PHILIPS TECHNICAL REVIEW

VOLUME 41
1983/84

PHILIPS

Philips Technical Review is published by Philips Research Laboratories, Eindhoven, The Netherlands, and is devoted to the investigations, processes and products of the laboratories and plants that form part of or cooperate with enterprises of the Philips group of companies. In the articles the associated technical problems are treated along with their physical or chemical background. The Review covers a wide range of subjects, each article being intended not only for the specialist in the subject but also for the non-specialist reader with a general technical or scientific training.

The Review appears in an English and a Dutch edition, both identical in contents. There are twelve numbers per volume, each of about 32 pages. An index is given for each volume and an index covering ten volumes appears every five volumes (the latest one was included in Volume 40, 1982).

Editors:	Dr J. W. Broer
	Dipl.-Phys. R. Dockhorn, Editor-in-chief
	Dr E. Fischmann
	Ir J. A. Klaassen
	Dr J. L. Sommerdijk
	Ir N. A. M. Verhoeckx
	Ir F. Zuurveen
Editorial assistants:	Ing. P. Post
	T. M. B. Schoenmakers
English edition:	D. A. E. Roberts, B.Sc., M. Inst. P., A.I.L.

© N.V. Philips' Gloeilampenfabrieken, Eindhoven, The Netherlands, 1985. Articles may be reproduced in whole or in part provided that the source 'Philips Technical Review' is mentioned in full; photographs and drawings for this purpose are available on request. The editors would appreciate a complimentary copy.

Subject index, Volume 41, 1983/84

	Page
Air bearings, measuring radial error of	334
Aspheric optical elements, fabrication, testing and application	296
Aspheric surfaces, design and optical advantages	289
Aspherics	285
Audio circuits, digital, computer simulations and listening tests	99
Bearings, air, measuring radial error of	334
Bearings, magnetic	348
Capacitors, ceramic boundary-layer	338
Capacitors, ceramic multilayer	89
Capacitors, switched, integrated filter for viewdata with	105
Ceramic boundary-layer capacitors	338
Ceramic multilayer capacitors	89
Communications network, experimental, with optical fibres	253
Compton-scatter radiation, X-ray imaging with	46
Computer, fault-tolerant, '(4,2) concept' for	1
Crystal structure, computer calculation of, from powder diagram	239
CVD, Chemical Vapour Deposition, for growth of silicon films	60
Digital audio circuits, computer simulation and listening tests	99
Digital optical recording with tellurium alloys	313
Digitization of speech	201
DIVAC	253
DOR, tellurium alloys for	313
Dye, organic, films of, for optical recording	325
Fault-tolerant computer, '(4,2) concept' for	1
Filter, integrated switched-capacitor, for viewdata	105
FM receivers on a single chip	169
Image intensifier, X-ray, with large input format	137
Integrating sphere, optical	347
Iridescence	149
Iron garnets, bismuth-substituted, optical switching with	33
Lens surfaces, inspecting the shape of	224
Lithography, X-ray, for VLSI	150
Low-friction films, wear-resistant, application by PVD	186
Magnetic bearings	348
Magnetic tape, porosimeter measurements of	260
MCR, lengthening of reverberation time by multiple-channel amplification	12
Mercury porosimeter measurements of magnetic tape	260
Metal/ceramic X-ray tube for medical diagnostics	126
Metal/ceramic X-ray tubes for non-destructive testing	24
Microbalance, piezoelectric	304
Multilayer capacitors, ceramic	89
NMR tomography	73
Nucleation and growth of silicon films by CVD	60
Optical fibre, stripping the protective coatings from	124
Optical-fibre communications network, experimental	253
Optical integrating sphere	347
Optical recording, digital, tellurium alloys for	313
Optical recording, organic-dye films for	325
Optical switching with bismuth-substituted iron garnets	33
Optomechanics	286
Organic-dye films for optical recording	325
Piezoelectric microbalance	304
Porosimeter measurements of magnetic tape	260
Powder diagram, computer calculation of structure model from	239
Precision air bearings, measuring radial error of	334
Protective coatings, stripping of, from optical fibre	124
Proton spin resonance tomography	73
PVD, Physical Vapour Deposition, for applying low-friction wear-resistant films	186
Radio receivers, integrated, for FM	169
Reflection filter, multilayer	149
Reflection filters, thin-film	225
Reverberation time, lengthening of, by multiple-channel amplification	12
Scandium for X-ray tube anode	267
Silicon films, nucleation and growth of, by CVD	60
Silicon Repeater, optical aspects of	268
Speech digitization	201
Switched-capacitor filter for viewdata	105
Tellurium alloys for digital optical recording	313
Tomography with proton NMR	73
Viewdata filter with switched capacitors	105
VLSI, X-ray lithography for	150
Wafer stepper for lithography	268
Wear-resistant films, low-friction, application by PVD	186
X-ray diffractometer, high-resolution	183
X-ray image intensifier with large input format	137
X-ray imaging with Compton-scatter radiation	46
X-ray lithography for VLSI	150
X-ray tube anode, rotating	24
X-ray tube anode, scandium for	267
X-ray tube, metal/ceramic, for medical diagnostics	126
X-ray tubes, metal/ceramic, for non-destructive testing	24

Author index, Volume 41, 1983/84

Page

Bartels, W. J.
High-resolution X-ray diffractometer 183
Berkhout, P. J., see Eggermont, L. D. J.
Bloem, J. and W. A. P. Claassen
Nucleation and growth of silicon films by chemical vapour deposition 60
Braat, J. J. M.
Aspherics, II. Aspheric surfaces: design and optical advantages 289
Claassen, W. A. P., see Bloem, J.
Coppelmans, P. M. C., see Roermund, A. H. M. van
Dimigen, H. and H. Hübsch
Applying low-friction wear-resistant thin solid films by physical vapour deposition 186
Eggermont, L. D. J. and P. J. Berkhout
Digital audio circuits: computer simulations and listening tests 99
Eijk, B. van der and W. Kühl
An X-ray image intensifier with large input format . . . 137
Frank, G., see Köstlin, H.
Gijsbers, T. G., see Haisma, J.
Gravesteijn, D. J. and J. van der Veen
Organic-dye films for optical recording 325
Hagemann, H.-J., D. Hennings and R. Wernicke
Ceramic multilayer capacitors 89
Haisma, J. and T. G. Gijsbers
Aspherics, I. Optomechanics, an ultra-high-precision machining technique 285
Haisma, J., W. Mesman, J. M. Oomen and J. C. Wijn
Aspherics, III. Fabrication, testing and application of highly accurate aspheric optical elements 296
Hansen, P., B. Hill and W. Tolksdorf
Optical switching with bismuth-substituted iron garnets . 33
Harding, G., H. Strecker and R. Tischler
X-ray imaging with Compton-scatter radiation 46
Hartl, W., D. Peter and K. Reiber
Metal/ceramic X-ray tubes for non-destructive testing . . 24
Hartl, W., D. Peter and K. Reiber
A metal/ceramic diagnostic X-ray tube 126
Heijden, J. van der
DIVAC — an experimental optical-fibre communications network 253
Hennings, D., see Hagemann, H.-J.
Hill, B., see Hansen, P.
Holster, P. L., J. A. H. M. Jacobs and B. Sastra
Measuring the radial error of precision air bearings . . 334
Hübsch, H., see Dimigen, H.
Huisman, H. F. and C. J. F. M. Rasenberg
Porosimeter measurements on magnetic tape 260
Jacobs, B. A. J., see Vriens, L.

Page

Jacobs, J. A. H. M., see Holster, P. L.
Kamerbeek, E. M. H.
Magnetic bearings 348
Kasperkovitz, W. G.
FM receivers for mono and stereo on a single chip . . . 169
Koning, S. H. de
The MCR system — multiple-channel amplification of reverberation 12
Köstlin, H. and G. Frank
Thin-film reflection filters 225
Krol, Th.
The '(4,2) concept' fault-tolerant computer 1
Kühl, W., see Eijk, B. van der
Locher, P. R.
Proton NMR tomography 73
Lüthje, H.
X-ray lithography for VLSI 150
Mauczok, R. and R. Wernicke
Ceramic boundary-layer capacitors 338
Mesman, W., see Haisma, J.
Mulder, B. J. and R. van der Schee
A piezoelectric microbalance 304
Oomen, J. M., see Haisma, J.
Peter, D., see Hartl, W.
Rasenberg, C. J. F. M., see Huisman, H. F.
Reiber, K., see Hartl, W.
Roermund, A. H. M. van and P. M. C. Coppelmans
An integrated switched-capacitor filter for viewdata . . 105
Sastra, B., see Holster, P. L.
Schee, R. van der, see Mulder, B. J.
Severijns, A. P. and P. J. W. Severin
Device for stripping protective coatings from glass fibre . 124
Severin, P. J. W., see Severijns, A. P.
Sluyter, R. J.
Digitization of speech 201
Strecker, H., see Harding, G.
Tischler, R., see Harding, G.
Tolksdorf, W., see Hansen, P.
Veen, J. van der, see Gravesteijn, D. J.
Verbakel, J. M. M. and J. H. N. van Vucht
From powder diagram to structure model on the computer 239
Vriens, L. and B. A. J. Jacobs
Digital optical recording with tellurium alloys 313
Vucht, J. H. N. van, see Verbakel, J. M. M.
Wernicke, R., see Hagemann, H.-J.
Wernicke, R., see Mauczok, R.
Wijn, J. C., see Haisma, J.
Wittekoek, S.
Optical aspects of the Silicon Repeater 268

PHILIPS TECHNICAL REVIEW

VOLUME 41, 1983/84, No. 1

The '(4,2) concept' fault-tolerant computer

Th. Krol

In many different fields the computer has gradually become an established and familiar tool. The more we come to rely upon it, however, the more one particular aspect gains in importance: reliability. A computer failure can soon become very expensive and cause a great deal of inconvenience, or may have even more disastrous consequences. A typical, fairly recent application of computers in which great reliability is required is in telephone exchanges. On average, in a period of 40 years, a computer-controlled exchange should not break down more than once and should not be completely out of action for more than two hours. This requirement cannot be met without making special provisions in both the hardware and the software. At Philips Research Laboratories a new method known as the '(4,2) concept' has recently been developed for building reliable ('fault-tolerant') computer hardware. The Philips Telecommunications Division is now studying the suitability of this concept for application in computer-controlled exchanges.

Introduction

Without computers there would be no space vehicles, certain chemical production processes could not be so accurately controlled and data processing in an airline reservation system would not take place so smoothly. These are just a few current examples of applications where the computer has proved its worth and which would be almost inconceivable without it. But in spite of the impressive performance of computers, seeming at times to outstrip the human brain itself, the computer is and remains a machine, consisting of a large number of components each with its own probability of failure. When we use a computer, therefore, we do well to look in advance at what can go wrong if the computer should fail, and to take any necessary precautions. In some cases the consequences of failure are so serious (human lives might be at stake), that failure must be avoided at all costs. Every effort is then made to design the computer in such a way that an internal fault does not perceptibly upset the operation of the system. In such cases a computer or computer system is said to be 'fault-tolerant'.

Ir Th. Krol is with Philips Research Laboratories, Eindhoven.

An illustrative example is to be found in the flight control of the American space shuttle. Five computers are available on the shuttle, one of them acting as a standby. The other four monitor each other continuously, bit by bit. In addition the synchronicity of the computers is checked 500 times a second. The moment one of the four indicates any deviation, it is automatically switched off. The other three carry on as usual. If another fault is detected later, a warning is signalled to the crew, who must then decide whether to switch over to the standby. All this takes place without interrupting the flight control.

A solution as rigorous as this will generally be too expensive. The introduction of the additional hardware also calls for expert knowledge: any increase in the hardware obviously increases the number of possible internal defects and hence the protection required. Consequently there are various possible ways of increasing the reliability of a computer system. The most direct method is to use components that possess the greatest possible intrinsic reliability. In general this is only feasible during the original design phase of

the system. In many professional applications, however, this does not give adequate results. The reliability can then only be increased by adding extra ('redundant') components; in normal circumstances they are not required for performing the actual function and serve merely to reduce the consequences of faults. The concept of redundancy is a familiar one in daily life: cars have spare wheels to minimize the delay due to punctures. From this example and from the previous one of the space shuttle we may also note, incidentally, that the concept of reliability, as used in this article, has a much wider significance than fault tolerance alone. A spare wheel cannot keep the car in operation if a tyre develops a puncture; all it can do is reduce the unwanted delay. In a truly fault-tolerant system a component can be repaired or replaced without any interruption in the normal operation of the system.

Strictly speaking, the *reliability* $R(t)$ of the system is defined as the probability that the system will continue to operate correctly after a time t, provided that the system was in perfect condition at $t = 0$. In the wider sense of the word as used in this article, reliability also comprises the aspects of fault tolerance and availability. A system has *fault tolerance* if it continues to operate correctly as long as the faults occurring within the system are of a predefined nature and extent. *Availability* is defined as the proportion of a given period in which a system functions correctly.

In modern telephone exchanges all the important functions, such as connecting subscribers, generating various signals (dialling tones, ringing or waiting tones, busy tones) and metering are controlled by a computer. The reliability of the computer largely determines the quality of the entire telephone service. Existing methods of maximizing this reliability are based on duplication or triplication of all the computer hardware.

In our studies of advanced telephone exchanges we have recently developed a new method that we call the '(4,2) concept'. A computer system built on this scheme is proof against practically all faults that might introduce confusion in an 'ordinary' computer. The occurrence of a fault for whatever reason (e.g. because of a defective transistor on a chip or because of a transient signal distortion due to noise) is signalled but does not affect the correct operation of the system. In the (4,2) concept the central processor part is quadrupled with respect to the non-fault-tolerant computer, but the memory capacity is only doubled. This scheme is particularly suitable for applications in which a relatively large memory capacity is required and the availability must be high. In this respect it compares favourably with methods such as triple modular redundancy.

In this article we shall first consider the existing methods of duplication (dual hot standby) and triplication (triple modular redundancy) of computer hardware. Next, the new (4,2) concept will be introduced, with a discussion of the principles, the special encoding rule adopted and the circuits for encoding and decoding. In passing we shall also deal with associated subjects such as data input and output, clocks and synchronization. Finally we shall show how the (4,2) concept may be regarded as a particular case of the general (n,k) concept.

Fault-tolerant computers

The basic architecture of a computer is shown in *fig. 1a*. It consists of a central processor, a memory, an input unit and an output unit. Between the various units there are connections for the transfer of data words (continuous lines) and for control (dashed lines). For our present purposes we shall confine ourselves to the combination of memory and central processor; fig. 1*b*. This combination occupies a place of central importance in the total operation of the computer. It also constitutes a distinct section that can easily be extended later by input/output units. For convenience we shall provisionally assume that all data words consist of 8 bits.

A notion that plays a leading part in fault-tolerant systems is the 'fault-isolation area'. Inside a fault-isolation area of a system faults may be interdependent, but its operation is unaffected by faults in other fault-isolation areas. The division into fault-isolation areas implies certain restrictions for the interaction (e.g. data exchange) between these areas. A complete fault-isolation area is always said to be either faulty or not faulty. It does not matter whether there is one single cause or a combination of causes.

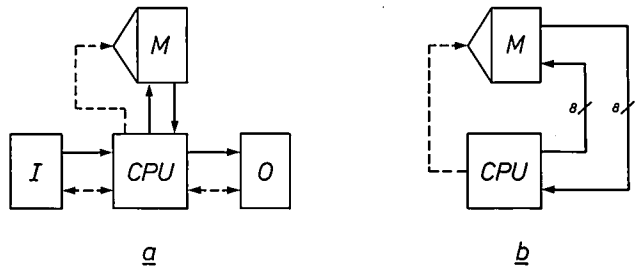

Fig. 1. *a*) Basic architecture of a computer with no special provisions for increasing the reliability. *I* input device, *CPU* central processor (or central processing unit), *M* memory, *O* output device. The continuous lines are the interconnections carrying the actual information (the data); the dashed lines carry the control signals. *b*) Simplified model used here as the basis for the treatment of a fault-tolerant computer. The data consists of groups (words) of 8 bits which are transferred in parallel. This is indicated by a small oblique stroke and the number 8.

Dual hot standby

In telephone exchanges the reliability of the extremely important control computer is often increased by duplication, referred to as 'dual hot standby'; see *fig. 2*. Two identical computers then execute the same program simultaneously and each forms a fault-isolation area. At a suitable point, for example in the bus carrying the data flow from the memory to the central processor, the signals in the two computers are continuously compared. This makes it practically 100% certain that any faults will be detected, provided we may assume that the probability of both machines incurring the same fault simultaneously is negligible. A disadvantage of this method is that, at the moment when a fault is detected, it is not clear which of the two machines is responsible. This will have to be determined in some other way. In one possible procedure, as soon as a fault is detected, it is reported to both central processors, which immediately stop the user program to check their own operation. Two evident disadvantages of this method are:

- the user program must be designed in such a way that it can be interrupted at any moment;
- a transient fault cannot be detected in this way, although it may have caused a permanent change in a memory.

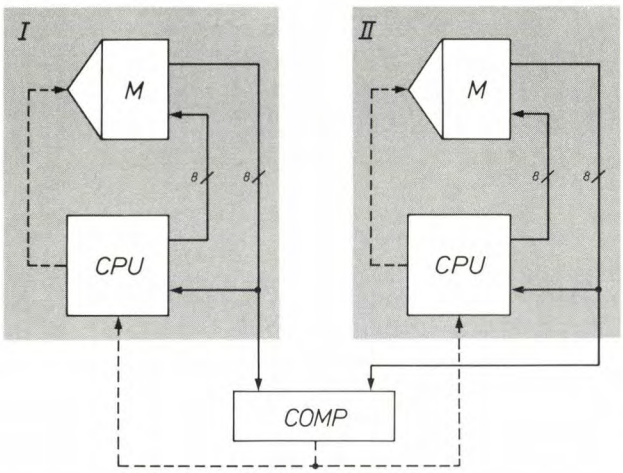

Fig. 2. Computer system with increased reliability, based on duplication (dual hot standby). Two identical computers execute the same program simultaneously. The two data flows from the memories *M* to the central processors *CPU* are continuously compared in the circuit *COMP*. Any discrepancy between them is signalled to the *CPU*s, which use a special diagnostic program to try and locate the fault. In this configuration faults are *detected* with practically 100% certainty if the probability of the same fault occurring in both machines simultaneously is negligibly small. This does not imply, however, that faults can be *located* with certainty. *I* and *II* represent fault-isolation areas, which we call 'slices'.

There is often an easy way of alleviating the difficulties of diagnosis. All data words can be given a parity bit, for example. Now if different signals appear in the two computers it is often possible to tell which computer has failed from a parity check of the data words.

Triple modular redundancy

A method that works better than dual hot standby is triplication, or 'triple modular redundancy'; see *fig. 3*. Here three identical computers are used in parallel as three fault-isolation areas. Each computer has a decision circuit that compares its own data with the data from the two other computers. A majority decision determines which data is correct. If the decision is not unanimous, this is recorded in a special error register as an indication that a fault has occurred. The contents of these registers are checked regularly by the central processors, which determine whether a fault has occurred and if so where. In this way we have obtained a real fault-tolerant computer which continues to operate correctly, provided any faults are contained within a single fault-isolation area. Disadvantages of this scheme are that it requires more than three times the hardware and many interconnections between the computers.

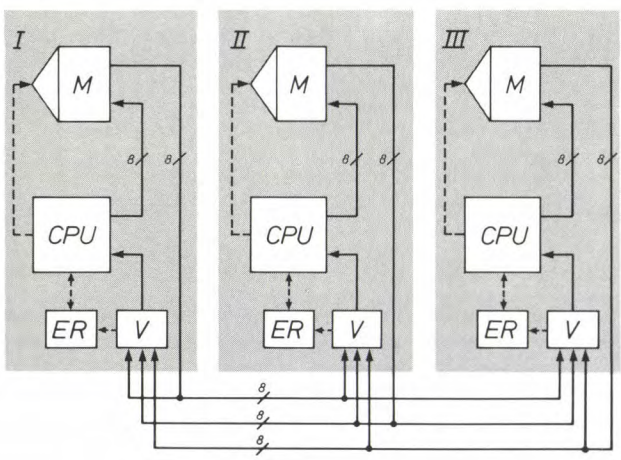

Fig. 3. Fault-tolerant computer system based on triplication (triple modular redundancy). Three identical computers now perform the same program simultaneously. The three data flows from the memories *M* to the central processors *CPU* are compared with each other in the decision circuits (voters) *V*. These circuits take a majority decision (vote) on the correct signal based on the three input signals, and also report any discrepancy detected in the input signals, thus indicating a fault. This information is stored in the error registers *ER*, whose contents are regularly checked by the central processors. *I*, *II* and *III* are fault-isolation areas (or slices).

The (4,2) concept

Principles

In the methods we have so far considered the increased reliability is achieved by duplicating or triplicating *all* computer activities in identical hardware. For the operations carried out in the central processor, which are many and varied, this is in fact the most

suitable method. The situation is entirely different, however, for operations that merely comprise the simple storage or transfer of information. Here the information is not altered by the operation, and any change that does occur is the result of a fault. We can establish the occurrence of such changes by making use of the extensive knowledge of error-detecting and error-correcting codes [1][2] now available, and for certain applications this will give a much more efficient solution. This is the idea behind the (4,2) concept. With a computer architecture based on this concept, fault tolerance is achieved by:

- quadrupling the central processor;
- protecting the memory functions by applying an error-correcting code, with only a duplication of the total memory hardware required. (Later we shall also see that data transfer to and from the input/output devices can be protected in a similar way.)

The basic architecture of such a computer is shown in *fig. 4*. There are four fault-isolation areas, which will be called 'slices' from now on, each containing an identical central processor (*CPU*) and an identical memory (*M*). Provided no faults occur, each *CPU* delivers the same 8-bit data word. From this a *different* 4-bit word is derived in each slice by the four different encoding circuits (*COD1* to *COD4*). Together these four circuits incorporate a carefully selected encoding rule, which determines the particular features of the (4,2) concept. This will be discussed in more detail later. The encoded information is stored in the memories, each memory being offered, in general, a different 4-bit word and no single memory receiving sufficient information to enable it to recover the original 8-bit data word. When the *CPU*s call information from the memories, identical decoders (*DEC*) in each of the four slices derive an 8-bit data word from the combined information delivered by all four memories. Provided any faults, whatever their nature, are confined to one slice, that slice will be positively identified in the decoding. The normal operation of the computer will not be affected, however. The occurrence of a fault, just as in the triple modular redundancy scheme, is recorded in an error register *ER*.

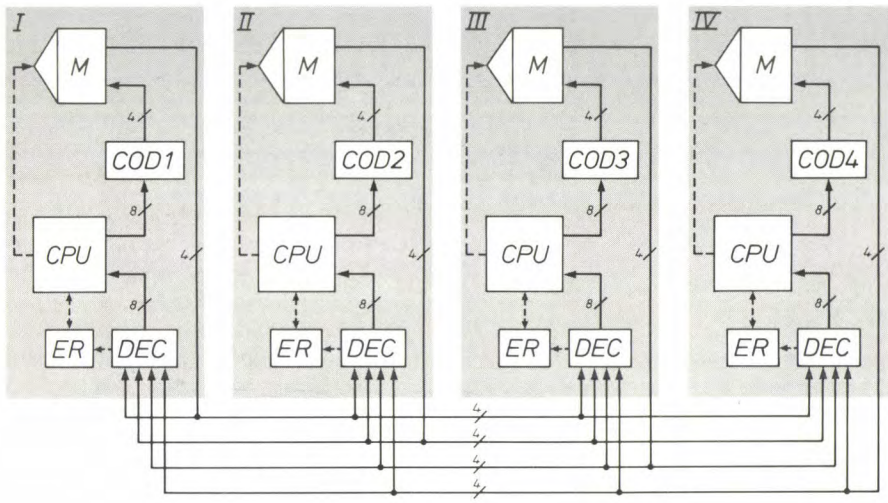

Fig. 4. Fault-tolerant computer based on the (4,2) concept. The complete system comprises four slices *I*, *II*, *III* and *IV*. Each of these slices consists of a central processor *CPU*, a memory *M*, a decoder *DEC* and an error register *ER*, which are identical in each slice. Each slice also contains an encoder (*COD1* to *COD4*); the encoders taken together incorporate one particular encoding rule, but are all different from one another. The contents of the four memories at any instant are therefore also different. The input signal to each encoder consists of eight bits (always the same for each encoder if there are no faults), while the output signal consists of four bits and is different for each encoder. Because of this reduction the (4,2) concept only requires duplication of the memory capacity compared with the original, non-fault-tolerant computer.

To achieve fault tolerance it is not necessary to check the control signals as well (e.g. the address or read/write instructions to the memories) in each slice. Errors in the control signals will show up sooner or later in the data words, which are checked.

The error-correcting code used for the (4,2) concept is rather ingenious [3], as the following illustration shows. If faults occur in one of the slices, that slice is then negated by the other slices (it is said to be 'erased'). In these circumstances the other three slices are still able, however, to correct a number of less serious but fairly frequent errors and hence continue to operate correctly.

The encoding rule

In the example given in fig. 4 the 8-bit output data word from the central processors is converted into a 16-bit code word in the encoders; four of the bits in this code word are calculated in each slice and stored in a memory. In the decoders the four groups of four bits are again interpreted as one 16-bit code word, from which the 8-bit data word has to be recovered. In deciding on the encoding rule the starting point was that the decoders should give the correct result provided any errors are produced in a single slice only. This means that we have to regard the groups of four bits that come from each slice as an entity or 'symbol'. We can thus choose a code in which the code words consist of four symbols and which can correct one incorrect symbol per code word (no matter how many bits of that symbol are incorrect). Since in this approach one symbol consists of four bits, we must consider the 8-bit data word from which we started as two symbols. The encoding thus converts *two* symbols into *four* symbols. This is referred to as a (4,2) code, and it is this terminology that led to the name '(4,2) concept'.

In general an error-correcting code in which k information symbols are converted into one code word of n symbols by the addition of n-k parity symbols is referred to as an (n,k) code. An important concept in such codes is the 'distance' d between two code words chosen at random. The 'distance' is the number of corresponding positions that have different symbols in the two code words. The minimum distance d_m is the lowest value of d that can occur in a particular code. From the theory of error-correcting codes [4][5] it is known that relations exist between d_m and the correcting properties of a code on the one hand and between d_m and the required number of parity symbols n-k on the other. If we wish to correct t random symbol errors, then we must have:

$$d_m \geqslant 2t + 1.$$

If, however, we wish to be able to correct t random symbol errors, while at the same time there are u other known symbols that are incorrect (erasures), then we must have:

$$d_m \geqslant 2t + u + 1.$$

Furthermore, we have as a general rule (the 'Singleton bound'):

$$d_m \leqslant n - k + 1.$$

If in this expression the equals sign is applicable for a particular code, we then have an *optimum code* or an *MDS (Maximum Distance Separable) code*, because we have the minimum number of parity symbols for a given d_m. The number of symbols added to the original information symbols during encoding is then as small as possible.

The class of MDS codes includes the established Reed-Solomon codes (RS codes) and a large number of codes derived from them, such as Extended RS codes and Shortened RS codes.

If we wish to design a fault-tolerant computer with n fault-isolation areas (slices), in which any single slice may fail, we can start from an (n,k) code with $t = 1$, $d_m \geqslant 3$ and $(n\text{-}k) \geqslant 2$. The optimum case is obtained with an $(n,n\text{-}2)$ code of the MDS type. The (4,2) code used in the (4,2) concept also belongs to this class, with $n = 4$ and $d_m = 3$.

Let the number of bits forming a symbol be s. From the theory of error-correcting codes [5] it is known that an MDS code does not exist for every combination of s and n. Although no general proof has yet been given, there are strong indications, based on a large number of known cases, that an MDS code of practical value requires the condition

$$s \geqslant \log_2(n - 1).$$

For the code used in the (4,2) concept we have $n = 4$, so that $s \geqslant 1.6$. With the actual value $s = 4$ we are well above the minimum. An older version of the (4,2) concept used $s = 2$. In that case we had a (4,2) code in which two 2-bit symbols were encoded into four 2-bit symbols. In each encoding or decoding operation *four* data bits were thus simultaneously encoded or decoded. However, since we started with data words of *eight* bits it was necessary to perform *two* encoding or decoding operations in parallel for each data word. Each slice therefore contained *two* encoders and *two* decoders. The advantage of this was that two decoders for a (4,2) code with $s = 2$ required much less hardware than one decoder for a (4,2) code with $s = 4$. A disadvantage of the solution with $s = 2$, however, was that the error-correcting properties were not so good. Our eventual choice was therefore $s = 4$.

Galois fields

In the literature on coding special methods of calculation for code analysis are described that are based on 'Galois fields'. A Galois field consists of a finite number of different elements, whereas conventional algebra embraces an infinite number of different elements (= numbers). All arithmetical operations, such as addition, subtraction, multiplication and division, that are carried out in a Galois field are defined in

[1] R. C. French and P. J. Mabey, Error control in mobile-radio data communication, Philips Tech. Rev. 39, 172-182, 1980.
[2] H. Hoeve, J. Timmermans and L. B. Vries, Error correction and concealment in the Compact Disc system, Philips Tech. Rev. 40, 166-172, 1982.
[3] An essential contribution to this work was made by B. J. Vonk, Philips' Telecommunicatie Industrie, Hilversum.
[4] S. Lin, An introduction to error-correcting codes, Prentice-Hall, Englewood Cliffs 1970.
[5] F. J. MacWilliams and N. J. A. Sloane, The theory of error-correcting codes, North-Holland, Amsterdam 1977.

such a way that they always yield an element from that same field. In calculations on codes in which the code words are built up from symbols of s bits the Galois field with 2^s elements is used, represented by GF(2^s). Each of the 2^s elements corresponds to a particular symbol, i.e. to a particular combination of s bits. Each element (with the exception of the 'zero element' $\emptyset$) can also be represented as an integral power i of α (i.e. as α^i) with $i = 0, 1, 2, \ldots, 2^s - 2$. The quantity α is an element from GF(2^s) with the special property that the integral powers referred to here correspond exactly to all the possible elements from GF(2^s) that differ from the zero element; α is called a *primitive element*. *Table I* lists the elements of the field GF(2^4), which is of most interest to us, in both notations. The notation using the primitive element is more suitable for theoretical treatments, and the representation in the form of 4-bit words is particularly suitable as a starting point in the design of encoding and decoding hardware, which is usually based on binary logic circuits.

The relation between the two notations in Table I can be uniquely described by a polynomial $P(\alpha)$. The same polynomial also indicates the interrelations between the different powers of the primitive element α. For the table given here the associated polynomial is $P(\alpha) = \alpha^4 + \alpha + 1$. Formally, Table I gives all elements of GF(2^4), generated with $\alpha^4 + \alpha + 1 = 0$. A more detailed description can be found in the literature on Galois fields [4][5].

The most commonly used error-correcting codes are known as *linear* codes. A code of this type is used in the (4,2) concept. Its encoding rule can be represented by means of a matrix. For the notation of this *generator matrix*, as it is called, the primitive element α can be used. For an (n,k) code we then obtain an $n \times k$ matrix G, which precisely defines how every k data symbols are encoded into the n symbols of the corresponding code word. To find a code word it is only necessary to perform a matrix multiplication of G by a column vector consisting of the k data symbols written as powers of α. The n symbols of the code word are then found similarly as powers of α. For our (4,2) code with 4-bit symbols

$$G = \begin{pmatrix} \alpha^0 & \emptyset \\ \emptyset & \alpha^0 \\ \alpha^7 & \alpha^{11} \\ \alpha^{11} & \alpha^7 \end{pmatrix}$$

where α is a primitive element of GF(2^4) and $\emptyset$ is the zero element.

It is also possible, however, to give for the same code a generator matrix G' that contains bits only ('ones' and 'zeros'). This matrix G' indicates how the encoder transforms each group of $k \times s$ data bits into the $n \times s$ bits of the corresponding code word. In our case G' would be a 16×8 matrix of ones and zeros.

Table I. The 16 different elements of the Galois field GF(2^4) shown as a combination of 4 bits and (except for the 'zero element' $\emptyset$) as an integral power of the primitive element α. The exact connection between the two notations can be uniquely described by a polynomial $P(\alpha)$ (here the polynomial is $P(\alpha) = \alpha^4 + \alpha + 1$). The quantity α^0 is often indicated by 1 (the 'unit element').

0000	$\emptyset$
1000	$\alpha^0 = 1$
0100	α
0010	α^2
0001	α^3
1100	α^4
0110	α^5
0011	α^6
1101	α^7
1010	α^8
0101	α^9
1110	α^{10}
0111	α^{11}
1111	α^{12}
1011	α^{13}
1001	α^{14}

The matrix G can be directly transformed into G'. In this case, however, each element of G is replaced not by a single 4-bit combination as in Table I, but by a 4×4 matrix. The conversion is made with the aid of the 'companion matrix' of the polynomial of the Galois field under consideration.

The encoders

In the (4,2) concept only one of the four symbols of each code word is calculated in each of the four fault-isolation areas (slices). Each of the four encoders in fig. 4 can therefore be described by a 2×1 matrix G_1 to G_4, corresponding always to one row of G:

$$G_1 = (\alpha^0 \ \emptyset) \qquad G_2 = (\emptyset \ \alpha^0)$$
$$G_3 = (\alpha^7 \ \alpha^{11}) \qquad G_4 = (\alpha^{11} \ \alpha^7).$$

For the same reason we may divide G', which contains only zeros and ones; into four submatrices G_1' to G_4', each describing the encoder of one slice:

$$G_1' = \begin{pmatrix} 10000000 \\ 01000000 \\ 00100000 \\ 00010000 \end{pmatrix} \qquad G_2' = \begin{pmatrix} 00001000 \\ 00000100 \\ 00000010 \\ 00000001 \end{pmatrix}$$

$$G_3' = \begin{pmatrix} 11010111 \\ 10111100 \\ 01011110 \\ 10101111 \end{pmatrix} \qquad G_4' = \begin{pmatrix} 01111101 \\ 11001011 \\ 11100101 \\ 11111010 \end{pmatrix}.$$

Each of these matrices is really a compact way of writing four equations that give the relations between the

eight bits $d_1, d_2, \ldots d_8$ entering each encoder, and the four bits $c_{i1}, c_{i2}, c_{i3}, c_{i4}$ of the output (i is the number of the slice). The matrix G_1' means:

$$c_{11} = d_1 \qquad c_{12} = d_2 \qquad c_{13} = d_3 \qquad c_{14} = d_4$$

and the matrix G_2' means:

$$c_{21} = d_5 \qquad c_{22} = d_6 \qquad c_{23} = d_7 \qquad c_{24} = d_8.$$

Also, from the matrix G_3':

$$\begin{aligned} c_{31} &= d_1 \oplus d_2 \oplus d_4 \oplus d_6 \oplus d_7 \oplus d_8 \\ c_{32} &= d_1 \oplus d_3 \oplus d_4 \oplus d_5 \oplus d_6 \\ c_{33} &= d_2 \oplus d_4 \oplus d_5 \oplus d_6 \oplus d_7 \\ c_{34} &= d_1 \oplus d_3 \oplus d_5 \oplus d_6 \oplus d_7 \oplus d_8 \end{aligned}$$

and from G_4':

$$\begin{aligned} c_{41} &= d_2 \oplus d_3 \oplus d_4 \oplus d_5 \oplus d_6 \oplus d_8 \\ c_{42} &= d_1 \oplus d_2 \oplus d_5 \oplus d_7 \oplus d_8 \\ c_{43} &= d_1 \oplus d_2 \oplus d_3 \oplus d_6 \oplus d_8 \\ c_{44} &= d_1 \oplus d_2 \oplus d_3 \oplus d_4 \oplus d_5 \oplus d_7. \end{aligned}$$

Here the sign $\oplus$ indicates a modulo-2 addition, that is to say $0 \oplus 0 = 0$, $1 \oplus 0 = 1$, $0 \oplus 1 = 1$ and $1 \oplus 1 = 0$. We now see immediately how to design the encoders (*fig. 5*). *COD1* and *COD2* are simply four straight-through connections. For *COD3* and *COD4* we need a number of modulo-2 adders ('EXCLUSIVE-OR' gates). These are just simple circuits.

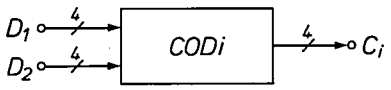

Fig. 5. Block diagram of the encoders *COD1* to *COD4* for the (4,2) concept. D_1 and D_2 are the data symbols, consisting of bits d_1 to d_4 and d_5 to d_8. C_i is the i^{th} symbol of the code word consisting of bits c_{i1} to c_{i4}. The circuits *COD1* and *COD2* contain only four straight-through connections. In *COD3* and *COD4* the bits of both data symbols are used to calculate the bits of C_3 and C_4 by means of modulo-2 adders.

The decoders

In decoding linear (n,k) codes we use the 'parity-check matrix' H of the code. This is an $(n\text{-}k) \times n$ matrix that is closely related to the generator matrix. For our code the parity-check matrix H is given by

$$H = \begin{pmatrix} \alpha^7 & \alpha^{11} & \alpha^0 & \emptyset \\ \alpha^{11} & \alpha^7 & \emptyset & \alpha^0 \end{pmatrix}.$$

With the parity-check matrix we can compute a *syndrome* of $n\text{-}k$ symbols from any group of n symbols. If these n symbols form one code word exactly, then the syndrome consists entirely of zero symbols. If this condition is not satisfied, the syndrome will contain other symbols. This occurs if for one reason or another errors have occurred in the symbols of the code word, or if the encoders in the different slices have not been supplied with exactly the same data symbols. The main task of the decoders is to determine the most probable error and to ensure that the correct symbols will nevertheless appear at their outputs. *Fig. 6* shows a block diagram of the decoder for our (4,2) concept. The four 4-bit symbols C_1 to C_4, each originating from one slice, are fed to the syndrome circuit *SYN*, in which the syndrome consisting of the symbols S_1 and S_2 is calculated. Next, the error location and evaluation circuit *ELE* determines from S_1 and S_2 whether it must be assumed that errors have occurred in C_1 to C_4. This is done in two stages: the incorrect symbol is first *located* (error location) and then the nature of the error is *evaluated* (error evaluation). From the results of these operations the actual correction circuit *COR* then derives the correct data symbols D_1 and D_2. As soon as the circuit *ELE* detects an error, the important information about the

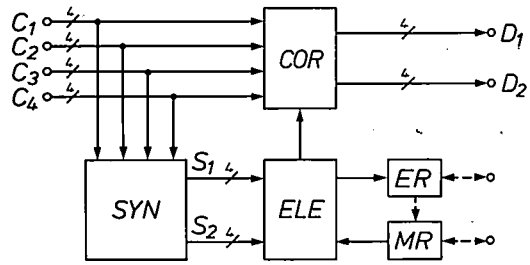

Fig. 6. Block diagram of the decoder for the (4,2) concept. The original data symbols D_1 and D_2 are recovered as accurately as possible from the four symbols C_1 to C_4 of the code word. First the syndrome, consisting of two symbols, S_1 and S_2, is calculated in the syndrome circuit *SYN*. The error location and evaluation circuit, block *ELE*, uses this information to determine whether a particular symbol is incorrect (error location) and if so, what the error is (error evaluation). The actual correction of the error then takes place in the block *COR*. Data on faults that have occurred are stored in the error register *ER*. The contents of this register are regularly called by the central processors. The block *ELE* can operate in different modes, depending on the contents of the mode register *MR*. (Note that *ER* is shown here as a part of the decoder, although in fig. 4 it was shown separately for clarity.)

fault that caused the error (for example the slice in which it has occurred) is stored in the error register *ER*, where it remains available as the starting point for further action (e.g. repair of the failed component or subsystem). The operation of the circuit *ELE* depends on the mode register *MR*, which indicates the mode of the decoding process. The mode determination depends partly upon the error register *ER*, but external intervention is also possible. This will be examined more closely in the next section.

Modes in decoding

There are three distinct modes in decoding:

- the random mode (the normal mode)
- the erasure mode
- the single mode.

There are four types of erasure mode and six types of single mode.

In the *random mode* all the fault-isolation areas (slices) are equivalent. As we have seen, in our code we have a minimum distance $d_m = 3$, so that the decoder can completely correct an arbitrary error in an arbitrary symbol ($t = 1$). It can be shown mathematically [6], however, that our code can deal with even more types of errors: if an error affects only one bit of a particular symbol, it is permissible for a single arbitrary bit to be incorrect in one of the three other symbols at the same time (*fig. 7a*). This is very important, because single-bit errors do frequently occur in computer memories (they may even account for 90% of the total) and are often a result of transient faults.

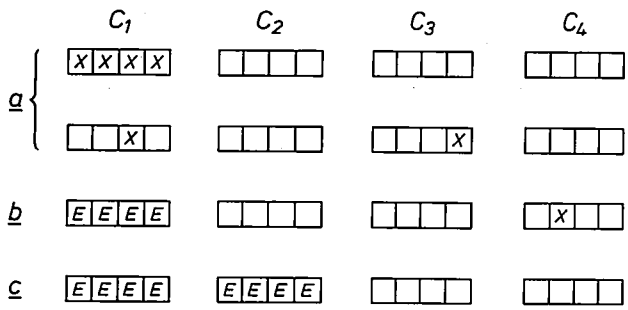

Fig. 7. Types of error that do not affect the operation of a computer based on the (4,2) concept. C_1, C_2, C_3 and C_4 represent the 4-bit symbols supplied to the decoder in each slice. An incorrect bit is indicated by an X and an erased bit by an E. In the normal (random) mode a single symbol may contain any number of incorrect bits or two symbols may each contain one incorrect bit (*a*). In the erasure mode a single symbol is completely erased and one incorrect bit may occur in the other symbols (*b*). In the single mode two symbols are erased. There must then be no errors in the remaining symbols (*c*).

As soon as the decoder concludes, from the computed syndrome symbols, that a particular symbol of the code word contains an error that affects more than one bit, the corresponding slice is erased and the decoder automatically switches into the *erasure mode*. Since this mode may relate to any of the four slices, there are four possible versions. From the theoretical relation mentioned earlier, relating the minimum distance d_m, the number of erasures u and the number of correctable symbols t, we know that $t = 0$ in our code with $d_m = 3$ and $u = 1$. In the erasure mode, therefore, our code is no longer able to correct an *arbitrary* symbol error. However, it can be shown [6] that in the erasure mode our special code does offer the possibility of correcting an arbitrary single-bit error in one of the three non-erased symbols (fig. 7*b*). This is extremely important because of the typical fault behaviour of memories as mentioned above. On the other hand, if more serious faults occur in the erasure mode, the decoder is generally no longer able to correct the resulting errors, although it may well be able to detect their occurrence and to report them to the error register (fig. 6).

The *single mode* of the decoding process can only be set up externally. In single-mode operation two symbols are erased (fig. 7*c*). This means that two slices can be taken out of use, e.g. for repair or replacement. However, the two remaining slices then no longer have any error-detecting or error-correcting capacity, and any fault that occurs may lead to observable malfunctioning of the computer. Single-mode operation is based on a typical general property of (n,k) codes of the MDS type: with these codes, provided no errors occur, the k information symbols can be retrieved from any arbitrary combination of k symbols in the code word. In our (4,2) code we can therefore retrieve the two original information symbols from any arbitrary pair of code word symbols. Since there are six different pairs, this mode has six forms.

The property of MDS codes just mentioned may also be used as the basis for the design of a decoder that differs to some extent from fig. 6. In this scheme all six possible combinations of two symbols of a presented code word are used for simultaneously calculating the original data symbols from established rules as if there were no errors anywhere. This gives six results that will all be the same only if there have been no errors. In addition to this the parity-check matrix is applied to determine the syndrome. From this information and the knowledge of the mode in operation, the best choice is then made from the six decoded symbol combinations. This design is particularly attractive if the decoder is integrated on a chip. In such an integrated circuit the decoding can be performed in an exceptionally short time. For example, we have designed a decoder that can be made in CMOS technology and requires less than 170 nanoseconds for each decoding operation.

Input and output

So far we have concentrated our attention on the heart of the computer: the combination of central processor and memory. Inevitably every computer works with a larger or smaller number of input and output devices (fig. 1*a*). These have to be connected in some way to the fault-isolation areas (slices) that we have been considering in detail. One thing is paramount. A defect in the input/output devices must never endanger the proper operation of the vital fault-tolerant part of the system; in other words it must never affect more than one slice. There are many ways of setting up the desired connections. The method chosen depends on the nature of the hardware to be connected (this could be a simple input/output device or another complete computer based on the (4,2) concept) and on the desired degree of fault tolerance. We shall illustrate this

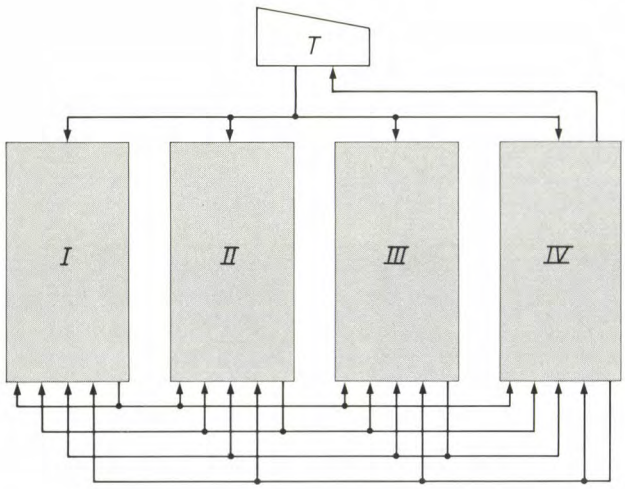

Fig. 8. Schematic representation of the way in which a single terminal T can be connected to a computer based on the (4,2) concept. The four slices are again indicated by *I*, *II*, *III* and *IV*. The terminal receives control and data signals from only one slice, but conversely sends all its output signals to all the slices.

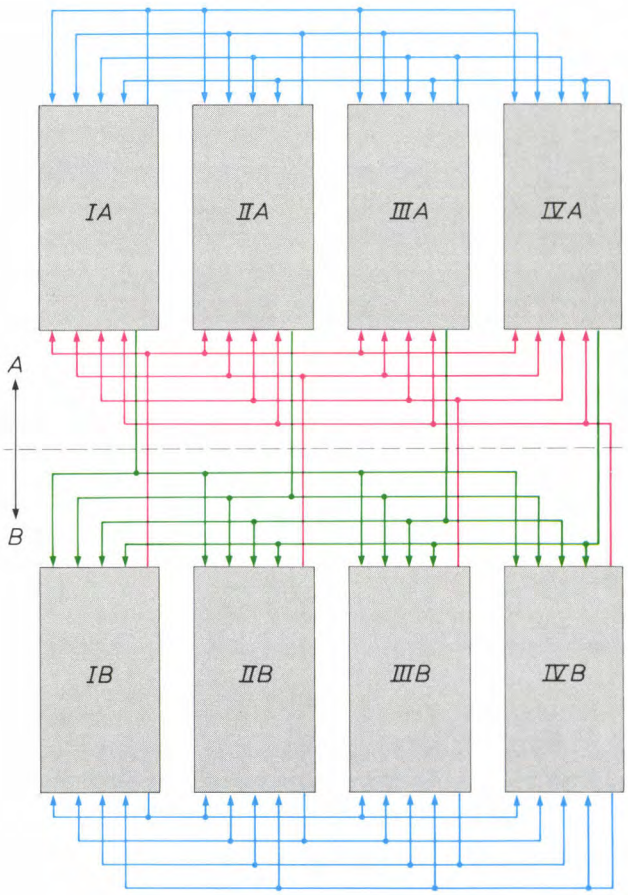

Fig. 9. Schematic representation of the method of interconnecting two computers, A and B, both based on the (4,2) concept. The method also protects the signal transfer between the two computers from the effects of certain faults. This can be done in various ways. The computers may, for example, exchange exactly the same information four times, or they may exchange signals encoded in the same code as the one on which the (4,2) concept is based. The interconnections (signal buses) for signal transfer inside the computers (blue) and between the two computers (green and red) are separate in this example.

by two examples. Each slice (fig. 4) is considered as a single entity requiring no detailed description. A very simple case is illustrated in *fig. 8*. This shows a terminal T in which no additional measures have been taken to obtain fault tolerance, connected to a computer based on the (4,2) concept.

The control and data signals for the terminal are available in each slice, but the terminal can only receive these signals from one slice (slice *IV*). Information from the terminal should be sent to each slice. The control required within the slices for these operations is carried out independently in each slice so as to prevent unwanted interactions. A consequence of the scheme in fig. 8 is that the terminal can only be used while there are no faults in slice *IV*.

A quite different example is given in *fig. 9*, which shows how two computers A and B, both based on the (4,2) concept, can be interconnected as a fault-tolerant system. Each slice can now send signals to all the other slices and receive signals from them. The information exchanged within either one of the computers is in general completely different from the information exchanged with the other computer. For this reason the transfer paths, called signal buses, are entirely separate. In this scheme signal transfer between the two computers is protected against certain errors resulting from failed slices, even though it is not yet established exactly how this is done. It may be, for example, that the computers exchange the same information with each other four times, with a majority decision being taken after reception. Another method is to exchange signals encoded in accordance with the (4,2) concept encoding rule, which are then decoded after reception. In this second case fewer symbols have to be transferred than in the first case, but the operations required are rather more complicated.

Clock and synchronization

Every digital computer carries out its sequence of operations to the regular beat of a fixed reference, called the clock. In a computer based on the (4,2) concept all four slices have to operate in full synchronism. The simplest way to achieve this is to supply them all with the same clock signal, but since fault tolerance is required this would not be advisable. Any defect in the common clock-signal source could then put the whole computer out of action. A multiple clock must therefore be provided (e.g. by giving each of the four slices its own clock) and these four clocks must be synchronized. The synchronization must also be fault-tolerant, of course, so that one defective clock can

[6] Th. Krol, The '(4,2) concept' fault-tolerant computer, Digest of Papers 12th Ann. Int. Symp. on Fault-tolerant computing (FTCS-10), Santa Monica 1982, pp. 49-54.

never upset the operation of the other clocks. Problems of this nature also occur when the entire fault-tolerant system has been out of action or if a slice has to be taken out of service temporarily. It is essential to ensure that all the slices will come back into clock synchronization. In general, however, this alone is not sufficient. Since most computer operations require more than one clock period, it is also necessary to ensure that all the slices start corresponding operations in the same clock period. This means that a special synchronization function is required, with extra hardware as well as extra software. In this respect the (4,2) concept does not differ essentially from other methods used to achieve fault tolerance.

Comparison of different methods

In conclusion, let us briefly consider the relative merits of the (4,2) concept and its two closest rivals, dual hot standby and triple modular redundancy. As we have seen, dual hot standby does not offer true fault tolerance, because the system only detects a fault at first: normal operation must be stopped for fault diagnosis. With triple modular redundancy, on the other hand, as with the (4,2) concept, one fault-isolation area can fail completely without disturbing the normal operation of the system. This alone indicates that the (4,2) concept provides at least the same improvement in reliability as triple modular redundancy. However, the (4,2) concept can also tolerate a large number of defects that cause single-bit errors. If 90% of all the faults are associated with the memory and cause single-bit errors — and this is by no means unlikely — then our (4,2) concept is ten times as reliable as triple modular redundancy (quite apart from the improvement in reliability resulting from the difference in memory capacity).

The main differences between the three methods mentioned above are listed in *Table II*. The (4,2) concept is especially suitable for applications in which a relatively large memory capacity is required and where availability is of the utmost importance. These circumstances are typical for computers used in telephone exchanges, and these computers might be the first to benefit from the advantages of the (4,2) concept [7][8].

The (n,k) concept

The (4,2) concept based on the (4,2) code, as described in the foregoing, is in fact only an example of the general (n,k) concept based on an (n,k) code. The familiar method of triplication of the hardware (fig. 3) could for example be regarded as an application of the (3,1) concept based on a (3,1) code. Since the coding corresponds simply to triplication of the data word, no separate encoders are necessary; the decision circuits V (voters) act as decoders.

If extremely high reliability is demanded of a computer, the (8,4) concept might be used. With an (8,4) code of the MDS type, the minimum distance is $d_m = 8 - 4 + 1 = 5$. By considering the properties mentioned earlier of codes with a particular d_m we can deduce the extent to which the resultant computer

Table II. Comparison of a non-redundant computer, with no special provisions for improving reliability (see the column 'Original') and the same computer after application of dual hot standby, triple modular redundancy or the (4,2) concept.

	Original	Dual hot standby	Triple modular redundancy	(4,2) concept
Memory hardware (*M*)	1×	2×	3×	2×
Number of central processors (*CPU*)	1×	2×	3×	4×
Number of interconnections between *M* and *CPU* (bus)	1×	2×	3×	2×
Complexity of encoder (number of logic gates)	—	—	—	low
Complexity of decoder (number of logic gates)	—	low	low	acceptable
Special software for locating faults	—	yes	no	no
Degree of fault tolerance	—	—	one faulty slice	one faulty slice + one single bit fault
Suitability for processing transient faults	—	poor	good	good

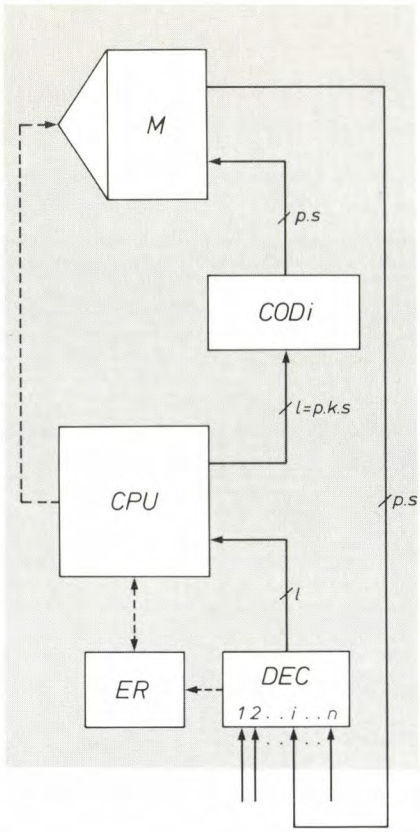

Fig. 10. General representation of the i^{th} slice based on the (n,k) concept for a data word length of l bits. An (n,k) code with symbols of s bits is used, in which l is divisible by the product $k \times s$, so that $l = p \times k \times s$.

is fault-tolerant. In the first place we see that the computer continues to operate correctly if errors are made in two arbitrary slices (i.e. if $t = 2$). If, however, the computer 'knows' that two slices are no longer to be trusted and therefore erases them ($u = 2$), any one of the other six slices can fail ($t = 1$) without affecting the proper operation of the system. The reliability of this computer based on the (8,4) concept is comparable with that of a five-fold system. An important advantage of the (8,4) scheme is that it only requires *twice* the memory capacity of the non-fault-tolerant computer. Furthermore, fewer interconnections between the slices are required. On the other hand, it requires eight times as much central-processor hardware, and some hardware is also required for encoding and decoding. The relative importance of the various advantages and disadvantages depends on the specific application.

The (4,2) concept for a computer with 8-bit data words (fig. 4) can easily be generalized to the (n,k) concept for a computer with a data word length of l bits. A computer designed on the basis of this generalized concept contains n slices (and hence n central processors) and a memory n/k times larger than the basic computer. In principle the design can be based on any existing (n,k) code in which the symbols have a length of s bits, provided l is divisible by the product $k \times s$. The quantity

$$p = \frac{l}{k \cdot s}$$

indicates how many code words are necessary to represent the l information bits of one data word. A computer of this type can thus be implemented by providing each slice with p encoders and p decoders of the original (n,k) code with s-bit symbols. It is also possible, however, to regard all the p encoders together or the p decoders together as a single encoding or decoding circuit for an (n,k) code with $(p \times s)$-bit symbols. This approach is illustrated in *fig. 10*, which shows a block diagram of one slice based on the general (n,k) concept for a computer with data words of l bits, starting from an (n,k) code with symbols of s bits. If the minimum distance of the code employed is known, the characteristics of the resulting fault-tolerant computer can be derived from the usual rules.

[7] F. J. Schramel, A. W. van 't Slot and S. H. Liem, The peripheral control domain, an all-digital intelligent terminal for subscribers and trunks in the PRX/D system, Proc. 10th Int. Switching Symp. (ISS '81 CIC), Montreal 1981, session 34A, paper 3 (9 pages).

[8] R. H. Bourgonjon and M. J. Hoek, The TCP16, a fault-tolerant control system for PRX/D, Proc. 10th Int. Switching Symp. (ISS '81 CIC), Montreal 1981, session 34A, paper 4 (6 pages).

Summary. In certain professional applications, such as in telephone exchanges, it is essential to make sure that a simple fault in the hardware will not put an entire computer system out of operation. The (4,2) concept is a new method of making such computers fault-tolerant. The hardware is divided into four fault-isolation areas (slices) and a special error-correcting (4,2) code is used. The encoding hardware is distributed among the four slices. During normal operation one arbitrary slice may fail completely or a less serious but more frequent type of fault may occur in two slices without upsetting the operation of the system. Components may be repaired or replaced without the need to shut down the computer system. The (4,2) concept requires four times as much central-processor hardware as the original non-fault-tolerant computer, but only twice the memory capacity. The new concept is especially suitable for applications that require a large memory capacity and high availability. It then compares well with methods such as triple modular redundancy. The (4,2) concept may be considered as a special case of the general (n,k) concept.

The MCR system — multiple-channel amplification of reverberation

S. H. de Koning

'... and no discussion was held as to the advantages and disadvantages of reverberation. The gentlemen present were asked to express their approval or disapproval of the room at each stage of the experiment, and the final decision seemed to be reached with perfectly free unanimity.'

The quotation [*] is from Wallace C. Sabine (1868-1919), the founder of modern auditorium acoustics. He was pointing out how closely different people agreed, just as they do today, on the desirable reverberation time for musical performances. The reverberation time can now be adapted to the musical needs of the moment.

Introduction

Reverberation time

The acoustics of concert halls has long been a subject of lively discussion. Everyone has an opinion on it — audiences, musicians, critics. The consensus view, as often with mass opinions, tends to come in black-and-white terms: an auditorium is either good or it is bad. A reputation for good acoustics is only slowly acquired. The few halls that are considered to be 'very good' are therefore invariably old; a well-known example is the large auditorium of the Amsterdam Concertgebouw (1888).

What makes the acoustics of a concert hall 'good'? Many attempts at answering this question have been expressed in vague terms; 'ambience' is a word often heard — there is a feeling of being 'caught up in the sound'. Wallace C. Sabine (1868-1919) identified the reverberation time as the most important parameter in auditorium acoustics; he used a stopwatch to measure the time it took for the reverberation of a pistol shot or a voiced organ pipe to decay to inaudibility. Although other factors turned out later to be of great importance — such as the direction and the intensity of the early reflections — the reverberation time is undoubtedly a principal characteristic of the acoustics of an auditorium.

Ir S. H. de Koning is with the Philips Electroacoustics Division, Breda.

[*] W. C. Sabine, Collected Papers on Acoustics, Harvard Univ. Press, Cambridge 1927, p. 77.

Adapting the acoustics of an auditorium to changing use

If the reverberation time of a concert hall is too long, the music will not be heard at its best. Successive tones will overlap and the music will lose in clarity. Measures can easily be taken to improve this situation, for there is nowadays a whole range of sound-absorbent materials available that can be applied to walls and ceiling, so reducing the reverberation time.

It may be precisely because the modern architect can so easily resort to acoustic absorption materials that many new auditoriums exhibit the opposite characteristic: a short reverberation time. This is not experienced as a disadvantage in every use that is made of the auditorium. Many auditoriums are built for a variety of functions. Sometimes the auditorium serves as a congress hall, at other times as a theatre, and occasionally as a concert hall. If intelligibility of speech is a primary requirement (as for meetings and plays), a short reverberation time, say 1 second, is an advantage. Music, however, sounds much better in an enclosure where the reverberation is longer, between say $1\frac{1}{2}$ seconds for chamber music and $2\frac{1}{2}$ seconds for a large symphony orchestra. Organ music requires an even longer reverberation time.

With electroacoustic techniques it is possible to adapt the acoustics of an auditorium to changing use. Speech reinforcement by electroacoustical amplification is now normal. But it is also possible to lengthen the reverberation time electroacoustically by increasing the energy of the reverberant sound field; this was first attempted some 20 or 30 years ago. There are two distinct systems here. One of them is used in the Royal Festival Hall in London; its ceiling contains 172 amplification channels — each consisting of a microphone, amplifier and loudspeaker — which register the diffuse sound field of the reverberation and reproduce it in an amplified form [1]. The idea is that each channel should reinforce one natural frequency of the auditorium; the microphones and the loudspeakers are tuned to this frequency by acoustic resonators. The resonant frequencies are about 2 to 5 Hz apart; the system covers the band from 58 Hz to 700 Hz. The reverberation time is only increased in this band, of course.

The other system, which is quite different, was developed some time ago by Philips [2]. In this system the sound near the source was picked up by microphones, delayed by magnetic recording on the circumference of a 'delay wheel' and then added by means of distributed loudspeakers to the diffuse sound in the auditorium. A system of this type, called 'ambiophony', was installed in many well-known theatres, including the Teatro alla Scala in Milan, where it is still in use.

Table I. Technical data for four MCR installations.

	ELA Studio, Eindhoven, 1977	POC Congress Centre, Eindhoven 1981	HansRosbaudStudio, Südwestfunk, Baden-Baden, 1981	Claude Debussy Theatre, Palais des Festivals et des Congrès, Cannes, 1983
Volume of auditorium (m^3)	1300	4000	6100	12000
Boundary surface area (m^2)	800	1900	2100	5500
Mean absorption coefficient	0.4	0.25	0.3	0.25
Reverberation time without MCR (s)	0.65	1.15	1.5	1.45
Reverberation time with MCR (s)	1.1	1.7	2.1	2.0
Number of channels	90	90	70	66
Increase in reverberant sound field (dB)	2.4	2.3	1.9	1.85
Bandwidth (Hz)	90-5000	70-6000	70-6000	140-6000
Maximum sound level (dB)	109	112	109	110

[1] P. H. Parkin and K. Morgan, "Assisted Resonance" in the Royal Festival Hall, London: 1965-1969, J. Acoust. Soc. Am. **48**, 1025-1035, 1970.

[2] R. Vermeulen, Stereo reverberation, Philips Tech. Rev. **17**, 258-266, 1956; D. Kleis, Modern acoustical engineering I, Philips Tech. Rev. **20**, 309-326, 1958/59; and II, **21**, 52-72, 1959/60.

MCR, a new system of artificial reverberation

Now Philips have developed another new system [3]. Although it bears some superficial resemblance to the one used at the Royal Festival Hall, it is based on a rather different approach. It consists similarly of a large number of independent amplification channels, with the microphones and loudspeakers in the ceiling and the walls of the auditorium, and therefore in the reverberant sound field. Each channel has the full audio bandwidth, however, and reinforces the total sound field as received by the microphone.

In the reverberant sound field as received by the microphone there are in fact certain frequencies that are dominant (see fig. 2). This is because every natural frequency of the auditorium has its corresponding standing-wave pattern, and the microphone is most strongly coupled to the field at the natural frequencies that have a pressure antinode at the location of the microphone. Something similar applies for the loudspeaker. The associated MCR channel, however, amplifies the entire spectrum and not simply its peaks. A system of this type has meanwhile been installed in several auditoriums (some examples are given in *Table I*); the name MCR stands for 'Multiple-Channel amplification of Reverberation'. The installation in Eindhoven will be described in some detail, and information will be given about similar installations at Baden-Baden and Cannes. First, however, we shall look at the principle of operation and also the limitations imposed by acoustic feedback.

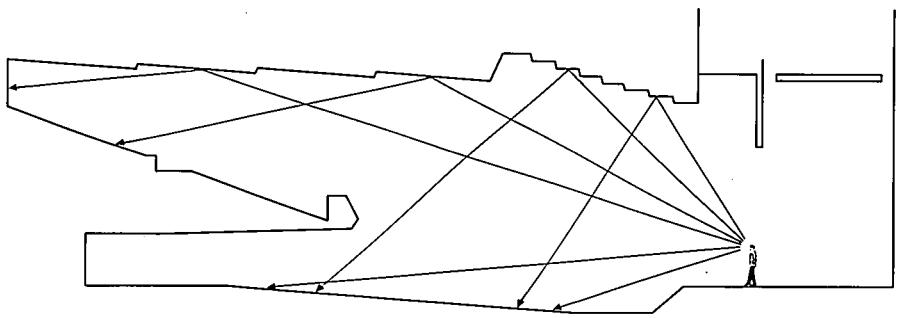

Fig. 1. Sound produced by a sound source on the stage propagates in all directions in the auditorium and is reflected by ceiling, walls and other boundary surfaces. The many reflections later merge to produce the reverberation.

Principles of the MCR system

Reverberation and energy density [4]

The sound waves emitted by a sound source situated in an enclosure (*fig. 1*) eventually reach a wall or some other boundary surface. On their way to that boundary surface they constitute the *direct sound*. Its intensity I (defined as the acoustic power in watts that passes through an area of 1 m^2) decreases as the inverse square of the distance r to the source:

$$I = \frac{P}{4\pi r^2} . \qquad (1)$$

In this equation P is the acoustic power radiated by the source.

At the boundary surface the wave is partly absorbed and partly reflected. It is absorbed in fibrous or porous materials, for example, in which the movement of the air particles is subject to friction. In a hall the floor surface is usually strongly absorbent (due to carpeting, seat upholstery and the clothing worn by the audience). The part of the sound that is absorbed varies from a few per cent for concrete and plaster to nearly a hundred per cent for a block of occupied seats.

The sound energy that is not absorbed is reflected. After a certain transit time the reflected sound wave strikes another boundary surface where it is again partially reflected. At the same time it spreads out, so that an increasing number of boundary surfaces take part in the reflections. The very numerous reflections from all directions surrounding a listener in an auditorium together constitute the *indirect sound* or reverberant sound field. Some early reflections reaching the listener from side walls and ceiling reinforce the clear perception of the direct sound, while the others merge together to form the reverberation.

In the greater part of the auditorium the intensity of the indirect sound is greater than that of the direct sound. In the immediate vicinity of the source, however, the situation is different; at only a few metres away from the source both intensities are the same. The distance at which the two intensities are equal is called the reverberation distance.

The acoustic energy introduced into the auditorium by the sound source thus disappears by absorption at the boundary surfaces. If there is little absorption a

sound wave will circulate for longer before it becomes attenuated to a given level. The reverberation time — defined as the time in which the reverberation has decreased to a millionth of its original intensity (i.e. has become 60 dB weaker) and denoted by T — is then longer and the total energy content of the reverberant sound field is greater. A measure of this energy content is the energy density, i.e. the number of joules per cubic metre. This differs at any given instant from place to place in a manner that defies exact description. For this reason we have to resort to statistical methods. We use the mean energy density throughout the auditorium in our calculations, and we make the simplifying assumption that the energy of the reverberant sound field is distributed uniformly throughout the auditorium.

The mean energy density w of the reverberant sound field and the reverberation time T are related:

$$w = 0.072\,(1 - \bar{\alpha})\,\frac{PT}{V}\,. \qquad (2)$$

We see in the first instance that w and T are linearly related. The reverberation time, for a given P, can be lengthened by increasing the energy in the reverberant sound field by means of electroacoustic amplification. Also, w is proportional to the power P of the sound source and inversely proportional to the volume V of the auditorium. The factor $(1 - \bar{\alpha})$ introduces a complication. The acoustic absorption coefficient, α, is a coefficient indicating the fraction of the incident sound energy that is absorbed by a wall; α therefore has a value between 0 and 1. In our calculations we take the mean value $\bar{\alpha}$, averaged over all the boundary surfaces of the auditorium. We can represent $(1 - \bar{\alpha})P$ as the power that enters the sound field after the first reflection of the sound waves.

The factor 0.072 in (2) is dimensionless. Equation (2) is derived by calculating the average acoustic energy density that is maintained in an auditorium of given characteristics by a sound source of power P. The relevant quantities are the volume V and the total acoustic absorption, which is considered to be concentrated in an area of A m^2 with an absorption coefficient of 100%. In the steady state the power that escapes outside through this 'open window' is equal to the power P supplied by the sound source. It is given by the product of the area A, the energy density in the plane of the window and the mean velocity of the energy propagation in the direction perpendicular to the window. The energy density here includes the direct sound, and the symbol w_{tot} is therefore used. Assuming that all directions of propagation in the auditorium are equally likely — and this is a reasonable assumption for a uniform energy distribution — the energy density in the plane of the window is $w_{tot}/2$, since no energy enters from outside and half of all the possible directions of propagation can be ignored. The propagation velocity in the direction perpendicular to the window is $c\cos\phi$, where c is the velocity of sound and ϕ is the angle between the direction of incidence and the normal to the plane of the window. Averaging over all possible directions in a hemisphere gives a mean propagation velocity of $c/2$, and this in turn gives

$$P = w_{tot}\,A\,c/4. \qquad (3)$$

We now require the relation with the reverberation time. If the sound source is switched off, the sound in the auditorium dies away. The total energy content of the auditorium at any instant t is $W(t) = w_{tot}(t)V$. The energy loss through the 'open window' is $-\mathrm{d}W/\mathrm{d}t$, so that we have the differential equation:

$$-\frac{\mathrm{d}W}{\mathrm{d}t} = \frac{WAc}{4V}$$

with the solution

$$W = W_0 \exp\left(-\frac{Ac}{4V}\,t\right).$$

Now the reverberation time T has been defined as the time for W to decrease to $10^{-6}\,W_0$, where W_0 is the acoustic energy at the time $t = 0$. Thus

$$10^{-6}\,W_0 = W_0 \exp\left(-\frac{Ac}{4V}\,T\right),$$

from which we have

$$T = 6 \ln 10\,\frac{4V}{Ac}\,. \qquad (4)$$

Combining this with the equation for P above, we obtain

$$w_{tot} = \frac{1}{6 \ln 10}\,\frac{PT}{V}\,.$$

For the reverberant sound field — i.e. after subtraction of the direct sound — we have:

$$w = (1 - \bar{\alpha})\,w_{tot} = \frac{1}{6 \ln 10}\,(1 - \bar{\alpha})\,\frac{PT}{V} = 0.072(1 - \bar{\alpha})\,\frac{PT}{V}\,.$$

Sound reinforcement, acoustic-feedback oscillation

It can be seen from equation (2) that the reverberation time can be increased by increasing the mean energy density of the reverberant sound field, for example by sound reinforcement. At first sight this looks like the conventional kind of amplification as used in public-address systems, which amplify the sound from a source close to the microphone. The effect of such a public-address installation on the acoustics of the auditorium as a whole is negligible, however: although the speaker on the platform is clearly intelligible to his audience, questions from the audience are unintelligible and the presence of a microphone on the platform does not help.

Increasing the gain of the system does not help either. This is because the electroacoustic amplification of sound is characterized by a fundamental limi-

[3] N. V. Franssen, Sur l'amplification des champs acoustiques, Acustica 20, 315-323, 1968 (in French).
[4] A. Th. van Urk, Auditorium acoustics and reverberation, Philips Tech. Rev. 3, 65-73, 1938.

tation: it operates within a closed-loop feedback system consisting of microphone-amplifier-loudspeaker-auditorium-microphone, and if the loop gain is too high the system becomes unstable and oscillates. This acoustic-feedback oscillation, or 'howl', makes the system useless; the gain must be kept below the level at which a tendency to howl sets in. Most public-address systems are kept just below this limit, much too close to it in fact, so that the system almost goes into oscillation now and again. The increased gain at the frequency at which the system tends to oscillate gives the sound a certain 'coloration'. This particular preferred note seems to linger, lengthening the reverberation time, but only for this particular note.

Many channels required

It becomes clear that our objective of increasing the reverberation time cannot be reached with only one channel. A single channel will not increase the energy content of the indirect sound field sufficiently to give the required increase in reverberation time.

If the transfer of sound from loudspeaker to microphone is measured as a function of frequency (*fig. 2*), the spectrum obtained is very irregular, with a large number of peaks and valleys close together and differences in sound level that may often be more than 30 dB from peak to valley (i.e. a power ratio > 1000). This pattern is obtained because an auditorium possesses a large number of resonances and antiresonances that lie close together in frequency. The peaks and valleys in the measured frequency spectrum are the resultant of the superimposition of a large number of partly overlapping resonance curves; as has been shown [5], the mean distance between a peak and the valley that follows it is about $4/T$. Resonance regeneration and eventual oscillation will occur at the frequency of one of the highest peaks in the spectrum. Oscillation will set in if at this frequency the signal circulating in the closed loop microphone-amplifier-loudspeaker-auditorium-microphone is not attenuated; the 'loop gain' is then equal to unity (a difference in level of 0 dB).

For reproduction without coloration the loop gain at the highest peak should be no more than -5 dB (1/3 in power). The mean transfer level over the whole frequency band is about 12 dB below the highest peak (measured in terms of power the average transfer is 1/16 of that at the highest peak; see fig. 2*b*). The mean loop gain over the complete frequency band should therefore not exceed a level of -17 dB (1/50 in power).

The loop gain at a given frequency is found to be closely dependent on the positioning of microphone and loudspeaker. If the position of either is moved, a different transfer function is measured; despite our initial assumption the sound field is far from uniform. Temperature fluctuations and even the presence or absence of an audience also affect the sound transfer. If the gain setting is fixed, an additional safety margin of 4 dB (a factor of 2.5 in power) is therefore required. The loop gain should not be made higher than 5 dB + 4 dB = 9 dB below the limit of oscillation. This means that the mean gain over the entire frequency

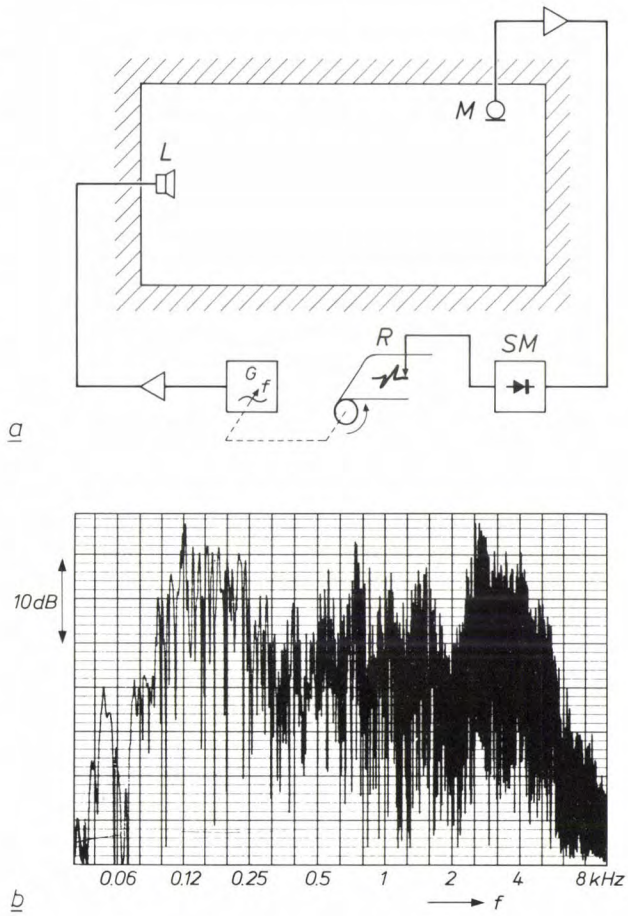

Fig. 2. The sound transfer from loudspeaker to microphone in an auditorium, measured as a function of frequency. *a*) Measurement system. A signal generator *G* of variable frequency *f* supplies a sinusoidal tone of very slowly rising frequency to a loudspeaker *L* via an amplifier. After amplification, the signal from the microphone *M* goes to a sound level meter *SM*, whose output is a varying direct voltage that is applied to a pen recorder *R*. The varying direct voltage determines the vertical excursion of the pen; the horizontal displacement of the paper matches the frequency variation of the signal generator *G*. *b*) The resultant pen recording.

band is -21 dB, which implies that the amplification channel adds 1/125 or 0.8% to the energy density of the reverberant sound field. The reverberation time is also lengthened by approximately this amount.

One channel therefore does little to change the acoustics of the auditorium. A second channel, independent of the first, does not 'know' whether the acoustics of the auditorium is a consequence of the

presence of the first channel or of natural circumstances, and adds 0.8% to the already existing energy density of the sound field and to the reverberation time. This second channel, if it goes into acoustic feedback oscillation, will almost certainly oscillate at a different frequency, since this channel excites a different resonance mode in the auditorium and it has a transfer function in which the peaks lie at different frequencies. Something similar happens with the $(n+1)^{th}$ channel that is added to a set of n channels. In this way, with the microphones and loudspeakers distributed at random in the auditorium, the energy contributions from more than one channel can be added together.

This points the way to the desired objective. A significant lengthening of the reverberation time can be achieved by installing a large number of independent channels in the auditorium. Each of these channels then operates in a reinforced sound field, incidentally; the limit of acoustic feedback oscillation is reached at a lower gain than if the relevant channel were the only one present in the auditorium, and the setting is adjusted accordingly.

How many channels?

The number of channels necessary for a desired increase in reverberation time is of vital interest, since the cost of the installation will largely depend on the number of channels.

If G_n is the gain in energy density of the sound field achieved with an installation of n channels, then from (2):

$$G_n = \frac{w_n}{w_0} = \frac{(1-\bar{\alpha}_n)T_n}{(1-\bar{\alpha}_0)T_0}. \qquad (5)$$

We see that the reverberation time T cannot simply be increased by the same factor, since the quantity $\bar{\alpha}$ — the mean absorption coefficient of the boundary surfaces of the auditorium — is obviously affected by the n amplification channels. When these are in operation, the sound striking the wall will here and there arrive at a microphone and be returned to the sound field elsewhere in the auditorium, having been amplified to some extent. In this way the wall, seen in its entirety, has become less absorbent; this may be described formally by the relation $\bar{\alpha}_n < \bar{\alpha}_0$.

What then are the magnitudes of $\bar{\alpha}_0$ and $\bar{\alpha}_n$? To find the answer let us start from the Sabine expression for the reverberation time:

$$T = 0.16\frac{V}{\bar{\alpha}S}, \qquad (6)$$

where S is the total area of all the boundary surfaces in the auditorium.

From this expression we find that

$$\bar{\alpha}T = 0.16\frac{V}{S}$$

is a constant for a given auditorium and depends only on its geometry. We put

$$\bar{\alpha}_0 T_0 = \bar{\alpha}_n T_n = \tau, \qquad (7)$$

so that (5) becomes

$$G_n = \frac{T_n - \tau}{T_0 - \tau}. \qquad (8)$$

The magnitude of τ has to be calculated from the dimensions of the auditorium, which can be taken from the architectural drawings.

Equation (6) is essentially the same as the earlier equation (4). In that equation the total absorption was considered to be concentrated in an 'open window' of area A, whereas here the absorption is assumed to be uniformly distributed over the total boundary surface S. It is interesting to note that the time constant τ is in a fixed ratio to the mean free path $\bar{l}$ of a sound wave in the auditorium between two reflections. It can be shown [4] that

$$\bar{l} = 4V/S; \qquad (9)$$

$\bar{l}$ is thus completely determined by the geometry of the auditorium. From (4) it follows that:

$$T = 6\ln 10\frac{4V}{\bar{\alpha}Sc},$$

so that

$$\tau = \bar{\alpha}T = 6\ln 10\,\bar{l}/c = 13.8\,\bar{l}/c. \qquad (10)$$

The time constant τ therefore corresponds approximately to the time in which a sound wave in the auditorium undergoes 14 reflections; the total attenuation of this sound wave is $(1-\bar{\alpha})^{14}$.

The presence of the term $-\tau$ in equation (8) means that the reverberation time is not lengthened by the full magnitude of the factor G_n by which the energy of the sound field increases. The outcome is less favourable; in practice it is found that for each channel about 0.8% is added to the energy of the sound field, but only 0.6% to the reverberation time. Increasing the reverberation time by a half thus requires 80 to 90 channels (see Table I).

The reverberation time is frequency-dependent

When we refer to 'the' reverberation time we mean an average over a broad frequency band, as measured for example with a pistol shot — a sound source with a broad frequency spectrum. It is obvious, however, that the absorption of sound at different wavelengths

[5] M. Schröder, Die statistischen Parameter der Frequenzkurven von grossen Räumen, Acustica 4, 594-600, 1954 (in German).

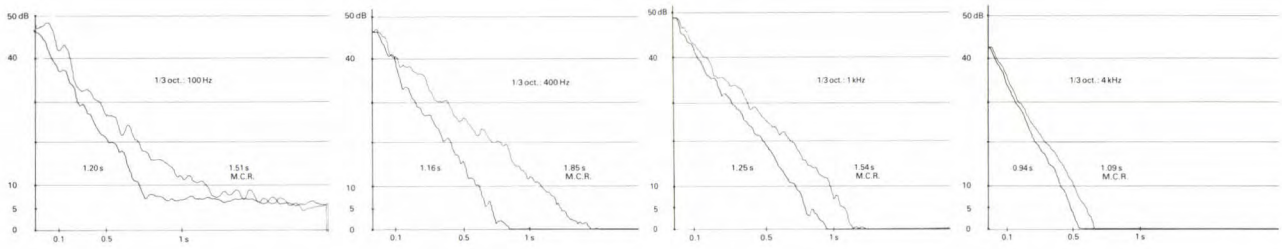

Fig. 3. Reverberation measurements made in the Philips POC Congress Centre in Eindhoven at the frequencies 100 Hz, 400 Hz, 1 kHz and 4 kHz, with MCR and without. The signal whose reverberation was measured was 'pink' noise with a bandwidth of a third of an octave. The falling curves represent the decay in the sound level after the sound source has been switched off. The shorter the reverberation, the steeper the curve. The reverberation time is calculated from the angle of slope of the curve.

in an auditorium is not the same, and the variation in wavelength from the lowest notes to the highest is enormous: from 10 m to 2 cm.

The reverberation time at a particular frequency is measured with a test signal of limited bandwidth, such as random noise with a bandwidth of an octave or a third of an octave. The test signal is introduced into the auditorium via loudspeakers and is picked up by a microphone connected to a pen recorder. When the test signal is switched off the decay is indicated by the recorder trace. The plot is logarithmic, in dB (see *fig. 3*); the paper runs at a constant, known speed, and if the decay of the sound is slower the curve will be less steep. Measurement of the angle of slope gives the reverberation time.

The curve of reverberation time as a function of frequency is a very important measure of the subjective impression produced by an auditorium. If the reverberation time increases towards the low frequencies, the auditorium sounds 'warm'; if the reverberation time is about the same at low and high frequencies, the hall has a 'thin' sound.

With an electronic reverberation system it is therefore necessary to have some means of influencing the frequency characteristic of the reverberation. There is also of course another reason for this. In the natural frequency characteristic of many auditoriums there is a preferred frequency band in which the amplification system will tend to howl when the gain is increased. A higher total gain can be achieved if attenuation is included in this band.

The Philips MCR installation in the Philips POC Congress Centre

The first theatre auditorium to be provided with an MCR system was the one in the Philips POC Congress Centre in Eindhoven, where it came into use in 1981. Before then some systems had been tried out in a demonstration studio belonging to the Philips Electro-acoustics Division (the 'ELA Studio'); see Table I. The POC auditorium is on the first floor of the building (see the photograph on page 12 and *fig. 4*); it has 796 seats and a volume of 3100 m^3 plus 900 m^3 on the stage below the orchestra canopy. It is used as a theatre as well as a concert hall, and concerts are given by groups ranging from a small chamber-music ensemble to a large symphony orchestra.

The auditorium contains 90 channels of amplification. When these are used the reverberation time can be increased from its natural value of about 1.1 s to 1.7 s, in nine steps. The corresponding increase in sound-field level is 2.3 dB (see *fig. 5*). The stage is included in the total volume of the auditorium by mounting the loudspeakers of 14 of the channels in the orchestra canopy. This also has the advantage of giving the musicians a better impression of the overall sound of the orchestra.

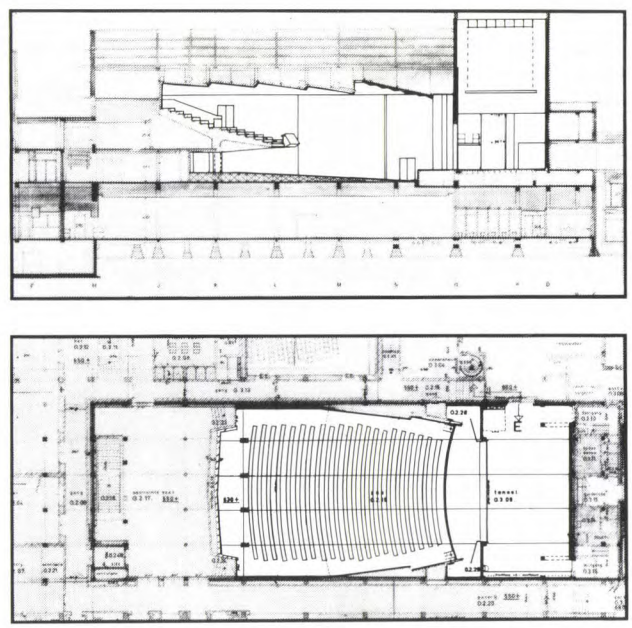

Fig. 4. Cross-sections of the POC Congress Centre in Eindhoven. The large auditorium contains 796 seats and has a volume of 3100 m^3 (plus 900 m^3 for the stage, below the orchestra canopy).

General arrangement of the system

The 90 microphones of the system are all mounted in the ceiling of the auditorium. In the photograph on page 12 they can be seen between the small lights at the front and also further back. The loudspeakers are located in the side walls, in the ceiling under the balcony and, as mentioned earlier, on the stage; in all there are 110 loudspeakers. The total power available to the loudspeakers is 90×16 W = 1440 W; this gives a maximum sound level of 112 dB in the auditorium.

fed to each channel in turn, and the channel response is monitored. For this operation the control desk contains a filter that has the inverse characteristic of the filter in each channel (see fig. 6). In measurements via this inverse filter the output signal should be constant. If any channel fails to give a constant output, an alarm is given. In addition the internal noise of each channel is checked; when a resistance of 200 ohms is connected across the input instead of a microphone the output signal should not exceed a specified small

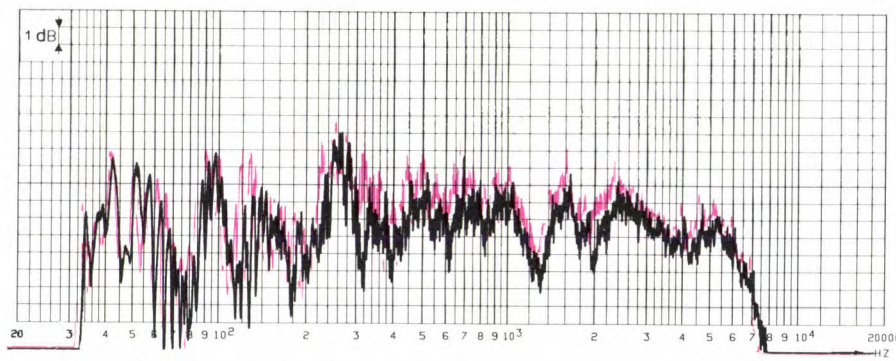

Fig. 5. Sound-transfer measurement in the large auditorium of the POC Congress Centre in Eindhoven, without MCR (*black*) and with MCR in position *8* (*red*). The difference between the red and black curves gives the reinforcement of the reverberant sound field by the MCR system.

The lengthening of the reverberation time can be adjusted in nine steps by simultaneously adjusting all the attenuators in the ninety channels. Except for switching the system on and off, this is the only adjustment necessary in daily use, and it is performed by remote control.

Each channel includes filters, for adjusting the frequency characteristic of the system during installation. The filters include treble and bass control with a range of $\pm$ 12 dB with respect to the level at 500 Hz, and four band filters. Three parameters of the band filters can be adjusted: the centre frequency, the bandwidth and the insertion loss or gain, depending on whether the filter is used as a bandstop filter or a bandpass filter. These filters have been used to give each amplification channel in the POC auditorium a frequency response as shown in *fig. 6*; the curve shows the signal transfer from microphone input to loudspeaker output.

The reliability of such an elaborate installation requires special attention. Provision is therefore made for monitoring the operation of the system from a control panel. A checking procedure is started automatically when the system is switched on, and can also be operated manually. Each channel contains a separate monitoring input and a monitoring output from the output amplifier. A sine-wave signal produced by a sweep oscillator incorporated in the control panel is

value. Finally, the output voltage is monitored at maximum level.

Overload protection is also provided. If a separate monitoring microphone picks up excessively high levels (above 112 dB in the POC auditorium) automatic gain controls come into operation to reduce the levels in the separate channels by 4 dB.

A block diagram of the installation is shown in *fig. 7*.

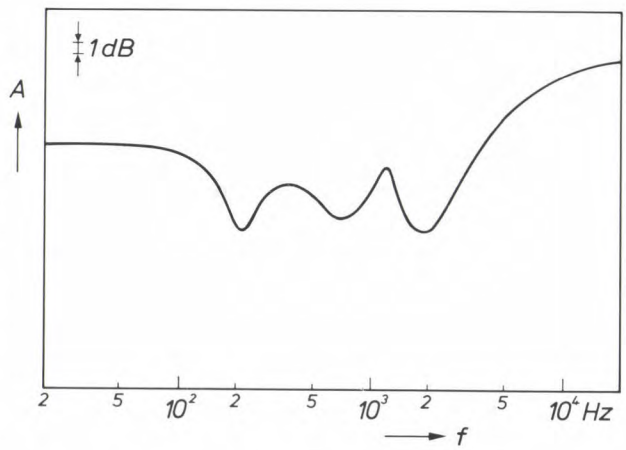

Fig. 6. The gain A of an MCR channel in the POC Congress Centre, plotted in dB against the frequency f. The filters incorporated in the channel equalize the total frequency response of the system, including the loudspeakers and the hall.

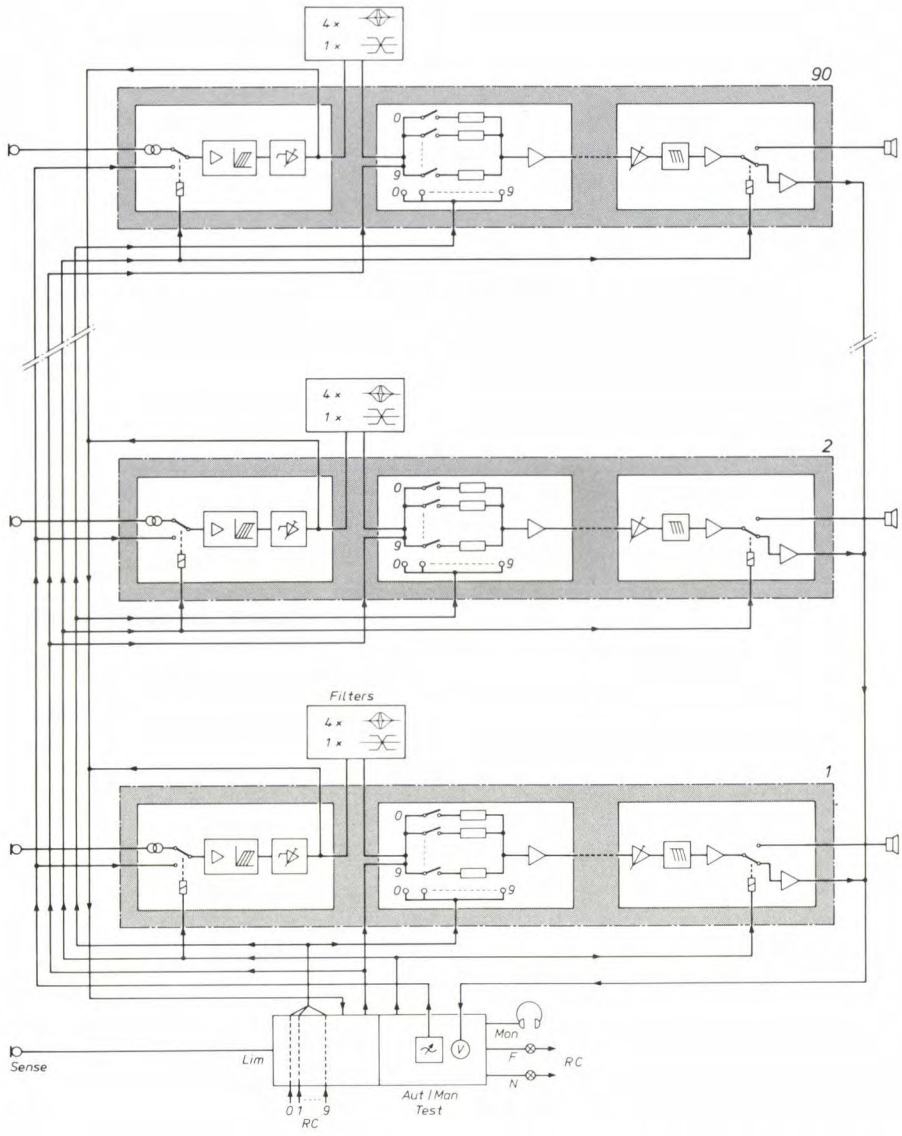

Fig. 7. Block diagram of the MCR installation in the POC Congress Centre. *1* . . . *90* amplification channels. *Filters* four bandpass/bandstop filters and one high/low tone control. *Aut/Man Test* automatic and manual monitoring of gain and noise. *Mon* monitor headphone. *Sense*, *Lim* sensor microphone and automatic limiter to prevent overloading. *RC* remote control for adjusting reverberation increase (settings *0* . . . *9*) and for testing (indicator lamps: *N* normal, *F* fault).

Improvement of the acoustics in the POC

In fig. 3 we showed a number of reverberation curves for four frequency bands, recorded in the POC with the MCR system switched on and switched off. *Fig. 8* shows a plot of the reverberation time against frequency with the MCR system in the settings *0* (off), *4* (mid-position) and *8* (almost at maximum). The measurements were made with 'pink' noise of one octave bandwidth. It can be seen that the reverberation time in the octave around 500 Hz can be increased from 1.1 s to 1.8 s. In other octave bands the lengthening of the reverberation is less; the settings have

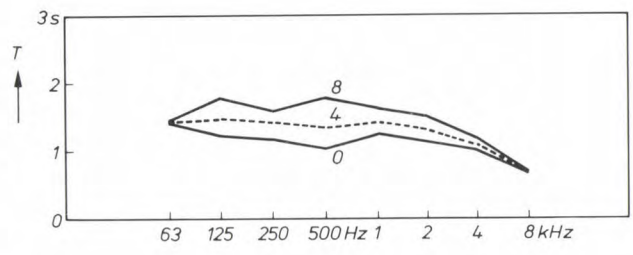

Fig. 8. The reverberation time of the large auditorium of the POC Congress Centre without MCR (*0*) and with MCR (*4*: mid-position, *8*: near maximum). Measurements were made with 'pink' noise octave bands. The largest increase in reverberation is located at 500 Hz (from 1.1 s to 1.8 s).

been deliberately chosen to produce the desired sound timbre. If a different timbre should be required, it is always possible to change the setting of the filters.

Musicians and music critics responded favourably to the introduction of the new system. The conductor and members of the Brabant Orchestra, who regularly perform in the POC auditorium, said there was a 'substantial improvement'. The musicians were sure that they could hear one another better than before, and that this improved their ensemble playing.

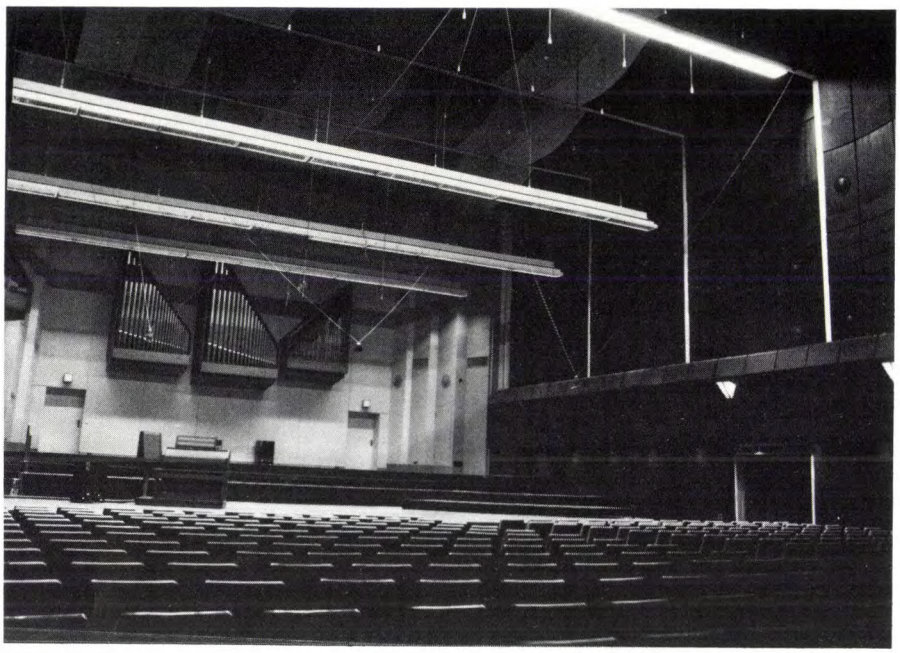

Fig. 9. The Hans Rosbaud Studio of the Südwestfunk broadcasting organization at Baden-Baden (Federal Republic of Germany). This studio has been provided with an MCR sytem of 70 channels. The microphones can be seen suspended from the ceiling; the loudspeakers are incorporated in the walls.

MCR installations at Baden-Baden and Cannes

More recently, MCR installations have been completed in the Hans Rosbaud Studio of the Südwestfunk broadcasting organization at Baden-Baden in the Federal Republic of Germany, and in the Claude Debussy Theatre of the Palais des Festivals et des Congrès at Cannes in France. Both auditoriums are larger than the one in Eindhoven.

The Hans Rosbaud Studio has a volume of 6100 m^3 and is of a conventional rectangular shape. There are 70 amplification channels; as can be seen in *fig. 9* the microphones are suspended from the ceiling. The loudspeakers are mounted in the side walls. The natural reverberation time is 1.5 s; in setting *6* of the system the reverberation time is increased to 2.0 s (*fig. 10a*). This value was specified in the contract; even longer reverberation times are also possible (fig. 10*a*, curve *8*) and are used for organ music. It can be seen from fig. 10 that the greatest increase is obtained in the octaves around 125 Hz and 250 Hz, thus boosting the lower octaves, which are only weakly represented in the natural reverberation. *Fig. 11a* shows the results of a measurement of the sound transfer from loud-

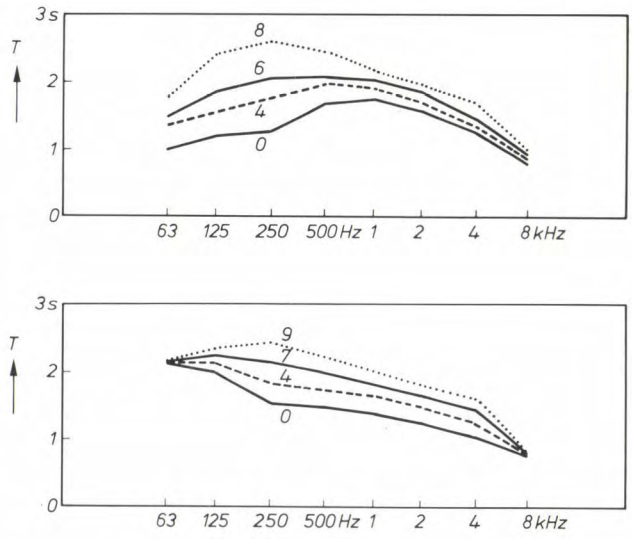

Fig. 10. The reverberation time in different octaves, without MCR (*0*) and with MCR in various settings (*4*... *9*). Measurements were made with 'pink' noise octave bands. *a*) Hans Rosbaud Studio, Baden-Baden. *b*) Claude Debussy Theatre, Cannes.

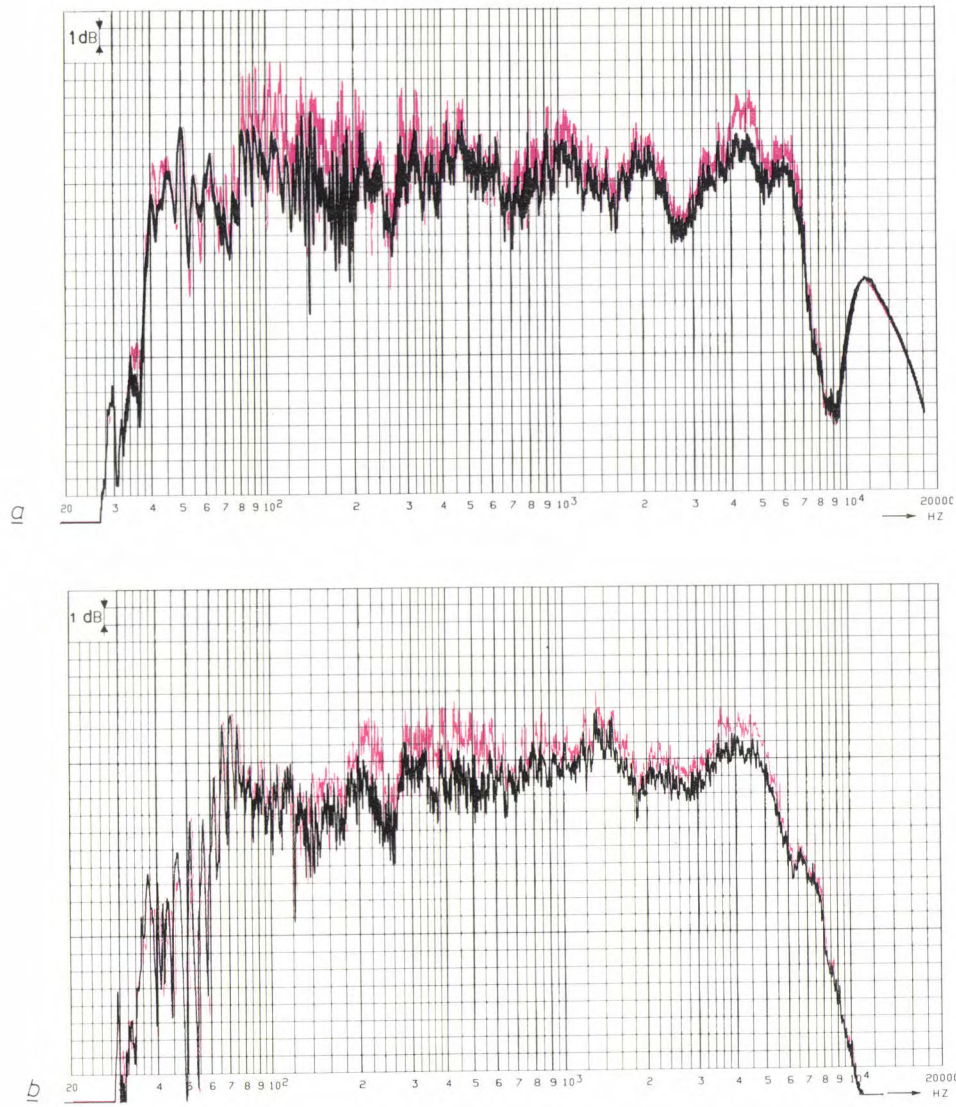

Fig. 11. Measurement of the sound-transfer level in the auditorium between a loudspeaker and a microphone as a function of the frequency; *black*: without MCR, *red*: with MCR. It can be seen that there is a mean difference in the level of the reverberant sound field of about 2 dB, with the greatest reinforcement in the frequency bands where the reverberation time is increased most, as indicated in fig. 10. *a*) Hans Rosbaud Studio, Baden-Baden; MCR in setting *8*. *b*) Claude Debussy Theatre, Cannes; MCR in setting *7*.

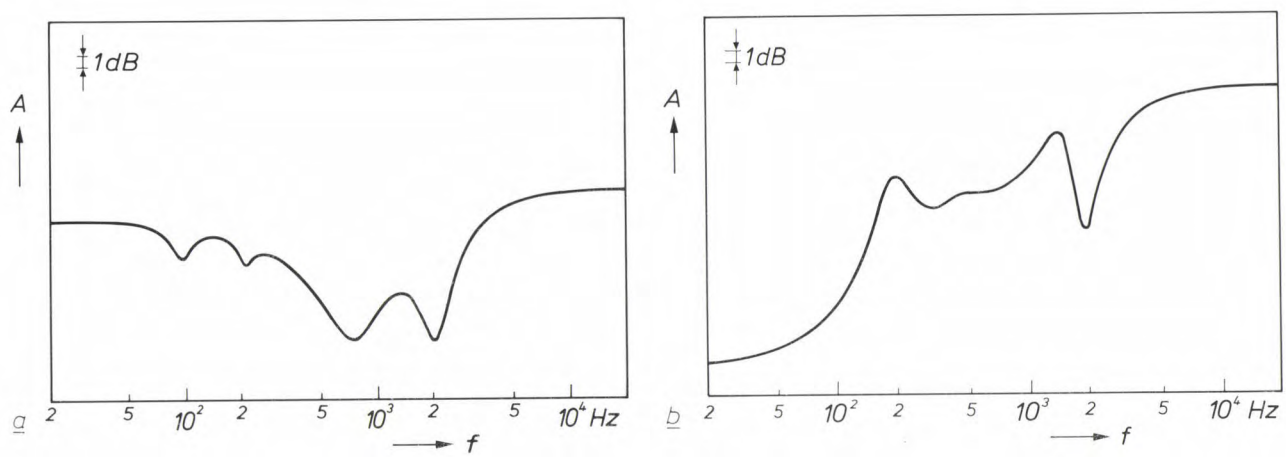

Fig. 12. The gain A of an MCR channel, shown in dB as a function of frequency f. *a*) Hans Rosbaud Studio, Baden-Baden. *b*) Claude Debussy Theatre, Cannes.

speaker to microphone without the MCR system (*black*) and with the system (*red*); the MCR system was set to setting *8*, and it can be seen that the mean reinforcement of the reverberant sound field is greater than 2 dB. *Fig. 12a* shows the response of the filters in each of the channels.

The Claude Debussy Theatre in the Palais des Congrès at Cannes is even larger; its volume is 12 000 m^3, including the part of the stage occupied by the orchestra. However, the natural reverberation time is shorter than at Baden-Baden: 1.45 s. With an MCR installation of 66 channels this can be increased to 2.0 s (in setting *7* of the system). This is accompanied by a mean increase of 1.85 dB in the reverberant sound field (fig. 11*b*). The response of the filters in the installation at Cannes is shown in fig. 12*b*.

Summary. Many auditoriums are used for different purposes (as congress halls, theatres and concert halls); when the hall is used for a concert hall a longer reverberation time is desirable. The MCR system (Multiple-Channel Reverberation) makes it possible to lengthen the reverberation time and correct the frequency characteristic of the reverberation. The system consists of a large number of identical amplification channels, with the microphones and loudspeakers scattered around the auditorium to reinforce the indirect sound. Each channel has its own preferred frequencies, determined by the location of microphone and loudspeaker. To avoid 'coloration' of the sound owing to excessive acoustic feedback, the gain has to be kept low enough for each channel to contribute no more than 0.8% to the energy of the indirect sound, thus adding about 0.6% to the reverberation time. In the large auditorium of the Philips POC Congress Centre in Eindhoven 90 channels have been built in, so that the reverberation time can be increased in steps from 1.1 s to about 1.7 s. The Hans Rosbaud Studio of the Südwestfunk broadcasting organization in Baden-Baden (Federal Republic of Germany) has been provided with 70 channels; the reverberation time of this hall can be increased from 1.5 s to about 2.1 s. An MCR installation has also been fitted at the Claude Debussy Theatre of the Palais des Festivals et des Congrès, Cannes (France). The 66 channels can be used to increase the mean reverberation time from 1.45 s to 2.0 s.

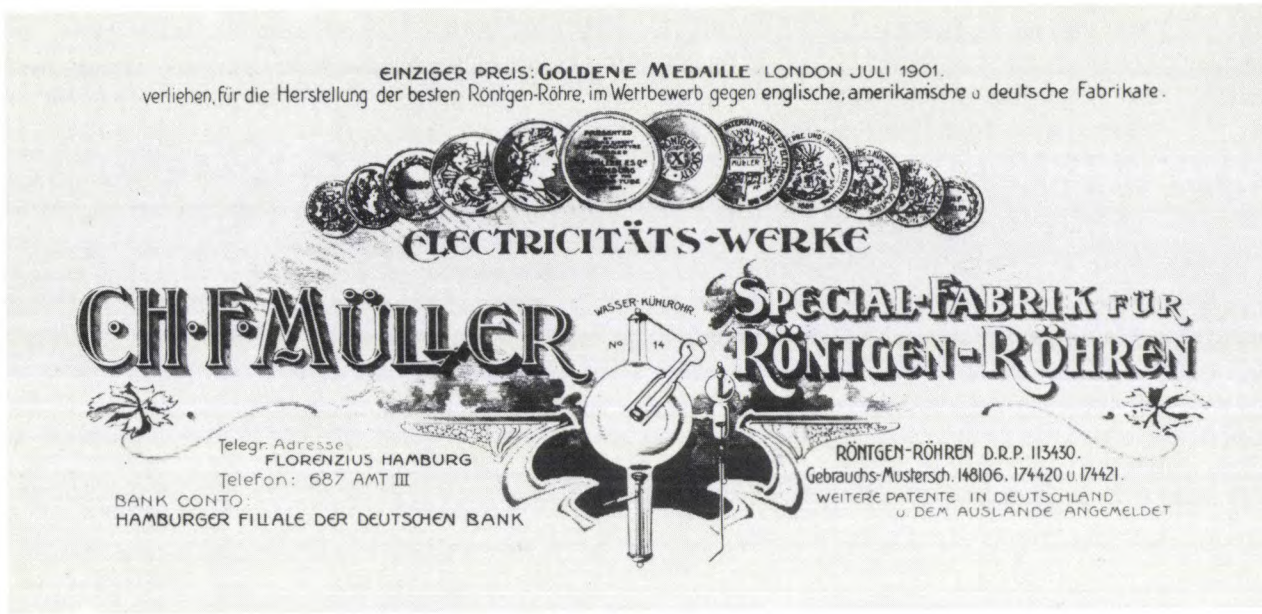

Metal/ceramic X-ray tubes for non-destructive testing

W. Hartl, D. Peter and K. Reiber

The Hamburg industrialist Carl Heinrich Florenz Müller was one of the first manufacturers of X-ray tubes, as appears from the following sentence describing a communication [*] made three months after the discovery of X-rays on the 8th of November 1895: 'One day in February K. informed me that there is a Mr Müller living in Hamburg who owns an electric power station and an electric-lamp factory, and who also engages in the manufacture of Geissler tubes, Hittorf tubes and X-ray tubes . . .'. The letterhead printed above, which refers to the first prize won by the firm in 1901 in a competition (with 28 entries) sponsored by the London Röntgen Society, bears witness to the firm's engineering skills in glass/metal technology. Those engineering skills enabled the factory — which has been part of the Philips group since 1927 — to grow into one of the biggest suppliers of X-ray tubes and equipment, both for medical applications and for the testing and investigation of materials. Although the construction of X-ray tubes has changed considerably in the course of the years, it was not until the sixties that there were any substantial changes in tube technology itself. It was the advent of metal/ceramic seals that set the manufacturing process on an entirely new course, making it possible to manufacture tubes that are much smaller and lighter, even though the specifications are the same or are improved.

Introduction

Soon after the discovery of X-rays the X-ray tube entered upon a period of vigorous development, to which the firm of C. H. F. Müller made important contributions. In 1899, for example, the firm was granted a patent, under the name of Prof. B. Walter, for the water-cooled anode. Ion tubes, filled with a rarefied gas, were followed by vacuum X-ray tubes, which had an anode/cathode configuration very similar to that of the X-ray tubes of today. The many and various applications of X-rays gave rise to a wide

Dr W. Hartl, Dipl.-Phys. D. Peter and Dr K. Reiber, are with C. H. F. Müller, Philips GmbH, Hamburg, West Germany.

[*] See page 31 of O. Glasser, Wilhelm Conrad Röntgen und die Geschichte der Röntgenstrahlen, Springer, Berlin 1959 (in German).

variety of types of X-ray tube; the tubes for medical applications and those used for the investigation of materials form two separate classes. The medical tubes can be subdivided into tubes for diagnosis and for therapy. X-ray tubes for materials investigations are subdivided into tubes for X-ray diffraction, X-ray fluorescence and macroscopic testing.

The medical tubes for diagnostics have to be capable of making a shadowgraph image of a moving object, and are therefore required to produce a high intensity of X-rays in a short time, from a point source (called the focus) on the anode. This explains why tubes of this type usually have a rotating anode; they do not have such a high voltage between anode and cathode as other X-ray tubes. The therapy tubes, used for destroying malignant tissue, call on the other hand for hard X-rays (i.e. radiation at a very short wavelength) and hence require a much higher voltage. The focus in these tubes can be larger and the exposure time is much longer. These tubes therefore operate with a fixed anode.

The tubes for investigating materials by means of X-ray diffraction and X-ray fluorescence are not included in the production programme at C. H. F. Müller; they are manufactured elsewhere in the Philips group. X-ray diffraction tubes are used in crystallographic research. X-ray fluorescence tubes are used for the quantitative analysis of elements in material samples, involving measurement of the height of the characteristic X-ray lines in a spectrum obtained by X-ray fluorescence. X-ray diffraction tubes have two or more windows, enabling the elongated focus to serve either as a 'point' focus or as a 'line' focus. The X-ray fluorescence tubes have a single window and the focus is not concentrated at a point. In view of the different properties required from the X-radiation, special anode materials (copper, silver, etc.) are generally used in diffraction and fluorescence tubes, while tungsten is most commonly used in other types of X-ray tubes.

The macroscopic testing of materials may be concerned with tracing welding and casting flaws in thick metal workpieces, or tracing foreign bodies in materials that present less of an obstacle to X-rays, for example foodstuffs. In these macroscopic inspections X-rays are required that are generated with voltages ranging from 50 kV to more than 400 kV. The tubes used in these applications, and described in this article, are therefore manufactured in a range of versions, for maximum voltages of between 100 kV and 420 kV. The power required from the tube, particularly at the lower voltages, is high. As in diagnostic tubes, the focus must approximate to a point source to give sharp definition in the shadowgraph image. The tube power is less than that of diagnostic tubes, but must be available for a relatively long period — ten minutes or sometimes more — to produce sufficient density on the photographic material. The long exposure time is permissible because the objects are stationary. Tubes of this type have non-rotating anodes with forced liquid cooling.

In electronic tubes of all kinds — evacuated devices whose operation depends on electron paths — the principal structural material for the tube wall has until recently always been glass. The reasons for this are well known. Glass is a cheap material, its properties can readily be adapted to a particular application by varying the composition, and it is easy to shape because of the long softening gradient as its temperature is increased. Although glass has many good properties that make it suitable for a wall material for evacuated enclosures, it does have certain disadvantages. These are particularly noticeable when high voltages are used, as in X-ray tubes. Scattered electrons may cause charge to build up on the inside of the glass wall, causing deflection of the electron beam. Electrons that strike the wall may also damage the glass and eventually cause voltage breakdown (flash-over). On the outside of the glass adsorbed moisture may cause external flash-overs. To avoid this, X-ray tubes of conventional design are enclosed in an insulating oil (transformer oil). Another kind of disadvantage is that shaping the glass when it is hot does not allow

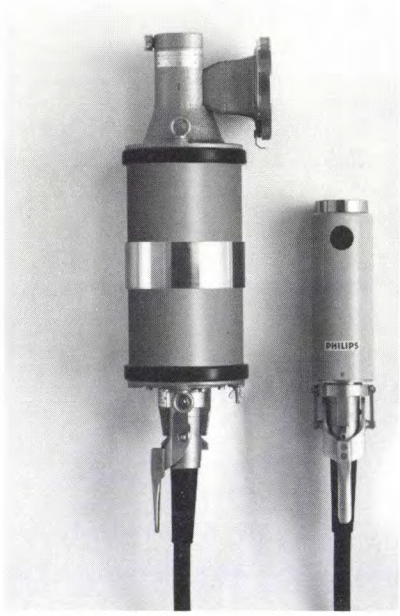

Fig. 1. Two X-ray tubes for macroscopic testing, both for a maximum power consumption of 3 kW. *Left:* A conventional tube for 150 kV maximum in glass/metal technology. *Right:* A tube of the new generation for 160 kV maximum in metal/ceramic technology. Both tubes are shown in their shields. The new-generation tube has linear dimensions that are about half those of a conventional tube and is only a quarter of its weight.

particularly accurate dimensional tolerances, and this may affect the relative position of the anode and cathode. Finally, glass is a fragile material.

In spite of all the difficulties, successful technologies for the use of glass have been developed. Many thousands of glass X-ray tubes have been manufactured; the availability of various alloys with expansion coefficients equal to those of the different glasses was a great help in their design.

In the sixties a need arose for more compact and lighter X-ray equipment for non-destructive testing. In testing heavy workpieces the bulk and weight of the test equipment, particularly for voltages higher than 400 keV, are a serious handicap. It is obviously much more convenient for the operator if either the workpiece or the equipment can be moved by hand.

A breakthrough in the efforts to develop a lighter, smaller and less fragile X-ray tube for direct voltage came with the advent of metal/ceramic technology. The combination of this technology with an entirely different tube design made it possible to reduce the weight to about a quarter and to halve the linear dimensions; see *fig. 1*. This dramatic improvement came about largely because there was no longer any need for the insulating oil around the tube. This is because the new tube has a metal wall, which is at earth potential. The improved design of the tube prevents the occurrence of flash-overs, since scattered electrons are conducted to earth via the wall.

In the 'single-pole' tubes the anode is also at earth potential. Double-pole tubes are supplied by twin generators and the anode voltage is above the potential of the earthed tube wall by the same amount that the cathode voltage is below it. With double-pole tubes, therefore, for the same cabling and two generators of the same size, the high voltage between anode and cathode can be twice as high as with single-pole tubes.

In the following we shall first look at the mechanism responsible for the occurrence of flash-over across an insulating wall in the tube. We shall then compare the design of a glass/metal tube with that of the same type of tube made in ceramic/metal technology and point out the characteristic differences between the two tube designs.

Flash-over across an insulator surface

To improve the design of an X-ray tube it was first of all necessary to gain a better understanding of the discharge effects occurring along an insulator inside the tube. Discharge effects across an insulating surface range from very small currents and micro-discharges to spark discharges. The first two effects are assumed to be associated with current paths across the insulator, and were first explained satisfactorily only in the sixties [1].

Fig. 2a shows a schematized diagram of the path that an electron released from the cathode by field emission (or a scattered or secondary electron) may describe in an X-ray tube of conventional design with a glass wall. The wall bridges the potential difference between anode and cathode at opposite sides of the tube, and the equipotential surfaces, indicated by thin

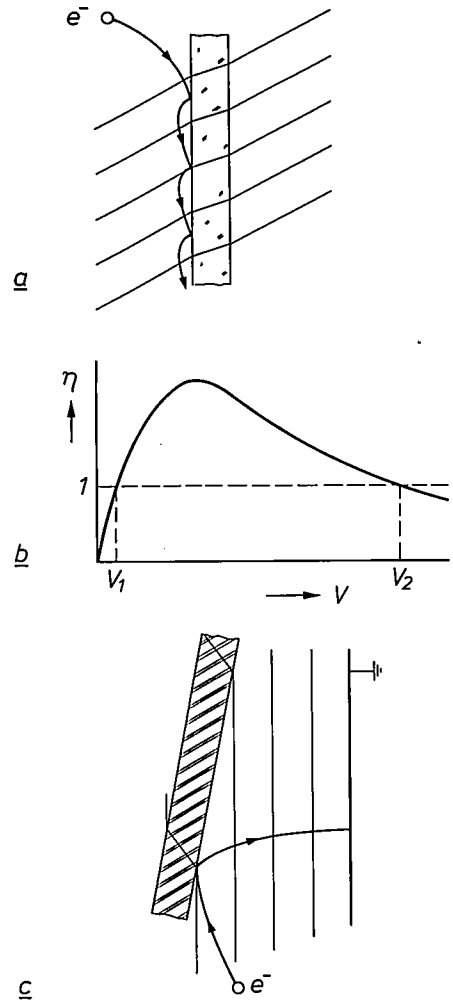

Fig. 2. The origin and avoidance of current paths across an insulator in an X-ray tube. *a*) Path of electrons e^- in a conventional tube. The thin lines represent the equipotential surfaces corresponding to the initial situation before any current path has formed or charge has built up. An electron released by field emission from the cathode (or a scattered or secondary electron) strikes the glass wall. Owing to secondary emission at the point of impact, new electrons are released which in their turn release electrons from a second point of impact, and so on. *b*) The yield η, the ratio of the number of secondary electrons to the number of primary electrons as a function of the voltage drop V that the primary electrons pass through (schematic). V_1 for glass is about 30 V, V_2 for glass is generally between 3 and 10 kV. When the electrons pass through voltage drops of the magnitude of V_2 between successive points of impact, a fairly stable situation arises referred to as 'hopping'. *c*) An electron path in a tube of the new generation. The equipotential surfaces are at an acute angle to the ceramic insulator owing to the earthed metal tube wall opposite to it (see fig. 3). Electrons now released by secondary emission from the insulator arrive at the tube wall, and no current paths are formed across the insulator.

lines, are therefore almost perpendicular to the wall. After colliding with the wall an electron liberates secondary electrons. The yield of secondary electrons as a function of the potential difference they pass through follows from the curve given in fig. 2*b*. Electrons of energy less than eV_1 ($V_1 \approx 30$ V) and of energy greater than eV_2 (V_2 is somewhere between 3 and 10 kV) produce on average less than one secondary electron.

The current path across the glass wall indicated in fig. 2*a* arises in the following way. When electrons of energy between eV_1 and eV_2 first strike a point on the wall, the environment of that point will acquire a positive charge because more electrons leave this area than arrive there. The potential difference that these primary electrons pass through will therefore increase until the electrons acquire an energy eV_2 and a stable potential difference V_2 is established. The electrons emitted from the first point of impact and its environment strike the wall again. The second point of impact is so far away from the first that they again pass through a potential difference V_2. In this way current paths arise across the insulator that are built up from separate, arc-like electron trajectories. The effect is referred to as 'hopping'. The discharge effects that we have described cause a shift in the equipotential surfaces shown in fig. 2*a*. The result is that over the part of the glass wall near the anode there is a greater voltage drop than was originally present.

Fig. 4. The series of metal/ceramic X-ray tubes for macroscopic materials inspection. The tube alone and the tube with its shield are shown side by side. *Left:* two single-pole tubes for 100 kV maximum (below) and 160 kV. *Centre:* double-pole tube for 320 kV maximum. *Right:* double-pole tube for 420 kV maximum. The ceramic anode insulators can be seen in the double-pole tubes.

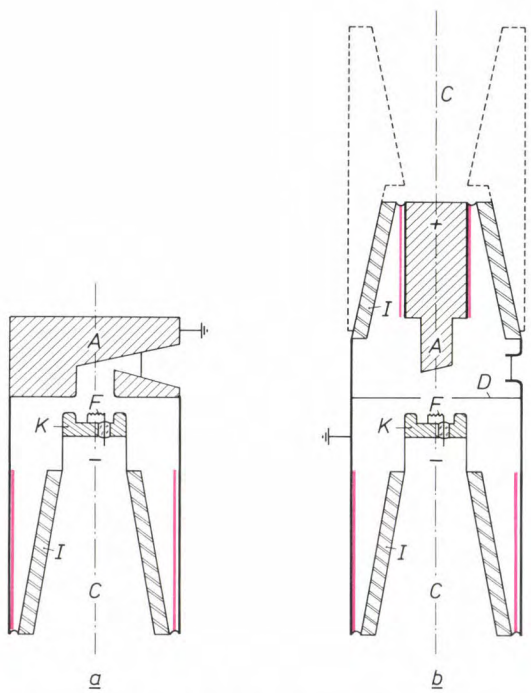

Fig. 3. Schematic design of the new-generation tubes. *K* cathode, *A* anode, *I* insulator, *C* tapered socket for cable termination, *F* filament of cathode. Since an insulator always has a metal surface opposite to it (indicated by red lines) at a higher potential, the hopping effect in fig. 2*a* is avoided (see also fig. 2*c*). *a*) A single-pole tube. Here both the tube wall and the anode are at earth potential. *b*) A double-pole tube. The anode voltage is above the potential of the earthed tube wall by the same amount that the cathode voltage is below it. *D* diaphragm that prevents scattered electrons from reaching the insulator between anode and tube wall. The dashed lines indicate a plastic spacer that serves as a connector for the anode cable. The new-generation tubes thus always have an axial cable connection.

A consequence of the small currents across the glass surface is that gas is desorbed from the glass. This has the effect, especially near the anode, of damaging the glass wall and ultimately flash-over will occur. By giving the anode a hollow projection it is possible to prevent most of the electrons scattered from the anode from reaching the tube wall. It is also possible to use materials that give relatively little secondary emission. In this way a reasonably long useful life can still be obtained with the conventional design of tube.

The understanding thus obtained of the origin of current paths across an insulator points the way to a tube design in which discharge effects of this kind can be avoided. It follows that if the equipotential surfaces are arranged to be at an acute angle to the insulator surface the secondary electrons will not be able to reach the insulator again. This can be achieved by placing close to the insulator a metal wall at a positive potential with respect to the insulator; see fig. 2*c*. *Fig. 3* shows very schematically the resulting configuration of anode, cathode and metal wall as used in

[1] H. Boersch, H. Hamisch and W. Ehrlich, Oberflächenentladungen über Isolatoren im Vakuum, Z. Angew. Phys. **15**, 518-525, 1963 (in German).

the new generation of metal/ceramic X-ray tubes; for a single-pole type in fig. 3*a* and a double-pole type in fig. 3*b*. It is obvious that this design principle is feasible only with d.c.-operated tubes.

The new generation of tubes

The design principles indicated above have been used in designing a range of X-ray tubes for macroscopic materials inspection. The tubes operate at maximum voltages of 100, 160, 320 and 420 kV; see *fig. 4*. The first two types are single-pole, the other two are double-pole. The 320-kV and 420-kV tubes therefore need twin high-voltage generators, which are built up from separate circuits for 160 kV and 210 kV.

As we said earlier, the new tubes are very much more compact and lighter than the tubes of the previous generation that were made of glass and metal, largely because there is no need for oil insulation. This is illustrated in *fig. 5*, which shows cross-sections of a conventional tube for 150 kV (left) and of a metal/ceramic tube for 160 kV (right), both with a power consumption of 3 kW and shown with the appropriate shields. The figure on the left clearly indicates the shielding effect of the hollow projecting part of the anode *A*, designed to prevent scattered electrons from colliding with the glass wall *G*. The space between the lead-clad outer wall *S* of the shield and the glass tube wall *G* is completely filled with insulating oil *O*. The tapered plug of the high-voltage cable fits into a separate insulator, made of epoxy resin, with a tapered socket *C*. Since the breakdown resistance of epoxy resin is greater than that of oil, this prevents voltage breakdown through the oil between the metal parts of the cathode connection and the earthed wall of the shield.

The space between the metal tube wall *W* and the wall *S* of the shield is filled with air in the metal/ceramic X-ray tubes, as can be seen in the right-hand part of fig. 5. The wall of the shield serves only to give protection against unwanted X-radiation. The sep-

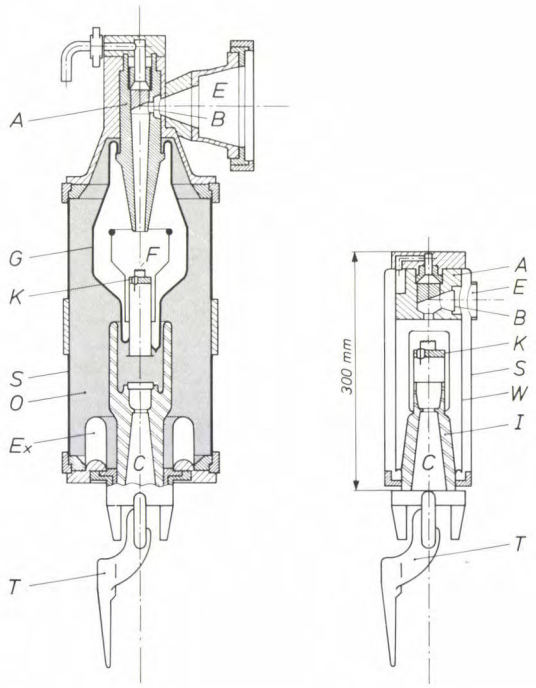

Fig. 5. Comparison of the designs of single-pole X-ray tubes (in shield) of the old and the new generation, both for a power of 3 kW; see also fig. 1. *Left:* The conventional tube in glass/metal technology for a voltage of 150 kV maximum. *Right:* A new-generation tube in metal/ceramic technology for a voltage of 160 kV maximum. Both tubes are thus reasonably comparable in performance. The new tube, however, is much less fragile and much smaller and lighter. *G* glass tube wall, *W* earthed metal tube wall, *O* insulating oil (shaded), *Ex* expansion space, *T* toggle for fixing the cable plug, *S* outer wall with lead shield, *E* exit for the X-ray beam, *B* beryllium window. The other symbols are as in fig. 3.

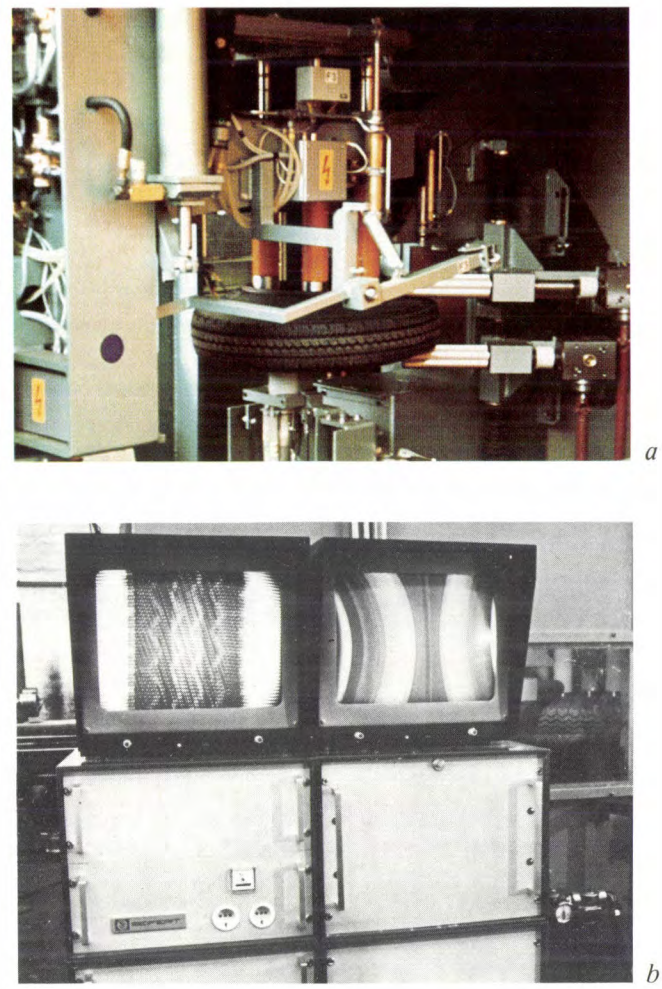

Fig. 6. Inspecting radial tyres in a car-tyre factory with the aid of three metal/ceramic X-ray tubes for 160 kV. *a*) The tyre rotating slowly during inspection. *b*) The pictures on the monitors; the left-hand picture shows the steel bands in the running surface and the right-hand picture shows the two side walls of the tyre.

arate epoxy insulator is superfluous here, because the tapered plug of the cable fits directly into the tapered socket *C* of the ceramic insulator *I* of the tube. Virtually all the air in the gap between the cable termination and the insulator can be expelled by the soft tapered rubber pressing against the hard ceramic. At the anode end of the double-pole tubes there is a plastic spacer, with an internal taper at the tube side and a tapered socket *C* for the cable termination (see the dashed line in fig. 3*b*). The new-generation tubes thus always have an axial cable connection.

Both tubes in fig. 5 have a water-cooled anode *A*. (The non-earthed anode of the double-pole tubes must be oil-cooled.) The coolant is sprayed through a nozzle on to the copper anode-insert, which holds the tungsten target. The X-ray beam in both the single-pole and double-pole tubes of the new generation emerges through a beryllium window, which absorbs far less X-radiation than the glass and the layer of oil through which it has to pass in the conventional double-pole tubes. The weight of the left-hand tube in fig. 5, including shield and oil, is 32 kg, while that of the tube on the right, including shield, is only 8 kg.

To conclude this article we show two applications of the tubes described. *Fig. 6* shows three 160-kV X-ray tubes in use for inspecting radial car tyres during the manufacturing process, *fig. 7* shows a 420-kV tube being used for inspecting a thick-walled casting.

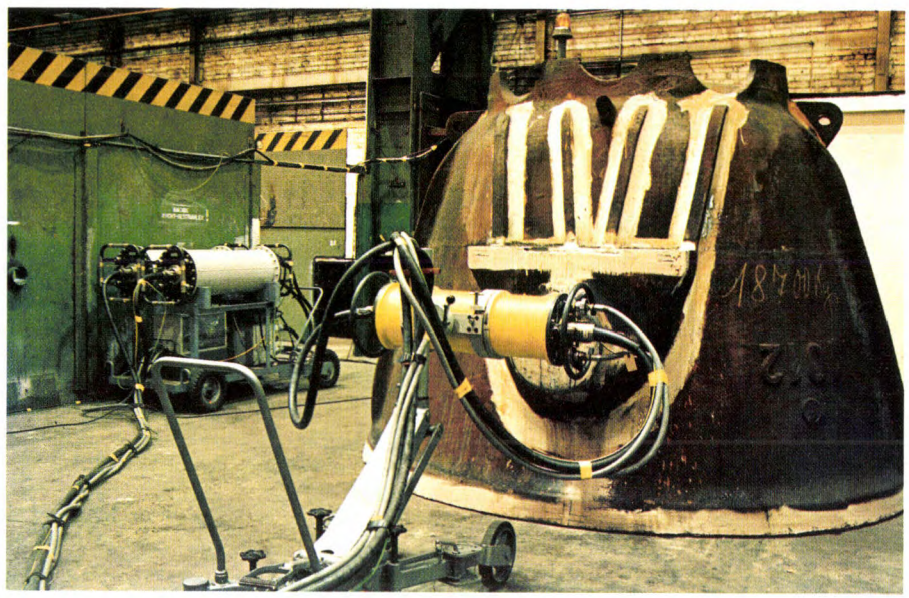

Fig. 7. A metal/ceramic X-ray tube for 420 kV used for inspecting a thick-walled casting in a foundry. The two high-voltage generators for the double-pole tube can be seen on the left.

Summary. As a wall material for X-ray tubes, glass has a number of disadvantages. The tube is relatively fragile, charge builds up on the tube wall, and current paths may form due to 'hopping' of electrons. These problems can be avoided by means of metal/ceramic technology and an improved tube geometry. In a new generation of d.c. X-ray tubes for macroscopic testing of materials, designed in accordance with these principles, it has been possible to halve the linear dimensions and to reduce the weight to a quarter of that of conventional tubes with a glass wall. This was accomplished largely because the new tubes have an earthed metal wall, so that there was no need for insulating oil around the tube. Cross-sectional drawings give a comparison between old-generation and new-generation X-ray tubes for non-destructive testing. The new-generation tubes have a wide variety of applications; typical examples are the inspection of radial tyres and thick-walled castings.

Scientific publications

These publications are contributed by staff of laboratories and plants that form part of or cooperate with enterprises of the Philips group of companies, particularly by staff of the research laboratories mentioned below. The publications are listed alphabetically by journal title.

Philips GmbH Forschungslaboratorium Aachen, Weißhausstraße, 5100 Aachen, Germany — *A*

Philips Research Laboratory Brussels, 2 avenue Van Becelaere, 1170 Brussels, Belgium — *B*

Philips Natuurkundig Laboratorium, Postbus 80000, 5600 JA Eindhoven, The Netherlands — *E*

Philips GmbH Forschungslaboratorium Hamburg, Vogt-Kölln-Straße 30, 2000 Hamburg 54, Germany — *H*

Laboratoires d'Electronique et de Physique Appliquée, 3 avenue Descartes, 94450 Limeil-Brévannes, France — *L*

Philips Laboratories, N.A.P.C., 345 Scarborough Road, Briarcliff Manor, N.Y. 10510, U.S.A. — *N*

Philips Research Laboratories, Cross Oak Lane, Redhill, Surrey RH1 5HA, England — *R*

Philips Research Laboratories Sunnyvale P.O. Box 9052, Sunnyvale, CA 94086, U.S.A. — *S*

E. C. H. Keung, C.-S. Keung & R. S. Aronson *N*	Passive electrical properties of normal and hypertrophied rat myocardium	Am. J. Physiol. **243**	H917-H926	1982
Z. L. Wu*, J. L. Merz* (* *Univ., Santa Barbara, CA*), C. J. Werkhoven, B. J. Fitzpatric & R. N. Bhargava *E, N*	Shallow N acceptor in N^+-implanted ZnSe	Appl. Phys. Lett. **40**	345-346	1982
K. H. Härdtl *A*	Electrical and mechanical losses in ferroelectric ceramics	Ceram. Int. **8**	121-127	1982
A. Broese van Groenou *E*	Theory of dust pressing	Ceram. Monogr., Suppl. Interceram **31** (No. 6)	1-4	1982
J. M. Woodcock & J. J. Harris *R*	Control of the height of Schottky barriers on MBE GaAs	Electron. Lett. **19**	93-95	1983
H. W. Werner *E*	Analytical assistance in semiconductor and electronic material technology	Fresenius Z. Anal. Chem. **314**	274-284	1983
B. M. J. Smets & R. G. Gossink *E*	Surface analysis of glass in the electronics industry	Fresenius Z. Anal. Chem. **314**	285-288	1983
H. C. M. van den Nieuwenhuizen (*Philips Lighting Div., Eindhoven*) & K. H. J. Buschow *E*	Explosive combustion of amorphous alloys in a cold oxidizing atmosphere	High Temp. Sci. **15**	301-309	1982
M. J. Powell & D. H. Nicholls *R*	Stability of amorphous-silicon thin-film transistors	IEE Proc. I. **130**	2-4	1983
S. B. Luitjens & A. van Herk *E*	A discussion on the crosstalk in longitudinal and perpendicular recording	IEEE Trans. **MAG-18**	1804-1812	1982
B. J. Minnis *R*	Classes of sub-miniature microwave printed circuit filters with arbitrary passband and stopband widths	IEEE Trans. **MTT-30**	1893-1900	1982
F. L. Engel, J. J. Andriessen & H. J. R. Schmitz *E*	What, where and whence: means for improving electronic data access	Int. J. Man-Mach. Stud. **18**	145-160	1983
D. Hennings, A. Schnell & G. Simon (*Tech. Univ., Braunschweig*) *A*	Diffuse ferroelectric phase transitions in $Ba(Ti_{1-y}Zr_y)O_3$ ceramics	J. Am. Ceram. Soc. **65**	539-544	1982
P. C. Scholten *E*	Comment on "Anisotropic suspension display"	J. Appl. Phys. **54**	421	1983
M. J. Sparnaay *E*	Four notes on van der Waals forces	J. Colloid & Interface Sci. **91**	307-319	1983
J. C. Jacco, G. Kostecky & G. M. Loiacono *N*	Solution crystal growth of ferroelectric $LiH_3(SeO_3)_2$ using cylindrical seeds	J. Cryst. Growth **60**	445-446	1982

J. S. Vermaak (*Univ., Port Elisabeth, South Africa*) & J. Petruzzello *N*	Radiation damage in N^+-implanted ZnSe	J. Electron. Mater. **12**	29-42	1983
W. Schnitker, H. Rau, P. Eckerlin & P. H. Smit *A, E*	Stabilizing oxide layers on iron particles	J. Magn. & Magn. Mater. **30**	93-98	1982
E. Dormann (*Univ., Bayreuth*), H. de Graaf*, R. C. Thiel* (* *Kamerling Onnes Lab., Leiden*) & K. H. J. Buschow *E*	Magnetic properties of $GdMg_2$ as studied by means of NMR and Mössbauer effect spectroscopy	J. Magn. & Magn. Mater. **30**	231-237	1982
P. G. van Engen, K. H. J. Buschow & M. Erman *E, L*	Magnetic properties and magneto-optical spectroscopy of Heusler alloys based on transition metals and Sn	J. Magn. & Magn. Mater. **30**	374-382	1983
P. C. M. Gubbens*, A. M. van der Kraan* (* *Interuniv. Reactor Inst., Delft*) & K. H. J. Buschow *E*	^{169}Tm Mössbauer effect and magnetic study of Tm_6Mn_{23} and its ternary hydride	J. Magn. & Magn. Mater. **30**	383-388	1983
K. H. J. Buschow, I. Vincze* & F. van der Woude* (* *Univ., Groningen*) *E*	Crystallization of amorphous Zr-rich alloys	J. Non-Cryst. Solids **54**	101-106	1983
H. Schaper & E. Schnedler *A*	Electrolyte-free electrochemiluminescence in thin-layer cells. Current efficiency studies	J. Phys. Chem. **86**	4380-4385	1982
M. E. Rosar, W. A. Smith & A. Bhalla (*Univ., University Park*, PA) *N*	Specific heat of SbSI	J. Phys. & Chem. Solids **44**	117-118	1983
K. H. J. Buschow *E*	Stability and electrical transport properties of amorphous $Ti_{1-x}Ni_x$ alloys	J. Phys. F **13**	563-571	1983
P. Blood, J. J. Harris, B. A. Joyce & J. H. Neave *R*	Deep states and surface processes in GaAs grown by by molecular beam epitaxy	J. Physique (Colloque C5) **43**	C5/351-C5/355	1982
J. P. Stagg, P. J. Hulyer, C. T. Foxon & D. Ashenford (*Imp. College, London*) *R*	Optimization of Sn doping in GaAlAs/GaAs DH lasers grown by MBE	J. Physique (Colloque C5) **43**	C5/377-C5/382	1982
H. A. van Sprang *E*	Surface-induced order in a layer of nematic liquid crystal	J. Physique **44**	421-426	1983
A. E. T. Kuiper, S. W. Koo, F. H. P. M. Habraken & Y. Tamminga *E*	Deposition and composition of silicon oxynitride films	J. Vac. Sci. & Technol. B **1**	62-66	1983
G. Verspui *E*	Chemisch opdampen	Natuur & Techniek **50**	712-729	1982
W. N. Schreiner, C. Surdukowski, R. Jenkins* & C. Villamizar* (* *Philips Electron. Instr., Mahwah, NJ*) *N*	Systematic and random powder diffractometer errors relevant to phase identification	Norelco Rep. **29** (No. 1)	42-48	1982
D. G. Bouwhuis (*Inst. for Perception Res., Eindhoven*)	Engels leren met spraak naar keuze	Onderwijs en de nieuwe media, eds E. J. W. M. van Hees & A. Dirkzwager, Swets & Zeitlinger, Lisse	51-61	1982
B. M. J. Smets & T. P. A. Lommen *E*	The role of molecular water in the leaching of glass	Phys. & Chem. Glasses **24**	35-36	1983
P. J. Dean (*Royal Signals and Radar Establishment, Great Malvern, Worcs*), W. Stutius (*Xerox Res. Centre, Palo Alto, CA*), G. F. Neumark, B. J. Fitzpatrick & R. N. Bhargava *N*	Ionization energy of the shallow nitrogen acceptor in zinc selenide	Phys. Rev. B **27**	2419-2428	1983
F. J. A. M. Greidanus, L. J. de Jongh*, W. J. Huiscamp* (* *Univ., Leiden*), A. Furrer (*E.T.H., Zürich*) & K. H. J. Buschow *E*	Crystal field splittings of PrX_2 compounds (X = Pt, Rh, Ir, Ru, Ni) studied by inelastic neutron scattering	Phyisca **115B**	137-155	1983
J. C. M. Henning *E*	The structure of the Pt^- center in silicon	Physica **116B**	332-334	1983
B. Fitzpatrick, G. Neumark, R. Bhargava & J. Vermaak *N*	Structural defects and p-type conductivity in ZnSe	Physica **116B**	487-491	1983
M. P. A. Viegers, C. W. T. Bulle-Lieuwma & W. J. Bartels *E*	Overcompensation of misfit strain by dislocation networks in phosphorus implanted (001) silicon	Physica **116B**	612-615	1983

J. F. van der Veen*, L. Smit* (* *FOM, Amsterdam*), P. K. Larsen & J. H. Neave *E, R*	Core level binding energy shifts for reconstructed GaAs (001) surfaces	Physica **117B & 118B**	822-824	1983
J. F. M. Pennings *E*	Analysis of vinyl copolymer surfaces by XPS and surface reactions	Physiochemical aspects of polymer surfaces, Vol. 2, ed. K. L. Mittal, Plenum, New York	1199-1211	1983
K. S. Chung *E*	A noncoherent receiver for GTFM signals	Proc. GLOBECOM '82, Miami 1982	334-338	1982
A. W. Ludikhuize *E*	High-voltage DMOS and PMOS in analog IC's	Proc. IEDM 82, San Francisco 1982	81-84	1982
R. C. Powell (*Univ., Stillwater, OK*) & W. K. Zwicker *N*	Spectroscopic properties of Nd-laser materials	Proc. Int. Conf. on Lasers '80, New Orleans 1980	356-360	1981
A. Nicia & D. Rittich (Felten & Guillaume, Köln) *E*	Ball lens connector system for optical fibres and cables	Proc. 30th Int. Wire & Cable Symp., Cherry Hill, NJ, 1981	341-351	1982
D. Paterson *R*	Engineering metrology software	Proc. NELEX 82, Glasgow 1982	8 pp.	1982
J. S. Nadan *N*	Recent advances in digital optical recording	Proc. SPIE **318** (Pt I)	32-35	1982
F. J. A. den Broeder & S. Nakahara (*Bell Labs, Murray Hill, NJ*) *E*	Diffusion induced grain boundary migration and recrystallization in the Cu-Ni system	Scr. Metall. **17**	399-404	1983
R. W. Cooper *R*	An investigation of recombination in gold-doped PIN rectifiers	Solid-State Electron. **26**	217-226	1983
J. A. T. Verhoeven & H. van Doveren *E*	An XPS investigation of the interaction of CH_4, C_2H_2, C_2H_4 and C_2H_6 with a barium surface	Surf. Sci. **123**	369-383	1982
J. H. Waszink & G. J. P. M. van den Heuvel *E*	Heat generation and heat flow in the filler metal in GMA welding	Weld. J. **61** (Weld. Res. Suppl.)	269s-282s	1982

Contents of Philips Telecommunication Review **41**, No. 2, 1983

T. M. Schuringa: The relevance of telecommunication for rural areas (pp. 97-99)

T. M. Schuringa: Planning of telecommunication services in rural areas in non-industrialised countries (pp. 100-112)

M. de Couesnongle & C. R. Garnier: IRT 1500 integrated rural telephony system (pp. 113-125)

Philips electromechanical switching systems (p. 126)

E. R. Lockie: Rural radio telephone with Telex facility (pp. 127-133)

J. C. Leguyt & I. B. J. Rots: A DAMA satellite system for thin-route telephone communication (pp. 134-144)

M. J. Laarakker & E. Webers: Experience with transportable PRX exchanges (pp. 145-150)

G. H. Siebers: Solar power systems and passive-cooled shelters for unattended telecommunication sites (pp. 151-161)

Contents of Electronic Components & Applications **5**, No. 3, 1983

R. Croes: CMOS gate arrays — the fast way to semi-custom logic (pp. 130-141)

A. Goldberger: Data communications (pp. 142-147)

U. Dibbern & A. Petersen: The magnetoresistive sensor — a sensitive device for detecting magnetic field variations (pp. 148-153)

W. Golombeck: Circulators and isolators for reducing transmitter intermodulation (pp. 154-158)

W. H. A. van Dooremolen & M. Hufschmidt: A complete f.m. radio on a chip (pp. 159-170)

L. P. M. Bracke: Progress in SMPS magnetic component optimisation (pp. 171-180)

S. Ohr: Data converters for robotics (pp. 181-187)

Volume 41, 1983/84, No. 1 pages 1-32 Published 12th October 1983

Supplement to Philips Technical Review
Bijlage van Philips Technisch Tijdschrift
No. 20

June 1983

Recent United States Patents

Abstracts from patents that decribe inventations from the following research laboratories, that form part of or cooperate with the Philips group of companies:

Philips Research Laboratories, P.O.Box 80 000, 5600 JA Eindhoven, The Netherlands — *E*
Philips Research Laboratories, Cross Oak Lane, Redhill, Surrey RH1 5HA, Engeland — *R*
Laboratories d'Electronique et de Physique Appliquée, 3 avenue Descartes, 94450 Limeil-Brévannes, France — *L*
Philips GmbH Forschungslaboratorium Aachen, Weißhausstraße, 5100 Aachen, Germany — *A*
Philips GmbH Forschungslaboratorium Hamburg, Vogt-Kölln-Straße 30, 2000 Hamburg 54, Germany — *H*
Philips Research Laboratory Brussels, 2 avenue Van Becelaere, 1170 Brussels, Belgium — *B*
Philips Laboratories, N.A.P.C., 345 Scarborough Road, Briarcliff Manor, N.Y. 10510, U.S.A. — *N*

4 314 326

Rectifying circuit with zero correction

R.E.J. van de Grift — *E*

The invention provides a substantial improvement of a known rectifying circuit for a.c. signals by adding a circuit which measures the d.c. unbalance at the output and subsequently cancels said unbalance by feeding back compensation currents to the rectifying circuit. A dynamic range of 1 to 10,000 or more is then attainable. The rectifying circuit supplies a current whose shape is similar to that of the a.c. input signal, thus enabling r.m.s. values to be measured, for example in voltmeters.

---

4 317 210

Coherent receiver for angle-modulated data signals

C.B. Dekker — *E*
K.M. Boschma

A receiver for angle-modulated signals of the type sin $((\omega)t + \varphi(t))$, comprising a frequency transposition stage incorporating a local oscillator. A frequency shift $\Delta\omega$ of the local oscillator relative to the carrier frequency ω may cause the angle modulation signal $\varphi(t)$ to become faded. An argument detector produces the signal $[\varphi(t) + (\Delta\omega)t]$ which is differentiated by a differentiator to provide the signal $[d\varphi(t)/dt + \Delta\omega]$. A DEC-shift detector determines the DC-component $\Delta\omega$ of this signal. This component is integrated by an integrator to provide the signal $(\Delta\omega)t$, which is thereafter subtracted from the output signal of the argument detector to provide a clear angle modulation signal.

---

4 318 086

(B + A)-bit-A/D convertor with B-bit auxiliary A/D convertor

J.B.H. Peek — *E*
W.F.G. Mecklenbräuker
T.A.C.M. Claasen
N. van Hurk

An analog-to-digital converter is described for converting an analog-signal into a sequence of (b + a)-bit code words by means of a b-bit auxiliary analog-to-digital converter. To reduce the quantizing noise resulting from the requise quantizing of the analog signal samples this analog signal is applied to an integrating network whose output is connected to an amplitude-limiting device which brings the integrated signal within the signal range of the auxiliary analog-to-digital converter, which in its turn produces a sequence of b-bit code words which are applied to a digital output filter via a cascade arrangement of an amplitude-restoration device and a difference network. Sampling pulses which occur at a frequency exceeding the Nyquist sampling frequency associated with the analog signal are applied to the auxiliary analog-to-digital converter.

---

4 354 269

Apparatus for the processing of an information stream with the aid of an error-correcting convolutional code and apparatus for the detection of an error still irremediable in this processing

L.B. Vries — *E*
M.A. Diepeveen

A sequence of k-tuples of information elements is converted by means of an error-correcting convolutional code into a sequence of n-tuples (n greater than k) of code elements. In the processing of the code elements use is made of first of all a syndrome former to form a sequence of (n − k)-tuples of syndrome elements from the n-receiver sequence of n-tuples of code elements. From a segment of a number of successive (n − k)-tuples of syndrome elements one or more correction bits are formed in each case so as to be able to correct the receiver code bits and also, if a correction is apllied, to be able to update a number of further syndrome bits from that same segment. Furthermore an (n − k)-tuple of secondary syndrome bits or residue bits is formed in each case from this updated segment. A first value of such an (n − k)-tuple indicates the state in which the decoder must be provisionally considered as having corrected all errors in a predetermined sequence of n-tuples of code elements. Any other values indicate that an error has remained uncorrected. Such other values are converted into unreliability signals. The unreliability signal indicates a sub-sequence of n-tuples of code elements, in which the errors not corrected are located. Outside this sub-sequence the n-tuples can be reliable again.

4 319 279

Television imaging panel

F.H.M. Bergen E
M.G. Collet
L.J. van de Polder

An imaging panel comprising a buffer register inputs of which are connectable to the outputs of one of the rows of elements or connectable one after the other to outputs of several rows of the elements and whose outputs are coupled to the panel output. The buffer register is connected to a control circuit for shifting in each first field period of the interlaced picture each recorded information of an element row directly and fully, and for shifting in each second field period of the interlaced picture half of each recorded information of an element row, the other half being retained in the buffer register for confining it to half of the information to be shifted of he next row of elements.

---

4 354 993

Method of manufacturing a magnet body

F.X.N.M. Kools E
S. Strijbos

A method of manufacturing a sintered permanent magnetizable body essentially consisting of a ferrite of the formula $MeO.6Fe_2O_3$, wherein Me is at least one of the metals barium, strontium and lead by adding an acid to a suspension of the powdered ferrite in a liquid which suspension is then supplied to one or more matrices of a press to form a compressed product which is then sintered. As a result of the treatment with acid, the compression time is reduced.

---

4 355 204

Speech synthesizing arrangement having at least two distortion circuits

K. Riemens E
J.G.M. van Thuijl

This improved voice-excited speed synthesizer expands the voice-band spectrum to generate high-frequency band excitation signal by using two separate distortion networks: a full-wave rectifer for lower frequencies, and a limiter for higher frequencies. Channel and formant type voice excited embodiments are shown.

---

4 356 392

Optical imaging system provided with an opto-electronic detection system for determining a deviation between the image plane of the imaging system and a second plane on which an image is to be formed

S. Wittekoek E
T.A. Fahner

An optical imaging system is described which is provided with an opto-electronic detection system for determining a deviation between the image plane of the imaging system and a second plane on which an image is to be formed by the imaging system. After a first reflection on the second plane an auxiliary beam which is obliquely incident on said plane is reflected along itself and mirror-inverted, is subsequently reflected a second time on the second plane, and is finally incident on two detectors. The difference signal of the detectors, which is a measure of the deviation, is unaffected by tilting of the second plane and by local variations in reflectivity of in said plane.

4 356 512

Television keying circuit

K.H.J. Robers E

A keying circuit for television, in the form of a special effect generator or chroma-keying circuit. In order to generate a keying signal which does not cause flicker phenomena in an interlaced television picture when there is a great contrast in the region of a signal switchover between two video signals in response to the keying signal, the circuit comprises a signal delay circuit and a signal combining circuit for the binary keying signal which occurs undelayed and delayed. The signal delay device has delay times of a field period minus and plus one line period or of one and two line periods, respectively. This results in a gradually changing keying signal there, where the flicker phenomenon in the interlaced television picture might occur.

---

4 356 772

Magnetically levitated object

H. van der Heide E

A magnetically levitated carriage provided with a magnetic system suspension consisting of support magnets which magnetically cooperate via an air gap. The levitated carriage is maintained in a stable condition by means of a stabilizing device which substantially comprises a row of first stabilizing magnets connected to the levitated carriage and a row of parallel arranged second stabilizing magnets. The dynamic stiffness due to the stabilizing device is greater than the static stiffness due to the support magnets.

---

4 357 546

Integrated frequency divider circuit

G.A. Govaert E

A frequency divider circuit realized by means of two piled bistable transistor pairs, the signal, whose frequency is to be divided, being applied in phase to the emitters of the lower transistor pair and in phase opposition to the auxiliary emitters of the upper transistor pair.

---

4 357 555

Rotary anode X-ray tube

J. Gerkema E
E.M.H. Kamerbeek

An X-ray tube having a rotary anode which is supported by a bearing system comprising an axial magnetic bearing and at least one radial sleeve bearing. In operation, mutually cooperating metal (e.g. W or Mo) supporting faces of the sleeve bearing are separated by a liquid layer wetting the supporting faces. The liquid layer consists of a metal or a metal alloy, such as Ga or a Ga alloy, whose vapor pressure at 300°C is below 10^{-5} N/m^2, and which does not attack the supporting faces to any substantial extent. The tube has a long life, produces little noise during operation, and is of relatively simple construction.

4 357 658

System for the asynchronous transporting of data between active functional units

E.M.A.M. van der Ouderaa E

For mutual bidirectional communication, two active functional units are connected by a bidirectional data bus line and one unidirectional control line for each of the two directions. Both active functional units are each time connected, via an output circuit, to the relevant single connections of the data bus line. The output circuits have at least one first state in order to produce per first state, at a low impedance, a first data stata on the connection, and one second state for generating, at a high impedance, a second data state for the connection. When such a first and a second data states are simultaneously present on one and the same connection, the former state dominates. The second state can thus also act as an inactive state. A bidirectional data transport cycle for the first active functional unit includes the following steps: supplying data – transmitting a request signal – detecting an acknowledge signal – deactivating the transmitted data – changing over to the receiver state – terminating the receive state – transmitting the acknowledge signal.

---

4 357 696

Optical scanning apparatus with focusing system

M.P.M. Bierhoff E
K.A. Immink

Disclosed is an apparatus for optically scanning a record carrier in which the scanning beam is focused on the record carrier by a focusing system. For automatically correcting an incorrect control point of the focusing system, the apparatus is provided with a phase detector to which are applied the focusing error signal generated by the focusing system and a signal corresponding to the amplitude of the information signal being read. The output signal supplied by the phase detector is applied to the focusing system as correction signal so as to automatically correct for an incorrect control point of the focusing system.

---

4 357 799

Hot-gas reciprocating machine

J. Vos E

A hot-gas reciprocating machine comprises two intercommunicating spaces of variable volume and two pistons for varying the volumes of these spaces. The two pistons are coupled to two parallel crank shafts and are movable with an adjustable phase difference. For balancing the engine a system of counterweights is provided comprising a counterweight on each crank shaft and a counterweight on each of two auxiliary shafts which are coupled one to each crank shaft for rotation therewith at the same speed as in the opposite direction, each auxiliary shaft extending parallel with the associated crank shaft on the side thereof remote from the other crank shaft. The counterweight on each crank shaft is so arranged that the centrifugal force of that counterweight in the operation of the machine equal half the force produced by the reciprocating parts coupled to the respective crank shaft, and the counterweight on each auxiliary shaft is so arranged that the horizontal and vertical components of the centrifugal force of that counterweight always act respectively in the opposite direction to and the same direction as the corresponding components of the centrifugal force of the counterweight on the associated crank shaft.

4 358 711

Circuit arrangement for starting and operating a gas and/or vapor discharge lamp

H. Bex A

A circuit arrangement for starting and operating a discharge lamp by means of an electronic ballast includes a series arrangement of a PTC resistor and an ohmic resistor connected in parallel with an electronic switch of the ballast, with only the PTC resistor being in parallel with a control circuit of the electronic switch. The value of the ohmic resistor is eight to twelve times the cold resistance of the PTC resistor.

---

4 358 736

Phase comparison circuit

J. de Boer E

A phase comparison circuit for comparing first and second pulse trains applied to first and second inputs respectively, comprises a sawtooth signal generator which is phase-locked to the first pulse train by means of a frequency control loop comprising a first sampling circuit and an amplifier. The output signal of the sawtooth generator is sampled when each pulse occurs in the second pulse train by means of a second sampling circuit. In order that a phase difference of zero between the two pulse trains can be accurately determined, whatever their actual repetition frequency, the output signal of the arrangement is formed by means of a differential amplifier as the difference between the output signals of the two sampling circuits.

---

4 358 799

Apparatus for recording and/or producing signals

E. de Niet E

A helical scan video recorder having a reduced drum diameter in comparison with a two-head video recorder by the use of n heads, n being greater than two, and a tape wrap angle greater than 360 (n – 1)/n degrees. An important additional advantage of this recorder is that reproduction during recording (monitoring) is possible without the use of additional heads.

---

4 358 801

Disk unit with rotatable circular information disk

J.W. Faber E
P. van der Giessen

A disk unit comprises a circular information disk accommodated in an enclosure, at least one major wall of the enclosure being formed with a slot for an information write and/or read head of a disk drive apparatus, which slot is closed by means of a sliding plate of a slot sealing device when the disk unit is disposed outside the drive unit, and which slot can be opened by sliding the slyding plate from the closed position to the open position when the disk unit is inserted into a drive unit. An actuating member for moving the sliding plate is constituted by a lever which is journalled on the major wall in which the slot is formed, in such a way that a transmission ratio greater than unity is obtained between a free end of the lever which is externally accessible to the drive unit and a second free end which is connected to the sliding plate.

4 359 776

Device for generating or amplifying coherent electromagnetic radiation, and method of manufacturing the device

G.A. Acket E
P.J. de Waard
G.D. Khoe
G.C. Wirtz
T.E. Rozzi

A semiconductor laser/amplifier is disclosed in which the radiation oscillates only in one longitudinal mode. According to the invention this is achieved by a stripshaped active region which exhibits periodic variations in amplification (and preferably also in the amplification profile) in its longitudinal direction over at least a part of its length. The period of the amplification variation is at least ten times the wavelength of the radiation.

---

4 359 892

Arrangement for measuring surface profiles

A. Schnell A
H. Oepen

A surface testing apparatus includes a bilaminar ceramic flexure element provided with means for generating a voltage which is proportional to the deflection of the flexure element. This voltage is compared with a reference voltage. After amplification the difference voltage is applied to the flexure element so that the applied force remains constant, independently of the deflection.

---

4 360 823

Semiconductor device having an improved multilayer wiring system

J.A.A. van Gils E

A semiconductor device includes a first metallization pattern which is sunken into a portion of a first insulating layer on the semiconductor body. This first metallization pattern is sunken through only a part of the thickness of the first layer and its surface substantially coincides with that of the first layer. The first metallization pattern and first insulating layer are covered with a second insulating layer, and a second metallization pattern is provided on the second insulating layer. In order to provide contact with desired regions of the semiconductor device, the second metallization pattern extends through contact holes in the underlying second layer to provide the desired electrical connections. This configuration results in a flatter, more efficient and at the same time a more reliable multiple-layer metallization system.

---

4 361 727

Sound reproducing arrangement for artificial reverberation

N.V. Franssen E

An artificial reverberation arrangement comprising a number of mechanical units each of which comprises a microphone, an amplifier and a loudspeaker. These units are arranged in such a way relative to each other that the microphone of one specific unit receives substantially less sound energy from its own associated loudspeaker than from all the other loudspeakers of the arrangement.

4 361 801

Microwave method for measuring the relative moisture content of an object

W. Meyer H
W. Schilz

The moisture content of an object is determined by placing the object in a field produced by a microwave applicator and measuring the dielectric properties of the applicator. The measured properties are used to derive the moisture content from known dielectric properties for the apllicator without the object present, and from known moisture/dielectric properties for the specific material of the object.

---

4 364 986

Drye-containing layer of a film-forming polymeric binder and the use thereof in an information recording element

D.J. Zwanenburg E
W.P.M. Nijssen
C.G.I. van der Staak

Dye-containing layer of a film-forming polymeric binder and the application thereof in an information recording element. The invention relates to a dye-containing layer in which dye, if desired in a very large weight percentage is dissolved or finely divided in a copolymer (1:1) of methyl vinyl ether and maleic anhydride or a semi-ester thereof. The dye-containing layer is particularly suitable for use as a recording layer in an optical information recording element.

---

4 365 323

Optical read unit for scanning a record carrier having a radiation-reflecting information structure

J.P.J. Heemskerk E
K.A. Immink
C.A.J. Simons

An optical read unit is described for scanning a record carrier with a radiation-reflecting trackwise-arranged information structure. The read unit utilizes a diode laser which generates the read beam and also detects the information stored on the record carrier. The read unit is also provided with an opto-electronic system for detecting the position of the read spot relative to a track to be read and the position of the plane of focusing. The diode is mounted in a housing and the unit includes electromechanical apparatus for moving the housing in two perpendicular directions so as to correct the position of the read spot. The objective system for the formation of the read spot is of simple construction.

---

4 366 346

Artificial reverberation apparatus

E.C. Dijkmans E
N.V. Franssen

Artificial reverberation apparatus comprising a delay device provided with a feedback circuit and a feed-forward circuit having a gain equal and opposite to that of the feedback circuit if the gain in the delay device is unity. In order to simulate a second echo having a different delay time using a minimum number of circuit components, the foregoing reverberation circuit is included in cascade with a second delay device and the resulting combination is provided with its own feedback circuit and feed-forward circuit. In order to simulate a third echo having yet another delay time, the resulting circuit may be included in cascade with a third delay device with the resulting combination having its own feedback circuit and feed forward circuit.

Supplement to Philips Technical Review
Bijlage van Philips Technisch Tijdschrift
No. 21

September 1983

Recent United States Patents

Abstracts from patents that describe inventions from the following research laboratories, which form part of or cooperate with the Philips group of companies:

Philips Research Laboratories, Eindhoven, The Netherlands	*E*
Philips Research Laboratories, Redhill, Surrey RH1 5HA, England	*R*
Laboratoires d'Electronique et de Physique Appliquée, 3 avenue Descartes, 94450 Limeil-Brévannes, France	*L*
Philips GmbH Forschungslaboratorium Aachen, Weißhausstraße, 51 Aachen, Germany	*A*
Philips GmbH Forschungslaboratorium Hamburg, Vogt-Kölln-Straße 30, 2000 Hamburg 54, Germany	*H*
Philips Research Laboratory Brussels, 2 avenue Van Becelaere, 1170 Brussels (Boitsfort), Belgium	*B*
Philips Laboratories, N.A.P.C., 345 Scarborough Road, Briarcliff Manor, N.Y. 10510, U.S.A.	*N*

4 366 564

Apparatus for writing digital information in a disc-shaped optically readable record carrier

M. R. de Haan *E*
M. G. Carasso

An apparatus for recording optically detectable information in a record carrier provided with information areas arranged in accordance with a spiral or concentric track pattern, which areas alternate with synchronization areas each containing the address of the associated information area. Recording is effected with a first modulated laser beam, while a second beam is projected after the first beam for reading the recorded information. The track pattern has previously been provided with a periodic track modulation of a frequency at which the power spectrum of the information to be recorded has a substantially zero value. The apparatus comprises a first and a second filter for filtering signal corresponding to the track modulation out of the signal derived by detecting the first or second laser beam reflected or transmitted by the record carrier. In series with the second filter there is included a delay network from which a synchronization signal is available. Furthermore, there is provided a phase comparator which, during reading of the synchronization areas, determines the phase difference between the signals obtained from the first and the second filter and which controls the delay network in such a way that the output signal of the delay network is in phase with the output signal of the first filter.

---

4 370 797

Method of semiconductor device for generating electron beams

G. G. P. van Gorkom *E*
A. M. E. Hoeberechts

The invention relates to a semiconductor cathode and a camera tube and a display tube, respectively, having such a cathode, based on avalanche breakdown in a p-n junction extending parallel to the surface of the semiconductor body. The released electrons obtain extra energy by means of an accelerating electrode provided on the device. The resulting efficiency increase makes the manufacture of such cathodes in planar silicon technology practical. Since the depletion zone of the p-n junction upon a avalanche breakdown does not extend to the surface, the released electrons show a sharp, narrow energy distribution. This makes such cathodes particularly suitable for camera tubes. In addition they find application, for example, in display tubes and flat displays.

4 371 748

Device for artificial reverberation

E. C. Dijkmans *E*
K. A. Immink

An artificial reverberation device comprising first, second, third and fourth delay lines and first and second adder circuits with at least a part of said first, second, third and fourth delay lines connected in a cascade arrangement with the first and second adder circuits. First and second feedback circuits and first and second transmission paths are coupled to the cascade arrangement so as to produce a multiple reverberation effect with a minimum number of components.

---

4 371 795

Dynamic MOS-logic integrated circuit comprising a separate arrangement of combinatory and sequential logic elements

C. Mulder *E*
L. Nederlof
C. Niessen
R. M. G. Wijnhoven
R. H. W. Salters

An integrated circuit in dynamic MOS logic is composed of combinatory and sequential logic elements. Each of the latter comprises a succession of an input gate, an intermediate gate and an output gate which are activated to conduct by a corresponding phase of the first one and subsequent phases of a clock pulse cycle. The combinatory logic elements are all composed of gates of a single type, while the input signals are applied via the sequential logic elements and the output signals are output again via the latter elements. Thus, in the combinatory network only a sole type of interference is still relevant.

---

4 371 868

Method and device for the automatic calibration of an analog-to-digital converter

R. E. J. van de Grift *E*
R. J. van de Plassche
E. C. Dijkmans

For the automatic calibration of an analog-to-digital converter an analog calibration quantity is measured and the digital signal is compared with a digital calibration signal associated with the calibration quantity. A digital difference signal is applied to a register

for influencing its counting capacity, while the register contents of pulses counted during the measurement also represents one of the parameters involved in the analog-to-digital conversion. Because of the fully digital character of the calibration, this calibration can be performed very rapidly and accurately.

4 374 302

Arrangement and method for generating a speech signal

L. L. M. Vogten E
L. F. Willems

LPC-synthesizing device, in which a modulation of the synthesized signal with a window signal is used to reduce the buzz which is characteristic for such devices. This window signal has an amplitude which initially increases gradually from substantially zero value to a constant value, and then decreases gradually from the constant value to substantially zero value. As a result of this modulation the signal in the transition between two segments of voiced speedh is forced to zero thereby eliminating any transition discontinuities, the existence of which causes the buzz.

4 374 324

Optical focusing device with inclination detection

G. E. van Rosmalen E
W. G. Opheij

In order to improve the focusing of radiation from a source onto an object, in example for a "VLP" or "Compact Disk" system, a further control signal from an object-inclination detector is added to the focusing error signal, yielding improved control stability and smaller focusing errors.

4 374 452

Apparatus for manufacturing a color display tube

J. Koorneef E

An apparatus for fabricating a quadrupole shadow mask includes a reel for storing a web of insulating material having a conductive layer on one side thereof, a reel for storing a long metal strip having a plurality of spaced apertures arranged in parallel rows, means for cutting the web into strips and a roller having circumferential grooves for positioning and then pressing the insulating strips onto the surface of the metal strip between the rows. The resulting strip is guided through a heating device and then is cut into sheets of predetermined length.

4 374 698

Method of manufacturing a semiconductor device

J. A. M. Sanders E
F. H. M. Sanders
H. Kalter
E. P. G. T. van de Ven

A method of manufacturing a semiconductor device in which layers of silicon nitride and silicon oxide are etched by bringing the layers into contact with constituents of a plasma which is formed in a gas mixture which contains a fluoride compound and an oxygen compound. By addition of from 1 to 15% by volume of a gaseous compound which contains a halogen other then fluoride to the gas mixture, silicon nitride layers can be etched at least five times faster than silicon oxide layers. The method is thus suitable in practice, for example, for manufacturing a silicon nitride mask for the formation of a field oxide in LOCOS processes.

4 374 699

Method of manufacturing a semiconductor device

J. A. M. Sanders E
F. H. M. Sanders

A method of manufacturing a semiconductor device in which an organic lacquer layer which is locally present on a substrate is etched by bringing the layer into contact with constituents of plasma which is formed in a gas mixture which contains a halogen compound and an oxygen compound. If the mixture contains more than 25% by volume of an oxygen compound from the group CO_2 and NO, the organic lacquer layer can be etched away from 500 to 1000 times faster than poly Si.

4 375 058

Device for reading a printed code and for converting this code into an audio signal

H. Bouma E
D. G. Bouwhuis
P. M. Boers
J. C. Jacobs

A carrier containing information which is suitable for visual perception, such as a text or a picture. By suitable positioning, a code also present on the carrier linked thereto. This code is visible to the user, but cannot be read directly. A device for reading the code having a scanner which can be moved into the area of the code by hand. The code is optically read, synchronization signals being obtained from the code itself. The information read is stored in an intermediate memory. The intermediate memory is subsequently read under the control of a clock. This data can either directly activate an acoustic generator for producing a sound signal, or can address an object memory which in its turn supplied data for controlling the acoustic generator. A sound signal is thus linked to the picture or the text. A device of this kind may from part of an educational system.

4 375 257

Hydrogen storage and supply device

H. A. C. M. Bruning
J. H. N. van Vucht
F. F. Westendorp
H. Zijlstra

A hydrogen storge and supply device in which a pressure vessel contains a hydride of the gross formula AB_nH_m, in which A is calcium or one of more of the rare earth metals with or without thorium, zirconium, or halfnium, B is nickel and/or cobalt, with or without iron and/or copper, n has a value between about 3 and 8.5 and m has a value exceeding 0 and up to about 7.

4 375 623

Arrangement for the transmission of audio signals

N. V. Franssen E
K. A. Immink
E. C. Dijkmans
M. H. Geelen

An arrangement for the transmission of audio signals, comprising a delay line provided with 5, 7 or 9 tappings situated at equal time intervals along the delay line. The tappings are each connected to a common adding circuit via an amplitude control device. The ratios between the amplitudes of the output signals of the amplitude control devices, viewed from one end of the delay line to the other end are $1:2n:2n^2:-2n:1$ for five tappings, $1:2n:2n^2:n^3-n:-2n^2:2n:-1$ for seven tappings, and $1:2n:2n^2:n^3-n:{}^1/_4(n^4-1)-2n^2:-(n^3-n):2n^2:-2n:1$ for nine tappings. This yields an arrangement having a flat frequency response from the input of the output. The invention also relates to a plurality of delay lines connected in series and to a reverberation unit provided with such a transmission arrangement.

4 375 686

Semiconductor laser

P. J. de Waard E

A semiconductor laser includes an active layer of a first conductivity type comprising a strip-shaped active region formed by a doping of the second conductivity type over at least a part of the thickness of the active layer. According to the invention, the active region consists of a number of zones of the second conductivity type which are

separated by material of the first conductivity type and which, viewed in the longitudinal direction of the active region, have a maximum dimension of at most 20 μm. Upon ageing, crystal defects in the zones will not expand beyond the zones, thus extending the usable lifetime of the laser.

---

4 375 832

Tube and fin radiator

G. A. Asselman
A. P. J. Castelijns
A. J. van Mensvoort

A radiator comprising a number of parallel cooling medium pipes having fin stacks secured thereto in which a metal strip of the desired width dimensions is zigzag folded to form a stack having successive fin parts and side parts, each fin part being divided into stepwise parallel portions by additional fold areas parallel to the side parts.

---

4 376 307

Semiconductor laser or intensifier

T. E. Rozzi E
J. H. C. van Heuven

A semiconductor laser or traveling wave intensifier has an active layer between two passive semiconductor layers, and a strip-shaped electrode geometry. The active layer is uniform in thickness, while at least one of the passive layers within the strip-shaped geometry comprises a strip-shaped zone which contains portions having different refractive indices n_1 and n_2. According to the invention it holds that $n_1 - n_2)(d_1 - d_2) > 0$, wherein n_1 is the refractive index of the portion which at least within said strip-shaped zone adjoins the active layer, d_1 is the thickness thereof within the strip-shaped zone, and d_2 is the thickness thereof beside the strip-shaped zone.

---

4 376 977

Computer system with scannable program memory

B. T. J. Bruinhorst E

A computer system having a program memory for machine instructions to be executed and for other data not included in machine instructions to be executed, also a keyboard, a display device and a processor. In the program memory a quantity of such other data is preceded by a special code from a pre-determined set of not-to-be-executed machine codes plus an adjacent indication giving the address distance between the beginning and the end of the other data in question. A decoder that can address specifically the machine-code set is connected to the instruction register. An address-distance detector is also connected. Together, these elements generate a signal to process the quantity of other data in a specific way and, in particular, not to treat them as further machine instructions. In the design phase of a program, no large capacity memory is required for the text because all relevant information can be stored in a program memory of limited capacity because the machine program has a very compact notation.

---

4 378 331

Hydrides of the formula A_DNH_M

H. A. C. M. Bruning E
J. H. N. van Vucht
F. F. Westendorp

Then invention is directed to hydrogen absorbing compounds which are useful for storing, keeping and releasing hydrogen gas. Such compounds have the formula $LA_\chi Ce_{1-\chi}Ni_5$ where χ lies between 0.4 and 1. The compounds may also be lanthanium/nickle compounds which contain copper zirconium or yttrium.

4 379 021

Method of manufacturing single crystals

J. P. M. Damen E
T. J. Berben

A method of manufacturing a single crystal of a composite oxide by gradual solidification of a melt with solidification starting from a seed crystal which initially is in contact with the melt, is provided wherein to obtain a single crystal having a composition which is as homogeneous as possible (homogeneous within 1 mol.%) the following measures are taken: first, initially the melt consists of no more than 25% by weight of the single crystal to be grown; and second, during the solidification process molten material is added to the melt at the same rate and having the same composition as material solidifies out from the melt.

---

4 379 030

Aluminium electroplating solution

T. E. G. Daenen E
G. A. R. van Dijk
S. A. Stolk

Electrolyte liquid for the electrodeposition of aluminum, consisting of a solution of a ligand of one or more aluminum halohydrides in an aprotic solvent. The ligand is, for example, tetrahydrofuran or triethylamine. This liquid makes it possible to deposit ductile aluminum up to high current densities.

---

4 379 230

Automatic beam correction in a scanning transmission electron microscope

G. Bouwhuis E
H. de Lang
N. H. Dekkers

In a scanning electron microscope, a periodic structure in the object plane is used for the detection of the focus condition of a spot-focused electron beam scanning an object in order to correct defocusing and astigmatism in the scanning electron beam spot. To achieve this the detector comprises a plurality of individual elements which can be pair-wise read and an electronic circuit for forming a control signal for controlling the excitation of a spot-forming lens and a stigmator, respectively, from signals representing movement of the electron interference pattern at the detector, relative to the object scan, due to an out of focus condition. The signals are derived from corresponding pairs of detector elements which are situated at a fixed distance from each other in order to correct the focus and compensate for the astigmatism in the electron beam respectively. In the case of astigmatism, signals from at least two pairs of detector elements spaced in directions at right-angles to one another, are used.

---

4 379 251

Cathode-ray tube

M. Brouha E
W. W. van den Hoogenhof
P. C. van Loosdregt

In a cathode-ray tube for displaying colored pictures comprising in an evacuated envelope means to generate a number of electron beams, a display screen comprising a number of regions luminescing in different colours, and colour selection means comprising a large number of apertures which assign each electron beam to luminescent regions of one colour, in which colour selection means a magnetic quadrupole field is generated to form a magnetic quadrupole electron lens in each aperture, which luminescent regions have the shape of substantially parallel strips the longitudinal direction of which is substantially parallel to the defocusing direction of the quadrupole lens, characterized in that the apertures are elongate, substantially hexagonal and symmetrical relative to theire longitudinal axes in a number of parallel rows which extend substantially parallel to the strips and the apertures of two juxtaposed rows are shifted relative to each other, it is possible, in spite of the large transmission of the colour selection means, to obtain a display screen having very uniform phosphor strips.

4 380 366

Detachable connector for optical fibres

A. J. J. Franken E
F. M. Coolen
G. D. Khoe
J. Langerhorst
H. W. W. Smulders

A connector for connecting optical fibres comprises three portions: centering means for centering the fibre with respect to a housing in which the fibre has been inserted, a profiled edge on each housing for centering housings with respect to each other, and fixing means for connecting two housings to each other. The edges of the housings are resilient with respect to the rest of the housing so that reference faces of the connector can be pressed together by springing back the edges.

---

4 380 708

I^2L with polysilicon diodes and interconnects

C. M. Hart E

An integrated circuit includes a number of diode-coupled gate circuits, each having an inverter transistor. The logic signals are coupled between the gate circuits by conductive tracks which also form the coupling diodes. These diodes are mono-poly or poly diodes, and are formed integrally with the conductive tracks to achieve a flexible yet simple construction.

---

4 381 967

Method of manufacturing a semiconductor device

F. H. M. Sanders E
J. A. M. Sanders
J. Dieleman

A method of manufacturing a semiconductor device where a layer which is present on a substrate and which is locally covered with an organic lacquer layer is etched by bringing the layer into contact with constituents of a plasma which is formed in a gas mixture containing a halogen compound and an oxygen compound. The rate at which the organic lacquer layer is removed by the constituents of the plasma is substantially reduced by the addition of from 1 to 15% by vol. of CO to this gas mixture.

---

4 383 227

Suspended microstrip circuit for the propagation of an odd-wave mode

F. C. de Ronde E

A suspended microstrip circuit having a dielectric substrate arranged in parallel between two parallel metal planes. First and second strip conductors are provided on the substrate, the second strip conductor being in parallel with the first strip conductor and coupled thereto. A wave phenomenon can propagate through the conductor pair in an odd mode. The metal box accommodating the microwave circuit may now be much greater so that in most cases one box is sufficient. Microwave components such as magic-T, series-T, shunt-T, circulators, filters, attenuators, can be implemented with the suspended microstrip line.

---

4 384 038

Method of producing integrated optical waveguide circuits and circuits obtained by this method

G. D. Khoe E, A
H. G. Kock
D. Küppers
H.-J. Lydtin

Optical waveguide circuits, such as signal splitters, can be produced by etching grooves in a transparent, glass substrate and by filling the grooves with glass having a higher refractive index than the material of the substrate. The grooves have a semicircular cross-section and the filling glass is produced by a low temperature plasma-activated chemical vapor deposition process. Two substrates can be placed on top of each other, with the surfaces in which the filled grooves have been provided in contact, to form an integrated optical circuit.

4 384 335

Method of and system for determining the pitch in human speech

H. Duifhuis E
L. F. Willems
R. J. Sluyter

Method of and arrangement for the determination of the pitch of speech signals in a system of speech analysis, wherein sequences of significant peak positions of the amplitude spectrum of a speech signal are derived from time segments of the speech signal by means of a discrete Fourier transform. In order to reduce the influence of noise signals and noise components, respectively, in the amplitude spectrum the significant peak positions are compared with different masks, which have apertures at harmonic distances of the associated fundamental tone. The mask which matches the sequence of significant peak positions best is selected. A probable value for the pitch is now computed with the harmonic numbers now known of the significant peak positions which are located in apertures of the selected mask. The mean square error between these significant peak positions and the corresponding harmonics of the finished tone can be used as a criterion.

---

4 385 916

Method of producing an optical fiber having a core which has a noncircular cross-section, and double crucible for use in this method

C. M. G. Jochem E
P. J. W. Severin

An optical fiber having a circular outer cross-section and having a core which has a noncircular cross-section is produced by using a double crucible. The outer crucible is provided with a ring-shaped channel of which at least one of the boundary walls has a noncircular cross-section. The glass of the outer crucible is passed through this channel before it is contacted with the glass of the inner crucible.

---

4 386 268

Envelope for a photodiode

H. G. Kock E

An envelope for a photodiode which serves as a detector of light signals comprises a support and a metal cap-shaped member connected hermetically to the support. A metallized glass light conductor passed through an aperture of the cap-shaped member is connected in the aperture by means of solder. One end of the light conductor extends up to the photodiode; the other end projects from the cap-shaped member and is surrounded by the wall of an aperture on one side of a blocked-shaped member, in which aperture an optical fiber can be incorporated on the other side.

---

4 386 323

Arrangement for synchronizing the phase of a local clock signal with an input signal

G. L. M. Jansen E

Synchronizing the phase of a locally generated clock signal with the phase of an input signal is usually effected by using a phase-locked loop, but this has a drawback that a certain run-in time is necessary to be sure that the phase of the clock signal is stable. The present arrangement comprises a delay line having taps, the delay line being driven by a crystal oscillator. Clock signal versions which are phase shifted relative to one another through 90° are available at the successive taps. A coincidence detection circuit comprising trigger circuits and a combining network detects the version of the clock signal whose ascending edge, for example, is located nearest to an ascending edge of the data signal, and this version is supplied as the clock signal at an output.

PHILIPS TECHNICAL REVIEW

VOLUME 41, 1983/84, No. 2

Optical switching with bismuth-substituted iron garnets

P. Hansen, B. Hill and W. Tolksdorf

Now that we stand on the threshold of the era of communication by means of optical fibres, the switching of optical signals has become very important. During the last thirty years the magnetic effects in garnet crystals have been extensively studied. This work was started because of the applications at microwave frequencies, but was later found to be of interest for the development of backing-storage systems, including the use of magnetic 'bubbles'. The investigations showed that the Faraday effect in garnets could be turned to good use in optical switching devices. In the early seventies, work by P. F. Bongers, T. J. A. Popma, J. M. Robertson and S. Wittekoek at Philips Research Laboratories in Eindhoven revealed that the Faraday effect could be greatly enhanced by substituting bismuth in gadolinium-iron garnet [*]. With this solid foundation established, the work on magneto-optical effects in garnets was continued at Philips Research Laboratories in Hamburg. The good understanding of the physical background and the mastery of the technology for making garnet single crystals and growing epitaxial layers on them paved the way for the manufacture of optical switching devices such as the LiSA 512 light-switching array.

Introduction

Magneto-optical effects in garnet crystals have been the subject of keen interest since the mid-sixties. In the efforts to develop computer memories with higher packing densities the Kerr effect and the Faraday effect seemed to offer good prospects [1]. At Philips laboratories as well there was research on the application of garnets and other magneto-optical materials as a basic material for storage devices. The work was concerned with 'bubble memories', storage devices in which magnetic domains can move [2], and with garnet storage wafers in which the data is written and read out by means of a laser beam [3].

Since then the enthusiasm for the large-scale manufacture of bubble backing-storage devices has lessened to some degree. It turns out that the costs associated with an entirely new technology were higher than expected, and in addition there have been unexpectedly rapid developments in the capacity and price of semiconductor backing-storage systems [4].

Although the outlook for garnets in bubble memories seems rather less promising, the application of garnets for controlling the transmission of visible light remains as interesting as ever. Possible applications include displays, printers and fibre-optics telecommunication systems. In all these applications a current

Dr P. Hansen, Dr B. Hill and Prof. Dr W. Tolksdorf are with Philips GmbH Forschungslaboratorium Hamburg, Hamburg, West Germany.

[*] These investigations have resulted in a Netherlands patent No. 160659 (granted 16th October 1979) and an American patent No. 3838450 (granted 24th September 1974).

[1] P. Dekker, Manganese bismuth and other magnetic materials for beam addressable memories, IEEE Trans. **MAG-12**, 311-327, 1976.

[2] J. A. Pistorius, J. M. Robertson and W. T. Stacy, The perfection of garnet bubble materials, Philips Tech. Rev. **35**, 1-10, 1975.

[3] H. Heitmann, B. Hill, J.-P. Krumme and K. Witter, MOPS, a magneto-optic storage wafer of the discrete-bit type, Philips Tech. Rev. **37**, 197-206, 1977.

[4] J. G. Posa, Memories, Electronics **54**, No. 21 (Oct. 20), 130-138, 1981.

pulse changes the transmission in a small domain in a material that is normally transparent to visible light.

The rotation of the plane of polarization of linearly polarized light under the influence of a magnetic field with a component in the direction of propagation of the light was first observed in 1845 by Michael Faraday, and is known as the Faraday effect. It arises because some media have different refractive indices for clockwise and anticlockwise circularly polarized light. The effect is not reciprocal, i.e. the rotation of the plane of polarization does not return to zero when the light passes through the medium in the opposite direction — unlike the rotation of the polarization plane in optically active substances.

The magneto-optical switching devices that are the subject of this article consist of a substrate of non-ferrimagnetic single-crystal garnet, to which has been applied a thin film of ferrimagnetic single-crystal garnet with the [111] direction of the cubic lattice perpendicular to the film. The Faraday rotation of polarized light passing perpendicularly through the film is caused by the internal magnetization in the same direction due to the presence of magnetic moments of iron and gadolinium atoms in the crystal structure. When the direction of the internal magnetization of the material is reversed, the Faraday rotation changes from anticlockwise to clockwise or vice versa; see *fig. 1*. Since there is an analyser *AN* for polarized light behind the substrate, there is contrast between domains in the ferrimagnetic film that are magnetized in opposite directions. The magnetization is 'frozen into' the material, because the temperature of operation is close to the compensation temperature of the film. (The term 'compensation temperature' will be clarified presently.) The magnetization can be locally reversed by raising the temperature while at the same time applying an external field. This makes it possible to obtain a different distribution of light and dark areas. These effects have been studied for some time in our laboratories and have also been described in this journal [2][3].

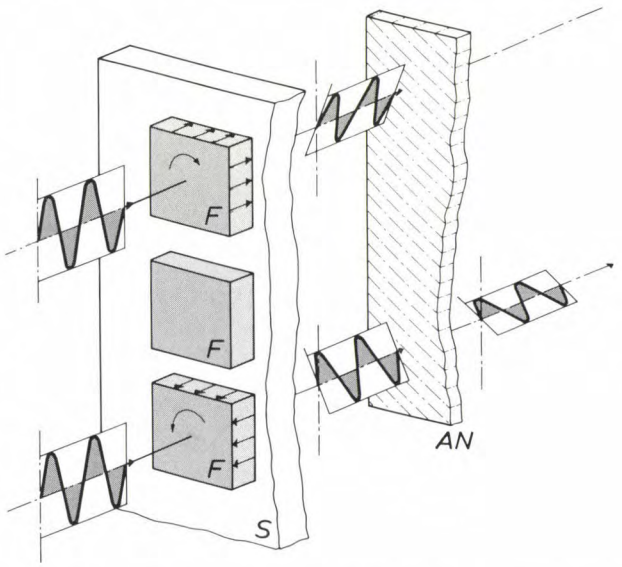

Fig. 1. Operation of a magneto-optical switching device. A substrate *S* of a single-crystal non-ferrimagnetic garnet is covered with a thin ferrimagnetic garnet film, parts of which have been removed by etching, leaving ferrimagnetic domains *F*. Polarized light passing through the ferrimagnetic domains undergoes Faraday rotation. The rotation of the plane of polarization is anticlockwise or clockwise, depending on the direction of the internal magnetization. The analyser *AN* produces a difference in contrast between domains magnetized in opposite directions.

The ferrimagnetic films for our devices must give a large Faraday rotation and low absorption, and their compensation temperature should be approximately equal to room temperature. We shall show how the physical properties of the gadolinium-iron garnet film material can be affected by substituting atoms of elements such as bismuth and gallium. The substitution of bismuth increases the Faraday rotation [5]; gallium is substituted to bring the compensation temperature closer to room temperature. With a film of the right composition a non-ferrimagnetic substrate material is required that has exactly the same lattice constant and minimum absorption. After extensive investigations we can now predict the ratio of the constituent elements for a single-crystal substrate with a defined lattice constant. This can be made equal to the lattice constant of the epitaxial ferrimagnetic film that will be grown later on a slice of the single crystal. Because of the importance of good process control, our laboratories continued to take an interest in the batch production of the LiSA 512 light-switching array. We designed LiSA 512 and it was put into production by the Philips Elcoma division (at Valvo, Hamburg).

We shall first look at the crystal structure of garnets, and then we shall consider the Faraday effect in more detail and examine the influence of the substituted elements in the film. We shall also discuss the matching of the lattice constant of a substrate to that of the film and describe the fabrication of substrate and film. In conclusion we shall consider some applications.

Crystal structure and magnetic properties of garnets

For completeness we shall first deal briefly with the structure of garnet crystals and with the magnetic properties that are relevant to this article.

The best-known magnetic garnet is yttrium-iron garnet, $Y_3Fe_5O_{12}$ or YIG, which is used in a modified form in microwave applications and in bubble memories. We have investigated the properties of yttrium-iron garnet and of gadolinium-iron garnet and varied the properties by substituting other elements. The

structure of $Gd_3Fe_5O_{12}$ is shown in *fig. 2*. The composition of the garnets discussed in this article is given by the formula $R_3A_2B_3O_{12}$, in which the trivalent R ions are rare earths such as lutetium, yttrium, gadolinium or other large ions, and the A and B ions are smaller ions, such as the transition metal ions Fe^{3+}, or diamagnetic ions, such as Ga^{3+} or Al^{3+}. The R ions are surrounded by a dodecahedron (not the regular one, but a 'distorted cube') of eight oxygen ions, the B ions by a tetrahedron of four oxygen ions and the A ions by an octahedron of six oxygen ions. The basic structure of garnets is cubic. The red body diagonal in the left-hand figure, corresponding to the [111] direction, forms a local axis of threefold symmetry owing to the presence of the two sets of three Gd^{3+} ions, shown as red dots.

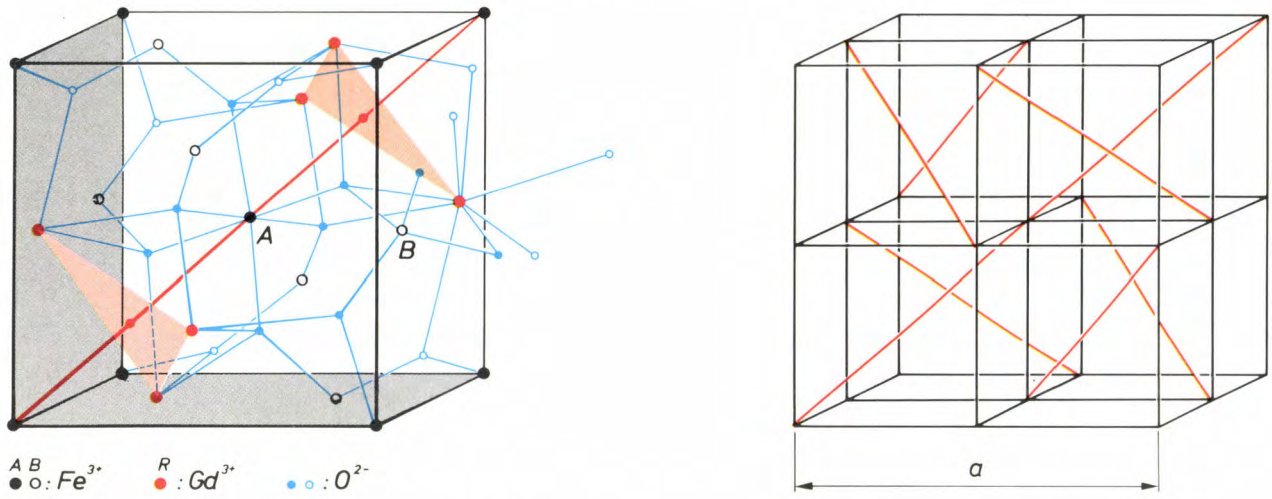

Fig. 2. Crystal structure of $Gd_3Fe_5O_{12}$ [6] (gadolinium-iron garnet), or in general $R_3A_2B_3O_{12}$. The diagram on the right shows a complete unit cell; a is the lattice constant; the diagram on the left gives the details of an eighth part of the unit cell. The positions of the ions in the complete cell are obtained when the cube with edge $a/2$ (the eighth part of a unit cell) on the left is made to overlap the cubes with edges $a/2$ on the right-hand figure, successively turned so that the red diagonals coincide. The Fe^{3+} ions, shown as black dots (A in $R_3A_2B_3O_{12}$), are surrounded by octahedrons of six oxygen ions and form a body-centred cubic lattice. The Fe^{3+} ions, shown as black rings (B in $R_3A_2B_3O_{12}$), are surrounded by tetrahedrons of four oxygen ions. The groups of six and four oxygen ions surrounding the two Fe^{3+} ions A and B are indicated by blue dots; the other oxygen ions by blue rings. The two groups of three Gd^{3+} ions, linked by a red plane (R in $R_3A_2B_3O_{12}$), give rise to threefold symmetry at the location of the Fe^{3+} ion A. This axis of symmetry coincides with the red diagonal.

When a thin ferrimagnetic garnet film is grown epitaxially on a (111) plane of a non-ferrimagnetic substrate, uniaxial magnetic anisotropy is produced in the [111] growth direction. As a consequence of this anisotropy the direction of the magnetic polarization — which would normally be in the plane of the film to correspond with a minimum of magnetic energy — is perpendicular to the film. This alignment of the polarization could be considered as the result of the presence of an effective magnetic field. This effective field is called the anisotropy field H_a and it depends on the composition of the film and the growth conditions [7].

The magnetic polarization J of the film can be regarded as the sum of all the magnetic dipole moments j of the Fe^{3+} ions in the tetrahedral and octahedral sublattices and the Gd^{3+} ions in the dodecahedral sublattice. The coupling between the sublattices is antiferromagnetic; see *fig. 3a* and *b*. In fig. 3*a* the magnitude of the total magnetic saturation moment m_s per unit of $Gd_3Fe_5O_{12}$ (an eighth part of a unit cell — see fig. 2) in Bohr magnetons μ_B is plotted as a function of absolute temperature. At absolute zero the total moment of 16 μ_B is composed of the moments of the electron spins of the Fe^{3+} ions ($+10$ and -15 μ_B) and of the Gd^{3+} ions ($+21$ μ_B); see fig. 3*b*. The antiferromagnetic ordering of the submoments of the individual ions is the characteristic of ferrimagnetism.

[5] Investigations at Philips Laboratories in Eindhoven and Redhill, Surrey, England, led to the design of a theoretical model in 1972 for describing the influence of bismuth on Faraday rotation in garnets; see S. Wittekoek and D. E. Lacklison, Investigation of the origin of the anomalous Faraday rotation of $Bi_xCa_{3-x}Fe_{3.5+0.5x}V_{1.5-0.5x}O_{12}$ by means of the magneto-optical Kerr effect, Phys. Rev. Lett. **28**, 740-743, 1972.

[6] From P. P. Ewald and C. Hermann, Strukturbericht 1913-1928, Akad. Verlagsges., Leipzig 1931, p. 364.

[7] P. Hansen, K. Witter and W. Tolksdorf, Magnetic and magneto-optic properties of lead- and bismuth-substituted yttrium iron garnet films, Phys. Rev. B **27**, 6608-6625, 1983.

It follows from fig. 3*a* that, as a result of differing local symmetry, the magnetic submoments of the three crystal lattices of $Gd_3Fe_5O_{12}$ depend on temperature in different ways. At slightly below 300 K — i.e. at about room temperature — the magnetic dipole moments cancel and the total polarization of the material is zero. The temperature at which this occurs is referred to as the compensation temperature (T_{comp}). At this temperature each sublattice has magnetic order: the situation differs from that at the Curie point (T_C). In fig. 3*c* the magnetic saturation polarization J_s[8] of the material, which follows from fig. 3*a*, is plotted as a function of temperature. The value of J_s in teslas corresponds to the magnetic moment $j_s = \mu_0 m_s$ in Wb·m per unit volume ($J_s = \mu_0 | m_s | \mu_B 8/a^3$, where μ_B is the magnetic moment in Am^2 associated with a Bohr magneton, and a is the lattice constant; there are eight units of $Gd_3Fe_5O_{12}$ per unit cell).

In the temperature range near the compensation temperature the saturation magnetic flux density of the film material is very low (in view of the high permeability the saturation flux density is approximately equal to J_s in fig. 3*c*). Since the energy required for reversing the magnetic polarization — equivalent to the area of the hysteresis loop — will not change very much as a function of temperature, the coercivity H_c in this temperature range should reach very high values. This is indeed so in practice, as can be seen from the curve for H_c in *fig. 4*. If we draw the hysteresis loop for three different temperatures above T_{comp} with the aid of the known values for the coercivity and the saturation flux density, we see that it becomes flatter as T_{comp} is approached. It thus becomes more difficult to change the magnetic polarization of the material by applying an external magnetic field.

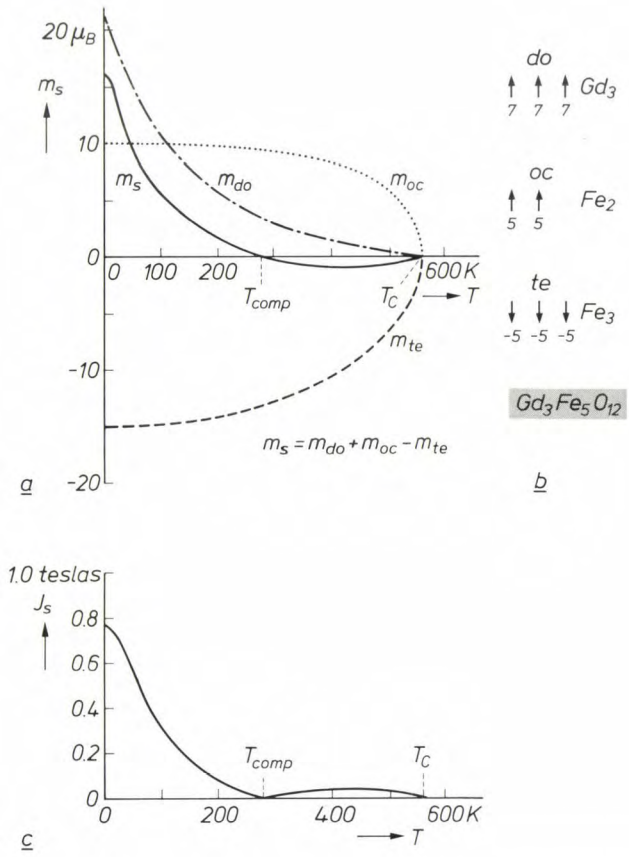

Fig. 3. *a*) The magnetic saturation moment m_s per unit of $Gd_3Fe_5O_{12}$ (an eighth part of a unit cell, fig. 2, left) in Bohr magnetons μ_B, as a function of absolute temperature T in a gadolinium-iron garnet film. The saturation moment m_s is the sum of the magnetic moments m_{oc}, m_{te} and m_{do} originating from the spins of the Fe^{3+} ions at the octahedral and the tetrahedral lattice sites and of the Gd^{3+} ions at the dodecahedral lattice sites. T_{comp} is the compensation temperature; when this temperature is exceeded and an external magnetic field is applied the direction of m_s rotates through 180°. T_C Curie point. *b*) Origin of the total saturation magnetization m_s as the sum of the magnetic moments of the sublattices for a unit $Gd_3Fe_5O_{12}$ at absolute zero. *c*) The magnetic saturation polarization J_s in teslas (the magnetic saturation moment $j_s = \mu_0 m_s$ Wb·m per unit volume) derived from fig. 3*a* for the material, as a function of the absolute temperature T. The saturation polarization is $J_s = \mu_0 | m_s | \mu_B 8/a^3$ teslas, where $\mu_B = 0.927 \times 10^{-23}$ Am^2 is the magnetic moment associated with a Bohr magneton, and a is the lattice constant (see fig. 2).

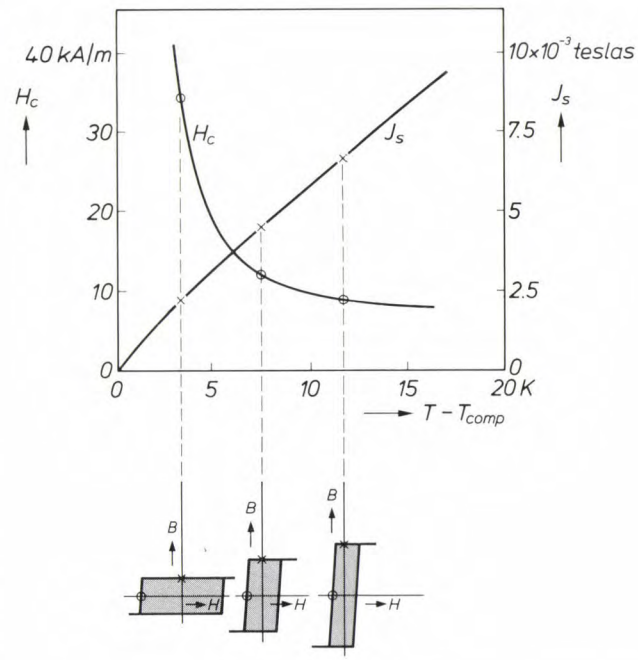

Fig. 4. Saturation polarization J_s (from fig. 3) and the coercivity H_c (from [3]) as a function of the temperature difference $T - T_{comp}$. Three hysteresis loops $B(H)$ are shown below for three different values of $T - T_{comp}$, based on values for H_c and J_s measured from the curves (the saturation flux density is approximately equal to the saturation polarization). As T approaches T_{comp} the hysteresis loop becomes flatter. Near the compensation temperature the direction of magnetization in the material can only be changed by means of a very strong external magnetic field (which approaches an infinite value for $T = T_{comp}$).

The effect just described is used in the optical switching devices that are the subject of this article. The direction of magnetization of the material is stabilized near the compensation temperature (i.e. at about room temperature): the magnetic polarization is 'frozen in'. However, when the temperature of certain areas of the film is raised by a few tens of degrees the magnetization can be reversed by a relatively weak external field (greater than $H_a - J_s/\mu_0$; for homogeneous single-crystal materials $H_c \approx H_a$). As we shall now explain, this also changes the sense of the Faraday rotation.

The Faraday effect

The Faraday rotation θ is proportional to the path δ travelled in the medium, so that

$$\theta = \theta_F \delta, \qquad (1)$$

where θ_F is the specific Faraday rotation, i.e. per metre.

The Faraday rotation occurs because certain solids have a different refractive index for clockwise and anticlockwise circularly polarized light. *Fig. 5* shows how this comes about. When a magnetic field is applied, an emission line is split into two closely spaced lines since the electron spin can be either parallel or antiparallel to the field. This is known as the simple Zeeman effect. (In the anomalous Zeeman effect there is an even finer quantum-mechanical subdivision.) In analogy with the simple Zeeman effect an absorption line in a magnetic field is also split by spin-orbit coupling into two closely spaced absorption lines, as shown in fig. 5*a*. Ordinarily the refractive index n increases monotonically with the frequency of the light. At an absorption line, however, there is a discontinuity in the refractive index. In a magnetic field, owing to the splitting of the absorption line, the curves of the refractive indices n^+ for clockwise and n^- for anticlockwise circularly polarized light are displaced in relation to one another; see fig. 5*b*. The difference $n^+ - n^-$, which will be found to be the main cause of the Faraday rotation, is plotted as a function of frequency in fig. 5*c*.

The difference $n^+ - n^-$ causes a rotation of the plane of polarization of linearly polarized light: this can be seen in *fig. 6*. The linearly polarized light may be regarded as the sum of clockwise and anticlockwise circularly polarized light. After passing through a magnetically polarized medium, e.g. a gadolinium-iron garnet film in the epitaxial growth direction, the two components will have different phase shifts. After recombination it is found that the polarization plane has rotated through an angle $\theta = \delta\theta_F$. Since the absorption is also usually different for clockwise and anticlockwise circularly polarized light (the effect is known as dichroism) the amplitudes of the emerging components are unequal. The Faraday rotation is therefore generally accompanied by Faraday ellipticity $\delta\psi_F$ — not usually a desirable effect. The Faraday

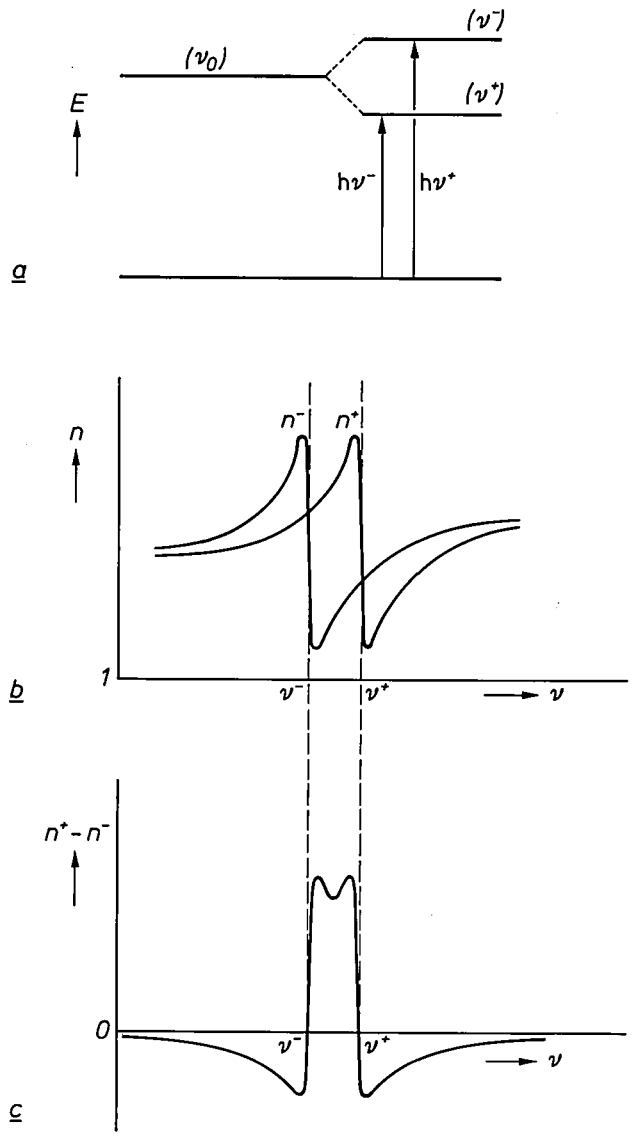

Fig. 5. Origin of the Faraday effect. *a*) Energy-level diagram; on left, no magnetic field, on right, with magnetic field. Owing to the simple Zeeman effect an absorption line of frequency ν_0 is split into two absorption lines of frequencies ν^- and ν^+. These absorption lines are produced by electron transitions from the ground state to higher levels with different potential energies $h\nu^-$ and $h\nu^+$; h is Planck's constant. The direction of the electron spin determines which transition takes place. *b*) Refractive indices n^- and n^+ for anticlockwise and clockwise circularly polarized light as a function of frequency ν. Since there are two absorption lines, one associated with anticlockwise and the other with clockwise circularly polarized light, the curves are displaced in relation to one another by a distance of $\nu^+ - \nu^-$. *c*) The difference $n^+ - n^-$ as a function of frequency ν. This difference is the cause of the Faraday rotation, as can be seen from fig. 6.

[8] $J_s = \mu_0 M_s$ in teslas corresponds to 10^4 times $4\pi M_s$ in gauss.

ellipticity is defined as the arc tangent of the ratio of the principal axes of the polarization ellipse. The specific Faraday ellipticity ψ_F is equal to the Faraday ellipticity per metre of path length travelled in the medium.

greatest when $\beta = 45°$. Substituting this in (2) we obtain

$$\Delta I = I_0 \, e^{-\alpha\delta} \sin 2\delta\theta_F. \qquad (3)$$

To find a maximum for ΔI as a function of film thick-

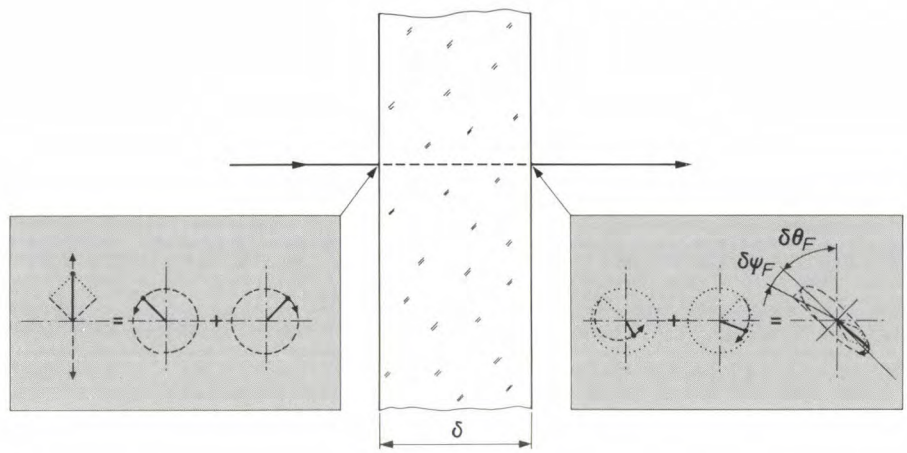

Fig. 6. Rotation of the plane of polarization of linearly polarized light after travelling a distance δ in a medium in which the refractive indices for clockwise and anticlockwise circularly polarized light are not equal. The light entering the medium may be considered as the sum of clockwise and anticlockwise circularly polarized light. The phase shifts for the vectors of the two kinds of circularly polarized light are different when the light travels through the medium. Since in general the absorption coefficients for clockwise and anticlockwise rotation are not equal (dichroism), there is also a difference in the lengths of the vectors. Recombination of the vectors gives elliptically polarized light with Faraday ellipticity $\delta\psi_F$ and Faraday rotation $\delta\theta_F$.

Optimum composition of a magneto-optical garnet film

We shall first look at the magnetic and optical requirements that a garnet film must satisfy in a good light-switching device. This will give an indication of the required composition of the garnet film.

The primary requirement is that there must be the greatest possible contrast between light beams that have passed through areas magnetically polarized in opposite directions. The intensities I_1 and I_2 of two emergent beams will be calculated with the aid of *fig. 7*[1]. These two beams have passed through two oppositely polarized areas and then through an analyser AN whose principal direction is at an angle β to the direction of polarization of the incident beams. The incident beams both have an intensity I_0, the thickness of the garnet film is δ and the mean absorption coefficient is α (per metre), no account being taken of the dichroism. The difference in intensity $\Delta I = I_2 - I_1$ is then equal to

$$\Delta I = I_0 \, e^{-\alpha\delta}\{\cos^2(\beta - \delta\theta_F) - \cos^2(\beta + \delta\theta_F)\}.$$

Rewriting the right-hand side of this equation gives

$$\Delta I = I_0 \, e^{-\alpha\delta} \sin 2\delta\theta_F \sin 2\beta. \qquad (2)$$

The intensity difference as a function of β is obviously

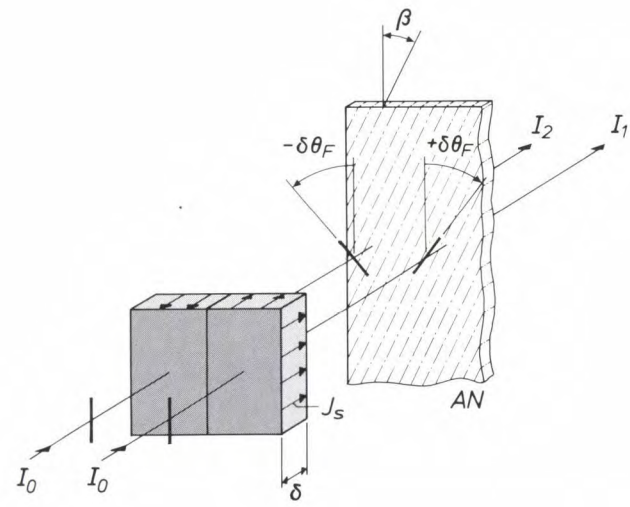

Fig. 7. Quantities used in the calculation given in the text for the intensity difference $\Delta I = I_2 - I_1$ of two light beams after they have passed through areas of opposite magnetic polarization J_s in a ferrimagnetic garnet film of thickness δ. The incident beams both have an intensity I_0 and are linearly polarized; the planes of polarization are parallel. After passing through the garnet film the planes of polarization are rotated through angles $-\delta\theta_F$ and $+\delta\theta_F$. The Faraday ellipticity has not been taken into account. Behind the garnet film is an analyser AN, whose principal direction is at an angle β to the plane of polarization of the two incident beams. The calculation shows that the intensity difference is greatest when $\beta = 45°$, and that the optimum thickness of the garnet film is $1/\alpha$, the reciprocal of the absorption coefficient.

ness δ we put $d(\Delta I)/d\delta = 0$. Then from (3) we have:

$$\tan 2\delta\theta_F = 2\theta_F/\alpha.$$

Since the films are thin, $\tan 2\delta\theta_F \approx 2\delta\theta_F$. The optimum film thickness δ_{opt} is then:

$$\delta_{opt} = 1/\alpha. \qquad (4)$$

The corresponding optimum intensity difference $(\Delta I)_{opt}$ is obtained by substituting (4) in (3):

$$(\Delta I)_{opt} = (1/e)\, I_0 \sin 2\theta_F/\alpha. \qquad (5)$$

$(\Delta I)_{opt}$ is large if the ratio $2\theta_F/\alpha$ is large. We therefore use

$$Q = 2|\theta_F|/\alpha \qquad (6)$$

as a figure of merit for the film. This quantity expresses the requirement, specified in the introduction, for a ferrimagnetic garnet film, that it should have a large Faraday rotation and low absorption.

Studies [7][9][10] have shown that a large Faraday rotation can be achieved by substituting bismuth at dodecahedral sites in the lattice. The exact explanation for this effect is not fully understood as yet. However, a qualitative explanation might run as follows. There is a large Faraday rotation if the two absorption lines (see fig. 5*b*) are relatively far apart, so that the difference $n^+ - n^-$ is large (see fig. 5*c*). The absorption-line doublet responsible for the Faraday rotation in garnets originates in the transition of electrons from 2p levels in the O^{2-} ions to 3d levels in the Fe^{3+} ions in the tetrahedral and octahedral sublattices. This comes about through charge transfer between the electron orbitals of the oxygen and iron ions in these sublattices. It appears that the substitution of the large Bi^{3+} ions at the dodecahedral sites also causes charge transfer between the outer 6p orbitals of Bi^{3+} ions and the 2p orbitals of O^{2-} ions. Since the electrons in these 6p orbitals have strong spin-orbit coupling, the effective spin-orbit coupling of the transitions of the absorption-line doublet is also increased. This has the effect of increasing the difference $h\nu^+ - h\nu^-$ in fig. 5*a* [5][9].

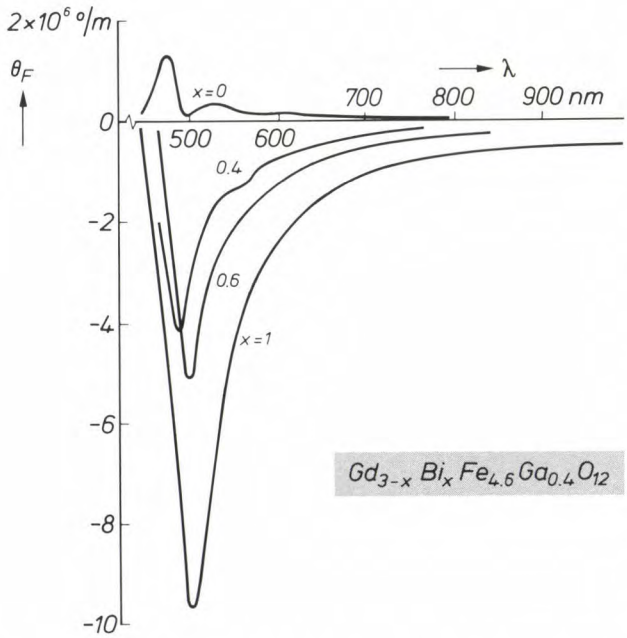

Fig. 8. The specific Faraday rotation θ_F in degrees per metre of $Gd_{3-x}Bi_xFe_{4,6}Ga_{0,4}O_{12}$ as a function of the wavelength λ in nm of the incident light, with the bismuth content x as parameter. θ_F is positive when the Faraday rotation is clockwise, viewed in the direction of propagation of the light beam. The curves have much the same shape as the left-hand part of the curve in fig. 5*c*, especially at large values of x.

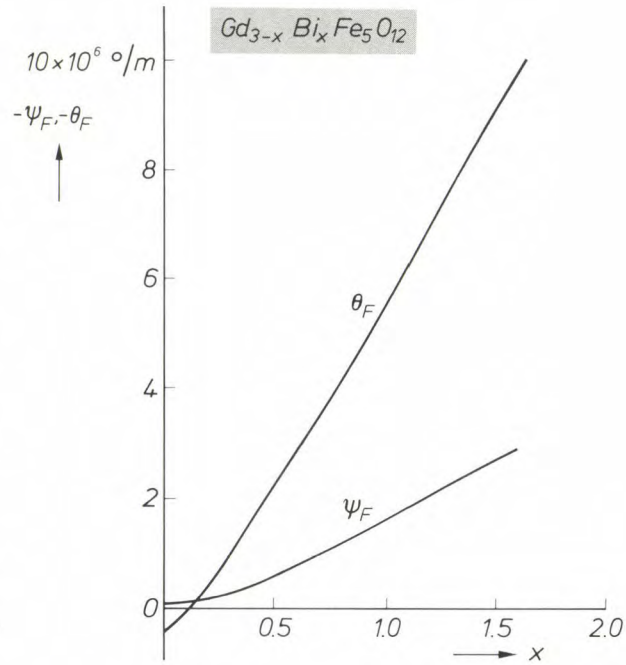

Fig. 9. The effect of bismuth substitution on the specific Faraday rotation θ_F and the Faraday ellipticity ψ_F, both in degrees per metre, for light at a wavelength of 546 nm and a temperature of 295 K. The results of measurements are plotted as a function of the bismuth content x of a ferrimagnetic garnet film of composition $Gd_{3-x}Bi_xFe_5O_{12}$.

During our study of garnet films we measured the optical and magnetic properties of bismuth-gadolinium-iron garnet $Gd_{3-x}Bi_xFe_5O_{12}$. First, *fig. 8* gives the dependence of the specific Faraday rotation θ_F on the wavelength of the incident light, with the bismuth content x as parameter, for the mixed crystal $Gd_{3-x}Bi_xFe_{4.6}Ga_{0.4}O_{12}$. (The role of the substituted gallium will be clarified later.) The curves in this figure for $x = 0.4$, 0.6 and 1.0 show the same behaviour as the left-hand part of fig. 5*c*. *Fig. 9* gives the specific

[9] S. Wittekoek, T. J. A. Popma, J. M. Robertson and P. F. Bongers, Phys. Rev. B **12**, 2777, 1975.
[10] P. Hansen, K. Witter and W. Tolksdorf, Magnetic and magneto-optic properties of bismuth-substituted gadolinium iron garnet films, Phys. Rev. B **27**, 4375-4383, 1983.

Faraday rotation θ_F and ellipticity ψ_F as functions of x for light at a wavelength of 546 nm, at a temperature of 295 K. *Fig. 10* shows the absorption coefficient α as a function of x at wavelengths 546 and 633 nm. The figure of merit Q at a wavelength of 546 nm is also shown as a function of x. It appears that the best optical properties are obtained at a bismuth content between $x \approx 0.5$ and $x \approx 1.1$. These properties are obtained when the film thickness is $\delta_{opt} = 1/\alpha$, which is in the range 3 to 10 μm, depending on the wavelength. *Fig. 11* gives a plot of the magnetic saturation polarization J_s as a function of absolute temperature T,

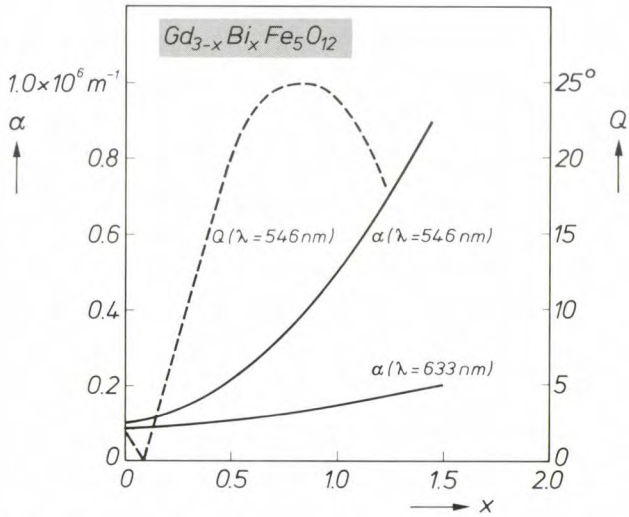

Fig. 10. Results of measurements of the figure of merit $Q = 2|\theta_F|/\alpha$ in degrees — at a wavelength of 546 nm — and the absorption coefficient α in m^{-1} — at wavelengths of 546 and 633 nm — as a function of the bismuth content x in $Gd_{3-x}Bi_xFe_5O_{12}$. The curve for Q is shown dashed.

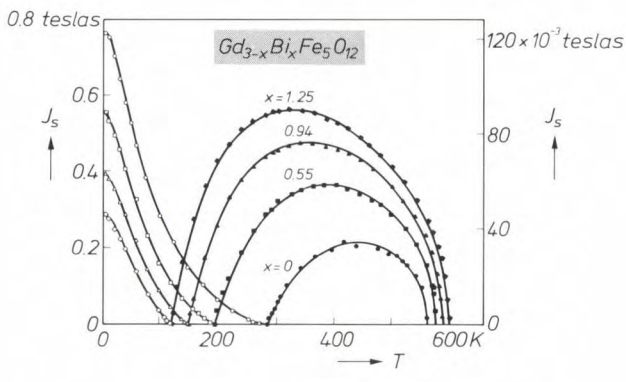

Fig. 11. The measured magnetic saturation polarization J_s in teslas (points, indicated in four different ways) as a function of absolute temperature T, for different bismuth contents x in $Gd_{3-x}Bi_xFe_5O_{12}$. For temperatures in the range between the compensation temperature and the Curie point a different scale has been used for J_s (on the right; see also fig. 3). The compensation temperature has been lowered by bismuth substitution. The continuous lines show the calculated behaviour of J_s (from molecular field theory). The calculations correspond closely to the measurements.

with the bismuth content x as parameter. The figure shows that an increase in bismuth content has the effect of lowering the compensation temperature T_{comp} and raising the Curie point T_C. This happens because the Bi^{3+} ions are not magnetic, so that the influence of the dodecahedral sublattice magnetization is reduced; see fig. 3*a*. Furthermore, the substitution increases the 'superexchange', i.e. the interaction between the spin moments of electrons of the Fe^{3+} ions in the octahedral and tetrahedral sublattices via the O^{2-} ions. The effect of the bismuth substitution can be calculated from molecular field theory [10][11]. The calculations — represented by the continuous lines in fig. 11 — correspond closely to the measurements.

As we noted earlier, the compensation temperature of the garnet film should be approximately equal to room temperature. The reduction in compensation temperature due to the bismuth substitution can be compensated by the partial substitution of non-magnetic ions for the magnetic Fe^{3+} ions of the tetrahedral sublattice. These non-magnetic ions must also be trivalent, e.g. Ga^{3+} or Al^{3+}. The effect of the substitution of gallium and bismuth on the Curie point and the compensation temperature has been calculated from molecular field theory and is shown in *fig. 12*. The compositions $Gd_{3-x}Bi_xFe_{5-y}Ga_yO_{12}$, where y is

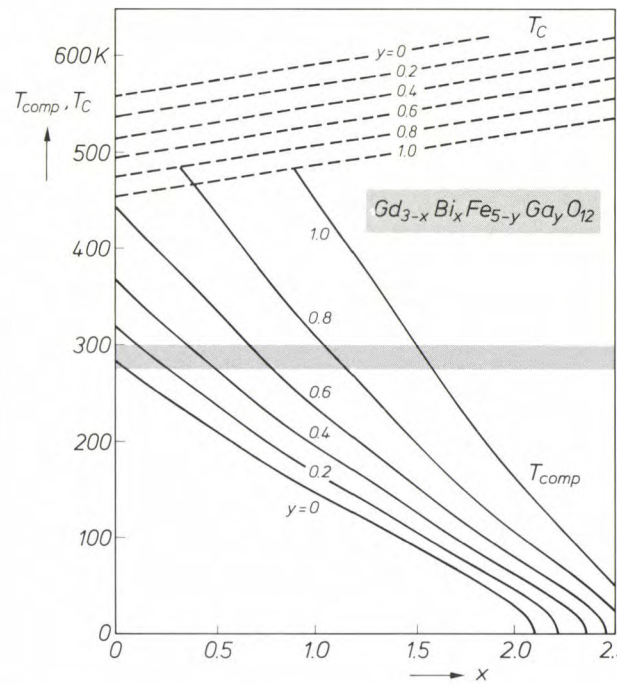

Fig. 12. Behaviour of the compensation temperature T_{comp} (continuous lines) and the Curie point T_C (dashed lines) as a function of bismuth content x, with the gallium content y as parameter, for $Gd_{3-x}Bi_xFe_{5-y}Ga_yO_{12}$, calculated from molecular field theory. The shaded area corresponds to a compensation temperature near room temperature: 280 K $< T_{comp} <$ 300 K. Optimum values for x and y are obtained from fig. 10 (high Q-value) and from the shaded area in this figure.

the gallium content, with a compensation temperature between 280 K and 300 K are found within the shaded strip in the figure. With a high value of Q, determined from fig. 10, it then follows that the combination (x, y) should lie between (0.7, 0.6) and (1.1, 0.8). A garnet with the appropriate composition then has practically the maximum Q-value combined with a compensation temperature that is at or near room temperature. We shall now show how we can determine the composition of a substrate material that matches this film material.

Choice of substrate material; fabrication of substrates and films

The substrate material should have:

- a garnet structure,
- no spontaneous magnetic polarization,
- minimum absorption in the wavelength range of visible light, and
- a lattice constant that deviates by no more than one pm (10^{-12} m) from that of the film material.

A widely used substrate material is the commercially available gadolinium-gallium garnet, which has a lattice constant a practically identical to that of yttrium-iron garnet; see *fig. 13*. In fact $Gd_3Ga_5O_{12}$ satisfies the first three requirements. Since the Gd^{3+} ions in this garnet are not surrounded by magnetic ions, it has no magnetic polarization, unlike $Gd_3Fe_5O_{12}$ (see fig. 2).

As explained earlier, we work with magneto-optical films of $Gd_3Fe_5O_{12}$ containing Bi and Al or Ga. The relatively large Bi^{3+} ions give a larger a than that of pure $Gd_3Fe_5O_{12}$, whereas the relatively small Ga^{3+} ions and even smaller Al^{3+} ions give a smaller a; see fig. 13. The lattice constant of the films we use is between 1.247 and 1.250 nm, depending on the exact composition, and is larger than that of $Y_3Fe_5O_{12}$. This is why we cannot use $Gd_3Ga_5O_{12}$ as a substrate material.

If some of the Ga^{3+} ions in $Gd_3Ga_5O_{12}$ are replaced by Zr^{4+} and Mg^{2+} ions in the ratio of 1:1 for charge compensation, it is possible to produce substrate single crystals that have a larger lattice constant. In general, however, there is a gradual and undesirable change in the lattice constant during the single-crystal growth process. We have succeeded in limiting this drift to a value less than $\Delta a/a = 2\times10^{-4}$ per single crystal by substituting Ca^{2+} ions as well. The general formula then becomes

$$Gd_{3-v}Ca_vGa_{5-v-2z}Mg_zZr_{v+z}O_{12}.$$

The combinations of the calcium content v and the zirconium content $v+z$ that result in this reduced variation of the lattice constant in a single crystal follow from *fig. 14* for 1.245 nm $< a <$ 1.251 nm [12].

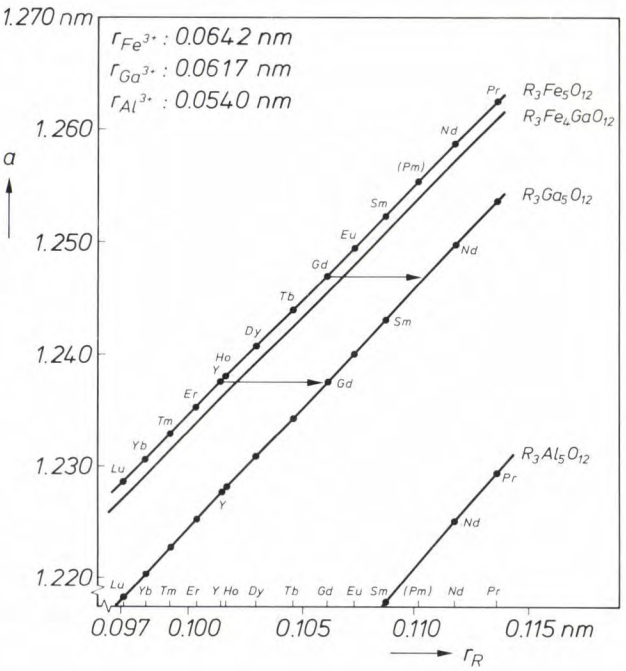

Fig. 13. The lattice constant a in nm of a garnet crystal as a function of the radius r_R in nm of the ion R^{3+} at the dodecahedral lattice sites. The lines give the lattice constants, calculated from the radii of the constituent ions, of $R_3Al_5O_{12}$, $R_3Ga_5O_{12}$, $R_3Fe_4GaO_{12}$ and $R_3Fe_5O_{12}$. Points along the lines and along the r_R-axis indicate a number of elements from the lanthanum series and also the element yttrium, all of which can occupy the site of R. The lattice constants of garnet crystals with various compositions can be derived from this diagram. The diagram can be used for choosing a substrate with the same lattice constant as a given ferrimagnetic garnet film, e.g. a substrate of $Gd_3Ga_5O_{12}$ matching to a film with the composition $Y_3Fe_5O_{12}$. A matching substrate material cannot be found directly for a film with the composition $Gd_3Fe_5O_{12}$.

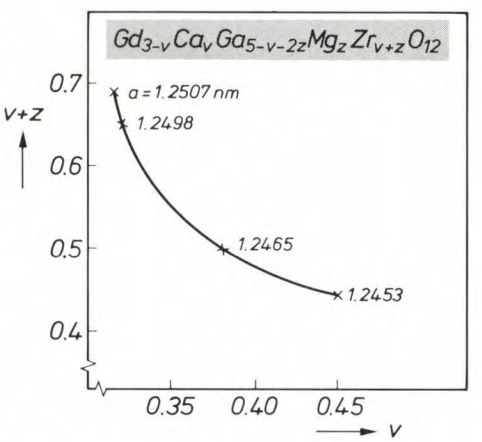

Fig. 14. The zirconium content $v+z$ as a function of the calcium content v in $Gd_{3-v}Ca_vGa_{5-v-2z}Mg_zZr_{v+z}O_{12}$, for single crystals grown with a relative lattice constant variation $\Delta a/a$ less than 2×10^{-4}. The lattice constant a in nm is given for the four experimental values around which the curve has been constructed.

[11] P. Röschmann and P. Hansen, Molecular field coefficients and cation distribution of substituted yttrium iron garnets, J. Appl. Phys. **52**, 6257-6269, 1981.

[12] D. Mateika, R. Laurien and Ch. Rusche, J. Cryst. Growth **56**, 677, 1982.

Fig. 15 shows a single crystal of the formula quoted above, with $v = 0.33$ and $z = 0.32$, and a lattice constant a of 1.2495 nm. These crystals were pulled by the Czochralski process [2] from a melt of the oxides of the constituent elements.

Our methods for making epitaxial films on slices of substrate material are partly derived from earlier studies at Philips Research Laboratories in Eindhoven [13]. The slices are sawn along a (111) plane from 3-inch single crystals, which are grown by the method described above. The carefully polished slices are then dipped two at a time in a 40 °C to 80 °C undercooled melt. Cohesion forces keep two surfaces of the two slices together during the process, preventing the melt from penetrating between them. The melt consists of oxides of lead and boron, containing dissolved oxides of the elements that will form the film. The temperature of the supersaturated melt is between 700 and 900 °C. During the growth process the slices are rotated about an axis perpendicular to their plane, and the direction of rotation is frequently changed. The growth rate is between 0.3 and 0.8 μm per minute. *Fig. 16* shows a double slice (of diameter 3 inches = 7.62 cm) being removed from the melt at the end of the process. The final composition of the film does not only depend on the proportions of the elements required in the film but also on the ratio of the concentrations of PbO and B_2O_3 and on the degree of supercooling [14].

Fig. 17 shows the magnetic domains that become visible when a 3-μm magneto-optical film is illuminated under polarized light. The high contrast between the light and dark areas indicates the large Faraday rotation produced by bismuth substitution in the film.

Applications

As we have seen, by applying an external magnetic field we can change the direction of magnetic polarization in a garnet crystal, and hence, through the Faraday effect, change the transmission for polarized light from '1' to '0' and vice versa; see fig. 1. The potential applications of this 'light switching' are innumerable, especially since the effect is not reciprocal, i.e. it does not change sign when the direction of incidence of the light is reversed.

In the very rapidly evolving technology of fibre-optics communication various kinds of light-switching elements are required, and these could be made with garnets. Devices analogous to the various 'switching' devices used in microwave technology [15][16], such as the isolator, the circulator and the modulator, can in principle be made for fibre-optics in garnet technology. The first two of these devices would utilize the non-reciprocity of Faraday rotation. Work is currently in progress in our laboratories on such fibre-optics switching devices.

Another field of application, which we have been studying for some considerable time, is that of imaging techniques, involving the use of 'compensation-temperature switching'. In such techniques, as explained earlier, the coercivity of defined regions of the film is reduced by heating these regions to a temperature above the compensation temperature, which is at or near room temperature. The active film is divided into small domains (e.g. 50 μm × 50 μm) by etching, and the temperature of the domains can be individually increased by means of a resistor applied to each small element. Each resistor can be supplied with current as required via metal conductors. Techniques familiar in semiconductor technology can be used for etching the magneto-optical film and for applying the resistors and conductors. Consequently the devices can be produced relatively inexpensively.

Fig. 15. Photograph of a 3-inch single crystal with the composition $Gd_{2.67}Ca_{0.33}Ga_{4.03}Mg_{0.32}Zr_{0.65}O_{12}$. The lattice constant a of this crystal is 1.2495 nm.

A 512-element device based on this principle is the LiSA 512 light-switching array, which we designed. This is now being produced and marketed by the Philips Elcoma Division. *Fig. 18a* shows the complete array, with the ICs for driving each element, including two 256-element CCD shift registers (CCD = charge-coupled device). Fig. 18*b* shows a scanning-electron-microscope (SEM) photomicrograph of the optical unit, in which the rectangular switching elements produced by etching can be seen. The resistors at the corner of each element can also be seen, as well as the metal conductors that supply the current. The bottom row of resistors is connected to one shift register, the upper row to the other. The digital information used for controlling the array is fed in series to the registers and then in parallel to the optical elements. The switching sequence can be seen from fig. 18*c*. First, a current I_R is supplied to the resistors of the elements in which the direction of the magnetic polarization is to be changed. Next a pulsed current I_H is supplied through a two-turn coil, thus applying an external

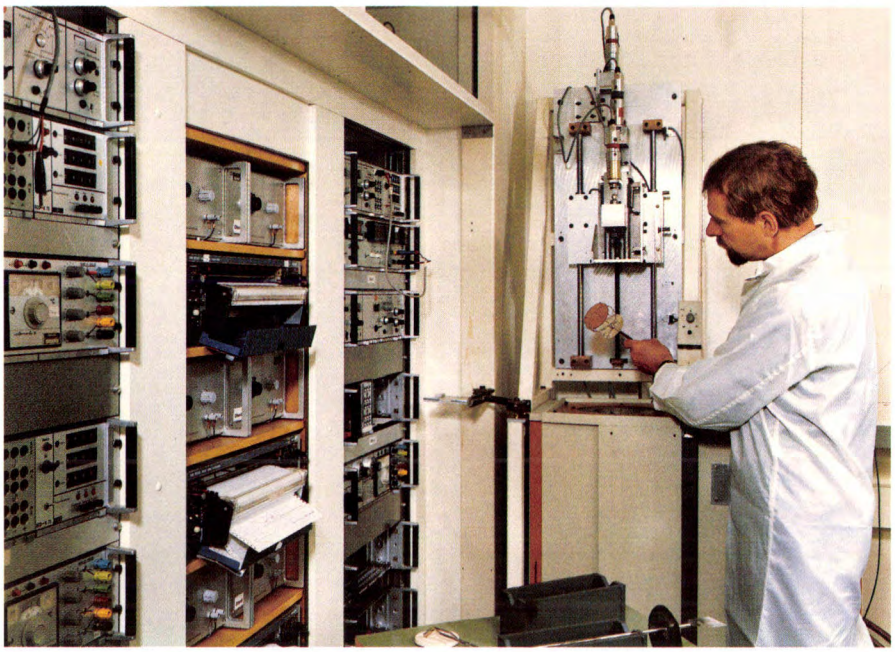

Fig. 16. Equipment for producing epitaxial films on slices sawn from garnet single crystals. The photograph shows a double slice being removed from the melt. The melt consists of oxides of lead and boron containing dissolved oxides of the constituent elements. The electronic units for measuring and regulating the melt temperature and for controlling the movement of the slice during the growth process can be seen on the left.

Fig. 17. Photomicrograph of the magnetic domains made visible when a 3-μm magneto-optical epitaxial film is illuminated by transmitted polarized light. The width of the domains is about 100 μm. The high contrast indicates a large Faraday rotation. This is achieved by bismuth substitution in the film.

[13] J. M. Robertson, S. Wittekoek, Th. J. A. Popma and P. F. Bongers, Preparation and optical properties of single crystal thin films of bismuth substituted iron garnets for magneto-optic applications, Appl. Phys. **2**, 219-228, 1973.

[14] C. P. Klages and W. Tolksdorf, LPE growth of bismuth substituted gadolinium iron garnet layers: systematization of experimental results; to be published shortly in J. Cryst. Growth.

[15] C. S. Aitchison, Lumped components for microwave frequencies, Philips Tech. Rev. **32**, 305-314, 1971.

[16] M. Lemke and W. Schilz, Microwave integrated circuits on a ferrite substrate, Philips Tech. Rev. **32**, 315-321, 1971.

magnetic field to all the elements. The direction of magnetic polarization, and hence the transmission of the polarized light, changes only in the elements that have been heated by I_R. The lower curve shows the variation in the intensity I_O of the light emerging from one element. The entire switching operation takes no more than about 20 µs. The complete LiSA 512 array — possibly combined with others to produce a multiple of $n \times 512$ pixels in a single row — can be used in printers, for example [17]. An optical system of this kind with 2560 pixels is shown in fig. 18*d*. The switching elements are illuminated by means of optical fibres. Five lenses produce an image of the switching elements on the paper to be exposed. A sheet of A4 format can be printed in two seconds, with a resolution of 12 pixels per mm.

Two-dimensional circuits can be made in a similar way. A magneto-optical display of this type has been made in our laboratories [18]; see *fig. 19*. The display is flicker-free and can be controlled pixel by pixel; the image information is not lost if there is a power failure. A display with these advantageous features has many potential applications.

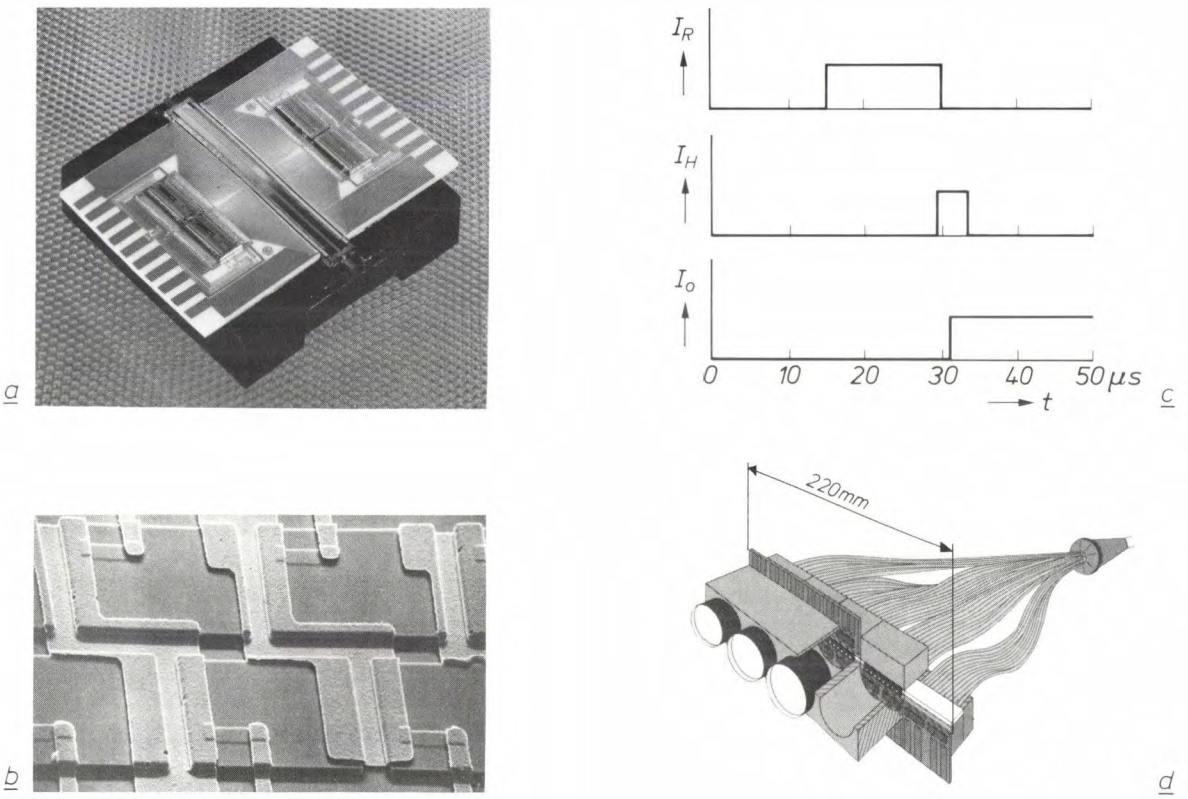

Fig. 18. The LiSA 512 light-switching array, with 512 elements. *a*) The complete array with the integrated circuits for electronic control (including two 256-element CCD shift registers). The actual dimensions are 38 mm × 40 mm. *b*) SEM photomicrograph of some optical switching elements each measuring 65 µm × 65 µm, mounted in two rows (in the horizontal direction in the photograph) of 256 elements. Each rectangular switching element has been etched into the ferrimagnetic layer. In each element there is a resistor for increasing its temperature (top left in the upper row, bottom left in the lower row). The current is supplied to the resistors via metal conductors, which connect to one of the shift registers. In the complete array there is also a two-turn coil, which applies a magnetic field perpendicular to the film to all elements simultaneously, but this is not shown here. *c*) The current I_R through the resistor of an element whose direction of magnetization is to be reversed, and the current I_H in the coil, as a function of time t. The quantity I_O is the intensity of the light transmitted through the element. The transmission coefficient is thus switched from '0' to '1'. The entire switching operation takes only 20 µs. *d*) A complete optical system, which can be used in a printer, with five LiSA 512 elements. The individual switching elements are illuminated by a halogen lamp via optical fibres. Five lenses produce images of the elements on the object, which could be light-sensitive paper or an electrophotographic photoconductor drum.

[17] B. Hill and K. P. Schmidt, Light-switching array for high-resolution pattern generation, Electron. Components & Appl. **4**, 169-174, 1982.

[18] B. Hill and K. P. Schmidt, Fast switchable magneto-optic memory-display components, Philips J. Res. **33**, 211-225, 1978.

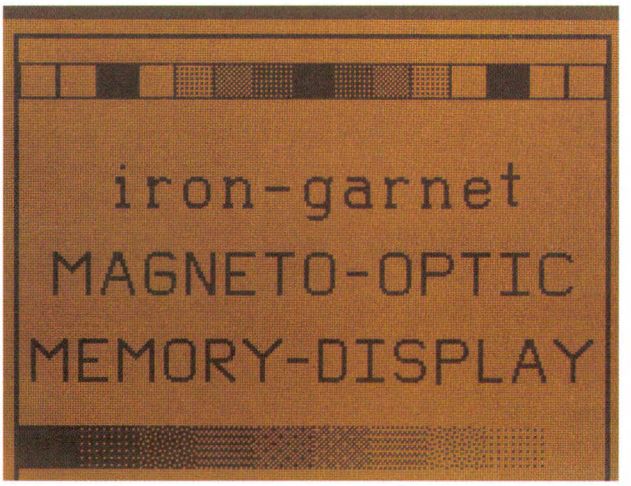

Fig. 19. A two-dimensional switching device of 256 × 256 pixels, which operates in the same way as the LiSA 512 array in fig. 18.

Summary. Optical switching devices can be made by utilizing the Faraday effect in ferrimagnetic garnet films. The magnetization of gadolinium-iron garnet consists of the sum of the individual magnetic dipole moments of the magnetic ions in the dodecahedral, octahedral and tetrahedral sublattices. At the compensation temperature (approximately equal to room temperature for $Gd_3Fe_5O_{12}$) the coercivity of the film is high, so that homogeneously magnetized domains are 'frozen in'. The direction of the magnetization can however be changed at a higher temperature. The Faraday rotation depends on the difference in refractive index for clockwise and anticlockwise circularly polarized light as a result of the magnetization of the material. Substitution of bismuth can enhance the Faraday rotation. Gallium or aluminium must then be added to prevent changes in the compensation temperature. The maximum contrast between domains magnetized in different directions is obtained when the film thickness is equal to the reciprocal of the absorption coefficient. The optimum values of x and y in a ferrimagnetic film of composition $Gd_{3-x}Bi_xFe_{5-y}Ga_yO_{12}$ can be determined from measurements and calculations. With the optimum garnet film a matching non-ferrimagnetic substrate can be found in the form of $Gd_{3-v}Ca_vGa_{5-v-2z}Mg_zZr_{v+z}O_{12}$, where the values of v and z can be found from our measurements. The results of the investigations are applied in the 512-element LiSA light switching array, which uses a kind of compensation-temperature writing.

X-ray imaging with Compton-scatter radiation

G. Harding, H. Strecker and R. Tischler

The physics department of London's well-known Hammersmith Hospital seems to be the home of the idea of applying Compton scattering for X-ray imaging. This alternative to Röntgen's transmission method was first described, we believe, by P. G. Lale in an issue of the journal 'Physics in Medicine and Biology', in October 1959. It may come as some surprise that the challenging problems signalled by Lale are still very worthy of investigation. The present article offers a good general picture of the work being done in this field at Philips Forschungslaboratorium in Hamburg. For some applications the sensitivity now within reach is at least of the same order of magnitude as that of computed-tomography scans, or even better. Complex reconstruction operations, with associated artefacts, are unnecessary. In particular the back-scattering mode of Compton scattering seems a good way of obtaining frontal views of organs, in slices that lie up to 5 to 10 cm below the surface of the human body, and also for discriminating tumours from the surrounding tissue in such superficial layers. For non-destructive testing in industry back-scatter imaging offers an even better prospect, since the radiation dose is very rarely harmful to inanimate material.

Imaging by scattering

Shadow projection, well-known as the principle of X-ray imaging, is no longer unique. For some years the Compton effect, the scattering of X-rays by atomic electrons, has attracted attention as a practical alternative [1]. Both medical and industrial applications have proved feasible.

Although the new approach is certainly not free from problems yet, this imaging by means of scattered X-rays has produced pictures that have some important advantages. For example, the depth information that can be gathered from the pictures — in other words, the location of the details along the ray path — is generally much better than from pictures made conventionally.

Dr G. Harding, Dipl.-Phys. H. Strecker and Dr R. Tischler are with Philips GmbH Forschungslaboratorium Hamburg, Hamburg, West Germany.

Conventional X-ray pictures are simple 'shadowgraphs', without any clear-cut physical effects that could represent the depth coordinate. In the transmission technique employed, information is obtained solely from the detection of 'unperturbed' quanta. ('Perturbed', i.e. scattered, quanta, some of which are also detected, form an undesirable background in this case.) It is a simple and time-honoured method, dating almost from the moment X-rays

were discovered (November 8, 1895). The distribution of the unperturbed quanta in some image plane at the detector can be obtained by applying the relation

$$I = I_0 \exp\{-\int_{\text{source}}^{\text{detector}} \mu(l)\mathrm{d}l\}, \quad (1)$$

where I is the irradiance dose (or particle fluence) of the X-rays incident at the detector, which can be a photographic film or a fluorescent screen; I_0 is the irradiance dose of the X-rays incident on the body under investigation; $\mu(l)$ is the linear attenuation coefficient at the coordinate of position l in the inhomogeneous material through which the radiation quanta pass. The cumulative increase in the absorption, i.e. the integration in eq. (1) of the attenuation over the *total* ray path, implies the complete loss of any depth information. (By 'depth information' we really mean a knowledge of the behaviour of the attenuation coefficient μ, within the body, as a function of the coordinate l.) Each 'point' (or pixel) of a shadowgraph therefore represents the integrated properties of the irradiated body along a *line* (this is termed here 'superposition effect'). This absence of depth information has repeatedly given misleading indications, especially in industrial radiography for non-destructive testing of materials.

When the alternative principle of X-ray imaging is used, it is not the unperturbed quanta but the *perturbed* quanta that are detected. With this approach it is possible to record 'individual' attenuation events — at least those that scatter the X-rays, and the superposition of attenuation is avoided; depth information then remains available.

The new pictures permit much easier identification of low-contrast objects, another advantage of the alternative approach. A good example from the medical field is the detection of a tumour surrounded by a mass of soft tissue. Shadowgraphs usually give too little contrast in such situations. Again, with the classical technique overlying material can cause masking and hence uncertainty in the identification of low-contrast objects. In medical applications high-contrast structures such as bone can cause such problems easily.

In fairness we should not forget to mention that more effort has been spent, in earlier years and also recently, in circumventing the superposition effect in X-ray imaging. This has led to successful techniques like computed tomography [2] and what is termed flashing tomosynthesis [3]. In these methods the object is exposed as in the classical shadow-projection method, but with a multitude of projection directions. With the aid of a computer program or an optical decoding process [3] the depth information can then be derived from the perspective information available from the complete set of shadowgraphs. The depth information these techniques provide is accompanied, however, by a considerable increase in system complexity.

Basing an imaging method on the detection of unperturbed quanta alone is less 'natural' than many people have come to believe since the first appearance of that famous picture of the hand of a German anatomy professor (title picture) [4]. In fact, our ordinary view of the objects around us depends on the scattered light that enters our eyes, to form a focused image on the retina. The human visual system therefore detects the perturbed quanta, providing us with a useful analogy for X-ray imaging based on Compton-scatter radiation.

The four principal components of an X-ray scatter system are on that account an X-ray source, the scatterer (the object), a focusing element (analogous to the cornea and lens of the eye), and a detector (like the retina). Also somewhat surprisingly, it seems that about 90 per cent of all the possible interaction events between X-rays and the soft-tissue material of the human body involve Compton scattering — at least for energies in the 50 to 70 keV range, typical of diagnostic radiology. For harder tissues the percentage is lower, but still appreciable (50 per cent for bone, for example).

The interactions that occur when X-rays pass through matter comprise three distinct physical processes: Rayleigh (or coherent) scattering, Compton (or incoherent) scattering, and photoelectric absorption [5]. The energy lost by the X-ray quanta in Compton scattering is imparted to atomic electrons in the irradiated body, and reappears ultimately as radiation dose absorbed by the body. In the region of 60 keV the energy loss is relatively low, and for material with properties similar to those of water — such as the soft tissue in the human body — the received dose has a minimum value.

The only difficulties with the four principal components of an X-ray scatter system are associated with the focusing element. Since there is no significant refraction at the energies normally used for medical applications (about 60 keV) and industrial radiography (about 200 keV), lenses cannot be used.

The only focusing element at present available is the pinhole, as in the earliest cameras. It focuses by merely rejecting all the rays that do not arrive at the correct point of the pinhole plane; only the rays that pass through the pinhole are detected. In this way an inverted projection image of moderate sharpness is obtained. Since the beam is extremely narrow the sensitivity is very poor, and a large radiation dose is necessary for a satisfactory image. In medical applica-

[1] See for example B. C. Towe and A. M. Jacobs, X-ray backscatter imaging, IEEE Trans. **BME-28**, 646-654, 1981.

[2] F. W. Zonneveld and C. Albrecht, Computed Tomography: a review of the past and present and a perspective of the future, Medicamundi **26**, 81-92, 1981.

[3] E. Klotz, R. Linde, U. Tiemens and H. Weiss, Flashing tomosynthesis, Philips Tech. Rev. **38**, 338-346, 1978/79.

[4] We acknowledge the kind assistance of the staff of the Deutsches Röntgen-Museum at Remscheid, Lennep, West Germany, in obtaining this picture.

[5] C. M. Davisson, Interaction of γ-radiation with matter, in: K. Siegbahn (ed.), Alpha-, beta- and gamma-ray spectroscopy, Vol. 1, North-Holland, Amsterdam 1968, pp. 37-78. For quantum energies higher than about 1020 keV pair formation occurs, another interaction effect.

tions the X-ray exposure must of course be kept well within safe limits; in industrial radiography, on the other hand, the objects are usually free from any such restrictions.

The next section describes our first scatter-imaging system, with pinhole collimation. This basic system has been used to check aluminium castings used in car engines; even though it is a somewhat primitive system it shows that the method has considerable promise for non-destructive testing in industry. Cavities (shrink holes) down to about 1 mm size in the aluminium can be detected.

We conclude the article with a summary of the advantages and disadvantages associated with Compton-scatter imaging in its present state of development, and a brief look at the future prospects.

The fan-beam experiments

Fig. 1 shows a photograph of our earliest experiment in scatter imaging. The object for X-ray inspection was an aluminium casting, in fact a car part obtained from the automobile industry. An arrangement based on this experiment could be used in developing an

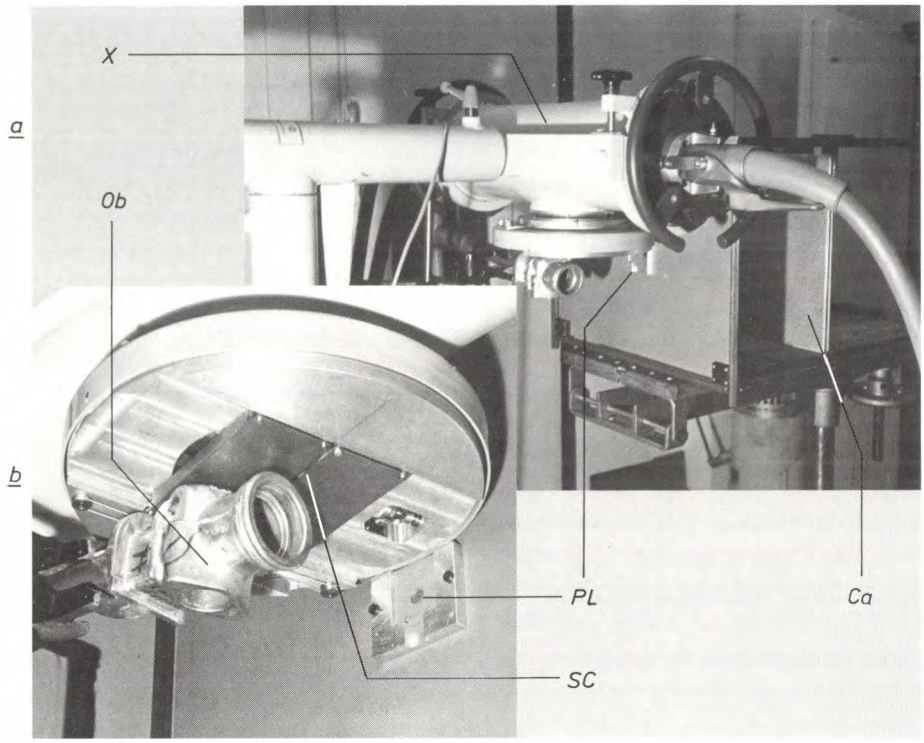

Fig. 1. The first scatter-imaging experiment at Philips Forschungslaboratorium in Hamburg. *a*) General arrangement. *X* is a Philips industrial X-ray tube, type MCN 320, used at 200 kV. *b*) Detailed view of the test object *Ob*, an aluminium car-engine component, and of the slit collimator *SC*, which is mounted on the window of *X* to define the primary beam. There is scattering from the primary beam, which has the shape of a fan, through an angle of about 90°. The detector *Ca*, consisting of film in a cassette, produces a two-dimensional image of an entire slice (thickness 2 mm) of the object, as determined by the fan-shaped beam. The plane of the beam is parallel to that of the detector. *PL* is the pinhole lens.

The third section deals briefly with some of the more important physical properties of Compton scattering. It is intended as an introduction to a more detailed account of calculations, for data correction — necessary because of attenuation and multiple-scatter effects — and for numerical comparison of the sensitivities of scatter imaging and conventional imaging.

The fourth section discusses the design and performance of COMSCAN, the laboratory version of the scatter-imaging system we are now testing. We draw attention to the importance of back-scatter imaging in medical applications.

automatic device for checking to ensure that there are no cavities (shrink holes) in the castings — a very important aspect of quality control in the modern automobile industry.

The X-ray tube (Philips MCN 320) gives a primary beam in the shape of a fan; the shape of the beam is determined by the slit collimator mounted on the tube window. The fan-shaped beam is combined with a two-dimensional detector — merely a flat film in a cassette — to produce an image of an entire slice of the object in a single exposure. The pinhole 'lens' that collects the scattered rays has an aperture with a diam-

eter of 0.5 or 1 mm, in a lead plate of thickness 6 mm. The aperture has a profiled edge, to minimize the occurrence of spurious quanta (such as edge-scattered quanta or Kα-Pb quanta) among the scattered quanta that produce the image of the object slice.

A complete volume scan of the object can be produced by effectively moving the slice of interest within the object. This can be done by displacing either the fan beam or the object.

The mean scattering angle is about 90 degrees (fig. 1). The scattered quanta therefore move in a direction approximately perpendicular to the plane of the slice scanned. The X-ray inspection can then be made with the maximum 'transverse' spatial resolution, equal to the thickness of the slice. This thickness is approximately equal to the slit width (2 mm) of the primary-beam collimator, because the object is mounted directly in front of it. The spatial resolution in the plane of the slice is approximately equal to the diameter of the pinhole, as can readily be seen from elementary geometry.

To make maximum use of the scattered-ray intensity, the pinhole lens is placed as close to the object as possible. As might be expected, there are a few problems. Since the pinhole is very small (0.5 to 1 mm diameter), the acceptance angle is proportionally small, so that the exposure times must be long and the absorption doses correspondingly large — especially with a fan-shaped primary beam. Our object is not affected by the radiation, and like many other industrial products, it contains only two types of material: metal and air. Metal scatters the primary beam considerably (in aluminium with 100-keV quanta some 90 per cent of the interaction events are due to Compton scattering), but air — the undesirable component — gives little scatter. Non-destructive testing for industry by means of scatter imaging offers the attractive feature of a 'binary' intensity distribution. This binary behaviour makes automatic inspection of materials relatively easy [6].

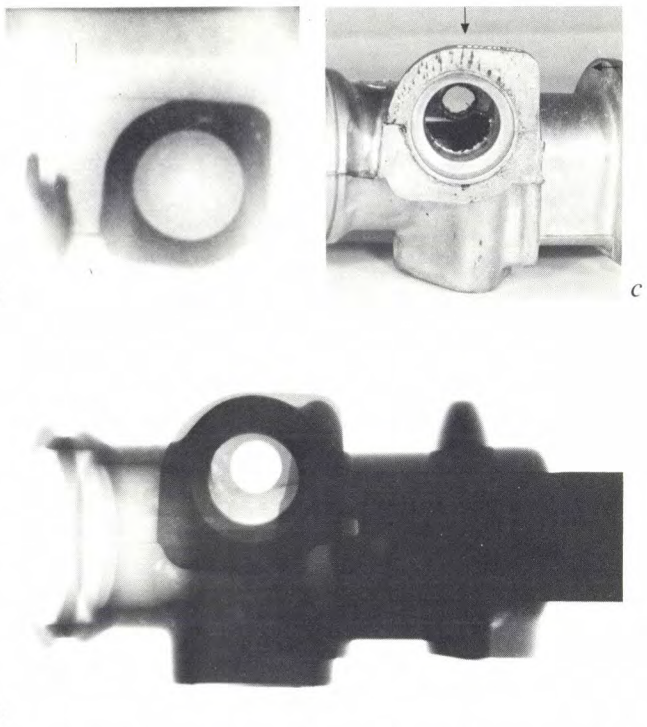

Fig. 2. Results obtained with the scatter-imaging arrangement of fig. 1, as used for non-destructive testing of materials. The aluminium car-engine component (*Ob* in fig. 1) was inspected for the presence of possible shrink holes in the material. *a*) Our first scatter image. The scattered radiation from the primary fan beam (which is parallel to the plane of the picture) can be used to produce images for the inspection of individual slices of material, only 2 mm thick, all parallel to the plane of this picture. The slice shown is between 4 and 6 mm below the upper surface of the flange. There are at least three undesirably large shrink holes in this slice. *b*) The same object, as revealed by a shadowgraph, the conventional radiograph. The ubiquitous superposition effects make clear-cut interpretation of the test results almost impossible. *c*) The same object, photographed.

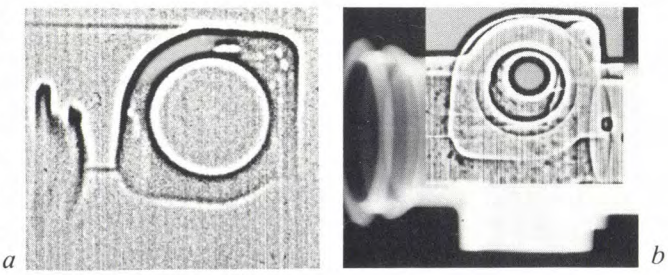

Fig. 3. *a*) An edge-enhanced scatter image, corresponding to fig. 2*a*. The visibility of the shrink holes is improved. The image was obtained by highpass filtering of the spatial frequencies present in fig. 2*a*. *b*) A similarly enhanced image, corresponding to fig. 2*b*. Depth coordinates cannot be assigned to the many shrink holes in the image, because of superposition.

The first scatter radiograph

Fig. 2a shows the first scatter image obtained with the arrangement of fig. 1. The scanned slice lies between 4 and 6 mm below the upper surface of the central flange. For comparison a conventional radiograph of the same object is also shown (fig. 2*b*). The complete absence of the superposition effect gives the first picture its strikingly 'clean' appearance. The third picture is an ordinary photograph of the same object (fig. 2*c*). A number of shrink holes in the aluminium, of dimensions ranging from 1 to 2 mm, are reasonably apparent in the scatter radiograph (fig. 2*a*). The visibility of the shrink holes in fig. 2*a*, however, can be improved by digital image processing to give an edge-enhanced image. This was done on a computer, by highpass filtering of the spatial frequencies present in fig. 2*a*. The resulting picture (*fig. 3a*) is a scatter image with much sharper contours, in which the shrink holes

[6] See for example W. Spiesberger and M. Tasto, The automatic measurement of medical X-ray photographs, Philips Tech. Rev. **35**, 170-180, 1975.

are now clearly visible. Similarly, fig. 3*b* is the edge-enhanced image of fig. 2*b*, the conventional radiograph. In this picture the contour enhancement has produced a confusing mass of shrink holes, whose depths are all unknown. A comparison of figs 3*a* and *b* shows that our scatter-imaging method permits a much better determination of the depth coordinates.

Improvements and limitations

If the film cassette in the arrangement of fig. 1 is replaced by a standard X-ray image intensifier connected to a TV camera and monitor, direct scatter images can be obtained on the TV screen. The image represented by a single video frame (0.04 seconds) is not acceptable, however, because of picture noise. The difficulty can be overcome by adding a real-time video digitizer. This integrates 16 successive video frames to build a single-slice image of reasonable quality in only 0.64 seconds (*fig. 4*). Such fast imaging represents an enormous improvement; producing a single scatter image like fig. 2*a* with the film cassette, under identical conditions (1 mm pinhole), takes some 2 hours — far too long for automated industrial inspection.

We can also see that the intensity distribution in the two scatter images (figs 2*a* and 4) is not purely binary, so that the attractive feature mentioned earlier is in fact missing. The images are not binary because of attenuation and multiple scatter. Quanta scattered from neighbouring regions in the object can be scattered again in the slice being examined, and this reduces the contrast or causes pictorial artefacts. Because of this multiple scatter, neighbouring regions affect the intensity distribution. The other effect, beam attenuation, arises because the primary beam and the scattered rays are subject to attenuation wherever they pass in the object. So in this case too the neighbouring regions influence the intensity distribution. This explains effects such as edge fading in fig. 2*a*.

The experience obtained so far with fan-beam scattering suggests that a complete volume scan with a spatial resolution of about 1 mm can easily be produced within five or ten minutes for all aluminium parts of dimensions below about 10 cm. The peak voltage of the X-ray tube must be 300 kV or higher; otherwise attenuation effects are likely to degrade the picture quality unacceptably.

The irradiation time necessary for a desired picture quality — expressed in terms of contrast, for example — is proportional to the 5th power of the object dimension and inversely proportional to the 6th power of the spatial resolution. Both relations — the first for fan beams only, the second of general validity — can be calculated from simple considerations that neglect absorption and multiple scatter [7]. They give some indication that the usefulness of scatter imaging for rapid industrial testing might remain limited in scope, mainly because of unfavourable irradiation times.

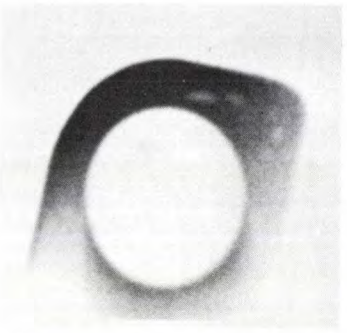

Fig. 4. A single-slice scatter image, again of the object *Ob* (fig. 1). This picture was made by means of a standard X-ray image intensifier connected to a television camera with a real-time video digitizer and a computer (for real-time processing of the video signal). Exposure time 0.64 seconds.

The gain in sensitivity, theoretical considerations

Calculations have been made that enable sensitivities to be compared. Our objective was to establish the conditions for which scatter imaging on film gives better image quality than conventional X-ray imaging, with particular reference to differences in grey scale (or contrast). The sensitivity calculations will not be accurate, of course, unless they are corrected for the intensity changes due to the beam attenuation and multiple scatter mentioned in the previous section. Both corrections should be applied to the primary rays and to the scattered rays. Before going into the calculations in more detail we should first briefly consider some of the more important physical properties of the Compton effect [8].

Physical properties

Compton scattering obeys the relativistic laws for conservation of linear momentum and total energy, as applied to a simple elastic collision between two particles, i.e. an incident X-ray quantum and an atomic electron. *Fig. 5* depicts the situation. The path of the recoil electron — whose atomic binding energy is assumed negligible compared with the energy ($h\nu$) of the incident X-ray quantum — lies in the plane defined by the incident X-ray and the scattered X-ray.

From the conservation laws we have the Compton shift:

$$\lambda_{\text{scatt}} - \lambda = 2\frac{h}{m_0 c}\sin^2(\tfrac{1}{2}\theta), \qquad (2)$$

where λ_{scatt} and λ are the wavelengths of the scattered

and the incident rays; θ is the scattering angle (fig. 5); m_0 is the rest mass of the electron, h is Planck's constant and c is the velocity of light. (The constant h/m_0c, known as the 'Compton wavelength' and equal to 2.426 pm, represents the wavelength of an X-ray quantum whose energy is 511 keV, the rest energy of an electron.)

From eq. (2) it can be seen that Compton scattering always increases the wavelength, so that there is a partial energy loss. The wavelength of the incident radiation does not affect the change of wavelength — the shift depends only on the scattering angle chosen. It is found that the energy loss increases continuously as the scattering angle increases from 0 to 180° and the energy of the incident radiation is kept constant. If, on the other hand, the incident energy is varied and the scattering angle kept constant, there is a *relative* energy loss that continuously increases with the energy of the incident radiation.

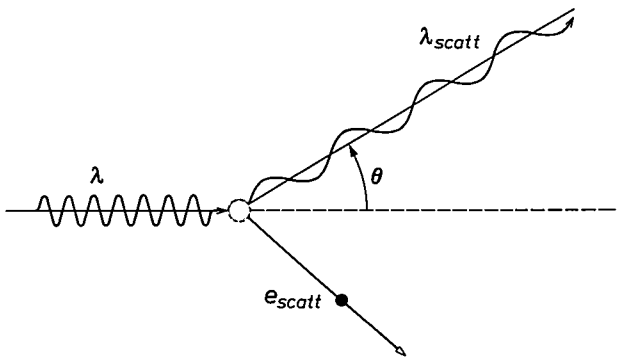

Fig. 5. Compton scattering. An incident X-ray of wavelength λ is scattered by an electron that is assumed to be free and at rest. The electron can be an atomic electron, provided that its binding energy is negligible compared with $h\nu$, the quantum energy of the incident X-rays. λ_{scatt} is the wavelength of the scattered ray. e_{scatt} is the recoil electron. θ is the scattering angle.

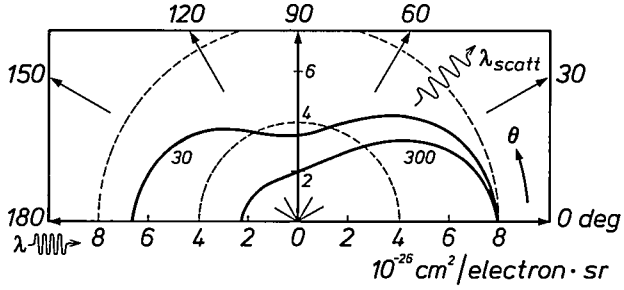

Fig. 6. Polar plot of the differential cross-section for the number of X-ray quanta scattered into unit solid angle at the mean scattering angle θ. The cross-section, calculated per free electron, is given here for two incident energies (30 and 300 keV). More information can be found in A. T. Nelms, Graphs of the Compton Energy-Angle Relationship and the Klein-Nishina Formula from 10 keV to 500 MeV, U.S. Nat. Bureau of Standards, Circular 542, Washington D.C. 1953.

If a comparison is made for incident energies of, say, 50 keV and 400 keV, it can be shown that the 50-keV quanta lose about 9 per cent of their energy and the 400-keV quanta almost 44 per cent, five times as much (both for $\theta = 45$ deg). Such results are most easily derived from the energy equation:

$$E_{scatt} = \frac{E}{1 + 2\frac{E}{m_0c^2}\sin^2(\frac{1}{2}\theta)}, \qquad (3)$$

where E and E_{scatt} are the quantum energies. Eq. (3) is easily derived from eq. (2). The absorbed radiation dose is therefore much smaller with the 50-keV quanta, so that they are safer than the 400-keV quanta.

The spatial distribution of the intensity of scattered X-rays possesses rotational symmetry, with the direction of the incident ray as axis. In spite of this symmetry, the distribution is not completely isotropic. The degree of anisotropy varies strongly with the incident energy. At higher energies, above about 100 keV, the quanta are mostly scattered forwards, indicating a strong anisotropy; at energies around 30 keV the distribution is much more isotropic (*fig. 6*). A consequence of this is that the use of radiation at an energy in the range of these lower values makes it possible to detect scatter radiation at reasonably constant efficiency at any value of the scattering angle θ. In particular we should point out that the back-scatter radiation is almost as strong as the forward-scatter radiation. The practical significance of this will become evident in the next section. In any case, in determining the best geometrical layout for X-ray imaging with Compton-scatter radiation, we can add the spatial intensity distribution as a 'free' parameter — which is not possible in the conventional transmission method. The best example of the greater freedom is that of the detector. The detector position can be chosen so that effects such as beam attenuation are minimized. In the new method a large number of different detector positions are potentially available; in the conventional method, however, there is only one (mainly determined by the incident beam).

The scatter-signal contribution from a small volume element δV in an irradiated body and located at the intersection of a primary-ray path p and a scattered-ray path q is given by:

$$S(\delta V; p,q) = K n_e \delta V . \exp\{-\int_p \mu(l)\mathrm{d}l\} . \exp\{-\int_q \mu'(l)\mathrm{d}l\} + M(\delta V; p,q). \qquad (4)$$

[7] H. Strecker, Scatter imaging of aluminum castings using an X-ray fan beam and a pinhole camera, Mater. Eval. 40, 1050-1056, 1982.

[8] The subject is well described in the standard texts on low-energy nuclear physics. A good example is R. D. Evans, The atomic nucleus, McGraw-Hill, New York 1955.

The proportionality constant K includes the differential scattering cross-section and the various factors for solid angle, detector efficiency and X-ray tube output, as well as all other body-independent effects. The constant n_e is the number of 'free' electrons (= scattering centres) per unit volume in δV. The two exponential functions represent the attenuation of the primary rays and the scattered rays. The dash (') in the second integral is used to indicate that the attenuation of the scattered rays occurs at a *different* energy (E_{scatt}, see eq. (3)). The additional term $M(\delta V;p,q)$ is the multiple-scatter contribution; it represents the signal from all X-ray quanta scattered more than once inside the body and reaching the detector along the path q.

In order to determine the imaging sensitivity of a body-scanning method, it is necessary to find the minimum detectable mass-density variation. The electron density, n_e in eq. (4), which is proportional to the mass density, is therefore the major quantity to be derived from the measurement of the scattered radiation.

The scattering volume element δV and data correction

The use of a simple 'pencil-beam' geometry, with suitable diaphragms for the selection of a primary-ray path p and a scattered-ray path q leading to the detector, gives a straightforward way of determining the *position* of a scattering volume element δV.

Measuring the intensity of a scattered signal and using eq. (4), the required *mass density* in δV, or rather the electron density, can also be found. However, since the attenuation of the primary and scattered rays and the intensity of the multiple-scatter radiation are unknowns too, the solution is by no means as straightforward as finding the position.

The required correction of the measured data is obtained here from the approximate assumption that the scattering properties of the scanned object are the same as for water. This is a reasonable initial assumption in most medical applications (except bone-tissue investigations). The true attenuation can then be estimated from the attenuation in a reference object — of similar shape but filled with water. The scatter signal from the actual object can be compared with the scatter signal from the reference object. Any local differences between the two scatter signals, if statistically significant, should be interpreted as the result of local variations in mass density — the variations we are looking for — rather than local variations in attenuation. In this way a 'first-order' corrected image is obtained, even if the attenuation coefficients in the reference object are not exactly identical to those in the scanned object. Obviously the shapes of the two objects should be as similar as possible; surrounding the scanned object with a water-bag is an easy way of improving the equivalence between the two objects.

The use of a reference object to correct for the attenuation of the scatter signal has the added advantage that the multiple-scatter term, M in eq. (4), simultaneously disappears in the signal subtraction. The multiple scatter is only approximately corrected, of course, because the effect depends on the exact composition of the scanned object, though usually only to a limited degree.

The ratio of the numbers of single-scatter quanta to multiple-scatter quanta at the detector, as measured in our experiments so far, is about 10 or even higher. Any residual multiple-scatter radiation therefore reduces contrast in the scatter images to a negligible extent in practice.

Expressions for contrast and sensitivity

To compare the sensitivities of scatter imaging and conventional imaging (i.e. transmission imaging), it is useful to consider the scanning of a spherical body whose attenuation coefficient is equal to μ except in a small central region, where it is $\mu + \Delta\mu$. By definition, the contrast that the central region will produce in an image is equal to the relative change in the detected signal that would occur on decreasing the attenuation coefficient of the central region from $\mu + \Delta\mu$ to μ. It is also assumed that the central region in the image becomes visible (or detectable) as soon as the contrast obtained exceeds the statistical fluctuations in the signal that arise from the quantum nature of the radiation. This lower limit of detection, corresponding to the minimum detectable value of $\Delta\mu$, represents the sensitivity of the imaging technique.

To simplify our initial calculations we have assumed that the attenuation is entirely due to scattering; any photoelectric absorption of the X-rays is neglected. It was also assumed that the dimension d of the central region in the direction of the incident beam is small compared with the diameter L of the spherical body.

The contrast produced by the central region is given by the approximate expressions [9]:

$$C_{conv} = d\,\Delta\mu \qquad (5a)$$

for a conventional image, and

$$C_{scatt} = \frac{1}{\mu}\Delta\mu \qquad (5b)$$

for a scatter image.

An illustrative case of the possible gain in contrast is that of a small tumour whose linear attenuation coefficient could be 0.22 cm^{-1} while the surrounding tissue has a μ equal to 0.20 cm^{-1}. With d equal to 0.5 cm, say, it is clear that C_{scatt} is a whole order of magni-

tude larger than C_{conv} — a considerable gain in contrast. This could be most useful indeed, since it would not be possible to detect such a tumour in a conventional image with the naked eye, because the contrast is only 1 per cent.

A higher contrast is only of practical value if the levels of the statistical fluctuations are the same in the two images (and sufficiently small). The usual convention is to take the standard deviation of the mean number of detected X-ray quanta as the level of statistical fluctuations. The Poisson distribution is applicable to this detection process [8], so that the relative image fluctuation levels are $1/N_{conv}^{1/2}$ and $1/N_{scatt}^{1/2}$, where N_{conv} and N_{scatt} represent the mean numbers of detected quanta.

From the definition of sensitivity as given above, it will be clear that in both types of images the ratio $C/N^{-1/2}$ determines whether the region of deviating contrast will be seen or not. This ratio, which we call the detectability D, is the numerical quantity that should be used as a figure of merit in predicting the conditions for which scatter imaging will outperform conventional imaging. Finally, therefore, the ratio of the two detectability values is required:

$$\frac{D_{scatt}}{D_{conv}} = \frac{1}{\mu d}\left(\frac{N_{scatt}}{N_{conv}}\right)^{\frac{1}{2}}. \qquad (6)$$

N_{scatt} and N_{conv} are given by the approximate expressions:

$$N_{conv} \approx N_0 \exp(-\mu L) \qquad (7a)$$

and

$$N_{scatt} \approx N_0 \exp(-\mu L) \cdot \{1 - \exp(-\mu d)\} \cdot \frac{\Delta\Omega}{4\pi}, \qquad (7b)$$

where N_0 is the number of primary-beam quanta incident on the spherical body per unit time, $\exp(-\mu L)$ represents the total attenuation — for scatter imaging this attenuation refers to both the primary beam and the scattered rays, $\Delta\Omega$ is the solid angle subtended by the detector and $1 - \exp(-\mu d)$ is the proportion of the quanta that are scattered into a complete sphere (or 4π steradians). If it is assumed that there is a cylindrical slit collimator of slit width d at a distance $\frac{1}{2}L$ from the central scattering region, and that all the quanta passing through the slit are received by an annular detector, then eq. (7b) takes the form:

$$N_{scatt} \approx N_{conv} \cdot \mu d \cdot \frac{d}{L}, \qquad (8)$$

where μd is an approximation for $1 - \exp(-\mu d)$ and $\Delta\Omega/4\pi$ is equal to d/L. Substituting eq. (8) into eq. (6) we finally obtain the simple result:

$$\frac{D_{scatt}}{D_{conv}} = (\mu L)^{-\frac{1}{2}}. \qquad (9)$$

The ready comparison of sensitivities via eq. (9) is not the only advantage obtained through the adoption of full-circle geometry and the use of a 2π annular detector. There is also a substantial reduction (about 40 times) of the radiation dose absorbed by the irradiated body, at least in the case of the simple pencil-beam geometry described earlier.

From eq. (9) it can be seen that the sensitivity of scatter imaging in 'ring-slit' geometry is superior to conventional imaging provided the object is radiologically 'thin' (or $\mu L < 1$). The two methods are equivalent in practice when the object dimension L is equal to the reciprocal of the object's linear attenuation coefficient.

For 60-keV radiation soft body tissue has $\mu \approx 0.2$ cm^{-1}, and the limiting dimension is therefore about 5 cm. This low value seems to imply, at least in medical applications, that scatter imaging should be restricted to the superficial organs and the extremities of the human body (hands, feet, see title picture). It is worth remembering, however, that scatter imaging offers great freedom in choosing the measurement geometry. In particular, a back-scatter configuration could be used to obtain an image of organs near the surface of the body. The dose required is much smaller than for the conventional method — in which the radiation passes right through the body.

In non-destructive testing there are situations where conventional X-ray transmission cannot be used. In checking surface welds in large-diameter pipes, for example, it is sometimes impractical to place a radiation source inside the pipe or behind it.

The COMSCAN laboratory equipment

The foregoing theoretical considerations have given strength to our conviction that, at least in a number of cases, a scatter-imaging technique can provide better results than transmission imaging, the conventional method. We have therefore extended our earlier work on fan-beam experiments by setting up a new and, again, rather experimental piece of imaging equipment, which we have called COMSCAN.

This equipment (*fig. 7a*) is a typical laboratory version, built entirely from proven components from standard X-ray equipment to form a modular system. The modular arrangement offers considerable scope for experiments on image-quality parameters,

[9] G. Harding, On the sensitivity and application possibilities of a novel Compton scatter imaging system, IEEE Trans. NS-29, 1260-1265, 1982.

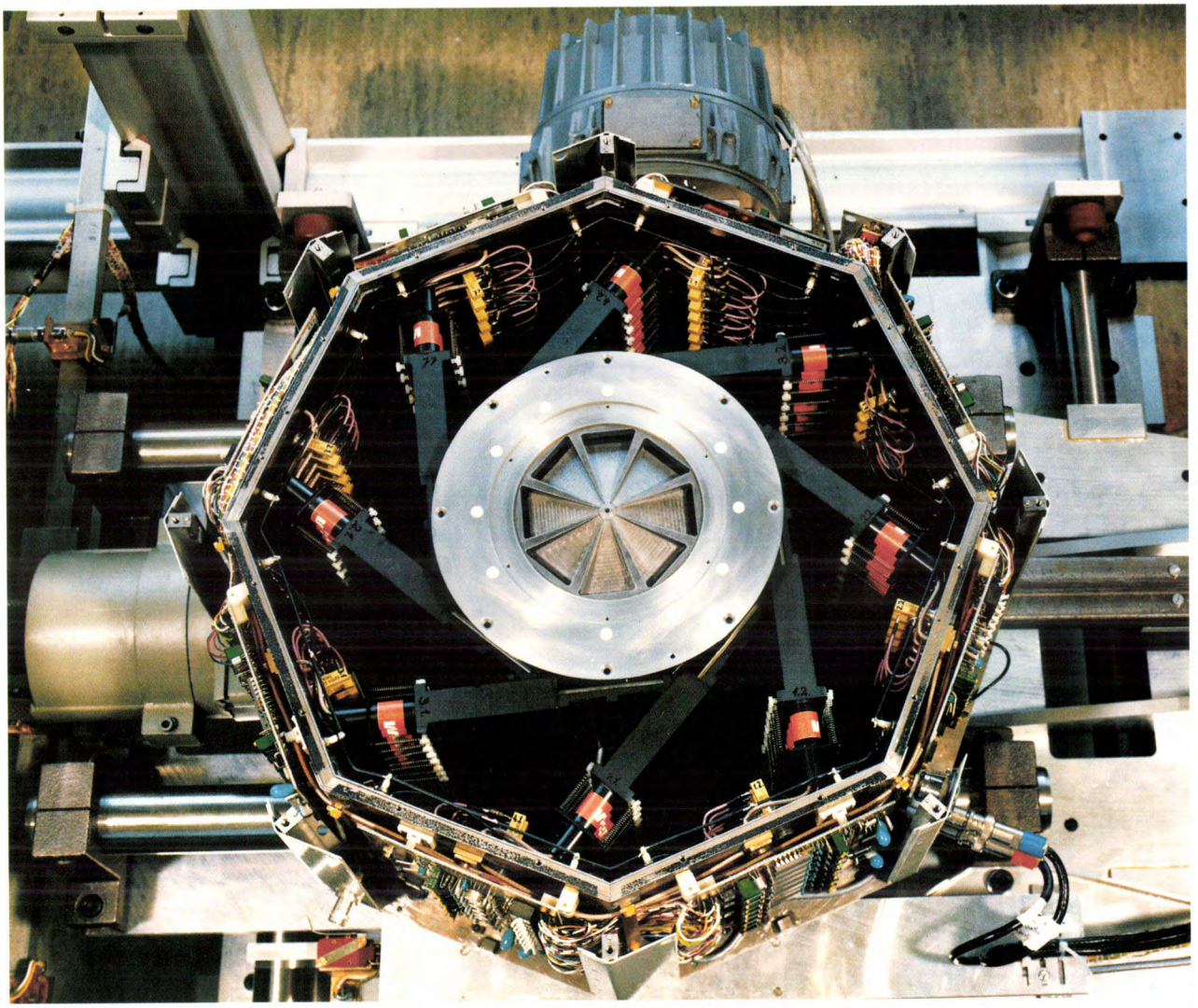

a

Fig. 7. *a*) COMSCAN, the latest laboratory equipment developed at Hamburg for investigation of X-ray back-scatter imaging. The X-ray tube, near the floor of the room, can be seen just to the left of the octagonal housing. The small (1 mm × 1 mm) aperture at the centre of the eight 'spokes' of the flange in the middle of the photograph helps to define the primary beam. The eight collimator slits (seven are clearly visible) at the end of the spokes focus the back-scatter radiation on to 32 pairs of scintillation counters, all mounted in the octagonal housing. The four uppermost pairs can be seen clearly (the tangential black structures). The arrangement of the counters permits simultaneous full-circle detection throughout a body depth of about 6 cm, at a best axial resolution of 8 mm (see text). The object table, normally mounted over the octagonal housing, was removed for the photograph. *b*) The geometry of COMSCAN, partially of the pencil-beam type. *B* test object, located on the object table *OT*. The X-rays are produced by the tube *X*; the square (1 mm × 1 mm) apertures *RA* in the lead shields *LS* shape the cross-section of *PB*, the primary beam. *SC* eight collimator slits (fig. 7*a*); these all admit back-scatter radiation simultaneously at scattering angles ranging from 105° to 150°. *S* detector unit, consisting of 32 pairs of scintillation counters (1-1*, 2-2*, . . . , 32-32*, see small diagram for position), distributed over 8 'rings'. (The top ring consists of the counter pairs 1-1*, 2-2*, 3-3*, 4-4*, and the pattern continues in the lower rings.) The detector unit, the shields *LS*, and the tube *X* can all be moved simultaneously for certain scanning operations. *OT* and *B* remain fixed (see fig. 8).

at present especially in back-scatter methods. Fast-scanning methods will also be studied soon, since these could become of interest in the near future, e.g. for following the ventricular motions of the human heart.

Design

The COMSCAN system is based on a simple geometry, partially of the pencil-beam type (fig. 7*b*). The X-ray tube, again of an industrial type, is operated at a nominal 3 kW with a maximum voltage of 150 kV. The average energy of the emitted X-ray spectrum, 65 keV, is sufficiently low to guarantee a reasonably isotropic scatter (fig. 6) — a prerequisite for an efficient back-scatter method. The primary beam is defined by two square apertures (1 mm × 1 mm) in lead shields (thickness 10 mm); the edges of the apertures are specially shaped to reduce edge scattering and to suppress the production of the characteristic Kα-Pb radiation as well as possible.

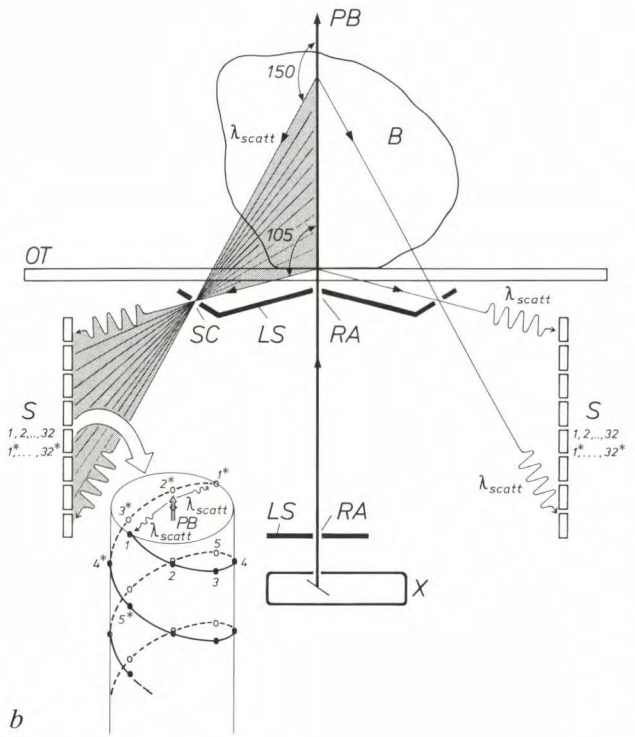

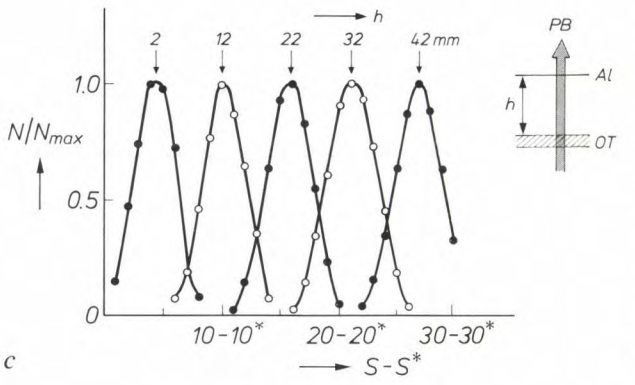

c) Scatter distributions (or 'point-spread functions') measured with COMSCAN. Vertically plotted: N/N_{max}, the relative number of quanta, obtained from the individual counts from 8 (up to 11) subsequent pairs of detectors. *S-S** pair number of the detectors. The scattering object *Al* (a small piece of aluminium wire, thickness 3 mm) has been mounted at five distances (*h*) above *OT*. From the measurement of a scatter distribution an unknown *h* can be found with a uncertainty of less than 2 mm.

At the centre of the photograph (fig. 7*a*) there are eight collimator slits for focusing the back-scatter radiation on to a number of BGO scintillation detectors [10], all located in the large octagonal housing. In total the collimator slits, which are separated by eight radial lead wedges, admit about 85 per cent of the total radiation available from the annular scattering zone at the scattering angle concerned. The edges of the slits are specially shaped, and to suppress the detection of spurious radiation sets of steel lamellae (not visible in the photograph) have been inserted in front of the scintillation crystals. The lamellae are particularly efficient for the suppression of multiple-scatter radiation.

The arrangement of the scintillation crystals in the housing is such that the detectors count — effectively in full-circle geometry and also simultaneously — the back-scatter radiation originating from a linear array of 32 volume elements. This array covers a depth of some 6 cm along the axial (= primary-beam) direction in the body to be scanned. Each volume element has a cross-sectional area of 1 mm × 1 mm, as defined by the primary beam, while the axial dimension is 7 mm, a value that follows from the crystal and collimator-slit geometry. A dimension of 7 mm implies a considerable overlap between neighbouring volume elements, of course. Their relative displacement in the axial direction is about 1.8 mm.

The centre points of the 64 scintillation crystals are arranged in pairs, diametrically opposite to one another, on two parallel helices that start at the top face of the housing and finish at the lower face (fig. 7*b*, diagram). In this way a cylindrical surface around the incident primary beam is monitored by 32 pairs of scintillation crystals arranged in a uniform spatial distribution. This arrangement provides detection over 360° and over the total height of the housing. Each pair corresponds to a single back-scattering angle, or more accurately to a small range of angles, dependent upon the axial coordinate of the pair. For the top pair the angle is 105°, and for the bottom pair it is 150°.

The counts registered by each of the 32 pairs are stored separately, thus representing each of the 32 volume elements whose scatter radiation has been measured. The acceptance angle of the collimator slits is sufficiently large to reduce the statistical counting errors (or picture noise) for one pair of detectors to values as low as 1 per cent in a counting time of 10 ms. For full-circle geometry the counts from four consecutive pairs have to be added together. This decreases the axial resolution slightly (to about 8.0 mm), with the advantage, however, of a picture-noise reduction to 0.5 per cent in the same counting period of 10 ms.

The irradiation dose in 10 ms at the surface of the scanned body amounts to a dose equivalent of about 1.7 mSv [11]. This relatively low value for the irradiation dose is due to the presence of a thin copper shield

[10] BGO, for $Bi_4Ge_3O_{12}$ or bismuth germanate, is a promising high-*Z* gamma-ray detector. See for example A. E. Evans, Jr., IEEE Trans. **NS-27**, 172, 1980.

[11] The sievert, 1 joule/kg, is the unit of dose equivalent, the quantity that expresses the risk of the deleterious effects of ionizing radiation upon living organisms. 1 Sv = 100 rem, the older unit (see International Standard ISO 31/10, February 1982). In the natural environment man is exposed to about 1.5 mSv/year.

(150 μm) in front of the window of the X-ray tube; the shield removes most of the low-energy quanta from the primary beam before it enters the body. If they were not removed these quanta would increase the absorbed dose via the photoelectric effect strongly.

Fig. 7*c* gives a number of scatter distributions (or 'point-spread functions') that have been obtained from the individual counts from about ten pairs of detectors. The scattering object was a thin piece of aluminium wire that could be mounted at five different distances above the object table (in air). The similarity of the different distributions confirmed in the first place that the counters could provide reasonably uniform detection of the scatter radiation originating from the primary beam. The full width at half height of such a point-spread function is a direct consequence of the slice thickness (7 mm); the latter follows from the geometry used. Moreover, the distance from the centre of the object — the centre-line of the wire — to the object table can be determined from a measured scatter distribution, with a constant uncertainty of less than 2 mm. The uncertainty is therefore independent of the distance to the object table, at any rate up to 5 cm.

Separate storage of the counts from each pair of detectors is recommended if axial-resolution values obtainable with COMSCAN are to be improved further in the future. Bringing down the present 7-mm resolution to, say, the 2-mm precision of the point-spread functions experiment of fig. 7*c* would in addition require smaller crystals and, unfortunately, considerably longer irradiation times (to maintain the image quality in other respects).

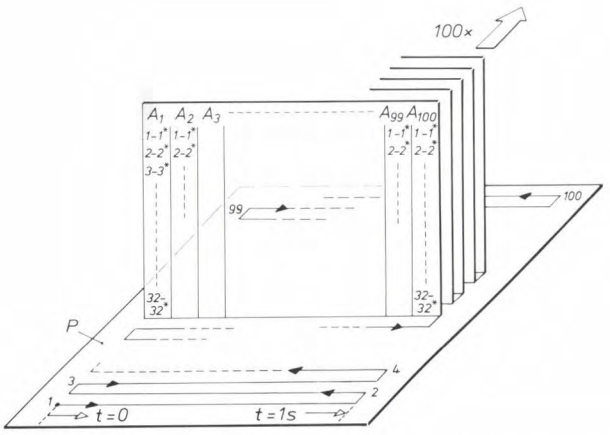

Fig. 8. The line pattern 1, 2, 3, . . . , 99, 100 in the horizontal plane *P* indicates the scanning movement the tube *X* and the detectors *S* (fig. 7*b*) execute together. Each line scan (length 100 mm) takes 1 second to register sequentially 100 arrays A_i of counts — represented by one vertical plane. An array contains back-scatter radiation from 32 volume elements, as detected by the scintillation-counter pairs 1-1*, 2-2*, . . . , 32-32*, respectively. Completed in 100 s, the total scan covers an irradiated volume of 100 mm × 100 mm × 60 mm (the depth is 60 mm). Thus the back-scattering radiation from 32×10^4 different volume elements is read and stored individually.

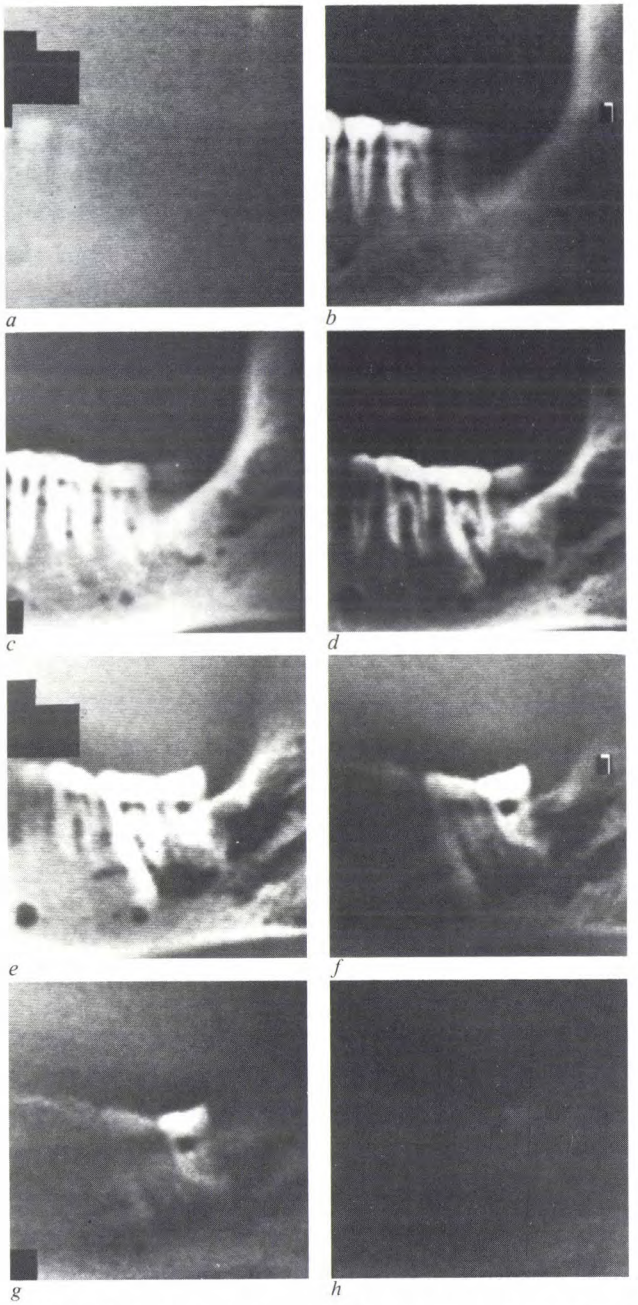

Fig. 9. Eight back-scatter images of a human mouth, obtained with COMSCAN. *a-h* order of increasing depth. Each slice represents 60 mm × 60 mm of irradiated surface; the separation of adjacent slices is 3.8 mm. White: high density regions. For details of the teeth, jawbone, and tissues observed, see text. Experimental conditions: cross-section of primary beam 1 mm × 1 mm; axial resolution 8.0 mm (obtained by connecting the pairs of detectors in groups of four).

Fig. 8 shows the scanning movement of the detector housing and the X-ray tube. The object to be scanned and the table on which it lies do not move. The total volume scan takes 100 seconds; it consists of 100 vertical planar slices, each resulting from 100 linear arrays of 32 volume elements. The counts registered are read and stored every 10 ms. Finally, a simple re-sorting of the stored data gives the distribution of the

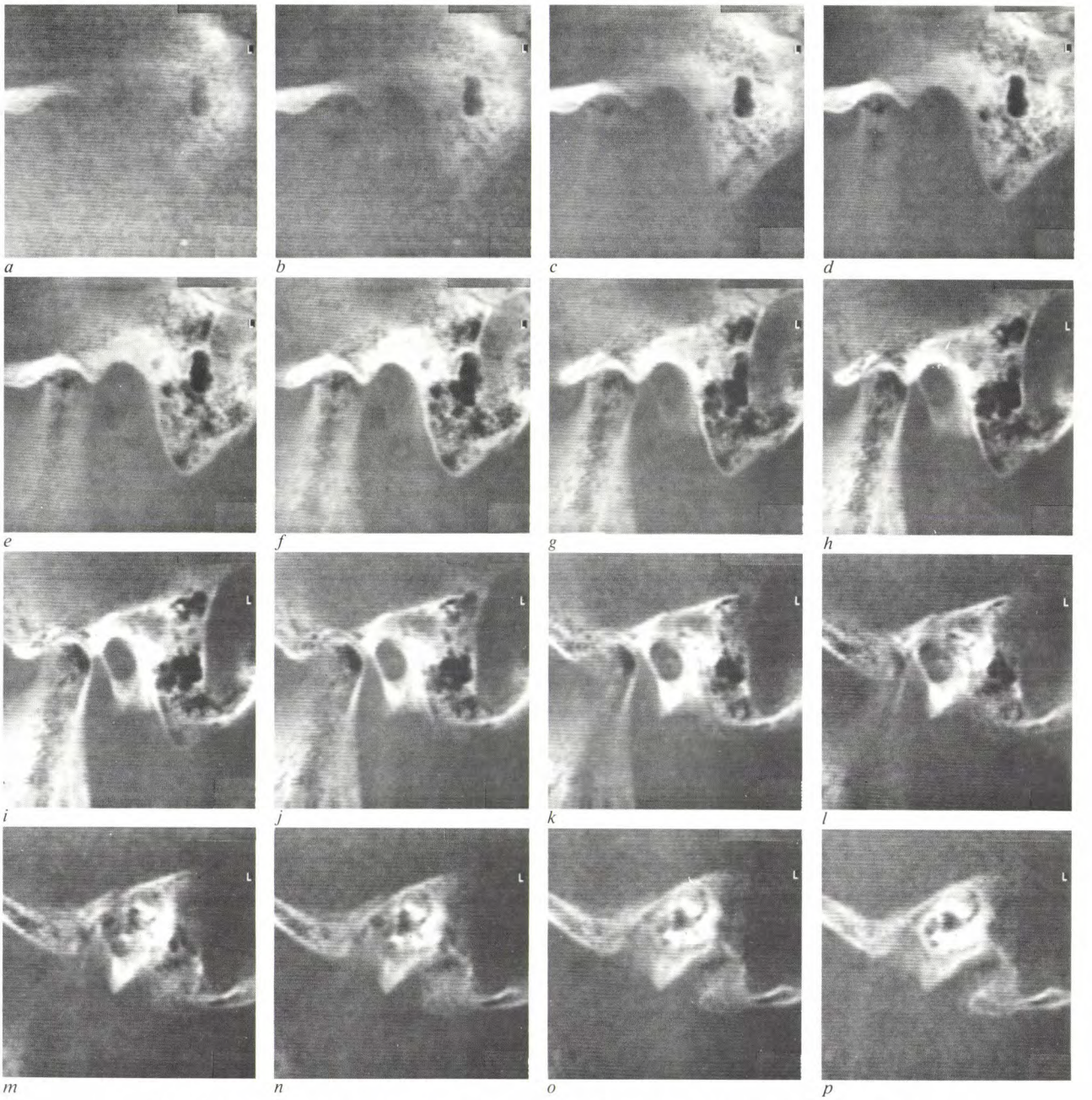

Fig. 10. Sixteen back-scatter images of a human skull, showing ear and lower jaw, obtained with COMSCAN. The images are focused at 1.875-mm intervals, in order of increasing depth into the skull. Each slice represents an area of 60 mm × 60 mm. For anatomical details of the imaged structures, see text. Experimental conditions: cross-section of primary beam 0.5 mm × 0.5 mm; axial resolution 8.0 mm (obtained by connecting the pairs of detectors in groups of four).

back-scattering intensity in each of the horizontal plane slices, 32 in number, each comprising 100×100 volume elements. The individual slices can be inspected on a black-and-white monitor, with a grey scale of up to 256 levels.

Two examples of back-scatter imaging

Fig. 9 shows a set of eight slices of a human mouth, obtained with COMSCAN. Taken through the side of the jaw, the slices are all oriented parallel to the cheek; they are given here in order of increasing depth. The teeth at the front of the jaw are closer to the equipment than those at the back, so that moving the imaged slice deeper into the mouth has the effect of bringing into focus first the canine tooth (see fig. 9*b*, *c*), then the molars (fig. 9*d*, *e*), and finally the wisdom tooth (fig. 9*f*, *g*). In these pictures various anatomical details are immediately apparent: the enamel (white) of the

teeth, the dentine (grey) and the pulp (black) tissue of the teeth, the teeth roots with attached vessels, and the porous structure inside the jawbone.

It is clear that much useful information will be lost by superimposing all these images on top of one another, as well as on the image of the other side of the jaw, as could happen in a conventional X-ray picture of the mouth.

The second example (*fig. 10*) of back-scatter imaging with COMSCAN shows sixteen slices through a human skull and ear, all parallel to the side of the skull. Fig. 10*a*, the one taken at minimum depth, shows some of the temporal arch and the side of the skull (temporal bone) superimposed on the uniform background of the object table. These structures become clearer in figs 10*b* to 10*d*, which also reveal the highly porous nature of the mastoid outgrowth (bottom right). Figs 10*e* to 10*h* show the joint of the lower jawbone and the interior of the mastoid. Deeper in the skull (fig. 10*i*) the exterior ear channel becomes visible, disappearing again in the slices of figs 10*l* to 10*p* to make way for detail of the middle and inner

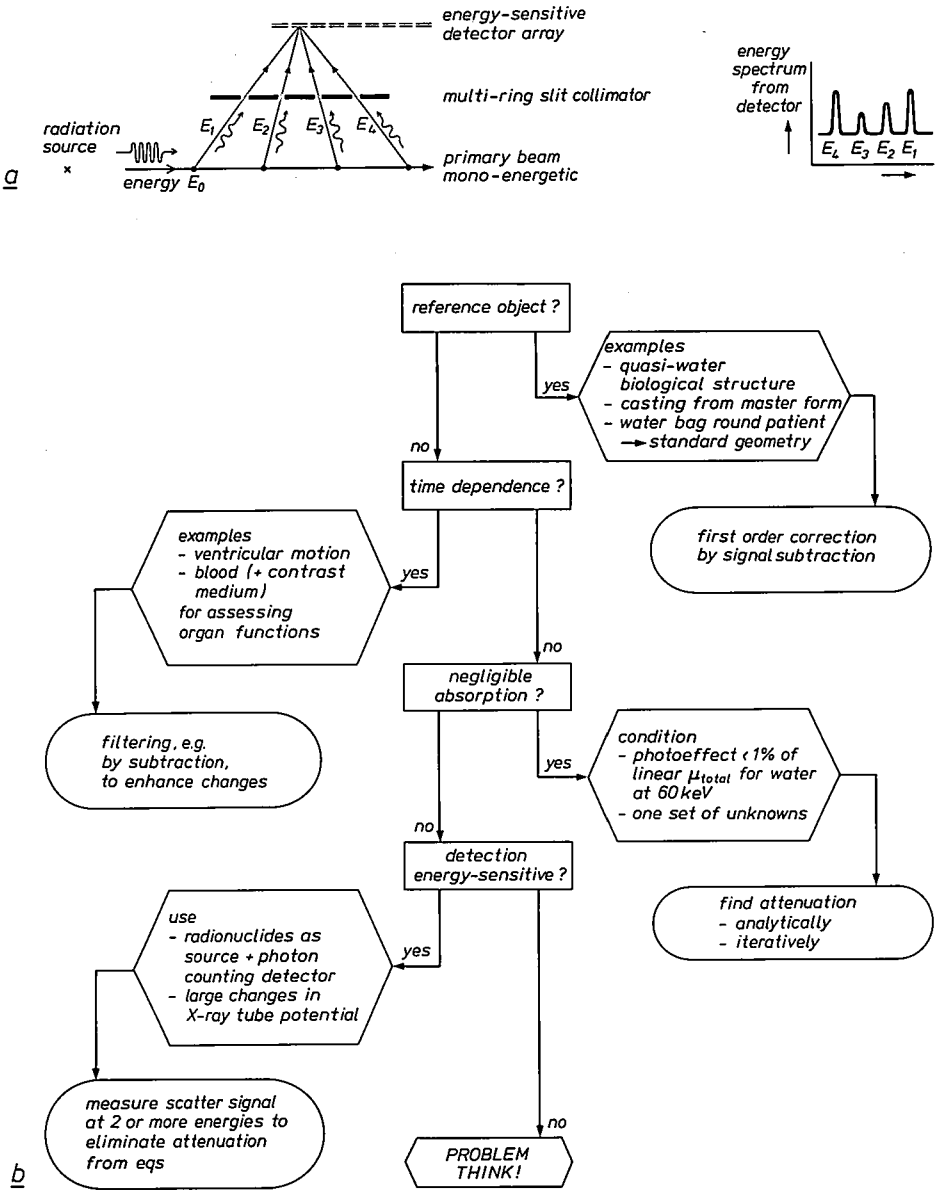

Fig. 11. Topics for new research in back-scatter X-ray imaging. *a*) Imaging by means of an energy-sensitive detector array via multi-ring slit collimator, using a reasonably mono-energetic primary beam. The detector signals would show a spectrum with four lines. Such an 'indirect' scatter-imaging method could reduce the absorbed dose values for constant image qualities considerably. *b*) The attenuation problem. The purpose of this decision tree is to set the general strategy for dealing with the attenuation effects, which should introduce some badly needed 'streamlining' in this complex situation.

ear, with the cochlea (figs 10*n* to 10*p*) now the most obvious feature.

Because of the large amount of bone material present in these images, we have corrected the data for photoelectric attenuation using a 'dual energy' scan technique [12], in which the object is scanned twice, once with a low X-ray energy, once with a high X-ray energy.

The two examples have been used here mainly to demonstrate how useful scatter imaging can be in avoiding superposition problems. X-ray pictures like figs 9 and 10 have even more advantages to offer, however. With the aid of data-correction methods of the kind described earlier it is easy to use them for determining any small local differences in mass density. Such deviations from uniformity in small areas could reveal the presence of malformations at an early stage.

Assessment and prospects

The experimental results presented indicate that the scattering technique is a realistic option for X-ray imaging. The main advantages are first, the direct three-dimensional imaging — which allows an unusually wide range of objects to be investigated and avoids any reconstruction from projections — and secondly, the free choice of the measurement geometry. In one almost 'extreme' configuration, with both the X-ray source and the detector on the same side of the object, it is possible to make high-sensitivity scans of organs close to the body surface. This back-scatter mode gives interesting results — the best so far — both in medical applications and in industrial non-destructive testing. However, the relatively poor use of the X-ray tube output and the non-availability of versatile high-efficiency detectors (with acceptance angles amounting to the better part of 4π steradians) do present challenging problems worthy of research.

One such promising topic for further research would be the investigation of a multi-ring slit collimator combined with an energy-sensitive detector array in situations where the primary beam is reasonably mono-energetic (*fig. 11a*). Such studies would provide a stimulus to the application mentioned earlier of a fast-scanning technique for dynamic recording of the ventricular motions of the heart. Another topic with some hope of progress in the near future is a general study of more accurate methods of correction for the attenuation effects. Fig. 11*b* gives some information on present methods of dealing with the attenuation problem. The information is presented as a decision tree, to show where research would be most appropriate.

Valuable support and cooperation in this work was given by K. H. Fischer, A. Meyer, H. Schroeder and W. Selke.

Summary. The production of images by detection of Compton-scatter radiation is an alternative to transmission X-ray imaging. Calculations show that with ring-slit geometry and objects for which dimension × absorption coefficient < 1, scatter imaging is more sensitive than transmission imaging. Tumours in breast tissue can be diagnosed and voids in aluminium castings can be detected. Since there is no superposition, three-dimensional resolution of 2 mm or better is feasible. COMSCAN, an equipment designed at Philips Forschungslaboratorium in Hamburg for scatter-imaging investigations, is a modular system constructed from standard X-ray equipment components. Pencil-beam (1 mm × 1 mm) geometry is used, with full-circle detection (by BGO-scintillation counters) of back-scatter radiation at angles from 105° to 150°. A narrow ring slit (85 per cent free aperture) functions as a pinhole focusing element. At a surface dose equivalent of about 1.7 mSv, a volume of dimensions 100 mm × 100 mm × 60 mm (the depth 60 mm) is line-scanned in 100 s. The scatter data are read out and stored every 10 ms, at a spatial frequency of 1 mm^{-1}. Frontal slices with a depth resolution of about 8 mm and a picture noise of 0.5 per cent are shown on a monitor. Corrections are made for beam attenuation and multiple scatter. The development of versatile arrays of annular energy-sensitive detectors with multi-ring collimators is considered.

[12] J. Coumans, J. Kosanetzky and F. W. Zonneveld, Computerized dual-energy imaging: a technical description, Medicamundi 27, 125-132, 1982.

Philips Tech. Rev. 41, 60-69, 1983/84, No. 2

Nucleation and growth of silicon films by chemical vapour deposition

J. Bloem and W. A. P. Claassen

Chemical vapour deposition (CVD) is a long-established method, widely used in IC technology, for depositing a thin silicon film on a hot substrate from a chemically reactive gas mixture. The article below describes an experimental study of the nucleation and growth of silicon by CVD, which has provided a better understanding of the molecular processes that take place in the gas phase and at the substrate surface. The knowledge thus gained may contribute to better control of the CVD process and the properties of the silicon films.

Introduction

Since the sixties silicon has become a very important material in the electronics industry. Single-crystal silicon is a basic material for all IC technology, and thin films of polycrystalline silicon are widely used as conductors and as gate electrodes in MOS transistors, for example, and in ICs. Increased interest has recently been shown in amorphous silicon because of its possible application as a basic material for solar cells.

A good method of producing thin silicon films is chemical vapour deposition (CVD), in which silicon is deposited from the gas phase on to a hot substrate from a chemically reactive mixture of gases. The gas phase consists of a reactive mixture of a carrier gas and a silicon compound. The growth rate and the properties of the films depend closely on the conditions during deposition, such as the pressure and the composition of the gas mixture and the temperature of the substrate.

At Philips and elsewhere a great deal of knowledge has been gained through the years about the conditions necessary for producing silicon films that possess the required properties. This article describes an investigation that included a systematic study of the way in which silicon nuclei form at the substrate surface and how this nucleation leads to further growth [1]. The investigation was particularly concerned with growth on substrates of amorphous silicon dioxide (SiO_2) and silicon nitride (Si_3N_4), which are widely used in IC technology for the deposition of polycrystalline films. In the CVD process there are two separate phases: nucleation, in which the nuclei grow until they coalesce, and the subsequent growth, which is essentially the growth of silicon on silicon. The investigation has provided a clearer picture of the part played by the various molecules and stages in the overall growth process, and in many cases the effects of the different process conditions can now be satisfactorily explained.

The article starts with a short description of the CVD method that we used. The nucleation of silicon on SiO_2 and Si_3N_4 and the subsequent growth of silicon on silicon are then dealt with. Finally a brief account is given of the control of some of the properties of the silicon films.

Prof. Dr J. Bloem, formerly with Philips Research Laboratories, Eindhoven, is a Professor at the Catholic University of Nijmegen; Dr Ir W. A. P. Claassen is with Philips Research Laboratories, Eindhoven.

The CVD method for silicon

In the growth of thin silicon films by the CVD method, gaseous silicon compounds such as silane (SiH_4) and chlorosilanes (SiH_2Cl_2, $SiHCl_3$ and $SiCl_4$) are passed over a hot substrate. Hydrogen (H_2) is usually employed as reducing agent and carrier gas in this process. Occasionally nitrogen (N_2) is used as the carrier gas and hydrogen chloride (HCl) is added to the gas mixture to influence the nucleation and growth rate. *Fig. 1* gives a diagram of a CVD arrangement used mainly for producing single-crystal films on single-crystal substrates of materials such as silicon or sapphire. The substrates to be coated are placed on a graphite block (a 'susceptor'), which is heated by a radio-frequency generator. To prevent the deposition of silicon on the vitreous-silica envelope of the reactor, the reactor is cooled by water or air. The equipment also includes gas-flow controllers for H_2, HCl and the gaseous silicon compound, in this case SiH_4. When the gases flow over the hot substrates, chemical reactions occur accompanied by the deposition of silicon.

The rate at which a silicon film grows decreases with the temperature of the substrate. In *fig. 2* the growth rate is plotted on a logarithmic scale as a function of $1000/T$ for silicon growth from four gas mixtures of H_2 with SiH_4, SiH_2Cl_2, $SiHCl_3$ or $SiCl_4$. Although the mixtures have very different growth rates, their behaviour as a function of temperature is very similar. In all cases a temperature reduction at high temperatures causes a small decrease in growth rate, whereas at low temperatures the decrease is much more pronounced. This is attributable to the difference in the rate-determining step during growth. At high temperatures the gas-phase diffusion of the reactive molecules to the substrate determines the rate of growth. Since the diffusion coefficients in the gas phase are only slightly temperature-dependent ($\propto T^{3/2}$), the temperature does not have much effect on the growth rate. At low temperatures the surface reactions determine the growth rate. Reactions such as adsorption, desorption, surface diffusion and the incorporation of silicon atoms in a lattice possess an activation energy, so that as the temperature falls the reaction rates decrease exponentially. The decrease in the growth rate becomes greater with increasing activation energy of the rate-determining surface reaction. For the growth of silicon from silane and chlorosilanes it turns out that this activation energy is always about 160 kJ/mol.

As would be expected from what we have said above, the effect of the total gas pressure is particularly marked at high temperatures, as can be seen in *fig. 3*. When the gas pressure is reduced, the molecules diffuse more freely. As a consequence the growth rate

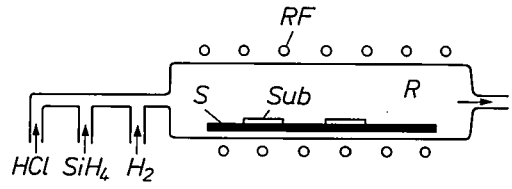

Fig. 1. Diagram of the CVD equipment for depositing silicon films. The reactor *R* consists of a vitreous-silica tube, cooled by water or air. Inside the reactor the substrates *Sub* to be coated are positioned on a graphite susceptor *S*. The susceptor and the substrates are heated to the required temperature by a radio-frequency coil *RF*. The gas flow in the reactor in this case consists of hydrogen (H_2), silane (SiH_4) and hydrogen chloride (HCl).

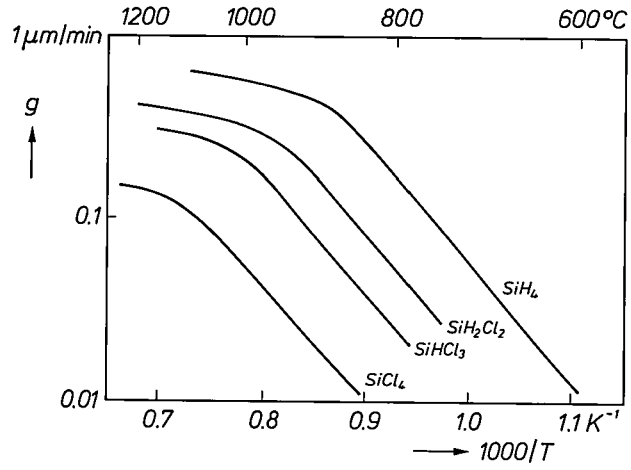

Fig. 2. Growth rate *g* plotted on a logarithmic scale against $1000/T$ (T is the absolute temperature) for silicon films produced by CVD from SiH_4, SiH_2Cl_2, $SiHCl_3$ or $SiCl_4$ (100 Pa) and hydrogen at atmospheric pressure (10^5 Pa). In each of these cases the decrease in growth rate is much greater at lower temperatures than at higher temperatures.

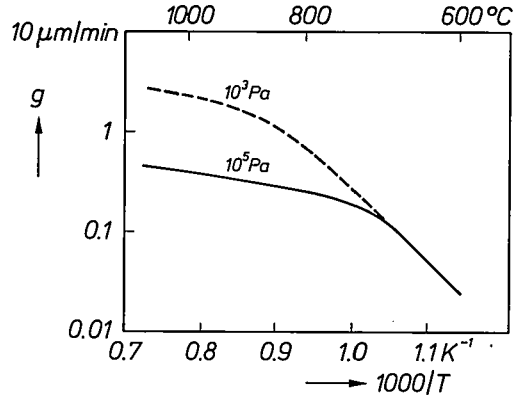

Fig. 3. Growth rate *g* plotted on a logarithmic scale against $1000/T$ for the deposition of silicon from nitrogen and silane (10^2 Pa) at atmospheric pressure (10^5 Pa) and at low pressure (10^3 Pa). At high temperatures the reduction in total pressure causes a marked increase in the growth rate.

[1] A more detailed description is given in: W. A. P. Claassen, Kinetic studies on the nucleation and growth of silicon via chemical vapour deposition, Thesis, Nijmegen 1981.

increases, provided the partial pressure of the silicon compound in the gas phase remains unchanged.

The partial pressure of the silicon compound in the gas phase can also have a considerable influence. As an example *fig. 4* shows a plot of the growth rate against the partial pressure of $SiCl_4$ in H_2 [2]. With increasing $SiCl_4$ pressure the growth rate increases linearly to a maximum value, and then decreases to zero. This can be explained by assuming that there is a thermodynamic equilibrium between two competing reactions:

$$SiCl_4(g) + 2H_2(g) \rightleftarrows Si(s) + 4HCl\ (g) \quad \textit{growth} \quad (1)$$
$$Si(s) + 2HCl(g) \rightleftarrows SiCl_2(g) + H_2(g) \quad \textit{etching} \quad (2)$$

With increasing $SiCl_4$ pressure the etching reaction becomes more important, so that the growth rate decreases. When the $SiCl_4$ pressure is very high the growth rate on a silicon substrate can in fact become negative, so that silicon is etched away instead of being deposited.

Nucleation and growth on the surface of a single-crystal substrate can be described with the aid of a simple model [3], shown schematically in *fig. 5*. In this model the crystal surface contains a series of atomic 'steps'. An adsorbed silicon atom, formed by the decomposition of an adsorbed silicon-containing molecule, diffuses over the surface to a more stable position at a step. It then diffuses along this step until it arrives at a 'kink' position. The atom has then reached a stable 'semicrystalline' (or 'half-crystal') position and is regarded as part of the lattice. For such two-dimensional growth to take place the surface diffusion must be sufficiently fast. Single-crystal films can therefore only be formed if the substrate temperature is sufficiently high. At a somewhat lower temperature there is more chance of nucleation between the steps because of the slower diffusion, and this may give rise to relative misorientation between the nuclei, ultimately giving a polycrystalline film. At even lower temperatures the diffusion may be so slow that one atom may not have diffused away before another arrives at the same place. This leads to the formation of an amorphous film, in which only short-range order exists. We shall not discuss nucleation on single-crystal substrates further [4].

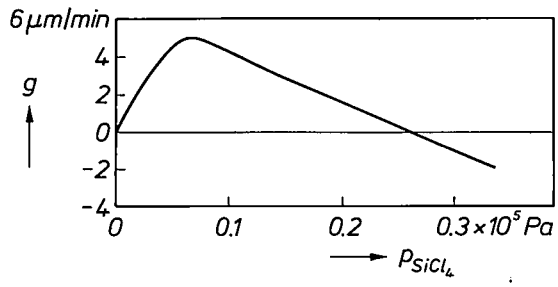

Fig. 4. Growth rate g of silicon on a silicon substrate as a function of the $SiCl_4$ pressure p_{SiCl_4} at 1270 °C with hydrogen (10^5 Pa) as carrier gas [2]. At high $SiCl_4$ pressures the etching effect of the hydrogen chloride released is so strong that the growth rate can become negative.

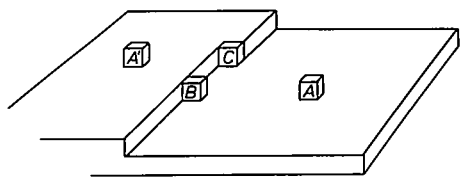

Fig. 5. Simple model for two-dimensional growth of silicon films. An adsorbed atom A diffuses to a more stable position B at a 'step' formed by a linked series of atoms [3]. It then travels along the step to arrive at a still more stable 'kink' position C. The same thing can happen with an atom A' adsorbed one step higher.

On amorphous substrates of materials such as SiO_2 and Si_3N_4 so much three-dimensional growth occurs that purely polycrystalline and amorphous films are formed. Properties such as the electrical resistivity of polycrystalline silicon films are chiefly determined by grain size. To obtain grains of the required size, accurate control of the process conditions is essential. We shall now demonstrate the part played in this process by the nucleation of silicon on amorphous SiO_2 and Si_3N_4.

Nucleation of silicon on SiO_2 and Si_3N_4

Before nucleation occurs an equilibrium concentration of adsorbed atoms is first built up, which depends on the adsorption rate and the rates of desorption and chemical reactions [5]. The next stage is the formation of nuclei of varying sizes, until at a critical size the nuclei start to grow by attracting neighbouring atoms. As soon as the diameter of the nuclei is larger than about 0.02 μm the progress of the nucleation can clearly be followed with a scanning electron microscope (SEM) and a transmission electron microscope (TEM). *Fig. 6* shows eight SEM photomicrographs made at different times from the start of the deposition on SiO_2 from a mixture of H_2, SiH_4 and HCl. At three seconds no nuclei are visible. Between 6 and 25 seconds an almost constant number of nuclei can be observed that steadily increase in size, the average diameter growing from about 0.2 μm to about 0.5 μm. Then the number of nuclei decreases, because the growing nuclei start to coalesce. The nucleation density can be derived from photomicrographs such as this. The density varies from 10^4 to 10^{11} per cm^2, depending on the supersaturation in the gas phase, the composition of the gas mixture and the substrate temperature.

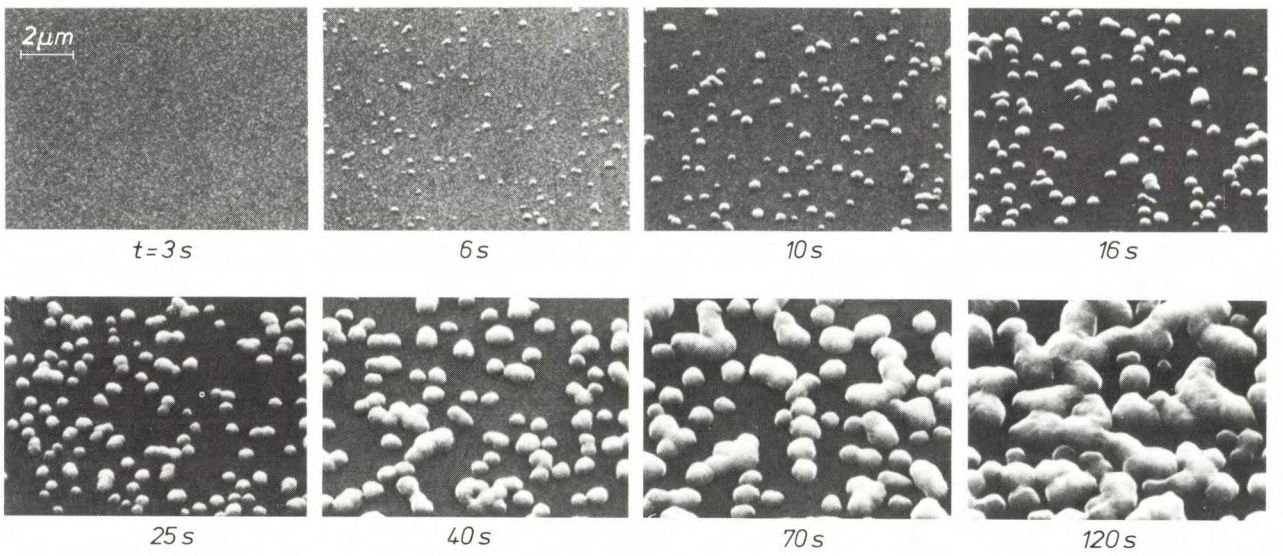

Fig. 6. SEM photomicrographs of the silicon nuclei at different times during the deposition from silane (88 Pa), hydrogen chloride (440 Pa) and hydrogen (10^5 Pa) on an SiO_2 substrate at 1000 °C. Between 6 and 25 seconds after the start of deposition the nuclei become larger but the density of the nuclei remains practically constant. Eventually the nuclei come increasingly into contact with each other and coalesce.

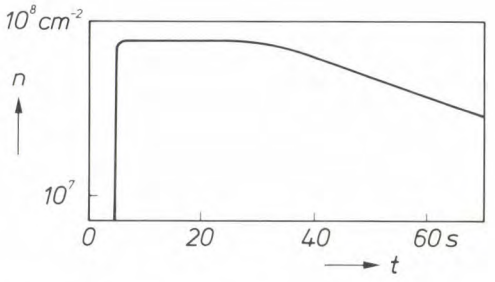

Fig. 7. Nucleation density n as a function of time t for the deposition shown in fig. 6. After an incubation period of about 3 seconds, n rises very rapidly to a steady value, the saturation density. After about 25 seconds there is a gradual decrease as a result of the coalescence of the nuclei.

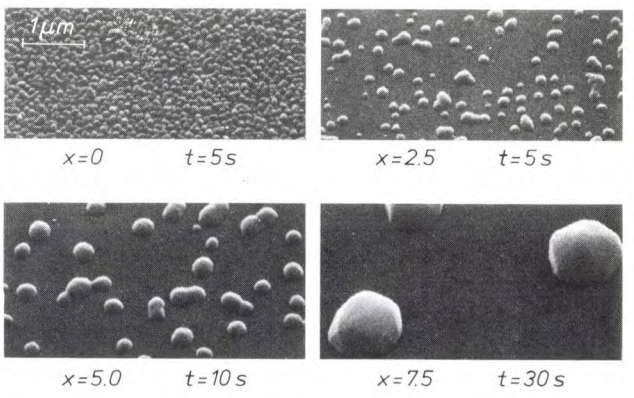

Fig. 8. SEM photomicrographs of silicon nuclei during deposition from silane (88 Pa), hydrogen chloride and hydrogen (10^5 Pa) on an SiO_2 substrate at 1000 °C and at four different HCl partial pressures. The photomicrographs were taken at the time t when saturation density was reached. A larger ratio x between the partial pressure of hydrogen chloride and silane gives a lower saturation density.

Fig. 7 shows the nucleation density for the gas mixture in fig. 6 plotted as a function of the time during which the mixture was supplied. After a short 'incubation period' the nucleation density very quickly reaches a steady value, the saturation density. From then on the number of nuclei counted remains constant, while the nuclei continue to grow. After about 30 seconds the nucleation density slowly decreases because of coalescence of the nuclei. From the size distribution of the nuclei and the occurrence of an incubation period it appears that the visible nuclei are formed in a very short time. The time needed to reach the saturation density is shorter for an Si_3N_4 substrate than for an SiO_2 substrate. It is also shorter when the SiH_4/HCl ratio in the gas mixture is greater and the substrate temperature higher.

The saturation density depends strongly on the gas composition. *Fig. 8* shows SEM photomicrographs for four SiO_2 substrates subjected to mixtures of different HCl/SiH_4 ratio. The highest saturation density is observed for silane in hydrogen. Adding HCl to the gas mixture gives an appreciable reduction of the saturation density.

[2] H. C. Theuerer, J. Electrochem. Soc. **108**, 649, 1961.
[3] W. K. Burton, N. Cabrera and F. C. Frank, Phil. Trans. R. Soc. **243**, 299, 1951.
[4] See for example:
H. A. Abbink, R. M. Broudy and G. P. McCarthy, J. Appl. Phys. **39**, 4673, 1968;
B. A. Joyce, Rep. Prog. Phys. **37**, 363, 1974;
J. Blanc and M. S. Abrahams, J. Appl. Phys. **47**, 5151, 1976.
[5] W. A. P. Claassen and J. Bloem, J. Electrochem. Soc. **127**, 194, 1980.

The saturation density is also considerably affected by the temperature of an SiO_2 substrate; see *fig. 9*. When the temperature is reduced from 1200 to 925 °C the saturation density rises steeply. Addition of HCl increases the temperature dependence as well as reducing the nucleation density. Similar behaviour is observed for Si_3N_4 substrates, but the decrease in the nucleation density on the addition of HCl is smaller than for an SiO_2 substrate.

The saturation density n_s between 925 and 1200 °C depends on the partial pressures p_{SiH_4} and p_{HCl} and the substrate temperature T in the following way:

$$n_s \propto \left[\frac{p_{SiH_4}}{1 + 6\times10^{-4}p^2_{HCl}}\right]^{(i+1)/2} \cdot \exp(E/kT), \qquad (3)$$

where E is the activation energy for nucleation and k is Boltzmann's constant. The parameter i is the number of atoms of a 'critical' nucleus, i.e. a nucleus whose dimensions are such that the probability of continued growth is the same as the probability of extinction. *Fig. 10* gives a plot of the saturation density at 1000 °C against the ratio $p_{SiH_4}/(1 + 6\times10^{-4}p^2_{HCl})$ for the deposition of silicon on an SiO_2 or an Si_3N_4 substrate. This ratio can be taken as the effective silane partial pressure. An increase in this pressure can cause a marked increase in the saturation density. On Si_3N_4 the saturation density is substantially higher than that on SiO_2. It can also be seen that the pressure at which nucleation takes place is always higher than 0.1 Pa, the equilibrium vapour pressure of silane in contact with solid silicon and hydrogen gas. From the slopes of the curves for SiO_2 and Si_3N_4 it appears that the value of i at a high effective silane pressure is about 1. This implies that every adsorbed silicon atom can be regarded as a nucleus. At lower pressures the value of i increases, and for an SiO_2 substrate it does so more strongly than for an Si_3N_4 substrate.

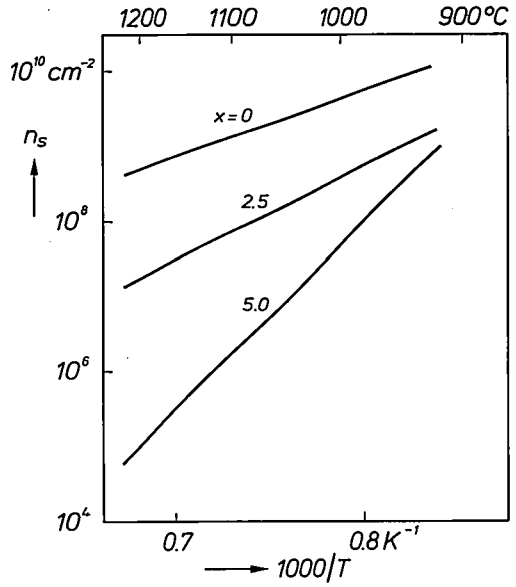

Fig. 9. Saturation density n_s of silicon nuclei on an SiO_2 substrate as a function of $1000/T$, for deposition from three mixtures of silane (73 Pa), hydrogen chloride and hydrogen (10^5 Pa). A larger ratio x of the partial pressure of the hydrogen chloride to that of the silane gives a stronger temperature dependence and a lower saturation density.

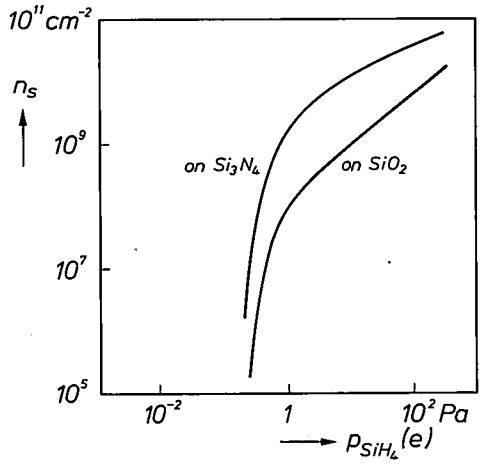

Fig. 10. Saturation density n_s of silicon nuclei on SiO_2 and Si_3N_4 at 1000 °C for deposition from silane, hydrogen chloride and hydrogen (10^5 Pa) as a function of the effective silane partial pressure $p_{SiH_4}(e) = p_{SiH_4}/(1 + 6\times10^{-4}p^2_{HCl})$. The saturation density on Si_3N_4 is substantially higher than that on SiO_2.

The change in the critical nucleus size with the effective silane partial pressure is reflected in the values of the activation energy of nucleation, which may be derived from curves like those in fig. 9. *Fig. 11* gives a plot of the activation energy against the effective silane pressure for nucleation on SiO_2 and Si_3N_4. The activation energy for SiO_2 is higher than for Si_3N_4. When the silane pressure is reduced the activation energy for SiO_2 increases much more strongly than for Si_3N_4 and this difference can be attributed to the reaction of adsorbed silicon atoms with the SiO_2 substrate,

$$Si\,(s) + SiO_2\,(s) \rightleftarrows 2SiO\,(g), \qquad (4)$$

which is accelerated by the presence of hydrogen [5]. This reaction is more likely to occur at a lower silane pressure: owing to the lower nucleation density it takes longer before the whole surface is covered with silicon. No such reaction is found with an Si_3N_4 substrate.

At lower temperatures the difference in saturation density between an SiO_2 and an Si_3N_4 substrate is much greater [6]. Whereas in the case of Si_3N_4 the saturation density continues to increase linearly with $1/T$, for SiO_2 there is a marked decrease at temperatures lower than 925 °C; see *fig. 12*. If nitrogen is used as carrier gas for the CVD process instead of hydrogen, the substrates have practically the same saturation density. This indicates that atomic hydrogen is

adsorbed at the SiO_2 surface, partially blocking the adsorption sites for SiH_4. This effect is less pronounced on Si_3N_4 because N-H has a much lower binding energy than O-H: 347 as against 426 kJ/mol.

Our experiments have given us a better understanding of the nucleation of silicon on substrates of amorphous SiO_2 and Si_3N_4. This also applies to the experiments in which we used a chlorosilane instead of silane as a silicon compound in the gas phase [7]. The better understanding thus obtained permits better control of the grain size and hence of other properties of the polycrystalline films. Owing to the marked variation in nucleation density — 10^4 to 10^{11} per cm^2 — the grain size may also vary considerably. After coalescence of the growing nuclei the grains in the film give further columnar growth, which may be regarded as the growth of silicon on silicon. We shall now look more closely at the kinetics of this process.

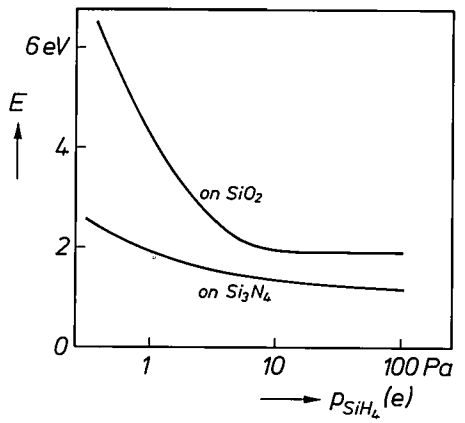

Fig. 11. Activation energy E for nucleation during the deposition of silicon from silane, hydrogen chloride and hydrogen on an SiO_2 and an Si_3N_4 substrate, as a function of the effective silane partial pressure $p_{SiH_4}(e)$. The nucleation on SiO_2 has a much higher activation energy than that on Si_3N_4, especially at low silane pressures.

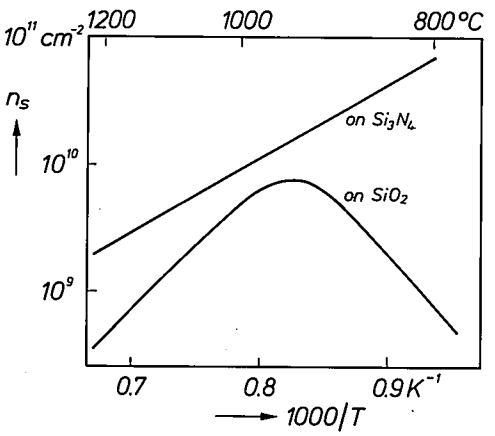

Fig. 12. Saturation density n_s of silicon nuclei on SiO_2 and Si_3N_4 for deposition from silane (100 Pa) and hydrogen (10^5 Pa), as a function of $1000/T$. At lower temperatures the saturation density falls rapidly for deposition on SiO_2.

Growth kinetics of silicon on silicon

The CVD growth of single-crystal silicon on a single-crystal silicon substrate usually takes place at temperatures above 1050 °C in order to obtain films with the fewest possible defects. At these temperatures the reactions at the surface are so rapid that the gas phase diffusion is the rate-determining step (fig. 2). Growth in this temperature range has been the subject of much investigation and reasonable explanations have been given for the different effects on the growth rate and the properties of the films [8].

The situation with the growth of polycrystalline and amorphous films, usually at lower temperatures, is quite different. The growth rate here is determined by reactions at the surface that are not very well understood. Until recently the descriptions given were therefore usually of a speculative nature. It was partly for this reason that we performed experiments designed to give us a better understanding of the growth kinetics at low temperatures (700-1000 °C). We again used silane and chlorosilanes as the silicon compound in the reactive gas mixture.

Growth via silane

The growth of polycrystalline silicon films via silane was studied at atmospheric pressure using hydrogen or nitrogen or a mixture of the two as the carrier gas. The growth rate depends closely on the silane pressure and the composition of the carrier gas. At a given silane pressure the rate is highest in pure nitrogen and lowest in pure hydrogen. The effect of the silane pressure is shown in *fig. 13* for three different carrier gases,

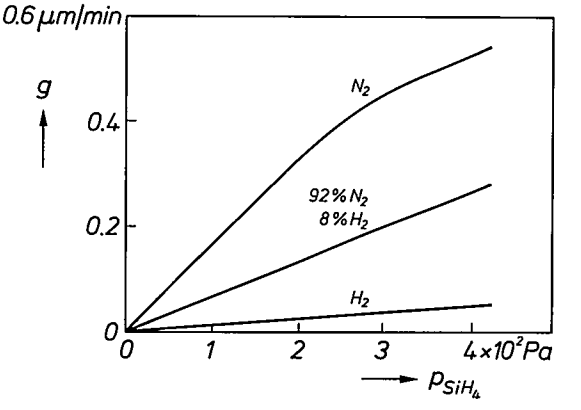

Fig. 13. Growth rate g of silicon during deposition at 700 °C from silane, hydrogen or nitrogen or a mixture of hydrogen and nitrogen as a function of the silane partial pressure p_{SiH_4}. The growth rate increases when the silane pressure is raised and when the relative amount of hydrogen in the gas mixture is reduced.

[6] W. A. P. Claassen and J. Bloem, J. Electrochem. Soc. **128**, 1353, 1981.
[7] W. A. P. Claassen and J. Bloem, J. Electrochem. Soc. **127**, 1836, 1980.
[8] See for example J. Bloem, J. Cryst. Growth **50**, 581, 1980.

hydrogen, nitrogen and a mixture of the two. The growth rate is seen to be proportional to the silane pressure and inversely proportional to the hydrogen pressure in the gas mixture.

We were able to deduce from these results that SiH_2 molecules adsorbed at the surface play a leading part [9]. Close to the silicon surface the following reaction occurs:

$$SiH_4\,(g) \rightleftarrows SiH_2\,(g) + H_2\,(g). \qquad (5)$$

This reaction is followed by adsorption of SiH_2 at the surface. It appears from the observed dependence of the silane and hydrogen pressures that the decomposition of silane and the adsorption of SiH_2 is very rapid; the growth-rate-determining step does not occur until later. An adsorbed SiH_2 molecule diffuses over the surface until it reaches a stable position; see fig. 5. Finally the hydrogen atoms are released:

$$SiH_2\,(s) \rightleftarrows Si\,(s) + H_2\,(g). \qquad (6)$$

This desorption is probably the rate-determining step of growth via silane.

The addition of hydrogen chloride to silane has the effect of reducing the growth rate. The reduction increases as the substrate temperature decreases and the amount of hydrogen contained in the carrier gas decreases. The effect of the HCl pressure for different silane contents at 900 °C is shown in *fig. 14*. When the partial pressure p_{HCl} increases the growth rate first drops sharply by an amount proportional to p^2_{HCl}, then decreases gradually at a rate that is also proportional to p^2_{HCl}. The sharp fall due to a small addition

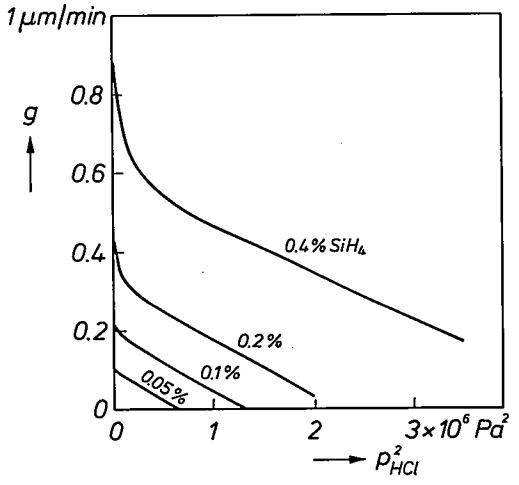

Fig. 14. Growth rate g of silicon for deposition from silane, hydrogen chloride and hydrogen (10^5 Pa) at 900 °C, plotted against the square of the HCl partial pressure, at four different SiH_4 partial pressures. In each of these cases an addition of hydrochloric acid first causes a sharp drop in the growth rate followed by a more gradual decrease, both approximately proportional to p^2_{HCl}.

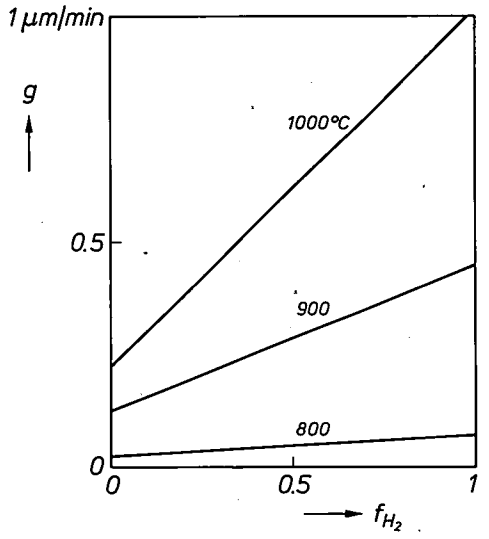

Fig. 15. Growth rate g of silicon from SiH_2Cl_2, hydrogen and nitrogen as a function of the hydrogen content f_{H_2} in the gas mixture, at three different temperatures. The growth rate rises linearly with the hydrogen content, and rises more steeply as the temperature increases.

of HCl is attributable to the reaction of HCl with adsorbed SiH_2:

$$SiH_2\,(s) + 2HCl\,(g) \rightleftarrows SiCl_2\,(s) + 2H_2\,(g). \qquad (7)$$

Adsorbed $SiCl_2$ molecules diffuse over the surface and are trapped at a step (fig. 5). They then yield silicon by reduction:

$$SiCl_2\,(s) + H_2\,(g) \rightleftarrows Si\,(s) + 2HCl\,(g). \qquad (8)$$

This reaction takes place relatively slowly, however, so that an excess of $SiCl_2$ is produced on the surface, giving rise to desorption and sharply reducing the growth rate. Besides initiating the conversion of SiH_2 into $SiCl_2$, an addition of HCl also attacks the silicon lattice itself by the etching reaction of equation (2). The rate of the etching reaction is proportional to p^2_{HCl} and inversely proportional to the hydrogen pressure [10]. This reaction causes the gradual drop in growth rate, until growth changes to etching.

Growth via chlorosilanes

With the chlorosilanes SiH_2Cl_2, $SiHCl_3$ and $SiCl_4$ as silicon compound in the gas phase we carried out the same experiments as with silane. It appears that $SiCl_2$ molecules play a leading part in growth via chlorosilanes. These molecules are formed near the silicon surface by the following reactions:

$$SiH_2Cl_2\,(g) \rightleftarrows SiCl_2\,(g) + H_2\,(g) \qquad (9)$$

$$SiHCl_3\,(g) \rightleftarrows SiCl_2\,(g) + HCl\,(g) \qquad (10)$$

$$SiCl_4\,(g) + H_2\,(g) \rightleftarrows SiCl_2\,(g) + 2HCl\,(g) \qquad (11)$$

The $SiCl_2$ molecules are adsorbed at the surface, and

then diffuse over it until they reach a stable position (fig. 5). After this they are reduced to silicon by the reaction of equation (8). For growth via SiH_2Cl_2 and $SiHCl_3$ this reduction turns out to be the rate-determining step [11].

A consequence of the involvement of hydrogen in the rate-determining step is that the growth rate increases almost linearly with the partial hydrogen pressure in the gas mixture. For mixtures of SiH_2Cl_2, H_2 and N_2 this increase becomes smaller as the temperature decreases; see *fig. 15*. This is because the decomposition of SiH_2Cl_2 expressed by equation (9) is slower at lower temperatures.

At 1000 °C there is a large linear increase in the growth rate when the SiH_2Cl_2 pressure in hydrogen is raised, whereas at lower temperatures saturation occurs; see *fig. 16*. This points to a higher concentration of adsorbed $SiCl_2$ molecules waiting for reduction. We have found a similar effect with $SiHCl_3$ in hydrogen. In this case some saturation occurs at 1000 °C as well, but this is a consequence of the etching effect of HCl, which arises during the decomposition of $SiHCl_3$ described by equation (10).

With $SiCl_4$ in hydrogen there is no saturation at low temperatures [11]. The etching effect of the hydrogen chloride released is so strong that above a particular $SiCl_4$ partial pressure the growth rate decreases and may even go negative (fig. 4). Saturation does not occur at low temperatures because the $SiCl_2$ molecules important to growth are produced only to a limited extent by the gas-phase reduction of equation (11) but much more by the action of $SiCl_4$ on silicon:

$$SiCl_4\,(g) + Si\,(s) \rightleftarrows 2SiCl_2\,(s). \qquad (12)$$

At low temperatures this reaction is the rate-determining step for growth via $SiCl_4$, so that the $SiCl_2$ concentration at the surface remains relatively low.

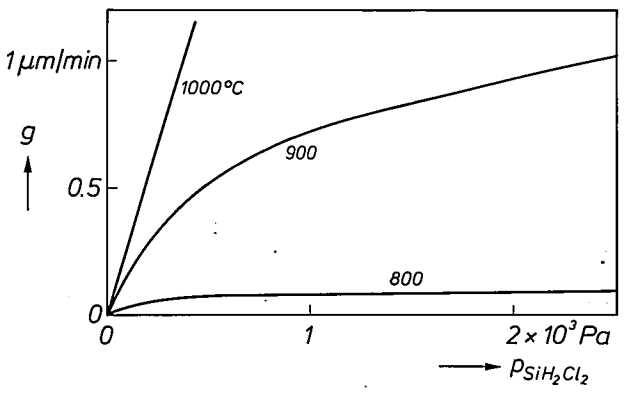

Fig. 16. Growth rate g of silicon from SiH_2Cl_2 and hydrogen (10^5 Pa) as a function of the partial SiH_2Cl_2 pressure, at three different temperatures. At lower temperature there is a definite saturation.

The difference in kinetics is also reflected in the decrease in the growth rate when HCl is added to the gas phase. With SiH_2Cl_2 in hydrogen a small addition of HCl does not give an abrupt decrease at 1000 °C, while at lower temperatures the decrease in growth rate is linear with the HCl pressure, not quadratic. The reason for this is the reduction in the $SiCl_2$ concentration by the reaction

$$SiCl_2\,(g) + HCl\,(g) \rightleftarrows SiHCl_3\,(g). \qquad (13)$$

The same effect is observed with $SiHCl_3$ in hydrogen. Here the linear dependence arises mainly because the addition of HCl opposes the dissociation of equation (10). With $SiCl_4$ in hydrogen the dependence with small quantities of HCl is relatively strong, but with an excess of HCl it is weaker and linear [11]. These results can be explained reasonably well by taking into account the effects of adding HCl on the parallel reactions that give $SiCl_2$. At lower temperatures $SiCl_2$ is more likely to be formed via the reaction of equation (12). This is less sensitive to the addition of HCl than the reaction of equation (11).

Control of properties

The results obtained provide a better understanding of the effect of the various parameters on the CVD growth of silicon films. This in turn permits better control of the properties of the films. An important parameter in this context is the growth rate. Economic considerations will always dictate the highest possible growth rate, so that a relatively large number of substrates can be covered in a short time. However, to obtain films with the desired properties it may be essential to have a low growth rate.

The growth rate and the temperature both help to determine the structure of films deposited on single-crystal substrates [12]; see *fig. 17*. For example, a high temperature and a low growth rate are required if single-crystal films are to be deposited in the manufacture of integrated circuits. Lowering the temperature and increasing the growth rate can introduce such distortion of two-dimensional growth (fig. 5) that polycrystalline films are ultimately produced. At even lower temperatures and higher growth rates amorphous silicon films are obtained, because the deposition is much faster than the surface diffusion.

[9] W. A. P. Claassen and J. Bloem, J. Cryst. Growth 51, 443, 1981.
[10] P. van der Putte, L. J. Giling and J. Bloem, J. Cryst. Growth 31, 299, 1975 and 41, 133, 1977.
[11] J. Bloem, W. A. P. Claassen and W. G. J. N. Valkenburg, J. Cryst. Growth 57, 177, 1982.
[12] J. Bloem and L. J. Giling, Current topics in materials science 1, E. Kaldis (ed.), North-Holland, Amsterdam 1978, chapter 4; J. Bloem, Pure & Appl. Chem. 50, 435, 1978.

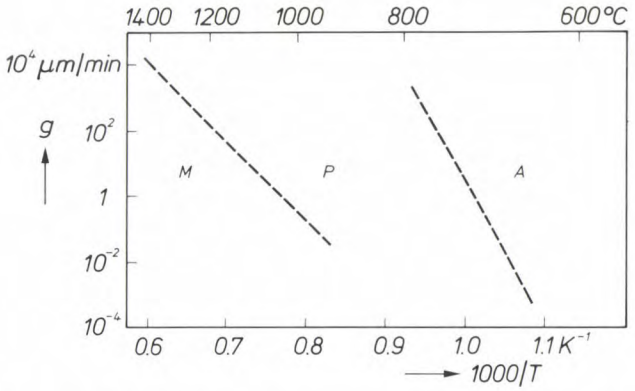

Fig. 17. Existence regions of single-crystal (*M*), polycrystalline (*P*) and amorphous (*A*) silicon as a function of $1000/T$ and the growth rate g.

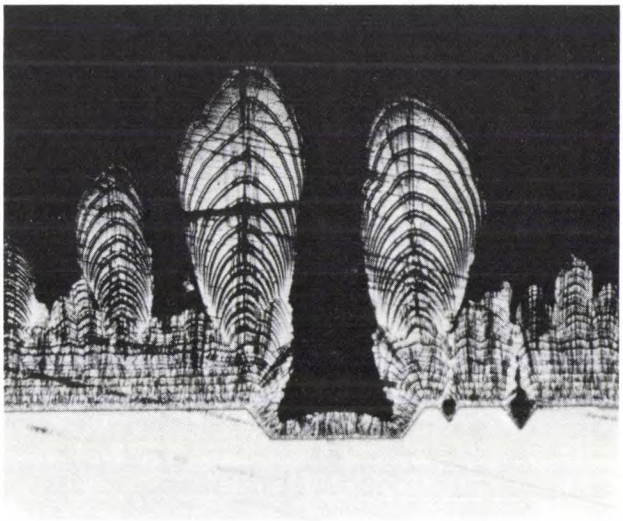

Fig. 18. Photomicrographs of silicon deposition from $SiHCl_3$ and hydrogen on an uneven substrate. At high temperatures severe bulging occurs (*above*). This can be avoided (*below*) by performing the deposition at lower temperatures or by increasing the $SiHCl_3$ partial pressure [15].

To deposit polycrystalline films at a low temperature (600-900 °C) and a low growth rate it is common practice to use a hot-wall reactor, consisting of a vitreous-silica tube that is heated in a furnace. The tube contains a silica crucible in which the substrates to be coated are mounted vertically [13]. Frequently the deposition is performed at low pressure (about 100 Pa). Because of the relative slowness of the surface reactions there is only a small concentration gradient in the gas flow, so that the growth rate is virtually independent of the position of the substrate. A large number of substrates can therefore be coated uniformly in the reactor at the same time. A hot-wall reactor is not so suitable for the deposition of single-crystal layers: at low temperatures the adsorbed molecules are not sufficiently mobile, and at high temperatures the SiO_2 wall reacts as indicated by equation (4).

The surface morphology of a deposited film is very important for applications in semiconductor technology. At high temperatures in particular, large fluctuations in film thickness may occur on substrates with uneven surfaces. As an example *fig. 18* is a photomicrograph of a film deposited on such a substrate via $SiHCl_3$ in hydrogen [14]. Raised parts of the surface and corners receive much more of the diffusion flux than the rest of the substrate, resulting in severe bulging. As can be seen in the other photomicrograph in fig. 18, this can be avoided by using a lower substrate temperature, so that the growth is slower and the rate of growth is determined by the surface reactions. It is however possible to obtain uniform coatings at high temperatures if the concentration of $SiHCl_3$ is increased to a level at which some etching occurs additionally [15]. Adding HCl to the gas mixture gives the same result. A further improvement in uniformity can be achieved by carrying out the deposition at a low pressure (about 100 Pa). This has the effect of increasing the gas-phase diffusion, so that the growth rate becomes more strongly dependent on the rate of the surface reactions.

The electrical properties of silicon films are closely dependent on the dopant content. For the same growth rate and composition in the gas phase the dopant content in a polycrystalline film is almost identical with that in a single-crystal film, but the conductivity values can differ considerably [16]; see *fig. 19*. With low doping the conductivity in a polycrystalline film is a great deal lower than that of a single-crystal film. This is because charge carriers are trapped at the grain boundaries [17]. With smaller grains there is more trapping, and the conductivity is then lower. Largely as a result of the better understanding of nucleation

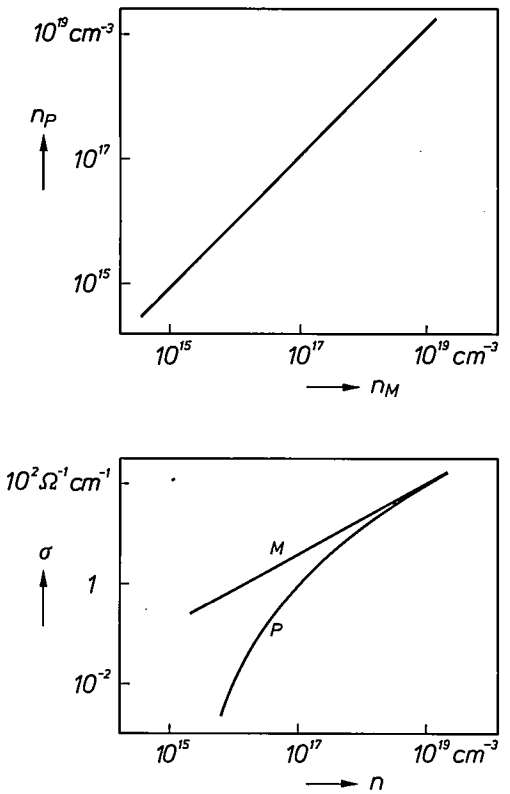

Fig. 19. *Above:* Dopant contents n_M and n_P in single-crystal and polycrystalline silicon, respectively, under identical conditions during deposition. With both weak and with strong doping n_P is virtually identical to n_M. *Below:* Electrical conductivity σ as a function of the dopant content n for single-crystal silicon (*M*) and polycrystalline silicon (*P*). With weak doping the conductivity of *P* is considerably lower than that of *M*.

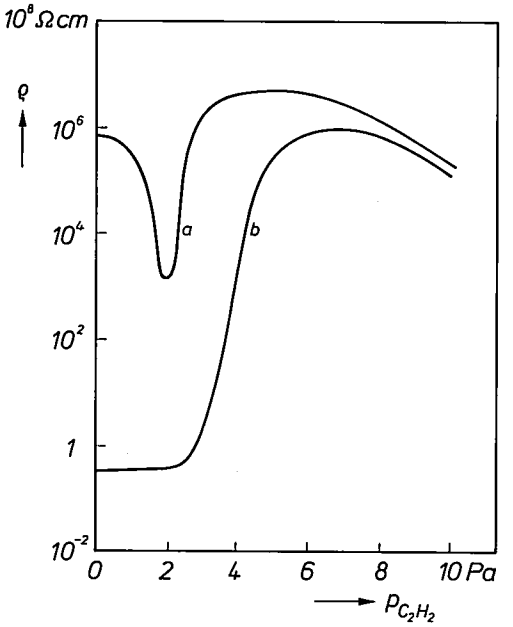

Fig. 20. Resistivity ϱ of phosphorus-doped polycrystalline silicon layers as a function of the ethyne partial pressure $p_{C_2H_2}$ during deposition from silane (200 Pa), phosphine (PH_3), ethyne and hydrogen (10^5 Pa) at 850 °C. With a ratio of 10^{-6} between the partial pressures of phosphine and silane an increase in the ethyne pressure first causes a sharp fall in resistivity, followed by a marked increase and finally a weak decrease (curve *a*). When the ratio is 10^{-4}, the resistivity at low ethyne pressure is considerably lower (curve *b*). At high ethyne pressure, however, there is little difference compared with curve *a*.

behaviour it has become possible to obtain better control of the electrical properties of polycrystalline silicon films.

Our last example shows how carbon can affect the grain size and electrical resistivity of polycrystalline silicon films. Carbon doping is obtained by adding ethyne (C_2H_2) to the reactive gas mixture [18]. In *fig. 20* the resistivity of two phosphorus-doped films is plotted against the ethyne pressure during growth via silane, phosphine (PH_3), ethyne and hydrogen. In the low-phosphorus film the resistivity first decreases sharply with increasing ethyne pressure. This is because the presence of carbon at the grain boundaries releases a number of charge carriers and increases their mobility [18]. At ethyne pressures above 2 Pa the solubility of carbon in silicon is exceeded. The addition of carbon then causes faster nucleation and results in smaller grains. This has the effect of reversing the initial drop in resistivity. The total grain surface becomes larger so rapidly that there is not enough carbon to keep the resistivity low. At high ethyne pressure (> 5 Pa) there is a further drop in resistivity, because the films become amorphous. The film with a high phosphorus content already has such a low resistivity that a small addition of carbon has practically no effect. At high ethyne pressure there is little difference compared with the low-phosphorus film.

Summary. Chemical vapour deposition (CVD) is a method widely used in IC technology for depositing a thin silicon film on a substrate. The reactive gas mixture from which the deposition takes place consists of a carrier gas (H_2 and/or N_2) and a silicon compound such as SiH_4, SiH_2Cl_2, $SiHCl_3$ or $SiCl_4$, occasionally supplemented with HCl. The nucleation of polycrystalline silicon on substrates of amorphous SiO_2 and Si_3N_4 is strongly dependent on the gas composition, the type of substrate and the substrate temperature. In the further growth of silicon on silicon the SiH_2 and $SiCl_2$ molecules adsorbed at the surface play a significant part in the process. The influence of the process conditions on the growth rate can be brought into relation with the diffusion and the chemical reactions in the gas phase and at the substrate surface. The improved understanding of these relationships permits better control of the properties of the silicon films.

[13] C. H. J. van den Brekel and L. J. M. Bollen, J. Cryst. Growth 54, 310, 1981.
[14] C. H. J. van den Brekel, Philips Res. Rep. 32, 118, 1977.
[15] C. H. J. van den Brekel and J. Bloem, Philips Res. Rep. 32, 134, 1977.
[16] J. R. Monkowski, J. Bloem, L. J. Giling and M. W. M. Graef, Appl. Phys. Lett. 35, 410, 1979.
[17] J. Y. W. Seto, J. Appl. Phys. 46, 5247, 1975 and 47, 5167, 1976;
C. H. Seager and D. S. Ginley, Appl. Phys. Lett. 34, 337, 1979.
[18] J. Bloem and W. A. P. Claassen, Appl. Phys. Lett. 40, 725, 1982.

Scientific publications

These publications are contributed by staff of laboratories and plants that form part of or cooperate with enterprises of the Philips group of companies, particularly by staff of the research laboratories mentioned below. The publications are listed alphabetically by journal title.

Philips GmbH Forschungslaboratorium Aachen, Weißhausstraße, 5100 Aachen, Germany — *A*

Philips Research Laboratory Brussels, 2 avenue Van Becelaere, 1170 Brussels, Belgium — *B*

Philips Natuurkundig Laboratorium, Postbus 80000, 5600 JA Eindhoven, The Netherlands — *E*

Philips GmbH Forschungslaboratorium Hamburg, Vogt-Kölln-Straße 30, 2000 Hamburg 54, Germany — *H*

Laboratoires d'Electronique et de Physique Appliquée, 3 avenue Descartes, 94450 Limeil-Brévannes, France — *L*

Philips Laboratories, N.A.P.C., 345 Scarborough Road, Briarcliff Manor, N.Y. 10510, U.S.A. — *N*

Philips Research Laboratories, Cross Oak Lane, Redhill, Surrey RH1 5HA, England — *R*

Philips Research Laboratories Sunnyvale P.O. Box 9052, Sunnyvale, CA 94086, U.S.A. — *S*

F. Bregman* & A. Kastelein* (* *Philips Science & Industry Div., Eindhoven*)	The evolution of the oscilloscope	Acta Electron. **24**	291-295	1982
C. Loty *L*	L'oscilloscopie numérique et les systèmes à conversion de balayage	Acta Electron. **24**	297-300	1982
R. Brun *L*	De l'oscilloscope conventionnel à l'oscilloscope à mémoire numérique	Acta Electron. **24**	301-308	1982
K. W. M. P. Zeppenfeld (*Philips Elcoma Div., Heerlen*)	Oscilloscope tubes: past, present and future	Acta Electron. **24**	309-316	1982
T. Vriz *L*	Amplificateur large bande pour oscilloscope	Acta Electron. **24**	317-331	1982
W. N. Schreiner & R. Jenkins (*Philips Electron. Instr., Mahwah, NJ*) *N*	Automatically correcting for specimen displacement error during XRD search/match identification	Advances in X-ray analysis, Vol. 25, eds J. C. Russ *et al.*, Plenum, New York	231-236	1982
G. Leyendecker*, J. Doppelbauer*, D. Bäuerle* (* *Univ. Linz*), P. Geittner & H. Lydtin *A*	Raman diagnostics of CVD systems: determination of local temperatures	Appl. Phys. A **30**	237-243	1983
J. H. Neave, B. A. Joyce, P. J. Dobson* & N. Norton* (* *Imp. College, London*) *R*	Dynamics of film growth of GaAs by MBE from RHEED observations	Appl. Phys. A **31**	1-8	1983
J. P. Gowers *R*	TEM image contrast from clustering in Ga-In containing III-V alloys	Appl. Phys. A **31**	23-27	1983
A. J. van Roosmalen *E*	Plasma parameter estimation from rf impedance measurements in a dry etching system	Appl. Phys. Lett. **42**	416-418	1983
A. R. Miedema & A. K. Niessen *E*	The enthalpy of solution for solid binary alloys of two 4d-transition metals	CALPHAD **7**	27-36	1983
A. K. Niessen, F. R. de Boer*, R. Boom (*Hoogovens, IJmuiden*), P. F. de Châtel*, W. C. M. Mattens* (* *Univ. Amsterdam*) & A. R. Miedema *E*	Model predictions for the enthalpy of formation of transition metal alloys II	CALPHAD **7**	51-70	1983
M. Davio & C. Ronse *B*	Rotator design	Discrete Appl. Math. **5**	253-277	1983
L. Vriens, A. H. M. Smeets & H. J. Cornelissen *E*	Modeling of a glow discharge	Electrical breakdown and discharges in gases, Pt.B, eds E. E. Kunhardt & L. H. Luessen, Plenum, New York	65-117	1983
P. M. Ballard *R*	Waveguide-bandwidth millimetric mixer with IF to 18 GHz	Electron. Lett. **19**	46-47	1983

J. M. Woodcock & J. J. Harris	*R*	Bulk unipolar diodes in MBE GaAs	Electron. Lett. **19**	181-183	1983
G. D. Khoe, J. Poulissen & H. M. de Vrieze	*E*	Efficient coupling of laser diodes to tapered monomode fibres with high-index end	Electron. Lett. **19**	205-207	1983
R. J. van de Plassche & H. J. Schouwenaars	*E*	A monolithic 14 bit A/D converter	IEEE J. **SC-17**	1112-1117	1982
P. Piret & T. Krol	*B, E*	MDS convolutional codes	IEEE Trans. **IT-29**	224-232	1983
P. Delsarte, Y. V. Genin & Y. Kamp	*B*	A polynomial approach to the generalized Levinson algorithm based on the Toeplitz distance	IEEE Trans. **IT-29**	268-278	1983
L. Thurlings	*E*	On the noise power spectral density of particulate recording media	IEEE Trans. **MAG-19**	84-89	1983
J. E. Knowles	*R*	The coercivity of multiple acicular particles	IEEE Trans. **MAG-19**	90-94	1983
H. K. Kuiken	*E*	A class of backward free-convective boundary-layer similarity solutions	Int. J. Heat & Mass Transfer **26**	655-661	1983
P. J. Severin	*E*	Single-mode optical fiber technology I. Propagation properties and material dispersion in single-mode fibers	Integrated optics, eds S. Martellucci & A. N. Chester, Plenum, New York	73-86	1983
P. J. Severin	*E*	Single-mode optical fiber technology II. Silica-based single-mode fiber technology, loss and polarization properties	Integrated optics, eds S. Martellucci & A. N. Chester, Plenum, New York	87-99	1983
P. J. Severin	*E*	Single-mode optical fiber technology III. Double-crucible drawing technology and compound glass fibers	Integrated optics, eds S. Martellucci & A. N. Chester, Plenum, New York	101-109	1983
D. J. Breed, A. B. Voermans, P. Q. J. Nederpel & B. A. H. van Bakel	*E*	Magnetic properties and growth conditions of manganese-containing iron garnet films for magnetic bubbles	J. Appl. Phys. **54**	1519-1527	1983
G. Leyendecker*, H. Noll*, D. Bäuerle* (* *Univ. Linz*), P. Geittner & H.Lydtin	*A*	Rapid determination of apparent activation energies in chemical vapor deposition	J. Electrochem. Soc. **130**	157-160	1983
B. J. Mulder & S. van Heusden	*E*	Mechanism of glass darkening by a low pressure mercury discharge	J. Electrochem. Soc. **130**	440-449	1983
H. K. Kuiken, F. E. P. Mikkers (*Philips Elcoma Div., Eindhoven*) & P. E. Wierenga	*E*	Laser-enhanced electroplating on good heat-conducting bulk materials	J. Electrochem. Soc. **130**	554-558	1983
J. W. Smits, S. B. Luitjens, F. J. A. den Broeder & A. G. Dirks	*E*	Magnetic properties and microstructure of CoCr based vertical recording materials prepared by ion beam sputtering	J. Magn. & Magn. Mater. **31-34**	920-922	1983
J. W. Smits, H. A. Algra, U. Enz & R. P. van Stapele	*E*	Ion beam sputter deposition of layered magnetic thin films	J. Magn. & Magn. Mater. **35**	89-92	1983
F. Crowet & C. Dierieck	*B*	Stream function formulation of the 2-*d* Stokes problem in a multiply-connected domain	J. Mec. Theor. Appl. **2**	67-74	1983
D. M. Krol & R. K. Janssen	*E*	Raman study of the chemical reactions during the melting of a $15Na_2CO_3$-$10BaCO_3$-$75SiO_2$ batch	J. Physique **43** (Colloque C9)	C9/347-C9/350	1982
B. M. J. Smets & T. P. A. Lommen	*E*	The leaching of sodium containing glasses: ion exchange or diffusion of molecular water?	J. Physique **43** (Colloque C9)	C9/649-C9/652	1982
G. A. Beck *et al.*	*E*	High density frame transfer image sensor	Jpn. J. Appl. Phys. **22** (Suppl. 22-1)	109-112	1983
R. J. Sluyter	*E*	Spraakcodering voor het mobiele radiokanaal	K.I.V.I. Leergang Mobiele Communicatie, Eindhoven 1983	52-60	1983
P. van Dooren	*B*	Reducing subspaces: definitions, properties and algorithms	Matrix pencils, eds B. Kagstrom & A. Ruhe, (Lect. Notes Math. **973**), Springer, Berlin	58-73	1983
A.E.T.Kuiper, F.H.P.M.Habraken, A. van Oostrom & Y. Tamminga	*E*	Chemical composition of LPCVD silicon nitride and silicon oxynitride layers	Philips J. Res. **38**	1-18	1983

F. H. P. M. Habraken, A. E. T. Kuiper & Y. Tamminga	*E*	Thermal nitridation of monocrystalline silicon, polycrystalline silicon and silicon dioxide films	Philips J. Res. **38**	19-36	1983
J. L. Gentner	*L*	Vapour phase growth of GaAs by the chloride process under reduced pressure	Philips J. Res. **38**	37-76	1983
P. M. Th. M. van Attekum, J. J. Ramekers, J. A. Pals & A. A. M. Hoeben	*E*	Supercurrent dependence of the microwave enhancement of the order parameter in superconducting aluminum	Phys. Rev. B **27**	1623-1628	1983
J. C. M. van Dongen*, T. T. M. Palstra*, A. F. J. Morgownik*, J. A. Mydosh* (* *Univ. Leiden*), B. M. Geerken (*Vrije Univ. Amsterdam*) & K. H. J. Buschow	*E*	Crystal-structure transformations and magnetic-ordering phenomena in $GdCu_{1-x}Ga_x$	Phys. Rev. B **27**	1887-1902	1983
P. Blood & A. D. C. Grassie	*R*	Optical excitation of defects in molecular beam epitaxy grown GaAs with polarized light	Phys. Rev. B **27**	2548-2550	1983
A. M. van der Kraan (*Interuniv. Reactor Inst., Delft*) & K. H. J. Buschow	*E*	^{57}Fe Mössbauer isomer shift in various amorphous Fe-base alloys	Phys. Rev. B **27**	2693-2697	1983
K. H. J. Buschow, J. H. N. van Vucht, P. G. van Engen, D. B. de Mooij & A. M. van der Kraan (*Interuniv. Reactor Inst., Delft*)	*E*	Structure, magnetic and magneto-optical properties, and ^{57}Fe Mössbauer effect in a new variety of Heusler alloy: PtFeSb	Phys. Stat. Sol. a **75**	617-623	1983
K. H. J. Buschow, H.-J. Eifert* & B. Elschner* (* *T.H., Darmstadt*)	*E*	Electronic structure and stability of amorphous Pd-Si alloys	Phys. Stat. Sol. b **115**	455-462	1983
J. E. Ralph & J. M. S. Schofield	*R*	$1/f$ noise in positive temperature coefficient thermistors	Physica **115B**	35-40	1982
G. Lütteke, A. J. Bock & K. Stips	*A*	S-band second harmonic VCO with auxiliary fundamental frequency output for PLL stabilization	Proc. 12th European Microwave Conf., Helsinki 1982	193-198	1982
C. Niessen	*E*	Hierarchical design methodologies and tools for VLSI chips	Proc. IEEE **71**	66-75	1983
A. Emami-Naeini (*Systems Control Technol. Inc., Palo Alto, CA*) & P. van Dooren	*B*	On computation of transmission zeros and transfer functions	Proc. 21st IEEE Conf. on Decision & control, Orlando, FL, 1982	51-55	1982
R. A. Walker*, A. Emami-Naeini* (* *Integrated Systems Inc., Palo Alto, CA*) & P. van Dooren	*B*	A general algorithm for solving the algebraic Riccati equation	Proc. 21st IEEE Conf. on Decision & control, Orlando, FL, 1982	68-72	1982
G. Louis & A. Pirotte	*B*	A denotational definition of the semantics of DRC: a domain relational calculus	Proc. 8th Int. Conf. on Very large data bases, Mexico City 1982	357-369	1982
W. K. Zwicker, S. Colak, J. Khurgin & J. M. Robertson	*N, E*	Spectroscopic properties of TbP_5O_{14}, $TbLiP_4O_{12}$ and $TbAl_3(BO_3)_4$	Proc. SPIE **335**	5-9	1983
D. M. Krol	*E*	The application of Raman spectroscopy in the study of glass melting and fining	Riv. Staz. Sper. Vetro (1982, No. 5)	194-199	1982
C. Ronse	*B*	Optimization of cost and delay in cellular permutation networks	SIAM J. Comput. **11**	784-788	1982
V. Belevitch	*B*	The Gauss hypergeometric ratio as a positive real function	SIAM J. Math. Anal. **13**	1024-1040	1982
A. Pirotte	*B*	A precise definition of basic relational notions and of the relational algebra	SIGMOD Rec. **13**	30-45	1982
H. W. Werner, J. Hornstra & N. Warmoltz	*E*	The influence of the simultaneous action of several independent stochastic processes on the crater-shape during sputter depth profiling	Surf. & Interface Anal. **5**	87-88	1983
A. J. A. Nicia	*E*	Micro-optical devices for fiber communication	Thesis, Eindhoven	—	1983
J. E. de Jong	*E*	Numerical analysis of metalforming processes	Thesis, Eindhoven	—	1983
H. K. Kuiken	*E*	The cooling of a low-heat-resistance sheet moving through a fluid: a rejoinder	Wärme- & Stoffübertrag. **16**	101-103	1982

Volume 41, 1983/84, No. 2 pages 33-72 Published 17th November 1983

Supplement to Philips Technical Review
Bijlage van Philips Technisch Tijdschrift
No. 22

November 1983

Recent United States Patents

Abstracts from patents that describe inventions from the following research laboratories, which form part of or cooperate with the Philips group of companies:

Philips Research Laboratories, Eindhoven, The Netherlands	*E*
Philips Research Laboratories, Redhill, Surrey RH1 5HA, England	*R*
Laboratoires d'Electronique et de Physique Appliquée, 3 avenue Descartes, 94450 Limeil-Brévannes, France	*L*
Philips GmbH Forschungslaboratorium Aachen, Weißhausstraße, 51 Aachen, Germany	*A*
Philips GmbH Forschungslaboratorium Hamburg, Vogt-Kölln-Straße 30, 2000 Hamburg 54, Germany	*H*
Philips Research Laboratory Brussels, 2 avenue Van Becelaere, 1170 Brussels (Boitsfort), Belgium	*B*
Philips Laboratories, N.A.P.C., 345 Scarborough Road, Briarcliff Manor, N.Y. 10510, U.S.A.	*N*

4 388 636

Static memory cell and memory constructed from such cells

J. Lohstroh *E*

A static cross-coupled bipolar memory cell has a large read current/stand-by current ratio and short write time. The nonlinear load element includes a resistor with a parallel-connected pnp transistor serving as a diode and an inversely-operating npn transistor for dissipating charge carriers.

---

4 389 101

Device for pivoting an optical element under electrodynamic control

G. E. van Rosmalen *E*

To reduce the susceptibility of an electrodynamically controllable pivoting mirror device to stray magnetic fields, said device comprises a pivoting mirror which is mounted on a frame so as to be pivotable by means of a suitable bearing arrangement, on which mirror permanent-magnetic means are arranged on which a pivoting torque can be exerted by means of control coils mounted on the frame. By providing the permanent-magnetic means, on the side where they are located, with two zones of north polarity and two zones of south polarity, which are situated on diametrically opposed sides relative to a pivoting axis, and by moreover having the turns on the control coil extend over zones of north and of south polarity, a pivoting mirror device is obtained whose control coils dissipate a minimum amount of heat and which is less susceptible to external magnetic stray fields produced by components located in the vicinity, such as transformers and electric motors.

---

4 389 273

Method of manufacturing a semiconductor device

J. Bloem *E*
C. H. J. van den Brekel

A method of manufacturing a semiconductor device in which a monocrystalline material is epitaxially grown on a disc-shaped monocrystalline substrate. The substrate is placed in an elongate reactor and a gas flow in the longitudinal direction is passed over the substrate while a temperature gradient is maintained in the gas flow. The gas flow initially contains the reaction components in equilibrium with the material to be grown, and the gas flow becomes undersaturated with respect to the material to be grown, etching will take place.

4 389 276

Method of manufacturing an electric discharge device comprising a glass substrate having a pattern of electrodes

G. H. F. de Vries *E*

In a method of manufacturing an electric discharge device having a pattern of electrodes impressed in a glass plate, the starting material for the manufacture of the pattern of electrodes is a metal foil which has a relief pattern. The relief pattern comprises thick portions which are connected together by thin portions of the foil and in which the thick portions constitute the desired pattern of electrodes. At a temperature T_1 which is lower than the melting-point of the metal of the foil and in which the glass of the glass plate has a viscosity of approx. 10^7 to 10^{13} Pa.s, the surface of the metal foil comprising the relief is impressed in the glass plate. After cooling, the desired pattern of electrodes is obtained by etching away the thin portions of the foil. In order to improve the adhesion, the metal foil can be rigidly adhered to the glass plate by means of an anodic bonding process prior to etching away the thin portions. The invention is particularly suitable for use in the manufacture of gas discharge display panels.

---

4 389 277

Method of manufacturing an electric discharge device

G. H. F. de Vries *E*

A method of manufacturing an electrid discharge device comprising a pattern of electrodes bonded to a glass substrate. It is necessary for certain gas discharge display devices to use metal electrodes which are at least 20 μm thick and adhere satisfactorily to a glass substrate. A metal foil is placed on a glass substrate and this assembly is heated to a temperature T_1 which is below the melting-point of the metal of the foil and at which the viscosity of the glass of the substrate is in the range from 10^7 to 10^3 Pa.s. The foil is pressed uniformly against the substrate at the temperature T_1 for a time which is sufficient to produce uniform contact between the foil and the substrate. The foil is then bonded to the substrate by an anodic bonding process, and the desired electrode pattern is produced by locally removing metal from the foil.

4 389 567

Semiconductor switching device for guiding and amplifying radiation

G. D. Khoe E
L. J. Meuleman
T. E. Rozzi

A semiconductor switching device for guiding and amplifying electromagnetic radiation is disclosed. An electrode pattern which defines a number of strip-shaped guiding members is profided on a layer structure analogous to that of a semiconductor laser. According to the invention the radiation guiding members have tapering juxtaposed ends in a transition area. Adjacent radiation guiding members in the transition area are situated within each other's amplification profile. The radiation guiding members are preferably separated from each other by insulation areas which do not extend to the common active layer. The invention may be used, for example, in switching radiation signals between two or more radiation paths in optical communication.

---

4 390 808

Picture display device having a gas discharge display panel

G. H. F. de Vries E
H. B. Bulle

A display device having a gas discharge display panel which comprises a plurality of sets of discharge cells. Each set comprises N discharge cells arranged according to a matrix of n rows and N/n columns where $n \geqq 2$. Each set furthermore comprises first and second electrode means for selectively energizing the N discharge cells. The first electrode means comprises N column conductors with n column conductors for each column of discharge cells. The column conductors each have a discrete discharge surface element such that in each column of cells each cell has associated therewith for selectively energizing the cell a respective one of the discrete surface elements and a surface element of the second electrode means. Per set the surface elements of the second electrode means are electrically interconnected. The sets are driven successively and in a driven set all discharge cells in accordance with the display information for that set. By simultaneously energizing all discharge cells in a set the duration of operation per cell is increased and an increased brightness is obtained.

---

4 390 894

Noise suppression circuit for a video signal

J. G. Raven E

In a noise suppression circuit for a video signal, the input video signal is separated into its high and low frequency components by a separating circuit. The signal at an output of a delay circuit is combined with the separated low frequency signal in a combining circuit whose output is applied to the input of the delay circuit. The time delay of the delay circuit is switched from field to field by means of a change-over switch so that this time delay changes from field to field to a field period minus and a field period plus half a line period. The noise-suppressed low frequency output from the combining circuit is added to the separated high frequency component in an adder circuit. In use such a noise suppression circuit produces substantially no travelling noise patterns on a television display.

---

4 391 622

Method for the precision manufacture of glass articles

C. L. Alting E
R. Brehm
J. Haisma

By using special dies, lenses from glass can be manufactured with great precision. Such dies are manufactured from quartz glass. Quartz glass can be worked with the required shape accuracy and the required smoothness, for example, by a polishing treatment succeeded by sputtering.

4 392 163

Magnetic tape recording and/or reproducing apparatus with automatic head positioning

A. M. A. Rijckaert E
E. de Niet
J. P. Beun

A magnetic tape recorder or playback apparatus, especially suitable for tape having a large number of parallel longitudinal tracks, has a positioning device for independently correcting tracking and skew errors. A first positioning system uses two piezo-electric elements parallel to each other and equally spaced on opposite sides of the pivot axis, and a second positioning system arranged between the first two piezo-electric elements, having at least three piezo-electric elements regularly spaced around and extending longitudinally about the pivot axis.

---

4 392 167

Magnetic head, method of producing the magnetic head

H. J. M. Joormann E

Magnetic head and method of producing a magnetic head which is formed by a core assembled from two pole pieces. At least one layer of a non-magnetizable material which forms the useful gap is provided between the pole pieces. One embodiment of the method includes the step of deposition on the pole pieces by means of a sputtering method a layer of a glass which comprises 12-20% by weight of Al_2O_3, 40-48% by weight of B_2O_3 and a total of 35-45% by weight of one or more of the oxides BaO, CaO or SrO. Thereafter the pole pieces are pressed together, with the glass layers in contact, and bonded together by heating the glass to the softening point, followed by cooling.

---

4 392 939

Magnetron cathode sputtering

J. E. Crombeen E
P. W. H. M. Crooymans
J. Visser

In a magnetron cathode sputtering system the target (plate of material to be sputtered) is held against a backing plate by a vacuum, enabling the backing plate to be reused. By providing the backing plate with a layer of soldering material which adheres to the backing plate, but does not adhere to the target, heat transfer between the two plates is improved.

---

4 393 273

FM-receiver with transmitter characterization

T. A. C. M. Claasen E
G. C. M. Gielis
J. M. Schmidt
H. B. Schoonheijm

An FM-receiver with transmitter characterization, having a tuning unit, an IF-amplifier, a demodulation circuit for demodulating a discrete transmitter characterization signal, a clock regeneration circuit, a decoding device for decoding the discrete transmitter characterization signal and a siganal processing unit. The clock regeneration circuit regenerates a clock signal the period of which is obtained by dividing the frequency of the stereo pilot signal. Synchronization of the clock signal phase with the phase of the clock signal used in the transmitter is carried out by detecting, using of a periodic window signal, the average phase of the code edges in the discrete transmitter characterization signal and by choosing the phase of the regenerated clock signal to be equal thereto.

---

4 393 396

Video signal processing circuit for noise reduction

J. G. Raven E
M. C. W. van Buul

In a noise suppression circuit for a video signal the number of elements required can be reduced when a separation circuit for a high-frequency and a low-frequency component is used and the

noise suppression is effected in the low-frequency component by means of a comb filter which, in order to realize a still further savings in components, may comprise a delay circuit having a delay which is switchable between a field period plus half a line period and a field period minus half a line period. The noise suppression circuit is therefore particularly suitable for use in television receivers.

---

4 393 471

Memory cell arrangement for a static memory

C. M. Hart *E*
J. Lohstroh

A memory cell for a static memory, in which the number of control lines is reduced to a maximum of three by the use of a diode in one collector circuit and the series connection of a diode and a resistor in the other collector circuit of an Eccles-Jordan flip-flop, which diodes have an exponential characteristic with an exponent smaller than that of conventional diodes.

---

4 394 438

Method of manufacturing an optically readable information carrier using deep U.V. radiation

P. van Pelt *E*
G. J. M. Lippits

A method of manufacturing an optically readable information carrier in which a substrate which is provided on at least one surface with a material which is sensitive to deep ultraviolet light having a wavelength from 190-300 nm, is exposed to deep ultraviolet light via a contact mask which on one side has a layer of a material which is not permeable to deep ultraviolet light in which an information track has been provided, after which the exposed plate is developed and if desired is provided with a reflection layer.

---

4 395 588

MFB system with a by-pass network

N. V. Franssen *E*
A. J. M. Kaizer
C. A. M. Wesche

A device for driving an electroacoustic transducer comprising a feedback amplifier and a pick-up whose output signal is a measure of the acoustic output signal of the transducer. A by-pass network bypasses at least the transducer and the pick-up and produces an output signal that for frequencies outside the operating range of the transducer is large and for frequencies in the operating range (f_l to f_h) of the transducer is small relative to the pick-up output signal. The sum of the output signals of the pick-up and the by-pass network serves as a feedback signal. This widens the transducer frequency range and reduces distortion. The device may include a limiter and a network before the transducer. The network has a frequency response inverse to that of the signal path from the electroacoustic transducer to the pick-up to provide an additional reduction in the distortion.

---

4 395 768

Error correction device for data transfer system

J. M. E. B. Goethals *B, E*
T. Krol

An error correction device for digital data storage and transfer systems wherein data are transferred over a plurality of channels. Synchronously with the transfer of a group of data bits, a coding device forms a first correction bit for a first correction channel and a second correction bit for a second correction channel. The first correction bit is formed on the basis of a second group of data bits, the second correction bits being formed on the basis of a third group of data bits. Each data channel supplies the data of two sub-groups of data bits for this purpose. The delay operator having a length of one bit cell being represented by D, a series of directly successive bits can be represented by a polynomial in D: $x0.D^0 + x1.D^1 + x2.D^2 + \ldots$, in which xj (j = 0, 1 . . .) represents the bit value. The quotient of the polynomials relating to the two sub-groups of a data channel is different for each data channel in order to enable correction of an arbitrary error pattern in a single data channel. When the data bits and correction bits are received, a first and a second error elimination bit are calculated from the extracted data bits by using the same algorithm. Comparison of first/second correction/elimination bit produces two error detection bits. When a given number of successive error detection bits do not indicate a discrepancy, the transfer medium is error-free. When a given configuration of discrepancies is detected, a correction vector is formed which indicates, after storage, the channel containing an error, while further error detection bits indicate the error pattern which can thus be corrected.

---

4 396 446

Method for producing an optical telecommunication element

A. J. J. Franken *E*

An optical communication element comprises an optical fiber bonded in a state of axial compression to a metal tape. The tape may be folded up into a tube and sealed by soldering. Such elements are strong and not sensitive to stress corrosion. Such an optical communication element may be produced by passing a metal tape and an optical fiber on the outside. An adhesive, which solidifies or cures during the passage around the drum is applied to the metal tape.

---

4 397 669

Method for the precision moulding of glass articles, method of manufacturing a mould, and mould for the precision moulding of glass articles

J. Haisma *E*
J. K. A. Boesten
H. de Vroome

A method for the manufacture of a mould intended for the precision moulding of glass articles, notably aspherical lenses. The desired shape and dimensional accuracy are imparted to a mechanically treated preform by an accurate polishing operation. Subsequently, the polished preform is prestressed and reinforced by a chemothermal treatment. The surface of the mould thus obtained comprises an edge zone which is subject to compressive stress and which changes over, via a neutral stress-free zone, to the core which is subject to tensile stress. The mould in accordance with the invention has a longer life and produces moulded products having a quality which is higher than that of products made by means of known moulds.

---

4 397 774

Method of preparing resistance material and resistor bodies produced therewith

A. H. Boonstra *E*
C. A. H. A. Mutsaers

A method of preparing resistance material in accordance with which metal oxides and/or metal oxidic compounds are heated together with a binder and, possibly, metal. A resistor having a temperature coefficient which is low and independent of the dilution, that is to say the level of the resistance value, is obtained by choosing particles which are smaller than 100 nm and vary within a very narrow range only as the starting material.

---

4 397 796

Method of manufacturing an anisotropic oxidic permanent magnet

F. K. Lotgering *E*
P. H. G. M. Vromans

In order to obtain a sintered oxidic permanent magnetic material with improved properties, a mixture is prepared which forms a magnet having a composition defined by the formula $MeFe_2^{2+}Fe_{16}^{3+}O_{27}$, where Me is one or more of the metals barium or strontium, optionally partly replaced by calcium and/or lead. A prefired product having a ferrous iron content which corresponds to the stoichiometric ferrous content of the product composition is sintered at a temperature between 1160 and 1250 °C in an atmosphere having such an oxygen concentration that substantially no oxygen exchange takes place between the product and the atmosphere.

4 397 930

Record carrier for deformation images

U. Killat *H*
G. Rabe
H. J. Schmitt

The record carrier according to the invention comprises a substrate on which an electrode is provided which, on the side remote from the substrate, has a low-ohmic photoconductive layer which is covered with a second transparent electrode which is provided with a thermoplastic layer. For storing information the electrodes are connected to a voltage source and the thermoplastic layer is charged electrostatistically and exposed in known manner. Upon exposure of an area of the thermoplastic layer, the light will fall through the transparent electrode on the low-ohmic photoconductive layer. As a result of the current passage, Joulean heat is produced which heats the thermoplastic layer in the place of the exposed area and softens it thereby deforming the layer by electrostatic forces in accordance with the charge. The thermoplastic layer may, in known manner, also have photoconductive properties or be provided with a further photoconductive layer.

---

4 398 217

Method of and arrangement for digitizing a time-discrete video signal using a picture transform coding

J. H. Peters *E*

A method of an arrangement for digitizing a video signal using a picture transform coding, wherein a group of N video signal samples is converted into a group of N coefficients y(m) wherein m = 1, 2, 3, ... N which are each adaptively encoded. In order to prevent a coefficient y(m) which is on average small to very small, from being insufficiently accurately encoded, or not encoded at all, when it is occasionally large, the group of coefficients is compared with a number of fixed classification groups A(j) each consisting of M elements a(j,m), wherein $a(j+1,m) \geqq a(j,m)$ and j = 1, 2, 3, ... M. The j is determined in such manner that $y(m) < a(j,m)$ for all m. A bit-assignment group B(j) having elements b(j,m) is associated with each classification group A(j) and each one of the N coefficients y(m) is now converted into a code word z(m) which contains a number of bits which is characterized by b(j,m) and which is, for example, equal to the value of b(j,m).

---

4 398 896

Method of de-burring and cleaning electrode systems

W. M. van Alphen *E*

A method of de-burring and cleaning an electrode system, a printed circuit board, or the like comprising at least two conductors positioned at a predetermined distance from each other by means of insulation material. The electrode system is immersed in a dielectric liquid and an electric potential difference is then applied between the conductors which is sufficiently large to generate an electric flash-over between the conductors. As a result of the small free path length in the dielectric liquid metal sputtered from the conductors can not deposit on the insulating parts of the electrode system.

---

4 398 935

Method and device for the high-precision manufacture of glass articles, in particular lenses

H. F. G. Smulders *E*
G. E. Bartman

A method of and a device are provided for the high-precision manufacture of glass lenses where a roughly metered volume of softened glass is transferred in a product holder from a furnace to a position between two moulds, the moulds being subsequently moved towards one another and the excess glass being pressed from between the moulds. The moulds and the product holder are moved at such a mutual speed that both moulds simultaneously contact the article, and the movement of the moulds is terminated when they reach a given position with respect to one another.

---

4 399 090

Method of producing mouldings and layers of inorganic materials

W. Sprangers *E*
R. Dijkstra

Bake out is accelerated and made possible at a lower temperature when at least one metal organic compound defined by the general formula MR_n in which M = V^{III}, Mn^{II}, Mn^{III}, IN^{III}, Ca, Co^{III}, Ni^{II} $(VO)^{II}$ or $(VO)^{III}$, n = 2 or 3, R is an organic residue of the compound classes of polyunsaturated compounds, aminoalcohols, aminoacids, carboxylic acids, hydroxycarboxylic acids, mercaptocarboxylic acids, enolisable ketones, ketoximes, aldoximes, amines, and phosphines, which is capable of changing into an oxide of M when heated to 150 to 420 °C is dissolved in the starting mixture or added to the starting mixture in the form of a solution.

---

4 399 328

Direction and frequency independent column of electro-acoustic transducers

N. V. Franssen *E*

An electro-acoustic arrangement comprising a plurality of transducer units including five, seven or nine equally spaced transducers situated in line with the transducers connected to a transmission channel via individual amplitude control devices. The amplitude control devices are adjusted so that the ratios between the conversion factors of the transducer units viewed from end to end are $1:2n:2n^2:-2n:1$ for five transducers to produce an output signal substantially independent of direction and/or frequency. The invention also relates to a combination of five, seven or nine of the foregoing arrangements situated adjacent each other or in line at equal distances with further amplitude control devices connected to a transmission channel. The amplitude control devices are adjusted so that the ratios between the conversion factors of the arrangements, viewed from end to end, form a special relationship.

---

4 399 375

Current stabilizer comprising enhancement field-effect transistors

A. Sempel *E*

A current stabilizer having two parallel current paths coupled by means of two different current coupling circuits in order to obtain a stabilizing point. At least one of the two coupling circuits comprises two enhancement field-effect transistors which are each included in one of the two current paths. One of said field-effect transistors has a gate-source voltage which has a constant voltage difference with respect to the gate-source voltage of the other transistor by including between the gate electrodes of the two field-effect transistors, a biased bipolar semiconductor junction.

---

4 399 450

ROM with poly-Si to mono-Si diodes

J. Lohstroh *E*

In a diode matrix of a permanent memory (ROM) the word line and bit line system is formed by a system of strip-shaped zones of one conductivity type provided in the silicon body and in the another system is formed by polycrystalline silicon tracks of the opposite conductivity type provided on the surface and forming monopoly p-n junctions with the strip-shaped zones. High packing density and high speed are obtained.

PHILIPS TECHNICAL REVIEW

VOLUME 41, 1983/84, No. 3

Proton NMR tomography

P. R. Locher

Nuclear magnetic resonance (NMR) has developed through the years into a branch of physics with a wide range of applications. In this technique a substance is placed in a constant homogeneous magnetic field. Nuclei that have a spin will then show a very pronounced resonance with high-frequency magnetic fields. The resonance frequency is proportional to the strength of the constant field, and the details of the spectrum provide accurate information about the structure of the substance. In the early seventies it was suggested that it should also be possible to produce images of — for example — the interior of the human body by using spatially dependent fields, since the spectra would then contain spatial information. This led to the technique known as NMR imaging, which is attracting considerable attention today — especially in the medical world — because of its great promise as a diagnostic aid.

Soon after these ideas were first put forward, investigations were started at Philips Research Laboratories into the possible applications of NMR imaging. This led to the formation of a project group including people from the laboratories and from the Philips Medical Systems Division. An NMR tomograph built by this group is now being used by physicists, medical practitioners and technicians to gain experience with this new technique. Building on this experience, Philips Medical Systems Division started the production of NMR imaging systems, to which they gave the name 'Gyroscan'.

The article below discusses the principles of NMR imaging and describes some examples of practical applications.

Introduction

When a proton is placed in a constant magnetic field of flux density B its spin describes a precessional motion around the direction of the field. The angular frequency ω of this 'Larmor precession' is proportional to the flux density: $\omega = \gamma B$; the quantity γ is called the gyromagnetic ratio of the proton. An r.f. magnetic field perpendicular to the constant field excites the precession if its frequency is equal to the precessional frequency. This is the basis of nuclear magnetic resonance (NMR). It is also possible to observe NMR by using other atomic nuclei provided that, like the proton, they have an angular momentum and thus possess a magnetic moment. Since its discovery, NMR has developed into an important tool for studies such as the investigation of molecular structures. The details of the resonance effect depend on a number of variables. The only variables of interest in this article are the proton density (ϱ) and the relaxation times (T_1 and T_2) that describe the return from the excited state to the state of thermal equilibrium.

In 1971 and 1972 R. Damadian drew attention to the potential applications of NMR for medical diagnosis [1]. He had in mind point-by-point measurements of the characteristic NMR variables, which is a very time-consuming procedure. In 1973 and 1974 P. C. Lauterbur and others proposed methods in which many points in an entire region could be measured simultaneously [2]. These ideas were taken

Dr P. R. Locher is with Philips Research Laboratories, Eindhoven.

[1] R. Damadian, Science **171**, 1151, 1971.

[2] P. C. Lauterbur, Nature **242**, 190, 1973.
P. C. Lauterbur, Pure & Appl. Chem. **40**, 149, 1974.
J. M. S. Hutchison, J. R. Mallard and C. C. Goll, in: P. S. Allen, E. R. Andrew and C. A. Bates (eds), Magnetic resonance and related phenomena, Vol. 1, North-Holland, Amsterdam 1975, p. 283.
A. N. Garroway, P. K. Grannell and P. Mansfield, J. Phys. C **7**, L457, 1974.

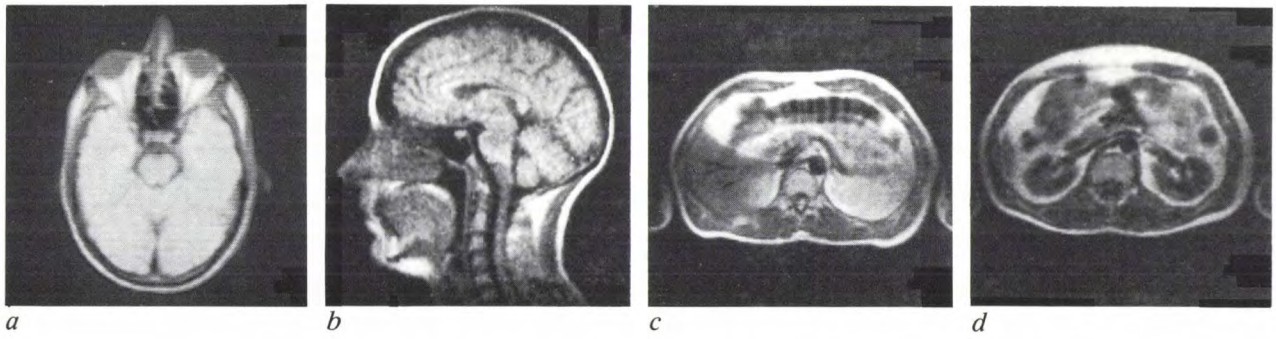

Fig. 1. NMR images of cross-sections of the body, made with the equipment described in the article. The layers depicted have a thickness of about 1 cm. Tissues with a low proton concentration (ϱ) or a short 'transverse relaxation time' (T_2) are shaded dark, e.g. the skull and the nasal cavity in (*a*). *a*) Transverse section through the head, at eye height. The optic nerve can be seen in the 'cones' of fatty tissue behind the eyes. The 'circle' at the centre marks the region of transition from brain to spinal cord. *b*) Sagittal section through the head. The image shows clearly that brain and spinal cord form a single entity. *c*) Section through the body, at the height of the 'horizontal' part of the large intestine (at the top of the picture). Just below the centre of the picture there is a vertebra, and directly above it to the right the aorta, as a dark silhouette. The large area on the left is the liver, and the spleen is on the right. *d*) A section 6 cm lower down. The kidneys show up clearly, with the main renal blood vessels.

further in the years that followed, and a stage has now been reached where good NMR images of 'slices' of the human body are being made in various research centres around the world. NMR imaging equipment for diagnostic applications has also been developed at Philips by cooperating teams from the Research Laboratories and the Medical Systems Division. NMR images made with this equipment are shown in *fig. 1*.

To explain very briefly the basic idea of NMR imaging, let us imagine that we have a thin tube in which protons (e.g. in water) are distributed inhomogeneously over the length (*fig. 2a-b*). To make a one-dimensional NMR image of this distribution, we proceed as follows. We place the tube between the poles of a magnet that produces a highly uniform magnetic field, and produce a gradient in the field along the tube, using separate coils. The flux density then varies along the tube, e.g. from $B_0 - \frac{1}{2}\Delta B$ to $B_0 + \frac{1}{2}\Delta B$ (fig. 2*c*). Next we excite all the protons in the tube by applying a short relatively broad-band r.f. pulse, and at the end of the pulse we measure the voltage that the protons induce in a detector coil. This signal is a superimposition of all the signals from the individual protons, which precess at angular frequencies between $\gamma(B_0 - \frac{1}{2}\Delta B)$ and $\gamma(B_0 + \frac{1}{2}\Delta B)$. The *spectrum* (the Fourier transform) of the signal (fig. 2*d*) gives the number of protons precessing in each frequency range, and this is a direct representation of the spatial distribution of the protons because of the direct relation between frequency, field and location. Translation of the spectrum into a grey-level pattern finally yields the required image (fig. 2*e*). The essence of the technique is therefore that the accurate

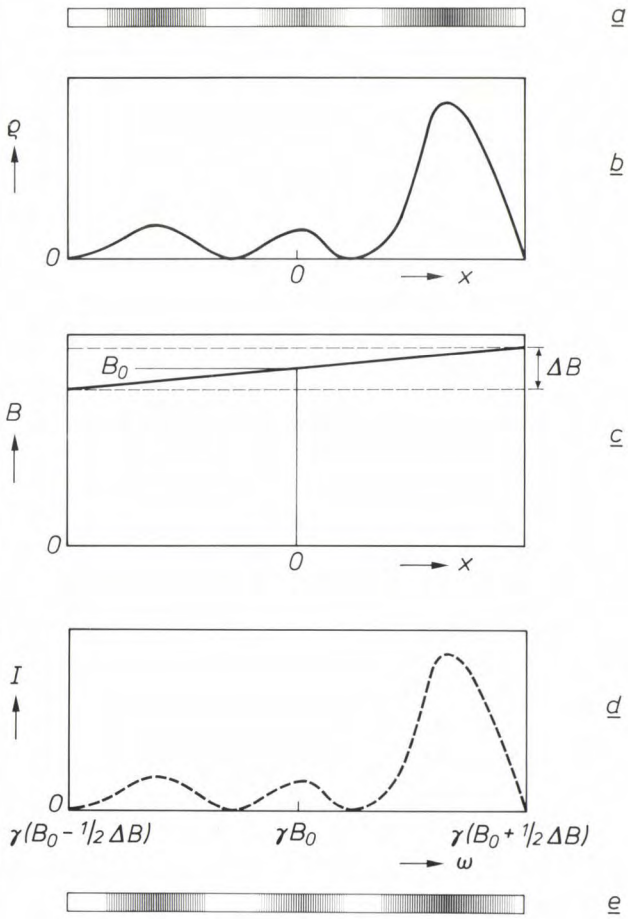

Fig. 2. Principle of one-dimensional NMR imaging. *a*) Tube in which the proton concentration ϱ is spatially dependent. *b*) ϱ as a function of position x, measured along the tube. *c*) Absolute value B of magnetic flux density as a function of x (the direction of $\boldsymbol{B}$ relative to the tube does not matter). The Larmor frequency varies along the tube from $\gamma(B_0 - \frac{1}{2}\Delta B)$ to $\gamma(B_0 + \frac{1}{2}\Delta B)$. *d*) Signal spectrum of freely precessing protons, giving a faithful representation of $\varrho(x)$. *e*) Image of the tube: the spectrum translated into a pattern of grey levels.

discrimination of field-strength that is possible with NMR is converted into spatial discrimination by the use of a field gradient. Two-dimensional images can be obtained in a similar way by appropriate manipulations of field gradients and pulse trains. The method will be explained in this article.

The following are some typical values for our tomograph: flux density of the magnetic field B_0 about 0.14 T (1400 Gs), field homogeneity 1 part in 10^5 throughout a volume of 40 cm × 40 cm × 30 cm; precessional frequency $\omega_0/2\pi$ of the protons in this field: about 6 MHz ($\gamma/2\pi$ = 42.576 MHz/T for protons in water); gradients: 5 to 20×10^{-4} T/m, which amounts to a difference of about 0.15 to 0.6 per cent from one end of the region of homogeneity to the other; time for measuring one slice about five minutes. *Fig. 5* shows a photograph of our magnet.

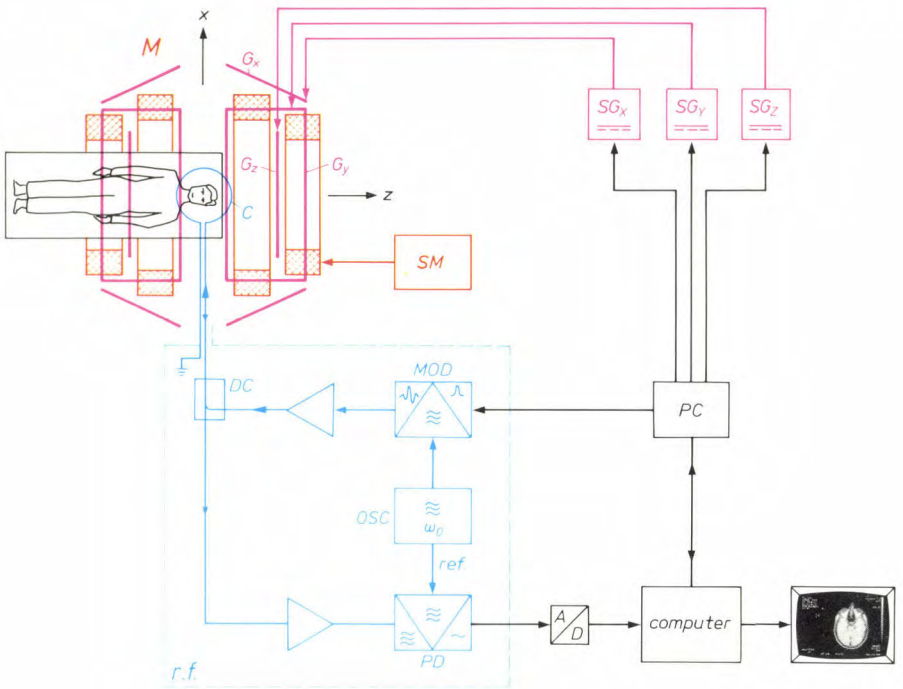

Fig. 3. Diagram of the NMR tomograph discussed in this article. *M* magnet, consisting of four coils, generating a highly uniform magnetic field (flux density B_0) in a part of the patient. G_x, G_y, G_z coils producing field gradients (see fig. 4). The patient, the magnet and the gradient coils are shown in plan view or in horizontal cross-section (the *y*-axis is vertical). *SM*, SG_x, SG_y, SG_z power supplies for the magnet and the gradient coils. The oscillator (*OSC*) in the r.f. unit (*r.f.*) is 'tuned' to the magnet ($\omega_0 = \gamma B_0$). The oscillations are modulated to form pulses (*MOD*), which excite the spins in the patient via the r.f. coil *C*; the *z*-gradient selects an *x*,*y*-slice. After a pulse the signal of the freely precessing spins (the 'FID signal', where FID stands for Free Induction Decay), after phase-sensitive detection (*PD*) and analog-to-digital conversion (*A*/*D*), is stored in the computer. After a sequence of say 200 or 250 pulses with the FID signals following them, each with a different combination of gradients, the computer contains sufficient information for the construction of an image of the slice. The computer program consists in part of a 2D Fourier transformation. The succession of pulses and gradients is controlled by the process-control unit *PC*. The unit *DC* is a directional coupler, ensuring that the phase-sensitive detector receives only the FID signal and no signal from the pulse amplifier.

An NMR tomograph thus consists of the following components (see *fig. 3*):

- a magnet (*M*), large enough to enclose a human subject, and producing a highly uniform field in a space of dimensions say 40 cm × 40 cm × 30 cm;
- gradient coils (G_x,G_y,G_z). *Fig. 4* shows how various gradients can be produced;
- r.f. excitation and detection equipment (*r.f.*);
- a unit that controls the sequences of gradients and r.f. pulses (*PC*);
- a computer to translate the scanning signals into an image; a two-dimensional Fourier transformation is an important part of the computer program.

NMR tomography is attracting keen interest in the medical world. The interest arises because in some cases the technique gives clearer and simpler indications than other diagnostic methods of certain internal features of the human body, such as a difference between healthy and diseased tissue. Nor does it seem that the technique can possibly cause physiological damage; this is certainly not true of X-rays.

In our tomograph the relative orientations of patient and magnet are as shown in fig. 3: the longitudinal axis of the patient is horizontal, in the direction of the field (the z-axis). Other orientations can also be adopted, for example with the axis of the coils and hence the direction of the field vertical; the patient — again horizontal — is then placed *between* the coils [3]. In this article we shall only consider the orientations of fig. 3.

Since NMR tomography is based entirely on nuclear magnetic resonance, we shall first review the principal aspects of this method of investigation. We shall be concerned in particular with 'pulse NMR', a version that has now almost completely superseded 'continuous-wave NMR', which was previously more widely used. In this review we shall take the z-axis (the direction of the magnetic field) vertical, as is the convention in NMR; fig. 3 and the rest of the article do not follow that convention, however.

Next we shall discuss the principles of the two best known versions of NMR imaging: 'NMR projection reconstruction' and 'Fourier zeugmatography'. The discussion will be limited to the production of two-dimensional images, and particularly of x,y-cross-sections. This limitation will simplify the treatment without the loss of anything essential; the extension to differently oriented cross-sections, and also to three-dimensional images — where the distribution of the proton density or of some other NMR variable is determined in three dimensions — is more or less self-evident.

Finally, we shall look at some of the practical aspects in more detail. An actual pulse and gradient sequence will be used to show how the method works in practice, and to indicate the factors that determine the image quality.

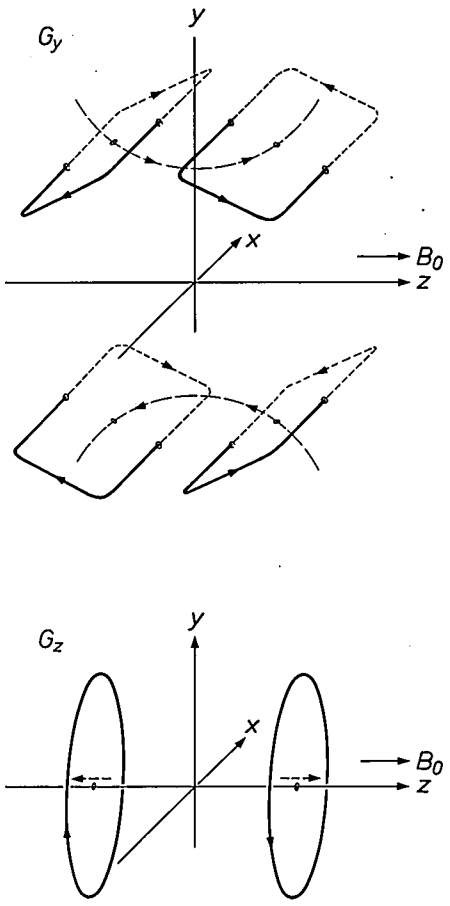

Fig. 4. Coils for the y-gradient (*above*) and the z-gradient (*below*), schematic. The coils for G_x are rotated by 90° about the z-axis relative to those for G_y. In our tomograph there are four G_z coils.

Nuclear magnetic resonance

We shall now briefly review four main features of pulse NMR: the Larmor precession, relaxation, excitation of the precession and detection. One or two conclusions of relevance to NMR imaging will occur incidentally in the discussion.

Larmor precession

When a substance that contains protons is located in a homogeneous magnetic field and is in thermal equilibrium, it has a *nuclear magnetization* in the direction of the field, since there are more spins aligned with the field than spins aligned in the opposite sense. The excess of spins aligned with the field is always very small: in a field of say 0.3 T (3000 Gs) at room temperature it is no more than about 1 in 10^6. The magnetization then amounts to only 10^{-6} of the theoretical saturation value (which holds for all spins pointing in the same direction).

Now let us assume that, at a certain moment, the magnetization ($\boldsymbol{M}$) is rotated through an angle α, e.g. about the x-axis (*fig. 6a*), by applying an 'α-pulse'; just how this is done will be explained later. From that time onwards $\boldsymbol{M}$ describes a precession around the z-axis (the direction of the magnetic field; fig. 6*b*). This precession is described in complex notation by the equations:

$$M_z = \text{constant}, \tag{1a}$$

$$M_\perp = M_{\perp 0}\, e^{-j\omega t}, \text{ where } \omega = \gamma B. \tag{1b}$$

Here $M_\perp$ is the 'complex transverse magnetization':

$$M_\perp = M_x + jM_y.$$

$M_{\perp 0}$ is the complex transverse magnetization at the time $t = 0$.

If now the 'spectrum' of the precession of a specimen in a homogeneous constant magnetic field of flux density B is determined, then from the above there should be a single sharp resonance line at the Larmor

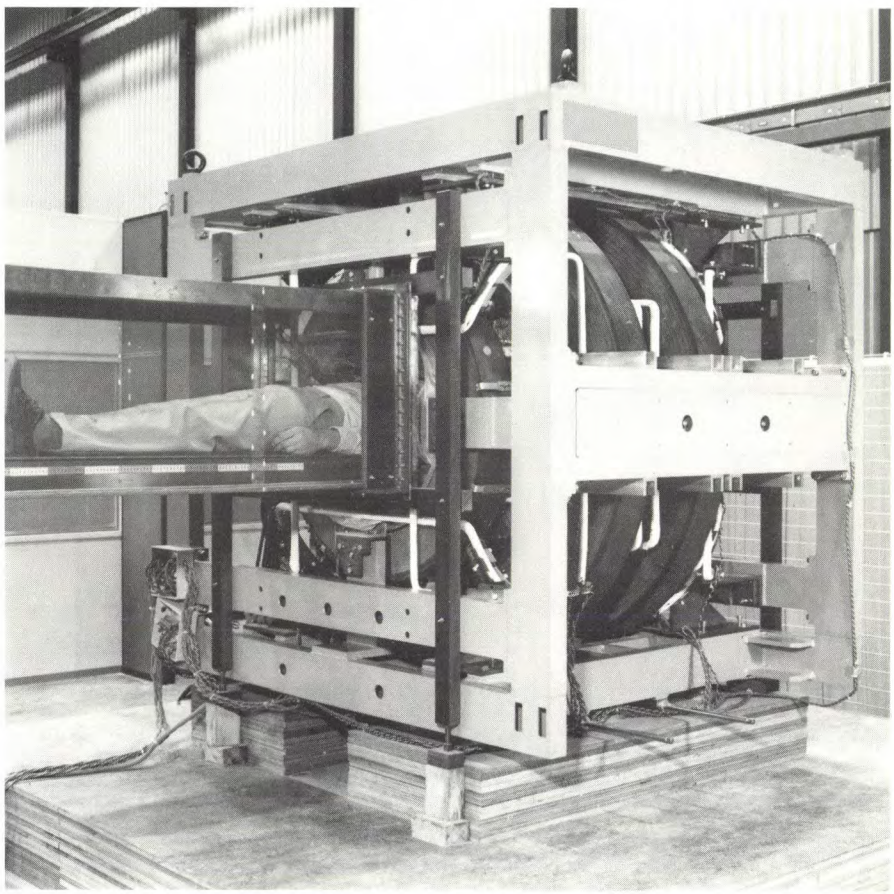

Fig. 5. The magnet used in our tomograph. The four coils are of water-cooled copper tubing. The inside diameter of the inner coils is 1.10 m, that of the outer coils 0.70 m. The flux density of 0.14 T is obtained at a power of 50 kW. The patient is inserted into the magnet in a Faraday cage to exclude external interference. The white conductors (except the ones between the large coils) form part of the G_x and G_y gradient coils. The G_z coils are not visible.

angular frequency γB. For various reasons this line always has a certain width, or can even extend to form a spectrum with fine structure. In NMR spectroscopy the interest is centred on this fine structure, which is caused by 'chemical shift' or 'spin-spin coupling', subjects that we shall not consider further here. In proton NMR imaging the fine structure is of no interest, since the spectrum of protons in body fluids has little or no structure. The 'spectrum' in this case is due to the gradient in the magnetic field.

The precession occurs because the magnetic moment $\boldsymbol{\mu}$ of a proton is inseparably connected with the spin angular momentum $\boldsymbol{p}$ by the relation $\boldsymbol{\mu} = \gamma \boldsymbol{p}$. Consequently the set of spins also has a net angular momentum per unit volume $\boldsymbol{J}$, for which we have: $\boldsymbol{M} = \gamma \boldsymbol{J}$. Since the time derivative $\dot{\boldsymbol{J}}\mathrm{d}v$ of the angular momentum of the spins in the volume element $\mathrm{d}v$ is equal to the couple $[\boldsymbol{M}\times\boldsymbol{B}]\mathrm{d}v$ acting on it, it follows that $\dot{\boldsymbol{M}} = \gamma[\boldsymbol{M}\times\boldsymbol{B}]$. From this we can easily derive equations (1a) and (1b). It is also immediately clear from this that the change in magnetization is always perpendicular to the magnetization itself and to the direction of the magnetic field. This gives at once the precession in fig. 6*b*.

From eq. (1b) we can now derive an expression that is of special significance for NMR imaging. In view of our limitation in this article to 2D imaging of x,y-cross-sections, the 'specimen' here is always a thin layer parallel to the x,y-plane. The r.f. signal is induced by the *transverse magnetic moment of this layer*. This is the sum of the transverse moments of small domains $\mathrm{d}x\mathrm{d}y$. If there is a field gradient in the layer, ω is position-dependent, and if the protons are not homogeneously distributed or are not precessing in phase, this also applies to the $M_{\perp 0}$ of eq. (1b). For the

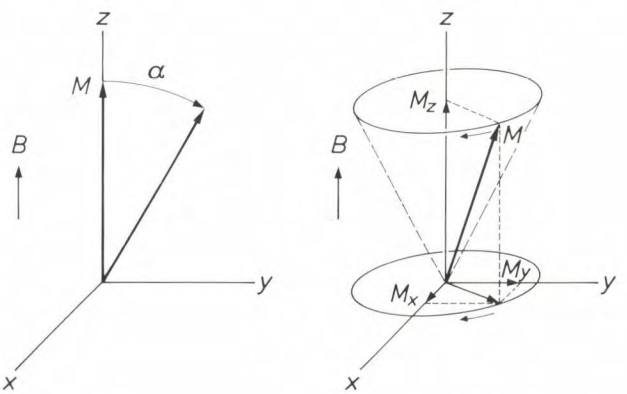

Fig. 6. The Larmor precession. The magnetic field is directed along the z-axis. After rotation of the magnetization $\boldsymbol{M}$ through an angle α from the z-axis, with the aid of an α-pulse (*a*), $\boldsymbol{M}$ describes a precessional motion about the z-axis (*b*).

[3] J. M. S. Hutchison, W. A. Edelstein and G. Johnson, J. Phys. E **13**, 947, 1980.

complex transverse magnetic moment m of the layer we therefore have the general expression:

$$m(t) = \iint f(x,y)\, e^{-j\omega(x,y)t} dx dy, \qquad (2)$$

where $f(x,y)$ is the complex *two-dimensional* transverse magnetization (transverse moment per unit area of the layer) at the time 0, i.e. $M_{\perp 0}$ times the thickness of the layer. In special cases the modulus of $f(x,y)$ gives the two-dimensional proton distribution in the layer directly. What NMR imaging systems have to do is to reconstitute $f(x,y)$ from measurements of m.

Relaxation

If an excited spin system is left to its own devices, the Larmor precession decays away and the system returns to the state of thermal equilibrium. In the case of an ideal homogeneous magnetic field there are two processes. In the first place the transverse magnetization decays gradually, because of the interaction, usually very slight, between the spins themselves and between the spins and their environment (transverse relaxation). The characteristic time of this decay is the *transverse relaxation time* T_2 (*fig. 7a*). In the second place the z-component of the magnetization also returns to its equilibrium value (longitudinal relaxation). The characteristic time here is T_1, the *longitudinal relaxation time* (fig. 7*b*).

The two processes arise from different causes, and T_1 and T_2 are not therefore in general identical. T_2 can never be longer than T_1, of course, but it is often much shorter. The values differ considerably for different substances, depending on quantities such as the viscosity and on certain impurities. In solids T_2 is generally much smaller than T_1 (e.g. $T_1 \approx 10$ s, $T_2 \approx 10^{-5}$ s), whereas in liquids T_2 and T_1 are not so very different from each other (e.g. $T_2 \approx T_1 \approx 0.1$ s).

In reality the field is never truly homogeneous. Different parts of the spin system are thus located in fields of slightly different strengths. Consequently the 'submagnetizations' have slightly different angular velocities. For this reason, they immediately begin to fall out of step after the α-pulse and differ increasingly in phase; as a result the transverse magnetization decreases more rapidly than it does in a homogeneous field. This is sometimes described by a relaxation time T_2^*, which is therefore shorter than the 'true' transverse relaxation time T_2. In NMR imaging, the inhomogeneities fall into two categories: *undesired inhomogeneities* and deliberately applied *gradients*.

Excitation

The r.f. equipment comprises an r.f. oscillator with an angular frequency ω_0 approximately equal to the central Larmor frequency of the spin system. During an r.f. pulse the oscillator generates an r.f. magnetic field in the spin system by means of an excitation coil. We can think of this field as being resolved into two circularly polarized components; only one of these is important, the component that rotates with the spins; the component that rotates in the opposite sense has little or no effect. We therefore treat the r.f. field as a field of flux density B_1 that is circularly polarized in the x,y-plane and of angular velocity ω_0.

The behaviour of the magnetization $\boldsymbol{M}$ is now most conveniently described in the 'rotating frame of reference' x',y',z'. The z'-axis coincides with the z-axis. The frame rotates synchronously with the r.f. oscillator at an angular velocity ω_0 about the z'-axis in the direction of the spins and of the r.f. field. In this frame the r.f. field is thus stationary. If the angular frequency of precession of $\boldsymbol{M}$ is exactly equal to ω_0, then $\boldsymbol{M}$ in this system no longer 'feels' the constant field; the field is 'taken into account' by the rotation. *Before* and *after* a pulse $\boldsymbol{M}$ is therefore stationary in

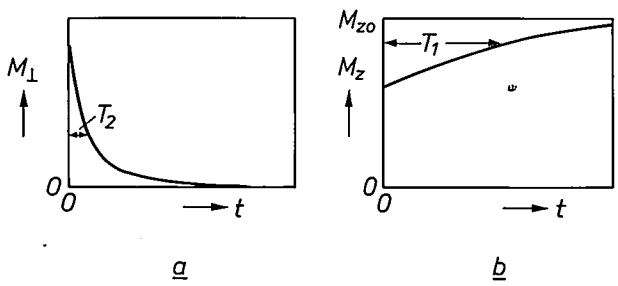

Fig. 7. *a*) Transverse relaxation. After an α-pulse the transverse magnetization decreases exponentially because the spins go out of phase. This process is characterized by the transverse relaxation time T_2. *b*) Longitudinal relaxation. The z-component of the magnetization returns, also exponentially, to its thermal equilibrium value. The characteristic time here is the longitudinal relaxation time T_1. As a rule the two relaxation times are not the same, since the two processes do not arise in the same way.

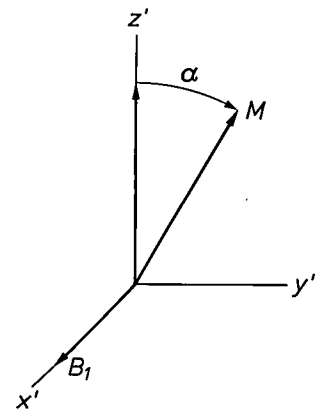

Fig. 8. The α-pulse in the rotating frame of reference x',y',z'. Because of the rotation the static field is 'removed', and the r.f. field is stationary. In this frame the magnetization therefore precesses about $\boldsymbol{B}_1$ during a pulse. This is equivalent to a spiral motion in the static frame.

this frame. During a pulse, however, $\boldsymbol{M}$ does 'feel' the r.f. field and consequently describes a Larmor precession about the vector $\boldsymbol{B}_1$ [4].

With the aid of this knowledge a simple description of the α-pulse can be given (*fig. 8*). The phase of the rotating frame is chosen to make $\boldsymbol{B}_1$ lie along the x'-axis. $\boldsymbol{M}$ then rotates from its initial position along the z'-axis in the direction of the y'-axis, at an angular velocity γB_1, so that $\boldsymbol{M}$ describes an angle $\gamma B_1 \Delta t$ in a time Δt. An α-pulse is thus obtained by choosing the r.f. flux density B_1 and the pulse duration Δt in such a way that $\gamma B_1 \Delta t$ is equal to α. It is normal practice to use 90° pulses for excitation.

Besides 90° pulses, 180° pulses are also widely used. *Figs 9* and *10* show what can be done with 90° and 180° pulses. The 'inversion-recovery sequence' in fig. 9 is used for measuring T_1. After a 180° pulse (*1* → *2* in fig. 9*b*) the spin system starts to recover its thermal equilibrium (*2* → *3*) as shown in fig. 9*c*. After a time τ a 90° pulse is given (*3* → *4*); the detector signal immediately after this pulse is a measure of the value of M_z immediately before the pulse. By determining M_z in this way for a series of τ-values we find the variation of M_z in fig. 9*c*, and hence the value of T_1.

Fig. 10 illustrates a 'spin echo' experiment. After a 90° pulse (fig. 10*a-b*) the transverse magnetization starts to relax. In addition, however, the transverse magnetization also decreases owing to the dephasing of submagnetizations mentioned earlier as a consequence of field inhomogeneities. This process is illustrated in fig. 10*c*; the submagnetization *1* is situated in a stronger field and thus 'runs fast'; the submagnetization *2* is in a weaker field and 'runs slow'. After the period τ a 180° pulse is given (fig. 10*c-d*). Since *1* still runs fast and *2* still runs slow, *they start to converge*, and after another period τ the transverse magnetization has recovered (fig. 10*e*), *resulting in an echo signal*. Owing to the transverse relaxation the recovery is not complete. The transverse relaxation time T_2 can be determined by repeating the experiment for different values of τ.

As we shall shortly see, spin echoes can be very useful in NMR imaging.

Detection

After an excitation pulse the Larmor precession of the spins induces an r.f. voltage across the ends of a detector coil whose axis is parallel to the y-axis. This signal, called the 'FID signal' (free induction decay), has the nature of a modulated carrier with a centre angular frequency ω_0; the modulation contains the information. This is recovered by means of *double phase-sensitive detection* (*PD* in fig. 3). Two low-frequency signals $S_1(t)$ and $S_2(t)$ are produced, each of which is obtained by mixing the r.f. signal with (i.e. multiplying it by) a reference signal from the r.f. oscillator and filtering with a lowpass filter. The two reference signals differ in phase by 90°. The signals obtained can be combined to form a complex signal $S(t) = S_1 + jS_2$.

In this process the spectrum of the signal is shifted from the r.f. region at ω_0 to the l.f. region at zero frequency (*fig. 11*). In fact this is also what happens when the magnetic moment of the specimen is viewed

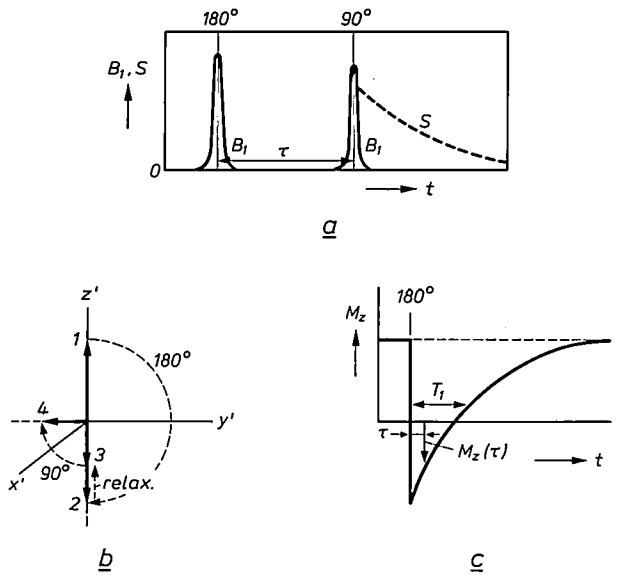

Fig. 9. Inversion-recovery sequence. *a*) Pulses (B_1) and signal (S) as a function of time. *b*) Magnetization in the rotating frame. *c*) Longitudinal relaxation. After the inversion by the 180° pulse (*1* → *2* in *b*) the spin system starts to recover thermal equilibrium (*2* → *3*). After a time τ the recovery is interrupted by a 90° pulse (*3* → *4*). The r.f. signal immediately after the 90° pulse is a measure of the value of M_z immediately before the pulse (*3* in *b*); a point is thus found on the relaxation curve (*c*). Repetition of the experiment for different values of τ gives the complete curve and hence T_1.

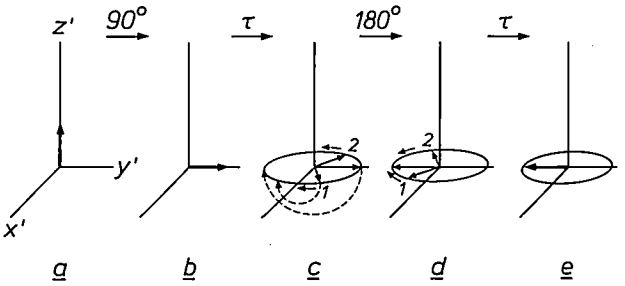

Fig. 10. Spin echo. After a 90° pulse (*a* → *b*) the magnetizations of different domains immediately start to dephase (*b* → *c*) as a consequence of field inhomogeneities. After a time τ all submagnetizations are rotated 180° about the x'-axis (180° pulse, *c* → *d*). The submagnetizations then start to converge, and after a further time τ they are back in phase again (*e*); they then give an echo signal. Owing to the transverse relaxation the recovery is not complete. T_2 can be determined from the echo signal as a function of τ.

[4] T. C. Farrar and E. D. Becker, Pulse and Fourier Transform NMR, Academic Press, London 1971, pp. 10-15.

from the rotating frame. In essence the two processes are the same, and the equipment can be arranged in such a way that the *complex output signal* $S(t)$ directly gives the *complex transverse magnetic moment in the rotating frame.*

In NMR imaging, where the 'specimen' is a thin x,y-layer, the complex transverse magnetic moment in the rotating frame of reference is obtained by substituting $\omega - \omega_0$ for ω in eq. (2). The complex output signal, except for a constant factor, is thus equal to:

$$S(t) = \iint f(x,y)\, e^{-j(\omega-\omega_0)t}\, dx\,dy, \qquad (3)$$

where ω also is a function of x and y, as before.

A more rigorous derivation of equation (3) runs as follows. The r.f. signal, except for a constant factor, is equal to the y-component of the magnetic moment, or to $\mathrm{Im}\, m$, the imaginary part of m (see eq. (2)). As reference signals we take $-\sin\omega_0 t$ and $\cos\omega_0 t$. Multiplication gives the two r.f. signals

$$s_1(t) = -(\mathrm{Im}\, m)\sin\omega_0 t,$$
$$s_2(t) = (\mathrm{Im}\, m)\cos\omega_0 t.$$

For the complex r.f. signal $s = s_1 + js_2$ we find:

$$s = j(\mathrm{Im}\, m)\, e^{j\omega_0 t} = j\,\frac{m - m^*}{2j}\, e^{j\omega_0 t} =$$

$$= \tfrac{1}{2}\iint f(x,y)\, e^{-j(\omega-\omega_0)t}\, dx\,dy - \tfrac{1}{2}\iint f^*(x,y)\, e^{j(\omega+\omega_0)t}\, dx\,dy.$$

After the lowpass filters, only the first, low-frequency term, remains, and this, again except for a constant factor, is equal to the expression given in (3).

Two-dimensional NMR projection reconstruction

To obtain an image of a cross-section of the body a 'slice' of thickness say 0.5 cm is 'selected', e.g. by exciting only the spins in that slice. The way in which this is done will be explained presently. One of the methods of obtaining a 2D image of this slice is known as '2D projection reconstruction'.

In general terms the procedure is as follows. A direction $\boldsymbol{u}$ in the plane of the slice is selected, and a field gradient is applied in that direction. In each narrow strip of the slice perpendicular to $\boldsymbol{u}$ the spins have the same frequency and are thus added together in the spectrum of the FID signal. The spectrum is thus a *projection* of the proton distribution. The measurement is repeated for, say, 200 directions $\boldsymbol{u}$ and the 2D distribution itself is reconstructed from the projections obtained.

This account of the procedure requires a small correction. We should first note that reconstructing the distribution of a material from its projections is a problem that can be approached mathematically in different ways. We are concerned here only with a relatively simple version, based entirely on Fourier transformation. In this version the first step is usually the determination of the Fourier transform of each projection. In NMR projection reconstruction, however, this step is not present, since the measured FID signal is already the Fourier 'partner' of the projection ('the projection is the spectrum of the signal') so that the reconstruction can be started immediately here without first having to resort to the projections. The projections are only included here for purposes of explanation. However, we will retain the name 'NMR projection reconstruction', in accordance with conventional usage.

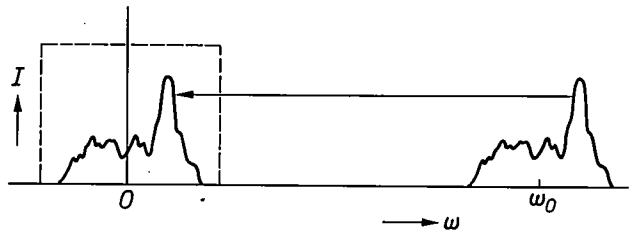

Fig. 11. Phase-sensitive detection (*PD* in fig. 3). The spectrum of the r.f. signal covers a frequency band at ω_0 with a width given by the variation of the field over the length of the object. By mixing with a reference signal of frequency ω_0 the spectrum is shifted towards the origin. A lowpass filter (the rectangle) eliminates all signals and interference from outside this frequency band.

Let us now consider the method in more detail with the aid of *fig. 12.* The function $f(x,y)$ we are looking for — in the simplest case the proton distribution in the x,y-plane (see page 78) — is shown for a hypothetical case in fig. 12*a* by means of 'contour lines'. In general $f(x,y)$ is a complex function; the simple presentation in fig. 12*a* is only intended as an aid to explanation. The reconstruction now takes place via the *2D Fourier transform* of $f(x,y)$:

$$F(k_x,k_y) = \iint f(x,y)\, e^{j(k_x x + k_y y)}\, dx\,dy. \qquad (4)$$

All integrals in this section run from $-\infty$ to $+\infty$. $F(k_x,k_y)$ is a function (again complex) in the plane of the variables k_x,k_y shown by contour lines in fig. 12*b*. The reconstruction is based on the theorem: *the FID signal, recorded with a gradient* $\boldsymbol{G}$ *in the direction* $\boldsymbol{u}$*, is a 'cross-section' of* $F(k_x,k_y)$ *along a corresponding line* k_u *in the* k_x,k_y *plane.* 'Cross-section' here refers simply to $F(k_x,k_y)$ itself on the line k_u. 'Corresponding' means that k_u in the k_x,k_y-plane has the same orientation as $\boldsymbol{u}$ in the x,y-plane. A cross-section of $F(k_x,k_y)$ is shown at the lower right in fig. 12*b*. The theorem above states that this curve has the same shape as the signal $S(t)$, recorded with a gradient in the corresponding direction.

Starting from this theorem, which will be proved shortly, we proceed as follows in NMR projection reconstruction. The FID signal is recorded for a large

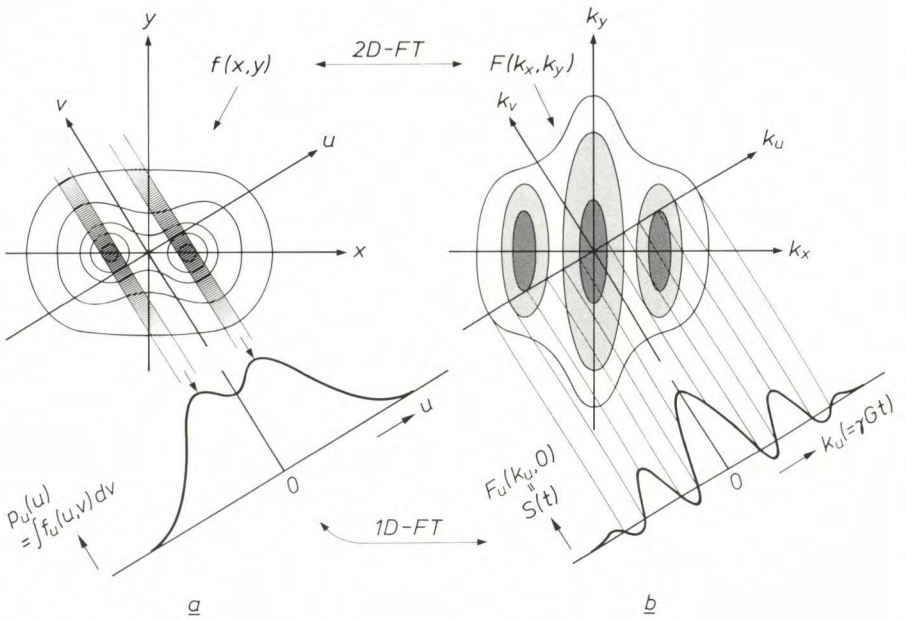

Fig. 12. NMR projection-reconstruction method. *a*) The proton distribution in a slice, $f(x,y)$, and *b*) its two-dimensional Fourier-transform $F(k_x,k_y)$ (see eq. (4)), both represented by means of lines of equal value ('contour lines'). At the *lower right* in *a* is a *projection* ($p_u(u)$) of $f(x,y)$ and at the *lower right* in *b* is a *cross-section* (or 'slice') of $F(k_x,k_y)$ in the corresponding direction. According to the 'projection-slice theorem' these are one-dimensional Fourier transforms of one another. The projection $p_u(u)$ is the spectrum of the NMR signal for a gradient in the direction $\boldsymbol{u}$ (see text); the cross-section referred to is therefore the NMR signal itself (since 'signal' and 'spectrum' are Fourier partners). $F(k_x,k_y)$ can thus be directly reconstructed from the signals for a large number of directions. A 2D Fourier transformation is used to find $f(x,y)$.

number of directions $\boldsymbol{u}$. From the cross-sections of $F(k_x,k_y)$ thus obtained $F(k_x,k_y)$ itself is determined. A 2D Fourier transformation completes the reconstruction of $f(x,y)$ [5].

One indication is still missing here: the 'horizontal scale' on which we find a cross-section of F if we identify it with $S(t)$; in other words, the relation between t and k_u. This will be found in the proof of the theorem mentioned above, which will now be given. To start with, the transformation (4) is restated in terms of the coordinates of the rotated systems $u,v;k_u,k_v$ (see fig. 12):

$$F_u(k_u,k_v) = \int\int f_u(u,v)\, e^{j(k_u u + k_v v)}\, du\, dv, \qquad (5)$$

where $F_u(k_u,k_v)$ is the function $F(k_x,k_y)$ in terms of k_u and k_v, and $f_u(u,v)$ is the function $f(x,y)$ in terms of u and v. For the 'cross-section' of F along $\boldsymbol{k}_u$, $F_u(k_u,0)$, we therefore have:

$$F_u(k_u,0) = \int\int f_u(u,v)\, e^{jk_u u}\, du\, dv. \qquad (6)$$

On the other hand, the FID signal with the gradient $\boldsymbol{G}$ in the direction $\boldsymbol{u}$ is found from eq. (3) by the substitution:

$$(\omega - \omega_0)t = \gamma(B - B_0)t = \gamma G u t.$$

This gives:

$$S(t) = \int\int f_u(u,v)\, e^{j\gamma G u t}\, du\, dv. \qquad (7)$$

Here again the integration is carried out in terms of the coordinates u,v. We see now that the signal (7) is identical to the cross-section (6) if we put:

$$k_u = \gamma G t. \qquad (8)$$

This provides the proof and at the same time the desired relation between k_u and t.

The method can also be formulated as follows. If the signal $S(t)$ is recorded with a gradient $\boldsymbol{G}$ in the direction $\boldsymbol{u}$, a $\boldsymbol{k}_u$-line in the k_x,k_y-plane is described at a rate given by (8); the signal value at every instant gives the value of F at the point reached. If sufficient measurements are made, F is obtained and f can be derived. This formulation will presently be extended to the case where different gradients are applied successively.

The proof given is not quite complete, since it may not be immediately clear that the transformations (4) and (5) of $f(x,y)$ — in (5) in the form $f_u(u,v)$ — do indeed give the same result. The results do agree, for if the coordinate systems in fig. 12 are rotated through the same angle, $k_x x + k_y y$ becomes $k_u u + k_v v$. This is self-evident, since the expression gives the scalar product $(\boldsymbol{r}.\boldsymbol{k})$ of the radius vectors $\boldsymbol{r}$ and $\boldsymbol{k}$ in the two planes, and is thus invariant on rotation.

Finally, a comment is in order about other cases of projection reconstruction that differ from NMR projection reconstruction in that the projections themselves do have to be taken as the point of departure. This is the case, for example, with computerized tomography (CT), where X-ray scanning in a plane of directions gives the projections from which the distribution of the material in that plane is reconstructed. First the Fourier transforms of the projections are calculated (the 'first step' mentioned earlier that is missing in NMR projection reconstruction). These are then identified with cross-sections of $F(k_x,k_y)$, so that $F(k_x,k_y)$ can be determined and hence $f(x,y)$, by transformation. For these cases, the theorem is often formulated (see fig. 12) as: *a projection of $f(x,y)$ and the 'corresponding' cross-section (or 'slice') of $F(k_x,k_y)$ form a 1D Fourier pair.* In this form the theorem is known as the 'projection-slice theorem'.

[5] Since $F(k_x,k_y)$ is obtained in polar coordinates in k-space, whereas $f(x,y)$ is preferably obtained in Cartesian coordinates, the 2D Fourier transform takes the special form here known as 'filtered back projection', but without the first step, which is the 1D Fourier transform of the individual projections.

Two-dimensional Fourier zeugmatography

With 2D projection reconstruction the information is obtained in the k_x,k_y-plane from points along a large number of lines through the origin (*fig. 13a*). This has its disadvantages. The data acquisition is very inhomogeneous: very dense at the centre and thin at the edge. It is therefore better — and for other reasons as well — to collect the information from points along a number of parallel lines (fig. 13*b*). This is done in 'Fourier zeugmatography' [6].

The method can be explained by extending the formulation of NMR projection reconstruction given above. A succession of different gradients can be considered as an 'excursion' in the k_x,k_y-plane, with the instantaneous velocity given by the instantaneous gradient $\boldsymbol{G}$ via the relation

$$\frac{d\boldsymbol{k}}{dt} = \gamma \boldsymbol{G}; \qquad (9)$$

for such an excursion the instantaneous signal value $S(t)$ gives the F-value at the point reached.

This follows immediately from expression (3) for the signal $S(t)$ and the Fourier relation (4). In a time δt the signal $S(t)$ changes because the phase angle $(\omega - \omega_0)t$ changes, and F changes because of the excursion in the k_x,k_y-plane as described by equation (9). The change in the phase angle is $(\omega - \omega_0)\delta t = \gamma(G_x x + G_y y)\delta t$, and from (9) this is equal to $x\delta k_x + y\delta k_y$. Consequently δS is always exactly equal to δF in such an excursion.

In projection reconstruction, excursions are only made at constant velocity along straight lines through the origin. In Fourier zeugmatography excursions of the type shown in *fig. 14* are made, which amounts to the following procedure. In the 'preparation period' the system is excited by a 90° pulse, and a positive y-gradient and a negative x-gradient are applied. An excursion is then made along the line a. When the point P is reached, both gradients are removed. Next a positive x-gradient is applied and the detector signal is recorded (detection period). This gives the cross-section of F along the line b. Selecting different values for the y-gradient in the preparation period gives different starting points and hence different cross-sections. It would of course be possible to record the detector signal during the excursion along line a as well, but this would require a more complicated processing program.

Some pitfalls

The situation would be exactly as described above if the transverse magnetization after a pulse were determined solely by the successive gradients. The actual situation is different; there are two main reasons for this.

In the first place the signal decays as a result of transverse relaxation. The time during which a signal can be recorded is thus limited to about T_2. This is one of the reasons why the entire k_x,k_y-plane is not traced out after a single pulse, but a start is made again for each cross-section of F.

In the second place the signal becomes degraded by dephasing of the spins owing to the undesired field inhomogeneities. It is usually necessary to accept field inhomogeneities of 1 in 10^5. This corresponds to a frequency uncertainty of $(10^{-5} \times 6$ MHz $=)$ 60 Hz, which means that the dephasing amounts to $60 \times 360°$ per second, or about 20° per ms. After a preparation period of 10 ms the phase uncertainty has therefore risen to 200°. The spin-echo method (fig. 10) offers a solution here. In the centre of the echo the dephasing is cancelled out and the signal is detected in a period that contains most of the echo signal including the initial and final parts of its waveform.

Finally the layer selection, which we have so far neglected, also has its complications [7].

To show the effects of all this, a pulse and gradient sequence as used in practice will now be considered in detail.

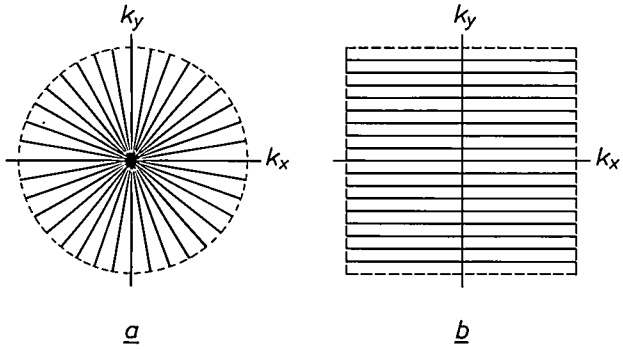

Fig. 13. Projection-reconstruction method versus Fourier zeugmatography. NMR signals are cross-sections of the function $F(k_x,k_y)$ (see fig. 12). The projection-reconstruction method detects the signals along lines through the origin in the k_x,k_y-plane (*a*), Fourier zeugmatography detects the signals along parallel lines (*b*).

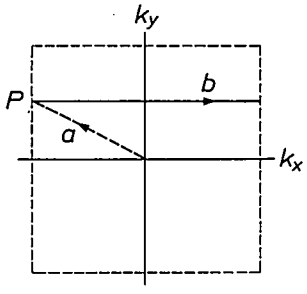

Fig. 14. Excursion in the k_x,k_y-plane for detection along one of the lines in fig. 13*b*. The path a (preparation period) is covered by taking G_x negative and (in the case illustrated) G_y positive; the detection path b is covered by taking G_y zero and G_x positive.

An actual pulse and gradient sequence

Fig. 15 shows a pulse and gradient sequence that we have actually used in NMR imaging (e.g. fig. 1). At the times P and Q, separated by 25 ms, a 90° pulse and a 180° pulse are applied; 25 ms after Q the centre of the echo appears; this time is defined as $t = 0$. The signal is recorded from R to S, i.e. from $t = -12.8$ to $+12.8$ ms. The gradient G_z selects the layer, the gradients G_x and G_y determine the path of the excursion in the k_x,k_y-plane.

During the 90° pulse only the spins in a thin layer perpendicular to z are excited, because of the gradient G_z (layer selection). To keep this layer as thin as possible, a pulse is used that has an approximately Gaussian profile and an effective duration of about 3 ms; the bandwidth Δf is thereby limited to 0.3 kHz. (In NMR spectroscopy the pulses are normally much shorter, e.g. 10 μs, with a bandwidth of the order of 100 kHz.) The relation between the bandwidth Δf and the thickness Δz of the layer of resonating spins is:

$$\Delta f = \Delta\omega/2\pi = \gamma\Delta B/2\pi = \gamma G_z \Delta z/2\pi.$$

For a gradient of 1.2×10^{-3} T/m the value of $\gamma G_z/2\pi$ is about 50 kHz/m; this is a gradient of about 0.3 per cent over the region of homogeneity (page 75). Under these conditions, with $\Delta f = 0.3$ kHz, the layer thickness is thus equal to (0.3/50)m = 0.6 cm.

As a consequence of the z-gradient the spins in the different sublayers of Δz have different frequencies; after the 90° pulse they therefore start to dephase. The 180° pulse, however, reverses the process (rephasing). Fig. 10 again shows what happens to the spins. When the detection starts at R, the dephasing has just been cancelled, because G_z is switched in such a way that the two integrals $\int_P^Q G_z dt$ and $\int_Q^R G_z dt$ are equal.

The excursion in the k_x,k_y-plane after the 90° pulse (*fig. 16*) is determined by the x-gradients, the y-gradient and the 180° pulse. The 180° pulse is equivalent to a reflection of the transverse magnetizations of the subdomains in the x',y'-plane relative to the x'-axis (fig. 10*c* and *d*). In complex notation this represents a reflection relative to the real axis ($j \rightarrow -j$) and hence a jump from k_x,k_y to $-k_x,-k_y$ (see eq. (4); this applies only if $f(x,y)$ is real, but this is always the case with our sequences). Along the detection path RS a cross-section of F is determined. The procedure is carried out for 128 G_y values. Between the determinations of two cross-sections it is necessary to allow a time of

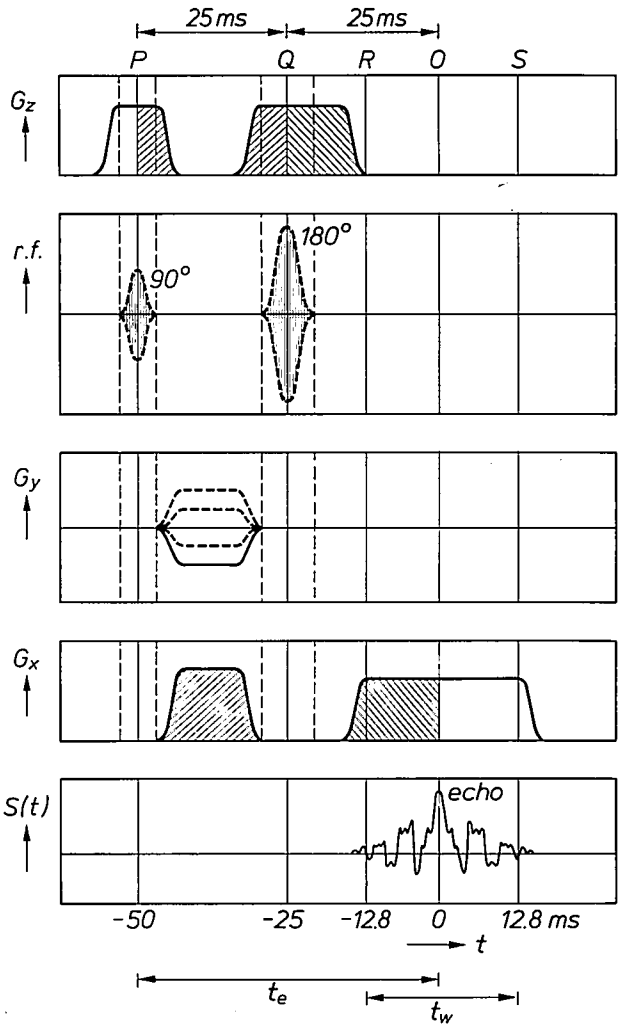

Fig. 15. Practical example of a pulse and gradient sequence. The 90° pulse in P and the 180° pulse in Q give an echo signal with the centre at O. PR preparation period, RS ($= t_w$) detection time, PO ($= t_e$) echo time. The gradient G_z is used in selecting a layer. The gradients G_x and G_y determine the path scanned in the k_x,k_y-plane. To measure a complete body slice the sequence is repeated 128 times, with a slightly different G_y-value each time.

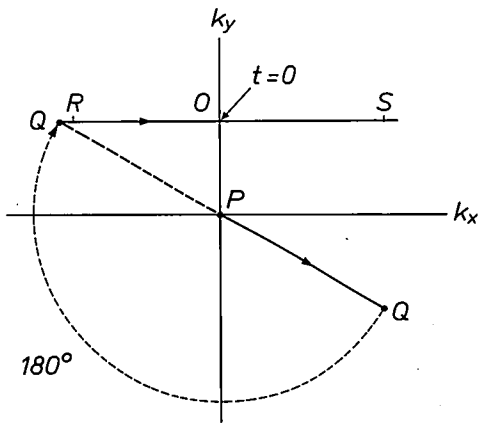

Fig. 16. Path scanned in the k_x,k_y-plane with the pulse sequence of fig. 15. The points P, Q, R, O and S correspond to those in fig. 15. The 180° pulse corresponds to a reflection in the origin.

[6] A. Kumar, D. Welti and R. R. Ernst, J. Magn. Resonance **18**, 69, 1975. The rather strange term 'zeugmatography' was coined by P.C. Lauterbur from the Greek word *zeugma* meaning 'that which joins together'; the locally resonant spins 'join' the r.f. field with the static spatially-dependent magnetic field. See the articles by Lauterbur [2].

[7] P. R. Locher, Philos. Trans. R. Soc. London B **289**, 537, 1980.

about one second to elapse, to give the spin system an opportunity to return more or less to thermal equilibrium. It thus takes about two minutes to measure one complete body slice.

For the digital processing the low-frequency signals S_1 and S_2 (see page 79) are sampled during detection at a typical rate of one sample per 0.2 ms. Each pair of samples yields a value for the complex function $F(k_x,k_y)$. After measurement of the complete body slice we thus have the values of $F(k_x,k_y)$ in a matrix of points in the k_x,k_y-plane. The computer then calculates $f(x,y)$ from these values, and the result is displayed on the screen as a pattern of grey levels.

Image quality

Let us now consider the factors that determine the image quality, taking a representative example of our measurements. We shall consider a pulse sequence as in fig. 15, with a 'detection time' t_w of 25.6 ms. Such a pulse sequence can only be used when the transverse relaxation time T_2 is not much less than the echo time t_e of 50 ms. For our example we take T_2 equal to 50 ms.

Resolution

One aspect of the image quality is the resolution or its reciprocal, the size of an 'object element'. 'Object elements' are the smallest elements of the body slice that can be reproduced in the image. The element size is primarily determined by the detection period t_w. This is because we cannot discriminate between frequencies in the signal $S(t)$ that are closer together than $\Delta\nu = 1/t_w$. Consequently, we cannot discriminate between points in the x,y-plane closer together than Δx, where

$$\Delta x = 2\pi\Delta\nu/\gamma G. \qquad (10)$$

In our example $\Delta\nu$ ($= 1/t_w$) is approximately equal to 40 Hz; once $\Delta\nu$ is fixed, Δx is determined by the gradient. Let us assume that we wish to make images with object elements that are 2 mm square. This means that the gradient should satisfy the relation:

$$\gamma G/2\pi = \Delta\nu/\Delta x \approx 20 \text{ kHz/m}$$

or

$$G \approx 4.7\times10^{-4} \text{ T/m}.$$

We shall return presently to this choice for Δx and G, but first we shall consider its consequences for the measurement program. Let the main dimension of the object be 25 cm. The original r.f. signal then covers a frequency band of 20 kHz/m $\times$ 0.25 m = 5 kHz, around the centre Larmor frequency of 6 MHz. Phase-sensitive detection shifts this to the band -2.5 to $+2.5$ kHz (fig. 11). The directly detected signals ($S(t)$ in fig. 15) thus have frequencies from 0 to 2.5 kHz (negative frequencies are only of significance for the complex signal). To take these frequencies into account properly, it is necessary to sample the signals — in accordance with the 'sampling theorem' — at a frequency of at least (2×2.5 =) 5 kHz, i.e. once in each 0.2 ms. For the detection time t_w this amounts to 128 samples, so that we obtain values for F at 128 points on the detection path RS in fig. 16. For the same data density in the k_y-direction the detection must be repeated for 128 k_y-values. The matrix of 128×128 F-values thus obtained is converted by the computer into 128×128 f-values, so that with an object of 250 mm $\times$ 250 mm there is one value for each object element of 2 mm $\times$ 2 mm. In reality, there are twice as many samples, F-values and f-values, because the signals and functions are complex.

Two corrections to this rather simplified account should be mentioned here. In the first place, the analog filter that reduces the bandwidth to 2.5 kHz would have to be an ideal filter to permit correct sampling at 5 kHz. Obviously any practical filter will not be ideal. We compensate for this by 'digital filtering', which implies oversampling — we take one sample in each 0.1 ms. In the second place the matrix of 128×128 f-values is not converted directly into 128×128 grey values, but translated first — by means of a refined method of interpolation — into a matrix of 256×256 values; the image thus has 'greyness elements' of dimensions 1 mm $\times$ 1 mm. This is done to give the best visual display of the information available.

Signal-to-noise ratio

We now return to the choice of the gradient and the size of the object element. Equation (10) might give the impression that, for a given frequency uncertainty $\Delta\nu$, the uncertainty of position (Δx) might be made arbitrarily small by making the gradient sufficiently large. This is only apparently so. If the object elements are too small the proton content can no longer be determined: the signal is swamped in the thermal noise. This is because the signal voltage from an element is proportional to the element volume: if an element with coherently precessing spins is divided into two identical elements, the induced voltage per element is twice as small. On the other hand the noise voltage of the element is determined only by the corresponding bandwidth $\Delta\nu$, and is thus independent of the gradient; the r.m.s. noise voltage $\bar{V}_n$ is $\sqrt{4kT_c\Delta\nu R_s}$, where T_c is the 'equivalent noise temperature', R_s is the 'equivalent series resistance' of the circuit, and k is Boltzmann's constant.

The equivalent resistance R_s represents the total losses. A considerable proportion of these losses arises in the body, because it has electrical conductivity. The

noise from the actual ohmic resistance of the coil might be reduced by cooling the coil, but the human body will always produce noise at 310 K.

An upper limit to the power signal-to-noise ratio is given by the relation:

$$(\tilde{V}_s/\tilde{V}_n)_{av}^2 \leqq \frac{\omega^2 L v_p^2 \chi^2 B_0^2}{2\mu_0 v_c} \cdot \frac{T_2}{4kT_c R_s} \cdot N \qquad (11a)$$

$$= \frac{Q v_p^2 \gamma \chi^2 B_0^3 T_2}{8\mu_0 v_c k T_c} \cdot N. \qquad (11b)$$

The expression on the right in (11a) has been divided into three factors. The first factor is an upper limit for $\tilde{V}_s^2$, the square of the r.m.s. value $\tilde{V}_s$ of the signal voltage during the echo: it can be shown that $\tilde{V}_{si}^2$, the corresponding value *immediately after a 90° pulse*, is given by this factor, and $\tilde{V}_s^2$ is certainly smaller. In this first factor v_p represents the volume of an object element, L and v_c are the inductance and the 'effective volume' of the detector coil, and χ is the volume susceptibility of the substance being investigated ($M = \chi B_0/\mu_0$; χ is dimensionless); B_0, as before, is the flux density of the static field. The second factor is an upper limit for $1/\tilde{V}_n^2$, which is equal to $1/4kT_c\Delta\nu R_s = t_w/4kT_c R_s$, and t_w is certainly smaller than T_2. In our example $t_w \approx \frac{1}{2}T_2$. In expression (11b) these two factors have been combined, and use is made of the relations $\omega = \gamma B_0$ and $\omega L/R_s = Q$, where Q is the Q-factor of the coil.

The factor N is the number of paths RS used for the measurement of a complete body slice (128 in our example). This factor represents the effect of time averaging, a familiar method of dealing with noise problems. Each object element corresponds to an extended wave pattern in the k_x,k_y-plane (a one-dimensional sine function; see *fig. 17*), and all N detections contribute 'coherently' to the information about this pattern, so that the accumulated signal energy is proportional to N^2; on the other hand the noise energy, which accumulates 'incoherently', is only proportional to N.

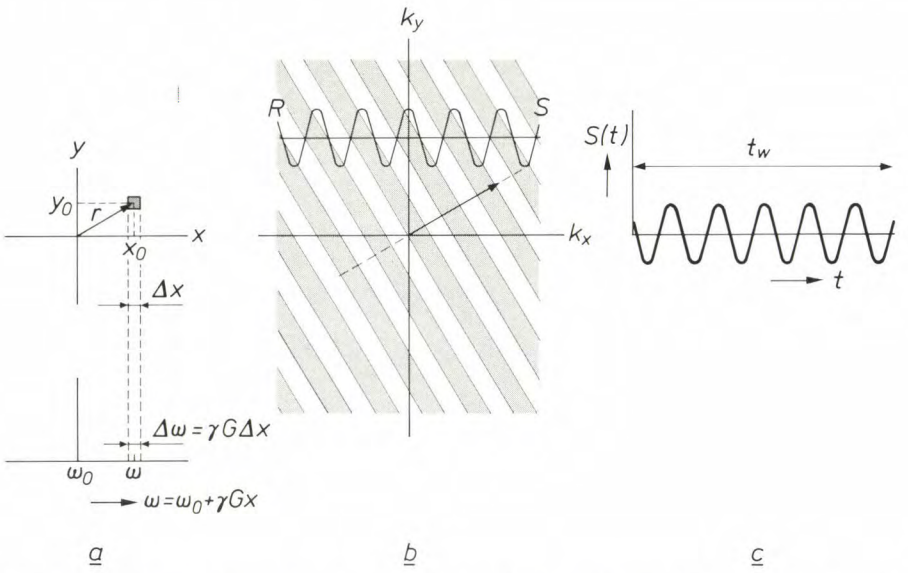

Fig. 17. Contribution of one object element to the signal. *a*) The element in the x,y-plane. *b*) Contribution to $F(k_x,k_y)$, a sinusoidal wave pattern. In the grey strips the contribution is positive, between them it is negative. The arrow indicates the direction of the wave pattern, and this is the same as the direction of the radius vector $\boldsymbol{r}$ in (*a*). The cross-section of the pattern along the line RS gives the contribution to the signal (*c*) when this line is scanned. The detection time t_w determines the uncertainty in the angular frequency, $\Delta\omega$, and, together with the gradient, the element size Δx (equation (10)). All detection paths RS (fig. 13*b*) contribute coherently to the information about the wave pattern.

The number N determines the total measurement time τ for a slice. Between two detection paths a time of about $2T_1$ has to elapse to allow the spin system to return to equilibrium. The total measurement time is thus about:

$$\tau = 2NT_1. \qquad (12)$$

It will be shown here that $\tilde{V}_{si}^2$ is indeed equal to the first factor of (11a) if the detector coil is a long solenoid (*fig. 18*). $\tilde{V}_{si}$ is the voltage induced across the coil by the precessing spins immediately after a 90° pulse. The object element then has a magnetization that precesses with an amplitude $\hat{M}$ equal to the equilibrium magnetization before the pulse: $\hat{M} = \chi H_0 = (1/\mu_0)\chi B_0$. This precessing magnetization is equivalent to an oscillating flux density of amplitude $\hat{B}_i = \mu_0 \hat{M} = \chi B_0$. For a coil homogeneously filled with coherent spins there would be an oscillating flux ϕ of amplitude $\hat{\phi} = A\hat{B}_i$, and therefore an induced voltage $-n\dot{\phi} = -\omega n\phi$ of amplitude $\omega nA\hat{B}_i$, where A is the cross-sectional area of the coil and n the number of

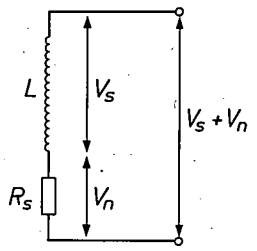

Fig. 18. Diagram of the detector coil. L inductance, R_s series resistance, V_s signal voltage, V_n noise voltage.

If now the signal-to-noise ratio and the scanning time are calculated for different sizes of the object elements, using equations (11) and (12), the results presented in *Table I* are found (columns B and A). The values taken are typical for our tomograph and for elements of 100% water. The calculation was made for elements of depth 5 mm (the thickness of the slice) and cross-sections of 2×2, 1×1 and $\frac{1}{2}\times\frac{1}{2}$ mm^2. Associated with these square elements is a square matrix of F-values. This implies that N has to be chosen twice as large when we go from the 2×2 to the 1×1, or from the 1×1 to the $\frac{1}{2}\times\frac{1}{2}$ mm^2 element, so that the measurement time becomes twice as long and the signal-to-noise ratio $8\times$ as small (in eq. (11) v_p^2 is $16\times$ as small and N twice as large).

Equation (11) gives a fairly generally valid upper limit. In our example the power signal-to-noise ratio is at least 15 times smaller, for the following reasons. The signal is not measured until 50 ms after the 90° pulse, and since in our example T_2 also has this value, the signal voltage is about e times smaller and the signal power e^2 (≈ 7.5) times smaller. Moreover, the

Table I. A typical numerical example. The first two boxes on the left give values of the characteristic quantities for object elements of 100% water and for our equipment. The upper right-hand box shows how χ is calculated (linear Langevin equation with a quantum-mechanically corrected value for μ^2, the square of the magnetic moment of the nucleus; ϱ is the proton density, T_s the temperature of the sample, I is the spin-quantum number). The lower box gives the results of a calculation of the measurement time (column A) and of the signal-to-noise ratio (column B) with equations (12) and (11). Column C gives a more realistic upper limit (see text). The *voltage* signal-to-noise ratio $\bar{V}_s/\bar{V}_n$ determines the contrast.

Substance

protons in water at 295 K	$\gamma/2\pi = 42.576$ MHz/T $\chi = 4.10\times10^{-9}$
typical relaxation times in tissue	$T_2 = 50$ ms $T_1 = 0.5$ s

$\chi = \dfrac{\mu_0\varrho\mu^2}{3kT_s}$, $\mu^2 = \gamma^2 I(I+1)\hbar^2$

$\varrho = 6.67\times10^{28}$ m^{-3}
$T_s = 295$ K
$I = \frac{1}{2}$

Equipment

magnet frequency	$B_0 = 0.14$ T $\omega_0/2\pi = \gamma B_0/2\pi = 6$ MHz
coil, losses	$v_c = 0.1$ m^3 $Q = 100$ $T_c = 295$ K

Fundamental constants

$\mu_0 = 4\pi\times10^{-7}$ Vs/Am (permeability of free space)
$k = 1.38\times10^{-23}$ J/K (Boltzmann's constant)
$h = 6.63\times10^{-34}$ Js (Planck's constant)
$\hbar = h/2\pi$

Measurement time and signal-to-noise ratio

volume of object element	N	A (from (12)) τ	B (from (11)) $(\bar{V}_s/\bar{V}_n)_{av}^2$	B (from (11)) $(\bar{V}_s/\bar{V}_n)_{av}$	C (realistic) $(\bar{V}_s/\bar{V}_n)_{av}^2$	C (realistic) $(\bar{V}_s/\bar{V}_n)_{av}$
$v_p = 2\times2\times5$ mm^3 = 20 mm^3	128	128 s ≈ 2 min	780	28	52	7.2
$1\times1\times5$ mm^3 = 5 mm^3	256	256 s ≈ 4 min	98	9.9	6.5	2.6
$\frac{1}{2}\times\frac{1}{2}\times5$ mm^3 = 1.25 mm^3	512	512 s ≈ 9 min	12	3.5	0.8	0.9

turns. As the field in a long thin coil is uniform, the spins should contribute equally to this induced voltage. The contribution of one object element to the induced voltage is thus $\bar{V}_{si} = (v_p/v_c)\omega nA\hat{B}_i$. It follows that:

$$\bar{V}_{si}^2 = \tfrac{1}{2}\hat{V}_{si}^2 = v_p^2\omega^2(nA)^2\chi^2B_0^2/2v_c^2,$$

With the aid of the relations $L = \mu_0 n^2 A/l$ and $v_c = Al$ (where l is the length of the coil) the quantities A and n relating to the details of the coil shape can be translated into the more general concepts L and v_c; we have $(nA)^2 = Lv_c/\mu_0$. On substitution, the first factor of (11a) is obtained for $\bar{V}_{si}^2$.

It is possible to show that this result is also valid for coils other than long solenoids. The effective volume v_c must then be defined by the relation:

$$\tfrac{1}{2}LI^2 = \tfrac{1}{2}v_cH_cB_c,$$

where $\frac{1}{2}LI^2$ is the magnetic energy of the coil at a current I such that field and flux density at the centre are equal to H_c and B_c.

reciprocal of the noise power, t_w/kT_c, is twice as small as T_2/kT_c. Column C gives the results. Columns B and C also give the *voltage* signal-to-noise ratio, $\tilde{V}_s/\tilde{V}_n$, which determines the contrast.

It will now be clear why we decided to adopt elements of 2×2 mm^2. With the conditions described, and with elements of this size, differences of 1 part in 7 of water (14%) can be distinguished. The discrimination rapidly deteriorates with smaller elements, and with elements of $\frac{1}{2} \times \frac{1}{2}$ mm^2 the signal for 100% of water is completely swamped in the noise. Smaller elements also imply longer scanning times (column A).

The above analysis can be summarized as follows. After an appropriate detection time t_w has been chosen, the element size may be made arbitrarily small by making the gradient sufficiently large, but there is no point in making it smaller than the size for which the signal-to-noise ratio (11b) is about 1. One of the variables in this procedure is N, the number of detections per slice (the number of 90° pulses). In our example N has been linked to the number of elements per slice, but this is not necessary: N — and hence the power signal-to-noise ratio — can be doubled, for example, by carrying out each r.f. measurement twice. However, the total scanning time τ (12) will then also be twice as long. A compromise therefore has to be made between image quality and speed of imaging.

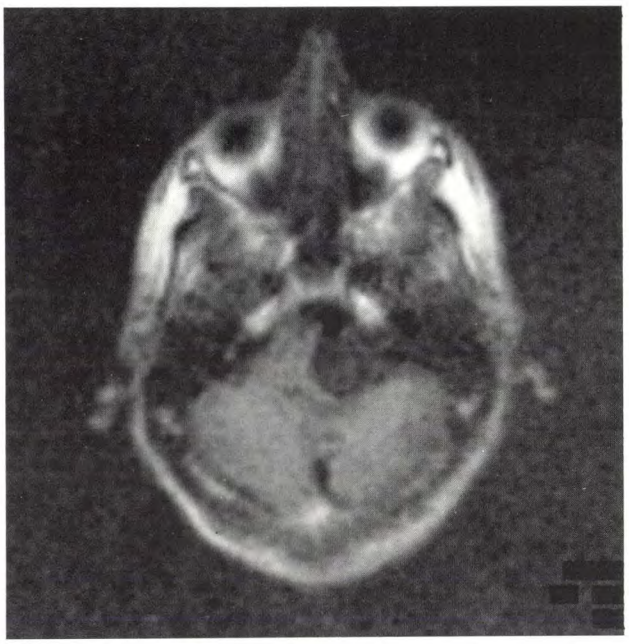

Fig. 19. T_1-sensitive image. The dark asymmetric area just to the right of the centre is a benign tumour projecting from the auditory nerve.

Concluding remarks

ϱ-, T_1- or T_2-sensitive images

In this article it has been assumed for simplicity that the discrimination between tissues depends entirely on the proton concentration ϱ in the tissues. Now we should note first that there are some protons that take no part at all in the process, because their transverse relaxation time (T_2) is too short. However, apart from this, the brightness in the image would indeed be a perfect measure of the concentration of the protons that do take part, provided these all had identical T_1's and identical T_2's. Now T_1 is usually much greater than the echo time t_e (see fig. 15). In such a case the effect of T_1 can in principle be completely eliminated by making the waiting time between two pulses so long that the thermal equilibrium is fully restored between pulses. However, T_2 is often of the same order as t_e. A substance with the same concentration but with a smaller T_2 therefore gives a noticeably weaker echo signal. The same applies to other pulse sequences than the one we have discussed, because there is always some 'preparation time' between pulse and detection.

In practice a virtue has been made of necessity: the pulse sequences are as a rule deliberately designed to ensure that the image brightness does depend strongly on T_1 or T_2, so that it is T_1 or T_2 that is 'imaged' rather than ϱ. This can often give greater contrasts because tissues and body fluids tend to differ more in relaxation time than in proton concentration. Moreover, other things are 'seen'. In particular, it has been found that healthy tissue and tumour tissue generally give very different values of T_1 and of T_2, whereas ϱ is much the same. Thus, a T_1- or T_2-sensitive image discriminates more clearly between healthy and diseased tissue. A T_1-sensitive image can for example be made by using the inversion-recovery method illustrated in fig. 9; if the time between the 180° and the 90° pulses is selected about midway between the two T_1-values, strong contrasts are obtained. *Fig. 19* gives an example of such an image. Images can also be made showing other effects; for example the difference between static and flowing body fluids (such as the blood in the arteries) can be visualized distinctly.

It is probably true to say that the art of NMR imaging no longer consists so much in the visualization of many details of an internal structure, but more in establishing precisely what is seen.

Further development of equipment and method

Expression (11b) was used to find the best element size for our tomograph. This expression also shows how the signal-to-noise ratio and the image quality might be improved. In the first place stronger fields could be used ($V_s/V_n \propto B_0^{\frac{3}{2}}$, if for simplicity it is as-

sumed that there is no change in the Q of the coil). In present magnet designs with ordinary wire the cost increases so steeply with field-strength that for fields of 0.2 to 0.3 T and above, superconducting magnets are preferable. The estimated cost per additional tesla of superconducting magnets is also much lower in this range, so that the use of such magnets for very much stronger fields (1.5 to 2 T) becomes a practical possibility. As will appear below, this is particularly important for NMR tomography with other nuclei.

To return to protons, the use of higher field-strengths would entail a proportionate increase in frequency and hence other complications. In the first place, the penetration of the r.f. field into the body is less, because of the skin effect in such an electrically conductive medium. At 10 MHz the penetration depth into a physiological salt solution ($\sigma = 2.0\ \Omega^{-1}\mathrm{m}^{-1}$) is only about 10 cm. But this does not really apply for the human body, since the conductivity of the body is fortunately lower than that of a physiological solution; but above about 20 MHz the skin effect should be taken into account. In the second place it becomes increasingly difficult to design good high-Q r.f. coils for higher frequencies. Good images with noticeably less noise have been made at about 20 MHz (about 0.5 T).

The characteristics of the coil are expressed in the factor $Q/v_c T_c$ in equation (11b). The shape of the coil affects both v_c and Q. A simple calculation for a long solenoid shows that a coil of few turns wound closely around the object gives the best performance. This calculation only applies to the copper losses in the coil. The Q, however, is inversely proportional to the sum of *all* the losses, including the copper loss, the radiation loss and the losses due to induction in neighbouring conductive objects, in particular the body. As already noted, the copper losses can be reduced by cooling the coil. This has the double advantage of increasing Q and making T_c smaller. It would entail further technical complications, of course.

Finally, NMR imaging is possible with nuclei other than protons. Since the gyromagnetic ratio γ of the nuclei that appear to be most suitable (^{31}P, ^{23}Na, ^{13}C) is three to four times smaller than that of protons, much higher fields have to be used at the same frequency; the field gradients required are also much larger. Moreover, the image quality for a given concentration variation will be much worse, as can be seen from eq. 11b, since $\gamma\chi^2 B_0^3$ is proportional to γ^2 at a given frequency (χ is given in Table I). For these reasons, and also because of their relatively high concentration in biological material (ϱ comes into equation (11) via χ (see Table I)), protons are clearly the best choice if distinct high-contrast images of body tissues and organs are required. Nevertheless, there is very considerable interest in imaging with other nuclei because of the completely different kind of information it can provide. In particular, the chemical shift can be put to use for observing interesting chemical states. It may for example become possible to monitor certain metabolic processes locally by discriminating between phosphorous chemically combined in ATP and phosphorus combined in inorganic phosphates.

Summary. In NMR imaging the accurate field-strength discrimination possible with nuclear magnetic resonance is converted by gradients in the magnetic field into spatial discrimination. An NMR tomograph consists of a large coil-magnet, gradient coils, r.f. equipment (for excitation and detection of the nuclear spin precession), program-control electronics and a computer for translating signals into images. Pulse NMR methods are used, generally with 90° and 180° pulses for excitation. The best-known versions of NMR imaging are 2D projection reconstruction and 2D Fourier zeugmatography. In the first of these a z-gradient is used to select a slice of thickness say 5 mm and parallel to the x,y-plane. Next a gradient is applied in a direction u in the x,y-plane. The NMR spectrum is then a one-dimensional projection of the two-dimensional proton distribution $f(x,y)$ in the slice. The 2D proton distribution $f(x,y)$ is reconstructed from the projections for say 200 directions of u. The reconstruction takes place via the 2D Fourier transform $F(k_x,k_y)$ of $f(x,y)$. Analysis shows that the NMR signal with a gradient in the direction u is a faithful representation of a 'cross-section' of F. It is thus possible to use the signals from different gradient directions to construct F and subsequently f. In the 2D projection reconstruction method the k_x,k_y-plane is in fact scanned via lines through the origin. In 2D Fourier zeugmatography this is done via parallel lines. The method is illustrated with an actual pulse and gradient sequence and the image quality is discussed. In addition to proton-density images it is also possible to produce images that are sensitive to relaxation times; these generally provide much more information.

Ceramic multilayer capacitors

H.-J. Hagemann, D. Hennings and R. Wernicke

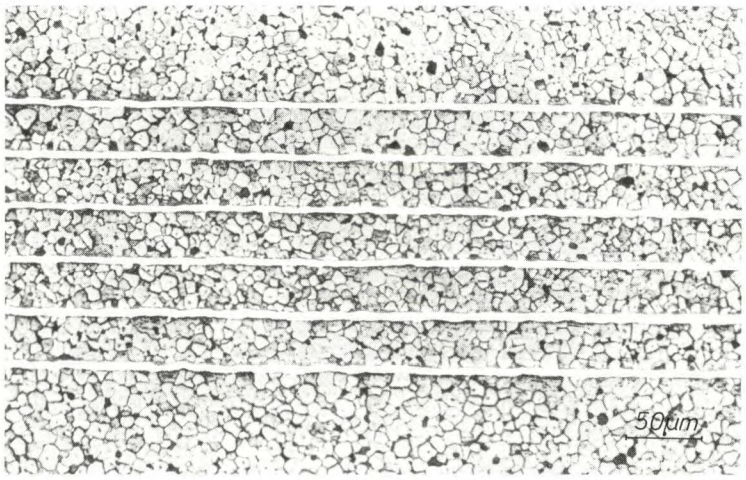

The progressive miniaturization of electronic circuits has created an increased need in recent years for capacitors of small dimensions and high capacitance. If such capacitors are to be widely used in consumer products, inexpensive manufacturing methods are required. Ceramic multilayer capacitors do indeed have a high capacitance per unit volume, and their construction makes them very suitable for automatic mounting. But at present they are not cheap, because expensive noble metals such as palladium have to be used for the internal electrodes of the multilayer structure (see title photograph). This article describes the principle of the conventional multilayer capacitor and discusses two approaches to the development of new and cheaper versions; in one approach the palladium is partially replaced by silver, and in the other it becomes possible to replace the palladium by nickel.

Approaches to further development

In recent years there have been radical changes in the manufacture of electronic devices. Since the production of the first integrated circuit twenty years ago such great strides have been made in the technology of integrating active components that a complete microcomputer can now be built on a single chip [1]. However, a comparable integration and miniaturization of *passive* components, especially *capacitors*, has been much more difficult. For ceramic capacitors the challenge has been taken up, and there has been worldwide activity in the development of capacitors of small size and high capacitance.

The prospects and the difficulties are best discussed by starting from the well-known equation for the capacitance of a parallel-plate capacitor:

$$C_A = \frac{\varepsilon_0 \varepsilon_r}{d},$$

where C_A is the capacitance per unit area, ε_0 is the permittivity of free space, ε_r is the relative permittivity

Dr H.-J. Hagemann, Dr D. Hennings and Dr R. Wernicke are with Philips GmbH Forschungslaboratorium Aachen, Aachen, West Germany.

[1] See H. Bosma and W. G. Gelling, Philips Tech. Rev. **37**, 267, 1977.

(or dielectric constant) of the dielectric and d is the spacing of the plates. It follows at once from the equation that there are two possible ways of increasing the capacitance per unit area: increasing ε_r or decreasing d.

Increasing the dielectric constant

The first approach, trying to obtain a larger permittivity, has been tried ever since ceramic capacitors first came into use and has led to the development of a wide variety of dielectric materials. But after the discovery of the ferroelectric properties of barium titanate in 1943, which for the first time brought ε_r-values of 1000 and more within reach, research and development have been increasingly concentrated on this material [2]. *Fig. 1* shows the relative permittivities as a function of temperature for some of these now well-established ceramics, which are all modifications of $BaTiO_3$. Their relative permittivities at room temperature range from 1000 to 15 000, depending on the temperature characteristic.

Research on these ferroelectric materials revealed that an increase in the permittivity is generally gained at the expense of the temperature characteristic (see fig. 1). Such an effect can be predicted from fundamental considerations on ferroelectrics, since the factors that cause the permittivity to increase also make it more sensitive to temperature changes [3].

Small improvements in the permittivity of individual ferroelectrics are still possible, of course, but on the whole the limits of the attainable ε_r-values have now been reached with this group of materials, at any rate for a given temperature characteristic. There seems to be little further to be gained in trying to increase the capacitance per unit area in this way.

Reducing the thickness

The other approach, trying to increase the capacitance by reducing the thickness of the capacitor, has also been followed since the sixties. Unlike the first approach, this is mainly a problem of technology. The conventional flat capacitors now in use are shaped by pressing, extruding, or calendering a mixture of a ceramic powder and binders. These techniques can reduce the thickness to 100 μm. In addition, pieces of ceramic thinner than 200 μm are very difficult to handle in the manufacture of the capacitors (e.g. in soldering the leads and encapsulation).

Considering the dielectric material alone, it seems that the idea of a much thinner layer is promising. Modern ceramics are able to withstand a rated electric field-strength (i.e. the maximum value quoted in the specification) of between 2 and 3 V/μm. Since ceramic capacitors are normally rated for a voltage of about

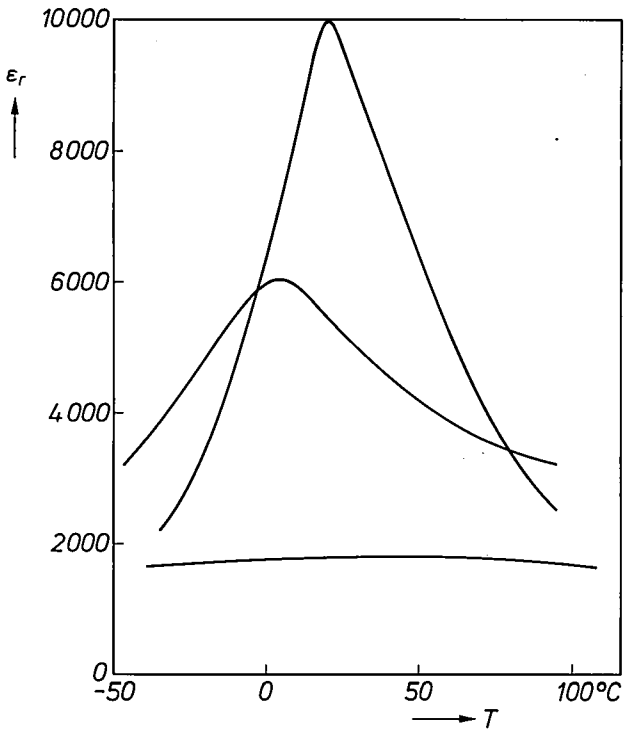

Fig. 1. Relative permittivity ε_r of some widely-used ceramic materials, based on $BaTiO_3$, as a function of temperature.

50 V, it ought to be possible to reduce the thickness to between 20 and 25 μm. This means that there is a factor of *at least eight* to be gained, compared with the conventional capacitors, if all the technical difficulties associated with production can be overcome.

This line of thought has resulted in the development of two new types of ceramic capacitor. The first type is the 'ceramic barrier-layer capacitor' (CBC), which is based on the formation of a thin insulating layer at the surface or at the grain boundaries of a piece of semiconducting ceramic. In this way *dielectric* thicknesses of a few microns can be obtained in pieces of ceramic with a practical *physical* thickness of a few hundred microns, which present no problems of manufacturing technology. This type of capacitor will be the subject of a forthcoming article in this journal. The second new type of capacitor, resulting from efforts to reduce the thickness, is the 'ceramic multilayer capacitor' (CMC), which is the subject of this article.

Advantages and disadvantages of the multilayer capacitor

As can be seen from the cut-away view in *fig. 2*, a multilayer capacitor consists of a ceramic body with embedded electrode layers, which are alternately connected to the metallized end terminations on the left

and right of the capacitor. With this electrode arrangement the individual capacitors formed by the ceramic layers between the electrodes are all connected in parallel, so that their capacitances add up to the required total capacitance.

The manufacture of multilayer capacitors is in essence as follows. A powder of the ceramic material is mixed with binders to form a suspension, and strips of thickness of about 50 μm are cast from the suspension. The strips or 'tapes' are then cut into sheets, and a metal paste is applied by screen printing. The sheets, with the electrodes printed on them in a repetitive pattern, are stacked and consolidated under pressure, and the individual units are then cut apart and heated to burn off the binder. The complete assembly is then fired to produce a coherent, integral structure of ceramic and metal. During the screening, stacking and cutting the sheets are aligned in such a way that the electrodes on successive layers are exposed at opposite faces. These two faces are then metallized, so that the individual ceramic capacitors are all connected in parallel.

Clearly a capacitor constructed in this way can be made with a high capacitance per unit volume: the small thickness of the ceramic layer (about 25 μm after firing) is effectively of double benefit to the total capacitance — in the magnitude of each subcapacitance and in the number of subcapacitors per unit volume.

Multilayer capacitors are made from three main types of materials, often described as NPO, X7R and Z5U materials [4]. The NPO-type materials have relatively low permittivities, which are nearly independent of temperature, the Z5U materials have very high permittivities, which vary strongly with temperature, and X7R materials come somewhere between the two. With these materials, and with dimensions ranging from 2 mm × 1.2 mm × 1 mm to 6 mm × 5 mm × 2 mm, capacitance values between 0.5 pF and 1 μF can be obtained. The great advantage of multilayer capacitors is also illustrated in *fig. 3*, which shows capacitors of this type beside a number of others of the same capacitance (100 nF) and comparable secondary characteristics but made by different technologies.

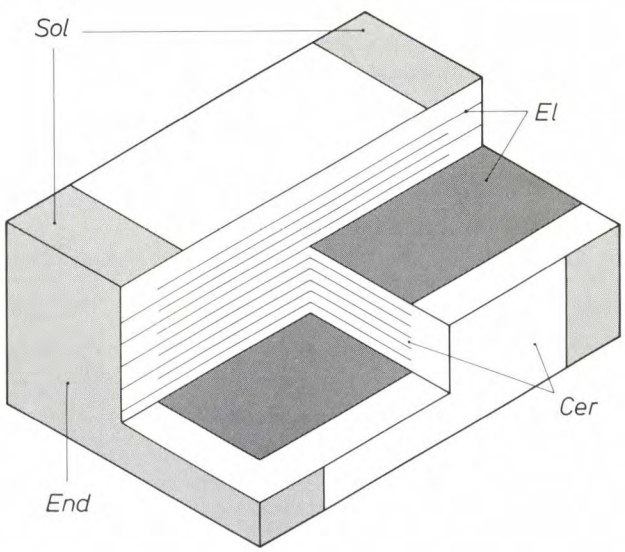

Fig. 2. Cut-away view of a ceramic multilayer capacitor. *Cer* ceramic material. *El* electrodes. *End* metallized end terminations. *Sol* solder lands. The electrodes are connected alternately to the end terminations on opposite sides of the capacitor, so that all of the 'subcapacitors' are in parallel with each other. The capacitor requires no leads, and is suitable as a chip component for automatic mounting.

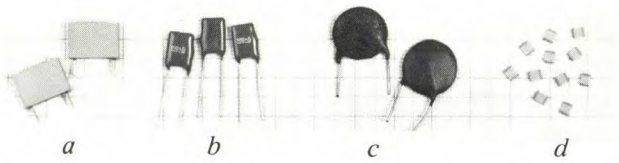

Fig. 3. Four types of capacitors (*a* to *d*), with a capacitance of 100 nF, made by different technologies: a film capacitor, a ceramic flat tubular capacitor, a ceramic disc capacitor and a multilayer capacitor. The last is clearly the smallest.

A second and equally important advantage of multilayer capacitors is that the metallized end terminations are located at the two end faces of the ceramic body, making these capacitors 'chip components'. These are leadless electronic components that can be soldered directly to the conducting paths of a printed-circuit board [5]. Components of this type have become particularly important in recent years, since the introduction of automatic mounting techniques that can only handle chip components [6]. It is of course a great advantage of the CMC that it is already essentially a chip component and therefore does not have to be redeveloped for this kind of application. Except for tantalum capacitors, which offer a different range of capacitances anyway, the ceramic multilayer capacitor is the only other type of chip capacitor available in quantity on the market today.

The palladium problem

Although it has many advantages, the multilayer capacitor is expensive to manufacture. In the first place the technological processes used for making them are

[2] See G. H. Jonker and A. L. Stuijts, Philips Tech. Rev. **32**, 79, 1971.

[3] See H. J. Martin, Die Ferroelektrika, Geest & Portig, Leipzig 1964;
D. Hennings, A. Schnell and G. Simon, J. Am. Ceram. Soc. **65**, 539, 1982.

[4] See Philips Data handbook: Components and Materials, Part 15, 1982.

[5] See R. J. Klein Wassink and H. J. Vledder, Philips Tech. Rev. **40**, 342, 1982.

[6] See Electron. Eng., June 1981, p. 108; and Markt und Technik, No. 49, 87, 1981.

Ned. Philips Bedrijven B.V.
PHILIPS NATUURKUNDIG LAB
BIBLIOTHEEK WY - 1
P.O. Box 80.000
5600 JA EINDHOVEN

fairly complex compared with those used for conventional capacitors, and have indeed until recently been rather expensive. Many manufacturers have now succeeded, however, in reducing these costs, through automation, to a level at which they are no longer a major obstacle. The second problem here still exists, however: the materials used for the electrodes are expensive.

As we explained earlier, in the manufacture of conventional multilayer capacitors the internal electrodes are fired together with the ceramic material. Since dielectric ceramics are normally fired in air at temperatures between 1200 and 1400 °C, only non-oxidizing noble metals with high melting points can be used for the electrodes of the conventional multilayer capacitor. In practice this means that the metal must be palladium, or platinum which is even more expensive. These noble metals can in fact account for nearly half the cost of manufacture of the capacitor, depending on the capacitance value. If ceramic multilayer capacitors are to be used as components in an automatic chip-mounting system and in mass-produced consumer articles, it is essential to find an answer to the 'palladium problem' first.

Work on three fundamentally different methods of avoiding or at least reducing the use of expensive metals in multilayer capacitors is going on in many countries. The first method is called the 'back fill process', in which the electrode metal is not applied until after firing [7]. This method, like the one discussed above, also includes screen printing, not with a metal paste but with special inks that contain a ceramic powder and a large amount of binder. During the firing the binder burns off to form volatile components, leaving behind a porous ceramic at the electrode locations. After firing these porous layers are filled with a relatively inexpensive fusible alloy, e.g. of Pb and Sn, which forms a more or less continuous electrode layer. Although this method seems at first sight to offer an elegant solution to the palladium problem, the process has been found difficult to control.

Investigations at Philips Research Laboratories in Aachen, and further developments in Eindhoven, have resulted in two new types of multilayer capacitor [8]. In both types the electrodes are fired with the dielectric. The first type, which is discussed in the next section, requires dielectrics that can be fired at a lower temperature without loss of the desired properties, so that electrode material with a relatively low melting point can be used; we used Pd-Ag alloys. The second type requires dielectrics that can be fired in a reducing atmosphere, so that a base metal such as nickel can be used for the electrodes.

Firing at reduced temperature

An inexpensive alternative to palladium as an electrode material is silver, which is about a tenth of the price. However, the very much lower melting point of silver (961 °C) would entail firing at a very much lower temperature than the usual 1300 to 1400 °C. Since the difference is so large, some compromise is desirable; this could consist in using an alloy of silver and palladium. As *fig. 4* shows, these two metals are completely miscible, and the melting point of the alloy changes monotonically from 961 to 1552 °C.

Reducing the firing temperature enables the silver content to be increased. It is therefore necessary to consider how far the firing temperature can be reduced without deterioration of the dielectric properties, and to find out how to counteract any deterioration.

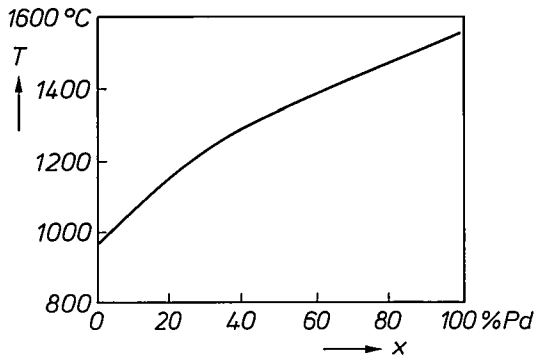

Fig. 4. The melting diagram of Ag-Pd [9]. The quantity x represents the percentage by weight of palladium.

High permittivities are found, as we noted above, in materials based on ferroelectric barium titanate. But if the material is also required to have a temperature characteristic compatible with use as a dielectric, it is necessary to consider mixed crystals of $BaTiO_3$ with other perovskites such as $CaTiO_3$, $BaZrO_3$ etc. The ones most widely used as dielectrics are mixed crystals of the system $(Ba_{1-x}Ca_x)(Ti_{1-y}Zr_y)O_3$. If Zr is incorporated in the $BaTiO_3$ the maximum of the permittivity curve (at the Curie point) is shifted from 130 °C to room temperature, whereas the non-ferroelectric $CaTiO_3$ broadens this maximum [10]. The broadening arises because $CaTiO_3$ has only a limited solubility in $BaTiO_3$ and small undissolved particles of $CaTiO_3$ act as grain-growth inhibitors in the ferroelectric matrix. As *fig. 5* shows, decreasing the grain size makes the permittivity peak at the Curie point lower and broader. To obtain a fairly high permittivity maximum with an acceptable Z5U temperature characteristic — the problem on which we have concentrated our efforts — the grain size in the system $(Ba,Ca)(Ti,Zr)O_3$ should be about 10 μm.

To understand the way in which the temperature affects the sintering processes during firing we must bear in mind that the rate-determining step in the densification and grain growth is a diffusion process. This diffusion may take place entirely in the solid phase or also in a liquid phase formed during the sintering. Since solid-state diffusion is a rather slow process, in perovskites as in other materials, densification of a system like (Ba,Ca)(Ti,Zr)O_3 is almost impossible if solid-state diffusion is the only transport mechanism. Reducing the sintering temperature of these materials would therefore never produce a dense ceramic with acceptable dielectric properties.

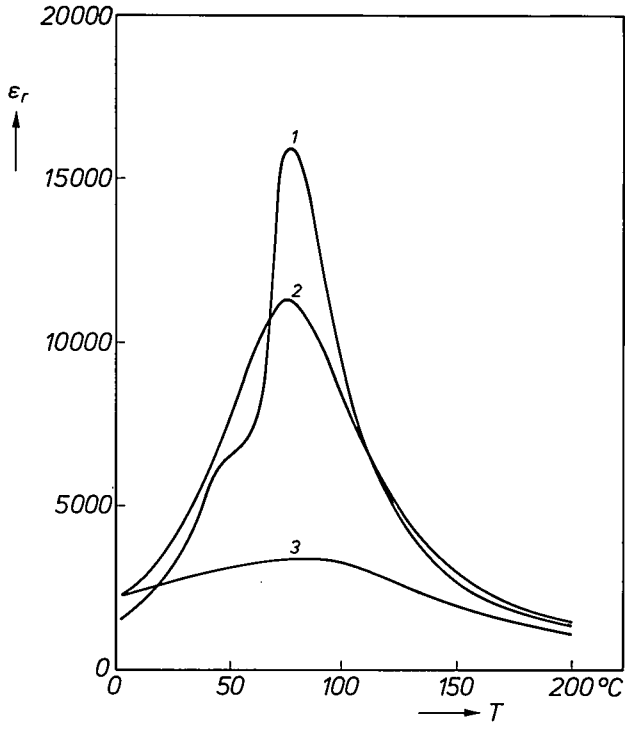

Fig. 5. The relative permittivity ε_r as a function of temperature for mean grain sizes of 40 μm (*1*), 15 μm (*2*) and 3 μm (*3*) in $(Ba_{0.87}Ca_{0.13})(Ti_{0.88}Zr_{0.12})O_3$.

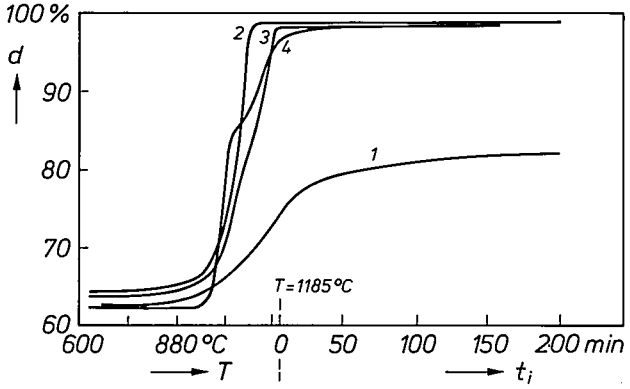

Fig. 6. Relative density *d*, measured with a dilatometer, of $BaTiO_3$ ceramic as a function of temperature (left) and as a function of time t_i at a temperature of 1185 °C; in the first case the heating rate is 3K/min. The graphs show the effect of the addition of small amounts of CuO and TiO_2 to the ceramic on the densification. The amounts added per mol of $BaTiO_3$ are: curve *1*, 0.0025 mol CuO + 0.0025 mol TiO_2; curve *2*, 0.005 mol CuO + 0.005 mol TiO_2; curve *3*, 0.01 mol CuO + 0.01 mol TiO_2; curve *4*, 0.02 mol CuO + 0.01 mol TiO_2. Addition of 0.5 to 1 mol% (curves *2* and *3*) gives the best result.

To stimulate the formation of a liquid phase during the firing it is customary to add a small excess of TiO_2 to the barium-titanate ceramic. The TiO_2 reacts with $BaTiO_3$ to form the phase $Ba_6Ti_{17}O_{40}$, which forms a eutectic with the $BaTiO_3$ at 1320 °C. For our purposes we must obviously look for other additives that form eutectics at lower temperatures.

Although many low-melting-point eutectics are to be found in the literature, only a few of them can be used with any success in practice for liquid-phase sintering of $BaTiO_3$ dielectrics. Most of these low-melting-point eutectics react with the barium titanate, forming inactive phases with high melting points, or they dissolve in large amounts in the perovskite, unacceptably modifying the properties of the dielectric.

We have found a highly effective eutectic, which meets most of the requirements, in the system $BaTiO_3$-CuO-Cu_2O, melting at 1070 °C [11]. The eutectic occurs when CuO is added to the $BaTiO_3$ and the CuO partly decomposes into Cu_2O during the sintering. Since the chemical equilibrium for $4CuO \leftrightarrows 2\ Cu_2O + O_2$ at the eutectic temperature of 1070 °C has an oxygen partial pressure of 0.4×10^5 Pa (0.4 bar), this eutectic occurs only in a strongly oxidizing atmosphere ($p_{O_2} > 0.4 \times 10^5$ Pa), because otherwise the CuO would long before have completely decomposed into Cu_2O below 1070 °C, and no liquid phase would be formed. This drawback to the use of CuO-Cu_2O can be overcome by introducing co-additives such as TiO_2, GeO_2 or Al_2O_3, which reduce the eutectic temperature to about 1000 °C so that the firing can be carried out normally in air.

Further investigation of sintering behaviour

We shall now look at the results of a more detailed investigation carried out in our laboratory into the effect of the combination of additives on the sintering behaviour of $BaTiO_3$ during firing. In practice the sintering additive is added as a mixture of CuO and the co-additive to the pre-reacted pervoskite powder. *Fig. 6* shows the effect of different amounts of CuO

[7] T. C. Rutt and J. A. Stynes, IEEE Trans. **PHP-9**, 144, 1973.
[8] The development of the new multilayer capacitors based on these investigations was carried out by W. Noorlander and N. P. Slijkerman of the Philips Elcoma Division, Passive Components Department, Eindhoven.
[9] M. Hansen and K. Anderko, Constitution of binary alloys, McGraw-Hill, London 1958, p. 41.
[10] See G. H. Jonker, Philips Tech. Rev. **17**, 129, 1955/56.
[11] D. Hennings, Ber. Dtsch. Keram. Ges. **55**, 359, 1978.

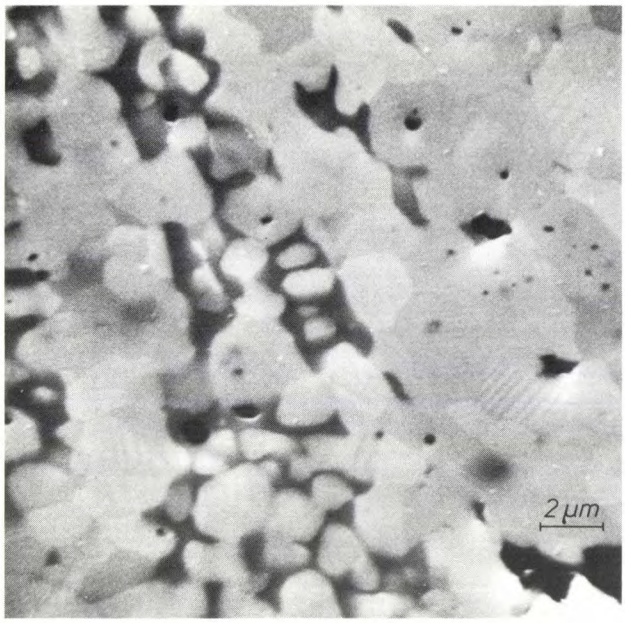

Fig. 7. SEM photomicrograph of a quenched sample of $BaTiO_3$ ceramic with added CuO-Cu_2O in the solution-precipitation phase. Small grains in the surrounding (darker) melt are going into solution, whereas the larger grains grow at the expense of the smaller ones.

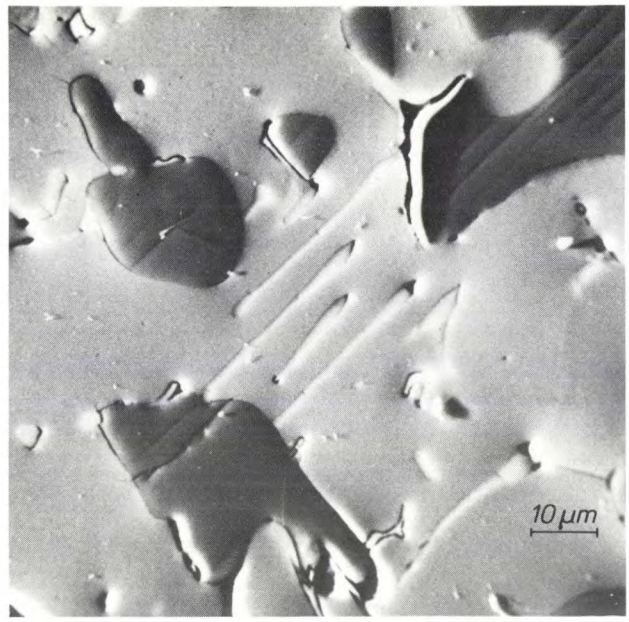

Fig. 8. A quenched eutectic melt of $BaTiO_3$ with CuO-Cu_2O additive. The $BaTiO_3$ dissolved in the CuO-Cu_2O system (shown white in the centre) has segregated in the form of lamellae. The other phases consist alternately of Cu_2O (grey) and CuO (black).

and TiO_2 on the densification of $BaTiO_3$, measured with a dilatometer. The graph is divided into two parts: on the left the relative density d is plotted against the temperature, which was increased uniformly to a maximum of 1185 °C; on the right the relative density is plotted as a function of the time during which the material was subjected to a temperature of 1185 °C. The densification starts very rapidly at about 1000 °C, which is approximately the eutectic temperature. The best results were obtained with sintering additives of 0.5 to 1 mol% (curves *2* and *3*). Larger amounts of sintering additives and lower amounts both produced poorer results. Similar findings were obtained with a number of other additives. The lowest sintering temperature of $BaTiO_3$ was found at 1020 °C with equimolar mixtures of CuO and GeO_2.

These results can be understood by considering the mechanism of liquid-phase sintering. Investigations of this rather complex mechanism have shown that there are three characteristic stages in the process of liquid-phase sintering.

First stage: melting and wetting. After melting of the eutectic mixture, the liquid phase wets the ceramic powder more or less completely. In most cases, including the case of $BaTiO_3$ with CuO considered here, effective densification only takes place when the perovskite particles are completely covered by a thin film of the liquid phase.

Second stage: disintegration and rearrangement. Above a certain temperature larger agglomerates and aggregates of particles, which are always present in a ceramic powder, start to disintegrate, and the individual particles are then drawn together again by the action of capillary forces, so that there is a marked shrinkage of the whole sample. (This shrinkage is usually not observed in samples that have been subjected to strong mechanical predensification before sintering.)

Third stage: solution-precipitation. This is the stage in which the actual densification is completed. The solution of the perovskite material in the eutectic melt is a process in which small particles are preferentially dissolved because of their slightly higher surface energy. The dissolved material passes through the liquid-phase film by diffusion and precipitates on larger grains that have a slightly lower surface energy and therefore a slightly lower solubility in the liquid.

Fig. 7 shows a photomicrograph of a sample that was quenched during the solution-precipitation stage. Near the centre of the photograph a number of small grains (white) can be seen that are in the process of being dissolved in the surrounding melt (black).

For effective densification the $BaTiO_3$ must be readily soluble in the CuO-Cu_2O eutectic, of course. Indications that this is so can be seen in the SEM photomicrograph in *fig. 8*, which shows a quenched eutectic melt of CuO-Cu_2O from which the dissolved $BaTiO_3$ has segregated in typical eutectic lamellae. The two different copper oxides can be distinguished from each other because of their different contributions to back-scattering in the electron microscope.

The grey phase is the more strongly scattering Cu_2O and the black phase is the CuO.

Since the diffusion in the liquid phase is the rate-determining step in the sintering process, it seems reasonable that the diffusion paths should be as short as possible for effective liquid-phase sintering. This is in agreement with the results of our sintering experiments, as shown in fig. 6. If too little additive is used the densification is poor, probably because of insufficient wetting of the grains by the liquid phase. Too much additive also gives poor results, presumably because the liquid layers between the grains are too thick and the diffusion path consequently too long.

The individual stages in liquid-phase sintering are not really as readily distinguished from each other as suggested here. In addition, an effect known as exaggerated grain growth is also encountered. This is a discontinuous process starting more or less at random at a few grains and then proceeding very rapidly at the expense of the neighbouring grains and resulting in a coarse ceramic structure with a pronounced variation in grain size. Liquid-phase sintered titanate dielectrics may therefore have coarse-grained microstructures with grain sizes up to 100 microns. As mentioned earlier, such coarse-grained materials have inferior dielectric properties.

By using a few other special additives, such as Tl_2O_3, we have succeeded in reducing and controlling exaggerated grain growth in liquid-phase sintering so as to achieve an almost uniform grain-size distribution in the end-product. This has enabled us to fire ceramic perovskites at temperatures below 1100 °C, producing completely dense end-products with grain sizes of no more than a few microns.

Investigation of the dielectric properties

Materials prepared as just described have relative permittivities between 8000 and 10 000 combined with the Z5U temperature characteristic. This means that the permittivity varies at the most between +22% and −56% of the value at 25 °C when the temperature is varied from 10 to 85 °C.

These materials can be used for making multilayer capacitors that have a sufficiently low conductivity, as appears from life tests at elevated temperatures [8]. The added CuO has practically no effect on the dielectric properties of these capacitors. At high temperature it forms the required liquid phase, dissolving only in traces in the perovskite lattice, and during the cooling it segregates preferentially at the triple junctions of the grains, where it has little effect on the dielectric properties of the capacitor.

Since the ceramic material can be fired at temperatures of about 1050 °C with this method, an Ag-Pd alloy with more than 70% of Ag can be used for the electrodes (see fig. 4).

The conclusion is that an answer to the palladium problem has been found for Z5U-type dielectrics, with a 60% reduction in electrode cost compared with pure palladium. A similar approach can also be taken with the X7R and NPO materials.

Nevertheless, silver is also a fairly expensive metal, and we have therefore investigated at the same time the possibility of using a base metal for making the electrodes. This investigation is described in the section that follows.

Sintering in reducing conditions

Acceptors and their general effect on conductivity

If a base metal such as nickel is to be used for the internal electrodes of a ceramic multilayer capacitor, and if the electrodes are to be sintered with the dielectric, the normal sintering conditions will have to be changed [12]. The normal firing cycle in air would cause oxidation of the nickel, leading to undesired reactions between the NiO and the ceramic material and delamination of the multilayered structure. To avoid this a sufficiently reducing atmosphere to prevent oxidation of the nickel is required. A mixture of N_2, H_2 and H_2O or of CO and CO_2 can be used.

The barium titanate and its modifications conventionally used as dielectrics, however, are not directly suitable for sintering in reducing conditions. After such treatment they tend to become semiconducting owing to loss of oxygen; the oxygen vacancies generated then act as donors of conduction electrons. This unwanted effect of the treatment can be counteracted by means of acceptor-type dopants, which trap the conduction electrons. The acceptors most commonly used are ions that occupy sites of the tetravalent Ti in the $BaTiO_3$ host lattice with a valency lower than four, especially ions of the transition metals Cr, Fe, Ga, Mn or Ni.

However, the acceptor dopants not only trap electrons, they also change the concentration of the oxygen vacancies. If Ti^{4+} ions in the perovskite lattice are replaced by trivalent or divalent acceptor ions, a corresponding number of oxygen vacancies will be formed in the lattice to maintain charge neutrality. At temperatures higher than 500 to 600 °C these oxygen vacancies take part in a chemical equilibrium and their concentration is then determined not only by the acceptor concentration but also by the temperature and the partial pressure of the oxygen in the ambient atmosphere. The establishment of this equilibrium

[12] See L. S. Darken and R. W. Gurry, Physical chemistry of metals, McGraw-Hill, New York 1953, pp. 347-359.

may in turn change the valence state of the acceptors. In short, a complete picture of the defect chemistry of the material is necessary to explain the effects of doping on the electrical properties of the dielectric.

The main objective of our investigation, of course, was to control the electrical conductivity of the specimen after cooling to room temperature. At practical cooling rates, however, complicated kinetic processes influence the defect concentrations [13] and hence the electrical conductivity. We therefore started by attempting to control the conductivity of the material after *quenching* from well-defined equilibrium conditions at high temperatures. We found that in these conditions the conductivity was determined by the valence states of the acceptors and the concentration of oxygen vacancies.

We measured these quantities for barium-titanate samples doped with Cr, Mn, Fe, Co or Ni (in concentrations of 0.1 to 2.0 mol%), after subjecting the samples to annealing treatments in different well-defined equilibrium conditions. We determined the valence states of the acceptors by measuring the magnetic susceptibility of the samples [14], and determined the concentration of the oxygen vacancies independently by measuring the changes in weight when the equilibrium conditions were varied [15]. We shall now take a closer look at these two methods of measurement.

Determining the valence states of the acceptors

The dopant ions of the transition metals that we used have a magnetic moment that depends on the number of electrons in the 3d shells. A Faraday balance was used to measure the force exerted by an inhomogeneous magnetic field on the ceramic samples. This force is directly proportional to the magnetic susceptibility of the samples. As shown in *fig. 9* for samples doped with Fe, Mn or Ni, the susceptibility measured in this way at room temperature is a linear function of the dopant concentration. *Fig. 10* shows that between 80 and 300 K the magnetic susceptibility — after subtracting the diamagnetic contribution — is inversely proportional to the absolute temperature, in agreement with Curie's law for paramagnetic substances.

The paramagnetism is due to the angular momentum of the unpaired electrons in the outer 3d shell of the acceptor dopants. The orbital angular momentum of ions in the transition metals is in many cases 'quenched' and the magnetic moment then only depends on the total spin angular momentum S of the 3d electrons. Since S is determined solely by the number of unpaired electrons, the valency of the acceptors can generally be uniquely determined in this way.

All the measurements were carried out after subjecting the samples to an annealing treatment at 700 °C, a temperature high enough to achieve the desired equilibrium of the defect chemistry. This heat treatment was applied at two different partial pressures of oxygen for each sample: one measurement was made after annealing in pure oxygen at high pressure and the other after annealing in a wet mixture of H_2 and N_2 (in this case a strongly reducing gas atmosphere was provided by the low oxygen partial pressure of the H_2-H_2O equilibrium).

The results of the magnetic measurements are given in the second and third columns of *Table I*. It can be seen that the valencies of the Cr, Mn and Co dopants depend on the oxygen partial pressure used in the annealing treatment, but this does not apply to Fe and Ni. It is not always easy to interpret the magnetic measurements for Ni and Co [16], but a definitive determination can be made with the aid of the results obtained from the measurements of the oxygen vacancy concentration, which we shall now describe.

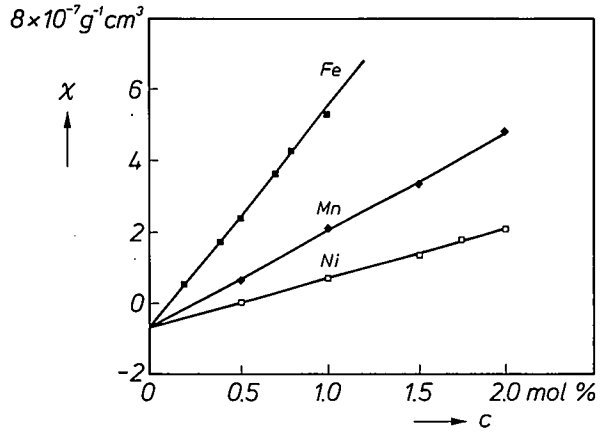

Fig. 9. Magnetic susceptibility χ of $BaTiO_3$ ceramic at 300 K as a function of the concentration c of the dopants Fe, Mn or Ni. The specimens were all fired in an oxidizing atmosphere.

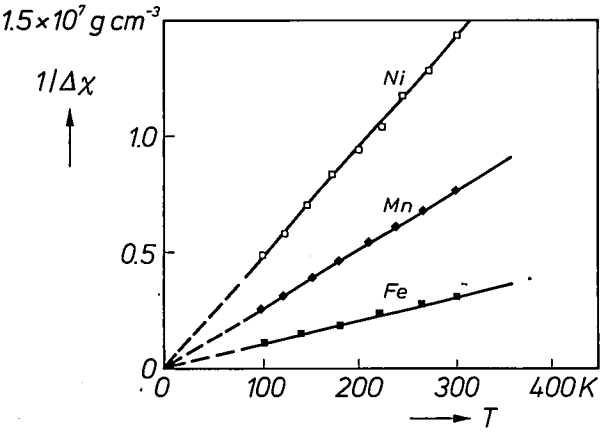

Fig. 10. Reciprocal of the magnetic susceptibility $1/\Delta\chi$ of $BaTiO_3$ ceramic doped with 0.5 mol% (8×10^{19} cm^{-3}) of Fe, Mn or Ni, as a function of temperature. The diamagnetic contribution has been subtracted from the measured susceptibility values.

Table I. Results of measurements on ceramic specimens of $BaTiO_3$, doped with the transition metals listed in the first column. The second and third columns give the valence states of these dopants as derived from magnetic susceptibility measurements on samples previously annealed in an oxidizing (ox.) or reducing (red.) atmosphere. The fifth column gives the relative changes $\Delta[V_o]$ in the oxygen-vacancy concentration, calculated from measurements of the relative weight change $\Delta m/m$ (fourth column) that occur when the dopants change from one valence state (in column 2) to the other (in column 3), due to successive annealing in the same oxidizing and reducing atmospheres as above.

Dopant (8×10^{19} cm^{-3})	Valence state		$\Delta m/m$ (10^{-6})	$\Delta[V_o]$ (10^{19} cm^{-3})
	ox.	red.		
Cr	4+	3+	164 ± 9	3.7 ± 0.2
Mn	4+	2+	342 ± 22	7.7 ± 0.5
Fe	3+	3+	27 ± 9	0.6 ± 0.2
Co	3+	2+	178 ± 18	4.0 ± 0.4
Ni	2+	2+	31 ± 9	0.7 ± 0.2

Measuring the oxygen-vacancy concentration

As mentioned already, the incorporation of acceptor dopants requires charge compensation by oxygen vacancies. One doubly ionized oxygen vacancy compensates two trivalent ions at Ti^{4+} sites or one divalent ion at a Ti^{4+} site. If the valency of the acceptor ions is altered by annealing, the concentration of the charge-compensating oxygen vacancies is also changed, and this is reflected in a slight increase or decrease in weight. These small changes in weight can be measured with a sensitive balance. Assuming that the dopant concentration is 0.5 mol% (8×10^{19} cm^{-3}) and that, as a result of annealing, the valency of the dopants has been lowered by one unit, then 0.25 mol% or 4×10^{19} cm^{-3} additional oxygen vacancies are created, which means that a sample initially weighing 2.5 g loses 425 μg in weight.

The fourth and fifth columns of Table I give the relative weight changes $\Delta m/m$ and the corresponding changes $\Delta[V_o]$ in oxygen-vacancy concentrations observed when a sample is annealed successively in oxidizing and reducing atmospheres. Comparison with the results of the magnetic measurements, also included in the Table, show that there is indeed a close relation between the valency of the acceptors and the concentration of the oxygen vacancies. Whenever the valency, as determined by the magnetic measurements, changes by one unit as a result of the annealing, a corresponding change of about 4×10^{19} cm^{-3} is observed in the oxygen-vacancy concentration. And when the valence state is not changed by annealing, as is the case with Fe^{3+} and Ni^{2+}, only a relatively small change in the oxygen-vacancy concentration is observed.

Our assumption that acceptors and oxygen vacancies are the most important quantities for describing the defect chemistry in the experimental conditions we have discussed is therefore verified.

Effects of acceptor dopants on conductivity

In the further course of our investigation we used a thermobalance to determine the concentration of the oxygen vacancies as a function of the oxygen partial pressure in the full pressure range experimentally accessible. The determinations were made for barium-titanate samples doped with 0.5 mol% (8×10^{19} cm^{-3}) of Co, Mn, Fe or Cr, after an equilibrium at 1000 °C had been established (*fig. 11*).

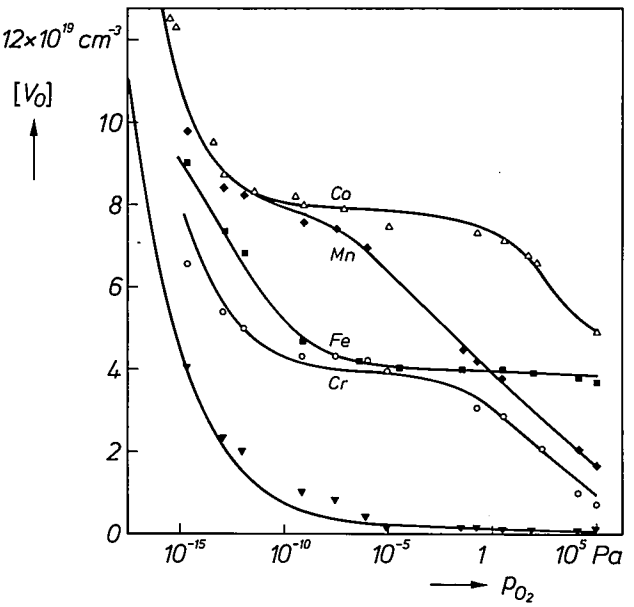

Fig. 11. Oxygen-vacancy concentration $[V_o]$ in undoped (*lower curve*) and acceptor-doped $BaTiO_3$ (acceptors Co, Mn, Fe or Cr) as a function of oxygen partial pressure p_{O_2} during annealing at 1000 °C.

Two distinct ranges can be recognized in the resultant graph. There is a range of relatively high oxygen pressure (10^{-5}-10^{5} Pa), where the oxygen-vacancy concentration does not exceed the limits imposed by the acceptor dopants, that is to say the concentration in that region does not assume values greater than are required to maintain charge neutrality. For Co and Mn, which become divalent in reducing conditions (Table I), the upper limit is twice as high as for Fe and Cr, which become at the most trivalent under the same conditions (see Table I). In the range of low oxygen pressures ($<10^{-5}$ Pa) the concentration does exceed the limits imposed by the acceptors.

When the samples are quenched from these latter conditions to room temperature, a high electrical con-

[13] See J. Daniels, K. H. Härdtl and R. Wernicke, Philips Tech. Rev. 38, 73, 1978/79.
[14] H.-J. Hagemann and H. Ihrig, Phys. Rev. B 20, 3871, 1979.
[15] H.-J. Hagemann and D. Hennings, J. Am. Ceram. Soc. 64, 590, 1981.
[16] H.-J. Hageman.., Thesis, Aachen, 1980.

ductivity is found, because in that case the excess oxygen vacancies are no longer fully compensated by the acceptors but to some extent by conduction electrons. We therefore call this the 'intrinsic' region, and the other one discussed above the 'extrinsic' region.

If in fig. 11 we compare the behaviour of the oxygen-vacancy concentration in the doped samples with that in the undoped samples, we see that the range in which a high electrical conductivity may be expected has been considerably displaced towards lower oxygen partial pressures as a result of the doping. This result is confirmed by measurements of the electrical conductivity itself, as shown in *fig. 12*. For this purpose the electrical conductivity was measured in undoped samples and in samples doped with Mn, which had been annealed in atmospheres of different oxygen partial pressures and then quenched to 150 °C. The result of the measurements shows clearly that the transition from a state of low conductivity to one of high conductivity is shifted considerably towards the range of small oxygen partial pressures by the Mn acceptors.

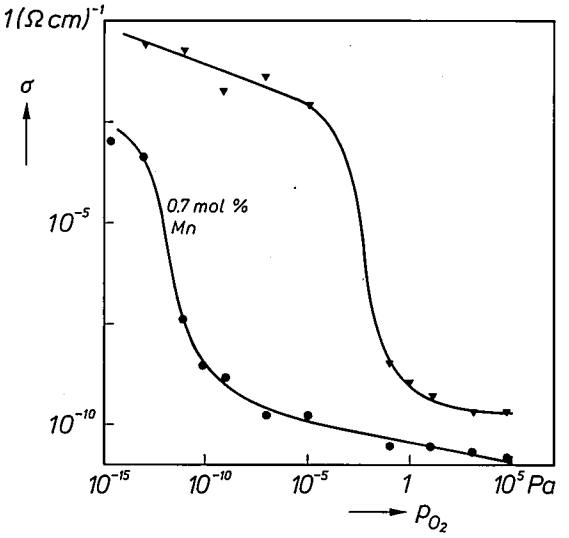

Fig. 12. Electrical conductivity σ of undoped (*upper curve*) and Mn-doped $BaTiO_3$ (0.7 mol% Mn) as a function of the oxygen partial pressure p_{O_2} during annealing at 1000 °C. The conductivity was measured at 150 °C — and not at room temperature — to avoid complications due to ferroelectric effects.

Further investigations on the complete capacitor

A shift as described above is a prerequisite for the preparation of multilayer capacitors with base-metal electrodes. This is because such a shift has the result that it is possible to find an oxygen partial pressure for which an insulating ceramic can exist side-by-side with an electrode consisting of a base metal such as Ni, Co or Fe. Or, to put it another way: with undoped barium titanate no oxygen partial pressure can be found for which the base metal does not oxidize or the ceramic does not become conductive.

The determination of the valence states and the weight measurements described above have been performed for a range of acceptor concentrations and annealing temperatures [14][15]. We have used the results to develop a thermodynamic model, which corresponds in general terms to the model used for explaining the PTC effect (positive temperature coefficient) of $BaTiO_3$, described earlier in this journal [13]. The model has been useful in calculations on the defect chemistry of acceptor-doped $BaTiO_3$ as a function of temperature, oxygen partial pressure, and the type and concentration of the acceptors. This enabled us to choose the best type of acceptor, its concentration and the other conditions necessary for the preparation of multilayer capacitors with base-metal electrodes.

Multilayer capacitors with base-metal electrodes have been developed on the basis of these investigations [8]. They include the Z5U type with nickel electrodes shown in the title photograph. The dielectric consists of Cr-doped (Ba,Ca)(Ti,Zr)O_3. The capacitors are fired in a reducing atmosphere containing hydrogen. The electrical characteristics of these capacitors certainly equal those of conventional types with Pd electrodes. A multilayer capacitor of the NPO type has also been developed, which has a relative permittivity of about 35. The development of the third type (X7R) has run into problems because the control of the defect chemistry has to be combined with special sintering properties to obtain a very fine-grained ceramic microstructure and an inhomogeneous distribution of the dopant within the small grains. We are continuing to investigate methods of overcoming these problems.

Summary. Ceramic multilayer capacitors offer the advantage of a high capacitance per unit volume. In their manufacture alternating dielectric layers, e.g. of (Ba,Ca)(Ti,Zr)O_3, and metal electrode layers, usually of palladium, are fired simultaneously at a temperature of 1300 to 1400 °C in air. At Philips Research Laboratories in Aachen the firing temperature has been reduced to 1100 °C by the addition of small amounts of CuO and other additives such as TiO_2 and Tl_2O_3, so that 70% of the expensive palladium can be replaced by silver. Various types of ceramic multilayer capacitors, with the temperature characteristics Z5U, X7R and NPO have been made in this way. Multilayer capacitors have also been made in which palladium has been replaced by nickel. In this process the dielectric material is doped with a transition metal, e.g. Cr, which acts as an acceptor, and the firing process is carried out in a strongly reducing atmosphere. A thermodynamic model of the defect chemistry has been devised that has been useful for determining the conditions necessary to obtain a material that does not have a high electrical conductivity. On this basis capacitors have been developed with the temperature characteristics Z5U and NPO, and work is in progress on a type that will have the X7R temperature characteristic.

Digital audio circuits: computer simulations and listening tests

L. D. J. Eggermont and P. J. Berkhout

Digital audio technology has arrived — we now have digital recording on tape and on the Compact Disc [*]. We should now be able to enjoy a great improvement in quality. Representing the sound signal by a series of digits and recording it in this form make it possible to choose the level of accuracy required. In practice, of course, it is necessary to compromise between the desired accuracy on the one hand and the size, speed and dissipation of the circuits on the other. At Philips Research Laboratories in Eindhoven a computer system has been installed and a listening room built for the specific purpose of simulating digital signal processing on a computer and subjectively appraising the audible result. In this way it is the ear that ultimately decides how many bits are needed in each signal processing step in order to reach the high quality that is possible with digital audio technology.

Introduction

In audio engineering wide use is now made of digital techniques both for storing audio signals and for processing them. This enables a higher audio quality to be maintained than is possible with traditional analog methods. A frequency-response curve flat from 20 Hz to 20 kHz, a signal-to-noise ratio of more than 90 dB and nonlinear distortion of no more than a fraction of a per cent are all feasible.

To achieve such values the audio signal to be digitally processed must be represented by numbers ('words') containing a sufficiently large number of bits. Words of 16 bits are usual at the beginning and end of the digital path, but during the signal processing the number of bits required is generally much larger. This has an immediate impact on the design of the circuits and on their size, of course. If the number of bits per word is too small it can give rise to additional distortion of various kinds. If the number of bits is larger than strictly required, the circuit is made unnecessarily complicated. During the design of a circuit it is therefore important at an early stage to have some understanding of the effect of the number of bits per word on the output signal.

Ir L. D. J. Eggermont is with Corporate Product Development Coordination, Philips International B.V., Eindhoven; Dr P. J. Berkhout is with Philips Research Laboratories, Eindhoven.

It is a great advantage for the designer to be able to simulate the intended functions with a computer. A complete algorithm or a single logic element can be programmed, so that simulation is also possible at the level of the logic operations in an integrated circuit — and ICs are usually the ultimate objective of the design. Parameters relating both to the algorithm and to the circuits can then be varied in the program, so as to arrive at an optimum result in a flexible, interactive method of design. If in addition the simulation can be performed in 'real time', this may often be a further argument for dispensing with 'breadboards', i.e. trial circuits with discrete components, thus considerably shortening the design time.

For evaluation of a digital audio circuit criteria are necessary. Objective criteria, such as the frequency-response characteristic, signal-to-noise ratio and distortion, can sometimes be calculated in advance at the design stage; later they can then be measured with the aid of test signals. For music and speech, however, such measurements may not provide the necessary information, since the original recording may already have contained imperfections. Nor is it always possible to calculate the effect of a finite word length analytically. What is more, it is not possible to predict

[*] Philips Tech. Rev. 40, 149-180, 1982.

how combinations of different types of distortion will be perceived by the listener. So tests with real listeners are essential for an evaluation of the quality of a digital audio circuit.

At Philips Research Laboratories in Eindhoven a computer system has been installed for the specific purpose of simulating digital audio signal processing, where possible in real time. An adjoining room has been fitted out for listening to the results (see *fig. 1*). We shall now take a closer look at both of these installations.

Fig. 1. Listening room and adjoining computer room. The listening room is well insulated against extraneous noise (background sound level 18 dB(A)). A computer terminal provides the listener with a direct control of the digital audio signal processing.

The computer system

The computer system (see the block diagram in *fig. 2*) is grouped around a 32-bit minicomputer, which has a main memory of 2.5 Mbyte (1 byte = 8 bits). A large memory capacity is necessary for processing audio signals: 1 second of digitized audio (stereo) occupies 200 kbyte ($2 \times 50\,000$ samples of 16 bits). Four disc systems are therefore provided as on-line random-access mass storage. One disk will store 16 minutes of stereo music. The other disks are used for temporary storage of provisional results of signal processing not performed in real time, and also for storing programs. There is also a magnetic-tape storage facility for signal archiving and program exchange.

The *data input/output* block (fig. 2) deals with the input and output of analog or digital audio signals either through on-line interfaces or from an off-line data-collection system. Two audio signals can be digitized or converted back into analog signals with an accuracy of 16 bits at a maximum sampling rate of 100 kHz for each channel. The off-line data-collection system consists of a digital magnetic-tape recorder, developed for this application, which is used for recording digitized music and also for mass storage.

During listening tests a person can enter his assessment into the computer from an input terminal. Properties of the audio signal heard in the listening room can be shown on a display, permitting a direct comparison of visual and auditive presentations. It is possible, for example, to display the frequency spectrum

or the waveform of a selected audio fragment. The output equipment also includes a plotter and a printer.

Digital signal processing may sometimes require a very large number of arithmetical operations such as multiplications and additions. The computer is therefore connected to an array processor, designed to perform high-speed vector operations with a maximum of 16000 numbers. This array processor can perform 12 million floating-point operations per second. Therefore processing digital audio signals in real time is possible for many algorithms.

A software package in a high-level language is available for the analysis of original and processed signals. The package includes modular programs for interactive signal processing and synthesis. A well-organized file-management system stores and retrieves the data required for the programs. Also contained in the software package are programs for simulating various digital operations on the audio signals, such as encoding, equalization and 'teeth' filters for digital reverberation.

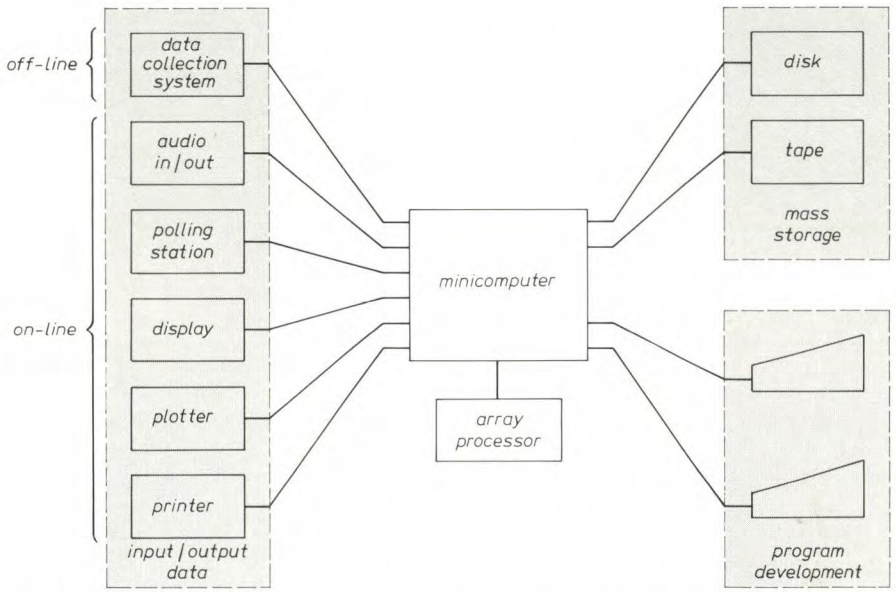

Fig. 2. Block diagram of the computer system for simulating digital audio signal-processing operations. Some of the peripherals grouped around a 32-bit minicomputer were developed for this application. The *data-collection system* is a digital tape recorder, the *polling station* enables the listener to give his assessment as direct computer input. The *array processor* performs vector operations on 16000 numbers, enabling the digital audio signals to be processed in real time.

The listening room

The listening room, where the effect of the signal operations can be evaluated without disturbance from extraneous sounds, has a volume of about 45 m^3. One of the main requirements to be met by such a room is a very low interference noise level. This is because of the very wide dynamic range made possible by digital audio technology; we have already mentioned a signal-to-noise ratio of more than 90 dB. If a person listening to audio programmes with such a dynamic range is to be able to perceive weak noise and distortion without having to increase the gain to such an extent that signal peaks approach the threshold of pain (about 120 dB above the threshold of audibility, i.e. above an acoustic power of 10^{-12} W/m^2 carried by the sound wave), then the background sound level in the listening room must be low.

In our listening room this level is 18 dB(A). (The 'A' indicates that the frequencies in the measurement were weighted with respect to a standard curve A, which approximates to the sensitivity curve of the human ear at low levels.) This level is only found in good recording studios. Such a low level can only be reached by careful sound insulation: a 'floating floor' is fitted, i.e. a floor with a resilient connection to the concrete floor of the building structure, and the walls, which stand completely free from the concrete structure, are weighted with lead.

The intention is that the sound reaching the listener from the loudspeakers should be affected as little as possible by the acoustics of the room. The walls are therefore made highly sound-absorbent, so that the listener perceives the sound as coming mainly from the loudspeakers. This gives an exceptionally short reverberation time, between 0.2 and 0.3 seconds.

As mentioned earlier, there is a display in the listening room on which frequency spectra, waveforms etc.

can be shown. One can vary the signal-processing algorithm, as well as the parameters involved, from the listening room, so that the design procedure can be interactive.

Two examples of the design of a signal-processing algorithm

Physiological volume control

The human ear does not have a flat frequency response. Moreover, its response depends on the sound level: the weaker the sound, the more the frequency-response curve differs from a straight line. At low levels there is a pronounced maximum in the sensitivity between 2000 Hz and 5000 Hz (see *fig. 3*).

This has its effect on the fidelity of the sound reproduction. If a piece of music is played back at a level different from the level at which it was recorded — the playback level will usually be lower — the tonal balance perceived will not be the same as during the recording.

This was realized long ago, and since then efforts have been made to apply a correction by connecting a simple filter network to a tap on the volume control. A more accurate correction is possible, however, by building a digital filter whose coefficients vary with the position of the volume control. *Fig. 4* shows the corrections that are necessary at different sound levels to maintain the tonal balance, taking a reference sound level of 60 dB where the filter curve is flat.

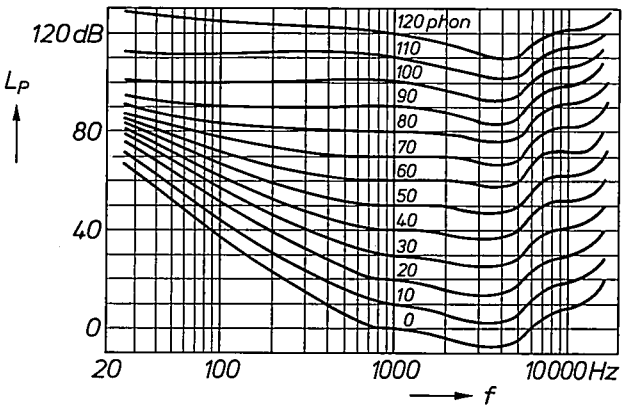

Fig. 3. The human ear does not have a flat frequency response. In the above graph (after H. Fletcher and W. A. Munson [1]) each curve connects sinusoidal tones of different frequency f that sound equally loud to the human ear even though the power level L_P is different: the level of subjective loudness (expressed in phons) is constant on each curve. The curve for 0 phon is the audibility threshold; it gives the power level of the tones that are only just audible, i.e. have a loudness level of 0 phon. The deviation from a flat response differs for different sound levels and increases as the level decreases. When music recorded on tape or disc is played back at a level different from the recording level, the subjective balance between low and high tones is different from that at the original level. Attempts are made to correct for this with a filter whose characteristic depends on the volume setting (physiological volume control).

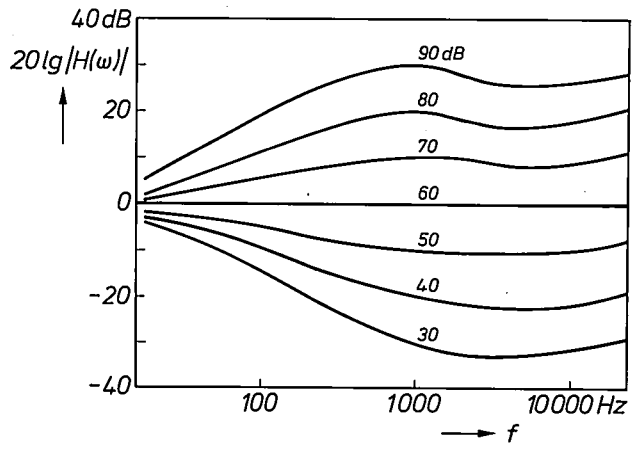

Fig. 4. Various correction curves for the frequency response during sound reproduction at different levels (*30 dB ... 90 dB*; physiological volume control). The transfer function $H(\omega)$, obtained by means of a digital filter, is adjusted to the position of the volume control.

The curves in fig. 4 could not be obtained by using standard programs for the design of filters, since these were written for designing highpass, lowpass or bandpass filters. The characteristics of fig. 4 were therefore modelled interactively with a minimum number of poles and zeros. The result was visually compared with the curves indicated by fig. 3, and assessed by listening tests.

A problem encountered when translating the computer-simulated curves of fig. 4 into hardware concerns the effect of finite word length. Digital words sometimes have to be rounded off to a given number of bits, or are truncated. A theoretical analysis was made of the effects of quantization and overflow and a computer simulation was performed. Listening tests were made to give a comparison with a simulation using the full computer word length.

It turns out that at least three poles and zeros are necessary to give a good approximation to the curves in fig. 4. The general form of the filter transfer function is then

$$H(z) = \frac{a + bz^{-1} + cz^{-2} + dz^{-3}}{1 + ez^{-1} + fz^{-2} + gz^{-3}}.$$

To find the frequency response it is necessary to calculate the absolute value of this transfer function for $z^{-1} = e^{-j\omega T}$, where ω is the angular frequency and T the sampling period. For an approximation to the upper curve (90 dB) in fig. 4 the coefficients are found to be: $a = 23.9397$, $b = -43.2$, $c = 24.417$, $d = -4.1406$, $e = -1.7721$, $f = 0.7838$ and $g = 0$. With these coefficients an accuracy of 12 bits gives a satisfactory sound quality, as confirmed in comparisons with a simulation using the full computer word length in listening tests.

For analysing the effects of quantization the impulse response is calculated from the point where the quantization is introduced as far as the output. 'Overflow', i.e. the result of exceeding the signal amplitude that can be expressed by the given number of bits, is de-

tected by applying a pulse to the input and seeing whether the response at a particular point exceeds a certain amplitude. To avoid overflow 10 extra bits are required for the internal representation and the word length at the output must be 6 bits longer than at the input. With a 16-bit input signal the internal word length must thus be 26 bits and the word length at the output 22 bits. If the output signal is subsequently quantized to 16 bits, this final quantization step will determine the signal-to-noise ratio at the output.

Reverberation

In connection with an investigation of electronic reverberation systems being carried out elsewhere in the laboratory, simulations of digital reverberation circuits were made. Reverberation is the sum of a large number of delayed versions of the sound signal, each with its own delay. In digital audio technology reverberation is produced by means of delay lines. The output of such a delay line can be fed back through a filter to the input, so that the filtered signal travels along the delay line again, and so on (*fig. 5*). We prefer to call the circuit thus produced a 'teeth filter' [2]. In this way the long delays necessary for reverberation can be built up.

These long delays create problems in an investigation of the consequences of finite word length and overflow, however, because it is difficult to find a closed-form expression for the desired impulse response. In this way it is only possible to estimate the number of bits required in the worst case.

The transfer function of the teeth filter in fig. 5 is

$$\frac{Y(z)}{X(z)} = \frac{z^{-m}}{1 - z^{-m}H(z)},$$

where m is the number of signal samples stored in the delay line and $H(z)$ is the transfer function of the filter in the feedback loop. This filter was introduced to give the reverberation a natural tonal colour, i.e. a natural frequency response. The number of poles ranges from 2000 to 4000 at sampling rates of 40 to 50 kHz; this large number makes the analysis difficult. An analysis has been given of the effects of finite word length and overflow for the case where $H(z)$ is a first-order recursive filter [3]. However, the results of this analysis only apply directly to a signal whose amplitude does not change significantly during the entire duration of the impulse response (1-5 s), and this is not generally the case with music.

A digital reverberation system will have not just one teeth filter but a combination of teeth filters, and they will also be connected to other processing modules. To limit the word length it is necessary to scale the amplitude of the signals between the different operations. The scale factors are obtained in part from a statistical analysis, but with a signal that varies as greatly as music the scale factors have to be verified in listening tests. It has been found that a word length of more than 22 bits is necessary in the filters for 16-bit quality to be maintained from input to output, corresponding to a signal-to-noise ratio of more than 90 dB.

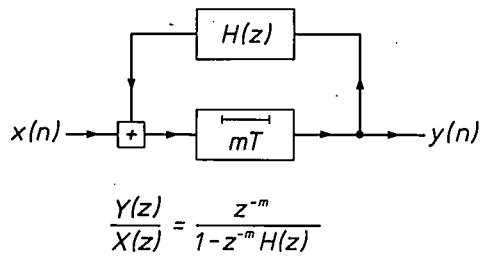

Fig. 5. Teeth filter for artificial reverberation. The digital input signal $x(n)$ (where n is the serial number of the signal sample) is stored in a delay line for m sampling periods, each of duration T, and then passed as $y(n)$ to the output. The output signal $y(n)$ is then added to the input signal, via a filter H, and delayed once again. If in a hypothetical case the input signal consisted of one very short pulse (one sample differs from zero, all the others are zero), then this pulse would appear at the output after mT seconds and again after each successive period of mT seconds, although affected by the filter H. The representation of the transfer function of the feedback system in the frequency domain has a series of maxima at regular intervals, which suggests the name 'teeth filter'.

The example of digital reverberation, like that of physiological volume control, shows that it is a great advantage at the design stage if computer simulation is available, preferably interactive, and with real-time signal processing capability. The listening tests that are indispensable in such a design process can then be made immediately. The facilities outlined here meet these requirements and considerably reduce the design time for digital audio circuits.

Summary. At Philips Research Laboratories, Eindhoven, facilities are available for rapidly and flexibly designing the algorithms used in the digital processing of audio signals. The facilities consist of a computer system and a well-insulated listening room in which the background level is 18 dB(A). The algorithms can be simulated by the computer system and immediately applied to music signals stored in digital form on magnetic disks or tapes. While listening to the results the listener can vary parameters and can also see the resulting spectrograms or waveforms on a visual display. Algorithms that have been developed for physiological volume control and for artificial reverberation are discussed as examples of the capabilities of the system; the number of bits of word length that should be used in the signal processing if the operations are not to impair the sound quality has been indicated.

[1] H. Fletcher and W. A. Munson, J. Acoust. Soc. Am. **5**, 82, 1933/34.

[2] This filter is not really the same as the well-known *comb* filter. If $H(z)$ is a constant its frequency characteristic consists of a succession of real-frequency poles, whereas the frequency characteristic of a comb filter consists of a succession of real-frequency zeros. See L. R. Rabiner *et al.*, Terminology in digital signal processing, IEEE Trans. **AU-20**, 322-337, 1972.

[3] P. J. Berkhout and L. D. J. Eggermont, Some design issues in digital signal processing for digital-audio systems, Proc. ICASSP 82, Paris 1982, pp. 81-84.

Scientific publications

These publications are contributed by staff of laboratories and plants that form part of or cooperate with enterprises of the Philips group of companies, particularly by staff of the research laboratories mentioned below. The publications are listed alphabetically by journal title.

Philips GmbH Forschungslaboratorium Aachen, Weißhausstraße, 5100 Aachen, Germany — *A*

Philips Research Laboratory Brussels, 2 avenue Van Becelaere, 1170 Brussels, Belgium — *B*

Philips Natuurkundig Laboratorium, Postbus 80000, 5600 JA Eindhoven, The Netherlands — *E*

Philips GmbH Forschungslaboratorium Hamburg, Vogt-Kölln-Straße 30, 2000 Hamburg 54, Germany — *H*

Laboratoires d'Electronique et de Physique Appliquée, 3 avenue Descartes, 94450 Limeil-Brévannes, France — *L*

Philips Laboratories, N.A.P.C., 345 Scarborough Road, Briarcliff Manor, N.Y. 10510, U.S.A. — *N*

Philips Research Laboratories, Cross Oak Lane, Redhill, Surrey RH1 5HA, England — *R*

Philips Research Laboratories Sunnyvale P.O. Box 9052, Sunnyvale, CA 94086, U.S.A. — *S*

A. Daniels, M. Gasser* & A. Sherman* (* *Goddard Space Flight Center, Greenbelt, MD*) *N*	Magnetically suspended Stirling cryogenic space refrigerator: status report	Advances in cryogenic engineering, Vol. 27, ed. R. W. Fast, Plenum, New York	711-719	1982
H. M. Meehan & R. C. Sweet *N*	Novel titanium-aluminum joints for cryogenic cold finger structures	Advances in cryogenic engineering, Vol. 27, ed. R. W. Fast, Plenum, New York	721-726	1982
A. K. Niessen *E*	Note on the prediction of the enthalpy of formation of solid compounds of the transition and noble metals with chalcogens and halogens	High Temp. — High Pressures **14**	649-651	1982
S. Hoekstra, M. A. Munnig Schmidt-van der Burg, H. Galenkamp & H. van Wijngaarden *E*	Quantitative determination of stress and strain distributions during high axial compression of aluminium with the aid of small ruby particles	J. Appl. Mech. **105**	194-198	1983
S. Colak & W. K. Zwicker *N*	Transition rates of Tb^{3+} in TbP_5O_{14}, $TbLiP_4O_{12}$ and $TbAl_3(BO_3)_4$: an evaluation for laser applications	J. Appl. Phys. **54**	2156-2166	1983
O. Boser *N*	Internal friction due to hysteretic dislocation motion in solid solution crystals	J. Appl. Phys. **54**	2338-2343	1983
J. M. F. van Dijk & M. F. H. Schuurmans *E*	On the nonradiative and radiative decay rates and a modified exponential energy gap law for 4*f*-4*f* transitions in rare-earth ions	J. Chem. Phys. **78**	5317-5323	1983
P. C. M. Gubbens*, A. M. van der Kraan* (* *Interuniv. Reactor Inst., Delft*) & K. H. J. Buschow *E*	First order transition and magnetic structure of $TmCo_2$	J. Magn. & Magn. Mater. **29**	113-116	1982
A. L. J. Burgmans & A. H. M. Smeets *E*	The ionisation coefficient in Ar-Hg mixtures	J. Phys. D **16**	755-762	1983
R. Boom (*Hoogovens, IJmuiden*), F. R. de Boer (*Univ. Amsterdam*), A. K. Niessen & A. R. Miedema *E*	Enthalpies of formation of liquid and solid binary alloys based on 3d metals, III	Physica **115B**	285-309	1983
A. G. van Nie & G. Kersuzan (*TRT, Le Plessis-Robinson*) *E*	Accurate 'fixed-angle' models for calculating the temperature rise of rectangular heat sources in hybrid circuits	Proc. 4th Eur. Hybrid Microelectron. Conf., Copenhagen 1983	523-530	1983
S. Nakahara (*Bell Labs, Murray Hill, NJ*) & F. J. A. den Broeder *E*	Diffusion-induced grain boundary migration in heated Cu-Ni alloy targets during sputtering	Scr. Metall. **17**	607-610	1983
P. K. Larsen & J. F. van der Veen (*FOM, Amsterdam*) *E*	Photoemission from MBE grown III-V surfaces and interfaces	Surf. Sci. **126**	1-19	1983

PHILIPS TECHNICAL REVIEW

VOLUME 41, 1983/84, No. 4

An integrated switched-capacitor filter for viewdata

A. H. M. van Roermund and P. M. C. Coppelmans

Any ordinary colour television set can be adapted for the display of 'videography' by adding a special decoder circuit. We use the general term 'videography' as a name for a large number of different systems in which text and simple graphics are converted into a digital signal in accordance with fixed rules. This digital signal can be transmitted as part of a television signal (teletext) or sent upon request to one particular subscriber via an ordinary telephone line (videotex, or more specifically, viewdata). A subscriber to a viewdata system needs a 'viewdata modem' for the connection between his television set and the telephone line. An important component in the modem is the receive filter. The authors of this article have realized this filter as a single integrated circuit by making use of the rather new technique of switched-capacitor filters.

Introduction

The theory and design of electrical filters have long had an important part to play in electronic engineering. Filters enable the different frequency components of a signal to be treated in different ways. The great majority of filters are used to stop the transmission of certain frequencies (or frequency bands) while others are passed. Filters are therefore very widely used in all kinds of telecommunication equipment (in radio, television, telephony and so on). At first filters were built up from the three basic elements encountered in the theory of electrical networks: inductors (L), resistors (R) and capacitors (C). As time went by, whole classes of filters evolved, each with their advantages and disadvantages. There are for example doubly terminated LC filters, built entirely from inductors and capacitors except for the two terminating resistors. The great advantage of these filters is the relatively small change in filter characteristics when the element values depart from the theoretically ideal values. These filters are therefore said to have low parameter sensitivity. They do have one great disadvantage, however: they include inductors. These are relatively large, heavy and expensive, especially for applications at low frequencies. Also, it is almost impossible to make inductive elements as part of an integrated circuit. New filter types in which there are no inductors have therefore been sought for many years [1]-[3]. This objective can be achieved by using active elements, such as amplifiers. Well-known examples are active RC filters, composed of resistors, capacitors and operational amplifiers, and gyrator filters. Unfortunately, active RC filters have poorer parameter sensitivity. On the other hand, the low parameter sensitivity of LC filters can be retained, if the rules for design are properly 'translated' for other types of filter. The LC filters therefore still remain of considerable interest, as we shall see later in this article.

Ir A. H. M. van Roermund and P. M. C. Coppelmans are with Philips Research Laboratories, Eindhoven.

[1] D. Blom, H. W. Hanneman and J. O. Voorman, Some inductorless filters, Philips Tech. Rev. 33, 294-308, 1973.

[2] J. O. Voorman, W. H. A. Brüls and P. J. Barth, Integration of analog filters in a bipolar process, IEEE J. SC-17, 713-722, 1982.

[3] M. S. Ghausi and K. R. Laker, Modern filter design: active RC and switched capacitor, Prentice-Hall, Englewood Cliffs, 1981.

All the filters we have mentioned so far are *analog* filters. The signals in these filters can change in value at any moment and can take any value between two extremes. These analog signals are thus continuous in time and in amplitude (*fig. 1a*). Another kind of filter that has been known for some time is the *digital* filter. These filters rather resemble small computers: the signals consist of series of numbers and the filter operations are implemented as a succession of simple arithmetical operations such as multiplication, storage and addition. Since these digital signals are built up from clearly separated successive numbers ('samples') that can each take only a finite number of different values, they are discrete in time and in amplitude (fig. 1*b*). A digital filter is in general highly suitable for design in integrated-circuit form and represents an interesting method of making filters.

Recently a very promising third category of filters has attracted increasing attention: *sampled-data* filters. In these filters the signals can change value at certain instants only, but then they can take any value (between two extremes). Signals of this type can be obtained by periodically taking samples of an analog signal with a sampling circuit (*fig. 2a*). The signal level after sampling is often held constant for a time by a holding circuit. We then obtain signals like those shown in fig. 2*b* or *c*. All these signals can be considered to consist of a series of signal elements of fixed shape and duration but of arbitrary value. To put it another way, they are discrete in time and continuous in amplitude. In most sampled-data filters now in use the signal elements are represented by packets of electric charge, which are passed on within the filter at regular intervals and thus processed. This can be done for example by means of capacitors that are periodically switched to give a continuing redistribution of the charge packets. This gives a switched-capacitor filter, often abbreviated to SC filter. Some of the properties of SC filters correspond to those of analog filters, while others more closely resemble those of digital filters. We shall have more to say about this later. For the moment the most important feature is that SC filters are readily fabricated in integrated-circuit technology, although for the present the frequency range in which they offer the greatest advantage goes no higher than 100 kHz.

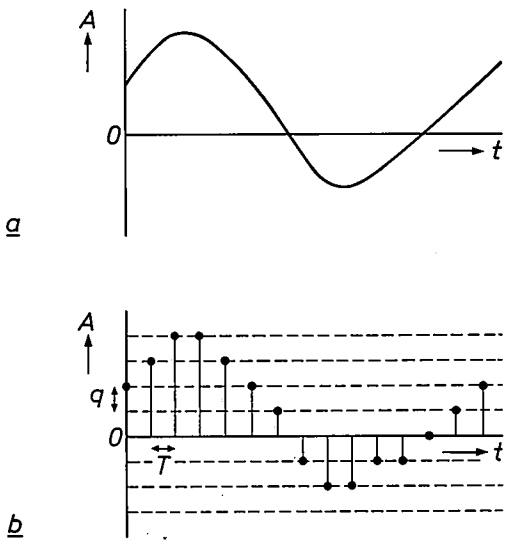

Fig. 1. *a*) An *analog signal* can have any amplitude A at any time t; it is continuous in time and continuous in amplitude. *b*) A *digital signal* is discrete in time and discrete in amplitude; it can be completely represented by a series of numbers that can each take only a finite number of different values. A digital signal is usually represented graphically by a sequence of points on a fixed 'grid' as shown here. q quantization step, T sampling interval.

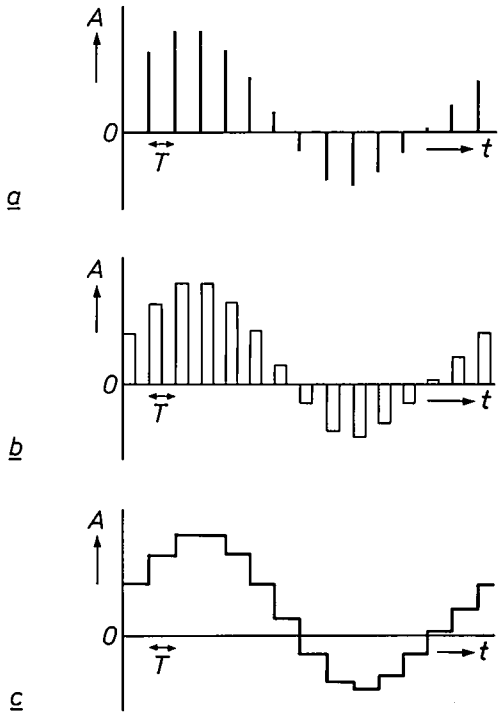

Fig. 2. A *sampled-data signal* can take any value A, but only at certain times, separated by T, the sampling interval. It can be obtained by sampling the value of a given analog signal at regular intervals (*a*). The level of the sampled-data signal is often held constant for a time after sampling (*b* and *c*). In all these cases the signal can be considered as a series of signal elements of fixed shape and fixed duration T, but of arbitrary amplitude. These signals are therefore said to be discrete in time, but continuous in amplitude. The exact shape of the signal elements is *not* of importance for the information (e.g. speech or music) carried by the signal. The signals in (*a*), (*b*) and (*c*) are fully equivalent in this respect.

However, we should note that a sampled-data signal can also be considered as an analog signal that is subject to certain constraints: its value is indeed defined for every time t, but cannot vary freely. If we consider a sampled-data signal in this way and process it accordingly, e.g. in an analog filter, then the exact form of the signal elements *is* of importance for the final result. The same analog processing of the signals (*a*), (*b*) and (*c*) can then lead to slightly different final results.

In this article we shall describe an integrated viewdata filter fabricated in MOS technology [4] as an example of an SC filter. The description will include a discussion of the fundamental principles of these filters and of the essentials of the design process that resulted in a filter on a single chip, which is ready for use without any adjustment. First of all, however, we must say something about the viewdata system, for which the filter is intended.

Videography

A conventional analog TV signal can represent practically any picture, complete with movement. In videography, on the other hand, a binary digital signal — i.e. a succession of bits ('ones' and 'zeros') — is used to give an encoded representation of letters, numbers and simple graphic symbols only. Videography is also usually limited to stationary pictures and its resolution is rather less than that of ordinary TV. However, much less information has to be transmitted. It is therefore possible to accommodate broadcast videography (*teletext* [5]) in an unused part of the transmitted television signal or to provide interactive videography (*videotex*, or more specifically *viewdata*) via the ordinary telephone system.

Although a teletext picture may look remarkably like a videotex picture, the two systems are quite different. In teletext the pictures to be added to the ordinary TV signal at a fixed rate are selected centrally at the studios. The viewer only decides which of the 'passing' teletext pictures will be displayed. To keep down the average waiting time, the number of different pictures (or 'pages') that can be consulted is restricted to a few hundred at the most. These pages therefore mainly contain subjects of general interest, such as the latest news, the weather forecast, sports results, traffic information, summaries of radio and TV programmes or subtitles for TV programmes transmitted simultaneously.

In videotex the viewer orders each picture separately from a central computer via the telephone network; hence the designation *interactive* videography. There is no direct relation between the number of different pages available and the average waiting time. In principle this number is therefore unlimited.

The videotex system can make all kinds of data bases accessible to anyone, with contents from stock-exchange prices and tourist information to catalogues of mail-order companies and encyclopaedias. Videotex offers a number of facilities that teletext does not have. It is possible for example to charge the subscriber for a transmitted page, since the information is only provided on demand. It is also possible to make certain pages available only to certain users (e.g. regular subscribers). Also, in certain circumstances a user can respond by booking a journey, say, or placing an order ('teleshopping'). It is also possible for videotex subscribers to send certain messages (e.g. greetings telegrams) to one another. So in this way videotex offers a simple form of electronic mail.

The introduction of videography has been accompanied by a flood of new terms, which sometimes are very confusing to both outsiders and insiders. The definitions for videography, teletext and videotex, as given above, have recently been proposed by some international bodies, including the IEC and the ITU [6]. *Teletext* has different names in different countries: Teletekst (the Netherlands), Videotext (Germany), Ceefax and Oracle (United Kingdom), Didon-Antiope (France). For *videotex* the situation is even more complicated. The original idea for videotex came from Britain, where it was first called viewdata. Then systems with different technical aspects and different names began to appear in other countries. At the same time some of the operating organizations introduced new names for technically identical systems. So now we have Viditel (the Netherlands), Bildschirmtext (Germany), Prestel and, shortly, Panda (United Kingdom), Teletel (France), Videotel (Italy), Telidon and Vista (Canada), Datavision (Sweden), Teledata (Denmark and Norway), Telset (Finland) and Captain (Japan).

To increase confusion even further a service called teletex has recently become available in some countries. However, this has nothing at all to do with videography, but is an improved version of the long-established telex.

In this article we shall pay particular attention to a filter from a modem for the original viewdata system. Such a filter is suitable for a large number of the other videotex systems, but is not automatically suitable for all of them. To emphasize this point, we shall continue to use the term viewdata in this article, even though this name seems to be falling out of favour in some quarters.

Viewdata modem

An essential condition for the use of videotex is the existence of a two-way connection between the subscriber and the videotex computer. This connection is set up via the telephone network (*fig. 3* and *4*). To connect the subscriber's television set to the telephone network there must be a modem (from *mo*dulator/*demo*dulator). In the viewdata system, the series of ones and zeros that represent the subscriber's commands are first of all encoded in the modem into series of tones at 390 or 450 Hz. These series of tones can be sent to the computer via the telephone connection. Another series of tones, at 1300 or 2100 Hz, is

[4] It is interesting to note that the same viewdata filter has been described as an example in [2]. However, there a completely different approach was used to obtain an integrated-circuit version. The filter was an *analog* filter, based on *gyrators*, and fabricated in a *bipolar* process.

[5] J. O. Voorman, P. J. Snijder, J. S. Vromans and P. J. Barth, An automatic equalizer for echo reduction in Teletext on a single chip, Philips Tech. Rev. 40, 319-328, 1982.

[6] IEC = International Electrotechnical Commission.
ITU = International Telecommunication Union.

received in the modem and translated back into the ones and zeros that represent the viewdata pictures. Information can be sent from the subscriber to the computer at the rate of 75 bits/s and simultaneously in the reverse direction at 1200 bits/s. An important component of the viewdata modem is the receive filter. This filter must pass the signal arriving for the subscriber with the minimum of distortion and at the same time it must attenuate all interfering signals (particularly 50-Hz mains hum, the signal sent by the subscriber himself and noise) as much as possible. In more specific terms this requires:

- low distortion due to attenuation and group delay in the passband (1100 to 2300 Hz),
- more than 50 dB of attenuation at 50 Hz,
- more than 50 dB of attenuation between 390 and 450 Hz and
- more than 28 dB of attenuation above 3400 Hz.

A computer program that can simulate a viewdata connection has been used to find a filter transfer function that meets this specification. The result was a 9th-

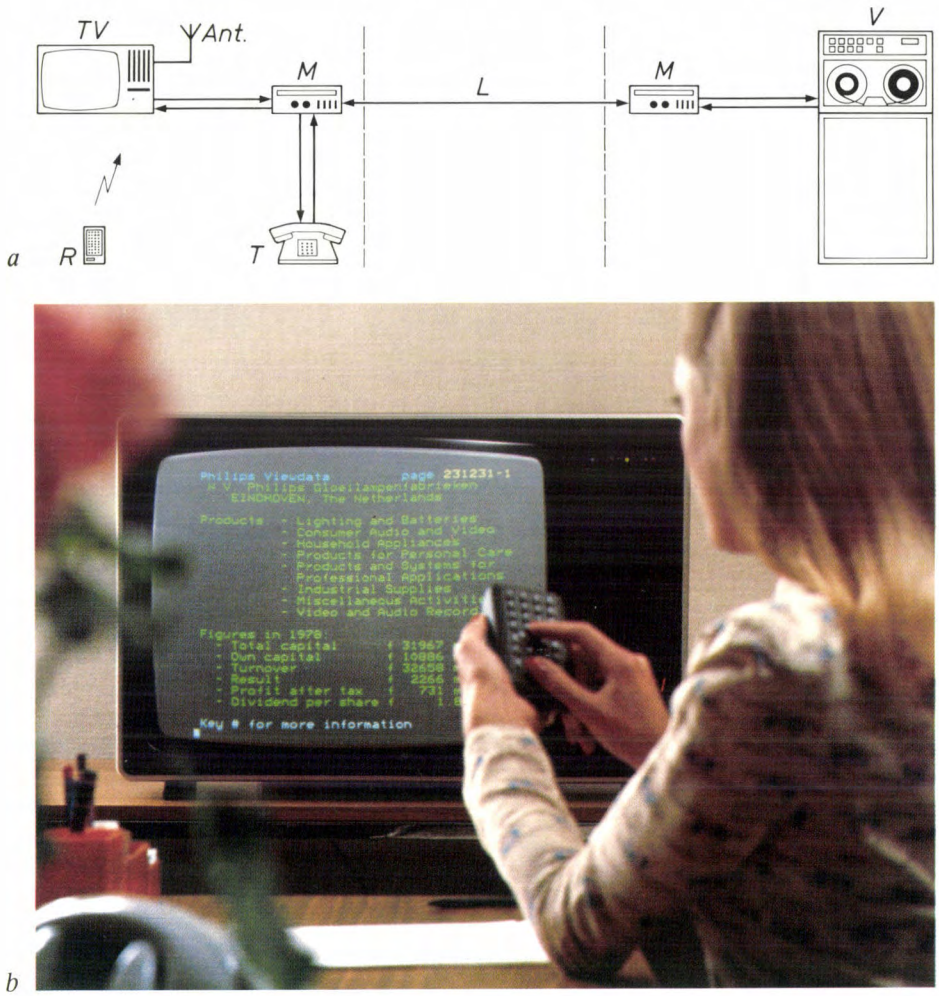

Fig. 3. *a*) Basic diagram of a videotex connection. The TV receiver is connected to the videotex computer *V*, which contains all the information, via two modems *M* and the telephone line *L*. The telephone *T* is used for making the connection. Once this has been made, the user communicates with the computer via the TV remote control *R*. Ordinary television programmes, including teletext signals, can be received with the antenna *Ant*. *b*) A videotex system in use. The telephone handset has been replaced on its cradle, since the connection has been made and the user provides all further commands via the remote control.

[7] All the computer calculations for the simulation of the viewdata connection and for the specification of the filter of fig. 6 were performed by our colleagues B. Huber, J. Kunze and R. Lücker of the TEKADE Company, Nürnberg, West Germany. They also decided on the signal flow diagram for the viewdata filter and carried out the final optimization.

[8] Recently our colleagues at Mullard Application Laboratory, Mitcham, Surrey, England, have made a 'two-chip' version of a videotex modem. One of these chips contains an SC filter with roughly the same characteristics as the ones given in fig. 5. The main differences from the integrated filter of this article are: their filter has an 8th degree transfer function, it is formed from 4 second-order sections ('biquads') and it has been fabricated in NMOS technology. Further details are given in: R. Sharpe, LUCY/LUCINDA — A fully integrated solution to Videotex terminal interfaces, IEEE Trans. **CE-29**, 492-497, 1983. A publication on the same subject will also appear shortly in Electron. Components & Appl.

degree transfer function with the attenuation characteristic and group-delay characteristic shown in *fig. 5*. Other computer programs that have been available for a long time could then be used to calculate a fully doubly terminated *LC* filter, could be directly applied in the viewdata modem. But because of the inductors (and especially the coupled inductors L_3, L_4 and L_5) it cannot be made as an integrated circuit. However,

Fig. 4. The business user often prefers to use special versions of videotex equipment. The colour TV receiver is then replaced by a simpler colour monitor and a complete keyboard is substituted for the remote control. The photograph also shows special equipment for making a print of the information on the screen. The modem can be seen below the telephone.

specified filter from these curves. In *fig. 6* we show as an example a doubly terminated *LC* filter that has been derived in this way [7]. In principle there are a large number of *LC* filters with the desired characteristics. One of the special features of the filter shown here is the small ratio of the largest to the smallest values of the different elements. The circuit of fig. 6, which meets all the stated filter requirements and also has the desirable low parameter sensitivity of the we shall show later that this circuit is very useful as the starting point for the design of an integrated SC filter [8].

SC filters

Fundamentals

SC filters are readily integrated because they are built up from three kinds of components that are

highly suitable for fabrication in a single process. These are switches, capacitors and amplifiers, which can all be integrated successfully in the well-known MOS (Metal-Oxide Semiconductor) technology [9]. In these components use is made of the following unique combination of features, which MOS circuits have but bipolar circuits do not.

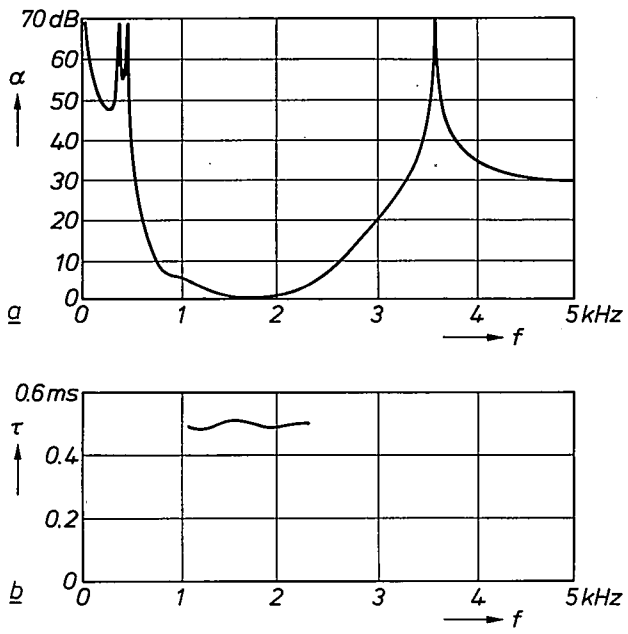

Fig. 5. *a*) Attenuation characteristic of the receive filter of a view-data modem. The figure clearly shows the passband (centre 1700 Hz) for the received signal and the stopband (centre 420 Hz) for the subscriber's own signal. Attenuation is also necessary at lower and higher frequencies because of 50-Hz mains hum and noise. *b*) Group-delay characteristic of the same filter in the passband. The distortion of the received signal is determined by the shape of both curves in this band. α attenuation, τ group delay, f frequency.

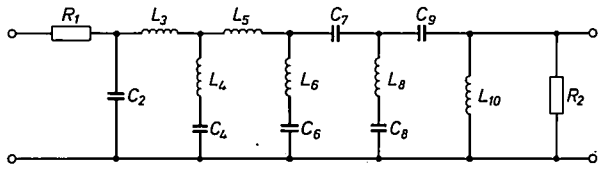

Fig. 6. A possible implementation of the characteristics of fig. 5 in the form of a doubly terminated LC filter. L inductance, C capacitance, R resistance. For this filter $L_3L_4 + L_3L_5 + L_4L_5 = 0$, which implies that at least one of the three inductances L_3, L_4 and L_5 must be negative. This can be achieved by combining L_3, L_4 and L_5 in a transformer.

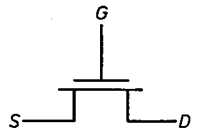

Fig. 7. Symbolic representation of an MOS transistor. S source, G gate and D drain. If the transistor is used as a *switch*, a gating signal is applied to G; this gating signal is used to make or break the connection between S and D as required. If the transistor is used as an *amplifier*, the signal to be amplified is generally applied to G.

- An MOS transistor used as a switch has a very high impedance between the source S and the drain D in the switched-off state (*fig. 7*). Electric charges on small capacitors (e.g. 1 pF) connected to the source or drain will therefore continue to be stored for a relatively long time (up to several milliseconds). In a bipolar transistor the minority carriers cause recombination currents and hence a change in the stored charge.
- The coupling between the gate G (fig. 7) of an MOS transistor and the source and drain is purely capacitive. This has two consequences. If the transistor is used as a *switch*, there will be no loss of charge from G to S or D. If it is used as an *amplifier*, the quantity of charge stored in a capacitor can be read out continuously and non-destructively via G.
- An MOS transistor can be made completely symmetrical, so that the source and drain cannot be distinguished from one another and have completely interchangeable roles. It therefore makes no difference to the transistor whether the voltage difference between S and D is positive, negative or zero. (To emphasize this point we have used a symmetrical symbol for the MOS transistor; there is also an asymmetrical symbol in which G is shown opposite to S.)
- Both the dimensions and the parasitic capacitances of an MOS transistor can be very small.

As the name indicates, SC filters contain switched capacitors. These can be compared with resistors in some respects. *Fig. 8a* shows the combination of a changeover switch with a capacitor of capacitance C. If we assume that in a period T the switch first takes the left-hand position and then the right-hand position, the capacitor will be charged first to a value

$$q_1 = Cv_i$$

and then to

$$q_2 = Cv_o.$$

In time T a total charge Δq will travel from left to right, where

$$\Delta q = q_1 - q_2 = C(v_i - v_o).$$

This corresponds to a *mean* current $\bar{i}$ given by

$$\bar{i} = \frac{\Delta q}{T} = \frac{C(v_i - v_o)}{T}.$$

If the frequencies in which we are interested are sufficiently low compared with the switching frequency $1/T$ (we usually speak of the *sampling rate* or *clock rate*), then we can consider the switched capacitor in fig. 8*a* as a resistance of value $R = T/C$ (fig. 8*b*). We can make the changeover switch in fig. 8*a* with the aid of two MOS transistors that are switched alternately on and off by clock signals ϕ_1 and ϕ_2 of period T (*fig. 9*).

An RC network of the 1st order with a time constant $\tau_A = R_1C_2$ can be approximated by combining a switched capacitance with a fixed one (*fig. 10*). The associated time constant τ_{SC} is then given by

$$\tau_{SC} = \frac{C_2}{C_1} T$$

(if the sampling rate $1/T$ is sufficiently high). This demonstrates two general properties of SC filters: time constants are proportional to *capacitance ratios* and inversely proportional to the *clock rate*. In modern integration processes capacitance ratios can be reproduced to an accuracy of 0.1% without difficulty and clock rates can be even more accurately set. In addition the capacitance ratios of integrated capacitors vary only slightly with temperature or capacitor voltage, especially if the capacitors are close to one another on the chip. If moreover we decide on a type of filter that intrinsically has low parameter sensitivity, then we can obtain the following impressive combination of desirable features:

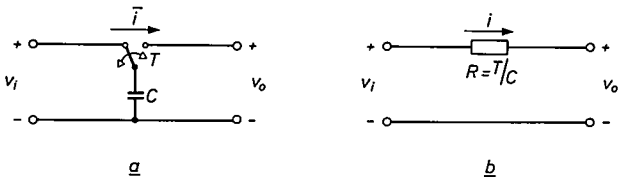

Fig. 8. *a*) A switched capacitor C is charged alternately to a voltage v_i and a voltage v_o at a frequency $1/T$. The charge transfer thus produced corresponds to a *mean* current $\bar{i} = C(v_i - v_o)/T$. *b*) At low frequencies this circuit is equivalent to a resistor $R = T/C$.

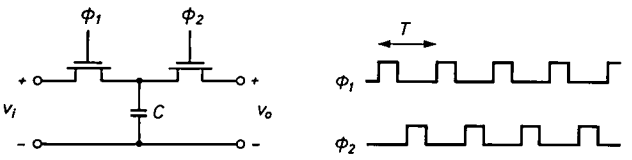

Fig. 9. In MOS technology the switched capacitor of fig. 8*a* can be made with a fixed capacitor C and two switching transistors, operated by two different clock signals, ϕ_1 and ϕ_2. Each transistor only makes its connection when its clock signal has a high value. The two clock signals are never allowed to have a high value both at the same time.

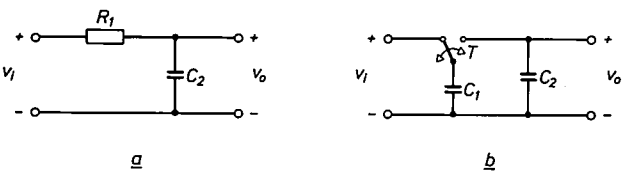

Fig. 10. *a*) Passive 1st-order RC filter and *b*) the SC filter derived from it with $C_1 = T/R_1$. The SC filter is a good approximation to the RC filter for frequencies that are low with respect to the switching frequency or sampling rate $1/T$.

- filter can be fully integrated;
- very high accuracy, without trimming (e.g. deviations of only 0.05 dB in the passband);
- very low temperature coefficients;
- processing conditions for manufacture are not critical, so that SC filters can easily be combined on a single chip with other circuits, such as logic circuits, oscillators, rectifiers and comparators;
- small dimensions (e.g. 0.2 mm^2 per filter pole) so that high-order filters can be produced on a single chip;
- low power consumption (e.g. 0.1 to 1 mW per filter pole);
- no analog-to-digital or digital-to-analog converters are necessary for applications with analog signals;
- frequency response can be scaled by changing the clock rate;
- no quantization as in digital filters and hence none of the accompanying negative effects it introduces (stability problems, preference for certain filter structures).

Beside these advantages there are a number of limitations. The most important ones are:

- The desirable features of SC filters (especially those relating to surface area, power and accuracy) are for the present only available in a limited frequency range (for signals up to about 100 kHz).
- An extra analog filter may be necessary before or after the SC filter to suppress frequency components higher than half the sampling rate.
- If an SC filter is the only component in a system that requires a clock signal, this implies a certain complication.
- SC filters introduce noise into the signal (typical signal-to-noise ratios are 70 to 80 dB).
- Like all active filters, SC filters take some electrical power from the supply; usually this is very low, however.
- SC filters can introduce more distortion than LC filters. (Distortion, power consumption and signal-to-noise ratio can be traded against one another at the design stage.)
- SC filters can off-set the d.c. level of the signal (by 10 to 100 mV).

SC filters with amplifiers

With the aid of fig. 8 we showed how a switched capacitor could be modelled as a resistor. In principle with such a model we could replace any resistor from any passive RC filter by a switched capacitor and

[9] Special issue on MOS transistors and MOS circuits, Philips Tech. Rev. 31, 205-295, 1970;
B. B. M. Brandt, W. Steinmaier and A. J. Strachan, LOCMOS, a new technology for complementary MOS circuits, Philips Tech. Rev. 34, 19-23, 1974.

hence derive an SC version of that filter. Indeed, that was what we did for an *RC* filter of the first order (fig. 10). However, this approach will not take us very far. In the first place our model is only an approximation. Moreover, we can only apply the technique to passive *RC*-filter prototypes with their inherently low selectivity. Finally, this approach yields SC filters that turn out to be very sensitive to the parasitic capacitances encountered in a practical integrated circuit. To avoid these difficulties and to make use of as many of the advantages listed in the previous subsection as we can, we have to include special amplifiers in our SC filters. In the literature these amplifiers are usually called 'operational amplifiers', or just 'op-amps'. Since we think the term 'operational' is something of a misnomer here, we shall not apply it for these amplifiers in the rest of the article.

An operational amplifier is a universally applicable amplifier with two inputs. The difference voltage between these two inputs acts as the input signal, and there is usually a single output. The input impedance, the gain and the bandwidth are very high, while the output impedance is extremely low. Between the output and the (inverting) input negative feedback is almost always used to give the desired amplifier response.

The differential amplifiers that we use in SC filters have a high input impedance and a reasonably high gain (e.g. a voltage gain of 10 000), but a fairly high output impedance and a bandwidth that must be separately 'tailored' for each amplifier, and should not be larger than strictly necessary, because of noise (e.g. 400 kHz). These amplifiers clearly have a number of features that are specific to their application, and are not really the same as the universal operational amplifiers. We shall return to these special amplifiers later.

The use of amplifiers in SC filters can be illustrated with the aid of *fig. 11*. This figure shows first of all an analog integrator, as widely used in active *RC* filters. It consists of a resistor, a capacitor and an amplifier. Next to it an SC approximation to it is shown. Making use of the complex variable p and the Laplace transforms $V_i(p)$ and $V_o(p)$ of the input and output voltages v_i and v_o, we can describe the analog integrator [10] in terms of the *transfer function* $H(p)$:

$$H(p) = \frac{V_o(p)}{V_i(p)} = \frac{-1}{pR_1C_2}. \qquad (1)$$

The transfer characteristics of the analog integrator for a sinusoidal signal of angular frequency ω rad/s are given by the *frequency response* $H_A(\omega)$. We can derive $H_A(\omega)$ from $H(p)$ by putting $p = j\omega$, where j is the imaginary unit ($= \sqrt{-1}$). We find

$$H_A(\omega) = \frac{-1}{j\omega R_1C_2}. \qquad (2)$$

(The subscript A indicates 'analog'.)

To determine the frequency behaviour of the SC filter from fig. 11 we first consider its operation in the time domain. During clock phase *1* (i.e. when the clock signal ϕ_1 is 'high', see fig. 9) the switch is in the left-hand position. At the end of this phase, e.g. at time $t = nT$, the charge on the capacitor C_1 is $C_1v_i(nT)$. At that the moment there is a charge $C_2v_o(nT)$ on the capacitor C_2 as the result of all the previous events in the filter. During clock phase *2* the switch is in the right-hand position. The amplifier always tries to bring the voltage difference between its two inputs back to zero. This is done by compensating the charge on C_1 with charge from C_2. The charge on C_2 therefore diminishes by $C_1v_i(nT)$ and then remains constant during the rest of the period T, i.e. until $t = nT + T$. The relation between the charges on C_2 at the times nT and $nT + T$ is given by:

$$C_2v_o(nT + T) = C_2v_o(nT) - C_1v_i(nT). \qquad (3)$$

By varying the number n, which is an integer, we can use this equation to determine the behaviour of the SC filter at all times separated by a multiple of T; we shall not consider what exactly happens between these times and we shall therefore consider the SC filter purely as a sampled-data filter. In fact equation (3) is an example of the description of a discrete-time sys-

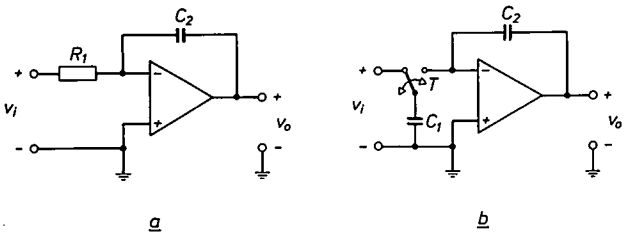

Fig. 11. *a*) Active 1st-order *RC* filter or analog integrator and *b*) the SC filter derived from it with $C_1 = T/R_1$. Here again the properties of the two filters only correspond well for frequencies that are low with respect to $1/T$.

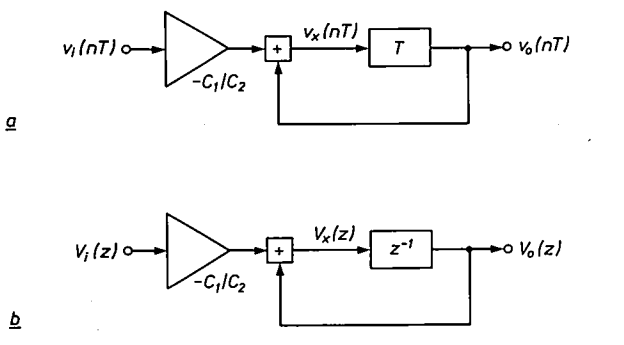

Fig. 12. Discrete-time equivalent circuit for the SC integrator of fig. 11 in the time domain (*a*) and in the complex-frequency domain or z-domain (*b*). We clearly recognize three basic elements of discrete-time systems: adder, delay element (indicated by T and z^{-1}) and constant-factor multiplier (here $-C_1/C_2$).

tem by a *difference equation*. Just as we can directly convert the description of a continuous-time system in terms of a *differential equation* into a description in terms of the complex variable p (the 'Laplace transform'), we can convert a difference equation into a description in terms of the complex variable z (the 'z-transform'). To do this we replace $v(nT)$ by $V(z)$, $v(nT+T)$ by $V(z).z$ and in general $v(nT+mT)$ by $V(z).z^m$. The equation above then becomes

$$C_2 V_o(z) . z = C_2 V_o(z) - C_1 V_i(z). \qquad (4)$$

The ratio of $V_o(z)$ to $V_i(z)$ is called the *transfer function* $G(z)$ of the discrete-time system, and in this case is given by

$$G(z) = \frac{V_o(z)}{V_i(z)} = -\frac{C_1}{C_2}\frac{1}{z-1}. \qquad (5)$$

From this $G(z)$ we can derive the transfer characteristics for a sinusoidal signal of angular frequency ω rad/s in the form of the *frequency response* $G_D(\omega)$. We find $G_D(\omega)$ from $G(z)$ by putting $z = e^{j\omega T}$, where j is again the imaginary unit, e the base of the natural logarithms and $1/T$ the sampling rate of the discrete-time system. Therefore:

$$G_D(\omega) = -\frac{C_1}{C_2}\frac{1}{e^{j\omega T}-1}. \qquad (6)$$

(The subscript D indicates 'discrete'.) For frequencies that are very much smaller than the sampling rate $1/T$ (i.e. $\omega T \ll 1$), $e^{j\omega T}$ is approximately equal to $1 + j\omega T$.

The validity of this approximation can easily be seen by starting from $e^{j\omega T} = \cos\omega T + j\sin\omega T$ and applying the approximations $\cos\omega T \approx 1$ and $\sin\omega T \approx \omega T$ for small values of ωT.

In this way we find the frequency response $G_{SC}(\omega)$ of the SC integrator of fig. 11 at low frequencies:

$$G_{SC}(\omega) = -\frac{C_1}{C_2}\frac{1}{j\omega T}. \qquad (7)$$

A comparison with $H_A(\omega)$, found earlier in equation (2), shows us that at low frequencies the two circuits in fig. 11 are equivalent, provided that $R_1 = T/C_1$. This corresponds to our earlier derivation with fig. 8. Also, we see again that the frequency behaviour is determined by a capacitance ratio and the clock rate.

In equations (3), (4) and (5) we have given descriptions in the time domain and the complex-frequency domain ('z-domain') of the SC integrator of fig. 11 as a purely discrete-time system. These equations can also be represented by block diagrams (discrete-time equivalent circuits). This has been done in *fig. 12a* and *b*. A delay of T in the time domain corresponds to a multiplication by z^{-1} in the z-domain, as we have indicated above. For the block diagram of fig. 12*a* we have:

$$v_x(nT) = -\frac{C_1}{C_2} v_i(nT) + v_o(nT)$$

and

$$v_o(nT+T) = v_x(nT).$$

Eliminating $v_x(nT)$ from these two equations gives equation (3).

For the block diagram of fig. 12*b* we have:

$$V_x(z) = -\frac{C_1}{C_2} V_i(z) + V_o(z)$$

and

$$V_o(z) = z^{-1} . V_x(z).$$

Eliminating $V_x(z)$ here gives equation (4) directly. Equivalent diagrams like those of fig. 12 are a very useful aid in the analysis of SC filters as discrete-time systems. They are particularly useful for filters of complicated structure.

In going from the analog integrating circuit of fig. 11*a* to the SC integrator of fig. 11*b* we have gone from a description in terms of $H(p)$ to a description in terms of $G(z)$. We have also seen that for low frequencies both integrators are equivalent if $R_1C_1 = T$. With this condition we can characterize this particular transition as the substitution of $(z-1)/T$ for p in $H(p)$; we then obtain $G(z)$ directly. This transition is called a *transformation* or *mapping*. In fig. 11 we are concerned with 'forward-difference mapping'. If in any active RC filter of transfer function $H_{tot}(p)$ every analog integrator is replaced by the SC integrator of fig. 11*b*, we obtain the resulting $G_{tot}(z)$ by substituting $(z-1)/T$ for every p in $H_{tot}(p)$. The transformation rule thus completely establishes the nature of the relationship between the frequency behaviour of the original filter and that of the new filter. In practice different transformations from the one in fig. 11 are usually used, since that particular transformation entails relatively large differences between the frequency responses corresponding to $G_{tot}(z)$ and $H_{tot}(p)$. We shall return to this in the following section.

SC integrators

The SC integrator is a good starting point for building complicated SC filters. We have already encountered one possible version of such an integrator in fig. 11. There are a countless number of variations, however, and a few of them are shown in *fig. 13*, with a discrete-time equivalent circuit and the associated transfer function $G(z)$. The switches in this figure are shown in the position that they take during clock phase *1*, i.e. when the clock signal ϕ_1 is 'high'. The other position is associated with clock phase *2* (ϕ_2 'high').

[10] See p. 77 of [3].

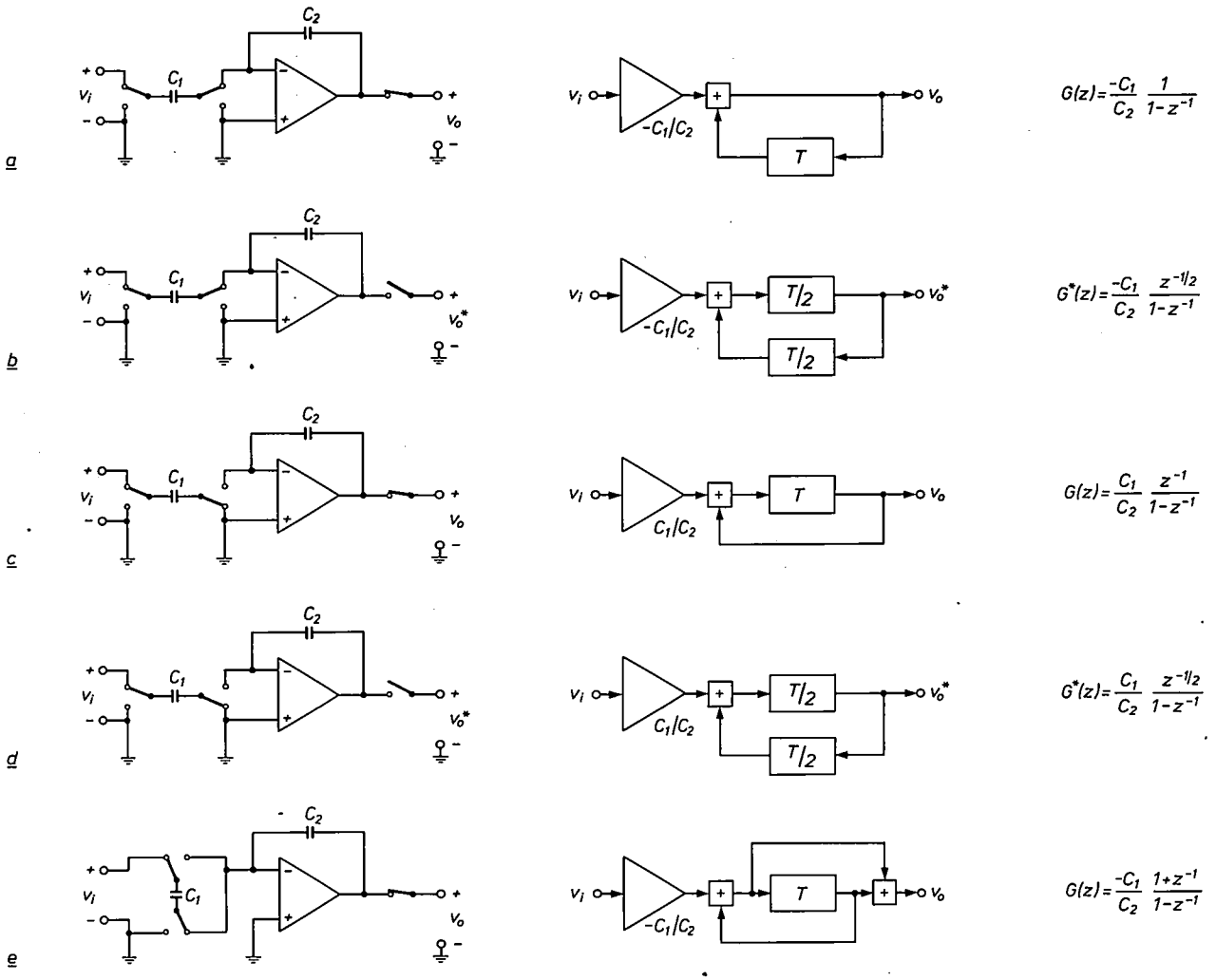

Fig. 13. Various types of SC integrator with corresponding discrete-time equivalent circuit and transfer function in z. Comparing *a* with *b* and *c* with *d* shows that the clock phase with which the output signal is read out clearly affects the behaviour of the circuit. All the switches are shown in the position they adopt during clock phase *1*. Signals that occur during clock phase *2* are indicated by an asterisk. Circuits *b* and *d* are of the LDI type (LDI stands for Lossless Discrete Integrator). Circuit *e* represents the bilinear transformation of an analog integrator.

We see that in some cases input signal and output signal occur during the same clock phase but not in other cases. We must therefore take proper care when connecting different integrators together. Signals that occur during clock phase *2* are indicated by an asterisk. If the input signal occurs during clock phase *1* and the output signal during clock phase *2*, the associated transfer function has also been indicated by an asterisk: $G^*(z)$. A difference in clock phase between input and output is manifest by the occurrence of fractional powers of z in $G^*(z)$. In practice there are no output switches, but the input switches of the following integrators will automatically fulfil this function by operating them in the required clock phase. We shall keep to the same convention in all the succeeding figures.

The integrators in fig. 13 differ from one another in several respects; the following are the most important:

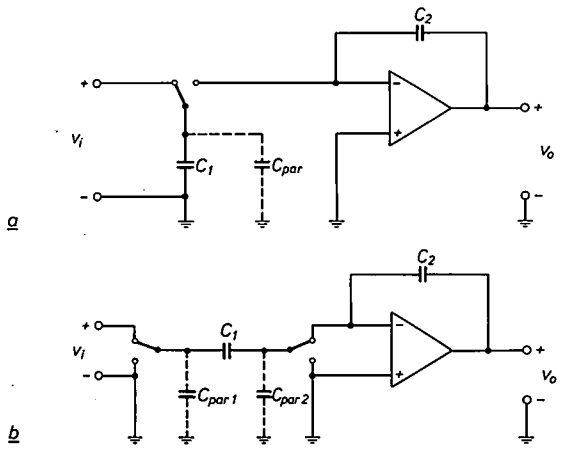

Fig. 14. When an SC integrator is fabricated as an integrated circuit, unintended capacitances C_{par} have to be taken into account. In some configurations these parasitics have much more effect on charge transfer from C_1 to C_2 than in others. The configuration of fig. 11*b* is not very good in this respect (*a*); the configuration of fig. 13*a*, *b*, *c* and *d* is much less affected by parasitics (*b*).

• The frequency behaviour of an analog integrator is approximated in various ways. This can be seen from the fact that each of the SC integrators has a different transfer function ($G(z)$ or $G^*(z)$).
• The sensitivity to parasitic capacitances, which are always present in practical circuits, differs considerably. If the sensitivity is high, a practical version of an SC-filter design can behave completely differently from the calculated version.

Of the SC integrators that we have considered so far, the ones from fig. 13*a* to *d* are the most interesting, since they are the least affected by parasitic capacitances [3][11]. We can explain this better with the aid of *fig. 14*. Here the parasitic capacitances that have to be taken into account in practical circuits have been included for two different integrator structures. In fig. 14*a* there is one such parasitic C_{par}, which is completely described by a departure from the desired value of the capacitance C_1. In fig. 14*b* there are two parasitics, but neither of them causes any trouble. The charge that is collected on C_{par1} during clock phase *1* is discharged to earth during clock phase *2* and does not reach C_2. Since the amplifier keeps the voltage difference between its two inputs as close to zero as possible, C_{par2} is connected to the same constant voltage during both clock phases; this parasitic will therefore also have no effect on the charge transfer from C_1 to C_2. It can be shown in a similar way that the integrator of fig. 13*e* is very sensitive to parasitic capacitance and therefore less suitable.

In the integrators of fig. 13*b* and *d* the input and output switches are in antiphase. In a cascade of such integrators the clocks ϕ_1 and ϕ_2 of adjacent stages alternate in role.

The SC integrators of fig. 13*b* and *d* are 'lossless discrete integrators' (LDIs) [12][13], and the SC integrator of fig. 13*e* is a 'bilinear integrator' (BI) [11]. In the LDI transformation $G^*(z)$ is obtained from $H(p)$ by substituting $K_1(z^{1/2} - z^{-1/2})/T$ for p and in the bilinear transformation $G(z)$ is obtained from $H(p)$ by substituting $K_2(z-1)/(z+1)T$ for p, where K_1 and K_2 are constants. These transformations are the only two known simple frequency transformations in which a direct relation can be found between the imaginary axis ($p = j\omega$) of the p-plane and the unit circle ($z = e^{j\omega T}$) of the z-plane and hence between the frequency responses before and after transformation. They are therefore highly suitable for 'translation' of analog filters into discrete-time filters. There are a number of clear differences between the two transformations, however [14]. One difference is that in the bilinear transformation the *entire* imaginary axis is mapped on to the unit circle, whereas in the LDI transformation there is a direct relation only if $|p| < |2K_1/T|$. In the first case the entire frequency response of the analog filter translates to the frequency band from 0 to $1/2T$ Hz in the discrete-time filter. In the second case the frequency behaviour of the analog filter below $K_1/\pi T$ Hz translates to the frequency band from 0 to $1/2T$ Hz in the discrete-time filter. The bilinear transformation is also widely used in the design of digital filters.

We can readily extend any SC integrator to make it into a circuit module that offers even more scope. This can be done in various ways; an integrator can for example be provided with more than one input (*fig. 15*), so that a linear combination of a number of signals can be integrated. For fig. 15:

$$V_o(z) = -\frac{C_1}{C_2}\frac{V_1(z)}{1-z^{-1}} - \frac{C_3}{C_2}\frac{V_2(z)}{1-z^{-1}},$$

where we have made use of the z-transforms of the input and output signals. The combination integrator/adder is also widely used. This is shown in *fig. 16* for the circuit of fig. 13*b*. Such a combination circuit can not only be used for integration but can also be used to 'weight' and add signals. For fig. 16 we have

$$V_o^*(z) = -\frac{C_1}{C_2}\frac{z^{-1/2}}{1-z^{-1}}V_1(z) - \frac{C_3}{C_2}V_2^*(z).$$

We have to remember here that we are considering the output signal during clock phase *2*. This signal contains a contribution from the preceding signal values of v_1 during clock phase *1* and from the current signal value of v_2^* during clock phase *2*. To emphasize this

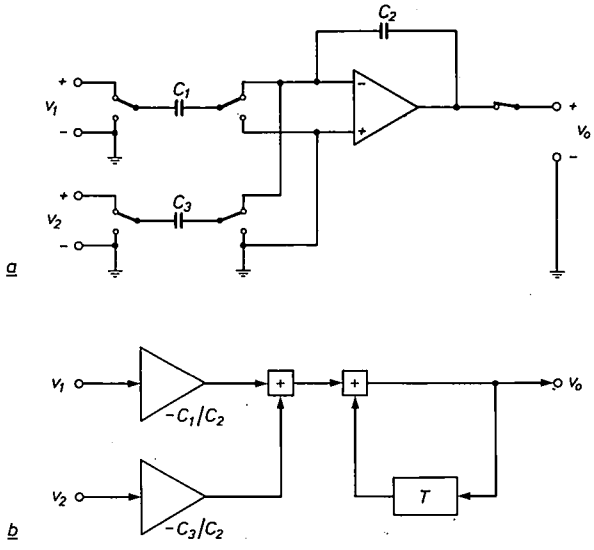

Fig. 15. An SC integrator can be extended in various ways to form a more complex module; here the integrator of fig. 13*a* has been extended by adding a second switched capacitor at the input. The input signal now consists of a linear combination of the signals v_1 and v_2 (*a*). This can clearly be seen from the discrete-time equivalent circuit (*b*).

[11] K. Martin and A. S. Sedra, Strays-insensitive switched-capacitor filters based on bilinear z-transform, Electron. Lett. **15**, 365-366, 1979.
[12] L. T. Bruton, Low-sensitivity digital ladder filters, IEEE Trans. **CAS-22**, 168-176, 1975.
[13] G. M. Jacobs, D. J. Allstot, R. W. Brodersen and P. R. Gray, Design techniques for MOS switched capacitor ladder filters, IEEE Trans. **CAS-25**, 1014-1021, 1978.
[14] M. S. Lee and C. Chang, Switched-capacitor filters using the LDI and bilinear transformations, IEEE Trans. **CAS-28**, 265-270, 1981.

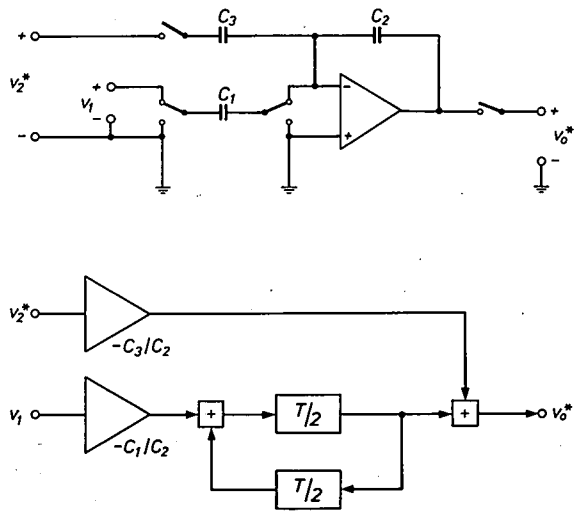

Fig. 16. The combination of a summation circuit or 'adder' and an LDI integrator with discrete-time equivalent circuit. Such circuits form a versatile module for making complicated SC filters (*a*). The discrete-time equivalent circuit gives a clear representation of the operation (*b*).

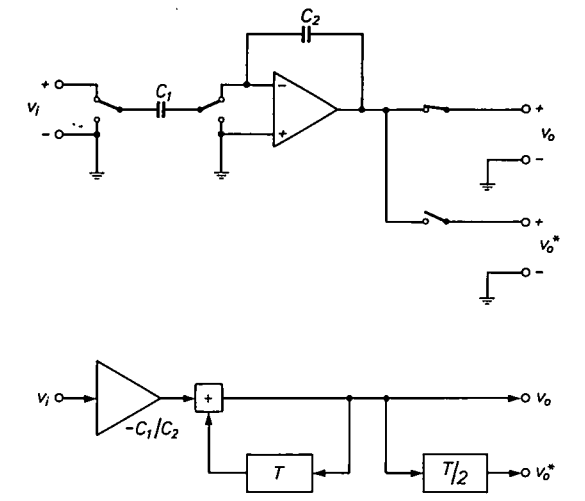

Fig. 17. In some cases the output signal of an SC integrator is used during both clock phases (*a*). This gives a combination of two simpler circuits, in this case from fig. 13*a* and 13*b*, as can clearly be seen from the discrete-time equivalent circuit (*b*).

we have provided C_3 with an input switch, but in practice there would not be a separate switch.

Another extension frequently found in practice is obtained if the output signal of an amplifier is used for further processing during both clock phases. A simple example is shown in *fig. 17*. In fact this represents a combination of two simpler circuits, for the circuit of fig. 17 can be considered as the combination of fig. 13*a* and *b*.

Continuous-time and discrete-time

So far we have placed the emphasis on the discrete-time nature of SC filters: we have shown how the filter operation can be described by considering only times separated by an integral number of sampling periods (or sometimes half-periods). This discrete-time approach is the natural method of describing SC filters built up from smaller constituent parts as a complete entity, e.g. so that the overall transfer function can be determined. One characteristic discrete-time property of SC filters is that the overall transfer function can be varied linearly with the clock rate (this is also true for digital filters). Another discrete-time aspect is the requirement that the bandwidth of the signals we wish to filter must satisfy the sampling theorem. They must contain no frequencies higher than half the sampling rate; otherwise there could be trouble from 'aliasing' in the SC filter. This usually requires a simple 'pre-filter'. In addition, the frequency spectrum of the sampled-data signal at the output of an SC filter is in principle unlimited in bandwidth. Therefore at that point we often have need of an analog filter that suppresses frequency components higher than half the sampling rate (a 'post-filter'), as in digital filters.

On the other hand, some of the things that can happen in an SC filter are impossible in true discrete-time filters. For example, an SC filter can contain closed loops in which there are no delay elements, yet some signal processing can take place. Also, in addition to various switched paths, an unswitched (and hence continuous-time) path can exist between input and output during one or both clock phases. In these cases a discrete-time approach gives an incomplete and sometimes unsatisfactory description of the filter.

Something related occurs if we wish to process the output signal of an SC filter as an analog signal (see the caption to fig. 2): here again the discrete-time description as an sampled-data signal is inadequate. In this case the exact waveform of the signal elements must be taken into account. For example, the amplitude characteristic $|G_D(\omega)|$ calculated by discrete-time methods must still be multiplied by a frequency function corresponding to this exact waveform. For the signals from fig. 2*b* and *c* this is a $\sin(x)/x$-function, with $x = \omega T/4$ and $x = \omega T/2$ respectively.

It is easily shown by Fourier analysis that a signal $b(t)$ consisting of a single rectangular pulse of width τ and height 1 has an amplitude spectrum given by

$$|B(\omega)| = \left| \frac{2\sin(\omega\tau/2)}{\omega} \right| = \tau \left| \frac{\sin x}{x} \right| ,$$

where $x = \omega\tau/2$.

It could be said that the discrete-time treatment of SC filters represents a 'macroscopic' approach, which confines itself to a description *at* (or really just after) the switching or sampling times. On the other hand,

there is also a 'microscopic' treatment, which is concerned with the electrical behaviour *between* the switching times. This kind of treatment is of use in the design of the components (switches, amplifiers) of SC filters and in analysing an SC filter with maximum accuracy. In these cases the electrical behaviour of an integrated circuit that is to be fabricated is calculated on a computer, with as many practical constraints as possible (such as parasitic elements and noise) taken into account. The resulting computer programs are fairly complicated [15], since the switched capacitors give rise to continuous-time *periodically varying* systems.

SC-filter design

Signal flow graphs

If we take an analog filter as the starting point, we have various ways of designing an SC filter built up from integrators. One of the most widely used procedures [13] is based on the derivation of a *signal flow graph* of the analog filter. A filter description of this type comes somewhere between the abstract description by means of a transfer function and the practical description in terms of a detailed circuit diagram. A signal flow graph is more detailed than the transfer-function description but more abstract than the circuit diagram. In addition it is a non-unique description: for any one filter there is an unlimited choice. For our purposes we require a signal flow graph that only includes integrating operations, additions and multiplications by a constant — the operations that can be performed by the SC modules of the preceding section. We shall illustrate the principle of working with signal flow graphs with the aid of *fig. 18*. This gives a diagram of a simple analog filter with the transfer function

$$H(p) = \frac{V_o(p)}{V_i(p)} = \frac{1}{p^2LC + pCR + 1}.$$

We can also describe this filter by a number of equations that each represent at the most a single integrating operation (corresponding to a multiplication by $1/p$):

$$V_1 = V_i - RI_1, \qquad I_1 = \frac{1}{pL}(V_1 - V_2),$$

$$V_2 = \frac{I_1}{pC}, \qquad V_o = V_2.$$

These equations can be represented graphically in the form of the signal flow graph of fig. 18*b*. By introducing an arbitrary scaling resistance R_s we can put $I_1 = U_1/R_s$, where U_1 is a fictitious voltage proportional to I_1. The filter of fig. 18*a* is then described by:

$$V_1 = V_i - \frac{R}{R_s}U_1, \qquad U_1 = \frac{R_s}{pL}(V_1 - V_2),$$

$$V_2 = \frac{U_1}{pR_sC}, \qquad V_o = V_2.$$

The nodes of the associated signal flow graph represent voltages only (fig. 18*c*).

The dimensions of the quantities indicated by the nodes of a signal flow graph are not of essential interest. The treatment above was based upon voltages and thus we found a scaling factor R_s with the dimensions of *resistance*. If it had been based upon currents, we would have found a scaling factor with the dimensions of *conductance*.

In principle the design of the SC filter is now complete: each of the integrating operations is performed by an appropriate SC integrator, the multiplications by a constant are obtained by a correct choice of capacitance ratio and the summations are produced by the correct interconnections. If we replace the integrating operations in the signal flow diagram by the corresponding discrete-time block diagrams of the SC

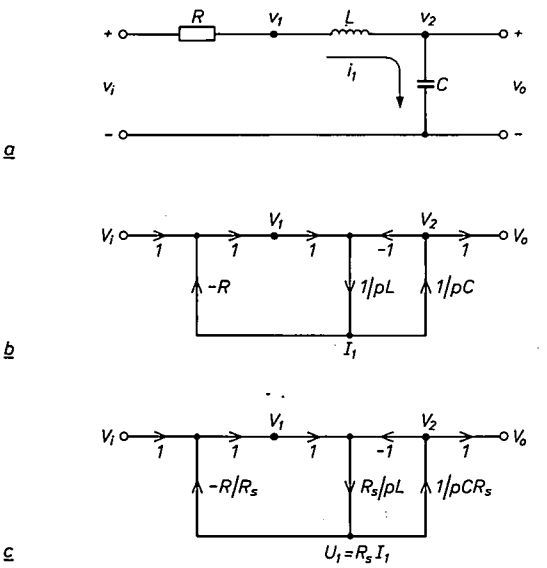

Fig. 18. Any filter can be represented in many ways by a signal flow graph. A simple analog filter of the 2nd order (*a*) is represented here by a signal flow graph in which the Laplace transforms of the actual voltages and currents can be identified (*b*) and as a signal flow graph with voltages alone (*c*). R_s is a scaling factor with the dimension of resistance. The signal flow graphs are chosen in such a way that all the frequency-dependent operations correspond to integration (multiplication by $1/p$) and can therefore readily be carried out by SC integrators.

[15] See for example the following articles:
Y.-L. Kuo, M. L. Liou and J. W. Kasinskas, An equivalent circuit approach to the computer-aided analysis of switched capacitor circuits, IEEE Trans. **CAS-26**, 708-714, 1979;
R. Lücker, Frequency domain analysis of switched-capacitor circuits using *z*-domain transfer function evaluation, Arch. Elektron. & Übertragungstech. **36**, 383-392, 1982.

modules, we have immediately a complete discrete-time model of the practical SC filter at our disposal.

Signal flow graph of viewdata filter

We now return to the doubly terminated *LC* filter from fig. 6 that satisfies all the specifications of the viewdata filter. This filter is shown again in *fig. 19a*, with a number of currents and voltages now introduced. The filter can be completely described by the set of equations [16]:

$$V_2 = \frac{1}{pC_2}\left[\frac{1}{R_1}(V_i - V_2) - I_3\right] \quad \text{(a)}$$

$$I_3 = \frac{1}{\varrho}\left[I_5 + \frac{1}{pL}(V_2 - V_4)\right] \quad \text{(b)}$$

$$V_4 = \frac{1}{\varrho}\left[V_2 + \frac{1}{pC}(I_3 - I_5)\right] \quad \text{(c)}$$

$$I_5 = I_7 + \frac{V_4 - V_6}{pL_6} \quad \text{(d)}$$

$$V_6 = \frac{1}{pC_6}(I_5 - I_7) \quad \text{(e)}$$

$$I_7 = I_9 + \frac{V_8}{pL_8} \quad \text{(f)}$$

$$V_8 = V_4 + \frac{1}{p}\left(-\frac{1}{C_{78}}I_7 + \frac{1}{C_8}I_9\right) \quad \text{(g)}$$

$$I_9 = V_{10}\left(\frac{1}{R_2} + \frac{1}{pL_{10}}\right) \quad \text{(h)}$$

$$V_{10} = V_8 + \frac{1}{p}\left(\frac{1}{C_8}I_7 - \frac{1}{C_{89}}I_9\right) \quad \text{(i)}$$

where $\varrho = 1 + L_3/L_4$, $C = C_4/(\varrho - 1)$, $L = -L_5 = L_3L_4/(L_3 + L_4)$, $C_{78} = C_7C_8/(C_7 + C_8)$ and $C_{89} = C_8C_9/(C_8 + C_9)$. The corresponding signal flow graph is shown in fig. 19*b*, in which we again represent each current I_j as a fictitious voltage U_j by multiplying by a freely chosen resistance R_s. To explain our design procedure more clearly we have selected a part of the filter, the fourpole consisting of L_3, L_4, L_5 and C_4 (fig. 19*a*). The electrical behaviour of this fourpole is completely described by the equations (b) and (c) above. The corresponding part of the signal flow graph is shown in colour in fig. 19*b*. This contains two integrating operations, both included in a single loop; this pattern can be found repeated many times in the signal flow graph.

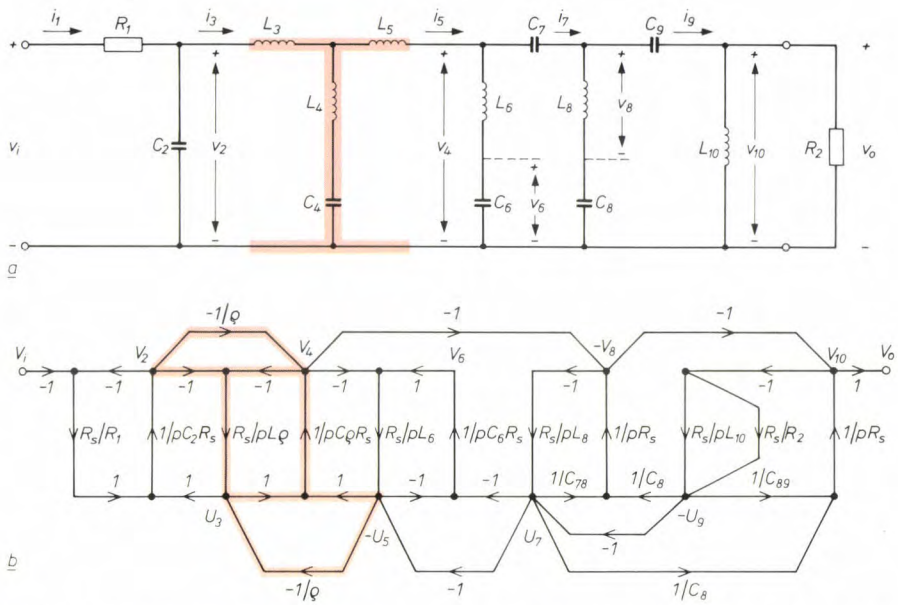

Fig. 19. The viewdata filter of fig. 6, but now with currents and voltages shown (*a*), so that a signal flow graph can be set up (*b*). In the signal flow graph every current I_j is shown as a fictitious voltage $U_j = I_jR_s$. The value of R_s is fixed, but can in principle take any value. As an aid to the explanation the fourpole $L_3L_4L_5C_4$ in the filter circuit and the corresponding part of the signal flow graph are shown coloured.

Choice of SC integrator

The determination of the signal flow graph brings the design of the SC filter to an advanced stage. A crucial decision still has to be made, however: the choice of the type or types of SC integrator to be used. Earlier in this article we encountered a number of basic types, and we considered the most important differences (approximation of the analog integrator and sensitivity to parasitic capacitances). This led to a preference for the integrators of fig. 13*a* to *d*. How can we narrow the choice further? The necessary criteria can be derived from the signal flow graph: let us examine fig. 19*b* again. We find that the pattern of a closed loop containing two integrators is repeated many times (the coloured part contains such a loop).

Two conditions must be satisfied for the realization of such loops:

- the overall transfer function of all the branches of an (open) loop must be negative (this is related to the required stability of the circuit);
- the input switches of either of the two integrators must be capable of acting as the output switch of the other one (if not, the effect is as if the integrators are connected by two switches in series that are never both 'on' at the same time, so that no closed loop can exist).

These conditions allow of only two options:

- a closed loop contains one integrator as in fig. 13*a* and one as in fig. 13*c*;
- a closed loop contains one integrator as in fig. 13*b* and one as in fig. 13*d*, with the role of the clocks ϕ_1 and ϕ_2 exactly interchanged for the two integrators.

In both cases the overall transfer function for the (open) loop is

$$G_L(z) = \frac{-Kz}{(z-1)^2},$$

where K is a positive constant whose value is determined by capacitance ratios.

In converting an analog filter of transfer function $H_{tot}(p)$ into an SC filter of transfer function $G_{tot}(z)$ a complication arises: since at least two kinds of integrators are required, the relation between $H_{tot}(p)$ and $G_{tot}(z)$ is not as simple as it might have appeared so far. For every closed loop containing *two* integrators the transfer function is $G_L(z)$ as given above. Now for both of the cases quoted we can interpret this as the LDI transformation of a combination of two continuous-time integrators. At the beginning and end of the signal flow graph, however, a special situation arises: there is always one loop with only *one* integrator (this is associated with the real terminating impedances R_1 and R_2). If we were to realize this integrator in the way shown in fig. 13*a* or *c*, the LDI-transformation rule would not apply to this part of the signal flow graph. On the other hand, we cannot use the LDI circuit of fig. 13*b* or *d*, since there would never then be a closed loop: the input and output switches of an LDI are always out of phase. This provides an interesting problem, for which various solutions exist [17][18]. Sometimes, however, they yield a slight modification of the transfer function. If this is unacceptable, a filter designer always has the option of abandoning the signal-flow-graph approach and using another design method in which this problem does not arise [3][11][19].

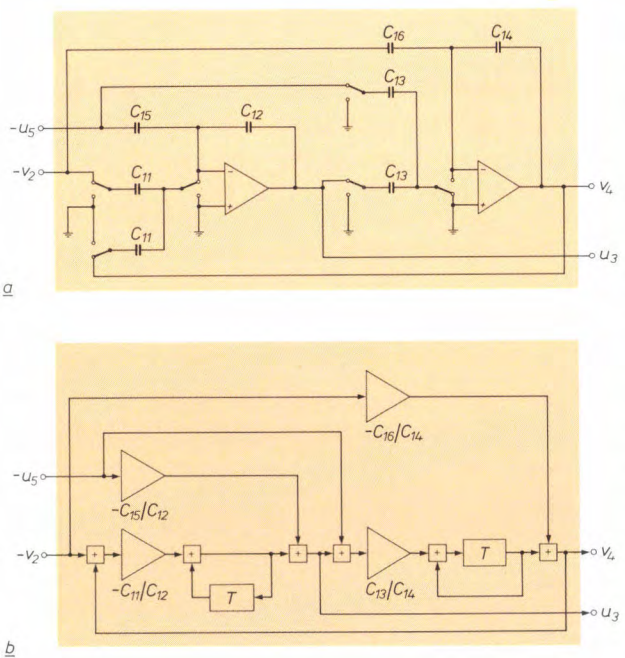

Fig. 20. An SC circuit derived for the coloured part of fig. 19 with the aid of SC integrators (*a*) and a corresponding discrete-time equivalent circuit (*b*).

In our viewdata filter we mainly use the integrators of fig. 13*a* and 13*c*. As an illustration we show in *fig. 20a* what the SC circuit derived for the coloured part of fig. 19 looks like. The capacitances in fig. 20*a* and the quantities in fig. 19*b* are related as follows:

$$\frac{C_{15}}{C_{12}} = \frac{C_{16}}{C_{14}} = \frac{1}{\varrho}, \quad \frac{C_{11}}{C_{12}} = \frac{R_s T}{L\varrho}, \quad \frac{C_{13}}{C_{14}} = \frac{T}{CR_s\varrho},$$

where $1/T$ is again the switching frequency of the capacitors. We can give a fully discrete-time model for fig. 20*a*; this is shown in fig. 20*b*.

SC-filter components

The most important components used in the construction of an SC filter are switches, capacitors and amplifiers. We shall now give some attention to the realization of each of these components.

The switches

As we have seen, an SC filter contains many change-over switches, each formed from two on/off switches (fig. 8). These on/off switches are operated by two clock signals ϕ_1 and ϕ_2 (fig. 9). Each on/off switch can consist of a single NMOS transistor, a single PMOS transistor or a combination of both. In comparison with a PMOS transistor an NMOS transistor has a lower resistance in the conducting state, but (in the fabrication process that we used) it also has a higher parasitic capacitance. The combination of both types

[16] B. Huber, J. Kunze, R. Lücker, A. H. M. van Roermund and P. M. C. Coppelmans, Design of a switched-capacitor filter for Viewdata modems, Arch. Elektron. & Übertragungstech. **36**, 141-147, 1982.
[17] R. W. Brodersen, P. R. Gray and D. A. Hodges, MOS switched-capacitor filters, Proc. IEEE **67**, 61-75, 1979.
[18] P. Lutz, Real terminations of SC-filters using LDI-Integrators, Frequenz **35**, 93-95, 1981.
[19] S. O. Scanlan, Analysis and synthesis of switched-capacitor state-variable filters, IEEE Trans. **CAS-28**, 85-93, 1981.

gives a switch that has fewer limitations to signal voltage swing, but it requires two clocks of opposite polarity and has an even higher parasitic capacitance. In our viewdata filter we use PMOS switches.

The capacitors

The frequency-dependent behaviour of an SC filter is primarily determined by *ratios* of capacitances. It is very important to keep this in mind at the design stage. We base our design on a 'unit capacitor', which represents the smallest capacitance used. Larger capacitances are obtained by stringing unit capacitors together (*fig. 21a*). An error that is essentially proportional to the *periphery* of a capacitor will now also be proportional to the *area* and hence its capacitance. In

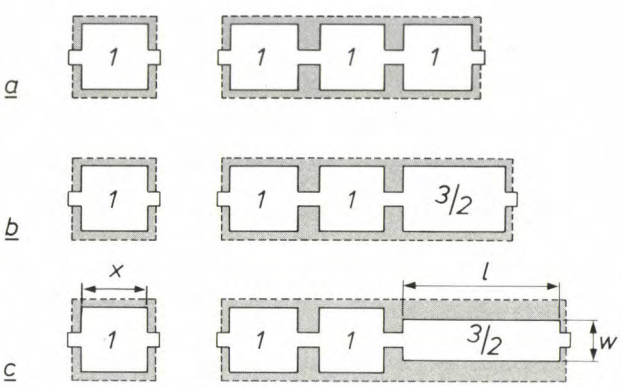

Fig. 21. To obtain accurate capacitance *ratios*, in spite of small dimensional errors in the fabrication process, larger capacitances are built up by stringing together a row of unit capacitors (*a*). For non-integral ratios, such as 1:3.5, one of the sub-capacitors is given a different shape. Even better results follow if the ratio of the periphery to area is always kept constant. This can be done by choosing length l and breadth w suitably (*c*). If the side of a unit capacitor is equal to x, then in our example $w = 0.634x$ and $l = 2.366x$. The top plate of each capacitor is represented by a continuous line, the lower plate by a dashed line.

this way certain variations in the etching process in the production will give a change in the *absolute values*, but not in the *ratio* of two capacitances. Since not all the capacitance ratios will generally correspond to an integer, we cannot pursue this system to the utmost. A ratio of 1:3.5, for example, can be obtained as shown in fig. 21*b*. A better solution, however, is the one shown in fig. 21*c*, where we make a capacitor with a relative capacitance of 3.5 by combining two unit capacitors with a capacitor of relative capacitance 1.5 that has the same ratio of periphery to area as the unit capacitor. This approach gives a capacitor that is almost unaffected by the production variations mentioned earlier.

Another cause of error is the occurrence of parasitic capacitances: in an integrated capacitor these appear both between the upper plate and the substrate and between the lower plate and the substrate. The first can be largely eliminated by making the upper plate slightly smaller than the lower plate; this can be seen clearly in fig. 21. The effect of both kinds of parasitic capacitance can be greatly reduced at the design stage by ensuring that both capacitor plates are switched only between earth and a low-impedance voltage source or between two points of equal voltage (fig. 14*b*).

To make the chip on which an SC filter is fabricated as small as possible, we should keep both the *ratio* and the *absolute values* of the capacitances small. We can influence the ratios through the shape of the signal flow graph, the value of the scaling resistance R_s and the magnitude of the sampling rate $1/T$. However, the signal flow graph and the scaling resistance also determine the dynamic range of the signals in the filter; similarly there are some constraints on the choice of the sampling rate. There is a lower limit to the absolute value of the capacitances, because the unit capacitor must have at least some minimum dimensions to ensure a certain accuracy. A high absolute value for the capacitances has the advantages of insensitivity to parasitics, noise, interference from clock signals and off-set voltages, but high absolute values are also associated with high power dissipation and slower circuits. We see that there are various conflicting factors, which have to be set against one another in the design process.

The capacitance per unit area depends upon the fabrication process. In our integrated viewdata filter we used capacitors with a capacitance of 340 pF/mm^2.

The amplifiers

The most critical component is the amplifier. This determines to a great extent the specifications that a particular filter can or cannot meet. The amplifiers that are used in SC filters have a number of special features, so from now on we shall call them SC amplifiers. An SC amplifier always has a capacitive load, for example, and never a purely resistive load. Since a capacitance has a high impedance at low frequencies, it is not necessary to use an output buffer, which would have an undesirable effect on the noise performance and stability of the amplifier. Another special feature is that the output voltage of an SC amplifier only has to reach the correct value at the instant when the input switch of the following stage is switched to 'on'. After any change in input voltage, the SC amplifier therefore has a certain time available in which the output voltage can settle to the corresponding value (*fig. 22*).

Since we have fabricated our integrated viewdata filter by a LOCMOS process [20], we can build up an SC amplifier from NMOS and PMOS transistors. The

result is shown in *fig. 23*. The complete amplifier consists of an input stage that operates as a differential amplifier and a final stage formed by a PMOS transistor and an NMOS transistor, with the NMOS transistor acting as a constant-current source. The compensation that produces the desired gain characteristic takes place between the two stages. It is realized on the chip by a Miller capacitance C_M in series with a resistance formed by the combination of a PMOS transistor and an NMOS transistor [21].

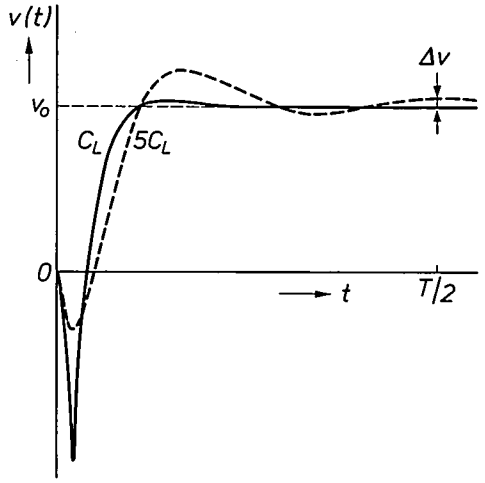

Fig. 22. Typical variation of the output voltage $v(t)$ of an SC amplifier as a function of time for two different capacitive loads C_L and $5C_L$. It can clearly be seen that the load of $5C_L$ is too large for a stabilized final value v_o to be reached within the desired half clock period $T/2$: at $t = T/2$ there is still a difference Δv.

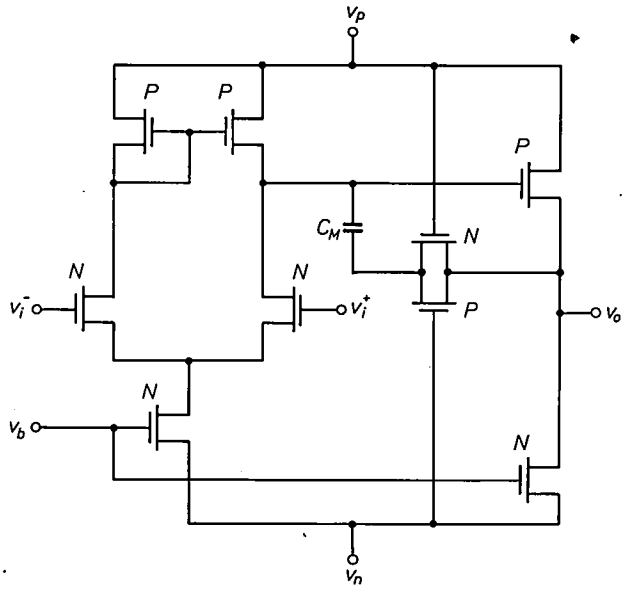

Fig. 23. SC amplifier for the integrated SC filter for viewdata. A CMOS process (CMOS = complementary MOS) is used in the fabrication, so that both PMOS transistors (*P*) and NMOS transistors (*N*) can be included. The amplifier consists of a differential stage with inputs v_i^- and v_i^+ and a final stage with output v_o. Between the two stages compensation is provided by a Miller capacitance C_M and a resistance formed by the combination of an NMOS and a PMOS transistor. v_p positive supply voltage, v_n negative supply voltage, v_b bias voltage.

In the ordinary way the Miller capacitance would provide direct negative feedback from the output to the input of the second stage. Since this output has a high impedance, the Miller capacitance then also provides feedforward. This has a significant and undesirable effect on the performance of the amplifier (more phase shift). We have corrected this by including a resistance in series with the Miller capacitance.

The area taken up by this amplifier in the integration is about 0.1 mm^2 and for most applications its power dissipation is between 0.1 and 5 mW. The exact dimensioning of the SC amplifier is closely dependent on the surrounding circuits. A large capacitive load requires a relatively large output transistor, for example, which also dissipates a relatively high power.

Integrated viewdata filter

In the previous section we saw that too large a capacitive load can upset the proper operation of an SC amplifier. The requirements that the amplifiers have to meet can become less exacting as this capacitive load is reduced. Now it is found that a direct realization of the signal flow graph of fig. 19*b* as an SC filter is not particularly satisfactory in this respect; the trouble seems to be mainly caused by the paths connecting points that are not directly adjacent and having a transfer function of -1. This is because these paths are formed with the aid of a summation circuit (see fig. 16) with $C_3 = C_2$. Consequently there is a large capacitive load, especially for the *preceding* SC amplifier. It would therefore be preferable to reduce the ratio C_3/C_2. This is done in the integrated filter by first making a number of changes [7] in the signal flow graph (*fig. 24*). Although the result looks more complicated than the original signal flow graph, the number of integrating operations remains the same and the maximum summation ratio has been reduced from -1 to -0.178. Furthermore, this is accompanied by a reduction in the total capacitance contained in the filter of no less than 30%. A detailed circuit diagram of the integrated viewdata filter is shown in *fig. 25*. Finally, *fig. 26* is a photograph of the integrated SC version of the viewdata filter. The separate components are clearly recognizable in the photograph; they

[20] See the article by B. B. M. Brandt *et al.* [9].

[21] W. C. Black Jr., D. J. Allstot and R. A. Reed, A high performance low power CMOS channel filter, IEEE J. SC-15, 929-938, 1980.

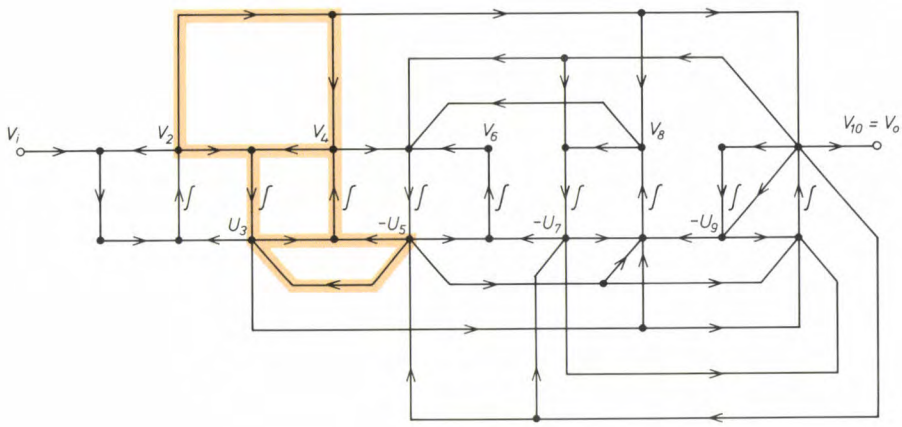

Fig. 24. Modified version of the signal flow graph of fig. 19*b*, in which the transfer between non-adjacent nodes has been minimized. This enabled the maximum capacitive load on the SC amplifiers to be reduced by a factor of about six, greatly easing the conditions that these amplifiers have to satisfy. For simplicity the exact values of the transfer between all the nodes have been omitted. Although this signal flow graph looks more complicated than the original one, the number of integrating operations ($\int$), and hence the number of SC amplifiers, remains the same. Moreover, the total capacitance required is 30% smaller.

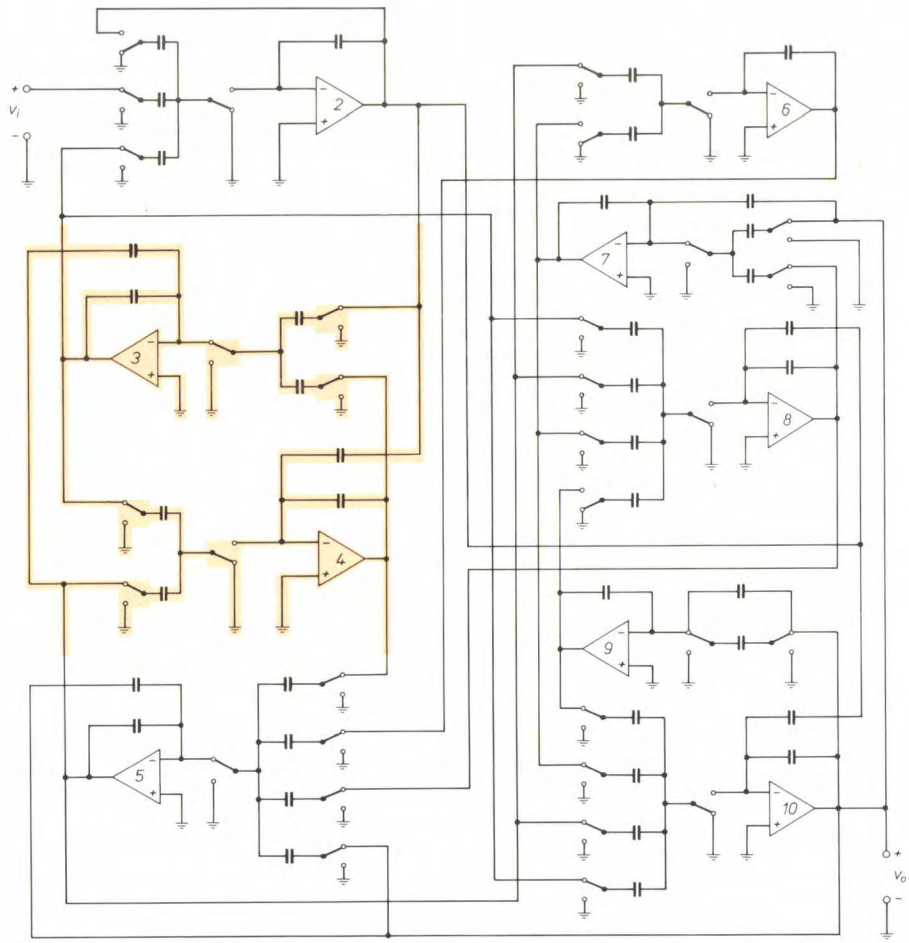

Fig. 25. Detailed circuit diagram of the viewdata filter corresponding to the signal flow graph of fig. 24. Each integrating operation is performed with the aid of an SC module, which is characterized by a low sensitivity to parasitic capacitance. The number of each amplifier corresponds to the subscript of the output voltage in the previous figure. We should also point out that some of the amplifiers (Nos *2*, *6* and *8*) form part of more than one type of integrator, since the input capacitors are switched in more than one way. The coloured part again corresponds to the coloured part in previous figures.

include the strings of unit capacitors, the long 'residual' capacitors and ten SC amplifiers. The measured attenuation and group-delay characteristics are very close to the calculated characteristics for the SC filter: the deviation from the attenuation characteristic in the passband is smaller than 0.05 dB and never more than 3 dB in the stopband (at 430 Hz); the maximum deviation for the group delay is 12 μs. The area of the integrated circuit (not including bonding pads) is about 3.3 mm^2. The power dissipation is about 10 mW at a supply voltage of 10 V. Recent developments in SC amplifier design and IC technology indicate that the required power can be reduced even further, to about 1 mW.

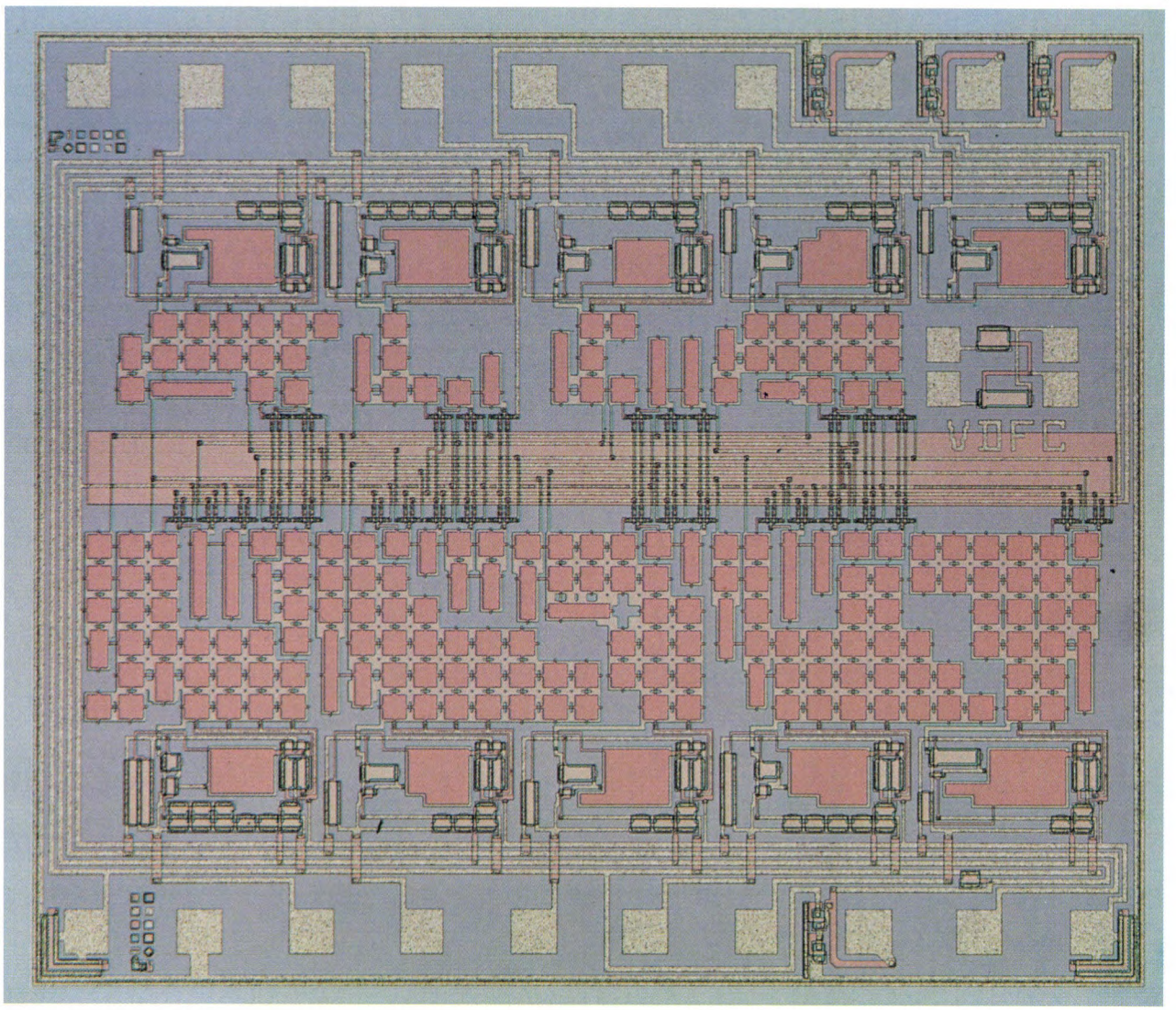

Fig. 26. The integrated viewdata filter. The strings of unit capacitors can clearly be seen on either side of the interconnection pattern, which is almost central. At the top and bottom of the picture there are five SC amplifiers, readily visible because of the large Miller capacitors. Nine of these amplifiers correspond to the amplifiers of fig. 25. The tenth (top right, close to the letters VDFC) is used for testing only. The area of the chip is about 3.3 mm^2.

Summary. In the last few years switched-capacitor filters (or 'SC filters') have been found very suitable for making fully integrated electrical filters. Since the signals in these filters are discrete in time but continuous in amplitude ('sampled-data signals'), the filters behave in some ways like analog filters and in others like digital filters. SC filters consist of switches, capacitors and amplifiers. All these components are readily integrated in MOS technology. The starting point for the design can be a doubly terminated *LC* filter. By setting up a signal flow graph in which the only frequency-dependent operations are integrations, a filter built up from SC integrator/adder modules can be derived fairly directly. The method gives a filter on a single chip, with very small dimensions, low parameter sensitivity and low power consumption. No trimming is necessary in production, temperature effects are very low, the circuit can be combined with others on the same chip and analog signals can be processed without analog-to-digital conversion. The chief limitation of SC filters is the frequency range in which they can be used to advantage (up to about 100 kHz at present). A number of the above aspects are illustrated with the aid of an integrated viewdata filter, fabricated in a LOCMOS process. Its area is about 3.3 mm^2. The power dissipation is about 10 mW at a supply voltage of 10 V.

Device for stripping protective coatings from glass fibre

Glass fibres for light transmission must not only have excellent optical properties; they must also be mechanically strong. Their strength is determined mainly by the quality of the fibre surface. Any cracks in the surface may propagate into the interior especially when the fibre is in tension, resulting eventually in fracture. The chance of damage to the surface should therefore be kept to a minimum, and during the drawing process a plastic protective coating is applied to the fibre under dust-free conditions before it is wound on to the reel.

The properties and nature of the coating are also extremely important. The optical losses introduced by local mechanical pressure of the coating on the fibre must be kept as low as possible. The coating must not be so thick and stiff that it limits the minimum radius of curvature. The coating must also adhere firmly to the fibre, so that under flexure, for example, the fibre will not protrude from the end. Depending on the type of fibre and its application various types of plastic can be used: silicones, UV-curing epoxy-acrylates, Saran and polyamide imide (PAI).

For joining the glass fibres together, e.g. by hot splicing [1], and for joining them to a connector, the fibres have to be broken off smoothly and accurately at right angles to the axis [2]. In practice this is only possible after first removing the coating at the place where the break is to be made. The methods used until now have been rather empirical, and each has had its disadvantages: heating in a flame causes sooting up, the use of a cutter or pincers may damage the fibre and removal by etching generally requires the use of highly reactive chemicals. There is therefore a need for a simple and reliable device for stripping various types of coatings from all kinds of glass fibres.

A device of this description has recently been developed at Philips Research Laboratories. The stripping is effected by a combination of heating and the application of a very small force. This device removes the coating automatically over lengths ranging from a few millimetres to more than half a metre on all known combinations of coating and glass fibre. The design of the device is shown schematically in *fig. 1*. A roller driven by a small electric motor feeds the glass fibre into a furnace. The furnace contains a plug with a spark-machined hole in it, of diameter slightly greater than the diameter of the uncoated fibre. The small hole in the plug is lined up with the guides in the drive unit with the aid of a microscope stage. The fur-

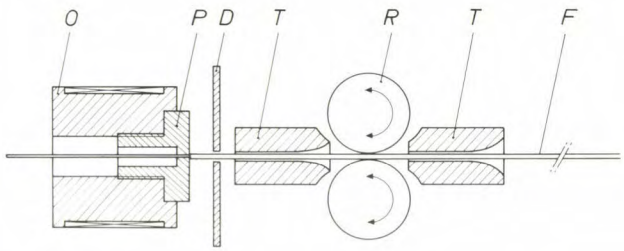

Fig. 1. Diagram of device for stripping protective coating from a glass fibre. *O* furnace. *P* plug. *D* metal diaphragm. *T* Teflon guide. *R* drive roller. *F* glass fibre.

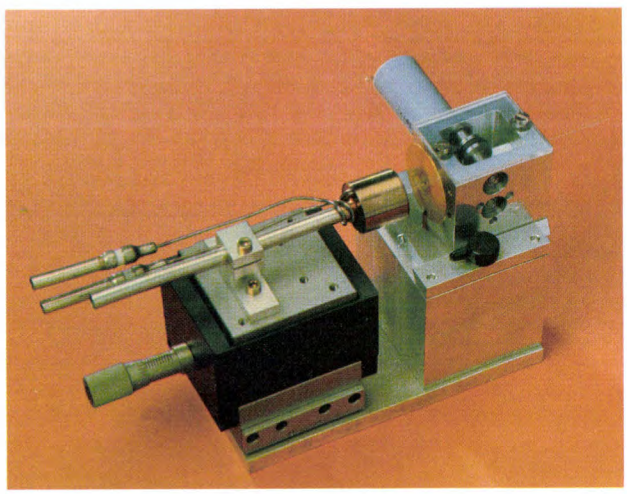

Fig. 2. Prototype of the device, developed in cooperation with C. J. G. Verwer of Philips General Design Office and J. W. T. Nent of the Mechanical Engineering Department of Philips Research Laboratories. The trials on this device were made in cooperation with F. A. Coolen.

[1] A. J. J. Franken, G. D. Khoe, J. Renkens and C. J. G. Verwer, Philips Tech. Rev. **38**, 158, 1978/79.

[2] W. J. J. van Hoppe, G. D. Khoe, G. Kuyt and H. F. G. Smulders, Philips Tech. Rev. **37**, 89, 1977. See also Philips Tech. Rev. **39**, 245, 1980.

[3] Quartz-glass fibres in which the core has a diameter of about 50 μm and a refractive index decreasing gradually from the centre outwards are intended for telecommunications with a semiconductor laser; see for example Philips Tech. Rev. **36**, 177-216, 1976. Quartz-glass fibres in which the refractive index is constant over the core diameter of about 100 μm are intended for short-distance transmission with a light-emitting diode as light source. Soft-glass fibres are also used in this application and in various kinds of complicated 'bundles' of fibres.

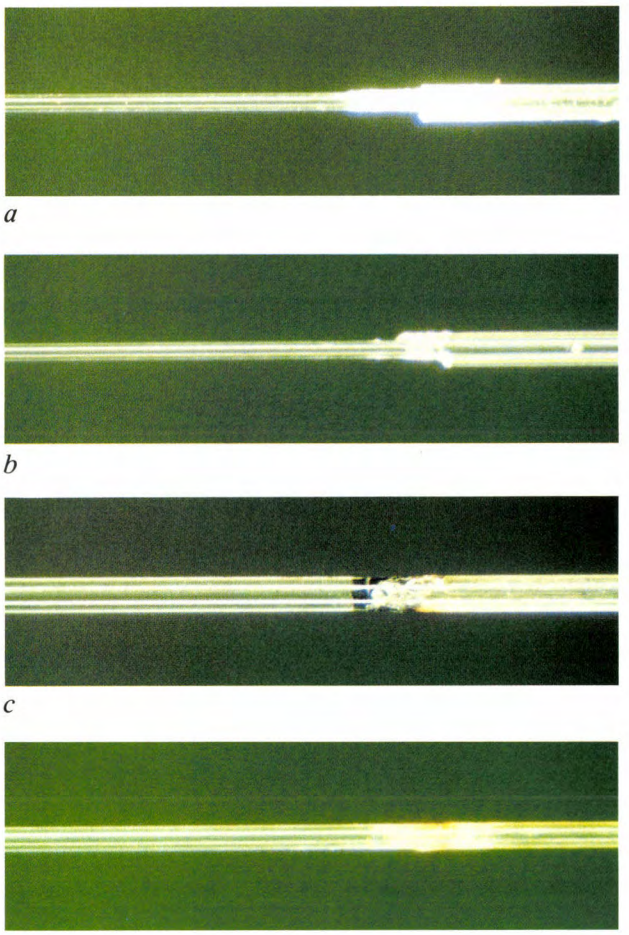

a

b

c

d

Fig. 3. Microscope photographs of glass fibres whose protective coating has been partially removed with our device. *a*) Quartz-glass fibre (diameter 120 μm) with a silicone coating of about 30 μm. *b*) Quartz-glass fibre (diameter 120 μm) with a UV-curing acrylate coating of about 30 μm. *c*) Soft-glass fibre (diameter 250 μm) with a Saran coating of about 10 μm. *d*) Soft-glass fibre (diameter 170 μm) with a PAI coating of about 5 μm.

nace is electrically heated to between 300 and 500 °C, depending on the type of protective layer. When the fibre is driven through the hole in the plug, the protective coating is stripped away and remains on the right of the plug. A metal diaphragm prevents the Teflon guide close to the furnace from becoming too hot. *Fig. 2* shows a photograph of a prototype of our device.

The first results are promising for both quartz-glass and soft-glass fibres [3]. *Fig. 3* shows four microscope photographs of glass fibres with a partially removed protective layer. Thick coatings (about 30 μm) of silicones (fig. 3*a*) and UV-curing acrylates (fig. 3*b*) can also be removed easily. A silicone coating comes away from the fibre in the form of shavings, while an acrylate layer crumbles and scatters in all directions. In both cases a clean surface is immediately revealed. Materials such as Saran (fig. 3*c*) and PAI (fig. 3*d*), which are applied in thin coatings (5 to 10 μm), leave a slightly charred film on the fibre. A clean surface can quickly be obtained, however, by rubbing the fibre with a piece of cotton wool.

A. P. Severijns
P. J. W. Severin

A. P. Severijns and Dr P. J. W. Severin are with Philips Research Laboratories, Eindhoven.

A metal/ceramic diagnostic X-ray tube

W. Hartl, D. Peter and K. Reiber

As early as 1896 the American physicist R. W. Wood put forward a proposal that an X-ray tube with a swinging cathode should be rotated about its axis during use, to prevent overheating of the glass envelope by cathode rays [*]. This idea can be considered as the origin of the rotating-anode X-ray tube, a type now widely used in X-ray diagnostics. A precursor of the well-known Philips Rotalix X-ray tubes was demonstrated by A. Bouwers as long ago as 1929 [**]. Since that time the performance of the Rotalix tubes has been continuously improved. An important step in this process is the recent development of the 'Super Rotalix Ceramic' diagnostic tube by the Philips firm C.H.F.Müller of Hamburg. Metal/ceramic technology is applied in this tube. The anode is energized by means of an induction motor of a new design, based on studies made by E. M. H. Kamerbeek of Philips Research Laboratories, Eindhoven.

Introduction

In conventional medical X-ray diagnostics an image of the part of the human body to be investigated is made by means of shadowgraph projection. This image is produced on a screen sensitive to X-rays. To avoid blurring due to penumbra the radiation source must be of small dimensions, preferably no larger than a few tenths of a millimetre. The electrons that strike the anode of the X-ray tube must therefore be concentrated as closely as possible to a single point (the focus). Since the objects (e.g. the heart or stomach) are often moving, the exposure time must be short — a few thousandths to a few tenths of a second. Nevertheless, the tube must deliver in this short time sufficient radiation energy to produce adequate photographic density on the X-ray-sensitive film or to liberate sufficient electrons at the input-screen photocathode of an X-ray image-intensifier tube [1]. The energy efficiency of the conversion of electrons into X-radiation in the tube is unfortunately less than 1%: more than 99% of the energy so briefly applied to the tube is dissipated as heat in the material of the anode. To prevent the anode material from melting during exposure, the anode is made to rotate rapidly. The dissipated heat is thus spread around a circular track on the anode surface.

Dr W. Hartl, Dipl.-Phys. D. Peter and Dr K. Reiber are with C.H.F.Müller, Philips GmbH, Hamburg, West Germany.

Although the principle of the rotating anode seems simple, there are many difficulties in practice. The bearings that support the rotating anode (now always ball bearings) are mounted in vacuum and cannot be lubricated with oil or grease. The anode must be driven by an induction motor, with the stator outside the tube because of the gas emission from the insulating material. The 'air' gap of the motor must be larger than would be required for an optimum design, since it has to include the glass wall of the envelope and the rotor is at anode potential, half the value of the high-voltage tube supply. The rotating anode cannot be cooled with a coolant, so that the heat in the anode must be removed by radiation. The anode temperature therefore becomes very high, which means that the anode material must meet some very special requirements. The bearings also become very hot. Partly because of the absence of lubrication they have a very short life, and therefore the anode is only rotated during the brief exposure. Usually it is run up to speed (accelerated) and brought to rest again (decelerated) for each exposure. The anode must be accelerated extremely rapidly — in a second or less — to avoid unnecessary delay for the radiologist operating the

[*] O. Glasser, Wilhelm Conrad Röntgen und die Geschichte der Röntgenstrahlen, Springer, Berlin 1959.

[**] A. Bouwers, Eine Metallröntgenröhre mit drehbarer Anode, Verhandl. d. D. Röntgen-Ges. **20**, 103-106, 1929.

equipment. The focus must also be extremely stable geometrically: the point source must remain as accurately as possible at the same place during a series of exposures.

In the successive generations of the Philips Rotalix tubes solutions have been found for many of the problems mentioned above. The ball bearings are lubricated with a suitable metal such as lead or silver. (The tube current can then be supplied to the anode via the bearings.) The anode is made of a material with a high melting point: tungsten or a tungsten alloy.

Until recently the various types of Rotalix X-ray tubes were always constructed in glass/metal technology. The advantages and disadvantages of this approach have been described in a previous article [2]. An attendant disadvantage of this technology is that at the high power levels in the rotating-anode tubes tungsten from the cathode filament and the anode is deposited on the glass envelope, where it eventually forms a conducting layer. In the last version but one, the Super Rotalix Metal (SRM) tube, the glass envelope is largely replaced by metal at earth potential. The problems that were caused by electric charge on the glass envelope and the deposition of tungsten on the glass were thus mainly avoided. The image contrast was also greatly improved, mainly by the removal of secondary electrons. Other disadvantages inherent in glass/metal technology, such as the fragility and the need for oil insulation between tube and shield, were still present in the SRM tube. Also, the SRM tube with shield is longer than its predecessor in its shield.

As will be explained later, the peak power that can be applied as a pulse to a rotating-anode tube is proportional to the anode velocity at the focus. For this reason the speed of rotation and the external diameter of the anode have been continuously increased through the years in the development of tubes of higher power. In the Super Rotalix (SRO) tube, for example, the predecessor of the SRM tube, the frequency of the supply voltage for the motor was increased from 50 to 150 Hz.

In the recent development of the Super Rotalix Ceramic (SRC) tube, which is the subject of this article, there were two main objectives: to overcome the difficulties of the glass/metal technology by only using metal and ceramic, and to improve the performance by using an anode with a larger external diameter (120 mm, instead of 100 mm in the SRM tube and 90 mm in the SRO tube). The peak power that can be delivered to the tube for a short time has been increased by 40% with respect to the SRO tube. *Fig. 1* shows the three types of tube. Fig. 1*a* shows the SRO tube with an envelope entirely of glass, fig. 1*b* shows the SRM tube with an envelope partly of metal, and fig. 1*c* shows the recently developed SRC tube in metal/ceramic technology.

The newest tube is again shown in *fig. 2*. Fig. 2*a* gives a cross-sectional diagram of the actual tube and fig. 2*b* shows the tube in its shield. It is interesting to

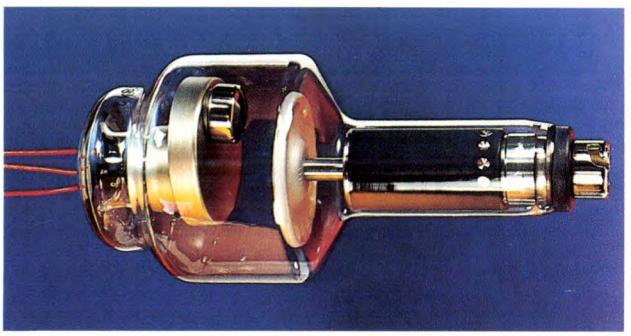

a

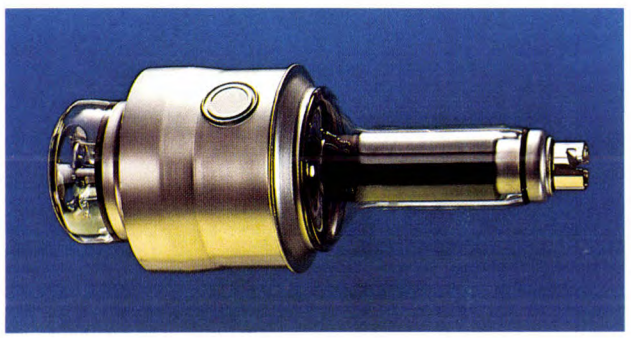

b

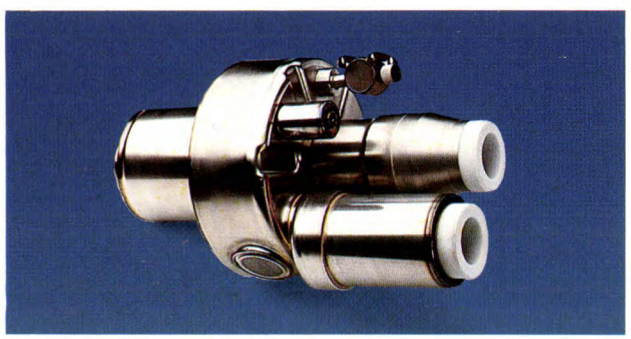

c

Fig. 1. Three successive types of Philips Rotalix diagnostic X-ray tubes. *a*) The Super Rotalix (SRO) tube with an entirely glass envelope. (The description 'Super' refers to the 150-Hz alternating-voltage supply for the induction motor that rotates the anode — an improvement in relation to the 50-Hz supply of earlier tubes.) *b*) The Super Rotalix Metal tube (SRM). In this tube part of the glass envelope has been replaced by metal, at earth potential. *c*) The newest tube, the Super Rotalix Ceramic (SRC), with ceramic instead of glass for the high-voltage insulation. The external diameter of the anode has been increased to 120 mm (as against 90 mm in the SRO tube and 100 mm in the SRM tube). The power that can be applied to the tube for a short time has thus been increased by 40% with respect to the SRO tube.

[1] See the article by B. van der Eijk and W. Kühl in the next issue: Philips Tech. Rev. **41**, 1983/84, No. 5.

[2] W. Hartl, D. Peter and K. Reiber, Metal/ceramic X-ray tubes for non-destructive testing, Philips Tech. Rev. **41**, 24-29, 1983/84.

note that the external diameter of the shield is the same as for the three earlier types, even though the anode diameter is larger. The shield is in fact considerably shorter than that of the SRM tube. It is therefore easy to fit the new tube in existing equipment. Oil is still used between shield and tube, but only for heat transfer (via a heat exchanger, not shown, no longer mounted inside the shield), and not for high-voltage insulation. The SRC tube, unlike the earlier tubes, has bearings on both sides of the anode. This arrangement gives a more stable construction, and the balancing procedure is simpler, since the anode assembly can be balanced in air. It can also be seen from fig. 2*a* that the rotor is at earth potential, so that the air gap of the motor is small. This required the rotor to be insulated from the anode by the ceramic insulator I_R. The two high-voltage cables are connected to the same side of the tube via the tapered sockets C in the insulators I_K and I_A.

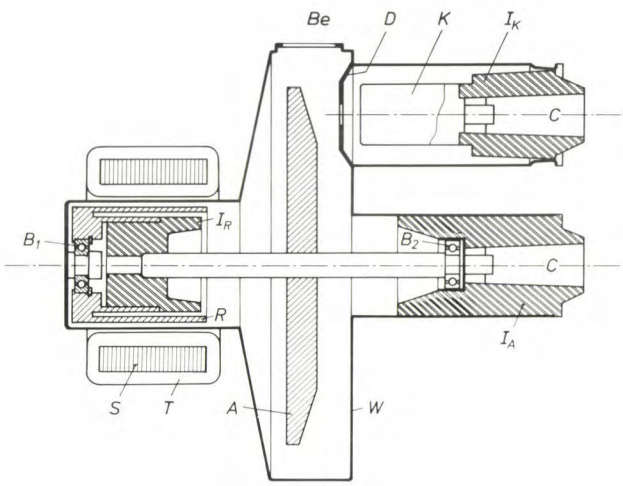

a

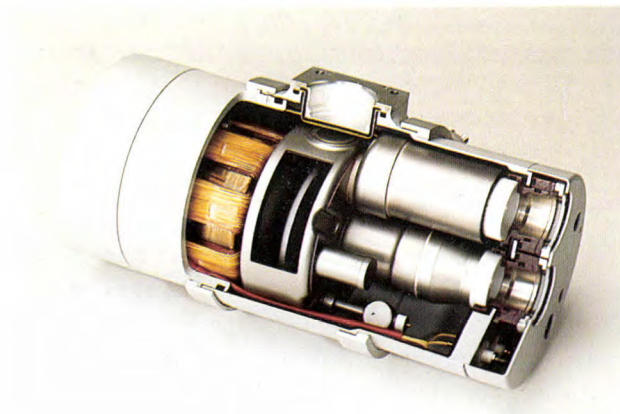

b

Fig. 2. *a*) Diagram of the Super Rotalix Ceramic tube without its shield. *A* anode. *K* cathode. *D* diaphragm. B_1, B_2 ball bearings. I_A ceramic anode insulator; I_K ceramic cathode insulator. Both have a tapered socket *C* for the connector on the high-voltage cable. I_R ceramic insulator on the anode shaft. The rotor *R* and the metal wall *W* of the tube are both at earth potential. *Be* beryllium window. *S* ring-shaped stator core with toroidal winding *T*. The components *R*, *S* and *T* comprise the induction motor for rotating the anode. *b*) The Super Rotalix Ceramic tube in its shield. The tube and shield have been partly cut away. The toroidal stator windings *T* can be seen on the left. Part of the anode *A* can also be seen next to the windings, and above it the exit window *Be* for the X-radiation. The external diameter of the shield is no larger than that of the SRM tube. The shield has in fact been made shorter, and with the cable connections now on the same side a saving in space can be made in mounting the tube in the diagnostic equipment.

The moment of inertia of the rotating anode of the new tube is three times as large as that of the anode of the SRO tube. Nevertheless the time required for acceleration and deceleration of the anode is still only about a second. To achieve this result the tube had to have a new design of motor that developed a much larger torque. As we said earlier, the new motor has a smaller air gap; it also has a toroidal stator winding on a ring-shaped core. The motor supply is an alternating voltage whose frequency varies in such a way that the slip frequency is constant while the motor is starting up (the slip frequency is the difference between the frequency of the supply voltage and the frequency corresponding to the actual rotor speed). As a result of these special measures the copper loss in the rotor is greatly reduced. The product of voltage and current has been doubled and the power taken up tripled.

In the following we shall first discuss the rotating anode and then consider the characteristics of the new tube as a complete unit. Finally, we shall deal with the new motor design.

The rotating anode

As long ago as the thirties W. J. Oosterkamp made calculations of the temperature distribution in the anodes of X-ray tubes [3]. For short exposure times and a stationary anode he found that the maximum temperature difference ΔT_{max} between the temperature at the centre of the focus on the anode surface and the mean temperature T_{av} of the anode was given by

$$\Delta T_{max} = 2W\sqrt{\frac{t}{\pi\lambda\varrho c}}, \qquad (1)$$

where W is the specific anode load in W/m^2, t the time of exposure in s, λ the thermal conductivity in $W\,m^{-1}\,K^{-1}$, ϱ the density in $kg\,m^{-3}$ and c the specific heat in $J\,kg^{-1}\,K^{-1}$.

If the anode is rotating, the electron beam is incident on the anode material for a time

$$t = \frac{b}{v\pi D} \qquad (2)$$

during each revolution, where b is the width in m of the focus in the circumferential direction, v the fre-

PHILIPS NATUURKUNDIG LAB
BIBLIOTHEEK WY - 1
P.O. Box 80.000
5600 JA EINDHOVEN
NEDERLAND

quency of rotation in s^{-1} and D the mean diameter of the focus track. If we assume that the exposure time is shorter than the time $1/\nu$ required for one revolution, the maximum temperature difference ΔT_{max} is found by substituting (2) in (1):

$$\Delta T_{max} = \frac{2W}{\sqrt{\pi\lambda\varrho c}}\sqrt{\frac{b}{\nu\pi D}}. \qquad (3)$$

For the power that can be delivered to the tube during a short exposure, the temperature $\Delta T_{max} + T_{av}$ at the anode surface at the centre of the focus is the determining quantity. The value of ΔT_{max} is inversely proportional to the factor $\sqrt{\nu D}$. Since in practice a series of exposures is usually made with the tube, T_{av} is dependent on the number and duration of the exposures that have been made with the tube immediately beforehand. T_{av} is low if the thermal capacity and the heat-radiating surface of the anode are both large. This can be achieved by increasing the external diameter of the anode. The power that can be delivered to the tube during an exposure can therefore be increased most readily by increasing the anode diameter. A somewhat smaller contribution can also be obtained by increasing the speed of rotation.

Oosterkamp was also able to find out what in theory should be the best material by using equation (3). The characteristic radiation emitted by the anode is not very important in diagnostic tubes. The intensity of the radiation emitted with a continuous spectrum (bremsstrahlung) is proportional to Z, the atomic number of the anode material. For a particular anode material, a particular exposure time and fixed dimensions of the focus, (1) and (3) show that the power we can deliver to the anode during a short time is proportional to $\Delta T_{max}\sqrt{\lambda\varrho c}$. If it is assumed that the maximum permissible temperature difference is a certain fraction of the melting point T_m, this tube power is proportional to $T_m\sqrt{\lambda\varrho c}$. The intensity of the X-radiation emitted by the anode is therefore proportional to the expression $ZT_m\sqrt{\lambda\varrho c}$ for short exposure times. *Table I* gives a summary of the values of Z, T_m, λ, ϱc and $ZT_m\sqrt{\lambda\varrho c}$ for a number of materials. It can be seen that for withstanding high temperatures and for radiation output tungsten is in theory the most suitable anode material.

Now that computers are available it is possible to calculate the temperature distribution in anodes more accurately. When Oosterkamp made his calculations he had to introduce certain simplifications so that he could obtain an analytical solution to the heat-transfer problem. At the Philips Aachen research laboratories the temperature distribution in a rotating anode has recently been calculated [5] with the aid of the program FEABL1 (developed at the Jülich nuclear research centre), which makes use of the finite-element method. *Fig. 3* shows some of the results of the calculations for $\nu = 50$ Hz (*a*) and $\nu = 150$ Hz (*b*). The absolute temperature of the anode at the centre of the focus is shown as a function of time, with the depth z below the anode surface as the parameter. The data used for the calculation are given in the caption to the figure. The influence of the speed of rotation is very clear. At $\nu = 50$ Hz the melting point is far exceeded; at $\nu = 150$ Hz the temperature maximum is 2800 K, which is considered permissible for tungsten. The swing in temperature becomes less as z increases, i.e. as the heat penetrates into the material.

Table I. The expression $ZT_m\sqrt{\lambda\varrho c}$ for a number of anode materials, and the values of the atomic number Z, the melting point T_m, the thermal conductivity λ and the product of density and specific heat ϱc (from [3], with the values for Mo from [4]).

Material	Z	T_m [K]	λ [W m^{-1} K^{-1}]	ϱc [J m^{-3} K^{-1}]	$ZT_m\sqrt{\lambda\varrho c}$ [J m^{-2} s$^{-0.5}$]
Cu	29	1350	390	3.5×10^6	1450×10^6
Ag	47	1230	420	2.5×10^6	1870×10^6
Ta	73	3270	53	2.4×10^6	2690×10^6
W	74	3620	160	2.7×10^6	5570×10^6
Pt	78	2040	70	2.8×10^6	2230×10^6
Au	79	1330	296	2.5×10^6	2860×10^6
Mo	42	2890	135	2.6×10^6	2270×10^6

It also appeared from the computer calculations that the relation found by Oosterkamp between anode temperature and exposure time (1) is not entirely valid. The computer calculations indicated that ΔT_{max} was approximately proportional to $t^{0.7}$ and not $t^{0.5}$. The discrepancy must be attributed to the simplifications that Oosterkamp was forced to adopt.

We have carried out an extensive investigation to find out which materials are suitable for practical application in a rotating anode. While tungsten has the best combination of radiation output and thermal properties (see Table I), it is unfortunately rather brittle. This means that it will permit little plastic deformation. Because of the alternating thermal stresses hairline cracks appear in the surface of a pure tungsten anode; see *fig. 4a*. The crazing of the surface produces an asymmetry in the intensity distribution of the emergent X-ray beam; see fig. 4*b*. This asymmetry gradually increases while the tube is in use, and the total intensity becomes smaller. In earlier tube types this effect often determined the life of the tube. The anode

[3] W. J. Oosterkamp, The heat dissipation in the anode of an X-ray tube I, Philips Res. Rep. 3, 49-59, 1948; II, *ibid.*, 161-173; III, *ibid.*, 303-317.
[4] R. C. Weast (ed.), Handbook of chemistry and physics, C.R.C. Press, Boca Raton 1982.
[5] H. Hübner, Calculation of three-dimensional distributions of temperatures, displacements and stresses in rotating X-ray anodes with the finite-element method, Philips J. Res. 37, 145-164, 1982.

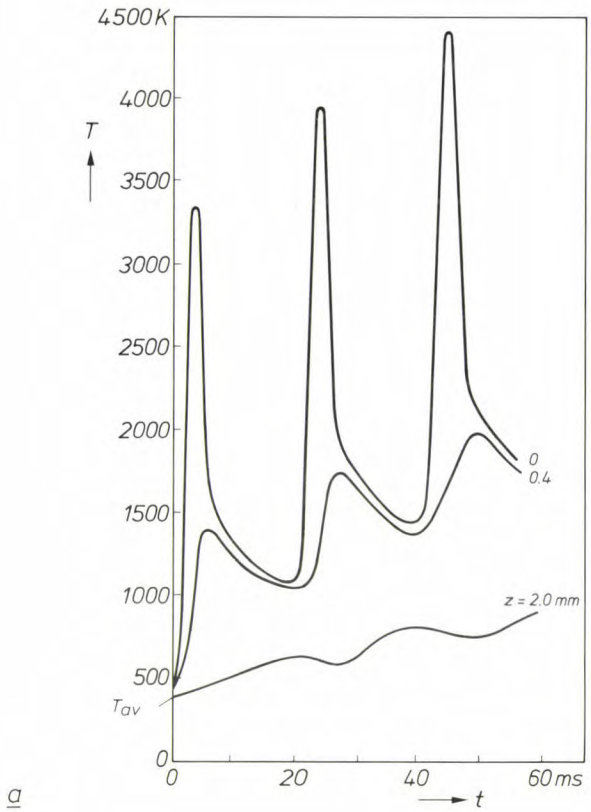

Fig. 3. Some results from a computer calculation of the temperature distribution in a rotating tungsten anode by the finite-element method [5]. The calculations were made for the rather unusual focus dimensions of 8 by 4.4 mm, a diameter at the focal track of 85 mm, an external anode diameter of 100 mm, an anode thickness of 10 mm and a delivered power of 100 kW for 50 ms. The temperature T of the anode at the centre of the focus is shown as a function of the time t in ms, with the depth z below the anode surface as parameter. A value of 400 K was assumed for the mean temperature T_{av} of the anode. *a*) The temperature distribution for a frequency of rotation of 50 Hz. By the second revolution the temperature at the surface of the anode has already reached the melting point of tungsten. *b*) The temperature distribution for a frequency of rotation of 150 Hz. After 50 ms the temperature at the anode surface is still well below the melting point.

is therefore now provided with a coating of tungsten-rhenium 0.7 mm thick. The addition of rhenium makes tungsten less brittle, while the melting point remains virtually unchanged.

The base material for the anode is molybdenum, alloyed with titanium and zirconium [6]. The great advantage of molybdenum is that its density is low, 10.2 g/cm^3 as against 19.4 g/cm^3 for tungsten. This means that the moment of inertia of the anode is smaller than for an anode made entirely of tungsten. The tungsten-rhenium layer must be thick enough to

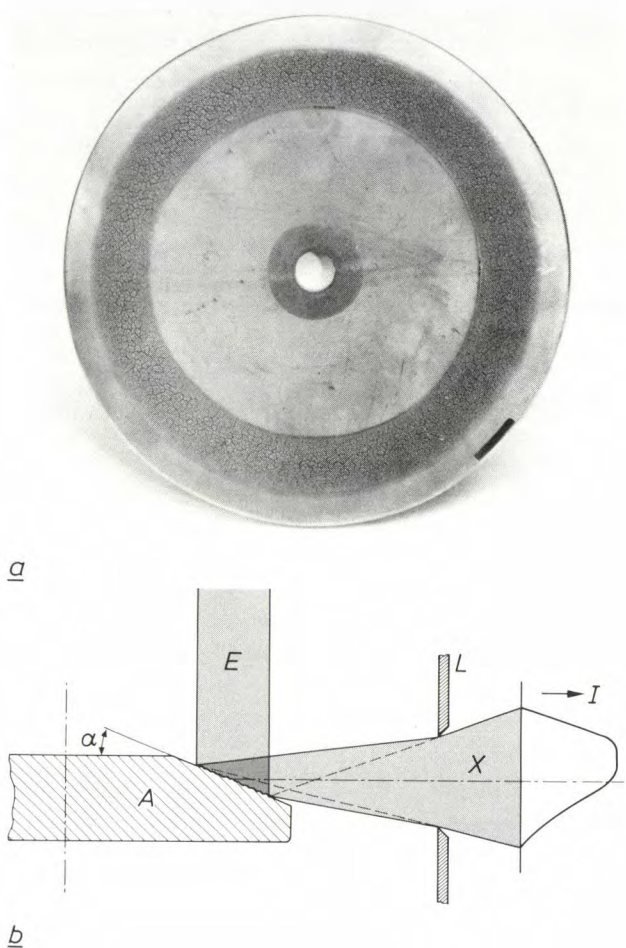

Fig. 4. Damage caused to a pure tungsten anode surface by varying heat stress. *a*) The heat stresses eventually produce hairline cracks in the surface, giving an effect known as 'crazing'. *b*) The consequences of the roughness of the anode surface caused by thermal cracks. The anode slopes at an angle α, so that the 'line' focus of the tube appears as a 'point' focus on the axis of the emergent beam and there is an enhanced brightness of the focus because of the isotropic distribution of the intensity of the X-ray beam. E electron beam that causes emission of X-radiation at A the anode. L lead exit diaphragm. The wall of the X-ray tube and the exit window are not shown. X emergent X-ray beam. I intensity of the X-ray beam, as a function of position (schematic). The X-radiation that leaves the anode at a 'grazing' angle is attenuated by the roughness of the surface. As the roughness increases, the intensity distribution of the X-ray beam becomes more asymmetric and the total radiation intensity also decreases. In earlier types of tube with a pure tungsten anode this effect frequently determined the life of the tube.

prevent the melting point of the molybdenum alloy from being reached. Fig. 3*b* shows that the thickness of 0.7 mm is sufficient. The anode is formed by sintering, followed by forging to reduce the porosity. To make the heat radiation from the anode as large as possible the surface is 'blackened' at the outside edge, by roughening it and coating it with aluminium oxide.

The special features of the new design

An important feature of the SRC tube is the stability of the focus. It is important that the focus should remain accurately in the same position if the tube is used to make a series of exposures at different voltages, and also if it is used for computed tomography. The focus stability has a thermomechanical component and an electrical component. The thermomechanical stability is maximized by combining an optimum geometry with materials with an appropriate thermal expansion coefficient: this is particularly important in the special tube for computed tomography. The electrical stability is ensured mainly because the metal envelope cannot collect a localized charge from scattered electrons, as can happen with a glass envelope.

The secondary electrons emitted at the focus may amount to some 30% of the tube current, depending on the accelerating potential. In conventional tubes these secondary electrons arrive at other parts of the anode, where they produce 'extrafocal' radiation, which reduces the contrast in the X-ray image. The earthed metal envelope of the SRC tube removes most of the secondary electrons, so that the extrafocal radiation has much less effect on the image contrast. Also, the removal of the secondary electrons reduces the mean anode temperature. The improvement in the image contrast has been confirmed by measurements; see *fig. 5*. If the edge of a copper plate is located at the centre of the X-ray beam and an image of the edge is made on a photographic film, the photographic density as measured by a densitometer varies in the way shown in fig. 5*a*. The contrast loss is defined as the ratio $(b-a)/b$. In fig. 5*b* the contrast loss is plotted as a function of the voltage for an image format of 35 cm × 35 cm. The dashed line indicates the variation of the contrast loss when a conventional glass-envelope tube is used; the continuous line indicates the variation with the new SRC tube. At a voltage of 100 kV there is an improvement of more than 20% with the new tube.

Another advantage of the new tube is that it has a beryllium exit window (*Be* in fig. 2*a*), which absorbs much less X-radiation than the glass envelope of the SRO tube in fig. 1*a*. There is a much thinner layer of oil between exit window and shield, because the oil is not used here for insulation, but only as a coolant. In the old tube the X-radiation had to pass through a plastic cap as well as the oil; in the new tube the cap is of aluminium. Oil and plastic have an undesirable

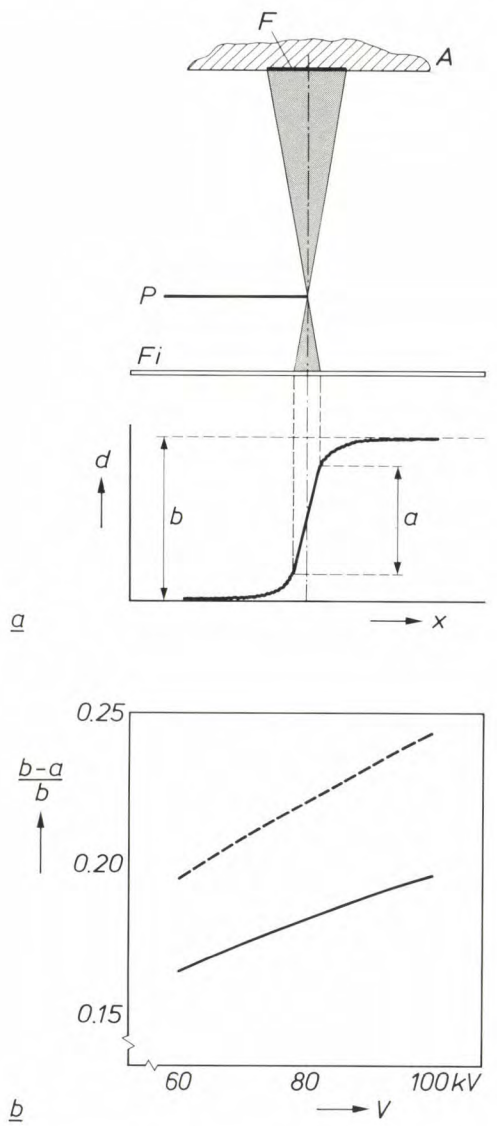

Fig. 5. Measurement of the contrast loss due to extrafocal radiation. *a*) Experimental arrangement. *A* anode. *F* focus. *P* copper plate. *Fi* photographic film. An image of the edge of *P* is produced on the film. After the film has been developed the photographic density *d* is measured, with a densitometer, as a function of position *x*. If no X-radiation were emitted by the anode surface outside the focus, the measured density curve would consist entirely of straight lines. However, since secondary electrons cause emission of X-radiation from the anode surface adjacent to the focus (extrafocal radiation), a curve of the type shown is obtained. The ratio $(b-a)/b$ is called the contrast loss. *b*) The result of a measurement of the contrast loss of an SRO tube (fig. 1*a*) — the dashed curve — and of an SRC tube — the continuous curve. The contrast loss is plotted as a function of the voltage *V* across the tube for an image format of 35 cm × 35 cm. At a voltage of 100 kV an improvement of more than 20% is obtained.

[6] P. Schreiber, New anode disc technology in Super Rotalix tubes, Medicamundi **20**, 87-90, 1975.

scattering effect on the X-radiation and also act as a filter, even where this is not desired.

In diagnostic work some of the long-wave X-radiation is removed by filters of aluminium or other material. Long-wave radiation contributes very little or nothing to the image formation, but contributes to the patient's dose. With the compact construction of the new tube the filters and shutters can be located close to the focus.

An interesting feature of the new tube is that the voltage between cathode and earth can be made higher than the voltage between earth and anode ('asymmetric high voltage'). Since the tube current depends only on the voltage between the earthed diaphragm *D* (see fig. 2*a*) and the cathode, a high tube current can be obtained even with a low anode/cathode voltage.

The motor

As we mentioned earlier, it was necessary to develop a new motor for the new tube. This motor has to be able to accelerate the anode, whose moment of inertia is three times that of the SRO tube of fig. 1*a*, in about a second and to bring it to rest in about the same time. This requires a very unconventional design of motor. Special attention was paid to the reduction of the copper loss in the rotor, since it is difficult to remove the heat dissipated in the rotor. As the rotor loss is the leading quantity in the design, it was possible in this way to increase the stator current and thus obtain a higher motor torque.

Normally the stator winding of an induction motor is wound in slots in the stator iron. The difficulty with this method is that the 'teeth' thus formed in the stator

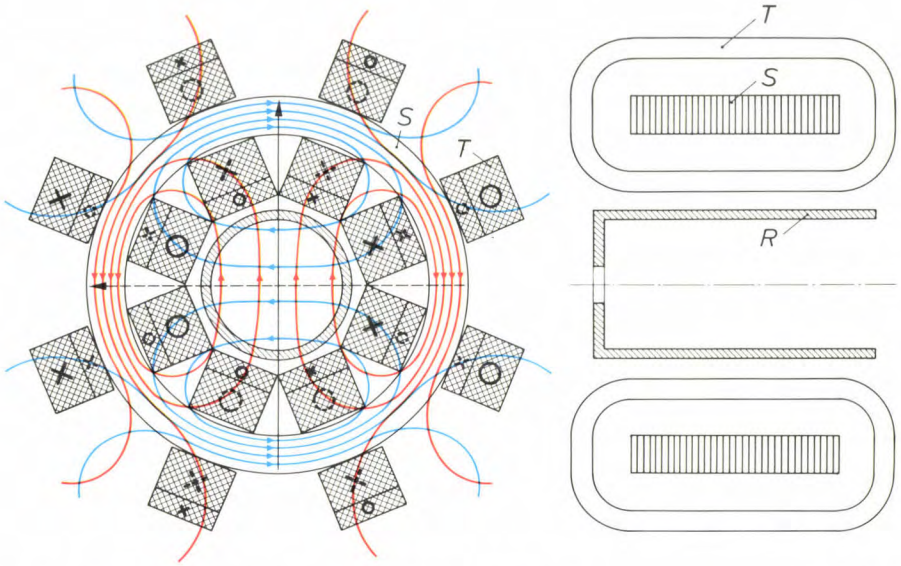

Fig. 6. Diagram of the new two-phase induction motor. *Left:* Transverse cross-section. *Right:* Longitudinal cross-section. *S* ring-shaped laminated-iron stator core. *T* toroidal stator coil. *R* copper rotor with iron core (not shown). The envelope wall (not shown) is situated in the space between *T* and *R*. The eight stator coils *T* each consist of two subcoils with the numbers of turns in the ratio 2:1. The continuous circles and crosses indicate a current direction for one of the phases, corresponding to the lines of force shown in *red*. The dashed circles and crosses indicate a current direction for the other phase, corresponding to the lines of force shown in *blue*. In the situation shown, the currents in the two phases are the same. The arrows indicate the main directions of the two fields associated with the current directions shown. The resultant field, the rotating field (not shown) is at an angle of 45° to the two main directions. The coil configuration shown gives an approximately sinusoidal distribution of the current for each phase along the rotor circumference. An appreciable stray field is set up around the motor, however. This is screened by the motor housing.

The tube then has to be connected to a special asymmetric generator.

In the earlier types of tube the life was mainly limited by erosion of the glass envelope wall by scattered electrons, damage to the anode surface and the formation of a conducting tungsten film on the envelope. In the new tube the life is mainly determined by the filament life and the bearing life. The mean life of the new tube — with its improved specification — is at least twice that of the earlier types.

iron also introduce higher-harmonic rotating fields. These fields cause braking torques and extra copper loss in the rotor, adversely affecting the efficiency.

We therefore designed a new motor, based on studies made by E. M. H. Kamerbeek of Philips Research Laboratories, Eindhoven. This motor has a toroidal stator winding; see *fig. 6* (and also fig. 2). The stator winding must fit in the space available between the rotor (increased in size by the ceramic insulator I_R) and the motor housing. The ring-shaped laminated

stator core S, with no slots, is surrounded by eight coils T, each consisting of two subcoils with the numbers of turns in the ratio 2:1. The motor is two-phase and two-pole. For each phase eight subcoils are connected in series. Four of these subcoils have twice the number of turns. The continuous crosses and circles in fig. 6 indicate a current direction in the coils of one phase and the dashed crosses and circles indicate a current direction in the other phase. The arrows indicate for each phase the main direction of the magnetic field associated with the current directions shown, with the lines of force shown red for one phase and blue for the other. The resultant magnetic field, the rotating field, rotates at the frequency of the alternating currents supplied with a 90° phase difference to the two phases. The method used for splitting up the coils for each phase gives a current distribution at the circumference that approaches a sine wave more closely than with conventional winding methods. The copper loss in the rotor R is therefore lower.

The stator winding described has the disadvantage that an alternating stray magnetic field is set up in the space around the motor. This stray field could upset the operation of other equipment (e.g. ECG or EEG equipment). There are also codes of practice that set maximum levels for interfering magnetic fields. The motor therefore has to be screened to contain this stray field. Various kinds of magnetic or electrically conducting screens were tested. It turned out that a combination of the two was most effective. In the final design the aluminium motor housing (fig. 2*b*), fitted with a soft-iron shield, serves as the magnetic screen.

Calculations have shown that the toroidally wound motor with its screening has a higher power factor ($\cos\phi$) than a conventionally wound motor. The product of voltage and current — which largely determines the dimensions of the equipment for the motor supply — can therefore be lower. The efficiency of our motor is a little smaller, however, because of the somewhat higher copper loss in the stator. The removal of the heat developed in the stator is not difficult, however.

We mentioned earlier that the motor is supplied by an alternating voltage of varying frequency while it is starting up. *Fig. 7* shows that this method is an improvement. Fig. 7*a* is a diagram of a torque-speed curve of an induction motor, the torque M as a function of the angular velocity ω_M of the rotor, for a fixed frequency $\omega_s/2\pi$ of the supply voltage. The angular velocity of the motor shaft after running up to speed, i.e. during the exposure in our case, is ω_e. The method that we used is shown schematically in fig. 7*b*. The frequency $\omega_s/2\pi$ of the supply voltage is increased in such a way while the motor is starting that the difference $\omega_s - \omega_M$ always remains the same. The resulting torque-speed curve is therefore rectangular.

Fig. 7*c* shows the results of calculations of the work required for starting, the rotor copper loss and the

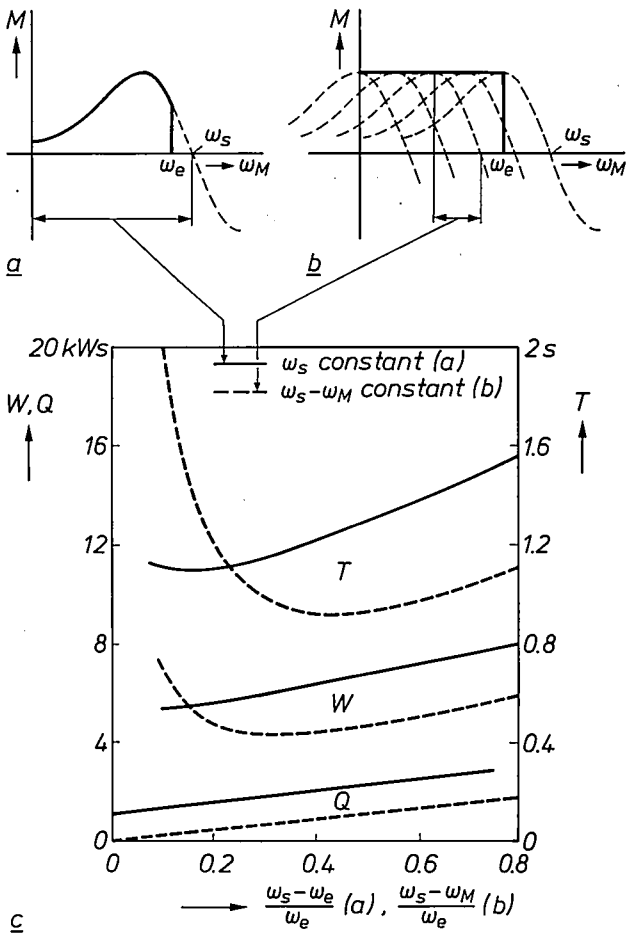

Fig. 7. *a*) Diagrammatic torque-speed curve (the torque M as a function of the angular velocity ω_M), for the motor of fig. 6, with an alternating-current supply of fixed frequency, ω_s synchronous angular velocity. ω_e the angular velocity of the rotor after running up to speed, i.e. during the exposure. *b*) The torque-speed curve of the same motor, supplied from an alternating-current generator whose frequency varies in such a way that the difference $\omega_s - \omega_M$ is constant. The torque is therefore constant during starting. The dotted curves (identical to those in *a*) are included to show that the point on the ω_M-axis corresponding to ω_s moves to the right during starting. *c*) Results of calculations of the work W in kWs required for starting, the rotor copper loss Q in kWs and the starting time T in s. The calculated quantities are shown as a function of the ratio $(\omega_s - \omega_e)/\omega_e$ for a fixed frequency of the stator current (continuous curves), and as a function of the ratio $(\omega_s - \omega_M)/\omega_e$ for a variable frequency (dashed curves). The calculations were made for $\omega_e = 838.5\ s^{-1}$ (corresponding to 133 Hz or about 8000 revolutions/min) and a moment of inertia of 0.33×10^{-2} kg m^2 for the rotating mass, at constant amplitude of the stator current. The shape of the torque-speed curve was assumed to be such that the maximum torque (the pull-out torque) occurred at 62% of the synchronous angular velocity with a 150-Hz motor supply. The smallest starting time is obtained when $(\omega_s - \omega_e)/\omega_e \approx 0.15$ for a fixed supply frequency (fig. 7*a*), and when $(\omega_s - \omega_M)/\omega_e = 0.43$ for a varying supply frequency. With a variable supply frequency the minimum starting time is about 20% smaller, while the rotor copper loss Q is less, so that less energy W has to be supplied during the start.

starting time. The calculations were made for a constant amplitude of the stator current, for the conventional method of fig. 7*a* (continuous lines) and for the new method of fig. 7*b* (dashed lines). It was found that for a fixed supply frequency the shortest starting time is obtained when $(\omega_s - \omega_e)/\omega_e \approx 0.15$, corresponding to a synchronous frequency of about 150 Hz (our motor was in principle designed for this frequency). With a varying supply frequency the minimum starting time is obtained when $(\omega_s - \omega_M)/\omega_e = 0.43$. This is found to correspond to a variation of the synchronous motor speed such that the motor always exerts the maximum torque (the pull-out torque) during starting; this is the situation shown in fig. 7*b*.

The desired motor supply with variable frequency is obtained by measuring the energy taken from the mains while the motor is starting up. This is a known function of the kinetic energy of the rotating mass, so that the angular velocity can be calculated. From the angular velocity the desired value of the frequency can be calculated. This desired value is applied to a control circuit.

If we compare the minimum starting times in the two methods, we find that the variable-frequency method gives a value about 20% smaller. This result is obtained with a lower copper loss Q and hence with less applied energy W. Even though the moment of inertia is tripled, the improved starting method and the modified motor design give a starting time of only about a second.

Summary. The SRC tube (Super Rotalix Ceramic), which is constructed entirely of metal and ceramic, has a number of important improvements with respect to the earlier types of Philips Rotalix tube. The metal wall conducts many of the secondary electrons away, so that the tube will take a higher load and the contrast of the images made with the tube is improved. More power can be supplied to the tube because the diameter of the rotating anode has been increased, yet the external diameter of the tube is unchanged. The temperature distribution in the anode can be determined from earlier analytical calculations by W. J. Oosterkamp and from recent computer calculations with the finite-element method. It can be shown that in theory tungsten is the best anode material; in practice, however, even better results can be obtained by combining tungsten-rhenium with a molybdenum alloy. To accelerate the anode in one second, even though it has a moment of inertia three times that of the anode of earlier tube types, a new motor has been designed. The stator of this motor has a toroidal winding. The frequency of the supply voltage increases during starting, so that the rotor is driven by the maximum torque during the start.

Scientific publications

These publications are contributed by staff of laboratories and plants that form part of or cooperate with enterprises of the Philips group of companies, particularly by staff of the research laboratories mentioned below. The publications are listed alphabetically by journal title.

Philips GmbH Forschungslaboratorium Aachen, Weißhausstraße, 5100 Aachen, Germany — *A*

Philips Research Laboratory Brussels, 2 avenue Van Becelaere, 1170 Brussels, Belgium — *B*

Philips Natuurkundig Laboratorium, Postbus 80000, 5600 JA Eindhoven, The Netherlands — *E*

Philips GmbH Forschungslaboratorium Hamburg, Vogt-Kölln-Straße 30, 2000 Hamburg 54, Germany — *H*

Laboratoires d'Electronique et de Physique Appliquée, 3 avenue Descartes, 94450 Limeil-Brévannes, France — *L*

Philips Laboratories, N.A.P.C., 345 Scarborough Road, Briarcliff Manor, N.Y. 10510, U.S.A. — *N*

Philips Research Laboratories, Cross Oak Lane, Redhill, Surrey RH1 5HA, England — *R*

Philips Research Laboratories Sunnyvale P.O. Box 9052, Sunnyvale, CA 94086, U.S.A. — *S*

H. A. van Sprang & R. G. Aartsen	*E*	Temperature dependence of liquid crystal tilt angles	Appl. Phys. Lett. **42**	669-671	1983
B. Aldefeld	*H*	On automatic recognition of 3D structures from 2D representations	Comput. Aided Des. **15**	59-64	1983
M. W. van Tol & J. van Esdonk	*E*	A high luminance high-resolution cathode-ray tube for special purposes	IEEE Trans. **ED-30**	193-197	1983
H. Ney	*H*	A time warping approach to fundamental period estimation	IEEE Trans. **SMC-12**	383-388	1982
H. Ney	*H*	Dynamic programming algorithm for optimal estimation of speech parameter contours	IEEE Trans. **SMC-13**	208-214	1983
U. Dibbern	*H*	Magnetoresistive Sensoren und ihre Anwendung	Ind. Elektr. & Elektron. **28** (No. 6)	36-38	1983
D. R. Wolters, J. J. van der Schoot & T. Poorter	*E*	Damage caused by charge injection	Insulating films on semiconductors, J. F. Verweij & D. R. Wolters (eds), Elsevier, Amsterdam	256-260	1983
T. Poorter & D. R. Wolters	*E*	Intrinsic oxide breakdown at near zero electric fields	Insulating films on semiconductors, J. F. Verweij & D. R. Wolters (eds), Elsevier, Amsterdam	266-269	1983
J. J. van der Schoot & D. R. Wolters	*E*	Current induced dielectric breakdown	Insulating films on semiconductors, J. F. Verweij & D. R. Wolters (eds), Elsevier, Amsterdam	270-273	1983
H. Heitman & P. Hansen	*H*	The healing behavior of nuclear tracks in yttrium iron garnet films	J. Appl. Phys. **53**	7321-7330	1982
K. H. J. Buschow	*E*	Magnetic properties of amorphous Co and Ni alloys	J. Appl. Phys. **54**	2578-2581	1983
P. C. Zalm	*E*	Energy dependence of the sputtering yield of silicon bombarded with neon, argon, krypton, and xenon ions	J. Appl. Phys. **54**	2660-2666	1983
H. J. de Wit & H. M. J. Boots	*E*	A geometric model of alternating current etching of aluminum	J. Appl. Phys. **54**	2727-2731	1983
K. H. J. Buschow & A. M. van der Kraan (*FOM, Amsterdam*)	*E*	Mössbauer effect and magnetization after hydrogen absorption in ^{57}Fe-doped $HoCo_2$ and YCo_2	J. Less-Common Met. **91**	203-208	1983
P. H. Woerlee, G. C. Verkade & A. G. M. Jansen (*Univ. Nijmegen*)	*E*	An experimental investigation on weak localisation, spin-orbit and interaction effects in thin bismuth films	J. Phys. C **16**	3011-3024	1983

G. Dittmer & U. Niemann	*A*	Heterogeneous reactions and chemical transport of molybdenum with halogens and oxygen under steady state conditions of incandescent lamps	Mater. Res. Bull. **18**	355-369	1983
P. Hansen, H. Heitmann & P. H. Smit	*H, E*	Nuclear tracks in iron garnet films	Phys. Rev. B **26**	3539-3546	1982
J. C. M. Henning & E. C. J. Egelmeers	*E*	Strain-modulated ESR study of Pt^- in silicon	Phys. Rev. B **27**	4002-4012	1983
P. K. Larsen, J. H. Neave, J. F. van der Veen (*FOM, Amsterdam*), P. J. Dobson (*Imp. College, London*) & B. A. Joyce	*E, R*	GaAs(001)-$c(4\times4)$: A chemisorbed structure	Phys. Rev. B **27**	4966-4977	1983
U. Enz	*E*	Unperturbed sine-Gordon solitons as Newtonian particles	Phys. Rev. B **27**	5815-5816	1983
K. H. J. Buschow & P. G. van Engen	*E*	Note on the magnetic and magneto-optical properties of Ni_2In type 3d transition metal compounds	Phys. Stat. Sol. a **76**	615-620	1983
P. C. M. Gubbens* W. Ras*, A. M. van der Kraan* (* *Interuniv. Reactor Inst., Delft*) & K. H. J. Buschow	*E*	Magnetization and ^{161}Dy Mössbauer effect study of $DyMn_2$ and Dy_6Mn_{23} and their ternary hydrides	Phys. Stat. Sol. b **117**	277-282	1983
W. A. M. van Bers, A. J. J. Franken & P. K. Larsen	*E*	Simple mechanism for *in situ* adjustment of gratings in UHV monochromators	Rev. Sci. Instrum. **54**	637-638	1983
H. Ney	*H*	Automatic speaker recognition using time alignment of spectrograms	Speech Commun. **1**	135-149	1982
J. J. Goedbloed	*E*	EMC en industrie	T. Ned. Elektron. & Radiogen. **48**	71-79	1983
J. H. Waszink & L. H. J. Graat	*E*	Experimental investigation of the forces acting on a drop of weld metal	Weld. J. **62** (Weld. Res. Suppl.)	109s-116s	1983

Contents of Electronic Components & Applications 5, No. 4, 1983

N. A. Anderson: Cobalt rare-earth high energy permanent magnets (pp. 194-199)

W. J. W. Kitzen: Multiple loudspeaker arrays using Bessel coefficients (pp. 200-205)

A. Petersen: Silicon temperature sensors (pp. 206-213)

A. Moelands: I^2C bus in consumer applications (pp. 214-221)

J. Dijk: High-voltage power transistor quality (pp. 222-232)

A. D. Schelling: Liquid crystal displays (pp. 233-244)

A. Otten, H. Schmickl & J. Slakhorst: Recent developments in wet aluminium electrolytics (pp. 246-253)

Contents of Philips Telecommunication Review **41**, No. 3, 1983

N. A. Buys & A. J. M. Dingjan: Optical fibre systems: towards long distances (pp. 165-173)

A. M. Giacometti & Ph. Uythoven: The 565 Mb/s 8TR640 system: equalisation design and performance analysis (pp. 175-192)

J. Wagenmakers: 8TR640, a 565 Mb/s coaxial line muldex system (pp. 193-201)

J.-C. Liénard: SOPHO-NET, a versatile private network (pp. 202-224)

P. Potgieser & P. Vervest: The P 5700 Teletex terminal (pp. 225-226)

K. Furnbom: Text editing easier on Philips teleprinters (p. 227)

P. Costantini & A. Scattolini: IRICON, an international message switching centre (pp. 228-232)

P. Buffet: The electronic telephone directory (pp. 233-234)

N. van Tol & W. Ros: VECOM short-range communication with vehicles (pp. 235-249)

J. McLean: A new family of FM portables (pp. 250-256)

Volume 41, 1983/84, No. 4 pages 105-136 Published 15th February 1984

PHILIPS TECHNICAL REVIEW

VOLUME 41, 1983/84, No. 5

An X-ray image intensifier with large input format

B. van der Eijk and W. Kühl

Philips Research Laboratories have played an important part in the development of the X-ray image-intensifier tube. Professor G. Holst, the founder and later director of the Laboratories, was himself actively involved in the development of an image converter in which an infrared image was transformed into a visible picture [*]. *This image converter may be regarded as a forerunner of the image intensifier. A series of six articles on the X-ray image intensifier appeared in this journal in 1955* [**]. *After several generations of X-ray image intensifiers with a glass input window, Philips have now put on the market a type with a thin metal input window and an input screen format of 36 centimetres diameter. With this large format a single exposure can simultaneously include, for example, both of the kidneys or the stomach as well as the duodenum.*

Introduction

In the classical method of X-ray screening (fluoroscopy) X-rays are projected on to a fluorescent screen from a focal spot on the anode of an X-ray tube [1]. The light produced at the screen, however, is of low brightness or luminance, about 0.005 cd/m^2. (A moonlit landscape has a luminance of about 0.01 cd/m^2 [2].) With this fluoroscopic method the radiologist therefore requires a long period of visual adaptation, and even then is unable to observe details. Another problem was that cinematographic recording of moving objects (for example the heart) exposed the patient to an excessive radiation dose, and also placed too high a load on the X-ray tube. Even in the early days of X-ray diagnostics there was therefore a demand for images of higher luminance.

From Abbe's sine condition it follows that the luminance of object and image in an optical system is theoretically constant. In practice the luminance of the image is lower than that of the object, owing to losses. In an electron-optical system the brightness of the image can indeed be increased because the electrons can be accelerated in an electric field (thereby causing each electron to produce a number of photons). An electron-optical image therefore resembles an optical image in a medium of increasing refractive index [2]; see *fig. 1*. To obtain a higher luminance it is therefore necessary to convert photons into electrons, and to follow this by a conversion in the opposite sense. Multiple wavelength conversions are a typical feature of image intensifiers, which include the X-ray image intensifier as a special case.

The authors are with the Philips Elcoma Division, Ir B. van der Eijk in Heerlen and Dr W. Kühl in Eindhoven.

[*] G. Holst, J. H. de Boer, M. C. Teves and C. F. Veenemans, An apparatus for the transformation of light of long wavelength into light of short wavelength, Physica **1**, 297-305, 1934.

[**] M. C. Teves, *et al.*, The application of the X-ray image intensifier I-VI, Philips Tech. Rev. **17**, 69-97, 1955/56.

[1] See the article by W. Hartl, D. Peter and K. Reiber, Philips Tech. Rev. **41**, 126, 1983/84.

[2] M. C. Teves and T. Tol, Electronic intensification of fluoroscopic images, Philips Tech. Rev. **14**, 33-43, 1952/53.

Since no substances are known in which X-ray quanta can be converted into free electrons with a sufficient yield, more than two wavelength conversions are necessary in an X-ray image intensifier. *Fig. 2* shows a diagram of an X-ray image intensifier of conventional design. The X-rays reach the X-ray screen through a glass input window, which forms part of the envelope of the evacuated tube. The screen consists of an aluminium substrate coated with a scintillation layer *S*, in which X-ray quanta are converted into photons. On this layer is a second layer, the photocathode *K*, in which the photons are converted into free electrons. An electrostatic lens, formed by the anode *A* with the photocathode and an auxiliary electrode *El*, produces a reduced electron image on the output screen *E*, which is at anode potential. Here, in a luminescent layer, the electrons are converted back into photons. The image can be observed through the glass envelope wall with a microscope, and photographed or converted into a video signal by means of a TV camera tube. The intensification of luminance is brought about not only by the supply of energy to the electrons but also by the reduction in size of the image.

In medical diagnostics, details of small thickness such as blood vessels give low contrast in an X-ray image in relation to the surrounding tissue. Contrasts cannot be observed until they amount to a certain multiple of the relative noise in the image. It is therefore important to obtain an image with the largest possible signal-to-noise ratio at the output screen of the image intensifier.

The input X-ray image always contains quantum noise, originating from the statistical fluctuations in the stream of X-ray quanta. The signal magnitude in the X-ray image must be kept to a minimum to minimize the radiation dose received by the patient. At the input screen of the X-ray image intensifier the image therefore always has a signal-to-noise ratio that is limited by and dependent on the radiation dose. It is therefore important to design an X-ray image intensifier so that the input window transmits the maximum of X-radiation while the scintillation layer on the X-ray screen absorbs as much of the radiation as possible. The absorption of the scintillation layer largely determines the extent to which the image intensifier affects the signal-to-noise ratio of the X-ray image.

Until recently the various types of Philips X-ray image intensifiers were made with glass for the envelope and metal for the parts that determine the electric potential. The new X-ray image-intensifier tube that is the subject of this article consists almost entirely of metal; see *fig. 3*. A notable feature of the tube is the concave shape of the input window, which consists of titanium foil 0.25 mm thick. The hollow shape is due to atmospheric pressure (the total force on it is 14 kN). The metal foil transmits 85% of the incident X-radiation, compared with a transmission of only 60% for a glass window, which would in addition give more X-ray scatter.

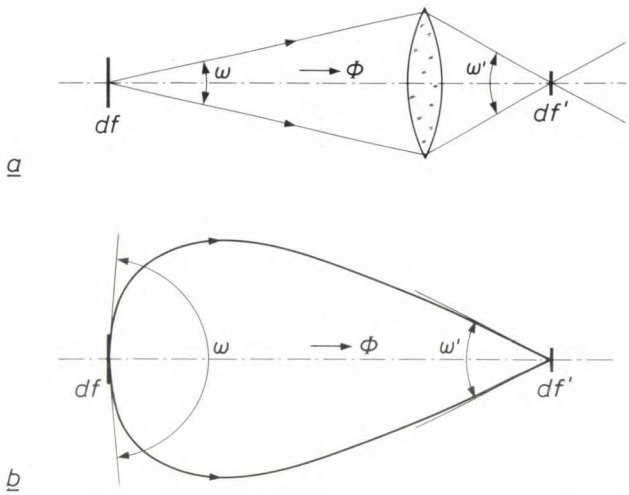

Fig. 1. Luminances of object and image in imaging systems. ω and ω' solid angles of the imaging beams. The area df of the object corresponds to the area df' of the image. Φ light flux. *a*) An optical imaging system. The luminance at the object is $\Phi/\omega df$, the luminance at the image $\Phi/\omega' df'$. Since $\omega df = \omega' df'$ (Abbe's sine condition), the luminances of object and image are equal. This applies only to optical systems using light if the refractive index in the object and the image space is the same. *b*) An electron-optical imaging system, in which the electrons are accelerated. The electron trajectories are curved so that $\omega df > \omega' df'$. The luminance of the image is thus greater than that of the object. Electron imaging may be compared with optical imaging in a medium of increasing refractive index, where B/n^2 = constant, B being the brightness (luminance) and n the refractive index. In an electron-imaging system the refractive index is proportional to the root of the kinetic energy delivered to an electron.

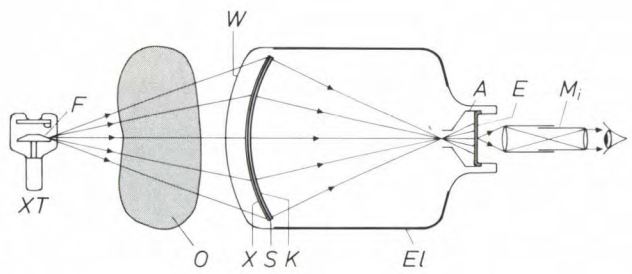

Fig. 2. Principle of an X-ray image-intensifier tube. *O* object. *W* input window (which forms part of the tube wall). *X* X-ray input screen with *S* scintillator and *K* photocathode. *A* anode. *E* output screen. *El* auxiliary electrode on the glass envelope wall. The anode *A* combined with *K* and *El* forms a positive electrostatic lens. *XT* the X-ray tube with focus *F*. In *S* the input X-ray quanta generate photons that are converted into electrons in *K*. The shadow image of *O* formed at *X* by central projection from *F* is produced at a reduced scale on the viewing screen *E*, which is at anode potential. The luminescent layer of *E* converts the electron image into an optical image, which can be viewed through the glass envelope wall with a microscope *Mi*. The increase in the luminance is produced by supplying energy to the electrons and reducing the size of the image. The image on the viewing screen can be focused by varying the voltage on the auxiliary electrode *El*.

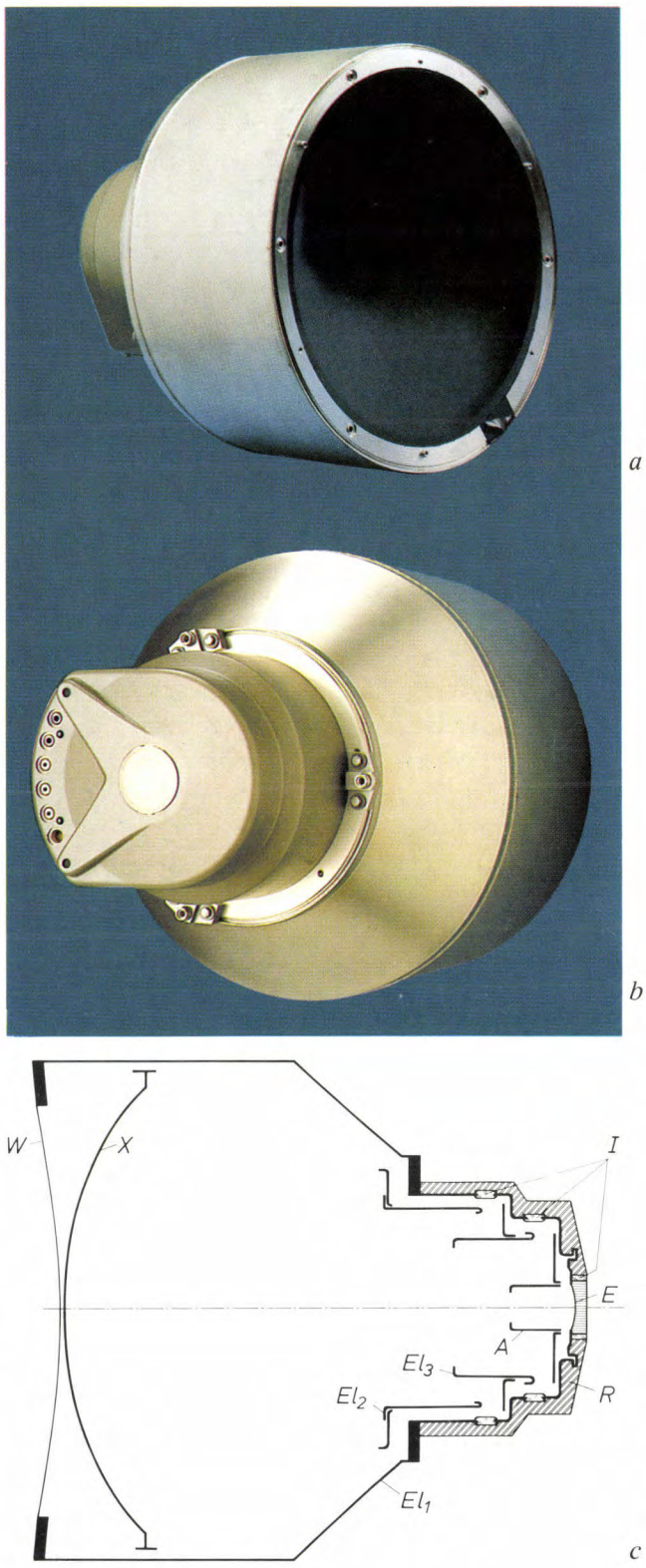

Fig. 3. The new 36-cm image intensifier. Unlike the conventional tube in fig. 2, this tube is made almost entirely of metal. *a*) The tube seen from the input-window side; the window consists of 0.25-mm titanium foil. *b*) The tube seen from the output-window side; the output window consists of a fibre-optic plate. *c*) A cross-section of the tube. El_1, El_2, El_3 auxiliary electrodes used for focusing and varying the magnification. With this tube the diameter of the input X-ray image can have fixed values of 36 cm, 25 cm or 17 cm or can be continuously varied. *I* glass rings, providing insulation between the various direct voltages in the tube. *R* rubber insulation, surrounding all live parts of the tube. The part of the envelope wall that is not enclosed in rubber is at earth potential. The output screen *E* is at the same potential as the anode *A*. Other symbols have the same significance as in fig. 2. ▶

The material of the scintillation layer on the X-ray screen is caesium iodide, which has a high atomic absorption for X-radiation because of the high atomic numbers of the constituent elements and the density of the evaporated layer. As the crystal anisotropy is perpendicular to the layer, there is little lateral scatter of the photons generated. The photocathode consists of caesium antimonide, which is formed *in situ* on the X-ray screen as a compound after the tube has been evacuated, since it is attacked by air. The output screen consists of zinc-cadmium sulphide, which is applied by sedimentation to a fibre-optic plate that also forms the output window of the tube. The viewing screen and the fibre-optic plate convert the sharp but curved electron image into a sharp flat optical image.

The diameter of the X-ray input screen is 36 cm (14 inches), compared with 23 cm (9 inches) in the previous largest types of Philips X-ray image intensifiers. With the new intensifier it is therefore possible to obtain an image of both kidneys, or of the stomach and duodenum, simultaneously. Since the electron-optical image can be curved because of the use of a fibre-optic plate, the length of the tube is relatively small: 48 cm. The outer diameter of the tube is also relatively small: 42 cm. The ratio of the diameter of the X-ray screen to the outer diameter of the tube is greater than with any other type of X-ray image intensifier. Since the tube is exceptionally compact, it can readily be mounted in existing diagnostic equipment, unlike other image intensifiers of large input format (or 'entrance field size').

When the new image intensifier is incorporated in an integrated diagnostic system with closed-circuit TV (CCTV), the radiologist can switch almost instantaneously from fluoroscopy with the TV monitor to radiography with a camera (or 'photofluorography'). This only requires short exposures, so that movement blur is avoided. The output image of the new tube is of such high quality that radiographs on 100-mm film are generally as good as conventional full-size radiographs, or better. Since film accounts for about half the running costs of a hospital X-ray department, considerable savings can be made by using 100-mm film. This also means that less storage space is required for film records, a not inconsiderable advantage. It has also been found that the new tube is very suitable for application in a system using digital signal processing. With such a system the visibility of blood

vessels can be improved, for example by subtraction of images with and without contrast medium.

In the following we shall first look at the electron-optical system and then deal with the concept of quantum noise. Next we shall discuss the properties of the various active layers in the tube, and consider the criteria used for establishing the quality and performance of an X-ray image intensifier. Finally we shall examine a few aspects of the use of the new tube in medical X-ray diagnostics.

The electron-optical system

The electron-optical part of an X-ray image intensifier is based in principle on the system with a single electrostatic positive lens (a system of concentric spheres) as proposed in 1952 by P. Schagen, H. Bruining and J. C. Francken of Philips Research Laboratories [3]; see *fig. 4*. It consists of a cathode K, an anode A, and a viewing screen E, which are all three curved spherically and have a common centre-point M. The viewing screen has the same potential as the anode, so that the space inside the anode is 'field-free'. The magnification is equal to the ratio of the radii of viewing screen and cathode.

An electron-optical system possesses a number of intrinsic physical and geometrical types of aberration. The first category includes chromatic aberration, due to a non-constant statistically distributed initial velocity of the electrons leaving the photocathode. (This type of aberration can be reduced by making the field-strength at the cathode large compared with the initial energy of the electrons.) One type of geometrical aberration is the pin-cushion or barrel distortion that occurs because the magnification increases or decreases as the object point moves away from the optical axis. Another type of distortion is caused by the curvature of the electron-optical image. A type of distortion not connected with the electron-optics is 'X-ray distortion' of the X-ray shadow image, due to the projection from the focus of the X-ray tube on to the convex cathode (see fig. 2).

The various aberrations can be minimized (although not reduced to zero) by modifying the shape of the cathode and by fitting auxiliary electrodes around the circumference of the tube. The first Philips X-ray image intensifier was a triode tube; see fig. 2. The tube described in this article, illustrated in fig. 3, is a pentode. The ratio of the diameter of the input X-ray image to the outside diameter of the tube can therefore be made larger than with the imaging system in fig. 4. In addition, different magnifications can be obtained by varying the voltages of the three auxiliary electrodes, which are also used for focusing the electron beams. The new tube can be used at three fixed magnifications, which are arranged so that the diameter of the input image can be 36 cm (14 inches), 25 cm (10 inches) or 17 cm (7 inches) to completely fill the viewing screen in all three cases. The magnification can also be continuously adjusted. The curvature of the electron-optical image is corrected by a plano-concave fibre-optic plate at the output side of the tube. The use of another fibre-optic plate between the scintillation layer and the photocathode might be considered as a means of correcting the X-ray distortion. At present, however, fibre-optic plates of such dimensions cannot be made at a reasonable price.

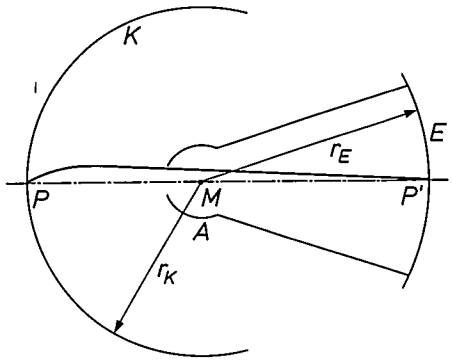

Fig. 4. Principle of the electron-optical imaging system proposed by P. Schagen, H. Bruining and J. C. Francken [3], which is the basis of all practical electrostatically focused image intensifiers. The photocathode K, the anode A and the output screen E have a convex curvature with a common centre point M. The image of the point P is produced at the point P'. The electrodes A and E are at the same potential, so that the space enclosed by A and E is 'field-free'. The magnification is equal to the ratio of the radii r_E and r_K of output screen and cathode.

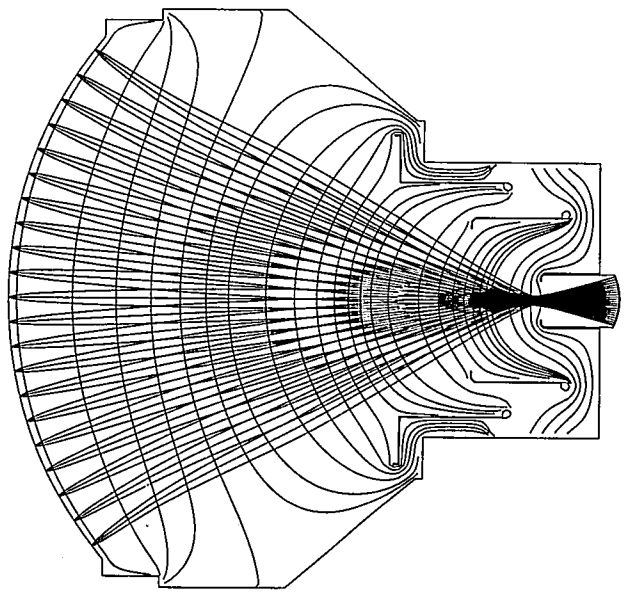

Fig. 5. Electron trajectories and equipotential lines in a 36-cm X-ray image intensifier, calculated and drawn with the aid of a computer.

Fig. 5 shows the electron-optical configuration after optimization by means of a computer program. The geometrical and chromatic aberrations were calculated for different geometries and different voltage combinations. The figure also shows a number of calculated equipotential lines and electron trajectories. With the parameters finally chosen the total pin-cushion distortion at the largest radius of the 36-cm input image is seven per cent (six per cent of this is due to X-ray distortion), as against 12% with earlier types of glass image-intensifier tubes (with a smaller input image).

Quantum noise

Fig. 6 illustrates the relative numbers of radiation quanta present in the image per unit time during the different phases of the image-forming process. The continuous and dashed lines give the relative numbers of quanta Q when an X-ray image intensifier is used and when an X-ray fluorescent screen is directly observed. G gives the increase in the photon yield when an image intensifier is used. Before the input window of the tube or before the fluorescent screen (at B in fig. 6) the image information is already present. In the following phases more quanta are produced, but the relative statistical fluctuation as compared with B increases, because not all the X-rays are absorbed in the X-ray screen. When the image intensifier is used, however, the number of quanta at the retina of the eye (at E in fig. 6) is so large that the image can be observed without lengthy adaptation.

The size of the details that can just be observed in the X-ray image — in spite of the statistical fluctuation due to their quantum nature — can be determined as follows. Let the average content of a detail in the X-ray image for a given dose be $\bar{Q}$ X-ray quanta. (At a dose of 100 μR and a typical X-ray tube voltage a detail of 1 mm^2 on the X-ray screen could contain 2×10^4 X-ray quanta.) The standard deviation of $\bar{Q}$ is equal to $\sqrt{\bar{Q}}$, since repeated observations of $\bar{Q}$ follow a Poisson distribution. A random contrast C_N caused by this distribution may be characterized by:

$$C_N = \{\bar{Q} - (\bar{Q} - \sqrt{\bar{Q}})\}/\bar{Q} = \frac{1}{\sqrt{\bar{Q}}}. \qquad (1)$$

If a cubic detail of edge x and absorption coefficient μ_x (in m^{-1}) is to be observed in a surrounding medium of absorption coefficient $\bar{\mu}$ (see *fig. 7a*), then the contrast C_A caused by the absorption difference is approximately proportional to the dimension of the detail in the direction of observation, and is thus equal to

$$C_A = x(\mu_x - \bar{\mu}). \qquad (2)$$

In (1) $\bar{Q}$ is proportional to the square of the dimension

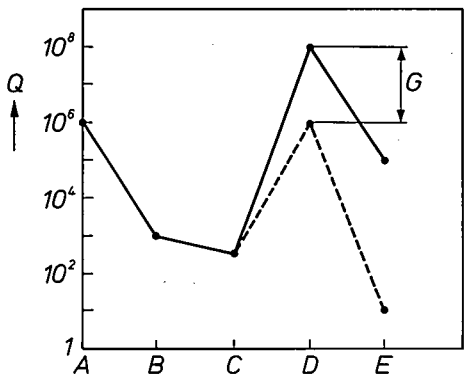

Fig. 6. The relative number Q of radiation quanta present per unit time during the image-forming process; A after leaving the X-ray tube, B after passing the object, C absorbed in the X-ray screen, D after passing through the output window of the image intensifier (continuous lines) or — without image intensifier — after passing through a fluorescent screen (dashed lines), E effective at the retina of the eye. G indicates the factor by which the photon yield is increased when an image intensifier is used.

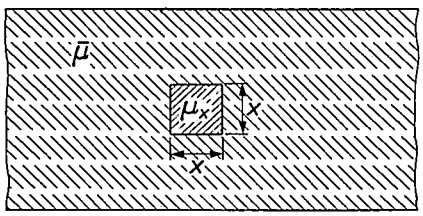

a

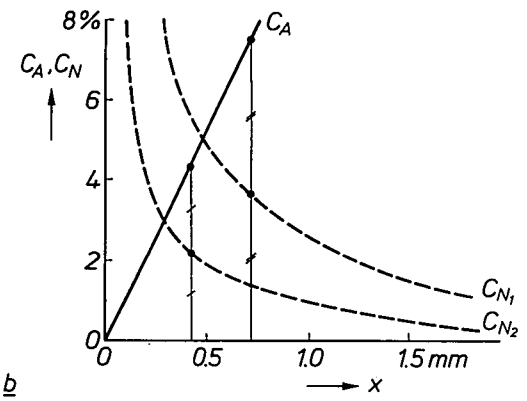

b

Fig. 7. Detail perceptibility in the X-ray image. *a*) A cubic detail of edge x and absorption coefficient μ_x in a medium with absorption coefficient $\bar{\mu}$ and approximately constant thickness. This idealized detail is a model of a blood vessel filled with contrast medium and located in a tissue environment (largely water). *b*) The contrast C_N due to the statistical quantum noise, and the contrast C_A due to the difference in absorption coefficient, both as a function of the edge x of the detail under observation. C_N depends on the dimension of the detail perpendicular to the direction of observation and is proportional to $1/x$; C_A depends on the dimension of the detail in the direction of observation and is proportional to x. The quantity C_N also depends on the X-ray dose. Curve C_{N_1} relates to a dose of 10 μR per exposure, C_{N_2} to a dose of 100 μR per exposure. Details are distinguishable from the statistical quantum noise if $C_A \geqslant kC_N$. It can be seen from the figure that for this example with $k = 2$ at a dose of 100 μR, details of 0.4 mm are only just perceptible. At a dose of 10 μR details of 0.7 mm are only just perceptible.

[3] P. Schagen, H. Bruining and J. C. Francken, A simple electrostatic electron-optical system with only one voltage, Philips Res. Rep. 7, 119-130, 1952.

of the detail perpendicular to the direction of observation, so that

$$C_N = \frac{1}{x\sqrt{D}}, \qquad (3)$$

where D is a quantity proportional to the radiation dose. Details can be distinguished from the quantum noise if $C_A \geqslant kC_N$. Work by A. Rose [4] has shown that k must be at least equal to 5. Others [5] have found lower limiting values for k. A reasonable value for the observation of details in X-ray images would seem to be $k = 2$. Fig. 7*b* shows the absorption contrast C_A and the quantum-noise contrast C_N as a function of the side x of a cubic detail filled with contrast medium, which is to be made visible when surrounded by water (or tissue). The details that are just visible for $k = 2$ when the dose is 10 μR (curve C_{N_1}) or 100 μR (curve C_{N_2}) can be read from the figure. In this example, a cubic object of 0.4 mm side can be made only just visible at a dose of 100 μR, and an object of 0.7 mm will be only just visible at a dose of 10 μR. In this case, increasing the dose ten times improves the perceptibility of detail by a factor of about two.

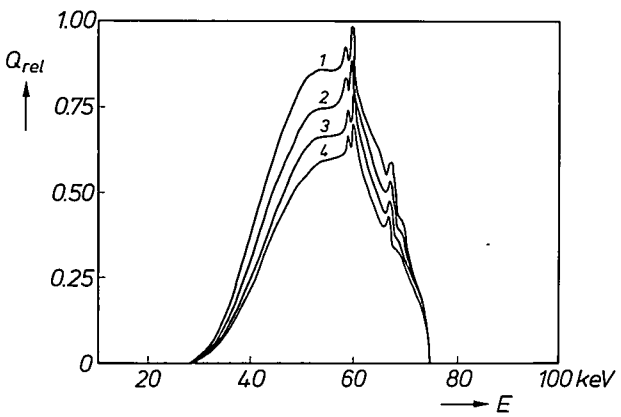

Fig. 8. The transmission of different input windows. The figure shows calculated X-ray spectra with the relative number Q_{rel} of quanta as a function of $E = hc/\lambda$, where λ is the wavelength, c the velocity of light and h Planck's constant. Curve *1* gives the measured spectrum of the radiation just before the image intensifier (at an anode voltage for the X-ray tube of 75 kV), curves *2*, *3* and *4* give the calculated spectra after an input window of 0.25-mm titanium, 3-mm glass and 4.5-mm glass, respectively. The associated mean transmission coefficients are 85, 77 and 69%.

As noted earlier, an X-ray image-intensifier tube should be designed in such a way that a minimum of noise is added during the successive phases of the image-forming process and the 'signal' (contrast) is attenuated as little as possible. The effect of the tube on the signal-to-noise ratio is characterized by the 'detective quantum efficiency' DQE. The DQE is defined as the ratio of the square of the signal-to-noise ratio at the output to its square at the input of the tube [6]. The DQE of the new tube is 0.53, as against about 0.4 for previous types of tube. The high value of the DQE is mainly due to the high absorption of the CsI layer. Another important feature is the low absorption of the titanium input window. *Fig. 8* shows the spectra of the X-radiation before and after passing through an input window of 0.25-mm titanium, of 3-mm glass and of 4.5-mm glass. The mean transmission coefficients for the three windows are 85, 77 and 69% respectively.

The active layers

The tube contains three layers in which the wavelength of the radiation is converted. The chemical composition of these layers and the nature of the wavelength conversions are listed in *Table I*. The last column gives the relative quantum flow between the active layers; the ratio of 10^5 for the entire image intensifier corresponds to the transition of phase *C* to phase *D* (continuous line) in fig. 6.

In earlier tubes the scintillation layer on the X-ray screen was made of sedimented zinc-cadmium sulphide. Because of the low packing density (50%) and the relatively low atomic numbers of the constituent elements of such a layer the absorption coefficient (i.e. the ratio of absorption to layer thickness) for X-radiation is not very high. This required a relatively thick layer (about 0.5 mm), to the detriment of the resolution. In the late sixties a vast improvement in X-ray image intensifiers was obtained by using *thin* layers of evaporated caesium iodide instead of relatively *thick* layers of sedimented zinc-cadmium sulphide. CsI has the advantages of high X-ray absorption, a packing density of nearly 100% and an anisotropic crystal structure — due to the evaporation process. *Fig. 9* shows the spectra of the X-rays absorbed in sodium-activated CsI and in silver-activated (Zn,Cd)S, compared with the spectrum of the input radiation [7]. The absorption is found to be approximately tripled. *Figs 10a* and *b* show cross-sections of a sedimented (Zn,Cd)S layer and of an evaporated CsI layer. In the photograph of the CsI layer the crystal anisotropy is clearly visible. Fig. 10*c* shows the images of a small light spot on the two layers. It can be seen that there is hardly any lateral scatter of the light in the CsI layer.

The scintillation layer and the photocathode (separated by a thin transparent film of aluminium oxide) are applied to the inside of the aluminium screen (*X* in fig. 3*c*). The photocathode consists of a 10-nm layer of caesium antimonide. This semiconducting compound reacts with water vapour and oxygen from the

air and therefore has to be formed *in situ* after the tube has been evacuated. Before the compound is formed, the caesium is stored in the tube as caesium chromate in 'dispensers', small tubes closed non-hermetically at both ends. The antimony has been deposited beforehand by evaporation on to the surface of the screen *in situ*. The contents of the dispensers are

Table I. Wavelength conversions in the successive active layers of the image intensifier, and relative quantum flows between them.

Layer	Chemical formula	Type of radiation	Wavelength [nm]	Quantum-flow ratio
		X-radiation	≈ 0.02 (at 75 kV and max. intensity, $\lambda = hc/eV$)	1
scintillator	CsI	↓ blue light	400	≈ 1000
photocathode	Cs_3Sb	↓ electrons	≈ 0.01 (at 35 kV tube voltage, $\lambda = h/\sqrt{2eVm}$)	≈ 100
phosphor	(Zn,Cd)S	↓ green light	535	≈ 100 000

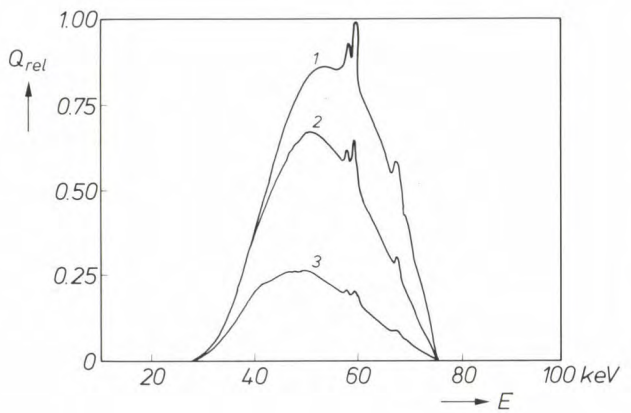

Fig. 9. The absorption of different scintillation layers. Curve *1* gives the X-ray spectrum just before the X-ray screen, curve *2* the spectrum of the radiation absorbed in evaporated CsI:Na, and curve *3* the spectrum of the radiation absorbed in sedimented (Zn,Cd)S:Ag. The layer thicknesses are 0.3 mm for CsI and 0.5 mm for (Zn,Cd)S. See also the caption to fig. 8.

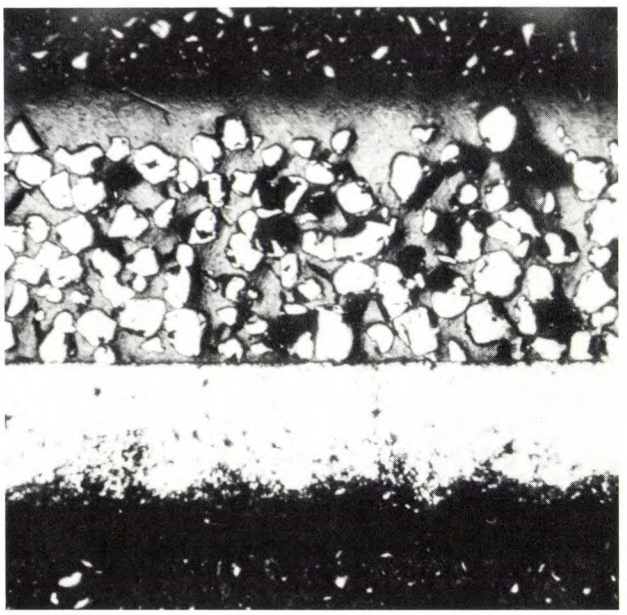

a

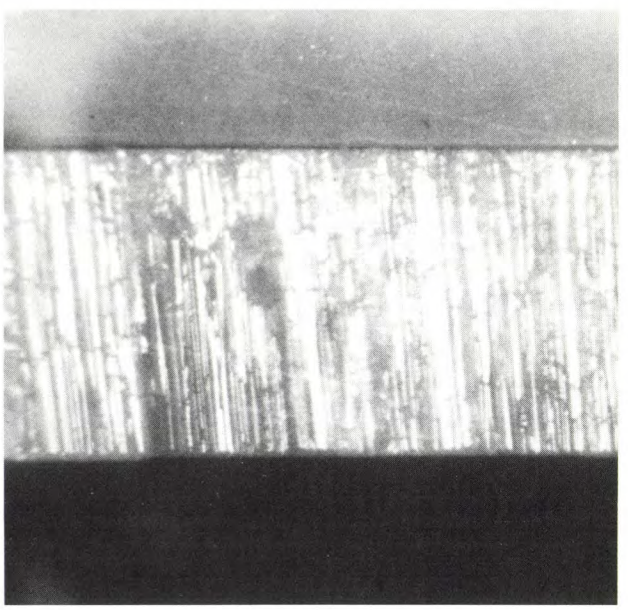

b

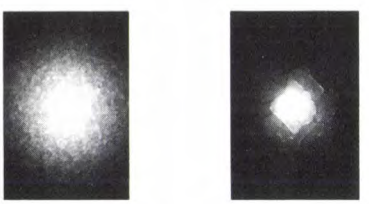

c

Fig. 10. Comparison of scintillation layers consisting of (Zn,Cd)S and CsI; see fig. 9. *a*) A sedimented layer of (Zn,Cd)S; the packing density is about 50%. *b*) Evaporated layer of CsI; the packing density is nearly 100%. The CsI layer also shows crystalline anisotropy; the photons generated by the X-ray quanta therefore undergo less lateral scatter. *c*) Image of a small light-spot on a layer of (Zn,Cd)S (*left*) and on a CsI layer. The low lateral scatter is evident from the greater sharpness of the image on the right.

[4] A. Rose, Vision: human and electronic, Plenum, New York 1973.
[5] A. D. Schnitzler, Image-detector model and parameters of the human visual system, J. Opt. Soc. Am. **63**, 1357-1368, 1973. W. Kühl, Information transfer with image intensifier systems, in: R. D. Moseley, Jr. and J. H. Rust (eds), Diagnostic radiologic instrumentation, Thomas, Springfield 1965, pp. 222-239.
[6] W. Kühl, Detection of X-rays for real-time imaging, in: D. A. Garrett and D. A. Bracher (eds), Real-time radiologic imaging: medical and industrial applications, (ASTM STP 716), Am. Soc. Test. & Mater., Philadelphia 1980, pp. 33-44.
[7] W. Kühl and J. E. Schrijvers, Design aspects of X-ray image intensifiers, Acta Electronica **20**, 41-51, 1977.

heated by passing a current, which causes the caesium to be released by reduction from the chromate. Caesium vapour leaves the dispenser and combines with the antimony on the X-ray screen to form the compound Cs_3Sb.

The luminescent layer on the output screen consists of a thin sediment of silver-activated zinc-cadmium-sulphide crystals ranging in size from 1 to 2 μm. This layer is coated with a thin film of evaporated aluminium to conduct the anode current and at the same time prevent light from the luminescent layer from reaching the photocathode. In the earlier image intensifiers these layers were applied directly to the glass envelope of the tube. The actual (Zn,Cd)S layer has a resolution of about 200 line pairs per mm, but this resolution is reduced by lateral scatter of the generated light and reflection from the back of the glass envelope wall; see *fig. 11a*, on the left. This 'halo' effect is almost completely suppressed by using the glass fibre-optic plate mentioned earlier as the substrate for the luminescent layer; see fig. 11*a*, on the right. The glass fibres have a diameter of about 10 μm. The fibre-optic plate therefore not only corrects the image curvature, but also performs three other functions: it acts as an anode-voltage insulator, as a vacuum seal, and as a substrate for the luminescent viewing screen. Fig. 11*b* shows pictures of a projected light spot, on the left for the case where the glass envelope forms the base for the luminescent layer, and on the right for the case where this is a fibre-optic plate. Elimination of halo effects has considerably improved the reproduction of contrast. However, the fibre-optic plate must be manufactured to very great accuracy, and this makes it one of the most expensive components of the image intensifier.

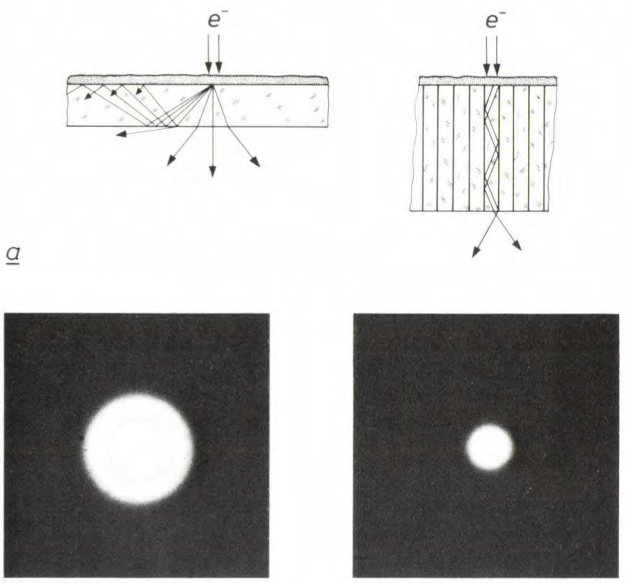

Fig. 11. The luminescent layer on the output screen. *a*) If the layer of sedimented (Zn,Cd)S is applied to the glass envelope wall (*left*), the photons generated by the electrons are partly reflected by the glass-air interface. This can be avoided by applying the luminescent layer to a fibre-optic plate (*right*). The electron-optical image can then also have greater curvature. *b*) Image of a small light spot on a layer sedimented on the glass tube envelope (*left*) and on a layer sedimented on a fibre-optic plate.

The measurement of quality

In the foregoing we have several times used the term 'resolution'. This has traditionally been *the* criterion for the quality of optical systems. Nowadays the criterion frequently used is the modulation-transfer function or MTF, which is the ratio of the modulation depths of sinusoidal changes in image intensity at the output and the input as a function of their spatial frequency in line pairs per mm; see *fig. 12a* and *b*. The resolution R is a quality criterion that is valid at high frequencies. However, it is at the high frequencies that the contrast of structures in the X-ray image is very low; see fig. 7. Furthermore, in resolution measurements (e.g. with 'Funk phantoms', line structures of varying fineness, made of lead foil) there is always a wide spread in the results because of subjective interpretation. The MTF therefore has greater significance and is more objective as a quality criterion than the resolution.

In recent years it has increasingly been recognized that the image quality of an X-ray image intensifier depends not so much on the MTF-value at high spatial frequencies — characterized by the resolution — as on the MTF-value at low frequencies. It has been customary to characterize the behaviour of the tube at low frequencies by the 'fogging' in the production of the image of a point object (P/Q in fig. 12*c*) or of a lead disc (S/T in fig. 12*c*, in accordance with a standard laid down by NEMA, the (American) National Electrical Manufacturers Association). The intensities P and S are due to stray X-ray quanta, photons and electrons in the tube. The behaviour of the tube at low frequencies — appearing as 'veiling glare', making the image look 'milky' — can be characterized more satisfactorily by the 'low-frequency drop' or LFD. The LFD is defined by the point of intersection of the M-axis and the extrapolated MTF curve at right angles to the M-axis; see fig. 12*b*. The LFD has been found to be a more reliable criterion for the subjectively experienced image quality than the criteria P/Q and S/T mentioned above and illustrated in fig. 12*c*. The LFD of the new tube is equal to 0.06 (as against 0.12 to 0.30 for earlier types of tube) and the MTF-

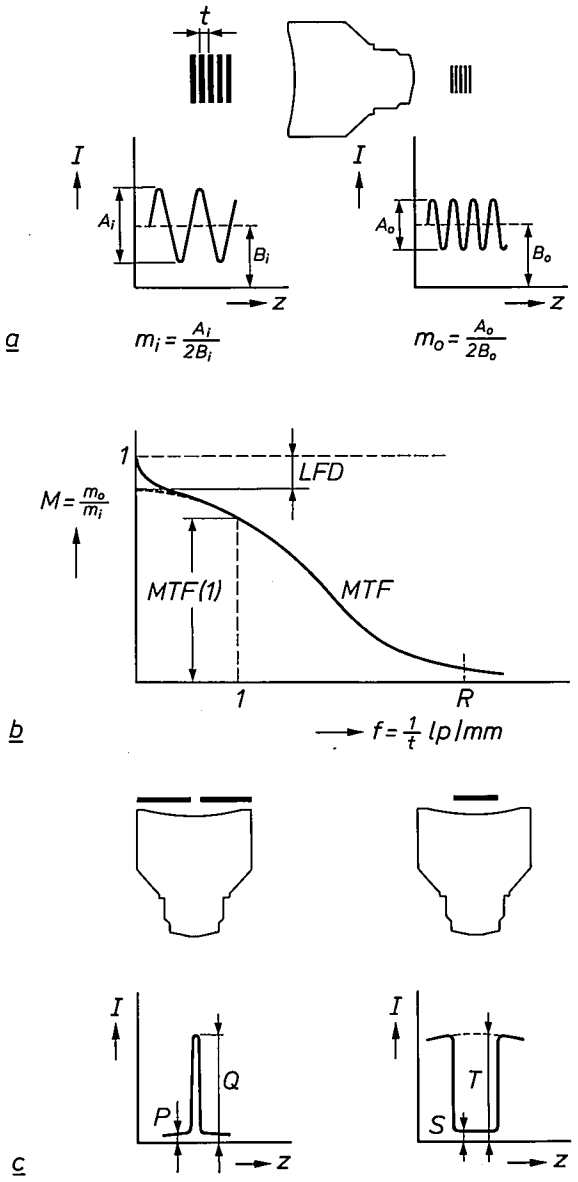

Fig. 12. The modulation-transfer function MTF. *a*) Illustrating the concept of modulation transfer. The intensity per unit area I as a function of position z is represented diagrammatically for the input and the output images in the case where an image is formed of a sinusoidal pattern of period t. The quantity m_i is the modulation depth of the input image, m_o the modulation depth of the output image. The modulation transfer is defined as the ratio $M = m_o/m_i$. *b*) Modulation transfer M as a function of the spatial frequency $f = 1/t$ in line pairs per mm of the sinusoidal pattern in the input image. The modulation-transfer function can be characterized by the following quantities: R resolution, the number of line pairs per mm of the sinusoidal structure that, in optical magnification, can only just be perceived; MTF(1) the value of M for $f = 1$ lp/mm; LFD the low-frequency drop or 'veiling glare'. The LFD can be determined by extrapolating the MTF curve in such a way that the M-axis is intersected at right angles. *c*) Other criteria for contrast reproduction at low frequencies. On the left, the fogging (or halation) P/Q in the image of a point object; on the right the fogging S/T in the image of a lead disc. It has been found that the LFD as in fig. 12*b* is a more reliable criterion of subjectively evaluated image quality than the other criteria.

value at a frequency of 1 lp/mm is equal to 0.40 (as against 0.30 to 0.35 for earlier tubes).

Another important criterion for judging the quality of an X-ray image intensifier is the luminance distribution of the output image. In image intensifiers, when the luminance distribution of the input image is constant the luminance of the output image generally decreases from the centre towards the edge. In earlier types of X-ray image intensifiers the luminance at the edges of the image was 75 to 80% of the value at the centre. In the new 36-cm image intensifier the luminance at the edges has increased to 90%, mainly because of the improved electron optics and the use of a plano-concave fibre-optic plate.

Apart from this unevenness in luminance on a large scale, luminance defects can also occur on a small scale. These latter defects may be caused by faults in the active layer or in the fibre optics, or by loose particles in the tube. Image defects of this type are referred to as 'spots'; the total number of spots determines the 'cosmetic quality' of the tube. If the output image is recorded photographically, the contrast in the image is increased about three times (by the 'gamma' of the film material). The increase in contrast enhances the effect of spots in the image. (In cine exposures, or when a TV camera tube is used, the contrast is only slightly increased, if at all.) At the end of the production process every X-ray image intensifier is carefully tested for the presence of spots and blemishes.

The new image intensifier in diagnostic installations

X-ray image intensifiers in medical diagnostics were at first used for screening (fluoroscopy) and for recording dynamic effects with cine cameras. The static photographs made with an image intensifier (photofluorography) were not generally acceptable, however, because of their unusual smaller format and their poorer image quality. Static X-ray images were therefore usually produced as a full-size radiograph of large format. The use of X-ray screens with thin CsI scintillation layers in image intensifiers gave an appreciable improvement in the modulation transfer and the detective quantum efficiency (DQE). An image intensifier could now be used in combination with a 70-mm fluorographic camera, and later with a 100-mm camera.

Compared with previous types of 'glass' image intensifiers with CsI scintillators, the 36-cm image intensifier described in this article has given a considerable improvement of the modulation transfer at low frequencies (LFD). With a given tube design an improvement in the modulation transfer usually corresponds to a degradation of the DQE, since a thinner scintillation

layer has to be used. The application of metal technology has made it possible however, to improve both DQE and LFD of the new image intensifier. *Fig. 13* shows two renal angiograms (radiographs of the kidney blood vessels) made with a dose of 100 μR [8]. The radiograph in fig. 13*a* was made with the 36-cm input format, and both kidneys are visible. Fig. 13*b*, for which the 17-cm format was used, only shows the right kidney.

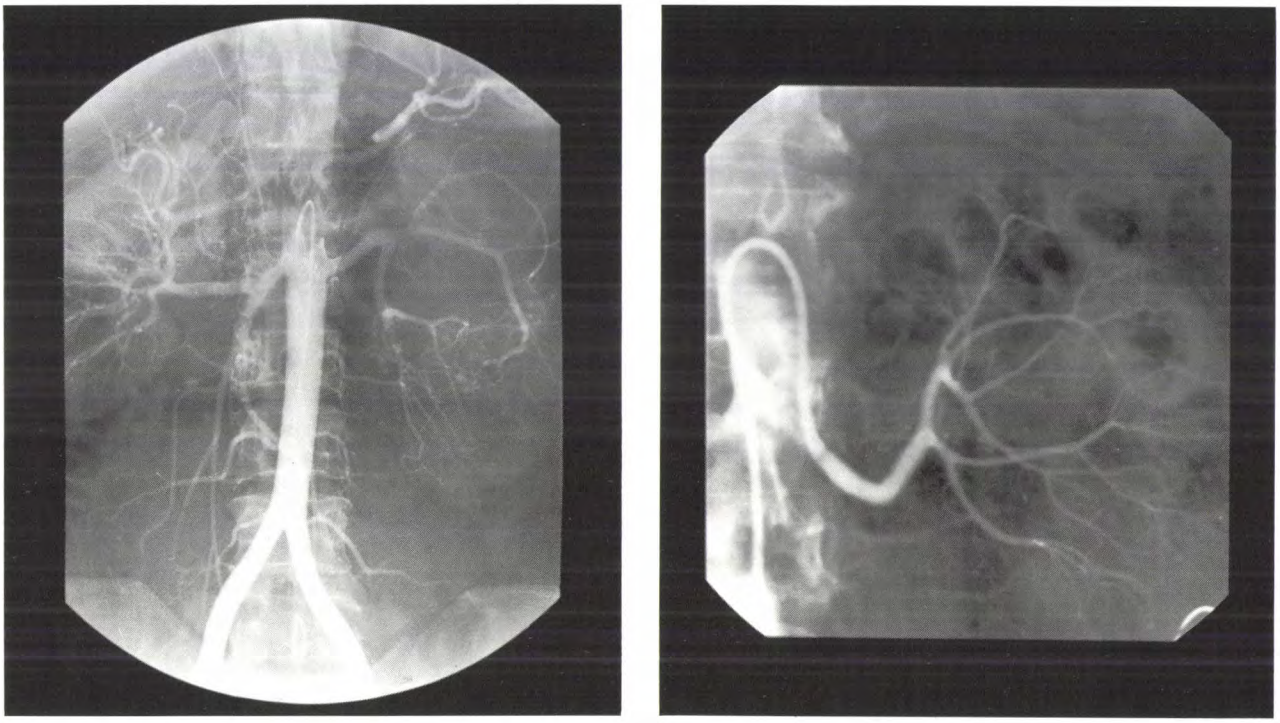

Fig. 13. Two radiographs (angiograms) of blood vessels in the kidneys, made on 100-mm film with the new 36-cm image intensifier. A contrast medium has been injected into the blood vessels. *a)* An angiogram made with an input format of 36 cm. The blood vessels in both kidneys and a part of the aorta are visible. *b)* An angiogram made with the 17-cm format. The good contrast rendering of both exposures is typical of the quality of the new tube.

The X-ray installation used by the radiologist usually comprises two detector systems, one with an X-ray image intensifier and CCTV system, the other with full-size film cassettes. Now that the new 36-cm image intensifier is available, the radiologist can use a single detector system in which all the functions are integrated. *Fig. 14* shows such a modern X-ray installation, the Philips DIAGNOST ARC, which includes the 36-cm image intensifier, a 100-mm camera giving a maximum of eight pictures per second, a cine camera and a CCTV system. The area under investigation can be examined with a low X-ray dose per second by means of a TV monitor. At the appropriate moment a single 100-mm exposure of the appropriate location or a series of 100-mm exposures is then made. Making radiographs at the wrong moment is now a rare occurrence because the image is observed on the TV monitor at the same time as the exposures are made. When a series of full-size radiographs is being made, complete cassettes have to be changed and a frequency of eight images per second is not feasible. The use of 100-mm film makes the X-ray examination more efficient, and as already mentioned in the introduction, cuts costs as well as saving film storage space and reducing patient dose.

In the X-ray diagnostic system shown in fig. 14 the dose control of the X-ray tube is linked to the exposure control of the camera tube and the photo camera. *Fig. 15a* illustrates this. The quantity of light leaving the image intensifier is measured by a light sensor *LS*. The exposure control *EC*, which is controlled by a microprocessor, is linked to the high-voltage generator *XG*, which supplies the X-ray tube *XT*. The exposure control also operates the iris diaphragm *ID* of the camera and the lead diaphragm *LD* for the X-ray tube. If the image intensifier is set for a smaller format than the maximum, the current in the X-ray tube is increased in inverse proportion to the diameter of the image on the X-ray screen. (This is necessary because

more details have to be visible in the smaller format.) The exposure control then causes a different lead diaphragm to be placed in front of the X-ray tube, so that a smaller area of the patient is irradiated and the patient receives a smaller total amount of radiation. On transition to the smaller image format the diaphragm setting in the photo camera is increased at the same time; see fig. 15*b* and *c*. In the conventional method, on the other hand, the diaphragm remains unchanged and for smaller formats the current in the X-ray tube must be increased in inverse proportion to the square of the diameter of the X-ray image, to keep the amount of X-ray quanta per exposure the same, regardless of the input format.

Because of its good modulation transfer for low frequencies, the new X-ray image-intensifier tube is particularly suitable for systems with digital image processing, which are of increasing importance. In these systems the video signal, obtained by means of a Philips Plumbicon 45XQ camera tube with high MTF, is converted into a digital signal. The digital signal can then be subjected to various kinds of digital processing. An example is the digital processing of angiograms (DVI: 'digital vascular imaging') [9]. Here a

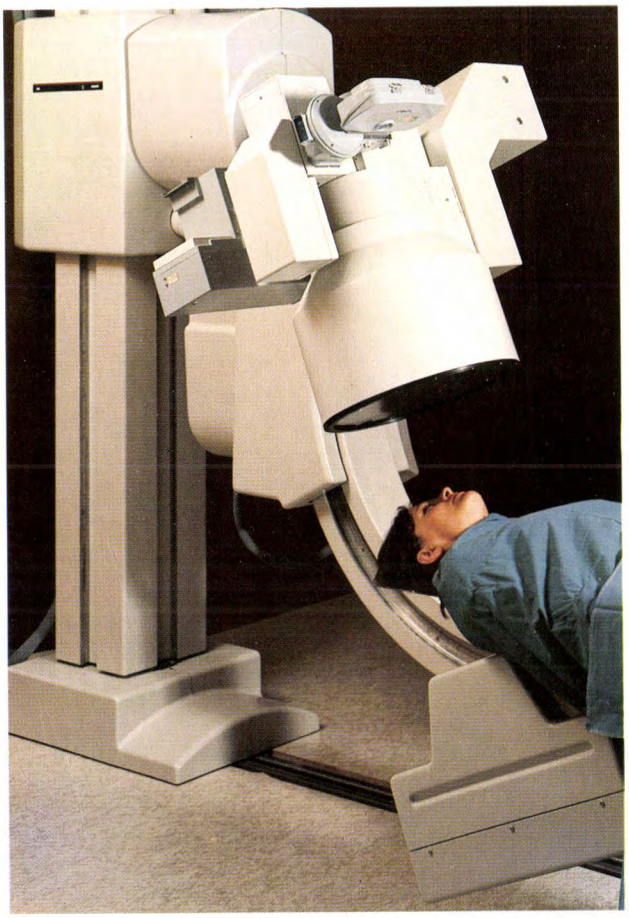

Fig. 14. The Philips DIAGNOST ARC X-ray system, in which a 36-cm X-ray image intensifier, a 100-mm camera, a closed-circuit TV with a Plumbicon camera tube, and a cine camera are integrated. Because of the high quality of the image intensifier, an installation of this kind does not require a separate cassette system for full-size radiographs. One of the advantages of using 100-mm film is a considerable saving in film and storage space.

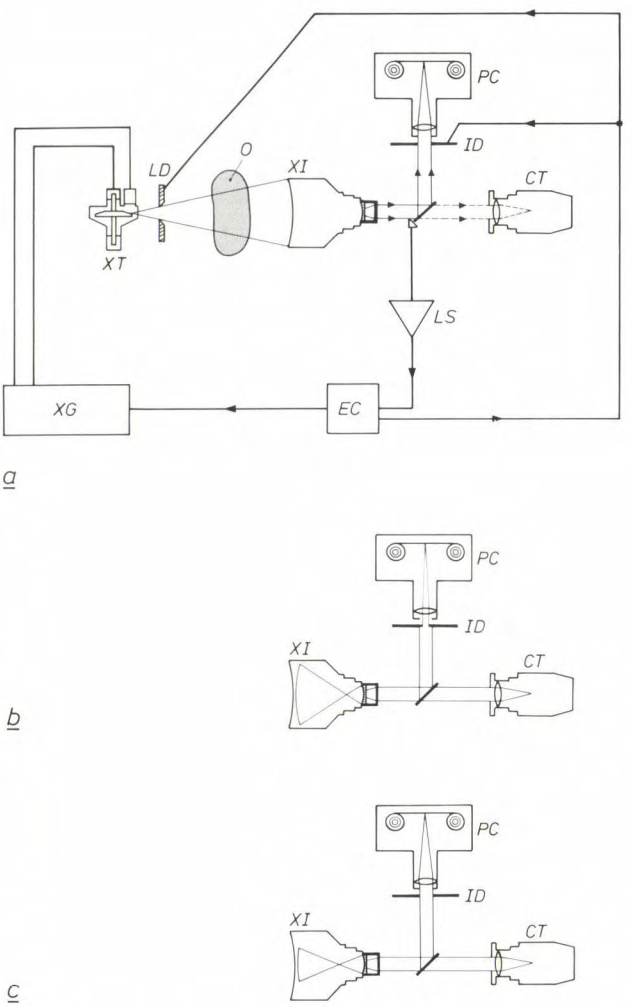

Fig. 15. *a*) Control of film exposure. *XT* X-ray tube with rotating anode [1]. *LD* lead diaphragm. *O* object. *XI* X-ray image intensifier. *PC* photo camera. *ID* iris diaphragm. *CT* camera tube. *LS* light sensor. *EC* exposure control. *XG* high-voltage generator for the X-ray tube. A smaller input image for *XI* permits the use of a smaller diaphragm *LD*. The current through the X-ray tube is then increased in inverse proportion to the diameter of the X-ray-screen image. With a smaller image format the patient is thus exposed to a smaller radiation dose than in the conventional procedure, where the current increases in inverse proportion to the square of the diameter of the X-ray image. *b*) *c*) On switching to a smaller image format, the opening of the camera diaphragm *ID* is increased.

[8] G. Hancken, L. P. Dietrich and H. Birken, Erste klinische Erfahrungen mit einem 36-cm-Bildverstärker, Röntgenstrahlen, No. 37, 12-23, 1977.

[9] C. A. Mistretta *et al.*, Digital vascular imaging, Medicamundi **26**, 1-10, 1981.

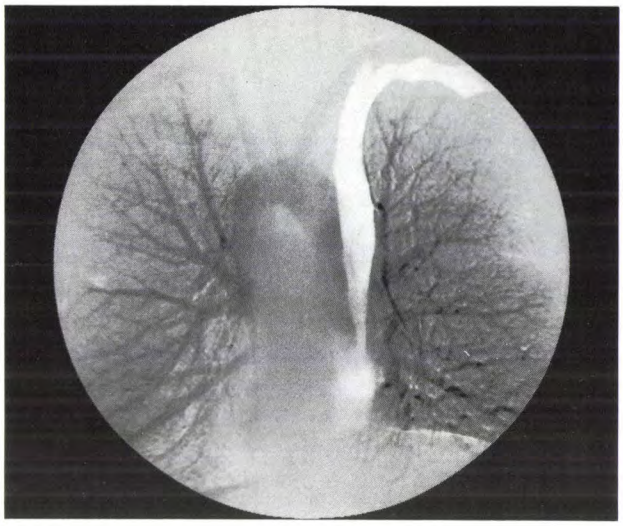

Fig. 16. Example of the digital processing of angiograms using DVI (digital vascular imaging). The picture shows an image of the branching of the pulmonary artery. As a result of digital subtraction of exposures with and without contrast medium, blood vessels can be seen more clearly in this angiogram, without surrounding tissue or bone. The good modulation transfer at low spatial frequencies makes the new image intensifier particularly suitable for diagnostic systems using digital signal processing.

high-contrast image of blood vessels is obtained by digital subtraction of exposures made with and without contrast medium in the blood. *Fig. 16* shows an example of a DVI angiogram of the pulmonary artery.

Summary. The new 36-cm X-ray image intensifier offers in addition to a large input format the advantage of enabling routine exposures of high quality to be made on 100-mm film. This image quality is due to an improved electron-optical system, a metal input window with low X-ray scatter, a CsI scintillation layer giving high absorption, and the use of a fibre-optic plate at the output. The use of a fibre-optic plate makes strong curvature of the electron-optical image permissible, so that — in spite of the large input format — the tube is still relatively compact and can be built into existing equipment. The detective quantum efficiency of the tube is high. This reduces the effect of statistical quantum noise, giving better detail perceptibility for the same dose per exposure. The image veiling glare or 'low-frequency drop' of the new tube is low, giving good contrast reproduction. The new tube is used in diagnostic systems in which a 100-mm camera and a Plumbicon TV camera are integrated. An automatic exposure control ensures that the average quantity of radiation per exposure is lower than previously. In combination with a TV camera the new tube is also very suitable for systems using digital image processing.

Iridescence in technology and nature

The objects in the two photographs shown here — a modern multilayer reflector and an old, weathered wine bottle — have a glossy, somewhat mother-of-pearl appearance. The reflector consists of a flat glass disc, with a diameter of 2.5 cm, on which there are more than 40 thin alternate layers of silica and titanium dioxide. The layers, deposited in a vacuum chamber in a series of evaporations of SiO_2 and TiO_2, each have a thickness corresponding to an optical pathlength of about 0.14 μm. This value is equal to a quarter of the 'mean' wavelength of visible light. The corresponding refractive indices are alternately low (SiO_2:1.47) and high (TiO_2:2.51). A '$\frac{1}{4}\lambda$-stacked element' of this type, which has a remarkably low absorption in the entire spectrum of visible light, possesses a very high reflection coefficient ($\geqslant 99\%$) in a particular wavelength range and can be used in all kinds of optical systems as a selective mirror (band filter). Its operation is based on interference of the reflected light waves. This interference can also explain the iridescence effect, which contributes to the smooth changes in colour.

The connection between the antique wine bottle and the reflector is that the surface of the bottle also has a multilayered structure. It is known that Nature can also produce such a structure, although in this case it took about ten million times longer to do so than it did the three members of the Research Laboratories (Dr Ir J. Haisma, J. J. M. Pasmans and P. G. M. Vos) to make the multilayer reflector and the photographs. The natural changes in temperature and humidity in the mud of an Amsterdam canal for more than 350 years were responsible for the flaky surface structure of the bottle, with its layers of alternating refractive index, higher for glass and lower for water/air. During the warmer seasons of the year water molecules will easily have penetrated into the glass and a relatively fast ion exchange will have occurred, e.g. Na^+ out and H_3O^+ in, making the glass brittle in places. Shrinkage due to falling temperature in cold seasons must then have led to flaking. The temperature drop in the Dutch climate has apparently not been severe enough for the brittle layers to have broken away completely, since the wall of the bottle has remained intact. In this way a multilayer structure must have formed in the glass, and the layers constitute a somewhat incomplete record of the seasonal variations of Mother Earth in an Amsterdam canal. Unfortunately, counting the layers in antique glass does not give a reliable indication of age, like the rings of a tree.

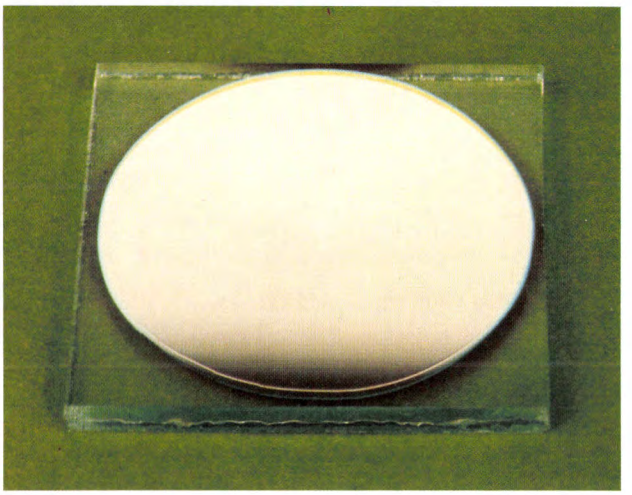

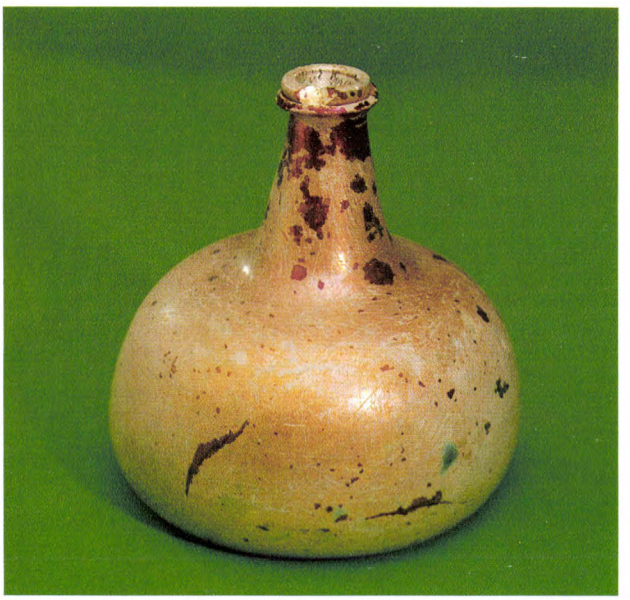

Philips Tech. Rev. **41**, 150-163, 1983/84, No. 5

X-ray lithography for VLSI

H. Lüthje

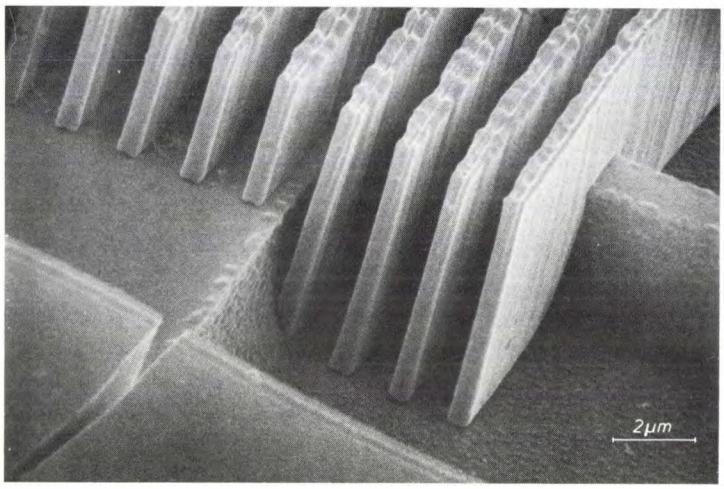

The photolithographic methods used in the production of integrated circuits (ICs) are also in use for large-scale integration (LSI), where the sizes of details are in the micron range. Owing to the occurrence of optical diffraction effects, however, photolithographic methods are often inadequate for the submicron structures required by the increasing miniaturization and complexity of the circuits in very-large-scale integration (VLSI). For this reason other lithographic methods are being developed for producing circuits of this kind. One of these methods, electron lithography, has been described in a previous article in this journal. The article below deals with the investigation of another promising method, X-ray lithography.

Lithographic methods for VLSI

The lithographic method used in IC technology for transferring patterns to the surface of a silicon slice is illustrated schematically in *fig. 1*. Radiation passes through a mask containing the required pattern on to a silicon slice coated with a thin layer to be structured (e.g. an oxide layer) and a layer of photosensitive resist. After development of the resist the uncovered parts of the layer beneath it are etched away, so that a pattern corresponding to that of the mask remains on the slice. In the production of an IC different patterns are applied successively to the same part of the slice. The corresponding masks must therefore be in exact alignment with one another. The mask patterns have to be transferred to the slice with sufficient accuracy and with sufficiently sharp demarcation to ensure that all the details of the patterns are preserved during further processing of the slice. The lithographic process must also be compatible with a number of general requirements of IC technology, such as rapid production, high reliability, high yield and low cost per unit.

A significant development in IC technology is the ever-increasing refinement of the pattern details. As circuits become smaller the IC components can have higher packing densities, and consequently higher switching rates, lower energy consumption, lower costs and improved performance. Since the introduction of ICs the packing density has almost doubled every year. In the circuits now being produced a single slice can

Dipl.-Ing. H. Lüthje is with Philips GmbH Forschungslaboratorium Hamburg, Hamburg, West Germany.

contain many hundreds of thousands of components. To indicate the extreme complexity of these circuits the term very-large-scale integration (VLSI) is used, as an extension of LSI [1].

The miniaturization of ICs imposes increasingly stringent requirements on the lithographic resolution. Whereas in LSI the minimum dimensions are still in the micron range, future VLSI circuits will have to contain details smaller than 1 μm. This has important consequences with regard to the choice of the lithographic method [2]. We shall now look briefly at a number of the methods that might be used.

Limitations of photolithography

The simplest and most widely used lithographic method in IC technology is photolithography. In this method a layer of photosensitive resist is irradiated with ultraviolet light. Each mask consists of a transparent substrate and a thin light-absorbing layer carrying the required pattern.

Until recently the masks were usually pressed against the slices, to give relatively fine details. Serious practical drawbacks of this 'contact printing' are the damage caused to the mask, leading to errors in subsequent slices, and local differences in the distance between mask and slice due to surface unevenness in the slices.

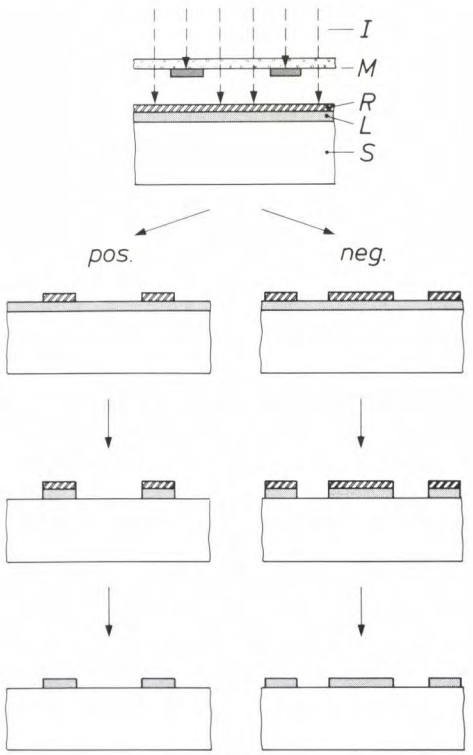

Fig. 1. Diagrammatic representation of lithography for producing the desired patterns on a silicon slice *S*. Radiation *I* passes through a mask *M* containing the required pattern and is incident on a layer of resist *R* that is sensitive to this radiation. After development of the sensitive layer only the non-irradiated parts remain for a *positive* resist and only the irradiated parts for a *negative* resist. The uncovered parts of the layer *L* to be structured are then etched away, and the remaining resist is then removed.

If some space is allowed between mask and slice the resolution is limited mainly by diffraction effects. The minimum detail size Δx is then given by:

$$\Delta x \approx \sqrt{\lambda d},$$

where λ is the wavelength of the light used and d the distance between mask and slice. At a distance of 30 μm and a wavelength of 400 nm details of 4 μm can be reproduced. Reducing the wavelength to say 200 nm gives a higher resolution but does not lead to the reproducible production of submicron structures.

Better results can be obtained with exposure by projection, especially when it is accompanied by reduction. A familiar example of this method is the use of the Silicon Repeater [3]. With this machine repeated projections of a single mask at a fifth of full scale are made directly on the slice. Successive patterns are accurately positioned with respect to the already existing part of the circuit. It is possible to compensate for small deformations of the silicon surface. The optical repeaters now in use can produce details down to about 0.7 μm and are therefore suited to the manufacture of the present VLSI circuits. Even these advanced machines, however, will not be able to produce the details smaller than 0.5 μm that will be required in future VLSI circuits. A disadvantage of repeating projectors is that they are complicated and therefore fairly expensive. Other disadvantages are that images can only be made of relatively small areas and that the reproduction of submicron structures requires very careful processing of the resists.

Possible use of electron and ion lithography

To permit the transition to smaller details some methods have been developed that use electrons or ions instead of light. The effective wavelength of these particles is much smaller than the dimensions of the details required, so that diffraction effects are no longer a problem.

In electron lithography a narrow beam of electrons is usually used to define the pattern in an electron-sensitive resist [4]. An electron-beam pattern generator, as described earlier in this journal [5], can be used for

[1] See the articles on LSI in Philips Tech. Rev. **37**, 265-356, 1977.
[2] An extensive review of lithography for VLSI has been given by R. P. Kramer, Ned. T. Natuurk. **A 46**, 4, 1980 (in Dutch) and by A. N. Broers, IEEE Trans. **ED-28**, 1268, 1981.
[3] A. G. Bouwer, G. Bouwhuis, H. F. van Heek and S. Wittekoek, Philips Tech. Rev. **37**, 330, 1977. An improved version of the Silicon Repeater will be described in a forthcoming issue of this journal.
[4] See for example M. J. Bowden, CRC Crit. Rev. Solid State & Mater. Sci. **8**, 223, 1978/79.
[5] J. P. Beasley and D. G. Squire, Philips Tech. Rev. **37**, 334, 1977.

drawing the pattern directly on the resist ('direct slice writing'), or for making masks, which can then be copied, for example with an electron-image projector [6], the electron-optical analogue of the optical image projector. The pattern generator is versatile: the electron-optical system can be electrically controlled and operated by a computer. Given favourable conditions the resolution obtainable is better than 0.1 μm. A disadvantage of this method is that lateral scatter of the electrons in the slice can cause distortion of closely adjacent details. This 'proximity effect' can be corrected to some extent, but at the expense of the writing speed. For direct slice writing in mass production this is an economic problem. For making masks, however, electron lithography, with its versatility and accuracy, is a suitable method, which is now widely used.

Direct writing on the slice is also possible with an ion beam [7]. Because the absorption in the resist is better, this method has higher sensitivity than writing with an electron beam. It is difficult, however, to find an intense and sufficiently stable ion source. Another problem is the proximity effect, which can also occur with ions. The other form of ion lithography, ion-optical imaging of the pattern, gives too much thermal deformation in the masks.

Investigation of X-ray lithography

Another promising method for VLSI is X-ray lithography [8], in which X-rays are used to produce an image of the mask pattern on a slice coated with X-ray-sensitive resist. The wavelength of the radiation varies from about 0.5 to 3 nm, so that no diffraction effects occur. The title photograph, made with a scanning electron microscope (SEM), shows a resist pattern applied to a silicon structure by X-ray lithography with a mask-to-slice distance of 400 μm. Even with a maximum layer thickness of 10 μm the width of the tracks in the resist is only 0.5 μm. The resolution obtainable is of the same order as with electron lithography (< 0.1 μm). As compared with the latter method, X-ray lithography at these wavelengths has the advantage that there is no proximity effect. On the other hand, many more problems are encountered in finding a suitable radiation source, alignment, and making the masks and resists.

The investigation described in this article is mainly concerned with the production and testing of different masks. We are also interested in finding suitable resists. A great deal of this work is being done in cooperation with other groups, both within Philips and outside. It all forms part of a comprehensive programme (the BESSY project), which is supported in the Federal Republic of Germany by the Ministry of Research and Technology, for the development of X-ray lithography for VLSI. Before dealing with our contribution to this work, a general description will be given of the procedure adopted for X-ray lithography.

Procedure for X-ray lithography

An X-ray lithographic system generally consists of an X-ray source, a mask with the required pattern, an alignment system and a slice coated with an X-ray-sensitive resist; see *fig. 2*. The choices of these components are closely interdependent.

Choice of X-ray source

In a conventional X-ray tube [9] X-radiation is generated by bombarding an anode with high-energy electrons (10 to 30 keV). Such a source is fairly monochromatic and is not expensive compared with other X-ray sources. A disadvantage is the relatively low intensity of the radiation, so that long exposures may sometimes be required (perhaps as much as 20 to 30 minutes or more). Because of the low radiation intensity the source has to be located close to the mask (e.g. at a distance of 20 cm). A difficulty then is that the divergence of the X-rays can cause considerable distortion in the image. This source therefore seems less suitable for producing submicron details.

Other sources consist of plasmas generated by a powerful laser [10] or by injection of an intense electron beam [11]. These sources provide X-radiation at very high intensity and are therefore of interest for

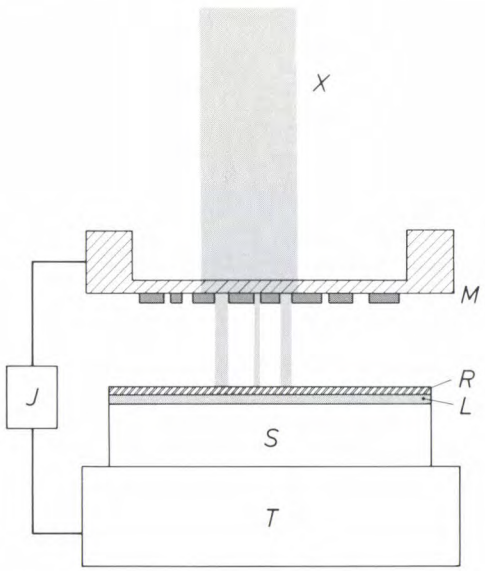

Fig. 2. Diagram of arrangement for X-ray lithography. *X* X-radiation. *M* mask with X-ray-transmitting membrane and X-ray-absorbing metal layer with the required pattern. *S* silicon slice coated with the layer *L* to be structured and an X-ray-sensitive resist *R*. *T* slice table. *J* system for aligning slice and mask.

lithographic applications. At present, however, they are still insufficiently developed.

Distinctly better prospects are offered by the use of synchrotron radiation generated tangentially by the circular movement of relativistic electrons; see *fig. 3*. The spectral distribution of this X-ray source extends over a wide wavelength range, e.g. from 0.1 to 100 nm. The high intensity of the radiation enables the exposure times to be kept short (a few seconds) and the distance between source and mask can be large enough (> 10 metres) to make the divergence of the incident radiation very small.

A problem with synchrotron radiation is that the source is extremely expensive. For the investigations with this source it was therefore decided to make a collective approach, with several firms and institutes participating, so as to keep the financial risk within bounds. The chief source is the BESSY storage ring set up in West Berlin. Work is now also under way in the project on the development of a compact cheaper version for individual use in IC factories.

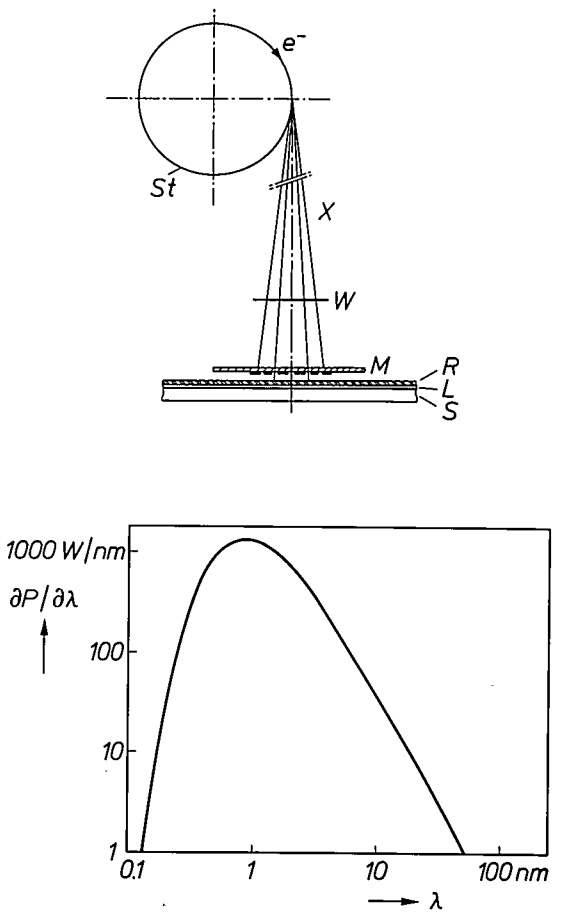

Fig. 3. *Above:* Diagram representing synchrotron irradiation for X-ray lithography. Relativistic electrons in the storage ring *St* generate tangential X-radiation *X*. This passes through the X-ray-transmitting vacuum window *W* and the mask *M* on to the slice *S* with the layer *L* to be structured and the resist layer *R*. In experiments with the BESSY storage ring in West Berlin the distance between X-ray source and mask is 13.5 m. *Below:* Spectral distribution ($\partial P/\partial\lambda$ as a function of λ) of the X-radiation generated by BESSY, at an electron current of 1 A and an energy of 800 meV.

Another problem is the limited homogeneity of the radiation in the vertical direction, perpendicular to the plane of the drawing in fig. 3. Only strips with a height of about 10 mm can be homogeneously irradiated. For larger surfaces the X-ray beam can be diffracted by means of reflectors [12]. It is also possible to enlarge the area that can be homogeneously irradiated by setting the storage-ring electrons into oscillation by means of an oscillating electrical or magnetic field [13]. Both methods have been successfully used with the BESSY storage ring.

In view of the extremely high accuracy required in making images of submicron structures it is necessary to use a 'step-and-repeat' process, in which repeated images of an X-ray mask of area a few square centimetres are made on the slice. The high accuracy required is achieved in this process by moving the slice into exact alignment with the mask.

Choice of alignment system

As the details required diminish in size the alignment of successive mask patterns on the same part of the slice must be improved. In practice it is found that an alignment accuracy better than a quarter of the smallest dimension is necessary. This means that the alignment has to be exceptionally accurate in X-ray lithography.

As in other lithography methods, the masks are provided with markers, which are scanned during the alignment process. Visible light in the form of laser radiation is preferably used for the alignment. Because of the high intensity of this radiation the identification time required is very short (e.g. 0.01 s), so that the alignment does not limit the rate of production. A further advantage of optical alignment in X-ray

[6] J. P. Scott, Philips Tech. Rev. 37, 347, 1977.
[7] See for example R. L. Seliger and P. A. Sullivan, Electronics 53, No. 7 (March 27), 142, 1980.
[8] See for example:
E. Spiller and R. Feder, in: H.-J. Queisser (ed.), X-ray optics (Top. Appl. Phys. 22), Springer, Berlin 1977, p. 35;
A. Heuberger, H. Betz and S. Pongratz, Festkörperprobl. 20, 259, 1980;
H. I. Smith and D. C. Flanders, J. Vac. Sci. & Technol. 17, 533, 1980.
[9] A description of metal/ceramic X-ray tubes is given by W. Hartl, D. Peter and K. Reiber, Philips Tech. Rev. 41, 24, 1983/84, and 41, 126, 1983/84.
[10] P. J. Mallozzi, H. M. Epstein, R. G. Jung, D. C. Applebaum, B. P. Fairand, W. J. Gallagher, R. L. Uecker and M. C. Muckerheide, J. Appl. Phys. 45, 1891, 1974.
[11] R. A. McCorkle and H. J. Vollmer, Rev. Sci. Instrum. 48, 1055, 1977;
R. A. McCorkle, J. Phys. B 11, L 407, 1978.
[12] P. M. Guyon, C. Depautex and G. Morel, Rev. Sci. Instrum. 47, 1347, 1976.
[13] See the article by A. Heuberger *et al.*, mentioned in [8], p. 300.

lithography is that it does not affect the resist on the slice, since most X-ray resists are virtually insensitive to visible light.

By means of a displacement measurement system using a laser interferometer [14], alignment can be carried out to an accuracy more than sufficient to achieve the required detail dimensions. A repeater is used for the stepped exposure to synchrotron radiation, permitting separate alignment of mask areas between the different exposure steps. This permits correction for overlay deformations in the slice. In the joint project a repeating projector of this type is now being built for the BESSY storage ring.

Requirements for resists and masks

The choice of synchrotron radiation, stepped 1:1 (original pattern size) imaging and optical alignment has important consequences for the resists and masks to be used.

In the search for suitable resists the sensitivity to synchrotron radiation is a major criterion. A highly sensitive resist only requires a short exposure, which means that the total production rate can be faster. In addition, high contrast is required between the exposed and unexposed parts of the resist, for the patterns to be properly transferred to the resist. Also important is the ability of the resist to withstand physical ion etching [15], reactive ion etching and plasma etching [16], which are the usual dry-etching methods used in VLSI technology. Other practical aspects include the bonding to the slice, temperature stability, availability and price.

The masks for X-ray lithography also have to meet exceptionally strict requirements. The transmission of materials for X-radiation is much less variable than for ultraviolet light. Nevertheless the mask substrates must give high X-ray transmission, while the structures placed on them should have a high absorption. Since the images of the patterns are at full scale, the details have to be the same as in the final circuits. To permit optical alignment, the masks must be sufficiently transparent to light, at certain places at least.

Investigation of X-ray resists

Because of the many and varying requirements imposed on resists for X-ray lithography, there is no one resist that has all the best properties. This means that the best compromise has to be found from a variety of candidates. Some resists that were developed for electron lithography have turned out to be suitable for X-ray lithography as well. They consist of organic polymer molecules with linear chains. On irradiation these chains can break, resulting in the formation of smaller molecules, but they can also form bonds with others, leading to cross-linking and the formation of a three-dimensional network. In a *positive* resist there is a much stronger tendency for chain breakage to occur than cross-linking. As a result the molecules become so much smaller that the resist dissolves in the liquid developer. In a *negative* resist cross-linking is predominant, so that irradiation has the opposite effect: it makes the resist insoluble in the developer.

The sensitivity and the contrast of an X-ray resist can be derived from its characteristic curve. This is obtained by plotting the thickness of the layer of resist after the developing process against the radiation dose. *Fig. 4* shows idealized characteristic curves for positive and negative resists. The sensitivity of a positive resist can be defined as the minimum radiation dose required for complete solution of the resist in the liquid developer. For a negative resist the sensitivity is then the minimum dose required to make the resist completely insoluble. The contrast of a resist is determined by the slope of its characteristic curve.

In our investigation to determine the usefulness of different resists we looked not only at the sensitivity and the contrast but also at the resist profile that can be achieved and at its ability to withstand dry etching. Some of the resists studied are commercially available, others were developed at Philips Research Laboratories at Redhill and at Philips Research Laboratories in Eindhoven. In some cases additives are added to the resists to improve their properties for X-ray lithography.

The irradiation of the resists by X-rays was initially carried out with the DORIS storage ring in Hamburg,

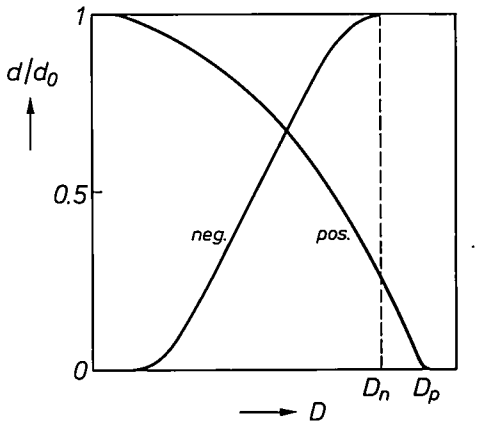

Fig. 4. Diagram showing the characteristic curves of positive and negative X-ray resists. The ratio of the thickness d after the development of the resist layer to the original thickness d_0 is plotted against the radiation dose D (logarithmic scale). A quantity that can be taken as a measure of the sensitivity of a positive resist is D_p, the minimum dose at which the resist is completely soluble in the liquid developer. The corresponding quantity D_n for a negative resist is the minimum dose at which the resist is completely insoluble in the developer.

but is now mainly done with the BESSY system in Berlin. Before irradiation the resists are first baked at a temperature above the glass transition temperature to give good bonding to the silicon slice. Depending on the temperature, baking time and atmosphere, other properties can also be improved by this pretreatment. The liquid developer we use is usually methyl isobutyl ketone (MIBK), or isopropyl alcohol (IPA) or a mixture of the two. The parts of the resist that are not soluble in the developer receive a second baking after development to improve the resistance to dry etching.

Results with positive X-ray resists

One of the best-known positive resists for X-ray lithography is polymethyl methacrylate (PMMA). Details of 0.01 μm can be produced in this resist, but the sensitivity is rather low [8]. The sensitivity can be improved by additives that increase the X-ray absorption (e.g. ferrocene). If the time for complete development of the layer of resist is kept constant, a smaller radiation dose is required; see *fig. 5*. Even with such an additive, however, PMMA resists have too low a sensitivity to be widely used in X-ray lithography.

Better results can be achieved with a positive resist consisting of methacrylate chains interconnected by acid anhydride cross-links. This resist, known commercially as PM15, was described as a suitable electron resist in a previous article in this journal [17]. On irradiation of PM15 the cross-links between the chains are broken, making the resist soluble in the liquid developer. A special property of PM15 is that the cross-linking increases at higher temperature, so that the solubility decreases. As a result of this, raising the pre-baking temperature has the beneficial effect of causing less (undesired) removal of non-exposed resist. On the other hand, the sensitivity to X-radiation will be reduced; see *fig. 6*. The optimum pre-baking temperature is about 110 °C. The sensitivity is then about three times higher than that of PMMA. As can be seen in the title photograph, a very sharp profile can be made in PM15. This profile changes hardly at all if the resist is post-baked at temperatures up to about 130 °C. Above this temperature it tends to become less sharp. *Fig. 7* shows sharp and less sharp profiles obtained in PM15 after post-baking the resist at temperatures of 110 °C and 150 °C.

Sharp profiles can also be obtained with positive resists consisting of polymers of fluoralkyl methacrylates, such as the commercially available resist FBM120. These resists also have a high sensitivity, about ten times that of PMMA.

The resists mentioned here are distinctly less resistant to dry etching than the AZ1350H resist widely used in photolithography; see *Table I*. The resistance of PMMA and PM15 is only high enough in a few cases to give sufficient protection to the underlying layer in the normal dry-etch conditions. The sensitive resist FBM120 has a relatively low resistance to reactive ion etching in CF_4 and CHF_3. Continued

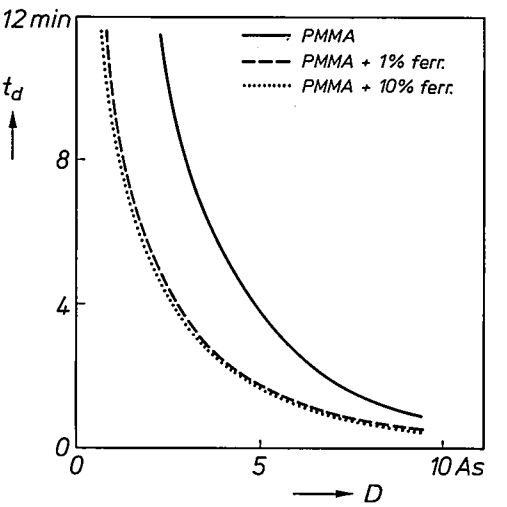

Fig. 5. Time t_d required for complete solution in the liquid developer MIBK, as a function of the radiation dose D, for positive resists based on PMMA. The resists were pre-baked for 30 min at 150 °C. Addition of 1% of ferrocene to PMMA gives a smaller value for t_d. A further increase of the ferrocene content has little effect.

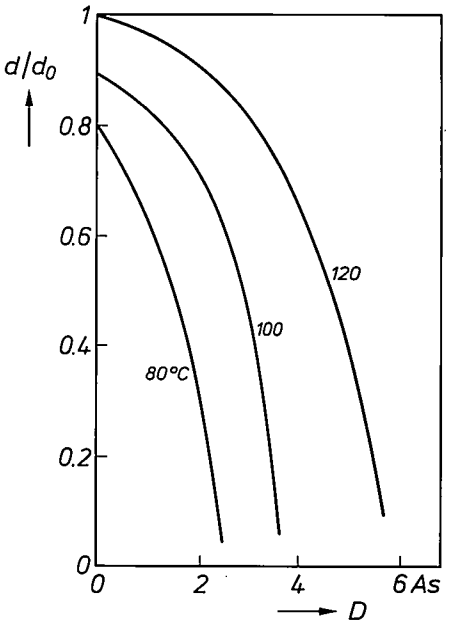

Fig. 6. Ratio of the thickness d after development in MIBK to the original thickness d_0, as a function of the radiation dose D, for the positive resist PM15 at three different pre-baking temperatures. A higher pre-baking temperature gives less removal of the 'non-irradiated' resist, but also gives a lower X-ray sensitivity.

[14] H. de Lang and G. Bouwhuis, Philips Tech. Rev. 30, 160, 1969.
[15] H. Dimigen and H. Lüthje, Philips Tech. Rev. 35, 199, 1975.
[16] H. Kalter and E. P. G. T. van de Ven, Philips Tech. Rev. 38, 200, 1978/79.
[17] E. D. Roberts, Philips Tech. Rev. 35, 41, 1975.

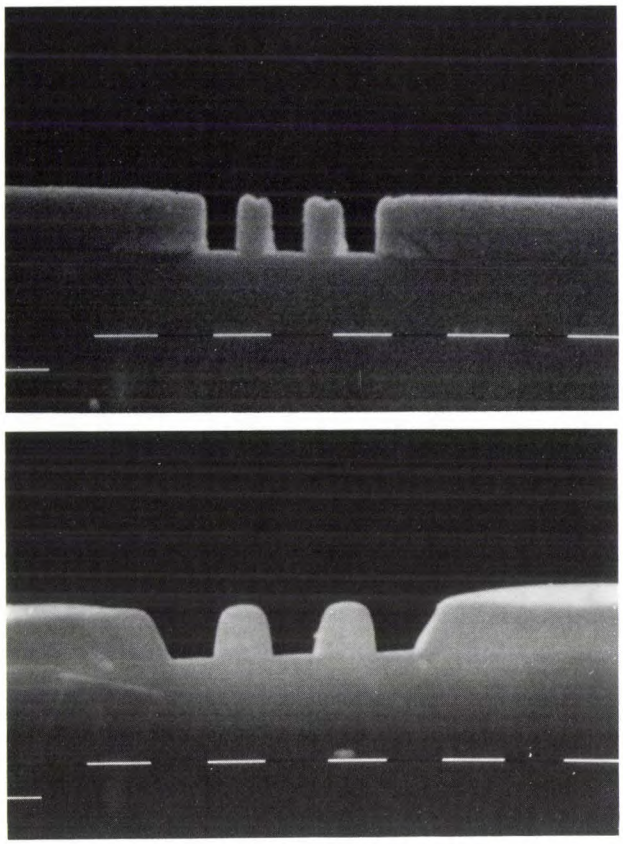

Fig. 7. SEM photographs of a pattern in the PM15 resist. *Above:* Track width about 0.5 μm, resist post-baked at 110 °C. *Below:* Track width about 0.7 μm, resist post-baked at 150 °C. The profile is less sharp as a result of the high post-baking temperature.

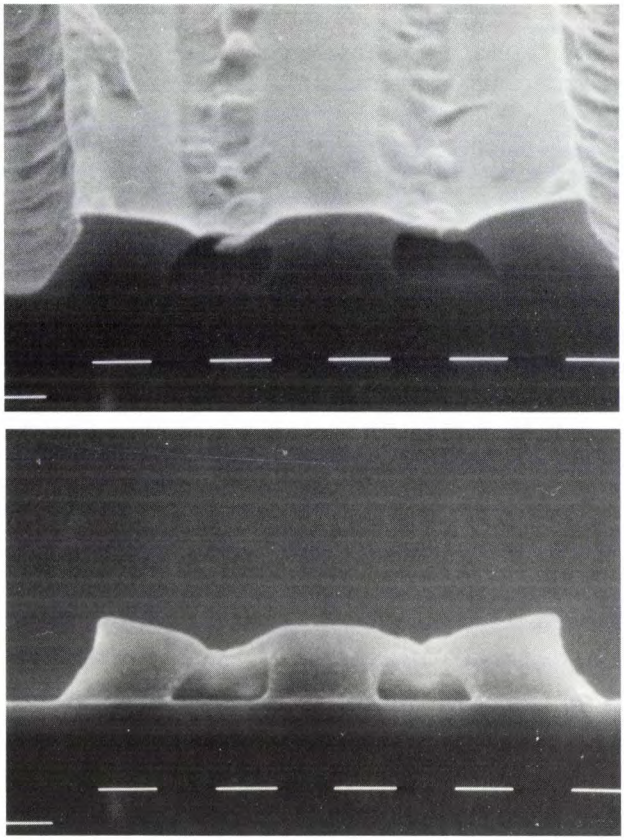

Fig. 8. SEM photographs of a pattern in the negative resist COP. Some cross-linking also occurs at 'non-irradiated' positions because the mask contrast is too low for the required pattern transfer.

efforts are being made to find a positive resist that has a high resistance to dry etching in addition to a high sensitivity.

Results with negative X-ray resists

The negative resist polyglycidyl methacrylate-co-ethyl acrylate (COP), widely used for electron lithography, is also very sensitive to X-radiation: about 30 times as sensitive as PMMA. The use of this highly sensitive resist requires very high contrast in the masks. Parts of the resist that lie below the absorber, and should really dissolve completely in the liquid developer, may give some cross-linking, which thus reduces their solubility. This undesirable effect is more pronounced if the mask has less contrast and the patterns are finer; see *fig. 8*. Another problem encountered with COP that also occurs when using it in electron lithography is that molecules of the liquid developer are taken up in the irradiated parts of the resist during development [18]. The swelling thus produced causes undesirable distortions that can upset the fine details in the pattern.

Other familiar negative electron resists are based on polystyrene [18]. The X-ray sensitivity of these resists depends closely on the mean molecular weight and the presence of foreign atoms. Polystyrene with a mean molecular weight of about 10^5 g/mol and without foreign atoms is rather less sensitive than PMMA. A higher sensitivity is achieved by incorporating chlorine before the polymerization. A resist made in this way is now commercially available as NS150. It is about twice as sensitive as PMMA. A much greater increase in sensitivity can be obtained by increasing the mean molecular weight. *Fig. 9* shows two characteristic curves of a polystyrene with a mean molecular weight of 3×10^6 g/mol. Curve *a*, obtained without post-

Table I. Etch rate of three positive (*p*) and two negative (*n*) X-ray resists divided by the etch rates of silicon, for physical ion etching in Ar (10^{-2} Pa) and reactive ion etching in CF_4 (0.5 Pa), CHF_3 (0.5 Pa) and SF_6 (2 Pa). For comparison the results are also shown for the well-known AZ 1350 H photoresist (Shipley).

Resist \ Medium	Ar	CF_4	CHF_3	SF_6
PMMA (*p*)	1.2	2.7	2.3	0.5
PM 15 (*p*)	1.2	2.7	2.2	0.5
FBM 120 (*p*)	1.3	4.6	4.0	0.6
COP (*n*)	1.2	2.4	2.3	0.5
NS 150 (*n*)	0.7	1.2	0.9	0.2
AZ 1350 H	0.8	1.4	1.2	0.2

baking, shows not only that the sensitivity is very high but also the presence of pronounced swelling: the thickness after exposure and development is considerably greater than the original thickness. An excessive radiation dose causes less swelling. On post-baking of the resist, the layer shrinks and returns to its original thickness (curve *b*). Efforts are now being made to find a negative resist that combines sufficient sensitivity with a low swelling.

The dry-etch behaviour of the negative X-ray resists we have investigated is generally better than that of the positive X-ray resists (Table I). Resists based on polystyrene, such as NS150, are even more resistant to dry etching than the photoresist AZ1350H.

At this stage of the investigation we cannot yet say which resist is most suitable for X-ray lithography. We do know there are a few positive resists that give reasonably good results, e.g. PM15 and FMB120. In the negative resists the swelling effect is still too troublesome for submicron structures, but here substantial improvements can be expected.

A study is currently being made of the effect of various resists on the dry-etch pattern transfer in silicon. The preliminary results look promising. *Fig. 10* shows how well a pattern in the PM15 resist can be transferred to polycrystalline silicon by plasma etching in Cl_2.

Making the masks

Because of the special requirements that masks for X-ray lithography have to meet, as mentioned earlier, they look very different from the conventional masks used for photolithography. The mask substrates consist of a membrane that on the one hand is thin enough to pass X-radiation sufficiently and on the other hand is thick enough to be mechanically stable. To compensate for thermal effects the membranes should be in slight tension. The preferred materials for the membrane consist of light elements with low X-ray absorption. Those that are suitable include inorganic materials such as silicon, silicon carbide and silicon nitride, titanium and magnesium and organic materials such as Kapton and Mylar [19]. Compared with organic membranes, inorganic ones have the advantage that they are more resistant to synchrotron radiation. From now on we shall therefore only be concerned with inorganic membranes.

The structured absorbing layer on the membrane must in the first place have high X-ray absorption. This implies that the layer must be sufficiently thick and that heavy elements (e.g. gold) must be used. In addition the layer must adhere well to the membrane, be mechanically stable and be a good conductor of heat. The patterns in the absorbent layer must be applied to at least the same accuracy as required for applying the patterns in the slice by X-ray lithography.

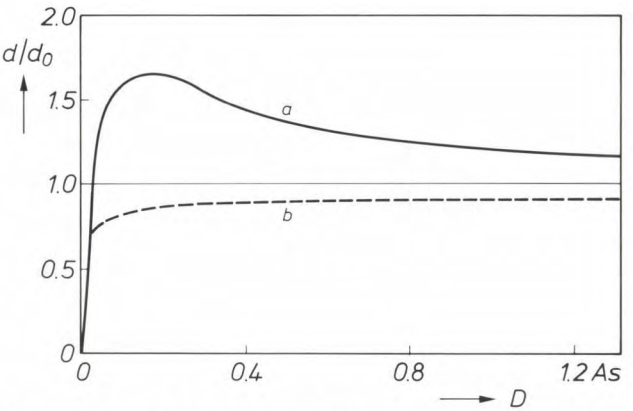

Fig. 9. Ratio of the thickness d after development in MIBK to the original thickness d_0, as a function of the radiation dose D, for a negative X-ray resist based on polystyrene with an average molecular weight of 3×10^6 g/mol. The layer of resist that has received no post-baking has swelled considerably; the swelling depends on the radiation dose (curve *a*). The post-baked layer has shrunk to less than its original thickness (curve *b*).

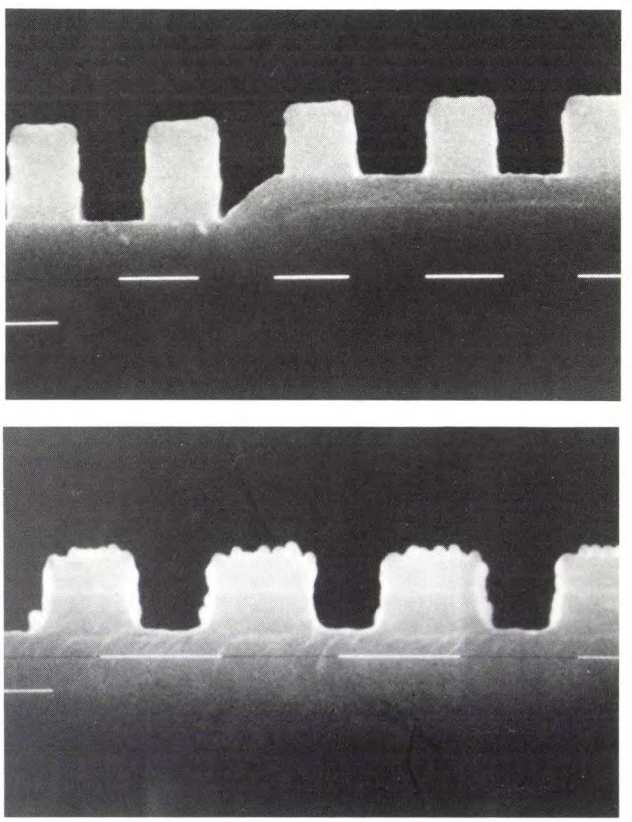

Fig. 10. SEM photograph (marker is 1 μm) of a pattern in the PM15 resist (*above*) and the pattern transferred to polycrystalline silicon by plasma etching in Cl_2 (*below*).

[18] J. C. Jagt and P. W. Whipps, Philips Tech. Rev. **39**, 346, 1980.
[19] A description of different membrane materials is given in the article by Heuberger *et al.* mentioned in [8], p. 265.

The contrast in the mask must be sufficient for the pattern definition to be fully preserved in the X-ray lithography.

We shall first consider the production of different membranes, followed by the application and structuring of the absorbing layer. Finally we shall consider deformation measurements on the masks.

Making the membranes

A silicon membrane with a thickness of say 2 μm can be obtained by partially etching away a silicon slice ('thin etching'). An etchant frequently used is EDP, a mixture of ethylene diamine, pyrocatechol and water. This etchant has a strongly anisotropic action: the etch rate in the [100] direction is much greater than that in the [111] direction. The part of the slice to be preserved for the membrane is made insoluble beforehand, for example by a boron diffusion.

A process commonly used for making thin silicon membranes consists of ten stages, as illustrated in *fig. 11*. A silicon slice with (100) orientation is first coated on one side in four stages with a layer of oxide, and the other side is then doped with boron. In the next four stages a window is made in the oxide layer. The final stage is the thin-etching with EDP; the remaining oxide mask now provides a supporting ring of the original thickness. A disadvantage of this process is that the large number of separate operations adversely affect the yield and quality of the membranes.

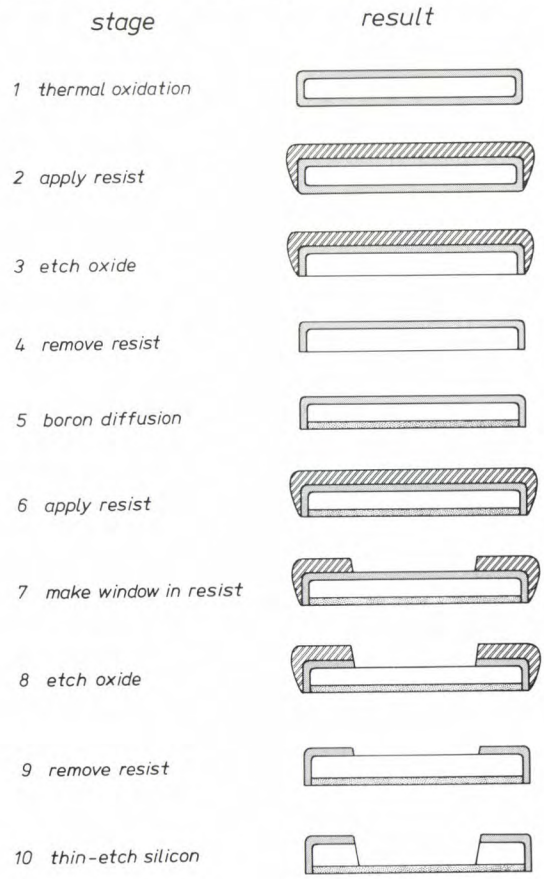

Fig. 11. Production of a thin silicon membrane by a conventional process consisting of ten stages. The various stages are indicated on the left and the diagrams show the result of each stage.

We achieved a considerable improvement by developing a process in which the membranes are made in only three stages; see *fig. 12*. In this process a silicon slice is first doped with boron on both sides, preferably by diffusion with boron tribromide. Next, a window is made on one side by reactive ion etching or plasma etching. The parts of the slice that support the membrane are screened off mechanically by a mask. After dry etching the thin-etching with EDP is carried out. It is also possible to make the silicon wafer thinner after first applying and structuring the metal layer, but this leads to impermissible deformations in the mask.

Making membranes from silicon has the advantage that a great deal is known about the technology and control of the properties of this material. The membranes have high elasticity and stand up well to X-radiation. The membranes are in considerable tension because of the doping, and are therefore not truly planar (the error is a few μm). This is tolerable because of the use of almost parallel synchrotron radiation. Problems can however arise during the optical alignment. In that case the membrane stress has to be reduced by tempering, or corrective layers have to be applied. The optical transmission required for the alignment can be obtained by incorporating light-transmitting windows at various locations or by coating the slice with a reflection-reducing film.

Silicon membranes are in principle suitable for use in X-ray masks. Nevertheless, because of the very stringent requirements for submicron X-ray masks it is certainly necessary to investigate other materials and methods as well. One particularly interesting material is the optically transparent silicon carbide (SiC). Thin membranes of SiC can be produced by applying the SiC to a silicon substrate by chemical vapour deposition (CVD) and then selectively etching the substrate. The CVD process is performed in a horizontal fused-silica tube, with the silicon substrate on a

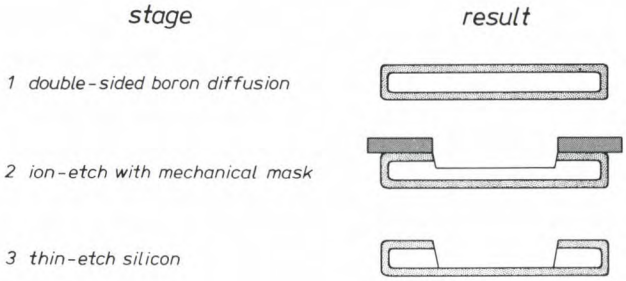

Fig. 12. Production of a thin silicon membrane by a process consisting of only three stages.

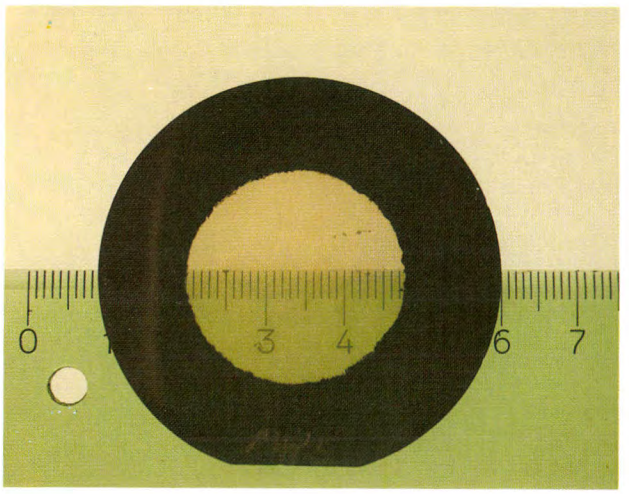

Fig. 13. Transparent SiC membrane 2 μm thick in a silicon ring.

graphite susceptor which is heated by a high-frequency generator to say 1250 °C [20]. Hydrogen is used as the carrier gas. The silicon carbide is formed by the decomposition of dichlorodimethyl silane:

$$(CH_3)_2SiCl_2\,(g) \rightarrow SiC\,(s) + CH_4\,(g) + 2\,HCl\,(g).$$

With an appropriate choice of process conditions such as temperature, gas composition and gas supply, we have succeeded in making membranes about 2 μm thick and with a diameter of about 30 mm that have far less deformation than silicon membranes with the same dimensions. The membranes are also highly stable when irradiated by X-rays. *Fig. 13* shows a silicon-carbide membrane in a silicon ring. The advantage of the high optical transmission is that no separate provisions for alignment are necessary.

In the methods described so far a thin-etching process is used: the substrate is etched away in the area where the membrane will be. Membrane and ring thus form a unit. The great advantage of these methods is that commercially available equipment for semiconductor technology can be used, so that inexpensive mass production becomes a practical possibility. Problems can arise, however, with the adjustment of the membrane tension and the flatness of the membranes. For this reason we are also experimenting with methods in which a thin metal membrane is made and then stretched over a frame. With titanium membranes made in this way [21] reasonably good results have been achieved for mechanical stability, resistance to fracture and flatness. The X-ray transmission of titanium is relatively limited, however, so that only membranes thinner than 1 μm can be used successfully. There are considerable technological problems in producing such thin membranes without defects.

Better prospects are offered by the use of magnesium membranes. These can be produced by sputtering a thin film of magnesium on a glass plate and then 'peeling off' the film. The glass plate is first given a very thin coating of gold to prevent the magnesium film from adhering too tightly to the glass. Diffusion of gold into the magnesium film can be effectively suppressed by applying an intermediate coating of titanium oxide (TiO_x). This is applied by sputtering titanium in an atmosphere containing oxygen. The sputtering of the magnesium film should be carried out at a low residual gas pressure and a low substrate temperature, otherwise the magnesium will be too highly oxidized. The peeling is done with a device with an auxiliary ring and double-sided adhesive tape. After it has been peeled off, the membrane is stretched over a smaller ring by a special tool and fixed to it with an adhesive. Suitable materials for this ring are glass, aluminium oxide and some alloys with a low coefficient of expansion. *Fig. 14* shows a 2-μm-thick magnesium membrane stretched over an aluminium-oxide ring.

The considerable flexibility of magnesium membranes enables the membrane stress to be adjusted in such a way as to compensate largely for thermal changes occurring during the subsequent processes. Some of the membranes used are remarkably flat, fracture-resistant and mechanically stable. A particularly

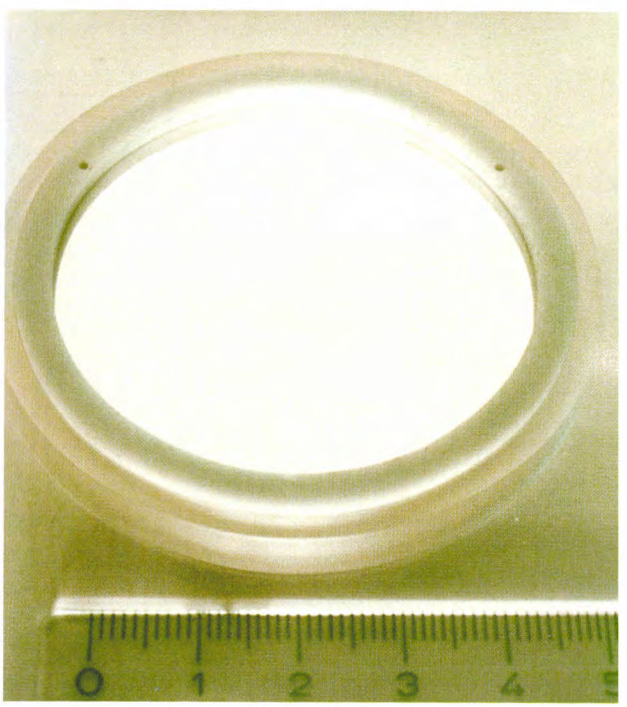

Fig. 14. Magnesium membrane 2 μm thick stretched over an aluminium-oxide ring.

[20] An earlier article in this journal described the CVD process for applying wear-resistant TiC and TiN coatings; see Philips Tech. Rev. **40**, 204, 1982 and for applying silicon films in IC technology, see Philips Tech. Rev. **41**, 60, 1983/84.

[21] W. D. Buckley, J. F. Nester and H. Windischmann, J. Electrochem. Soc. **128**, 1116, 1981.

useful property of these membranes is their low X-ray absorption, especially at wavelengths longer than 1 nm. This means that the exposure can be very short when a mask with a magnesium membrane is used. In addition, good contrast can be achieved with a structured X-ray-absorbing layer of very small thickness. Because of the optical opacity it is necessary to have separate alignment windows. Since the masks are very accurately made these windows can also be mounted in a glass ring.

Application of metal layers

In view of the high accuracy needed for obtaining submicron structures, it is necessary for all the masks discussed here to apply and structure the metal layer on the thin membrane. The metal coating of a mask for X-ray lithography must in the first place be highly absorbent for X-radiation in the relevant wavelength region. In addition it must bond well to the mask membrane, have a low expansion coefficient, be fine-grained and it must not give rise to mechanical stresses. Its properties must also be compatible with electron lithography, which is used for the structuring. In this process the metal layer is coated with an electron resist that is subsequently irradiated with an electron-beam pattern generator [5]. After development of the resist the required structure is produced in the metal layer by dry etching. Another method that can be used to obtain a structured metal layer is electrodeposition of the metal between electron-lithographically produced resist structures.

A suitable metal for the X-ray absorbing layer is gold. According to the literature the usual method is to use a gold layer deposited on a silicon membrane by evaporation, after first depositing a thin bonding layer of chromium by evaporation. With this combination of materials, however, severe mechanical stresses can occur. We have therefore investigated the possibilities of combining other materials with gold, and have also studied other methods of application such as sputtering and electrodeposition. We have also performed tentative experiments with a few other heavy metals that give high X-ray absorption and can be anisotropically etched, such as molybdenum, tantalum and tungsten.

Bonding layers of chromium or nickel chromium are often subject to unacceptable mechanical stresses. Furthermore, these materials can easily diffuse when the gold layer is applied, especially if the substrate temperature is high. This diffusion may partly be the cause of poor bonding and of ageing effects that lead to deformations of the mask. When titanium is used for the bonding layer no perceptible diffusion is found.

To solve the problem of the stresses we studied the effects of the conditions in which the metal coatings are applied. These effects were found to be particularly pronounced in the sputtering process. Gold layers are subject to a tensile stress that decreases if the argon pressure is higher during sputtering. Layers of chromium and titanium are subject to a compressive stress at low argon pressures and a tensile stress at higher argon pressures; see *fig. 15*.

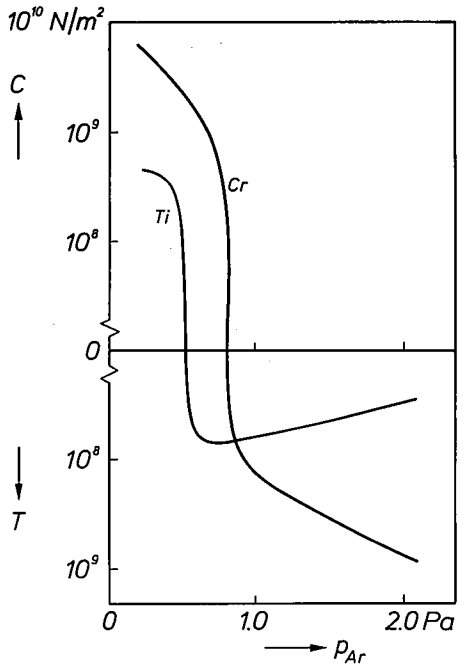

Fig. 15. Compressive stress C and tensile stress T of chromium and titanium layers as a function of argon pressure p_{Ar} during sputtering.

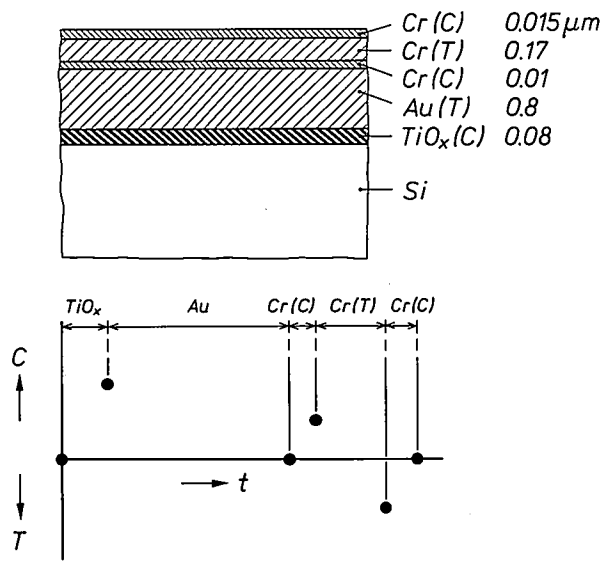

Fig. 16. *Above:* Diagram of structure of a stress-free, X-ray-absorbing coating on a silicon membrane. The sputtered layers give alternate compressive (C) and tensile stresses (T). *Below:* Diagram showing the resultant compressive stress C and tensile stress T before and after applying the different layers.

In principle it should be possible, with a given combination of materials, to select the application conditions in each case so as to minimize the stresses in the individual films. In practice, however, such a procedure is not readily reproducible. With our knowledge of the stress variations we therefore looked for combinations of materials in which the stresses in the different layers compensate one another. An example is shown diagramatically in *fig. 16*. The bonding layer consisting of titanium oxide is subject to a compressive stress that is almost completely compensated by the tensile stress in the gold layer. The presence of chromium can give better electron-lithographic structuring of the gold layer, as described later. We used a sandwich configuration of three chromium layers: two very thin layers with a compressive stress and between them a much thicker layer with a tensile stress sufficient to make the complete sandwich virtually stress-free. The advantage of such a sandwich is that sufficient compensation remains after the structuring of the gold layer, in which a substantial part of the chromium is etched away. This is because the dry-etching process removes the upper chromium layer completely and the central chromium layer only partly. The tensile stress in the remainder of this layer is then compensated by the compressive stress in the lower chromium layer.

Besides gold, other possible materials for the absorbing layer in masks for X-ray lithography are tantalum and tungsten. In combinations such as molybdenum-gold and tungsten-gold the compressive and tensile stresses can be effectively compensated.

Structuring

The structuring of the absorbent metal layer of masks for X-ray lithography is carried out with the aid of an electron-beam pattern generator. The dry-etching method often used is reactive ion etching, because of the problems of ditch formation and redeposition encountered with physical ion etching [15] and because plasma etching is often not sufficiently anisotropic [16]. Since the etching process is carried out on thin membranes, the choice of the high-frequency power level is particularly important. The electron-resist layer to be used has to be fairly thin (about 0.3 μm), otherwise the proximity effect will be too great during the electron irradiation. A thin resist layer, however, offers little protection to the underlying metal layer during etching, especially if the etch rates of these two layers are not very different. This is the case, for example, in the ion etching of a gold layer coated with an electron resist in an argon atmosphere. Here the etch rate of gold is not more than twice as high as that of the usual electron resists. The result is that oblique edges are formed in the resist structure and hence in the gold layer as well.

Since there is no known reactive ion-etching or plasma-etching process that has an anisotropic action on gold, we decided to structure gold layers by a process in which a thin chromium layer acts as an auxiliary mask. This is based on the relatively high resistance of chromium to ion etching in argon and oxygen; see *fig. 17*. The transfer of the resist structure to the chromium layer is performed by plasma etching in a mixture of C_2HCl_3 and $C_2H_2Cl_2$. The structure in the chromium layer is then transferred to the gold layer by ion etching. Because of the great difference in etch rates it is possible in this way to produce reasonably steep edges in the gold layer; see *fig. 18*. To obtain them it is necessary to etch longer, depending on the structure, than the etching time corresponding to the etch rate and thickness of the gold layer. This presents

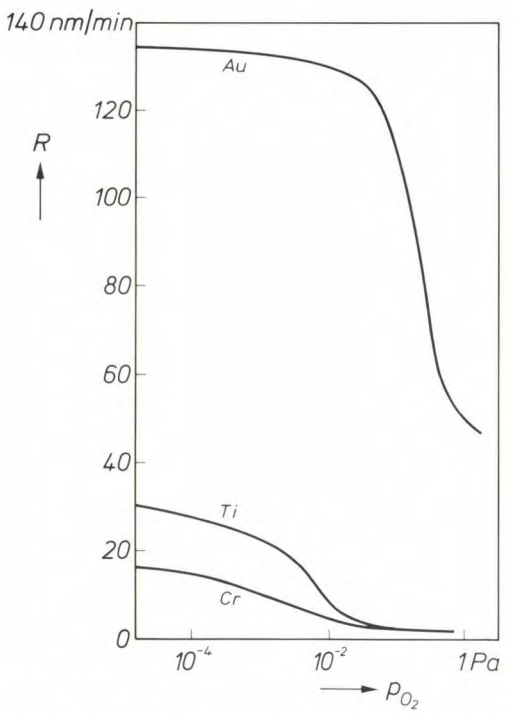

Fig. 17. Etch rate R in ion etching of gold, titanium and chromium layers as a function of the partial oxygen pressure p_{O_2}. At a low oxygen pressure the stability of chromium and titanium is much greater than that of gold.

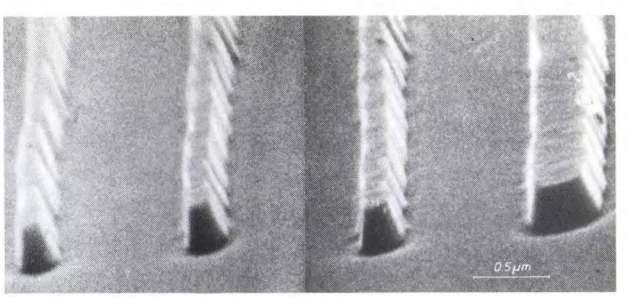

Fig. 18. SEM photographs of a gold pattern with fairly steep edges, obtained by ion etching in argon and oxygen with chromium as an auxiliary mask.

no problem, however, since the bonding and compensation layer of TiO_x is only slightly attacked in argon and oxygen.

When tungsten is used as the absorbing layer, good structuring is again not possible with an electron resist about 0.5 μm thick. Unlike gold, however, tungsten can be reactively etched. A gold layer of thickness about 0.2 μm can then be used as an auxiliary mask. The structure in the gold layer can be applied by ion etching in argon. Structuring of the tungsten layer is best performed by reactive ion etching in CF_4 at a pressure of about 0.8 Pa. The resistance of gold is then so much greater than that of tungsten that very steep edges can be obtained in the tungsten structure; see *fig. 19*.

As well as by etching, a structured gold layer can also be obtained by electrodeposition on an electrically conducting substrate coated with a structured layer of resist. The substrate used is a thin gold layer (e.g. about 0.02 μm thick). For the bonding to a mask membrane of silicon a thin titanium-oxide layer is used. The advantage of structuring by electrodeposition is that gold layers with very low stress can be produced.

For a faithful reproduction of a structure by electrodeposition a resist layer of about 1 μm with steep edges in its structure is required. For electron lithography, however, the layer of resist should be no thicker than about 0.3 μm because of the proximity effect. For this reason processes have been investigated in which the substrate is successively coated with a relatively thick resist layer, a thin inorganic layer and a thin electron-resist layer [22]. Possible combinations of layers include 1-μm-thick PIQ (Hitachi), 0.05-μm-thick tungsten and 0.3-μm-thick PM15. First the tungsten layer is structured by electron lithography and reactive ion etching in SF_6. This layer then serves as a mask for the ion etching (in oxygen) of the lower resist layer. This method will give reliable structures with very steep edges. An example is shown in *fig. 20*.

Measurements of mask deformations

A silicon slice coated with a bonding layer of titanium 0.01 μm thick and a structured gold layer is found after thin-etching to a 2-μm-thick membrane to have shrunk about 0.5 μm per centimetre. This means that impermissible dimensional variations from the original mask design have occurred in the metal pattern. This has led to the view that to obtain a reliable mask it is necessary to produce the membrane first and only then to apply and structure the X-ray-absorbing metal layer.

Although dimensional errors also occur during the structuring of the metal layer on a thin membrane, they can be kept sufficiently small by means of stress-compensating layers [23]. This is the case for example with a mask obtained after structuring the combination of materials in fig. 16 on a silicon membrane. *Fig. 21* shows the measured dimensional errors in the complete X-ray mask as compared with the original design. Because of the stress compensation the different process stages only introduce very small deformations

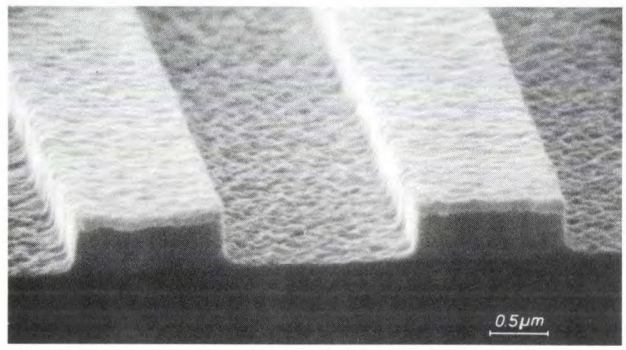

Fig. 19. SEM photograph of a tungsten pattern on a silicon substrate. The steep edges were obtained by reactive ion etching in CF_4 at 0.8 Pa, with a 0.2-μm-thick gold layer as an auxiliary mask.

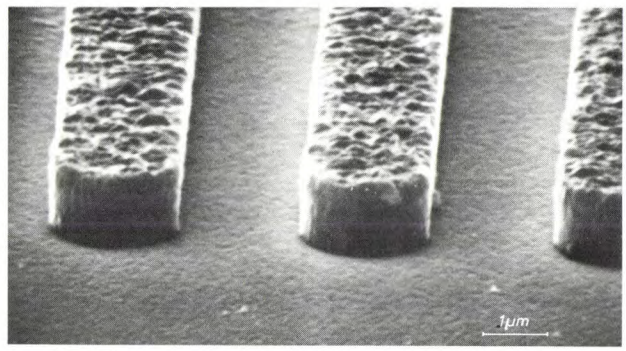

Fig. 20. SEM photograph of a gold pattern with steep edges, obtained by structuring with the electrodeposition process described in the text, in which the conducting substrate is first given a coating of three layers.

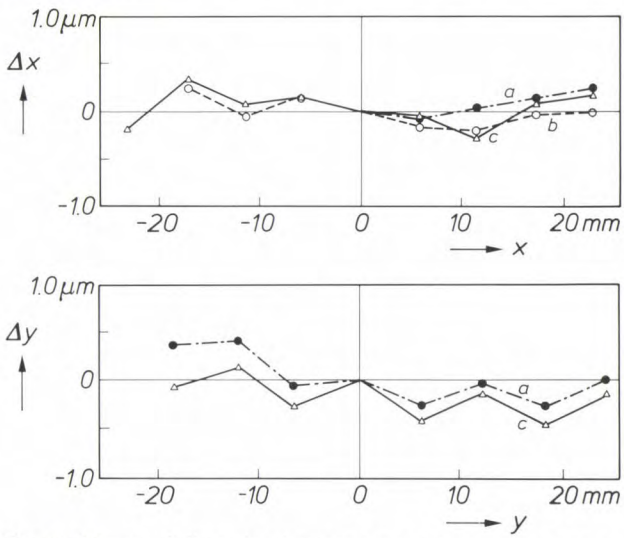

Fig. 21. Measured dimensional errors Δx and Δy as a function of the coordinates x and y in a silicon membrane as in fig. 16, after electron lithography (*a*), etching of the chromium sandwich (*b*) and etching of the gold layer (*c*). Each of these stages gives only slight deformation of the membrane.

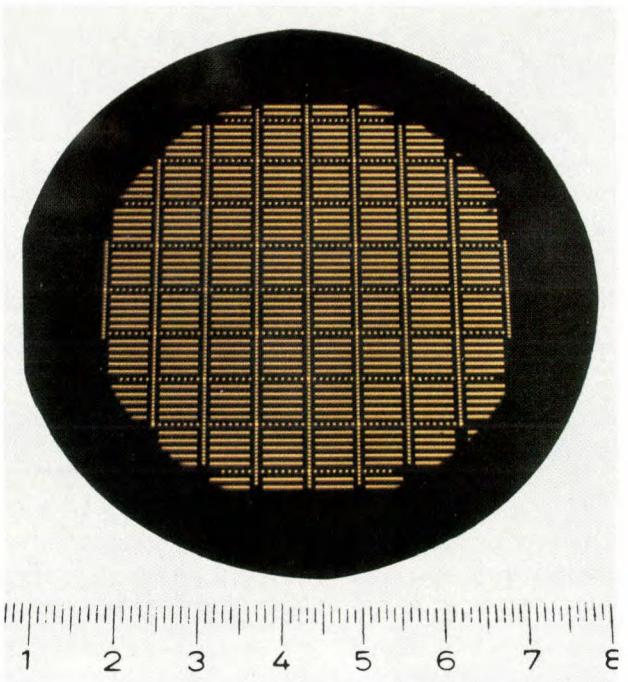

Fig. 22. Complete mask for X-ray lithography, consisting of a 2-μm-thick silicon membrane, an 0.08-μm-thick bonding layer of TiO_x and an 0.8-μm-thick structured gold layer.

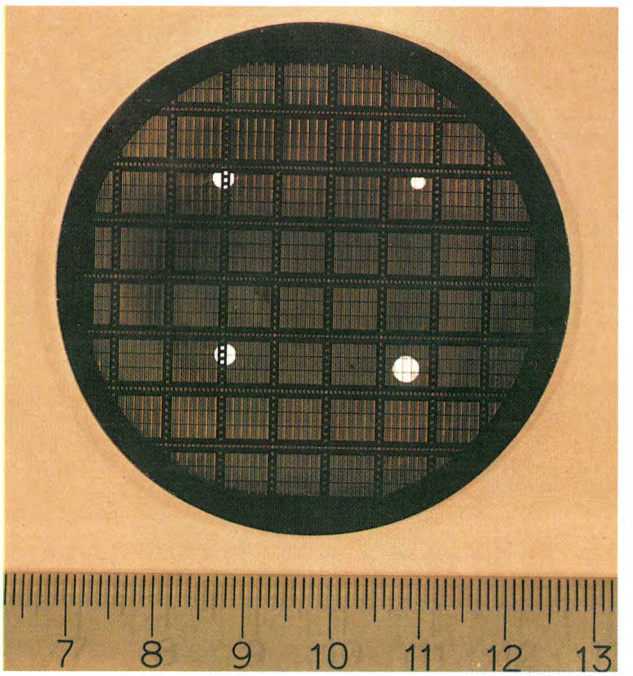

Fig. 23. Complete mask, with optically transparent alignment windows, consisting of a 2-μm-thick magnesium membrane and an 0.6-μm-thick structured tungsten layer coated with a 0.2-μm-thick gold layer.

of the membrane. The structure produced in the resist layer is transferred very accurately (error no greater than about 0.2 μm) to the gold layer. The errors in the y-direction are a little larger owing to an error in the design program, which had the result that every other point measured in the pattern was exposed twice. Taking this into account, we may deduce from the measurements that the dimensional variations in the complete mask relative to the original design are no greater than about 0.15 μm per centimetre. An example of such a mask with a silicon membrane is shown in *fig. 22*.

A further improvement can be obtained by stabilizing the frame of the membrane with a carrier plate matched to the X-ray silicon repeater used. The smallest dimensional errors we have measured were found in a complete mask with a magnesium membrane, shown in *fig. 23*. In a diameter of 50 mm the deformation measured here is less than about 0.2 μm.

We shall only know which mask technology is the best one after the X-ray stepper at BESSY has been in use for some time. Only then can we also assess the economic consequences. The prospects for the X-ray lithographic procedure described in this article nevertheless look promising, since large areas (about 4 cm^2) can be repeatedly exposed in the submicron range with each exposure lasting only a few tenths of a second. The speed of the total irradiation process is thus determined mainly by the mechanical components of the X-ray stepper.

In the investigation described here the author has worked in close technological cooperation with A. Bruns, M. Harms, A. Lentfer (all with PFH) and B. Matthiessen (with Valvo RHW), and also, in a wider organizational context, with Dr H. Dimigen (PFH) and Dr D. Sautter (Valvo UB). The work was carried out with the financial support of the Ministry of Research and Technology of the Federal Republic of Germany. The author alone is entirely responsible for the contents of this publication.

Summary. X-ray lithography is a promising method for producing submicron structures in VLSI. Good results are obtained with synchrotron radiation used in connection with a laser-aligned X-ray stepper. The resists employed have to meet the strictest requirements for X-ray sensitivity, pattern transfer and resistance to dry etching. Some resists have been investigated in view of these requirements. In the investigation described most attention was paid to the making of the masks. These consist of an X-ray-transmitting membrane and an X-ray-absorbing metal layer carrying the required pattern. Since these masks have to meet accuracy requirements for a prospective submicron technology, several mask materials have been investigated. Under optimized conditions X-ray masks that are sufficiently flat and geometrically stable can be made by different methods. The electron-beam-written patterns in these masks reproduce from the original design to within about 0.2 μm. X-ray masks based on Si, SiC and Mg proved to be stable when exposed to very intense synchrotron radiation.

[22] J. M. Moran and D. Maydan, J. Vac. Sci. & Technol. **16**, 1620, 1979.
[23] A. Bruns, M. Harms, H. Lüthje and B. Matthiessen, Proc. Microcircuit Engineering 82, Grenoble 1982, pp. 111-115.

Scientific publications

These publications are contributed by staff of laboratories and plants that form part of or cooperate with enterprises of the Philips group of companies, particularly by staff of the research laboratories mentioned below. The publications are listed alphabetically by journal title.

Philips GmbH Forschungslaboratorium Aachen, Weißhausstraße, 5100 Aachen, Germany — *A*

Philips Research Laboratory Brussels, 2 avenue Van Becelaere, 1170 Brussels, Belgium — *B*

Philips Natuurkundig Laboratorium, Postbus 80000, 5600 JA Eindhoven, The Netherlands — *E*

Philips GmbH Forschungslaboratorium Hamburg, Vogt-Kölln-Straße 30, 2000 Hamburg 54, Germany — *H*

Laboratoires d'Electronique et de Physique Appliquée, 3 avenue Descartes, 94450 Limeil-Brévannes, France — *L*

Philips Laboratories, N.A.P.C., 345 Scarborough Road, Briarcliff Manor, N.Y. 10510, U.S.A. — *N*

Philips Research Laboratories, Cross Oak Lane, Redhill, Surrey RH1 5HA, England — *R*

Philips Research Laboratories Sunnyvale P.O. Box 9052, Sunnyvale, CA 94086, U.S.A. — *S*

A. Besse (*S.A. Philips I.C., Fontenay-aux-Roses*)	Micro-informatique: qualité et innovation	Acta Electron. **25**	7-8	1983
L. Quéré (*S.A. Philips I.C., Fontenay-aux-Roses*)	Techniques d'intégration à grande échelle appliquées aux mini-ordinateurs	Acta Electron. **25**	9-13	1983
C. Fernandès (*S.A. Philips I.C., Fontenay-aux-Roses*)	Réalisation d'unités centrales à l'aide de circuits VLSI et de réseaux prédiffusés	Acta Electron. **25**	15-28	1983
M. Pauker (*S.A. Philips I.C., Fontenay-aux-Roses*)	Trois bus Euro: UPL, VME, P 896	Acta Electron. **25**	29-33	1983
P. Braffort (*GFI-Automatique, Paris*), A. Decroix (*S.A. Philips I.C., Fontenay-aux-Roses*)	Un outil de développement du logiciel: l'APL/P 800	Acta Electron. **25**	35-40	1983
A. Decroix (*S.A. Philips I.C., Fontenay-aux-Roses*)	Normalisation et certification du logiciel: intérêt et impact	Acta Electron. **25**	41-43	1983
A. Decroix (*S.A. Philips I.C., Fontenay-aux-Roses*)	Qualité et fiabilité du logiciel	Acta Electron. **25**	45-51	1983
G. Ségarra* & B. Geffrotin* (* *S.A. Philips I.C., Fontenay-aux-Roses*)	BIS, un réseau local à large bande	Acta Electron. **25**	53-60	1983
Y. Chaigneau (*Compagnie Française Philips, Paris*) & C. Vignaud (*S.A. Philips I.C., Fontenay-aux-Roses*)	Méthodes prévisionelles et suivi de qualité aux stades de développement et de fabrication	Acta Electron. **25**	61-85	1983
P. Le Marchant (*S.A. Philips I.C., Fontenay-aux-Roses*) & P. Parmentier (*RTC, Evreux*)	La carte à mémoire électronique: technologie et expérimentation	Acta Electron. **25**	87-92	1983
P. Le Marchant (*S.A. Philips I.C., Fontenay-aux-Roses*)	Carte à mémoire et systèmes de contrôle d'accès	Acta Electron. **25**	93-98	1983
W. N. Schreiner & R. Jenkins (*Philips Electron. Instrum., Mahwah, NJ*) *N*	Profile fitting for quantitative analysis in X-ray powder diffraction	Advances in X-ray analysis, Vol. 26, C. R. Hubbard *et al.* (eds), Plenum, New York	141-147	1983
J. Braat *E*	Optically read disks with increased information density	Appl. Opt. **22**	2196-2201	1983
G. M. Martin, P. Terriac, S. Makram-Ebeid, G. Guillot* & M. Gavand* (* *LPM, Villeurbanne*) *L*	Evidence for the creation of the main electron trap in bulk GaAs	Appl. Phys. Lett. **42**	61-63	1983
F. H. P. M. Habraken (*Univ. Utrecht*), A. E. T. Kuiper & Y. Tamminga *E*	Surface and interface nitridation of thin polycrystalline silicon films	Appl. Phys. Lett. **42**	950-952	1983

T. de Jong (*Philips Elcoma Div., Nijmegen*), W. A. S. Douma*, J. F. van der Veen*, F. W. Saris* (* *FOM, Amsterdam*) & J. Haisma	*E*	Silicon molecular beam epitaxy on gallium phosphide	Appl. Phys. Lett. **42**	1037-1039	1983
J. Hasker	*E*	Calculation of diode characteristics and proposed characterization of cathode emission capability	Appl. Surf. Sci. **16**	220-237	1983
M. Davio, J.-P. Deschamps & A. Thayse	*B*	Représentation d'algorithmes: architectures VLSI associées	Architecture des machines et systèmes informatique, Lille 1982	279-288	1983
J. R. Mansell, A. G. Knapp, A. W. Woodhead, D. Washington, R. Pook, C. D. Overall & P. Schagen	*R*	The metal-dynode multiplier: a new component in CRT design	Displays **4**	135-139	1983
D. Meignant & M. Binet	*L*	New ultra-high-speed GaAs strobed comparators	Electron. Lett. **19**	67-68	1983
K. A. Schouhamer Immink	*E*	Runlength-limited code with small error propagation	Electron. Lett. **19**	323-324	1983
G. Bergmann	*A*	Zur Wirtschaftlichkeit der solaren Brauchwassererwärmung in Privathaushalten	Energiewirtsch. Tagesfragen **33**	443-447	1983
J. D. B. Veldkamp (*Philips Glass Div., Eindhoven*), N. Hattu & G. de With	*E*	Deformation and cracking during high temperature scratching of some brittle materials	Fracture mechanics of ceramics, Vol. 5, R. C. Bradt *et al.* (eds), Plenum, New York	121-144	1983
L. Hollan & G. Hallais	*L*	Vapor phase epitaxy for GaAs FETs	GaAs FET principles and technology, ARTECH, Dedham, MA	67-99	1982
J. W. M. Biesterbos, R. P. Brouwer, A. Valster, J. A. de Poorter & G. A. Acket	*E*	The effect of active layer thickness on lateral waveguiding in narrow-stripe gain-guided AlGaAs DH laser diodes	IEEE J. **QE-19**	961-965	1983
D. C. van Eck	*E*	Wavefront measurements on semiconductor lasers	IEEE J. **QE-19**	966-968	1983
J. W. M. Biesterbos, A. J. den Boef, W. Linders & G. A. Acket	*E*	Low-frequency mode-hopping optical noise in AlGaAs channeled substrate lasers induced by optical feedback	IEEE J. **QE-19**	986-990	1983
R. Cuppens & L. H. M. Sevat	*E*	A 256 kbit ROM with serial ROM cell structure	IEEE J. **SC-18**	340-344	1983
F. C. Schoute (*Philips' Telecommun. Ind., Hilversum*)		Dynamic frame length ALOHA	IEEE Trans. **COM-31**	565-568	1983
R. Knoechel	*H*	Capabilities of multiapplicator systems for focused hyperthermia	IEEE Trans. **MTT-31**	70-73	1983
R. F. Milsom, D. T. Elliott*, S. Terry-Wood* & M. Redwood* (* *Queen Mary College, London*)	*R*	Analysis and design of coupled-mode miniature bar resonators and monolithic filters	IEEE Trans. **SU-30**	140-155	1983
J. P. André, C. Schiller, A. Mitonneau, A. Brière, J. Y. Aupied	*L*	(Ga,Al)As/GaAs MIS heterostructure with semi-insulating (Ga,Al)As grown by MOVPE	Inst. Phys. Conf. Ser. No. 65	117-124	1983
B. Ehlers, H.-D. Hinz, H. Löbl & R. Pape	*H*	Electrophoretic recording of color images	J. Appl. Photogr. Eng. **9**	1-6	1983
H. C. de Graaff & M. T. M. Huybers	*E*	$1/f$ noise in polycrystalline silicon resistors	J. Appl. Phys. **54**	2504-2507	1983
P. van de Weijer & R. M. M. Cremers	*E*	Determination of the oscillator strengths of the $6D$ 6^1P_1 atomic energy mercury transitions	J. App. Phys. **54**	2835-2836	1983
D. J. Breed & P. Q. J. Nederpel	*E*	The movement of magnetic bubbles in a rotating field gradient	J. Appl. Phys. **54**	4054-4058	1983
G. M. Loiacono, J. J. Zola & G. Kostecky	*N*	Growth of KH_2PO_4 crystals at constant temperature and supersaturation	J. Cryst. Growth **62**	545-556	1983
G. M. Loiacono, A. Shaulov, D. Dorman & T. Kovats	*N*	Crystal growth and properties of $V(PO_3)_3$	J. Cryst. Growth **63**	209-211	1983
H. J. de Wit & C. Crevecoeur	*E*	The CV product of etched aluminum anode foil	J. Electrochem. Soc. **130**	770-776	1983
D. Stoppels, P. G. T. Boonen, U. Enz & L. A. H. van Hoof	*E*	Monocrystalline high-saturation magnetization ferrites for video recording head application — I. Zn ferrous ferrites	J. Magn. & Magn. Mater. **37**	116-122	1983

D. Stoppels, P. G. T. Boonen, J. P. M. Damen, L. A. H. van Hoof & K. Prijs *E*	Monocrystalline high-saturation magnetization ferrites for video recording head application — II. MnZn ferrites with large Fe^{II} contents	J. Magn. & Magn. Mater. **37**	123-130	1983
D. Stoppels, L. A. H. van Hoof & P. G. T. Boonen *E*	Monocrystalline high-saturation magnetization ferrites for video recording head application — III. Co^{II} doped MnZn ferrites with large Fe^{II} contents	J. Magn. & Magn. Mater. **37**	131-137	1983
T. T. M. Palstra*, J. A. Mydosh*, G. J. Nieuwenhuys* (* *Univ. Leiden*), A. M. van der Kraan (*Interuniv. Reactor Inst., Delft*) & K. H. J. Buschow *E*	Study of the critical behaviour of the magnetization and electrical resistivity in cubic $La(Fe,Si)_{13}$ compounds	J. Magn. & Magn. Mater. **36**	290-296	1983
J. L. Gentner & R. Cadoret* (* *U.E.R., Aubières*) *L*	Low pressure vapour phase epitaxy of GaAs — the growth rate limiting processes	J. Physique **43** (Colloque C5)	C5/111-C5/118	1982
P. M. Frijlink & J. Maluenda *L*	Quantum well and modulation doped GaAs — $Ga_{1-x}Al_xAs$ heterostructures	J. Physique **43** (Colloque C5)	C5/185-C5/191	1982
J. L. Gentner *L*	Anisotropy in sulphur doping of GaAs grown by V.P.E.	J. Physique **43** (Colloque C5)	C5/267-C5/270	1982
N. Vodjdani, A. Lemarchand & H. Paradan *L*	Parametric studies of GaAs growth by metalorganic molecular beam epitaxy	J. Physique **43** (Colloque C5)	C5/339-C5/349	1982
J. J. Harris & J. M. Woodcock *R*	The growth of thin, heavily doped layers for hot electron devices	J. Vac. Sci. & Technol. B **1**	196-198	1983
W. J. Bartels *E*	Characterization of thin layers on perfect crystals with a multipurpose high resolution X-ray diffractometer	J. Vac. Sci. & Technol. B **1**	338-345	1983
J. M. Shannon & J. A. G. Slatter *R*	Monolithic hot electron transistors in silicon with $F_T > 1$ GHz	Jpn. J. Appl. Phys. **22** (Suppl. 22-1)	259-262	1983
M. Zijlstra (*Philips ISA-CQM, Eindhoven*)	A simple derivation of the waiting time distribution in an M/G/1 queueing system with vacation times	Kwantitatieve Methoden **6**	137-143	1982
G. Söllner *A*	Passive Solarnutzung	Licht-Forsch. **5** (No. 1)	25-34	1983
P. Röschmann & W. Tolksdorf *H*	Epitaxial growth and annealing control of FMR properties of thick homogeneous Ga substituted yttrium iron garnet films	Mater. Res. Bull. **18**	449-459	1983
G. B. McMillan*, J. M. Shannon & H. Ahmed* (* *Univ. Cambridge*) *R*	Processing of shallow (Rp < 150Å) implanted layers with electron beams	Mater. Res. Soc. Symp. Proc. **13**	437-442	1983
P. van Beek (*Agricult. Univ. Wageningen*), A. Bremer (*Philips Medical Systems Div., Eindhoven*) & C. van Putten (*Philips ISA-CQM, Eindhoven*)	An application of dynamic programming to integral lot-sizing in multi-level assembly networks with tree structure	Methods Oper. Res. **46**	645-652	1983
H. A. van Sprang *E*	Surface order in nematics	Mol. Cryst. & Liq. Cryst. **97**	255-261	1983
D. G. Bouwhuis (*Inst. Perception Res., Eindhoven*)	Visuele woordherkenning bij het lezen	Ned. T. Psychol. **38**	330-357	1983
P. C. Zalm, L. J. Beckers & F. H. M. Sanders *E*	On the role of physical sputtering in reactive ion beam etching	Nucl. Instrum. & Methods **209/210**	561-565	1983
W. J. M. J. Josquin *E*	The application of nitrogen ion implantation in silicon technology	Nucl. Instrum. & Methods **209/210**	581-587	1983
H. Dammann & M. Zinke *H*	Spatial frequency colour encoding by Fresnel images in the proximity of twin-gratings	Opt. Commun. **44**	317-322	1983
M. Lemonier, M. Fouassier, C. Piaget *L*	Imagerie à bas niveau de lumière par CCD	OPTO 82, Paris 1982	85-87	1982
V. Belevitch & J. Boersma (*Univ. of Technol., Eindhoven*) *B*	Some electrical problems for a torus	Philips J. Res. **38**	79-137	1983
K. A. Schouhamer Immink *E*	Some statistical properties of maxentropic run-length-limited sequences	Philips J. Res. **38**	138-149	1983
B. Hill *H*	Optical transmissivity of magneto-optic switching elements	Philips J. Res. **38**	150-163	1983
P. Hansen, K. Witter & W. Tolksdorf *H*	Magnetic and magneto-optical properties of bismuth-substituted gadolinium iron garnet films	Phys. Rev. B **27**	4375-4383	1983

J. C. M. Henning, J. J. P. Noijen & A. G. M. de Nijs	*E*	Excited states of the Zn and C acceptors in $Al_{0.47}Ga_{0.53}As$	Phys. Rev. B **27**	7451-7459	1983
R. A. de Groot*, F. M. Mueller* (* *Univ. Nijmegen*), P. G. van Engen & K. H. J. Buschow	*E*	New class of materials: half-metallic ferromagnets	Phys. Rev. Lett. **50**	2024-2027	1983
H. Rodot (*Equipe Technol. Croissance Crist., France*), J. C. Guillaume*, J. Chevallier* (* *C.N.R.S., Meudon*), M. Boulou, V. T. Kriapov+, F. R. Kashimov+, T. I. Markova+ & I. A. Zoubridski+ (+ *Acad. Sci., Moscow*)	*L*	Defects in gallium arsenide grown from solution under microgravity conditions	Physica **116B**	168-176	1983
G. M. Martin & S. Makram-Ebeid	*L*	Manifestations of deep level point defects in GaAs	Physica **116B**	371-383	1983
H. Kurz, J. M. Liu* & N. Bloembergen* (* *Harvard Univ., Cambridge, MA*)	*H*	Pulsed laser annealing of semiconductors; experimental facts and open questions	Physica **117B & 118B**	1010-1013	1983
F. J. A. M. Greidanus, L. J. de Jongh*, W. J. Huiskamp* (* *Univ. Leiden*), P. Fischer+, A. Furrer+ (+ *E.T.H., Zürich*) & K. H. J. Buschow	*E*	Magnetic properties of PrX_2 compounds (X = Pt, Rh, Ru, Ir) studied by hyperfine specific heat, magnetization and neutron-diffraction measurements	Physica **119B**	215-227	1983
F. J. A. M. Greidanus, G. J. Nieuwenhuys*, L. J. de Jongh*, W. J. Huiskamp*, H. W. Capel* (* *Univ. Leiden*) & K. H. J. Buschow	*E*	Specific heat, resistivity, and AC susceptibility of the cubic PrX_2 compounds (X = Pt, Ru, Ir, Rh)	Physica **119B**	228-242	1983
J. W. C. de Vries*, R. C. Thiel* (* *Univ. Leiden*) & K. H. J. Buschow	*E*	^{151}Eu isomer shifts and charge transfer in Eu-base intermetallic compounds	Physica **121B**	100-108	1983
J. G. Wagner	*N*	The frictional behavior of tungsten and molybdenum powders sliding on die materials	Powder Technol. **35**	47-50	1983
J. Geninet (*Portenseigne, Fontenay/Bois*) & P. Harrop	*L*	Direct reception from satellites	Proc. Conf. The video revolution, Reading 1982	92-101	1982
M. J. Coenen & A. Jongepier	*E*	Active broadband antennas in the 10 kHz to 30 MHz range	Proc. 1983 Electromagnetic Compatibility Symp., Zürich 1983	271-274	1983
J. J. Goedbloed, K. Riemens & A. J. Stienstra (*Philips Audio Div., Eindhoven*)	*E*	Increasing the RFI immunity of amplifiers with negative feedback	Proc. 1983 Electromagnetic Compatibility Symp., Zürich 1983	471-476	1983
V. Pauker	*L*	The matching and biasing circuits for broadband MIC microwave FET amplifiers	Proc. 12th European Microwave Conf., Helsinki 1982	143-147	1982
C. Tsironis & P. Lesartre	*L*	Temperature stabilization of GaAs FET oscillators using dielectric resonators	Proc. 12th European Microwave Conf., Helsinki 1982	181-186	1982
F. C. de Ronde	*L*	A multi-octave matched quarterwave microstrip taper	Proc. 12th European Microwave Conf., Helsinki 1982	617-621	1982
H. Sari	*L*	A comparison of equalization techniques on 16 QAM digital radio systems during selective fading	Proc. Globecom '82, Miami 1982	1240-1245	1982
P. Delsarte, Y. Genin, Y. Kamp & P. van Dooren	*B*	On the role of the partial trigonometric moment problem in speech modelling	Proc. ICASSP 83, Boston 1983	789-792	1983
S. Hoekstra	*E*	An accurate and general method of determining habit planes and orientation relationships in bainitic steels and a verification of the IPS theory	Proc. Int. Conf. on Solid to solid phase transformations, Pittsburg, PA, 1981	1017-1021	1981
F. C. Schoute (*Philips' Telecommun. Ind., Hilversum*)		Adaptive overload control for an SPC exchange	Proc. 10th Int. Teletraffic Congr., Montreal 1983	6 pp.	1983
P. J. M. Kallenberg (*Philips' Telecommun. Ind., Hilversum*)		Queuing systems with a finite number of sources and internal traffic	Proc. 10th Int. Teletraffic Congr., Montreal 1983	6 pp.	1983

J. de Boer (*Philips' Telecommun. Ind., Hilversum*)	Limits and asymptotes of overflow curves	Proc. 10th Int. Teletraffic Congr., Montreal 1983	7 pp.	1983
C. A. A. J. Greebe, L. J. van de Polder & S. L. Tan *E*	HiFi television — Its limitations and possibilities	Proc. 13th Int. TV Symp., Montreux 1983	5-19	1983
J. P. van der Fluit (*NKF, Waddinxveen*)	Optical transmission over long distances for CATV and CCTV	Proc. 13th Int. TV Symp., Montreux 1983	291-303	1983
H. Breimer (*Philips International, Eindhoven*)	Development in camera technology	Proc. 13th Int. TV Symp., Montreux 1983	307-315	1983
G. M. Kuyck (*Philips Electro-acoust. Div., Eindhoven*)	Experiments in multifunctional CATV-systems	Proc. 13th Int. TV Symp., Montreux 1983	391-397	1983
A. W. Woodhead, D. Washington, C. D. Overall, J. R. Mansell, A. G. Knapp & D. L. Lamport *R*	The channel multiplier cathode ray tube	Proc. S.I.D. **23**	113-122	1982
J. H. T. Pasman *E*	Rigorous diffraction theory applied to video disk geometries	Proc. SPIE **369**	674-680	1983
D. M. Connah & C. A. Fishbourne *R*	Segmentation by colour	Radio & Electron. Eng. **53**	153-156	1983
H. Ney *H*	A dynamic programming algorithm for nonlinear smoothing	Signal Process. **5**	163-173	1983
G. Frank, E. Kauer, H. Köstlin & F. J. Schmitte (*RWTH, Aachen*) *A*	Transparent heat-reflecting coatings for solar applications based on highly doped tin oxide and indium oxide	Sol. Energy Mater. **8**	387-398	1983
I. J. M. M. Raaijmakers, P. W. J. M. Boumans, B. van der Sijde* & D. C. Schram* (* *Univ. of Technol., Eindhoven*) *E*	A theoretical study and experimental investigation of non-LTE phenomena in an inductively-coupled argon plasma — I. Characterization of the discharge	Spectrochim. Acta **38B**	697-706	1983
P. W. J. M. Boumans *E*	An assessment of prominent lines in inductively-coupled argon plasmas with special reference to spectrographic general survey analysis	Spectrochim. Acta **38B**	747-776	1983
E. Bruninx & A. van Eenbergen *E*	Relative intra-element cross-sections and binding energies obtained from XPS wide scan spectra	Spectrochim. Acta **38B**	821-830	1983
J. de Kroon (*Philips ISA-CQM, Eindhoven*) & P. van der Laan (*Agricult. Univ., Wageningen*)	A generalization of Friedman's rank statistic	Stat. Neerlandica **37**	1-14	1983
J. Engel (*Philips ISA-CQM, Eindhoven*)	Analysis of variance on indirectly measured variables	Stat. Neerlandica **37**	59-68	1983
G. D. Khoe *E*	Advanced passive componentry for optical fiber communication systems	Tech. Digest IOOC'83, Tokyo 1983	4 pp.	1983
H. Schomberg, W. Vollmann & G. Mahnke *H*	Lateral inverse filtering of ultrasonic B-scan images	Ultrason. Imaging **5**	38-54	1983
A. Broese van Groenou *E*	The sphere-on-tape: a quick test on wear of materials used in magnetic recording	Wear of materials 1983, K. C. Ludema (ed.), ASME, New York	212-217	1983
M. Zijlstra (*Philips ISA-CQM, Eindhoven*)	Optimization of preventive maintenance for two-unit cold standby redundant systems with a general cost structure	Z. Oper. Res. **27**	55-63	1983

Contents of Philips Telecommunication Review **41**, No. 4, 1983

D. W. Rollema: The new IJmuiden maritime traffic centre (pp. 261-283)

L. Taschner: Transmitting two TV channels over a single coaxial tube (pp. 284-291)

J. T. van Leerdam & W. J. van Oeveren: Junction networks in the multi-exchange areas in Saudi Arabia (pp. 292-299)

F. C. Schoute: Overload control in SPC processors (pp. 300-310)

Volume 41, 1983/84, No. 5 pages 137-168 Published 4th April 1984

PHILIPS TECHNICAL REVIEW

Vol. 41, 1983/84, No. 6

FM receivers for mono and stereo on a single chip

W. G. Kasperkovitz

Most households now possess a number of radio receivers. This wide availability of a once-expensive technical product has come about only through a phenomenal fall in the cost of manufacture. This in turn is the result of greatly increased production runs — now into millions — but more than anything it is due to new technological developments. Every now and then a fundamental advance is made, a step towards other, and cheaper, methods of achieving the required functions in the receiver. One such earlier step was the change from thermionic valves to transistors. In the new technology, costs are gradually being brought down by greater efficiency and economies of scale in production, but in the long run this downward trend in production costs must stop and another fundamental step forward becomes necessary. The article below describes such a new step: the integration of a complete FM mono receiver on a single chip. The number of trimming points — an important cost factor — has been reduced to one: the externally connected oscillator inductor. The other external components are a few capacitors and resistors, which do not have to meet any particularly arduous requirements. The new chip (TDA 7010T) is so small that extreme miniaturization is possible — and some wrist-watches on the market now contain a built-in FM receiver based on this chip. But even in this new technology further improvements are on the way; the successor, TDA 7020T, already in pilot production, will work on lower battery voltages and requires fewer external components. The article also presents a fundamental solution of the next step forward: a completely integrated FM stereo receiver.

Introduction

Although the first attempts to use integrated circuits in radio receivers to reduce the cost were made more than 15 years ago, most receivers built today still consist of a printed-circuit board with manually inserted discrete transistors, diodes, resistors, capacitors and inductors; the inductors generally have to be aligned. Integrated circuits are now frequently included in high-performance receivers to make tuning easier, through additional features such as noise muting, deviation muting (off-tune signal suppression), station preset, frequency display, frequency synthesis, touch control and remote control. But the basic circuit used in most of the less-expensive portables and clock radios has remained essentially unchanged for ten years or more.

Dr Ing. W. G. Kasperkovitz is with Philips Research Laboratories, Eindhoven.

This gives some idea of the difficulties encountered in designing a successful substitute for inductors that will combine high Q-factors with high signal-to-noise ratios at high operating frequencies. In principle, gyrators [1] can be used instead of inductors. However, with increasing operating frequencies these circuits become less attractive because of the limitations of dynamic range and Q-factor and because of their complexity and power dissipation.

Instead of designing an integrated radio receiver in which the inductors in the resonant circuits are replaced by active RC circuits, it may be possible to adopt other approaches that are less handicapped by the limitations of IC technology. Various systems have been proposed in which fewer inductors are necessary

[1] B. D. H. Tellegen, The gyrator, a new electric network element, Philips Res. Rep. 3, 81-101, 1948.

for the receiver unit [2]-[7]. Compared with existing superheterodyne receivers the proposed receiver circuits use a significantly lower intermediate frequency, so that the intermediate-frequency bandpass filters may be replaced by *RC* filters that can be partly or completely integrated.

Depending on the choice of intermediate frequency, two classes of problems are encountered in FM receivers. With an intermediate frequency of zero [4]-[6] image-reception problems in superheterodyne receivers are eliminated. With these receiver systems, however, the amplitude of the i.f. signal cannot be limited before demodulation. This results in a 3-dB lower signal-to-noise ratio in the i.f. stage and in less suppression of unwanted amplitude modulation of the demodulated signal.

This problem is not encountered in a receiver system that has an intermediate frequency of 140 kHz [7], where a limiter/amplifier is used before the demodulator to suppress AM noise and peak distortions of the r.f. signal. With this system, however, there is an image response at a spacing of 280 kHz, almost coinciding with the centre frequency of a neighbouring channel at a spacing of 300 kHz. Because of this there are also two tuning positions for each station (quite apart from the double response on the outer slopes of the demodulator characteristic, which is dealt with below).

To be acceptable to the customer an integrated FM receiver should at least avoid the shortcomings of the proposed systems with low intermediate frequency. But if the shortcomings of today's superheterodyne receivers could also be eliminated, such an integrated receiver, in addition to being cheaper to produce, would have advantages for the user as well.

Compared with AM receivers, FM receivers have one fundamental weakness, which is that each station has at least three tuning positions. *Fig. 1* shows the amplitude of the demodulated audio signal of a typical superheterodyne portable receiver as a function of the tuning frequency, with the r.f. voltage V_{ant} at the antenna input as the parameter; the modulation is a constant 1000-Hz tone. Besides the correct response at the centre of fig. 1, there are two spurious responses, characterized by a reduced signal-to-noise ratio and increased harmonic distortion of the audio signal. The demodulation takes place on the sides of the demodulator curve, which are referred to here as 'noise slopes', because of the high noise level (see *fig. 2*). The position and relative intensity of the spurious responses depend on the antenna input voltage and the selectivity of the receiver. They are separated from the range for correct tuning by minima in the output voltage. It might seem as if these minima would make it easy to identify the spurious responses. However, this is not the case in the far more complex situation found in practice, where the modulation is not constant and sinusoidal as in fig. 1, but strongly time-dependent and often with significant overlap between the spurious responses of adjacent channels. These effects combine to give rather unsatisfactory tuning behaviour, especially for simple tuning by ear.

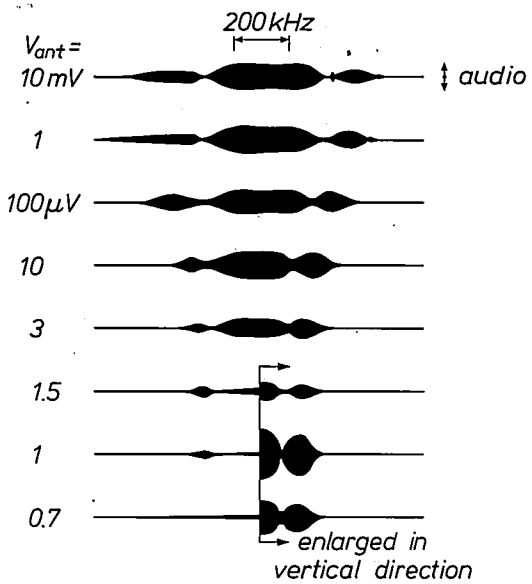

Fig. 1. The tuning behaviour of a conventional mono receiver at different antenna input voltages V_{ant}. The demodulated audio signal (vertical), here a 1000-Hz tone (*audio*), is shown as a function of the tuning frequency (horizontal). The audio signal has a maximum at the correct tuning position, and two secondary maxima to the left and right (on the outer slopes of the demodulator characteristic; see fig. 2). This makes it difficult to tune by ear. In the integrated FM receiver the two spurious responses are suppressed (see fig. 10).

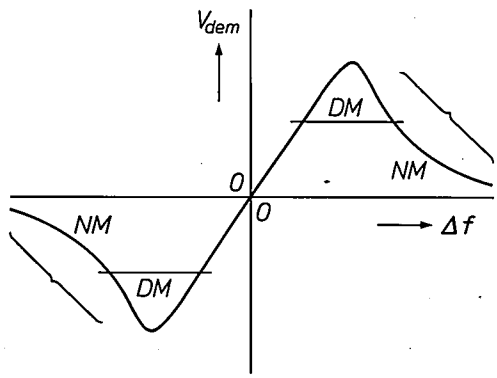

Fig. 2. Demodulator characteristic. This gives the relation between the demodulator output voltage V_{dem} and the frequency deviation Δf. The central part of the curve has the desired linear relation between the two. On detuning from the centre frequency, demodulation can also take place on the slopes *NS*; this is accompanied by distortion and noise. In our monolithic FM receiver these spurious responses are suppressed by a special circuit that reacts to frequency deviations (*DM*, 'deviation muting') or to excessive noise (*NM*, 'noise muting').

In the high-performance class of FM receivers squelch systems like noise muting [8] and deviation muting [9] are built in to suppress the spurious responses, and tuning meters are used to locate the correct tuning position. These features help to make tuning very much easier. Although cost reduction was the main objective in the integrated FM receiver presented here, it seemed a good idea to include these or similar features in the system. This had to be done, however, without unduly increasing the complexity, the power consumption or the number of external components and pins of the integrated circuit.

The integrated mono receiver circuit described in this article is now being marketed under the type designation TDA 7000 (or TDA 7010T) [10]. An improved design has recently been brought out under the type designation TDA 7020T. Some data are given in *Table I*. *Fig. 3* shows a wrist-watch, now commercially available, which contains an FM mono receiver built around this integrated circuit.

Fig. 3. A wrist-watch with a built-in FM receiver IC. The headphone lead also acts as the antenna.

A question that arises, of course, is whether it would also be possible to build an integrated FM stereo receiver. This is a much more complicated exercise in view of the large bandwidth (53 kHz) of the stereo multiplex signal compared with the bandwidth of the mono signal (15 kHz). Nevertheless, it does seem feasible, and a complete integrated circuit for a stereo receiver is now being studied. A block diagram of the design is presented at the end of this article.

Table I. Data for the integrated FM receivers TDA 7000/7010T and TDA 7020T.

	TDA 7000/ 7010T	TDA 7020T	
Supply voltage	4.5	3	V
Supply current	8	5.7	mA
Frequency range	1.5-110	0.5-110	MHz
Sensitivity (amplitude limiting −3 dB, input impedance 75 Ω, signal mute not operating)	1.5	1.5	μV
Max. input voltage (total harmonic distortion 10%, $\Delta f = \pm 75$ kHz, input impedance 75 Ω)	200	200	mV
Audio output voltage Minimum load	90 22000	100 35	mV Ω

[2] D. K. Weaver, Jr., A third method of generation and detection of single-sideband signals, Proc. IRE **44**, 1703-1705, 1956.
[3] J. P. Costas, Synchronous communications, Proc. IRE **44**, 1713-1718, 1956.
[4] J. G. Williford, U.S. patent No. 3 568 067.
[5] I. Vance, British patent No. 1 530 602.
[6] I. A. W. Vance, An integrated circuit VHF radio receiver, Proc. Int. Conf. on Land mobile radio, Bailrigg 1979, pp. 193-204.
[7] G. G. Gassmann, Ein neues Empfangsprinzip für FM-Empfänger mit integrierter Schaltung, Radio Mentor **32**, 512-518, 1966 (in German).
[8] J. Craft, U.S. patent No. 3 714 583.
[9] I. Fukushima *et al.*, U.S. patent No. 3 851 263.
[10] W. H. A. van Dooremolen and M. Hufschmidt, A complete f.m. radio on a chip, Electron. Components & Appl. **5**, 159-170, 1983.

Basic features of the FM mono receiver

The integrated FM mono receiver described here operates with an intermediate frequency of 70 kHz. This value would lead to unacceptable harmonic distortion at a frequency swing of ± 75 kHz, which is the maximum value allowed in FM broadcasting. This is evident, since there is no room in the intermediate-frequency band for a deviation of −75 kHz, which would extend into the range of 'negative frequencies'. The frequency scale is then 'folded' around 0 Hz (see fig. 13), resulting in unacceptable harmonic distortion. For this reason 'frequency feedback' is used in our system, to reduce the maximum frequency swing of the intermediate frequency to ±15 kHz. This frequency feedback is obtained by using the demodulated audio signal to control the frequency of the local oscillator in our superheterodyne receiver. This is done in such a way that the oscillator frequency 'travels some of the way' with the frequency deviation of the transmitter. If the transmitter has a frequency deviation of ± 75 kHz, then the oscillator is given a deviation of ± 60 kHz, resulting in an i.f. signal with a frequency deviation of only ± 15 kHz.

With our choice of intermediate frequency, image reception occurs at a spacing of 140 kHz, i.e. at the edge of the received channel. Background noise in this part of the frequency band is equal in strength to the background noise of the received signal. Thus, with a given input signal and a given bandwidth, the signal-to-noise ratio at the output of the mixer stage is in principle 3 dB lower than in systems with complete suppression of the image response. This entails an increase in the noise figure, but the increase is partly compensated by the reduced i.f. bandwidth [11], and partly by a lossless coupling between the r.f. amplifier and the mixer stage.

An advantage of using an intermediate frequency not equal to zero is that amplitude modulation in the received signal can be effectively suppressed. A high-gain limiter/amplifier is included before the demodulator. This gives good AM suppression and automatic volume control (AVC), even for weak input signals.

The circuit also includes 'deviation muting', a system that suppresses the audio signal if the tuning is incorrect or if the input signals are comparable with the input noise. It is based on the correlation between the i.f. signal and a delayed and inverted version of the i.f. signal. A qualitative description of the system is given in *fig. 4*. The signal *IF'* is derived from the amplitude-limited intermediate-frequency signal *IF* by delaying this signal by one half of its period at correct tuning, and inverting the delayed signal. This means that for correct tuning the two signals are identical (fig. 4*a*), giving high correlation. In this situation the demodulated audio signal is applied to the audio output. If the tuning is incorrect (fig. 4*b*), one half of the period of the signal *IF* no longer corresponds to the delay between the two signals *IF* and *IF'*. In this situation the correlation between the two signals is small or negative, and the demodulated audio signal is not applied to the output. In this way the spurious responses for large input signals are suppressed.

If the input signal is comparable in level to the input noise, the two signals *IF* and *IF'* are as shown in fig. 4*c*. Because of the low *Q* of the i.f. filter (about 0.7) the intervals between the successive zero crossings of the i.f. signal fluctuate considerably, again giving a low correlation between the two signals and hence muting of the demodulated audio signal. In this way the skirts of the spurious responses at large input signals (top of fig. 1) and the entire spurious responses for small input signals (bottom of fig. 1) are suppressed. Fig. 2 illustrates what is meant here by 'skirts'.

This muting system that comes into operation when correlation is low combines the characteristics of signal muting operated by noise (in which the noise on the envelope of the i.f. signal is detected [8]), and signal muting operated by incorrect tuning (which depends on the automatic frequency control [9]). The correlation system can be used in our receiver because the compressed frequency swing is never so large as to disturb the correlation seriously. In addition, advantage is taken of the delay network that is part of the demodulation circuit; this gives a delay of a quarter of a period. At the low intermediate frequency it is not necessary to use a tuned circuit either for this delay or for the additional quarter-period delay also required

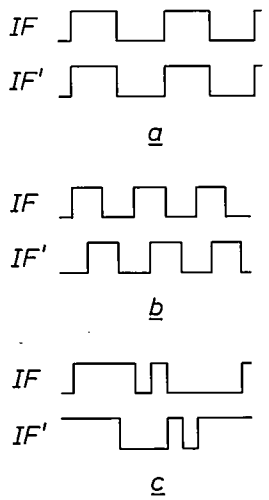

Fig. 4. Correlation measurement for signal muting. The i.f. signal is delayed by half a period, inverted (*IF'*) and compared with the original signal (*IF*). For correct tuning there is maximum correlation (*a*), for incorrect tuning less or no correlation (*b*), in the presence of noise alone there is no correlation (*c*). In cases *b* and *c* the signal is not supplied to the audio output.

for the muting, so that the entire signal-muting system requires few extra components and takes very little extra current. In our system the muting threshold is about five times as low as the muting thresholds of the most advanced systems based on detection of the noise on the envelope of the i.f. signal. It can therefore be high dynamic range at the output of the mixer, to a constant amplitude. To obtain the high gain of 90 dB at low current, LA_1 operates into a high impedance, and a buffer amplifier A_2 is added; this has a sufficiently low output impedance to reduce unwanted crosstalk between multipliers M_2 and M_3.

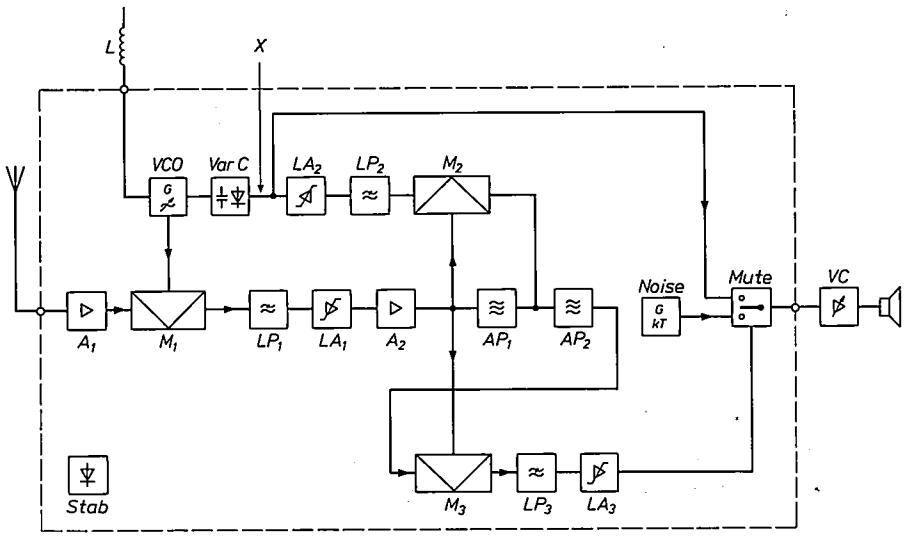

Fig. 5. Block diagram of integrated FM mono receiver. $A_{1,2}$ amplifier. $M_{1,2,3}$ multiplier circuit (mixer). $LP_{1,2,3}$ lowpass filter. $LA_{1,2,3}$ limiter/amplifier. $AP_{1,2}$ allpass network (gives 90° phase shift). *VarC* varactor. *VCO* voltage-controlled oscillator. *Noise* noise generator. *Mute* signal/noise switch. *Stab* stabilized direct voltage supply. *L* inductor (tunes *VCO* to the FM band). *X* point where the frequency-locked loop is regarded as open in the treatment of open-loop behaviour. *VC* volume control.

used in portable receivers, where many of the input signals are only slightly above the input noise level.

A noise generator is used in combination with the muting system to give an audible tuning indication in the absence of a tuning meter.

The integrated FM mono receiver

Fig. 5 shows a block diagram of the integrated circuit with its three essential connections to the outside world: the antenna input, the audio output and the connection to the circuit used for tuning to the desired station.

The antenna is connected to the input of the broadband amplifier A_1, which amplifies throughout the entire FM band. The output of A_1 is connected to the r.f. mixer M_1, which performs the conversion to the intermediate frequency. The signal gain from antenna input to mixer output is about 26 dB.

The i.f. signal is filtered by a fourth-order active lowpass filter (LP_1) to suppress signals outside the selected channel [12]. The response of this filter is shown in *fig. 6*. The limiter/amplifier LA_1, with a gain of more than 90 dB, limits the i.f. signal, which has a

Demodulation and limitation of the frequency swing are achieved by converting the frequency into a voltage, which is then used to correct the voltage-controlled oscillator *VCO*. Associated with this oscillator are an integrated varactor diode *VarC* (a variable-capacitance diode) and the external resonant circuit

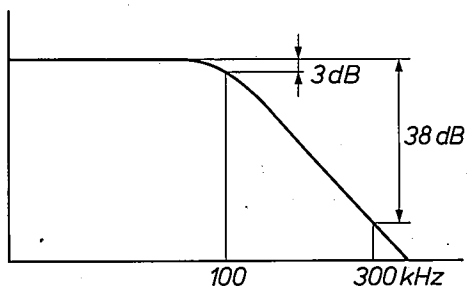

Fig. 6. Response of the lowpass filter LP_1. This fourth-order filter passes the band from 0 Hz to 100 kHz and acts as i.f. band filter in the integrated FM mono receiver, in which it determines the selectivity. A channel at a spacing of 300 kHz is attenuated by 38 dB.

[11] L. H. Enloe, Decreasing the threshold in FM by frequency feedback, Proc. IRE **50**, 18-30, 1962.

[12] A Sallen and Key configuration is used for this filter because it gives the best compromise between selectivity, current taken and signal-to-noise ratio. See R. P. Sallen and E. L. Key, IRE Trans. **CT-2**, 74-85, 1955.

mentioned above. The frequency is converted into a voltage by means of the multiplier M_2, in which the i.f. signal is multiplied by a version of the same signal shifted in phase by 90°. The phase shift takes place in the allpass filter AP_1. The combination of M_2 and AP_1 is called an FM quadrature detector (FMQD).

A mathematical description of quadrature demodulation is given on page 179, with a calculation of the signal delay in the quadrature demodulator.

The lowpass filter LP_2 is included in the frequency-locked loop thus formed. In addition to the audio frequency signal mentioned above, a d.c. signal also appears in the loop when the i.f. frequency does not have a value such that the delay in AP_1 is exactly a quarter-period of the carrier. This direct voltage provides automatic frequency control (AFC) by acting on the voltage-controlled oscillator *VCO*. The loop also contains a low-gain limiter/amplifier LA_2 to control the locking range of the AFC. Audio signals are extracted after this limiter/amplifier. The limiter does not distort the audio signals because as soon as it starts to operate the AFC is switched off; the receiver is then no longer tuned to the transmitter and the signal is suppressed.

The system that suppresses the signal in the absence of correlation (the correlation muting system) consists of two identical allpass filters AP_1 and AP_2, mixer M_3, lowpass filter LP_3 and limiter/amplifier LA_3. The correlation between the limited i.f. signal at the input of AP_1 and its delayed and inverted version at the output of AP_2 takes place in mixer M_3. The amplified and limited output signal of the correlator is used as a muting signal to suppress the audio signal for spurious responses.

Fig. 7 shows some of the control voltages in the integrated FM receiver as they would appear if the frequency-locked loop were opened at X in fig. 5; the responses shown are purely qualitative and relate to a particular level of the antenna signal. In fig. 7*a* and *b* the output voltages of demodulator M_2 and low-gain limiter/amplifier LA_2 are shown as a function of the difference between the antenna-signal frequency f_{ant} and the oscillator-signal frequency f_{osc}. With the loop closed the control makes this difference equal to the centre frequency f_c, giving correct tuning.

The output voltages of the correlator M_3 and of limiter/amplifier LA_3 are shown in fig. 7*c* and *d* as a function of $f_{ant} - f_{osc}$. There are two bands of $f_{ant} - f_{osc}$ where the signal is not suppressed but is applied to the output. One is centred around f_c, the point of correct tuning. The other band with no muting is defined by $-f_2 < f_{ant} - f_{osc} < -f_1$. This means that a

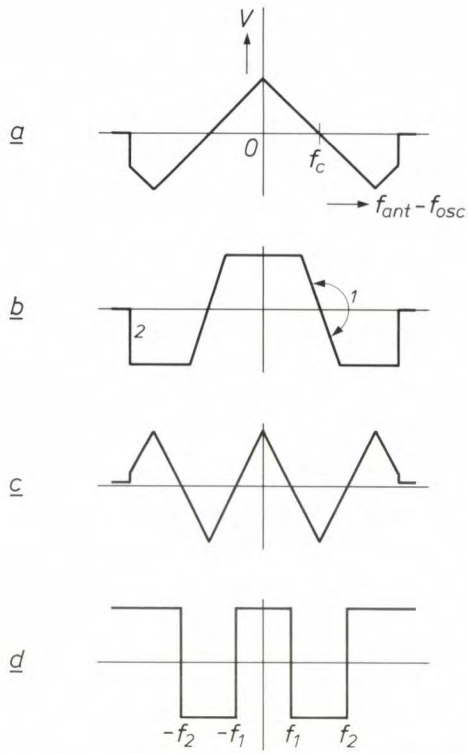

Fig. 7. Signal voltages V for frequency control and signal suppression (muting). Schematic representation of open-loop behaviour. *a*) Output voltage of mixer M_2 as a function of the difference $f_{ant} - f_{osc}$ between received frequency and oscillator frequency. f_c is the desired intermediate frequency to which $f_{ant} - f_{osc}$ is tuned in the closed loop. *b*) The same voltage after limiting and amplification in LA_2. Stable tuning positions are found on paths *1* and *2*, because if the value of $f_{ant} - f_{osc}$ is too high the control voltage is negative, so that $f_{ant} - f_{osc}$ is reduced again; the tuning position on path *2* (the slope) is one of the spurious responses. *c*) Output voltage of mixer M_3, used for deviation muting. *d*) The same voltage after limiting and amplification in LA_3. When the voltage is high, the output signal is suppressed (muted), thus eliminating the spurious respons on path *2*. The voltage is low in the desired frequency range between f_1 and f_2, and also at the image frequencies between $-f_2$ and $-f_1$; however, stable tuning is impossible at the image frequencies, because of the frequency control.

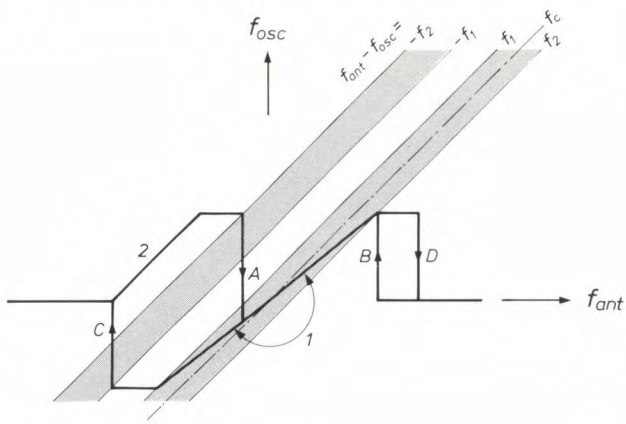

Fig. 8. Frequency control and signal muting with closed loop. (See fig. 7.) f_c desired intermediate frequency. *1* frequency trajectory at the correct tuning position; the frequency point moves to and fro along this path as a result of the frequency modulation. Because of the frequency feedback this line is not horizontal but sloping, and f_{osc} also varies. *Shaded area:* intermediate frequency bands where the audio signal is supplied to the receiver output; everywhere else the signal muting is operative. *2* second stable tuning position, but the signal is not supplied to the audio output. *A*, *B* frequency locking. *C*, *D* frequency release.

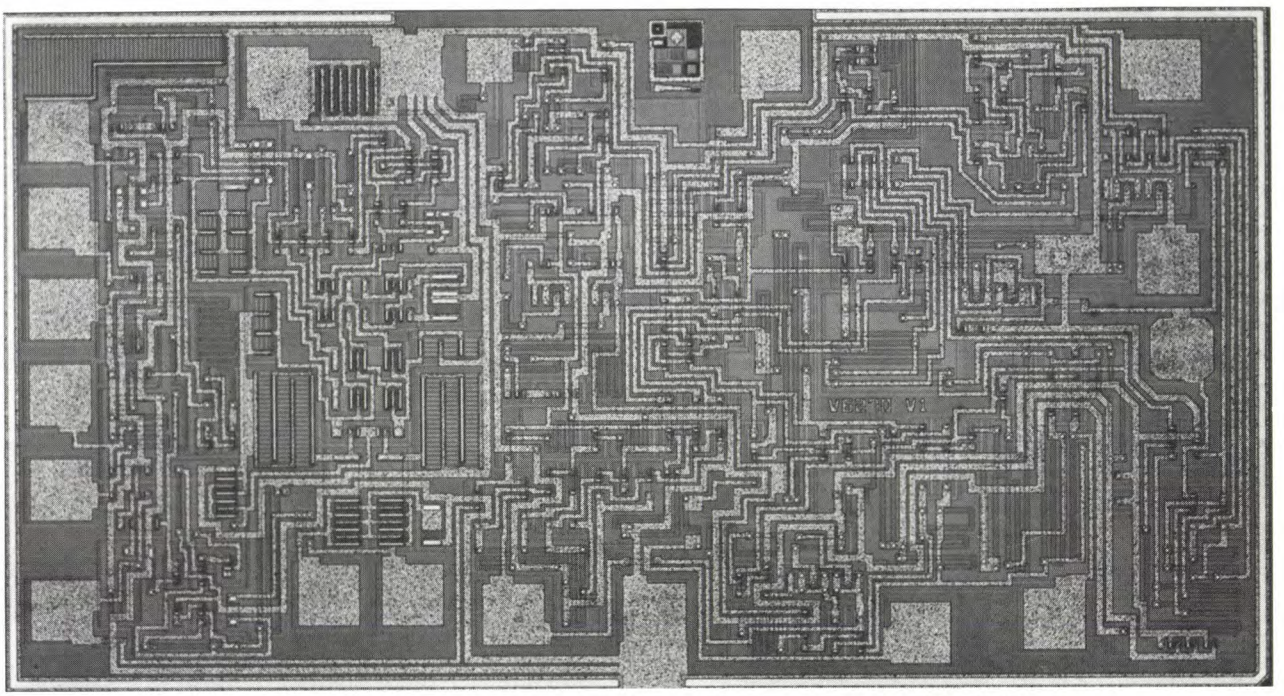

Fig. 9. Photomicrograph of the integrated FM mono receiver circuit TDA7000/7010T. Chip area 3.5 mm^2.

double tuning response is possible with an open loop. The second (spurious) response is at the image frequency.

When it is closed the frequency-locked loop gives positive feedback at the image frequency; a deviation from the image frequency generates a control voltage whose polarity is such that the deviation increases. Double tuning is therefore impossible with the loop closed.

This is illustrated in detail in *fig. 8*, which shows the paths taken by the control point as it moves towards the point of correct tuning in the plane f_{ant}, f_{osc}. The shaded areas indicate that there is no muting. The figure relates to the same antenna signal as in fig. 7.

With correct tuning (path *1*) the demodulated audio signal — which is a linear function of f_{ant} and also of f_{osc} — is not muted but is applied to the audio output (see fig. 7*d*). On path *2*, the noise slope of the demodulator characteristic, the frequency feedback is negative, so that a stable tuning position is also possible here. This path, however, lies in a region where signal muting is operative.

If the deviation from the point of correct tuning is too great the frequency-locked loop loses its hold on the oscillator frequency (fig. 8 *C*, *D*). As the point of correct tuning is approached, the transmitter eventually becomes 'locked' in the loop (fig. 8 *A*, *B*). Both events are accompanied by a sudden jump in the loop voltage, which would be audible in the audio signal if no countermeasures were taken. These transients in the audio signal are suppressed in two different ways.

The lock operation *B* and the loss of lock *D* take place in a region where $f_{ant} - f_{osc}$ is greater than f_2. In this region the signal muting is permanently in operation. The situation is different with loss of lock indicated by *C*; here the signal muting is not operative during the complete transition. The transition starts in a region where the mute is operative, then passes the region $-f_2 < f_{ant} - f_{osc} < -f_1$, where the signal is not muted and ends up in a region where the signal is muted again. To make this transition inaudible the time constant of the lowpass filter LP_3 (see fig. 5) has been made such that the input voltage of LA_3 remains positive during the short time interval necessary for crossing the region $-f_2 < f_{ant} - f_{osc} < -f_1$.

In a similar way the time constant of LP_3 also determines what can be heard during the locking operation *A*, where a transition takes place from the noise generator to the demodulated audio signal. Here the control point passes through four different regions with alternating states of the muting signal. A proper choice of the time constant ensures a smooth acoustical transition from the region $f_{ant} - f_{osc} < -f_2$, where the signal from the noise generator is passed to the output, to the region $f_{ant} - f_{osc} > f_1$ where the desired transmitter is heard at the output.

Measurements on the FM mono receiver

Fig. 9 shows a photograph of the integrated FM mono receiver circuit on a single chip. All the functions indicated in the block diagram in fig. 5 have been

optimized for chip area, power consumption and supply voltage variations. The current taken by the IC is 8 mA at 4.5 V, but it operates at any supply voltage between 3 V and 18 V. The chip area is 4.5 mm^2 and the number of bonding pads is 18.

Measurements have been made on an experimental receiver containing this IC. Apart from the integrated circuit, the receiver consists of a resonant circuit used for tuning to the desired station, a number of ceramic capacitors and a resistor. The resonant circuit is tuned by a varactor. No trimming is required apart from the adjustment of the direct-voltage range for tuning the resonant circuit through the FM band. Because of the low intermediate frequency i.f. trimming is unnecessary: the tolerance on the values of the most critical of the fixed capacitors is about 100 times greater than the tolerance on the *LC* products of the resonant circuits used in a conventional receiver.

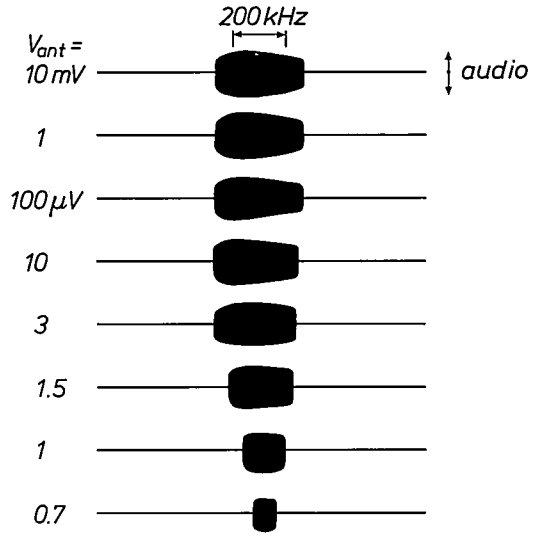

Fig. 10. Tuning behaviour of the integrated FM mono receiver (see also fig. 1).

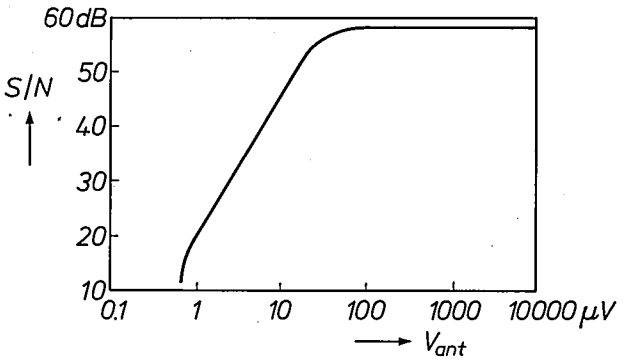

Fig. 11. Signal-to-noise ratio *S/N* of the demodulated signal (frequency 1 kHz, carrier frequency swing ± 22.5 kHz) as a function of the antenna voltage V_{ant} (across an input impedance of 40 Ω). At 1.5 μV the signal-to-noise ratio is 26 dB (this is the 'quieting sensitivity' as defined in the CCIR standard).

Fig. 10 shows the tuning behaviour of the experimental receiver. There are three improvements as compared with the tuning of a typical portable receiver, as shown in fig. 1:

- No spurious responses, at large or small input voltages. This is the result of the correlation muting system.
- Large range of correct tuning, even at small input voltages. This is achieved with the AFC. This function is illustrated by fig. 8, where a large variation in f_{ant} — which is equivalent to a large variation in the tuning frequency — is reduced to a small variation in the intermediate frequency $f_{ant} - f_{osc}$.
- No degradation of the audio signal for small antenna signals. This is due to the high gain of the limiter/amplifier LA_1 before the demodulator, which limits the i.f. signal even at input voltages lower than 1 μV. In conventional portable receivers, limiting at such low voltages results in stability problems because higher harmonics of the limited i.f. signal are radiated to the antenna. With the low intermediate frequency used in the design discussed here, it was possible to eliminate this radiation problem by careful layout of the integrated circuit.

In *fig. 11* the signal-to-noise ratio of the demodulated audio signal is shown as a function of the antenna input voltage; the frequency swing of the received signal is ± 22.5 kHz and the modulation frequency is 1 kHz. At 1.5 μV across an input impedance of 40 Ω the signal-to-noise ratio is 26 dB ('quieting sensitivity' as defined in the CCIR standard). The muting threshold is 0.7 μV, which practically coincides with the threshold of FM reception; below this level the signal-to-noise ratio decreases rapidly with decreasing input voltage. This means that with the correlation-muting system only audio signals of unacceptable reception quality are suppressed.

The fourth-order active *RC* filter LP_1 (figs. 5 and 6) has internal resistors and external capacitors. It provides 38 dB of attenuation for a neighbouring channel at a spacing of 300 kHz. The total harmonic distortion of the demodulated audio signal is defined by the characteristic curve of the integrated varactor diode. It has been measured as 1.8% at an input voltage of 1 mV and a frequency swing of ± 75 kHz. A better figure can be obtained by increasing the area of the integrated varactor.

Design of an integrated FM stereo receiver

Stability of frequency-locked loop

The bandwidth of the FM stereo signal that modulates the carrier is much larger than that of the FM mono signal (see *fig. 12*). As laid down in the inter-

national standards, the stereo signal, often called the stereo multiplex signal, consists of a baseband signal equal to the sum of the signals in the left and right channels (about 0-15 kHz), a pilot tone (19 kHz) and a subcarrier (38 kHz), modulated in amplitude by the difference between the left and right signals. This AM subchannel covers a band of 23 kHz to 53 kHz; the subcarrier is suppressed at the transmitter end and is reconstructed in the receiver from the pilot tone by frequency doubling [13].

The large bandwidth of the FM stereo multiplex signal (0-53 kHz) would lead to difficulties in a receiver like the one shown in fig. 5. The problem is connected with the stability of the frequency-locked loop, which

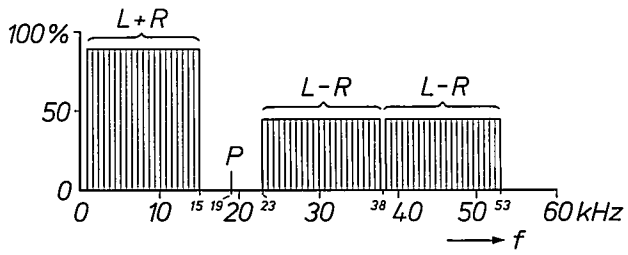

Fig. 12. Frequency spectrum of the stereo multiplex signal. The figure shows: from about 0 Hz to 15 kHz the stereo sum signal $L+R$, at 19 kHz the pilot tone P, from 23 kHz to 53 kHz the stereo difference signal $L-R$, amplitude-modulating a carrier at 38 kHz; this carrier is not transmitted. The vertical scale gives the contributions of each component to the frequency swing.

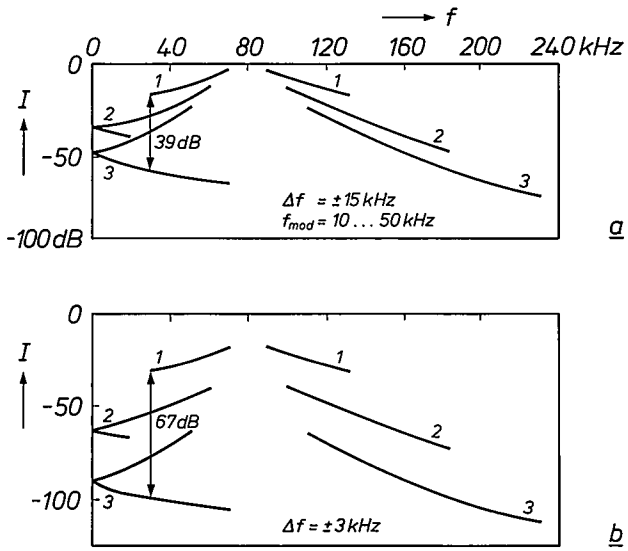

Fig. 13. Sideband 'folding'. The sideband level I for an FM signal is plotted against the frequency f (after conversion to an intermediate-frequency band centred on 80 kHz). The reference level of 0 dB corresponds to the unmodulated carrier. The diagram shows the sidebands of first, second and third order (*1*, *2*, *3*) for modulation by a sinusoidal tone at a frequency f_{mod} of 10 kHz to 50 kHz. The lower sidebands of second and third order extend further than the i.f. band permits; they are 'folded' around 0 Hz, causing harmonic distortion on demodulation. *a*) Weakly compressed or uncompressed frequency swing $\Delta f = \pm 15$ kHz. *b*) Highly compressed frequency swing $\Delta f = \pm 3$ kHz. The sidebands *2*, *3* of second and third order are much weaker and the harmonic distortion is therefore less.

is responsible for compression of the frequency swing. For reception of the stereo multiplex signal, frequency-swing compression is even more necessary than for the mono signal, because of the larger bandwidth. The improvement resulting from frequency-swing compression is illustrated in *fig. 13*, where the level of the sidebands of an FM signal with a swing $\Delta f = \pm 15$ kHz (little or no compression) is compared with the level at $\Delta f = \pm 3$ kHz (high compression). A frequency swing of ± 15 kHz is the contribution from the encoded stereo difference signal if one of the channels is fully modulated and the other is quiescent. Because of the low intermediate frequency (80 kHz) assumed in fig. 13, the lower sidebands are 'folded' around the limit of 0 Hz, giving rise to harmonic distortion. Since the sidebands of higher order (*2*, *3*) are disproportionately weaker when the swing is smaller, the resulting harmonic distortion is less.

The frequency-locked loop is a negative feedback system, which is only stable when the phase shift is less than 180° at the frequencies where the loop gain is greater than or equal to one. If the phase shift in this frequency range is 180°, the loop will oscillate spontaneously.

Now a phase shift is unavoidable in the filters used in this control loop: these are the i.f. filter (LP_1 in fig. 5), which determines the selectivity, the FM detector (AP_1 and M_2) and the loop filter (LP_2) that limits the bandwidth of the loop. To obtain a quantitative idea of the way in which the selectivity, the bandwidth of the closed frequency-locked loop and the transfer characteristic are affected by the stability condition, it is useful to have a simplified model of the frequency control system in the FM receiver. Let us first take another look at the mono receiver as shown in fig. 5.

Frequency control of mono receiver

Fig. 14 shows the model, including the transmitter. This is represented by the voltage-controlled oscillator VCO_1, to which the mono information V_i is supplied (there is no multiplex signal). VCO_1 delivers a frequency-modulated carrier. In the analysis that follows, the frequency of the unmodulated carrier is not relevant; we are more concerned with the frequency-deviation f_i. We shall therefore consider this alone in the following and merely state that VCO_1 delivers a signal f_i. This frequency deviation f_i is proportional to V_i.

All non-essential subfunctions in the receiver, such as the amplifiers and the signal muting, have been omitted. The oscillator VCO_2 is controlled by the

[13] N. van Hurck, F. L. H. M. Stumpers and M. Weeda, Stereophonic radio broadcasting, I. Systems and circuits, Philips Tech. Rev. 26, 327-339, 1965.

voltage V_o, which is produced by the control system, which gives it a frequency deviation f_o. The mixer M_1 produces the difference signal $f_i - f_o$; this passes through the i.f. filter LP_1, which determines the selectivity, and goes to the frequency demodulator AP_1/M_2, whose output signal $(V_i - V_o)_{del}$ is delayed. This signal passes through the loop filter LP_2 (bandwidth B) and its output signal is the control voltage V_o mentioned above.

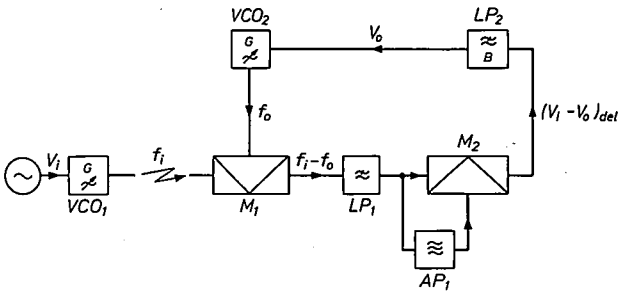

Fig. 14. Model of the frequency-locking system in the FM mono receiver. V_i mono signal. VCO_1 transmitter, frequency-modulated by V_i. f_i frequency deviation at receiver input. M_1 mixer. LP_1 i.f. filter. M_2 mixer for demodulation. AP_1 allpass filter (delay network) giving a 90° phase shift for the intermediate frequency. LP_2 loop filter. V_o control voltage. VCO_2 voltage-controlled oscillator. f_o deviation of the oscillator frequency. $(V_i - V_o)_{del}$ signal resulting from demodulation of $f_i - f_o$ and delayed by LP_1 and AP_1.

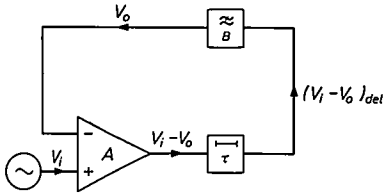

Fig. 15. Simplified version of fig. 14. The conversions from voltage to frequency deviation and frequency deviation to voltage have been omitted. The gain A is the product of the conversion factors of VCO_2 and AP_1/M_2.

The delay of $(V_i - V_o)_{del}$ is partly caused by the group delay of LP_1 and partly by the delay of the i.f. signal in AP_1. Both delays are added together to form a single delay τ.

When the voltage-frequency conversion in VCO_1 and VCO_2 is combined with the frequency-voltage conversion in demodulator AP_1/M_2, the result is a particularly simple model of an FM transmitter and FM receiver with a frequency-locked loop (*fig. 15*). The transmitter now consists only of the voltage source V_i, and the receiver consists of a differential amplifier of gain A, a delay element with delay τ and a loop filter of bandwidth B. The gain A is the product of the conversion gains of VCO_2 and AP_1/M_2.

The transfer function from transmitter to receiver is determined by these three quantities A, τ and B. The swing compression is $1/(1 + A)$. The part of the delay τ arising in LP_1 is connected with the selectivity, and the part arising in AP_1 is connected with the intermediate frequency. Finally, B is a quantity that determines the stability of the frequency-locked loop.

The contribution of the filter LP_1 to the delay τ can be determined quantitatively with the aid of *fig. 16*. The curves *Bu* represent the amplitude characteristic and the group delay of the filter as designed for the integrated FM mono receiver; it is a fourth-order Butterworth filter with a cut-off frequency of 100 kHz. It can be seen in fig. 16*b* that the group delay in the

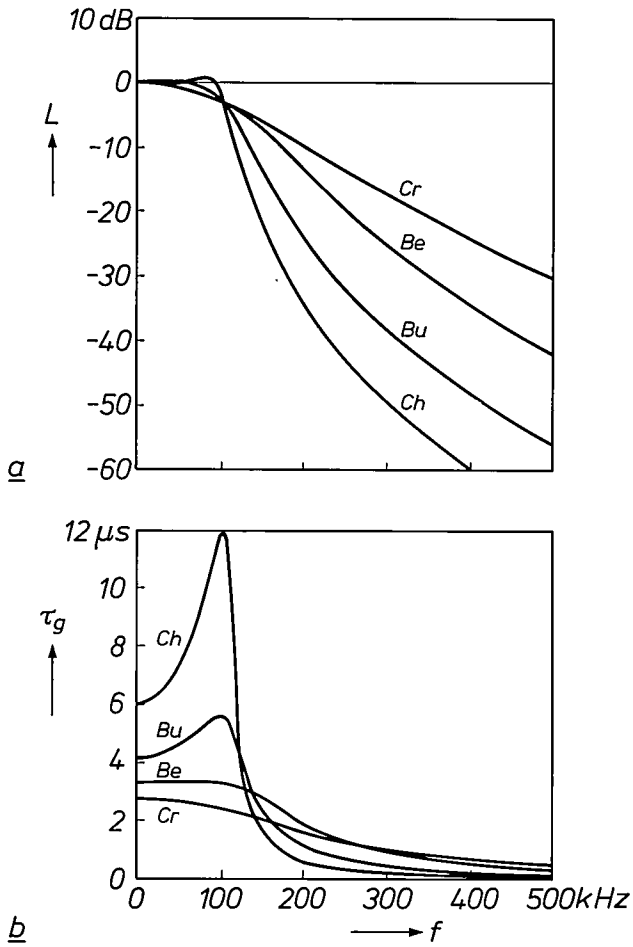

Fig. 16. Amplitude level L and group delay τ_g of the output signal as a function of frequency f for a fourth-order lowpass filter with a cut-off frequency of 100 kHz. *Cr* critically damped filter. *Be* Bessel filter. *Bu* Butterworth filter. *Ch* Chebyshev filter. The selectivity of the filters increases in this order, but at the same time the group delay in the passband increases.

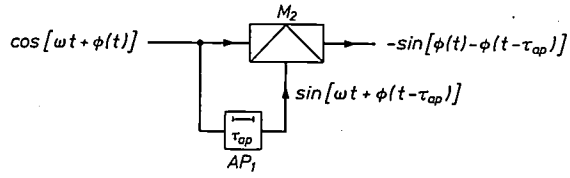

Fig. 17. Signal delay in the demodulator circuit AP_1/M_2. The delay τ_{ap} in the allpass filter AP_1 is a quarter of a period at the intermediate frequency. Because of the symmetry of the expression for the output signal a delay of $\frac{1}{2}\tau_{ap}$ can be assigned to it.

passband is reasonably constant and that LP_1 may be replaced by a frequency-independent delay element.

A further delay occurs in the frequency demodulator, which consists of the allpass filter AP_1 and the multiplier M_2 (*fig. 17*). The output signal of M_2 is the product of the i.f. signal and a delayed version of it obtained from AP_1; the delay in AP_1 corresponds to a phase shift of 90° at the nominal intermediate frequency. The symmetry of the contributions from the two input signals to the output signal suggests that the delay of the output signal is the average of the delays of the two input signals, i.e. half the group delay of AP_1.

This may be substantiated by a mathematical description of quadrature modulation. The product of the two input signals to M_2 (see fig. 17), taking τ_{ap} as the delay in AP_1, is:

$$\cos\{\omega t + \phi(t)\} \sin\{\omega t + \phi(t - \tau_{ap})\}$$
$$= \tfrac{1}{2} \sin\{2\omega t + \phi(t) + \phi(t - \tau_{ap})\}$$
$$- \tfrac{1}{2} \sin\{\phi(t) - \phi(t - \tau_{ap})\}.$$

The first term is at twice the intermediate frequency and is suppressed by the loop filter. The second term represents the low-frequency output signal; the variation of the phase $\phi(t)$ with time contains the audio information, since $d\phi/dt$ is the instantaneous value of the frequency deviation and hence of the audio signal. We can expand $\phi(t)$ and $\phi(t - \tau_{ap})$ about the time $t - \frac{1}{2}\tau_{ap}$ in a Taylor series and then subtract:

$$\phi(t) = \phi + \frac{\tau_{ap}}{2}\frac{d\phi}{dt} + \frac{\tau_{ap}^2}{8}\frac{d^2\phi}{dt^2} + \frac{\tau_{ap}^3}{48}\frac{d^3\phi}{dt^3} + \cdots$$

$$\phi(t - \tau_{ap}) = \phi - \frac{\tau_{ap}}{2}\frac{d\phi}{dt} + \frac{\tau_{ap}^2}{8}\frac{d^2\phi}{dt^2} - \frac{\tau_{ap}^3}{48}\frac{d^3\phi}{dt^3} + \cdots$$

$$\phi(t) - \phi(t - \tau_{ap}) = \tau_{ap}\frac{d\phi}{dt} + \frac{\tau_{ap}^3}{24}\frac{d^3\phi}{dt^3} + \cdots$$

All the terms on the right-hand side have the argument $t - \frac{1}{2}\tau_{ap}$. The terms of third and higher order are small, so that, to a good approximation,

$$\phi(t) - \phi(t - \tau_{ap}) \approx \tau_{ap}\frac{d\phi(t - \frac{1}{2}\tau_{ap})}{dt}.$$

The output signal thus carries the information of the time $t - \frac{1}{2}\tau_{ap}$, so that the delay in the demodulator circuit amounts to half the delay in the allpass filter AP_1.

Now that we know the total delay τ in the frequency-locked loop in fig. 15, we can calculate the effect of the bandwidth B of the loop filter on the transfer function V_o/V_i. *Fig. 18* gives three examples for bandwidths of 2 kHz, 3 kHz and 5 kHz. As might be expected, the −3-dB bandwidth of the closed loop increases and at the same time the stability decreases with increasing bandwidth B of the loop filter. Although a −3-dB bandwidth of 53 kHz is obtained at $B = 5$ kHz, there is a peak of 8 dB because of the reduced stability, and this is unacceptable for stereo reception. The bandwidth of 53 kHz is necessary, however, if the entire stereo multiplex signal is to contribute to the frequency-swing compression. The peaking can of course be reduced by making τ smaller, but this necessitates a less selective i.f. filter (see fig. 16, curves *Be* or *Cr*); in many situations there would then be unacceptable interference from strong adjacent stations.

There is therefore a dilemma between undistorted stereo reception on the one hand and sufficient selectivity on the other. We have succeeded in finding a solution, which will be explained here with the aid of a simplified model of a stereo transmitter and receiver.

Frequency control of a stereo receiver

The essence of our solution to the stability problem caused by the large bandwidth of the stereo multiplex signal is that the stereo difference signal that modulates the suppressed 38-kHz subcarrier does not pass through the loop filter. Instead it is first demodulated and passed through a lowpass loop filter of its own. The output is then remodulated, again producing an AM signal with suppressed carrier at 38 kHz. This in turn is added to the stereo sum signal, to provide oscillator control.

A simplified model of the system of frequency control in the combination of stereo transmitter and stereo receiver is illustrated in *fig. 19*. Here the signal from the stereo transmitter consists only of a subcarrier at 38 kHz, modulated in amplitude by V_i, the difference between the right and the left channels. The stereo receiver consists for the most part of the same components as the greatly simplified mono receiver in fig. 14: VCO_2, M_1, LP_1 and AP_1/M_2. Here, however, the loop filter LP_2 is replaced by mixer M_3, lowpass filter LP_3 and mixer M_4. The large-signal input to mixer M_4 is a 38-kHz subcarrier in phase with the subcarrier of the transmitter. The large-signal input to mixer M_3 is a delayed version of the subcarrier; the delay τ is equal to the delay in LP_1 and AP_1/M_2.

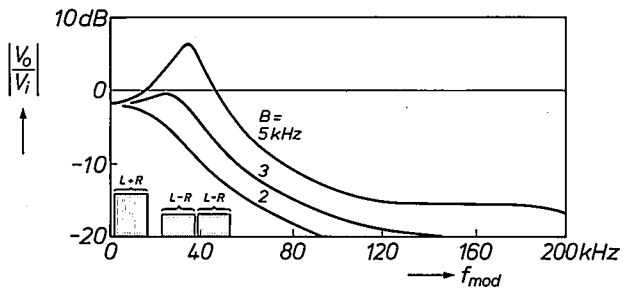

Fig. 18. Transfer function V_o/V_i in the closed frequency-locked loop; f_{mod} is the modulation frequency. The bandwidth B of the loop filter must be 5 kHz for all modulation frequencies up to 53 kHz of the stereo multiplex signal in fig. 12 to be passed, so that they can contribute to the swing compression. However, there is then an undesired peak of 8 dB, a sign of reduced stability.

The operation of the model is as follows. In M_0 the difference signal V_i modulates the subcarrier to produce V_i'; this then modulates VCO_1 to give the frequency deviation f_i. In a similar way the subcarrier is modulated in M_4 by the difference signal V_o obtained from the demodulation, resulting in a signal V_o', which

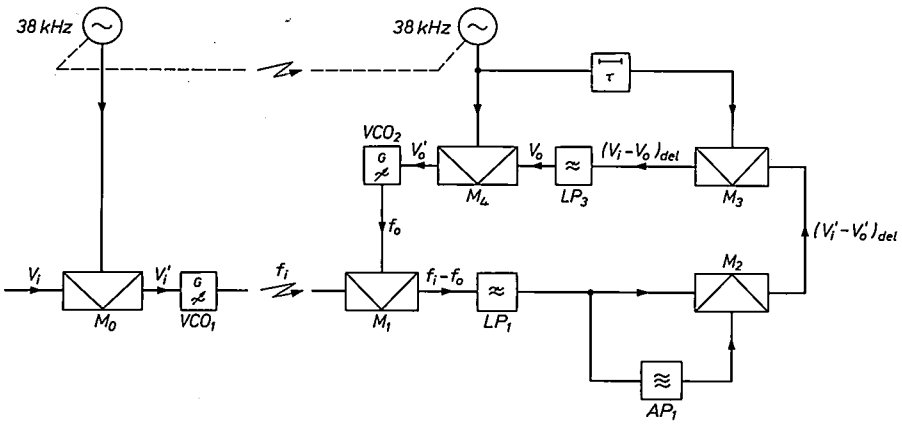

Fig. 19. Model of the frequency-control system in the FM stereo receiver. It is assumed that only a stereo difference signal V_i is transmitted; this is denoted as V_i' after modulation of the 38-kHz subcarrier. The model contains all the elements of the mono receiver in fig. 14. In the control loop now, however, demodulation of the 38-kHz subcarrier takes place in M_3 before the loop filter and remodulation to 38 kHz takes place in M_4 after the loop filter. In this model the 38-kHz generators in transmitter and receiver are assumed to be in phase; the signal delay τ in LP_1 and AP_1/M_2 makes it necessary to give the 38-kHz carrier the same delay to ensure correct phase in the demodulation in M_3.

then modulates VCO_2; the result is f_o. The output signal of mixer M_1 is the difference $f_i - f_o$. After filtering (in LP_1) and first demodulation (AP_1/M_2) this signal gives a delayed version $(V_i' - V_o')_{del}$ of the difference between the control signal V_i' of VCO_1 and V_o' of VCO_2. After a second demodulation in M_3, including compensation for the phase error introduced by LP_1 and AP_1/M_2, a delayed version $(V_i - V_o)_{del}$ of the difference between the difference signals V_i in the transmitter and V_o in the receiver is obtained. After filtering in loop filter LP_3 the output signal V_o is obtained in the same way as in the mono receiver.

Modulation by the 38-kHz subcarrier in M_0 and M_4 and corresponding inverse demodulation in M_3 take place without delay. The only delays in the receiver are the group delay of LP_1 and the delay in the demodulator AP_1/M_2. If the sum of these delays is equal to τ, and if the bandwidth of the loop filter LP_3 is equal to B, the transfer function V_o/V_i in the stereo receiver is the same as the transfer function in the highly simplified model of a mono receiver in fig. 15. The stability problem in the stereo receiver is therefore essentially the same as for the mono receiver and can therefore be solved with selectivity maintained.

Fig. 20 shows the calculated and measured transfer function V_o/V_i of a stereo receiver as in fig. 19 with open loop (*OL*) and closed loop (*CL*). There is good agreement between model and experiment up to modulation frequencies of about 30 kHz with an open loop, and to about 80 kHz with the loop closed. The highest frequency in the stereo difference signal is 15 kHz, which can be processed without difficulty by a receiver of this type.

A real stereo receiver must of course deal with the sum signal as well as the stereo difference signal. This means that the receiver must contain a loop as shown in fig. 14 in parallel with the loop shown in fig. 19.

In a practical receiver the subcarrier locking is obtained by means of a 19-kHz pilot tone, which has a delay τ with respect to the transmitter signal after demodulation. The regenerated 38-kHz subcarrier thus has the correct phase for the demodulation in M_3, but this phase must be advanced by an amount

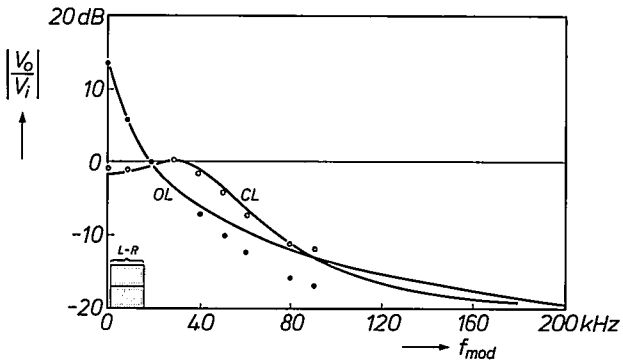

Fig. 20. Transfer function V_o/V_i in the open frequency-locked loop (*OL*) and in the closed loop (*CL*) in the stereo receiver; f_{mod} is the modulation frequency. The points indicate values calculated from a model like the one of fig. 19; the curves were measured for an experimental circuit. The stereo difference signal $L-R$ that the filter must pass has a bandwidth of 15 kHz.

$2\pi \times 38\,000 \times \tau$ for the remodulation in M_4. If, as assumed above, the i.f. filter LP_1 is a fourth-order Butterworth filter and the intermediate frequency is 70 kHz, the phase correction required at 38 kHz can even amount to about 90°. Without this phase correction the stereo difference signal modulated at 38 kHz would not contribute to the swing compression.

Block diagram of an integrated FM stereo receiver

The block diagram of the FM stereo receiver is given in *fig. 21*. The input stages are the same as in the FM mono receiver; the main additions are the more elaborate loop-filter network *LoopFi*, the subcarrier regenerator *SubcGen* and the matrix network *Matr*, in which the signals for the left and right channels are recovered from the sum and difference signals.

The stereo multiplex signal that appears at the output of the FM quadrature detector *FMQD* takes various paths in the loop-filter network. The lowpass filter LP_2 with a cut-off frequency of 5 kHz passes the baseband, but with an attenuation increasing by 6 dB/octave above 5 kHz (first-order filter). The multiplier circuit M_3 receives the 38-kHz subcarrier from the subcarrier regenerator and multiplies it by the multiplex signal. This results in demodulation of the difference signal, which is then limited in bandwidth in the first-order lowpass filter LP_3 (cut-off frequency also 5 kHz); after band limiting it is used for remodulating the amplitude of the subcarrier (multiplier M_4, amplitude modulation with suppressed carrier again). In this way a band filter centred on 38 kHz is obtained. In fact there is a temporary transformation from 38 kHz to 0 Hz, so that a simple lowpass filter is sufficient for limiting the passband.

A filtered multiplex signal is produced in an adder circuit and is returned via limiter/amplifier LA_2 to the

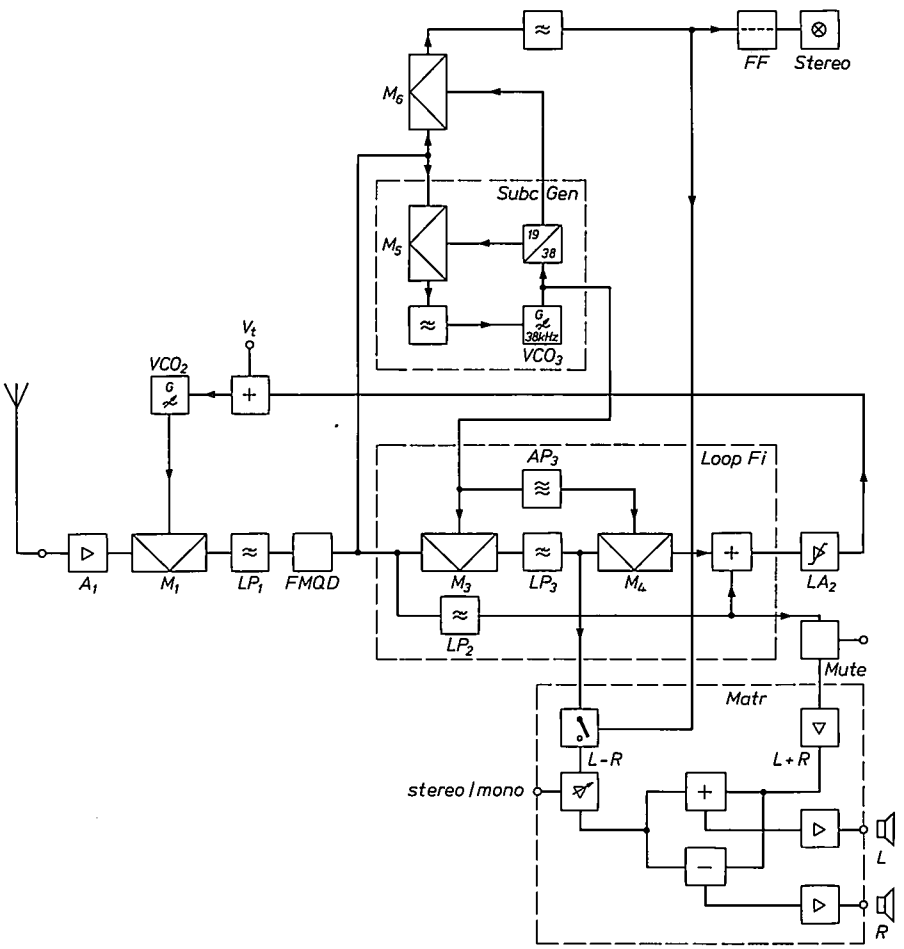

Fig. 21. Block diagram of an FM stereo receiver for integration. Many of the components are the same as in the mono receiver (see fig. 4). *FMQD* FM quadrature detector. *LoopFi* loop filter. *SubcGen* subcarrier generator. *Matr* matrix network (in which the left and right signals L and R are recovered from $L+R$ and $L-R$). *FF* bistable circuit. *Stereo* stereo indicator. *Mute* muting for off-tune signals.

voltage-controlled oscillator VCO_2 to give the required swing compression. The external tuning voltage V_t is added to the control signal.

The allpass filter AP_3 compensates for the delay of the 38-kHz carrier in the i.f. filter and the FM detector. As explained earlier, the phase of the subcarrier is advanced here by an amount τ, so that in M_4 the stereo difference signal modulates a carrier of the same phase as the subcarrier in the input signal of M_1.

The regeneration of the subcarrier for demodulating and remodulating the stereo difference signal in the loop-filter circuit *LoopFi* takes place in the stereo subcarrier regenerator *SubcGen*. This contains a phase-locked loop in which the 19-kHz pilot tone is multiplied by a 19-kHz signal, obtained by frequency division from a 38-kHz voltage-controlled oscillator (VCO_3). Any phase deviations cause a d.c. component in the product signal; this d.c. component is passed by a lowpass filter and is used to control the tuning of the oscillator.

The presence of the 19-kHz pilot tone is detected with the aid of multiplier M_6. Its output signal passes through a lowpass filter and controls a bistable circuit *FF*, which in turn switches on a stereo indicator; the same output signal operates the mono/stereo switch.

The demodulated stereo difference signal goes via this switch to a variable-gain amplifier and then to the matrix network, in which the signals for the left and right audio channels are derived from the difference and sum signals by addition and subtraction. The variable-gain amplifier makes it possible to vary the stereophonic effect (*stereo/mono*) in the reproduction. For a weak signal in noise it is better to attenuate the stereo difference signal; this reduces the stereo effect but improves the signal-to-noise ratio. On the other hand the stereo effect can be accentuated by amplifying the stereo difference signal more than proportionately, so that the sound sources seem to be further apart than the loudspeakers.

Summary. The article describes the integration of a complete FM mono receiver on a single chip. The external components are a single inductor (for the oscillator) and some capacitors and resistors. The use of a very low intermediate frequency (70 kHz) enables the i.f. bandpass filters to be replaced by lowpass filters. Harmonic distortion in such a limited i.f. band is avoided by compressing the frequency swing to ± 15 kHz. The IC is currently being marketed as type TDA 7000/7010T; an improved version, TDA 7020T, which operates with a lower battery voltage, is in pilot production. A monolithic FM stereo receiver is now being studied. In this receiver two frequency bands are selected from the stereo multiplex signal for oscillator control, since a frequency-locked loop with the full stereo multiplex bandwidth is not stable because of the group delay in a sufficiently selective i.f. filter.

High-resolution X-ray diffractometer

In an ideal mixed crystal (e.g. $Ga_{1-x}Al_xAs$) a linear relation exists between the lattice constant and the chemical composition of the substance. Changes brought about in the crystal by ion implantation, diffusion or epitaxy generally have an effect on the lattice constant. By measuring the change in the lattice constant it is possible to determine whether the required composition has been reached. This measurement can be made by means of X-ray diffraction. The double-crystal diffractometer [1], which is generally used for this purpose, has two major disadvantages. It can only be used to measure changes in the lattice constant, it cannot determine their absolute value. In addition, a suitably modified monochromator is required for every measurement. At Philips Research Laboratories in Eindhoven an X-ray diffractometer has been developed that does not have these disadvantages. Before taking a closer look at this instrument, let us first briefly consider the principle of X-ray diffraction.

When a parallel beam of X-rays of wavelength λ is incident at an angle θ on a crystal whose lattice planes are separated by a distance d, there is reflection when Bragg's law is satisfied:

$$2d \sin\theta = \lambda. \qquad (1)$$

The beam is then deflected through an angle 2θ. The variations $\Delta d/d$ that can be observed are determined by the spread in the angle of incidence of the beam ($\Delta\theta$) and the spread in the wavelength ($\Delta\lambda/\lambda$). It can be shown from (1) that the relation between these variables is

$$\frac{\Delta d}{d} = \frac{\Delta\lambda}{\lambda} - \frac{\Delta\theta}{\tan\theta}. \qquad (2)$$

The quantity $\Delta d/d$ represents the resolution of the diffractometer. If variations $\Delta d/d$ of the order of magnitude of 10^{-5} are to be measured, then $\Delta\lambda/\lambda$ and $\Delta\theta$ must be of the same order. However, the radiation emitted by an X-ray tube has a fairly broad wavelength spectrum, consisting of a broad background ('bremsstrahlung') on which a number of 'lines' are superimposed (the characteristic radiation). The natural linewidth of the characteristic radiation is still fairly large, however. For the CuKα_1 line, for example, it amounts to $(\Delta\lambda/\lambda)_{CuK\alpha_1} = 3\times10^{-4}$. The emitted radiation also has a fairly large divergence, amounting to a few degrees. Although this divergence can be limited to some extent by means of slits, the result is never much better than say $\Delta\theta = 0.1° = 1.7\times10^{-3}$ rad.

These problems are partly solved by the double-crystal diffractometer (*fig. 1*). The X-rays are collimated by the first crystal (the 'monochromator') to about $\Delta\theta = 2'' = 10^{-5}$ rad, and are then incident on the second crystal (the sample). The diffraction in the two crystals is in opposite directions. This is referred to as the (+, −) setting. The ratio of the X-ray intensity after diffraction from the sample to the intensity before diffraction is called the reflectivity. By measuring the reflectivity as a function of the angle between the incident beam and the sample a diffraction curve (called a 'rocking curve') is obtained. A sharp rocking curve is measured for a crystal only when the

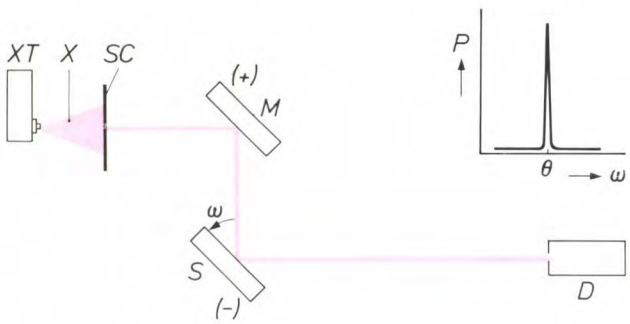

Fig. 1. Schematic arrangement of a double-crystal diffractometer. *XT* X-ray tube with Cu anode. *X* X-ray beam. *SC* slit collimator. *M* monochromator crystal. *S* sample. *D* detector. ω angle between the incident X-ray beam and the sample. By measuring the reflectivity *P* (the intensity of the reflected beam as a percentage of the intensity of the incident beam) as a function of ω, a diffraction curve (rocking curve) is obtained from which the Bragg angle θ can be read.

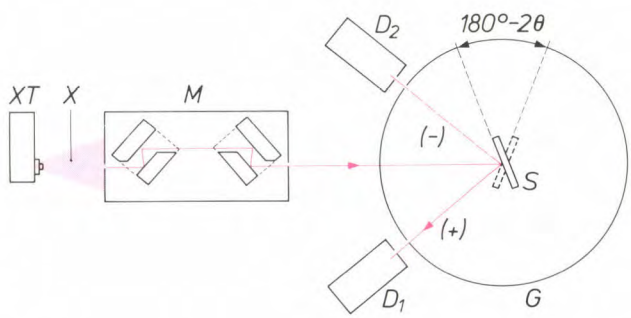

Fig. 2. Schematic arrangement of the high-resolution diffractometer. *M* monochromator with four-fold diffraction on germanium crystals. *G* goniometer carrying the detectors D_1 and D_2 and the sample *S*. The other symbols are as in fig. 1. The two positions of the sample are necessary for measuring absolute lattice constants [3].

[1] W. J. Bartels and W. Nijman, X-ray double-crystal diffractometry of $Ga_{1-x}Al_xAs$ epitaxial layers, J. Cryst. Growth **44**, 518-525, 1978.

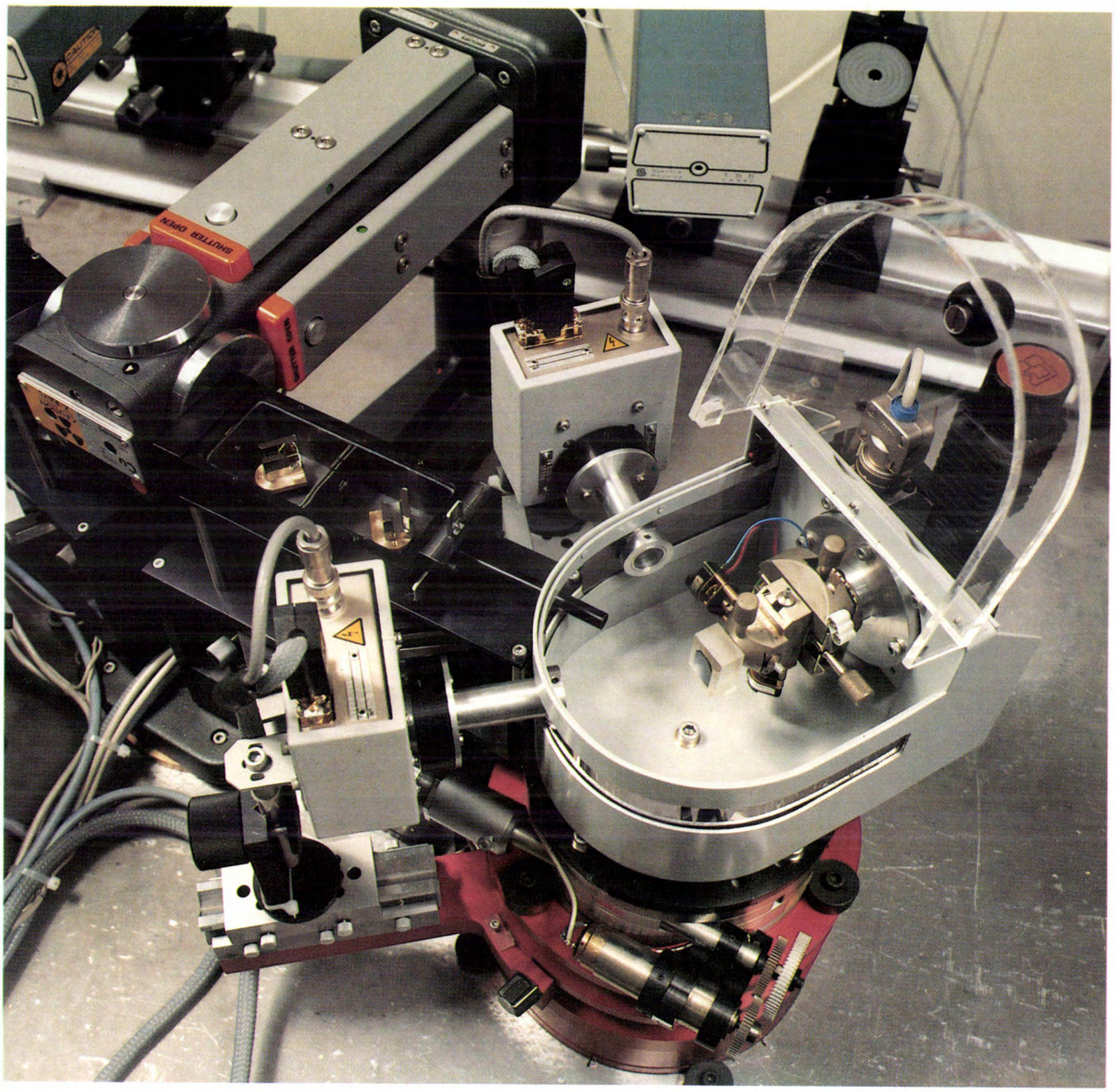

Fig. 3. The high-resolution X-ray diffractometer (see fig. 2). The X-ray tube can be seen at the upper left (grey), with the monochromator on its right (black). The top of the monochromator has been removed to show the germanium crystals. The sample holder and crystal, surrounded by a shield whose transparent cover has been raised, can be seen on the goniometer (red). The two detectors can be seen above the shield and to the left of it.

Bragg angle is exactly the same for both crystals, because only then is this configuration insensitive to a spread in the wavelength of the X-rays [2]. If the diffraction in both crystals is in the same direction (the (+,+) setting), then the configuration is no longer insensitive to such a spread. This results in a very broad rocking curve. Since a measurement for both configurations is necessary to determine the absolute value of the lattice constant [3], the double-crystal diffractometer is not suitable for this purpose. The requirement that the Bragg angle θ of both crystals should be identical is also a serious practical limitation, since it means that a different monochromator crystal is necessary for each material under investigation.

The X-ray diffractometer developed at Philips Research Laboratories has none of the disadvantages mentioned above [4]. The main components of the instrument (see *figs 2* and *3*) are the X-ray tube, the monochromator and a goniometer carrying two detectors and the sample holder with the crystal under investigation. The extremely compact monochroma-

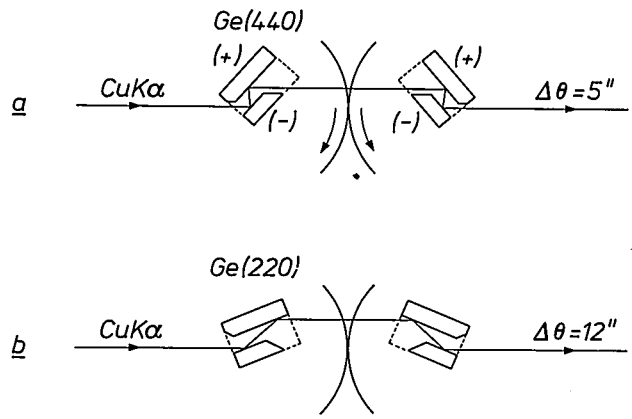

Fig. 4. Tuning the monochromator. *a*) The (440) reflection of the CuKα_1 line has a very small divergence. *b*) By rotating the two crystal blocks it is also possible to use the (220) reflection. This reflection has 30 times the intensity, but greater divergence. The monochromator can be tuned to a different wavelength and hence adapted to an X-ray tube with a different anode.

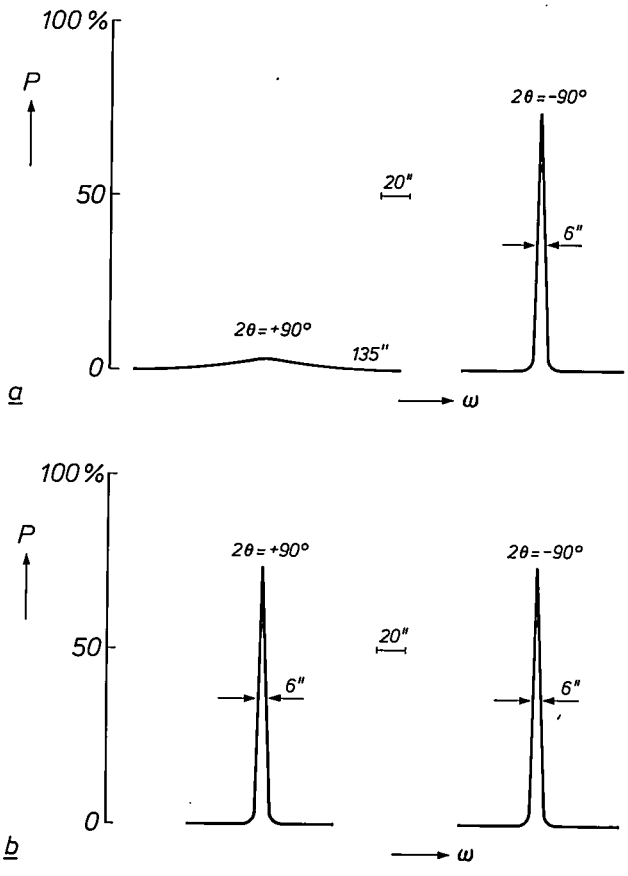

Fig. 5. Diffraction (rocking) curves of [001]-oriented GaAs. *a*) Measurement with a double-crystal diffractometer. As there is one sharp reflection and one broad one, only relative measurements of the lattice constant can be made. *b*) Measurement with the high-resolution diffractometer. There are now two identical sharp reflections, so that absolute measurements can now be made.

tor (about 15 cm long) consists of two U-shaped blocks made from dislocation-free germanium single crystals. The four-fold diffraction at the (440) planes of the germanium crystals results in an X-ray beam with a wavelength spread $\Delta\lambda/\lambda$ of 2.3×10^{-5} and a divergence $\Delta\theta$ of $5'' = 2.4\times10^{-5}$ rad. With this arrangement diffraction measurements can be performed for each lattice plane of any given material in any direction of diffraction, so that absolute measurements of the lattice constant can also be made.

A special feature of the monochromator is the possibility of 'tuning' (*fig. 4*). When the two blocks are rotated in opposite directions, the angle θ changes but the emergent beam does not change in direction or position. This enables the passband of the monochromator to be tuned to the different wavelengths of X-ray tubes with different anode materials.

Another feature is that the intensity of the emergent beam can be increased, although at the expense of the collimation (and hence the resolution). Instead of using the (440) diffraction in the germanium crystals (fig. 4*a*), the diffraction at the (220) planes can also be used (fig. 4*b*). If the (220)-plane diffraction is used, the intensity of the emergent beam is 30 times higher. The divergence, however, then increases from $\Delta\theta = 5''$ for the (440) reflection to $\Delta\theta = 12''$ for the (220) reflection, so that the resolution is rather less.

The improvement which the new diffractometer represents compared with a double-crystal diffractometer is illustrated in *fig. 5*, which shows the rocking curves for a GaAs crystal. Fig. 5*a* was made with a double-crystal diffractometer. The reflection in the (+,+) configuration cannot be used because of its low intensity and excessive width. The new diffractometer, on the other hand, gives two identical reflections (fig. 5*b*), so that an absolute measurement of the lattice constant is possible.

The diffractometer described here has been used for measuring the lattice constants of various crystals on both a relative and an absolute scale [4]. Other applications include the determination of mechanical stresses in epitaxial layers and of the thickness of such layers. It already seems that the instrument will be of great value in improving the processes used for growing single crystals and layered crystal structures.

Ned. Philips Bedrijven B.V.
PHILIPS NATUURKUNDIG LAB
BIBLIOTHEEK WY - 1
P.O. Box 80.000
5600 JA EINDHOVEN
NEDERLAND

W. J. Bartels

[2] See for example L. V. Azároff (ed.), X-ray spectroscopy, McGraw-Hill, New York 1974, p. 67.
[3] W. L. Bond, Precision lattice constant determination, Acta Crystallogr. **13**, 814-818, 1960.
[4] W. J. Bartels, Characterization of thin layers on perfect crystals with a multipurpose high resolution x-ray diffractometer, J. Vac. Sci. & Technol. B **1**, 338-345, 1983.

Drs W. J. Bartels is with Philips Research Laboratories, Eindhoven.

Philips Tech. Rev. 41, 186-197, 1983/84, No. 6

Applying low-friction wear-resistant thin solid films by physical vapour deposition

H. Dimigen and H. Hübsch

The techniques of applying thin solid films to substrates have made great advantages owing mainly to their many applications in IC technology. In recent years this has also led to a marked growth of interest in thin films that have a beneficial effect on mechanical properties such as friction and wear. Thin solid films of this type are the subject of extensive investigations at Philips GmbH Forschungslaboratorium Hamburg, where the films are applied to the substrates mainly by means of physical processes in the vapour phase, referred to as PVD (physical vapour deposition).

Introduction

For covering tools of various kinds a growing need has arisen in recent times for thin solid films possessing special mechanical properties. This is partly because of the increasing scarcity and expense of many raw materials, and partly because the use of such films makes it possible to optimize the surface properties of tools and their other properties independently of each other.

An important area of applications is the dry lubrication of moving parts under conditions where fluid lubrication is beset with difficulties, e.g. at high and low pressures, high and low temperatures and slow oscillations. For this dry lubrication the bearing surfaces are coated with a thin low-friction film. During operation this film must retain its good lubricating properties as long as possible, since the bearing cannot usually be lubricated again later. Some metals and alloys can be used for dry lubrication, but the materials that seem most suitable are certain chalcogenides. The one that has been most extensively studied is molybdenum sulphide [1]. Other suitable materials include oxides, fluorides and fluorinated hydrocarbons [2].

Another interesting application is the coating of tools to reduce surface wear, which can be a problem in metal-cutting operations. In this application the thin solid films have to be hard and wear-resistant. Materials of interest here include various carbides, nitrides, oxides and alloys [2], as well as diamond-like carbon [3] and mixtures of metal and carbon [4]. These materials cannot usually be used for the entire tool, mainly because they may be too brittle or too hard. However, they are very useful for improving the surface properties of tools.

The application of thin solid films possessing the required properties imposes its own special requirements on working procedures and materials. Precise control of the growth rate of a film is essential during the application. Depending on the application and the materials, it will be necessary to produce final film thicknesses from 0.1 to 10 μm. The substrate to be coated must be able to stand up to high temperatures during the application. To give a long useful life the film must adhere well to the substrate. It must also be possible to coat uneven surfaces uniformly.

There are various methods that can be used for applying thin solid films. One of them, 'chemical vapour deposition' (CVD), is particularly suited for applying wear-resistant films of materials like titanium carbide or titanium nitride on tool steel, as described earlier in this journal [5]. This method is preferred when the substrates to be coated are unaffected by high temperatures and very hard coatings with maximum adhesion are required. For coating substrates that cannot stand up to high temperatures, however, and to obtain thin films possessing good lubricating proper-

Dr H. Dimigen and H. Hübsch are with Philips GmbH Forschungslaboratorium Hamburg, Hamburg, West Germany.

ties, preference is given to other methods such as vacuum evaporation, sputtering and plasma deposition. These methods, in which physical processes in the vapour phase play a dominant role, are referred to as physical vapour deposition (PVD).

In the work described in this article we are mainly concerned with the application of low-friction, wear-resistant films by PVD. We have used various materials and PVD methods. The influence of the deposition conditions on the properties of the films is one of our subjects of investigation. We are also looking at the life of the films under different conditions of use. Some potential applications are also being investigated in cooperation with other groups.

We shall begin with a brief description of a number of PVD methods. Next, we shall deal with the results obtained with thin films of molybdenum sulphide, diamond-like carbon and metal-carbon films. Finally, we shall discuss some possible applications.

PVD methods

A simple and widely used method of coating substrates with a thin film is deposition by vacuum evaporation. This method is not so suitable, however, for the deposition of thin low-friction films. This is mainly because the adhesion is often inadequate, since the condensing particles, which have an average energy of only 0.01 to 0.1 eV, strike the substrate surface at too low a velocity. Developments aimed at improving the adhesion have led to the method known as 'ion plating' [6]. In this method argon is admitted into a vacuum chamber at a pressure of about 1 Pa and a high-voltage source is connected to the substrate holder; see *fig. 1a*. A gas discharge is set up in the vacuum chamber, so that some of the evaporated material is given a positive charge. Owing to the strongly negative substrate potential the positive particles formed land on the substrate at high velocity. In comparison with ordinary vacuum evaporation this process gives both better adhesion and a more uniform coating of non-flat substrates.

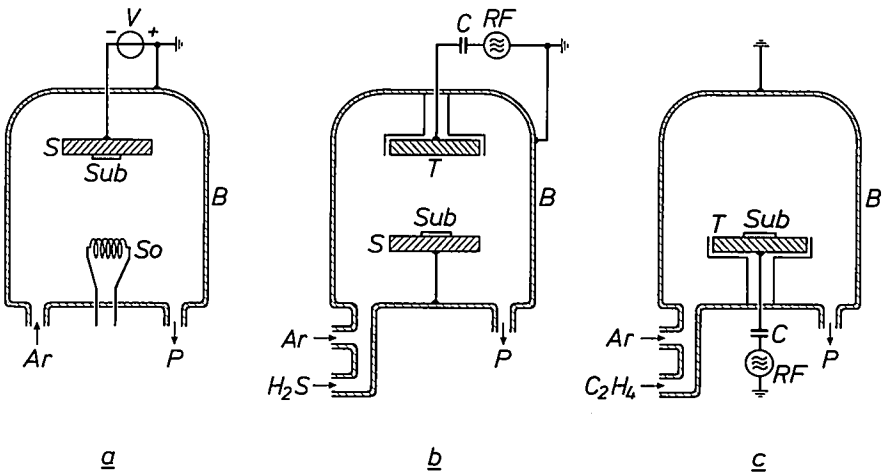

Fig. 1. Diagram showing the configurations for three PVD methods. *a) Ion plating.* Argon is admitted into the vacuum chamber *B* connected to the vacuum pump *P*, at a pressure of about 1 Pa and the material for the film to be deposited on the substrate *Sub* is evaporated by heating the source *So*. Since the substrate holder *S* is connected to the negative pole of a high-voltage source *V*, a gas discharge is produced in the vacuum chamber and the resultant positive particles of the evaporated material land on the substrate at high velocity. *b) Sputtering.* Here again the vacuum chamber contains argon at a pressure of about 1 Pa; the target *T* is connected via a capacitor *C* to a radio-frequency high-voltage source *RF*. In the resulting gas discharge the target acquires a negative potential, so that it is bombarded by the positive argon ions. The particles sputtered from the target settle on the substrate. The properties of the film deposited can often be improved by applying a negative potential to the substrate from a direct-voltage source. In addition the sputtered particles can first be allowed to react with a reactive gas, e.g. hydrogen sulphide (H_2S). *c) Plasma deposition.* In the vacuum chamber here the substrate is attached to a target connected to a radio-frequency high-voltage source. The vacuum chamber contains a mixture of argon and a reactive gas that provides the material for deposition, e.g. ethene (C_2H_4) to produce carbon films.

[1] See for example F. J. Clauss, Solid lubricants and self-lubricating solids, Academic Press, London 1972.
[2] A survey of suitable materials for low-friction and wear-resistant thin solid films is given by H. Dimigen and H. Hübsch in: Philips — Unsere Forschung in Deutschland, Vol. III, 256-261, 1980 (in German).
[3] K. Enke, H. Dimigen and H. Hübsch, Appl. Phys. Lett. **36**, 291-292, 1980.
[4] H. Dimigen and H. Hübsch, T.H. Darmstadt Schriftenreihe Wiss. & Tech. **20**, 257, 1983 (in German).
[5] P. J. M. van der Straten and G. Verspui, Philips Tech. Rev. **40**, 204-210, 1982.
[6] See for example D. M. Mattox, J. Vac. Sci. & Technol. **10**, 47-52, 1973.

Another method of applying thin low-friction films is sputtering. In this method argon is admitted into a vacuum chamber at a pressure of about 1 Pa and a radio-frequency high-voltage source is connected to a target; see fig. 1*b*. A gas discharge forms between the target and a substrate holder electrically connected to the vacuum chamber. Since electrons are more mobile than ions and since the target has a much smaller area than the combination of substrate holder and vacuum chamber, the substrate holder has about the same potential as the plasma, while the target acquires a much lower potential [7]. The positive argon ions produced in the discharge therefore strike the target with so much energy that they knock particles out of it. These particles then settle on the substrate to form a thin coating.

The use of high-energy ions makes sputtering a versatile method that can be used for coating all kinds of substrates with a wide variety of materials. Since the target is cooled during the sputtering there is no diffusion in it, so that targets made of alloys and chemical compounds can be sputtered virtually quantitatively. Some non-conducting targets can also be sputtered satisfactorily. The scope of the method can be widened by admitting a reactive gas during the sputtering. For example molybdenum-sulphide films can be deposited by sputtering with a molybdenum-disulphide (MoS_2) target in an argon atmosphere, and also by reactive sputtering with a molybdenum target in an atmosphere containing hydrogen sulphide. There are only few restrictions on the substrates that can be coated. During the deposition the substrate temperature is relatively low, between 100 and 300 °C. Substrates that are not completely flat can also be coated fairly uniformly, but for coating workpieces of complicated shape the uniformity that can be achieved is definitely less than with the CVD method [5]. To increase the uniformity the substrate is often given a negative potential, so that local protrusions can be etched away by the positive argon ions landing on them. A negative substrate potential also helps to improve the adhesion.

Depending on the process conditions and the materials, the deposition rate from sputtering can be varied between 0.005 and 0.5 μm/min. With magnetron sputtering [8] a deposition rate as high as 2.5 μm/min can be achieved. The various properties of the deposited films depend on a large number of parameters. Finding the optimum process conditions for a particular application therefore usually requires an extensive series of experiments to determine the effect of the different parameters.

A useful method for applying thin carbon films is plasma deposition [9]. In this method a plasma is generated in an argon-filled vacuum chamber by connecting a radio-frequency voltage source to a target carrying the substrate to be coated (fig. 1*c*). A gaseous hydrocarbon such as ethene (C_2H_4) or ethyne (C_2H_2) is added to the plasma. The ions in the plasma cause the hydrocarbon to break down and the carbon formed settles in the form of a thin film on the substrate. In this way carbon films with a thickness of 0.1 to 2.5 μm can be applied to substrates such as silicon, aluminium oxide, glass and steel. The properties of the films depend closely on the potential and the gas composition during the plasma deposition.

PVD methods are already applied in many different fields, and it seems highly likely that these methods will be very useful for applying low-friction wear-resistant films. The particular PVD method to be chosen for a particular application will depend on the workpiece to be coated, the material to be deposited and the properties required. In mass production the price will also be important. Careful consideration will have to be given to the cost of the equipment and materials required, and also to the deposition rate and the size and shape of the workpiece surfaces to be coated.

Molybdenum-sulphide films by sputtering

The production of molybdenum-sulphide films by cathode sputtering has already been extensively described in the literature. Until recently, however, little

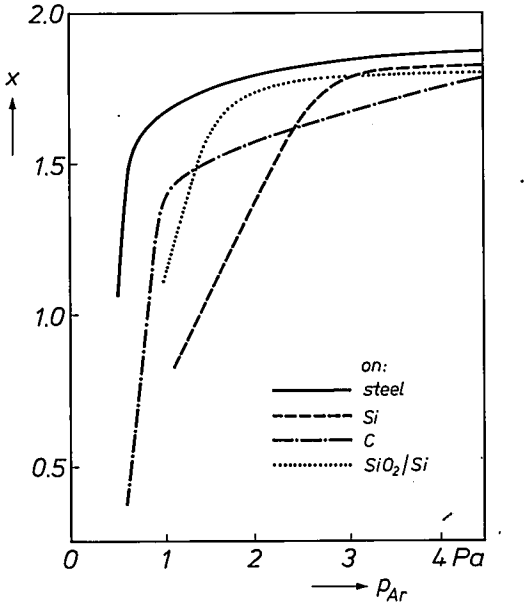

Fig. 2. Sulphur content x of MoS_x films as a function of the argon pressure p_{Ar} during sputtering with an MoS_2 target and different substrates. Increasing the argon pressure leads to an increase in the sulphur content, which depends on the substrate. At all argon pressures the films deposited on steel have the highest sulphur content. All the films have a sulphur deficit in relation to the composition MoS_2; the deficit is very considerable at low argon pressures.

was known about the effects of process conditions on the composition of the films or about the resultant effects on properties such as friction and wear. To gain a better understanding of these matters we have performed experiments in which various molybdenum-sulphide films were deposited under different conditions, and the composition of the films was then determined, usually by X-ray-fluorescence analysis [10]. In these experiments we paid particular attention to the influence of the gas composition and substrate temperature, and of the material and potential of the substrate. We applied the films with a molybdenum-disulphide target and also with a molybdenum target in an atmosphere of argon and hydrogen sulphide. During the sputtering the target potential was 1.5 kV, the residual gas pressure in the vacuum chamber was about 5×10^{-4} Pa and the distance between target and substrate was about 50 mm.

Films deposited by sputtering in an argon atmosphere with an MoS_2 target almost invariably contain less sulphur than would be expected from this composition. The magnitude of the deficit depends on the substrate material and increases rapidly as the argon pressure is decreased; see *fig. 2*. The sulphur deficit is caused by 'resputtering', an effect in which more sulphur than molybdenum is sputtered away from the growing film because of the weaker bonds between the sulphur atoms and the substrate [11]. The resputtering occurs because some of the argon ions are neutralized during the bombardment of the target and the reflected argon atoms then settle on the substrate. On the way to the substrate they collide repeatedly with other argon atoms, losing some of their energy at every collision. When the argon pressure is low the number of collisions is small, so that the argon atoms can land on the substrate with a high energy. This leads to strong resputtering and hence to a considerable sulphur deficit and a low growth rate.

The composition of molybdenum-sulphide films depends not only on the substrate material and the argon pressure but also on the potential and the temperature of the substrate. The use of a negative substrate potential considerably reduces the sulphur content and the growth rate. This is the result of increased resputtering, because high-energy positive argon ions can now land on the substrate as well. An increase in the substrate temperature from say 150 to 300 °C has the effect of increasing the sulphur content, particularly at low argon pressures. Less resputtering then takes place, probably because the sulphur atoms are more strongly bound to the molybdenum and substrate atoms. The results obtained show that reproducible deposition depends on good control of the process conditions. They also show that for sputtering with an MoS_2 target in an argon atmosphere the composition of the deposited film can come closest to MoS_2 when the substrate is made of steel.

Reactive sputtering by the addition of H_2S gas generally gives films of higher sulphur content. In *fig. 3* the composition of films deposited on steel and on silicon is plotted against the H_2S pressure during reactive sputtering with a molybdenum or molybdenum-disulphide target. As might be expected, with the molybdenum target the effect of the H_2S pressure is greater than with the MoS_2 target. When the H_2S pressure is

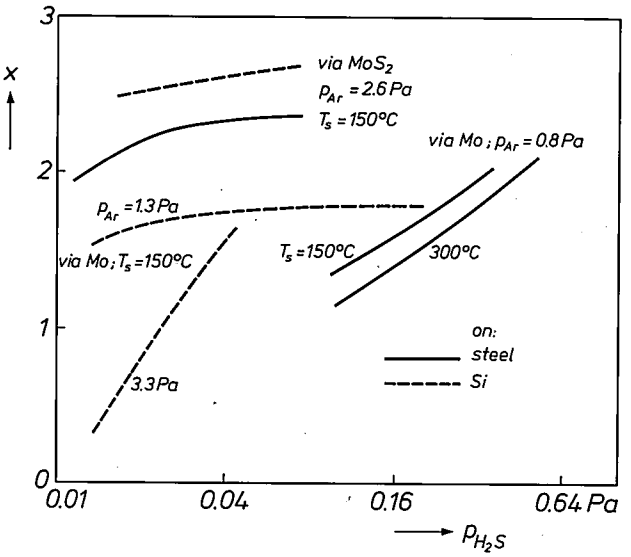

Fig. 3. Sulphur content x of MoS_x films as a function of the H_2S pressure p_{H_2S} (logarithmic scale) during reactive sputtering of a molybdenum target and a molybdenum-sulphide target on substrates of steel and silicon. The increase in the sulphur content at higher H_2S pressures depends on the target material, the argon pressure p_{Ar}, the substrate and the substrate temperature T_s.

low an increase in the argon pressure leads to films of lower sulphur content. Evidently the increased molybdenum sputtering has a greater effect on the composition than the reduction in the resputtering mentioned earlier. Even when the substrate temperature is increased, the reduction in the resputtering is of minor significance in view of the reduced sulphur content in the films. Reactive sputtering with a molybdenum target has not yet resulted in films with the composition MoS_2 or with an excess of sulphur. In reactive sputtering with a molybdenum-sulphide target, on the

[7] H. Dimigen and H. Lüthje, Philips Tech. Rev. 35, 199-208, 1975.
[8] J. J. Scheer and J. Visser, Philips Tech. Rev. 39, 246-255, 1980.
[9] An extensive list of references is given by K. Enke, Thin Solid Films 80, 227-234, 1981.
[10] M. L. Verheijke and A. W. Witmer, Philips Tech. Rev. 34, 339-343, 1974.
[11] W. R. Gesang, H. Oechsner and H. Schoof, Nucl. Instrum. & Methods 132, 687-693, 1976.

other hand, even a low H_2S pressure may be sufficient for the deposition of films with an excess of sulphur.

To measure the friction and wear of the films we use the 'pin-on-disc' method, which is illustrated in the diagram of *fig. 4a*. The substrate, in the form of a steel disc and coated with the film, rotates with a vertical shaft. A steel ball, fixed to a balance arm, is pressed against the rotating substrate with a force F_1. The resultant friction exerts a force F_2 on this arm in the sense of rotation of the substrate, and this force is measured with a transducer. The coefficient of friction μ is defined as the ratio F_2/F_1. Fig. 4*b* shows a photograph of a test arrangement frequently used. We have incorporated a similar arrangement in a high-vacuum system, in which measurements can be performed in the pressure range down to 10^{-7} Pa. The wear of a film is determined by means of life tests made in the configuration shown. The end of the life of the film shows as a sudden marked increase in the coefficient of friction. The number of substrate rotations made before failure is taken as a measure of the film life.

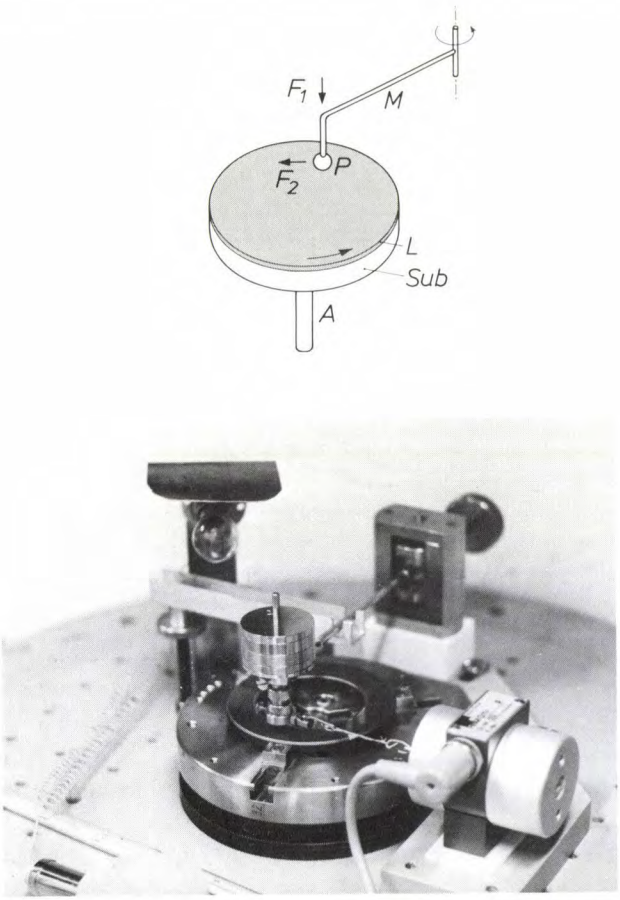

Fig. 4. *Above:* Diagram of the arrangement for friction measurements by the 'pin-on-disc' method. A substrate *Sub* with a diameter of about 75 mm, on which a film *L* has been deposited, rotates about a shaft *A*. Pressing on the substrate with a force F_1 (usually about 5 N) is a steel ball *P* of about 4 mm diameter, attached to a balance arm *M*. During the test a force F_2 acts on this pin; the force is measured by a force transducer. The coefficient of friction is defined as F_2/F_1. *Below:* Photograph of a widely used experimental arrangement for friction and wear measurements.

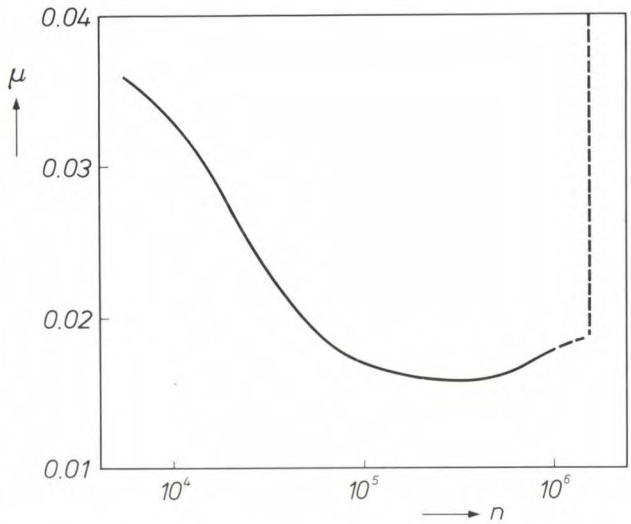

Fig. 5. Coefficient of friction μ for a film of composition $MoS_{1.7}$ sliding on steel, as a function of the number of rotations n in dry nitrogen with a load of about 5 N. After an initial period with a gradual fall, the coefficient of friction remains virtually constant for many rotations. Wear then begins to occur, so that the coefficient of friction first increases gradually, then suddenly rises very sharply.

The coefficient of friction for a molybdenum-sulphide film sliding on steel depends on the number of rotations already completed. An example is shown in *fig. 5*. During an initial period the coefficient of friction first gradually decreases. To some extent this is connected with an increasing orientation of the crystallites in the film, which tend to align themselves parallel to the surface [12]. We have found from experiments in high vacuum, however, that the reduced friction is mainly caused by strong desorption of water vapour. When most of the water vapour has disappeared from the film, the coefficient of friction is found to have a very low value. This remains unchanged for a large number of rotations. At the end of film life the coefficient of friction slowly rises again; this is an indication of incipient wear. Finally, at about 1.6×10^6 rotations, there is an abrupt and very marked increase of at least a factor of 10; the film has then become useless.

The coefficient of friction for molybdenum-sulphide films sliding on steel is closely dependent on the composition; see *fig. 6*. The smallest coefficient of friction (< 0.02) is obtained when the composition is approximately $MoS_{1.5}$. When the sulphur content is reduced further the friction remains fairly low. It only increases significantly (to about 0.5) at a composition of $MoS_{0.8}$.

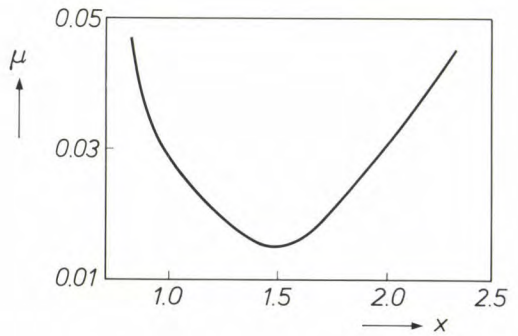

Fig. 6. Coefficient for friction μ of MoS_x films sliding on steel at a rate of rotation of 2500 min^{-1} and a load of about 5 N, as a function of x. The lowest value for the coefficient of friction is found when x is about 1.5. The very marked increase in μ (up to about 0.5) at $x \approx 0.8$ is not shown.

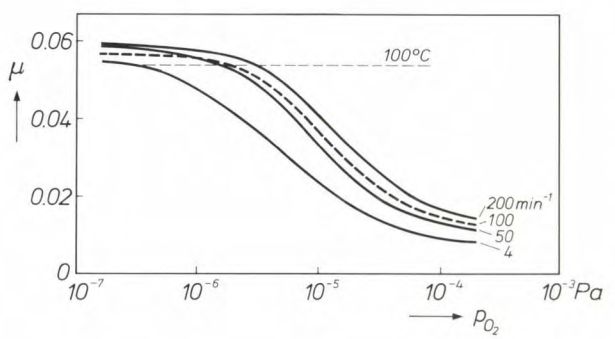

Fig. 7. Coefficient of friction μ for a film of composition $MoS_{1.44}$ sliding on steel, as a function of the oxygen partial pressure p_{O_2} with a load of about 5 N and at different rates of rotation. An increase in the oxygen partial pressure has the effect of reducing the coefficient of friction, the reduction becomes greater as the rate of rotation decreases. At 100 °C the coefficient of friction is almost independent of the oxygen pressure.

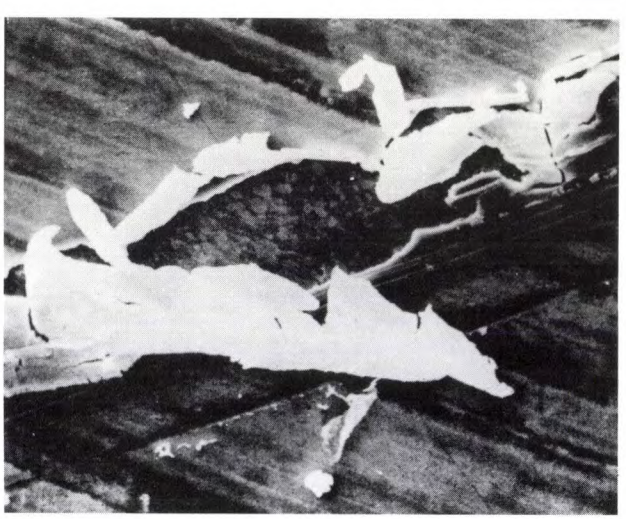

Fig. 8. Photograph of a poorly adhering molybdenum-sulphide film that has started to break away from the steel substrate after a scratch.

In general the results of the measurements in high vacuum are comparable with those in dry nitrogen. With a film deficient in sulphur a low oxygen partial pressure of say 10^{-4} Pa gives a considerable reduction in the friction. This reduction can be attributed to the adsorption of oxygen by the unsaturated bonds in the film, and this is confirmed by measurements of the pressure dependence at different rates of rotation; see *fig. 7*. The pressure at which the coefficient of friction begins to fall decreases as the rate of rotation decreases. At the lowest rate (4 min^{-1}) the probability of adsorption is greatest, so that even with an oxygen partial pressure of only 2×10^{-7} Pa there the friction coefficient has begun to fall. At a temperature of 100 °C, however, no decrease is observed; evidently there is no oxygen adsorption at this temperature.

Life tests in dry nitrogen and high vacuum show that the life of a film is proportional to its thickness. This indicates 'normal' wear, with the film being gradually worn away by contact with the pin (fig. 4). Usually, however, this wear is not the main cause of the end of film life. The life of a film is in fact found to depend strongly on the temperatures during the deposition of the film and the life test. The effect seems to be related to stresses between the film and the substrate. We have deduced from this that the adhesion to the substrate largely determines the life of a film. An indication of the quality of the adhesion can be obtained by making a scratch on the film. If the adhesion is insufficient part of the film will break away from the substrate; see *fig. 8*. The adhesion may often be improved by taking some precautionary measures, such as a special pretreatment for the substrate or the use of a bonding layer.

The measurements showed that molybdenum-sulphide films are suitable for lubrication both in dry nitrogen and in high vacuum. The coefficient of friction between the film and steel can be less than 0.02 and a life of about 3×10^6 rotations can be reached. In a humid atmosphere the properties of molybdenum-sulphide films are less satisfactory. Higher humidity leads to more friction and a shorter life. The effect of humidity decreases with the sulphur content of a film. At a relative humidity of say 80% the longest life (for $MoS_{2.3}$) is about 10^4 rotations, while the coefficient of friction is about 0.14.

Because of the less satisfactory properties of molybdenum sulphide in humid conditions we tried to find other materials that do have good friction and wear properties in a humid atmosphere. This led us to an investigation of films containing carbon.

[12] T. Spalvins, Thin Solid Films **73**, 291-297, 1980.

Plasma deposition of diamond-like carbon

The properties of carbon films produced by plasma deposition are closely dependent on the partial pressure of the hydrocarbon used (e.g. ethene) and on the potential of the target during deposition [13]. Hardness measurements on the films thus obtained show that there are three different existence regions; see *fig. 9*. At low target potentials ($\lesssim$100 V) soft polymeric films are produced that are transparent and electrically insulating. At high potentials ($\gtrsim$1000 V) hard graphitic films are obtained that are opaque and weakly conductive. In the intermediate regions hard diamond-like films are obtained. These are slightly transparent and electrically insulating.

The carbon films deposited have a compressive stress that is again closely dependent on the ethene pressure and the target potential. *Fig. 10* shows some schematized lines of equal compressive stress, derived from a large number of measured results. Relatively high compressive-stress values are observed in the diamond-like region. For this reason diamond-like carbon films thicker than 1 μm have a tendency to break away from the substrate. Relatively low values are obtained with polymeric films deposited at high ethene pressure and low target potential, and with graphitic films deposited at a low ethene pressure and high target potential. The low compressive stress usually found in polymeric films is not so surprising in view of their softness. The lower compressive stress of graphitic films compared to that of diamond-like films is probably connected with a reduced incorporation of the hydrogen contained in the plasma [13].

Films of diamond-like carbon have good lubricating properties. Because of the combination of high hardness and low coefficient of friction they show little wear. In some cases a life of more than 4×10^6 rotations can be reached. The coefficient of friction for diamond-like carbon sliding on steel is strongly dependent on the relative humidity in the test atmosphere; see *fig. 11*. Up to a humidity of about one per cent very low values (0.01 to 0.02) are found. Above one per cent there is noticeably more friction. At a humidity of nearly 100% the coefficient of friction has risen to about 0.2. This friction behaviour is the opposite of that in graphitic films, which have high friction and pronounced wear at low humidity. The friction between diamond-like carbon films and diamond or between two diamond-like carbon films is less sensitive to humidity than the friction between diamond-like carbon film and steel. In both dry and humid atmospheres the coefficient of friction is less than 0.05.

The wear of diamond-like carbon films is only partly connected with an increase in the coefficient of friction. Whereas the coefficient of friction for a dia-

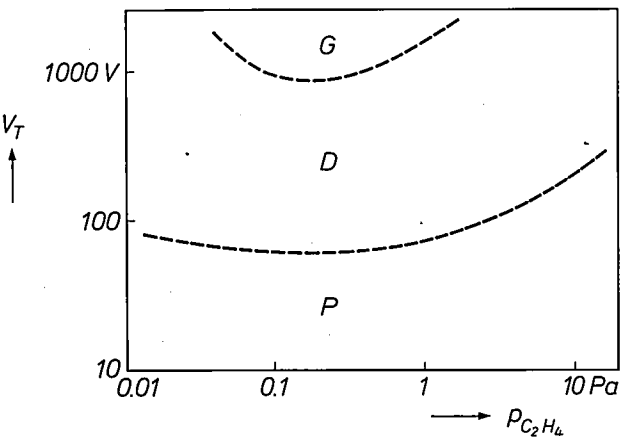

Fig. 9. Existence regions (schematic) of three modifications of carbon film, as a function of the ethene pressure $p_{C_2H_4}$ and the target potential V_T during plasma deposition. The dashed lines indicate the transitions between the regions where the carbon films are polymeric (*P*), diamond-like (*D*) and graphitic (*G*).

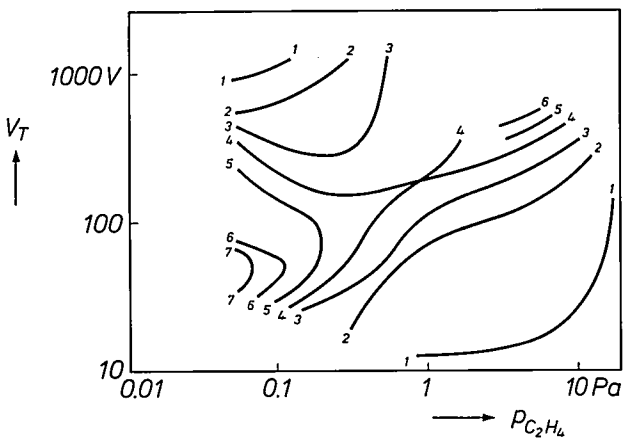

Fig. 10. Lines of equal compressive stress (schematic, in 10^9 N/m^2) in carbon films, as a function of the ethene pressure $p_{C_2H_4}$ and the target potential V_T during plasma deposition.

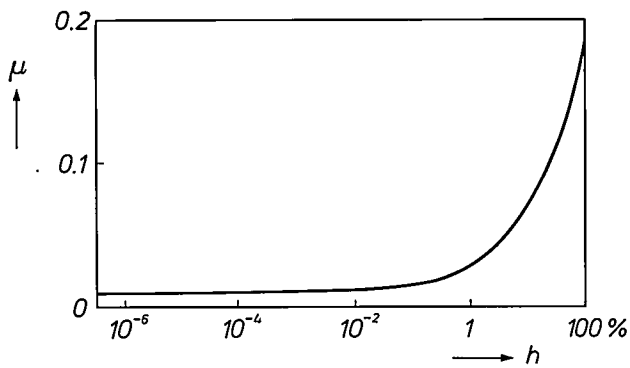

Fig. 11. Coefficient of friction μ for a diamond-like carbon film sliding on steel, as a function of the relative humidity *h*. Up to about one per cent humidity the coefficient of friction is very small; there is a marked increase when the humidity becomes greater.

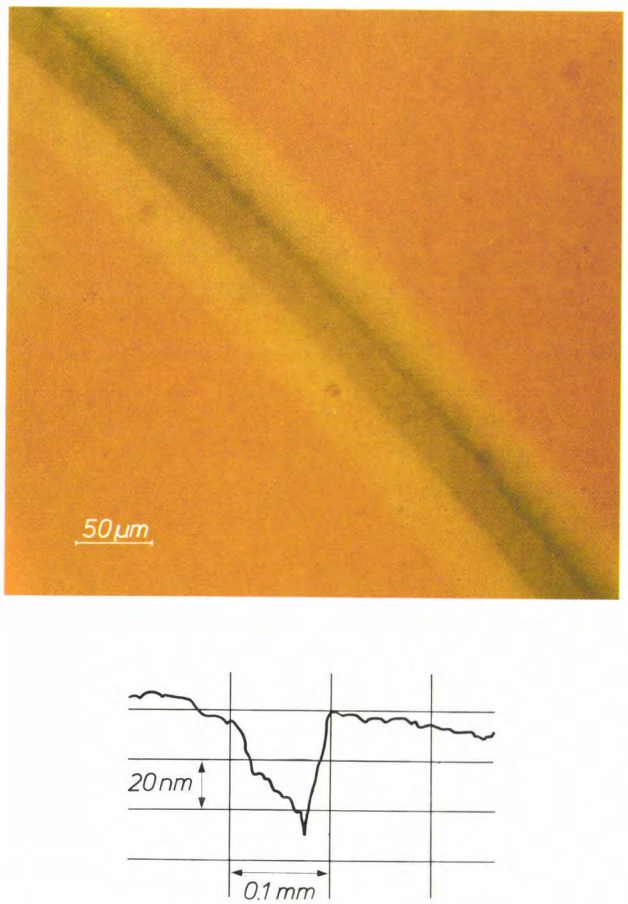

Fig. 12. Wear of a diamond-like carbon film due to sliding friction with a steel ball. *Above:* Photomicrograph of an indentation track after 10% of film life. *Below:* Height profile of the track.

mond-like carbon film sliding on steel rises monotonically with increasing humidity (fig. 11), maximum life is reached at a relative humidity of about 0.5%. The life of the film is virtually independent of the rate of rotation. As the load is increased, the life decreases sharply, since the film is more quickly destroyed by friction or breaks away from the substrate. Life is also adversely affected by surface roughness of the coated substrate. The film covering the higher parts of a rough steel surface may be prematurely rubbed away by a steel pin, so that high friction between steel and steel can arise. To counteract this effect the film should be appreciably thicker than 0.3 μm. In view of the high compressive stress in thicker films a film thickness of 0.5 μm is usually a good compromise.

As with molybdenum-sulphide films, the wear may be caused by gradual erosion of the film due to contact with the other frictional surface, and by the film breaking away from the substrate when the adhesion is insufficient to resist the forces that arise. To determine which of these two effects is more important, we interrupted the life-test experiments at different times to take photomicrographs and determine the height profile in the film. This revealed that the behaviour of a diamond-like carbon film is entirely different from that of a molybdenum-sulphide film: provided the load is not unduly high, the wear is mainly caused by the film being locally rubbed away. Early signs of this are found right at the start, when the pin only touches a very small part of the film and therefore produces a high local pressure. This becomes less as soon as the pin has rubbed away part of the surface. *Fig. 12* shows a photomicrograph and a height profile of a small indentation after 10% of film life. After about 30% of the life of the film the wear increases sharply because of the grinding action of the resulting carbon walls. Until about 90% of life has been reached the film shows no tendency to break away from the substrate.

The good wear characteristics of diamond-like carbon films can be seen from plots of the rate of wear at different contact pressures. We obtained these results by measuring the loss in thickness of the ball and the contact path travelled at various times during the friction experiments (fig. 4), at the prevailing contact pressure; the ratio of thickness loss to the path length is regarded as the rate of wear. In *fig. 13* the rate of

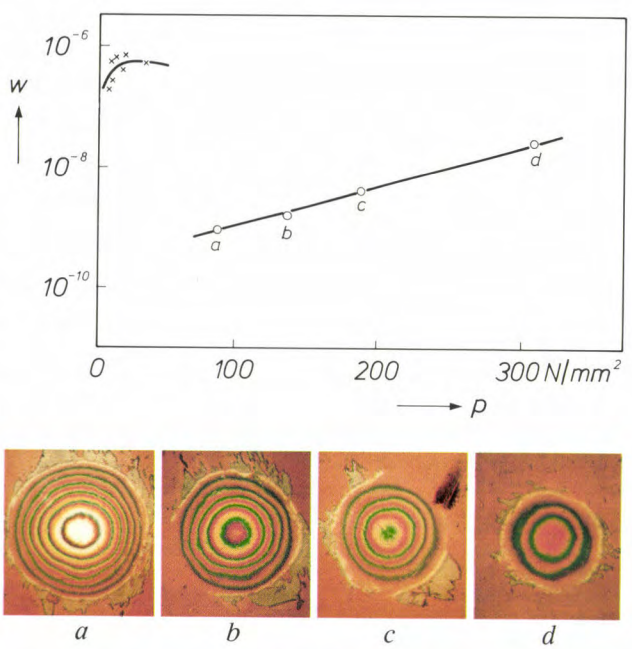

Fig. 13. *Above:* Rate of wear w — defined as the ratio of the thickness reduction to the pathlength — as a function of the contact pressure p, for the friction between a steel ball and a steel substrate, both coated with a diamond-like carbon film (*circles*) and both uncoated (*crosses*). The coating with a diamond-like carbon gives a considerable reduction in the rate of wear. *Below:* Interference fringes at the surface of the coated ball at different stages of the wear experiment. The patterns correspond to the four measured points indicated by circles (pattern *a* with circle *a*, etc.). An increase in the number of interference fringes indicates increasing wear, corresponding to a reduction in the contact pressure.

[13] See the article by K. Enke listed in [9].

wear determined at different times is plotted against the contact pressure, for the friction between a steel pin and a steel substrate, both with no coating and both with a coating of a diamond-like carbon film. With no coating the rate of wear is very high and can only be determined at low contact pressures. With a coating the rate of wear is considerably lower. For the coated surfaces the wear of the pin has been pictorially represented in the form of interference fringes that correspond to the four measured points. Greater wear, accompanied by a lowering of the contact pressure, appears as an increase in the number of interference fringes.

To summarize, therefore, diamond-like carbon films of thickness up to about 0.5 μm can readily be applied by plasma deposition; the films adhere firmly to the substrate and have great hardness and a low coefficient of friction. On a polished substrate they offer good protection against wear for moderately high loads and temperatures.

Metal-carbon films produced by sputtering

The favourable experience with diamond-like carbon films prompted us to investigate the possibilities of metal-carbon films. These films can be deposited on a steel substrate, for example, by reactive sputtering with a metal target in an argon-hydrocarbon atmosphere or by non-reactive sputtering with a metal-carbon target in an argon atmosphere. A great advantage of reactive sputtering is that after some initial ion etching of the substrate pure metal can be deposited on it, followed by metal-carbon in stages. This procedure results in very good adhesion to the substrate. In friction and life-test experiments we found no tendency for the films to break away from the substrate. Metal-carbon films deposited by non-reactive sputtering, on the other hand, have poor adhesion on a steel substrate.

Metal-carbon films with a metal content of less than 50% have a low coefficient of friction. *Fig. 14* shows the coefficient of friction for iron-carbon films sliding on steel and for tungsten-carbon films on steel at a relative humidity of about 40%, as a function of the metal content in the films. Below 50 at.% of metal the coefficient of friction depends very little on the composition. In this range the films have a hardness of 1500 to 2500 kg/mm^2. At high metal contents the coefficient of friction increases sharply from about 0.15 to 0.4.

As well as depending on the composition the coefficient of friction also depends to a great extent on the load and the other friction surface. *Fig. 15* shows the coefficient of friction for four combinations of materials at a relative humidity of about 40%, plotted against the contact pressure. There are marked differences in behaviour, especially at low contact pressures. Low values are found for the coefficient of friction at contact pressures higher than 1000 N/mm^2. Efforts are currently being made to find combinations of metal-carbon films that also have a small coefficient of friction at low loads.

Whereas with molybdenum-sulphide films and diamond-like carbon films the coefficient of friction always rises steeply with increasing humidity, the dependence of the friction coefficient of metal-carbon films on humidity is largely determined by the composition of the films. An example is shown in *fig. 16* for iron-carbon films. The coefficient of friction of a film

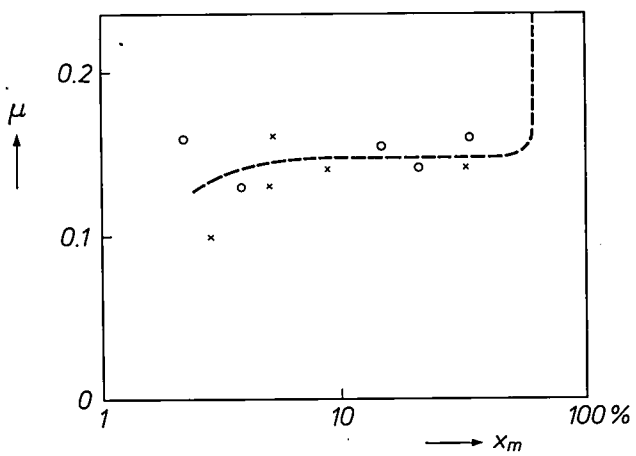

Fig. 14. Coefficient of friction μ for iron-carbon films sliding on steel (*circles*) and for tungsten-carbon films on steel (*crosses*) as a function of the metal content x_m at a relative humidity of about 40% and a load of about 3.5 N. Up to a content of roughly 50% the coefficient of friction is virtually constant; above 50% there is a marked increase.

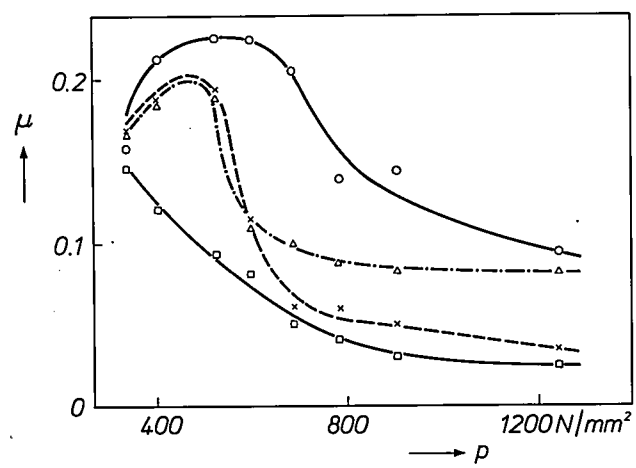

Fig. 15. Coefficient of friction μ as a function of contact pressure p at a relative humidity of about 40%, for the combinations $Ta_{32}C_{65}$-steel (*circles*), $Ru_{18}C_{81}$-steel (*crosses*), $Ta_{0.1}C_{95}$-steel (*triangles*) and $Ta_{0.1}C_{95}$-$Ru_{18}C_{81}$ (*squares*). The variation in the coefficient of friction differs considerably for the four combinations. The lowest values are found at high contact pressures.

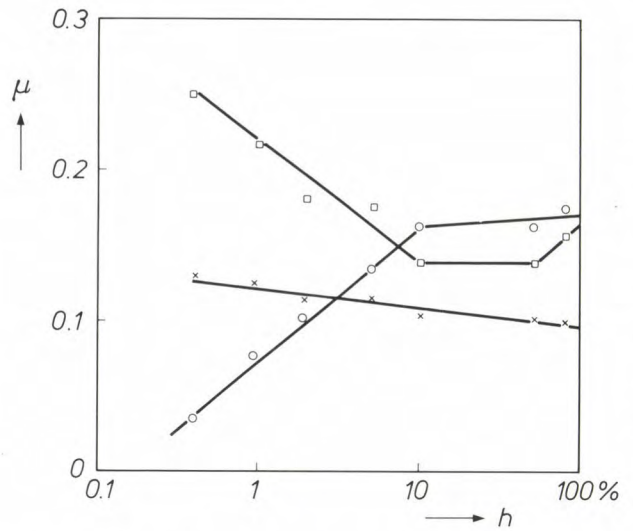

Fig. 16. Coefficient of friction μ for three iron-carbon films sliding on steel with a load of about 3.5 N, as a function of the relative humidity h. With increasing humidity, the friction coefficient for $Fe_{2.3}C_{93}$ (*circles*) increases sharply and the coefficient for $Fe_{15}C_{78}$ (*squares*) decreases sharply, whereas there is little variation for $Fe_{4.1}C_{84}$ (*crosses*).

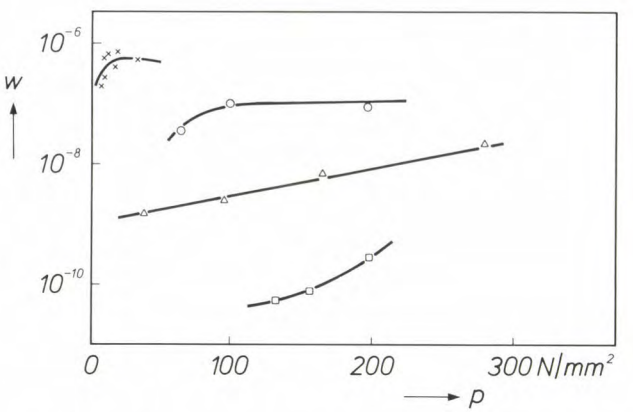

Fig. 17. Rate of wear w as a function of contact pressure p for the friction between a pin and a substrate (see fig. 13). With a steel substrate a solid tungsten-carbon pin of composition $W_{50}C_{50}$ (*circles*) gives a much lower rate of wear than a steel pin (*crosses*). Even lower rates of wear are obtained if the steel of the substrate and that of the pin are coated with $W_{2.8}C_{96}$ (*triangles*). Very low rates of wear are obtained when the substrate is coated with $Ta_{0.1}C_{95}$ and the pin with $W_{2.8}C_{96}$ (*squares*).

with the composition $Fe_{15}C_{78}$ decreases strongly with increasing humidity (from 0.26 to 0.14), whereas for a film with a composition $Fe_{2.3}C_{93}$ there is a sharp increase (from 0.03 to 0.17). The coefficient of friction of a film with a composition $Fe_{4.1}C_{84}$, on the other hand, remains virtually constant at about 0.12.

Another difference between metal-carbon films and molybdenum-sulphide films is that humidity has much less effect on the life of metal-carbon films. For example, under standard measuring conditions an iron-carbon film at a relative humidity of about 40% can reach a life of 2×10^7 rotations, whereas the life of molybdenum-sulphide films in a dry atmosphere, measured under otherwise identical conditions, is an order of magnitude less.

The use of metal-carbon can result in a considerable reduction of wear; see *fig. 17*. The rate of wear of a solid tungsten-carbon pin against an uncoated steel substrate is about 10 times less than that of an uncoated steel pin. When the steel is coated with metal-carbon films a very low rate of wear can be achieved even at relatively high contact pressures.

Applications

Thin solid films that can improve the frictional and wear properties of workpiece surfaces have various potential applications. We shall only mention a few examples here.

Fig. 18. Components of ball-bearings, coated with molybdenum sulphide (left) and uncoated.

Molybdenum-sulphide films would appear to be suitable for use in ball-bearings. *Fig. 18* shows the components of ball-bearings with a coating of a molybdenum-sulphide film and without a coating. Ball-bearings coated with our molybdenum-sulphide films are now being studied more extensively at the Darmstadt University of Technology [14]. The life of these completely dry-running bearings in a non-humid atmosphere is about 60% of the life of conventional grease-lubricated bearings under otherwise identical conditions.

We have made a detailed study of the possible application of low-friction solid films in plain bearings. *Fig. 19* is a diagram of the frictional torque plotted

[14] W. Rüblinger, T.H. Darmstadt Schriftenreihe Wiss. & Tech. **20**, 159, 1983.

against the rate of rotation of the shaft for two journal bearings with a bearing bush of sintered metal and a steel shaft, uncoated and with a coating of diamond-like carbon. In both cases, when the shaft is set in motion the frictional torque first decreases, because the contact between shaft and bearing bush steadily diminishes. At higher rates of rotation the hydrodynamic lubrication takes effect and the frictional torque gradually increases. Whereas at higher rates of rotation the divergence between the frictional torques of the two bearings steadily diminishes, there is a considerable difference during the starting-up period. Owing to the low friction of a diamond-like carbon film the bearing in which the shaft is coated with this film has a substantially smaller frictional torque than the bearing with the uncoated shaft. This has the desirable result of a marked reduction in bearing wear. The time that elapses before the first signs of wear are detected on the shaft can be increased in this way by more than 100 times.

Our investigations have shown that metal-carbon films on shafts running in sintered bearing bushes have wear properties equal to those of diamond-like carbon films. One possible application of metal-carbon films is on the capstan drives of audio tape recorders. *Fig. 20* shows a drive spindle coated with a film of tungsten-carbon and an uncoated spindle. These spindles can run in plastic or metal bearing bushes as shown in the figure. In this case the metal-carbon coating serves a dual function. On the one hand the film has the effect of reducing the friction between the spindle and the bearing bush. As indicated in fig. 19, the frictional torque at low rates of rotation is considerably reduced, so that there is much less wear. On the other hand the film has the effect of increasing the friction between the spindle and the tape, which is necessary for ensuring slip-free tape transport. *Fig. 21* shows the results of slip measurements with an uncoated spindle and with a spindle coated with a tungsten-carbon film, as a function of the tension in the tape. With the coated spindle virtually slip-free tape transport is possible even at high tape tension. With the uncoated spindle, on the other hand, considerable slip occurs even at low tape tension. Life tests have shown that a film about 0.2 μm thick gives trouble-free operation in the tape-transport mechanism for several thousands of hours.

Finally, we should note that for some potential applications of low-friction, wear-resistant films there are a number of problems still to be overcome in the manufacture of the films. Applications of films for optimizing the mechanical surface properties not only require special properties in the films but also require very good adhesion to the workpiece surface. Films

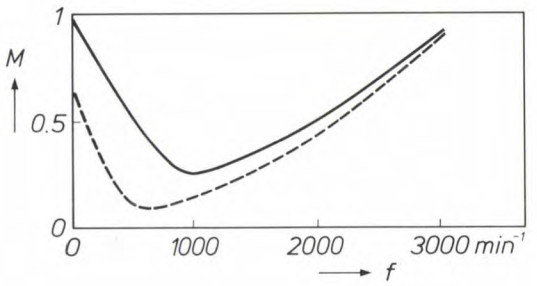

Fig. 19. Diagram of the frictional torque M in arbitrary units plotted against the rate of rotation f for two journal bearings consisting of a bush of sintered metal and a steel shaft. In one bearing the shaft is uncoated (*solid line*) and in the other it is coated with a diamond-like carbon film (*dashed line*). The presence of this film leads to a substantial reduction in the frictional torque during the starting-up period.

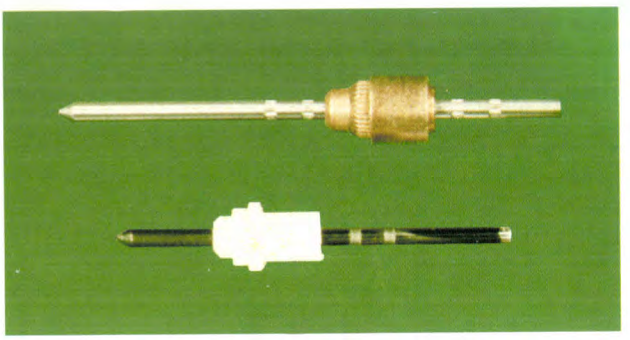

Fig. 20. Tape drive spindles of audio tape recorders. The spindle in the plastic bearing bush is coated with a tungsten-carbon film, the one in the metal bush is uncoated.

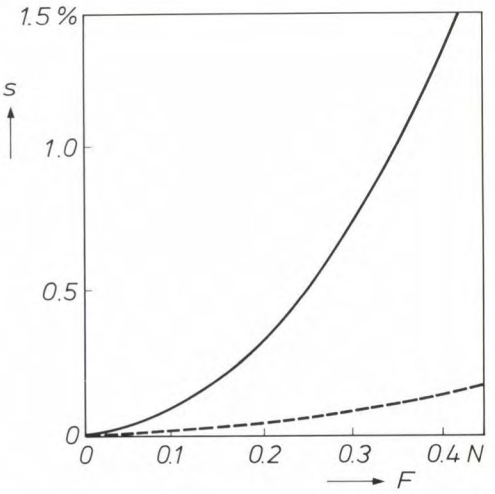

Fig. 21. Relative slip s plotted against the tension F in the tape in an audio tape recorder when the drive spindle is uncoated (*solid line*) and when it is coated with a tungsten-carbon film (*dashed line*). The presence of this film makes virtually slip-free tape transport possible even under high tape tension.

deposited from the gas phase at high temperatures (800-1000 °C) present very few problems here, because the diffusion zone formed as a result of the high temperatures ensures sufficient adhesion for the films. If, however, the deposition temperature for coating temperature-sensitive substrates is no higher than 100 to 300 °C, problems can then arise with the adhesion. Efforts are now being made in many laboratories to produce films that will give good adhesion at these temperatures as well. Another problem connected with deposition at low temperatures is the difficulty of obtaining an optimum film structure.

In the work described here we cooperated closely with Dr K. Enke and U. Schaal. The work received some financial support from the Ministry of Science and Technology in the Federal Republic of Germany. The authors alone are responsible for the contents of this publication.

Summary. The friction and wear properties of workpiece surfaces can often be considerably improved if they are coated with a low-friction, wear-resistant thin solid film, by means of 'physical vapour deposition' (PVD). The improvement depends on the PVD method used, the material deposited and the process conditions. Good results have been obtained with films of molybdenum sulphide, diamond-like carbon and metal-carbon, deposited by sputtering, plasma deposition and sputtering, respectively. Molybdenum-sulphide films give little friction in a dry atmosphere. Films of diamond-like carbon and metal-carbon films are outstanding for their good adhesion to steel and their high resistance to wear. Depending on their adhesion and wear characteristics the thin solid films described have various potential applications, such as lubrication of dry-running bearings and the protection of workpieces.

Scientific publications

These publications are contributed by staff of laboratories and plants that form part of or cooperate with enterprises of the Philips group of companies, particularly by staff of the research laboratories mentioned below. The publications are listed alphabetically by journal title.

Philips GmbH Forschungslaboratorium Aachen, Weißhausstraße, 5100 Aachen, Germany — *A*

Philips Research Laboratory Brussels, 2 avenue Van Becelaere, 1170 Brussels, Belgium — *B*

Philips Natuurkundig Laboratorium, Postbus 80000, 5600 JA Eindhoven, The Netherlands — *E*

Philips GmbH Forschungslaboratorium Hamburg, Vogt-Kölln-Straße 30, 2000 Hamburg 54, Germany — *H*

Laboratoires d'Electronique et de Physique Appliquée, 3 avenue Descartes, 94450 Limeil-Brévannes, France — *L*

Philips Laboratories, N.A.P.C., 345 Scarborough Road, Briarcliff Manor, N.Y. 10510, U.S.A. — *N*

Philips Research Laboratories, Cross Oak Lane, Redhill, Surrey RH1 5HA, England — *R*

Philips Research Laboratories Sunnyvale P.O. Box 9052, Sunnyvale, CA 94086, U.S.A. — *S*

M. Auphan	*L*	Distributions caractérisant la réponse acoustique impulsionnele des cibles sphériques rigides	Acustica **52**	68-85	1983
J. P. Boutot, J. Nussli (*Hyperelec, Brive*) & D. Vallat (*RTC, Paris*)	*L*	Recent trends in photomultipliers for nuclear physics	Adv. Electronics & Electron Phys. **60**	223-305	1983
M. Jatteau & C. Berche	*L*	Review of image reconstruction techniques in medical transaxial computed tomography	Ann. Radiol. **26**	13-22	1983
P. Friedel & S. Gourrier	*L*	Interactions between H_2 and N_2 plasmas and a GaAs(100) surface: chemical and electronic properties	Appl. Phys. Lett. **42**	509-511	1983
G. W. 't Hooft & C. van Opdorp	*E*	Temperature dependence of interface recombination and radiative recombination in (Al,Ga)As heterostructures	Appl. Phys. Lett. **42**	813-815	1983
M. D. Dawson*, W. Sibbett*, J. I. Vukusic* (* *Imp. College, London*), P. Dawson, G. Duggan & C. T. Foxon	*R*	Streak camera study of short pulse generation in an optically pumped GaAs/(GaAl)As laser	Appl. Phys. Lett. **43**	226-228	1983
H. W. M. Salemink (*RIV, Bilthoven*) & J. W. M. Biesterbos	*E*	Optical stability of narrow stripe, proton-isolated AlGaAs double heterostructure lasers with gain guiding	Appl. Phys. Lett. **43**	434-436	1983
P.-J. Courtois	*B*	Error minimization in decomposable stochastic models	Applied probability — computer science, Vol. 1, R. Disney & T. J. Ott (eds), Birkhauser Boston, Cambridge, MA	189-218	1982
A. K. Niessen & A. R. Miedema	*E*	The enthalpy effect on forming diluted solid solutions of two 4d and 5d transition metals	Ber. Bunsenges. Phys. Chem. **87**	717-725	1983
J. Landsbergen	*E*	Machine translation based on logically isomorphic Montague grammars	COLING 82, J. Horecky (ed.), North-Holland, Amsterdam	175-181	1982
M. Davio, J.-M. Goethals & J.-J. Quisquater	*B*	Authentication procedures	Cryptography, T. Beth (ed.), Lect. Notes Comput. Sci. **149**, Springer, Berlin	283-288	1983
M. Monnier & M. Monneraye	*L*	An original interconnection technique for an electronic payment card	Electrocomponent Sci. & Technol. **10**	23-29	1982
M. Rocchi & B. Gabillard	*L*	GaAs digital dynamic IC's for applications up to 10 GHz	IEEE J. **SC-18**	369-376	1983
M. P. A. Viegers, C. W. T. Bulle-Lieuwma & W. J. Bartels	*E*	Impurity drag on climbing misfit dislocations in phosphorus-implanted (001) silicon	Inst. Phys. Conf. Ser. No. 67	359-364	1983

A. H. van Ommen, Y. Tamminga & M. F. C. Willemsen *E*	Diffusion of ion implanted Ga, In and Tl in SiO_2	Insulating films on semiconductors, J. F. Verweij & D. R. Wolters (eds), Elsevier, Amsterdam	55-58	1983
A. E. T. Kuiper, F. H. P. M. Habraken (*Univ. Utrecht*), Y. Tamminga & G. E. Thomas *E*	Interface composition of thin silicon nitride and oxynitride films as prepared by different growth techniques	Insulating films on semiconductors, J. F. Verweij & D. R. Wolters (eds), Elsevier, Amsterdam	116-120	1983
F. H. P. M. Habraken*, E. J. Evers*, G. A. P. Engelbertink* (* *Univ. Utrecht*) & A. E. T. Kuiper *E*	The chemical composition of LPCVD silicon oxynitride films with emphasis on the hydrogen content	Insulating films on semiconductors, J. F. Verweij & D. R. Wolters (eds), Elsevier, Amsterdam	121-125	1983
M. J. Powell & J. Pritchard *R*	The effect of surface states and fixed charge on the field effect conductance of amorphous silicon	J. Appl. Phys. **54**	3244-3248	1983
G. J. Parker, S. D. Brotherton, I. Gale & A. Gill *R*	Measurement of concentration and photoionization cross section of indium in silicon	J. Appl. Phys. **54**	3926-3929	1983
S. Gourrier, L. Smit (*FOM, Amsterdam*), P. Friedel & P. K. Larsen *L, E*	Photoemission studies of molecular beam epitaxially grown GaAs(001) surfaces exposed to a nitrogen plasma	J. Appl. Phys. **54**	3993-3997	1983
H. P. Stormberg & R. Schäfer *A*	Time-dependent behavior of high-pressure mercury discharges	J. Appl. Phys. **54**	4338-4347	1983
P. F. Fewster & P. A. C. Whiffin *R*	Crystallographic polarity and etching of cadmium telluride	J. Appl. Phys. **54**	4668-4670	1983
A. H. van Ommen *E*	Examination of models for Zn diffusion in GaAs	J. Appl. Phys. **54**	5055-5058	1983
D. J. Breed & W. de Geus *E*	Static properties of magnetic bubbles in garnet films with orthorhombic anisotropy	J. Appl. Phys. **54**	5314-5321	1983
F. Hottier & R. Cadoret *L*	Analysis of silicon crystal growth using low pressure chemical vapour deposition	J. Cryst. Growth **61**	245-258	1983
R. Cadoret (*CNRS, Aubière*) & F. Hottier *L*	Mechanisms of silicon monocrystalline growth from SiH_4/H_2 at reduced pressures	J. Cryst. Growth **61**	259-274	1983
C. Jacob (*CNET Grenoble, Meylan*), M. Duseaux, J. P. Farges, M. M. B. van den Boom & P. J. Roksnoer *L, E*	Dislocation-free GaAs and InP crystals by isoelectronic doping	J. Cryst. Growth **61**	417-424	1983
W. H. de Roode & J. M. Robertson *E*	Inhibitors in LPE growth of garnets	J. Cryst. Growth **63**	105-110	1983
W. A. P. Claassen, J. Bloem & F. H. P. M. Habraken (*Univ. Utrecht*) *E*	Influence of carbon addition on the electrical and structural properties of phosphorus and boron doped silicon layers	J. Electrochem. Soc. **130**	1586-1592	1983
D. M. de Leeuw & G. W. 't Hooft *E*	Method for the analysis of saturation effects of cathodoluminescence in phosphors; applied to Zn_2SiO_4:Mn and $Y_3Al_5O_{12}$:Tb	J. Lumin. **28**	275-300	1983
K. H. J. Buschow, P. G. van Engen & R. Jongebreur *E*	Magneto-optical properties of metallic ferromagnetic materials	J. Magn. & Magn. Mater. **38**	1-22	1983
G. A. C. M. Spierings *E*	Properties and structure of glasses in the system $10K_2O.20BaO.70(SiO_2,GeO_2,B_2O_3)$	J. Mater. Sci. 18	2963-2968	1983
P. Friedel & S. Gourrier *L*	Review of oxidation processes in plasmas	J. Phys. & Chem. Solids **44**	353-364	1983
C. T. Foxon *R*	MBE growth of GaAs and III-V alloys	J. Vac. Sci. & Technol. B **1**	293-297	1983
J. H. Neave, P. K. Larsen, B. A. Joyce, J. P. Gowers & J. F. van der Veen (*FOM, Amsterdam*) *R, E*	Some observations on Ge:GaAs(001) and GaAs:Ge(001) interfaces and films	J. Vac. Sci. & Technol. B **1**	668-674	1983
J. Maluenda & P. M. Frijlink *L*	Modulation doped GaAs-$Ga_{1-x}Al_xAs$ heterostructures grown by atmospheric pressure MOVPE	Jap. J. Appl. Phys. **22**	L127-L129	1983
H.-P. Stormberg & R. Schäfer *A*	Excitation of acoustic instabilities in discharge lamps with pulsed supply voltage	Light. Res. & Technol. **15**	127-132	1983
J. F. Verwey *E*	Fysica en halfgeleiderelektronica	Ned. T. Natuurk. A **49**	55-58	1983

W. J. M. J. Josquin & Y. Tamminga *E*	De toepassing van implantatie van stikstofionen in de silicium-IC-technologie	Ned. T. Natuurk. A **49**	63-66	1983
P. A. Devijver & M. Dekesel *B*	Insert and delete algorithms for maintaining dynamic Delaunay triangulations	Pattern Recognition Lett. **1**	73-77	1982
R. W. Cooper & K. A. Jaggers (*Mullard Hazel Grove, Stockport*) *R*	Design and performance of fast high-voltage EPI-diodes	PESC '83 Record, Albuquerque 1983	150-153	1983
J. Hagelstein *B*	Proving properties of shared data structures; application of functional programming	Proc. ACM '82 Conf., Dallas 1982	142-148	1982
R. J. Sluyter *E*	The state of the art in speech coding	Proc. ESSCIRC'83 Lausanne 1983	33-40	1983
R. E. J. van de Grift & R. J. van de Plassche *E*	A monolithic 8-bit video A/D converter	Proc. ESSCIRC'83, Lausanne 1983	57-60	1983
C. K. Wong*, R. F. Wassenaar* (* *Univ. of Technol., Enschede*) & E. Seevinck (*Philips Elcoma Div., Nijmegen*)	A wideband accurate vector-sum circuit	Proc. ESSCIRC'83, Lausanne 1983	135-138	1983
W. A. P. Claassen, W. G. J. N. Valkenburg, A. E. T. Kuiper & Y. Tamminga *E*	Characterization of thin plasma silicon-nitride layers	Proc. 4th Eur. Conf. on Chemical vapour deposition, Eindhoven 1983	199-205	1983
C. H. J. van den Brekel & B. Lersmacher *E, A*	Low pressure CVD of pyrolytic carbon	Proc. 4th Eur. Conf. on Chemical vapour deposition, Eindhoven 1983	321-336	1983
P. J. M. van der Straten*, M. M. Michorius* & G. Verspui* (* *Philips Centre for Manufact. Technol., Eindhoven*)	The decarburization of steel during the CVD of TiC	Proc. 4th Eur. Conf. on Chemical vapour deposition, Eindhoven 1983	553-566	1983
C. Venet, P. Baudet, M. Levent-Villegas, M. Roussel *L*	A 1 W, 20 dB gain, 6-12 GHz FET amplifier	Proc. 13th Eur. Microwave Conf., Nürnberg 1983	213-218	1983
E. Rammos *L*	A new wideband, high gain suspended substrate line planar array for 12 GHz satellite T.V.	Proc. 13th Eur. Microwave Conf., Nürnberg 1983	227-231	1983
J.-P. Farges & A. Mircea-Roussel *L*	Growth of InP from "in situ" synthesized and from polycrystalline charges	Proc. 2nd NATO Workshop on Materials aspects of InP, Bailrigg 1983	9.1-9.6	1983
K. H. J. Buschow *E*	Effect of short-range ordering on the thermal stability of amorphous Ti-Cu alloys	Scr. Metall. **17**	1135-1139	1983
T. A. C. M. Claasen & W. F. G. Mecklenbräuker (*Tech. Univ., Wien*) *E*	Overview of adaptive technqiues in signal processing	Signal processing II; Theories and applications, H. W. Schüssler (ed.), Elsevier, Amsterdam	747-754	1983
P. Dolizy & F. Grolière *L*	AES investigations of chemical composition of some alkali compounds	Surf. & Interface Anal. **5**	4-12	1983
J. H. Neave, P. K. Larsen, J. F. van der Veen (*FOM, Amsterdam*), P. J. Dobson (*Imp. College, London*) & B. A. Joyce *R, E*	Effect of arsenic species (As_2 or As_4) on the crystallographic and electronic structure of MBE-grown GaAs(001) reconstructed surfaces	Surf. Sci. **133**	267-278	1983
P. G. van Engen *E*	An experimental study of the magneto-optical properties of ferromagnetic alloys	Thesis, Eindhoven	—	1983
H. W. Werner *E*	On the use of sector-type mass spectrometers for measuring partial pressures and total pressures	Vacuum **33**	521-523	1983
P. Friedel & S. Gourrier *E*	On the interactions between H_2 and N_2 plasmas and GaAs(100) surface; chemical and electronic properties	Vide Couches Minces **38**	141-143	1983
M. Davio, J.-P. Deschamps & A. Thayse *B*	Digital systems with algorithm implementation	Wiley, Chichester	—	1983

PHILIPS TECHNICAL REVIEW

VOLUME 41, 1983/84, No. 7/8

Digitization of speech

R. J. Sluyter

At first sight there seems to be a world of difference between human speech with its wide range of emotional expression and the unimpassioned ones-and-zeros 'language' of modern computers. We know from information theory, however, that speech, like any other analog signal, can be represented to any desired degree of quality by a digital signal that has the appropriate number of bits per second. The actual practical conversion is known as 'digitization of speech'. It offers possibilities for improvement in all kinds of communication, whether person-to-person or between man and machine. Unfortunately information theory does not tell us the best way of making that conversion. Extensive research has resulted in the development of a large number of methods. In recent times this development has been greatly stimulated by the increasing capabilities of signal processing with digital circuits. More and more frequently we are seeing that an initial rudimentary analog-to-digital conversion is directly followed by more refined digital operations to give the desired digital representation of speech. Philips are very active in all aspects of speech digitization, from research into the principles to selling complete 'speech chips'. The article below gives a general survey of speech digitization and is not limited to Philips activities, of course. A shortened version of this article was presented as an invited paper at the 9th European Solid-State Circuits Conference ESSCIRC '83, held at Lausanne, Switzerland [*].

Introduction

Speech is one of the oldest forms of human communication. Like the use of tools, it was one of the earliest features that distinguished the human species from most other living creatures. In two respects, however, natural speech has its limitations: it is ephemeral and has a limited range. Throughout history many and various attempts have been made to overcome these limitations in inter-human communication. These include the evolution of writing and the invention of printing, and also the use of smoke signals and the first forms of electrical communication signals (Morse signals).

In 1876 the American Alexander Graham Bell made a great invention that opened up completely new perspectives for speech as a means of communication and has been thought to rival the invention of the wheel in importance. This was the telephone, of course. The new invention was to become the nucleus of the largest communications network the world has ever known, with more than five hundred million connections today. This implies that there is on average more than one telephone to every ten people in the world; in some regions the ratio is nearly one to one. The telephone did indeed remove the limitation to the range of speech.

The conversion of the original acoustic speech signal into an electrical signal, which is the principle of the telephone, opened the way to even wider pros-

R. J. Sluyter is with Philips Research Laboratories, Eindhoven.

[*] R. J. Sluyter, The state of the art in speech coding, Proc. ESSCIRC '83, Lausanne 1983, pp. 33-40.

pects. Combination with other techniques (such as Edison's phonograph, 1877), has ultimately made it possible to record and reproduce speech with almost complete fidelity. Nowadays we can faithfully reproduce the spoken word wherever and whenever we wish.

The invention of the telephone soon stimulated some new questions. What were the characteristics of speech that would have to be retained in transmission or storage? What changes could be permitted before quality became unacceptable? These questions remain vital for efficient (and inexpensive) communication, and the studies resulting from them have produced a number of interesting conclusions [1]–[4] about the nature of the speech-production process ('the voice'), speech itself and the perception process ('hearing').

Right from the beginning of telephony conscious or unconscious use has been made of the 'redundancy' inherent in the speech signal. It turns out that the quality of speech is hardly affected if we limit the frequencies in it to the band from about 300 Hz to 3400 Hz. In a telephone conversation one is hardly aware of this limitation; it is not until a direct comparison is made with broadband speech (for example during an FM-radio broadcast in which a telephone call is heard) that the consequences become distinctly perceptible.

Another striking proof of the high degree of redundancy in speech is to be found in an experiment in which all amplitude information is removed from the speech. This can be done by processing a speech signal in such a way that at any moment it can only assume a fixed positive or negative value, depending on the original polarity. Although the speech is severely degraded in quality, it still remains reasonably intelligible [5][6].

Information theory, which made its debut with C. E. Shannon's classic articles of 1948 [7], tells us that for a given quality criterion, any information source can be characterized by the quantity of information supplied (in bits per second). How much information, in this sense, does a speech signal contain? It is fairly easy to give an answer to this with an upper and a lower limit. From theoretical and practical considerations we know that any sound signal perceptible to the human ear in terms of frequencies and level can be represented by a bit stream of at the most 10^5 to 10^6 bits/s. It can also be shown that speech, reproduced as written text, represents no more than 10^1 to 10^2 bits/s [8]. This corresponds roughly to the maximum capacity of the human brain for absorbing information, as measured in a variety of experiments. The information content of a speech signal must therefore come somewhere between the two limits. The exact value depends to a great extent on the quality criterion adopted and is difficult to derive theoretically. At the highest values all the characteristics of speech down to the smallest details are taken into account; at the lowest values characteristics such as speaker recognizability, speech accents, fine variations in pitch and sound level are left out of account.

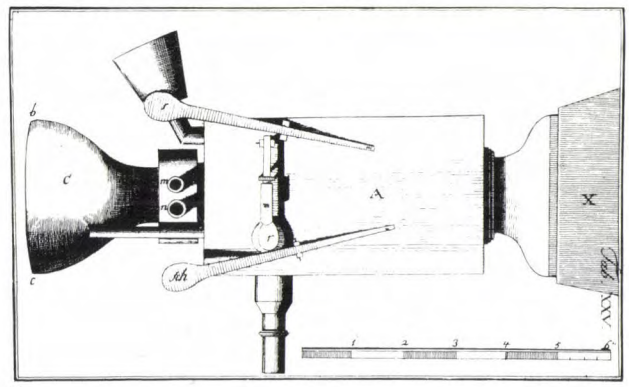

a

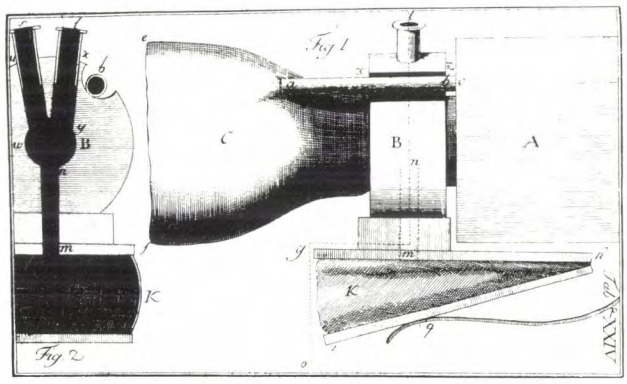

b

Fig. 1. Von Kempelen's speaking machine, reproduced from his original drawings; (*a*) top view and (*b*) side view and cross-section. *X* bellows. *A* chest in which different kinds of sounds are generated by a variety of methods. *C* horn resonator; the action of the human oral cavity is simulated by using the hand to vary the flow of air through the opening. There is even an imitation of the nostrils (*m* and *n* in the upper drawing). Von Kempelen was able to make the machine articulate any Latin, French or Italian word. In a sense it was an early forerunner of the modern voice-response systems now fitted in some of the more expensive cars, which give the driver a spoken warning if something is not in order (e.g. the oil pressure is too low).

Originally the concept of the 'information content' of a signal was mainly of theoretical significance, since it made the information 'quantifiable'. It shed new light, for instance on reversible and irreversible information-handling processes: in the irreversible information-handling processes the information content is reduced and in the reversible ones it is not. In the last 20 years or so, however, the actual conversion of speech signals into a stream of binary digits (or bit stream) has proved to be of great practical significance. This 'digitization' of speech has made it possible in the first place to improve the long-distance

transmission of speech signals by making the signals less sensitive to noise [9][10]. In addition it has made it possible to store speech in digital memories and enables 'scrambling' to be used for security. More recently the following important advantages have been added.

- The use of digital circuits permits highly advanced signal processing, which in many cases would not be possible in analog or other form. It is now possible to start with a digital signal representation with a large information content (i.e. a high bit rate) and to derive from this a well-defined representation with a low bit rate.
- The development of IC technology enables reliable, compact and cheap digital systems to be produced (complex systems can be contained on a single chip).
- After digitization all kinds of information (speech, data, picture) can easily be combined into a single digital signal ('multiplexing'). This results in efficient and versatile telecommunication networks in which the connections are switched by completely digital exchanges.

The central topic of this article is the digitization of speech. This includes not only the actual conversion of an analog speech signal into a digital one but also the subsequent operations that may be applied to reduce the bit rate to the required number of bits per second. The reconstitution of an analog speech signal from the digital version will also be discussed, and it will appear that such a reconstitution is often obvious if the digitization process is known. An attempt will be made to survey the evolution of voice coding to the present day. A proper understanding of the subject requires some elementary knowledge of the mechanisms of the human voice and hearing and of the characteristics of speech signals. These will also be discussed. The article closes with a brief treatment of a number of fundamental signal operations and a look at the available hardware, on which the success of speech digitization largely depends.

Background

It is about 200 years since the first successful attempt to build a machine that was capable of simulating the human voice (*fig. 1*). It was a manually operated contraption with some resemblance to certain musical instruments, and it could be made to articulate a wide variety of words [11]. Since then many variations on this machine have been built, with varying success. The young Alexander Graham Bell also worked on one, together with his brother. But no real advances were made before electronic systems became available. New results were achieved, mainly in the United States, at the end of the nineteen-thirties. At the 1939 New York World Fair an innovation that caused a stir was the Voder [12], a kind of electronic organ with some 15 keys on which specially trained operators were able to simulate human speech. This instrument was essentially a modified and popularized version of a scientific instrument that could analyse human speech and then synthesize it by a fully electronic method (*fig. 2*). This

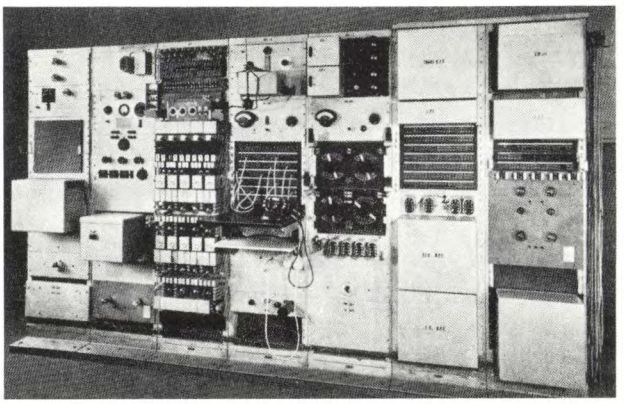

Fig. 2. General view of one of the oldest known electronic systems for speech analysis and synthesis (H. Dudley, 1936). The equipment occupies almost the entire wall (a telephone is just discernible on the middle rack). With speech digitization the same operations can now be performed by hardware consisting of a few chips, or perhaps just a single chip. (Photograph from Bell Laboratories Record, 1936; see [13].)

[1] R. J. Ritsma and B. Lopes Cardozo, The perception of pitch, Philips Tech. Rev. **25**, 37-43, 1963/64.

[2] A. Cohen, Phonetic research, Philips Tech. Rev. **25**, 43-48, 1963/64.

[3] K. Teer, The audibility of phase errors, Philips Tech. Rev. **25**, 176-178, 1963/64.

[4] J. 't Hart, S. G. Nooteboom, L. L. M. Vogten and L. F. Willems, Manipulation of speech sounds, Philips Tech. Rev. **40**, 134-145, 1982.

[5] J. C. R. Licklider and I. Pollack, Effects of differentiation, integration, and infinite peak clipping upon the intelligibility of speech, J. Acoust. Soc. Am. **20**, 42-51, 1948.

[6] This feature is turned to use in some speech-transmission systems. See for example F. de Jager and J. A. Greefkes, "FRENA", a system of speech transmission at high noise levels, Philips Tech. Rev. **19**, 73-83, 1957/58.

[7] C. E. Shannon, A mathematical theory of communication I, Bell Syst. Tech. J. **27**, 379-423, 1948; II, *ibid.*, 623-656.

[8] J. L. Flanagan, Speech analysis, synthesis and perception, 2nd edition, Springer, Berlin 1972.

[9] See for example the review article: F. W. de Vrijer, Modulation, Philips Tech. Rev. **36**, 307-360, 1976, in particular section III, Quantization and coding of analog signals, *ibid.*, 337-341.

[10] B. Gold, Digital speech networks, Proc. IEEE **65**, 1636-1658, 1977.

[11] W. von Kempelen, Mechanismus der menschlichen Sprache nebst der Beschreibung seiner sprechenden Maschine, Vienna 1791.
The mechanism is briefly described in:
Wolfgang von Kempelen's speaking machine, Philips Tech. Rev. **25**, 48-50, 1963/64, and in:
H. Dudley and T. H. Tarnoczy, The speaking machine of Wolfgang von Kempelen, J. Acoust. Soc. Am. **22**, 151-166, 1950.

[12] Pedro the Voder, Bell Lab. Rec. **17**, 170-171, 1938/39;
"My God, it talks!", Bell Lab. Rec. **17**, 177, 1938/39.

system, which was later called the 'Vocoder' (from 'voice coder'), could be used for studying many different speech characteristics, for example by synthesizing at a different pitch from the one found in the analysis [13]. The Vocoder marked the start of a new era in speech coding so clearly that the same term is still used today as a generic name for an entire class of systems. Although the purely scientific aspects were paramount in the original Vocoder, the early publications already referred to possible applications, not only for special sound effects in film and radio but also as a means of scrambling speech for security purposes or as a means of reducing the required bandwidth for speech transmission in telephony.

It is only in recent years, and largely because of digitization, that large-scale applications of speech coding have become feasible and of interest. Such applications, some of which have already been touched upon, include:

- Improvement of speech transmission quality and reduced costs in long-distance communications.
- Efficient use of transmission media (satellite communications, intercontinental cable links, mobile automatic telephone networks, new digital communication networks), especially when bandwidth is at a premium or different kinds of information have to be transmitted simultaneously.
- Efficient storage of speech in digital memories, including 'voice response' and answering equipment; this is already found in electronic talking toys and in speaking electronic teaching aids.
- Scrambling for security or privacy.
- Reproduction of speech at an increased or reduced rate *without* changing the pitch.
- Research into speech and language.
- Speaker verification and identification, in which the spoken word may in time act as a signature or a key [14].
- Speech recognition, which may eventually lead to the operation of machines by speech; there are even speculations about the feasibility of a typewriter that might one day, without manual aid, convert speech directly into typed text.
- Aids for people handicapped by speech or hearing deficiencies.
- Diagnostic aids in tracing disorders in the vocal organs.
- Improvement of speech quality, which can be achieved for example by the selective removal of echoes and interfering noises.

In most of these applications the digitization of speech is only a small part, but an indispensable one, of the total operation [8][15][16]. This article is mainly concerned with this digitization.

Voice and hearing

Natural speech is produced by means of the human vocal organs, shown in cross-section in *fig. 3*. Air is expelled from the lungs through the windpipe (the trachea). In speech production the air can cause vibration of the vocal cords or produce noise due to turbulences generated in a narrowing of the mouth cavity by the tongue. Some sounds are accompanied by a

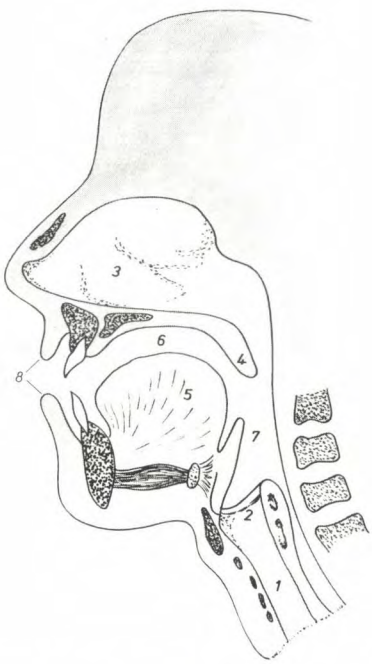

Fig. 3. Cross-section of the vocal organs. *1* Windpipe (the trachea). *2* Vocal cords. *3* Nasal cavity. *4* Soft palate. *5* Tongue. *6* Mouth cavity. *7* Pharynx. *8* Lips.

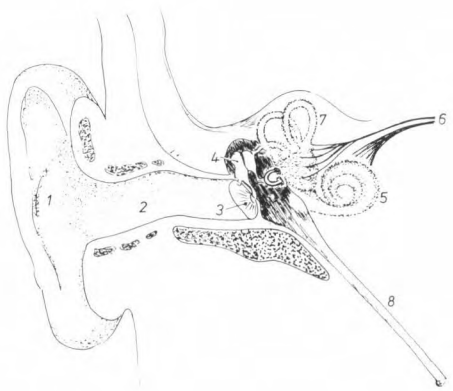

Fig. 4. Cross-section of the organs of hearing, showing the external ear, the middle ear and the internal ear. The external ear consists of the auricle (*1*) and the external auditory canal (*2*). The boundary between external ear and middle ear is formed by the eardrum or tympanic membrane (*3*). The middle ear contains the ear-ossicles (*4*) consisting of malleus, incus and stapes. Inside the internal ear is the cochlea (*5*), which is connected to the brain via the cochlear nerve (*6*), and the vestibular apparatus or organ of equilibrium (*7*). The middle ear is directly connected to the pharynx via the Eustachian tube (*8*). For clarity the various organs are not all shown at the same scale.

temporary complete closure of the mouth cavity. The vibration of the vocal cords determines the pitch of the speech. By changing the shape of the mouth cavity and opening or closing the passage to the nasal cavity the speaker is able to utter a wide variety of sounds. We shall see later how this knowledge can provide a basis for a simple model of the speech-production process.

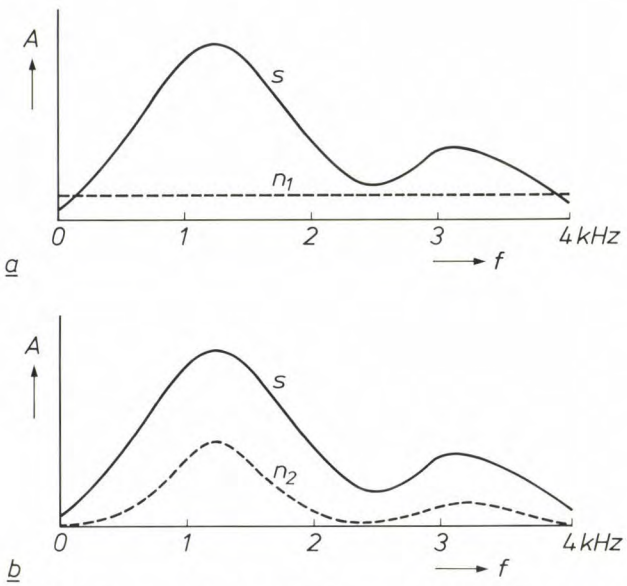

Fig. 5. *a*) Frequency spectrum A of a sound signal s and of a noise signal n_1 in which all frequencies f are represented at equal power ('white' noise). *b*) Frequency spectrum of the same sound signal s and of a 'shaped' noise signal n_2. In signal-to-noise measurements by the most current method the weight attached to noise in a particular frequency sub-band is independent of the position of that sub-band. With this method the same *objectively measured* signal-to-noise ratio is found for both the situations (*a*) and (*b*). In human hearing strong sounds tend to mask weaker sounds of the same frequency. Because of this the amount of noise *subjectively perceived* will be smaller for (*b*) than for (*a*). This effect ('auditory masking') is often utilized in digital speech coding by arranging that the spectrum of unavoidable interfering signals has approximately the same shape as the speech spectrum (this is called 'noise shaping'). The unwanted signals are then less perceptible and therefore cause less annoyance.

Speech is perceived by means of the human ear, shown in cross-section in *fig. 4*. The external ear consists of the auricle and the external auditory canal. The eardrum or tympanic membrane forms the boundary between the external ear and the middle ear. Sound entering the ear causes the tympanic membrane to vibrate. The vibration is conducted via the ossicles in the middle ear to the internal ear, where the sound is converted into nerve stimuli, which are conducted to the brain for further processing. Much less can be deduced about the functioning of the ear from visual inspection of the organs than is possible in the speech-production process. Nevertheless studies and experiments have provided much important information about speech perception. It has been found for example that the ear is relatively insensitive to the *phase* of the different frequency components of a sound. Then there is the familiar 'cocktail-party effect', in which a listener can use both ears to filter out one particular voice from a jumble of surrounding voices. Another important feature is that the perception of the pitch of speech is not determined by a *single* discrete frequency component but by the interrelationships of a *number* of frequency components. When the lower frequencies of speech up to say 300 Hz are suppressed, the pitch does *not* change, even if it is only 100 Hz [17][18]. Perhaps the most useful characteristic of hearing is that of *auditory masking*. This is based on the effect that stronger desired sounds diminish the perception of weaker undesired sounds, especially when both are in the same frequency range (*fig. 5*).

Speech signals

Studying the characteristics of speech signals provides a better understanding of the ways in which speech can be efficiently digitized. *Fig. 6* shows a speech signal as a function of time. In *fig. 7* two pieces of the same signal (the letters '*A*' and '*S*') are shown on a

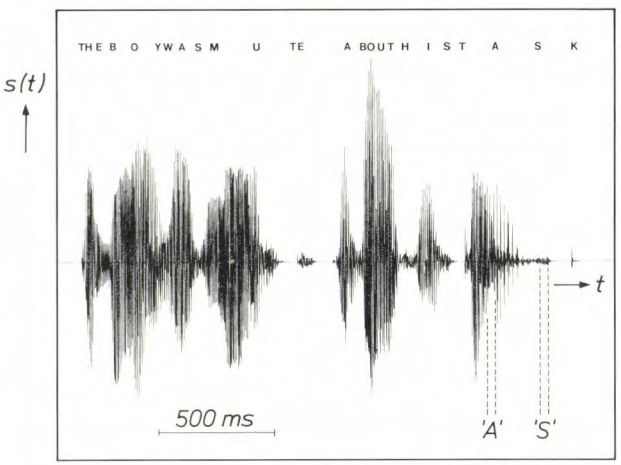

Fig. 6. Speech is converted by means of a microphone into a voltage that varies with time. Here the resultant signal $s(t)$ is given for the sentence: '*The boy was mute about his task!*' The signal varies considerably in strength. A distinction can be made between voiced sounds (such as the letter '*A*'), unvoiced sounds (such as the letter '*S*') and silent intervals or pauses between the words. The total duration of the signal is about 2.5 s.

[13] H. Dudley, Synthesizing speech, Bell Lab. Rec. **15**, 98-102, 1936/37;
H. Dudley, The vocoder, Bell Lab. Rec. **18**, 122-126, 1939/40;
H. Dudley, Remaking speech, J. Acoust. Soc. Am. **11**, 169-177, 1939.

[14] E. Bunge, Speaker recognition by computer, Philips Tech. Rev. **37**, 207-219, 1977.

[15] L. R. Rabiner and R. W. Schafer, Digital processing of speech signals, Prentice-Hall, Englewood Cliffs 1978.

[16] J. D. Markel and A. H. Gray, Jr., Linear prediction of speech, Springer, Berlin 1976.

[17] J. F. Schouten, The perception of pitch, Philips Tech. Rev. **5**, 286-294, 1940.

[18] H. Duifhuis, L. F. Willems and R. J. Sluyter, Measurement of pitch in speech: An implementation of Goldstein's theory of pitch perception, J. Acoust. Soc. Am. **71**, 1568-1580, 1982.

magnified time scale, together with the associated frequency spectra. These figures clearly illustrate a number of characteristic features of speech. In the first place it can be seen that the speech signal $s(t)$ varies strongly in amplitude; this effect is even more conspicuous when different speakers are compared with one another. The results is a *large dynamic range*. The speech signal as a function of time can also be divided up into a number of typical components. On the basis of figs 6 and 7 a distinction can be made between *voiced* sounds (the vowels and a number of consonants such as m, n, l, r, b and d, produced by vibrations of the vocal cords), *unvoiced* sounds (including f, s and sh, produced with the vocal cords at rest) and *pauses*. The voiced sounds have a more or less periodic structure, which gives a regular *line pattern* in the frequency spectrum (the fine structure). In a purely harmonic line pattern the distance between these lines represents the *fundamental frequency* and determines the *pitch* of the speech. In unvoiced sounds there is no regular fine structure and the sound produced has the character of *noise*. The envelope of the spectrum always determines the particular voiced or unvoiced sound. The local maxima in this envelope are called *formants*; four or five different formants can usually be found in the frequency band up to 5 kHz.

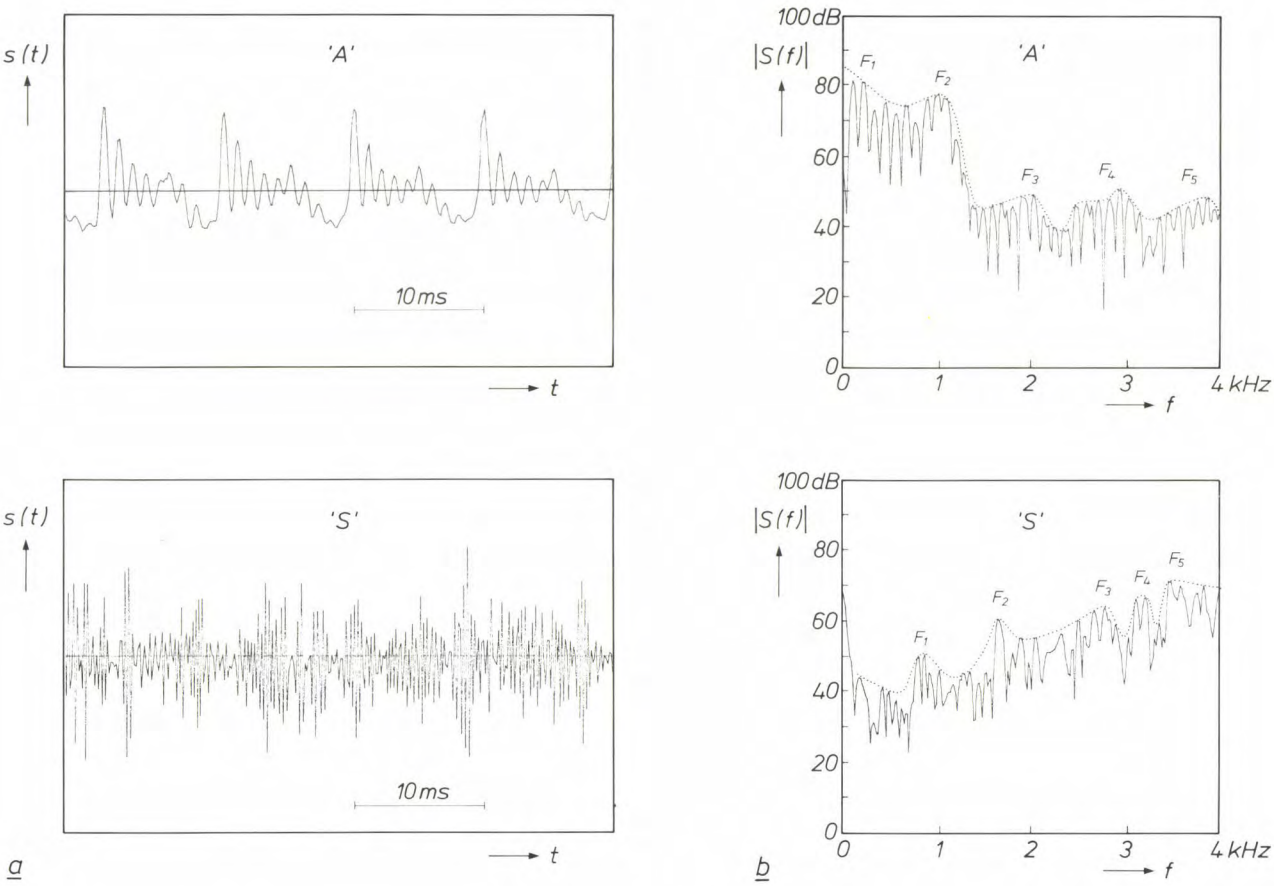

Fig. 7. *a*) Reproduction on an expanded scale (total duration 40 ms) of the letters '*A*' and '*S*' from the signal $s(t)$ of fig. 6 and *b*) the absolute value of the associated frequency spectra $S(f)$. The letter '*A*' gives a signal in which a distinct periodicity (the fundamental frequency or 'pitch') can be recognized. This produces a line structure in the frequency spectrum. (Because of the limited resolution with which this spectrum was calculated, the lines are not sharp but have the structure of narrow peaks or 'fingers'; however, the practically constant shape and the constant spacing between them characterize a regular line spectrum.) The letter '*S*' looks much more like noise. The spectral envelopes (indicated by dashed lines) determine the precise sounds. The maxima F_i of the spectral envelopes are called *formants*.

It is apparent from the foregoing that the characteristics of speech vary considerably as a function of time. For efficient digitization it is therefore often necessary to divide the speech signal into *segments* in which the characteristics are more or less constant, and to treat these segments separately. The segments are usually 20 to 40 milliseconds long and may partly overlap.

Digital coding of speech

There are two essentially different approaches to the digitization of speech. In one approach the aim of the conversion into a bit stream is to determine and preserve the shape of the original signal $s(t)$. This is referred to as *waveform coding*. In the other approach the aim is to derive a limited number (e.g. 10 to 20) of relatively slowly varying characteristic parameters of the speech signal and to represent these alone as a bit stream. This is referred to as *parametric coding* and the hardware used for this is called a *vocoder*. In parametric coding it is important to have a good model of the speech-production process, so that a good approximation to the original speech signal can be recovered from the parameters. Waveform coding is applied at the higher bit rates (about 50 kbit/s), where good quality can be achieved without undue complexity (*fig. 8*). With parametric coding lower bit rates are possible (about 5 kbit/s), but even when complex hardware is used some concessions to quality still have to be made. At bit rates of about 10 kbit/s the best results are obtained with a combination of both types of coding, which is referred to as *hybrid coding*.

It is fairly simple to explain intuitively that speech can be characterized by a number of *slowly varying* parameters. Essentially, these parameters represent the instantaneous 'setting' of the vocal organs. As the operation of the vocal organs is controlled by muscles, the changes in the 'setting' of these organs can only take place relatively slowly and each parameter can be adequately defined by some thirty or forty values per second.

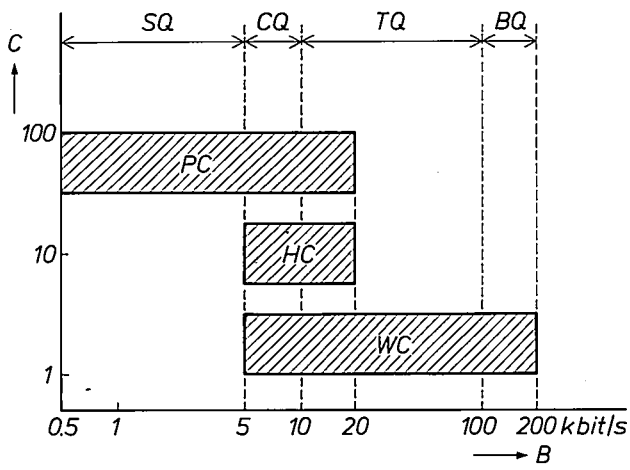

Fig. 8. Comparison of the three main types of digital speech-coding systems (*PC* parametric coding, *HC* hybrid coding, *WC* waveform coding). This figure gives a broad impression of the three main characteristics of each type: bit rate B in kbit/s, relative complexity C, in arbitrary units, and quality (*SQ* synthesis quality, *CQ* communications quality, *TQ* telephone quality, *BQ* broadcast quality). There is a clear correlation between these different characteristics; depending on the application each will have a different weight.

In the digital coding of speech the three most important design factors are:

- the resultant bit rate,
- the complexity of the electronic circuits, and
- the resultant speech quality.

The bit rate is the easiest to quantify (in bits/s). The circuit complexity can be measured in terms of the number of logic gates or the number of chips. Circuit complexity is directly related to cost and also to the often very important aspect of power dissipation. Quality is the most difficult to quantify; in waveform coding the accuracy to which the waveform is preserved can serve as a measure. By treating every deviation from the original shape as 'noise' a signal-to-noise ratio can be defined, and this is widely used with this type of coding. It constitutes an *objective* criterion of quality, whereas the *subjective* quality, which includes all the possible perceptive effects, ought to be the important factor. It has been found in waveform coding that a carefully selected objective criterion gives a reasonably good indication of the subjective quality. With parametric coding the situation is completely different: in this case there is no useful objective criterion because we may be concerned with features such as intelligibility or unintelligibility, naturalness or unnaturalness and recognizability or unrecognizability. We then have to rely entirely on subjective evaluation by means of auditory experiments with a sufficiently large number of speakers and listeners. An attempt is then made, often by comparison of different systems, to determine a 'mean-opinion score' on a scale that runs from 1 (not acceptable) to 5 (excellent) [19]. It is interesting to note that the present telephone quality is evaluated at 4.3. Another broad classification of quality sometimes used (from good to bad) is broadcast quality, telephone quality, communications quality and synthesis quality.

Waveform coding

Pulse-code modulation

The oldest form of waveform coding, which is also suitable for many more kinds of information than just speech, is pulse-code modulation, or *PCM*, invented in 1938 by A. H. Reeves. (This is the first of many abbreviations that will be used in this article, see *Table I*). The principle of PCM is illustrated in *fig. 9*. An analog speech signal, after band-limiting in a lowpass filter F_1, is converted by a sampling circuit into a series of samples s_n separated on the time axis by an interval T. The sampling rate is thus $1/T$.

[19] D. J. Goodman and R. D. Nash, Subjective quality of the same speech transmission conditions in seven different countries, IEEE Trans. **COM-30**, 642-654, 1982.

To avoid distortion ('aliasing') during the sampling process the analog signal should contain no frequency components above half the sampling rate. In telephone applications the rule is $1/T = 8$ kHz, which is more than sufficient for speech signals in the usual frequency band from 0.3 to 3.4 kHz. In the following it will be tacitly assumed that the sampling does not cause any aliasing.

The value of each sample s_n is then rounded off to $\hat{s}_n$ in a quantization circuit Q and converted into a code word of B bits in a bit coder *COD*.

The code words are linked together to form a continuous stream of bits as the final result of speech digitization. From this bit stream an analog speech signal can be reconstituted by means of a bit decoder *DEC* and a lowpass filter F_2. In accordance with current usage the entire digitization process will from now on be referred to as 'the transmitting end' or 'the transmitter' and the recovery of the analog speech signal as 'the receiving end' or 'the receiver'.

In the original PCM systems the relation between s_n and $\hat{s}_n$ (the 'quantization characteristic') is given by a stepped curve in which the distance between two neigh-

Table I. The principal abbreviations used in this article and their definitions.

ADM	Adaptive DM
ADPCM	Adaptive Differential PCM
ADPCM-AP	ADPCM with Adaptive Prediction
APC	Adaptive Predictive Coding
APCM	Adaptive PCM
ATC	Adaptive Transform Coding
DCDM	Digitally Controlled DM
DFT	Discrete Fourier Transform
DM	Delta Modulation
DPCM	Differential PCM
DSP	Digital Signal Processor
LDM	Linear DM
linPCM	Linear PCM
logPCM	Logarithmic PCM
LPC	Linear Predictive Coding
NFC	Noise-Feedback Coding
PCM	Pulse-Code Modulation
ΣDM	Sigma-Delta Modulation

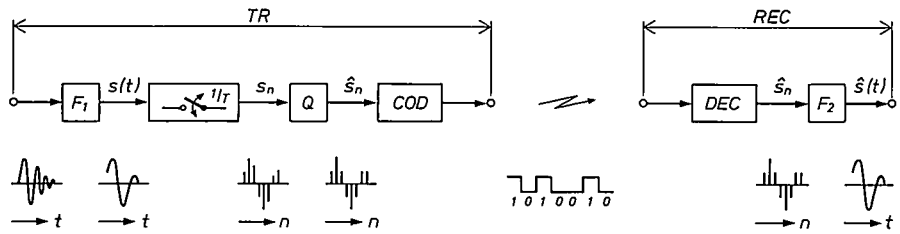

Fig. 9. Basic diagram of a *pulse-code modulation* (PCM) system. The analog input signal is first band-limited in a filter F_1. Samples of the signal $s(t)$ are then taken in a sampling circuit at a sampling rate $1/T$. The magnitude of each sample s_n is quantized to the nearest permitted value $\hat{s}_n$ in the quantization circuit Q and is converted into a word of B bits in the bit coder *COD*. The words are concatenated to produce a continuous bit stream as the end result of the digitization process. The complete circuit in which this is done is usually called the transmitter *TR*. The conversion of the bit stream into an analog signal $\hat{s}(t)$ takes place in the receiver *REC*. For PCM this consists of a bit decoder *DEC* and a lowpass filter F_2.

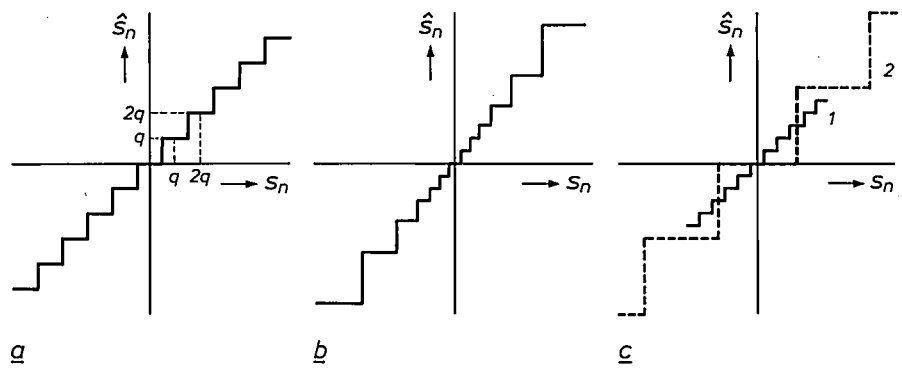

Fig. 10. The relation between the samples s_n and $\hat{s}_n$ is given by the quantization characteristic. *a*) In *linear* or *uniform PCM* this is a stepped curve with a fixed step size q (the quantization step). *b*) In *logarithmic PCM* the step size is not constant but is a fixed percentage of the value of s_n at which each step occurs. *c*) In *adaptive PCM* the step size is determined with reference to the average speech level. The curve changes as a function of time. The two curves drawn here relate to 'soft' speech *1* and 'hard' speech *2*. In all cases the number of possible levels of $\hat{s}_n$ depends on the number of bits per sample used in the bit coder.

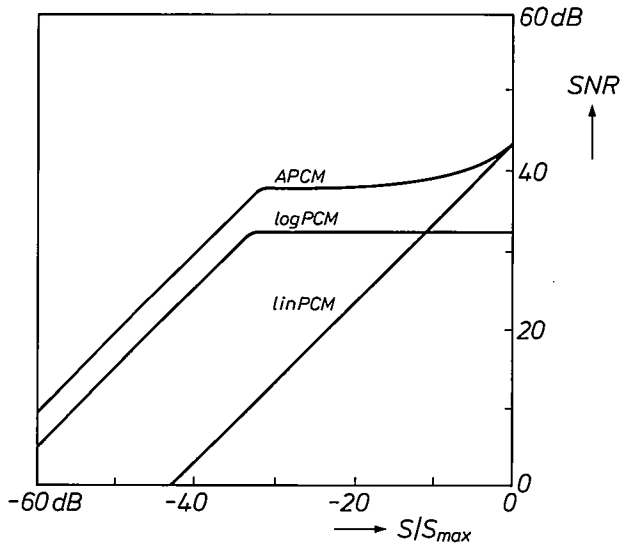

Fig. 11. Comparison of three PCM systems with different types of quantization at the same bit rate (56 kbit/s). The vertical scale represents the signal-to-noise ratio *SNR* in dB, which gives the power ratio of $s(t)$ to $s(t) - \hat{s}(t)$ in fig. 9. The horizontal scale represents the ratio of the power S of $s(t)$ to its maximum permissible value S_{max}. It can be seen that *APCM* and *logPCM* give a distinct improvement compared with *linPCM*.

bouring steps has the value q (the 'step size'); see *fig. 10a*. This is referred to as *uniform* or *linear PCM* (LinPCM). If B bits are used there are 2^B equidistant permissible amplitude values. To digitize speech of ordinary telephone quality in this way we require $B = 12$. At a sampling rate of 8 kHz this gives a bit rate of $12 \times 8 = 96$ kbit/s. However, in this case the characteristic features of speech and hearing are not used at all. As soon as this is done (even only to a limited extent), it is possible to obtain the same quality for $B = 8$, so that the bit rate can be reduced to $8 \times 8 = 64$ kbit/s. This can be done in two ways: by *instantaneous compression* or by *adaptive compression*, giving *logarithmic PCM* (logPCM) or *adaptive PCM* (APCM), respectively. In logPCM we take advantage of the characteristic feature that at larger amplitudes greater distortion (and therefore coarser quantization) is acceptable in relation to perception. The size of the step increases with the value of s_n, and is approximately a fixed percentage of the value of s_n at which the step occurs (fig. 10*b*). Such a quantization characteristic can be obtained by preceding linear quantization by logarithmic compression (hence the name logPCM) of the signal values of s_n, and by following this up with inverse (i.e. exponential) expansion.

LogPCM has become a widely used method in telephony systems. In various ways the logarithmic relationship can be approximated as closely as possible with this method. In the United States 'μ-law PCM' is used and 'A-law PCM' is used in Europe.

APCM depends on the relative slowness of the variation in the mean amplitude level of speech. The step size is adapted to this mean value. The effect is as if the entire quantization characteristic is 'elastic'. Fig. 10*c* shows two possible instantaneous characteristics. The actual number is of course much greater. The bit decoder of the receiver in APCM uses the same varying step size as the transmitter. Information about this is derived from the incoming bits.

The three PCM systems mentioned can be compared on the basis of a signal-to-noise ratio as described in the previous section. The quantity $s(t)$ is then treated as a signal and $s(t) - \hat{s}(t)$ as noise. This ratio varies with the power S of $s(t)$. For convenience we can use the normalized quantity S/S_{max}, where S_{max} is the maximum power of the speech signal. *Fig. 11* gives the result at a bit rate of 56 kbit/s. The figure clearly shows the gain that can be achieved with APCM and logPCM as compared with linPCM.

Differential coding

Speech signals can be represented more efficiently by making use of the close correlation that exists between the values of the successive samples s_n at the output of the sampling circuit in fig. 9. This is done in all sytems based on *differential* coding, for example. The principle is illustrated in *fig. 12a*. The output signal s_n of a sampling circuit is now not quantized directly but only after the preceding value s_{n-1} has been subtracted. Because of the reduction in correlation between the successive values, the difference signal $d_n = s_n - s_{n-1}$ will represent less signal power so that quantization with fewer bits per sample can provide the same quality. At the receiving end $\hat{s}_n$ is obtained by combining the output signal $\hat{d}_n$ of the bit decoder with the previously calculated value $\hat{s}_{n-1}$ from:

$$\hat{s}_n = \hat{d}_n + \hat{s}_{n-1}.$$

This compensates for the differential operation of the transmitter. In the basic system shown in fig. 12*a* errors introduced on quantization in the transmitter can accumulate at the receiving end. This is no longer so with the system shown in fig. 12*b*. The receiving end is the same as in fig. 12*a*, but in the transmitter the quantized output signal $\hat{d}_n$ is now processed in the same way as in the receiver: an estimate is made of the preceding speech sample $\hat{s}_{n-1}$ by integration. The difference

$$d_n = s_n - \hat{s}_{n-1}$$

is now quantized to $\hat{d}_n$. The operation of the system of fig. 12*b* is improved because the quantization circuit is now contained in a closed loop. The accumulation of quantization errors is avoided because at each

quantization the result of the previous operations is automatically discounted. This system may be regarded as the basis of a large number of other systems which all use differential coding based on the same principle.

The first generalization consists in replacing the delay element T by a general filter H. This makes it possible to reduce not only the correlation between successive samples of s_n but also the correlation between rather more widely spaced samples. The scheme thus obtained is called *differential PCM* (DPCM) (fig. 12*c*). An even more efficient system (with a lower bit rate) can be obtained by making the quantization circuit adaptive (as in fig. 10*c*). This is referred to as *adaptive differential PCM* (ADPCM).

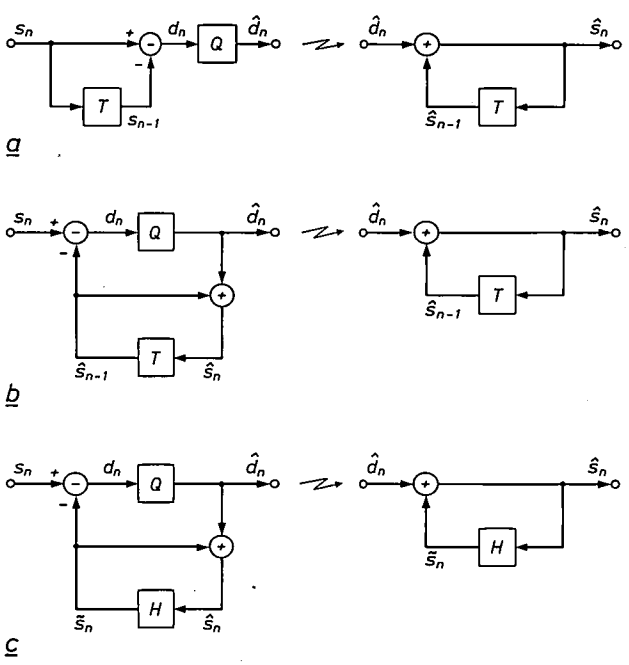

Fig. 12. *a*) In *differential coding* the output samples s_n of a sampling circuit are not directly quantized but are first preprocessed; the principle is shown here. Subtraction of the preceding sample s_{n-1}, which is stored in a delay element T, gives a difference signal d_n. The successive samples d_n show less correlation than the samples s_n. The power in d_n is therefore smaller and fewer bits per sample are then required in the quantization circuit Q. At the receiving end the differential preprocessing in the transmitter is compensated by an integrating operation. In this system an undesirable accumulation of quantization errors can occur in the receiver. *b*) Differential coding in which there is no accumulation of quantization errors; the transmitter now contains a copy of the receiver and the quantization circuit is contained in a closed loop. At every quantization the effect of previous operations is thus automatically discounted. *c*) When the delay element with a delay of one sampling interval T in (*b*) is replaced by any filter H, the general form of *differential PCM* (DPCM) is the result. This system can be further improved by making the quantization circuit adaptive (see fig. 10*c*). The system is then known as *adaptive differential PCM* (ADPCM). (For the transmission of $\hat{d}_n$ the transmitter is always provided with a bit coder and the receiver with a bit decoder as in fig. 9. For simplicity these are omitted here and in the following figures.)

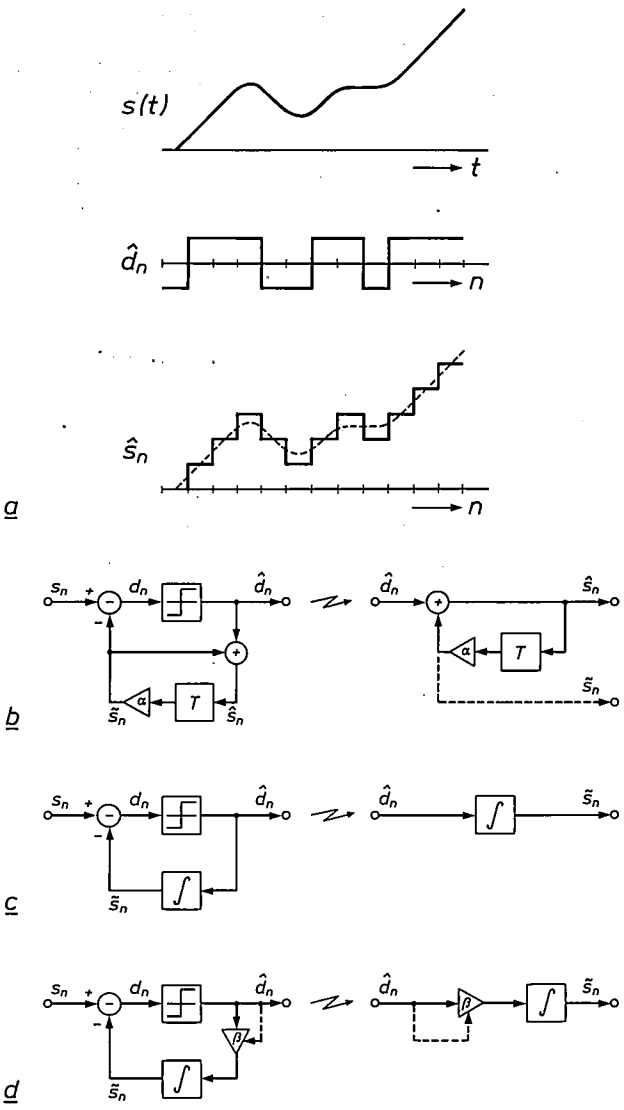

Fig. 13. *a*) When the speech samples s_n in fig. 12*b* are separated by a sufficiently small interval T, the quantization circuit Q need only have two levels. In fact this is *delta modulation*. The output signal $\hat{d}_n$ of Q is already a bit stream and no further bit coding is necessary here. The receiver is extremely simple: direct integration of $\hat{d}_n$ gives a 'staircase' signal $\tilde{s}_n$, which is a good approximation to the original speech signal $s(t)$. *b*) The delay T in transmitter and receiver can be combined with a gain $\alpha < 1$. In essence the receiver then constitutes a very simple filter, known as a 'leaky integrator'. Both the signal $\hat{s}_n$ and the signal $\tilde{s}_n$ can be used as an output signal; they differ only by a constant amplitude factor α and a constant time T. *c*) This accounts for a widely used schematic representation of a delta modulator and delta demodulator, which emphasizes the simplicity of the circuit. The integrator ($\int$) can be realized in many different ways, for example as a simple RC network. *d*) The resulting bit rate of the signal $\hat{d}_n$ can be reduced by introducing a variable gain β. The resultant system is referred to as *adaptive DM* (ADM) or *digitally controlled DM* (DCDM).

[20] J. F. Schouten, F. de Jager and J. A. Greefkes, Delta modulation, a new modulation system for telecommunication, Philips Tech. Rev. **13**, 237-245, 1951/52;
F. de Jager, Deltamodulation, a method of P.C.M. transmission using the 1-unit code, Philips Res. Rep. **7**, 442-466, 1952;
J. A. Greefkes and F. de Jager, Continuous delta modulation, Philips Res. Rep. **23**, 233-246, 1968.

[21] J. A. Greefkes and K. Riemens, Code modulation with digitally controlled companding for speech transmission, Philips Tech. Rev. **31**, 335-353, 1970.

The name 'ADPCM' is sometimes used differently in the literature. In this article the name ADPCM is used to denote the general system shown in fig. 12*c*, with a *fixed* filter H and an *adaptive* quantization circuit Q. Other authors use the term ADPCM to indicate that it is the *filter H* that is adaptive. We then have *adaptive prediction*, which will be discussed later in this article. However, we prefer to express this in the name, so that if both the filter H and the quantization circuit Q are adaptive, we refer to *ADPCM with adaptive prediction* (ADPCM-AP).

Delta modulation

Let us return for a moment to the system of fig. 12*b*. The number of different levels that the quantization characteristic of the circuit Q must contain to achieve a particular quality turns out to be dependent on the time interval T between each two speech samples. As this interval becomes smaller the number of levels required also becomes smaller. If T is made sufficiently small (say 10 µs) only two quantization levels will be sufficient. In fact this is *delta modulation* (DM) [20]. The signal $\hat{d}_n$ is then already a bit stream and no separate bit-coding circuit is required at the transmitting end or bit-decoding circuit at the receiving end. The complete receiver consists only of a closed loop with a delay element, which operates as an integrator (*fig. 13a*). Including a gain $\alpha < 1$ in the closed loop changes this into a 'leaky integrator' (fig. 13*b* and *c*). Undesirable effects such as bit errors then gradually 'leak away'.

By using a variable gain β, whose value is determined from the bit stream $\hat{d}_n$, this system can easily be made adaptive, so that a lower sampling frequency can be used (resulting in a lower bit rate); see fig. 13*d*. This is referred to as *adaptive DM* (ADM) or *digitally controlled DM* (DCDM) [21]. The original form of delta modulation without control is now called *linear DM* (LDM).

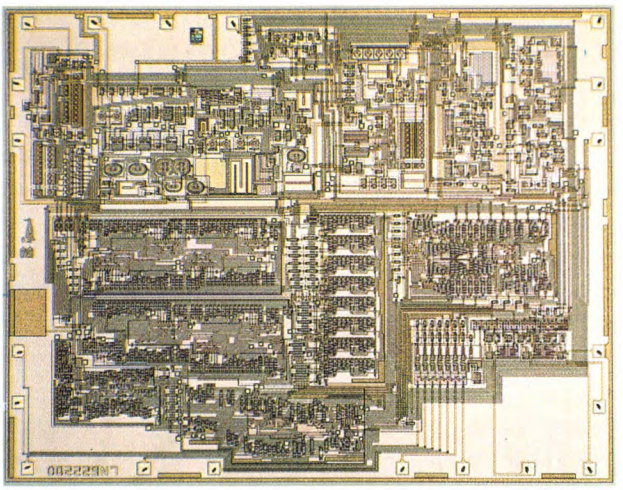

Fig. 14. Integrated circuit (type OQ 2229) for converting an analog speech signal into a digital signal or vice versa by DCDM. The maximum bit rate of the digital signal is 64 kbit/s, but may be freely chosen, so that this IC is also suitable for systems with a bit rate of say 16 or 32 kbit/s. The chip shown here is made in (bipolar) I^2L technology and contains some 1000 transistors. The chip area is about 25 mm^2.

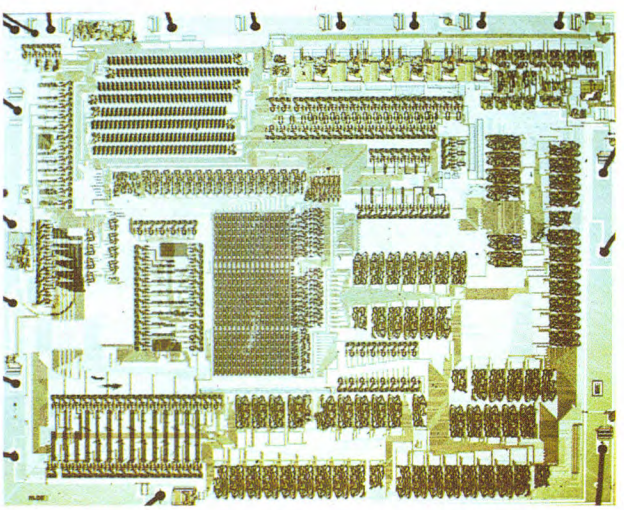

a

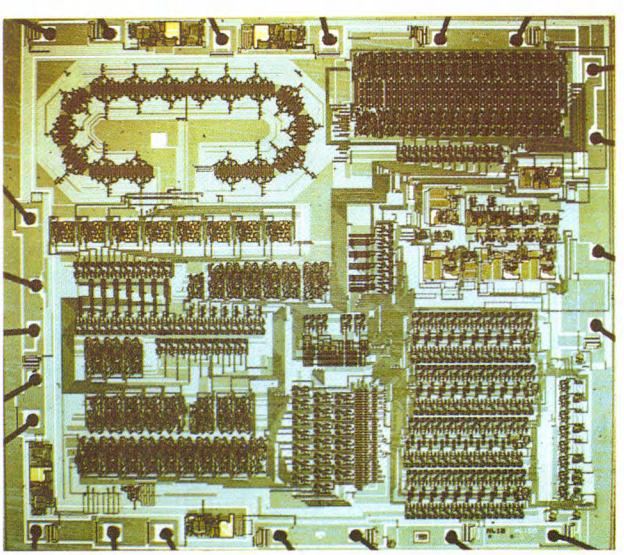

b

Fig. 15. *a*) Integrated circuit for converting an analog speech signal into a logPCM signal. The conversion takes place in different stages. It is preferable to convert the analog speech first into a special kind of DM signal (using linear sigma-delta modulation or ΣDM) at 256 kbit/s. A linPCM signal at $13 \times 8 = 104$ kbit/s is then derived from this and finally the required logPCM signal at a bit rate of $8 \times 8 = 64$ kbit/s is obtained. With a few exceptions, all the operations take place on this single chip of about 35 mm^2, produced in four-phase dynamic-NMOS technology. It contains about 35 000 transistors. *b*) Integrated circuit for the inverse operation: a logPCM signal is converted into an analog speech signal. This also takes place on a single chip in more than one stage. The incoming logPCM signal at 64 kbit/s is first converted into a linPCM signal at $32 \times 14 = 448$ kbit/s. From this another digital signal at $512 \times 7 = 3584$ kbit/s is derived. This signal represents a hybrid form of ΣDM and linPCM. In this circuitous way the actual conversion from digital to analog (in the 'stadium' structure, top left) is made without loss of quality with only 7-bit samples, which is a considerable simplification. The chip area here is about 30 mm^2. The chip is fabricated in four-phase dynamic-NMOS technology and contains about 20 000 transistors. The two chips in this figure represent the state of the art a few years ago. Now all the components (internal and external) of the two circuits described here can be contained in a single chip. This would be called a fully integrated PCM codec, where 'codec' means *co*der/*dec*oder.

In terms of complexity delta modulation is one of the simplest methods of digitizing speech [22]; see *fig. 14*. An important application is in some military communication networks [23]. DM is also an excellent starting point for obtaining PCM, since a DM signal can be converted into a PCM signal by fully digital circuits that are inexpensive and easily integrated [24]; see *fig. 15*.

To provide a comparison between the different methods of waveform coding, the signal-to-noise ratio introduced earlier is used (*fig. 16*). It is important to note here that the result of this comparison depends on the bit rate being considered. A system that functions best at one bit rate is not necessarily the best at another.

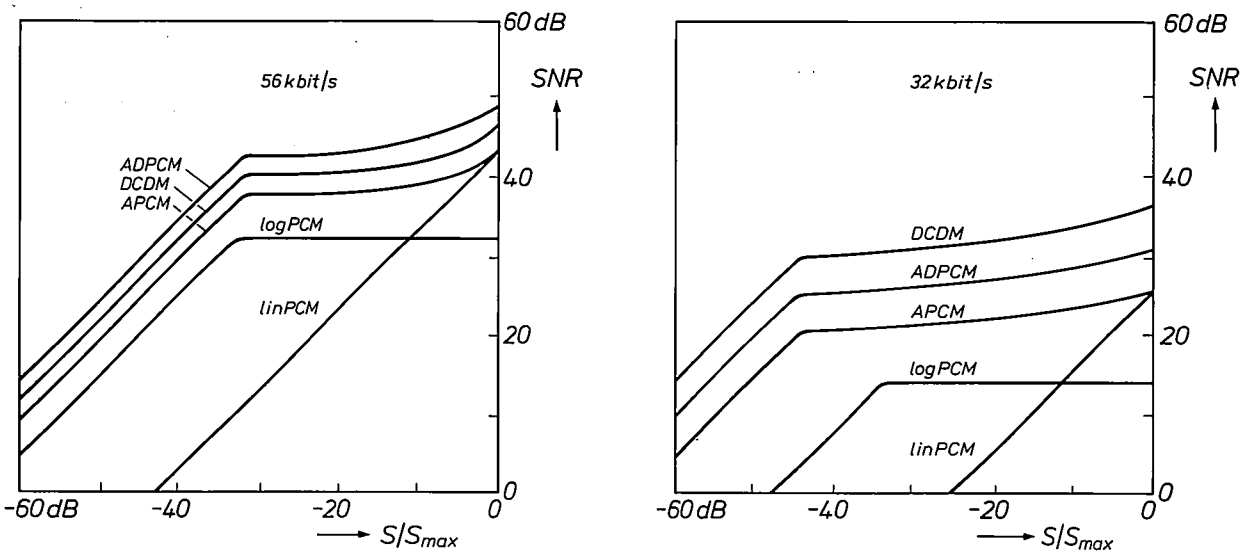

Fig. 16. Comparison of different methods of waveform coding (see also fig. 11) for two different bit rates of 56 kbit/s and 32 kbit/s. It can be seen that the result depends on the bit rate as well as on the method.

Predictive coding

The systems dealt with so far do not exhaust the possibilities of differential waveform coding. It has been found that the bit rate can be further reduced or the quality improved by adding a number of refinements. The concept of prediction is very important here. Indeed, another name for 'differential coding' is 'predictive coding'. The background to this is as follows. The function of the filter H in the general system in fig. 12*c* may be defined as: make the best possible prediction $\tilde{s}_n$ of the *present* value of s_n on the basis of *past* values of $\hat{s}_n$ ($\approx s_n$). Expressed mathematically:

$$s_n \approx \tilde{s}_n = a_1\hat{s}_{n-1} + a_2\hat{s}_{n-2} + \ldots \approx a_1 s_{n-1} + a_2 s_{n-2} + \ldots = \sum_i a_i s_{n-i} .$$

So far it has been tacitly assumed that H was a *fixed* filter using only the immediately preceding values of $\hat{s}_n$. It is evident, however, that better prediction should be possible if H is a *variable* filter, capable of adapting to the characteristics of speech as a function of the speaker and as a function of time. This can be achieved by making H adaptive. The precise setting of H then has to be calculated with a special circuit, and information about the setting must be sent to the receiver so that the filter H at the receiving end can be adjusted to the same setting. The calculation of the setting of the predictive filter [25] will not be dealt with here.

The prediction of the present speech sample s_n does not have to take place solely on the basis of the immediately preceding samples ('short-term prediction') but may also be based partly or entirely on earlier samples whose 'age' is approximately an integral number of periods of the fundamental frequency (p. 206). This is because, owing to the periodicity, there is a strong correlation between samples separated by such intervals. However, since the fundamental frequency can vary considerably, this second form of prediction ('long-term prediction') is only useful in adaptive form. The combination of these two forms of adaptive prediction is known as *adaptive predictive coding* (APC); see *fig. 17*.

Noise-feedback coding

A further extension applicable in each of the differential methods of waveform coding dealt with so far is '*noise-feedback coding*' NFC. The principle, illustrated in *fig. 18*, is as follows. The quantization

noise is determined as the difference between the signals at the input and output of the quantization circuit. This noise is fed back via a filter *NS*, which may be an adaptive filter. By using an appropriate filter, any required shape can be given to the frequency spectrum of the quantization noise. In this way it is possible to take optimum advantage of the masking effect in human hearing (auditory masking, p. 205). This may if desired be combined with a prefilter H_3, which provides optimum filtering of the signal s_n in advance. The filter action of H_3 is compensated by a filter H_4 in the receiver.

With the most advanced waveform-coding methods it is possible to achieve telephone quality at a bit rate of 16 kbit/s. Lower bit rates can also be used, but with some deterioration of quality.

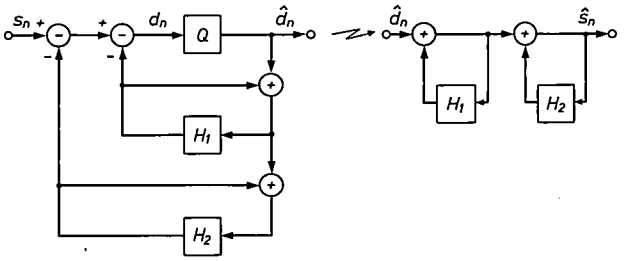

Fig. 17. Differential coding does not need to be based only on immediately preceding samples of the speech signal, as in the systems described previously ('short-term prediction' using H_1), but can be refined by prediction based on earlier samples, whose 'age' is approximately an integral number of periods of the pitch (H_2). Because of the continuing change of pitch this refinement only has any significance with *adaptive* prediction. The actual details of the adaptation process are not shown here. The instantaneous settings of H_1 and H_2 must be sent together with the bit stream $\hat{d}_n$ to the receiver so that its predictors can be given identical settings. This is done by means of a multiplexer and a demultiplexer, which form part of the bit-coder and bit-decoder circuits (not shown). The speech-digitizing method shown here is called *adaptive predictive coding* (APC).

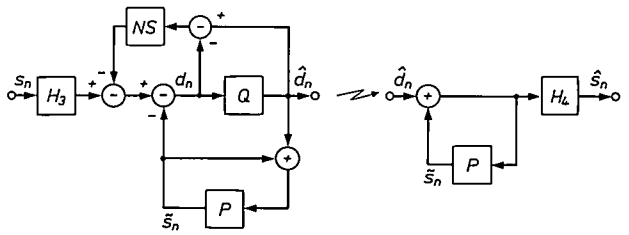

Fig. 18. Any form of differential coding can take advantage of the masking effect in human hearing (auditory masking) if the spectrum of the quantization noise is properly chosen. The quantization noise is obtained by subtracting the input signal from the output signal of the quantization circuit Q and feeding back the resultant signal via a noise-shaping filter *NS*. This can be combined with a prefilter H_3, which is compensated in the receiver by a post-filter H_4. The predictor, not specified further here, is indicated by *P*.

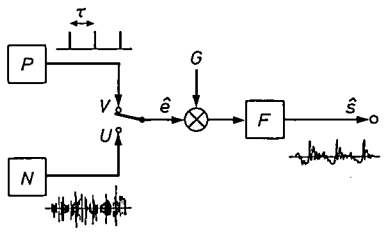

Fig. 19. Widely used speech-production model. It contains two signal sources: a source P for a periodic pulse train, whose repetition frequency $1/\tau$ corresponds to the pitch of the speech, and a source N for a noise-like signal. Source P or source N is selected on the basis of the voiced/unvoiced decision (V/U). This gives an excitation signal $\hat{e}$. The model also includes a variable gain G, which determines the magnitude of the sound signal, and a filter F that represents the vocal tract (the mouth cavity, nasal cavity and pharynx combined). When the values of all parameters are varied appropriately as a function of time, the signal $\hat{s}$ represents a synthetic speech signal.

Parametric coding

In the parametric coding of speech the speech-production model plays a leading part. A model is assumed, and the speech is analysed *segment by segment* (p. 206) at the transmitting end and then synthesized at the receiving end. The nearer the model approximates to reality, the better will be the ability to describe a given speech signal by a limited number of relatively slowly varying parameters. A widely used speech-production model is shown in *fig. 19*. It is based partly on the structure of the human vocal organs (fig. 3) and partly on the characteristic shapes of speech signals (figs 6 and 7). It contains two signal sources P and N. The source P delivers a series of periodic pulses whose repetition frequency $1/\tau$ corresponds to the fundamental frequency or pitch of the speech, and the source N delivers a noise-like signal. The source P generates voiced sounds and the source N unvoiced sounds. One or other of the two sources is selected on the basis of a voiced/unvoiced (V/U) decision. The magnitude of the source signal selected can be varied by means of the gain G, and its frequency spectrum can be modified by the filter F. In essence this filter performs a function comparable with that of the human vocal tract (pharynx plus nasal and mouth cavities). To make a reconstitution $\hat{s}$ of a real speech

[22] J. W. Glasbergen, This versatile IC digitizes speech, Philips Telecommun. Rev. 39, 147-154, 1981.
[23] C. Ziekman and P. Zwaal, DELTAMUX, a design element for military communication networks, Philips Telecommun. Rev. 32, 78-89, 1974.
[24] L. D. J. Eggermont, M. H. H. Höfelt and R. H. W. Salters, A delta-modulation to PCM converter, Philips Tech. Rev. 37, 313-329, 1977;
D. J. G. Janssen and L. van de Meeberg, PCM codec with on-chip digital filters, Electronic Components & Appl. 2, 242-250, 1980;
L. van de Meeberg and D. J. G. Janssen, A single-chip PCM codec with digital filters, Proc. 9. Int. Kongress Mikroelektronik, München 1980, pp. 69-74.
A forthcoming article in this journal, by J. J. van der Kam, will deal with analog-to-digital conversion by means of sigma-delta modulation and digital filtering for audio applications.
[25] B. S. Atal, Predictive coding of speech at low bit rates, IEEE Trans. **COM-30**, 600-614, 1982.

signal s with this model it is necessary first to derive the following time-varying parameters from s in the transmitter (*fig. 20*):

- the voiced/unvoiced (V/U) decision;
- for voiced sounds the fundamental frequency $1/\tau$ ('pitch detection' or 'pitch extraction');
- the magnitude of the gain G;
- some form of description of the filter F.

Because of the strong correlation the first two quantities are often derived together (excitation analysis) and so are the last two quantities (vocal-tract analysis). This yields two categories of problems that have long been predominant in parametric coding. A number of satisfactory alternatives have been found for characterizing the vocal tract. This is not so much the case with pitch detection, although a recent development like the 'harmonic-sieve method' (to which we shall return later) is a distinct step forward.

The speech-production model of fig. 19 has been the starting point for the design of many types of speech-coding systems (vocoders) [26]. However, various imperfections of this model are now beginning to be recognized. One of them is that some sounds cannot be clearly classified as voiced or unvoiced, but come somewhere between the two. Another point is that every speaker sometimes utters voiced sounds with no definite periodicity. Yet another aspect is that 'plosives' (such as p, t, k) are not really compatible with this model. This difficulty is connected with the required breakdown of the speech signal into segments; the sudden transients that are characteristic of plosives can only be properly simulated at the transitions between segments.

Excitation analysis

The determination of the fundamental frequency of speech involves a number of characteristic problems. In the first place the fundamental covers a relatively wide frequency band (from 50 to 500 Hz). In addition fairly rapid variations may occur in the period of the fundamental frequency ('non-stationarity'), even within the individual segments of a few tens of milliseconds into which the speech is broken down for processing. Yet another problem is connected with the formant structure. If the first formant is at low frequencies and is fairly narrow the corresponding periodicity in the speech signal may easily be confused with the periodicity associated with the fundamental. Furthermore, the background noises that accompany the speech, or just the absence of the low-frequency components (as in telephony up to about 300 Hz) can make pitch detection particularly difficult.

There are essentially two distinct approaches to pitch detection: one is the time-domain approach,

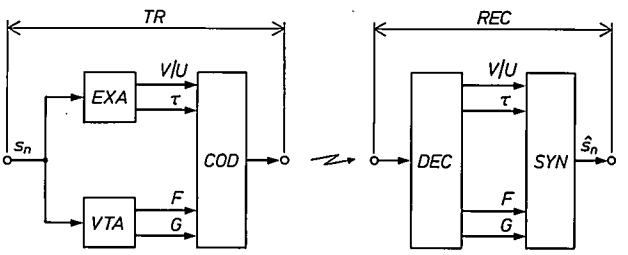

Fig. 20. In parametric coding a limited number of time-dependent parameters are derived from the speech signal s_n at the transmitting end (*TR*). With the speech-production model in fig. 19 a choice is made, by means of excitation analysis (*EXA*) and vocal-tract analysis (*VTA*) between voiced and unvoiced sounds (V/U), the fundamental frequency (pitch) $1/\tau$ is determined and the vocal tract is characterized by means of a filter function F and a gain G. In the bit coder *COD* this information is combined by a multiplexer to form a single bit stream. At the receiving end (*REC*) this bit stream is split up into its individual components again in a bit decoder *DEC* by a demultiplexer. These components are applied to a synthesizer *SYN*, based on the speech-production model; the output from the synthesizer is a synthesized speech signal $\hat{s}_n$. The combination of transmitter and receiver in parametric coding is called a *vocoder*.

often based on the autocorrelation function, and the other is the frequency-domain approach, based on spectral analysis [27]. The autocorrelation function $R(\tau)$ of a signal $s(t)$ indicates the extent to which a shifted signal version $s(t+\tau)$ will still resemble the original signal $s(t)$ (*fig. 21*). This means that an autocorrelation function always has the maximum value for $\tau = 0$ and that it has a local maximum at $\tau = T_1$, if $s(t)$ has a periodic structure of period T_1. It is this feature that enables the pitch of speech to be detected. The autocorrelation function can also be used as the basis for the voiced/unvoiced decision. For a voiced sound it is required that $R(\tau)$ outside the main peak (at $\tau = 0$) should exceed a critical threshold at least once. An alternative method consists in counting the number of zero crossings (changes of polarity) of the signal $s(t)$ per unit time; for an unvoiced sound this number is usually significantly higher than for a voiced sound (see fig. 7).

In the digitization of speech we do not in fact use the *continuous* autocorrelation function $R(\tau)$ of $s(t)$ but the related *discrete* autocorrelation function R_k of s_n. Formally this function is defined as

$$R_k = \lim_{N\to\infty} \frac{1}{2N+1} \sum_{n=-N}^{N} s_n s_{n+k} .$$

Since we are always dealing with speech segments of finite duration, this definition has to be adapted to the finite number of speech samples in each of these segments. This can be done in more than one way.

There are also a number of derived methods of pitch detection designed to simplify the computational effort involved in determining the autocorrelation function. Examples are the 'clipped autocorrelation method', the 'Average Magnitude Difference Function method' (AMDF) and the 'Simplified Inverse Filter Technique' (SIFT) [27].

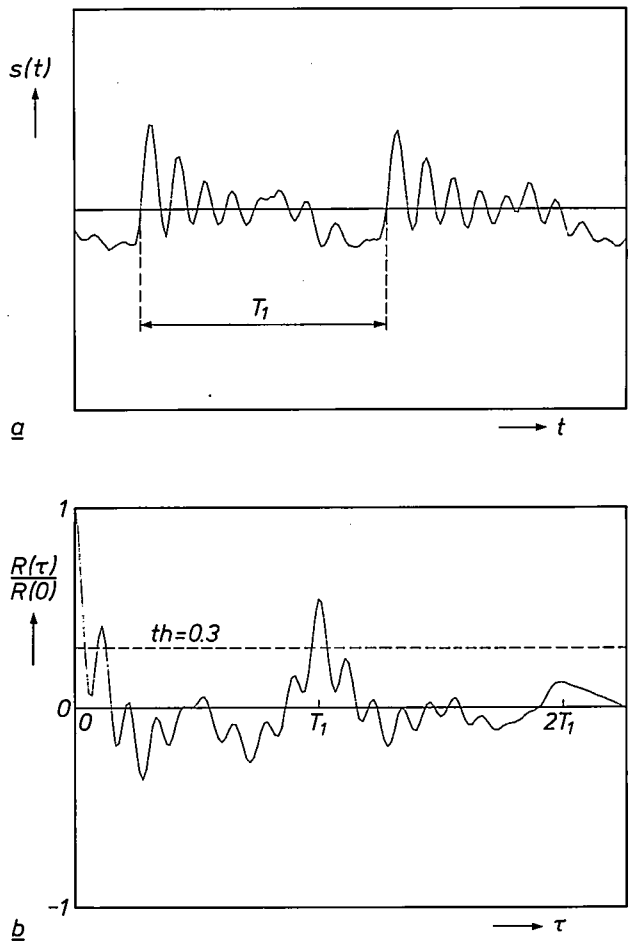

Fig. 21. Pitch detection in the time domain with the autocorrelation function. *a*) Speech signal $s(t)$ representing a voiced sound with a pitch period T_1, corresponding to the first half of the '*A*' from fig. 7*a*. *b*) The autocorrelation function $R(\tau)$ of this signal has a distinct peak at $\tau = T_1$. Dividing all values of $R(\tau)$ by $R(0)$ gives the normalized autocorrelation function $R(\tau)/R(0)$ shown here. This always has the value 1 for $\tau = 0$ and can also be used as the basis for the voiced/unvoiced decision. If the threshold value *th* (here $th = 0.3$) is not exceeded anywhere outside the immediate neighbourhood of the main peak, the sound is unvoiced; in the other case it is voiced.

A method of pitch detection by using spectral analysis that has been used for some time is found in the *homomorphic* processing of speech [15]. In this method the amplitude spectrum of the speech signal is first calculated by Fourier transformation; its logarithm is then taken and the result is transformed back again. A time-varying function called a 'cepstrum' is then obtained, from which various characteristic features of the speech signal can be derived.

A new method of pitch detection introduced fairly recently is known as the *harmonic sieve* [18][28]. In this method the frequency spectrum of a speech signal is first reduced to a limited number of low-frequency speech components $x_1, x_2, \ldots, x_K$ located at the positions of the original significant spectral peaks (*fig. 22*). Only the frequency of these components is important; they do not represent amplitude or phase information. A number of hypothetical 'sieves' whose 'meshes' correspond to harmonic frequency intervals are used to analyse the set of speech components. The analysis consists in determining whether each of the speech components will be located within one of the meshes of each of the sieves. There are L sieves, where L is about 40. Pitch extraction is achieved by determining which sieve gives the best general fit to a given set of speech components $x_1, x_2, \ldots, x_K$. The first mesh of the best sieve then represents the extracted pitch. Good results have been achieved with this method.

The voiced/unvoiced decision can also be based on a spectral analysis, since voiced sounds have a spec-

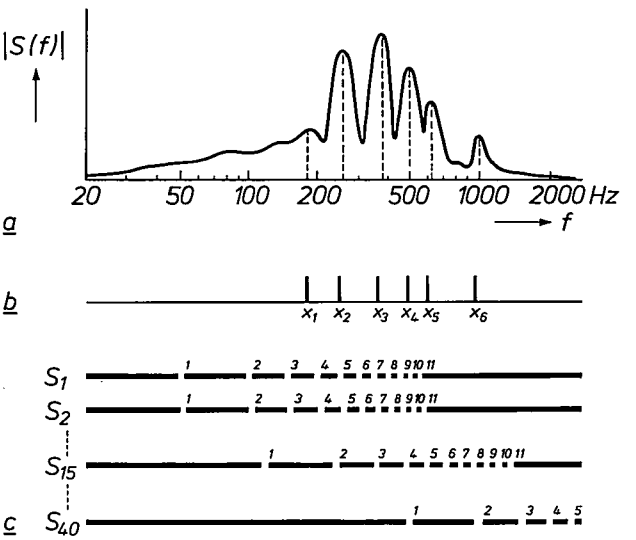

Fig. 22. Pitch detection in the frequency domain by the *harmonic-sieve* method. *a*) Low-frequency part of the amplitude spectrum of a portion of a speech signal. *b*) This spectrum is reduced to a number of components $x_1, x_2, \ldots, x_K$ at the positions of the original significant maxima. These components do not represent amplitude or phase information. *c*) From a number of 'sieves' $S_1, \ldots, S_{40}$, whose 'meshes' lie at harmonic frequency intervals, the sieve that best fits in with the set of components $x_1, x_2, \ldots, x_K$ is chosen (in this case it is S_{15}). This is done by determining which speech components fall through the meshes of each sieve and which do not. The first mesh of the best-fitting sieve represents the pitch (in this case 120 Hz). For clarity, the frequency scale in this figure is logarithmic.

[26] J. L. Flanagan, M. R. Schroeder, B. S. Atal, R. E. Crochiere, N. S. Jayant and J. M. Tribolet, Speech coding, IEEE Trans. **COM-27**, 710-737, 1979.

[27] L. R. Rabiner, M. J. Cheng, A. E. Rosenberg and C. A. McGonegal, A comparative performance study of several pitch detection algorithms, IEEE Trans. **ASSP-24**, 399-418, 1976.

[28] R. J. Sluyter, H. J. Kotmans and A. van Leeuwaarden, The harmonic-sieve method for pitch extraction from speech and a hardware model applicable to vocoder systems, Proc. 1980 Int. Zürich Seminar on Digital communications, Zürich 1980, pp. E2.1-E2.6;
R. J. Sluyter, H. J. Kotmans and T. A. C. M. Claasen, Improvements of the harmonic-sieve pitch extraction scheme and an appropriate method for voiced-unvoiced detection, Proc. ICASSP 82, Paris 1982, pp. 188-191.

trum that decreases with frequency while unvoiced sounds usually do not (fig. 7). Even from an analysis of the low-frequency part of the spectrum alone it is still possible to draw conclusions: voiced sounds have much more energy in that part of the spectrum than unvoiced sounds.

Vocal-tract analysis

The hardware used for parametric coding and decoding of speech (the vocoder) is generally identified

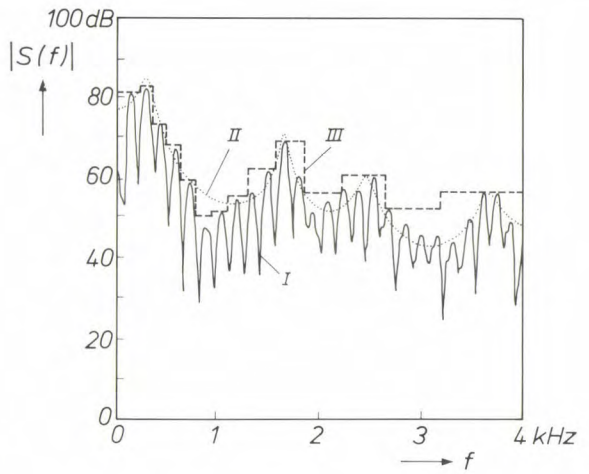

Fig. 23. In vocal-tract analysis the aim is to find a good description for the spectral envelope of a speech signal (*I*). To limit the number of bits required an approximation to this envelope is used. Two alternatives are shown here. One is an *all-pole* approximation (*II*), obtained as the result of linear prediction, and a *piecewise-constant* approximation (*III*), obtained as a result of a Discrete Fourier Transform.

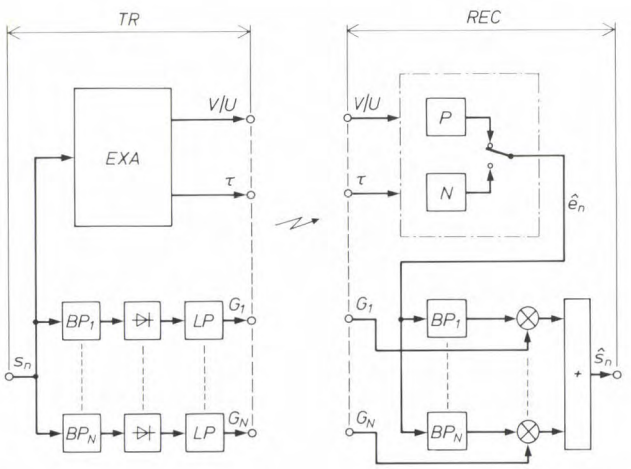

Fig. 24. Block diagram of a *channel vocoder*. At the transmitter *TR* the speech signal is split up by a bank (10 to 20) of bandpass filters $BP_1, \ldots, BP_N$ into different frequency sub-bands. The signal amplitude in each sub-band is measured by means of a rectifier and a lowpass filter *LP*. This information is transmitted to the receiver *REC* where it is used as a varying gain $G_1, \ldots, G_N$ to control the magnitude of the output signals of an identical bank of filters $BP_1, \ldots, BP_N$. The input signal for this filter bank is the excitation signal $\hat{e}_n$, generated in the usual manner. (For simplicity the bit coder and bit decoder have been omitted in this and subsequent figures.)

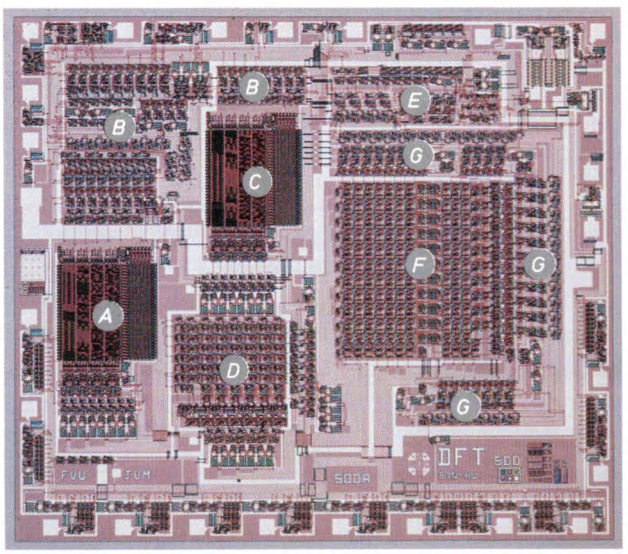

Fig. 25. Integrated circuit for performing a 256-point Discrete Fourier Transform. This circuit is designed for application in a variety of systems in which digital operations are performed on speech. With this IC a DFT can be performed in 6.5 ms on a speech segment containing 256 speech samples. The main components of this circuit are: two ROMs (*A* and *C*, 256 × 8 bits each), two parallel multipliers (*D* and *F*, 8 × 8 and 12 × 12 bits), an accumulator/shifter circuit (*G*, 30 bits) and control logic (*B* and *E*). This chip is fabricated in static-NMOS technology. It contains about 20 000 transistors and the chip area is about 12.5 mm².

by the kind of parameters used to characterize the vocal tract. This indicates the special importance of these parameters. The vocal-tract parameters always represent some sort of approximation to the *spectral envelope* during a speech segment (*fig. 23*). In principle any possible form of vocal-tract characterization may be combined with any of the forms of pitch detection and voiced/unvoiced decision mentioned above.

The oldest type of vocoder is the *channel vocoder*. The vocal tract is represented by a bank (10 to 20) of bandpass filters (*fig. 24*). At the transmitting end the average signal amplitude in each small frequency band is determined by means of a rectifier and a lowpass filter. The resultant information is transferred in coded form to the receiver, where it is used to adjust the gain in the branches of an identical bank of filters. The bandwidths of the individual filters in such a filter bank do not have to be equal; with a limited number of filters the best results are obtained when the filters for the lowest frequencies have the smallest bandwidth. This corresponds to the characteristics of human hearing. Digital versions of all the components in the block diagram shown in fig. 24 can be used for the digital implementation of a channel vocoder; the filter-bank function, however, can also be performed by means of a Discrete Fourier Transform (DFT).

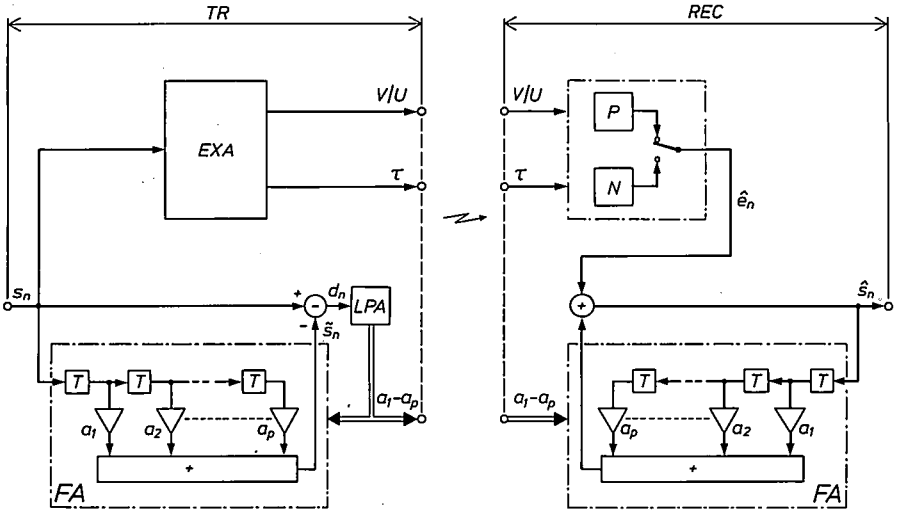

Fig. 26. Basic diagram of an *LPC vocoder*. The characterization of the vocal tract is now based on linear prediction with the aid of the filter *FA* with coefficients $a_1, \ldots, a_p$. In the analyser LPA these coefficients are calculated in such a way that the residual signal $d_n = s_n - \tilde{s}_n$ is as small as possible. The values found for $a_1, \ldots, a_p$ are transmitted to the receiver and used for deriving a synthesized speech signal $\hat{s}_n$ from the excitation signal $\hat{e}_n$. (The double arrows in this diagram are used for indicating more than one parameter at the same time.) For clarity the filter *FA* is explicitly shown at the transmitter end. In a real circuit this filter does not actually exist; it is implicitly included in the algorithm with which the set of coefficients $a_1, \ldots, a_p$ is directly calculated in *LPA* from a segment of s_n.

This gives a *DFT vocoder* [29]. *Fig. 25* shows an integrated circuit [30] suitable for use in such a vocoder.

Another method of characterizing the vocal tract is based on a description of the envelope of the speech spectrum in terms of formants (fig. 7), resulting in a *formant vocoder*. The vocal tract is now represented by four or five bandpass filters in which the bandwidth and the centre frequency vary as a function of time. The receiver contains the same number of filters with variable parameters. The required values are derived from the speech at the transmitting end. This can be done by means of linear predictive coding (LPC) [31]. A formant vocoder of this type is a member of the much larger family of *LPC vocoders*. The idea behind all these vocoders is again the assumption that any speech sample $\tilde{s}_n$ can be well approximated by a weighted sum s_n of preceding speech samples; see the equation on p. 212. This leads to the basic diagram of the LPC vocoder given in *fig. 26*.

The principle of linear prediction has been touched upon earlier in this article in the context of waveform coding, which included adaptive predictive coding (APC); see *fig. 27*. The main difference between APC and LPC is that in APC not only are the prediction coefficients (a_1 to a_p) sent from transmitter to receiver, but the associated residual error is sent as well in the form of $\hat{d}_n$. In an LPC vocoder $\hat{d}_n$ is replaced by information about the pitch and the voiced/unvoiced decision. A substitute excitation signal $\hat{e}_n$ is reconstituted from this in the receiver.

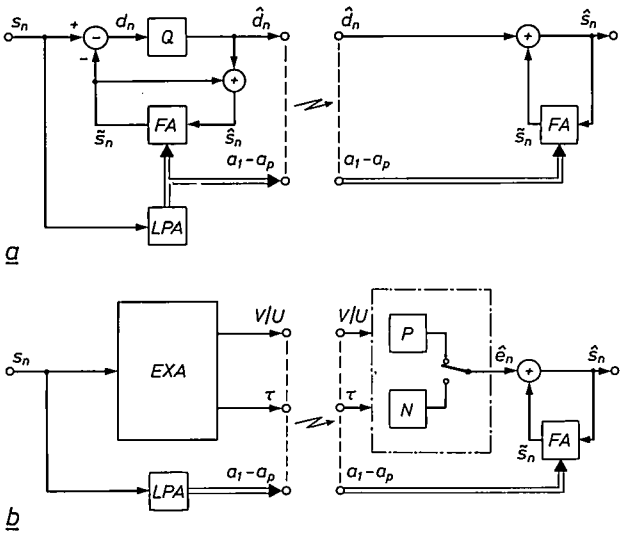

Fig. 27. A comparison of waveform coding by APC (*a*) and parametric coding by LPC (*b*) clearly shows a number of points of correspondence and difference. In both cases analysis on the basis of linear prediction (*LPA*) plays an important part. This gives the coefficients $a_1, \ldots, a_p$ of the predictive filter *FA*. The main difference between the two coding methods is that LPC does not use the residual prediction error ('the residual'), whereas in APC information about this in the form of $\hat{d}_n$ is sent from transmitter to receiver. This is the chief reason why increasing the bit rate will give better quality with APC than with LPC. (For convenience the prediction on the basis of pitch periodicity is not shown explicitly in this diagram of APC; see fig. 17.)

[29] G. J. Bosscha and R. J. Sluyter, DFT-vocoder using harmonic-sieve pitch extraction, Proc. ICASSP 82, Paris 1982, pp. 1952-1955.

[30] J. L. van Meerbergen and F. J. van Wijk, A 2μ NMOS 256-point Discrete Fourier Transform processor, IEEE 1983 Int. Solid-State Circuits Conf., New York 1983, pp. 124-125.

[31] J. Makhoul, Linear prediction: a tutorial review, Proc. IEEE 63, 561-580, 1975.

At the receiving end of an LPC vocoder the coefficients $a_1, \ldots, a_p$ are used for recovering the speech signal $\hat{s}_n$ from the reconstituted excitation signal $\hat{e}_n$. In fig. 27 this is done by including the digital predictive filter *FA* in a feedback loop. It is also possible, however, to derive $\hat{s}_n$ from $\hat{e}_n$ with any other digital-filter configuration that can give the same filter properties. Two examples are shown in *fig. 28b* and *c*. Fig. 28*b* shows a series arrangement of digital resonant circuits with coefficients $b_1, b_2, \ldots, b_q$; this filter is compatible with the formant structure of the speech spectrum (the resonance peaks being equivalent to the formants); see also *fig. 29* [32]. Fig. 28*c* shows a digital lattice filter with coefficients $r_1, r_2, \ldots, r_r$. This filter may be regarded as the electrical model of an acoustic tube with a cross-section that varies in discrete steps, giving a spatial approximation to the human pharynx and mouth cavity (for this reason the coefficients $r_1, \ldots, r_r$ are also referred to as 'reflection coefficients'). The various kinds of filter coefficients can in principle all be converted into one another [15]. There are, however, some important differences. With some types of filter it is much easier to ensure that no instabilities occur than with others. Furthermore, changes in the values of the coefficients (due to quantization or transmission errors) may in some cases lead to much smaller changes in filter properties than in others. For one thing, the lattice filter is far less affected by these anomalies than other types.

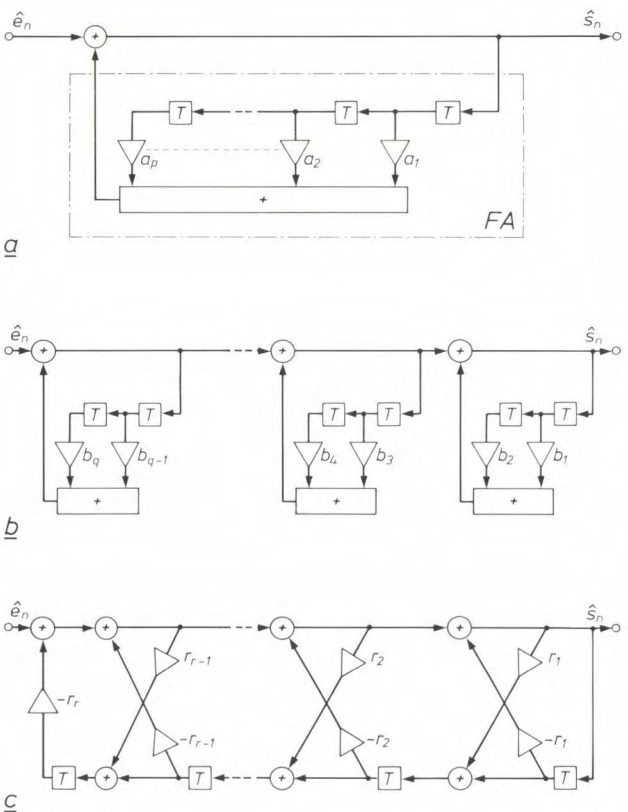

Fig. 28. In the reconstitution of a speech signal $\hat{s}_n$ on the basis of linear prediction a feedback-filter structure in which the prediction coefficients $a_1, \ldots, a_p$ can be recognized immediately is the most obvious configuration (*a*). However, any filter structure that will give the same characteristics can be used. A series arrangement of digital resonant circuits (*b*) or a digital lattice filter (*c*) could also be used. The filter coefficients then have different values but in principle they can always be expressed in terms of the other coefficients.

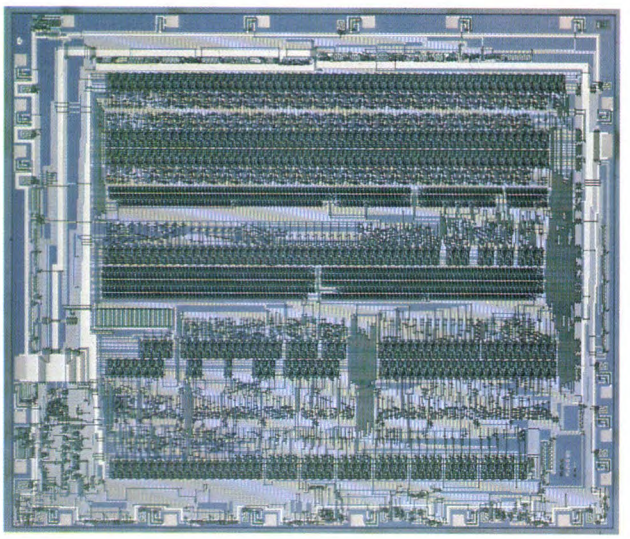

Fig. 29. Type MEA 8000 chip, containing the fully integrated receiving end of an LPC vocoder (or 'voice synthesizer'). The block diagram of this IC corresponds to the right-hand half of fig. 27*b*. The filter *FA* is now in the form of four digital (formant) resonators, whose bandwidth and (for three of the resonators) the centre frequency can be varied. These bandwidths and centre frequencies are reset for each speech segment, as are also the pitch, the signal amplitude and the voiced/unvoiced decision. The speech segments can have a length of 8, 16, 32 or 64 ms, depending on the application. Since the speech parameters for each segment are expressed in 32 bits, this synthesizer can be used for bit rates between 0.5 and 4 kbit/s. The chip is a product of dynamic-NMOS technology and the chip area is about 30 mm^2. It contains 14000 transistors.

Vocoders are preferably used at bit rates below about 5 kbit/s; higher bit rates do not give any significant improvement in speech quality, which always has to be a compromise anyway with vocoders. With careful selection of the number of parameters and the method of quantization, it is possible to use a bit rate of 2.4 kbit/s with relatively little further deterioration in quality. At rates lower than this the quality generally becomes unacceptably poor. An exception to this is the formant vocoder, which will give acceptable results at a bit rate of only 1 kbit/s. Vocoders are particularly suitable for applications in which a low bit rate is a primary requirement. Typical applications include the secure transmission of speech on standard telephone channels and the storage of speech in small digital memories. It has also been found that in certain long-distance radio links the limited vocoder quality obtainable is still preferable to the very mediocre quality obtained with current analog transmission systems.

Hybrid coding

At bit rates below 16 to 20 kbit/s there is a marked deterioration in speech quality with waveform coding. With vocoders, on the other hand, increasing the bit rate to more than 5 kbit/s gives hardly any improvement in quality. This means that there is a transition region (in the neighbourhood of 10 kbit/s) in which a relatively good quality might be achieved with relatively complex hardware [33]. In this transition region important potential applications of speech digitization could arise, such as mobile digital telecommunication networks (for example for mobile automatic telephony). Because of the limited channel space in these applications it is necessary to be very economical with the available bandwidth and hence to use a bit rate no higher than is strictly necessary to give the required quality. The result aimed at can perhaps be achieved with a combination of waveform coding and parametric coding. Interest in this *hybrid coding* has increased considerably in the last few years. Among the many different approaches to be found, two techniques have become fairly general: *noise shaping* and *residual coding*.

In noise shaping the aim is to make optimum use of the noise-masking effect of human hearing (see fig. 5). An example is to be found in *sub-band coding* (*fig. 30*). The speech signal is split into 4 to 16 frequency bands and the signals in each sub-band are separately coded using the method of waveform coding with adaptive quantization (APCM). In this way the signal-to-noise ratio obtained is about the same in each sub-band. Accurate matching of the width of the sub-bands to the characteristics of human hearing leads to the notion of 'critical bands'. With this approach, at a bit rate of 16 kbit/s, it has been possible to achieve a quality not very different from that of a standard telephone signal. A method that bears some resemblance to sub-band coding is *Adaptive Transform Coding* (ATC), in which the speech signal s_n is first subjected to a frequency transformation, and the transformation results are then adaptively coded as efficiently as possible. There are several modifications of this type of coding, some of them highly complex. Good results have been achieved at bit rates of about 16 kbit/s.

The principle of residual coding is based on the observation that the quality of LPC vocoders is limited, even when the permitted bit rate is increased, by the nature of the synthetic excitation signal $\hat{e}_n$ (fig. 27*b*). Efforts were initially made to replace the information about pitch and the voiced/unvoiced decision by a signal consisting of a narrow frequency sub-band of the original speech signal s_n. From this, by means of nonlinear operations such as rectification or squaring, a 'broadband' excitation signal was derived as a substitute for $\hat{e}_n$. These *voice-excitation* systems, as they are called, did not however produce any great improvements. Better results can be achieved by determining, at the transmitting end, the 'residual error' that occurs with linear prediction and by deriving from this an excitation signal for the receiver.

In effect this is a step in the direction of differential waveform coding, because in APC for example (fig. 27*a*) the residual signal is sent from transmitter to receiver practically unchanged, except for the quantization.

With this form of coding a distinction can be made between systems with a feedforward structure and systems with a feedback structure. An example of both is given in *fig. 31*. In the system shown in fig. 31*a* there is no feedback at the transmitting end. From the residual signal d_n a signal f_n is derived that can be transmitted at a lower bit rate than d_n. At the receiving end f_n is converted into an excitation signal $\hat{f}_n$ [34]. In these *residual-excited* systems, nonlinear operations of the same type as for the voice excitation mentioned earlier can be used. A more complex system of residual coding is given in fig. 31*b*. This shows a feedback system for the transmitter in which *analysis by synthesis* takes place. In the excitation generator *EG* the signal g_n is made such that after synthesis (in the transmitter) of $\hat{s}_n$ from g_n the signal $d_n = s_n - \hat{s}_n$ is kept as small as possible in accordance with some kind of criterion. This criterion can be based on the sum of all existing knowledge about human hearing, such as the noise-

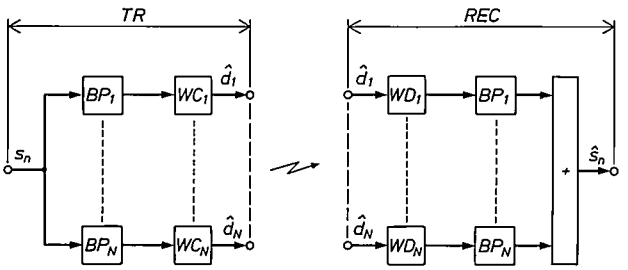

Fig. 30. One of the most direct forms of hybrid coding is *sub-band coding*. At the transmitting end the speech signal is split up into individual sub-bands by means of a number of bandpass filters $BP_1, \ldots, BP_N$. Each of the resulting signals is separately coded in a waveform coder $WC_1, \ldots, WC_N$. The receiver consists in principle of the corresponding waveform decoders $WD_1, \ldots, WD_N$ and bandpass filters $BP_1, \ldots, BP_N$ similar to the ones in the transmitter. These filter out as much as possible of the quantization noise in each branch. Virtually optimum *noise shaping* can be achieved by coding wih adaptive quantization.

[32] H. E. van Brück and D. J. A. Teuling, Integrated voice synthesiser, Electronic Components & Appl. 4, 72-79, 1982.
[33] See for example: Special issue on bit rate reduction and speech interpolation, IEEE Trans. **COM-30**, 565-814, 1982.
[34] R. J. Sluyter, G. J. Bosscha and H. M. P. T. Schmitz, A 9.6 kbit/s speech coder for mobile radio applications, Conf. Rec. ICC '84, Amsterdam 1984, pp. 1159-1162.

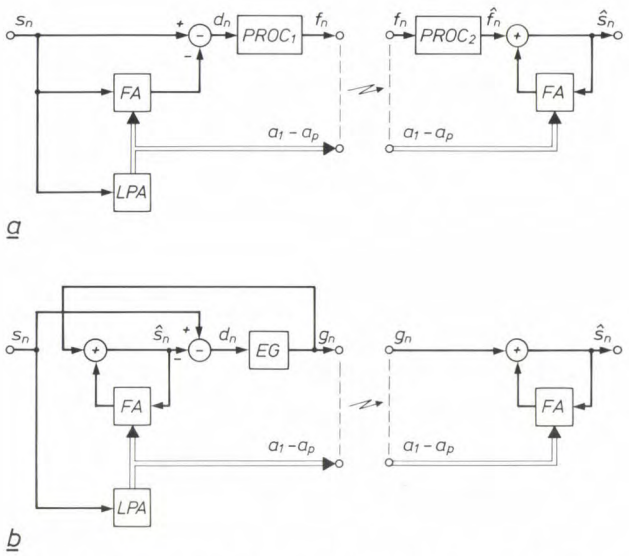

Fig. 31. Two more complex forms of hybrid coding, both based on *residual coding*. *a*) Feedforward configuration: a signal f_n that contains the most important information about the residual signal d_n but can be transmitted at a lower bit rate is derived from d_n in the processor $PROC_1$. At the receiving end an excitation signal $\hat{f}_n$ is derived from f_n in the processor $PROC_2$; nonlinear operations and sampling-rate conversion are often used here. *b*) Feedback configuration. At the transmitting end an optimum excitation signal g_n for the receiver is calculated for a given bit rate in the excitation generator *EG*. This is done by determining which signal g_n gives the best possible reconstituted speech signal $\hat{s}_n$. This is usually referred to as *analysis by synthesis*.

masking effect mentioned earlier. In a recently published application of this principle g_n consists of a pulse train in which several pulses occur at different intervals during each pitch period. This system is referred to as *multipulse-excited LPC* [35].

Both systems in fig. 31 can be expanded by including special coding and decoding circuits designed to transmit the signals f_n and g_n, coded by refined methods, as efficiently as possible from transmitter to receiver. Now that specialized processors are available for digital signal processing, much greater complexity of processing is acceptable in practice. There has been considerable recent interest in modern methods [36] such as *tree coding*, *trellis coding* and *codebook coding* or *vector quantization*, and these are also of interest for residual coding.

With residual coding acceptable speech quality can nowadays be achieved at about 10 kbit/s. However, it seems likely that there will be further improvement in the results that can be obtained with hybrid coding.

Signal-processing hardware

The oldest electronic equipment for speech coding, such as Dudley's Vocoder (see fig. 2) and the first PCM hardware, was relatively bulky, to such an extent that some sceptics initially doubted the practicality of these techniques. However, developments in semiconductors and especially in microelectronics brought a radical change in this situation [37], especially for waveform coding. Various circuits for PCM and DM are now available in integrated form. As an example *fig. 32* shows an IC that can be used as a transmitter or receiver in a PCM link [38]. For long-distance telephone links the logPCM system with a bit rate of 64 kbit/s has been standardized. There is however a very distinct trend in this application [39][40] toward the future use of a bit rate of 32 kbit/s with DPCM comprising both adaptive quantization and adaptive short-term prediction, referred to as ADPCM-AP (see p. 211). With this system the transmission capacity can be doubled without degrading the speech quality. Also under investigation is the possibility of achieving a much better speech quality with the bit rate of 64 kbit/s, for example a frequency band of 0-7 kHz. This would be an improvement in applications such as the loudspeaking telephone.

For parametric coding and hybrid coding very active development in signal-processing equipment continues. These coding methods require large numbers of digital operations per unit time [41]. A distinction can be made here between strongly structured operations ('vector operations') and ones that are less structured ('spaghetti operations'). The latter category includes many control functions, whereas the repeated calculation of a sum of a large number of products belongs to the first category. This distinction can have a bearing on the design of a speech-coding system, since the designer is faced with the choice between

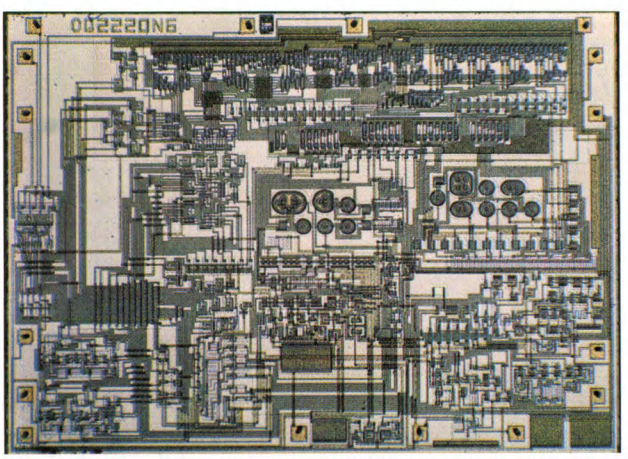

Fig. 32. Type OQ 2220 chip capable of performing the functions of two complete PCM codecs with a bit rate of 64 kbit/s. In this circuit two analog speech signals are simultaneously digitized by an internationally standardized type of logPCM ('*A*-law PCM'). Meanwhile two incoming digital speech signals are converted into the corresponding analog speech signals. This chip is primarily designed for use in certain multiplex telecommunication links. It is fabricated in I^2L technology, has an area of about 20 mm^2 and contains about 1000 transistors.

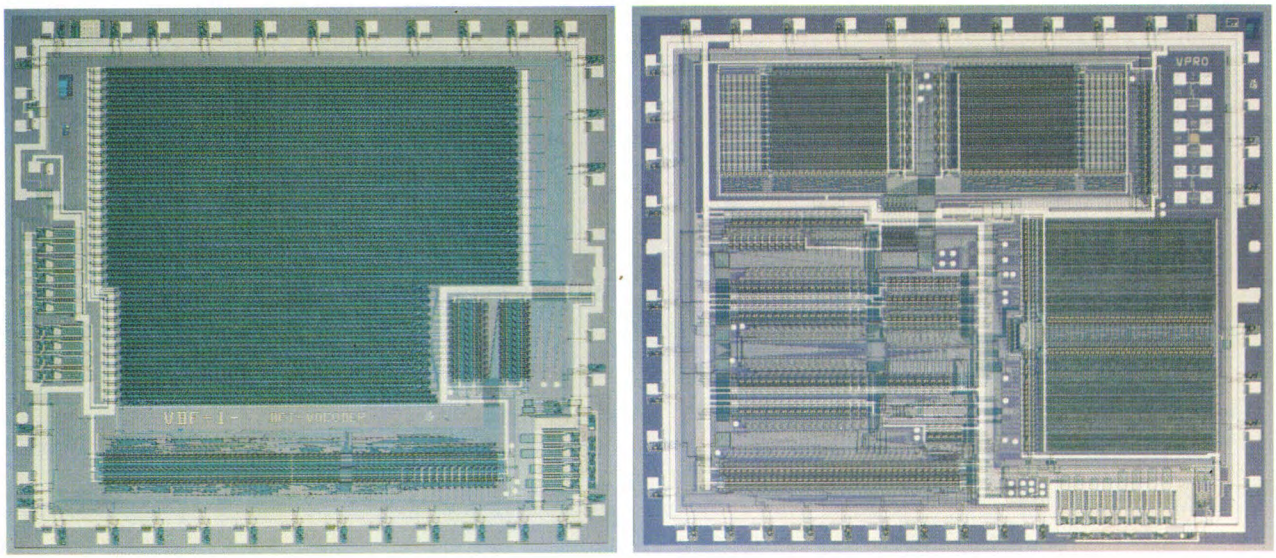

a *b*

Fig. 33. Two 'custom' ICs. The chips are fabricated in dynamic-NMOS technology, and can be used as modules in complex speech-processing systems. *a*) Digital segmentation buffer in which the continuous bit stream of a straightforwardly digitized speech signal can be divided into segments suitable for further processing. The chip has an area of about 39 mm^2 and contains 46 000 transistors. *b*) Programmable processor capable of performing a wide variety of operations, including the control of the segmentation buffer and the DFT chip in fig. 25. This processor has a chip area of about 46.5 mm^2 and contains about 35 000 transistors.

general-purpose ICs, such as microprocessors, and 'custom ICs', built for specific applications. The general-purpose ICs are attractive because of their versatility: different systems can be made with the same type of IC and it is usually a fairly simple matter to make modifications. A drawback, however, is the limited effectiveness with which the operations can be performed. This is largely because the vector operations mentioned earlier require many multiplications, which take a long time in standard microprocessors.

Many speech-digitizing systems require cross-correlation, autocorrelation, convolution and signal-transformation operations (such as the DFT mentioned earlier, and the 'cosine transform'). All these operations have the form:

$$w = \sum_i x_i y_i,$$

that is to say the result w is obtained as a large sum of products $x_i y_i$. This operation can be efficiently performed with a special type of processor known as the 'product accumulator' [42]. In this device the products are not calculated separately first, but the calculations overlap each other. Present-day microprocessors, however, do not have a separate multiplier (for the efficient calculation of individual products), let alone a product accumulator.

When a designer seeks the ultimate in aspects such as maximum processing rate, minimum chip area and minimum power consumption, he will generally prefer custom ICs. By building his design from a coherent family of devices he can then achieve a reasonable degree of flexibility. An example is to be seen in *fig. 33* in combination with fig. 25 [43]. Fig. 33*a* shows a digital buffer for splitting a speech signal into segments, and fig. 33*b* shows a digital processor suitable for a variety of spaghetti operations. Fig. 25 presents an IC for DFT of speech segments. The chips in fig. 25 and fig. 33 can be used to build a pitch detector that applies the harmonic-sieve method. The segmentation buffer and the DFT-IC are also used in spectral analysis for automatic word recognition [44].

[35] B. S. Atal and J. R. Remde, A new model of LPC excitation for producing natural-sounding speech at low bit rates, Proc. ICASSP 82, Paris 1982, pp. 614-617.

[36] H. G. Fehn and P. Noll, Multipath search coding of stationary signals with applications to speech, IEEE Trans. **COM-30**, 687-701, 1982.

[37] See for example: Joint special issue on integrated circuits for speech, IEEE Trans. **ASSP-31**, 249-346, 1983 (also published in IEEE J. **SC-18**, 1-99, 1983).

[38] A. Rijbroek and J. Drupsteen, Higher-order PCM multiplex systems, Philips Telecommun. Rev. **38**, 11-22, 1980.

[39] X. Maitre and T. Aoyama, Speech coding activities within CCITT: status and trends, Proc. ICASSP 82, Paris 1982, pp. 954-959.

[40] P. Noll, Trends in speech coding, in: H. W. Schüssler (ed.), Signal processing II: theories and applications (Proc. EUSIPCO-83, Erlangen 1983), North-Holland, Amsterdam 1983, pp. 363-370.

[41] R. W. Schafer and L. R. Rabiner, Digital representations of speech signals, Proc. IEEE **63**, 662-677, 1975.

[42] N. F. Benschop and L. C. M. Pfennings, Compact NMOS array multipliers with inverting full-adders, Philips J. Res. **36**, 173-194, 1981.

[43] P. Zuidweg, J. L. van Meerbergen and M. L. van der Meulen, Custom LSI chip-set for speech analysis, ICASSP 82, Paris 1982, pp. 521-524.

[44] R. Geppert and P. Schwartau, A DFT-based front-end for word recognition systems, Proc. ICASSP 84, San Diego, CA, 1984, pp. 44.14.1-44.14.4.

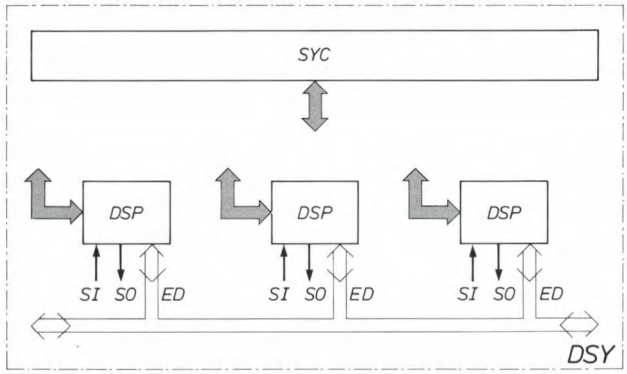

Fig. 34. With a parallel configuration of integrated digital signal processors *DSP* it is possible to build a complex digital system *DSY* as a compact unit. The *DSP*s communicate with one another via their external data bus *ED*, which carries data words (8 bits or 16 bits) in parallel. The 'traffic control' required here is one of the main tasks of the system control *SYC*. Usually each *DSP* has a series input *SI* and a series output *SO* for signal exchanges with devices such as external analog-to-digital and digital-to-analog converters.

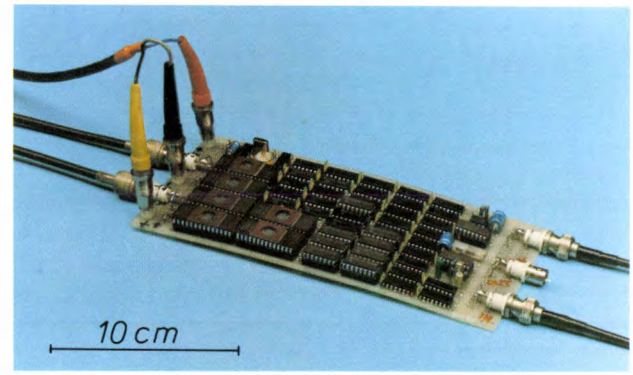

Fig. 35. Laboratory model of a complete speech-digitization system in the form of two parallel configurations of integrated DSPs. Altogether six DSPs of the type NEC μPD7720 are used (four for the transmitter and two for the receiver; on the left in the photograph). The other components serve primarily for controlling communication between the DSPs and for analog-to-digital conversion, digital-to-analog conversion and for generating the appropriate clock signals. The analog input of the transmitter and the analog output of the receiver are on the right; the digital output of the transmitter, the digital input of the receiver and three connections (upright) for the supply voltages are on the left. In this circuit the speech digitization is by residual coding in a feedforward system, using 16th-order LPC. The digitized speech signal has a bit rate of 9.6 kbit/s.

Initially efforts were made to increase the signal-processing capability of standard microprocessors by adding an external multiplier circuit. Recently it has become possible to accomodate a multiplier on the same chip. Through the addition of memory, both RAM (random-access memory) and ROM (read-only memory), and by giving special attention to the signal exchange between the different components (via the signal bus or data bus) a new type of IC has been produced that is well suited to digital signal operations and is known as a *digital signal processor* (DSP). The combination of a number of these DSPs in a parallel structure (*fig. 34*) enables highly complex speech-digitization systems to be built in a very compact form. In the design phase of such systems a number of specific questions have to be answered. How, for example, should the relevant algorithms be distributed among the different processors? And how should the communication between the processors take place? For this communication a common external data bus is used. However, this can only handle one 'message' at a time. In some way or another provision must be made for controlling the traffic. This is a system-con-

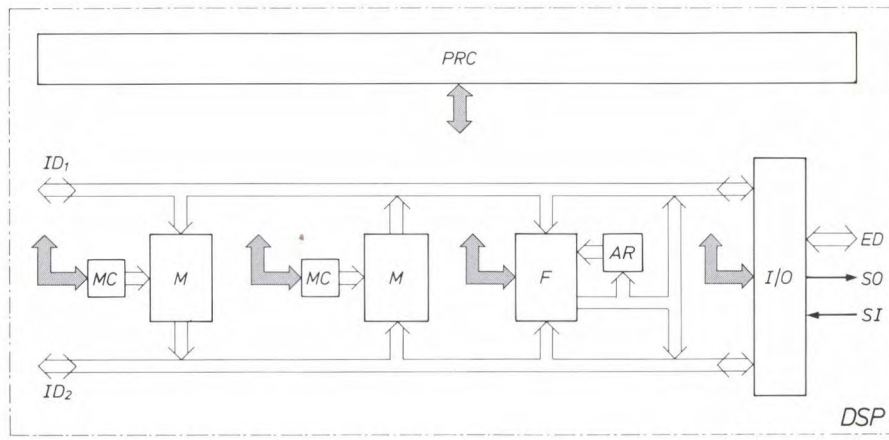

Fig. 36. Basic diagram of an advanced integrated digital signal processor *DSP*. The extensive use of parallelism gives greatly increased performance. Data transfer is highly efficient because there are *two* internal data buses ID_1 and ID_2. Unnecessary occupation of the internal data buses is avoided and the range of possibilities for parallel operation is increased by providing the memories *M* with their own memory controls *MC* and by providing functional blocks (multiplier, arithmetic unit) *F* with their own auxiliary registers *AR*. The external data bus *ED*, the series input *SI* and the series output *SO* are connected with the internal data buses via the input/output logic *I/O*. The total operation of the *DSP* is controlled by the processor control *PRC*.

trol task that can be accomodated, as a kind of traffic policeman, in a separate microprocessor called the 'bus master'. Another possibility consists in providing each DSP with an identical quantity of control logic, which controls the traffic between the DSPs on a 'democratic basis'. This approach has been adopted for the system shown in *fig. 35*. Here there are six digital signal processors (four for the transmitter and two for the receiver) to make a laboratory model of a complete speech-digitization system for 9.6 kbit/s, based on residual coding with a feedforward structure (fig. 31*a*).

The traffic density on the external bus in a parallel configuration of signal processors depends on the extent to which the processors are capable of independent operation. To avoid overloading in speech digitization it is therefore important to ensure that each processor has sufficient memory capacity to store at least one complete speech segment (e.g. 256 signal samples of 8 bits).

The strategies mentioned above, associated with the parallel use of DSPs, can be used to improve the internal structure of a DSP and hence increase its performance. Once again the keyword is 'parallelism'. This is applied both in the signal transport and in the manner in which the different operations are executed. The first leads to the introduction of a double internal data bus and the second to giving the maximum possible independence to the memory devices (ROM, RAM) and to the functional devices (multiplier, arithmetic unit). The independence is achieved by using separate memory controls and auxiliary registers. The block diagram of a DSP designed on these lines is shown in *fig. 36*. DSPs based on these new principles will be commercially available in the not too distant future.

Further developments in this field are expected. It would not be going too far to predict that a complete LPC vocoder (for a bit rate of say 2.4 kbit/s) will soon be available on a single chip. It seems fairly obvious that more applications will follow as the speech digitizing hardware becomes even more compact. The eventual outcome of these developments is still a matter for speculation.

Summary. There are many and various methods by which an analog speech signal can be converted into a digital signal at bit rates varying from about 1 to 100 kbit/s. Two important quantities here are the speech quality obtained and the complexity of the hardware required. A distinction is made between waveform coding, which will give good quality with relatively simple hardware at high bit rates, and parametric coding (using 'vocoders'), which will give moderate quality with complex hardware at low bit rates. In between (at about 10 kbit/s) is the area of hybrid coding in which interesting developments have been taking place in the last few years. With the increasing capabilities of integrated digital circuits for signal processing, hardware of greater complexity becomes acceptable. This will enable speech digitization to play an increasingly important part in human communications and in communications between man and machine. The article reviews the background to this development, the most common methods and the results achieved with speech digitization to the present day.

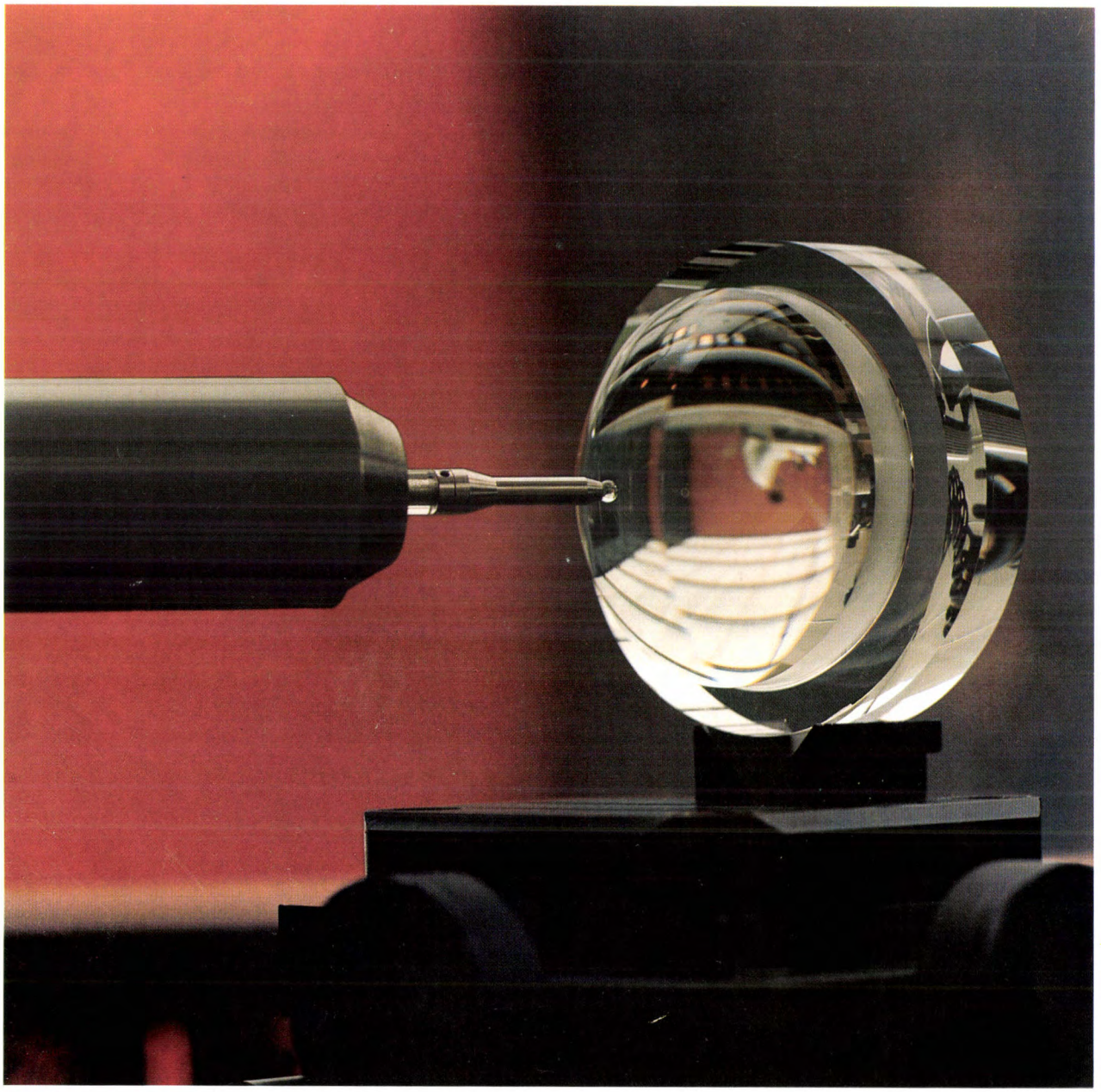

Inspecting the shape of lens surfaces

Complex lens systems are nowadays often replaced by a single lens with surfaces that are not spherical but aspheric. In lenses of this type the shape of the aspheric surfaces has to meet very exacting design specifications. Errors of only a tenth of a wavelength may be enough to cause distortion. At Philips Research Laboratories in Eindhoven an instrument [1] has been developed for inspecting these surfaces to an extremely high accuracy by means of a special measuring probe.

The photograph shows the probe resting against a lens under inspection. Information about the shape is obtained by rotating the lens about a vertical axis and measuring the displacement of the probe. The measuring error is about 10 nm. The plastic lens shown here (diameter 50 mm) is produced with the aid of the COLATH high-precision lathe [2].

[1] J. G. Dil, W. Mesman and J. C. Driessen, Proc. SPIE **235**, 85-90, 1980.
[2] T. G. Gijsbers, Philips Tech. Rev. **39**, 229-244, 1980.

Thin-film reflection filters

H. Köstlin and G. Frank

A great deal of attention is being paid to the economical use of energy today. Ways and means of minimizing energy losses are being carefully investigated everywhere. When energy is used in the form of visible light a substantial loss can arise from the generation of infrared radiation (heat radiation). A typical example is the incandescent lamp, in which most of the electrical energy supplied is lost as heat radiation. It has long been known that these losses can be reduced by using heat-reflecting filters. Filters that combine strong infrared reflection with good transmission of visible light consist of thin films deposited on glass. Various materials can be used for these films. A number of such filters are described in the article below, which deals with their manufacture, physical operation, optimization, characteristics and applications.

Introduction

Many optical applications require filters that reflect radiation in a particular wavelength range while transmitting it in another. The requirements to be met by a filter can be characterized by using spectral weighting functions for the reflected and transmitted radiation. The quality of a filter is determined by the weighted means of its spectral characteristics, i.e. the effective reflectance and transmittance. In designing a filter the aim is to achieve maximum effective reflectance in a certain wavelength range and maximum effective transmittance in another.

There is particular interest in filters that can function as transparent heat reflectors. These give high reflectance in the infrared (> 0.7 μm), which is the spectral range for heat radiation, but readily pass visible radiation (0.4-0.7 μm). The weighting function for the reflectance in this case is the spectral energy distribution of the incident infrared radiation, which is often approximately equal to the Planck distribution of a black-body radiator (e.g. heat radiation at 3000 K) in the infrared, while the weighting function for the transmittance is determined by the spectral-luminous-efficiency curve or the spectral energy distribution of the incident visible radiation or both; see *fig. 1*. The broad reflection and transmission bands required can be obtained with various types of filter. *Fig. 2* gives a plot of the reflectance R against wavelength for these types of filter. Since filters with low absorptance are generally used, the spectral transmittance does not differ much from $1 - R$. The differences between the reflection spectra are attributable to differences in the composition and physical operation of the different types of filter.

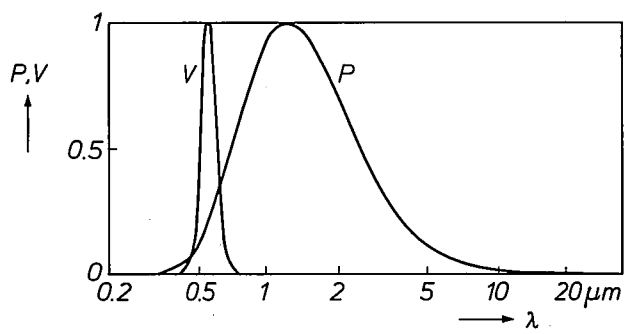

Fig. 1. Example of a spectral energy distribution in which the infrared is to be reflected and the visible light transmitted. The relative radiant energy P of a black body at 3000 K is plotted as a function of wavelength λ (on a logarithmic scale). The relative spectral luminous efficiency V is also shown as a function of λ.

Dr H. Köstlin and G. Frank are with Philips GmbH Forschungslaboratorium Aachen, Aachen, West Germany.

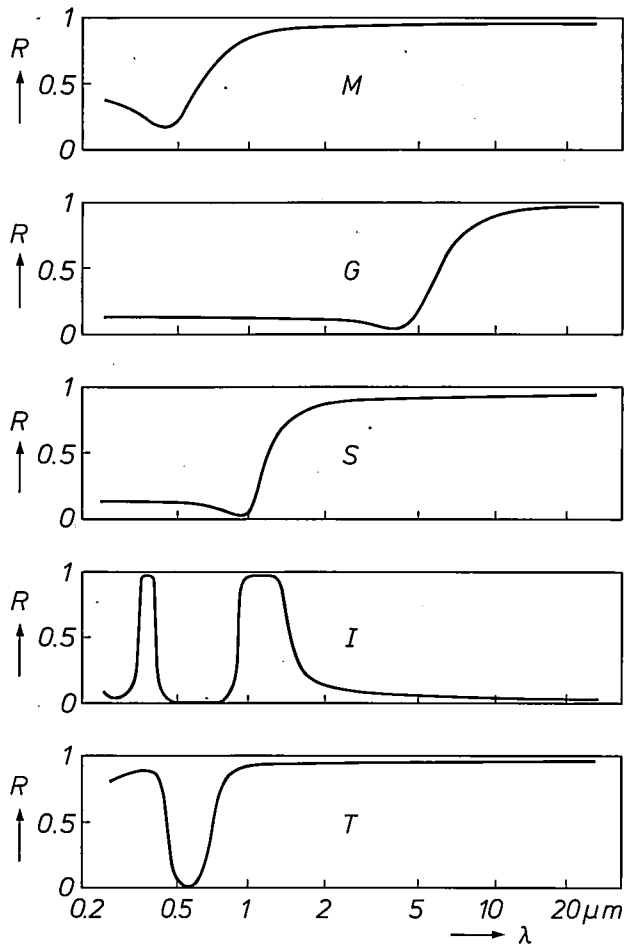

Fig. 2. Schematic plot of reflectance R against wavelength (logarithmic scale) for a metal film M, a metal mesh G, a semiconductor filter S, an interference filter I, and a metal filter with induced transmission T.

Filters consisting of a thin film of copper or gold give strong infrared reflection because of the presence of free charge carriers. At shorter wavelengths the reflectance decreases. The charge-carrier concentration and inter-band transitions determine the transition from high to low reflectance. For copper and gold this transition lies at the boundary between the infrared and the visible wavelength ranges. These metals are therefore often used as heat-reflecting filters on windows in houses and trains. Since such filters are to some extent reflectors and absorbers of visible light, however, they are less suitable for applications requiring maximum transmission of visible light, as in light sources [1].

Metal-mesh filters [2] with a technically feasible mesh-width of about 10 μm have a high-to-low reflectance transition that is too far into the infrared wavelength range for most practical applications.

A high infrared reflectance can also be obtained with a semiconductor film instead of a metal, provided the semiconductor is strongly doped to give a large number of free charge carriers. If the band gap of the semiconductor is sufficiently large and the film is not too thick, good transmission of visible light is possible. Suitable semiconductor materials include stannic oxide (SnO_2) and indium oxide (In_2O_3). Earlier articles in this journal described the use of SnO_2 filters in low-pressure sodium lamps [1][3] and of In_2O_3 filters in low-pressure sodium lamps [4] and in the form of coatings on the inner sides of double-glazed windows [5].

Another possibility is to use interference filters. These consist of a number of dielectric films that give little or no absorption and have alternate high and low refractive indices. Typical materials for such filters are zinc sulphide (ZnS) and silicon dioxide (SiO_2). The thickness of each film and the number of films can be chosen in such a way that a great deal of the infrared radiation is strongly reflected, while most of the visible light is transmitted [6].

The 'induced transmission' that occurs in metal films when anti-reflection films are used is also based on the interference effect. Anti-reflection films can be used to reduce the unwanted high reflectance of a metal film in the visible wavelength region to an acceptable value. This induced transmission can be obtained with a silver film coated on both sides by a layer of ZnS [7].

In this article we shall deal in some detail with the design and manufacture of filters mainly intended for use with light sources. We shall consider in turn filters consisting of a strongly doped semiconductor film, interference filters and filters consisting of a metal film with induced transmission.

Semiconductor filters

A semiconductor film that is to be used as a transparent heat-reflecting filter has to meet some difficult requirements. On the one hand, to achieve strong infrared reflection the concentration of free charge carriers must be high and the film sufficiently thick. On the other hand the semiconductor should have a large band gap and the film must be thin enough to transmit visible light satisfactorily. Relatively few semiconductors can meet all these requirements. The most suitable ones are SnO_2 and In_2O_3. These can be strongly doped to give materials that are good electrical conductors (n-type), with a conductivity up to about $7 \times 10^3\ \Omega^{-1}\,cm^{-1}$.

Thin films of SnO_2 and In_2O_3 can be made in various ways. The best results are obtained by deposition on a hot glass substrate (> 400 °C) from a chemically reactive gas mixture (chemical vapour deposition, CVD)

or from an aerosol (spray pyrolysis) [8]. The basic ingredients are usually chlorides of tin and indium. The preferred dopants are fluorine for SnO_2 and tin for In_2O_3. If too much oxygen is incorporated during the deposition of the films, this can later cause a reduction in the electrical conductivity and deterioration of the optical properties. To remove the surplus oxygen the films are usually baked in a weakly reducing atmosphere until the conductivity reaches a maximum [9].

Fig. 3 shows the reflectance and transmittance as a function of wavelength for a fluorine-doped SnO_2 film and two tin-doped In_2O_3 films, all three about 0.3 μm thick. The infrared reflectance of these films reaches values above 80%, while the transmittance in the visible wavelength range approximates to that of the glass substrate. The maxima and minima in the curves are the result of interference in the thin films. An increase in the concentration of charge carriers gives a higher reflectance in the infrared and also shifts the transition between low and high reflectance towards shorter wavelengths. At about the same charge-carrier concentrations the infrared reflectance of In_2O_3:Sn is a little higher than that of SnO_2:F.

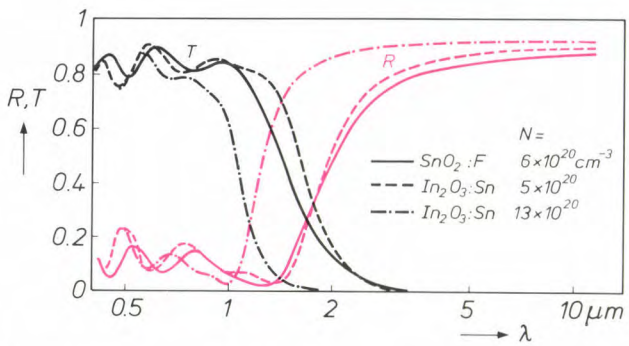

Fig. 3. Reflectance R(*red*) and transmittance T as a function of wavelength λ (logarithmic scale) for 0.3-μm films of SnO_2:F and In_2O_3:Sn on glass. The films have different carrier concentrations N. The most strongly doped In_2O_3 film gives the strongest infrared reflection with the transition from low to high reflectance at the shortest wavelength.

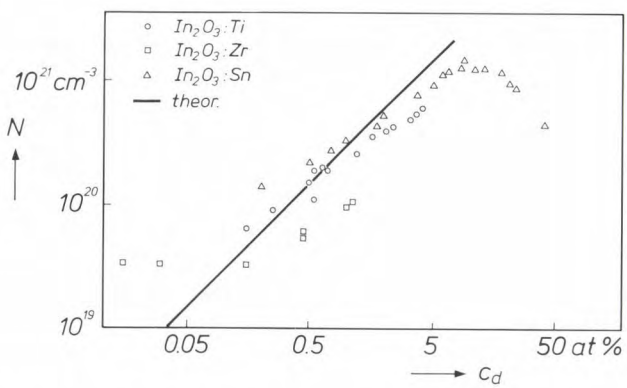

Fig. 4. Carrier concentration N as a function of doping level c_d of In_2O_3 films, doped with titanium, zirconium and tin. The continuous line corresponds to the delivery of one free electron per donor atom. For not unduly high and low values of c_d reasonably good agreement is found for the different doping levels.

The charge-carrier concentration depends on the material and the doping level [10]. In *fig. 4* the experimental values of the carrier concentration N are plotted against the doping level of In_2O_3 films, doped with the tetravalent metals titanium, zirconium and tin. The values correspond reasonably well to the straight line that would be expected if each donor atom supplied one free electron. Doping with titanium or zirconium appears to be rather less effective than with tin. At the highest value of N, about 15×10^{20} cm^{-3}, about 5% of the cation sites in In_2O_3 are occupied by tin atoms. With very weak doping the presence of charge carriers is mainly due to the presence of oxygen vacancies created during the reducing heat treatment. The drop in N at high Sn contents may be attributed to the formation of neutral pairs and clusters [9][11]. This prevents N from becoming higher than about 15×10^{20} cm^{-3}. With SnO_2 maximum values of only about 7×10^{20} cm^{-3} have been reached [12].

Another important quantity that affects the quality of a semiconductor filter is the d.c. mobility μ of the charge carriers. This determines the steepness of the reflectance and transmittance curves in the transition region (fig. 3). In *fig. 5* the measured mobility is plotted as a function of N for SnO_2 films doped with fluorine, and for In_2O_3 films doped with titanium, zirconium and tin. We have also shown the line calculated on the assumption that the mobility depends entirely on the scattering of electrons from ionized donor atoms [13]. The experimental results for the different doping levels in In_2O_3 films are in reasonable

[1] See for example E. Kauer, Philips Tech. Rev. **26**, 33-47, 1965.
[2] R. Ulrich, T. J. Bridges and M. A. Pollack, Appl. Opt. **9**, 2511-2516, 1970.
[3] R. Groth and E. Kauer, Philips Tech. Rev. **26**, 105-111, 1965.
[4] H. J. J. van Boort and R. Groth, Philips Tech. Rev. **29**, 17-18, 1968.
[5] H. Köstlin, Philips Tech. Rev. **34**, 242-243, 1974.
[6] See for example H. Koch, Feingerätetechnik **14**, 50-60, 1965; H. K. Pulker, Thin Solid Films **77**, 203-212, 1981.
[7] See for example M. M. Koltun and Sh. A. Faiziev, Sov. J. Opt. Technol. **42**, 397-398, 1975; H.-J. Gläser, Glass Technol. **21**, 254-261, 1980.
[8] The CVD method for other materials has been described in an earlier article in this journal by P. J. M. van der Straten and G. Verspui, Philips Tech. Rev. **40**, 204-210, 1982 and by J. Bloem and W. A. P. Claassen, Philips Tech. Rev. **41**, 60-69, 1983/84. Spray pyrolysis for SnO_2 and In_2O_3 films is also described in the articles of notes [3] and [4].
[9] G. Frank and H. Köstlin, Appl. Phys. A **27**, 197-206, 1982.
[10] G. Frank, E. Kauer, H. Köstlin and F. J. Schmitte, Proc. SPIE **324**, 58-66, 1982.
[11] H. Köstlin, R. Jost and W. Lems, Phys. Stat. Sol. a **29**, 87-93, 1975.
[12] P. Grosse, F. J. Schmitte, G. Frank and H. Köstlin, Thin Solid Films **90**, 309-315, 1982.
[13] E. Gerlach and P. Grosse, Festkörperprobl. **17**, 157-193, 1977.

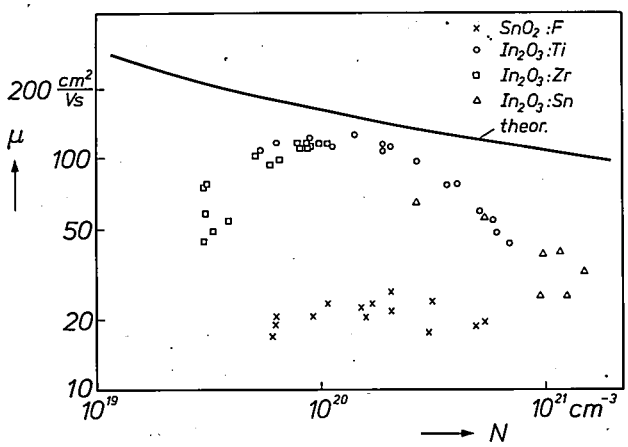

Fig. 5. Mobility μ as a function of the concentration N of the free charge carriers in SnO_2:F and In_2O_3 films doped with titanium, zirconium and tin. The continuous line was calculated for electron scattering from ionized donor atoms. With In_2O_3 films the measured points are much closer to this line than with SnO_2 films. The effect of the dopant is less marked.

agreement with each other. If the concentrations are not unduly low, they show the expected decrease of μ with increasing N. For SnO_2 films, on the other hand, μ hardly appears to depend on N at all, and most values of μ are much too low. The discrepancies found and the very adverse effect of oxygen on the mobility are probably the consequence of incidental scattering from neutral defects and grain boundaries.

Theory

The spectral reflectance and transmittance of a semiconductor filter are determined by the complex refractive index and the film thickness. The complex refractive index $\tilde{n}$ is equal to $n - jk$, where n is the real part of the refractive index, j is the imaginary unit ($= \sqrt{-1}$) and k is related to the absorption coefficient α at the wavelength λ by the expression $\alpha = 4\pi k/\lambda$. The effect of free charge carriers at a concentration N in a lattice of permittivity ε_1 can be described to a first approximation by the dispersion relations between n, k and the angular frequency ω of the incident radiation [14]:

$$n^2 - k^2 = \varepsilon_1 - \frac{Ne^2}{m^* \varepsilon_0(\omega^2 + \gamma^2)}, \qquad (1)$$

$$2nk = \frac{\gamma Ne^2}{m^* \varepsilon_0 \omega(\omega^2 + \gamma^2)}, \qquad (2)$$

where e is the electronic charge, ε_0 the permittivity of free space and γ the damping rate $e/\mu m^*$, where μ is the mobility and m^* the effective mass of the charge carriers. If the various constants of the material are known, n and k can be calculated from these equations. The reflectance R for radiation at normal incidence can be calculated from the well-known expression

$$R = \frac{(n-1)^2 + k^2}{(n+1)^2 + k^2}. \qquad (3)$$

It follows from the dispersion relations that the optical properties change radically when $n = k$. The angular frequency at which this occurs is called the plasma frequency ω_p; from eq. (1) it is equal to:

$$\omega_p = \left(\frac{Ne^2}{\varepsilon_0 \varepsilon_1 m^*} - \gamma^2 \right)^{1/2}. \qquad (4)$$

The plasma wavelength λ_p is given by $2\pi c_0/\omega_p$, where c_0 is the velocity of light in free space. At $\lambda > \lambda_p$ the film gives a metal-like reflection, whereas at $\lambda < \lambda_p$ the film behaves like a high-transmittance dielectric. In the materials considered here, which have an abrupt transition from high to low reflectance, the mobility of the charge carriers is so large that γ^2 in eq. (4) can be neglected. This implies that the plasma wavelength depends only on the carrier concentration:

$$\lambda_p \approx \frac{2\pi c_0}{e} \left(\frac{\varepsilon_0 \varepsilon_1 m^*}{N} \right)^{1/2}. \qquad (5)$$

In *fig. 6* λ_p^{-2} is plotted against N for a number of In_2O_3:Sn films. A straight line corresponding to eq. (5) is obtained. If $\varepsilon_1 = 4$, which is a reasonable value for undoped material in the optical range, the value of the slope indicates that m^* is approximately equal to 0.35 times the rest mass of the electron.

At very long wavelengths, with the film thickness much smaller than λ and ω much smaller than γ, the reflectance does not depend on the wavelength of the incident radiation. The reflectance can then be derived from the surface impedance Z of the film and the characteristic impedance Z_0 of free space [15]:

$$R = \left(\frac{Z - Z_0}{Z + Z_0} \right)^2. \qquad (6)$$

The impedance of free space is given by $1/\varepsilon_0 c_0$ ($= 377\ \Omega$). The surface impedance at long wavelengths is determined by the surface resistivity (or sheet resistance) of the film, in parallel with the impedance of the background. The surface resistivity is equal to ϱ/d, where ϱ is the resistivity ($= 1/Ne\mu$) and d is the thickness of the film. If the background impedance is equal to the foreground impedance $1/\varepsilon_0 c_0$, the reflectance is given by

$$R = (1 + 2\varepsilon_0 c_0 \varrho/d)^{-2}. \qquad (7)$$

We determined the relation between the reflectance and the surface resistivity experimentally by measuring the thermal radiation $(1 - R)$ at 80 °C for films of different surface resistivities. The results obtained

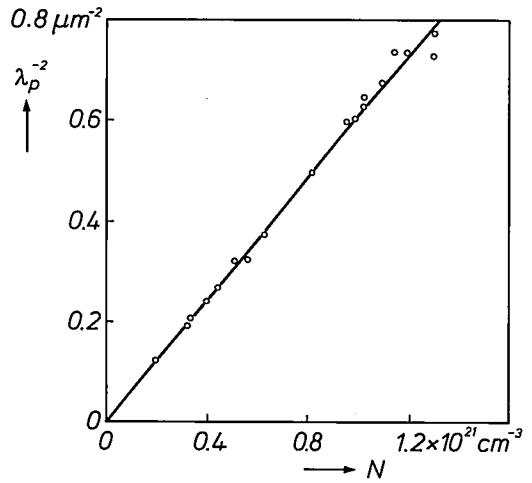

Fig. 6. Reciprocal of the square of the plasma wavelength λ_p, plotted against the carrier concentration N for In_2O_3:Sn films. The straight line through the points corresponds to equation (5).

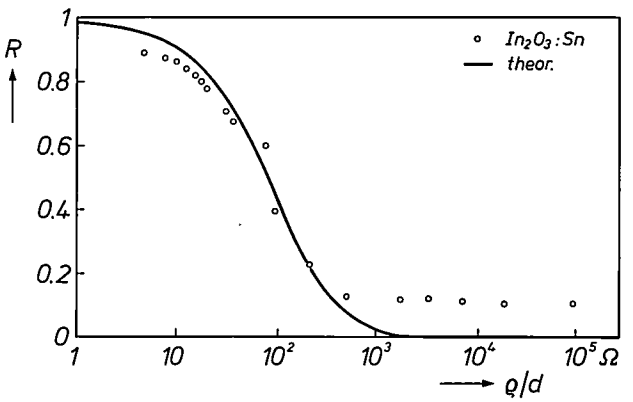

Fig. 7. Reflectance R for heat radiation at 80 °C, plotted against the surface resistivity (or sheet resistance) ϱ/d (logarithmic scale) of In_2O_3:Sn layers. The various values of surface resistivity are due to variations in the film thickness and the carrier concentration. The continuous curve was calculated from eq. (7). Reasonably good agreement is found in a wide range of surface resistivities.

with In_2O_3:Sn films on glass are presented in *fig. 7*. In a wide range of surface resistivities the experimental values for the reflectance agree reasonably well with eq. (7). At very high surface resistivities only the radiation from the glass substrate is measured; the reflectance is then equal to that of the substrate without the In_2O_3 film. The measured points at very low surface resistivities were obtained with films that were so thick that they showed bulk properties. In such a case the reflectance can be derived from equations (1), (2) and (3) by a long-wavelength approach ($\omega \ll \gamma$):

$$R \approx 1 - 4(\pi\varepsilon_0 c_0 \varrho/\lambda)^{1/2}. \tag{8}$$

In the experiment of fig. 7, λ is of the order of 10 μm. The film thickness that is just large enough for effective heat reflection can be estimated by combining eq. (7) with eq. (8). After some approximation we find that this film thickness is given by the well-known expression for the skin depth d_s [15]:

$$d_s = (\varepsilon_0 c_0 \varrho\lambda/\pi)^{1/2}. \tag{9}$$

It can be shown from this expression that at a wavelength of 10 μm and a resistivity of 3×10^{-4} Ω cm the film thickness should be about 0.3 μm.

The transmittance in the visible and in the near-infrared wavelength range is determined by the dielectric reflection and the absorptance of the film. Provided inter-band transitions and defects are insignificant, absorption is due to the free electrons in the film alone. They give a weak absorption, with the absorptance approximately equal to the product of the absorption coefficient α and the film thickness d. The transmittance is then given by:

$$T \approx 1 - R - \alpha d. \tag{10}$$

The value of α can be derived from equations (1) and (2):

$$\alpha \approx \frac{\gamma N e^2 \lambda^2}{4\pi^2 m^* n \varepsilon_0 c_0^3}. \tag{11}$$

At wavelengths slightly below the plasma wavelength this equation is reasonably accurate. At shorter wavelengths, however, it is necessary to take the special scattering mechanism of the electrons into account. This implies that the damping rate γ is then wavelength-dependent.

A more generally applicable expression for α can be arrived at by expressing the dispersion relations in terms of a frequency-dependent, complex resistivity:

$$\varrho' + j\varrho'' = \frac{m^*(\gamma + j\omega)}{Ne^2}. \tag{12}$$

This leads to

$$\alpha \approx \frac{N^2 e^4 \lambda^2 \varrho'}{4\pi^2 m^{*2} n \varepsilon_0 c_0^3}. \tag{13}$$

If γ is not wavelength-dependent, ϱ' is equal to $1/Ne\mu$ and eq. (13) changes to eq. (11). However, the theory of electron scattering indicates that ϱ' varies with wavelength, depending on the scattering mechanism. If the scattering from ionized donor atoms is the principal mechanism, then for short wavelengths ($\lambda < \lambda_p$) [13] we can show that:

$$\varrho' \approx \frac{e^2(2m^*)^{1/2}}{12\pi\varepsilon_0^2\varepsilon_1^2(0)} \cdot \left(\frac{\lambda}{hc_0}\right)^{3/2}, \tag{14}$$

where h is Planck's constant and $\varepsilon_1(0)$ is the relative

[14] P. Drude, Phys. Z. 1, 161-165, 1900.
[15] See for example H. B. G. Casimir and J. Ubbink, Philips Tech. Rev. 28, 300-315, 1967.

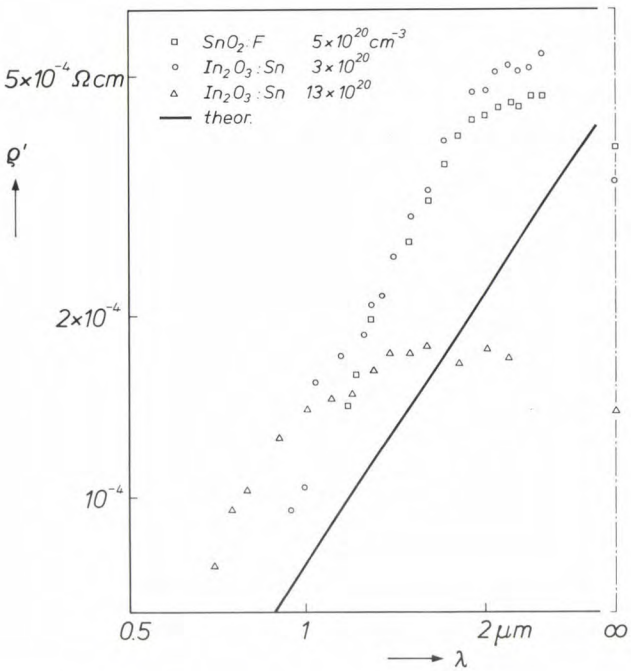

Fig. 8. The real part ϱ' of the complex resistivity as a function of wavelength λ for an SnO_2:F film and two In_2O_3:Sn films at different carrier concentrations N. At short wavelengths the measured points for the three films are fairly close to the continuous line, which was calculated from eq. (14). At long wavelengths, ϱ' comes close to the values of $1/Ne\mu$, which are indicated on the vertical axis for $\lambda = \infty$.

permittivity of the lattice in static fields, which is about 10 for SnO_2 and In_2O_3 [16].

In *fig. 8* the experimental relation between ϱ' and λ is compared with the theoretical relation of eq. (14) for an SnO_2:F film and two In_2O_3:Sn films. The experimental values of ϱ' were calculated from measurements of the reflectance, transmittance and film thickness by means of equations (1), (2) and (12) and the interference formulae to be discussed later. In the short-wavelength range equations (10) and (13) are sufficient. At long wavelengths ϱ' has a practically constant value that does not differ greatly from $1/Ne\mu$. At short wavelengths, ϱ' decreases sharply with decreasing λ, approximately as in eq. (14). Since m^*, ε_1 and $\varepsilon_1(0)$ do not differ greatly for the three materials, there is reasonably good agreement between their values of ϱ' in this wavelength range. These results confirm that scattering from ionized donor atoms is the principal damping mechanism. This damping is responsible for considerably reduced absorption in the visible wavelength region.

Applications

A major application of semiconductor filters is in low-pressure sodium lamps. To maintain the optimum sodium pressure the discharge tube in these lamps must be kept at a temperature of about 260 °C. The power for this heating is supplied by the gas discharge. Losses can occur here due to convection, conduction and radiation. In present-day low-pressure sodium lamps the convection and conduction losses are negligible, because the space between the discharge tube and the glass envelope is evacuated. The energy loss is thus mainly due to heat radiation: the glass of the discharge tube behaves like a black body at about 530 K, radiating its energy in the far infrared, with a maximum at about 5 μm. This loss can be substantially reduced by coating the inside of the glass envelope with a transparent heat-reflecting semiconductor film; see *fig. 9*. Originally SnO_2 filters were used, giving an increase in luminous efficacy of about 50% [3]. Later, even better results were obtained with In_2O_3 filters [4]. Modern low-pressure sodium lamps with In_2O_3 filters can have a luminous efficacy of 200 lm/W [17], about twice as much as that of the lamps without a filter. This gives them a luminous efficacy far higher than that of any other lamp.

Films of strongly doped SnO_2 and In_2O_3 can also be used in solar collectors [18]. They can reduce the energy loss due to heat radiation from the collector plate, while allowing most of the incident solar radiation to pass through. In double-glazed windows the energy loss can be reduced by coating the inside of the two panes with an SnO_2 or In_2O_3 filter [5]. An In_2O_3 filter can reduce the radiation loss through the glass by a factor of 6 without significantly reducing the transmission of visible light.

Semiconductor filters can also be used in incandescent lamps, as for example in the 'Spotlight' reflector lamp illustrated in *fig. 10* [19]. A sharply focused beam is formed in this lamp by the filament and the reflecting aluminium film applied to the inside wall. If this

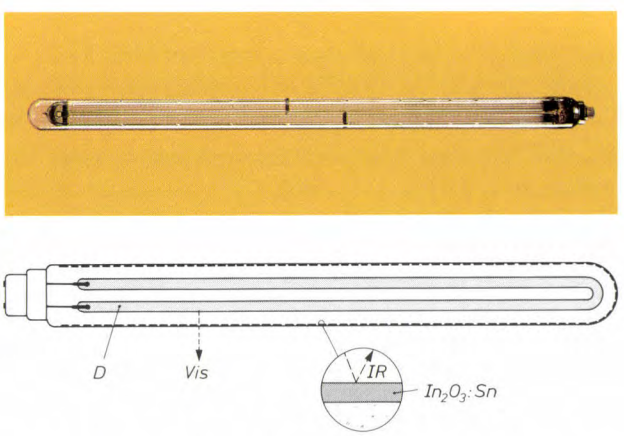

Fig. 9. Photograph and diagram of a low-pressure sodium lamp with a U-shaped discharge tube *D*. The inside of the outer envelope is coated with an In_2O_3:Sn film. This film reflects the heat radiation *IR* back to the discharge tube, but transmits the visible sodium light *Vis*.

beam is applied to an In_2O_3 filter, the emergent beam consists of 'cold' light. The spectral distributions shown indicate that more than 70% of the infrared radiation is suppressed. A further improvement is obtained by applying a protective SiO_2 coating to the In_2O_3 film, which at the same time acts as an anti-reflection coating for visible light (to be discussed later). The presence of In_2O_3:Sn and SiO_2 causes only a slight decrease in the luminous output, while the heat radiation is reduced to less than 30%.

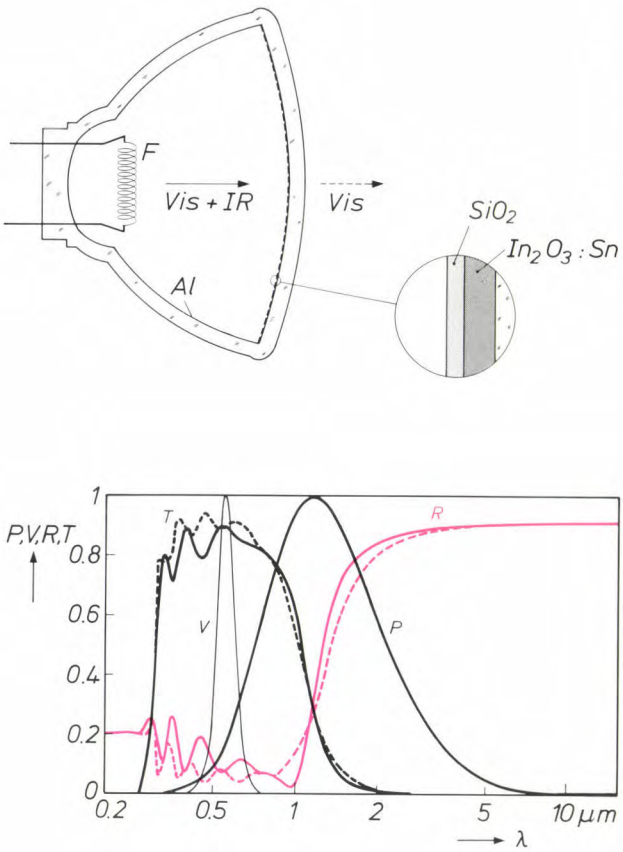

Fig. 10. *Above:* Diagram of a 'Spotlight' reflector lamp with filament F, a reflecting aluminium film Al, a transparent heat-reflecting film of In_2O_3:Sn and an anti-reflection SiO_2 film. The radiation leaving the lamp consists of 'cold' light, because the heat radiation IR is mostly reflected back and the visible radiation Vis is transmitted. *Below:* Spectral energy distribution P of the radiation emitted by the filament (2650 K), relative spectral luminous efficiency V, and reflectance R (*red*) and transmittance T of the In_2O_3 film as a function of wavelength λ (logarithmic scale). The dashed lines indicate the effect of the anti-reflection film.

A semiconductor filter in an incandescent lamp can not give such a great increase in luminous efficacy as it does in low-pressure sodium lamps. This is because in incandescent lamps the wavelength ranges for the transmitted and reflected radiation are much closer together, and the plasma wavelength of semiconductor filters cannot be shifted far enough towards the visible wavelength range. As we shall see in the following section, this difficulty can be countered by combining a semiconductor filter with an interference filter.

Interference filters

The optical characteristics of an interference filter can be derived from those of the separate films by the well-known formal methods of electrical network theory. The effect of a non-magnetic layer with a complex refractive index $\tilde{n}$ on an electromagnetic wave can be described by a characteristic transformation matrix M [20]:

$$\begin{pmatrix} E \\ H \end{pmatrix} = M \begin{pmatrix} E_b \\ H_b \end{pmatrix},$$

$$M = \begin{pmatrix} \cos\delta & \frac{j}{\tilde{n}}\sin\delta \\ j\tilde{n}\sin\delta & \cos\delta \end{pmatrix}, \qquad (15)$$

where E and H are the electrical and magnetic field-strengths in the film at the interface with the medium of incidence (e.g. air), and E_b and H_b are the field-strengths in the background material (i.e. the substrate) at the interface with the film. The quantity δ is the 'phase thickness', which is equal to $2\pi\tilde{n}d/\lambda$ for normal incidence. When there is more than one film, as in interference filters, M in eq. (15) must be replaced by the product of the separate characteristic film matrices.

The reflectance R of an interference filter is determined by the admittance $Y = H/E$ of the medium formed by the film and the substrate, and the admittance of the medium of incidence. If the admittance of the medium of incidence is put equal to 1 (free space, air), then:

$$R = \left(\frac{Y-1}{Y+1}\right)^2. \qquad (16)$$

To obtain the maximum reflection, Y must be as large as possible. Equations (15) and (16) show that an absorption-free film ($k = 0$) at wavelength λ gives the strongest reflection when its phase thickness δ is equal to $\pi/2$, $3\pi/2$, $5\pi/2$, ... Since $\delta = \pi/2$ corresponds to an optical thickness $nd = \frac{1}{4}\lambda$, a film of this type is sometimes referred to as a $\frac{1}{4}\lambda$ film. If a $\frac{1}{4}\lambda$ film of refractive index n is applied to a medium of admittance

[16] I. Hamberg and C. G. Granqvist, Thin Solid Films **105**, L83-L86, 1983.
[17] L. Sprengers, R. Campbell and H. Köstlin, Low-pressure sodium lamps with a luminous efficacy of 200 lm/W, submitted to J. Illum. Eng. Soc.
[18] G. Frank, E. Kauer, H. Köstlin and F. J. Schmitte, Solar Energy Mater. **8**, 387-398, 1983.
[19] G. Frank, E. Kauer and H. Köstlin, Thin Solid Films **77**, 107-117, 1981.
[20] See for example H. A. Macleod, Thin-film optical filters, Hilger, London 1969.

Y, eq. (15) shows that the admittance changes to n^2/Y. It therefore follows that for a stack of an odd number of $\frac{1}{4}\lambda$ films, of refractive indices $n_1, n_2, \ldots, n_s$, on a glass substrate of refractive index n_G, the admittance is given by:

$$Y = \frac{n_1^2 n_3^2 \ldots n_s^2}{n_2^2 n_4^2 \ldots n_{s-1}^2 n_G}. \qquad (17)$$

This equation shows that the admittance can be very high if the odd-numbered films have high refractive indices and the even-numbered films low ones. Usually only two different materials are used, with high and low refractive indices n_H and n_L. Equations (16) and (17) then show that the maximum reflectance of the stack is

$$R = \left(\frac{n_H^{s+1}/n_L^{s-1} n_G - 1}{n_H^{s+1}/n_L^{s-1} n_G + 1} \right)^2. \qquad (18)$$

With an increasing number of stacked films (larger s) the maximum reflectance increases; see *fig. 11*. The reflectance can come very close to 100%, as in the resonator mirrors used in lasers.

It is possible for an interference filter with a high reflectance in the infrared to have a high transmittance in the visible range. This can easily be seen from equation (15). If $\delta = \pi$, with $\frac{1}{2}\lambda$ films, radiation at wavelength λ is fully transmitted. The $\frac{1}{4}\lambda$ films mentioned above, with a maximum reflectance at $\lambda = \lambda_{IR}$, have their maximum transmittance at $\lambda_{vis} = \lambda_{IR}/2$, since they function as $\frac{1}{2}\lambda$ films at this wavelength.

The bandwidth $\Delta\lambda$ of the wavelength range with high reflectance for a stack of $\frac{1}{4}\lambda$ films is:

$$\Delta\lambda \approx \frac{4\lambda_{IR}}{\pi} \arcsin \frac{n_H - n_L}{n_H + n_L}. \qquad (19)$$

With $\lambda_{IR} = 1.1$ μm, $n_H \approx 2.3$ (ZnS) and $n_L \approx 1.5$ (SiO_2) this band extends from 0.93 to 1.27 μm. This is rather narrow for applications as a heat-reflecting filter. A considerable broadening can be achieved by using a stack of films that all have different thicknesses. With an appropriate choice of film thicknesses it is also possible to suppress the reflectance peaks at short wavelengths (see for example fig. 11). Good results are obtained with filters consisting of two stacks, one with average optical film thickness $\frac{1}{4}\lambda_{IR} + \frac{1}{8}\Delta\lambda$, the other with average optical film thickness $\frac{1}{4}\lambda_{IR} - \frac{1}{8}\Delta\lambda$.

Table I gives the optical film thicknesses of an optimized interference filter consisting of eight ZnS films and eight SiO_2 films alternately vacuum-evaporated on a glass substrate. The filter can be thought of as built up from two stacks of seven films with average optical thicknesses of about 0.33 μm and about 0.22 μm, supplemented by an intermediate film and a

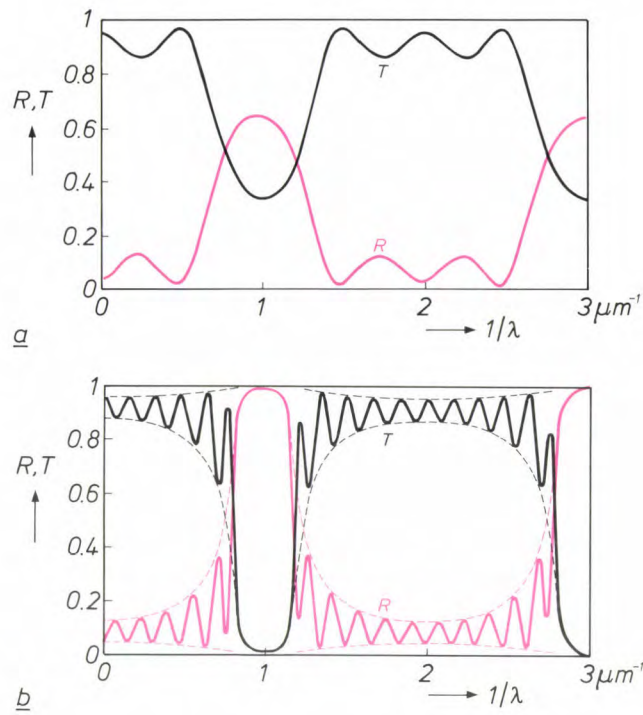

Fig. 11. Calculated reflectance R (*red*) and transmittance T, plotted against the wave number $1/\lambda$ for two interference filters consisting of a stack of non-absorbing $\frac{1}{4}\lambda$ films for $\lambda = 1$ μm. The layers have alternate high and low refractive indices ($n_H = 2.30$ and $n_L = 1.38$). *a*) Stack of three films, in the sequence *HLH*, on glass. The maximum reflectance at 1 μm is about 65%). *b*) Stack of eleven films, in the sequence *HLHLHLHLHLH*, on glass. The maximum reflectance here is close to 100%. The envelopes of the reflectance and transmittance curves are also shown.

Table I. Optical thicknesses nd of the films of optimized interference and combination filters deposited on a glass substrate. *H* film with high refractive index (ZnS). *L* film with low refractive index (SiO_2). *S* film of In_2O_3:Sn.

Film	nd (μm)	
	Interference	Combination
S	—	0.432
L	—	0.267
H	0.308	0.278
L	0.356	0.286
H	0.330	0.286
L	0.341	0.281
H	0.338	0.281
L	0.330	0.283
H	0.336	0.270
L	0.286	0.245
H	0.220	0.220
L	0.237	0.220
H	0.217	0.201
L	0.220	0.217
H	0.226	0.198
L	0.195	0.223
H	0.223	0.193
L	0.091	0.113

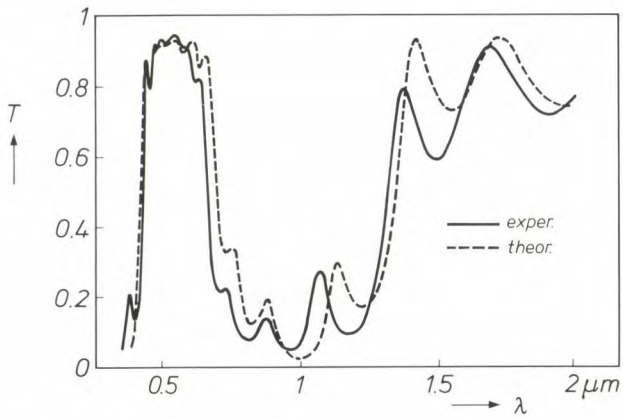

Fig. 12. Measured and calculated transmittance T as a function of wavelength λ for an interference filter consisting of 16 films (see Table I). The filter has a high transmittance in the visible wavelength range, and also in a part ($\lambda \gtrsim 1.2$ μm) of the infrared.

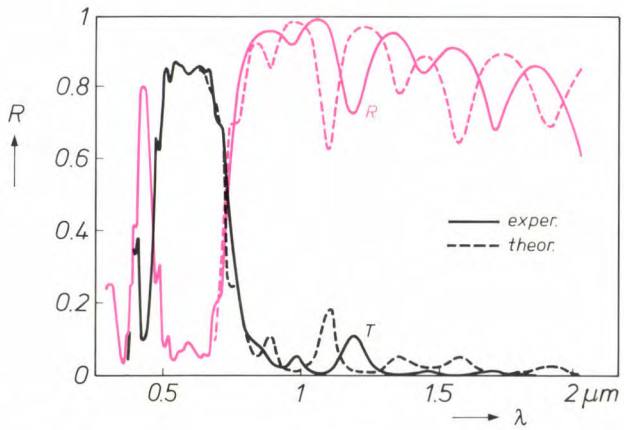

Fig. 13. Measured and calculated transmittance T and reflectance R (*red*) as a function of wavelength λ for a combination filter consisting of 18 films (see Table I). Compared with the filter in fig. 12 there is a decrease in transmittance that is much greater in the infrared than in the visible range. The reflectance is high in a wide wavelength range in the infrared.

thin anti-reflecting top coating of SiO_2. In *fig. 12* the measured and calculated transmission values of this filter are plotted against wavelength. The calculations also take into account the low reflectance and absorptance of the glass substrate [20]. The measured interference maxima and minima are found at slightly shorter wavelengths than the calculated ones, but the agreement between the two curves is nevertheless reasonably good. The effective transmittance of visible light is very high, about 90%. A disadvantage of this filter is that strong reflection occurs only in the near infrared ($\approx$ 0.8-1.2 μm). At longer wavelengths the transmittance of the filter is still fairly high. For example, only about 50% of the heat radiation of a black body at 3000 K is reflected.

A filter with much better heat reflection can be obtained by combining the interference films with a strongly doped semiconductor film [21]. As we have seen, an In_2O_3:Sn film of optimum thickness gives a very high reflectance in the long-wave infrared ($\gtrsim$1.5 μm), while the visible radiation is transmitted. In a combined filter the interference films and the semiconductor film complement each other, so that a high transmittance in the visible range is combined with a high reflectance in a broad infrared range.

Table I gives the optical thicknesses of an optimized combination filter with a total of 18 films. The first film, consisting of In_2O_3:Sn, is rather thicker than the other films. A transition film of SiO_2 is followed by two stacks of seven interference films, again with an intermediate film and a thinner top coating of SiO_2. The measured and calculated reflectance and transmittance are shown as a function of wavelength in *fig. 13*. The great difference compared with the filter without semiconductor film is the much higher infrared reflectance at longer wavelengths. While the effective transmittance in the visible wavelength range has dropped only slightly, the effective reflectance of the heat radiation of a black body at 3000 K has risen from about 50% to more than 80%.

Optimization

Theoretical values of the effective infrared reflectance R_{IR} and the effective transmission T_{vis} in the visible wavelength range can be obtained from the calculated reflection and transmission spectra (e.g. figs 12 and 13) and the associated weighting functions. For our calculations we usually assumed heat radiation at 3000 K. In addition to R_{IR} and T_{vis} the chromaticity coordinates x and y of a filter can also be calculated. The calculations then include the spectral luminous efficiency characteristic for the colours red, green and blue. For a white filter x and y should be about 1/3. This implies that a chromaticity factor, defined as

$$F = 1 - \sqrt{(x - 1/3)^2 + (y - 1/3)^2}, \qquad (20)$$

must be as large as possible. In looking for the optimum composition of a filter we have to remember that the requirements of high values for R_{IR}, T_{vis} and F are not independent. For this reason we have defined a quality factor Q:

$$Q = c_1 T_{vis} + c_2 R_{IR} + c_3 F, \qquad (21)$$

where c_1, c_2 and c_3 are constants. Optimization implies looking for a composition at which Q is a maximum. By making c_1, c_2 or c_3 larger more emphasis

[21] The realization of such a filter, by T. H. R. Almer and H. Köstlin, has already been described in German patent No. 2514494.

can be placed on good transmission of visible light, on strong infrared reflection or on good filter colour.

Because of the large number of layers required the optimization of interference filters and combination filters is highly complicated. For this reason we have developed iteration procedures in which Q is treated as a function of the separate film thicknesses or of the optical thicknesses. In general this leads to the same results. The filters listed in Table I were obtained by means of these procedures.

In the iteration procedures a set of s layers is considered as a spatial vector p in an s-dimensional space of the film thicknesses or of the optical thicknesses. The initial thickness chosen for most films corresponds to an optical thickness nd of 0.275 μm, resulting in a maximum transmittance at 0.55 μm and maximum reflectance at 1.1 μm. The optical thickness taken as the initial thickness for the In_2O_3 film in combination filters is twice as large because of the high reflectance required in the long-wave infrared. Because of the $\frac{1}{4}\lambda$ anti-reflection required at 0.55 μm from the top coating of interference and combination filters, the thickness taken for this coating corresponds to half the optical thickness of the underlying films.

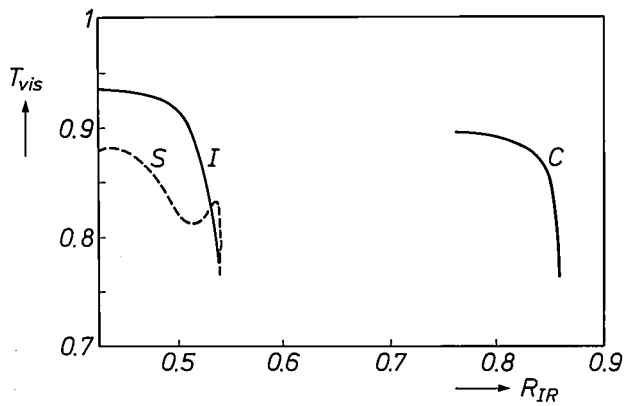

Fig. 14. Calculated effective transmittance T_{vis}, plotted against the calculated effective reflectance R_{IR} for heat radiation at 3000 K, for interference filters I, semiconductor filters S and combination filters C. The interference and combination filters, consisting of 16 and 18 films respectively, have been optimized for different values of c_1 and c_2 in eq. (21). The curve for the semiconductor filters was obtained with In_2O_3:Sn films using the thickness as parameter. The T_{vis}-values of the combination filters lie between those of the interference and semiconductor filters, but the associated R_{IR}-values are much higher.

To increase the rate of convergence of an iteration, p is varied in the direction of the strongest increase of $Q(p)$, until the coordinates of the maximum of a simple approximation function $\bar{Q}$ are reached. The increase in Q is determined by the gradient vector $q = (\partial Q/\partial d_1, \ldots, \partial Q/\partial d_k, \ldots, \partial Q/\partial d_s)$. The magnitude of the increase is the length q of this vector. The optimum direction of the film-thickness variation in the ith iteration step is then represented by the unit vector $n_i = q_i/q_i$. At each step in the iteration a new set of s partial derivatives is calculated. This is done by calculating Q at each step for the filter with film thicknesses $d_1, \ldots, d_k, \ldots, d_s$, and for the s filters with film thicknesses $d_1, \ldots, d_k + \partial d_k, \ldots, d_s$.

Near the optimum all the individual films have a comparable effect on the quality of the filter, and therefore the approximation function $\bar{Q}$ is taken to be a parabola that has the same thickness-dependence for all films. It then depends only on a single variable x, and the maximum is taken at $x = 0$. The desired variation width w — starting from p, where $\bar{Q} = Q$ and $d\bar{Q}/dx = q$, up to $x = 0$ — is given by:

$$w = \left(\frac{d\bar{Q}}{dx} \Big/ \frac{d^2\bar{Q}}{dx^2} \right)_{x=w} . \qquad (22)$$

In the first iteration step a value of w is introduced that serves as an upper limit in the subsequent steps to avoid possible divergence if the coordinates of the maximum are calculated too inaccurately. For the optimum variation width w_i in the ith iteration step an approximation of eq. (22) is used:

$$w_i = \left| \frac{Q_i - Q_{i-1}}{q_i - q_{i-1}} \right| . \qquad (23)$$

The optimized film thickness vector p_i is then:

$$p_i = p_{i-1} + w_i n_i . \qquad (24)$$

The iteration is terminated when the changes in Q remain below a particular limit value. In filters composed of many films the number of iteration steps is approximately equal to the number of films.

Some idea about the quality factor Q of different types of filter can be obtained from the calculated R_{IR}- and T_{vis}-values of filters that, except for their colour, have been optimized. *Fig. 14* gives a plot of T_{vis} against R_{IR} for optimized interference filters composed of 16 films and for combination filters with 18 films. The curves were obtained from a series of optimizing calculations in which different values were taken for c_1 and c_2 in eq. (21). When the same type of filter is used, with a given number of films of a given composition, these curves indicate limiting values that cannot be exceeded for any combination of film thicknesses. For comparison, T_{vis} is also given as a function of R_{IR} for semiconductor filters with an optimum composition (In_2O_3:Sn) with the film thickness as parameter. This figure clearly shows the higher quality of combination filters as compared with interference and semiconductor filters. With combination filters giving an effective transmittance of about 90% in the visible region it is possible to achieve an effective infrared reflectance of about 80%.

Application in reflector lamps

With appropriate choices of the number of films, the film thicknesses and the refractive indices, interference filters can provide very many variations for the positions and widths of the wavelength ranges giving high reflectance or high transmittance. This helps to explain why interference filters are used in such a wide range of applications, including TV cameras, lasers and spectroscopes.

They are also used as 'cold-light reflectors' in lamps, for example in slide and film projectors. These incandescent lamps produce a narrow and intense beam of light. To ensure that irradiated objects do not become too hot, the infrared radiation in the beam has to be minimized. The production of an intense 'cold' light beam is facilitated if the inside of the glass wall is

Fig. 15. Photograph and diagram of a 'cold-light' reflector lamp. *F* filament of halogen incandescent lamp. *M* reflector with interference filter *I* consisting of a number of films with alternate high and low refractive indices. Since this filter strongly reflects the visible light *Vis* and transmits the heat radiation *IR*, a beam of 'cold' light is produced.

partly coated with an interference filter that reflects as much as possible of the omnidirectional visible part of the radiation towards the beam and allows the infrared part to pass through. *Fig. 15* shows an example of a cold-light reflector lamp, used for the projection of super-8 films. The use of an interference filter here does not reduce the heat radiation emitted by the lamp, but it does reduce the heat radiation present in the emergent beam. The optical specification for the filter is exactly the opposite of that for transparent, heat-reflecting filters. This means that the range for maximum reflectance must be located at shorter wavelengths; this can be accomplished by using thinner films.

The combination filter described can also be used in conjunction with cold-light reflector lamps. The residual heat radiation of the beam is then mostly suppressed, without significantly affecting the visible radiation.

Metal filters with induced transmission

Metal films can give very strong infrared reflection (fig. 2), but for many applications their transmission of visible light leaves much to be desired. It has long been known, however, that the visible-light transmittance of some thin metal films can be appreciably increased by giving them a thin dielectric anti-reflecting coating. This induced transmission is possible when the real part of the refractive index in the visible wavelength range is much smaller than the imaginary part [22]. We shall show here how a metal filter with induced transmission can give an optimum compromise between maximum infrared reflectance and minimum loss of visible light.

The filter we shall discuss consists of a ZnS film, a silver film and a second ZnS film, successively deposited by vacuum evaporation on a glass substrate. Among the aspects studied when designing an optimum filter are the changes that take place in the complex admittance Y during the deposition of the three films. These changes are mapped in the complex admittance plane, with the imaginary part of the admittance plotted as a function of the real part. We shall confine our calculations to the wavelength for the maximum spectral luminous efficiency ($\lambda = 0.55$ μm) and we shall only consider normally incident radiation [23]. The calculated loci for the three depositions are shown in *fig. 16*. Let us now take a closer look at these curves.

The change in admittance during the deposition of a film on a substrate can be derived by the matrix method described earlier. In the deposition of a non-absorbing dielectric film, of refractive index n_D, on a non-absorbing glass substrate, of refractive index n_G, the admittance Y_D is given by:

$$Y_D = \frac{n_G + j\, n_D \tan \delta_D}{1 + j(n_G/n_D) \tan \delta_D}, \qquad (25)$$

where δ_D is the phase thickness $2\pi n_D d/\lambda$. The locus of

[22] A theoretical description of induced transmission is given in P. H. Berning and A. F. Turner, J. Opt. Soc. Am. **47**, 230-239, 1957.

[23] H. Köstlin and G. Frank, Thin Solid Films **89**, 287-293, 1982.

Y_D in the complex admittance plane is a circle with its centre on the real axis and passing through the points $Y = n_G$ and $Y = n_D^2/n_G$. In fig. 16 this circle is shown for $n_G = 1.5$ and $n_D = 2.3$ (ZnS).

In the application of a metal film, of complex refractive index $-jk_M$, on a substrate of refractive index n_D or on the ZnS film that has already been deposited on glass, the admittance Y_M is given by

$$Y_M = \frac{n_D - jk_M \tanh \delta_M}{1 + j(n_D/k_M) \tanh \delta_M}, \qquad (26)$$

where δ_M is the phase thickness $2\pi k_M d/\lambda$. The locus of Y_M in the complex admittance plane is an arc of a circle that intersects the real axis at the point $Y = n_D$ and the imaginary axis at the points $Y = \pm jk_M$. In fig. 16 this arc is shown for $n_D = 2.3$ and $k_M = 3.4$, a characteristic value for silver at $\lambda = 0.55$ μm.

When the second ZnS film is deposited the admittance must change in such a way that, when the deposition is stopped, the admittance value of air is reached ($Y = 1$). The requirement of optimum anti-reflection implies that the same admittance values should be obtained from air via filter to substrate as from substrate via filter to air. This means that in the deposition of the second ZnS film the change in admittance may be treated as the change that would occur in a deposition on a hypothetical substrate of air. For the admittance Y_D we then have:

$$Y_D = \frac{1 + jn_D \tan \delta_D}{1 + j(1/n_D) \tan \delta_D}. \qquad (27)$$

In the complex admittance plane this again gives a circle with the centre-point on the real axis, and in this case passing through the points $Y = 1$ and $Y = n_D^2$; see fig. 16.

The three admittance loci shown can be used for finding the optimum film thicknesses. Here again, optimum anti-reflection is required in the visible wavelength range and the metal film should be as thick as possible to give strong infrared reflection. In the deposition of the first ZnS film the admittance locus, starting from $Y = n_G$, is followed in the clockwise direction. The evaporation is stopped as soon as the point of intersection with the admittance locus for silver is reached. This locus is then followed in the downward direction during the deposition of the silver film, which is terminated when the admittance curve of the second ZnS film is reached. In the deposition of this film its admittance locus is again followed in the clockwise direction, until evaporation is stopped at $Y = 1$, the admittance of air.

To obtain the thickest possible metal film compatible with optimum anti-reflection in the visible wavelength range, it is generally necessary for the admit-

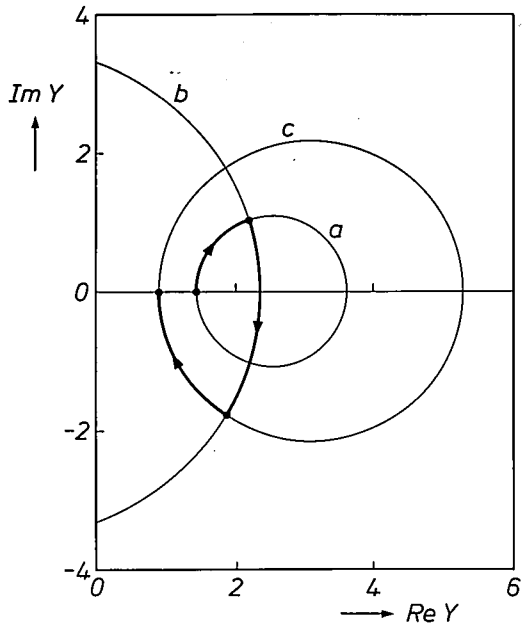

Fig. 16. The imaginary part ImY of the complex admittance plotted against the real part ReY, for a change in the phase thickness $\delta = 2\pi nd/\lambda$. *a*) ZnS ($n_D = 2.3$) on glass ($n_G = 1.5$), from eq. (25). *b*) Silver ($k_M = 3.4$) on ZnS, from eq. (26). *c*) ZnS 'on air', from eq. (27). The admittance route followed in the successive depositions of the three films is shown by the bold lines.

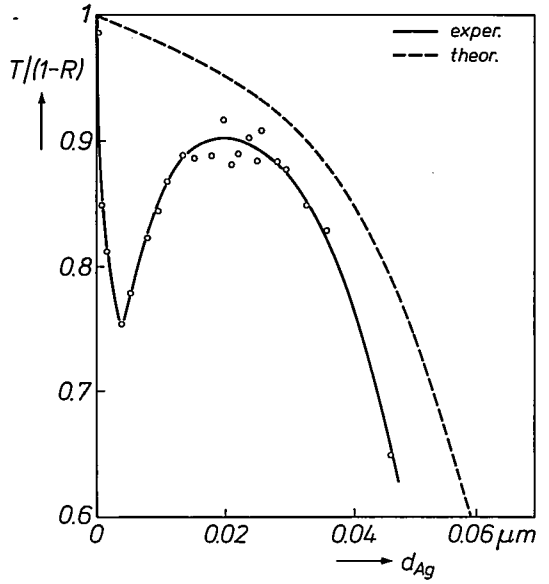

Fig. 17. Measured and calculated ratio $T/(1 - R)$ at a wavelength of 0.55 μm, as a function of the thickness d_{Ag} of the silver film in a filter in which this film is coated on both sides with a 0.03-μm ZnS film. For a very thin silver film the experimental values of $T/(1 - R)$ are unexpectedly low. The optimum film thickness is about 0.02 μm.

tance loci of the two dielectric films to intersect the metal-admittance locus more or less perpendicularly. The dielectric films should also have a high refractive index. Both requirements are met reasonably well by sandwiching a silver film between two ZnS films.

It can be shown from the equations given above that at the relevant points of intersection of the metal-admittance loci with the two ZnS loci the phase thickness δ_D of the ZnS layers is about $\pi/4$. This corresponds to an optical thickness $n_D d$ of about $\frac{1}{8}\lambda$. With $n_D = 2.3$ and $\lambda = 0.55$ μm this means that the ZnS films should be about 0.03 μm thick.

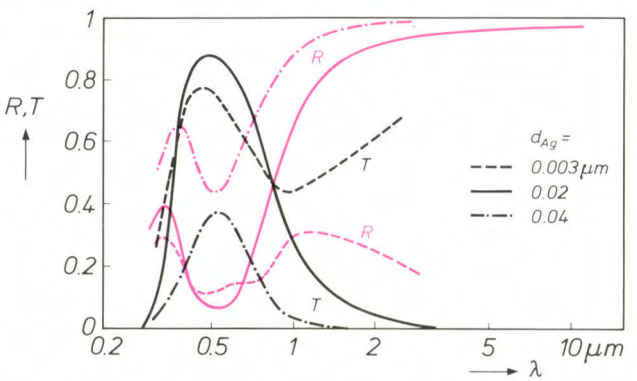

Fig. 18. Reflectance R (*red*) and transmittance T as a function of wavelength λ (logarithmic scale) for three thicknesses d_{Ag} of a silver film coated on both sides with a 0.03-μm ZnS film. For d_{Ag} = 0.02 μm there is both high transmittance in the visible range and high reflectance in the infrared.

The optimum thickness of the silver film cannot be derived directly from these equations, because they take no account of a slight absorption loss. Minimizing this loss implies maximizing the ratio $T/(1 - R)$. This ratio can be calculated from the admittance values on each side of the silver film, taking into account the real part (about 0.06) of the complex refractive index of silver at $\lambda = 0.55$ μm [24]. In *fig. 17* the theoretical curve and experimental values of $T/(1 - R)$ at λ = 0.55 μm are plotted against the thickness of the silver film. The unexpectedly low experimental values at film thicknesses smaller than 0.02 μm are due to the formation of small islands instead of a continuous silver film. The marked decrease at greater film thicknesses (> 0.04 μm) is a result of the skin effect [15].

The requirements of minimum absorptance and optimum anti-reflection at 0.55 μm and high infrared reflectance can best be met with a film thickness of about 0.02 μm. *Fig. 18* gives the experimental reflection and transmission spectra of three filters, in which the two ZnS films have the same thickness (0.03 μm) but the silver film has a different thickness. At a thickness of 0.003 μm the infrared reflectance is inadequate, whereas a thickness of 0.04 μm gives too high a reflectance in the visible range. At a thickness of 0.02 μm strong infrared reflection is obtained as well as good transmission of visible light.

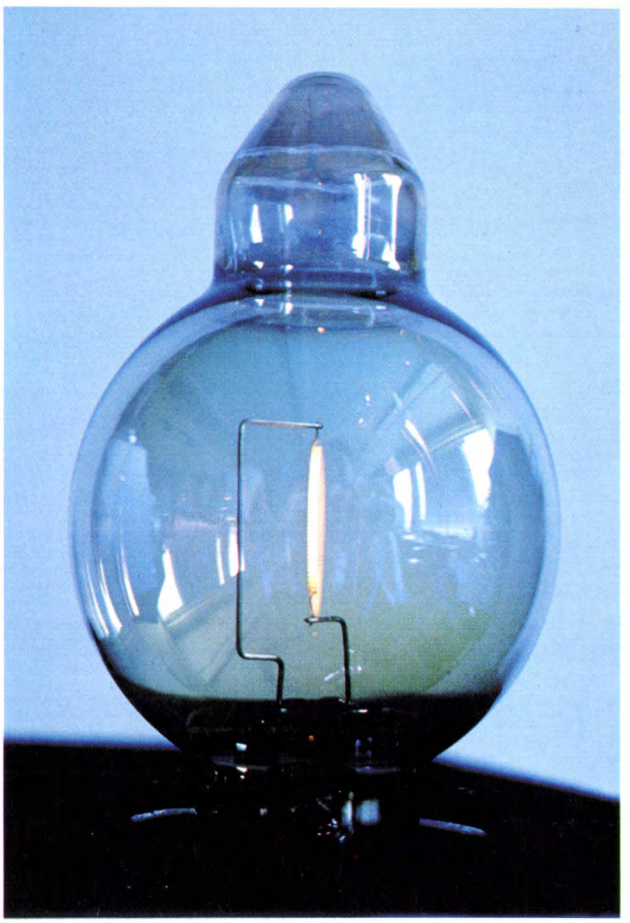

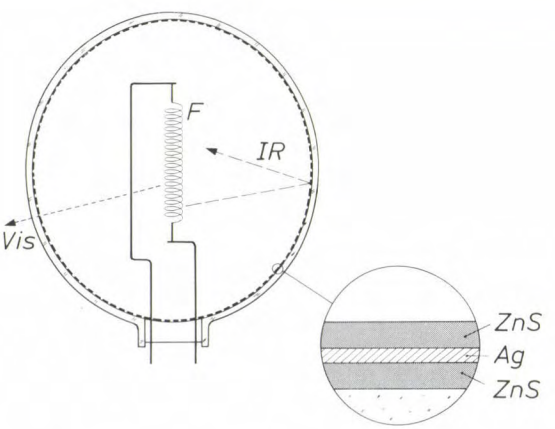

Fig. 19. Photograph and diagram of an incandescent lamp with a filter consisting of a silver film sandwiched between two ZnS films. The filter reflects the heat radiation *IR* back to the filament *F*, while the visible light *Vis* is transmitted.

[24] H. Köstlin, Festkörperprobl. **22**, 229-254, 1982.

Application in incandescent lamps

A reflector with the filter just described can give a considerable energy saving in incandescent lamps [25]. When the filament and the reflector have the appropriate geometry a substantial part of the reflected infrared radiation returns to the filament, so that much less power is needed to keep the filament at the required temperature (e.g. 2900 K). We have achieved good results with lamps with an elongated filament that absorbs strongly in the infrared. The most suitable shape for the reflector is found to be an ellipsoid; see *fig. 19*. Optimum reradiation of infrared from the reflector back to the filament is achieved when the filament is situated between the focal points of the ellipsoid. A filter with a high effective infrared reflectance and a high transmittance for visible light gives a lamp that requires only half the power of a conventional incandescent lamp and has a 40% higher luminous efficacy.

[25] H. Köstlin and B. de Vrijer, Power saving incandescent lamp with infrared reflecting filter, Third Int. Symp. on the Science and technology of light sources, Toulouse 1983 (not yet published).

The work described here is the result of cooperation between colleagues at the laboratories in Aachen, the Lighting Development Department in Turnhout and Weert, the Lighting Pre-development Department in Eindhoven, and the Research Laboratories in Eindhoven.

Summary. In light sources energy losses due to heat radiation can be reduced by means of transparent heat-reflecting filters consisting of thin films deposited on glass. Various types can be used: a film of a strongly doped semiconductor (e.g. In_2O_3:Sn), a stack of dielectric interference films (e.g. of ZnS and SiO_2) with alternate high and low refractive indices, and a film of metal (e.g. silver) between two dielectric films (e.g. of ZnS) inducing transmission in the visible wavelength range. The method of optimization used to obtain the required spectral reflection and transmission differs considerably for these three types. For a semiconductor filter the film thickness and the concentration and mobility of the free charge carriers are important quantities. With an interference filter the number of films and the film thicknesses are important. The optimum design for such filters can be found by means of a matrix method and an iteration procedure. A filter that has particularly interesting characteristics can be produced by combining an interference filter with a semiconductor filter. The optimum design of a filter consisting of a silver film between two ZnS films can be found by studying the changes in the complex admittance during the deposition of the films.

From powder diagram to structure model on the computer

J. M. M. Verbakel and J. H. N. van Vucht

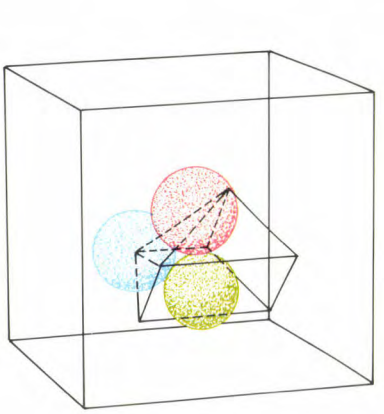

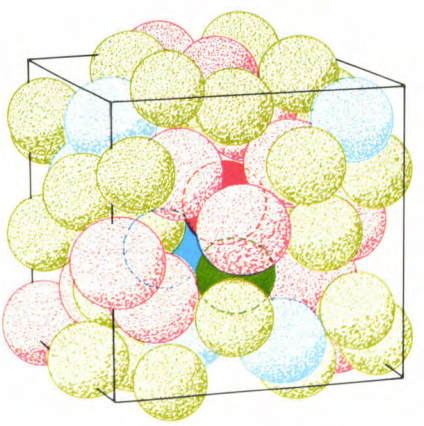

Can the crystal structure of metals and intermetallic compounds be calculated from powder diagrams? Can it be done on the basis of the purely geometric problem of filling space with atoms, represented in an idealized way as spheres, which must not overlap by more than a certain percentage? It can indeed, and in theory it is sufficient simply to try out all the possible atomic combinations in an arbitrary pattern. In practice, however, as the article below shows, it calls for great ingenuity in computer programming — even when the structures are not the most complicated ones.

Powder diagrams as 'fingerprints'

The properties of solids can seldom be properly understood without a model of their composition and structure. The method most generally used for determining the structure of crystalline solids is X-ray diffractometry; electron and neutron diffractometry are also used for this purpose [1].

The most complete information is obtained from single crystals. However, obtaining single-crystal specimens is usually a lengthy and expensive business. For most routine analysis of crystalline solids the crystallographer therefore wishes to be able to investigate the material in the polycrystalline form in which he normally receives it (*fig. 1*). Often, though not always, the material is supplied in the form of a powder.

Most powders are close-knit agglomerates of small crystals, not necessarily of the same type. When powders or other polycrystalline materials are exposed to monochromatic X-radiation (see *fig. 2*), the scattered beams of rays form a series of cones around the inci-

J. M. M. Verbakel and Dr J. H. N. van Vucht are with Philips Research Laboratories, Eindhoven.

[1] See for example P. B. Braun and A. J. van Bommel, Philips Tech. Rev. **22**, 126-138, 1960/61;
J. A. Goedkoop, Philips Tech. Rev. **23**, 69-82, 1961/62;
M. J. Buerger, Contemporary crystallography, McGraw-Hill, New York 1970.

Fig. 1. Photomicrograph of a compound of La and Ni (57.2 at% Ni), taken after rapid cooling from the melt. The picture shows a polished and etched section. The many phase regions in the specimen are clearly visible. Magnification 200×.

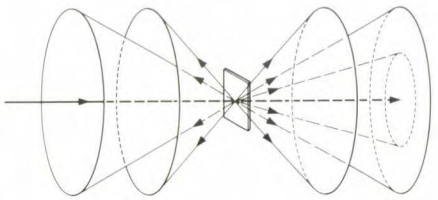

Fig. 2. Illustrating the ray paths in irradiation of a polycrystalline specimen by monochromatic X-rays. The diffractograms are shown in figures 3 and 4.

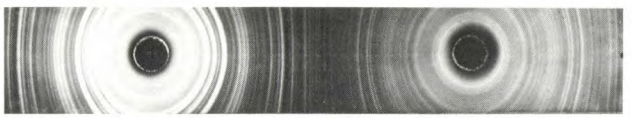

Fig. 3. Debije-Scherrer diffractogram.

dent beam. A classical method of observing this diffraction pattern is the Debije-Scherrer technique, in which the scattered radiation is recorded photographically (*fig. 3*). Nowadays diffractometers are widely used for this. In this technique the region in the plane through the incident beam and the normal to the specimen plane is systematically scanned for radiation by a radiation meter, which passes over each of the cones in succession. By recording the scattered intensity at every diffraction angle a 'powder diagram' is obtained (*fig. 4*). An instrument capable of performing such measurements fully automatically is incorporated in the PW 1700 Automated Powder Diffractometer System developed by Philips (*fig. 5*) [2].

A powder diagram can be regarded as a 'fingerprint' of the substance analysed; the relation is just as unambiguous and unique. To identify a solid we can therefore try to recognize its 'fingerprint', by comparing it with a collection (or data base) of fingerprints observed or calculated earlier. Various such collections are available, and the data in many of them can be retrieved by computer. It is also generally possible to identify the different components in powders consisting of crystals of more than one substance. This is obviously the fastest and often the cheapest method of identifying a crystalline solid. We can also try to determine the crystal structure of a solid in this way, provided of course that we know the structure of a closely related compound, which must be available in a data base.

Powder diagrams can however be used not only as fingerprints but also as a key to the elucidation of unknown crystal structures. For simple structures this approach has already proved successful in a few cases [3]. At Philips Research Laboratories in Eindhoven we have endeavoured for some years to develop this approach into a more systematic method that can be used for analysing more complex structures [4]. This method is the subject of the present article.

The powder diagram as the key to crystal structures

To describe a crystal lattice, or at any rate the lattice in its idealized form, all the crystallographer needs is a description of the 'unit cell' [1]. He arrives at the lattice by infinite repetition of the unit cell by translation.

From a powder diagram the crystallographer can measure the diffraction angles of the scattered radiation, and from the results he can usually deduce the *shape* and the *dimensions* of the unit cell. The intensity of the scattered radiation in these directions gives him information about the *arrangement of the atoms* within the unit cell. A direct determination of this arrangement from the intensity data, as is done from the diffraction data of single-crystal specimens [1], is not generally possible with powder diagrams because too many of the diffraction lines coincide. However, the intensity data in a powder diagram can often be used

[2] See for example R. Jenkins, Y. Hahm, S. Pearlman and W. N. Schreiner, Norelco Reporter **26** (No. 1), 1-15, 1979.

[3] See for example J. H. N. van Vucht, Philips Res. Rep. **16**, 1-40, 1961;
J. H. N. van Vucht, H. A. C. M. Bruning, H. C. Donkersloot and A. H. Gomes de Mesquita, Philips Res. Rep. **19**, 407-421, 1964;
J. C. M. A. Ponsioen and J. H. N. van Vucht, Philips Res. Rep. **22**, 161-169, 1967.

[4] A detailed description of the method is given in W. P. J. Fontein, J. M. M. Verbakel and J. H. N. van Vucht, Philips J. Res. **34**, 238-251, 1979.

[5] At Philips Laboratories, Briarcliff Manor, N.Y., U.S.A., work is being done on a powder diffractometer that can be used for the measurement and calculations of a moderately strong preferred orientation; see J. Ladell, U.S. Patent 4199678.

[6] N. F. M. Henry and K. Lonsdale (eds), International tables for X-ray crystallography, Vol. I, Kynoch, Birmingham 1952.

for the *verification* of crystal models derived in other ways [3]. In so far as crystal structures can be determined from powder it is usually done in this way. A condition, however, is that the crystallites in the powder should not acquire a texture, i.e. be aligned in a preferred relative orientation, as may be the case in needle- or plate-shaped crystallites. This gives certain diffraction lines a different intensity from the one arrived at by calculation [5].

The powder diagram also provides the crystallographer with information about the extent to which the atoms are symmetrically grouped within the unit cell. There are 230 conceivable combinations of symmetry elements in three-dimensional space, which are called space groups [1][6]. Symmetry elements such as axes of symmetry can be derived with a high degree of probability from the shape of the unit cell as constructed from the powder diagram. Other symmetry elements such as glide planes and screw axes appear from the systematic absence of certain diffraction lines in the powder diagram. Although this does not always indicate the space group of a crystal specimen with certainty, it does indicate a group of related space groups to which the crystal belongs.

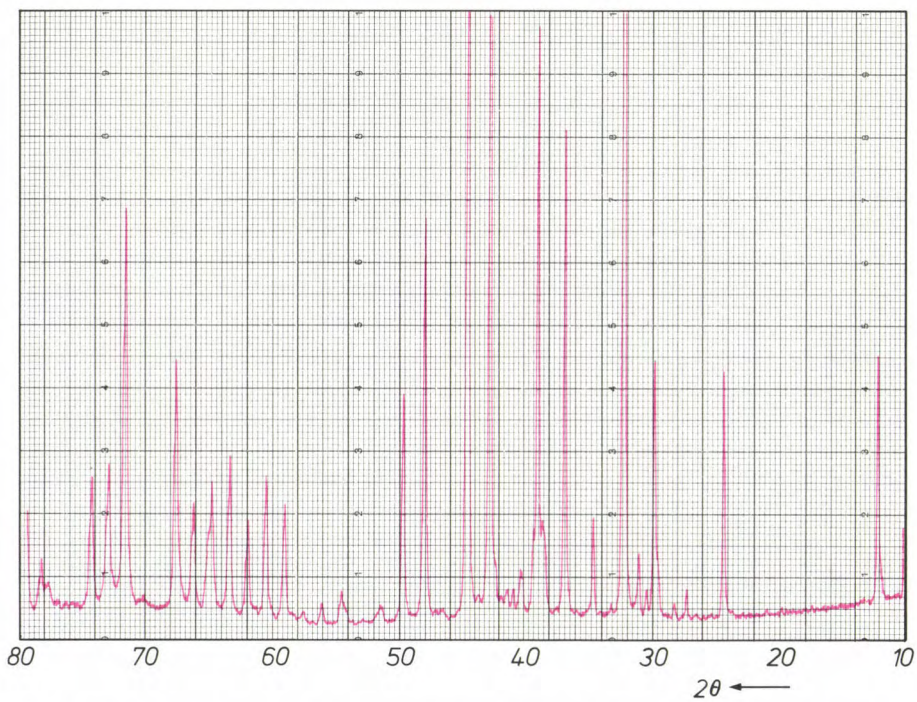

Fig. 4. Powder diagram of petzite (Ag_3AuTe_2), made with the Philips PW 1700 diffractometer. CuKα radiation was used. The intensity is shown as a function of the diffraction angle 2θ (from right to left).

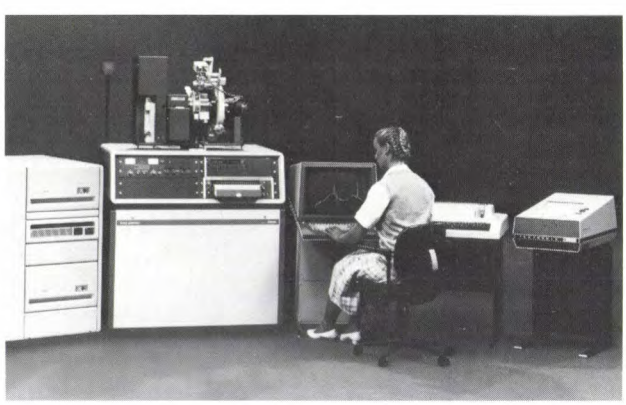

Fig. 5. The Philips PW 1700 Automated Powder Diffractometer System. The second cabinet from the left contains a high-voltage generator. Above it is an X-ray tube, which is connected to the diffractometer (on the right). The computer is at the far left, and on the right there are several output peripherals.

If we know the shape and dimensions of the unit cell, the number of atoms per cell (calculated from the chemical composition and the relative density) and the symmetry, we can try to determine the arrangement of the atoms by a trial-and-error procedure. A trial structure produced in this way can then be subjected to a process of verification and refinement, by minimizing the differences between the measured and calculated intensities of the diffraction lines in the powder diagram, for example by the method of least squares [1]. As we noted, this approach only has a chance of succeeding if the number of atoms in the unit cell is not too large and the degree of crystal symmetry is not too low. For slightly more complicated structures advan-

tage might be taken of earlier results obtained with related simpler compounds, but this cannot be expected to lead to more than occasional success.

In our attempts made a few years ago at Philips Research Laboratories to arrive at a more systematic approach along these lines, we confined ourselves to metals and intermetallic compounds. For these substances we wrote a computer program based on the geometric problem of filling the unit cell atom by atom so as to generate acceptable trial structures. The program also includes the cases where the number of atoms per unit cell is not small and the degree of symmetry is not particularly high. We assumed that the atoms were spheres of defined radius that should not overlap by more than a specified small percentage.

How realistic is it to treat atoms as spheres of defined radius? In modern physics a good picture of the structure of atoms has gradually been acquired. An atom can best be described as a very small positively charged nucleus, containing almost all of its mass, surrounded by a cloud of fast-moving negatively charged particles, the electrons. Because of the fast and random movement of the electrons, this cloud may be regarded as virtually spherical for a free atom. For combined atoms, however, we know that the spherical shape is not always the best model. Carbon atoms, for instance, will form bonds with other atoms only at certain defined angles, so the conclusion must be that at least the valence electrons are not uniformly distributed over a sphere. In metals, and also in the inert gases in the solid state, the spherical shape is a reasonable approximation: in metals because the valence electrons are shared by all the atoms of the lattice, in the inert gases because no electron exchange takes place. The radius of the spheres is determined by experiment and a certain degree of interpenetration has to be admitted, to make allowance for the inherent uncertainty of the values used [7].

Because of their spherical nature, the atoms of metals will pack fairly closely together in a manner determined entirely by the geometry. This makes these compounds much more amenable to calculation than organic compounds for example, where the *orientation* of the atoms in the unit cell would also have to be taken into account in the calculation, because of the angles between the bonds.

With the packing dependent purely on the geometry, the filling problem looks so much simpler that it begins to appear possible that modern aids like the computer, applied to the data of the powder diagram, might enable us to tell which atomic arrangements in the unit cell are possible and which are not. This question seems interesting enough to devote a separate section to the answer.

One question remains, however. Even if the *possible* arrangements for the crystal structure can be derived in this way from the powder diagram, will it be possible to derive the *actual* arrangements for the majority of metals and intermetallic compounds? We shall return to this later.

Potential and limitations of the computer [8]

Filling the unit cell

We shall try to elucidate the nature of the problem by giving an example based on calculations. Suppose that we wish to determine the possible atomic arrangements in the unit cell of the compound NaPb, with a maximum permitted atomic overlap of 10%. The unit cell of NaPb has a volume of 1970 Å^3, with 32 Na atoms and 32 Pb atoms; the location of the atoms has to satisfy the tetragonal symmetry of space group 142 (symbol $I4_1/acd$); this includes a fourfold screw axis and in three directions three different glide planes [6]. The compound belongs to an intermediate class of compounds in complexity of structure.

Before making computer calculations on crystal structures it is first necessary to 'discretize' the crystal space. This is done in our case by defining a grid in the unit cell. In the calculations the centre-points of the atoms are given a position on the nodal points of the grid. To limit the computer time, the mesh of the grid will have to be made as large as possible, yet not so large that possible solutions might be missed. An acceptable compromise is to take a mesh width equal to about a third of the smallest atomic radius.

In our example this means that the grid consists of 12 800 grid points. In searching for a location for the 64 atoms on these 12 800 grid points it is necessary to calculate the distance between every pair of atoms tried, so as to determine whether the maximum tolerated overlap has been exceeded or not. Calculation of these interatomic distances constitutes the bulk of the computing, and we therefore take this as the basis for estimating the total computer time.

If in our example there were no symmetry then the distance calculation, requiring 10^{-4} s for each distance, would have to be made $(12\,800)^{64} \times 64 \times 63/2$ times. This would take the rather unrealistic time of 10^{255} years. Taking into account, however, the symmetry required in our example because of the space group, which in general establishes the position of one atom within this unit cell for a further 31 other atoms, limits the number of distance calculations to $(12\,800)^2 \times 64 \times 63/2$ and the estimated computing time comes down to about a year.

This example indicates the limits of what is possible even with the fastest modern computer for calcula-

tions on problems of this kind, but what we have tried to emphasize is how important it is to make use of the symmetry present in the crystal structure. The symmetry can be even more fully exploited than here, but to understand how that can be done we must first know more about that part of the unit cell called the 'asymmetric unit'.

The asymmetric unit

The presence of symmetry in a crystal lattice means that not all atomic arrangements in the unit cell are permitted in our filling problem, because certain symmetry patterns are a precondition. The placing of one atom in a certain location implies the placing of a whole family of atoms, with the method of repetition or 'multiplication' given by the space group. In the example of NaPb such a family consist of 32 atoms, and in the highest symmetry classes a family can be a group of as many as 192 atoms.

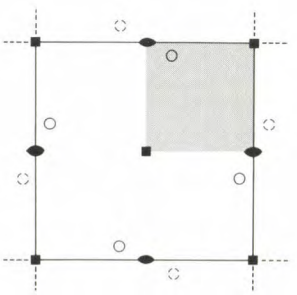

Fig. 6. 'Multiplication' of an atom (○ in the shaded part) to produce a complete two-dimensional lattice with the aid of the symmetry elements of the two-dimensional space group or planar group p4 [6]. ■ fourfold axis. () twofold axis. The multiplication can be performed by making repeated rotations of 90° about fourfold axes, first around the fourfold axes of the space group and then around the new fourfold axes, which appear at the outside as a result of the preceding multiplication operations. The continuous-line square is the unit cell; the shaded part, which, with the symmetry elements of the space group, contains all the information about the complete lattice, is called an 'asymmetric unit'. Any other number of asymmetric units are possible in addition to the one chosen here; see fig. 7.

Just as the lattice may be thought of as generated by multiple translations of the unit cell, the lattice can also be described as formed by repeated application of the symmetry operations comprised in the space group, which also include the translation operation (*fig. 6*). All the information about the crystal structure can then be given in the form of a 'recipe' for this method of multiplication with a description of the atomic arrangements in a part of the unit cell, the asymmetric unit. The size of the asymmetric unit depends on the multiplication factor of the space group, called the maximum multiplicity, and in the highest symmetry classes it can be as small as 1/192 of that of the unit cell.

This asymmetric unit is not generally used in conventional crystal-structure determinations largely because not one but any given number of asymmetric units may be chosen, all with the same volume but of different shape (*fig. 7*).

It will be clear from what we have said above that restriction to the asymmetric unit is absolutely necessary for a filling program like ours. We have solved the problem of the infinitely large number of choices for the asymmetric unit by *defining* one particular asymmetric unit for each space group. Our aim here was simplicity of description, with the fewest possible planes, edges and corner points, and the minimum number of neighbours (for reasons which will be dealt with presently).

In our example, in which the maximum multiplicity of the space group is 32, this restriction to the asymmetric unit reduces the number of calculations of interatomic distances to $(12\,800/32)^2$ and the estimated computer time to 16 seconds.

Special and general positions

In some cases the solution of the filling problem requires fewer distance determinations than the above example would suggest, because symmetry constraints impose specific positions in the unit cell, or asymmetric unit. These are known as special positions,

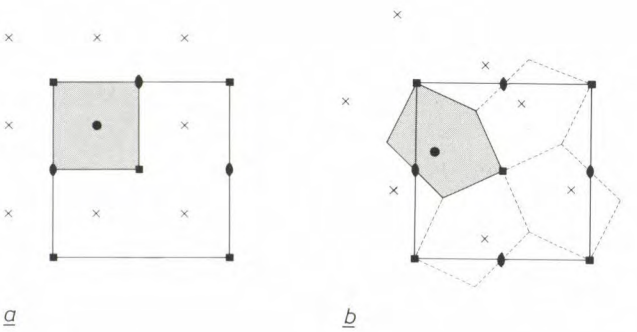

Fig. 7. Two of the asymmetric units of the (two-dimensional) space group p4, from the infinitely large number possible. In (*a*) it is a square (as in fig. 6), in (*b*) a pentagon. The structure here was built up by generating the entire family (×) from the points ● and then drawing the perpendicular bisectors of the connecting lines between the family members. It is clear that the shape of the asymmetric unit depends on the location of the chosen point ●. In (*b*) the multiplication was performed three times (dotted line) as described in fig. 6.

[7] Some tolerance in the overlapping must be accepted since in our method the atoms are located solely at the nodal points of a grid; see page 242, right-hand column.

[8] W. P. J. Fontein of these laboratories was also involved in studying the possibility of a computer solution to the filling problem.

situated at a symmetry element, for example at an inversion point, on an axis of symmetry, at an intersection of axes of symmetry, on a mirror plane, etc. An atom at a special position does not take part in the multiplication by the symmetry element where it is situated (except by coinciding with itself), in which all the atoms located outside that position do participate. It will be clear that an atom that does not occupy a special position but occupies a general position will be multiplied by all the symmetry elements present, and will thus have the highest multiplicity. A particular species of atom will have a prescribed special position if the number of atoms present in the unit cell is smaller (or not an integer number of times larger) than the multiplicity of the general position.

By way of illustration we shall now consider the crystal structure of petzite, Ag_3AuTe_2. The unit cell of petzite has a volume of 1070 Å^3; the space group 214 (symbol $I4_132$) belongs to the cubic class [6]; 24 Ag, 8 Au and 16 Te atoms have to find a place in the unit cell. If all the atoms were free to occupy a position at a general position, the computer time would be of the same order of magnitude as in the first example. Since, however, all atomic species occur in a smaller number than the maximum multiplicity (48) of the space group, all the atoms have to occupy special positions. The Au atoms can only occupy a corner point in our chosen asymmetric unit, so that the location of these atoms is established. The Ag atoms must be located on an edge of the asymmetric unit and the Te atoms on a line in a side plane of the asymmetric unit (*fig. 8*). Because of this considerable limitation of possible locations, the computer time in this case is estimated at only a fraction of a second.

Clearly, in solving the filling problem the number of distance determinations increases
1) with the size of the unit cell, and hence with the number of grid points that have to be included in the unit cell;
2) with the number of atoms in the unit cell;
3) as the degree of symmetry decreases, especially if the maximum multiplicity of the space group decreases;
4) and as the number of atoms that have to find a place at special positions decreases.

In the worst case (for computer time) where all the atoms can be located at general positions, we can express the computer time (t) as:

$$t = (p/m)^{n/m} \times \frac{1}{2}\frac{n}{m}\left(\frac{n}{m} - 1\right) \times 10^{-4} \text{ s}, \quad (1)$$

where p is the number of grid points in the unit cell, n is the number of atoms it contains, and m is the maximum multiplicity of the space group.

Suppose now that we wish to use no more than 100 s of computer time for investigating a structure. Let us also assume that the ratio p/n has a fixed value of 200 (the more atoms there are in the unit cell the greater in general the unit cell will be, and the more grid points will be needed for executing the filling program). Proceeding from these assumptions and using the above equation we can calculate how complex the structure may be that can just be determined, even in the worst case, by the filling program. For the least symmetrical, triclinic crystals, with an m-value of 1, the structure must not contain many more than two atoms in the unit cell, but for the most symmetrical, cubic crystals, with an m-value of 192, we estimate that the contents of the unit cell could be no fewer than 400 atoms.

Having given some idea of the scope and limitations of our method, we shall now give a broad description of the computer program that we use for the method. Our program has been run on the central computers at Philips Research Laboratories in Eindhoven and on the main computers of other establishments.

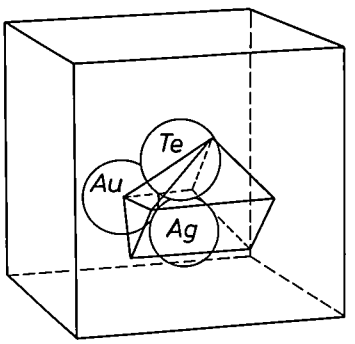

Fig. 8. The asymmetric unit as defined for the filling program for petzite (Ag_3AuTe_2), shown in the unit cell. Three special positions are indicated: a corner point, an edge and a line in the lower side plane at the back, where the atoms Au, Te and Ag (respectively) should be located; see also the left-hand part of the title picture.

The filling program

General procedure

The filling program consists of three main parts: the primary data input, the elimination of grid points as possible atom locations and the actual filling.

The principal primary data required for the input comprises the dimensions of the unit cell, the space group, the number and radius of the atoms, and the mesh width. Immediately after the input the (defined) asymmetric unit is read from the memory. Next a grid is constructed that extends beyond the asymmetric unit by a zone of width equal to twice the largest atomic radius. In this zone the atoms being placed, whose centre-points are always located within the

asymmetric unit, can come into contact with 'members of the same family'.

The next step is to determine the grid points that can be eliminated in advance as locations for an atom, because the multiplication operation would bring the atom in that position too close to one of the members of the same family, overlapping it by more than the permitted maximum percentage. (We want to keep the number of neighbours of the asymmetric unit as small as possible to minimize the number of members of the same family with which each atom could come into contact, thus reducing the number of times the computer has to calculate the overlap percentage.) The remaining grid points are next set out in a row or 'chain' always moving from special positions of low multiplicity to general positions.

The filling is done with a 'backtracking algorithm', in which the following instructions are successively carried out (*fig. 9*):

1) Look for a free grid point in the chain and place on it the largest possible atom.

2) Repeat until either all the atoms are placed (a solution has then been found) or no more atoms can be placed.

3) If no more atoms can be placed, replace the last atom by a smaller one.

4) If there is no smaller atom, remove the last atom placed.

5) Look for the next grid point in the chain and proceed as under instruction 1.

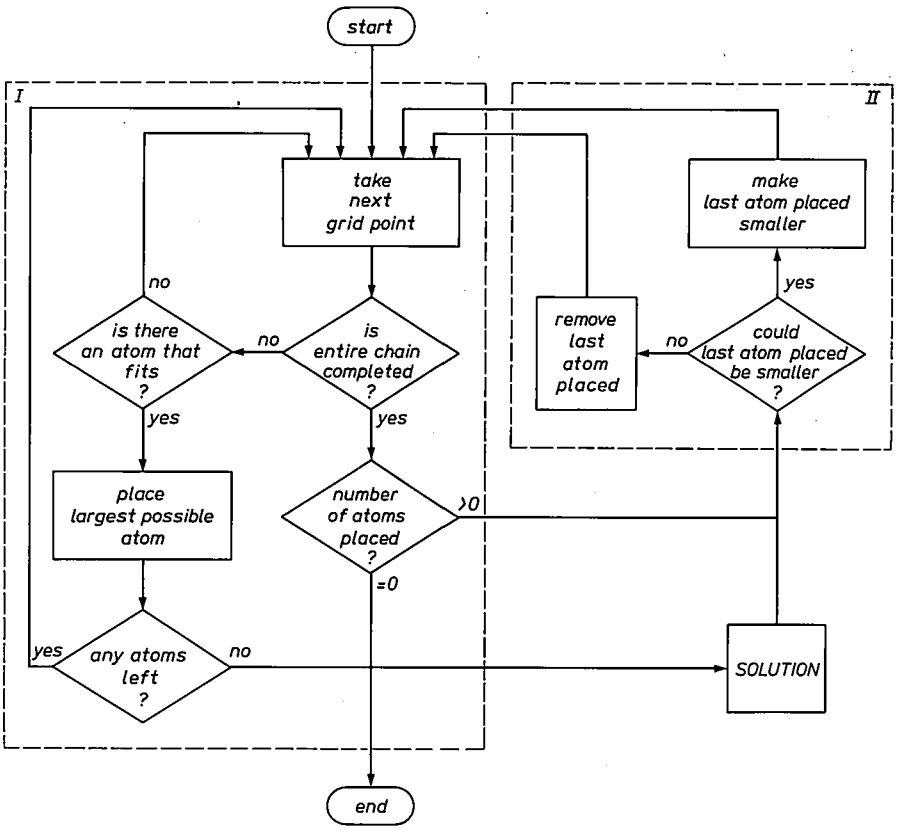

Fig. 9. General flow diagram for the filling program. I filling zone. II breaking-off zone.

Time-saving strategies

Running the filling program is like running through a maze with only a few exits — the solutions. Most of the time is spent on looking for the way out and encountering dead-ends. In making the filling program it was therefore important to find criteria that would help to show at the earliest possible stage that the way was leading to a dead-end. One such criterion is the ratio of the number of atoms still to be placed to the multiplicity of the grid points still to be tried.

We have seen that the computer runs through the grid points in the sequence of increasing multiplicity. Before the computer places atoms at grid points with a greater multiplicity, it always checks first to see whether the number of remaining atoms is still a multiple of the remaining multiplicities. If it is not, no solution is possible and an instruction to try another solution follows.

Another time-saving operation is to eliminate equivalent solutions, by determining in advance whether they are possible. If required, these can be printed out later. The detailed procedure of the advance search for equivalent solutions will not be described here, however.

Pictorial representation of the program

Fig. 10 illustrates how the computer carries out the calculations on petzite (Ag_3AuTe_2). Fig. 10*a* relates to the phase prior to the filling, when the computer performs a search to determine the grid points that can be used. For thirteen successive cross-sections through the asymmetric unit a calculation is made that will show by means of a code which atoms can be given a place and which cannot. If all the atomic species can be placed, a '3' is indicated; if tellurium, the largest

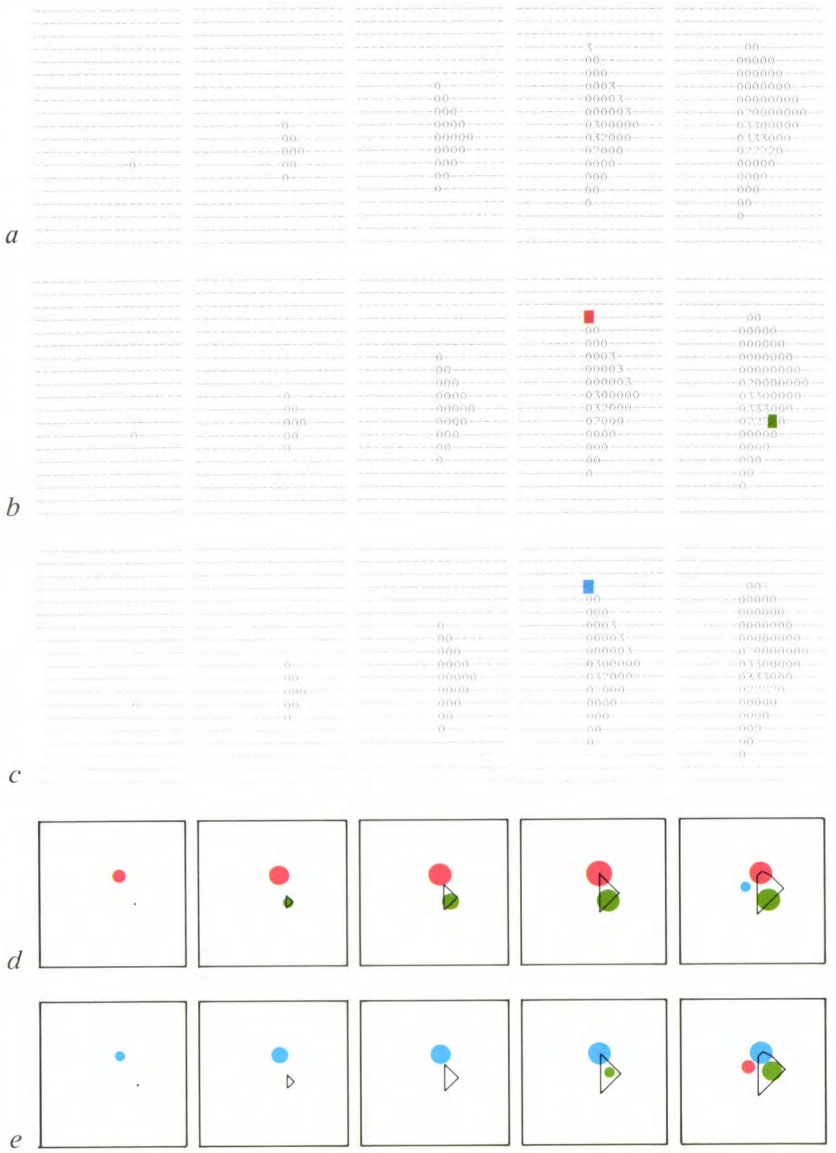

Fig. 10. Thirteen consecutive stages, shown side by side, of the grid for the asymmetric unit of petzite (Ag_3AuTe_2), calculated starting from space group 212. The distance between the stages is 1/24 of the edge of the unit cell. In (*a*) a calculation has been made for all grid points to find out whether an atom can be placed there, and if so, which one: a '–' indicates the grid points outside the asymmetric unit, a '*3*' indicates the grid points where there is room for the largest atom (Te), a '*2*' indicates there is room for the atom next in size (Au), a '*1*' marks the grid points (not found here) where only the smallest atom (Ag) can be located, and a '*0*' indicates that there is no room for any of the atoms. In (*b*) and (*c*) two possible fillings of the asymmetric unit are shown, where the green, blue and red patches represent the three atomic species in order of increasing size. (*d*) and (*e*) are the same solutions, this time indicating the cross-sections through the atoms (respectively green, blue and red). (*f*) and (*g*) are the constructed spatial representations of these two possible fillings, showing the earlier-indicated atoms and a number of neighbours. To give a clearer picture, these neighbouring atoms are considered to be transparent to the atoms mentioned earlier and only the circumferences and cross-sections of these neighbouring atoms alone are shown (in colour). From the solution shown in *c*, *e* and *g* it could be established that this solution is the correct one. It is not easy to compare the spatial representation of this filling with the one in the title picture because the filling shown here was calculated from the space group 212, whereas the one in the title picture was calculated from the space group 214. The difference in space group leads to a difference in asymmetric unit, which is twice as large in *g* and in addition has a different shape from the one in the title picture. This is also connected with the fact that the asymmetric unit in *g* contains *five* atoms, while the asymmetric unit in the title picture contains *three* atoms.

atom, is too large, a '*2*'; if gold is also too large, a '*1*' (in our example this possibility does not exist), and if no atomic species at all can be placed, a '*0*'. A dash '–' indicates that the grid points are outside the asymmetric unit.

Fig. 10*b* and *c* shows how the computer has filled up the asymmetric unit in two of its solutions. Silver is the smallest atom here that could be placed at the grid points *1*, *2* and *3*, but in this example it happens to fit only at the grid points *2* (green patch). Gold is the atom of medium size and can thus be placed at grid points *2* or *3* (here only at *3*; blue path). Tellurium is the largest atom, which only fits at the grid points *3* (red patch). In fig. 10*d* and *e* cross-sections of the placed atoms are given, and three-dimensional representations of these two solutions are shown in fig. 10*f* and *g*.

Uncertainties remaining after completing the filling program

We should emphasize once again that the filling program generates no more than a number of possible solutions (trial structures), and that a further analysis is generally necessary to determine the one correct solution. Various criteria can be used here. We might for example look for the solution with the lowest overlap percentage. It is also very common practice to follow the filling program with a 'refining' program, based on intensity data. This amounts to searching for the solution with the smallest *R*-factor (a measure of the agreement between the calculated and the measured intensity values).

After the filling program has been run it is by no means always certain that the correct space group was taken. To illustrate this complication we look again at

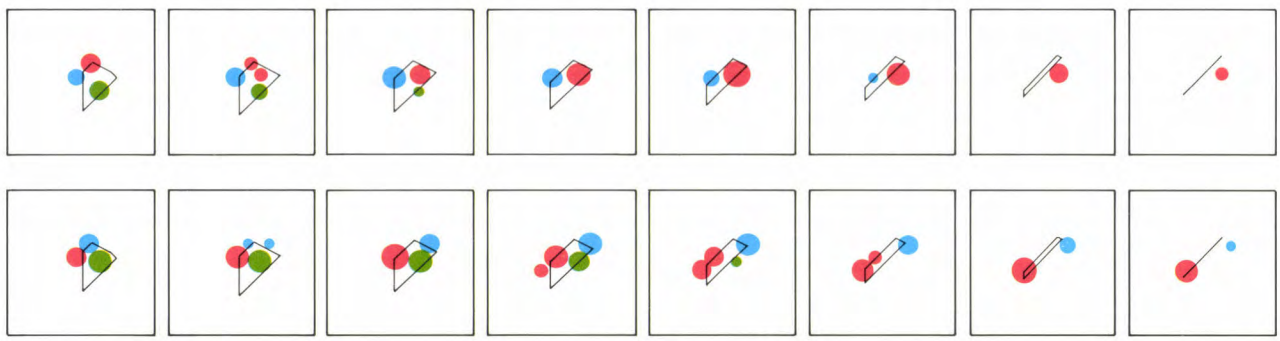

f

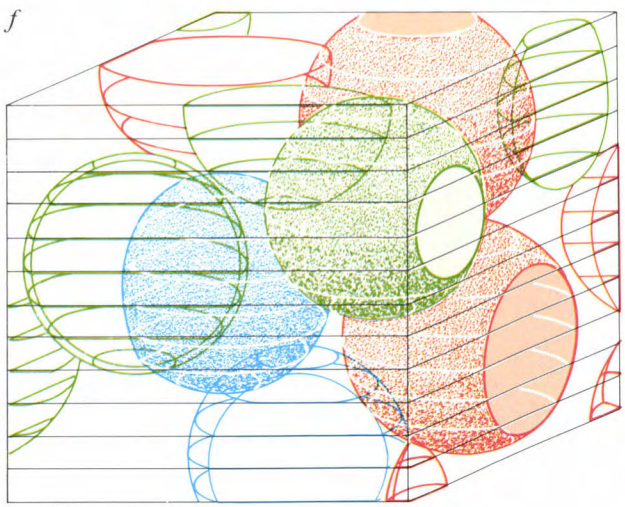

g

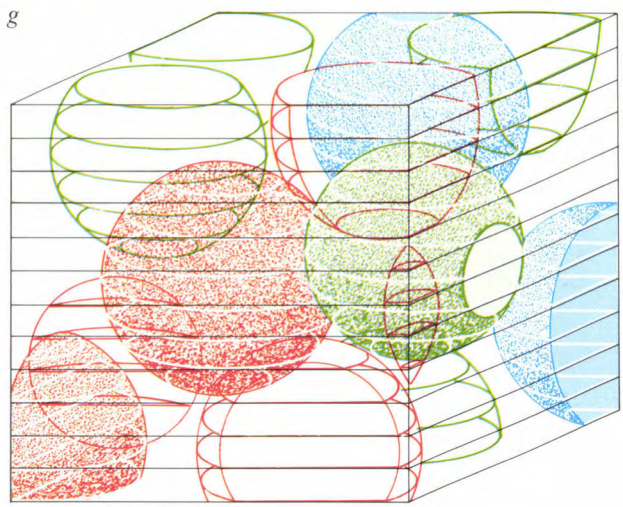

the case of petzite. Here the calculations started from space group 212 (symbol $P4_332$) and not from the actual space group 214 (symbol $I4_132$), which shows a repetition of the structure displaced by half a cell unit. Such an uncertainty in the choice of a space group is not so serious as may be thought, since this repetition also occurs in the solution found by starting from space group 212, so that this result points the way to the correct assignment of the space group.

Verifying the filling program; some results

We checked to see whether the solutions calculated by the filling program included the correct structures for 54 intermetallic compounds of known structure. This was always found to be the case.

For NaPb a total of 33 possible solutions were obtained in two seconds. For comparison *Table I* gives the atomic positions calculated by conventional methods [9] and the corresponding positions found with the filling program. It will be clear that the agreement in the values is limited because the positions obtained with the filling program can only be situated at nodal points of the grid. Nevertheless the agreement is so good that we may assume that a refinement using measured intensity values will lead to the correct structure.

The computer time of 2 s is a factor of 8 smaller than the time estimated from equation 1. This factor gives a very rough indication of the time saved by using the time-saving strategies followed in the program. (A rather more exact estimate of the computer time, including the grid points immediately *outside* the asymmetric unit — since of course there may also be some overlap between atoms placed on these points — indicates that the time saved corresponds to a factor of 30.)

For the calculations on petzite, starting from space group 214, the following procedure was adopted. In addition to the primary data, the input included intensity data and the instruction only to print out solutions with an *R*-factor smaller than 50%. A second instruction required the maximum tolerated overlap percentage (initially 20%) to be always reduced to the lowest value found. In two seconds this gave only one solution (really two, but equivalent), which was in

Table I. Atomic positions of NaPb, as found with the filling program, and as reported in the literature [9]. *m* is the multiplicity.

Atomic species		Atomic positions (filling program)			Atomic positions (literature)		
	m	*x*	*y*	*z*	*x*	*y*	*z*
Na	16	0.2500	0.8750	0.1250	0.2500	0.8750	0.1250
Na	16	0.3750	0.6250	0.2500	0.3750	0.6250	0.2500
Pb	32	0.0625	0.6250	0.1875	0.0696	0.6314	0.1867

```
GIVE THE SPACEGROUP NUMBER OR CODE
64
DO YOU DESIRE A DESCRIPTION OF THE ASYMMETRIC UNIT ?
n

SPACE GROUP NR  64  CODE: C m c a
C.C. ORTHORHOMBIC

GIVE A, B AND C
5.1138, 9.7316, 7.9075
DO YOU GIVE MEASURED DATA ?
y
FROM THE TERMINAL (T) OR FROM THE DATA FILE (F) ?
f
GIVE THE IDENTIFICATION NAME (<21 CHARACTERS)
LA2NI3

          REFLEXIONS (LAMBDA = 1.54056  )
      THETA                    INDEXING        INTENSITY
MEASURED      CALCULATED      H    K    L     MEASURED
 10.71          10.71         0    2    1      5.00
 11.23          11.23         0    0    2      5.00
 11.31          11.31         1    1    1     30.00
 14.54          14.54         0    2    2      5.00
 14.99          14.99         1    1    2    234.00
 17.31          17.31         1    3    1    253.00
 17.53          17.53         2    0    0     30.00
 18.46          18.46         0    4    0     23.00
                19.34         0    4    1
 19.37          19.41         0    2    3    209.00
 19.76          19.76         1    1    3     45.00
                19.90         2    2    0
 19.95          20.00         1    3    2     19.00
 20.73          20.73         2    2    1    130.00
 21.02          21.02         2    0    2     85.00
 21.82          21.82         0    4    2      2.00
 23.09          23.09         2    2    2      7.00
 24.90          24.87         0    2    4     26.00
 25.16          25.16         1    1    4     29.00
 25.52          25.52         0    4    3      5.00

GIVE PER ELEMENT THE RADIUS, THE NUMBER OF ATOMS PER UNIT CELL AND
THE CHEMICAL SYMBOL (AND CHARGE), FINISH WITH 100.
1.87,8,LA, 1.24,12,NI, 100

      SCATTERING FACTORS
SINTET/LAM     Ni          La
   .00       28.000      57.000
   .05       27.330      55.940
   .10       25.600      53.190
   .15       23.440      49.710
   .20       21.370      46.290
   .25       19.590      43.170
   .30       18.030      40.300
   .35       16.610      37.640
   .40       15.340      35.230
   .50       13.250      31.090
   .60       11.560      27.630
   .70       10.200      24.760

GIVE A REAL NUMBER OF MESHES ( .5<N<4 )
PER RADIUS LENGTH OF THE SMALLEST ATOM FOR THE X, Y AND Z DIRECTIONS
3,3,3

MESHPOINTS ALONG A, B AND C RESP.   16    24    20
WITH MESH LENGTHS RESP.  .3196    .4055    .3954  ANGSTROM

GIVE THE MAXIMUM OVERLAP FRACTION OF THE RADII AND
ITS MINIMUM VALUE TO WHICH IT MAY AUTOMATICALLY DECREASE
.2,0
GIVE THE MAXIMUM R FACTOR (%) FOR WHICH A RESULT IS TO BE PRINTED
50

NUMBER OF MESHPOINTS OF ASYMMETRICAL UNIT  715
NUMBER OF ASSOCIATED POINTS  599

GIVE FOR THE INITIAL FILLING FOR EACH ATOM (OR ION) 3 COORDINATES
AND THE CHEMICAL SYMBOL (AND CHARGE). FINISH WITH 100
100

                SOLUTION NR    1
        SPACE GROUP NR  64  CODE: C m c a
 NR  SYMB RADIUS  MULT.        COORDINATES
  1  Ni    1.24     4    +.0000    +.0000    +.0000
  2  Ni    1.24     8    +.2500    +.0417    +.2500
  3  La    1.87     8    +.0000    +.3333    +.1000
R FACTOR=   25.54   ,  OVERLAP =+.1401  ,  TIME =    2  SEC       5

                SOLUTION NR    2
        SPACE GROUP NR  64  CODE: C m c a
 NR  SYMB RADIUS  MULT.        COORDINATES
  1  Ni    1.24     4    +.0000    +.0000    +.0000
  2  Ni    1.24     8    +.2500    +.0833    +.2500
  3  La    1.87     8    +.0000    +.3333    +.1000
R FACTOR=   10.17   ,  OVERLAP =+.0866  ,  TIME =    2  SEC       6

                SOLUTION NR    3
        SPACE GROUP NR  64  CODE: C m c a
 NR  SYMB RADIUS  MULT.        COORDINATES
  1  Ni    1.24     4    +.0000    +.0000    +.0000
  2  Ni    1.24     8    +.2500    +.4167    +.2500
  3  La    1.87     8    +.0000    +.1667    +.4000
R FACTOR=   10.17   ,  OVERLAP =+.0866  ,  TIME =    2  SEC       7

RUN NR 1 : BEST SOLUTION IS NR  2  WITH R FACTOR  10.17  ,  TIME= 2
```

Fig. 11. Computer print-out for the filling of the asymmetric unit of La_2Ni_3. The print-out shows the questions asked by the program, the answers keyed in and the three solutions obtained (two of them are equivalent).

fact the correct one (the title picture gives the fillings found for the asymmetric unit and the unit cell; this solution corresponds to the one shown in fig. 10*g*, calculated starting from space group 212). At first the *R*-factor was not particularly small, but by applying the refinement program it was possible to reduce it to 20.5%. This would seem to be reasonable in view of the quality of the powder diagram. After the refinement, the atomic positions did indeed deviate by no more than 0.01 Å from those calculated for measurements on a single crystal [10].

So far we have only been considering compounds of known structure. Some years ago, in an investigation on powder diagrams of compounds between La and Ni, not only were lines of known phases like LaNi, $LaNi_2$, La_2Ni_7 and $LaNi_5$ found, but also lines originating from an unknown phase, with the approximate composition $LaNi_{1.4}$ [11]. It is very difficult to make single crystals from compounds like this. The unidentified lines in the powder diagram may be attributed to an orthorhombic structure with unit-cell edges of 5.1138, 9.7316 and 7.9075 Å in length. The absence of certain lines indicated a symmetry of space group 64 (symbol Cmca) [6]. From this, and from the approximate composition, it was possible to conclude with a fair degree of probability that the unit cell contained 8 La and 12 Ni atoms.

With the same procedure as just described, three solutions were found, two of which were equivalent. *Fig. 11* shows by way of example the complete result for this case printed out by the computer. The much lower *R*-factor of the two equivalent solutions led us to accept this structure as the correct one. The same structure was later found for the related compound La_2Co_3.

We have also explained the previously unknown structure of the compound PtFeSb [12], and the same structure was later found to occur in PtCrSb. The result of the filling program indicated that the most probable solution having an *R*-factor of 29.3% was a structure in space group 198 (symbol $P2_13$). Only by allowing interchangeability of the positions of Pt and Fe atoms was it possible to obtain good agreement between measured and calculated intensities ($R = 9.4\%$), see *Table II*. The resultant 'mixing' of the magnetic Fe atoms with the non-magnetic Pt atoms led us to expect characteristic magnetic effects, which were indeed found in the Mössbauer spectrum [12].

Table II. Atomic positions of PtFeSb found with the filling program, and the calculated occupancy for the Fe and Pt atoms with interchangeable positions.

Atomic species		Atomic positions (filling program)			Occupancy in %
	m	*x*	*y*	*z*	
Pt	4	0.000	0.000	0.000	77
Fe	4	0.000	0.000	0.000	23
Fe	4	0.625	0.625	0.625	77
Pt	4	0.625	0.625	0.625	23
Sb	8	0.375	0.375	0.375	—

Limitations and possibilities

We have said that a fundamental limitation of the method is that it can only be applied to compounds that consist of spherical atoms, and then only to those compounds that are not too complex. However, we have not yet discussed the possibility that one or more atomic species of a compound can be much smaller than the other atomic species. Where this is so the computer time will be relatively long because of the finer mesh required. One step further, and between the larger atoms there are a variety of interstices, any of which could contain atoms of the smaller species. In such a case our filling program obviously cannot provide definitive solutions for the locations of the small atoms.

We do not want to conclude our article by listing the main limitations of the method; we should also mention its potential application to non-metallic compounds, i.e. not basing the method entirely on the spherical shape with all-round symmetry. A filling program like ours could conceivably be used for generating trial structures with other basic units of known shape and dimensions. This does of course require the introduction of a different definition for the spacing between the basic units, and a different overlapping criterion and a different verification procedure will also have to be tried out. The basic units might for example be SO_4^{2-} groups and other ion conglomerations, always structured in the same way, of course, or they might be benzene rings and similar organic molecular structures of well-known shape and dimensions.

[9] W. B. Pearson, A handbook of lattice spacings and structures of metals and alloys, Vol. I, Pergamon, London 1958.
[10] A. J. Frueh, Jr., Am. Mineral. 44, 693-701, 1959.
[11] K. H. J. Buschow and H. H. van Mal, J. Less-Common Met. 29, 203-210, 1972.
[12] K. H. J. Buschow, J. H. N. van Vucht, P. G. van Engen, D. B. de Mooij and A. M. van der Kraan, Phys. Stat. Sol. a 75, 617-623, 1983.

Summary. The article describes a method that can be used to calculate crystal structures of metals and intermetallic compounds on a computer. The unit cell and the space group are derived from powder diagrams, and are taken as the basis for defining an 'asymmetric unit'. A grid is introduced in this asymmetric unit and the atoms are placed at the grid points by trial and error. The atoms are not allowed to overlap by more than a specified percentage (e.g. 10%). A number of time-saving strategies are discussed. The reliability of the method has been checked for 54 known structures. The application of the method to compounds of previously unknown structures (La_2Ni_3, La_2Co_3, PtFeSb, PtCrSb) is also discussed.

Scientific publications

These publications are contributed by staff of laboratories and plants that form part of or cooperate with enterprises of the Philips group of companies, particularly by staff of the research laboratories mentioned below. The publications are listed alphabetically by journal title.

Philips GmbH Forschungslaboratorium Aachen, Weißhausstraße, 5100 Aachen, Germany — *A*

Philips Research Laboratory Brussels, 2 avenue Van Becelaere, 1170 Brussels, Belgium — *B*

Philips Natuurkundig Laboratorium, Postbus 80 000, 5600 JA Eindhoven, The Netherlands — *E*

Philips GmbH Forschungslaboratorium Hamburg, Vogt-Kölln-Straße 30, 2000 Hamburg 54, Germany — *H*

Laboratoires d'Electronique et de Physique Appliquée, 3 avenue Descartes, 94450 Limeil-Brévannes, France — *L*

Philips Laboratories, N.A.P.C., 345 Scarborough Road, Briarcliff Manor, N.Y. 10510, U.S.A. — *N*

Philips Research Laboratories, Cross Oak Lane, Redhill, Surrey RH1 5HA, England — *R*

Philips Research Laboratories Sunnyvale P.O. Box 9052, Sunnyvale, CA 94086, U.S.A. — *S*

P. Blood & J. W. Orton *R*	Recent developments in the characterisation of semiconductors by transport measurements	Acta Electron. **25**	103-121	1983
S. Martin & G. Jacob (*CNET, Meylan*) *L*	Propriétés électriques des lingots d'arséniure de gallium	Acta Electron. **25**	123-132	1983
G. M. Martin & S. Makram-Ebeid *L*	Les défauts ponctuels dans l'arséniure de gallium	Acta Electron. **25**	133-145	1983
G. W. 't Hooft, C. van Opdorp & A. T. Vink *E*	Carrier lifetime in (Al,Ga)As epilayers and double heterostructure lasers grown with metalorganic vapour-phase epitaxy and liquid-phase epitaxy	Acta Electron. **25**	193-200	1983
J. N. Sandoe & J. R. Hughes *R*	EBIC and LBIC techniques for characterisation of reverse biased power devices	Acta Electron. **25**	201-209	1983
S. Gourrier & P. Friedel *L*	Caractérisation électrique des états électroniques d'interface isolant/semiconducteur	Acta Electron. **25**	217-240	1983
S. Makram-Ebeid & P. Minondo *L*	Effets parasites dans les transistors à effet de champ en GaAs: rôles de la surface et du substrat semi-isolant	Acta Electron. **25**	241-260	1983
C. Tsironis *L*	Influence de la technologie sur le bruit en basse fréquence des transistors à effet de champ en arséniure de gallium: importance pour des applications en amplificateur, mélangeur et oscillateur	Acta Electron. **25**	281-286	1983
D. J. Broer & L. Vriens *E*	Laser-induced optical recording in thin films: modelling of the hole opening and experiments with organic sublayers	Appl. Phys. A **32**	107-123	1983
J. H. Neave, P. J. Dobson (*Imp. College, London*) J. J. Harris, P. Dawson & B. A. Joyce *R*	Silicon doping of MBE-grown GaAs films	Appl. Phys. A **32**	195-200	1983
M. J. Powell *R*	Charge trapping instabilities in amorphous silicon-silicon nitride thin-film transistors	Appl. Phys. Lett. **43**	597-599	1983
T. G. J. van Oirschot (*Philips Elcoma Div., Eindhoven*), A. Valster & J. A. de Poorter *E*	Ridged substrate internally diffused stripe AlGaAs laser emitting in the visible wavelength region	Appl. Phys. Lett. **43**	809-811	1983
A. I. Goldman*, E. Canova*, Y. H. Kao* (* *Univ., Stony Brook, NY*), B. J. Fitzpatrick, R. N. Bhargava & J. C. Phillips (*Brookhaven Natl. Lab., Upton, NY*) *N*	Extended x-ray absorption fine structure studies of diffused copper impurities in ZnSe	Appl. Phys. Lett. **43**	836-838	1983
W. J. M. J. Josquin, P. R. Boudewijn & Y. Tamminga *E*	Effectiveness of polycrystalline silicon diffusion sources	Appl. Phys. Lett. **43**	960-962	1983

J. van Esdonk & H. H. van der Sluis (*TNO, Apeldoorn*)	*E*	Ceramic to metal seals by metallising and/or active brazing	Brazing & Soldering (No. 5)	22-25	1983
J. M. Shannon	*R*	Hot electron diodes and transistors	ESSDERC/SSSDT 1983, Canterbury 1983 (Inst. Phys. Conf. Ser. No. 69)	45-62	1983
P. A. Moore, S. K. Salmon	*R*	Surface acoustic wave reference oscillators for UHF and microwave generators	IEE Proc. H **130**	477-482	1983
G. F. M. Beenker & K. A. Schouhamer Immink	*E*	A generalized method for encoding and decoding run-length-limited binary sequences	IEEE Trans. **IT-29**	751-754	1983
E. Arnold & J. P. Karins	*N*	Electrical properties of doped semi-insulating polycrystalline silicon	Insulating films on semiconductors, J. F. Verweij & D. R. Wolters (eds), Elsevier, Amsterdam	149-152	1983
M. J. Powell	*R*	Instability mechanisms in amorphous silicon — silicon nitride thin film transistors	Insulating films on semiconductors, J. F. Verweij & D. R. Wolters (eds), Elsevier, Amsterdam	245-251	1983
W. N. Schreiner, C. Surdukowski & R. Jenkins (*Philips Electron. Instrum., Mahwah, NJ*)	*N*	A probability-based scoring technique for phase identification in X-ray powder diffraction	J. Appl. Crystallogr. **15**	524-530	1982
S. D. Brotherton, G. J. Parker & A. Gill	*R*	Photoionization cross section of electron irradiation induced levels in silicon	J. Appl. Phys. **54**	5112-5116	1983
R. G. Pratt, J. Hewett, P. Capper* C. L. Jones* & M. J. Quelch* (* *Mullard, Southampton*)	*R*	Minority carrier lifetime in *n*-type Bridgman grown $Hg_{1-x}Cd_xTe$	J. Appl. Phys. **54**	5152-5157	1983
G. M. Blom	*N*	Hole formation in tellurium alloy films during optical recording	J. Appl. Phys. **54**	6157-6182	1983
D. Y. Lou & G. M. Blom	*N*	Measurements on ablative hole formation process in thin tellurium-selenium alloy films	J. Appl. Phys. **54**	6637-6640	1983
H. K. Kuiken & R. P. Tijburg	*E*	Centrifugal etching: a promising new tool to achieve deep etching results	J. Electrochem. Soc. **130**	1722-1729	1983
G. de With	*E*	Note on the temperature dependence of the hardness of boron carbide	J. Less-Common Met. **95**	133-138	1983
J. R. Mansell & A. W. Woodhead	*R*	Contrast loss in image devices due to electrons backscattered from the fluorescent screen	J. Phys. D **16**	2269-2278	1983
M. J. Jongerius & A. J. M. J. Ras	*E*	Optogalvanic detection of acoustic resonances in a high-pressure sodium discharge	J. Physique **44** (Colloque C7)	C7/377-C7/384	1983
E. E. de Kluizenaar (*Philips Plastics & Metalware Fact.*)		Surface oxidation of molten soft solder: An Auger study	J. Vac. Sci. & Technol. A **1**	1480-1485	1983
A. Shaulov	*N*	Advantages of obliquely cut pyroelectric crystals for infrared detectors	Laser Focus/Electro-Optics (Sept. 1983)	216-218	1983
P. K. Larsen & J. F. van der Veen (*FOM, Amsterdam*)	*E*	Geometrische en elektronische structuur van halfgeleideroppervlakken, vervaardigd met molecuulbundel epitaxie	Ned. T. Natuurk. A **49**	68-70	1983
H. A. Harwig	*E*	Ontwikkelingen in de technologie van geïntegreerde geheugenschakelingen	Ned. T. Natuurk. A **49**	77-81	1983
G. A. Wesselink	*E*	Compact fluorescent lamps	Philips J. Res. **38**	166-179	1983
A. L. J. Burgmans & P. R. van IJzendoorn	*E*	The three-bulb lamp; a very compact fluorescent lamp	Philips J. Res. **38**	180-187	1983
		Erratum	Philips J. Res. **38**	312	1983
W. J. van den Hoek (*Philips Lighting Div., Eindhoven*)		Diagnostic methods in lamp research	Philips J. Res. **38**	188-213	1983
		Erratum	Philips J. Res. **38**	313	1983
P. Tielemans* & F. Oostvogels* (* *Philips Lighting Div., Eindhoven*)		Electrode temperatures in high pressure gas discharge lamps	Philips J. Res. **38**	214-223	1983
E. Schnedler	*A*	Description of tungsten transport processes in inert gas incandescent lamps	Philips J. Res. **38**	224-235	1983

E. Schnedler	*A*	Description of tungsten transport processes in halogen incandescent lamps	Philips J. Res. **38**	236-247	1983
S. Garbe & S. Hanloh	*A*	Growth of potassium-filled bubbles in doped tungsten and its relation to hot spot development and intergranular fracture	Philips J. Res. **38**	248-262	1983
J. W. Denneman (*Philips Lighting Div., Eindhoven*)		Acoustic resonances in high frequency operated low wattage metal halide lamps	Philips J. Res. **38**	263-272	1983
J. E. Curran	*R*	The use of plasmas to deposit and etch materials	Phys. Technol. **14**	283-296	1983
K. van Berkel	*E*	VLSI-layout design requires a new language	Proc. IEEE Int. Conf. on Computer design: VLSI in computers, Port Chester, NY, 1983	485-490	1983
D. Paterson	*R*	Automatic inspection of fine lines	Proc. SPIE **376**	94-98	1983
A. Huijser, B. Jacobs, L. Vriens, J. Markvoort*, A. Spruijt* & P. Vromans* (* *Philips Opt. Media Labs, Eindhoven*)	*E*	Ageing characteristics of digital optical recording (DOR) media	Proc. SPIE **382**	270-275	1983
H. M. van Noort	*E*	A transient layer in Sendust on a silicon substrate, as studied by conversion electron Mössbauer spectroscopy	Solid State Commun. **48**	495-497	1983
S. D. Brotherton	*R*	The width of the non-steady state transition region in deep level impurity measurements	Solid-State Electron. **26**	987-990	1983
J. H. Neave, P. K. Larsen, J. F. van der Veen (*FOM, Amsterdam*), P. J. Dobson (*Imp. College, London*) & B. A. Joyce	*R, E*	Effect of arsenic species (As_2 or As_4) on the crystallographic and electronic structure of MBE-grown GaAs(001) reconstructed surfaces	Surf. Sci. **133**	267-278	1983
B. H. Verbeek, P. K. Larsen & W. M. Gerits		Electronic structure of PdGa(110) by photoemission spectroscopy	Vacuum **33**	813-814	1983
M. Davio, J.-P. Deschamps & A. Thayse	*B*	Digital systems with algorithm implementation	Wiley, Chichester	—	1983

Contents of Electronic Components & Applications **6**, No. 1, 1984

P. Sijbers: Versatile speech/transmission ICs suit all telephone architectures (pp. 2-6)

N. Q. Burnham & C. F. Cowling: Fault-tolerant software in real-time single-chip microcontroller systems (pp. 7-14)

J. R. Kinghorn: Computer controlled teletext (pp. 15-29)

J. K. Chay: Fast co-processor meets factory's real-time needs (pp. 30-36)

J. W. Beunders & A. Garskamp: New techniques for accurately tuning a.m. and f.m. radios (pp. 37-43)

J. Exalto & H. Kern: Modifying Teradyne 283 programs to test high-speed CMOS logic ICs (pp. 45-47)

C. H. J. Bergmans: Twin-switch power pack for 110° colour tv (pp. 48-55)

P. Moors & T. H. Uittenbogaard: Wideband i.f. amplifier for satellite tv receiving systems (pp. 56-59)

Contents of Philips Telecommunication Review **42**, No. 1, 1984

P. G. L. Potgieser: Communicating typewriters (pp. 1-12)

F. L. van den Berg: An RF up-down converter for SCPC satellite communication (pp. 13-22)

Fifty years ago (pp. 23-27)

J. Scheepstra & G. B. Siebers: Passively cooled shelters for unattended telecommunication sites (pp. 28-34)

J. de Boer & J. B. de Jager: The trunking of radio channels in private mobile radio networks (pp. 35-45)

Volume 41, 1983/84, No. 7/8 pages 201-252 Published 11 September 1984

PHILIPS TECHNICAL REVIEW

VOLUME 41, 1983/84, No. 9

DIVAC — an experimental optical-fibre communications network

J. van der Heijden

Nowadays 'optical communication' usually means the exchange of information with the aid of optical fibres. The term is also applicable, however, to visual communication by semaphore or similar methods. In France between 1793 and 1852, for example, a visual communication network designed by Claude Chappe was in use. This worked with a system of moving arms that could be viewed by telescope from distances of up to 20 km. The network eventually had 556 stations and covered a total length of 4000 km [*]*. Although this network was very successful, it probably delayed the introduction of the electric telegraph in France by 20 years or more.*

Today something similar is happening. The introduction of optical-fibre networks is being delayed by the presence of conventional networks that work well, although optical fibres undoubtedly have distinct advantages over conventional copper cables for many communication applications.

To provide a general insight into the many possibilities offered by optical-fibre networks the DIVAC project was set up (DIVAC is an acronym for the Dutch words standing for digital connection between subscriber and exchange via optical fibres). In the DIVAC project experience is being gained not only with new technologies but also with new services. The parties cooperating in the project are the Dr Neher Laboratory of the Netherlands Posts and Telegraph Service, the Delft and Eindhoven Universities of Technology, Philips' Telecommunicatie Industrie B.V. and Philips Research Laboratories.

Introduction

A term encountered more and more widely today is 'information society'. The thinking behind this term is that we are now experiencing a transition from an industrially oriented society to an information-oriented society. The production of goods — mainly concentrated in western countries since the industrial revolution — will, it is considered, move increasingly to the countries of the third world. (The changes in the textile industry are a particular case in point.) The western countries will then become more engaged in 'intellectual production', that is to say in generating and disseminating information and in providing the necessary tools for that purpose.

We shall not enquire here into the social and political implications to which these changes would lead. What is relevant in this context, however, is that the changes have been made possible by a number of technological developments, two of which will be mentioned here. The first is the transition from analog to digital information transmission. The second is the move towards ever-higher signal frequencies, partly brought about by the perfection of optical fibres as a medium for signal transmission [1].

In telecommunication digital signal transmission has a number of interesting advantages. Since the sig-

Ir J. van der Heijden is with Philips Research Laboratories, Eindhoven.

[*] G. R. M. Garratt, The early history of telegraphy, Philips Tech. Rev. 26, 268-284, 1965.

[1] A. P. Bolle, Het gebruik van glasvezelkabel in lokale telecommunicatienetten, Staatsuitgeverij, 's-Gravenhage 1982 (in Dutch).
G. Mogensen, Wide-band optical fibre local distribution systems, Opt. & Quantum Electronics 12, 353-381, 1980.
N. Bjornandersen, M. Earl, O. Holst and E. Mumford (eds), Information society — for richer for poorer, North-Holland, Amsterdam 1982.

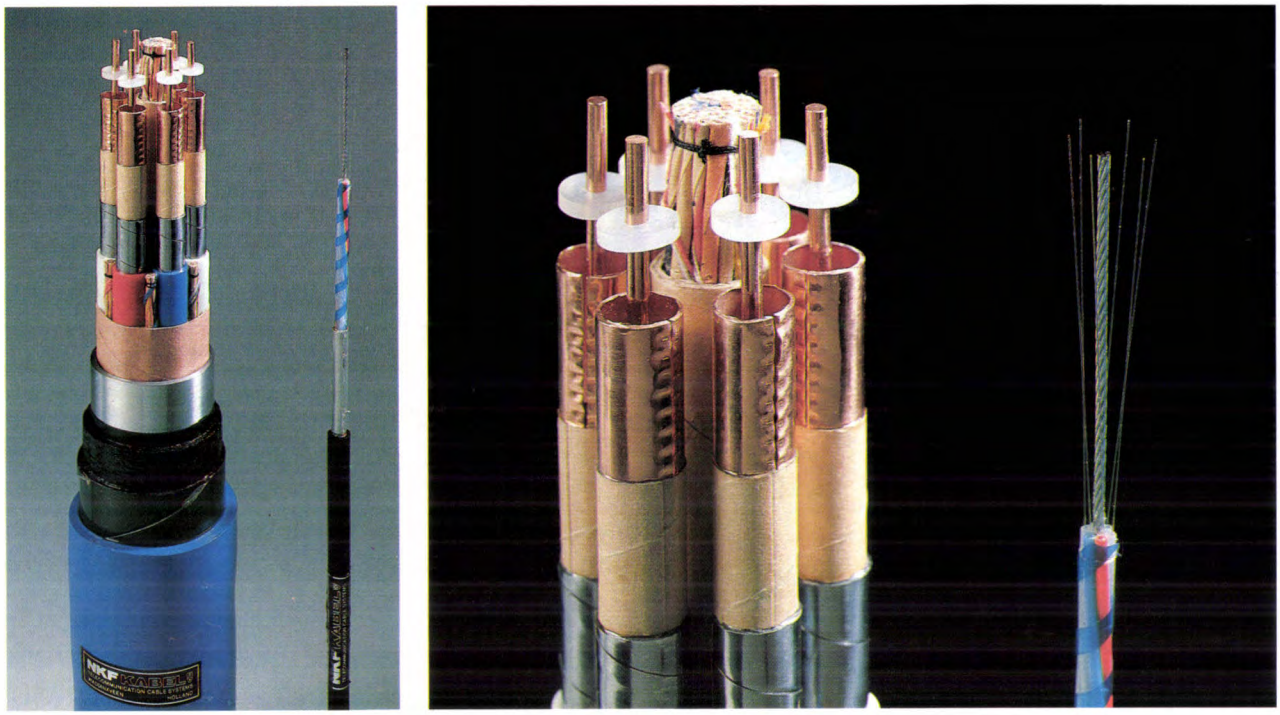

Fig. 1. Comparison of the dimensions of an optical-fibre cable and a coaxial cable, both with six cores. *Left:* general view; *right:* close-up. The copper conductors in the centre of the coaxial cable supply the signal amplifiers. The external diameter of the coaxial cable is 62 mm, the external diameter of the optical-fibre cable is 8 mm.

nals are built up from discrete voltage levels, there is less interference from the environment. A distorted signal can be restored during transmission or afterwards. Different digital signals can be 'multiplexed', so that they can be transferred as a single combined signal. The electronics required for multiplexing digital signals can be integrated more easily than the circuits required for multiplexing analog signals.

The techniques that can be used for multiplexing digital signals in optical-fibre cables are known as TDM (time-division multiplex), WDM (wavelength-division multiplex), SDM (space-division multiplex) and FDM (frequency-division multiplex). In TDM bit-groups of different signals follow one after the other in time. In WDM, signals formed from light of different 'colours' are transferred along a fibre simultaneously. In SDM a separate fibre in the cable is used for each signal. In FDM, signals of different frequency are added together. This originally analog method is used in digital technology for multiplexing signals with different bit rates, and can only be used here by virtue of coding techniques that modify the frequency spectra of the separate signals to prevent them from overlapping.

The modern optical-fibre cable for communication applications has exceptionally low attenuation — less than 1 dB per kilometre — which means that fewer repeaters are required than with coaxial cables. It also has various other advantages. The signal is not susceptible to interference from electromagnetic fields set up by nearby cables or other sources. An optical-fibre cable is also much smaller in diameter and lighter than a coaxial cable (see *fig. 1*), so that an optical-fibre cable can often be found accommodation in an existing cable duct. Then again, the raw materials for manufacturing the glass optical fibres are widely distributed in the Earth's crust. Finally, the price of optical-fibre links is still falling, so that they can already compete economically with coaxial-cable links — especially when the costs of the repeaters are taken into account. For this reason optical-fibre cables are already in use for connections between telephone exchanges.

Many homes in Western Europe are connected to a telephone network consisting of pairs of copper wires and to coaxial-cable systems for broadcast-signal transmission via a central antenna; see *Table I*. The telephone network can be used for two-way communication, whereas the broadcasting network is intended for purely one-way communication. Limited intervention by the user is possible only in the case of Videotex (picture information is obtained here by making telephone connections).

A local optical-fibre star network, which connects an exchange directly to a number of subscribers, offers

many more possibilities than present-day communication networks. With such a network the user can obtain a wide variety of information, and he can also communicate with the exchange or with other users. The optical fibre that connects the user's home to the exchange can be made to carry different signals simultaneously through the use of multiplexing methods, and signals can be sent in both directions simultaneously by using light of different spectral composition. In local optical-fibre star networks the present communication facilities can be combined with newer services such as video telephone, pay television, video-library services, electronic shopping and electronic banking.

The concept of 'service' should be understood as a facility offered to the user via the exchange and the optical-fibre star network. A service can be a programme, a video signal, a bit stream or a stream of photons, depending on the level at which it is being considered. A hierarchical model of this kind can be assigned to any service; see *fig. 2*. The user is not interested in the technical aspects of the video signal, nor in the method of manufacture of the cable that enters his home. He is however interested in the programmes he can watch on the screen of his television set. At the various levels in the hierarchical model different persons or bodies are involved: users, television-set manufacturers, network controllers, suppliers and installers of cable networks, programme suppliers and broadcasting organizations. The rules observed by the persons and bodies involved rest to a large extent on government regulations. The advantages of integrating all existing and new services in a multiservice network are that if new systems are installed the costs are relatively low and the user can benefit from a multiplicity of services, which can be extended as required.

In countries like Canada, West Germany, France and Japan experiments on a limited scale with local optical-fibre networks have already been undertaken or will be carried out in the near future [4]. The object of these experiments is to gain knowledge and experience with new technologies, to assess the reaction and acceptance of the persons and bodies involved, and to encourage the enactment of appropriate legislation, rules and regulations (e.g. should the users pay for the services individually or as a package). Standards institutions can also be encouraged to consider the standardization of signals, signal processing and equipment.

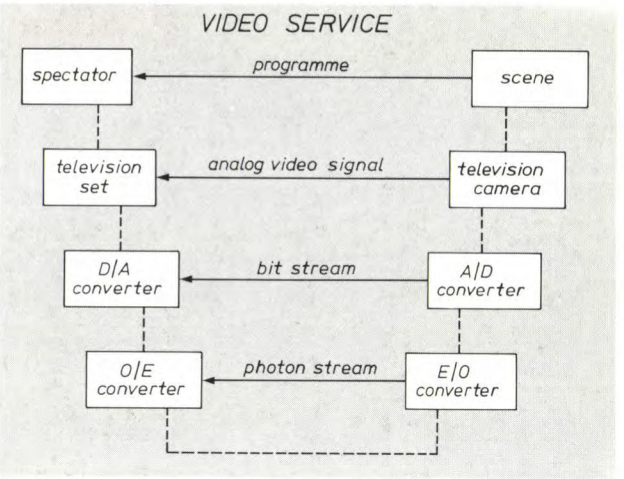

Fig. 2. Hierarchical model of a service (the video service). *A/D* analog/digital, *D/A* digital/analog, *E/O* electronic/optical, *O/E* optical/electronic.

Table I. The degree of penetration of telephony and central-antenna systems (CATV) in some countries of western Europe.

	Number of telephone connections per 100 *inhabitants* [2]	Number of CATV connections per 100 *families* [3]
Belgium	37	85
Denmark	64	61
Finland	50	44
France	46	44
Netherlands	51	65
Switzerland	73	59
United Kingdom	50	14
West Germany	46	41

An experimental local optical-fibre network has also been designed in the Netherlands. This design has resulted in a trial system that was put into operation some time ago. The project is called DIVAC (an acronym for the Dutch words standing for 'digital connection between subscriber and exchange via optical fibres'). The trial system differs from other experimental networks: all the signals are digitized, and it includes a very large number of services. To make it more readily accessible to interested parties, the system has been accommodated in a laboratory, and comprises one exchange and two 'subscribers'. The participants cooperating in the project were: Eindhoven University of Technology (audio activities), Delft University of Technology (design of the video switching network), Philips' Telecommunicatie Industrie B.V. (design of the optical units), the Dr Neher Laboratory of the Netherlands PTT (telephony), and Philips

[2] The world's telephones, AT&T Long Lines, Morris Plains, NJ, 1981.

[3] Cable TV communications in Western Europe, CIT Research, London 1982.

[4] J. van der Heijden, Fibre optic broadband multiservice networks, Proc. 9th ECOC (invited & post-deadline papers), Geneva 1983, 8 pp.

Research Laboratories (coding of video signals and new services). The integration of all these fields to form a complete system was undertaken by a working group in which all the partners were represented. The system was accommodated in the Geldrop Projects Centre of Philips Research Laboratories, Eindhoven. It was in operation there for more than a year, gave full technical satisfaction and attracted a great deal of interest, both at home and abroad. The system has recently been transferred to the Dr Neher Laboratory at Leidschendam to be used for demonstrations.

In the following we shall first look at the system aspects of DIVAC and at the services made available. Some of the technical features will then be discussed, and a few of the services will be examined in more detail.

The system

As we have just seen, DIVAC is a laboratory system, with one exchange and two subscribers. The subscribers are each connected to the exchange by two optical fibres 5 km in length, partly incorporated in a twelve-core cable; see *fig. 3*. The experimental network is the simplest form of a star network with long arms, each subscriber being connected to the exchange without the intermediary of distribution stations. (A telephone network is built up in the same way; in a cable-television network, on the other hand, the subscriber is usually connected to the exchange via intermediate distribution points.) The subscribers to DIVAC can communicate with each other via the exchange, but they also have access to services offered by the exchange, originating from outside sources such as broadcasting stations or generated in the exchange itself.

Most of the signals that enter the exchange or are generated in the exchange are analog signals. The subscriber sets (which are mainly modified standard sets) usually work with analog signals. Since the optical fibres in DIVAC only carry digital signals, analog-to-digital conversions and vice versa are required. In addition to these conversions the signals on the way from exchange to subscriber have to undergo electronic/optical and optical/electronic conversions, and may also have to pass through switching networks. The various possible successive operations are summarized in *Table II*.

Table II. Possible successive operations on the signals in DIVAC.

analog/digital conversion	in the exchange
switching	
electronic multiplexing (TDM and/or FDM)	
electronic/optical conversion	
optical multiplexing (WDM)	
optical demultiplexing	at the subscriber's home
optical/electronic conversion	
electronic demultiplexing	
switching	
digital/analog conversion	

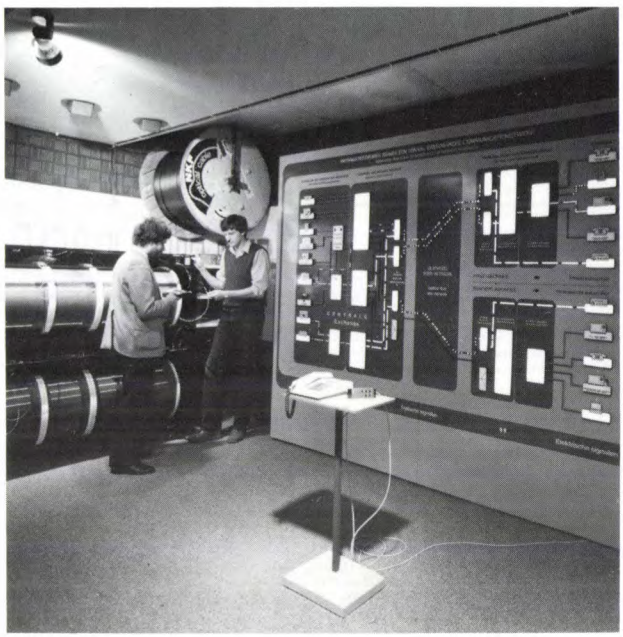

Fig. 3. Part of the experimental system in the laboratory. The reels of optical-fibre cable are on the left, and a demonstration display for the signal transfer can be seen on the right.

Because of the general lack of standardization in digital signal processing, we had to design most of the signal-processing equipment for DIVAC ourselves. It is therefore rather bulky and expensive. Standardization and the use of integrated circuits should make future equipment less costly and more compact.

Services

The following services are available for users of DIVAC:

- Distribution of audio signals. The subscriber receives 31 stereo signals simultaneously with the appropriate station and programme identifications (SPI) [5]. The definition of the audio signals in DIVAC is sufficient to give 'Compact Disc' quality for the subscriber's audio reproduction.
- Telephony. The subscriber has four telephone channels available. These signals can be fed to a 'dataphone', which is a combination of a loudspeaking telephone and a data terminal. It can be used at the same time for telephone calls and data transmission. For example, 'electronic shopping' with the dataphone

can be followed by 'electronic payment'. It is also possible to receive 'electronic mail', an 'electronic newspaper' or an 'electronic telephone directory'.

• Distribution of video signals. Selection television is used in DIVAC: the subscriber can operate a switching network via a control signal on a telephone channel to select the two video signals that he can receive simultaneously. When the system specification for DIVAC was adopted in 1981, the available bandwidth allowed the transmission of only one video signal per colour in an optical fibre. With the improved quality of fibres it would now be possible to transmit several video signals per colour by means of TDM. Another reason for using selection television is that some video services are only individually available. For instance, in addition to seven broadcast video channels and one channel for local television the user also has a video-library channel available. There are also two channels for pay television and a further three channels for test signals. The video library in the DIVAC laboratory system offers a choice from a total of 150 feature films, children's programmes and musicals, together with encyclopaedic information and interactive study courses.

• Broadband services. The broadband services provided include the video telephone, with which the subscriber can send and receive image and sound signals simultaneously [6], and surveillance television, capable of being used as a 'video baby alarm'. DIVAC also includes a connection to the electronic document-handling system MEGADOC [7], which uses digital optical recording (DOR) discs. It is also possible to send in personal video recordings for local television.

Some technical aspects

The fibres used for the transmission of optical signals are glass graded-index fibres with a core diameter of 50 μm and an outside diameter of 125 μm. The two fibres per subscriber transmit light at wavelengths of 820, 845 and 1300 nm, in wavelength multiplex. (In the present state of the art the number of wavelengths per fibre could be larger and one fibre per subscriber would be sufficient.) *Table III* indicates how the signals for the various services are distributed among the two fibres and the three wavelengths. *Fig. 4* shows a block diagram of the DIVAC trial system, giving the bit rates and bandwidths of the various signals.

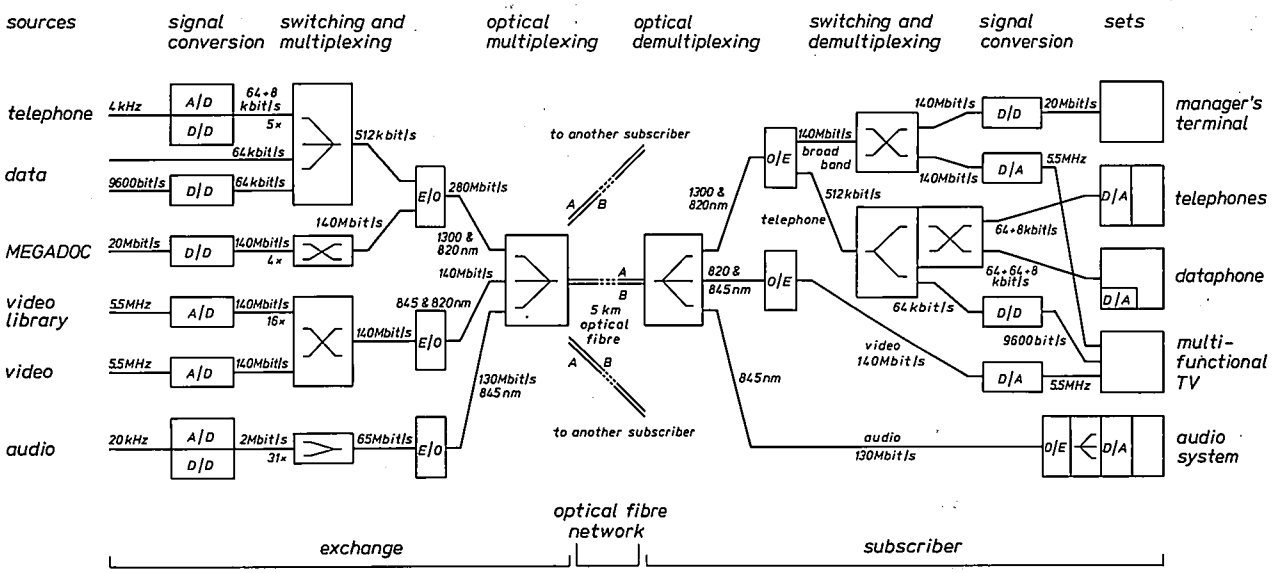

Fig. 4. Block diagram of the laboratory system. The signal sources in the exchange are shown on the left, the user sets are shown on the right. The signal operations, running from left to right, are summarized in Table II. *D/D* indicates conversions of digital signals into differently defined digital signals (e.g. for bit rate); see also the caption to fig. 2. The distribution of the electronic signals among the optical signals is as shown in Table III. The bandwidths of analog signals and the bit rates of digital signals are indicated beside the appropriate connecting lines, as are also the light wavelengths of the optical signals. The equipment for processing the signals at the user end is contained in a connection box, which can be made more compact in future by using special integrated circuits.

[5] G. C. M. Gielis, J. B. H. Peek and J. M. Schmidt, Station and programme identification in FM sound broadcasting, Philips Tech. Rev. 39, 216-225, 1980.

[6] Some general aspects of the video telephone are discussed in the introduction to: E. A. Aagaard, P. M. van de Avoort and F. W. de Vrijer, An experimental video-telephone system, Philips Tech. Rev. 36, 85-92, 1976.

[7] J. A. de Vos, Megadoc, a modular system for electronic document handling, Philips Tech. Rev. 39, 329-343, 1980.

All of the video signals except two are digitized by means of a one-bit/two-bit line-coding operation [8], resulting in signals at 140 Mbit/s. For comparison, one of the two remaining signals is digitized by pulse-code modulation (PCM), with a sampling rate of 14 MHz, and eight bits and two added bits per sample. After a five-bit/six-bit line-coding operation, with the object of removing the direct-voltage component from the signal, a signal is obtained with a bit rate of 168 Mbit/s. The other remaining signal is first frequency-modulated with a 22-MHz carrier and a frequency deviation of 11 MHz, and is then amplitude-limited ('clipped FM') [9].

The digitized signal of the broadband services (starting from the source 'MEGADOC' in fig. 4) has a bit rate of 140 Mbit/s. After a one-bit/two-bit line-coding operation the resultant bit rate is 280 Mbit/s. The coding removes the low-frequency components, so that the frequency spectrum of the broadband-services signal supplements that of the telephone signal, and both signals can be combined by frequency multiplexing; see Table III. The digitized telephone signal consists of a multiplex (TDM) of four signals for digital speech or for data transmission, and of the control signal that operates the switching matrices for the video signals and the broadband services. The resulting bit rate of the narrowband telephone signal is 384 kbit/s. After a six-bit/eight-bit line-coding operation a bit rate of 512 kbit/s is obtained with no high-frequency components. The narrowband and broadband signals are added together at the transmitting end and are separated by filters at the receiving end.

Each of the analog signals of the 31 stereo-audio signals is sampled at a rate of 64 kHz. With 12 or 14 bits per sample this results in a PCM signal. Bits for station and programme identification are then added to each signal. Multiplexing (TDM) of the 31 signals results in a bit rate of 65 Mbit/s, from which, after a one-bit/two-bit line-coding operation, a signal with a bit rate of 130 Mbit/s is obtained.

Table III. Distribution of the various optical signals among the wavelengths and fibres A and B, with the corresponding bit rates.

Optical fibre	Wavelength [nm]	Direction		Service	Bit rate [Mbit/s]
		exchange ↓ subscriber	subscriber ↓ exchange		
A	820	×		telephone	0.512
A	820	×		broadband	280
A	1300		×	telephone	0.512
A	1300		×	broadband	280
A	845	×		audio	130
B	820	×		video 1	140
B	845	×		video 2	140

Fig. 5. The telephone adapted for DIVAC, with keys for abbreviated dialling, automatic redialling, and for cancelling an incorrect digit (*R*). It has a small screen for displaying a dialled number or a caller's number.

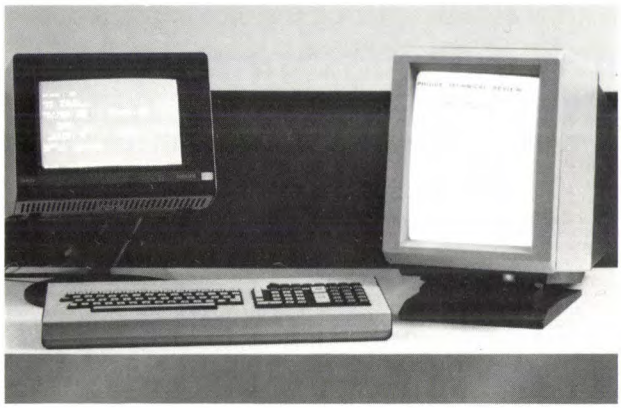

Fig. 6. The manager's terminal. This can be used to connect the user to the MEGADOC system and to show stored documents on a screen. The manager's terminal can be extended to include other functions such as electronic mail and access to data bases.

Some examples of services

The telephone modified for DIVAC is shown in *fig. 5*. It has a small display of 32 characters in two lines. The keyboard contains extra keys for new functions such as 'abbreviated dialling' and 'automatic redialling'.

Fig. 6 shows the 'manager's terminal'. This terminal can be used to connect the user to the MEGADOC system and to display documents on a high-resolution screen. Document retrieval requires the high bit rate of 20 Mbit/s. In the trial configuration of DIVAC the manager's terminal is confined to the MEGADOC

[8] E. Roza, An optical 1-bits video link, Proc. 7th ECOC, Copenhagen 1981, 4 pp.

[9] The various modulation techniques and some coding methods are described by F. W. de Vrijer, Modulation, Philips Tech. Rev. **36**, 305-362, 1976.

facility, but in a practical situation other functions may be added such as electronic mail and access to data bases.

The screen of the 'multifunctional' television set, which can be used for a wide variety of video facilities, is shown in *fig. 7a* and *b*. The first figure shows the picture that the user receives as soon as he switches on the set. From this 'menu' he can select entertainment, communication or education, using his remote-control unit. If, for example, 'video library' is selected, a connection is made to the computer of the electronic video library and the picture shown in fig. 7*b* appears on the screen. The computer at the same time records the charge for the use of the video library. Selections from successive menus can give feature films, interactive courses, children's programmes or subjects from a video encyclopaedia. The information is stored on LaserVision video discs. The 'juke box' that retrieves these discs and puts them on a LaserVision player is shown in *fig. 8*. The computer controls this juke box and also controls the transfer of the information on the disc to the user requesting it. The computer can also keep a record of such requests. This record can be used for combining requests so that the same information can be sent simultaneously to more than one user; the subscriber charges can be arranged to encourage this more efficient mode of operation.

a

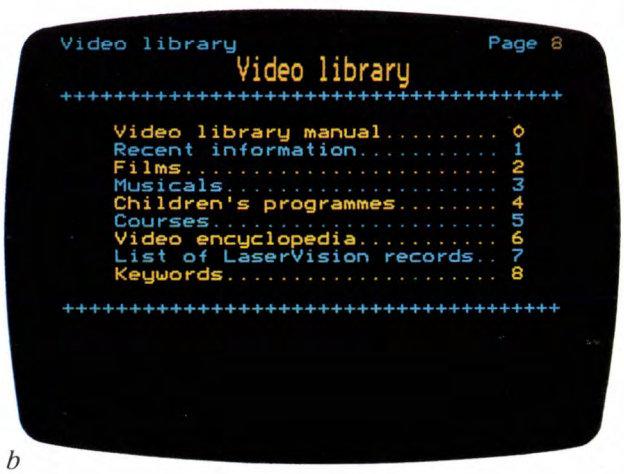

b

Fig. 7. The screen of the multifunctional television set, *a*) when the set is switched on, *b*) after the user has selected 'video library'. The services can be selected using the TV remote control unit.

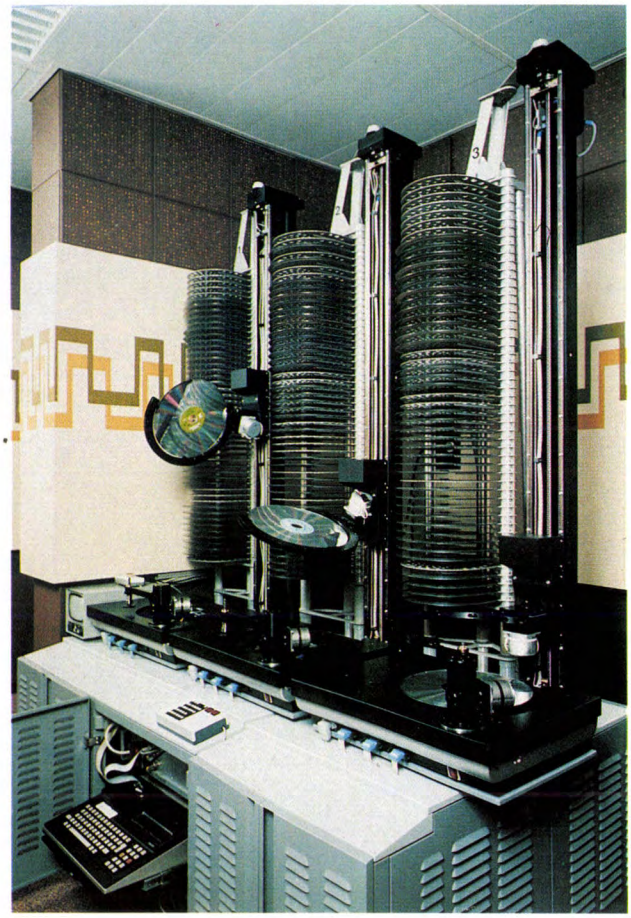

Fig. 8. The 'juke box' forming part of the video library in the exchange. The juke box consists of modules, each containing a LaserVision video player, a storage rack for fifty LaserVision discs and a retrieval and transport system. The mechanical system is arranged so that a player can also receive discs from other modules. The entire system is controlled by the computer of the video library.

Summary. The DIVAC project has resulted in an experimental optical-fibre communications network, which connects an exchange with two 'subscribers'. Five organizations have participated in this trial project, with the object of gaining experience with new technologies and assessing the reactions of potential users and bodies. Various digital signals, for telephony, audio, video and broadband services can be carried simultaneously and in two directions by means of TDM, WDM and FDM on a pair of optical fibres for each subscriber. The various services made available include selection television. The subscriber uses this to operate a switching network to select the required service: broadcast television, local television, a video library or pay television. The video library contains a collection of LaserVision discs, and has a control computer, a number of LaserVision players and a mechanical retrieval and transport system.

Porosimeter measurements on magnetic tape

H. F. Huisman and C. J. F. M. Rasenberg

To record half an hour of music with his Telegraphone in 1898 Valdemar Poulsen required nearly 4 km of piano wire. Today this can be done with about 85 m of thin magnetic tape, which takes up very much less space. The high quality demanded of a magnetic tape requires a complicated manufacturing process, conducted entirely in clean-room conditions. To determine the correct design data and for supervising the production process advanced analytical methods are necessary. In one such method used in the PDMagnetics magnetic-tape factory (PDMagnetics is a Du Pont-Philips joint venture), the porosity of the magnetic lacquer layer is measured with an extremely sensitive mercury porosimeter.

Introduction

Magnetic tape plays an important part in modern society. After the development of the Compact Cassette for sound recording at the end of the sixties [1], and its international standardization, audio magnetic tape 3.81 mm wide is now produced in large quantities throughout the world. As a consequence of the growing popularity of the video cassette recorder there is a considerable demand for 12.7-mm video magnetic tape. Because of its high information density video tape has to meet a much tighter specification than audio tape.

In the design and manufacture of magnetic tape the aim is to store as much information on the tape as possible within the wound volume. This can be achieved by applying a carefully distributed and structured magnetic material to a very thin carrier. Thus, modern magnetic tape consists of a polyester base material 7 μm to 25 μm thick coated with a thin layer of lacquer; the coating consists of a polymer binder with γ-Fe_2O_3, CrO_2 or metal-powder particles embedded in it. The particles have a length of about 0.5 μm and a diameter of about 0.1 μm. The ratio of particle volume to coating volume must be as high as possible because of the electromagnetic requirements for the tape.

Dr H. F. Huisman and Ing. C. J. F. M. Rasenberg are with PDMagnetics, Oosterhout.

During the manufacturing process a suspension of magnetic particles in a binder solution is poured on to the base material. (By analogy with paint manufacture the magnetic particles are usually referred to as 'pigment'.) Before the solvent has entirely evaporated, the needle-shaped particles are oriented in the longitudinal direction of the tape by means of a magnetic field. After this operation the particles must stack in such a way that the binder with the embedded particles takes up the minimum volume. The ratio of particles to coating in this stacking arrangement, on condition that the space between the particles is entirely filled with binder, is called the critical pigment-volume concentration (CPVC).

The suspension of magnetic particles in the binder solution is not stable. The mobility of the particles is increased by adding dispersing agents or stabilizers [2] and stirring the solution. Magnetic forces cause the formation of clusters of needle-shaped particles, which are found in the lacquer coating on the tape; see *fig. 1*.

The concentration of particles in the magnetic layer must of course be as high as possible, but if the concentration is too high interstices form between the clusters, and pores form in the actual clusters. In practice a concentration slightly above the critical pigment-volume concentration is found to give the best

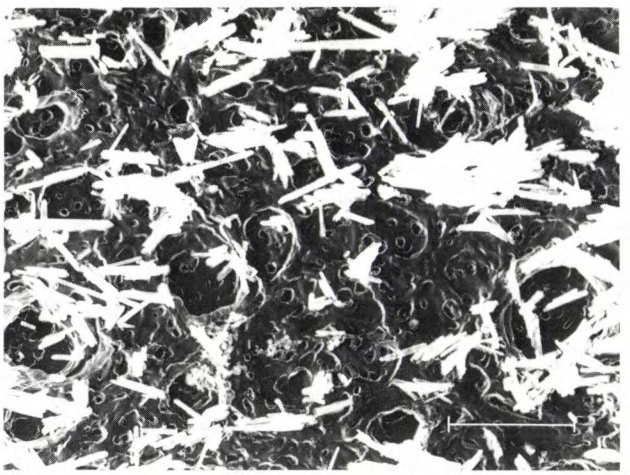

Fig. 1. Transmission electron micrograph of magnetic tape etched with hydrochloric acid. The white areas are clusters of CrO_2 particles. The black areas give the locations of the clusters of Fe_2O_3 particles; these particles were removed on etching. The Fe_2O_3/CrO_2 volume ratio was 95:5. The length of the line in the photograph corresponds to 1 μm in the sample.

results. After the drying process the interstices and pores are compressed and to some extent completely closed by calendering the tape, which consists in passing it between a number of extremely smooth rollers under pressure. The calendering improves the surface quality of the tape, so that there is less wear as the tape travels past the heads and the guide pins in the recorder. This improved surface quality also reduces the average distance between tape and head, so that reproduction of the higher frequencies is also improved.

If the tape is not calendered, interstices and pores caused by exceeding the critical pigment-volume concentration cause tape wear and shorten the useful life of the tape. Irregularities in the tape due to an excessively high local concentration of pores may even cause loss of contact between tape and head, resulting in a 'drop-out', i.e. a brief loss of information. In some cases, on the other hand, pores in the tape are desirable. In video tape, for example, pores may be created by certain additives at a fairly critical pigment concentration. In the cured coating these pores are partly filled by lubricant that was dispersed in the liquid lacquer. During use the lubricant diffuses to the tape surface and gradually becomes available to improve the sliding of the tape. These deliberately introduced pores are smaller in cross-section than the unwanted pores. It is obviously very important to keep the number of pores and their dimensions under careful control during the manufacturing process.

A method of measuring the porosity of materials was described as long ago as 1945 [3]. In this method the materials are first immersed in mercury, the pressure is then increased and the change in the mercury volume is measured. This is the principle of the type 200 Carlo Erba mercury porosimeter, which we have used. Since this instrument was designed for measuring the porosity of powders, and since only small quantities of material are used in measurements on magnetic tape, it was necessary to improve the sensitivity of the mercury porosimeter. We therefore modified the instrument to make it ten times more sensitive. The results of measurements with the modified porosimeter can be used to calculate the total number of pores and their dimensions.

In the rest of the article we shall first consider the construction of the porosimeter and the interpretation of the curves obtained. We shall then show how the porosity information is obtained from these curves, and finally we shall discuss some actual measurements.

The mercury porosimeter and the penetration curve

The principle of the mercury porosimeter is illustrated in the diagram of *fig. 2*. The sample — a rolled-up piece of magnetic tape — is introduced into a quartz-glass dilatometer with a calibrated neck. The dilatometer is evacuated and filled with mercury. The dilatometer is then placed in a pressure vessel filled with ethanol, in which the pressure is gradually raised to about 2000 bars. The mercury is forced into the interstices and pores of the sample, so that the total volume of mercury and sample is reduced, producing a drop in the mercury level. The compression acting on the dilatometer decreases its internal volume. This effect alone would cause an increase in the mercury level. In addition the mercury and the sample are compressed.

The different changes in volume result in a fall in the mercury level in the neck of the dilatometer. This fall is measured with a metal pin. After a certain pressure increase the pin is screwed downwards until it touches the surface of the mercury. This is detected by a sharp decrease in the electrical resistance between the pin and a contact in the base of the dilatometer. The rotation of a disc attached to the pin gives a measure of the mercury level in the neck. (The accurate determination of this angular displacement by means of a light source with a photocell and a hundred slits

[1] P. van der Lely and G. Missriegler, Audio tape cassettes, Philips Tech. Rev. **31**, 77-92, 1970.

[2] G. Frens, H. F. Huisman, J. K. Vondeling and K. M. van der Waarde, Suspension technology, Philips Tech. Rev. **36**, 264-270, 1976.

[3] H. L. Ritter and L. C. Drake, Pore-size distribution in porous materials, Ind. & Eng. Chem. Analyt. Edn **17**, 782-786, 1945; L. C. Drake and H. L. Ritter, Macropore-size distribution in some typical porous substances, *ibid.*, 787-791.

arranged around the circumference of the disc is one of the modifications we have introduced.)

When tape with initially open pores is measured in the porosimeter the result shown by curve *A* in *fig. 3a* is obtained. The linear parts *1*, *2*, *3* and *4* of this curve each belong to a different part of the compression and penetration process. Part *1* of the curve, almost coincident with the $-\Delta V$ axis, corresponds to the filling of the spaces between the turns of the tape. Part *2* corresponds to the compression of the tape, without the mercury penetrating into the pores. Part *3* corresponds to the penetration of mercury into the pores. Part *4* shows the change in the volume of the mercury, the dilatometer and the sample with the filled pores.

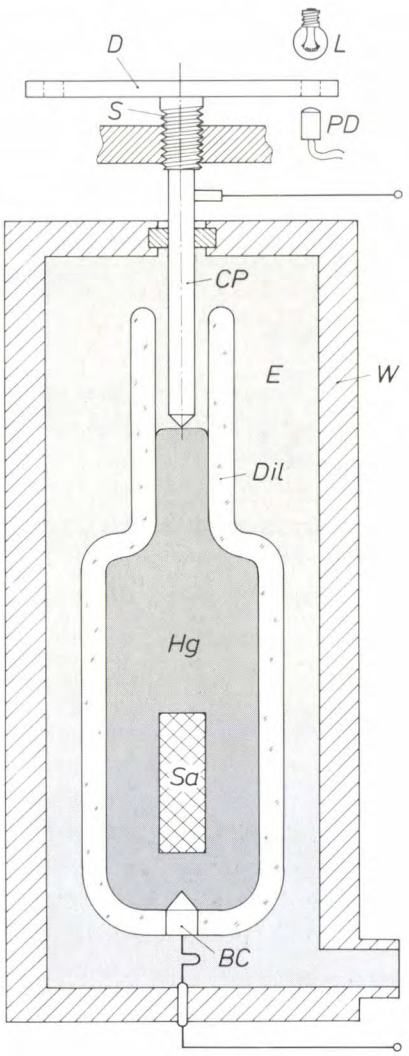

Fig. 2. Diagram of cross-section of part of the interior of the mercury porosimeter. *Sa* sample. *Hg* mercury. *Dil* quartz-glass dilatometer. *E* ethanol, whose pressure is slowly increased during the measurement. *W* pressure vessel. *CP* contact pin. *BC* contact in base of dilatometer. *S* screw with 1 mm pitch. *D* disc containing 100 slits evenly spaced around the circumference. After each increase in pressure, *S* is screwed downwards until the electrical resistance measured between *CP* and *BC* has fallen almost to zero. The change in the volume of *Hg* is obtained from the rotation of *D*. This is measured by counting the number of slits in *D* that have passed the light source *L* and the photodiode *PD*.

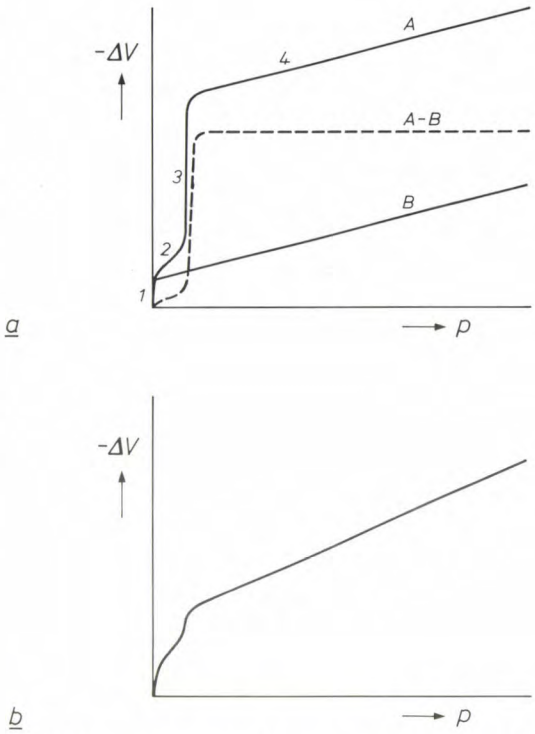

Fig. 3. The change $-\Delta V$ in the volume of the mercury (*Hg* in fig. 2) as a function of the pressure *p*. *a*) For magnetic tape with initially open pores. *A* measured curve: *1* filling the spaces between the rolled-up tape, *2* compression of the tape, *3* penetration of mercury into the pores, *4* remaining change in volume of mercury, dilatometer and sample (with filled pores). *B* correction line to allow for the changes of volume corresponding to lines *1* and *4*. $A - B$ penetration curve, the difference between curve *A* and correction line *B*. *b*) Curve from measurements on tape in which the pores have been closed by calendering.

Since we are not interested in the changes of volume corresponding to *1* and *4*, we correct the measured curve *A* by using line *B*, which represents these changes in volume alone. The result is the curve $A - B$, which we shall refer to as the 'penetration curve'. For this correction and other operations on the result of the measurement, as described below, the instrument is connected to a Philips PM 4410 microcomputer, which also controls the measuring process [4], see *fig. 4*. During this process the pressure is continuously increased by certain amounts — the size of step can be adjusted — and commands are given to measure the change in volume. The pairs of points $(p,\Delta V)$ thus obtained provide the result, which is displayed on a Philips PM 8151 digital plotter.

When magnetic tape whose pores have been closed by calendering is measured with this system, a different curve from curve *A* is obtained. Part *3* is then very small, but part *4* has a larger slope because of the increase in the compressibility of the sample (see fig. 3*b*). It is therefore possible to see from the shape of the measured curve how the tape has been calendered.

Calculation of some pore parameters

Information on the pores in the magnetic tape can be deduced from the shape of the penetration curve ($A-B$ in fig. 3*a*) if a simplified pore geometry is assumed. We shall assume that the pores do not widen with depth (no 'ink-bottle' pores) and are cylindrical in shape.

It is known that the surface of most solids is not wetted by a drop of mercury. This implies that the contact angle θ of the mercury droplet is in most cases greater than 90° (see *fig. 5a*). For mercury and the coating of magnetic tape the contact angle is between 130° and 160°. The consequence is that mercury will not spontaneously penetrate into an evacuated pore of the tape, but that a certain pressure p is required in the mercury. The relation between p and the radius for a cylindrical pore has been calculated by E. W. Washburn [5]. The radius r of this simplified pore will be referred to here as the 'equivalent pore radius'. The force F_1 ($= -2\pi r\sigma \cos\theta$), due to the surface tension σ (in N/m), has to be overcome by the force F_2 ($= \pi r^2 p$), due to the pressure in the mercury; see fig. 5*b*. From this we have the Washburn relation

$$p = -\frac{2\sigma \cos\theta}{r}. \qquad (1)$$

This equation shows that the pressure required for the penetration of mercury into the pore is related to the equivalent pore radius.

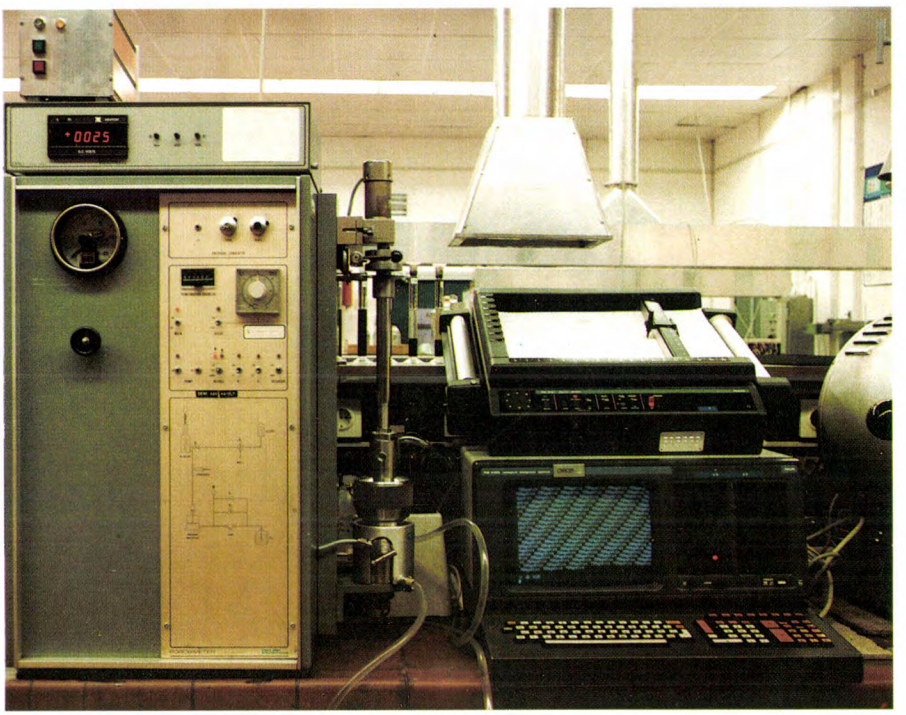

Fig. 4. Photograph of the complete measurement system. Left, the Carlo Erba type 200 mercury porosimeter; top right, Philips PM 8151 digital plotter; bottom right, Philips PM 4410 microcomputer, which controls the measuring process and calculates the results.

With the aid of fig. 5*b* we can also derive the expression given by H. M. Rootare and C. F. Prenzlow for the total theoretical surface area of all the pores [6]. The work that must be performed to force the mercury completely into the pores is equal to $\int_0^{V_m} p\,dV$, where V_m is the total pore volume; V_m is therefore equal to the change in the volume of the mercury during the penetration process. This work must be equal to the work performed by the force F_1, integrated over all the pores. Hence

$$\int_0^L (-2\pi r\sigma \cos\theta)\,dl = \int_0^{V_m} p\,dV,$$

where l is the displacement of the mercury in the direc-

[4] H. F. Huisman, C. J. F. M. Rasenberg and J. A. van Winsum, An improved mercury porosimetry apparatus — some magnetic tape applications, Powder Technol. **36**, 203-213, 1983.

[5] E. W. Washburn, The dynamics of capillary flow, Phys. Rev. **17**, 273-283, 1921.

[6] H. M. Rootare and C. F. Prenzlow, Surface areas from mercury porosimeter measurements, J. Phys. Chem. **71**, 2733-2736, 1967.

tion of the pore and L is the total length of all the pores. Putting $\int_0^L 2\pi r \mathrm{d}l$ equal to the total pore area S (and hence neglecting the 'bottom' of the pore), we find

$$S = \frac{-1}{\sigma \cos\theta} \int_0^{V_m} p \mathrm{d}V, \qquad (2)$$

where $\int_0^{V_m} p\mathrm{d}V$ corresponds to the hatched area in *fig. 6a*, so that the total pore area can be calculated from the penetration curve.

We are also interested in the distribution of the volume of the pores as a function of the pore radius, expressed as $\mathrm{d}V/\mathrm{d}r$. The relative pore-volume distribution is equal to $\mathrm{d}V/(V_0\mathrm{d}r)$, where V_0 is the volume of the sample. With the aid of equation (1) this can be rewritten as

$$\frac{1}{V_0}\frac{\mathrm{d}V}{\mathrm{d}r} = \frac{p^2}{2\sigma V_0 \cos\theta}\frac{\mathrm{d}V}{\mathrm{d}p}. \qquad (3)$$

In the part of the penetration curve that corresponds to the filling of the pores, the pressure changes very little, so p may be taken equal to the mean value p_m (see fig. 6*a*). The required pore-volume distribution is then equal to

$$\frac{1}{V_0}\frac{\mathrm{d}V}{\mathrm{d}r} = \frac{p^2{}_m}{2\sigma V_0 \cos\theta}\frac{\mathrm{d}V}{\mathrm{d}p}. \qquad (4)$$

The relative pore-volume distribution as a function of r can thus be obtained, except for a constant, by differentiating the penetration curve, taking $\Delta V = V - V_0$ and using $r = -(2\sigma\cos\theta)/p$ from equation (1); see fig. 6*b*. For normal values of the surface tension and the contact angle, $\sigma = 0.485$ N/m and $\theta = 140°$, the pressure range from 1 to 2000 bars corresponds to a change in the equivalent pore radius of 7.5 μm to 3.75 nm.

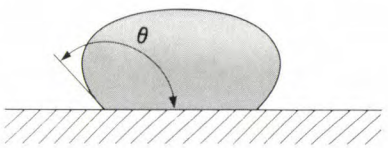

a

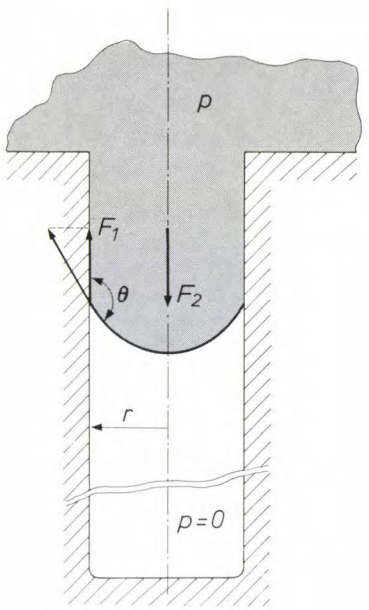

b

Fig. 5. *a*) A drop of mercury on the surface of a solid. θ contact angle. Since θ is greater than 90°, the surface of the mercury is not wetted. *b*) Penetration of mercury into a cylindrical pore of radius r. Since $\theta \geqslant 90°$, the mercury must have a pressure p. F_1 resultant of the forces acting on the mercury surface at the pore wall and due to the surface tension. (In reality the operating line of F_1 coincides with the centre-line of the pore.) F_2 downward force in the pore cross-section, due to the pressure p in the mercury. For the mercury to penetrate into the pore the condition $F_2 > F_1$ must be fulfilled.

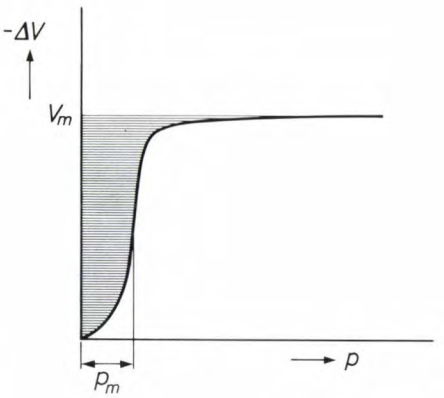

a

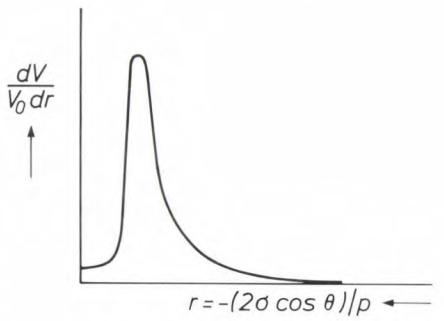

b

Fig. 6. *a*) Calculation of the total pore area from the penetration curve (see fig. 3*a*). The hatched area is a measure of the total pore area. V_m total pore volume: change in mercury volume in the porosimeter during the penetration process. *b*) Calculation of the relative pore-volume distribution $\mathrm{d}V/(V_0\mathrm{d}r)$. This distribution can be found, except for a constant, by differentiation of the curve from *a*. The pore radius $r = -2\sigma\cos\theta/p$ must then be plotted along the horizontal axis in the opposite direction.

Some results of measurements

Fig. 7a shows the measured relative pore-volume distribution of iron-oxide tape with a pigment concentration that is higher than the critical concentration.

The average equivalent pore radius is about 40 nm; the spread in the values of the pore radii is small. From repetitions of such measurements it was found that variation of the pigment concentration up to values far above the critical concentration caused little change in the pore-volume distribution. The total pore volume does change, of course. The equivalent pore radius thus appears to be fairly constant and only depends on the wetting and packing properties of the magnetic particles.

Fig. 7*b* shows the influence of the curing time of the coating on the effect of calendering. In an incompletely cured coating the pores can easily be closed under the pressure of calendering. On some tapes for which the curing times between the drying and calendering were not the same, measurements were made of the pore volume per unit mass, V_m/M. It was found that after a curing time of more than a week the pore volume was still not constant. The curing of the coating is obviously a slow process. The usual method of measuring the degree of curing is to determine the remaining quantity of isocyanate hardener. This can be done by means of infrared spectrometry. This analysis is not very reliable, however, since the pigment absorbs most of the useful infrared radiation. A wet-chemical analysis is also unreliable because the lacquer layer becomes insoluble after a certain amount of curing.

A method of determining the critical pigment concentration is shown in fig. 7*c*. The graph gives the measured relative pore volume V_m/V_0 as a function of the pigment concentration in percentage by weight. If the critical pigment concentration is exceeded, the porosity of the lacquer layer increases sharply. The critical pigment concentration is found from the intersection of the line through the measured points with the horizontal axis. This determination is much more accurate than the usual method, measuring Young's modulus of samples with different pigment concentra-

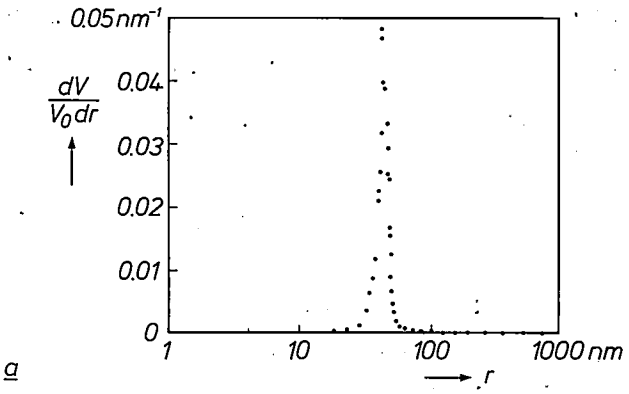

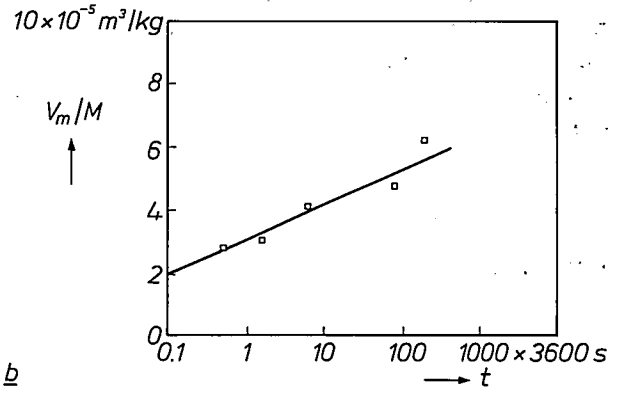

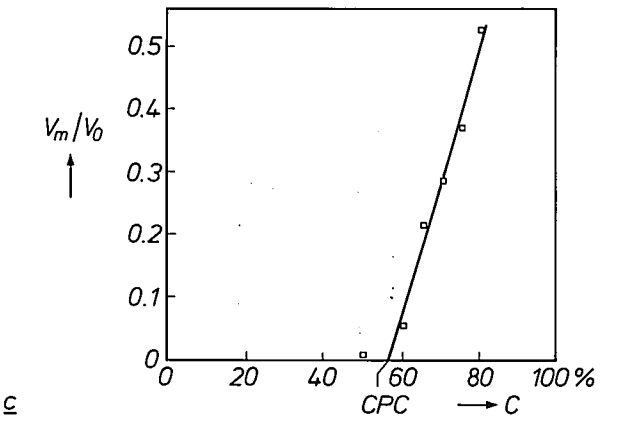

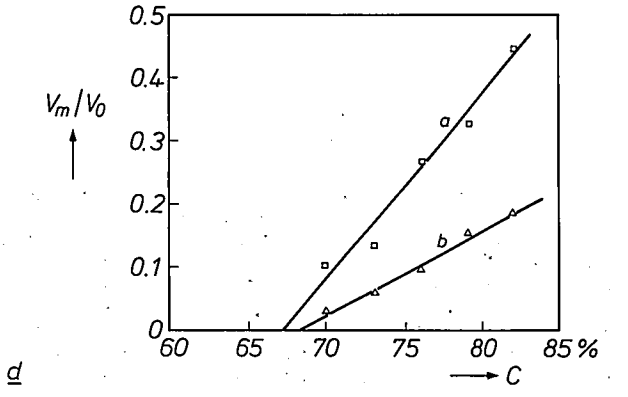

Fig. 7. Some results of measurements. *a*) The relative pore-volume distribution $dV/(V_0 dr)$ as a function of pore radius r, for iron-oxide tape with a pigment concentration higher than the critical value. *b*) The ratio of pore volume V_m to mass M for five tape samples, as a function of the time t between drying the lacquer layer and calendering. The time t thus determines the degree of curing of the lacquer layer. The pores in an incompletely cured layer can easily be closed by calendering. The continuous rise of the line through the measured points shows that the layers are not completely cured at the time of calendering. *c*) Determination of CPC, the critical pigment concentration, in percentage by weight. The relative pore volume V_m/V_0 of a number of samples is measured and plotted as a function of the pigment concentration C in percentage by weight. V_0 volume of the sample. The CPC can be found from the point of intersection between the line through the measured points and the C-axis, since the pore volume increases approximately linearly when the critical pigment concentration is exceeded. *d*) The same measurements on uncalendered (*a*) and calendered (*b*) metal-powder tape. In calendered tape the pores are thus partly closed and the critical pigment concentration is slightly higher.

Table I. Effect of calendering on the relative pore volume and useful life of metal-powder magnetic tape with a pigment-weight concentration of 73.5%, as a result of measurements. The useful life is indicated on a relative scale with values of 1 (short) to 5 (long).

Relative pore volume (percentage)	Relative useful life	Degree of calendering
31	1	uncalendered
18	1	lightly calendered
6	3	normally calendered
4	4-5	intensively calendered

tions. The latter method is hardly feasible for magnetic tape since the coating has to be measured without the base material. It would also be very difficult to calender unsupported layers of lacquer.

Fig. 7*d* shows the effect of calendering on the total pore volume of metal-powder tape. The graph gives measured results comparable with those in fig. 7*c* for uncalendered (*a*) and for calendered (*b*) tape. Calendering thus results in less porosity and, as pointed out earlier, increases the useful life of the tape. This also appears from *Table I*, which gives the relative pore volume and relative useful life of four samples of metal-powder tape subjected to different calendering conditions. The pilot-production proces that gave the measured results in the bottom line is now the standard method in the PDMagnetics tape factory at Oosterhout.

Summary. With a commercial mercury porosimeter, modified in various ways to give higher sensitivity, measurements can be made of the pore volume, the total pore area and the pore-volume distribution of magnetic tape. In calculating the results the curve giving the change in mercury volume as a function of mercury pressure has to be corrected for the compressibility of the mercury and the change in the volume of the dilatometer. The total pore area and the pore distribution are obtained by integration and differentiation of the corrected curve. From pore-volume measurements on different tape samples the critical pigment concentration can be determined. If this concentration is exceeded, pores are formed, but this negative effect can be eliminated by calendering.

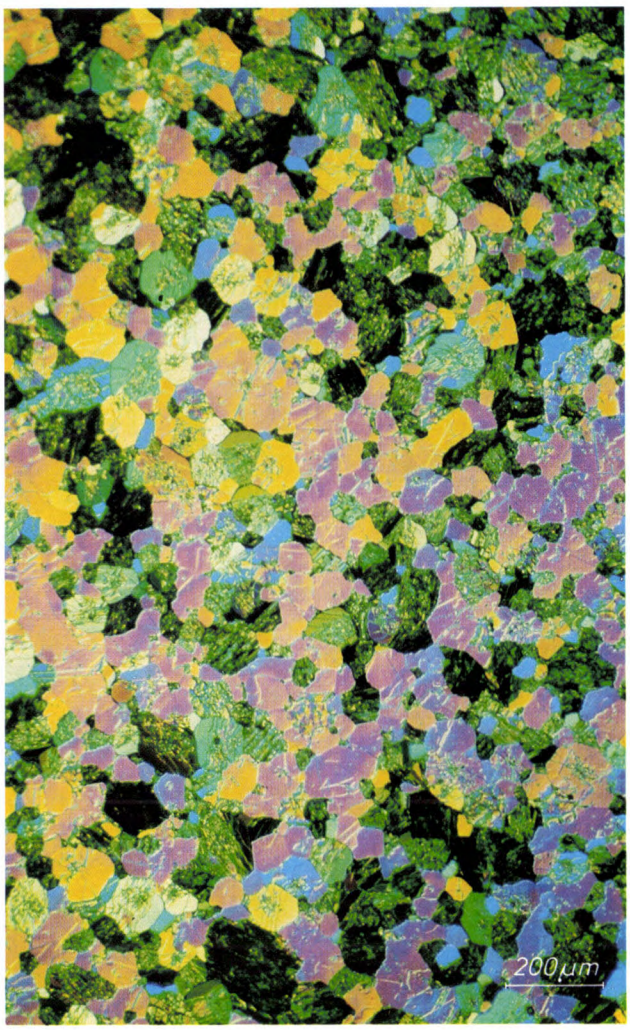

a

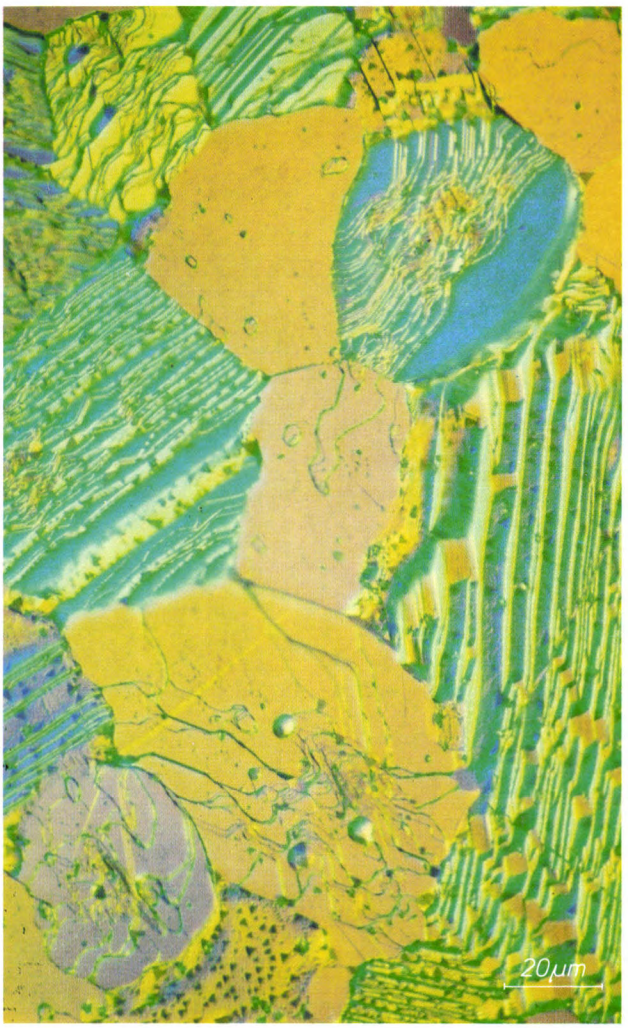

b

Scandium for X-ray tube anode

The photomicrographs above were made during an investigation into suitable materials for the anodes of X-ray tubes for X-ray fluorescence spectrometry. They show a scandium surface after heat treatment in vacuum. Interference contrast has been used to make the crystallites in the surface clearly visible (*a*). A higher magnification (*b*) exposes the surface structure of the crystallites themselves, revealing features such as steps (right) and pits (below).

X-ray fluorescence spectrometry is a method of non-destructive testing in which a specimen is irradiated with X-rays. Absorbed X-rays can release electrons from the K or L shells of the atoms. When the sites which then become vacant are filled by other electrons, X-ray fluorescence radiation may be emitted. The wavelength of this radiation depends on the nuclear charge of the atom, not on the chemical valence state. X-ray fluorescence can therefore be used to determine the constituent elements of a specimen. For efficient excitation the wavelength of the incident X-rays should not be much longer than that of the excited fluorescence radiation. In this respect scandium seems to be an attractive anode material. Since the wavelength is fairly long ($\lambda_{ScK\alpha} = 0.303$ nm) lighter elements (carbon to calcium) can be detected more easily than with an X-ray tube that has a chromium anode, such as the tubes commonly used in X-ray fluorescence spectrometry.

Optical aspects of the Silicon Repeater

S. Wittekoek

The Silicon Repeater, designed for the repeated projection of photomasks on a silicon wafer in the fabrication of integrated circuits in our laboratories, has been briefly described in an earlier issue of this journal [*]. *Meanwhile some substantial improvements have been made: the equipment is now faster and a larger silicon wafer can be exposed with higher resolution of details. The article shows that the Silicon Repeater owes its excellent specifications — largely determined by physical limits associated with the use of visible light — to the advanced design of the optical system.*

Introduction

At the start of each process step in the manufacture of integrated circuits an intricate and highly detailed light pattern (the photomask) has to be projected on to the thin film of photosensitive lacquer (photoresist) that covers the surface of the silicon wafer. Because of the continuing developments in IC manufacture the performance required of the imaging equipment also has to show a steady improvement: photomask details are becoming smaller, IC dimensions and wafer diameters larger, and the production rates required continue to grow.

At present the method most widely used in IC manufacture is the projection of the photomask on to the wafer surface by means of visible light. The projection equipment used generally gives an actual-size image of the mask, extending over the entire surface of the wafer. This procedure has some disadvantages. The 5-inch wafers currently used require a projection lens system with a large image field, so that the numerical aperture must remain small to minimize imaging errors at the edges [1]. This small aperture limits the resolution of the objective lens. Another serious drawback of 1:1 projection is that it is virtually impossible to make the large masks required completely without faults. There are other disadvantages: departures from flatness of the wafer can cause blurring of the image, no allowance can be made for wafer deformations, and it is difficult to modify the projection equipment to suit larger wafer dimensions.

Dr S. Wittekoek is with Philips Research Laboratories, Eindhoven.

The wafer stepper designed at Philips Research Laboratories, which we have called the 'Silicon Repeater', does not expose the wafer in its entirety but only parts of it in steps. A photomask that contains much less information is projected on to the wafer at a fifth of full scale. After each exposure step the wafer is rapidly and accurately displaced through a distance of say 10 mm, and the next part of the wafer is then exposed. Because of the small image field the projection lens has a numerical aperture of 0.3, a high value, giving a high resolution. The objective can be refocused at each step, so that departures from flatness of the wafer need not cause blurring in the image. At every step allowance can also be made for wafer deformation during manufacture, by aligning the wafer in relation to the photomask.

The masks for the Silicon Repeater have details five times larger than those in the masks for 1:1 projection. They are therefore not so difficult to make — partly because they contain less information. Faults in the mask can sometimes be corrected or repaired. A disadvantage is that a tiny speck of dust — and this can appear even in clean-room conditions — is repeatedly projected on to the wafer and can render it useless. This problem can be solved, however, by fitting an extremely thin 'pellicle' on both sides of the mask.

[*] A. G. Bouwer, G. Bouwhuis, H. F. van Heek and S. Wittekoek, The Silicon Repeater, Philips Tech. Rev. 37, 330-333, 1977.

The improved ('Mark 2') Silicon Repeater is shown in *fig. 1*. The optical system is illustrated schematically in *fig. 2* and the principal numerical data are summarized in *Table I*. The mechanical movement can thus displace the wafer through 10 mm in 0.3 s with an accuracy of 0.1 μm. This short displacement time partly accounts for the considerable production rate of sixty exposed 4-inch wafers an hour. The exceptionally high mechanical accuracy required is achieved by using a wafer table mounted on air bearings, hydraulic servocontrol and a laser-interferometer measuring system. The details of the wafer-table control system will not be discussed in this article, which is concerned solely with the optical aspects of the equipment.

Fig. 1. The Mark 2 Silicon Repeater, an improved version of the earlier Silicon Repeater designed at Philips Research Laboratories and described in this journal [*]. The improved Silicon Repeater can expose sixty 4-inch silicon integrated-circuit wafers per hour.

In designing the optical system of the Silicon Repeater it was necessary to satisfy a number of more or less conflicting requirements [2]. To avoid chromatic aberration in the projection the mask should ideally be exposed to monochromatic light. However, this causes intensity differences in the photoresist because of interference between the incident beam and the beam reflected from the wafer surface. This has the result that the widths of linear tracks are not constant after development. The projection lens is required to have a high resolution and hence a large aperture angle on the image side. However, a large aperture angle entails a small depth of focus, and any departure from flatness of the wafer must not cause blurring or variation in the magnification of details.

The problems indicated above have been solved in the Silicon Repeater in the following way. The mask is illuminated by a high-pressure mercury-vapour lamp of high luminous output. The radiation at *two* different wavelengths in the spectrum of this light source

[1] In one method of 1:1 projection the image errors are minimized by limiting the image field in one direction to a few millimetres. The mask and wafer are then moved through the image field together. However, the numerical aperture with this method is no larger than 0.16.

[2] S. Wittekoek, Step-and-repeat wafer imaging, Solid State Technol. **23**, No. 6 (June), 80-84, 1980.
R. Kramer, R. Vervoordeldonk, S. Wittekoek, R. Beem and G. van der Looij, Philips wafer stepper: characterization and processing experience, Proc. SPIE **334**, 95-104, 1982.

is used: 405 and 436 nm, corresponding to the h and g lines respectively. With practical photoresist thicknesses between 0.7 and 1.1 μm this method is virtually free of interference effects. A two-sided telecentric optical system [3] has been designed for the projector. This has a numerical aperture of 0.3, and is corrected for the narrow wavelength range from 400 to 440 nm. (It is more difficult to design an optical system for a *range* of wavelengths than for a single wavelength.) To obtain optimum focusing the upper surface of the wafer is first positioned with a levelling mechanism for coarse focusing and angular adjustment (see fig. 2). An automatic fine-focusing system comes into operation at each projection step. The residual focusing error is less than 0.3 μm.

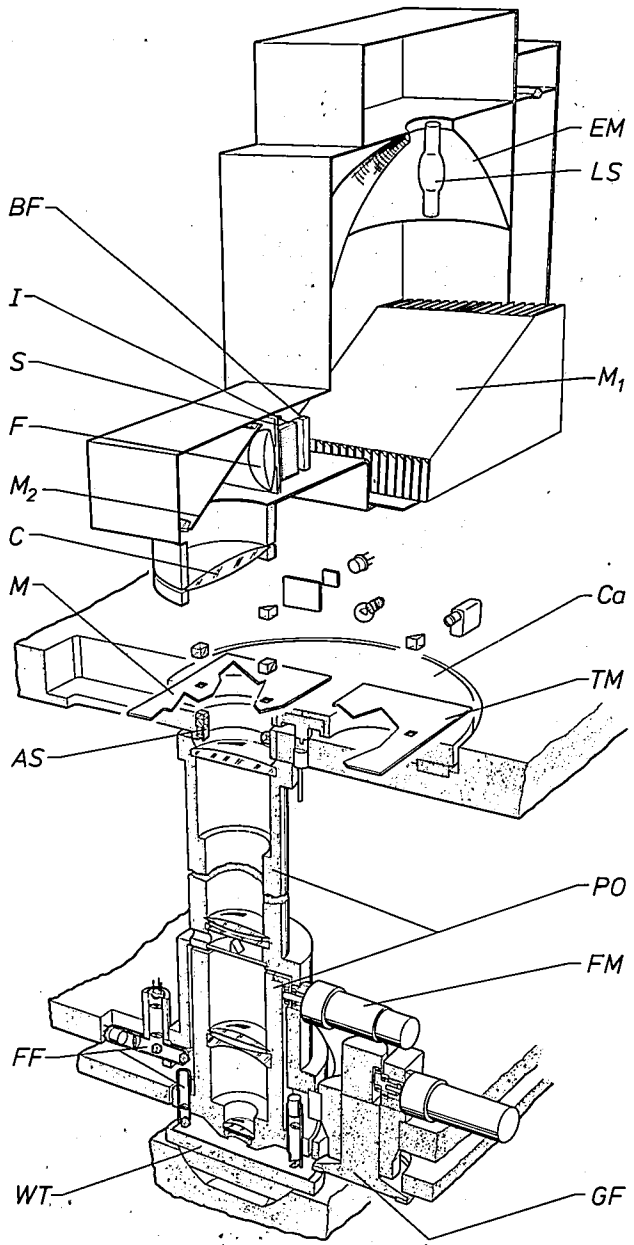

Fig. 2. Drawing of the optical system. *LS* high-pressure mercury-vapour lamp, 350 W. *EM* elliptical reflector, M_1 and M_2 flat reflectors. (M_1 is at the same time a multilayer interference filter that only reflects radiation at wavelengths below 450 nm.) *BF* bandpass filter (also a multilayer interference filter), which passes radiation of 395 to 440 nm. *S* shutter, necessary because the mercury-vapour lamp is not switched off between the projections. *F* field lens. *C* condenser. *I* optical integrator, whose operation is explained in fig. 3. *Ca* carousel for two masks; masks can be changed in 1.5 s. *M* mask. *TM* mask for test patterns. *AS* optics of alignment system. *PO* projection optics consisting of two parts. *FM* motor for displacing the lower part of *PO* for fine focusing. *FF* optical system for fine focusing. *WT* wafer table. *GF* mechanism for adjusting the upper surface of the wafer to a predetermined height (coarse focusing) and perpendicular to the optical axis. (In *WT* the spherical bearing for the angular displacement is shown but not the bearing for the vertical adjustment.)

The origin for the displacements is accurately determined by aligning the wafer relative to the mask in such a way that the exposures corresponding to the successive process steps are in exact register. The alignment system makes use of gratings, located both in the mask and on the wafer. The total registration error, summed vectorially for the x- and y-directions, does not exceed 0.25 μm.

We now go on to consider first the exposure of the mask and wafer, and the projection of the mask on to the wafer. We shall then consider the alignment of the wafer in relation to the mask.

Table I. Some numerical data for the Mark 2 Silicon Repeater.

Dimensions:	
Mask (maximum)	from 50 mm × 50 mm to 60 mm × 30 mm
Mask diagonal, maximum	70 mm
Diameter of silicon wafer	7.5, 10 or 12.5 cm (3, 4 or 5 inch)
Area of wafer movement	135 × 135 mm²
Smallest detail in projection	1.25 μm
Wavelengths for mask illumination	405 and 436 nm
Wavelength for alignment system	633 nm
Time:	
Exposure per projection	0.2 s
Wafer displacement (10 mm)	0.3 s
Mask-changing time (carousel)	1.5 s
Total exposure (4-inch wafer)	1 min
Tolerances:	
Non-parallelism of wafer	3 μm/cm
Capture range for automatic focusing	± 35 μm
Capture range of optical alignment system	88 μm
Accuracy:	
Max. focusing error	0.3 μm
Max. alignment error	0.08 μm
Max. positioning error	0.1 μm
Max. orthogonality error of wafer movement	0.1 arc second
Max. registration error (x and y summed vectorially)	0.25 μm
Miscellaneous:	
Numerical aperture of objective	0.3
Magnification of projection optics	0.2 ×
Max. non-uniformity of exposure	2%
Number of automatically interchangeable masks	2

Exposure of the mask

Since we wish to expose the maximum number of wafers per unit time, the exposure for each projection must be short and the luminous intensity on the wafer therefore high. In addition, to produce integrated circuits of the highest quality, the illumination of the exposed areas of the wafer must be highly uniform. This means that the mask must also be uniformly illuminated with light of the highest possible intensity.

The optical system for the exposure of the mask is shown in the upper part of fig. 2. The compact light source of the 350 W mercury lamp is located at one of the focal points of an elliptical reflector. An image of the light source is thus produced at the other focal point, which is located just in front of the integrator *I*. (The function of the integrator will be discussed later.) The reflector M_1 is at the same time a multilayer interference filter [4], which only reflects radiation of wavelength less than about 450 nm and passes the rest. The reflector and the bandpass filter *BF*, which is also an interference filter, together ensure that more than 90% of the radiation in the wavelength range from 395 to 440 nm is transmitted. More than 95% of the radiation in the rest of the wavelength range is stopped. After spectral filtering, spatial losses and scattering, the power of the light that reaches the integrator is only 4 W. The amount of light incident on the mask has a power of about 2 W and the wafer finally receives about 1 W of light. This power is one of the factors that determine the number of wafers that can be exposed per hour.

The operation of the integrator will be explained with reference to *fig. 3*. The integrator consists of a large number — 168 — of small rod lenses, whose focal length is almost the same as their physical length. The integrator and the field lens have the important task of 'smoothing out' the non-homogeneous distribution of the luminous intensity of the light-source image. The integrator also acts as a fibre-optic system with an aperture angle such that nearly all the light that reaches the second focal point of the elliptical mirror is transmitted. The lower side of the integrator can therefore be regarded as the actual light source for the projection system. An image of this 'secondary light source' is produced by the condenser in the diaphragm of the projection lens.

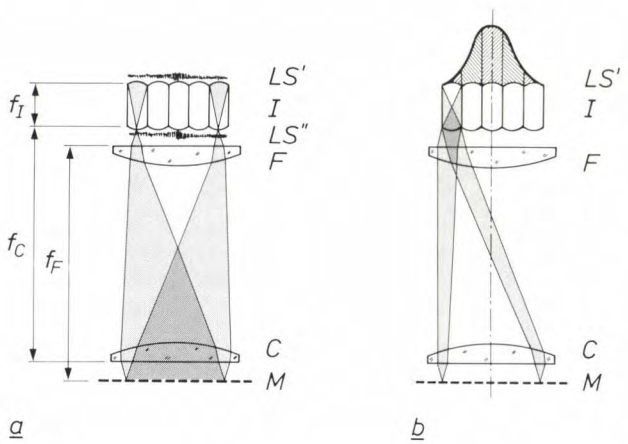

Fig. 3. Operation of the optical integrator *I*; see fig. 2. (For clarity, M_2 has been omitted, so that *I* and *F* are shown rotated by 90°.) *I* consists of 168 rod lenses (only five are shown) of focal length f_I. The lower and upper surfaces of the integrator are each virtually coincident with a focal plane and a principal plane of the rod lenses. *F* field lens of focal length f_F. *C* condenser lens of focal length f_C. *M* mask. *a*) The function of the condenser lens *C*. An image of the light source *LS* (see fig. 2) is produced as *LS'* just in front of the integrator. The integrator also functions as an optical-fibre system, so that the lower side of the integrator may be regarded as a 'secondary light source' *LS''*. The condenser *C* produces an image *LS'''* of this in the diaphragm of the projection optics (see also fig. 6). *b*) Function of the field lens *F*. The intensity distribution of *LS'* (and hence of *LS''*) is not homogeneous, as indicated diagrammatically by the bell-shaped curve at the top of the figure. With the aid of *F*, each rod lens spreads out the incident light over the full surface of the mask; the intensity of the incident light on one rod lens corresponds to the area of a hatched part under the bell-shaped curve. The illumination of *M* is therefore much more uniform than the intensity distribution of *LS'*.

Exposure of the wafer

When the photoresist is developed after exposure in the Silicon Repeater, patterns must remain that faithfully reproduce the mask pattern at a fifth of full scale. There is the problem here of interference in the transparent photoresist, between the incident light and the light reflected from the surface of the wafer. *Fig. 4a-d* shows what would happen if the photoresist was exposed to monochromatic light only. If there is a step in the layers of silicon oxide and aluminium originating from previous process operations (fig. 4*a*), the thickness of the photoresist varies at the step (fig. 4*b*). For a linear trace there is also a variation in the width of the positive photoresist that remains behind after development (fig. 4*c*), which comes about in the following way. In the ideal case the intensity of the light incident on the wafer varies with position perpendicular to the direction of the line to give a 'rectangular' pattern. However, since the optical system is not perfect, the sides of the intensity curve are not absolutely vertical. The amount of radiant energy absorbed in the photoresist varies correspondingly, but in addition it varies as a function of the film thickness (fig. 4*d*). The linewidth after development is therefore not the same for different film thicknesses.

We have found a solution to this problem by making simultaneous use of *two* kinds of monochromatic

[3] The projection optical system was designed by the firm Cerco of Paris and given the name of 'Super Tulipe'.

[4] H. Köstlin and G. Frank, Thin-film reflection filters, Philips Tech. Rev. **41**, 225-238, 1983/84.

light, originating from the g and h lines of the mercury-vapour spectrum. This was achieved by means of the spectral filtering from 395 to 440 nm mentioned above. The intensity functions given in fig. 4*d* are thus added for both wavelengths. Fig. 4*e* shows the beneficial effect of this bichromatic exposure [5]. (A difficulty is that a projection-lens system corrected for two wavelengths is more difficult to make than a system corrected for a single wavelength only.) With bichromatic exposure the linewidth variations approximately cancel out in a given range of film thicknesses. If we wish to limit the variation of the linewidth to ± 0.1 μm, we can allow the thickness to have a spread of ± 0.15 μm for a photoresist film of thickness 0.9 μm. (In practice film thicknesses outside this range may have to be used, in which case the spread in

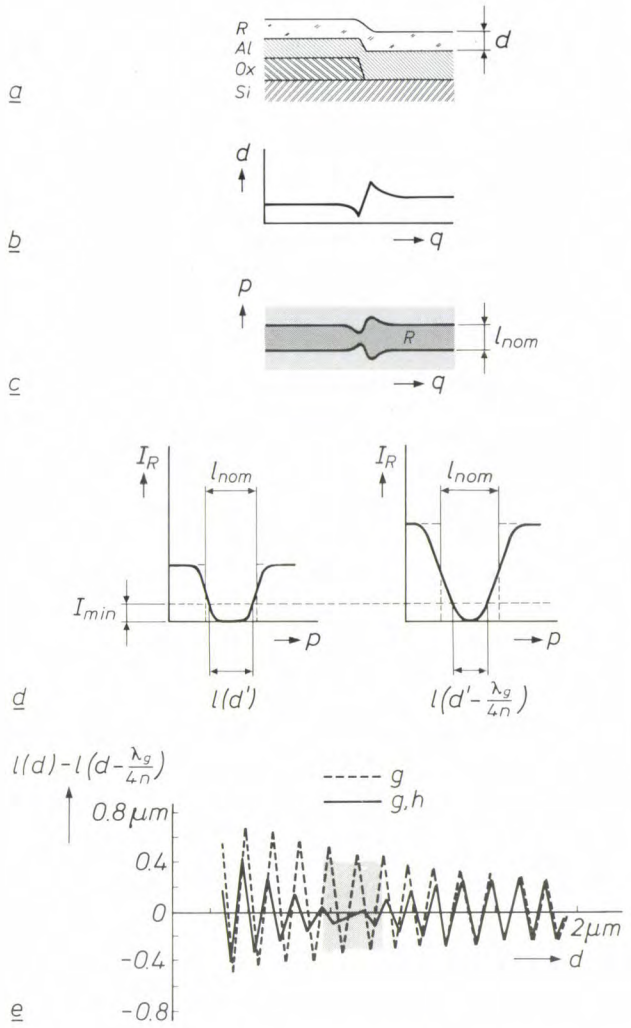

Fig. 4. Monochromatic as against bichromatic illumination of the silicon wafer. *a*) The various layers. *Si* silicon substrate, *Ox* silicon oxide, *Al* aluminium, *R* positive photoresist of thickness *d*. (When a positive photoresist is used the illuminated zone is removed in the development.) Because of the step in the layers *Ox* and *Al*, *d* is not the same everywhere. *b*) The thicknes *d* as a function of the position *q*. *c*) When monochromatic illumination produces a linear track (of nominal width l_{nom}) in *R* the linewidth varies at the position of the steps in *Ox* and *Al*. (*p* and *q* are position coordinates in the plane of the wafer.) *d*) The origin of the linewidth variation with monochromatic illumination. I_R is the light absorbed per unit area of *R* and is plotted as a function of *p*. The light incident on *R* does not have perfectly sharp transitions, so that the sides of the curve for I_R slope slightly and are rounded. Because of interference, I_R is also dependent on *d*. *Left:* The variation of I_R for a value *d'* of *d* that gives a minimum in the light absorbed. *Right:* The variation of I_R for a value *d* that is $\lambda_g/4n$ smaller than *d'*; λ_g wavelength of the monochromatic light, *n* the corresponding refractive index of the photoresist. I_{min} minimum light intensity necessary to dissolve *R* on development. The linewidths after development are equal to $l(d')$ and $l(d' - \lambda_g/4n)$. *e*) The difference $l(d) - l(d - \lambda_g/4n)$ as a function of *d* for monochromatic illumination (dashed lines) and for bichromatic illumination (continuous lines). The dashed lines have been calculated for light of the g line (436 nm), the continuous lines for light of the g and h lines (405 nm) together. With bichromatic illumination the linewidth variations partly cancel out. The range $d = 0.9 \pm 0.15$ μm in which there is little linewidth variation is shown shaded.

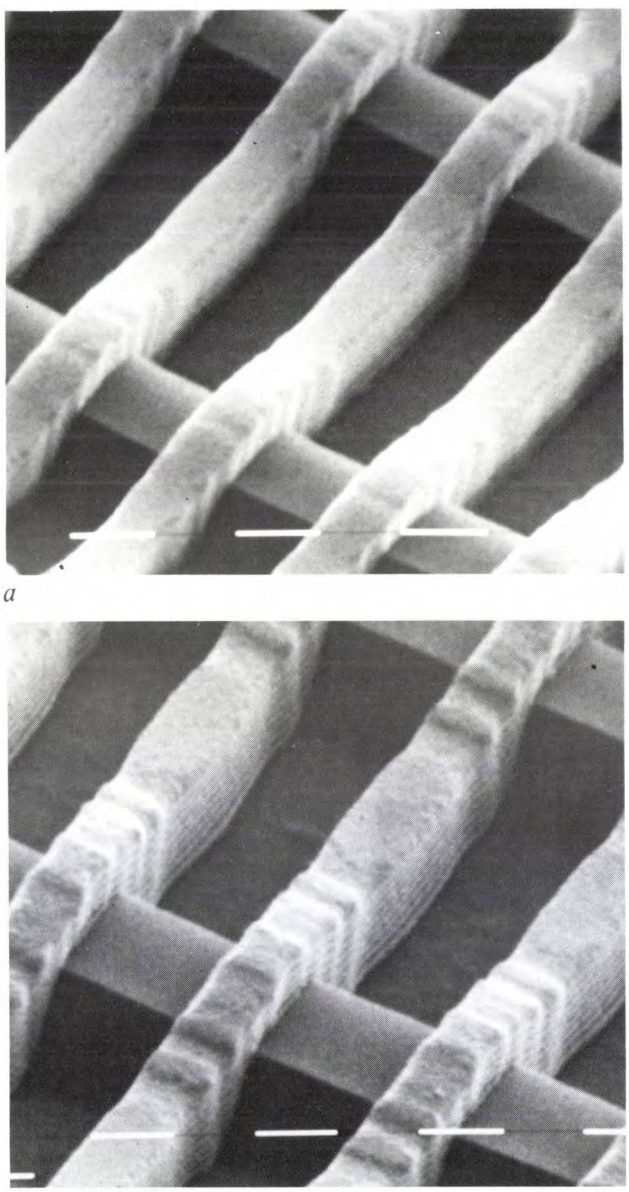

Fig. 5. Scanning electron micrographs of 1.1-μm-wide photoresist tracks over 1-μm steps of SiO_2 in the centre of the image field *a*) for bichromatic illumination, *b*) for monochromatic illumination. In the latter case there is undesirable variation in the track width. The steep edges and uniform width of the tracks in *a* are typical of the quality of the exposure and projection optics.

linewidth will be greater and at the most equal to the variation with monochromatic exposure.)

Fig. 5 shows scanning electron micrographs of tracks of width 1.1 μm resulting from (*a*) bichromatic and (*b*) monochromatic exposure. In case (*b*) the undesired variation in linewidth can clearly be seen.

The optical projection system

The first part of the optical projection system — the collimator — produces an image of the mask at infinity, while the second part — the objective — produces an image on the upper surface of the wafer; see *fig. 6*. To focus the image of the mask on the surface of the wafer it is only necessary to move the objective.

The special feature of the projection system is that both the entrance and exit pupils are located at infinity (two-sided telecentricity), so that the axes of symmetry of the light beams from the object and to the image are parallel to the optical axis. The entrance and exit pupils are both images of the diaphragm D in the common focal plane of the collimator and the objective. Fig. 6 also shows the image LS''' in D of the secondary light source LS'' (see fig. 3*a*). This image does not completely fill the aperture of the diaphragm. The 'relative pupil filling' σ is defined as the ratio of the diameter of the light-source image to the diameter of the diaphragm aperture. The pupil filling determines the degree of coherence in the exposure of the wafer. With increasing σ the coherence decreases; when $\sigma = 1$ the exposure is incoherent. It will be shown later that the modulation transfer function of the projection optical system depends on the coherence. Fig. 6 also shows the aperture angle α, which determines the magnitude of the numerical aperture $n \sin\alpha$ and hence — with the wavelength of the light — the resolution of the projection optics.

The collimator consists of three elements and its focal length f_{co} is 330 mm. The objective consists of thirteen elements and its focal length f_{ob} is 66 mm. The magnification is equal to the ratio $f_{ob}/f_{co} = 0.2$. The numerical aperture is 0.3 and the diameter of the image field is 14 mm. With this relatively small diameter, the image distortion is less than 0.2 μm.

The imaging quality of the optical system can be evaluated by means of the modulation transfer function (MTF) [6], which gives the variation of the modulation transfer M as a function of the spatial frequency f in line pairs per mm. The shape of the MTF curve depends mainly on the wavelength, the aperture and the relative pupil filling σ. *Fig. 7* shows some theoretical MTF curves for different values of σ. With increasing coherence (i.e. with decreasing σ) the resolution decreases but the modulation transfer for low frequencies increases. In practice it has been found that a modulation transfer of at least 0.6 is required to produce an image of a particular detail on the photoresist in such a way that it will not be lost after development. From fig. 7 it might therefore appear that the pupil filling σ ought to be as small as possible. However, the resulting high degree of coherence causes unacceptable diffraction effects ('ringing'). A good compromise is $\sigma = 0.7$. This value cor-

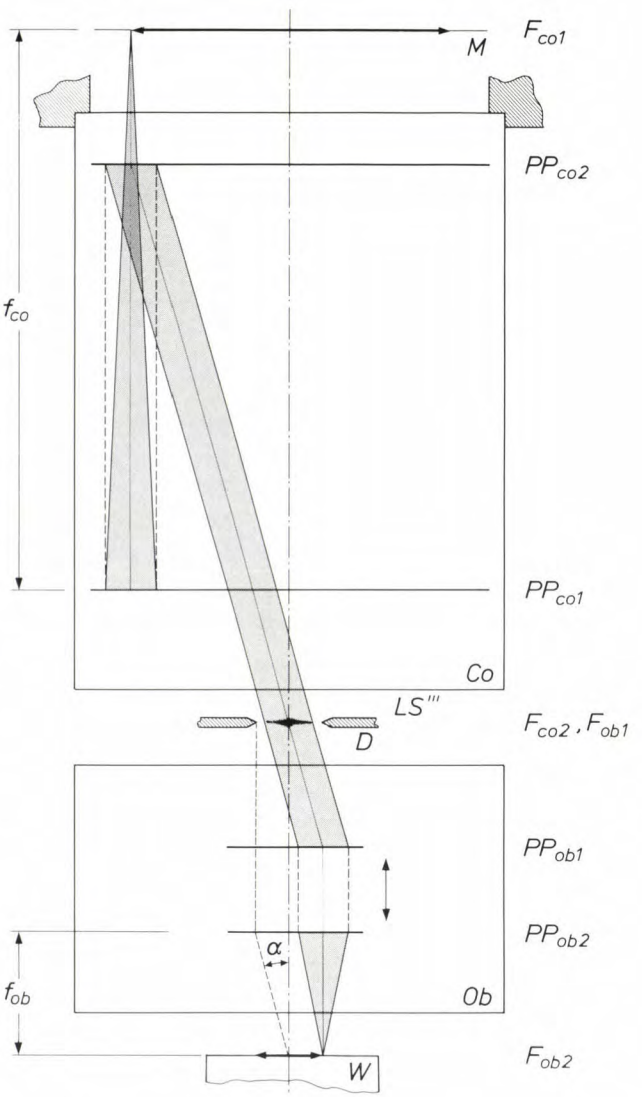

Fig. 6. Diagram of the optical projection system [3] with magnification 0.2. The optical system consists of two parts, the collimator *Co* and the objective *Ob*. *M* mask. *W* wafer. PP_{co1}, PP_{co2}, PP_{ob1}, PP_{ob2} principal planes. F_{co1}, F_{co2}, F_{ob1}, F_{ob2} focal planes; F_{co2} and F_{ob1} are coincident. f_{co} focal length of collimator. f_{ob} focal length of objective. The optical system is telecentric on both sides (both the entrance pupil and the exit pupil are at infinity). The entrance and exit pupils are both images of the diaphragm D in the common focal plane F_{co2}, F_{ob1}. The image LS'' of the light source (see fig. 3*a*) appears at D as LS'''. Owing to the 'parallel' path of rays between *Co* and *Ob*, only *Ob* has to be moved for focusing, without any change in magnification. The aperture angle α determines the numerical aperture, which is equal to 0.3.

[5] S. Wittekoek, Optical lithography for microcircuits, Proc. Microcircuit Engineering 80, Amsterdam 1980, pp. 155-170.

[6] B. van der Eijk and W. Kühl, An X-ray image intensifier with large input format, Philips Tech. Rev. **41**, 137-148, 1983/84.

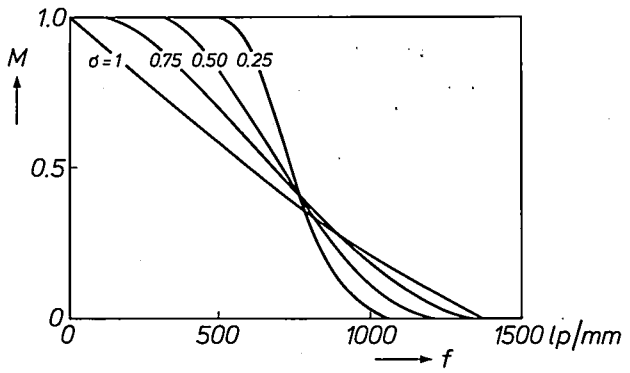

Fig. 7. The modulation transfer M of the projection optics as a function of the spatial frequency f in line pairs per mm with the relative pupil filling σ (the ratio of the diameters of LS''' and D, see fig. 6) as parameter. In a wafer stepper a high modulation transfer at low spatial frequencies is more important than a high resolution (the value of $1/(2f)$ for $M \rightarrow 0$).

responds to $f \approx 600$ lp/mm at $M = 0.6$, so that, in favourable conditions, details of about 0.8 μm can still be made visible in the centre of the image.

Focusing

After a wafer is introduced it is first clamped to the wafer table by means of gentle suction and then brought into coarse focus within ± 10 μm from the image plane of the projection optics; see fig. 2. At each projection the objective section of the projection optics is then displaced in such a way that the deviation from correct focus is less than 0.3 μm (fine focusing). This is necessary because the wafer might still not be truly flat, even though it is clamped against the flat surface of the table, and the error could increase during the process steps.

The fine focusing is done by means of an optical focusing device as illustrated in *fig. 8*. The light from a semiconductor laser is focused on to the wafer surface. After reflection from this surface, another image of the laser is formed on the wafer surface by a lens and reflectors. This second image of the laser is of the same size and inverted with respect to the first. Any beam asymmetry caused by the structure is therefore compensated by the double reflection on the wafer. Finally, the light beam is focused on to the photodiodes D_1 and D_2. Vertical displacement of the objective lens has the effect of moving the laser image on the photodiodes.

The motor used for displacing the objective is incorporated in a control loop in which the difference between the output currents of the photodiodes is used as feedback. The displacement therefore stops when the two output currents are identical. The optics of the focusing system are arranged in such a way that the virtually constant distance between the objective and the wafer surface corresponds to the image distance.

The quality of the exposure and projection optical system described above is demonstrated by the sharp delimitation and uniform width of the tracks in fig. 5*a* and *fig. 9*.

Alignment of the wafer

In the successive process steps the exposed zones on the wafer must be in exact register with each other. The wafer therefore has to be brought into alignment with the mask. To make this alignment possible the wafer is provided with alignment marks before the actual process steps start. These consist of phase gratings used in reflection, which are etched into the wafer. The alignment marks on the wafer are compared with similar marks in the mask, which consist of amplitude gratings used in transmission.

The alignment marks are illustrated in *fig. 10*. The marks Gr_1 etched into both sides of the wafer are used for the alignment of the complete wafer at the start of a series of projections for a step in the process. Each wafer has two of these alignment marks, each consisting of four separate gratings. The pitch of the two

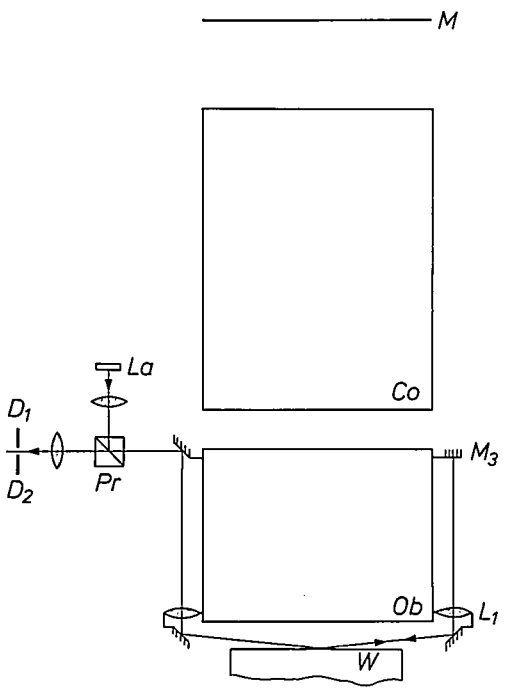

Fig. 8. The optical fine-focusing system (see also fig. 6). The light from the semiconductor laser La is focused on to the surface of the wafer W through the prism Pr with a half-silvered surface, two mirrors and two lenses. The light is reflected from W to form another image of La on W by means of a mirror, the lens L_1 and a mirror M_3. Mirror M_3 and the intersection point of the rays with W are located at the focal planes of L_1. After the second reflection from W, a final image of La is formed on the photodiodes D_1 and D_2. The difference signal produced by D_1 and D_2 is used for controlling the focusing motor (*FM* in fig. 2) for the vertical movement of the objective *Ob*.

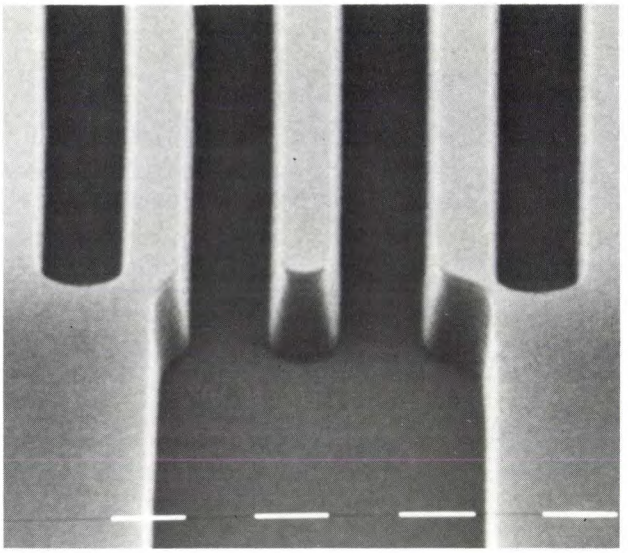

Fig. 9. Scanning electron micrograph demonstrating the quality of the exposure and projection optics. Photoresist tracks are shown with a width of 1.2 μm and a thickness of 1.2 μm on a silicon-oxide film with a thickness of 0.3 μm.

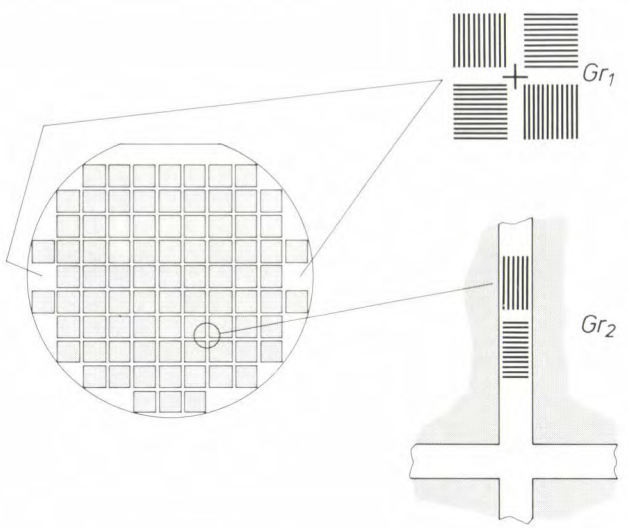

Fig. 10. The alignment marks consisting of phase gratings applied to the 'virgin' wafer. The marks Gr_1 serve for aligning the wafer in relation to the mask at the start of a series of projections. There are two alignment marks Gr_1, each consisting of four gratings, applied to opposite sides of the wafer. The two left-hand gratings of Gr_1 have a pitch of 16 μm, the two right-hand gratings a pitch of 17.6 μm. The dimensions of Gr_1 are 400 μm by 400 μm. The alignment marks Gr_2 serve for alignment at each projection and are mainly used when the wafer has nonlinear deformation. For each projection zone (shown shaded) there is one alignment mark Gr_2 consisting of two gratings. The gratings of Gr_2 have a pitch of 16 μm. The dimensions of Gr_2 are 80 μm by 400 μm.

gratings on the left is 16 μm, that of the two on the right is 17.6 μm.

The marks Gr_2 are only 80 μm wide. They are located between the projection areas (shaded), which are intended for the actual circuits on the wafer. These gratings are used for realignment before each projection. Each projection zone has an alignment mark Gr_2, consisting of two separate gratings. The pitch of these gratings is 16 μm.

When a wafer is introduced into the Silicon Repeater the wafer table is displaced in such a way that the two marks Gr_1 on the wafer coincide in turn with a mark on the mask. The computer in the wafer stepper then calculates, from the measured coordinates of each mark, the origin for the displacements and the angle that the line through the two marks makes with the x-direction of the table movement. The wafer is then rotated through this angle.

If a nonlinear deformation of the wafer is suspected, the marks Gr_2 can be used to align the wafer for each projection. The marks Gr_2 can also be used when the Silicon Repeater is used with a 1:1 projector in IC manufacture ('mix-and-match' procedure). A 1:1 projector as mentioned in the introduction can be used for the process steps that do not require such high accuracy. The processing time for a wafer can then be reduced. When a 1:1 projector is used the gratings are applied to the wafer with this projector at the start of production. Deviations due to image distortion produced by this projector are then recorded on the wafer by the positions of the marks Gr_2. When these marks are used for aligning the wafer at each projection in the Silicon Repeater, the quality of the integrated circuit is almost unaffected by errors due to the 1:1 projector.

The alignment system is illustrated in *fig. 11a* [7]. One of the alignment gratings on the wafer W is illuminated through a prism by a helium-neon laser at a wavelength of 633 nm. The reflected radiation is diffracted by the grating. In diffraction, light is reflected only at an angle of θ_k to the normal to the grating surface and in a plane perpendicular to the grating lines, where $\sin\theta_k = k\lambda/p$; k is the order and λ the wavelength of the reflected light, and p is the pitch of the grating. In the common focal plane of collimator and objective there is an order diaphragm, made from material that transmits the light for illuminating the wafer but not the light from the helium-neon laser. The order diaphragm has holes in it at locations such that light of order $k = 1$ and $k = -1$ reflected from the grating at a wavelength of 633 nm is transmitted; see fig. 11*b*. This light is then incident on the mask. Here, as a result of interference, a periodic pattern is again formed with a pitch 2.5 times greater than that of the grating on the wafer. The position of the mask does indeed correspond to a five-fold magnification, but only the images of the second harmonics (with $k = 1$ and $k = -1$) of the gratings are formed on the

[7] G. Bouwhuis and S. Wittekoek, Automatic alignment system for optical projection printing, IEEE Trans. **ED-26**, 723-728, 1979.

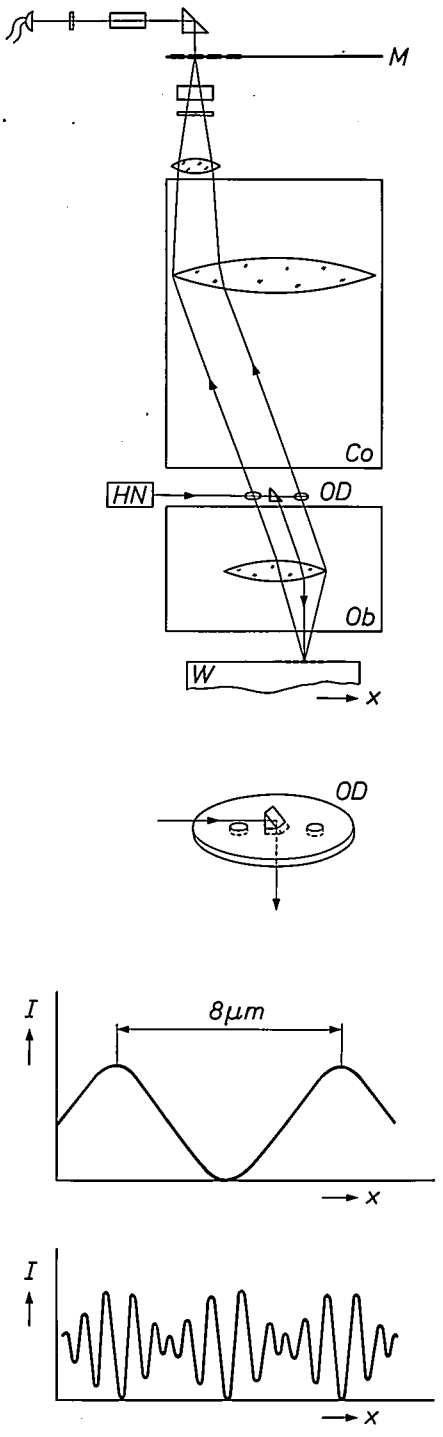

Fig. 11. The optics of the alignment system. *a*) A reflection phase grating on the wafer *W* is illuminated through the lower prism by a helium-neon laser *HN* with a wavelength of 633 nm. The projection optics produces an image of this grating on a corresponding transmission amplitude grating on the mask *M*. The gratings lie with their lines perpendicular to the plane of the drawing, so that alignment can take place in the *x*-direction. The order diaphragm *OD*, which is located at the common focal plane F_{co2}, F_{ob1} (see fig. 6), transmits the light for illuminating the wafer but stops most of the 633-nm light. The operation of the other components of the alignment system is explained in fig. 12. *b*) The order diaphragm *OD* and the lower prism, shown in perspective and on a rather larger scale. The material of the diaphragm has two holes for alignment in the *x*-direction (there are two other holes, not shown, for alignment in the *y*-direction), which transmit only the light of order 1 and −1 at a wavelength of 633 nm. *c*) When the intensity *I* of the 633-nm light transmitted through the grating on the mask is measured as a function of the wafer displacement *x*, the curve shown in the upper part of the figure is obtained. Its spatial period is 8 μm if the gratings on the wafer and mask with pitches of 16 and 40 μm coincide. The upper signal is sensitive to electrical interference and the maximum or minimum cannot easily be detected. To get around this difficulty, the signal is modulated at a frequency of 50 kHz, as indicated in the lower figure (for a constant wafer velocity). This modulation is explained in fig. 12.

wafer, resulting in a doubling of the spatial frequency. Assuming that the 16-μm grating of the alignment mark Gr_1 is observed, then the corresponding grating on the mask must have a pitch of 40 μm. A measurement of the intensity of light *I* at a wavelength of 633 nm that is transmitted through the grating surface in *M* would show that this varies with a spatial period of 8 μm when the wafer is displaced; see fig. 11*c*, *above*. In principle this can be used for aligning the wafer in relation to the mask. In such a case, however, the wafer must not be more than ± 4 μm from the correct position, and the accuracy with which the position of the minimum or the maximum of the periodic signal can be detected is not particularly high. The alignment accuracy can be increased by modulating the output signal from the alignment system by a signal at a fixed frequency, as illustrated in fig. 11*c*, *below*. This will now be explained, and also a method for increasing the capture range of the alignment system.

Signal processing in the alignment system

The detection system is illustrated in detail in *fig. 12a*, which also indicates the function of the various optical elements. Before the light at a wavelength of 633 nm reaches the mask, it first passes through a polarizer and a birefringent crystal. In this way the light is first linearly polarized and then split into two beams whose planes of polarization are rotated through −45° and +45°. The beams are also displaced relatively by half the pitch of the grating (i.e. by 20 μm). The light then passes through the mask and an optical modulator. This consists of a quartz crystal to which a 50-kHz alternating voltage V_{ref} is applied in such a way that the polarization plane of the light is rotated by −45° during the positive part of V_{ref} and by +45° during the negative part of V_{ref}. The light next passes through an analyser that has the same principal direction as the polarizer. Finally the light reaches a detector. The electronic signal from the detector is amplified and then processed in a phase-sensitive detector, to which V_{ref} is also applied.

Fig. 12*b* shows the operations performed on the light in the various optical elements, on the left for positive V_{ref} and on the right for negative V_{ref}. Fig. 12*c* indicates the electronic processing performed on the signal from the detector at three different places in the

circuit and for three different positions of the wafer. Because the output signal is modulated by the alternating voltage V_{ref} the phase-sensitive detector responds strongly to variations in alignment. In this way variations down to 0.02 μm can be detected. The output signal is also much less sensitive to electrical interference and variations in the optical transmission or the supply voltage.

If the alignment system were actually designed in the manner described above, the alignment field would

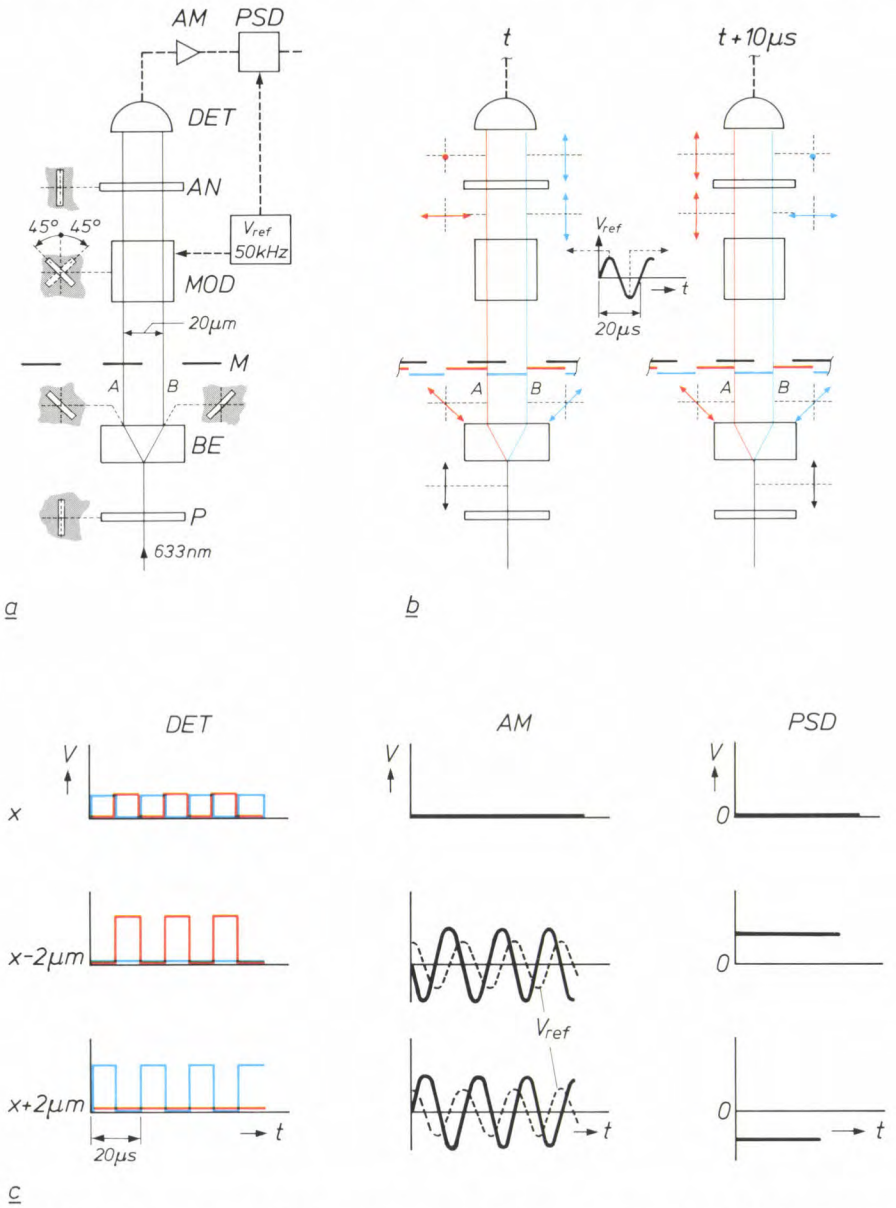

Fig. 12. Signal detection in the alignment system. *a*) The various optical and electronic components, and the effect of the optical components on the state of polarization of the 633-nm laser light. *P* polarizer. *BE* birefringent crystal, splitting the light into beams *A* and *B* (shown as lines) with plane of polarization rotated −45° and +45°, and displaced −10 μm and +10 μm. V_{ref} 50-kHz alternating voltage. *MOD* optical modulator: periodic rotation of the plane of polarization by −45° (during positive V_{ref}) and +45° (during negative V_{ref}). *AN* analyser. *DET* optical detector, which produces a direct voltage proportional to the light intensity. *AM* alternating-voltage amplifier. *PSD* phase-sensitive detector. *b*) Effect of the optical components on the beams *A* (red) and *B* (blue) during positive (left) and negative (right) V_{ref}. The position of the wafer is such that the beam-*A* and beam-*B* images of the wafer grating are displaced 10 μm to the left and 10 μm to the right in relation to the mask grating. In this position *DET* therefore only receives a signal from beam *B* on the left and only receives a signal from beam *A* on the right. *c*) The electronic signals after *DET* (left-hand column), after *AM* (centre column) and after *PSD* (right-hand column). In the upper row the wafer is in the position *x* (as in *b*); in the centre row it is in the position $x - 2$ μm, and in the lower row in the position $x + 2$ μm. (The square-wave voltage after *DET* is in reality sinusoidal; see fig. 11*c*.) The alternating voltages produced at positions $x - 2$ μm and $x + 2$ μm by *AM* are shifted in phase by −90° and +90° with respect to V_{ref}. Since *PSD* responds both to amplitude differences and to phase differences, *PSD* produces a direct voltage that is highly sensitive to small displacements of the wafer.

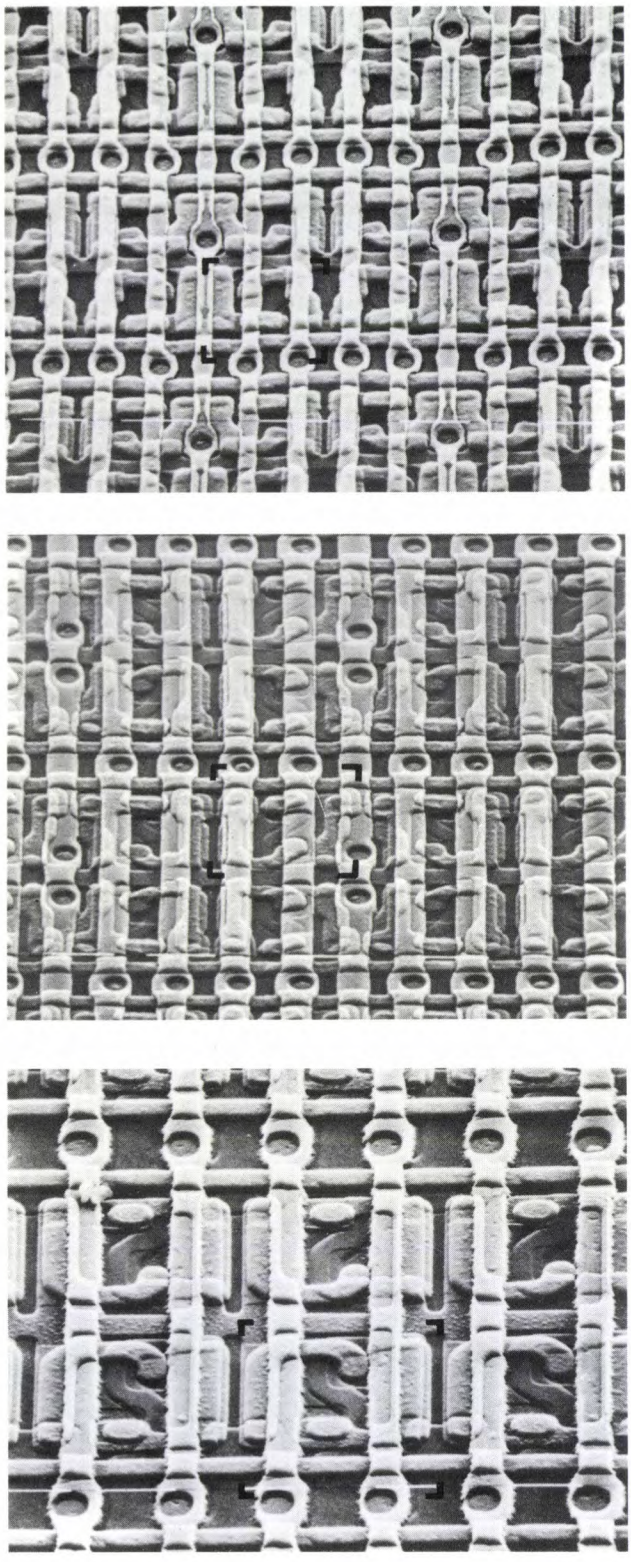

Fig. 13. Scanning electron micrographs of 16-K memory circuits of the static-RAM type (random-access memory) in NMOS technology. In each micrograph the corners of a memory cell are indicated. From bottom to top the dimensions of a cell are 28 μm by 38 μm, 21 μm by 28.5 μm and 17.5 μm by 21 μm. (The dimensions quoted first are measured horizontally in the photograph.) The increase in packing density of the circuits was achieved by process improvements and mainly by using the Silicon Repeater for the upper circuit. The centre and lower circuits were both made with the aid of a 1:1 projector. In the circuits 'pits' are visible, for making contact between the aluminium tracks running from top to bottom of the photograph and the underlying diffusion layers. The pits in the upper circuit are clearly much more accurately centred with respect to the tracks. This is due to the high alignment accuracy of the Silicon Repeater.

be very small. It has already been mentioned that the pitches of the two left-hand gratings of Gr_1 in fig. 10 are equal to 16 μm and those of the two right-hand gratings to 17.6 μm, resulting in pitches of 40 and 44 μm for the corresponding gratings on the mask. The detector *DET* has four quadrants, so that the degree of overlap between the gratings of pitch 16 and 40 μm and the gratings of pitch 17.6 and 44 μm can be measured at the same time. The capture range of the alignment system is considerably widened by taking the simultaneous production of a minimum in the output signal of both detector systems as the alignment criterion (rather like a vernier). The coincidence of the two minima is repeated with a periodicity of $8(8 + 0.8)/0.8 = 88$ μm in the displacement of the wafer. The capture range of the alignment system is thus increased 11 times, and is sufficient for the use of automatic wafer feed with mechanical pre-alignment.

Fig. 13 shows that the packing density of a memory circuit can be considerably increased by using the Silicon Repeater in its fabrication. The circuit shown in the upper part of the figure was made with this wafer stepper, the two others with a 1:1 projector. The upper picture clearly shows that the depositions made in the successive process steps are in much more exact register because of the highly advanced alignment system of the Silicon Repeater.

The development of the Silicon Repeater was the work of a group of research workers, in particular of H. J. Bartelings (electronics and software), A. G. Bouwer (mechanical design), T. Fahner (focusing system), G. C. van de Looij (exposure), R. H. Munnig Schmidt (servosystems) and J. E. van der Werf (alignment system). The author of this article was responsible for coordinating the development project.

Summary. With the Silicon Repeater sixty 4-inch silicon wafers for integrated circuits can be exposed per hour. This high production rate is possible because of the high intensity and the high efficacy of the illumination from a 350-W high-pressure mercury-vapour lamp with an elliptical reflector. The illumination of the mask is highly uniform, partly through the use of an optical integrator. Linewidth variations due to interference in the photoresist are largely avoided by using light at two wavelengths (405 and 436 nm). Image details of 1.25 μm can be produced, through the use of a specially designed two-sided telecentric projection system with high resolution, and because the repeater has a focusing system that reduces focusing errors to 0.3 μm or less. An alignment system ensures that the exposures for the successive steps of the process are in accurate register. This system uses phase gratings on the wafer, which are brought into register with amplitude gratings on the mask. Alignment errors as small as 0.02 μm can be detected.

Scientific publications

These publications are contributed by staff of laboratories and plants that form part of or cooperate with enterprises of the Philips group of companies, particularly by staff of the research laboratories mentioned below. The publications are listed alphabetically by journal title.

Philips GmbH Forschungslaboratorium Aachen, Weißhausstraße, 5100 Aachen, Germany — *A*

Philips Research Laboratory Brussels, 2 avenue Van Becelaere, 1170 Brussels, Belgium — *B*

Philips Natuurkundig Laboratorium, Postbus 80000, 5600 JA Eindhoven, The Netherlands — *E*

Philips GmbH Forschungslaboratorium Hamburg, Vogt-Kölln-Straße 30, 2000 Hamburg 54, Germany — *H*

Laboratoires d'Electronique et de Physique Appliquée, 3 avenue Descartes, 94450 Limeil-Brévannes, France — *L*

Philips Laboratories, N.A.P.C., 345 Scarborough Road, Briarcliff Manor, N.Y. 10510, U.S.A. — *N*

Philips Research Laboratories, Cross Oak Lane, Redhill, Surrey RH1 5HA, England — *R*

Philips Research Laboratories Sunnyvale P.O. Box 9052, Sunnyvale, CA 94086, U.S.A. — *S*

C. Ronse	*B*	A three-stage construction for multi-connection networks	Acta Inf. **20**	197-206	1983
M. Auphan	*L*	Réponse impulsionelle des sphères molles ou rigides	Acustica **54**	50-51	1983
P. van Dooren	*B*	Reducing subspaces: computational aspects and applications in linear system theory	Analysis and optimization of systems, A. Bensoussan & J. L. Lions (eds), Springer, Berlin	935-953	1982
K. H. J. Buschow	*E*	Some fundamental and technological aspects of research on rare-earth base metal systems	Ann. Meeting Rare Earth Soc. Japan, Osaka 1983	15-37	1983
P. van de Weijer & R. M. M. Cremers	*E*	Hook method: improvement and simplification of the experimental setup	Appl. Opt. **22**	3500-3502	1983
J. A. van Steenwijk	*E*	Correct relation between the impulse response of GRIN fibers and the excitation by a laser diode	Appl. Opt. **22**	3864-3868	1983
J. J. Harris, D. E. Ashenford (*GEC Hirst Res. Centre, Wembley*), C. T. Foxon, P. J. Dobson (*Imp. College, London*) & B. A. Joyce	*R*	Kinetic limitations to surface segregation during MBE growth of III-V compounds: Sn in GaAs	Appl. Phys. A **33**	87-92	1984
M. Erman & P. M. Frijlink	*L*	Interface analysis by spectroscopic ellipsometry of $Ga_{1-x}Al_xAs$-GaAs heterojunctions grown by metal organic vapor phase epitaxy	Appl. Phys. Lett. **43**	285-287	1983
M. Erman, N. Vodjdani, J. B. Theeten & J. P. Cabanié	*L*	Low loss waveguides grown on GaAs using localized vapor phase epitaxy	Appl. Phys. Lett. **43**	894-895	1983
H. Rau, H. A. Friedrichs* & W. Mathia* (* *RWTH, Aachen*)	*A*	*p-V-T* and bubble-point measurements in the system HBr-H_2O and its critical behaviour	Ber. Bunsenges. Phys. Chem. **87**	1181-1187	1983
V. Belevitch	*B*	On the anti-sidetone telephone circuit	Circuits Syst. & Signal Process. **2**	99-117	1983
J. L. W. Kessels	*E*	On-the-fly optimization of data structures	Commun. ACM **26**	895-901	1983
R. Memming	*H*	Processes at semiconductor electrodes	Comprehensive treatise of electrochemistry, Vol. 7, B. E. Conway *et al.* (eds), Plenum, New York	529-592	1983
C. Tsironis & D. Hennings	*L, A*	Highly stable FET DROs using new linear dielectric resonator material	Electronics Lett. **19**	741-743	1983

P. Bachmann, P. Geittner, H. Hübner, D. Leers & M. Lennartz *A*	Material dispersion characteristics of optical fibres prepared by the PCVD process	Electronics Lett. **19**	765-767	1983
L. Fortuin (*Philips ISA-CQM, Eindhoven*)	Initial supply and re-order level of new service parts	Eur. J. Oper. Res. **15**	310-319	1984
A. Shaulov & W. A. Smith *N*	Optimum cuts of monoclinic m crystals for pyroelectric detectors	Ferroelectrics **49**	223-228	1983
A. M. van der Kraan (*Interuniv. Reactor Inst., Delft*), K. H. J. Buschow & T. T. M. Palstra (*Univ. Leiden*) *E*	Magnetic behaviour of the cubic $La(Fe,Al)_{13}$ compounds	Hyperfine Interactions **15/16**	717-720	1983
C. A. A. J. Greebe, L. J. van de Polder & S. L. Tan *E*	Consumer displays for hi-fi television	IBA Tech. Rev. No. 21	42-45	1983
A. R. Cusdin & N. C. W. Fane (*RSRE, Great Malvern*) *R*	Performance of an interferometer angle-measuring receiver against non line-of-sight transmitters	IEE Proc. **130**	695-700	1983
J. W. Slotboom, M. J. J. Theunissen & A. J. R. de Kock *E*	Impact of silicon substrates on leakage currents	IEEE Electron Device Lett. **EDL-4**	403-406	1983
J. L. van Meerbergen & F. J. van Wijk *E*	A 256-point discrete Fourier transform processor fabricated in a 2 μm NMOS technology	IEEE J. **SC-18**	604-609	1983
V. Pauker & M. Binet *L*	Wideband high gain small size monolithic GaAs FET amplifiers	IEEE MTT-S Int. Microwave Symp. Digest, Boston 1983	50-53	1983
P. Röschmann & K. M. Lüdeke *H*	A ferrimagnetic resonance sensor for remote wireless temperature measurements in organic tissue	IEEE MTT-S Int. Microwave Symp. Digest, Boston 1983	192-194	1983
C. Tsironis, R. Stahlmann (*Tech. Univ. Aachen*) & R. Meierer *L*	Modelling and evaluation of dual gate MESFETs as low-noise, self-oscillating and image-rejection mixers	IEEE MTT-S Int. Microwave Symp. Digest, Boston 1983	443-445	1983
S. Shokoohi (*Bell Labs, Holmdel, NJ*), L. M. Silverman (*Univ. Los Angeles*) & P. M. van Dooren *B*	Linear time-variable systems: balancing and model reduction	IEEE Trans. **AC-28**	810-822	1983
M. H. Kuhn & H. H. Tomaschewski *H*	Improvements in isolated word recognition	IEEE Trans. **ASSP-31**	157-167	1983
Y. Kamp & C. J. Wellekens *B*	Optimal design of minimum-phase FIR filters	IEEE Trans. **ASSP-31**	922-926	1983
T. A. C. M. Claasen & W. F. G. Mecklenbräuker (*Techn. Univ. Wien*) *E*	The aliasing problem in discrete-time Wigner distributions	IEEE Trans. **ASSP-31**	1067-1072	1983
M. Lemonier & C. Piaget *L*	Characterization of local transfer defects in CCD's using a multireversal transfer mode	IEEE Trans. **ED-30**	1414-1416	1983
A. Broese van Groenou & M. I. L. Uijterschout *E*	A quick test on wear of head materials by recording tapes	IEEE Trans. **MAG-19**	1674-1676	1983
W. F. Druyvesteyn, L. Postma, G. H. J. Somers & J. de Wilde *E*	Thin-film read head for analog audio application	IEEE Trans. **MAG-19**	1748-1750	1983
R. L. Maresca *N*	An integrated magnetic actuator and sensor for use in linear or rotary magnetic bearings	IEEE Trans. **MAG-19**	2094-2096	1983
C. Tsironis & V. Pauker *L*	Temperature stabilization of GaAs MESFET oscillators using dielectric resonators	IEEE Trans. **MTT-31**	312-314	1983
A. J. M. Houtsma (*Inst. Perception Res., Eindhoven*)	Estimation of mutual information from limited experimental data	J. Acoust. Soc. Am. **74**	1626-1629	1983
M. T. M. Scheffers (*Inst. Perception Res., Eindhoven*)	Simulation of auditory analysis of pitch: An elaboration on the DWS pitch meter	J. Acoust. Soc. Am. **74**	1716-1725	1983
A. Broese van Groenou & R. C. D. Lissenburg *E*	Inhomogeneous density in die compaction: experiments and finite-element calculations	J. Am. Ceram. Soc. **66**	C/156-C/158	1983
F. Evers (*Hermal-Chemie, Hamburg*), K. Kobs, R. Memming & D. R. Terrell (*Agfa-Gevaert, Mortsel*) *H*	Intramolecular excimer emission of poly(*N*-vinylcabazole) and *rac*- and *meso*-2,4-Di-*N*-carbazolylpentane. Model substances for its syndiotactic and isotactic dyads	J. Am. Chem. Soc. **105**	5988-5995	1983
D. J. Breed, P. Q. J. Nederpel & W. de Geus *E*	Domain-wall dynamics in garnet films with orthorhombic anisotropy	J. Appl. Phys. **54**	6577-6583	1983
S. C. Abrahams*, R. Liminga*, P. Marsh* (* *Bell Labs, Murray Hill, NJ*) & G. M. Loiacono *N*	Strontium nitrite monohydrate: A new pyroelectric nonlinear optic material	J. Appl. Phys. **54**	6776-6778	1983

G. J. van Gurp, A. H. van Ommen, P. R. Boudewijn, D. P. Oosthoek & M. F. C. Willemsen *E*	Ion implantation and diffusion of Zn in GaAs	J. Appl. Phys. **55**	338-346	1984
J. Hasker *E*	Comment on 'A study of cathode edge emission'	J. Appl. Phys. **55**	792-793	1984
J. W. D. Martens, W. L. Peeters, P. Q. J. Nederpel & M. Erman *E, L*	Polar magneto-optical Kerr effect and the dielectric tensor elements of $CoFe_{2-x}Al_xO_4$ $0.1 \leqslant x \leqslant 1$ in the photon energy range $0.65 \leqslant h\nu \leqslant 4.5$ eV	J. Appl. Phys. **55**	1100-1104	1984
M. Zijlstra (*Philips ISA-CQM, Eindhoven*)	Characterizations of the geometric distribution by distributional properties	J. Appl. Prob. **20**	843-850	1983
M. Duseaux *L*	Temperature profile and thermal stress calculations in GaAs crystals growing from the melt	J. Cryst. Growth **61**	576-590	1983
C. Belouet*, C. Texier-Hervo*, M. Mautref* (* *CGE, Marcoussis*), C. Belin, J. Paulin & J. Schneider *L*	Growth of polysilicon sheets on a carbon shaper by the RAD process	J. Cryst. Growth **61**	615-628	1983
R. B. Heimann (*McMaster Univ., Hamilton, Canada*) & W. Tolksdorf *H*	Dissolution forms of gadolinium gallium garnet and yttrium iron garnet obtained in lead oxide/boron trioxide flux	J. Cryst. Growth **62**	75-86	1983
L. de Jonge (*Philips ISA-CQM, Eindhoven*) & W. M. Oppedijk van Veen (*Univ. Tilburg*)	Accounting for data inconsistencies in a longitudinal mail survey	J. Econ. Psychol. **4**	377-400	1983
W. A. P. Claassen, W. G. J. N. Valkenburg, F. H. P. M. Habraken (*Univ. Utrecht*) & Y. Tamminga *E*	Characterization of plasma silicon nitride layers	J. Electrochem. Soc. **130**	2419-2423	1983
A. van Eenbergen & E. Bruninx *E*	A study of some instrument characteristics of an LHS-10 electron spectrometer	J. Electron Spectrosc. & Rel. Phenom. **33**	51-60	1984
J. B. Clegg, J. B. Mullin (*RSRE, Malvern*), K. J. Timmins (*MQAD, Royal Arsenal East, London*), G. W. Blackmore (*Admiralty Mater. Technol. Est., Poole*), G. L. Everett (*Johnson & Matthey Chem. Ltd, Royston*) & R. Snook (*Imp. College, London*) *R*	Measurement of impurities in a multi-doped sample of cadmium mercury telluride	J. Electronics Mater. **12**	879-889	1983
J. J. Daniele & A. Lewis *N*	Electroepitaxial (Peltier-induced) liquid phase epitaxy, compositional stabilization and X-ray analysis of thick (120 μm) $In_{1-x}Ga_xP$ epilayers on (100) GaAs	J. Electronics Mater. **12**	1015-1031	1983
K. H. J. Buschow & D. B. de Mooij *E*	Note on the crystal structure of $EuGa_2$	J. Less-Common Met. **97**	L5-L8	1984
K. H. J. Buschow *E*	Magnetic properties of Y_2Ni_7 and its hydride	J. Less-Common Met. **97**	185-190	1984
P. C. Scholten *E*	How magnetic can a magnetic fluid be?	J. Magn. & Magn. Mater. **39**	99-106	1983
K. H. J. Buschow *E*	Magnetic properties of La_2Ni_7 and its hydride	J. Magn. & Magn. Mater. **40**	224-226	1983
K. H. J. Buschow, P. G. van Engen & D. B. de Mooij *E*	Magnetic and magneto-optical properties of Heusler alloys of the type $Ni_{3-x}Mn_xSn$	J. Magn. & Magn. Mater. **40**	339-347	1984
G. de With *E*	High temperature fracture of boron carbide: experiments and simple theoretical models	J. Mater. Sci. **19**	457-466	1984
K. M. Lüdeke & J. Köhler *H*	Microwave radiometric system for biomedical 'true temperature' and emissivity measurements	J. Microwave Power **18**	277-283	1983
D. M. Krol & J. G. van Lierop *E*	The densification of monolithic gels	J. Non-Cryst. Solids **63**	131-144	1984
B. J. Mulder *E*	Simple piezoelectric microbalance based on a vibrating quartz wire	J. Phys. E **17**	119-121	1984
P. C. M. Gubbens*, A. M. van der Kraan* (* *Interuniv. Reactor Inst., Delft*) & K. H. J. Buschow *E*	Magnetic interactions in Tm_6Fe_{23} and its hydride as studied by means of ^{169}Tm and ^{57}Fe Mössbauer spectroscopy	J. Phys. F **14**	235-243	1984
K. H. J. Buschow *E*	Short-range order and thermal stability in amorphous alloys	J. Phys. F **14**	593-607	1984

M. Duseaux, C. Schiller, J. P. Cornier, J. P. Chevalier (*C.N.R.S., Vitry-sur-Seine*) & J. Hallais	*L*	Elimination of dislocations in GaAs single crystals	J. Physique **44** (Colloque C4)	C4/397-C4/407	1983
M. Erman, J. B. Theeten, N. Vodjdani & Y. Demay	*L*	Chemical and structural analysis of the GaAs/AlGaAs heterojunctions by spectroscopic ellipsometry	J. Vac. Sci. & Technol. B **1**	328-333	1983
J. Maluenda & P. M. Frijlink	*L*	Abrupt transitions in composition and doping profile in GaAs-$Ga_{1-x}Al_xAs$ heterostructures by atmospheric pressure MOVPE	J. Vac. Sci. & Technol. B **1**	334-337	1983
K. H. Nicholas, R. A. Ford, H. E. Brockman & I. J. Stemp	*R*	The magnitude and significance of proximity effects in electron image projector defined layers	J. Vac. Sci. & Technol. B **1**	1020-1022	1983
A. A. van Gorkum	*E*	Correction of spherical aberration in charged particle lenses using aspherical foils	J. Vac. Sci. & Technol. B **1**	1312-1315	1983
Y. Genin, P. van Dooren, T. Kailath*, J.-M. Delosme* & M. Morf* (* *Stanford Univ., CA*)	*B*	On Σ-lossless transfer functions and related questions	Linear Algebra & Appl. **50**	251-275	1983
P. van Dooren & P. Dewilde (*Univ. of Technol., Delft*)	*B*	The eigenstructure of an arbitrary polynomial matrix: computational aspects	Linear Algebra & Appl. **50**	545-579	1983
P. Delsartre, Y. Genin & Y. Kamp	*B*	On the Toeplitz embedding of an arbitrary matrix	Linear Algebra & Appl. **51**	97-119	1983
H. Dötsch, D. Mateika, P. Röschmann & W. Tolksdorf	*H*	Growth and properties of epitaxial barium hexaferrite films	Mater. Res. Bull. **18**	1209-1216	1983
E. D. Roberts & C. E. Fuller	*R*	A positive-working cross-linked electron resist with improved resistance to plasma-etching processes	Microcircuit Engineering **83**	297-304	1983
P. Willich, A. P. von Rosenstiel* & N. Drost* (* *TNO, Apeldoorn*)	*H*	Quantitative electron probe microanalysis of sputtered FeC dry lubrication films	Mikrochim. Acta Suppl. **10**	211-216	1983
Y. Tamminga, M. F. C. Willemsen & R. van Silfhout	*E*	Optimization and application of glancing angle Rutherford backscattering spectrometry	Nucl. Instrum. & Methods Phys. Res. **218**	107-110	1983
W. J. Dallas & R. Linde	*H*	X-ray coded-aperture image reconstruction using an array of kinoforms	Opt. Acta **30**	1561-1572	1983
P. A. Devijver & M. Dekesel	*B*	Computing multidimensional Delaunay tessellations	Pattern Recognition Lett. **1**	311-316	1983
H. K. Kuiken	*E*	An analysis of the temperature drop across a double-layered medium	Philips J. Res. **38**	273-294	1983
D. Hennings & P. Schnabel	*A*	Dielectric characterization of $Ba_2Ti_9O_{20}$ type ceramics at microwave frequencies	Philips J. Res. **38**	295-311	1983
R. Knöchel, K. M. Lüdeke & W. Meyer	*H*	Mikrowellen in der Medizin	Phys. Bl. **39**	337-342	1983
P. Hansen & K. Witter	*H*	Magneto-optical properties of gallium-substituted yttrium iron garnets	Phys. Rev. B **27**	1498-1506	1983
P. Hansen, K. Witter & W. Tolksdorf	*H*	Magnetic and magneto-optic properties of lead- and bismuth-substituted yttrium iron garnet films	Phys. Rev. B **27**	6608-6625	1983
B. H. Verbeek, H. W. A. M. Rompa, P. K. Larsen, M. S. Methfessel* & F. M. Mueller* (* *Univ. Nijmegen*)	*E*	Mixed states in RhAl, RhGa, and RhIn studied by photoemission spectroscopy and band-structure calculations	Phys. Rev. B **28**	6774-6779	1983
P. Dawson, G. Duggan, H. I. Ralph & K. Woodbridge	*R*	Free excitons in room-temperature photoluminescence of GaAs-$Al_xGa_{1-x}As$ multiple quantum wells	Phys. Rev. B **28**	7381-7383	1983
P. M. T. M. van Attekum, P. H. Woerlee, G. C. Verkade & A. A. M. Hoeben	*E*	Influence of grain boundaries and surface Debye temperature on the electrical resistance of thin gold films	Phys. Rev. B **29**	645-650	1984
G. F. Neumark	*N*	Pair spectra and evaluation of the dielectric constant: Application to ZnSe	Phys. Rev. B **29**	1050-1051	1984
M. M. Broer*, D. L. Huber*, W. M. Yen* (* *Univ. Wisconsin, Madison, WI*) & W. K. Zwicker	*N*	Fluorescence quenching and spectral diffusion in $La_{1-x}P_5O_{14}:Nd_x^{3+}$	Phys. Rev. B **29**	2382-2389	1984
G. F. Weston	*R*	Developments in high-vacuum pumps	Phys. Technol. **15**	37-44	1984
M. F. H. Schuurmans & J. M. F. van Dijk	*E*	On radiative and non-radiative decay times in the weak coupling limit	Physica **123B**	131-155	1984

F. A. Vollenbroek, E. J. Spiertz & H. J. J. Kroon	*E*	Profile modification of resist patterns in optical lithography	Polym. Eng. & Sci. **23**	925-930	1983
E. D. Roberts	*R*	A dry-etch resistant positive-working electron resist	Polym. Eng. & Sci. **23**	968-974	1983
B. Sastra & G. M. Dohmen	*E*	High-precision numerically-controlled measuring system for cylindrical surfaces	Precision Eng. **6**	12-16	1984
M. Davio, J.-P. Deschamps & A. Thayse	*B*	Machines algorithmiques	Presses Polytechniques Romandes, Lausanne	—	1983
M. H. Kuhn & R. Geppert	*H*	Performance criteria and the role of integrated circuit technology for voice input systems	Proc. Conf. on communications equipment and systems, Birmingham 1982	80-86	1982
P. J. Severin	*E*	Chromatic launching, a new method for optical fibre profile, single-mode, and mode-dependent measurements	Proc. 9th ECOC, Genève 1983	185-188	1983
P. B. Hesdahl*, A. M. J. Koonen* & M. Weeda* (* *Philips' Telecommun. Ind., Huizen*)		A multi service single fibre subscriber network with wideband electro-optical switching	Proc. 9th ECOC, Genève 1983	331-334	1983
G. D. Khoe, J. A. Luijendijk & A. C. Jacobs	*E*	Application of UV-excited fluorescence for the preparation of single mode fibre connectors and splices	Proc. 9th ECOC, Genève 1983	413-416	1983
J. van der Heijden	*E*	Fibre optic broadband multiservice networks	Proc. 9th ECOC (invited & post deadline papers), Genève 1983	8 pp.	1983
H. Baudry & G. Kersuzan (*T.R.T., Le Plessis Robinson*)	*L*	Individual encapsulation for integrated circuits: how to use thermal analysis to optimize curing conditions towards reliability	Proc. 4th Eur. Hybrid Microelectronics Conf., Copenhagen 1983	111-121	1983
M. Monneraye, H. Baudry & D. Bricout (*RTC, Evreux*)	*L*	The adhesion of thick-film copper conductors	Proc. 4th Eur. Hybrid Microelectronics Conf., Copenhagen 1983	240-249	1983
P. Frey, B. Gabillard & M. Rocchi	*L*	Subnanosecond 8 bit normally-off GaAs SRAM	Proc. ESSCIRC'83, Lausanne 1983	65-68	1983
H. Dötsch, G. Martens & W. Meyer	*H*	Fibre optic components for industrial control	Proc. First Int. Conf. on Optical fibre sensors, London 1983	67-71	1983
B. Aldefeld	*H*	Automatic 3D reconstruction from 2D geometric part descriptions	Proc. IEEE Comput. Soc. Conf. on Computer vision and pattern recognition, Washington, D.C., 1983	66-72	1983
G. M. Martin, M. Duseaux & J. P. Farges	*L*	Characterization of GaAs and InP crystals for integrated optics	Proc. 4th Int. Conf. on Integrated optics and optical fiber communication, Kobe 1983	13-16	1983
H. Ney	*H*	Dynamic programming as a technique for pattern recognition	Proc. 6th Int. Conf. on Pattern recognition, München 1982	1119-1125	1982
H. K. Kuiken	*E*	Etching: a two-dimensional mathematical approach	Proc. R. Soc. London A **392**	199-225	1984
E. Lindale & D. Lehrfeld (*Magnavox, Mahwah, NJ*)	*N*	Life test performance of a Philips rhombic-drive refrigerator with bellows seals	Proc. SPIE **364**	103-108	1983
R. Ward, A. R. Franklin, P. Gould, M. J. Plummer & I. H. Lewin	*R*	Prospects for the 1:1 electron image projector	Proc. SPIE **393**	233-239	1983
J. Braat	*E*	Aspherical lenses in optical scanning systems	Proc. SPIE **399**	294-298	1983
A. T. Eventoff	*N*	Improved Philips Air Sandwich Disk	Proc. SPIE **420**	150-159	1983
R. H. Coursant, C. Méquio & P. Pesqué	*L*	Simulation of the acousto-electric response of ultrasonic narrow strip transducers with mechanical losses	Proc. Ultrasonics International 83, Halifax 1983	414-419	1983
H. W. Werner & R. P. H. Garten (*Inst. Spektrochem. & angew. Spektrosk., Dortmund*)	*E*	A comparative study of methods for thin-film and surface analysis	Rep. Progr. Phys. **47**	221-344	1984

C. Alibert*, F. J. Hua* (* *Univ. Sci. & Tech. Languedoc, Montpellier*), M. Erman, P. Frijlink, P. Jarry & J. B. Theeten	*L*	Electroréflexion et ellipsométrie spectroscopique d'hétérostructures InGaAsP/InP et GaAlAs/GaAs	Revue Phys. Appl. **18**	709-717	1983
P. Delsarte, Y. Genin & Y. Kamp	*B*	Equivalence classes of Hermitian matrices and their Schur parametrization	SIAM J. Algebraic & Discrete Methods **4**	279-289	1983
A. J. E. M. Janssen	*E*	A note on Hudson's theorem about functions with nonnegative Wigner distributions	SIAM J. Math. Anal. **15**	170-176	1984
H. Strecker	*H*	A local feature method for the detection of flaws in automated X-ray inspection of castings	Signal Process. **5**	423-431	1983
C. R. Hill	*N*	A real-time microprocessor debugging technique	SIGPLAN Not. **18** (No. 8)	145-148	1983
M. Barthelmes, P. Bressler, D. Bünz, K. Gütschow, J. Heeger & H.-J. Lemke	*H*	CATPAC: a software package for computer-aided control engineering	Simulation in engineering sciences, J. Burger & Y. Jarny (eds), Elsevier Science, Amsterdam	73-78	1983
J. Hallais	*L*	Metal organic vapour phase epitaxy: the key issues	Solid state devices 1982, A. Goetzberger & H. M. Zerbst (eds), Verlag Chemie, Weinheim	51-72	1983
M. J. Sparnaay & G. E. Thomas	*E*	Surface segregation in $Au_{0.1}Cu_{0.9}$ crystals	Surf. Sci. **135**	184-198	1983
J. W. D. Martens, W. L. Peeters & P. Q. J. Nederpel	*E*	A non-destructive analysis of the influence of sputter etching on the magnetic surface properties of manganese zinc ferrite	Surf. Sci. **135**	334-340	1983
M. Erman & J. B. Theeten	*L*	Analysis of ion-implanted GaAs by spectroscopic ellipsometry	Surf. Sci. **135**	353-373	1983
J. van der Heijden	*E*	Het DIVAC project	T. Ned. Elektron. & Radiogenoot. **48**	171-177	1983
R. L. J. Roetering (*Philips' Telecommun. Ind., Huizen*)		A/D-conversie van video-signalen en lijncodering	T. Ned. Elektron. & Radiogenoot. **48**	189-199	1983
S. Gourrier, P. Friedel & J. P. Chané	*L*	Interface properties of metal/oxide/semiconductor and metal/insulator/semiconductor structures on $Ga_{1-x}In_xAs$ with $x = 0.35$ and 0.10	Thin Solid Films **103**	155-166	1983
M. Fink, F. Hottier & J. F. Cardoso	*L*	Ultrasonic signal processing for *in vivo* attenuation measurement: short time Fourier analysis	Ultrason. Imaging **5**	117-135	1983
H. W. Werner & P. R. Boudewijn	*E*	A comparison of SIMS with other techniques based on ion-beam solid interactions	Vacuum **34**	83-101	1984
J. M. Shannon & J. B. Clegg	*R*	Nanometre structures in semiconductors formed by low energy ion implantation	Vacuum **34**	193-197	1984
A. J. van Roosmalen	*E*	Review: dry etching of silicon oxide	Vacuum **34**	429-436	1984
R. Memming	*H*	Photoelektrochemische Wasserstoff-Erzeugung durch Solarenergie	Wärme **89**	62-66	1983

Contents of Philips Telecommunication Review **42**, No. 2, 1984

Q. Renni & J. R. Lange: PFX, a new universal portable (pp. 49-62)

A. Brinkman & A. L. Bloemendaal: A motorway traffic control system (pp. 63-73)

A. J. W. van Daal & P. van der Vlist: DELTACS — a versatile tactical communications system (pp. 74-89)

W. J. A. Vonk: AEROPP 0 message and data switch for smaller airports (pp. 90-94)

P. G. L. Potgieser: The LAM91/95 family of data circuit terminating equipments (pp. 95-105)

Volume 41, 1983/84, No. 9 pages 253-284 Published 25th October 1984

PHILIPS TECHNICAL REVIEW

VOLUME 41, 1983/84, No. 10

Aspherics

I. Optomechanics, an ultra-high-precision machining technique

II. Aspheric surfaces: design and optical advantages

III. Fabrication, testing and application of highly accurate aspheric optical elements

One of the few surviving microscopes made by Antoni van Leeuwenhoek (1632-1723) contains a double convex lens that is aspheric and in all probability was not made by grinding. The asphericity gives the lens its high resolving power. The value can still be measured at 1.35 μm, at least one and a half times better than for the lenses in the other microscopes made by Van Leeuwenhoek. Whether this is purely fortuitous or additional proof of Van Leeuwenhoek's keen powers of perception we do not know, nor do we know whether Van Leeuwenhoek made the lens himself and exactly how. A Dutch optical physicist has recently shown that when a glass sphere with a diameter of a few centimetres is blown a thickening at the top can sometimes be used as a strongly magnifying aspheric lens. The title photograph shows such a sphere with the thickening at the top. Two Germans, the Von Uffenbach brothers, visited Van Leeuwenhoek in Delft when he was seventy-eight, and many years later one of them reported what they had talked about in the book 'Merkwürdige Reisen durch Niedersachsen Holland und Engelland' (Ulm 1754). It appears that Van Leeuwenhoek's claim that he could make such lenses, which were not spherical, by blowing was regarded by the other brother at the time as a 'Dutch tall story'. This Von Uffenbach considered that glass-blowing could not produce anything but a pure spherical shape. He spoke a prophetic word, perhaps, since aspheric lenses are not in fact made by blowing today. Instead of hazardous manual operations Philips technicians use more certain methods: a technique of ultra-high-precision turning and grinding on a special lathe called COLATH, which was described in Volume 39 of this journal (1980, No. 9). In spite of much automation, this modern machining technology remains a fascinating activity, producing outstanding 'optomechanical' results, such as a surface roughness of under 5 nm (less than one per cent of the wavelength of red light). This article in three parts on the subject of aspherics highlights the advantages of using aspheric refracting surfaces in applied geometrical optics, and describes the methods of designing them, making them and measuring their performance. To correct for image errors on the scale of 1 μm and less — as necessary for example in the read-out systems for Compact Disc and LaserVision — requires manufacturing methods with corresponding, exceptionally small tolerances for the shape of the lenses, etc. The 'optomechanical' machining technique described here for making aspheric optical elements offers practical answers to the problems, and has now been in use for eight years. In this technical journal, as in that historical discussion between the Von Uffenbachs and Van Leeuwenhoek, the main emphasis will be on how it is done.

I. Optomechanics, an ultra-high-precision machining technique

J. Haisma and T. G. Gijsbers

Optomechanics is a term that we commonly use to describe the fabrication of aspheric *optical* elements of extreme accuracy by means of numerically controlled *mechanical* (i.e. machining) operations. The measurements carried out to monitor such operations, which include turning and grinding to an optical finish, are also optical in nature.

In this first part we introduce the new method of fabrication and consider its position within applied geometrical optics. In this field the great changes that have taken place in recent years are mainly attributable to the ever-increasing refinement of turning as a method of machining. Much of the optomechanical work done at Philips Research Laboratories on the computer-controlled precision lathe called COLATH, brought into use in 1978, illustrates this progress in applied geometrical optics [1][2]. The results achieved do not seem to be fortuitous; taking advantage of a new method of manufacture, including measurement and testing, in applied optics has more than once improved the prospects for success. Optomechanics is such a method, and for that reason we begin this article with some information on its qualities and something of its history.

In the seventies only a few institutions and firms were actively engaged in the technological and scientific investigation of this new method of manufacture. With a few numerically controlled machines and diamond-tipped cutting tools, a machining accuracy was achieved that was then only possible on manually operated precision lathes for simple shapes, such as flat surfaces and cylinders of revolution. This machining quality may be reasonably compared with the results of conventional ultra-high-precision grinding and polishing. The latter operations, still performed manually sometimes, were — and are — used for making lenses and mirrors of the highest quality.

For a number of materials, such as machinable plastics and non-ferrous metals with their alloys, it proved possible in the second half of the seventies to keep dimensional errors in the aspheric workpieces smaller than a few tenths of 1 μm during machining and to reduce surface roughness to values of less than 20 nm (peak-to-valley) [1].

During the same period a method of 'transparent' single-point turning, using cutting tools of materials such as hafnium nitride, was developed for some types of optical glass, though without numerical control [3]. The surface roughnesses achieved had comparable values, but dimensional variations were an order of magnitude worse than the figure just mentioned.

Like turning, the art of grinding and polishing is a technical skill with a long pedigree. Spectacle lenses were probably ground and polished in the 14th century, if not earlier. Machining various materials on a kind of lathe must have already been familiar to the Romans.

Turning and grinding and polishing are thus ancient skills, but this by no means implies that little is happening in this field now. Since these two skills were raised to about the same level of accuracy and reproducibility not so very long ago, the continuing developments, which can now run hand in hand, may be expected to provide an increased stimulus to innovation.

In this way, within a few years, optomechanics, extending the pattern of existing skills, has taken shape as an ultra-high-precision machining technique. As the name suggests, the problems of optics — usually of applied geometrical optics — are a powerful stimulus to those who have access to the new machining facilities. The features of a highly developed numerical control system give a lathe flexibility and versatility. The ability to make all kinds of aspheric surfaces, and of course spherical surfaces too (both with rotational symmetry), seems almost to be simply a question of indicating the coordinates of the contours required. ('Almost' is here a word of caution. In spite of the automation, working with machines like COLATH still requires the greatest care and skilled attention as well as regular inspection, especially during the preparatory operations.)

Further work on COLATH at Philips Research Laboratories has led to the development of a 'grinding spindle'. This can be mounted on the machine instead of the cutting tool, and can also be used with the numerical control.

Dr Ir J. Haisma and Ir T. G. Gijsbers are with Philips Research Laboratories, Eindhoven.

It has proved possible in this way to combine turning and 'optical' grinding as precision machining operations in a single largely automated technique of 'point-coordinate' machining. The term 'point-coordinate' implies that this turning and grinding technique (grinding to a polish finish) uses a 'point' area of contact (the largest dimension is a few tens of μm).

COLATH has an inaccuracy of about 1 μm (absolute) within its total working area (of 200 mm × 200 mm). This figure includes the alignment errors in the machine and the rounding-off errors due to the numerical control. With the smaller surfaces the absolute accuracy achieved is even better: the error is less than 0.2 μm. The surface roughness of workpieces can be reduced to values of less than 10 nm (peak-to-valley). Workpieces meant to be identical show dimensional differences that can be less than 50 nm.

The grinding technique that we use ensures that hard and brittle materials (such as optical glass and various types of steel) can also be accurately machined, and do not have to be rejected as workpiece materials.

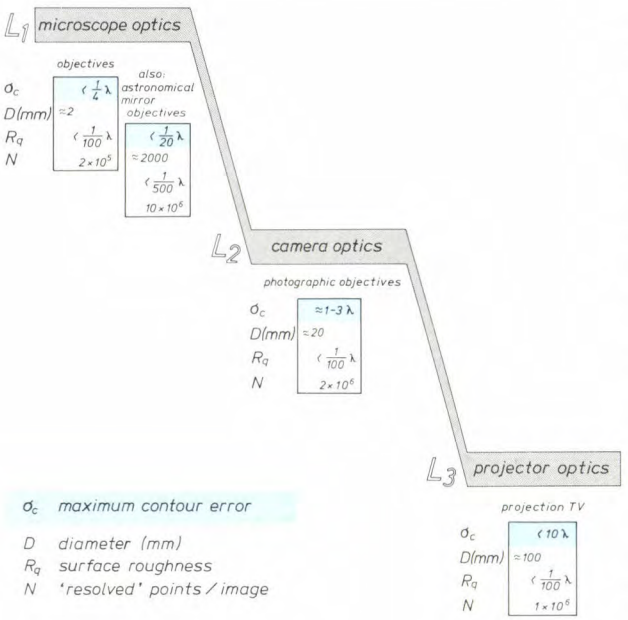

Fig. 1. The appropriate accuracies for the manufacture of lenses and mirrors in applied geometrical optics. The three different levels (L_i), which relate to the highest accuracy, a middle range and the lower values, are indicated by 'microscope optics', 'camera optics' and 'projector optics'. These names refer to the most commonly made instruments or devices for each level. The differences lie mainly in the permissible maximum contour error (or slow form error) of the lenses and mirrors. All variations — measured with respect to an ideal shape — are expressed in terms of λ, the mean wavelength of the part of the spectrum used in the particular instrument. The surface-roughness tolerances (R_q) are a measure of the smoothness of the surfaces. (See the subsection on 'checking the machining' in Part III.) Examples of the various lenses and mirrors, with a characteristic dimension (the diameter D), are included in the figure. The quantity N is a measure of the resolving power; the number is an estimate of the maximum number of object points that can be observed clearly separated in the image.

With few exceptions, the requirements of applied geometrical optics — often very strict — can readily be met in practice.

Generally speaking, these requirements correspond to three levels of accuracy. They are given in *fig. 1* with some of their characteristic values, together with examples of the different types of optical components or systems involved. The 'mean' wavelength of the relevant part of the spectrum is a good unit of length for considering cases of this kind. Optomechanics is expected to contribute most to applications at the highest level of accuracy. Within the Philips company interest is already clearly being shown in such applications on an industrial scale. In the somewhat longer term, however, a shift in interest toward the two groups with lower accuracy is not impossible.

The manufacture of highly aspheric surfaces of optical quality is the greatest advantage that optomechanics has been able to offer in its short existence. This is of such importance because it has long been known from calculations that the replacement of two spherical surfaces in an optical system by *aspheric* surfaces of revolution should permit the elimination of spherical aberration and coma, two of the more serious aberrations.

At this point we should also mention planar optics. This has recently been the subject of intensive development, with particular emphasis on geodesic components [4]. These are optical components that guide light beams along geodesic lines *on their surface*. (Geodesic lines of a surface are the shortest lines connecting pairs of points and which are completely contained in the surface.) Such surfaces can be highly aspheric surfaces of revolution; the guidance is designed to control light beams, i.e. to deflect, split or focus them (*fig. 2*).

For highly accurate lenses and mirrors the inclusion of aspheric surfaces today seems to have gone all the way from a theoretical idea, attractive but hardly practical, to reliable industrial manufacture, fast and efficient [5]. To illustrate more clearly the changes ushered in by optomechanics, it is interesting to recall the classical method of optical manufacture [6]. As-

[1] T. G. Gijsbers, COLATH, a numerically controlled lathe for very high precision, Philips Tech. Rev. **39**, 229-244, 1980.
[2] J. Haisma, E. Hugues and C. Babolat, Realization of a bi-aspherical objective lens for the Philips Video Long Play system, Opt. Lett. **4**, 70-72, 1979.
[3] R. Brehm, K. van Dun, J. C. G. Teunissen and J. Haisma, Transparent single-point turning of optical glass: A phenomenological presentation, Precision Eng. **1**, 207-213, 1979.
[4] S. Sottini, V. Russo and G. C. Righini, Geodesic optics: new components, J. Opt. Soc. Am. **70**, 1230-1234, 1980.
[5] Aspheric optics: design, manufacture, testing, Proc. SPIE **235**, Soc. Photo-Opt. Instr. Eng., Bellingham, WA, 1980.
[6] R. M. Scott, Optical manufacturing, in: R. Kingslake (ed.), Applied optics and optical engineering, Vol. III, Academic Press, New York 1965, pp. 43-95.

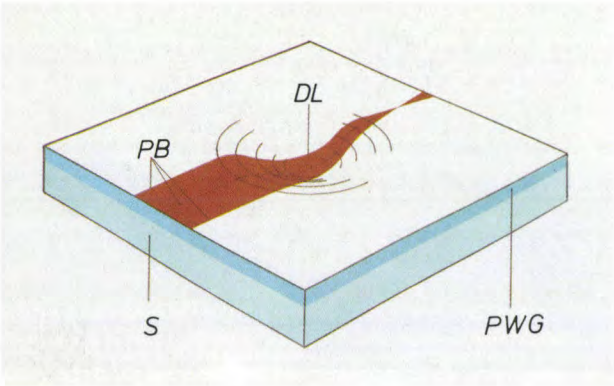

Fig. 2. In the relatively new field of planar optics studies are made of the propagation of light in a planar waveguide (*PWG*). An aspheric deformation of the surface of the waveguide can produce a lens effect, as shown here. This 'depression lens' is sometimes called a geodesic lens, since the light rays follow geodesic curves. *PB* the plane beam to be focused. *S* substrate of the waveguide.

pheric elements especially gave considerable problems, mainly because, as R. M. Scott put it [6], 'the natural actions of grinding and polishing force optical surfaces towards spheres'. The standard technique of grinding and polishing, with contact over the entire surface, offers the advantage of improving the dimensional accuracy and the surface quality (smoothness) of the optical component at the same time. This advantage is lost, however, as soon as aspheric surfaces have to be machined, because permanent contact over the whole surface during rotating movements is then in general no longer possible.

The standard method of grinding and polishing used in the manufacture of optical elements employs machines with two rotating parts whose surfaces are in slipping contact. The first part, the 'block', carries the lens or mirror being worked upon; by means of the second part, the 'cup' or 'polishing' tool, a gentle abrasive is provided, such as powdered aluminium oxide mixed with water. The grinding (or polishing) takes place in the contact region common to both rotating parts. One of the two, usually the block, is driven by a vertical spindle, which gives the other part a rotation such that each point of the lower surface contacts each point of the upper surface. The work is done here collectively by an 'infinite' number of (separate) grains of powder; this is very different from the single-point operation on a lathe, as performed on COLATH.

The manufacture of spectacle lenses is really the only branch of the established optical industry in which there is large-scale production of aspheric lenses. The optically permissible tolerances for spectacle lenses have such large values that the problems indicated and fundamental difficulties lose their significance. Making the appropriate shape of lens and polishing can be performed *separately*. A satisfactory lens shape produced by grinding can be finish-polished without this having any visually perceptible effect on the shape. Obviously, spectacle lenses do not belong to the level of highest accuracy in fig. 1. Cylindrical lenses are a second, though less important, example of aspheric lenses that can be produced by conventional methods. In classical technology a *linear* contact tool, a 'scraper', can also be used for making aspheric surfaces [6][7]. The inaccuracy of such scrapers is of the order of 10 μm, which is far too large for applications such as microscope optics (fig. 1).

Fig. 3 gives examples of what can nowadays be done optomechanically. The row of bi-aspheric lenses shown here, only limited by natural diffraction at the edges and thus possessing maximum resolving power, was made by turning a piece of plastic on COLATH. They have a numerical aperture of 0.43. The lens in the middle foreground has an even greater numerical aperture (0.85). The back row shows four steel moulds used for pressing glass lenses, together with two quartz-glass moulds for the same purpose. All six moulds were ground to an optical finish on COLATH.

These good results, enhanced by the greatly increased scope for introducing variation in the shapes of the lenses, do not mean that optomechanics is without its problems. Almost all the requirements for the lathe, the tools and the workpiece are exceptionally strict, especially with regard to control systems, quality of the tools, stability, and shape of the premachined workpiece. Premachining here implies that the preform of the required optical component must have no irregularities that might introduce mechanical resonances during the machining.

The *technician* operating the machine has to be aware that all the parts of an optical system and all the tools and materials used must be accurately compatible with one another. He must also make sure that his tools are in the best possible condition for the ultra-high-precision operations. The *designer* of an optical system must in his turn be aware of certain limitations of the machine, with regard for example to setting up the workpiece, and the maximum permissible aspheric 'steepness'. Good communication between the technician and the optical designer right from the beginning is a prerequisite for success in optomechanics. The application of optomechanics continues to call for technical consultation in connection with functional innovations, design development and quality control during preparation and manufacture (shape, surface, centring and clamping during setting up).

Part II of the article deals briefly with the theory of the advantages offered by aspheric surfaces of revolu-

[7] In finishing surfaces of revolution based on conic sections, such as a paraboloid, the natural and interactive correction between surface and 'scraper' can be used. See L. C. Martin, Technical optics, Vol. II, 2nd edition, Pitman, London 1961, pp. 353-356.

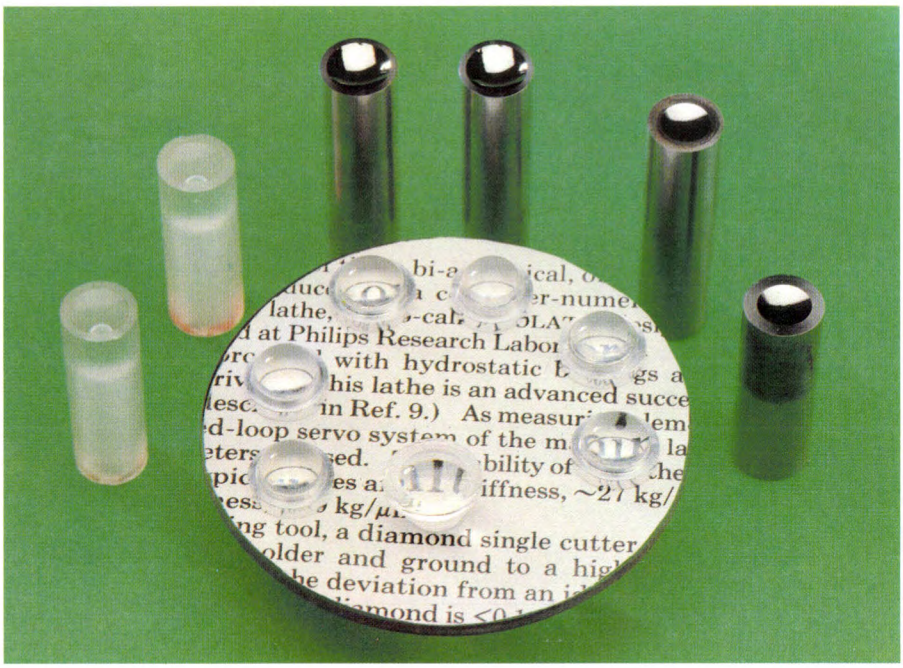

Fig. 3. The objects shown were produced by 'optomechanical' methods on the COLATH lathe. The lenses, each with two aspheric surfaces, were made by turning polymethyl methacrylate, with no further finishing. The residual surface roughness and any inaccuracies in the lens shape are so small that the greatest image imperfection is the diffraction due to the finite nature of the lens apertures. The other objects are moulds, of steel and quartz glass, for pressing glass lenses. These moulds were ground on COLATH and meet the tightest specifications for optical finish and accuracy of shape.

tion to the designer of optical systems. The description is based on two methods of solving design problems. A résumé is also given of the basic information required for optical design, including the main requirements of users of optical systems, together with some historical background.

The third part describes a group of bi-aspheric lenses made with COLATH as an example of ordinary manufacture. Particular aspects of the machining techniques are discussed. Attention is paid to the close relation between manufacture and measurement (or testing), and to a classification of errors of form. Also treated are the periodic tool-marks produced in machining the surface and their effect on quality monitoring, together with surface roughness. Finally, the applications of aspherics in optical read-out units in the LaserVision and Compact Disc systems are discussed. A summary description follows of the bi-aspheric objective (shown in fig. 3) with an exceptionally large numerical aperture (0.85). This is intended for making the master discs in the reproduction processes both for Compact Disc and LaserVision.

II. Aspheric surfaces: design and optical advantages

J. J. M. Braat

In designing a lens system the unavoidable lens errors for each of the separate components should ideally be given values and signs, positive or negative, such that the sum, calculated over all the components, is as small as possible. If this is done, the system will be capable of giving an image with a minimum of aberrations. It has long been known that this rather subtle balancing out of the individual lens errors can be considerably simplified by including aspheric surfaces in the design.

Dr Ir J. J. M. Braat is with Philips Research Laboratories, Eindhoven.

Until recently the state of technology did not really permit the introduction of aspheric surfaces into optical systems of the highest grade of accuracy as categorized in part I of this article (see also fig. 1), for a number of practical reasons. The only exceptions were the occasional astronomical telescope in which the skilful technicians had managed to produce aspheric surfaces by the classical approach — the difficult and extremely time-consuming method of repeated local polishing and remeasurement.

In the case of simple spherical surfaces the final quality of a system is determined by a carefully considered choice of the radii of curvature of the surfaces, the distances between the separate components and the lens thicknesses, and also the types of optical glass to be used. The deflection angles of the light rays at the lens surfaces should be small, since otherwise the permissible mechanical tolerances for the maker would no longer be realistic specifications. The total strength of such a purely spherical system is for these reasons often distributed over a large number of components (ten or more is not unusual).

The direct consequence of the admissibility of aspheric surfaces is the rigorous suppression of at least one aberration, sometimes more. The balancing out of the remaining aberrations also requires the presence of fewer components in the system than in the comparable classical case with simple spherical surfaces. In practice the reduction amounts to a factor of two or more. Moreover, in spite of the reduction in the number of components, the final image quality of the system can be better than in the classical design.

The extra freedom offered by the admissibility of aspheric surfaces has thus greatly eased the design problem. Now the difficulties that are still encountered are mainly those associated with fabrication. The main features of this have already been indicated in part I of this article. On their part, the designers obviously have to select from the multiplicity of possible aspheric surfaces, the ones that in steepness (the 'magnitude' of the asphericity) and sensitivity to position (permissible decentring, tilt) will present the fewest problems for the maker. Optical designers and mechanical engineers therefore work in close cooperation, especially when they are designing products that must be suitable for quantity production.

Desirable features

The users of an optical system often require it to have a high 'light-gathering power', i.e. a high aperture angle (expressed as the numerical aperture N.A. = $n \sin u$, where u is half the maximum angle of a pencil of image-producing rays on the object side and n is the refractive index in the object space). Users need this light-gathering power as soon as they need a high resolving power in the object plane. At the same time such users usually require the largest possible 'field'. ('Field' here means the part of the selected object plane corresponding to an adequately faithful image in the image surface — usually planar.) Both requirements can be seen as the desire to transfer the maximum number of bits of information (resolvable points) from object plane to image plane.

Unfortunately an optical system becomes more sensitive to aberrations as the N.A. increases. The aberrations can become so serious that further increase in the N.A. does not give an improvement in the resolving power but makes it *worse* instead. A trade-off then becomes unavoidable. In television cameras, for example, and also in cine and photographic equipment, designers always try to maximize the N.A., because of the essential importance of the illuminance at the image plane (it is proportional to the square of the N.A.). A small loss of resolving power then has to be taken into the bargain, certainly in conventional optical systems. This compromise can turn out better when aspheric elements are used.

The design of aplanatic systems

A good example of better image correction combined with a high N.A. is the achievement of aplanatism in an optical system through the use of *two* aspheric surfaces. (An 'aplanatic' system is one completely corrected for spherical aberration and coma.) The theory of this problem was first treated in 1948, by G. D. Wassermann and E. Wolf [8]. The design formulae that they derived, based on ray tracing, show that the specification of a *single* aspheric surface can lead to stigmatic image formation at the optical axis. In other words, the spherical aberration of the rays originating from one object point on the optical axis can be completely suppressed, even for systems that admit pencils with a large aperture angle. A lens with one such aspheric surface is rather thicker towards the edge than the equivalent lens with two spherical surfaces. The associated increase in optical pathlength compensates for the spherical aberration and makes the emergent wavefront perfectly spherical. This means that all rays intersect the axis at the same point, whether they are paraxial rays or marginal rays.

Wassermann and Wolf also showed that *two* aspheric surfaces are sufficient to extend the stigmatism of the object point on the axis to its immediate environment. This means that the introduction of *two* aspheric surfaces can ensure that Abbe's sine condition is exactly satisfied, so that there is no coma. In this case a small circular zone perpendicular to the optical axis and with its centre on the optical axis at the object point will give a sharp image in a plane. The validity of this aplanatism is again *guaranteed up to high values of the N.A.* This was the most important advance resulting from Wasserman and Wolf's theoretical work.

[8] G. D. Wassermann and E. Wolf, On the theory of aplanatic aspheric systems, Proc. Phys. Soc. B 62, 2-8, 1949. See also J. J. M. Braat and P. F. Greve, Aplanatic optical system containing two aspheric surfaces, Appl. Opt. 18, 2187-2191, 1979.

[9] See M. Born and E. Wolf, Principles of optics, 5th edition, Pergamon, New York 1975, p. 211, and also W. de Groot, Philips Tech. Rev. 9, 301-308, 1947/48.

A maximum permissible N.A. is always the quantity that limits the validity of design calculations for optical systems. Such calculations are made at three levels.

The first or 'lowest' level relates to very small values of the N.A., up to about 0.01, or 0.02 at the most. The calculations here are those of 'paraxial' optics; they give results such as the position of the image plane (for a given object plane) and the associated lateral magnification, the focal length, etc. However, they offer no way of determining aberrations, let alone reducing them.

The calculations at the second level are valid for N.A.-values up to almost 0.10. This method, originally devised in 1856 by the German astronomer L. P. von Seidel, can be used to influence five of the different aberrations: spherical aberration, coma, astigmatism, curvature of field and distortion [9]. All these primary aberrations (or Seidel aberrations) correspond to particular wavefront errors, i.e. deviations reckoned from an assumed perfect spherical wavefront (*fig. 4*). Only if a wavefront remains perfectly spherical will it be able to converge at an ideal point image.

Von Seidel's treatment starts by considering a perfectly spherical lens surface. The contour function $z(y)$ of the lens (its profile curve), a part of a circle, can be represented by:

$$z = r[1 - \{1 - (y/r)^2\}^{1/2}],$$

where z is the coordinate along the optical axis of the lens and y a coordinate perpendicular to the axis (identical to the radial coordinate of the surface); r is the radius of the circle. (The point (0,0) is the intersection of the optical axis and the lens surface.) Expressing the right-hand side as a power series in $(y/r)^2$ gives:

$$z = \frac{r}{2}\{(y/r)^2 + \tfrac{1}{4}(y/r)^4 + \tfrac{1}{8}(y/r)^6 + \ldots\}.$$

With Von Seidel's restrictions on the N.A.-values, the first two terms of the series (one more than in paraxial optics) are sufficient to enable the influence of a spherical surface on the image formation to be calculated. The spherical surface is therefore approximated by a surface whose radius of curvature is exactly equal to r only at the

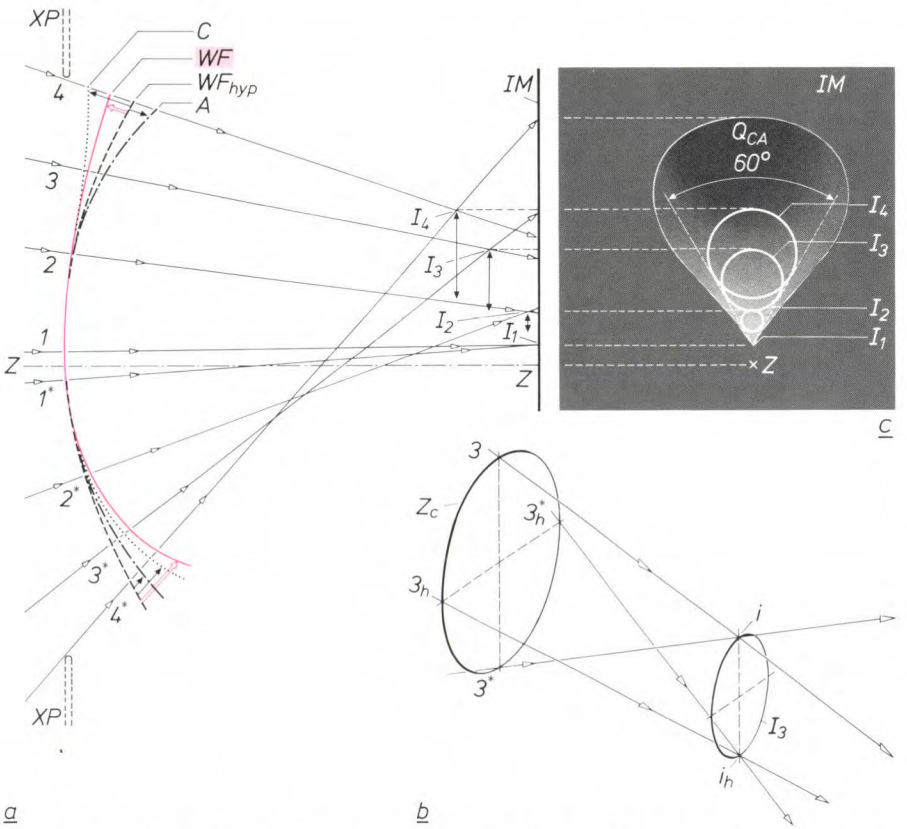

Fig. 4. *a*) Illustration showing, in vertical section along the axis, how spherical aberration and coma deform an ideal spherical wavefront (WF_{hyp}) to an aspheric wavefront (*A* and *C* respectively). They combine to give the ray-path determining wavefront *WF*, opposing one another on the side of ray *4* and reinforcing one another on the other side (at *4**). The pair of light rays *4,4** forms an image point on the 'ring' I_4, the pair *3,3** on the smaller ring I_3, etc. The ring I_1 is so small that it can be considered to be a point, the image point in the paraxial image plane *IM*. All the rays can be considered as originating from a point source (not shown) located a short distance from the optical axis (*Z-Z*) in the object space of the lens system (not shown), in the vertical (i.e. meridional) plane. *b*) The perspective drawing shows how an image ring, I_3 in the actual case, is completely filled with image points by pairs of rays that have passed through the same circular zone Z_c in the exit pupil, *XP* in (*a*), of the lens system. Each pair has two corresponding points in the circular zone, diametrically opposite one another. Pairs of rays rotated 90° with respect to one another (e.g. the 'sagittal' pair $3_h,3_h^*$ and the meridional pair *3,3**) give image points 180° apart (i_h and i respectively). *c*) The circular images I_1, I_2, ... are seen to fill a cone of apex angle 60° in *IM* (see for example A. K. Ghatak and K. Thyagarajan, Contemporary optics, Plenum Press, New York 1978). Q_{CA} is the 'comet-like' image pattern resulting in *IM* from I_1, I_2, ... The spherical aberration, see (*a*), has caused the rings to be displaced from the paraxial image plane in the direction of *XP*.

point (0,0); it differs from r at other points. Any *aspheric* surface with rotational symmetry can then be described by

$$z = \frac{r}{2}\{(y/r)^2 + \tfrac{1}{4}(1 + A)(y/r)^4\}.$$

The 'aspheric residue' $(y/r)^4 A$, which corresponds to a departure from a spherical surface (in Von Seidel's approximation), can be used to influence the five primary aberrations.

The calculations at the third level are necessary if the N.A. is greater than about 0.1. Von Seidel's approximation would fail here, essentially because it substitutes the 'third-order' approximation $u - (1/6)u^3$ for $\sin u$ (u is the angle of slope of the incident ray). This approximation is completely inadequate for calculating the aberrations to an accuracy typically better than 0.01 λ, a value of relevance for lenses of the highest quality. At this highest level the analysis can only be based on an 'exact' ray-path calculation. This is made by considering a pencil of rays leaving an object point and filling the entire entrance pupil of the system; the differences in pathlength between the various optical paths to the image plane are then calculated. These differences in optical pathlength determine the shape of the perturbed wavefront in the image space and hence the aberrations. The description 'exact' refers to the exact application of Snell's law; this must be done at each lens surface, for each light ray that goes through it. 'Shooting' all the rays through a system, and in this 'exact' fashion, was formerly a time-consuming activity. Fortunately, that difficulty has disappeared with the arrival of the computer. This method based on ray-tracing is an analysis of the *total system*, since it only gives the sum of the individual contributions of the various surfaces to the aberrations found, and hence not the effect of each individual surface — at least not in a readily usable fashion.

The two aspheric surfaces, which have rotational symmetry, can be specified as contour functions $z(y)$, with z the axial coordinate and y the radial coordinate of the surface. They are found here from two simultaneous differential equations of the first order, which are obtained by applying Snell's law consistently to all the reflecting surfaces. A numerical solution of the differential equations provides a number of points on the two desired curves $z(y)$. The complete curves can be approximated between these calculated points by using an interpolation method.

The original authors, Wassermann and Wolf, working in pre-computer days, used Taylor series for their calculations. We used a series expansion of $z(y)$ in Chebyshev polynomials, which is much better suited to computer calculations [10], as our interpolation expression. These expansions in Chebyshev polynomials usually converge more rapidly than the corresponding Taylor series. The expansion can be continued until the difference from the original function is no greater than a predetermined value. If this value is taken as 0.001 λ, say, we should be able to obtain lenses whose shape ensures the best possible image quality. The only remaining image imperfection is then diffraction at the edge of the lens, provided of course that the surfaces are polished to give the highest degree of optical-quality finish.

Polynomials of the sixth, eighth and even higher degree sometimes contribute appreciably to the series expansion for the interpolation, depending on the N.A. This confirms that Von Seidel's approximation [9] cannot be correct, at least for these high N.A.-values. Von Seidel's approximation 'of the third order' has remained of interest ever since it was first put forward more than a century ago. It provides a simple means of correcting the five primary aberrations, but the N.A.-value must not exceed 0.10.

Diffraction

The design analysis described above, for use in the specification of aspheric lens surfaces in high-aperture aplanatic lenses, is purely a matter of geometrical optics; no account can therefore be taken of diffraction effects, although they are present. Fortunately these effects can usually be taken into consideration through the application of a simple two-stage analysis. In the second stage the Fresnel-Kirchhoff diffraction equation [11] is applied to the bounded wavefront as calculated from geometrical optics (the first stage, in which the edge of the lens is simply considered as the abrupt boundary of a refracting zone). In this way the correct distribution of the light intensity in the image plane, which represents the total diffraction image, can be calculated. An example of this is the well-known Airy pattern, consisting of a small bright disc surrounded by alternate dark and light concentric rings; the pattern is formed even when an image of a 'true' point source is produced by a lens that itself could produce an aberration-free image. In this case the diffraction is purely due to the edge of the lens, which behaves as a circular aperture. Such a lens is an example of an 'ideal' element in geometrical optics. The quality of the lens is then diffraction-limited, since the unavoidable diffraction at its edge is the only 'aberration' present.

Examples of aspheric aplanatic lenses

The design of lenses for the LaserVision and Compact Disc systems [12] is a good example of practical results that the method of analysis originating from the work of Wassermann and Wolf can provide [8].

A feature of both systems is that the information density on the discs is very high, e.g. 100 Mbit/cm^2 on a Compact Disc, and for read-out they require a microscope objective with an N.A. greater than 0.4 and a useful field diameter varying from at least 100 μm to 500 μm.

E. Hugues and C. Babolat were the first to design a bi-aspheric lens with such a large N.A. (0.43) [2]. Their method is somewhat different from the method described in the text: they used a purely

iterative matching of incident and emergent light rays, with specified conditions for the behaviour in the image space. At the same time a number of specific boundary conditions have to be satisfied. These include tolerances for residual decentring and tilt for each aspheric surface, and these have to be optomechanically acceptable.

The objective that has been designed consists of only one lens, of diffraction-limited quality, with two aspheric surfaces (*fig. 5*). In the Table in fig. 5 a number of calculated contour parameters for the two desired surfaces are shown. The dimensional differences from perfectly spherical surfaces are not very large — the asphericity is a few tens of μm at most, but their significance is more obvious when they are expressed in wavelengths. This lens (we often call it a 'bi-aspheric'), gives an image free from coma and spherical aberration. Slight astigmatism and field curvature are present, near the edge of the useful field.

In a conventional design with spherical surfaces some four lenses would be necessary for the same image quality (fig. 5*b*). Accurate alignment is easier with a single lens than with four, and therefore preferable. (Alignment is the bringing into coincidence of the optical axes of the refracting surfaces. Faulty alignment, the main cause of coma, must be avoided. Coma is the very troublesome aberration that occurs transverse to and to one side of the optical axis and distorts an image point to a 'comet's tail', see fig. 4.)

More recent design work for the LaserVision and Compact Disc systems showed that a single lens with *one* aspheric surface can sometimes be sufficient (*fig. 6*). Such lenses cannot of course satisfy Abbe's sine condition exactly. Fortunately the discrepancies remain small provided that an 'equivalent' lens with spherical surfaces gives little coma and in addition the desired field radius in the image space is no larger than 50 to 100 μm. (The word 'equivalent' means that the lens thicknesses and the paraxial curvatures of both lenses are the same.)

contour function $z = \frac{1}{2} c y^2 + \sum_{i=2}^{5} c_i y^{2i}$

(z and y in mm)

	RAS_1	RAS_2
	$n = 1.5618$ at $\lambda = 632.8$ nm	
c	0.173 283 20	−0.107 723 09
c_2	0.000 236 301 390	0.002 440 229 5
c_3	−0.000 000 216 374	−0.000 207 306 8
c_4	−0.000 000 007 483	0.000 014 075 3
c_5	−0.000 000 002 299	−0.000 000 594 2

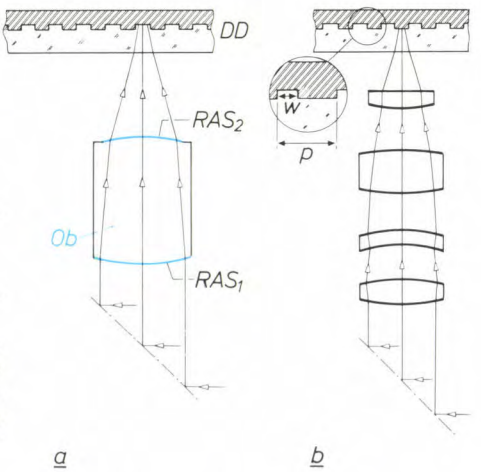

Fig. 5. *a*) For read-out of the information on an optical disc (*DD*), in vertical-radial section (shown in part), the microscope objective *Ob*, with the contour parameters given in the table, was designed as a bi-aspheric aplanat. $RAS_{1,2}$ aspheric refracting surfaces (*blue*), of diameter 7.32 mm and 4.14 mm respectively. *b*) A conventional objective for read-out, consisting of four spherical lenses. It is clear that adequate reduction of errors in the alignment of the eight refracting surfaces — to keep the image free of coma — is less simple than for the lens in (*a*). The width (*w*) of the pits is about 0.6 μm; the 'pitch' (*p*) is 1.7 μm.

Twenty years before a general theory for the calculation of aspheric surfaces was published, B. Schmidt's correction plate [13] appeared. This was the first really convincing application of an aspheric refracting surface (a surface of revolution, but not obtained from a conic section). This optical element corrected the spherical aberration of a concave spherical mirror. Originally applied in astronomical telescopes, it improves the resolution and the field angle. The device that we now call a Schmidt corrector is also used in projection television [14].

In the 17th and 18th centuries some theoretical knowledge already existed of the advantages that certain aspheric surfaces (paraboloids, etc., all of them surfaces of revolution obtained from conic sections) could offer in the correction of aberrations, but the manufacturing methods were so poor that in general no improve-

[10] See for example R. Bulirsch and J. Stoer, Darstellung von Funktionen in Rechenautomaten, in: R. Sauer and I. Szabó (eds), Mathematische Hilfsmittel des Ingenieurs, Teil III, Springer, Berlin 1968, pp. 352-446.

[11] See p. 380 of Born and Wolf in [9].

[12] See Philips Tech. Rev. **33**, 177-193, 1973 and Philips Tech. Rev. **40**, 149-180, 1982.

[13] See also H. Rinia and P. M. van Alphen, The manufacture of correction plates for Schmidt optical systems, Philips Tech. Rev. **9**, 349-356, 1947/48.

[14] H. Howden, Production of optical correction plates for projection television, Philips Tech. Rev. **39**, 15-18, 1980.

ment in the image quality could be obtained. There was one curious exception, however: the microscopes of Antoni van Leeuwenhoek (1632-1723). Recent measurements have shown that in one of the few surviving microscopes made by him the tiny lens is aspheric. We now know that the resolving power of about 1.3 μm — unusually good for its day — is due to its shape. The little lens looks like a small glass 'bead' about 1 mm thick. Just how Van Leeuwenhoek managed to make it is no longer known. It is almost certain that the lens was blown, and not ground. An empirically based theory (title photograph) has been put forward to explain how Van Leeuwenhoek performed the glassblowing [15].

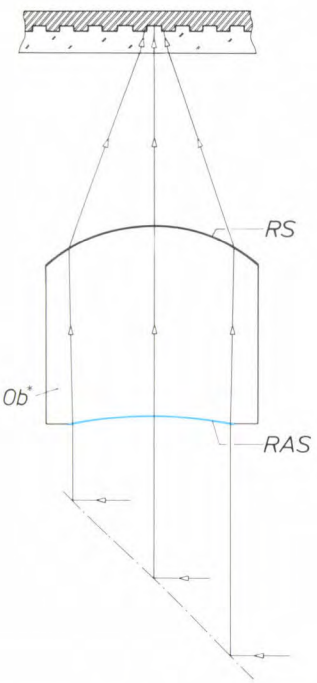

Fig. 6. The microscope objective *Ob** shown here has one aspheric refracting surface (*RAS*) and one spherical refracting surface (*RS*). Objectives of this design are also intended as read-out lenses for the LaserVision and Compact Disc systems; their useful field diameter is a little smaller than that of the bi-aspheric microscope objectives *Ob* (fig. 5*a*).

Designing for minimal wavefront errors in a large field

Photographic objectives, with their wide field of view, form an excellent example of optical systems whose design can be considerably improved by including aspheric lenses. This should be done not in the same way as described in the previous subsection, but by a direct optimization procedure. Such a procedure is based on general mathematical methods and allows a number of functions — for which wavefront deviations (= errors) have been chosen — to be minimized; this minimization is obtained by adapting the variables of the system. The solution obtained provides no information about the 'internals'; the relationship between the various image-forming properties and the individual refracting surfaces cannot be recovered, for example. Our earlier approach, making a design analysis that relates to certain optical concepts such as axial stigmatism and aplanatism, seems to be particularly difficult to carry out in the present case where a large field (or aperture angle) and high, although not completely diffraction-limited, image quality are required at the same time.

The method that we have followed for such designs of aspheric elements is a global minimization, a procedure that modifies the coefficients of a polynomial $z(y)$. This contour function, a series expansion of orthogonal polynomials in y, represents the unknown surface.

For the orthogonal polynomials in this global minimization we again decided to use Chebyshev polynomials; these are orthogonal in the interval $[-1, +1]$. By specifying a maximum optical diameter of a lens surface the distance from the axis of an arbitrary point on

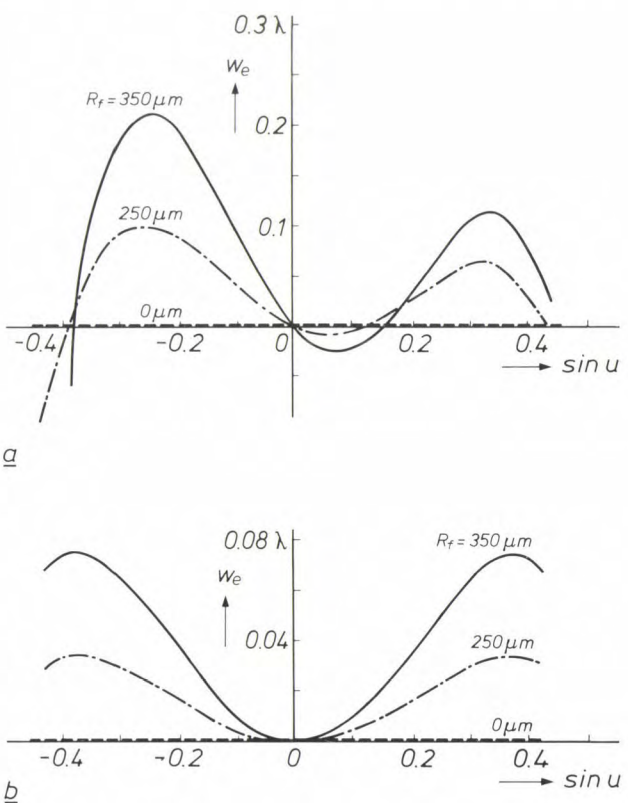

Fig. 7. The wavefront error w_e expressed in terms of the mean wavelength of the light to be used (λ, functioning as the unit of length), as a function of the sine of the angle of slope u of the incident ray. The field radius R_f in the image space is the parameter. These curves were produced as the result of computer calculations for a bi-aspheric thick lens with a numerical aperture of 0.40. *a*) The curves for the ray paths in the meridional plane (i.e. the plane that contains the optical axis and the assumed point source away from the axis). In this design the wavefront errors in the meridional plane remain acceptable up to a field radius of about 350 μm; beyond this value, where w_e is greater than $\frac{1}{4}\lambda$, the image quality can no longer be said to be that of a diffraction-limited element. *b*) The curves for the ray paths in the sagittal plane (i.e. the plane that contains the incident principal ray and is perpendicular to the meridional plane). In this plane the wavefront errors are clearly less serious. In both (*a*) and (*b*) the wavefront errors have been eliminated for the special case $R_f = 0$, i.e. with the source on the optical axis.

the lens surface can be expressed as a *fraction* of this diameter, and can thus be 'scaled' into the interval $[-1, +1]$. In the global minimization we use a matrix of derivatives that describe the effect of the different variables on the wavefront errors. To 'condition' this matrix appropriately in making a lens surface aspheric, i.e. to ensure that the dependence between the different rows of derivatives is as small as possible, it is highly advisable to choose a series expansion in terms of *orthogonal* polynomials. This is because it usually gives better and faster *convergence* of the optimization. Also, the numerical 'noise' of the aspheric surfaces thus found is less than if the method is based on a power-series expansion.

The coefficients of the various polynomials function together in a minimization algorithm as a part of the group of variables (as well as other variables, such as distances between surfaces and curvatures of surfaces). This algorithm minimizes a number of functions simultaneously, by finding a suitable set of values for the variables, the desired solution. Usually the minimized functions are the wavefront errors — corresponding to aberrations — of pencils of rays leaving points in the object plane.

The design calculations in such cases thus lead 'automatically' to a better appreciation of the residual wavefront errors as functions of various quantities that are characteristic of the desired optical system. As an example *fig. 7* shows three cases for which the angle of slope of an incident ray and the field radius in the image space are the characteristic optical quantities that are varied in the calculations. The wavefront errors that arise, which correspond to optical path differences below the 'Rayleigh limit' ($\frac{1}{4}\lambda$), indicate that the lens design is diffraction-limited. The undesirable effect of possible variations in construction parameters such as the thickness of the system or the alignment of refracting surfaces (in centring and slope) can also be rapidly calculated as extra wavefront errors (*fig. 8*). (Wavefront errors here mean residual local deviations with respect to a perfectly spherical wavefront.)

The optimization procedure suffers from an imperfection: the minimum or maximum it finds is *local*, dependent on the particular starting point selected. In theory many other minima can exist, some of these perhaps giving better image correction; this procedure cannot provide the extra information as to the relative nature or otherwise of a minimum in a simple way, however. Although the computer can give considerable help in optical design, we see here nevertheless that the experience of the user and the sound intuition of the designer are indispensable.

Fig. 9 shows an example of an optical system that was designed in the way just described. Four of the six lens surfaces are aspheric. This system can be used in projection television. A system with conventional lenses and the same degree of image correction would need seven or eight elements instead of three. This example shows clearly the great advantage of the introduction of aspheric surfaces into lenses: fewer elements giving simpler mounting and alignment, at lower cost.

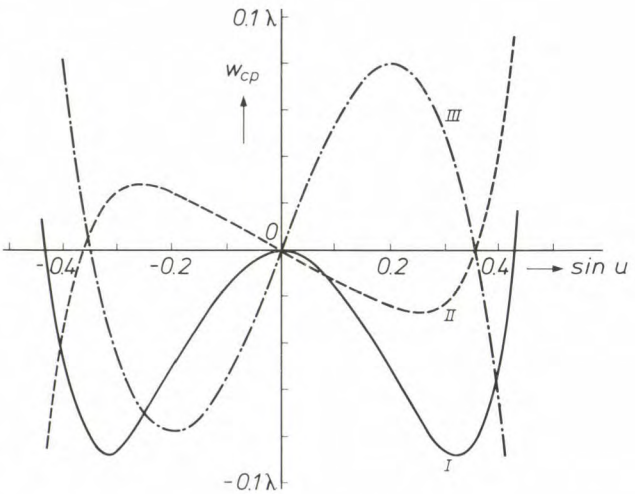

Fig. 8. Wavefront error w_{cp}, expressed in terms of the mean wavelength (λ) of the light to be used, as a function of the sine of the angle of slope u of the incident ray. These three curves apply for rays in the meridional plane, and were also calculated for evaluation of the design for the thick lens referred to in fig. 7. Curve *I*: the effect of increasing the lens thickness by 100 μm. Curve *II*: the effect of a 25-μm parallel displacement of the optical axis of the front surface of the lens with respect to the axis of the rear surface of the lens. Curve *III*: the effect of tilting the front surface of the lens. The change in angle is assumed to be 1 mrad with respect to the optical axis. These curves help to give an idea of the extent to which variations in the design parameters lead to an unacceptable total wavefront error, so that the design would no longer be of diffraction-limited quality. In the sagittal plane there is no wavefront error of any significance.

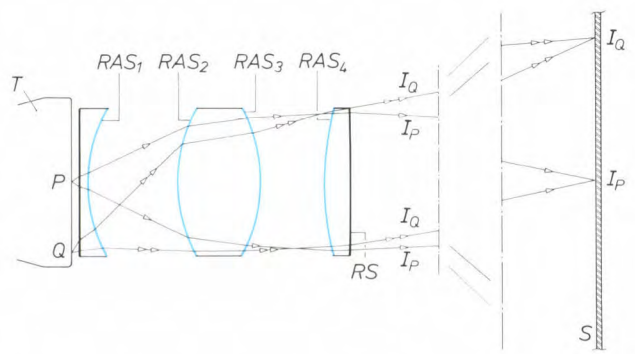

Fig. 9. An aspheric lens system designed for projection television. $RAS_{1,2,3,4}$ aspheric refracting surfaces. *RS* spherical refracting surface. *T* picture tube. *S* projection screen. The distance between the system and *S* is about 1.5 m. $I_{P,Q}$ image points of the object points *P* and *Q*. Magnification 10 times. The lens system was designed by the method based on a global minimization of the wavefront errors (see text).

[15] J. van Zuylen, The microscopes of Antoni van Leeuwenhoek, J. Microsc. **121**, 309-328, 1981. The authors would like to thank Dr Van Zuylen for making available the photograph used as the title illustration.

III. Fabrication, testing and application of highly accurate aspheric optical elements

J. Haisma, W. Mesman, J. M. Oomen and J. C. Wijn

Experimental fabrication with COLATH

Fig. 10 shows five lenses made with COLATH. Four of them are bi-aspherics, made from various materials, such as special glass with a high refractive index, quartz glass and a transparent plastic. The numerical aperture of two of the lenses is very high (0.85). The fifth lens, on the right in the photograph, is a plano-convex lens with a perfectly spherical surface. This was one of the first products made on COLATH, and was turned from a plastic (polymethyl methacrylate) with a diamond tool, mainly to establish the machining quality (the residual inaccuracy of form and surface roughness) that can be achieved in practice with the numerically controlled lathe [1].

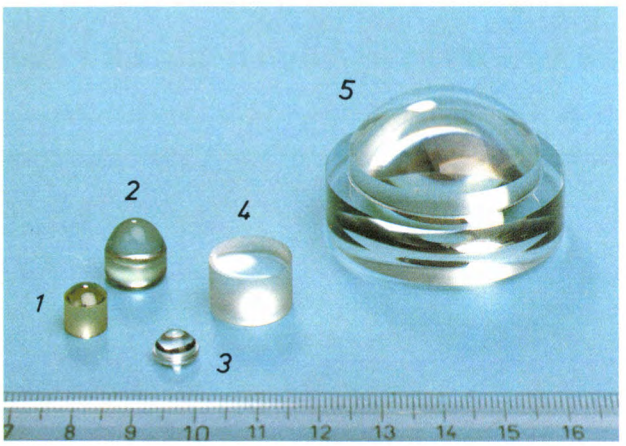

Fig. 10. Five examples of experimental manufacture of opto-mechanical parts on COLATH. Lens *1*: 'bi-aspheric' intended for a 'write' lens for master discs. The material is glass (SF59, with $n = 2.00097$ at $\lambda = 0.458$ μm). The numerical aperture is 0.85. Lens *2*: 'bi-aspheric' for the same application, numerical aperture again 0.85. The material is quartz glass (with $n = 1.4650$ at $\lambda = 0.458$ μm). The much lower refractive index, compared with that of lens *1*, is associated with a noticeably greater curvature of the upper surface. Lens *3*: 'bi-aspheric' intended as read-out lens for optical discs (see fig. 17). The material is the plastic PMMA (polymethyl methacrylate, with $n = 1.4908$ at $\lambda = 0.633$ μm). The numerical aperture is 0.43. Lens *4*: 'bi-aspheric', material quartz glass, numerical aperture 0.11. This lens is a component of a holographic interferometer (which will be used in checking the accuracy of form of aspheric moulds). Lens *5*: planoconvex lens with perfectly spherical surface. The material is PMMA. This lens was one of the first optical elements turned on COLATH (with a diamond-tipped tool). The ruler is calibrated in cm.

Dr Ir J. Haisma, W. Mesman, J. M. Oomen and J. C. Wijn are with Philips Research Laboratories, Eindhoven.

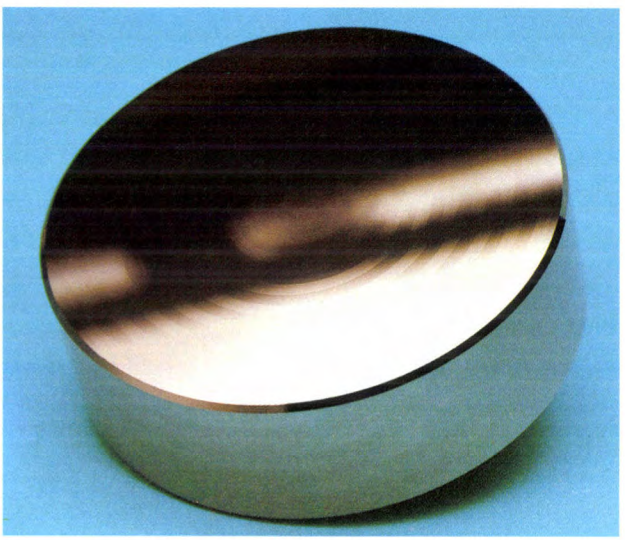

a

b

Fig. 11. *a*) Copper workpiece (diameter 80 mm, height 30 mm), turned on COLATH. The upper surface has been extremely accurately profiled in the machining. The radial section of the contour is a row of adjoining triangles, base 4 mm and height 1 μm. *b*) A stylus profile taken along a radius. The residual asperities in the sides of the triangles are smaller than about 50 nm.

Fig. 11 gives another example of the many possibilities that COLATH offers for turning complicated and yet extremely accurate profiles. In the upper surface of the copper workpiece a periodic wave pattern of extremely 'flat' triangles has been turned. The height of the triangles is only 1 μm, and the base is 4 mm (so that the apex angle is approximately three minutes of arc less than 180°). The raised sides show deviations (asperities) that are smaller than about 0.05 μm; this appears from measurements of the contour (fig. 11*b*). The cutting tools for such accurate work have to meet a very tight specification. In the case shown the tool had a diamond tip ground to a radius with a departure of less than 0.1 μm from a perfectly circular cutting edge (radius 1 mm). The maximum tolerance of 0.1 μm applies for the full angle of roll.

In the meantime a great deal of experience has been gained with COLATH. From this it appears that the accuracy of form attainable in turning is limited by the rounding-off errors in the numerical-

control system and by our deliberate restriction to a series of straight-line sections, as a linear approximation to the ideal contours required. (This approximation can be made very accurately, within a 'tolerance zone' of width only 0.01 μm.) Fundamentally better approximations than the linear interpolation are possible, and the control system is now being modified to suit these approximations. Mechanical limitations, such as imperfections in the bearings and inertia in servomotors and control valves appear to contribute little in the present situation to the dimensional imperfections still existing in the products.

well to the deviations in the straight lines of the interference fringes.

The small aspheric surface was also examined with the stylus, and this gave the third series of measurements (T_2 in fig. 12). There was little correlation between this series of measurements and the interferogram, no doubt because of the relative flatness of this particular contour.

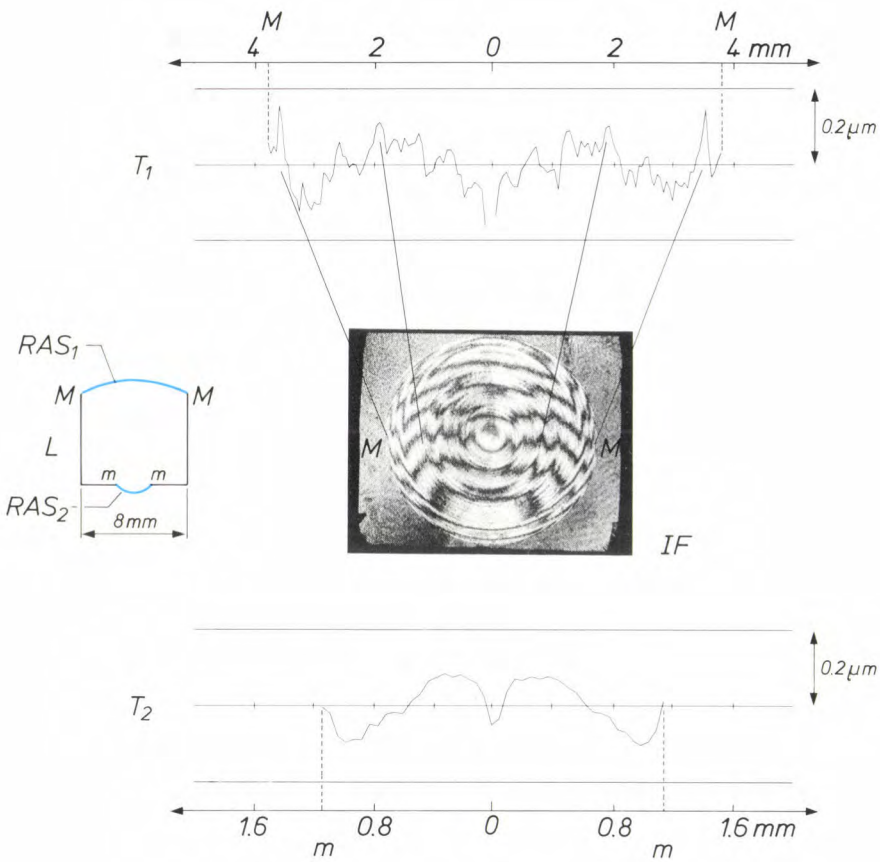

Fig. 12. Three test measurements made on a bi-aspheric lens *L* turned on COLATH. The lens, shown in longitudinal section (see also fig. 10, lens No. *1*), has a numerical aperture of 0.85. *IF* interferogram of the lens. The deviations in the straight lines are mainly determined by the large aspheric surface (RAS_1). T_1 stylus profile, taken approximately along the 'centre-line' *M-M* of RAS_1. There is good agreement between the two measurements. T_2 stylus profile along the line *m-m* of the lower surface of the lens, the small aspheric surface (RAS_2). The size of the tolerance range indicated (0.2 μm) helps to provide an impression of the residual deviations in form, in both RAS_1 and RAS_2. Details of the methods of measurement are given in the section entitled 'Quality control'.

Three test measurements of the surface quality obtained for a bi-aspheric lens are illustrated in *fig. 12*. The good thing about this test is that two series of measurements can be made, one mechanically with a stylus and the other by an optical interference method. A comparison shows that the deviations of the large aspheric surface measured with the stylus correspond

The curve of the stylus readings along the complete contour gives an impression of the precision of form attainable with COLATH. The measured results indicate that maximum deviations in form of 0.2 μm or even less can be considered realistic. We shall come back to the special nature of the bi-aspheric lens of fig. 12 at the end of the article.

Quality of finish and optical aberrations

The quality of a mirror or lens is essentially determined by only two factors: design and manufacture. The influence of the design chosen and its details on the aberrations has been discussed in part II of this article — and here we can take it that the computations, with their many internal checks for consistency, etc., can provide complete and sufficiently accurate manufacturing specifications.

In the manufacturing process, which follows the specifications closely, of course, it is found that the surfaces produced can suffer from three kinds of errors, which can impair the image. The first is the 'slow form error'. (This is usually classified as 'the' form error.) The form or contour produced does not correspond to the specified shape, when considered over a relatively large distance. The imperfections that this may cause in the image are essentially like the aberrations that were treated in part II of this article.

The second kind of errors are called 'fast form errors'. These are errors of form with a 'noise-like' nature, which relate to the roughness of the surface and represent deviations from the specified shape that vary over relatively small distances. The surface texture is then too rough locally, scattering some of the light passing through the element. The result is that the image intensity is reduced, at the very least.

The third kind of error, probably best called the 'purely periodic form error', consists of a regular shallow track over the entire finished surface. This imperfection arises from turning with a tool, or even — though then much less serious — from using the grinding spindle. Here again the main effect is a loss of intensity, due to scattering. (In COLATH it soon proved possible to reduce the depth of machining marks on the workpieces, with a pitch of 5 to 10 μm, to about 20 nm.)

Every variation in the shape of the lens or mirror corresponds to a wavefront error. If the form error is h, the wavefront error for a mirror is $2h$ and for a lens it is h times the difference in refractive indices. For refraction from air (with $n = 1$) to glass (with $n = 1.5$, say) it would therefore be $0.5h$. It is usual to indicate the magnitude of the wavefront errors in terms of the standard deviation of the wavefront from a perfectly spherical wavefront at the same position. The elementary image, even of a perfect point source, consists of a central diffraction disc with a number of rings around it, as noted earlier in part II.

The larger the wavefront errors, the more energy disappears from the centre of the diffraction pattern to be lost in the surroundings. This scattering of the light would easily make it impossible to use the modern optical discs. In discs for LaserVision and Compact Disc the optical read-out of the stored information requires an image spot of diameter no more than about 1 μm and with no significant ring structure outside that diameter.

The disappearance of energy from the centre of the diffraction pattern comes about in general in three ways corresponding to the three kinds of form error. With the slow form errors light appears mainly in a narrow zone around the central bright disc. This light

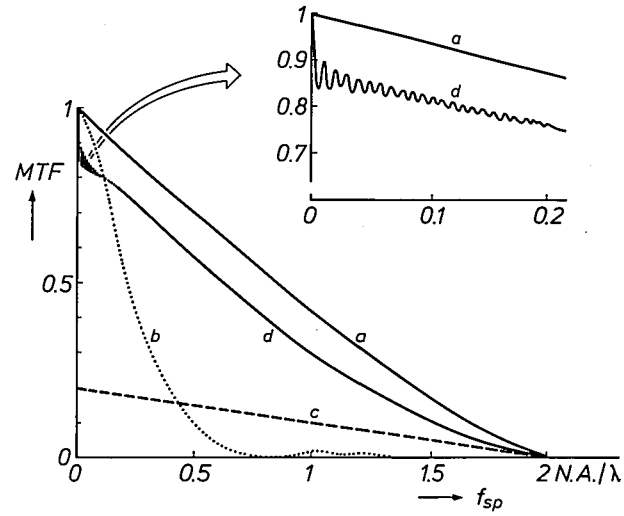

Fig. 13. Calculated curves for the modulation transfer function *MTF* of a lens, as a function of f_{sp}, the spatial frequency (expressed in terms of N.A./λ as unit). The maximum resolving power of the lens is equal to 2 N.A./λ, the spatial frequency at which the *MTF* is exactly zero. *a*) Curve for the case where the lens is of diffraction-limited quality. *b*) Curve associated with a slow form error. *c*) Curve associated with surface roughness. *d*) Curve associated with machining marks. The standard deviations of the wavefront are 0 (*a*), 0.2 λ (*b*), 0.2 λ (*c*) and 0.06 λ (*d*). The depth assumed for the machining marks is about ten times the value that can be achieved in practice[1]. The variation of curve (*b*) would be typical for camera optics, for example (see fig. 1).

reduces the contrast between the dark and bright rings of the diffraction pattern in this zone. The 'Seidel' aberrations (part II) are connected with this structure of the image.

In the case of fast form errors there is a fairly uniform background illumination, by a broad cone of scattered light.

In the case of purely periodic form errors there is a grating effect; much of the light scattered in this way can become concentrated in a single fairly broad ring of diameter many times larger than the central bright disc.

The three kinds of form error can have a very different effect on the behaviour of a lens. This can be made clear most easily by considering how they change the spatial frequency response. *Fig. 13* gives a number of calculated response curves[16]; the curve for an error-free lens is at the top (*a*). In this curve the

response loss has increased to 50% — a given modulation depth will then be exactly halved in the image — when the spatial frequency has risen to about half the cut-off frequency. (The cut-off frequency is the highest of the spatial frequencies that the lens passes as an 'optical filter'; this frequency limit corresponds to the maximum resolving power of the lens.) The curves *b*, *c* and *d* show the influence of the assumed standard deviation in the wavefront, of magnitude 0.2 λ due to slow form error (curve *b*), 0.2 λ due to roughness (curve *c*) and 0.06 λ due to machining marks (curve *d*). The slow form error, which also gives rise to a lower-order aberration, considerably reduces the spatial frequency at which the response loss is equal to 50%. This reduction thus indicates the introduction of a marked limitation of the bandwidth in the spatial-frequency domain. The roughness does not affect the shape of the curve, but causes a fixed relative reduction in the response, independent of the spatial frequency. In this example the reduction is severe; a lens with such a rough surface would be rather like frosted glass. Since in practice an optical system will always have several lenses, the designer will want to keep the total effect of the surface roughness to a tenth or less of that in the example of curve *c*; it will therefore be desirable to achieve a standard deviation of the wavefront not exceeding 0.01 λ. Such a value indicates that maximum tolerances for surface roughness of 10 to 20 nm should be included in the specification for quality of finish. The fast form error sometimes has much more serious consequences than the slow form error. In various image-forming systems for X-ray diagnostics, for example, a cone of scattered light would be disastrous; the peak-to-valley height for the surface roughness here should be well below 10 nm. The slow form error in X-ray diagnostics may in general be much larger [1]. Machining marks, rather like surface roughness, reduce the response throughout the spectrum. The shape of curve *d* is therefore rather like that of curve *c*. There is one great difference, however: the periodic variation in the response, due to the grating action of the machining marks. In the example shown, the machining or tool marks form a groove pattern of 200 turns with a pitch of 20 μm and peak-to-valley height of 200 nm (this is a few tens of times greater than the peak-to-valley height that can be achieved). In this case the periodic variation is limited to a range of very low spatial frequencies (see the enlarged portion of the curves *d* and *a* in fig. 13. If the peak-to-valley height is reduced curve *d* will rapidly approach curve *a*. In practice, when the value has been reduced to 20 nm, measurement of the response curve shows that it is no longer affected by the machining marks.

Setting up and alignment

In the manufacture of an aspheric lens on COLATH one of the lens surfaces is completely finished first before starting the other. This requires an accurate reversal and alignment of the lens with respect to the main spindle of the lathe, between the two machining operations. Each of the two refracting surfaces has its own optical axis. If the lens is to function satisfactorily later, these two optical axes must be correctly aligned. If great care is taken in setting up the lens and reversing it, the two optical axes can be brought to within 1 μm of the axis of the main spindle, with the front face of the lens tilted by no more than 0.2 mrad. The optical designer must also pay due attention here to one of the mechanical requirements. His design must provide sufficient 'chuck length' along the side of the lens, e.g. 3 mm for lenses whose thickness and diameter are about 8 mm.

Quality control

The manufacture of aspheric lenses and mirrors proceeds in parallel with two kinds of test measurements. To begin with, regular checks are made during the machining to see if any errors have occurred that require intervention. COLATH has a manual control panel, so that the technician can make such corrections with a direct view of the workpiece. The completed workpiece is subjected to an acceptance test, a kind of functional check to find out whether it will function as desired. This second kind of test is often deferred until a complete unit has been assembled from a number of optical elements. With regard to the optical characteristics, the function of this unit in its system should preferably be such that it is easily checked. To achieve the highest accuracy, it is often necessary to go through the full pattern of operations of machining, testing, re-machining, testing again, and so on.

The acceptance test

The best quantitative assessment of an aspheric lens system, say, to find out whether it will give the predicted performance is still obtained from a detailed knowledge of the resolving power. We therefore start by measuring the spatial frequency response of the system [16]. The extent to which the system causes loss of modulation depth is then determined, dependent on the spatial frequencies present in the image of a standard test pattern (*fig. 14a*). If the image is ob-

[16] For a discussion of the spatial frequency response or 'transmission factor' see p. 480 of Born & Wolf in [9], and chapter 9 of E. B. Brown, Modern optics, Reinhold, New York 1965. The authors would like to thank Dr J. J. M. Braat for making the calculations.

tained in the form of a photograph — an X-ray photograph (radiograph) is a good example [1] — the reduced modulation depth appears as a loss of contrast. These losses therefore also depend on the spatial frequency. This type of functional test makes it possible to find out quickly the extent to which the completed system will function differently from a fault-free version. The test in this form gives very little indication about the exact location of any faults in the system, however.

Another functional test, which corresponds rather more closely to the use of a completed system and also permits the place of origin of an image error to be found more readily, is the production of an interferogram by means of a Twyman-Green interferometer (fig. 14*b*) [17]. In the 'ideal' situation the interferogram consists of a number of parallel straight fringes. Local variations in the optical pathlength show up as deviations from parallelism and straightness, at the corresponding place in the interferogram. The sensitivity of this interferometric test is high, especially for slow form errors; variations of a few per cent of the mean wavelength of the visible part of the spectrum can be detected.

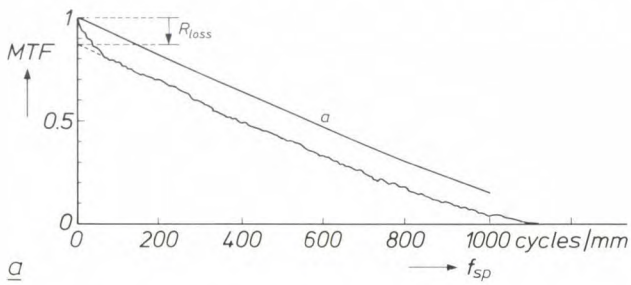

a

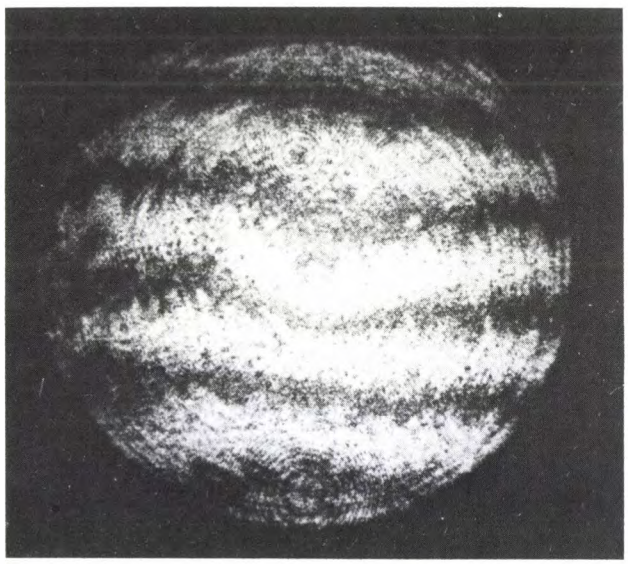

b

Fig. 14. The acceptance test of a completed aspheric lens system comprises the determination of its spatial frequency response (*MTF*, see also fig. 13) and making a Twyman-Green interferogram. *a*) Example of a measurement of *MTF* as a function of the spatial frequency (in cycles/mm; one cycle corresponds to one line pair on a test pattern). The bi-aspheric lens under test, with N.A. equal to 0.40, was uncoated; the reflection loss (R_{loss}) shifted the experimental curve to values about 0.15 lower than the theoretical maximum values (curve *a*). This measurement shows that the quality of the lens can be taken as diffraction-limited. *b*) A Twyman-Green interferogram made for the same lens. The shape of the dark fringes indicates deviations in optical pathlengths that must be smaller than about 0.1 μm, which agrees with the lens data given in (*a*). The concentric rings visible in the interferogram are related to the machining process and the surface quality; they are not associated with the slow form error.

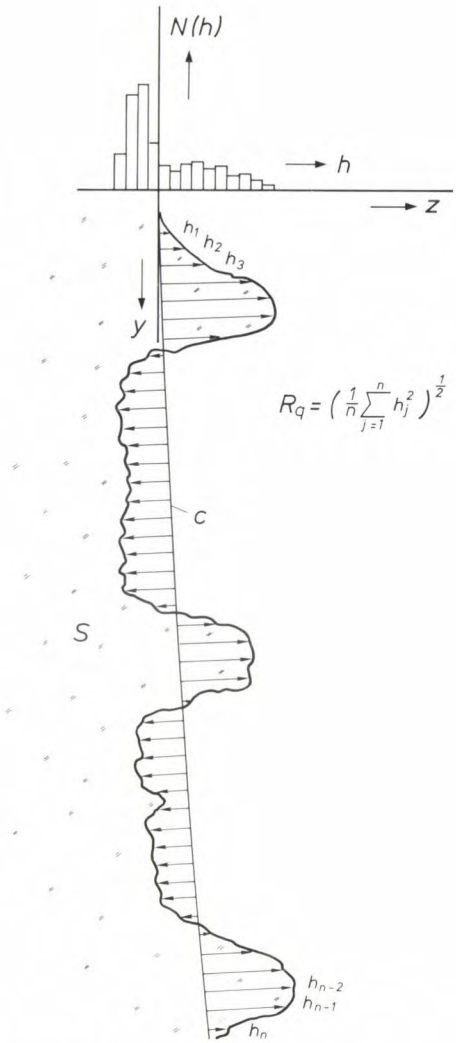

Fig. 15. Definition of surface roughness by means of a standard deviation R_q. The surface of an optical element S would follow the ideal contour $C(y,z)$ if it was perfectly smooth. The asperities still present can cause light scattering, and this effect can be used to calculate an R_q-value for the surface. The histogram $N(h)$ shown is an approximation to the 'amplitude-density function' of the surface. Statistical quantities characteristic of the topography of a finished surface can also be derived from this function [21].

Checking the machining

As we said earlier, it is necessary to pay close attention to three kinds of errors: contour errors, surface roughness and machining marks. The first kind of error, departure from the desired shape for a lens surface, for example, we determine with extremely sen-

sitive mechanical styluses [18]. The instrument we use, which gives differential measurements by means of an optical method, has a standard deviation of less than 5 nm in its reproducibility, even though the styluses are mechanical. The absolute inaccuracy of the instrument is about 0.1 μm. This degree of accuracy of form is no exaggerated luxury for aspheric elements; the correct performance of the completed lens systems for example is indeed closely dependent on it.

The 'optical smoothness' obtained from the machining can be checked by calculating the residual surface roughness from measurements of light scattering at the surface [19]. In principle, the light-scattering measurements can also be used to find the depth of the grooves caused by turning or grinding (the periodic form error).

The method developed in our laboratories for such measurements [20] is especially suitable for strongly curved surfaces (radius of curvature from 50 to 1 mm), as found fairly often in aspheric lens systems. The amplitude of surface roughness that can be measured in this way can amount to a fraction of 1 nm to several tens of nm.

The test consists in the measurement of the angular distribution of monochromatic light scattered by little pieces of the finished surface. The *intensity* of the scattered light shows a correlation with the 'amplitude' of the roughness, while the *direction*, i.e. the scattering angle, provides information about the spatial frequency that is characteristic of a particular imperfection (roughness) of the surface.

As with wavefront errors, it is usual to express the amplitude of the roughness numerically in terms of standard deviations. The definition of the standard deviation is in principle based on a contour of the 'actual' surface and a smooth 'mean' contour chosen at the same place (*fig. 15*). The values for the standard deviations only apply within a certain band of spatial frequencies. The limits of this frequency band are characteristic of the optical test method, rather than the surface under test. (Through the choice of measurement method a 'functional filtering' of the structure patterns present in the surface is fixed [21].)

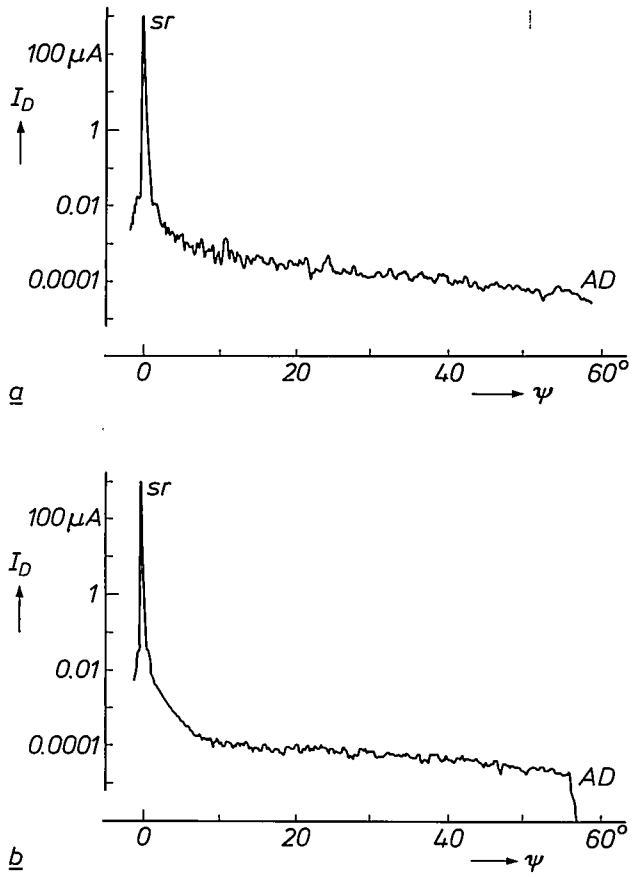

Fig. 16. Optical check of residual surface roughness after grinding for an element of quartz glass finished on COLATH. The two curves are angular-distribution spectra (*AD*) of monochromatic light that has been scattered by the surface, which was concave. The intensity of the scattered light, measured with a photodiode and expressed in terms of the photocurrent I_D, is plotted against the scattering angle ψ (measured with respect to the direction of the 'ordinary' specular reflection, the peak *sr*). The jagged peaks in the two spectra are completely reproducible (the 'speckles' in the distributed light, not noise). *a*) This measurement was made in the direction perpendicular to the direction of grinding. The spectrum is formed from two random patterns of irregularities, a one-dimensional pattern and a two-dimensional pattern. *b*) This measurement, which was made in the direction parallel to the direction of grinding, gave a spectrum of lower intensity than (*a*), since the one-dimensional random pattern in this direction of measurement cannot contribute to the scattering. The standard deviations $R_q^{(1)}$ and $R_q^{(2)}$ calculated from the measurements (*a*) and *b*) are given in Table I.

In the scattering measurements the alignment of the surface under test was again found to present difficult problems. These have been solved through the use of an optical method [20], with no need for contact with the surface.

Fig. 16 shows two examples of measured angular distributions of light scattered by a surface of quartz glass finished on COLATH. The surface roughness calculated from these measurements can be characterized by means of two standard deviations ($R_q^{(1)}$ and $R_q^{(2)}$, *Table I*). The residual roughness of the ground surface contains both a random one-dimensional pattern of irregularities — associated with the direction of grinding — and a two-dimensional pattern. If a check is made *parallel* to the direction of grinding the one-dimensional roughness pattern does not show up,

[17] See for example p. 414 of the book by E. B. Brown, in [16], and also p. 318 of the book by L. C. Martin in [7].

[18] J. G. Dil, W. Mesman and J. C. Driessen, High-precision measurement of aspheric surfaces, Proc. SPIE 235, 85-90, 1980. See also J. G. Dil, P. F. Greve and W. Mesman, Appl. Opt. 17, 553-557, 1978.

[19] E. L. Church, H. A. Jenkinson and J. M. Zavada, Measurement of the finish of diamond-turned metal surfaces by differential light scattering, Opt. Eng. 16, 360-374, 1977. See also T. V. Vorburger and E. C. Teague, Optical techniques for on-line measurement of surface topography, Precision Eng. 3, 61-83, 1981.

[20] The authors would particularly like to thank Dr Ir P. P. J. van Engelen, of Philips Research Laboratories, who investigated the method of measurement, put it into practical operation and performed the measurements and calculations quoted.

[21] T. R. Thomas, Characterization of surface roughness, Precision Eng. 3, 97-104, 1981.

Table I. Results of light-scattering measurements (an example is given in fig. 16) carried out to determine the residual roughness of a number of material surfaces obtained by optical grinding or turning. The spectrometer [20] used for this permits the quantities $R_q^{(1)}$ and $R_q^{(2)}$ to be determined, both standard deviations of extremely small random variations in shape (measured with respect to a smooth 'mean' surface, see fig. 15); $R_q^{(1)}$ characterizes any possible one-dimensional pattern of noisy roughness, and $R_q^{(2)}$ characterizes the two-dimensional pattern. The values measured only correspond to the variations in shape whose 'wavelength' lies between 1.0 and 60 μm.
n.d. not determined. *r* radius of curvature in mm.

Material	Surface	Roughness (nm)		Treatment
		$R_q^{(1)}$	$R_q^{(2)}$	
Quartz glass	concave, spherical $r = 10.0$	0.5	1.4	optically ground on COLATH fig. 16*a*,*b*
Quartz glass	concave, spherical $r = 7.0$	0 [b]	1.6	conventional grinding and polishing [a]
Steel	concave, aspheric $r \approx 6.7$	4.4	4.4	optically ground on COLATH
Copper	concave, spherical $r = 6.7$	n.d.	4.4	machined with diamond-tipped tool on COLATH

[a] by hand
[b] conventional grinding with the spherical tool (or 'cup') does not produce a one-dimensional pattern

and the resulting angular distribution of the scattered light is due only to the two-dimensional pattern.

The entire angular distribution spectrum in fig. 16 forms a kind of 'background', with completely reproducible asperities (the 'speckles' in the light distribution). Superimposed on this background is the peak of the specular reflected ray, at zero scattering angle (by definition). The 'ordinary' specular reflection is in fact only an unwanted effect in the performance of this test.

Only some of the spatial frequencies present in the roughness patterns determine the measured result. The lowest of these contributing frequencies is related to the lowest scattering angle that will give scattered light unaffected by reflected light; the highest causes scattered light at grazing incidence along the surface under test. In the tests the highest spatial frequency was 10^6 m^{-1}, the lowest about 1.7×10^4 m^{-1} (corresponding to 'wavelengths' of 1 μm and 60 μm).

As can also be seen from the results collected in Table I, the method used for measuring surface roughness offers a relatively simple and rapid comparison.

Applications of bi-aspheric lenses

Bi-aspheric objectives intended for use in the players for the LaserVision and Compact Disc systems [12] have been made for some time. Such lenses also seem an attractive proposition for read-out in the Philips DOR system (Digital Optical Recording). In addition to these applications, which are more associated with quantity production, work has also been done on an extremely advanced bi-aspheric, with an N.A. of 0.85, suitable for use as the 'write' lens for the equipment in which a master disc can be made (for LaserVision or Compact Disc). In both kinds of application the quality required is so high that it is limited only by diffraction at the lens edges. As we have already seen (fig. 10), it has in the meantime become possible to make such lenses of diffraction-limited quality.

At a rather later stage a third kind of application of bi-aspheric elements will probably arise from the possibility of using an optimized number of aspheric surfaces in zoom lenses. This would reduce the number of components required in a zoom lens by more than a half, yet for the same optical quality, as calculations have shown [22].

Read-out in LaserVision

The information on an optical disc for the LaserVision system is stored as a long spiral track of pits. The smallest distance between two successive turns of the track (the pitch) is 1.7 μm. The read-out of the information — the detection of the length of the pits and their repetition frequencies — is accomplished by 'scanning' with a spot of light that follows the track accurately [12]. The detector signal, the resulting modulation in the reflected light, must not be exposed to 'crosstalk' from pits in the adjacent turns. The light spot is therefore extremely small: the '50% diameter' is 0.9 μm. It is produced by using a helium-neon laser

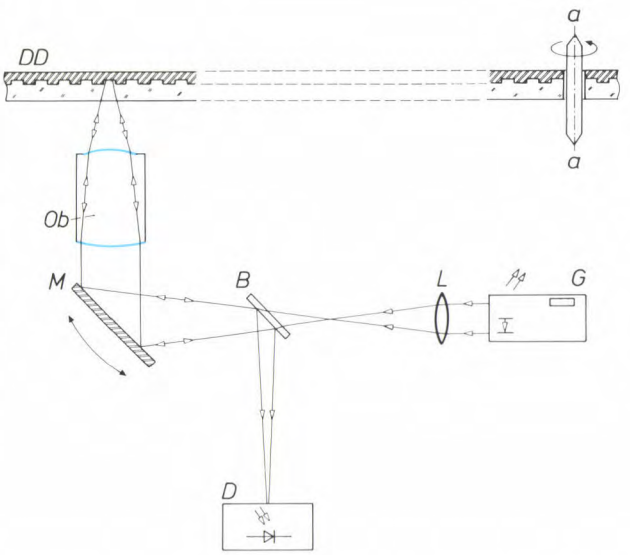

Fig. 17. The 'bi-aspheric' *Ob* (see also fig. 5*a*) can be used as a read-out lens in a player for optical discs. *DD* optical disc, rotating about the axis *a-a*. *G* laser light source. *L* optics for beam conditioning. *B* beam-splitter. *D* light-detector circuit. *M* tilting mirror, connected to a servosystem that keeps the light spot centred on the track [12].

as the light source (λ = 632.8 nm) with a bi-aspheric of diffraction-limited quality to form the image. (In the other system, Compact Disc, an AlGaAs laser is used, with wavelength λ = 820 nm.) The N.A. of the bi-aspheric must be at least 0.40 to be certain of obtaining an image spot with a dimension as small as 0.9 μm.

The introduction of a bi-aspheric here offers the well-known advantage (fig. 5, part II) of reducing the number of optical elements from four (with spherical lenses) to one (the bi-aspheric lens). In quantity production the accurate alignment of all the refracting surfaces for four lenses would certainly have been a difficult and expensive operation. A second advantage is the free space between the lens and the disc. This is larger than previously, so that the position of the image can be further away with the new lens.

The rotation of the optical disc is bound to have some slight eccentricity [12]. The bi-aspheric must therefore produce a reasonably constant image over a field diameter of about 500 μm. The spot of light will then scan the pits properly in spite of the small oscillation of the centre of the disc during rotation.

For completeness, *fig. 17* shows how the bi-aspheric is used as a component in the read-out system of a disc player [12]. The contour details for this bi-aspheric have already been given in fig. 5. An acceptance test for this lens has also been described earlier (fig. 14*a*). Comparison with the calculated curve, whose shape corresponds well to that of the measured curve, shows that there is a constant loss of modulation depth. This loss can be ascribed to reflection at the lens surfaces (which have no antireflection coating). From the interferogram of fig. 14*b* it can be shown that the slow form error is less than 0.1 μm for this lens.

The write lens for master discs

When information is written on to a master disc, for either LaserVision or Compact Disc, the resolution must be so high that an N.A. of 0.85 is necessary. Fortunately the diameter of the useful field does not have to be greater than 5 μm. The fabrication of such an unusual lens on COLATH, and the tests required, although not simple, can now be considered part of the available expertise (fig. 12). The tolerances alone provide a proof of optomechanical ability: about 3 μm for the lens thickness, about 1.5 μm for decentring and less than 0.2 mrad for tilt.

We should not conclude the article without the comment that at Philips, and elsewhere, the production of aspherics is now well past the initial phase. The way to a new kind of optical industry is open.

[22] E. A. Hugues, J.-M. Bacchus and J. Haisma, U.S. Patent No. 4416518.

Summary. Aspheric surfaces in optical systems can improve image correction, increase the numerical aperture and reduce the number of refracting surfaces required. The design work includes the calculation of aplanatic systems (N.A. 0.4 and higher, field diameter 100-500 μm) and designing for minimum wavefront errors and large field (photographic objectives). Bi-aspheric objectives have been calculated for read-out in LaserVision and Compact Disc, and also for writing the information on to the master discs for both systems. An aspheric system for projection television and a zoom lens have also been designed. The fabrication was 'optomechanical': the surfaces were turned and ground to an optical finish on COLATH. The optical elements produced are of diffraction-limited quality. The description of the fabrication includes quality of finish and optical aberrations, the alignment of the refracting surfaces and quality control (checking the machining and acceptance tests). Inaccuracies of form of 0.2 μm and surface-roughness values of less than 5 nm (standard deviation) have been achieved for small areas. Deterioration in quality due to machining marks is negligible. Measurement methods included interferometry (Twyman and Green), scattering measurements, stylus measurements and the determination of the spatial frequency response (MTF).

A piezoelectric microbalance

A microbalance is an instrument that can be used to measure very small changes of mass (e.g. less than 1 μg). Such changes might for example occur when a tiny piece of plastic film absorbs water. A microbalance can then be used to determine the effect of temperature or the relative humidity of the air on the absorption. The microbalances commonly used, however, are fragile instruments [1]. They do not stand up well to shocks and their sensitivity is affected by vibrations or by the ambient gas pressure. Measurements cannot be made at high relative humidity or temperature. We have now developed an experimental microbalance [2] that is simple in construction, insensitive to gas pressure and gas composition, performs well at high relative humidity and temperature and can be used for both relative and absolute measurements. Our microbalance determines the mass of an object from the resonant frequency of a vibrating quartz-glass filament from which the object is suspended. At a load of 3 mg the microbalance has a resolution of 10 ng. After first describing the construction of our balance we shall briefly outline the theoretical background and indicate how the mass of the object is calculated from the measurements. In conclusion we discuss the general features of the microbalance and give an example of a measurement.

As shown in the diagram of *fig. 1*, the balance consists of a quartz-glass filament bent in the shape of a hairpin and fused to two small quartz-glass plates. The tip of the hairpin is bent down to obtain a well-defined point of suspension. The load is attached to the microbalance by a slack loop of thin gold wire linked with the filament. The wire and plates were coated with about 50 nm of chromium by sputtering. One side of the plates was also coated with NiCr and with nickel that could be 'tinned', and the plates were then soldered to two piezoelectric flexure elements, taken from a record-player pick-up. These elements in turn were soldered to a metal support. (Since the quartz-glass filament and the plates have a conducting coating of chromium, any build-up of electrostatic charge is removed through the earthed support.) When a sinusoidal voltage is applied to one of the two flexure elements, the quartz-glass filament with the load suspended from it is set in vibration. The amplitude of the vibration is sensed by the other element. When the r.m.s. value of the voltage generated in the sensing element is measured as a function of the frequency of the voltage applied to the excitation element, a response curve is found as shown in *fig. 2*, curve *1*. The amplitude of the excitation voltage must be constant at all frequencies. Higher excitation voltages cause bouncing of the load and distortion of the response curve, as shown by curve *2* in fig. 2. The mass of the load can be calculated from the observed response curve.

The relation between the resonant frequency and the mass can be derived from the theory of a damped spring-mass system [3]. Suppose that a periodically varying force $F = F_0 \cos \omega t$ acts on an object of mass m, and that the object is subjected to an elastic force $-kx$ and a damping force $-\beta \mathrm{d}x/\mathrm{d}t$. Here x is the deflection of m from the equilibrium position, k the spring constant of the deflected quartz-glass filament and β the damping constant. The equation of motion is then

$$m \frac{\mathrm{d}^2x}{\mathrm{d}t^2} = F_0 \cos \omega t - \beta \frac{\mathrm{d}x}{\mathrm{d}t} - kx.$$

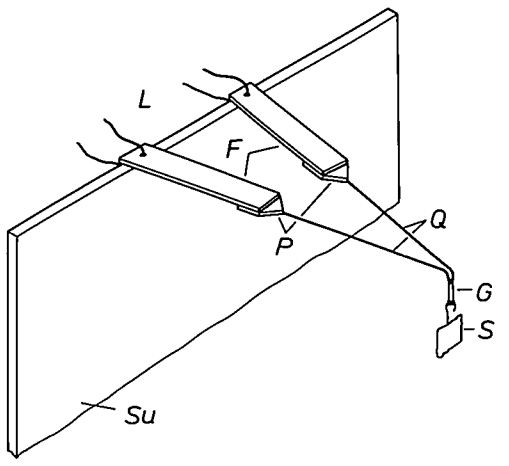

Fig. 1. Diagram of the microbalance. *Q* quartz-glass filament (diameter 140 μm, length about 50 mm), which is bent to the shape of a hairpin (angle about 10°). *P* quartz-glass plates (dimensions 2 mm × 1.5 mm × 0.3 mm). *F* piezoelectric flexure elements. *L* leads. *Su* support. *S* specimen to be weighed. *G* gold wire loop.

If we *define* γ and ω_0 such that $2\gamma = \beta/m$ and $\omega_0^2 = k/m$, the equation of motion becomes

$$\frac{d^2x}{dt^2} + 2\gamma \frac{dx}{dt} + \omega_0^2 x = \frac{F_0}{m} \cos \omega t.$$

Solution of this differential equation reveals that the maximum value of x (the amplitude A) of the vibration of the load is given by

$$A = \frac{F_0/m}{\sqrt{(\omega^2 - \omega_0^2)^2 + 4\gamma^2\omega^2}}.$$

This expression can be normalized by dividing by the amplitude A_M associated with the (otherwise arbitrary) frequency ω_M. We then find

$$A = A_M \sqrt{\frac{(\omega_M^2 - \omega_0^2)^2 + 4\gamma^2\omega_M^2}{(\omega^2 - \omega_0^2)^2 + 4\gamma^2\omega^2}}. \quad (1)$$

We now have an equation with only two unknowns: γ and the *undamped* resonant frequency ω_0. With a number of measured points (ω_i, A_i) it is now possible to determine γ and ω_0 by a numerical method.

If we assume that the mass m is composed of the mass m_s of the load and an effective mass m_e of the quartz-glass filament, we can now calculate the required mass m_s from our knowledge of ω_0 and an adapted form of the definition $\omega_0^2 = k/m$:

$$\omega_0 = \sqrt{\frac{k}{m_s + m_e}}. \quad (2)$$

The values of k and m_e can be found from at least two measurements with calibrated weights.

The determination of ω_0 and m_s is completely automatic. A microcomputer controls a frequency-programmable voltage source (a frequency synthesizer) and a voltmeter. After the load has been attached to the microbalance, the frequencies at which the measurements are to be performed are derived. This is done by the computer, with the limits of the frequency interval within which the measurements are to be made and the number of steps in which the interval is to be covered as its input data. The amplitude of the vibrating quartz-glass filament is measured at all the frequencies established in this way (perhaps 20). Around the frequency at which the largest amplitude so far has been measured, another small interval is covered in smaller frequency steps. The point with the largest measured amplitude is finally used as (ω_M,A_M) for normalizing the other measured points. With eq. (1) the values of γ and ω_0 are now found by means of the least-squares method. Since k and m_e are known from the calibration, the unknown mass m_s of the load can be calculated from eq. (2).

To evaluate the resolution of the microbalance a load of mass 3 mg was applied to the filament and measurements were taken at 20-minute intervals for 10 hours. The mass values determined from these measurements had a spread of less than 10 ng. With heavier loads, and hence lower resonant frequencies, the resolution decreases to about 100 ng at a maximum load of 8 mg.

It can be seen from eq. (2) that the measurements are not affected by the ambient gas pressure (which only affects γ). We see, however, that ω_0 does depend on k and consequently on temperature, since Young's modulus and the length of the quartz-glass filament are a function of temperature. This explains, for example, the change in the resonant frequency of the unloaded balance from 189.682 Hz to 190.654 Hz when the temperature is raised from 20 °C to 90 °C. The same relative change was found when the microbalance carried a load. The changes in frequency, however, proved to be perfectly linear with temperature, and were reversible without noticeable hysteresis. This does imply an apparent change in the measured mass when the temperature changes. For a 5 mg load the apparent change is about 0.8 μg/°C. The ambient temperature should therefore be accurately monitored and taken into account when interpreting results. A disadvantage resulting from this temperature dependence is that the device is not immediately suitable for measurements in vacuum, because the temperature of the filament would not be accurately known. The

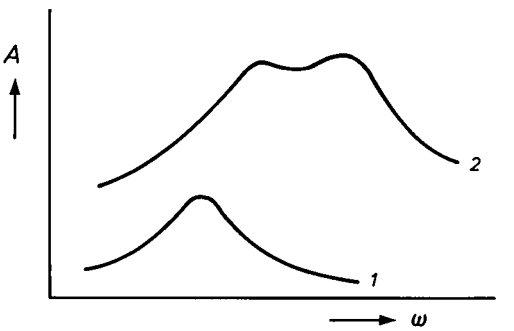

Fig. 2. Response curve, giving the observed amplitude A of the vibration as a function of the excitation frequency. If the voltage on the excitation element is not too high, a response as shown by curve *1* is obtained. Higher excitation voltages cause the load at the end of the quartz-glass filament to 'bounce', resulting in a distorted response curve (curve *2*). The highest and lowest frequencies at which measurements are made are about $2\pi \times 0.5$ Hz apart.

[1] A. W. Czanderna and S. P. Wolsky (eds), Microweighing in vacuum and controlled environments, Elsevier Scientific, Amsterdam 1980.

[2] B. J. Mulder, Simple piezoelectric microbalance based on a vibrating quartz wire, J. Phys. E **17**, 119-121, 1984.

[3] M. R. Spiegel, Theory and problems of theoretical mechanics, McGraw-Hill, New York 1967.

problem might be solved by giving the filament an inorganic coating that acted as a temperature-dependent resistance between the 'earthed' contacts of the piezoelectric flexure elements.

The microbalance can be used at all temperatures below the Curie point of the piezoelectric flexure elements (in our case below 180 °C). Changes in the properties of the flexure elements, e.g. resulting from a change in temperature, will not affect the results, since the response curve is normalized (see eq. (1)). Weighings can be carried out at higher temperatures if a piezoelectric material with a higher Curie point is used, for instance $LiNbO_3$, which has a Curie point of 1210 °C.

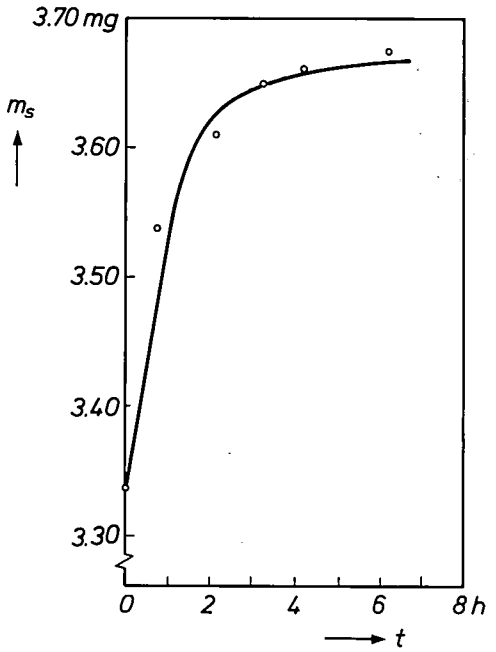

Fig. 3. The mass m_s of a piece of nylon film as a function of the time t exposed to an extremely humid environment with a relative humidity of 98% and a temperature of 40 °C. Even under these conditions the microbalance works well.

In conclusion we show in *fig. 3* the results of a series of measurements performed with our microbalance. After calibration a piece of nylon film was brought from an enclosure of low relative humidity (RH = 10%) into an enclosure where the humidity was extremely high (RH = 98%) at a temperature of 40 °C. The mass of the film was then determined at certain intervals over a number of hours. It can be seen that the increase in mass (and hence the water absorption) gradually slows down. After about 6 hours the mass of the film has increased about 10% due to water absorption. What is more interesting, however, is that our microbalance still works well under these extreme conditions.

B. J. Mulder
R. van der Schee

Dr B. J. Mulder and Ing. R. van der Schee are with Philips Research Laboratories, Eindhoven.

Scientific publications

These publications are contributed by staff of laboratories and plants that form part of or cooperate with enterprises of the Philips group of companies, particularly by staff of the research laboratories mentioned below. The publications are listed alphabetically by journal title.

Philips GmbH Forschungslaboratorium Aachen, Weißhausstraße, 5100 Aachen, Germany — *A*

Philips Research Laboratory Brussels, 2 avenue Van Becelaere, 1170 Brussels, Belgium — *B*

Philips Natuurkundig Laboratorium, Postbus 80000, 5600 JA Eindhoven, The Netherlands — *E*

Philips GmbH Forschungslaboratorium Hamburg, Vogt-Kölln-Straße 30, 2000 Hamburg 54, Germany — *H*

Laboratoires d'Electronique et de Physique Appliquée, 3 avenue Descartes, 94450 Limeil-Brévannes, France — *L*

Philips Laboratories, N.A.P.C., 345 Scarborough Road, Briarcliff Manor, N.Y. 10510, U.S.A. — *N*

Philips Research Laboratories, Cross Oak Lane, Redhill, Surrey RH1 5HA, England — *R*

Philips Research Laboratories Sunnyvale P.O. Box 9052, Sunnyvale, CA 94086, U.S.A. — *S*

R. P. de Wit (*Dr. Neher Lab., Leidschendam*), A. J. M. Kaizer & F. J. op de Beek *E*	Numerical optimization of the cross-over filters in a multiway loudspeaker system	75th AES Convention (preprint), Paris 1984	21 pp.	1984
J. C. Bermond*, C. Delorme* (* *Univ. Paris*) & J.-J. Quisquater *B*	Grands graphes de degré et diamètre fixés	Ann. Discrete Math. **17**	65-73	1983
P. Delsarte & P. Piret *B*	Algebraic codes achieving the capacity of the binary symmetric channel	Ann. Discrete Math. **17**	265-269	1983
L. Vriens & W. Rippens *E*	Optical constants of absorbing thin solid films on a substrate	Appl. Opt. **22**	4105-4110	1983
P. van der Werf & J. Haisma *E*	Broadband antireflective coatings for fiber-communication optics	Appl. Opt. **23**	499-503	1984
D. Y. Lou, A. Martinez & D. Stanton *N*	Surface profile measurement with a dual-beam optical system	Appl. Opt. **23**	746-751	1984
J. H. Neave, B. A. Joyce & P. J. Dobson (*Imp. College, London*) *R*	Dynamic RHEED observations of the MBE growth of GaAs	Appl. Phys. A **34**	179-184	1984
F. H. P. M. Habraken*, E. J. Evers* (* *Univ. Utrecht*) & A. E. T. Kuiper *E*	Hydrogen content of thermally nitrided thin silicon dioxide films	Appl. Phys. Lett. **44**	62-64	1984
J. Robertson (*Central Elect. Res. Labs, Leatherhead*) & M. J. Powell *R*	Gap states in silicon nitride	Appl. Phys. Lett. **44**	415-417	1984
T. de Jong (*Philips Elcoma Div., Nijmegen*), F. W. Saris (*FOM, Amsterdam*), Y. Tamminga & J. Haisma *E*	Solid phase epitaxy of silicon on gallium phosphide	Appl. Phys. Lett. **44**	445-446	1984
A. Eventoff, J. G. Wagner & Y. Chun (*Villanova Univ., PA*) *N*	Lateral deflection analysis of a rotating composite disk	ASME Paper No. 83-WA/DE-9	11 pp.	1983
S. Larochelle (*Inst. for Perception Res., Eindhoven*)	Some aspects of movements in skilled typewriting	Attention & Performance **10**	43-54	1984
S. M. Marcus (*Inst. for Perception Res., Eindhoven*)	Recognizing speech: on the mapping from sound to word	Attention & Performance **10**	151-163	1984
C. Ronse *E*	Sur les points fixés par les involutions dans un groupe transitif	Bull. Classe Sci. Acad. R. Belgique **69**	152-160	1983
E. Rammos *L*	Nouvelles structures d'antennes planes à rendement élevé en lignes triplaques óu en lignes à substrat	Coll. Int. sur le Radar, Paris 1984	154-157	1984
J. Durieu & M. Petit *B*	A 2-D solution of the contact problem in the capstan/tape/roller mechanism of magnetic recorders	Comput. Methods Appl. Mech. & Eng. **43**	21-35	1984

S. Moridi & H. Sari	*L*	Analysis of decision-feedback carrier recovery loops with application to 16 QAM digital radio systems	Conf. Rec. ICC'83, Boston 1983	671-675	1983
J. J. Kelly & P. H. L. Notten	*E*	Hole injection reactions and the potential distribution at the *p*-GaAs/electrolyte interface under anodic polarization	Electrochim. Acta **29**	589-596	1984
P. Bachmann, P. Geittner, D. Leers, M. Lennartz & H. Wilson	*A*	Low OH excess loss PCVD fibres prepared by fluorine doping	Electronics Lett. **20**	35-37	1984
R. Meierer & C. Tsironis	*L*	Modelling of single- and dual-gate MESFET mixers	Electronics Lett. **20**	97-98	1984
P. C. P. Bouten & H. H. M. Wagemans	*E*	Double mandrel: a modified technique for studying static fatigue on optical fibres	Electronics Lett. **20**	280-281	1984
J. J. Goedbloed	*E*	EMC en industrie	Elektronica **32** (No. 6)	11-21	1984
M. J. Coenen	*E*	Kabelkeuze: Een middel om EMC te bereiken?	Elektronica **32** (No. 6)	39-45	1984
J. J. Goedbloed, K. Riemens & A. J. Stienstra	*E*	Verbetering HF-immuniteit van versterkers met tegenkoppeling	Elektronica **32** (No. 6)	65-71	1984
J. J. Goedbloed	*E*	Terminologie van EMC	Elektronica **32** (No. 6)	101-103	1984
P. A. H. Hart	*E*	Physikalische Aspekte der Siliciumtechnologie für integrierte Schaltkreise	Elektrotech. & Maschinenbau **101**	156-162	1984
R. P. van Stapele & P. R. Locher	*E*	Nuclear magnetic resonance tomography	Europhysics News **15** (No. 5)	10-13	1984
H. Ney	*H*	Connected utterance recognition using dynamic programming	Fortschritte der Akustik, FASE/DAGA '82	915-918	1982
D. M. Krol & P. J. Rommers	*E*	Oxidation-reduction behaviour of antimony in silicate glasses prepared from raw materials and cullet	Glass Technol. **25**	115-118	1984
D. M. Krol & R. K. Janssen	*E*	The influence of batch preparation on the melting behaviour of 15 Na_2CO_3 - 10 $BaCO_3$ - 75 SiO_2 batches	Glastech. Ber. 56K (XIII. Int. Glaskongress, Hamburg 1983)	1-6	1983
B. M. J. Smets	*E*	The incorporation of divalent cations in sodium silicate and aluminosilicate glasses	Glastech. Ber. 56K (XIII. Int. Glaskongress, Hamburg 1983)	1023-1028	1983
A. W. Woodhead, D. Washington, J. R. Mansell, C. D. Overall, A. G. Knapp & P. Schagen	*R*	Channel multiplier CRT	IEE Proc. I **131**	2-5	1984
A. G. Knapp, D. Washington, A. J. Guest, R. W. A. Gill, R. Pook & L. H. Francis	*R*	Large-area channel electron multiplier for CRT applications	IEE Proc. I **131**	6-9	1984
D. L. Lamport, A. W. Woodhead, D. Washington & C. D. Overall	*R*	Flat deflection system for a channel multiplier CRT	IEE Proc. I **131**	10-12	1984
J. R. Mansell, A. W. Woodhead, A. G. Knapp & H. D. Stone	*R*	Colour selection in the channel-multiplier CRT	IEE Proc. I **131**	13-16	1984
R. J. van de Plassche & H. J. Schouwenaars	*E*	A monolithic high-speed sample-and-hold amplifier for digital audio	IEEE J. **SC-18**	716-722	1983
J. Lohstroh, E. Seevinck & J. de Groot	*E*	Worst-case static noise margin criteria for logic circuits and their mathematical equivalence	IEEE J. **SC-18**	803-807	1983
N. A. M. Verhoeckx & T. A. C. M. Claasen	*E*	Some considerations on the design of adaptive digital filters equipped with the sign algorithm	IEEE Trans. **COM-32**	258-266	1984
W. J. van Gils	*E*	Two topics on linear unequal error protection codes: bounds on their length and cyclic code classes	IEEE Trans. **IT-29**	866-876	1983
J. W. Smits, S. B. Luitjens & R. W. J. Geuskens	*E*	Comparison of surface and volume coercive field of sputtered CoCr thin films	IEEE Trans. **MAG-20**	60-62	1984
J. E. Knowles	*R*	The measurement of the anisotropy field of single 'tape' particles	IEEE Trans. **MAG-20**	84-86	1984
J. Paulin, J. C. Richard, J. P. Boutot & M. Jatteau	*L*	A diode intensifier tube designed for scintillation detection	IEEE Trans. **NS-31**	433-437	1984
J. Pergrale, C. Berche, D. Iachetti, G. Normand & M. Jatteau	*L*	Influence of the depth effect on quantitative results in single photon emission tomography with attenuation correction	IEEE Trans. **NS-31**	516-520	1984

M. Lacroix & A. Pirotte	*B*	Comparison of database interfaces for application programming	Inf. Syst. **8**	217-229	1983
H. K. Kuiken	*E*	The heat spreader: some quantitative results	Int. J. Heat & Mass Transfer **27**	942-943	1984
J. A. Clarke & R. J. Dewey	*R*	Millimeter wave imaging lens antenna	Int. J. Infrared & Millimeter Waves **5**	91-101	1984
J. 't Hart (*Inst. for Perception Res., Eindhoven*)		A phonetic approach to intonation: from pitch contours to intonation patterns	Intonation, accent and rhythm, D. Gibbon & H. Richter (eds), De Gruyter, Berlin	193-202	1984
A. Broese van Groenou & D. J. C. van Oers	*E*	Sphere-on-tape method of rapid selected-area thinning of samples for transmission electron microscopy	J. Am. Ceram. Soc. **66**	C/223-C/224	1983
G. A. C. M. Spierings	*E*	Influence of As_2O_3 on the optical properties of ultrapure multicomponent silicate glasses and optical fibers	J. Am. Ceram. Soc. **67**	124-127	1984
R. A. Kubiak, J. J. Harris & P. Dawson	*R*	Electrical and optical properties of Si- and Sn-doped $In_xGa_{1-x}As$ ($x \approx 0.53$) grown by molecular beam epitaxy	J. Appl. Phys. **55**	598-600	1984
S. D. Brotherton, P. Bradley, A. Gill & E. R. Weber (*Univ. Cologne*)	*R*	Electrical observation of the Au-Fe complex in silicon	J. Appl. Phys. **55**	952-956	1984
E. G. Visser	*E*	Effect of uniaxial tensile stress on the permeability of monocrystalline $MnZnFe^{II}$ ferrite	J. Appl. Phys. **55**	2251-2253	1984
J. W. Smits, S. B. Luitjens & F. J. A. den Broeder	*E*	Evidence for microstructural inhomogeneity in sputtered Co-Cr thin films	J. Appl. Phys. **55**	2260-2262	1984
T. T. M. Palstra*, G. J. Nieuwenhuis*, J. A. Mydosh* (* *Univ. Leiden*) & K. H. J. Buschow	*E*	Magnetic properties of cubic $La(Fe_xAl_{1-x})_{13}$ intermetallic compounds	J. Appl. Phys. **55**	2367-2369	1984
G. Marest*, A. Perez* (* *Univ. Claude Bernard, Villeurbanne*), J. L. Ponthenier+, P. Gerard+ (+ *L.E.T.I., Grenoble*) & J. M. Robertson	*E*	Mössbauer study of H^+ and Ne^+ implanted YIG	J. Appl. Phys. **55**	2560-2562	1984
M. J. Jongerius, A. J. M. J. Ras & Q. H. F. Vrehen	*E*	Optogalvanic detection of acoustic resonances in a high-pressure sodium discharge	J. Appl. Phys. **55**	2685-2692	1984
S. C. Abrahams (*AT&T Bell Labs, Murray Hill, NJ*), J. Ravez*, S. Canouet*, J. Grannec* (* *CNRS, Talence*) & G. M. Loiacono	*N*	Phase transitions and ferroelectric behavior in the $Pb_3(MF_6)_2$ family (M = Ti, V, Cr, Fe, Ga)	J. Appl. Phys. **55**	3056-3060	1984
W. H. de Roode & C. A. P. W. van de Pavert	*E*	Annealing effects and charge compensation mechanism in calcium-doped $Y_3Fe_5O_{12}$ films	J. Appl. Phys. **55**	3115-3124	1984
S. D. Brotherton	*R*	Photocurrent deep level transient spectroscopy in silicon	J. Appl. Phys. **55**	3636-3643	1984
A. W. Kolfschoten, R. A. Haring*, A. Haring* & A. E. de Vries* (* *FOM, Amsterdam*)	*E*	Argon-ion assisted etching of silicon by molecular chlorine	J. Appl. Phys. **55**	3813-3818	1984
H. Rau	*A*	The chlorination equilibrium of germanium oxides	J. Chem. Thermodyn. **16**	287-293	1984
E. Bannai (*Univ. Columbus, OH*), A. Blokhuis*, J. J. Seidel* (* *Univ. of Technol., Eindhoven*) & P. Delsarte	*B*	An addition formula for hyperbolic space	J. Comb. Theory A **36**	332-341	1984
M. Furtado & G. Jacob	*L*	Study on the influence of annealing effects in GaN VPE	J. Cryst. Growth **64**	257-267	1983
C. Cadoret (*Lab. Phys. Milieux Condensés, Aubière*) & F. Hottier	*L*	Mechanism of Si polycrystalline growth on a Si_3N_4 substrate from SiH_4/H_2 at reduced pressures	J. Cryst. Growth **64**	583-592	1983
P. J. Roksnoer & M. M. B. van Rijbroek-van den Boom	*E*	The single crystal growth and characterization of indium phosphide	J. Cryst. Growth **66**	317-326	1984
J. J. Kelly & P. H. L. Notten	*E*	Surface charging effects during photoanodic dissolution of n-GaAs electrodes	J. Electrochem. Soc. **130**	2452-2459	1983
G. A. R. van Dijk & H. C. A. M. Smoorenburg	*E*	Analysis of an aluminum plating bath using ^{27}Al-NMR spectroscopy	J. Electrochem. Soc. **131**	345-347	1984
J. F. Dijksman	*E*	Hydrodynamics of small tubular pumps	J. Fluid Mech. **139**	173-191	1984

K. H. J. Buschow & D. B. de Mooij	*E*	Crystal structure and magnetic properties of PtMnGa and PtMnAl	J. Less-Comm. Met. **99**	125-130	1984
A. L. J. Burgmans & H. J. H. Merks-Eppingbroek	*E*	The ionisation coefficient in Kr-Hg mixtures	J. Phys. D **17**	1159-1166	1984
P. C. Zalm & L. J. Beckers	*E*	Sputtering of silicon nitride with hydrogen ions	J. Vac. Sci. & Technol. **B2**	84-85	1984
A. W. M. van den Enden & T. Krol	*E*	A proposal for a wideband digital satellite switch	Links for the future (ICC'84, Amsterdam), P. Dewilde & C. A. May (eds.), Elsevier, Amsterdam	299-302	1984
T. Krol & A. W. M. van den Enden	*E*	A mathematical description of the behaviour of time division multiplex exchanges	Links for the future (ICC'84, Amsterdam), P. Dewilde & C. A. May (eds.), Elsevier, Amsterdam	303-306	1984
K. J. Wouda*, S. J. M. Tol* (* *Philips Telecommun. Ind., Hilversum*) & W. J. M. Reijntjes	*E*	An ISDN transmission system with adaptive echo cancelling and decision feedback equalization — a two chip realization	Links for the future (ICC'84, Amsterdam), P. Dewilde & C. A. May (eds.), Elsevier, Amsterdam	685-690	1984
J. van der Heijden	*E*	DIVAC: a Dutch integrated services glass fibre experimentation system and demonstration set-up	Links for the future (ICC'84, Amsterdam), P. Dewilde & C. A. May (eds.), Elsevier, Amsterdam	1145-1149	1984
R. J. Sluyter, G. J. Bosscha & H. M. P. T. Schmitz	*E*	A 9.6 kbit/s speech coder for mobile radio applications	Links for the future (ICC'84, Amsterdam), P. Dewilde & C. A. May (eds.), Elsevier, Amsterdam	1159-1162	1984
D. M. Ball & P. J. Stein	*R*	A rapid access protocol for trunked mobile radio systems	Links for the future (ICC'84, Amsterdam), P. Dewilde & C. A. May (eds.), Elsevier, Amsterdam	1214-1218	1984
J. Biellmann*, B. Prevot*, C. Schwab* (* *Lab. Spectrosc. & Opt. Corps Sol., Strasbourg*), J.-B. Theeten & M. Erman	*L*	Non destructive optical analysis of implanted layers in GaAs by Raman scattering and spectroscopic ellipsometry	Mater. Res. Soc. Symp. Proc. **14**	517-522	1983
E. Rammos	*L*	Suspended-substrate line antenna fits 12-GHz satellite applications	Microwave Systems News **14** (No. 3)	110-126	1984
A. J. M. Houtsma (*Inst. for Perception Res., Eindhoven*)		Pitch salience of various complex sounds	Music Perception **1**	296-307	1984
R. A. Haring* A. W. Kolfschoten & A. E. de Vries* (* *FOM, Amsterdam*)	*E*	Chemical sputtering by keV ions	Nucl. Instrum. & Methods Phys. Res. **B2**	544-549	1984
M. H. L. M. van den Broek	*E*	The influence of current density distribution on spot growth	Optik **67**	69-77	1984
J. W. Orton	*R*	On the analysis of space-charge-limited current-voltage characteristics and the density of states in amorphous silicon	Phil. Mag. B **49**	L1-L7	1984
B. A. Joyce, J. H. Neave, P. J. Dobson (*Imp. College, London*) & P. K. Larsen	*R, E*	Analysis of reflection high-energy electron-diffraction data from reconstructed semiconductor surfaces	Phys. Rev. B **29**	814-819	1984
H.-J. Eifert*, B. Elschner* (* *T.H., Darmstadt*) & K. H. J. Buschow	*E*	Electronic properties of amorphous Zr_xT_{1-x} alloys (T = Cu, Ni, Pd, Pt, Co, or Rh)	Phys. Rev. B **29**	2905-2911	1984
G. A. Acket & H. Koelmans	*E*	Semiconductor injection lasers	Phys. Technol. **15**	67-72	1984
A. W. Woodhead	*R*	Flat cathode ray tubes	Phys. Technol. **15**	86-91	1984
H. M. J. Boots & R. B. Pandey (*Univ. Cologne*)	*E*	Kinetic gelation model	Polymer Bull. **11**	415-420	1984
F. Manola & A. Pirotte	*B*	CQLF — a query language for CODASYL-type databases	Proc. ACM SIGMOD Conf., Orlando 1982	94-103	1982

M. Davio & J.-J. Quisquater	*B*	Cryptographic techniques in nuclear material control	Proc. 5th Ann. Symp. on Safeguards & nucl. mater. management, Versailles 1983	171-175	1983
P. Delsarte, Y. Genin & Y. Kamp	*B*	Generalized Schur positivity test and Levinson recursion	Proc. 6th Eur. Conf. on Circuit theory & design, Stuttgart 1983	321-323	1983
G. Normand, M. Jatteau, P. Lelong & J. Ott	*L*	Computer simulation of the light collection process in scintillation gamma-ray cameras	Proc. Int. Conf. Advances in scintillation counting, Banff, Alberta, 1983	176-189	1983
M. Jatteau & G. Normand	*L*	Influence of optical and geometrical parameters on scintillation detection in gamma camera heads	Proc. Int. Conf. Advances in scintillation counting, Banff, Alberta, 1983	190-207	1983
R. Bishop*, E. Bordelon*, R. Cheung*, M. R. Feay*, G. Louis & C. H. Smedema* (* *British Telecom, Ipswich*)	*B*	Separate compilation and the development of large programs in CHILL	Proc. 5th Int. Conf. on Software eng. for telecommun. switching syst., Lund 1983	80-86	1983
H. W. Zelle*, J. R. de Pijper* & J. 't Hart* (* *Inst. for Perception Res., Eindhoven*)		Semi-automatic synthesis of intonation for Dutch and British English	Proc. 10th Int. Congr. of phonetic sciences, Utrecht 1983	247-251	1984
M. T. M. Scheffers (*Inst. for Perception Res., Eindhoven*)		Pitch and the perceptual separation of simultaneous vowel sounds	Proc. 10th Int. Congr. of phonetic sciences, Utrecht 1983	434-438	1984
J. M. B. Terken (*Inst. for Perception Res., Eindhoven*)		The effect of accentuation on comprehension: an experiment	Proc. 10th Int. Congr. of phonetic sciences, Utrecht 1983	558-561	1984
J. 't Hart & J. R. de Pijper* (* *Inst. for Perception Res., Eindhoven*)		Experiments on the stylization of British English intonation	Proc. 10th Int. Congr. of phonetic sciences, Utrecht 1983	570-573	1984
B. A. G. Elsendoorn (*Inst. for Perception Res., Eindhoven*)		Production and perception of English vowel duration by Dutch speakers of English	Proc. 10th Int. Congr. of phonetic sciences, Utrecht 1983	673-676	1984
N. J. Willems (*Inst. for Perception Res., Eindhoven*)		English intonation from a Dutch point of view	Proc. 10th Int. Congr. of phonetic sciences, Utrecht 1983	706-709	1984
K. A. Schouhamer Immink & R. M. Aarts	*E*	Maximization of recording density obtainable in Te-alloys	Proc. SPIE **396**	181-188	1983
P. Saraga, C. V. Newcomb, P. R. Lloyd, D. R. Humphreys & D. J. Burnett	*R*	Unpacking and mounting TV deflection units using visually controlled robots	Proc. SPIE **449**	488-495	1983
J. J. Goedbloed	*E*	Analyse van stoorproblemen	PT/Elektrotech. Elektron. **39** (No. 3)	26-29	1984
M. L. G. Thoone & R. M. A. M. Breukers (*Philips Audio Div., Eindhoven*)	*E*	Application of the Compact Disc in car information and navigation systems	SAE Int. Congr. & Exposition, Detroit 1984	105-111	1984
M. P. A. Viegers	*E*	TEM work on grain boundaries	Science of Ceramics Vol. 12, P. Vincenzini (ed.), Ceramurgica, Faenza	245-256	1984
D. Hennings	*A*	Recrystallization of barium titanate ceramics	Science of Ceramics Vol. 12, P. Vincenzini (ed.), Ceramurgica, Faenza	405-409	1984
G. de With & H. Parren	*E*	Fracture of PTC ceramics	Science of Ceramics Vol. 12, P. Vincenzini (ed.), Ceramurgica, Faenza	537-542	1984
R. Wernicke	*A*	Ceramic multilayer capacitors and nonlinear resistors	Science of Ceramics Vol. 12, P. Vincenzini (ed.), Ceramurgica, Faenza	677-686	1984

A. Shaulov	*N*	Broad band infrared thermal detector	Sensors & Actuators **5**	207-215	1984
G. W. 't Hooft & C. van Opdorp	*E*	Analysis of LED degradation; proton-bombarded GaAs	Solid-State Electronics **27**	253-259	1984
C. van Opdorp & G. W. 't Hooft	*E*	Current-voltage and light-voltage relations for the linear-graded *pn* junction	Solid-State Electronics **27**	261-266	1984
W. J. J. Rey	*B*	Introduction to robust and quasi-robust statistical methods	Springer, Berlin	—	1983
J. C. Compter	*E*	Microprocessor-controlled reluctance motor	Thesis, Eindhoven	—	1984
F. J. A. den Broeder, J. M. Vandenberg (*Bell Labs, Murray Hill, NJ*) & C. W. Draper (*Western Electric Eng. Res. Center, Princeton, NJ*)	*E*	Microstructures of Cu-Zr phases formed by laser surface treatment	Thin Solid Films **111**	43-51	1984
J. M. Robertson & M. W. van Tol (*Philips Sci. & Ind. Div., Almelo*)	*E*	Cathodoluminescent garnet layers	Thin Solid Films **114**	221-240	1984
J. E. Curran	*R*	The properties and applications of low energy plasmas	Vacuum **34**	343-345	1984
B. C. Easton, J. A. Chapman, O. F. Hill & M. J. Powell	*R*	The plasma-enhanced deposition of hydrogenated amorphous silicon	Vacuum **34**	371-376	1984
G. F. Weston	*R*	Ultra-high vacuum line components	Vacuum **34**	619-629	1984
D. Fauvel & S. Gourrier	*L*	Étude de quelques résines développables en plasma	Vide Couches Minces **38** (suppl. to No. 218)	233-236	1983
F. Khodr, M. Bernheim (*Univ. Orsay*), D. Arnoult & S. Gourrier	*L*	Gravure plasma de GaAs	Vide Couches Minces **38** (suppl. to No. 218)	237-241	1983
G. Bergmann	*A*	Solare Niedertemperaturanwendungen unter technisch-ökonomischen Gesichtspunkten	Wärmetechnik **28**	426-434	1983

Contents of Philips Telecommunication Review **42**, No. 3, 1984

K. Hubée: A new force in telecommunications (pp. 109-110)

H. J. Goebertus: 5ESS-PRX architecture (pp. 111-131)

W. Lemstra: Network planning with 5ESS-PRX (pp. 132-147)

J. Drupsteen: 140 Mb/s single-mode optical connection inaugurated by Dutch PTT (p. 148)

C. G. Golder, D. W. Johnson, C. W. Kemp, M. P. Krishnan & N. Ostrove: The multifunction operations system (pp. 149-169)

R. H. Bourgonjon: 5ESS-PRX software (pp. 170-182)

Contents of Electronic Components & Applications **6**, No. 2, 1984

Surface-mounted devices in printed circuit board assembly (pp. 66-70)

H. Eng, A. Goldberger & J. Goodhart: Video display and attributes controller ICs (pp. 71-78)

M. Klewer & B. Vernooij: The 68000 microprocessor design philosophy (pp. 79-82)

H. Fiedeldij: VHF power amplifiers with broadband input circuitry (p. 83-86)

R. Blauschild & R. Fabbri: Two-chip modem for FSK data transfer (pp. 87-92)

A. Woodworth: The BTV60 — first in a new generation of GTOs (pp. 93-95)

J. G. A. Scholten: Thermal aspects of flange-mounted r.f. power transistors (pp. 96-106)

W. H. A. van Dooremolen: A new stereo decoder IC suits all classes of radio (pp. 107-111)

G. Hine: Quality of small-signal, low and medium power diodes (pp. 112-124)

Supplement to Philips Technical Review
Bijlage van Philips Technisch Tijdschrift
No. 24

December 1984

Recent United States Patents

Abstracts from patents that describe inventions from the following research laboratories, which form part of or cooperate with the Philips group of companies:

Philips GmbH Forschungslaboratorium Aachen, Weißhausstraße, 5100 Aachen, Germany *A*
Philips Research Laboratory Brussels, 2 avenue Van Becelaere, 1170 Brussels, Belgium *B*
Philips Natuurkundig Laboratorium, Postbus 80000, 5600 JA Eindhoven, The Netherlands *E*
Philips GmbH Forschungslaboratorium Hamburg, Vogt-Kölln-Straße 30, 2000 Hamburg 54, Germany *H*
Laboratoires d'Electronique et de Physique Appliquée, 3 avenue Descartes, 94450 Limeil-Brévannes, France *L*
Philips Laboratories, N.A.P.C., 345 Scarborough Road, Briarcliff Manor, N.Y. 10510, U.S.A. *N*
Philips Research Laboratories, Cross Oak Lane, Redhill, Surrey RH1 5HA, England *R*
Philips Research Laboratories Sunnyvale, P.O. Box 9052, Sunnyvale, CA 94086, U.S.A. *S*

4 423 502

Record carrier having an optically readable information structure

J. G. Dil *E*

A record carrier is disclosed in which information is recorded in an optically readable information structure of track-wise arranged information areas which alternate with intermediate areas. Adjacent information track portions are situated at different, parallel planes spaced from each other by a predetermined distance such as to reduce crosstalk from neighbouring tracks thereby permitting the information density to be substantially increased.

4 425 043

Device for detecting the position of an object

G. E. van Rosmalen *E*

A device is described for detecting the position of an object, which device comprises a radiation source, beam-splitting prism, and a detection system comprising a plurality of radiation-sensitive detectors. The object to whose position is to be measured carries only the prism, and each detector is divided into a plurality of subdetectors. The device enables changes in both position and inclination of the object to be measured.

4 425 478

Conference system for telephony

J. F. P. van Mil *E*
A. W. M. van den Enden
T. A. van Harreveld

A conference system for establishing simultaneous interchange of information among a plurality of participants ($E_o - E_k$) comprises a conference network (CN). Each participant is connected to a terminal ($n_o - n_k$) which is connected to a hybrid network ($CS_o - SW_k$). The output ($SW_o - SW_k$) from the hybrid networks ($CS_o - CS_k$) are fed to summing amplifiers ($SA_o - SA_k$) in the conference network CN. The outputs of the summing amplifiers are fed to the participants via the hybrid networks ($CS_o - CS_k$). The summing amplifiers ($SA_o - SA_k$) are arranged so that the signals contributed by the participant to which the particular summing amplifier output is connected is multiplied by a factor β while the signals contributed by the other participants are multiplied by a factor α. By returning a portion of the signal generated by a participant to that participant it is possible to construct a system having a lower attenuation while maintaining stability.

4 425 562

Device for coding signals which are distributed between a number of channels

E. de Niet *E*

A device for introducing digital data into a medium having bivalent or multivalent states and having a coding device and a commutation device. The coding device receives under the control of a first clock pulse series, data signals and forms therefrom a number of code bits which are combined as an input to the commutation device. The coding efficiency is smaller than 1. Under the control of a second clock pulse series, the commutation device switches each input to apply the code bits to a number of channels of the medium, so that for each channel certain code restrictions are satisfied.

4 425 577

Television camera equipped with a colour-separating arrangement disposed behind the objective

F. H. M. Bergen *E*
W. W. J. Degger
S. L. Tan

In order to minimize the effects of magnetic fields in a colour television camera, the colour prism arrangement is constructed so that at least two camera tubes can be arranged parallel to each other.

4 425 593

Magnetoresistive head

L. Postma *E*

A magnetic head having an elongate magnetoresistive element bearing a pattern of equipotential strips extending obliquely to its longitudinal axis for adjusting a suitable workpoint. With its edges extending parallel to the longitudinal axis, the element bears on components of magnetically permeable material one of which, in operation, is in direct flux coupling with a magnetic recording medium and the other of which is in flux coupling with the recording medium via a further element of magnetically permeable material which may be ferrite.

4 425 809

Measuring of tension and moments in a thin flexible tape

B. L. M. van Bakel E
G. P. C. van Kooijk
B. P. Videc

A device, and method of using such a device, for measuring tension in a thin flexible tape by guiding the tape along a curved path between two parallel curved guides, supplying pressurized gaseous medium to each side of the tape, and measuring the difference in gas pressure between the two sides of the tape. Measuring ducts, terminating substantially opposite each other in the curved guide surfaces are connected to at least one pressure transducer which in turn is connected to an electrical measuring circuit.

4 426 442

Method of producing metal images or patterns on and/or below the surface of a substrate comprising a semiconducting light-sensitive compound

A. Molenaar E
P. E. Wierenga

Producing metal images or patterns on and/or below the surface of a substrate material comprising a semiconducting light-sensitive compound, such as titanium dioxide or zinc oxide which after exposure of a metal compound releases this metal in the form of nuclei. Exposure takes place in the solution of the metal compound by means of a moving beam of laser light whereby the nuclei pattern is directly 'written'. Thereafter, the nuclei image is intensified in a known manner to produce a visible image or a conductive pattern, for example by means of an electroless plating solution. Use: the recording of information as well as the production of printed circuit boards.

4 427 524

Magnetron cathode sputtering system

J. E. Crombeen E
J. Visser
G. E. Thomas

Such a system comprises in an envelope a flat cathode from the material to be sputtered and a substantially circular anode situated coaxially with respect to said cathode. Behind the cathode, magnetic means are provided to generate at least one closed tunnel of field lines over a part of the cathode surface (a so-called electron trap). Between an anode and an edge of the cathode is present according to the invention a coaxial, substantially cylindrical auxiliary electrode. From the center of the cathode a rod-shaped auxiliary electrode moreover extends axially. Said auxiliary electrodes modify the electric field in such a manner that the electrons which are not captured in the tunnel of magnetic field lines are directed substantially towards the anode. The distance from the rod-shaped electrode to the substrate must be chosen to be comparatively small. By using the invention the substrate is less heated and not so much damaged by electron bombardment.

4 428 736

Methods of manufacturing a colour display tube having a magnetic quadrupole post-focusing mask

J. Verweel E
H. Zijlstra

In a first method, a meander-shaped coil is provided on each side of a mask having apertures. The coils are oriented perpendicularly relative to each other. If a current flows through the coils in the correct direction, a magnetic quadrupole is formed along circumference of each aperture. In a second method, a holder with permanent magnetic strips is provided on each side of the mask. The strips in the one holder are oriented perpendicularly relative to the strips in the other holder. A coil is provided around the holders and with which a decaying magnetic alternating field is generated which initially drives the material of the mask on both sides of the hysteresis curve into saturation. After the decay of said alternating field, a magnetic quadrupole is present along the circumference of each aperture.

4 429 337

Magnetic head unit having thermally dissipating cover plate

J. de Wilde E

An integrated magnetic head unit includes a housing and a substrate provided in the housing. The substrate supports a plurality of electromagnetic transducing elements including respective transmission elements which are connected to bonding pads on the substrate. A silicon plate covers the transducing elements and is arranged in a good thermally-conducting relationship with the transducing elements and with the housing. The cover plate is arranged such that the bonding pads are exposed.

4 429 396

Semiconductor laser having a doped surface zone

P. J. de Waard E

A semiconductor laser with a double hetero junction includes a strip-shaped semiconductor contact layer which is present on a passive layer of the same conductivity type, with a highly doped zone of the same conductivity type which extends over at least a part of the thickness of the contact layer and beside the contact layer in the passive layer so as to increase the radiation mode stability. According to the invention, the highly doped zone extends only over a part of the thickness of the passive layer in such a manner that below and beside the contact layer a difference in effective refractive index of at least 0.0005 and at most 0.005 is obtained.

4 430 609

Signal transfer device having a transfer characteristic which is adjustable in steps

T. J. van Kessel E
E. C. Dijkmans
A. J. P. M. van Uden

A step-controlled attenuator circuit which, in order to avoid audible switching clicks in audio equipment, employs current-controlled switches. A switch is switched on by means of a gradually increasing control current and a switch to be switched off is turned off by means of a gradually decreasing control current.

4 431 267

Optical system which provides a collimated light beam

J. C. J. Finck E
H. M. M. Kessels

An optical system which provides a collimated light beam, having a tubular holder, a semiconductor laser and a system of lenses incorporated in the holder, in which the semiconductor laser is positioned against an abutment in the axial direction of the holder and a resilient element is placed between the system of lenses and the abutment, while on the side of the system of lenses remote from the resilient element a locking element is present which, after axial adjustment in the holder, is fixed in such a location that the system of lenses, after moving in the axial direction against the presure of the resilient element, is in the position in which its focus coincides with the laser element in the semiconductor laser.

4 432 066

Multiplier for binary numbers in two's-complement notation

N. F. Benschop E

A device for multiplying two binary numbers in two's-complement notaton having an array for forming bitwise partial products and a further array for successively forming the result bits therefrom. The modules of the further array form either a full adder or a full subtractor under the control of a one-bit control signal. The negative sign of the most-significant bits of the factors can thus be taken into

account. Devices of this kind can be linked in order to realize multiplications with higher precision, variation of the control signal signalling that only the device to which a most significant factor bit is applied takes into account a negative sign. A pipe line product-accumulator device is formed by construction in n-MOS dynamic logic circuits, with an inherent trigger function on the outputs of full adders/subtractors.

---

4 432 738

Camera tube and method of manufacturing same

J. H. T. van Roosmalen E
F. C. M. de Haas

An electron gun for a camera tube includes an anode and a cathode. The cathode is assembled in a cathode support which can very readily be adjusted relative to the anode in the non-connected condition. In particular, the cathode support and the anode are movable radially with respect to each other and with respect to an axis. An emissive cathode surface and a part of the anode extending perpendicular to the axis remain accurately parallel to each other during the radial movement. As a result of this it is possible to cause the central path of the generated electron beam and the gun axis to coincide so that extra correction coils for aligning the electron beam may be omitted.

---

4 434 212

Device for propagating magnetic domains

J. M. Robertson E
D. J. Breed
A. B. Voermans

A device for propagating magnetic domains, comprising a monocrystalline nonmagnetic substrate of a material having a garnet structure, and a layer of an iron garnet grown epitaxially on the nonmagnetic substrate. In the dodecahedral lattice sites, the iron garnet comprises at least a bismuth ion and a rare-earth ion selected from the group consisting of lutetium, thulium, and ytterbium. Such a magnetic garnet combines very high uniaxial anisotropy with a high domain mobility, which properties make the device extremely suitable for the propagation of magnetic domains having diameters from approximately 1 to approximately 2 μm under the influence of comparatively low driving fields.

---

4 434 445

Magnetic head for high track density

A. van Herk E

A magnetic head for writing and/or reading information in mutually parallel tracks of a magnetic recording medium includes a transducing gap having a depth of the same order of magnitude as the longest wavelength on the recording medium. The gap also has a slope of less than or equal to 45° relative to the head surface which faces the medium.

---

4 435 200

Method of preparing precision pressed glas object

H. J. M. Joormann E
H. Verweij
J. Haisma

Glass objects, lenses in particular, can be pressed with precision from a glass which contains 45-55 mol% P_2O_5, 15-40 mol.% BaO, 5-15 mol.% Li_2O, 5-35 mol.% PbO, 0-2 mol.% Al_2O_3 and 0-6 mol.% F. A cube of glass is made from the above composition and preheated to a temperature of 20-60 °C above the American softening point to obtain a polishing effect. The preheated cube is then inserted into preheated dies which are closed to form a precision pressed object of the glass.

4 435 484

Device for propagating magnetic domains

D. J. Breed E
B. A. H. van Bakel
A. B., Voermans
J. M. Robertson

A device for propagating magnetic domains includes a monocrystalline nonmagnetic substrate of a rare earth gallium garnet bearing a layer of an iron garnet capable of supporting local enclosed magnetic domains. The iron garnet layer is grown in compression on a face of the nonmagnetic substrate. The iron garnet comprises manganese in part of the iron sites of its crystal lattice, and comprises yttrium and at least one representative selected from the group comprising bismuth and the rare earth metals in the dodecahedral lattice sites. Such a magnetic garnet has a very high unaxial anisotropy and a high domain mobility. These properties make the device extremely suitable for propagating submicron magnetic domains having diameters as small as 0.4 μm.

---

4 435 728

Field-frequency doubling circuit for a television signal

J. G. Raven E
M. J. J. C. Annegarn

A field-frequency doubling circuit for a television signal having two field memories may alternatively be employed as a picture memory for the television signal when it is slightly extended by providing a re-write circuit and an adapted output circuit. This picture memory may be included in, for example, a noise suppression circuit or a movement detector.

---

4 435 774

Method of and arrangement for calculating the discrete Fourier transform by means of two circular convolutions

T. A. C. M. Claasen E
W. F. G. Mecklenbräuker

Method of a N-point discrete Fourier transform. The original set, consisting of N input signal values $\{a(k)\}k = 0, 1, 2, \ldots N-1$ is converted into two sets of signal values $\{b_1(q)\}q = 1, 2, \ldots M$ and $\{b_2(q)\}q = 1, 2, \ldots M$, which each comprise $M = (N-1)/2$ signal values, each value being a linear combination of two of the original input signal values $a(k)$. These sequences are circularly convolved with the impulse response $h_1(v) = \alpha\cos((2\pi/N)g^v)$ and $h_2(v) = j\beta\sin((2\pi/N)g^v)$, respectively, for generating a set of third data elements $y_1(p)$ and a set of fourth signal values $y_2(p)$. Herein N is a prime and α,β and g represent constants and it holds that $p, v = 1, 2, \ldots M$, whereas $j = \sqrt{-1}$. The desired output signal value can be obtained by means of a linear combination of the signal values $y_1(p)$, $y_2(p)$ and a(0).

---

4 435 806

Device for testing a circuit comprising sequential and combinatorial logic elements

M. T. M. Segers
C. Niessen
K. Kuiper

A device for processing digital signals includes combinatorial and sequential logic elements. For the testing of the device, a shift register can be formed from the sequential elements. A test pattern is applied thereto. The result of the processing of the test pattern is applied to the shift register. The output of the shift register is connected to a second shift register which forms a moving multibit sum pattern from a received series of result patterns by way of a feedback circuit to at least one Exclusive-OR-element. An output of the feedback circuit is connected to an input of the first shift register in order to apply a subsequent test pattern thereto. After completion of the test, the sum pattern formed is checked.

4 435 900

Method of manufacturing a magnetic head unit

J. de Wilde E

A method of manufacturing an integrated magnetic head unit includes providing a substrate which supports a plurality of electromagnetic transducing elements connected to bonding pads. The transducing elements are then covered by a silicon plate which is arranged in good thermally-conducting relationship with the transducing elements and with a housing.

---

4 436 381

Precision pressed glass object

H. J. M. Joormann E
H. Verweij
J. Haisma

Glass objects, lenses in particular, can be pressed with precision from a glass which contains 45-55 mol.% P_2O_2, 15-40 mol.% BaO, 5-15 mol.% Li_2O, 5-35 mol.% PbO, 0-2 mol.% Al_2O_3 and 0-6 mol.% F.

---

4 439 008

Optical fiber of the graded index type and method of producing same

H. J. M. Joormann E
G. A. C. M. Spierings

An optical fiber of the graded index type consisting of a glass having predominantly the composition 60-70 mol.% SiO_2, 15-30 mol.% alkali metal oxides, and 10 to 15 mol.% MgO in combination with at least one oxide selected from the group formed by CaO, SrO, BaO and ZnO. The impurity content of the fiber is less than 0.01 ppm. In the fiber the MgO content increases from the axis of the fiber to the circumference of the fiber. The oxide or the other oxides, having cations which can be exchanged for the magnesium cation, decrease to a corresponding extent in this direction.

---

4 439 294

Reactive ion etching of soft-magnetic substrates

T. W. Bril E
W. G. M. van den Hoek

A method of providing grooves in a body of a soft-magnetic, iron-containing material. The method includes reactive ion etching the body in a chlorine-containing or bromine-containing plasma after providing the body areas not to be etched with a mask of an inorganic material such as Al_2O_3.

---

4 439 529

Glass and glass objects

H. J. M. Joormann E
H. Verweij
J. Haisma

Glasses consisting of 45-55 mol.% P_2O_6, 15-40 mol.% BaO, 5-15 mol.% Li_2O, 5-35 mol.% PbO, 0-2 mol.% Al_2O_3 and 0-6 mol.% F are suitable for the precision pressing of lenses.

---

4 440 470

Optical transmission system coupling a semiconductor laser diode to a multimode optical fiber

G. D. Khoe E

Optical transmission system comprising a laser diode which is coupled to a transmission fiber via a coupling path. The coupling path includes a monomode fiber or the series arrangement of a monomode fiber and a plurality of multimode fiber lengths, the cross-section of which, seen from the laser, increase in size. As a result thereof the modal noise and the reflection noise in the optical system in drastically reduced.

---

4 440 586

Method of manufacturing a die for duplicating plastics information carriers

G. J. M. Lippits E
A. J. M. van den Broek
A. J. G. op het Veld
R. Dijkstra
J. de Jonge

The invention relates to a method of reproducing plastics record carriers, in particular duplicating video records. According to the invention, a metal die is used which is provided with a thin-liquid molding resin of a particular composition which can be polymerized by radiation. A radiation-pervious substrate which is manufactured from synthetic material, for example polymethylmethacrylate, is provided on the molding resin. The molding resin is exposed to light via the substrate after which the cured molding resin together with the substrate connected thereto is removed from the die. The molding resin used in the process comprises low-molecular monomers or oligomers which contain on a average 25-70% by weight of hydrocarbon groups and/or phenyl groups. The molding resin is aprotic and has a functionality as regards unsaturatedness which is between the values 2 and 6. A suitable molding resin contains mono-, tri- or tetra esters of acrylic acid. The molding resin preferably has a swelling capacity with respect to the substrate and for that purpose preferably comprises a vinylmonomer. The metal die used in the method preferably is a quite flat die which is obtained by providing the master disk which is a flat glass plate with information track with a nickel layer, gluing hereon a flat stiffening plate and then removing the master disk. The resulting father disk may be used as a die. Alternatively, further metal copies may be made herefrom which are provided in a simpler manner with a flat stiffening plate. The invention also extends to the molding resin, substrate and die used in the method, as well as the resulting plastics record carriers.

---

4 440 699

Method and device for moulding a transparent object

A. Smid E
J. Haisma

A method of and a device for high-precision moulding of transparent objects is described. Before the object assumes its final shape, a radiation beam is passed through the moulds of a moulding device and the material contained therein, and the intensity distribution of the radiation spot formed by the beam is compared with a reference, thereby enabling the moulds to be aligned very accurately, so that high-quality products can be manufactured.

---

4 441 964

Method of depositing a metal

F. E. P. Mikkers E
P. E. Wierenga

The invention relates to a method of depositing a metal on a heat-conducting substrate, in which a surface of the substrate is irradiated at at least one area in a bath by a laser beam and the metal is deposited from the bath at that area on the substrate. In order to improve the localization of the deposited metal at the irradiated area and in its immediate surroundings, according to the invention, the metal is deposited on a layer of the substrate located at least at the irradiated area and in its non-irradiated surroundings. The layer has a heat conduction coefficient which is smaller than the heat conduction coefficient of the material of the substrate adjoining the layer.

PHILIPS TECHNICAL REVIEW

VOLUME 41, 1983/84, No. 11/12

Digital optical recording with tellurium alloys

L. Vriens and B. A. J. Jacobs

For some considerable time the electronics industry has been working on compact systems that will store large amounts of data for long periods reliably and yet allow them to be retrieved quickly. The Philips DOR (digital optical recording) system is a major breakthrough in this field: some ten billion data bits (corresponding to 500 000 A4 pages) can be written on a disc no bigger than an LP disc and read out by means of a semiconductor laser. The development of this system drew on the knowledge and experience gained at Philips Research Laboratories, Eindhoven, in work on the LaserVision ('VLP') system, semiconductor lasers and optical recording materials. Work at Philips Research Laboratories in Briarcliff, U.S.A., also contributed to this development. When it was presented to the press in November 1978 the DOR system was still in an experimental phase; since then it has been developed further and it is now on the professional equipment market. These further developments came about largely through the materials research initiated in the Eindhoven laboratories by P. Zalm and later undertaken jointly with the DOR laboratory of the Data Systems Division. One of the findings was that the quality of DOR discs can be substantially improved if the recording material used is not pure tellurium but an alloy of tellurium, selenium, antimony and sulphur. The article below describes this work, and the article that follows deals with an investigation into the potentialities of recording materials consisting of organic dyes.

Digital optical recording

In digital optical recording (DOR) on discs the information is written and read out by means of a laser beam. The most usual form of DOR uses a focused laser beam (effective diameter ≈ 1 μm), which is intensity-modulated by the information to be recorded, and makes small holes in the recording layer on the disc [1]. A focused laser beam is also used for reading out the stored information, but with a much lower power than is used for writing. Read-out is based on detection of the changes in reflectance caused by the presence of holes. The DOR system differs from the LaserVision [2] and 'Compact Disc Digital Audio' [3] systems described earlier in this journal: in LaserVision and 'Compact Disc' the information is prerecorded on the disc in the factory. In the DOR disc the information is written by the user himself [4].

In a preferred design of the DOR disc a transparent lacquer layer is sandwiched between the substrate and the recording layer. For tracking purposes a groove structure is produced in the lacquer layer during manufacture, provided with pits containing address

Dr L. Vriens and Ing. B. A. J. Jacobs are with Philips Research Laboratories, Eindhoven.

[1] K. Bulthuis, M. G. Carasso, J. P. J. Heemskerk, P. J. Kivits, W. J. Kleuters and P. Zalm, IEEE Spectrum **16**, No. 8 (August), 26-33, 1979.

[2] H. C. Haverkorn van Rijsewijk, P. E. J. Legierse and G. E. Thomas, Philips Tech. Rev. **40**, 287-297, 1982.

[3] Special issue, in Philips Tech. Rev. **40**, 149-180, 1982.

[4] An example of the application of DOR is found in the Megadoc system, as described by J. A. de Vos, Philips Tech. Rev. **39**, 329-343, 1980.

information and a sinusoidal profile for synchronization [1]. The user writes in the grooves by making holes in the recording layer. *Fig. 1* shows a micrograph, made with a scanning electron microscope (SEM), of part of a DOR disc.

Lacquer layers with the required pattern are produced by the same method as used in the manufacture of LaserVision discs [2][5]. A liquid lacquer, polymerizable with ultraviolet light (2p lacquer, from *p*hoto-*p*olymerization) is made to flow over the surface of a mould into which the substrate is pressed. The lacquer is cured by exposing it to ultraviolet light, so that it adheres to the substrate. After the substrate with the cured lacquer is removed from the mould, the recording layer can be applied.

The choice of material for the recording layer must be matched to the laser used for writing and read-out. Preference is given to an AlGaAs diode laser with emission in the near infrared (about 820 nm). This means that the recording layer must absorb and reflect sufficiently in this wavelength range. A suitable material is one whose properties not only make fast recording and good read-out possible but also ensure that both the disc and the stored information will not deteriorate with time.

Investigations in various laboratories have shown that different types of materials can be considered for use as the recording layer on DOR discs [6]. Good recording is achieved with thin polycrystalline films of tellurium. This element has a number of desirable properties, such as sufficient absorption in the near infrared, a low melting point, low thermal conductivity and low specific heat. This means that little energy is necessary to melt small areas with an AlGaAs laser. With tellurium this gives a low threshold energy for hole formation. The films also provide sufficient infrared reflection, making good focusing, tracking and read-out possible. A problem with tellurium films is their limited useful life. In a humid environment they quickly become oxidized, which reduces their sensitivity for the formation of new holes and leads to the loss of information already written. Another problem is the difficulty of controlling the transition from the amorphous phase to the polycrystalline phase; this can cause stresses and cracks in the films.

DOR layers of better durability can be produced with alloys of tellurium [7]. The presence of selenium, for example, considerably reduces the tendency to oxidation, and the presence of other elements helps to minimize stresses and crack formation. A disadvantage of tellurium alloys as compared with pure tellurium is their lower absorption in the near infrared, which in general means a higher threshold energy for hole formation. It has however been possible to find alloys that have much better durability and at the same time a low threshold energy.

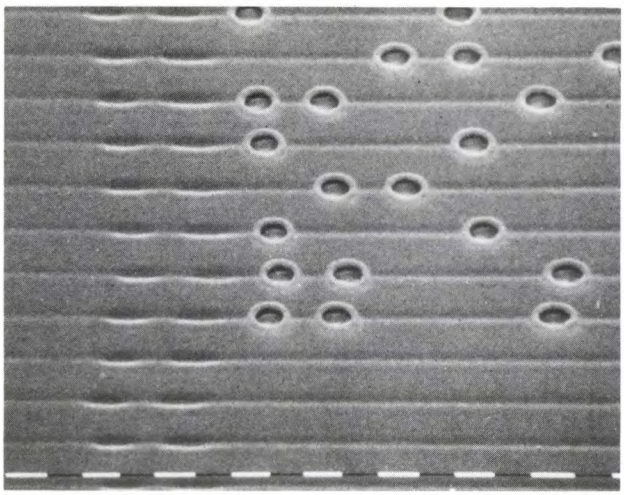

Fig. 1. SEM micrograph (scale divisions 1 μm) of part of a DOR disc [1]. The pregrooved structure is followed during writing and read-out. This structure contains small elongated pits containing address information (*left*) and data stored by means of writing small holes in the recording layer (*right*).

An entirely different class of materials for non-erasable optical recording are the organic dyes. The potentialities of these materials will be discussed in the next article [8].

The material for the recording layer has to meet some additional requirements if the stored information is also to be erasable. An example of erasable recording is magneto-optical recording with amorphous magnetic layers, e.g. of an alloy consisting of gadolinium, terbium and iron [6][9].

Erasable optical recording is also possible with polycrystalline films of some tellurium alloys [10]. Localized areas of the film are melted with a laser. During cooling after the laser pulse, the melted areas become amorphous. Information read-out is based on the difference in reflection between the amorphous phase and the polycrystalline phase. The written information can be erased by making the amorphous areas polycrystalline again, for example by treatment in an oven. With some alloys a laser can be used for local erasures.

In the investigation described in this article, we were mainly concerned with non-erasable DOR with a tellurium alloy. The main objective was to find an alloy of suitable composition. Important considerations include the optical and thermal properties of the recording layer, the structure of the layer and the holes formed, the durability and also the effect of the 2p lacquer. To study these properties we applied a large number of tellurium alloys to small plates of

polymethyl methacrylate (PMMA) and tested their suitability for DOR. Combinations with different 2p lacquers were also investigated.

An important result of these investigations was that alloys with the correct composition of tellurium, selenium, antimony and sulphur are capable of meeting the requirements of DOR. Some combinations of alloys and 2p lacquers were studied for their behaviour on DOR discs. It was found that with a suitable alloy and 2p lacquer DOR discs can be made that have good writing and read-out characteristics as well as a long useful life.

In this article we shall first give a brief description of the Philips DOR system. We shall then look at the requirements that the materials must meet. After an account of experiments with small discs, we discuss results obtained with large DOR discs.

The Philips DOR system

The use of a disc with a pregrooved structure is one of the main features of the Philips DOR system [1]. This structure, produced in the 2p lacquer, consists of a spiral groove with a pitch of 1.6 μm, a width of 0.6 μm and a depth of 0.07 μm. During writing and read-out this groove is tracked by the laser beam. Each track is divided into sectors that start with pits 0.14 μm deep containing address information. The remaining part (> 90%) is earmarked for the writing of information in the recording layer, with synchronization provided by a sinusoidal profile in the groove. *Fig. 2* shows a diagram of a part of a sector, with the signal obtained on read-out. At present the disc contains 32 000 tracks of 32 sectors. The number of bits that can be stored per sector in one track is about 8200. This means that one side of a DOR disc has a storage capacity of about 8×10^9 bits. At a rate of rotation of 8 Hz the writing speed is about 2×10^6 bits/s.

In the same way as in the manufacture of LaserVision discs [2][5], the lacquer structure is applied extremely accurately by means of a 'stamper' manufactured with a 'mastering recorder'. This method has the advantage that the mechanical parts of the DOR recorder do not have to meet such a critical specification as would be required if the discs were not pregrooved. Rapid and accurate positioning of the laser beam is achieved by simple monitoring of the tracking and synchronization signal. Shifting the accuracy of positioning to the surface of the disc keeps the price of the DOR recorder low. Another advantage is the random access: the address information can be used to direct the laser beam to any location of the disc within an average time of about 200 ms.

The 820 nm AlGaAs laser of the DOR system has the advantages of compactness and low price [11]. In addition, the beam intensity can be modulated by the electric current, so that no external light modulator is required. The pulse duration and output power for writing are matched to the frequency of rotation of the disc and to the threshold energy for hole formation. Reliable recording is achieved with a pulse duration of 50 ns and an output power of 50 mW. Because of the transmission losses in the optical system the power incident on the disc is in fact 10 to 20 mW. The output power used for read-out is a factor of 10 lower, so that there is no risk of melting the recording layer.

Recorded information is immediately checked by making use of the DRAW principle ('Direct Read After Write'). If more than one error is found in a sector, all the data of that sector is rewritten in another sector. By 'interleaving' the data within a sector and adding parity bits [3], errors that occur after writing can frequently be corrected. In this way the

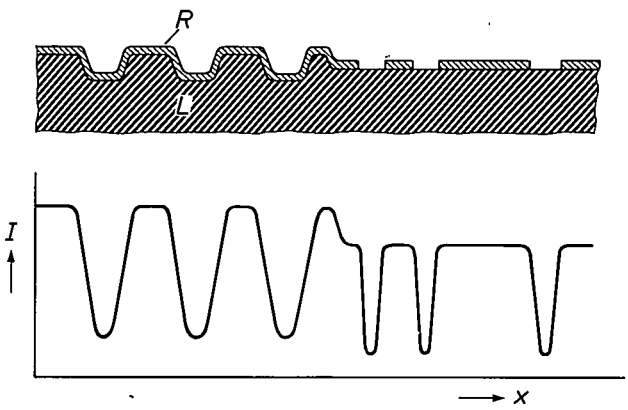

Fig. 2. *Above:* Cross-section of part of a sector of a DOR disc. The lacquer layer *L* has a groove 0.07 μm deep for tracking and is coated with a recording layer *R* about 0.03 μm thick. Located on the left are pits 0.14 μm deep containing address information, and data is stored on the right in the form of holes in the recording layer. The sinusoidal profile for synchronization is not shown. *Below:* Schematic representation of the signal current *I* obtained on read-out, as a function of the position *x* of the laser beam. At the location of the pits and holes an attenuation of the read-out signal occurs as a result of reduced reflectance.

[5] J. G. Kloosterboer, G. J. M. Lippits and H. C. Meinders, Philips Tech. Rev. 40, 298-309, 1982.
[6] A survey of the various possibilities is given in H. Brody, Laser Focus 17, No. 8 (August), 47-52, 1981.
[7] M. Terao, K. Shigematsu, M. Ojima, Y. Taniguchi, S. Horigome and S. Yonezawa, J. Appl. Phys. 50, 6881-6886, 1979.
[8] D. J. Gravesteijn and J. van der Veen, this issue, pp. 325-333.
[9] An article on magneto-optical recording will appear in a forthcoming issue of this journal.
[10] R. J. von Gutfeld and P. Chaudhari, J. Appl. Phys. 43, 4688-4693, 1972;
S. R. Ovshinsky, J. Appl. Photogr. Eng. 3, 35-39, 1977;
K. Watanabe, N. Sato and S. Miyaoka, J. Appl. Phys. 54, 1256-1260, 1983.
[11] J. C. J. Finck. H. J. M. van der Laak and J. T. Schrama, Philips Tech. Rev. 39, 37-47, 1980.

probability of a bit being read out erroneously (the bit error rate or BER) is reduced from 10^{-5}-10^{-6} to less than 10^{-12}.

A preferred version of the DOR disc is the 'Philips Air Sandwich' [12]; see *fig. 3*. It consists of two glass substrates 1.3 mm thick and of 300 mm diameter, each coated on the inner side with a 2p lacquer and a recording layer. The substrates are separated by an inner spacer with a centring hole, and a metal outer

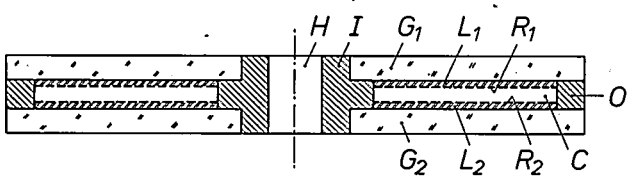

Fig. 3. Diagram of the cross-section of the Philips Air Sandwich for DOR discs [12]. The inner surfaces of the glass substrates G_1 and G_2 are coated with lacquer layers L_1 and L_2 and with recording layers R_1 and R_2. The plates are kept apart by a metal inner spacer I with centring hole H and a metal outer spacer O. The cavity C between the two plates, which is filled with dry air, is hermetically sealed.

spacer; the internal space is filled with dry air. Originally, when the recording layer was a thin film of tellurium, the Air Sandwich was designed chiefly to exclude humidity. Through the use of tellurium alloys, which are much less sensitive to humidity, the principal advantage of the Air Sandwich is that it keeps the recording layer free from dust and scratches. Writing and reading take place through the substrate. Particles of dust, fingerprints and scratches on the outside of the disc have no adverse effects since the thickness of the sandwich keeps them well beyond the depth of focus of the objective that focuses the laser beam. An additional advantage of the Air Sandwich is that the user is not exposed to the slight toxicity of the tellurium alloy [13].

Material requirements

The material for the recording layer must satisfy many special requirements [14]. This material has to be applied in the form of a thin homogeneous film that reflects and absorbs the infrared radiation at 820 nm adequately. In view of the limited output power of AlGaAs lasers and the reduction in their useful life if the output power is increased, the threshold energy for the formation of holes must be low. A secondary reason for keeping the threshold energy low is that writing at a lower energy generally results in smaller holes [15]. This means that a higher information density can be obtained or, for the same information density, the crosstalk between neighbouring data bits can be reduced. A low threshold energy also gives well-shaped ('regular') holes. The material displaced during the writing of a hole should form a uniform deposit around the edge of the hole. The formation of such a deposit is determined by the hole-forming mechanism, which depends on the properties of the material [16][17]. As an example *fig. 4* shows SEM micrographs of holes produced in films of different tellurium alloys. The top two pictures show regular submicron holes with a neat rim. The holes in the other pictures are less suitable either because they contain 'droplets' or 'half droplets' of displaced material, because they have not been completely formed or because they have an irregular edge due to spattering of molten material during the writing.

For the production of small regular holes at a low threshold energy a material is required that not only gives sufficient infrared absorption but also has good thermal and hydrodynamic properties. Since the holes are formed by melting parts of the recording layer, the material must have a low melting point. But the melting point is not the only important factor. It turns out that a low boiling point will also tend to give a low threshold energy [16]. In addition the material must have a low specific heat and low thermal conductivity, so that the heat supplied by the laser is effectively utilized. The recording layer must not be liable to cracks caused by stresses and it must be corrosion-resistant. Since the threshold energy must be practically constant over the entire layer, good homogeneity is necessary both on a submicron scale and for the entire disc.

The lacquer layer must also meet special requirements. Properties of this layer affect the formation of the holes in the recording layer. Special importance is attached to the thermal properties, the surface properties and the adhesion between the lacquer and recording layers [17]. There are also special requirements that apply to the processing of 2p lacquers, relating for example to the adhesion on the glass substrate, viscosity, curing rate, dimensional stability and hardness.

Since it is essential to be able to store data for a long time (ten years at least), the durability of the materials must also meet some rather special requirements. When tellurium or a tellurium alloy is used the greatest problem is oxidation. This is accelerated at higher humidity. Dust particles can also initiate accelerated localized electrochemical corrosion. Oxidation reduces the absorption of the layer, causing increased transmission and in general diminished reflection, and makes the layer less homogeneous. These effects lead to a higher threshold energy and a lower signal-to-

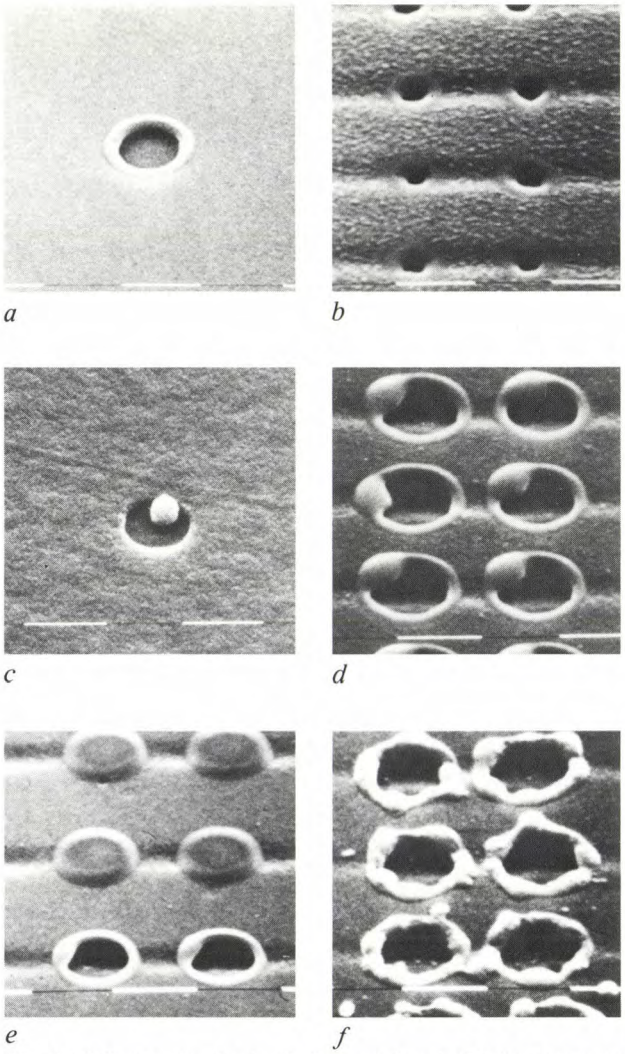

Fig. 4. SEM micrographs (scale divisions 1 μm) of holes written in layers of different tellurium alloys [17]. *a*) Well-shaped hole with thickened edge. *b*) Well-shaped holes with ring-shaped edge. *c*) Hole with a droplet of displaced material. *d*) Holes with an edge thickened with half a droplet. *e*) Holes not fully formed. *f*) Holes with an irregular edge.

noise ratio during read-out. During ageing cracks may form in the recording layer, depending on its composition, the method of applying it and the choice of 2p lacquer. Blisters may also be formed, so that particles from 1 to 10 μm in size may flake off. This is due to the swelling and shrinking of the 2p layer as humidity and temperature change. Another problem is deformation of the pregrooved structure of the 2p layer, again caused by the absorption of moisture and swelling.

Optimization of the tellurium alloy

In the search for the optimum composition of the recording layer different tellurium alloys were applied to plates (5 cm × 5 cm) of PMMA and, incidentally, to glass substrates [18]. Thin films were obtained by flash-evaporation [19] or magnetron sputtering [20]. The composition of the films was verified by X-ray fluorescence [21] and by Rutherford backscattering with high-energy helium ions [22]. Optical transmittance and reflectance were measured at 820 nm and other wavelengths. The recording characteristics were studied by writing and reading holes with a laser beam. The microstructure of the films and the holes were examined by scanning and transmission electron microscopes (SEM and TEM).

All these experiments were performed immediately after the films were evaporated, and also at different times during ageing. To assess the effect of different ageing conditions, the plates were made in identical sets of six by simultaneous vacuum evaporation. The plates were tested at room temperature, in an oven at 90 °C and in an environmental test chamber, in which the temperature was cycled between 25 °C and 65 °C at a relative humidity of about 93% (the Z/AD test [23]). It turns out that these three tests provide complementary information. In general the Z/AD test is the most severe; it greatly accelerates the oxidation.

One tellurium alloy (with thallium) gave good corrosion resistance in the environmental chamber but deteriorated rapidly in the oven at 90 °C. It turned out that this was due to the formation of volatile products. Other tellurium alloys stood up well to the oven and the Z/AD test but deteriorated at room temperature. This was the case with amorphous films, which slowly and inhomogeneously changed to the polycrystalline phase. In the oven and in the environmental chamber fast crystallization occurred, giving rise to homogeneous fine-polycrystalline films.

[12] G. C. Kenney, D. Y. K. Lou, R. McFarlane, A. Y. Chan, J. S. Nadan, T. R. Kohler, J. G. Wagner and F. Zernike, IEEE Spectrum **16**, No. 2 (February), 33-38, 1979.

[13] J. van der Veen and C. Rooijmans, Proc. SPIE **420**, 141-143, 1983.

[14] L. Vriens, B. Jacobs, D. Broer and W. de Poorter, SID 83 Digest, Philadelphia 1983, pp. 52-53.

[15] R. C. Miller, R. H. Willens, H. A. Watson, L. A. D'Asaro and M. Feldman, Bell Syst. Tech. J. **58**, 1909-1998, 1979;
D. Y. Lou, G. M. Blom and G. C. Kenney, J. Vac. Sci. & Technol. **18**, 78-86, 1981.

[16] P. Kivits, R. de Bont, B. Jacobs and P. Zalm, Thin Solid Films **87**, 215-231, 1982;
G. M. Blom, J. Appl. Phys. **54**, 6175-6182, 1983.

[17] D. J. Broer and L. Vriens, Appl. Phys. A **32**, 107-123, 1983.

[18] The search for suitable recording layers and the ageing tests were performed in cooperation with A. W. de Poorter. The work on 2p lacquer layers for DOR discs was carried out in cooperation with D. J. Broer. The principal results of the experiments with the small plates are to be found in the articles quoted in [14] and [17].

[19] See for example D. S. Campbell and B. Hendry, Br. J. Appl. Phys. **16**, 1719-1725, 1965.

[20] See for example J. J. Scheer and J. Visser, Philips Tech. Rev. **39**, 246-255, 1980.

[21] See for example M. L. Verheijke and A. W. Witmer, Philips Tech. Rev. **34**, 339-343, 1974.

[22] See W. K. Chu, J. W. Mayer and M. A. Nicolet, Backscattering spectrometry, Academic Press, New York 1978.

[23] IEC Publ. No. 68-2-38, Test Z/AD: Composite temperature/humidity cyclic test, IEC, Geneva 1974.

Tellurium films oxidize easily, with the result that their transmittance increases. The oxidation can be slowed down considerably if instead of tellurium a tellurium alloy is used that contains selenium. *Fig. 5* shows the transmittance of tellurium and of four selenium-containing tellurium alloys as a function of the time in the environmental chamber. Whereas the transmittance of the tellurium film has become unacceptably high after only a few days, the transmittance of the alloy films containing more than 10% of selenium is still low after thirty days. Various life tests indicate that the Z/AD test accelerates ageing by a factor of at least 250 as compared with office conditions. The thirty days in the environmental chamber will then correspond to a life of twenty years in normal operating conditions [24]. From the transmittance measurements we may therefore conclude that the susceptibility to oxidation can be sufficiently reduced by using tellurium alloys containing selenium. With a selenium content of about 10%, ageing is slowed down by a factor of 100. Increasing the selenium content to more than 15%, at the expense of the tellurium content, gives hardly any increase in corrosion resistance and has the unwanted effects of reducing the infrared absorption and increasing the threshold energy.

In alloys of tellurium and selenium the transition from the amorphous phase to the polycrystalline phase is generally rapid. The accompanying contraction in volume is considerable, and this leads to stresses in the film. As a result, small cracks may spread over the entire film during ageing; see *fig. 6*. The addition of antimony, whose valency is different from that of selenium and tellurium, inhibits the crystallization (although still rapid at higher temperatures), and at the same time reduces the volume contraction. This follows experimentally from a smaller difference in transmittance between the amorphous and polycrystalline films. Because of the reduced contraction there is less stress in the film on crystallization and therefore no cracking. It was found that even 1% of antimony has a beneficial effect, but 3% provides a good safety margin. The higher the selenium content the greater is the tendency to cracking. The special feature of antimony is that it amply compensates for the adverse influence of selenium on cracking without affecting the resistance to oxidation. At the same time, well-shaped holes can be made with the laser (fig. 4*a* and *b*). The replacement of antimony by some other element, such as indium, thallium, germanium, tin, lead, arsenic or bismuth, gives more corrosion, or less satisfactory holes or volatile products are formed at 90 °C.

With 3 to 5% of antimony, preferably with 1 to 2% of sulphur, the activation energy for the amorphous-to-polycrystalline transition is on the one hand high

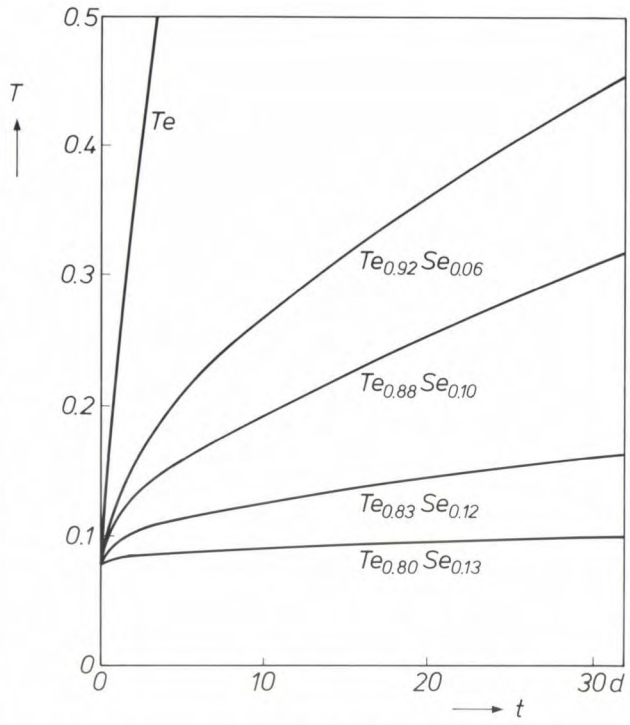

Fig. 5. Transmittance T at 750 nm as a function of time t (in days) in the environmental chamber for the Z/AD test, for a tellurium film and for four tellurium-alloy films of different selenium content. The alloys contain in addition a small amount of antimony and sulphur. The tellurium film gives a much larger increase in transmittance than the alloy films. As the tellurium content in the alloy decreases and the selenium content increases, the increase in transmittance with time becomes smaller. The transmittance of the film with 13% of selenium is no higher than about 10% after 30 days. These films are applied to glass substrates coated with a 2p lacquer. On the PMMA plates the degradation is between 5 and 10 times slower.

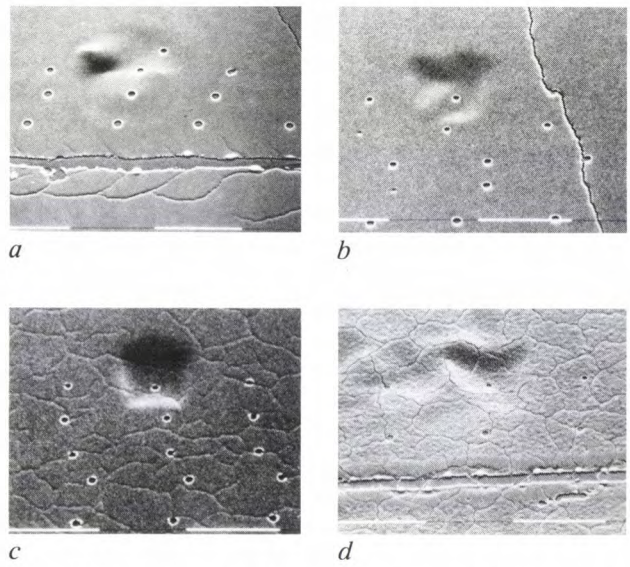

Fig. 6. SEM micrographs of a recording layer of the composition $Te_{0.82}Se_{0.14}S_{0.04}$ under different conditions (scale divisions 10 μm). The local distortion of about 10 μm perceptible in each picture occurred while the SEM micrographs were being made. Before ageing (*a*) and after 7 days of ageing under normal conditions (*b*) the film already shows some cracks. After 7 days of Z/AD test (*c*) and after 120 days at 90 °C (*d*) a pattern of cracks has formed over the entire surface.

enough to prevent a rapid, uncontrolled transition. On the other hand the activation energy is low enough to permit transition to the completely crystalline state in a short time ($\leqslant 15$ min) at a higher temperature. This transition may take place, for example, at 90 °C, during the sealing of the sandwich. At this temperature, high-density nucleation occurs in the film, resulting in the formation of small crystallites. TEM micrographs show that films with a very fine polycrystalline structure are obtained in this way, with grain dimensions of less than 0.05 μm; see *fig. 7*. Well-shaped holes can be written in such fine-polycrystalline films. Since they have good oxidation resistance, this also applies after ageing. *Fig. 8* shows SEM micrographs of films of this type in which a hole has been written after ageing in a normal environment, in an oven at 90 °C, and in the environmental chamber. In all cases the films have kept their high uniformity. With antimony contents greater than 5% the activation energy for the amorphous-to-polycrystalline transition is so high that crystallization cannot take place fast enough at 90 °C: a longer heat treatment is required.

Our experiments showed that good recording layers can be made with alloys based on tellurium, selenium, antimony and sulphur. The best results were obtained with the alloys $Te_xSe_ySb_qS_z$ in the composition region x = 81-85%, y = 11-13%, q = 3-4% and z = 1-2%. Within this region the threshold energy, reflectance and transmittance are practically constant. The films have good recording characteristics and behave well during ageing. They are not susceptible to cracking and have an appropriate activation energy for a rapid but controlled transition from the amorphous phase to the polycrystalline phase.

Effect of the 2p layer

In principle 2p lacquers as used for LaserVision discs [5] are also suitable for use in DOR discs, provided, however, that some additional requirements are met with regard to hole formation in the recording layer. To investigate the effect of the 2p layer the 5 cm × 5 cm plates of PMMA were coated with different 2p lacquers and identical tellurium alloys [17].

Hole-formation studies [15]-[17] have shown that if a low threshold energy is to be achieved the adhesion between the lacquer and the recording layer must not be too strong. The adhesion energy between these two layers is determined mainly by dispersive (Van der Waals) forces and polar (dipole-dipole) forces at the interface. To a good approximation the adhesion energy E_a [25] can be expressed as

$$E_a = 2(\gamma_{1,d}\gamma_{2,d})^{1/2} + 2(\gamma_{1,p}\gamma_{2,p})^{1/2},$$

where $\gamma_{1,d}$ is the dispersive component of the surface tension γ_1 of the recording layer and $\gamma_{2,d}$ is the dispersive component of the surface tension γ_2 of the 2p layer; $\gamma_{1,p}$ and $\gamma_{2,p}$ are the corresponding polar components. Defining the polarity p_i of the recording layer (i = 1) and the 2p layer (i = 2) as:

$$p_i = \gamma_{i,p}/(\gamma_{i,d} + \gamma_{i,p}),$$

we can express E_a as [17][26]:

$$E_a = 2(\gamma_1\gamma_2)^{1/2}\{[(1 - p_1)(1 - p_2)]^{1/2} + (p_1 p_2)^{1/2}\}.$$

For a given recording layer the values of γ_1 and p_1 are

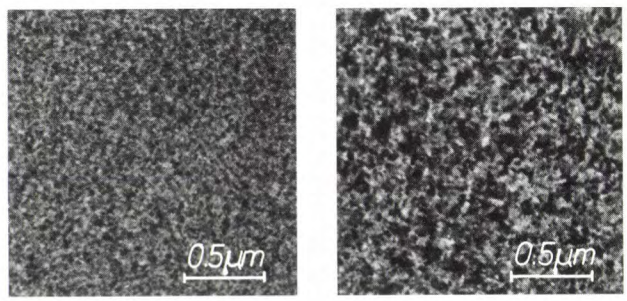

Fig. 7. TEM micrographs of recording layers of composition $Te_{0.75}Se_{0.15}Sb_{0.05}S_{0.05}$ (*left*) and $Te_{0.81}Se_{0.13}Sb_{0.035}S_{0.025}$ (*right*). Both layers have a fine-polycrystalline structure with grains smaller than 0.05 μm.

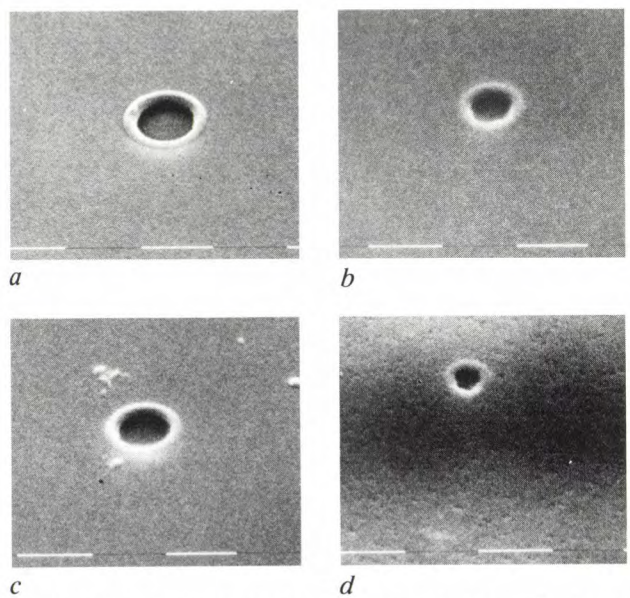

Fig. 8. SEM micrographs (scale divisions 1 μm) of recording layers of the composition $Te_{0.78}Se_{0.14}Sb_{0.05}S_{0.03}$ in which a hole is written after ageing for 6 and 200 days in a normal environment (*a* and *b*), 120 days in an oven at 90 °C (*c*) and 120 days of Z/AD test (*d*). In all cases the layers are still very uniform and the holes are formed correctly.

[24] 'Normal' DOR discs in a (sealed) Air Sandwich are hermetically sealed as an extra safety provision. This was separately tested and was shown to have a life of at least 100 days in a Z/AD test.

[25] D. K. Owens and R. C. Wendt, J. Appl. Polym. Sci. **13**, 1741-1747, 1969.

[26] B. W. Cherry, Polymer surfaces, Cambridge University Press, Cambridge 1981.

fixed, whereas γ_2 and p_2 depend on the composition of the 2p layer.

This equation shows that when the value of p_2 is constant the adhesion energy decreases as γ_2 decreases. This situation occurs for example during the copolymerization of 1,6-hexanediol diacrylate (HDDA) [5] with hexafluorisopropyl acrylate (HFPA) with increasing HFPA content; see *fig. 9*. The decrease in E_a does indeed result in a decrease in the threshold energy.

It may also be deduced that, for constant values of γ_1, p_1 and γ_2, the adhesion energy decreases as the difference between p_2 and p_1 increases. This effect is found in the copolymerization of HDDA with the polar monomer N-vinylpyrrolidone (NVP) [5], where the lacquer layer has a higher polarity with respect to the recording layer. *Fig. 10* shows that an increase in p_2 as a result of an increasing NVP content leads to a considerable drop in threshold energy [17].

The generation of holes in the recording layer also depends on the cross-linking in the lacquer and the average molecular weight of the lacquer polymers. As the cross-linking of the polymers in the lacquer and their molecular weight decrease, the threshold energy decreases [17]. In linear PMMA, for instance, the threshold energy is much lower than in the strongly cross-linked poly-HDDA, although it has almost the same values for γ_2 and p_2. This behaviour does not

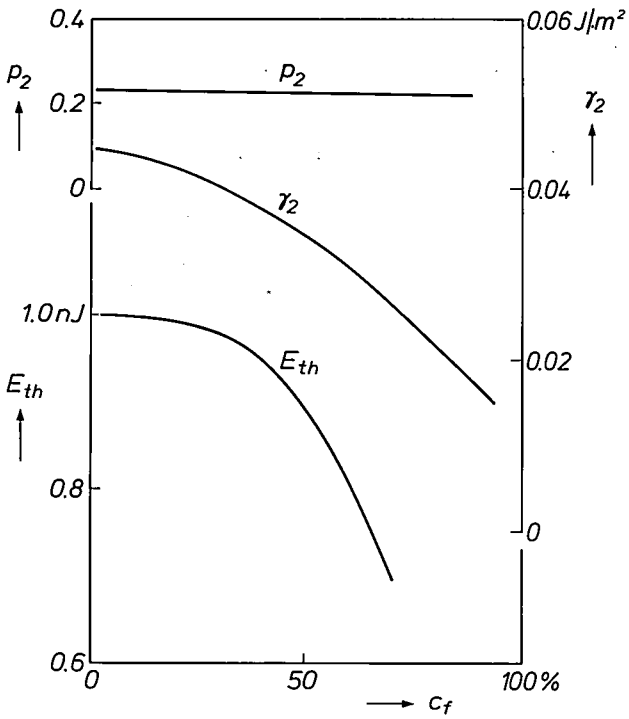

Fig. 9. Effect of the copolymerization of the monomers HDDA and HFPA on the polarity p_2 and the surface tension γ_2 of the lacquer layer, and on the threshold energy E_{th} for hole formation in a 0.03-μm recording layer deposited on it [17]. An increase in the HFPA content c_f (wt.%) has very little effect on p_2 but causes a marked decrease in γ_2 and hence in E_{th}.

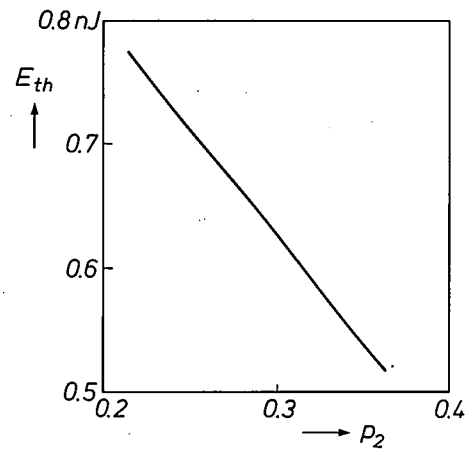

Fig. 10. Effect of lacquer polarity p_2 on the threshold energy E_{th} for hole formation in an 0.03-μm recording layer that has a lower polarity [17]. The lacquer layers were obtained by copolymerization of the monomers HDDA and NVP. The increase in p_2 at a higher NVP content results in a marked drop in E_{th}.

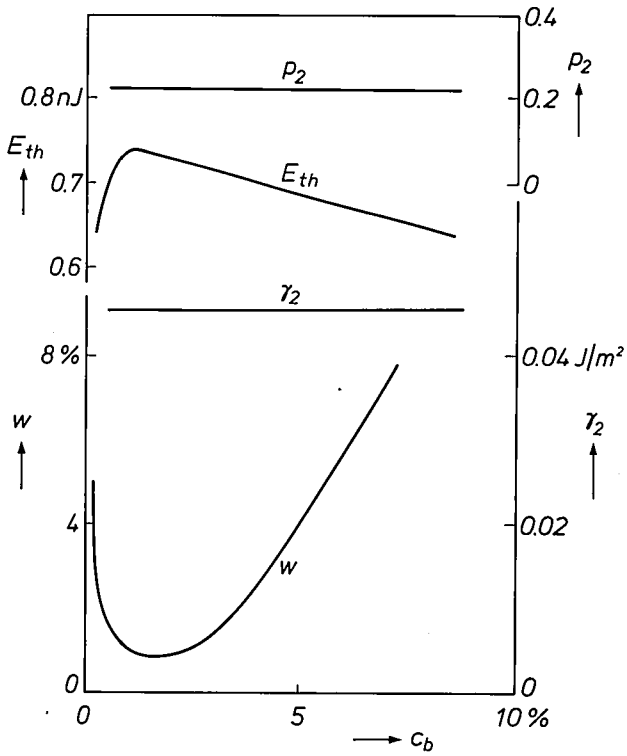

Fig. 11. Effect of the copolymerization of HDDA and the photoinitiator BME on the polarity p_2 and the surface tension γ_2 of the lacquer layer, the relative number w (wt.%) of mobile molecules in this layer and the threshold energy E_{th} for hole formation in a 0.03-μm recording layer deposited on it [17]. Unlike p_2 and γ_2, the value of w is closely dependent on the BME content c_b (wt.%). With a low BME content the lacquer layer still contains a large number of HDDA monomers, with a high BME content there are still many free BME molecules. The presence of mobile molecules has the effect of reducing E_{th}.

follow from the equation given for E_a. It is assumed that as well as the static adhesion energy, the dynamic behaviour at high temperature is also important. With linear polymers the 'dynamic' adhesion energy is low.

The dynamic adhesion energy is also reduced by the presence of small mobile molecules in the lacquer. This is found, for example, when the quantity of mobile molecules in the HDDA lacquer is changed by varying the content of the photo-initiator benzoin methyl ether (BME); see *fig. 11*: When less than 1% of BME is used, incomplete polymerization occurs, so that there is a high content of monomer molecules in the cured lacquer. With more than 2% of BME there will be a residue of unreacted initiator molecules. Fig. 11 shows that in these cases the lowest threshold energy is obtained. The surface tension and the polarity of the lacquer are independent of the BME content. Although mobile molecules in the lacquer layer have the advantage of reducing the threshold energy, experiments have shown that they lead to the increased occurrence of stresses and cracks in the recording layer.

The factors that favour a low threshold energy — low γ_2, a large difference between p_2 and p_1, linear polymers and mobile molecules — have the disadvantage, however, of reducing the dimensional stability and the durability of the 2p layer. Since the dimensional stability of DOR discs is essential for the maintenance of the pregrooved structure, a compromise has to be found.

Table I. Composition of six tellurium alloys used for the recording layer in the experiments on DOR discs.

Notation	at.% Te	Se	Sb	S
$TS_3(60)$	60	25	10	5
$TS_3(75)$	75	15	5	5
$TS_3(79)$	79.5	13.5	4	3
$TS_3(83)$	83	12	3	2
$TS_3(86)$	86	11	1.5	1.5
$TS_3(88)$	88	10	1	1

Table II. Composition of three lacquer layers used in the experiments on DOR discs.

Notation	Composition (wt.%)
LA 467	20% trimethylolpropane triacrylate (TMPTA) 20% 1,4-butanediol diacrylate (BDDA) 58% 2-ethylhexyl acrylate (EHA) 2% benzoin isobutyl ether [a]
LA 511	10% TMPTA 57% tripropylene glycol diacrylate (TPGDA) 29% N-vinylpyrrolidone (NVP) 4% 1,1-dimethoxy-1-phenyl acetophenone (DMPA) [b]
L 10044	96% 1,6-hexanediol diacrylate (HDDA) 4% DMPA [b]

[a] Photo-initiator, marketed under the name of Vicure 10.
[b] Photo-initiator, marketed under the name of Irgacure 651.

The experiments with different 2p layers made important contributions to the understanding of the mechanism of hole formation [17]. Experimental results support the model in which hole formation occurs through the melting of the tellurium alloy, the vaporization of some material (in general from the 2p layer) at the interface of the recording film and the 2p layer, and the formation of a small blister. The blister formation is accompanied by a radial flow of the molten alloy, caused by surface tension and surface-tension gradients, to the edge of the molten area.

The investigation with the small plates yielded a great deal of information about the choice of materials for the recording film and the lacquer layer. To establish the extent to which the results are also applicable to DOR discs, and to make further optimization possible, some combinations of materials were investigated to determine their behaviour in DOR discs.

Experiments with pregrooved DOR discs

The experiments with DOR discs [27] were made with substrates of toughened glass, of diameter 300 mm. These were coated with a 2p lacquer layer 2 to 20 μm thick, containing a spiral groove with address and synchronization information. A tellurium alloy film about 0.03 μm thick was then applied by either flash evaporation or magnetron sputtering. In each case one of the discs thus produced was sealed to a blank substrate to form an Air Sandwich (fig. 3).

On the basis of the results with the small plates six tellurium alloys and three lacquers were used. The compositions are given in *Tables I* and *II*. To study accelerated ageing two vent holes, 5 mm × 0.5 mm, were made in the outer spacer of the Air Sandwich. This was done because an ageing test on a hermetically sealed sandwich is mainly a test of the quality of the seal rather than the quality of the recording layer and the lacquer [24]. Before and during the ageing the transmittance and reflectance of the discs were measured, together with the threshold energy for hole formation, the signal-to-noise ratio (SNR), the pilot-to-

[27] The research on DOR discs was carried out in cooperation with A. Huijser and W. G. V. M. Rippens of these laboratories and with J. A. Markvoort, A. M. J. Spruijt and P. H. G. M. Vromans of the DOR laboratory of the Data Systems Division, later with Optical Media Laboratories.

noise ratio (PNR), i.e. the signal-to-noise ratio of the synchronization profile in the groove, and the bit error rate (BER). The quality of the layers and the holes produced was investigated with an optical microscope and, after ageing, with a scanning electron microscope as well.

The signal-to-noise ratio that can be achieved during read-out depends on the energy with which the information is written into the recording layer [28]. The lacquer layer also plays an important part here. As an example *fig. 12* gives a plot of the signal-to-noise ratio against the writing energy for the tellurium alloy $TS_3(79)$; the lacquers used were LA 467 and LA 511. When the writing energy is low the laser has no effect on the recording layer, so that there is no signal on read-out. At a rather higher energy (about 0.18 nJ) the laser pulse causes localized melting of the alloy, but holes are not produced. Because the melted areas cool very rapidly, amorphous regions with a lower reflectance form after termination of the laser pulse. These regions are detected on read-out, and the signal-to-noise ratio rises to more than 40 dB. At a further increase in the writing energy the molten areas acquire such a high temperature that hole formation starts. This initially gives a decrease in the signal-to-noise ratio because the holes are not yet formed at all writing locations. At this writing energy the effect of the lacquer layer is clearly observable [28]. It appears for example, in differences in threshold energy for complete hole formation, caused by differences in adhesion and vaporization. At an even higher writing energy only holes are formed, producing saturation of the signal-to-noise ratio at about 56 dB.

As expected, the signal-to-noise ratio of the information written on a disc decreases during ageing. The rate of decrease depends on the ageing conditions [29]. *Fig. 13* shows the behaviour of the signal-to-noise ratio for a disc with the alloy $TS_3(75)$ and the lacquer LA 511 during ageing at 45 °C and 95% humidity and during the Z/AD test. The greater decrease during the Z/AD test is attributable to alternating swelling and shrinking of the lacquer caused by the cyclic alternations of temperature at high humidity. This damages the recording layer and hence the information written in it (e.g. because of blistering).

The swelling and shrinking of the lacquer also adversely affects the information prerecorded in the lacquer layer. Because of the low modulation depth of the synchronization profile the PNR-value is highly sensitive to any degradation of the pregrooved structure. The decrease in the PNR-value depends on the type of lacquer layer and the ageing conditions. *Fig. 14* shows the effect of ageing in the Z/AD test for the three lacquers in Table II. With the lacquer L 10044 only a slight decrease is observed. This is attributable to the relatively high cross-linking in this lacquer, which therefore shows little tendency to swell or shrink.

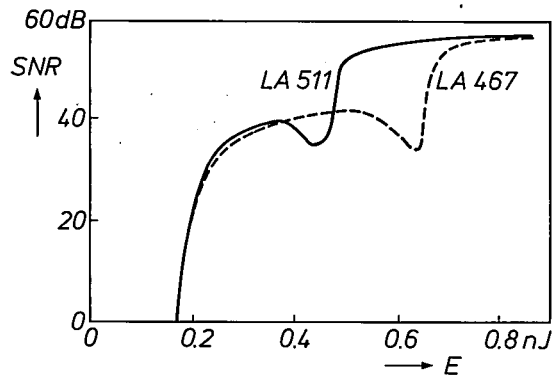

Fig. 12. Signal-to-noise ratio *SNR* as a function of the writing energy *E* for a $TS_3(79)$ film on the lacquers LA 467 and LA 511 [28]. As the writing energy increases beyond an energy value of about 0.18 nJ the *SNR* first increases sharply, then decreases slightly before rising finally to a saturation value of about 56 dB. The effect of the lacquer layer is clearly noticeable in the range where *SNR* decreases with the writing energy.

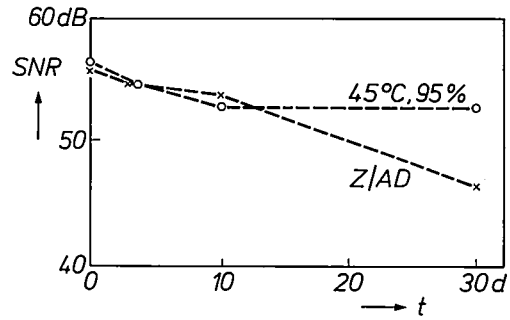

Fig. 13. Signal-to-noise ratio *SNR* as a function of the time *t* at a relative humidity of 95% and a temperature of 45 °C and during the Z/AD test, for a $TS_3(75)$ film on the lacquer LA 511 [29]. For long periods of exposure the Z/AD test results in a greater decrease in *SNR*.

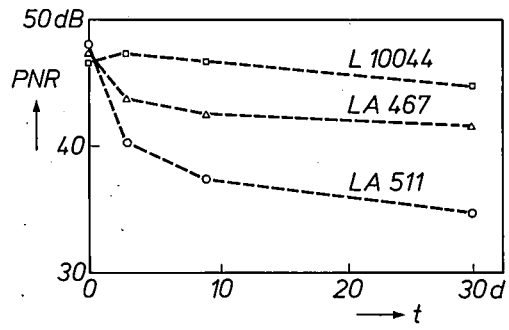

Fig. 14. Pilot-to-noise ratio *PNR* in a $TS_3(79)$ film on the lacquers indicated in Table II, as a function of time *t* in the Z/AD test. The decrease in *PNR* is closely dependent on the lacquer [28]. Only a slight decrease is found with the lacquer L 10044.

A lower signal-to-noise ratio is also observed when the information is written after the disc has been aged. Here again the compositions of alloy and lacquer are important. *Fig. 15* shows SEM micrographs of a $TS_3(75)$ layer and a $TS_3(60)$ layer with holes written before and after a Z/AD test for a total of 100 days. The holes written before ageing have a well-shaped edge. After ageing, poorly defined holes are generated. Since the oxides formed during ageing have a higher melting point than the corresponding elements and the homogeneity of the recording layers is affected, the holes are not so easily generated and hole formation is less regular.

The BER of DOR discs is determined by initial errors and ageing errors. The initial errors are due to imperfections in the substrate, the lacquer layer and the recording layer. With the alloys and lacquers described the initial BER-values found without corrections range from 10^{-5} to 10^{-6}. Accelerated ageing in the Z/AD test caused the BER-values to double within 10 to 50 days. This is mainly due to the occurrence of new errors in the recording layer, generally in the form of blisters. As mentioned, blistering is attributed to cyclic swelling and shrinking of the lacquer. This causes deformations in the recording layer of magnitude between 1 and 10 μm in areas where there is inadequate adhesion to the lacquer layer or insufficient cohesion in the lacquer. An important factor here is the difference in surface tension on the lacquer side and on the air side, causing the film to peel off and curl up at some places; see *fig. 16*. The conditions in the Z/AD test are exceptional, however. This effect will not occur in normal office use. The hermetic sealing of the discs gives an extra safety margin.

The results obtained with DOR discs generally agree well with the expectations based on the experiments with the small plates. The agreement was particularly good for the optimum compositions of the recording and lacquer layers. A marked difference, however, was the five to ten times faster degradation of the recording layers in the Z/AD test. This relates to the oxidation, as measured by optical transmission, and also to the blistering and decrease in homogeneity, as measured with the SEM. Further investigation showed that these differences are largely connected with the use of a different type of substrate: for DOR discs glass is used instead of PMMA to give a hermetic seal and protection from scratches. Results obtained with ESCA (Electron Spectroscopy for Chemical Analysis), Rutherford backscattering and SIMS (Secondary-Ion Mass Spectrometry) [30] showed that sodium and potassium can diffuse from a toughened glass substrate through the 2p lacquer into the recording layer. This does not happen when a quartz-glass or PMMA substrate is used. The alkali content in the recording layer can rise to between 10 and 20% as a result of this diffusion. It may be assumed that sodium and potassium are each chemically combined in the recording layer, resulting in accelerated degradation of the tellurium alloy.

The degradation is less pronounced for a thicker 2p layer. The type of lacquer also has an effect: with

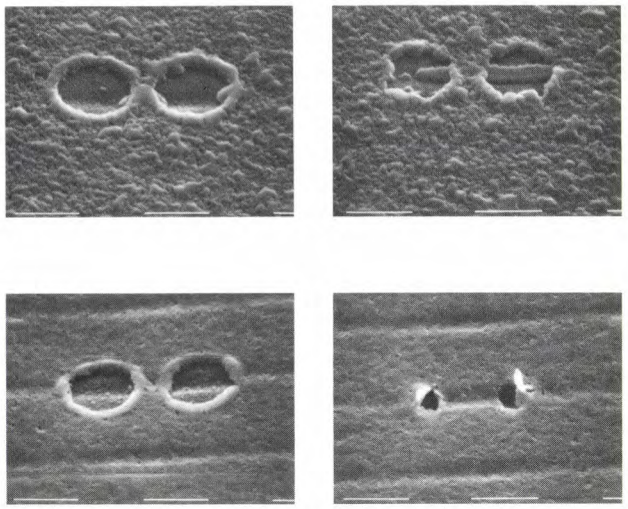

Fig. 15. SEM micrographs (scale divisions 1 μm) of a $TS_3(75)$ film (*above*) and a $TS_3(60)$ film (*below*) in which holes were written before (*left*) and after ageing of 100 days in a Z/AD test (*right*). After ageing, irregular holes are formed. The micrographs were made after 100 days of Z/AD test [29].

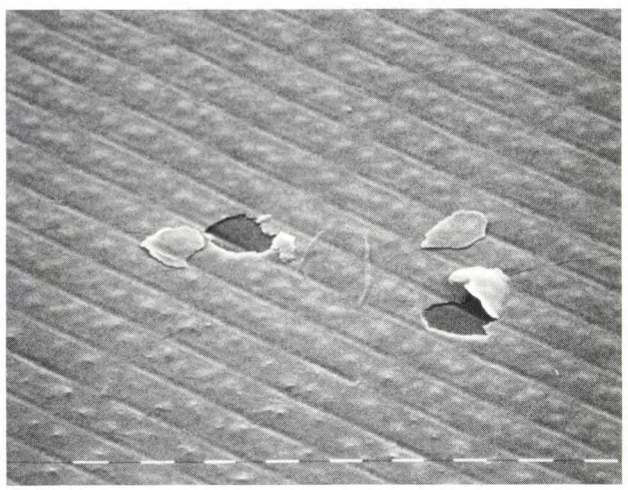

Fig. 16. SEM micrographs (scale division 1 μm) of a severely blistered recording layer, after 100 days of Z/AD test [29]. At some places the recording layer has peeled away from the lacquer layer.

[28] J. A. Markvoort, A. M. J. Spruijt, P. H. G. M. Vromans, A. Huijser, B. Jacobs, W. Rippens and L. Vriens, Proc. SPIE **420**, 134-140, 1983.

[29] A. Huijser, B. Jacobs, L. Vriens, J. Markvoort, A. Spruijt and P. Vromans, Proc. SPIE **382**, 270-275, 1983.

[30] See H. H. Brongersma, F. Meijer and H. W. Werner, Philips Tech. Rev. **34**, 357-369, 1974.

L 10044 the degradation is much less than with LA 511. This is attributed to the much higher cross-linking in L 10044 and to the smaller amount of mobile molecules in this lacquer, with the result that diffusion through the lacquer layer is inhibited.

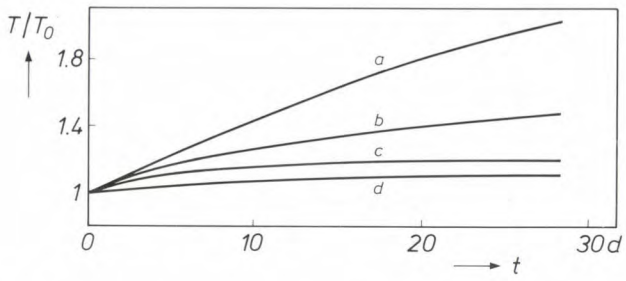

Fig. 17. Increase in transmittance with ageing of a single $TS_3(75)$ film on a glass substrate (*a*) and with an intermediate layer of Y_2O_3 with thicknesses of 6 nm (*b*), 13 nm (*c*) and 21 nm (*d*). The ratio of the transmittance T after ageing to the transmittance T_0 before ageing is plotted as a function of the time t in the Z/AD test. With sufficient thickness of the intermediate layer, the increase in transmittance is substantially reduced.

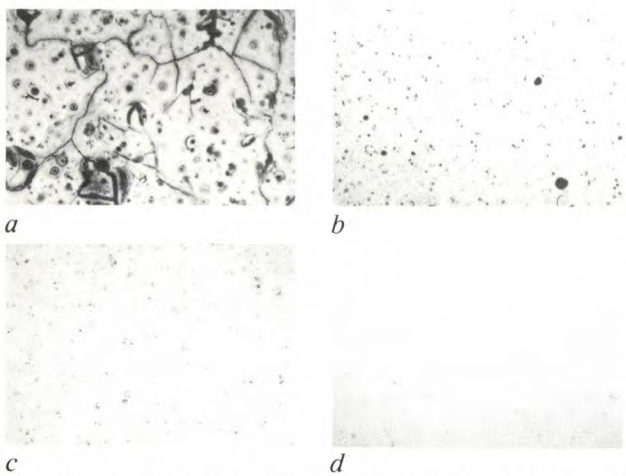

Fig. 18. Micrographs (magnification 100×) made after 24 days of Z/AD test, of a single $TS_3(75)$ film on a glass substrate (*a*) and with an intermediate layer of Y_2O_3 with thicknesses of 6 nm (*b*), 13 nm (*c*) and 21 nm (*d*). The favourable influence of Y_2O_3 is clearly noticeable.

The degradation can be reduced by first depositing a diffusion-inhibiting intermediate layer such as silicon nitride (Si_3N_4), titanium nitride (TiN) or yttrium oxide (Y_2O_3) on the substrate. The inhibiting effect is strong when Y_2O_3 is used, as appears for example from transmission measurements: see *fig. 17*. Whereas the transmittance of the disc without a Y_2O_3 layer has almost doubled after 24 days of Z/AD test, a disc with a 0.02-μm Y_2O_3 layer gives only a slight increase in transmittance. The advantageous effects of the intermediate layer on durability can also be seen in photomicrographs; see *fig. 18*. The use of a diffusion-inhibiting intermediate layer is therefore to be recommended for non-hermetically sealed sandwiches or for open discs. Such a layer is not required for hermetically sealed DOR discs in an Air Sandwich, since alkali diffusion does not occur in dry 2p layers.

Summary. With the Philips DOR (digital optical recording) system large amounts of data (10^{10} bits, 500 000 A4 pages) can be stored on discs the size of an LP disc. Writing and reading are carried out with a pulsed and focused light beam (effective diameter about 1 μm) from an AlGaAs laser emitting at 820 nm. A DOR disc consists of a glass substrate coated with a UV photopolymerized lacquer layer and a recording layer. The lacquer layer is pregrooved for tracking purposes and provided with information for addressing and synchronization. The recording layer consists of a material in which the laser beam can easily write holes with a significant difference in contrast on read-out. Experiments on small PMMA plates showed that some fine-polycrystalline films of tellurium alloyed with selenium, antimony and sulphur meet the special requirements for DOR much better than the tellurium films originally used; ageing is a hundred times slower. The lacquer layer also has a considerable effect on the recording and ageing behaviour. The results obtained have largely been confirmed by experiments with DOR discs. An important difference was the accelerated degradation of non-hermetically sealed DOR discs as a consequence of alkali diffusion from the glass substrate. This effect can be suppressed by using a less penetrable lacquer, by applying an intermediate layer of a material such as Y_2O_3, or by using a hermetically sealed sandwich.

Organic-dye films for optical recording

D. J. Gravesteijn and J. van der Veen

Like the tellurium alloys described in the previous article, some organic dyes have optical, thermal and mechanical properties that enable them to satisfy the requirements made on optical recording materials. The use of organic-dye films can have advantages: they are easy to prepare, permit high writing speeds, and both digital and analog (video) information can be recorded. Although the search for suitable dyes is by no means at an end, interesting results have already been achieved with a number of dyes and with the recording characteristics of films prepared from them.

Introduction

Organic dyes consist in general of unsaturated conjugated hydrocarbon compounds in which heteroatoms (e.g. nitrogen, oxygen, sulphur) are incorporated. The 'pi electrons' of the delocalized double bonds are excited with relatively little energy. Depending on the type of compound, the first absorption band, corresponding to the lowest excitation energy, may be situated in the near infrared, in the visible wavelength range or in the near ultraviolet.

To be useful as a material for optical recording with an AlGaAs laser the dyes must adequately absorb infrared light at 820 nm. Most organic dyes, however, give strong absorption only at shorter wavelengths and are therefore ruled out. A number of the dyes that absorb well at 820 nm have been investigated with a view to their use for optical recording. Experiments have included single-dye films [1], polymer films containing dyes [2] and combinations of dye films and tellurium films [3]. Various studies have shown that with some organic dyes it is possible to prepare films that have good recording properties. These dyes not only have an intense narrow-band absorption at about 820 nm, but also have a low melting point and low thermal conductivity. Pits are formed in such films with a laser beam of relatively low energy. The films can also give strong reflection at 820 nm, thus readily allowing tracking and read-out of information written into the film. Some dyes in addition possess sufficient physical and chemical stability, thus ensuring the durability of the discs and the information stored in them.

Organic-dye films may offer advantages over tellurium alloys [4]. In many cases smooth homogeneous films can be applied by means of a 'spin-coating' process. The threshold energy for the formation of pits is low, enabling high writing speeds to be achieved. Provisions can also be made for the storage of analog video information, by varying the length of the pits and the spacing between them, and for increasing the information density (packing density) by varying the depth of the pits.

In the investigation described in this article, aimed at finding a suitable dye, a provisional selection was

Dr D. J. Gravesteijn and Dr J. van der Veen are with Philips Research Laboratories, Eindhoven

[1] V. Novotny and L. Alexandru, J. Appl. Phys. **50**, 1215-1221, 1979 and J. Appl. Polym. Sci. **24**, 1321-1328, 1979;
V. B. Jipson and C. R. Jones, J. Vac. Sci. & Technol. **18**, 105-109, 1981.

[2] K. Y. Law, P. S. Vincett, R. O. Loutfy, L. Alexandru, M. A. Hopper, J. H. Sharp and G. E. Johnson, Appl. Phys. Lett. **36**, 884-885, 1980;
K. Y. Law, P. S. Vincett and G. E. Johnson, Appl. Phys. Lett. **39**, 718-720, 1981;
D. G. Howe and J. J. Wrobel, J. Vac. Sci. & Technol. **18**, 92-99, 1981.

[3] A. E. Bell and F. W. Spong, IEEE J. **QE-14**, 487-495, 1978;
P. Kivits, R. de Bont and J. van der Veen, Appl. Phys. A **26**, 101-105, 1981.

[4] L. Vriens and B. A. J. Jacobs, this issue, pp. 313-324.

first made on the basis of general understanding of the physical and chemical properties of organic dyes. Use was also made of data from the literature concerning the advantages and disadvantages of dyes as recording materials. In view of the coating method adopted, it was necessary to determine whether the dyes are sufficiently soluble in certain organic solvents, while at the same time insoluble in water to ensure stability.

The dyes investigated were applied in the form of films of different thicknesses on substrates of glass, with and without a pregrooved 2p lacquer layer [4], and polymethyl methacrylate (PMMA). The reflectance and transmittance were measured as a function of the thickness and morphology of the films. During the writing of information in the films the intensity and duration of the laser pulse were varied. During the read-out of written information the signal-to-noise ratio was measured. The geometry of the pits generated and the mechanism of pit formation were also studied, as well as the ageing behaviour of the films and the information stored in them. The investigation extended to the effects of high temperature, frequent temperature alternations at high humidity, prolonged irradiation with light and repeated read-out with a laser beam.

The investigation showed that there are a number of dyes that satisfactorily meet the requirements for optical recording. This article will deal mainly with the results obtained with two of them. We shall first explain how we came to choose these particular dyes. After describing the method of applying them and the properties of the films, we shall deal with their recording characteristics and their behaviour on ageing.

Choice of dye

Few organic dyes are known that will give the required strong absorption at 820 nm. These generally belong to the class of unsaturated compounds in which the pi electrons of the double bonds are delocalized over an odd number of atoms.

At a delocalization over $2N+1$ atoms molecular orbital theory [5] indicates that the energy diagram for the pi electrons contains a 'nonbonding' level E_{N+1} between the highest bonding level E_N and the lowest antibonding level E_{N+2}. For the neutral radical and the mononegative ion with $2N+1$ and $2N+2$ electrons respectively, the first absorption band corresponds to the transition $E_{N+1} \rightarrow E_{N+2}$, while for the monopositive ion with $2N$ electrons the first absorption band corresponds to $E_N \rightarrow E_{N+1}$. Because of the relatively small difference between E_{N+1} and E_{N+2} (or E_N) the first absorption band may be at a relatively long wavelength.

The position of the first absorption band depends to a great extent on the presence of hetero-atoms in the conjugated system, on the length of this system and on the presence of conjugated end-groups [6][7]. Thus in the polymethine dyes, for example, the first absorption band may vary between the near ultraviolet at 300 nm and the near infrared at 900 nm. These dyes possess a conjugated system that extends over an odd number of atoms and contains 'vinyl' units (—CH=CH—). For a symmetrical polymethine dye the following resonance structures may in general be written:

$$R\text{-}(\text{-CH=CH-})_m CH=R^+ \leftrightarrow R^+=CH\text{-}(\text{-CH=CH-})_m R,$$

where the R group is both a donor and acceptor, and m is the number of vinyl units. The positive charge can be compensated by a negative charge in another part of the compound and also by a counter-ion (e.g. Cl^- or ClO_4^-); such compounds are known as ionogenic dyes. The group R often contains a heterocyclic ring system including nitrogen, oxygen or sulphur. By variation of R and m the position of the first absorption band can be very considerably changed. In *fig. 1*, by way of example, the wavelength λ_{max} of the maximum of the first absorption band is plotted as a function of m for two types of polymethine dyes (denoted by A and B). For both types, λ_{max} increases strongly and almost linearly with m and hence with the length of the conjugated system. Each new vinyl unit gives a wavelength shift of about 100 nm. The effect of R is considerable: with a given number of vinyl units, λ_{max} for type B is almost 300 nm longer than for type A.

As fig. 1 shows, type B with two vinyl units meets the requirement of maximum absorption at about 820 nm. This requirement is also met by polymethine dyes with other end groups and a specific number of vinyl units. In all these cases the total length of the conjugated system is fairly large. Since the oscillator strength of the first absorption band increases linearly with this length [6], the absorption can be high.

The choice of dye is also limited by the requirements for the stability of the recording layer. In general, polymethine dyes are less stable as the conjugated system becomes longer. This means that although certain dyes with a long conjugated system have a high absorptance at 820 nm, they are not stable enough for optical recording. Insufficient stability of the dye film may also be the result of solubility in water. Among the ionogenic dyes this rules out the chlorides.

A further selection of dyes depends on the method of application adopted, in which the dye is first dissolved in an organic solvent that does not react with the substrate (glass or plastic). Suitable solvents include acetonitrile (CH_3CH), n-propanol ($CH_3CH_2CH_2OH$) and ethyl acetate ($CH_3COOC_2H_5$). The dye must be readily soluble in at least one of these solvents. In

some cases the solubility of a dye in an organic solvent is appreciably increased by the application of space-filling substituents such as tertiary butyl groups $(CH_3)_3C$—. Such groups have the effect of increasing the stacking distance in the crystal lattice, thus reducing the intermolecular interaction energy so that the dye dissolves more readily.

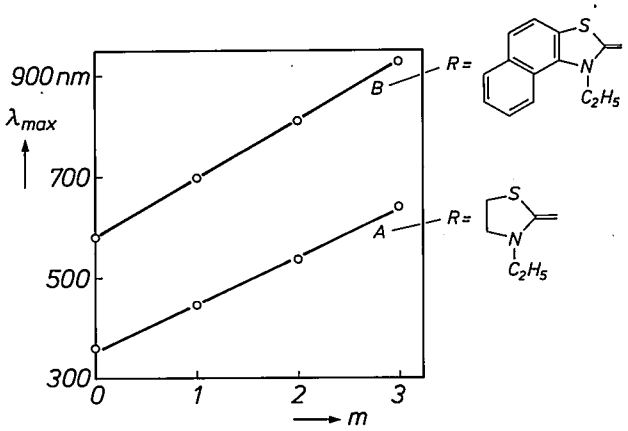

Fig. 1. Wavelength λ_{max} of the maximum of the first absorption band as a function of the number of vinyl units m, for two types of polymethine dyes with the general formula $R\text{-}(\text{-}CH=CH\text{-})_m\text{-}CH=R^+$ for one resonance structure. For both types λ_{max} increases by about 100 nm per vinyl unit. At a given value of m it can be seen that λ_{max} for type B is about 300 nm longer than for type A. At $m = 2$, the maximum absorption with type B is found at about 820 nm.

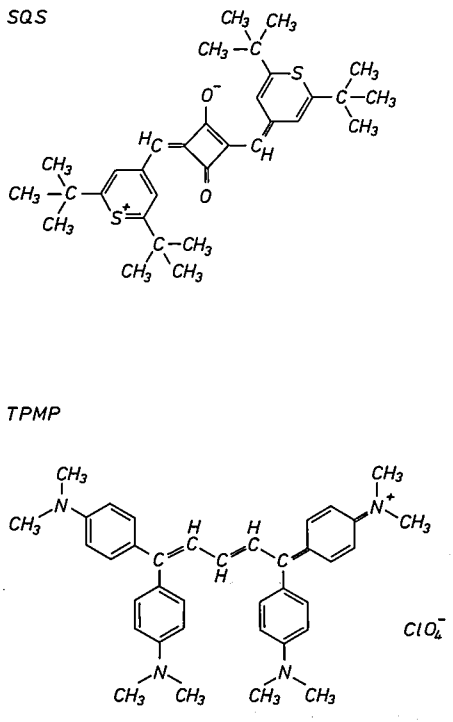

Fig. 2. Structural formulae of SQS and TPMP, two organic dyes suitable for optical recording. Only one resonance structure is given for each of the two dyes.

Two dyes that easily meet the requirements for infrared absorption, stability and solubility are shown in *fig. 2*. The non-ionogenic dye referred to as SQS consists of a squarylium nucleus with thiopyrylium end-groups. These ensure that the strong absorption that is characteristic of squarylium dyes is at a maximum in the neighbourhood of 820 nm. Because of the presence of the four tertiary butyl groups, this dye dissolves readily in solvents such as *n*-propanol. The other dye, tetradimethyl aminophenyl pentamethine perchlorate (TPMP) is one of the many ionogenic polymethine dyes. This also absorbs strongly at 820 nm. Unlike the chloride form of this pentamethine, TPMP is insoluble in water, so that waterproof films can be obtained.

Method of application and film properties

The spin-coating process is a suitable method for applying thin SQS and TPMP films [8]. A solution of the dye is poured on to a substrate fixed to a turntable in a clean room. The substrate is then rotated at a frequency of 3 to 30 Hz, so that the solution spreads out over the surface. During the spinning the liquid film becomes steadily thinner as most of the solution is flung off the surface and the solvent evaporates. After a short time a thin amorphous dye film remains. The thickness of the film depends on factors such as the frequency of rotation, the solvent and the initial concentration of the dye in the solution. A film thickness of between 40 and 200 nm is generally obtained.

To obtain a smooth homogeneous layer the solubility of the dye in the solvent should preferably be at least 10 g/l and the solvent should have the correct viscosity and volatility. The surface tension of the solvent should also be lower than that of the substrate, to permit effective wetting. In addition the solvent must not react with the substrate and must leave no vaporization residues. For the application of SQS and TPMP films the solvents acetonitrile, *n*-propanol and ethyl acetate mentioned above meet these requirements reasonably well. The spin coating can be carried out at normal pressure and temperature. Dust and other contaminants can be removed from the solution beforehand, e.g. by filtration, and highly homogeneous films can thus be obtained.

[6] See A. Streitwieser, Jr., Molecular orbital theory for organic chemists, Wiley, New York 1961.
[6] See J. Griffiths, Colour and constitution of organic molecules, Academic Press, London 1976.
[7] J. Fabian and H. Hartmann, Light absorption of organic colorants: theoretical treatment and empirical rules, Springer, Berlin 1980.
[8] More information on the spin-coating process, in particular for the application of thin photolacquer films on semiconductor substrates, will be found in: D. Meyerhofer, J. Appl. Phys. 49, 3993-3997, 1978.

An important difference compared with films deposited by vacuum evaporation or sputtering is encountered when the films are applied to a grooved substrate, as used in the manufacture of digital optical recording discs [9]. In this case the substrate has a pregrooved layer of lacquer or pregrooved PMMA. When the film is deposited on such a substrate by vacuum evaporation or sputtering the pattern of grooves is followed exactly, so that the film acquires virtually the same surface structure and the thickness is virtually constant over the entire surface. In the spin-coating process for dyes, on the other hand, the grooves in the substrate are filled up with dye solution and the final result is a film with a completely smooth surface.

The films of SQS and TPMP applied by the spin-coating process have strong absorption and acceptable reflection in the near infrared. *Fig. 3* shows the measured reflectance and transmittance of a 75-nm SQS film on a glass substrate as a function of the wavelength of the incident light. In the reflection measurements the light is incident from the substrate side, as it is in the writing and reading of optical recording discs. At 820 nm the reflectance is about 20% and the transmittance about 10%, so that the absorptance is about 70%. Roughly the same values are found with TPMP films.

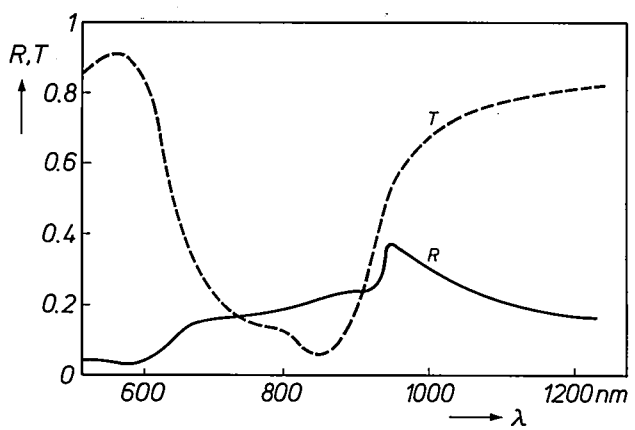

Fig. 3. Reflectance R and transmittance T, as a function of wavelength λ, for a 75-nm SQS film on a glass substrate, with the light incident from the substrate side. At a wavelength of 820 nm the reflectance is about 20% and the transmittance about 10%.

The measured reflectance and transmittance at a given wavelength and the measured film thicknesses can be used to calculate the complex refractive index of the dye films [10]. This is equal to $n - jk$, where n is the real refractive index, and the absorption index k is related to the linear absorption coefficient α at the wavelength λ; the relation is $k = \alpha\lambda/4\pi$. As would be expected, the complex refractive index of SQS and TPMP films depends strongly on the wavelength. *Fig. 4* shows as an example the values of n and k calculated for a TPMP film plotted against wavelength. The maximum value of k, which is about 1.3, is obtained at 830 nm, when n is about 2.1.

The calculated values of n and k can now be used to predict the reflectance and transmittance at a given wavelength as a function of the thickness of the dye film. *Fig. 5* gives the results of such calculations for SQS layers at a wavelength of 800 nm, where $n \approx 1.9$ and $k \approx 1.5$. The experimental values of the reflectance and transmittance of films of different thickness agree reasonably well with the predicted curves. The reflectance of SQS and TPMP films has a maximum at a thickness of about 90 nm.

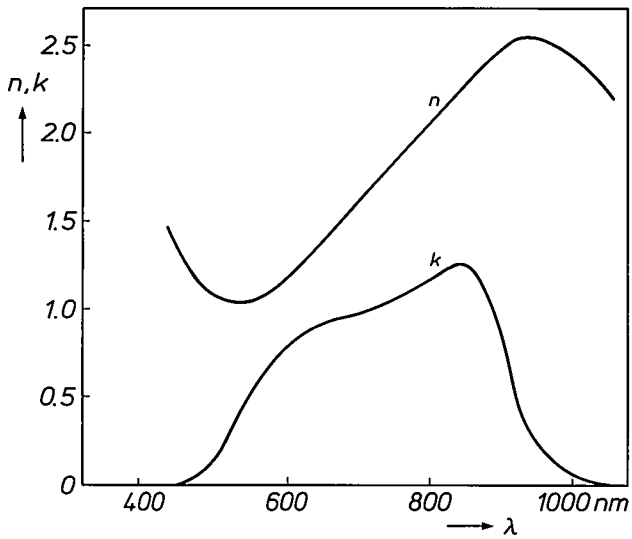

Fig. 4. The calculated real part n and imaginary part k of the complex refractive index $n - jk$, as a function of wavelength λ, for a 90-nm TPMP film on a glass substrate. The value of the absorption index k has a maximum at a wavelength of 830 nm. Practically the same curves are obtained with other film thicknesses.

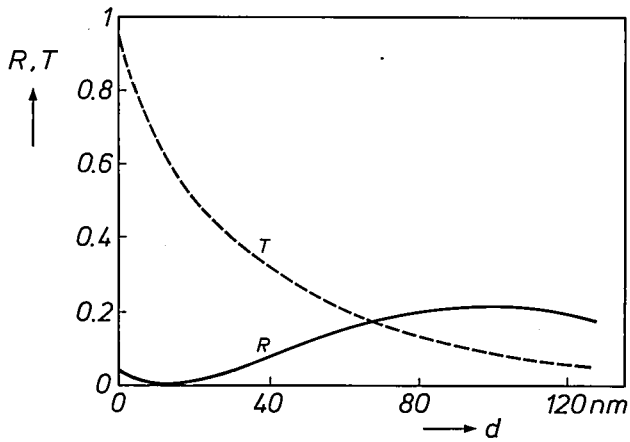

Fig. 5. Calculated value of the reflectance R and transmittance T at a wavelength of 800 nm, as a function of film thickness d, for an SQS film on a glass substrate with light incident from the substrate side. The reflectance has a maximum at a film thickness of about 90 nm.

Recording characteristics

The recording characteristics of a dye film can be determined by focusing the beam from a krypton-ion laser emitting at 799 nm on to a disc coated with the film. The laser beam is incident on the substrate side, and is focused by an objective with a numerical aperture of 0.5, giving a light spot with an effective diameter of about 1 μm. During the exposure the disc rotates at a frequency of say 25 Hz, giving a tangential velocity of 10 to 20 m/s. The 'writing' is done by a pulsed laser beam with a repetition frequency of 5.7 MHz, which is equivalent to recording a 'carrier' [11] at this frequency. During the writing the energy is varied from 0.08 to 1.2 nJ per pulse by varying the power of the laser beam at the recording layer from 1 to 15 mW, with a pulse duration of 80 ns. For focusing, tracking and read-out the laser beam on the film has a continuous power of about 0.5 mW.

The carrier-to-noise ratio, CNR, on read-out is highly dependent on the laser energy used in writing the carrier into the dye film. In *fig. 6* the carrier-to-noise ratio (at a bandwidth of 30 kHz) measured for SQS and TPMP films on a pregrooved PMMA sub-

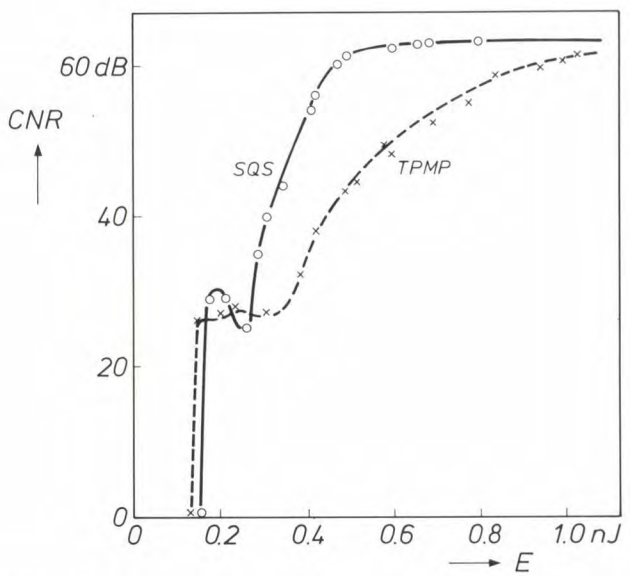

Fig. 6. Carrier-to-noise ratio CNR on read-out as a function of the writing energy E, for recording in 80-nm SQS and TPMP films on a pregrooved PMMA substrate. The measurements were made at a bandwidth of 30 kHz and a rotation frequency of 25 Hz. For writing the pulse rate is 5.7 MHz and the pulse duration 80 ns. In both cases a measurable signal is only obtained after a threshold energy (about 0.15 nJ) is exceeded. Above this threshold the CNR-value increases steeply with E. With the SQS film a saturation value of 63 dB is reached at 0.6 nJ.

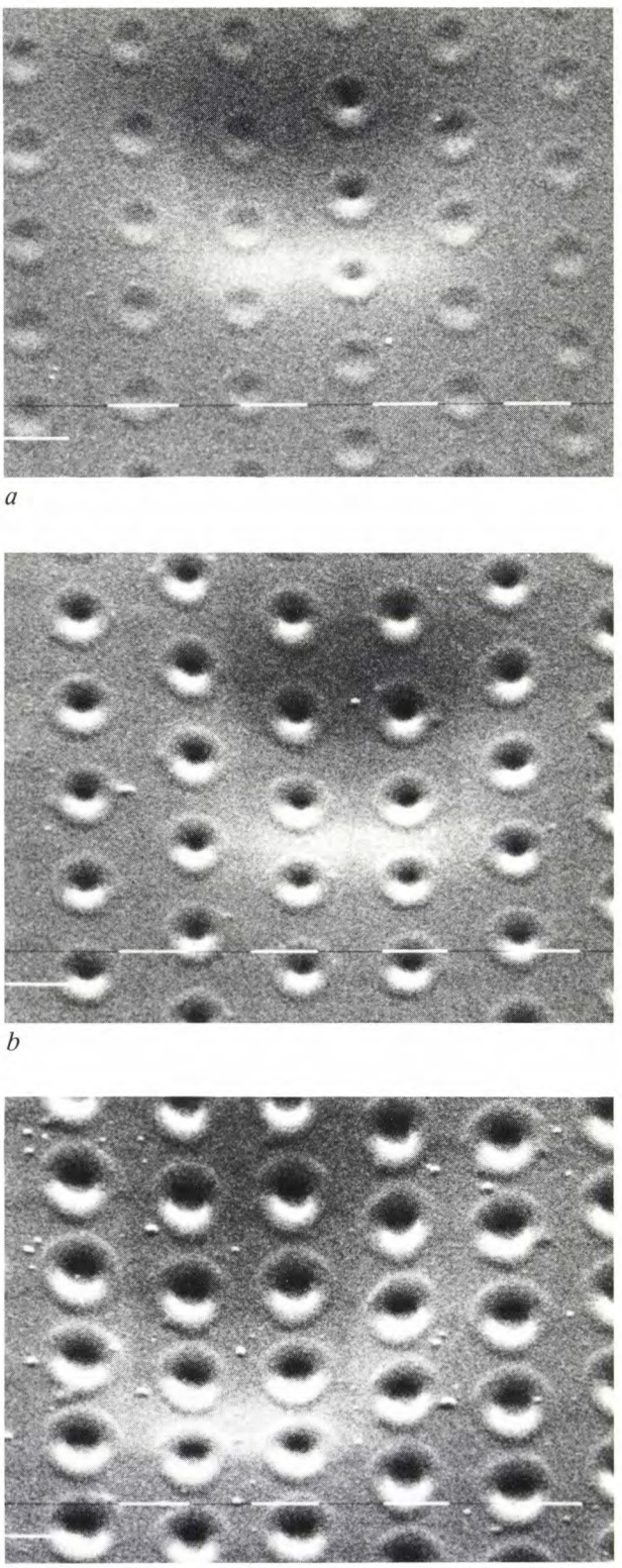

Fig. 7. Micrographs made with the SEM (scanning electron microscope) of pits in an SQS film, formed at a writing energy of 0.23 nJ (*a*), 0.27 nJ (*b*) and 0.42 nJ (*c*); the scale divisions are 1 μm. At a higher writing energy deeper and broader pits are produced. During writing, the disc rotates at a frequency of 8 Hz and the tangential velocity at the writing positions is about 5 m/s. During a laser pulse of duration 80 ns the write locations hardly move at all, so that circular pits are produced. For video recording the rotation frequency is higher (e.g. 25 Hz) and elongated pits are formed.

[9] K. Bulthuis, M. G. Carasso, J. P. J. Heemskerk, P. J. Kivits, W. J. Kleuters and P. Zalm, IEEE Spectrum **16**, No. 8 (August), 26-33, 1979.

[10] See O. S. Heavens, Optical properties of thin solid films, Butterworths, London 1955.

[11] See the series of articles on modulation published in this journal: F. W. de Vrijer, Philips Tech. Rev. **36**, 305-362, 1976.

strate is plotted as a function of writing energy. The threshold energy for obtaining a measurable signal is relatively low in both cases: about 0.15 nJ. Above the threshold energy the CNR-value rises steeply with the writing energy. At a writing energy higher than 0.6 nJ a CNR-value of 63 dB is reached with the SQS film. Slightly lower values are found with the TPMP film. values are high enough for recording video information as well, which requires a minimum of 57 dB. This was confirmed by initial experiments with video recording on SQS films.

From micrographs made with the scanning electron microscope (SEM) it can be concluded that writing on SQS and TPMP films produces pits with a ring at the

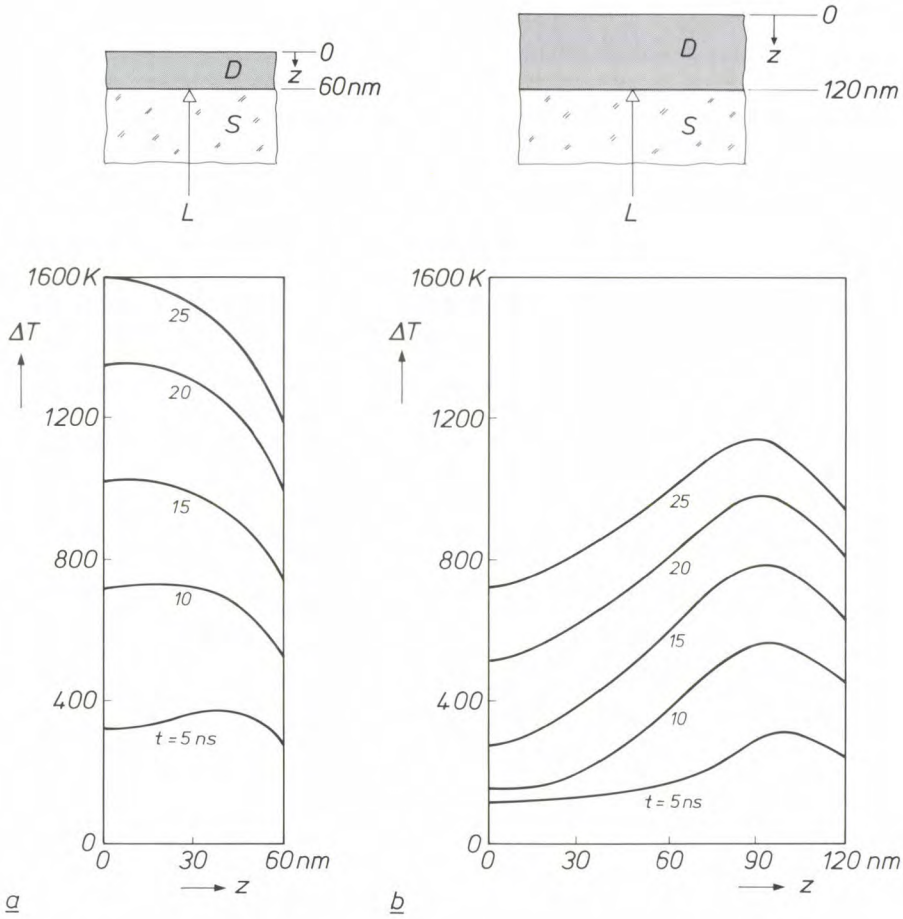

Fig. 8. Schematic temperature profile in a dye film D during writing with a laser beam L entering from the substrate side S. The calculated temperature increment ΔT at different times t during a 25-ns pulse is plotted against the vertical position z in the dye film. The calculations do not include possible changes in the film as a result of the temperature increases. In a 60-nm film (*a*) the temperature rises steeply from the interface with the substrate up to the surface of the dye film. In a film 120 nm thick (*b*) the internal temperature is much higher than at the surface or at the interface with the substrate.

Writing is found to have no effect on the noise: the noise level is the same at all writing energies and is determined solely by the surface structure of the substrate, in this case a pregrooved PMMA substrate. When the substrate surface is completely flat, even higher CNR-values can be obtained, e.g. 67 dB for an SQS film on a flat PMMA substrate.

The results obtained show that the CNR-values that can be achieved with SQS and TPMP are much higher than the minimum value required for digital optical recording. It was also found that the attainable CNR-surface. In TPMP films this ring is relatively thick. Read-out of the written information is based on the lower reflectance at the location of the pits, since the film at these locations is thinner (see fig. 5). Since relatively little energy is necessary to form readily 'readable' pits in SQS and TPMP films, the sensitivity of these films for optical recording is high. Higher writing energies produce deeper and broader pits; see *fig. 7*. A deeper pit gives a more marked reduction in reflectance, so that the CNR-value rises with the writing energy (fig. 6). It may also be deduced from the SEM

micrographs that writing does not give rise to any 'grain' and that the pits are regular in shape. This agrees with our earlier observation that writing is not accompanied by any additional noise.

It is possible to explain why writing from the substrate side generates pits in the surface of the dye film and not in the interface with the substrate by making use of calculations of the temperature profile produced in the film; see *fig. 8a*. Since the absorption length ($\lambda/4\pi k$) of SQS and TPMP is about 50 nm, films with a thickness of this order are fairly homogeneously heated by the laser beam. Heat dissipation to the substrate produces a steep temperature gradient in the film, with the highest temperature at the surface.

Because of the temperature increase that occurs at the surface during writing, the dye film melts at the places exposed to the beam and partially vaporizes or decomposes. The evaporating dye molecules or their decomposition products cause a pronounced recoil effect, producing considerable pressure on the surface of the molten dye. This sets up radial movement of material towards the outside, so that a pit with a ring is formed.

With thicker dye films and a high writing energy, holes may be formed at the writing locations, i.e. pits extending down to the substrate. With TPMP films more than 110 nm thick a writing energy of more than 0.5 nJ is necessary to produce such holes. Near the holes some grain is usually found, probably as a result of a kind of eruption. Holes are formed in a thick film and not in a thin one because the temperature profile produced in a thick film is completely different; see fig. 8*b*. Since only the first 50 nm of the film is heated effectively, with poor thermal conductivity in the film and heat dissipated to the substrate, a steep temperature gradient is obtained in the film with the highest temperature on the inside. This results in considerable gas generation inside the film, caused by the evaporating dye or its decomposition products. At a high writing energy the gas pressure in the interior of the film can become so high that the 'cold' upper layer tears open, producing a hole right through the thickness of the film at the writing location.

With a film thickness of about 90 nm, the optimum for reflection at 820 nm, no holes but only pits are formed. With this thickness, however, it is not possible to produce good recording *inside* the groove tracks when a grooved substrate is used. This is because the film *between* the groove tracks would be only 20 nm thick at the normal groove depth of 70 nm [9], and it would therefore not reflect sufficiently (fig. 5). Good recording is possible, however, if the information is written *between* the groove tracks, and if the dye film has a thickness of 90 nm there.

A special feature of the organic-dye films described here is that the dimensions of the pits can be adjusted fairly accurately by taking appropriate values for the frequency of rotation of the disc, the laser power and the pulse duration. As an example, *fig. 9* shows the length of the pits as a function of pulse duration for recording on an SQS film. At a given rotation frequency and laser power the pit length can be seen to increase linearly with the pulse duration.

Because the pit dimensions are adjustable, organic-dye films widen the scope for optical recording. For instance, in addition to digital recording, which is a matter of generating or not generating pits, they can also be used for analog recording in which the length of the pits and the spacing between them are varied. This means that video information can also be recorded. *Fig. 10* shows an SEM micrograph of an SQS

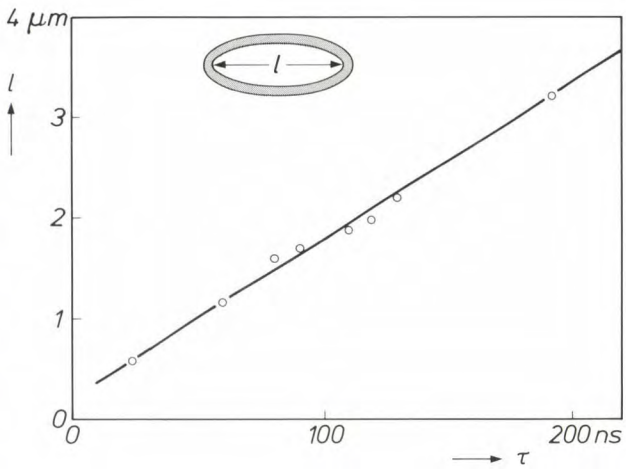

Fig. 9. Length l of the pits formed in an SQS film, as a function of the pulse duration τ at constant laser power (13 mW). The pit length increases linearly with the pulse duration.

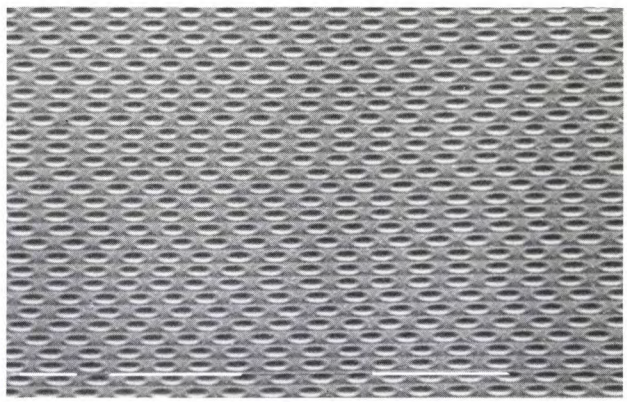

Fig. 10. SEM micrograph (scale divisions 10 μm) of a pattern of pits in an SQS film after recording video information at a rotation frequency of 25 Hz, a laser power of 7 mW and a pulse duration of 80 ns. Because of the movement of the writing locations during a laser pulse, the pits are elongated. The slight differences in length and in the spacing between the pits are typical of video recording.

film with a pattern generated by the writing of video information. As remarked earlier, the available signal-to-noise ratio is high enough to ensure reliable video recording. Another capability is the storage of information by writing pits of different depths. In this way the information density can be considerably increased. The practicability of the various potential applications will depend largely on the ageing behaviour of the dye films.

Ageing behaviour

In view of the different potential applications of organic dye films for optical recording, only a few general stability tests have so far been made on unprotected dye films. To study the effect of heat on ageing, we kept the films for some time in an oven at 90 °C. We also subjected films to rapid alternations in temperature at high humidity as specified in the Z/AD test [12]. For this test the films were stored in an environmental test chamber in which the temperature is cycled between 25 and 65 °C at a relative humidity of about 93%. Measurements were also made of the light-fastness of the films by subjecting them to prolonged irradiation from an intense light source and a large number of laser irradiations under read-out conditions.

During most of the tests SQS films gave unwanted crystallization. This can be prevented by the addition of a small amount of certain polymers, without in any way affecting the recording characteristics.

Transmittance measurements before and after ageing showed that TPMP films stand up well to high temperatures. After 200 days in an oven at 90 °C the transmittance only went up from 20 to 22%. SQS films, however, are adversely affected by storage at high temperatures. The transmittance of an SQS film on a PMMA substrate doubles after 20 days at 90 °C. At room temperature, on the other hand, SQS layers are very stable. On a pregrooved PMMA substrate SQS layers still had a CNR-value of more than 60 dB after keeping them in an ordinary office for a year.

In the Z/AD tests both SQS and TPMP films are found to be very stable. In *fig. 11* the transmittance of an SQS film on a PMMA substrate and a TPMP film on a lacquer-coated glass substrate are shown as a function of the time spent in the environmental chamber. In both cases the observed increase in transmittance is small. The stability in the Z/AD tests also appears from measurements of the read-out signal from discs containing prerecorded information. A disc consisting of a glass substrate, a lacquer layer and a TPMP film with information recorded in it showed hardly any reduction of the read-out signal after a

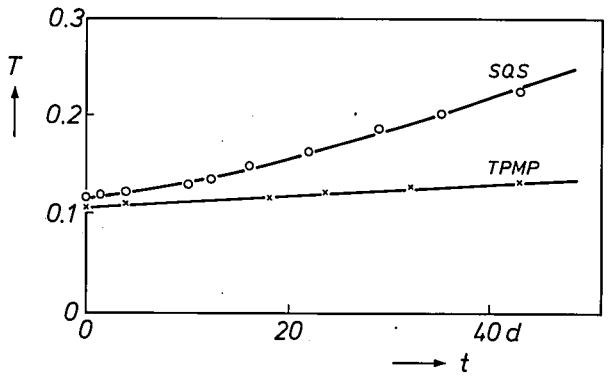

Fig. 11. Transmittance T for an SQS film on a PMMA substrate and for a TPMP film on a laquer-coated glass substrate during ageing in a Z/AD test [11], as a function of time t (in days) in the environmental test chamber. In both films the transmittance increases only slightly during ageing.

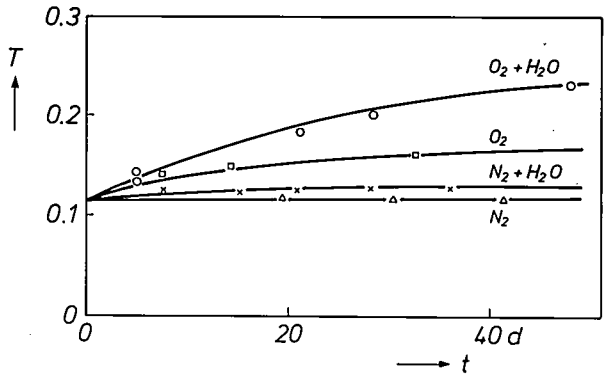

Fig. 12. Effect of the ambient atmosphere on the fading rate of SQS films on irradiation with white light of intensity 1000 W/m^2 at 40 °C. As a measure of fading the transmittance T is plotted as a function of the irradiation time t (in days). The transmittance increases more slowly in dry oxygen (O_2) than in wet oxygen (O_2/H_2O). The light-fastness is even better in wet nitrogen (N_2/H_2O) and in dry nitrogen (N_2).

period of several days in the environmental chamber. The CNR-value of this disc decreased by about 1 dB per day, owing to an increase in disc noise.

The light-fastness of the dye films was studied in a 'Xenotest', in which the films were irradiated with white light of 1000 W/m^2 intensity — about 500 times the illuminance in an ordinary office. During the irradiation the temperature was maintained at about 40 °C and the relative humidity at about 65%. The transmittance and reflectance were measured at different times. The fading caused by the irradiation was much slower with TPMP films than with SQS films. An increase in the transmittance by a factor of about 2 was found with SQS films after 100 hours of irradiation, and not until after 400 hours of irradiation for TPMP films. The fading rate of SQS films is strongly affected by the ambient atmosphere; see *fig. 12*. In dry oxygen the fading is much slower than in wet oxygen

[12] IEC Publ. No. 68-2-38, Test Z/AD: Composite temperature/humidity cyclic test, IEC, Geneva 1974.

or in an office at 20 °C and a relative humidity of about 60%. Even slower fading takes place in an atmosphere of wet or dry nitrogen. It may be deduced from these results that the combination of oxygen and water vapour plays an important part in the fading of SQS films under the action of light. It is probable that the fading is mainly determined by the oxidizing action of peroxides formed from oxygen and water vapour.

To determine the fastness of the dye films to laser light the transmittance and reflectance were measured after a large number of irradiations under read-out conditions with a focused beam from an AlGaAs laser emitting at 820 nm. The laser light-fastness of both SQS and TPMP films are found to be very high. With the laser powers commonly used for read-out a total of at least 10^8 read-outs can be made in both cases without any demonstrable degradation in the form of an increase in transmittance or decrease in reflectance. Above a particular laser power, however, some increase in transmittance is observed. It may be concluded from this that the fading is due to a photochemical process rather than a thermochemical process. To check the laser light-fastness we looked at the effect of repeated read-out from a few written tracks on the signal-to-noise ratio. After 5×10^5 read-outs of information written in an SQS film on a PMMA substrate almost the same CNR-value was found as with the first read-out.

The investigation described here was made in cooperation with W. P. M. Nijssen, Dr C. J. van der Poel, Dr Ir C. Steenbergen, Ing. H. T. L. P. Stockx and Ing. R. H. J. Striekwold.

Summary. An investigation into the possible applications of organic-dye films for optical recording with an AlGaAs laser emitting at 820 nm has indicated two suitable dyes: the non-ionogenic SQS, consisting of a squarylium nucleus with thiopyrylium end-groups, and the ionogenic tetradimethyl aminophenyl pentamethine perchlorate (TPMP). With both dyes, applied by a simple coating method, smooth and homogeneous films are obtained that give sufficient absorptance and reflectance at 820 nm. With a laser beam of relatively low energy, pits of adjustable size can be written into these films very rapidly giving a high signal-to-noise ratio (> 60 dB) on read-out. An advantageous feature is that both digital and analog (video) information can be recorded in this way. The films and the information recorded in them have good storage life.

Philips Tech. Rev. 41, 334-337, 1983/84, No. 11/12

Measuring the radial error of precision air bearings

The unit in which distances are expressed may often provide an idea of the accuracy with which those distances can be determined. Thus, for instance, an astronomer reckons in light years, a surveyor in kilometres or metres, a carpenter in centimetres and a metal worker in millimetres or microns. The radial error of the aerostatic precision bearings made at Philips Research Laboratories is so small that it is expressed in nanometres. A method of measuring this radial error has recently become available and will be discussed in this article.

The path described by a point of a bearing shaft during a single revolution will in general be approximately circular; see *fig. 1a*. When this path is magnified by means of a measuring instrument we see that it can be characterized by a number of quantities; see fig. 1*b*. The quantity e_0 is the eccentricity of the measuring instrument relative to the average position of the axis of rotation. The quantity e_1 is the eccentricity of a point of the shaft relative to this average position. Both quantities can be made virtually equal to zero by careful adjustment and do not therefore say much about the quality of the bearing. The quantity ε_r, the 'radial runout', does however express the quality of the bearing very well. This quantity is the difference between the radius of the highest peak and the radius of the lowest valley of the path of the point on the shaft; it is measured perpendicular to the best-fitting circle, found for instance by the method of least squares. The quantity ε_r is thus a measure of the radial runout of the shaft in the plane of the measurement. Complete characterization of the bearing requires a second measurement in another plane. Usually, however, it is only the runout at one position that is important. In this article we shall not be concerned with the axial runout, because it can usually be determined with far fewer difficulties.

Aerostatic bearings were already being used at Philips Research Laboratories in the sixties [1]. In these bearings the pressure of the lubricant — air — is derived from an external source, whereas in dynamic bearings the pressure is generated in the bearing gap itself. Some of the advantages of aerostatic bearings are low friction, no contamination and the absence of metallic contact, even when stationary. Another advantage is that geometrical errors in shaft and bearing bore introduce very little runout error. Aerostatic bearings with a tapered bearing gap (see *fig. 2*) have lately been used at our laboratories, because they give even smaller runout, are not so difficult to make, and are less sensitive to dust particles in the air supply. Bearings of this type are used at our laboratories in equipment for measuring roundness or straightness [2], in experimental apparatus depending on accurate movements, in high-precision machine tools, and in

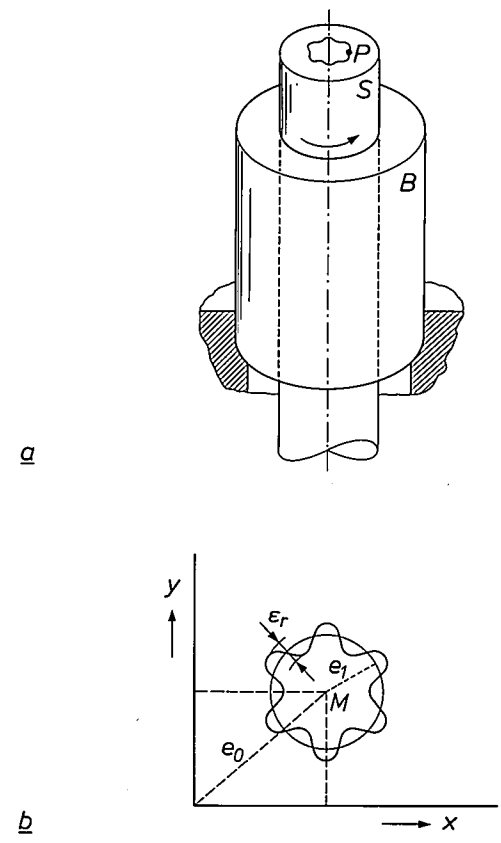

Fig. 1. Definition of the radial runout of a bearing shaft. *a*) The path described by a point *P* on the shaft during one revolution. *S* shaft. *B* bearing bush. *b*) The measured path of the point *P* in an (x,y)-coordinate system. *M* point where the average position of the axis of rotation intersects the plane of the measurement. The quantities e_0 and e_1, the eccentricities of the measuring instrument and the point *P* relative to *M*, can be minimized by adjustment. The radial runout ε_r is the difference in radius between the highest peak and the deepest valley of the path and is measured perpendicular to the best-fitting circle.

equipment for measuring forces and torques via low-friction joints.

The radial runout of a bearing is usually measured by attaching an accurately lapped cylindrical or spherical workpiece to the shaft, centring it, and then keeping the stylus of a displacement transducer held against it during one revolution of the shaft. The runout is equal to the difference between the maximum and minimum readings of the transducer. The measuring errors of the most sensitive displacement transducers, however, are too large for measuring the runout of our air bearings, and during the measurements these transducers also exert a slight radial force on the bearing.

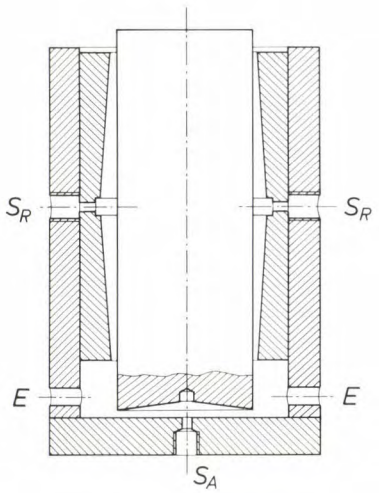

Fig. 2. An aerostatic bearing with tapered gap. S_R compressed-air supply for the journal bearing, S_A similar supply for the thrust bearing. *E* exit. The gap of the journal bearing tapers from the centre to the ends, from about 32 μm to 12 μm.

Fig. 3a shows the principle of the measuring instrument that has been designed in our laboratory for determining the runout by measuring the displacement of a point of the rotating shaft without making contact with the shaft. The instrument is a modified version of the 'optical pick-up' of the Compact Disc player [3]. This is a small and stable optical system and has the additional advantage that the components

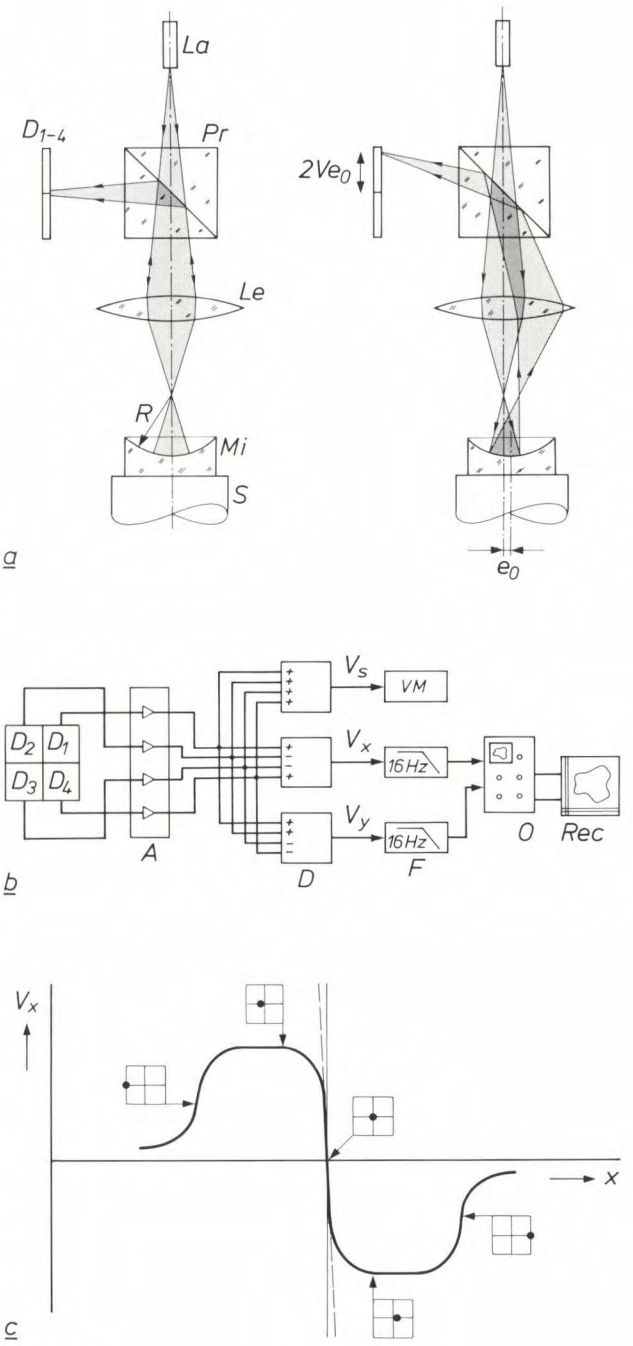

Fig. 3. Principle of the measuring instrument. *a*) Optical system. *La* semiconductor laser. *Pr* prism with half-silvered dividing surface. *Le* positive lens. *Mi* concave mirror of radius *R*. *S* shaft. D_{1-4} quadrant cell, consisting of four photodiodes (seen from above in *b*). *La*, *Pr* and *Le* are components of the 'optical pick-up' of the Compact Disc player, D_{1-4} is a component of the LaserVision player. *Left:* ray paths when the centre-point of *Mi* coincides with the optical axis. *Right:* ray paths when the shaft with *Mi* is displaced by a distance e_0. The image of *La* on the quadrant cell is then displaced through a distance $2Ve_0$; *V* optical magnification. *b*) Electronic signal processing. *A* signal amplifiers. *D* sum and difference circuits. *F* lowpass filters. *VM* voltmeter. *O* two-channel storage oscilloscope. *Rec* XY recorder. V_s sum signal. V_x, V_y difference signals for the displacements in *x*- and *y*-directions. *c*) Calibration curve, the signal V_x as a function of the displacement *x* of the shaft *S*. The associated laser images on the quadrant cell D_{1-4} are shown beside the curve. The steep central part of the curve is used for measuring the runout. The corresponding sensitivity is 4 V/μm.

[1] See p. 264 of E. A. Muijderman, New forms of bearing: the gas and the spiral groove bearing, Philips Tech. Rev. **25**, 253-274, 1963/64.

[2] A. F. Foederer, J. L. M. Hagen and A. G. van Nie, An instrument for measuring the curvature of reflecting surfaces, Philips Tech. Rev. **40**, 338-341, 1982.
B. Sastra and G. M. Dohmen, High-precision numerically-controlled measuring system for cylindrical surfaces, Precision Eng. **6**, 12-16, 1984.

[3] M. G. Carasso, J. B. H. Peek and J. P. Sinjou, The Compact Disc Digital Audio system, Philips Tech. Rev. **40**, 151-155, 1982.

are in accurate alignment. The row of photodiodes in the optical pick-up has been replaced by a quadrant cell, consisting of photodiodes arranged in a square as shown in fig. 3*b*. The quadrant cell is taken from the LaserVision player. A concave mirror is mounted on the rotating shaft; the laser image that in the ordinary way would fall on the surface of the Compact Disc is reflected by the mirror to form a second image at approximately the same place. If the distance from the centre of the mirror to the optical axis is e_0, the second image is a distance $2e_0$ from the optical axis. From the second image a third image is then formed on the quadrant cell. If the magnification of the optical system is V, the eccentricity of the laser image on the quadrant cell is $2Ve_0$. The optical magnification of the measuring instrument is thus $2V$. Unlike the method described above, the measuring result is not affected by local errors (for example dust and pits) in the rotationally symmetrical object — in this case the concave mirror, in the previous case a cylinder or sphere.

Fig. 3*b* also shows how the photodiodes of the quadrant cell are connected. Three output voltages are obtained, which are related to the luminous intensity I_{D1} to I_{D4} on each of the diodes as follows:

$$V_s \propto I_{D1} + I_{D2} + I_{D3} + I_{D4},$$
$$V_x \propto I_{D1} + I_{D4} - (I_{D2} + I_{D3}),$$
$$V_y \propto I_{D1} + I_{D2} - (I_{D3} + I_{D4}).$$

The signals V_x and V_y are applied to the x and y inputs of a two-channel storage oscilloscope. Both signals are also fed to an XY recorder. The signal V_s is measured with a voltmeter and is used for aligning the optics with the mirror.

Fig. 3*c* shows the output voltage V_x as a function of the displacement x of the concave mirror; the figure also shows the circular laser image on the quadrant cell for five different values of x. For measuring the runout we use the steep central part of the curve where it deviates by no more than 5% from a straight line. We calibrated our configuration by displacing the mirror and found a sensitivity, corresponding to the slope of the curve, of 4 V/μm The effective part of the calibration curve corresponds to a mirror displacement of 0.95 μm. (A larger range, with a correspondingly lower sensitivity, can be obtained if the image of the laser on the quadrant cell is slightly out of focus.) It is just possible to observe displacements of one nanometre, because of the high sensitivity resulting from the small diameter of the laser image on the quadrant cell. (The figure of one nanometre does not of course refer to the actual accuracy of the measurements.)

Before a measurement of the runout is made, the optical axis and the centre of the mirror are made to coincide as closely as possible with the axis of rotation of the shaft. Next, the path described by the centre of the mirror is displayed much enlarged on the oscilloscope screen. The resultant curve resembles the one shown in fig. 1*b*. The eccentricities e_0 and e_1 are then reduced still further (to zero if possible) by very careful adjustments. The value of ε_r can then be measured or calculated from a curve made on the XY recorder.

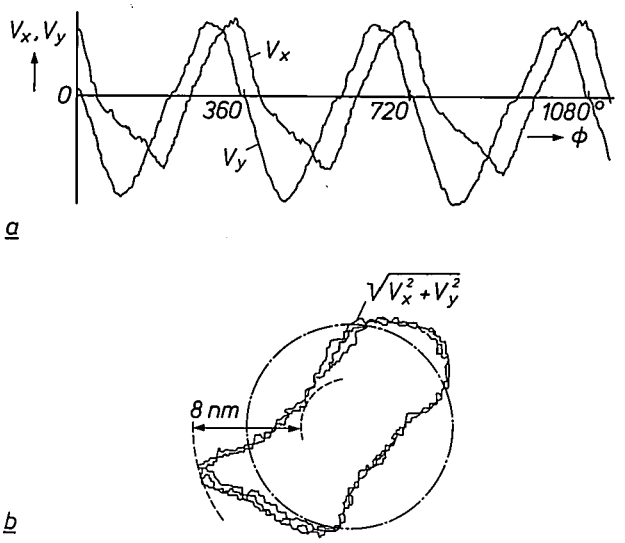

Fig. 4. Result of measurements on an unloaded air bearing, as in fig. 2, plotted with *Rec* in fig. 3*b*. *a*) The signals V_x and V_y as a function of the angle of rotation ϕ of the shaft. The signals are virtually identical for the first, second and third revolutions. *b*) The resultant vector sum of length $(V_x^2 + V_y^2)^{0.5}$. A runout value of 8 nm is measured perpendicular to the best-fitting circle (a dot-dash line drawn 'by eye'); see also fig. 1. This value includes the inaccuracy of the measuring instrument.

The inaccuracy of the measuring instrument depends on the errors of the optical components, the noise in the electronics, thermal effects and mechanical vibrations in the measuring configuration. The inaccuracy is generally different for the x- and y-directions, because of slight out-of-roundness of the laser image. In our case the mechanical vibrations proved to be mainly caused by 20-Hz vibrations of the laboratory building. These were eliminated from the results of the measurements by a 16-Hz lowpass filter; see fig. 3*b*. The shaft should therefore rotate at a low speed during the measurement, e.g. one revolution in 3.5 s. We estimate the total inaccuracy of our measurement of the runout at about 4 nm.

The measuring instrument described here has been used for measuring the runout of a precision air bearing made in the workshops of Philips Research Laboratories (see fig. 2), for use in a system for surface metrology. The diameter of the shaft is 70 mm and the

length of the bearing bush 150 mm. The bearing gap tapers from 32 μm at the centre to 12 μm at the ends. The bronze bearing bush was made on the COLATH lathe [4]. The out-of-roundness of the bush, measured at two places, is less than 0.3 μm. (The out-of-roundness can be determined with a 'Talyrond' instrument, which scans the workpiece during one accurate rotation, followed by an evaluation of the result more or less as shown in fig. 1*b*.) The out-of-roundness of the ground shaft, measured at three places, is less than 0.2 μm. The result of the runout measurement of the (unloaded) shaft in the bearing bush is shown in *fig. 4*. The runout determined from fig. 4*b* amounts to 8 nm; this value includes the inaccuracy of the instrument. The traces are virtually identical for three successive revolutions of the shaft. When the concave mirror is rotated through an angle of about 90° or 180°, the shape of the traces changes but the measured runout is consistently less than 8 nm [5]. The shape of the lapped glass mirror and the variation of its reflection coefficient appear to affect the accurcy of the runout measurement. Our aim is therefore to improve the quality of the mirror so that the race between manufacturing technology and metrology of precision bearings can be decided in favour of metrology.

[4] T. G. Gijsbers, COLATH, a numerically controlled lathe for very high precision, Philips Tech. Rev. **39**, 229-244, 1980.

[5] In assessing this figure it should be remembered that the runout of the most accurate standard ball-bearings is about 4 μm. The special ball-bearings for the head movement in certain types of video recorder have a runout of about 1 μm. The runout of the grease-lubricated spiral-groove bearings used in Philips V 2000 system video recorders is even less. See E. A. Muijderman, G. Remmers and L. P. M. Tielemans, Grease-lubricated spiral-groove bearings, Philips Tech. Rev. **39**, 184-198, 1980.

P. L. Holster
J. A. H. M. Jacobs
B. Sastra

Ing. P. L. Holster, Ing. J. A. H. M. Jacobs and Ir B. Sastra are with Philips Research Laboratories, Eindhoven.

Ceramic boundary-layer capacitors

R. Mauczok and R. Wernicke

The miniaturization of capacitors is much more of a problem than the miniaturization of transistors. An article recently published in this journal outlined the development of ceramic multilayer capacitors, showing the progress that has been made in this respect. The article below deals with an alternative method for the miniaturization of capacitors.

Miniaturization of ceramic capacitors

With LSI it is now possible to integrate 400 000 transistor functions on a single chip to form a complete microcomputer. Such a high degree of miniaturization is still far from feasible with passive electronic components, such as capacitors. The efforts being made in many laboratories around the world to make miniaturization possible by increasing the capacitance per unit volume have been described in a previous article in this journal [1]. Attempts to do this by increasing the relative permittivity (dielectric constant) soon run into the problem of deterioration of the temperature characteristic. Increasing the capacitance by merely reducing the thickness of the capacitor is only possible to a limited extent since it is difficult to reduce the thickness much below 200 μm with conventional methods. Pieces of ceramic as thin as this are very difficult to handle. If this difficulty could be circumvented so that we only had to consider the material properties such as the permissible operating voltage, it would be possible to reduce the thickness to about 25 μm and hence increase the capacitance by a factor of 8.

One of the ways of meeting these technological difficulties has been the development of ceramic multilayer capacitors (CMCs), which were the subject of the article mentioned earlier. Another approach makes use of ceramic barrier-layer capacitors (CBCs), whose operation depends on the formation of thin insulating layers in semiconducting materials. In this way dielectric thicknesses of less than a few microns can be obtained in pieces of ceramic that have a practical physical thickness of a few hundred microns and so are easy to handle.

R. Mauczok and Dr R. Wernicke are with Philips GmbH Forschungslaboratorium Aachen, Aachen, West Germany.

Although the capacitors produced in this way do not have such small dimensions, nor, as a rule, such good characteristics as CMCs, the method does have advantages in other respects. In the first place it is not so very different from the conventional methods of manufacture, so that CBCs are more compatible with the existing production facilities than CMCs are. Secondly, production costs are lower. For these reasons CBCs are still being produced in large quantities, mainly in the Far East, but also elsewhere.

There are three distinct types of barrier-layer capacitor (*fig. 1*). In the first type (surface-layer capacitors; fig. 1*a*), which we shall touch on only very briefly in this article, the thin insulating layers are present only at the surface. This type can be made by subjecting $BaTiO_3$ to a heat treatment in a reducing atmosphere. During this treatment the material becomes semiconducting because of the formation of oxygen vacancies, which are compensated by conduction electrons [2][3]. The material is then given a brief heat treatment in an oxidizing atmosphere, causing oxygen to diffuse into the bulk and fill up the oxygen vacancies, over a layer thickness that depends on the duration and temperature of the oxidation. This annihilation of the oxygen vacancies gives rise to a thin insulating layer at the surface of the piece of ceramic. A disadvantage of this type of capacitor is that such thin surface layers can easily be damaged during the production process, especially when the connection leads are soldered.

This disadvantage can be avoided by creating insulating layers at the grain boundaries of a semiconducting material [4]; see the types of capacitor illustrated in fig. 1*b* and *c*. The type shown in fig. 1*b* consists of single-phase polycrystalline material, usually $BaTiO_3$ or $SrTiO_3$, with internal boundary layers that

are formed by diffusion of barium or strontium vacancies. As a result of this diffusion a thin layer of the semiconducting grain becomes insulating when the specimen is cooled after sintering or during a special subsequent treatment. The same mechanism plays an important part in PTC materials (materials with a positive temperature coefficient of resistivity), which were the subject of an earlier article in this journal [2]. While this method results in insulating layers that have virtually the same composition as the rest of the grain, it is also possible to use a two-phase system with the insulating layers in the form of a second phase, that is to say with a quite different composition (fig. 1*c*).

After this brief introduction, we shall take a closer look in the next section at the general features of these two types of boundary-layer capacitor, and in the rest of the article we shall confine ourselves to an example of the second type, the SBL capacitor (SBL stands for $SrTiO_3$ Boundary-Layer).

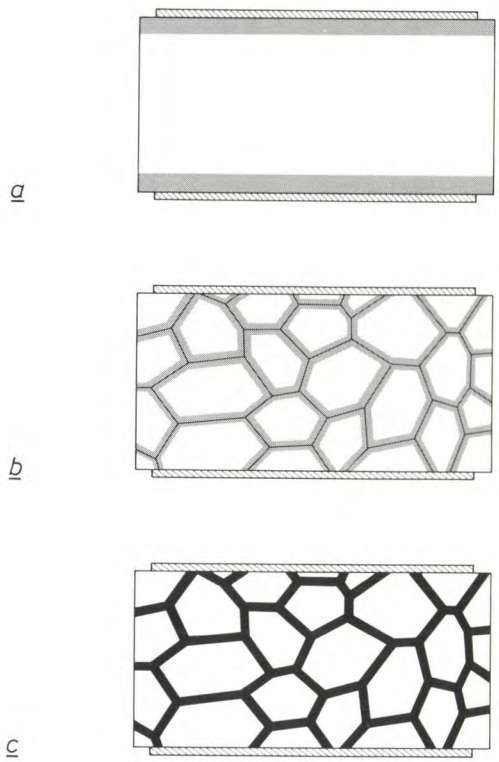

Fig. 1. Three types of barrier-layer capacitor, shown schematically. *a*) Surface-layer capacitor, consisting of single-phase semiconductor material (white), insulating layers at the surface, produced by diffusion of vacancies (shaded) and electrodes (hatched). *b*) Boundary-layer capacitor, as in (*a*), but with the insulating layer at the grain boundaries. *c*) Boundary-layer capacitor consisting of a two-phase system, where the first phase is a semiconducting grain and the second phase a thin insulating layer at the grain boundaries (black). Otherwise as in (*a*) and (*b*).

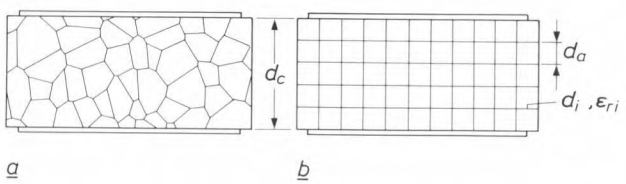

Fig. 2. Boundary-layer capacitor with a typical microstructure (*a*), approximated by cubic grains (*b*). This cubic approximation is used to calculate an effective relative permittivity for the dielectric of boundary-layer capacitors (see text). d_c thickness of capacitor. d_a average grain size. d_i and ε_{ri} thickness and relative permittivity of the insulating layers at the grain boundaries.

General features of boundary-layer capacitors

We shall first look at the manner in which the dielectric properties of a material consisting of semiconducting grains and insulating grain-boundary layers can be described in terms of an effective relative permittivity $\varepsilon_{r,ef}$. *Fig. 2a* shows a ceramic specimen with a thickness d_c and an average grain size d_a, with a typical grain structure as found in boundary-layer capacitors. Fig. 2*b* shows an approximation of this structure using cube-shaped grains. In this cubic approximation the material forms a capacitor that consists of $n = d_c/d_a - 1 \approx d_c/d_a$ insulating layers, connected in series by the semiconducting grains. Since each layer has a capacitance $\varepsilon^n \varepsilon_{ri} A/d_i$ (A is the surface area, d_i the thickness and ε_{ri} the relative permittivity of the insulating layers), the total capacitance of the specimen built up from cubic grains (fig. 2*b*) is $\varepsilon_0 \varepsilon_{ri} A/(d_i n) = \varepsilon_0 \varepsilon_{ri} d_a A/(d_i d_c)$. Assuming that this cubic approximation is admissible, we may assign to the ceramic specimen in fig. 2*a* the effective relative permittivity:

$$\varepsilon_{r,ef} = \varepsilon_{ri} d_a/d_i. \qquad (1)$$

This depends only on material constants.

We have already mentioned that boundary-layer capacitors are not very sensitive to mechanical damage, because their dielectric layers are not at the surface of the material but are situated in the bulk. This also means that the electrodes do not come into direct contact with the dielectric, and therefore can have no effect on the dielectric properties of the specimen, as they could in surface-layer capacitors. On the other hand, to obtain boundary-layer capacitors with readily reproducible characteristics, more attention has to be paid to the homogeneity of the microstructure.

For the product to be well-defined it would be best if all the grains were of the same size. However, a fun-

[1] H.-J. Hagemann, D. Hennings and R. Wernicke, Philips Tech. Rev. **41**, 89-98, 1983/84.
[2] See J. Daniels, K. H. Härdtl and R. Wernicke, Philips Tech. Rev. **38**, 73-82, 1978/79.
[3] See J. Daniels and K. H. Härdtl, Philips Res. Rep. **31**, 489-504, 1976.
[4] See J. Daniels and R. Wernicke, Philips Res. Rep. **31**, 544-559, 1976.

damental feature of a ceramic specimen is that the grain size has a fairly broad statistical distribution about a mean value. A few large grains might therefore cause a short-circuit. The probability of this happening increases as the ratio of the thickness of the capacitor to the average grain size d_c/d_a approaches unity. This factor is therefore very important and should be kept above the specified minimum value. Depending on the microstructural homogeneity, it appears that this factor should have a value between at least 5 and 10 for satisfactory practical results.

Fig. 3 shows how the resistivity of barrier-layer capacitors varies as a function of this factor. With vacuum-evaporated electrodes of CrNi the resistivity at small values of d_c/d_a is low, owing to the presence of a large number of leakages (in the form of large single grains that interconnect the two electrodes). In this case the resistivity is largely determined by the relatively low contact resistance of the metal-to-semiconductor transition at these positions. With increasing value of d_c/d_a the probability of such leakages decreases, and at a value of 5 or more the resistivity is found to be fairly constant, and mainly dependent on the insulating layers at the grain boundaries. As can be seen in fig. 3, the behaviour is entirely different if fired silver electrodes are used instead of vacuum-evaporated CrNi films. This is because firing silver paste at temperatures of about 800 °C, may produce insulating surface layers, which increase the resistivity substantially at the leakage locations. In this case the capacitor can be regarded as a mixed form of a surface-layer capacitor and a boundary-layer capacitor. With sufficiently high values of d_c/d_a the behaviour of this type of capacitor is again largely determined by the grain-boundary layers, so that the resistivity is hardly affected by the electrode.

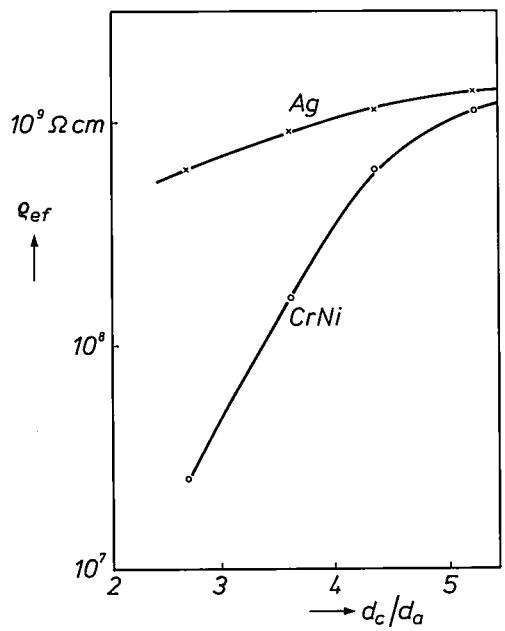

Fig. 3. The effective resistivity ϱ_{ef} of $BaTiO_3$ barrier-layer capacitors as a function of the factor d_c/d_a. The upper curve (*Ag*) relates to capacitors with fired silver electrodes, the lower curve (*CrNi*) to capacitors with vacuum-evaporated CrNi electrodes.

In practice both types of insulating layers are encountered. For optimizing the characteristics of a boundary-layer capacitor it is then important to know the details of its specific structure. Since it may be impossible to determine from outside the extent to which surface layers or boundary layers are responsible for the behaviour of a particular specimen, we have devised a method for obtaining more information about capacitors of this type, with particular reference to the degree of homogeneity of the ceramic. For this purpose we grind away a succession of thin layers of the capacitor under investigation, and after each grinding operation we measure the reduction in thickness and the capacitance. The result of such an investigation is given in *fig. 4*.

In principle there are three possibilities. *a*) The reciprocal of the capacitance decreases steeply after a layer of a certain thickness (e.g. 10 μm) has been ground away and remains constant after further grinding. This is the behaviour shown by a pure surface-layer capacitor. *b*) The reciprocal of the capacitance plotted as a function of the thickness reduction gives a straight line between the values corresponding to the initial capacitance and the original thickness. This is the behaviour shown by an ordinary dielectric, and it is also the behaviour one would expect from a pure boundary-layer capacitor with a well-defined effective relative permittivity. *c*) The curve shows the behaviour of a mixed form of the two types of capacitor. In the first and last cases the dielectric properties of the capacitor cannot be described adequately by an effective relative permittivity, as they can be with the second type. Grinding tests like these, in combination with other measurements [5], can provide a good understanding of the structure and operation of barrier-layer capacitors.

Another important step in this development has been the use of $SrTiO_3$ as the basic material. In the past, semiconducting $BaTiO_3$ was mainly used in the manufacture of barrier-layer capacitors, owing to the exceptionally high permittivity of this ferroelectric material. Its disadvantages, however, were high losses, relatively poor temperature characteristics, dielectric nonlinearities and hysteresis effects. In 1975 results were published for the first time on the application of boundary-layer capacitors based on the non-ferroelectric material $SrTiO_3$. Although in principle this has a lower permittivity than $BaTiO_3$, attempts to compensate this can be made by using exceptionally thin layers

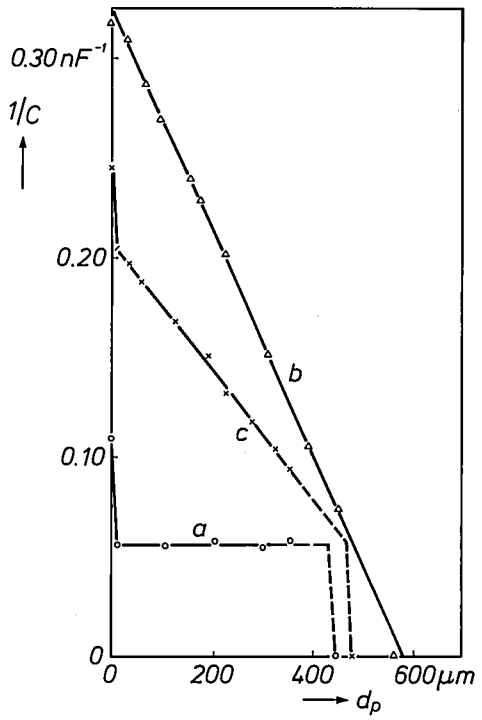

Fig. 4. Reciprocal of the capacitance $1/C$ of different barrier-layer capacitors as a function of the thickness d_p that has been removed from the surface successively. The shape of the curve depends on whether the capacitor is a pure surface-barrier-layer capacitor (curve *a*), a pure boundary-layer capacitor (curve *b*), or a mixed form of the two (curve *c*). Knowledge of the type of capacitor, determined by such tests, is important for optimizing its characteristics.

at the grain boundaries. When this was done it turned out that high effective relative permittivities, up to 80 000, could be combined with much better secondary properties than are possible with $BaTiO_3$ [6]. In the rest of this article we shall confine ourselves to these $SrTiO_3$ boundary-layer capacitors, often called SBL capacitors.

Manufacture of the dielectric material for SBL capacitors

The ceramic material for SBL capacitors is generally prepared in two stages. First, coarse-grained semiconducting $SrTiO_3$ is made, and insulating layers of a second phase are formed later at the grain boundaries.

In the first stage the composition of the material and the preparation conditions are chosen appropriately for the required microstructure (grain size, homogeneity) and the required conductivity. A grain size between 20 and 50 μm, which is indicated for a suitable d_c/d_a-value, can only be achieved with materials of this type by liquid-phase sintering [7]. A small excess of TiO_2 (about 1 mol%) is therefore added to the ingredients; this has the result that the desired liquid phase forms at temperatures above 1440 °C during the sintering process [8]. If necessary, further additives such as Al_2O_3, SiO_2, GeO_2 or ZnO can be used to reduce the eutectic temperature and hence lower the sintering temperature. This provides further means of controlling the size of the grains and the grain size distribution [9]. In this way it is possible to satisfy the condition of a suitable d_c/d_a-value.

Table I. Preparation process for SBL material.

Wet mixing of $SrCO_3$, TiO_2 and Nb_2O_5 for a composition $Sr(Ti_{1.01-x}Nb_x)O_3$ ($x = 0.01$-0.05).
Prefiring at 1150 °C in air.
Dry milling.
Pressing into discs 0.5 mm thick and 6 mm in diameter.
Sintering at 1450 °C in a gas mixture of N_2, H_2 and H_2O.
Painting with a mixture of PbO, Bi_2O_3 and B_2O_3.
Second firing in air, now at 1100 °C.
Electrode formation.

The conductivity can be controlled by doping with donors such as Nb and Ta. In general the same considerations apply for $SrTiO_3$ as for the preparation of n-type $BaTiO_3$, which has been described some time ago in this journal [2]. At a doping concentration of 1-5 mol% a conductivity of 0.5-2 S/cm is obtained after sintering under reducing conditions.

For the second stage in the preparation, forming an insulating second phase at the grain boundaries, the semiconducting product is coated ('painted') with a mixture of appropriate oxides, and then heat-treated at 1000 to 1200 °C in an oxidizing atmosphere. The mixture, usually combined with suitable binders, might typically consist of PbO, Bi_2O_3 and B_2O_3. The entire preparation process is summarized in *Table I*.

The formation of insulating second-phase layers at the grain boundaries

This second firing process has a particularly marked influence on the final characteristics of SBL capacitors. We shall therefore pay special attention to this process here, and also to the mechanism that initiates the formation of the second phase at the grain boundaries.

Fig. 5 shows SEM micrographs of two polished cross-sections of a specimen consisting of SBL material, one before the second firing process and the

[5] See R. Wernicke, Ber. Dtsch. Keram. Ges. 55, 356-358, 1978.
[6] T. Yuden, German patent 2433661 of 6th February 1975.
[7] This problem with barium-titanate materials is discussed in the article of note [1].
[8] See E. M. Levin, C. R. Robbins and H. F. McMurdie, Phase diagrams for ceramists, 1969 Supplement, American Ceramic Society, Columbus, OH, 1969.
[9] See J. Klerk and P. J. H. Sanders, in: L. M. Levinson (ed.), Advances in ceramics, Vol. 1, American Ceramic Society, Columbus, OH, 1983, pp. 282-289.

other after it. *Fig. 6* shows that a second phase, of different composition from the rest of the specimen, has formed at the grain boundaries.

An investigation of specimens of SBL material that had been initially sintered, then painted with the oxides mentioned above and finally subjected to a further heat treatment, gave the following results. At temperatures up to 600 °C the applied oxides are seen to change into other modifications, indicated by changes in colour. At about this temperature the oxides start to melt and form a glassy layer that spreads over the entire surface of the specimen because of its strongly 'wetting' properties. No significant changes are observed in this glassy layer in the temperature range from 600 to 800 °C. At about 900 °C the glassy melt penetrates rapidly into the specimen. This takes place so quickly that at 1000 °C the molten oxides are distributed throughout the volume of a specimen 10 mm thick in two or three minutes.

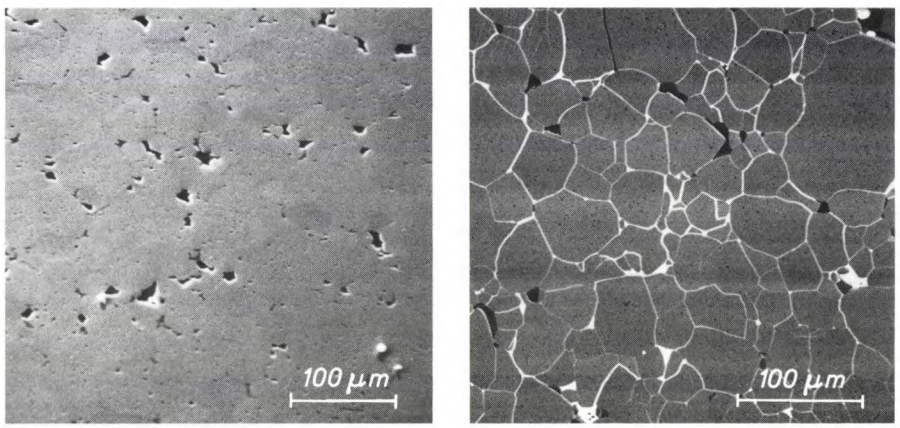

Fig. 5. SEM micrographs of polished cross-sections of SBL material, before (*left*) and after the second firing. The picture on the right shows the occurrence of a second phase at the grain boundaries, which appears very bright due to the presence of Pb and Bi.

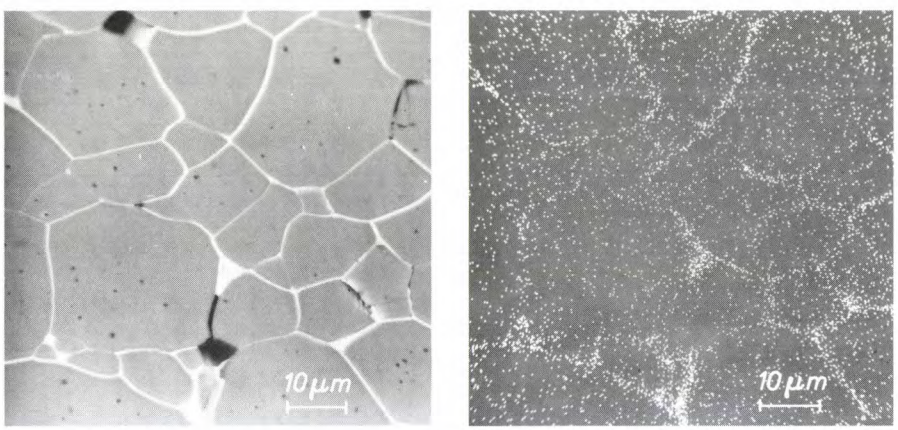

Fig. 6. Electron-microprobe micrographs of polished cross-sections of SBL specimens. The picture on the left was obtained by means of backscattered electrons; the picture on the right, showing the distribution of Pb, was obtained by means of X-ray analysis. The Pb content at the grain boundaries is clearly different from that in the grains themselves.

How might such a rapid material transport be explained?

The hypothesis of selective melting reactions

If solid-state diffusion is assumed to be the mechanism for this rapid material transport, then the diffusion coefficient must be in the region of 10^{-5}-10^{-4} cm^2/s at 1000 °C. Such a high value seems improbable for perovskite material, even allowing for the possibility of accelerated diffusion along the grain boundaries. Another argument against the hypothesis of solid-state diffusion is that diffusion fronts have never been observed and that a well-defined temperature exists (at about 900 °C) below which the melt is completely unable to penetrate into the specimen.

It therefore seems more likely that the transport takes place via liquid phases. The transport rates then attainable will in any case be sufficiently high, as may be deduced for example from data on liquid-phase sintering at low temperature [1]. This is the transport

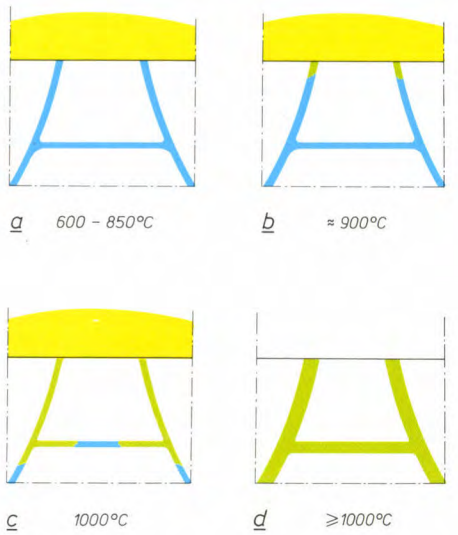

Fig. 7. Illustrating the hypothesis of selective melting reactions. *a*) In the temperature range from 600 to 850 °C the oxides 'painted' on the surface melt to form a glassy layer (*yellow*). At the grain boundaries there is a solid second phase of TiO_2, formed after sintering (*blue*). *b*) At about 900 °C the glassy melt begins to penetrate the specimen along the grain boundaries by dissolving the TiO_2 present at the boundaries (*green*). *c*) At 1000 °C this process has proceeded so far that the grains are almost entirely encircled by a melt. *d*) The final state, in which the melt has been completely taken up by the specimen.

mechanism underlying the hypothesis of *selective melting reactions*, which we shall now try to explain by reference to *fig. 7*.

We know that in the temperature range between 600 and 900 °C a melt forms on the surface of the semiconducting $SrTiO_3$ ceramic from the Pb, Bi and B oxides (*fig. 8a*). In the ceramic there is already a small amount of second phase present at the grain boundaries in the form of solid TiO_2. This has formed there from the slight excess of TiO_2 that was added to the original ingredients to improve the sintering properties (see page 341). At these temperatures the melt hardly reacts at all with any of the constituents of the ceramic. At about 900 °C the melt starts to react selectively with the solid second phase of TiO_2 found at the grain boundaries at the surface of the ceramic (fig. 7*b*). In this reaction the TiO_2 dissolves in the melt. This solution process continues along all the grain boundaries of the specimen (fig. 7*c*), aided by the wetting properties of the melt. The transport of Pb, Bi and B necessary for the solution process is easily made available via the liquid phase that had already formed at the grain boundaries. In this process the melt reacts much less with the rest of the material, the $SrTiO_3$ grains [10]. Eventually all the grains become surrounded by a thin liquid film (fig. 7*d*), and can thus easily move in relation to one another. A new arrangement of the grains can therefore be formed, and this usually causes the liquid film to become thicker than the original TiO_2 layers present as a second phase (compare fig. 7*a* with 7*d*). This rearrangement is accompanied by an increase in the volume of the specimen, as has been found experimentally.

During cooling the liquid phase crystallizes to form thin layers of a solid second phase, which separates all the grains from one another. The ultimate thickness of these layers is determined by a number of factors. The thickness depends first on the amount of second phase formed at the grain boundaries during the first sintering process [9], and secondly on the wetting properties and viscosity of the resultant melt. The latter properties depend in turn on the composition of the melt and on the temperature of the second firing.

Analysis of such a thin boundary layer is not easy and its composition is not exactly known in all cases. Presumably it is always a PbBiTi or SrBiTi compound with a layered perovskite structure. In some cases, where a fairly thick layer had formed, it was possible to identify the compound by X-ray diffraction as $Pb_2Bi_4Ti_5O_{18}$ or $Sr_2Bi_4Ti_5O_{18}$, depending on the mixture of oxides used.

Some confirmations of the hypothesis

The foregoing hypothesis is based on the assumptions that TiO_2 is rapidly soluble in the melt of the mixture of oxides used (PbO, Bi_2O_3 and B_2O_3) whereas under the same conditions there is only slight reaction with the $SrTiO_3$ grains. To test these assumptions we made the investigations that gave the results shown in *fig. 8*. From a specimen of ceramic TiO_2 that was painted on one side with the oxide mixture mentioned above, and subsequently heat-treated for

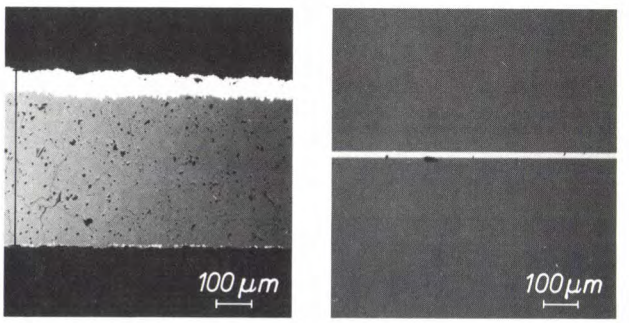

Fig. 8. Results of experiments designed to confirm the selectivity of the melting reactions. *Left:* TiO_2 ceramic painted with oxides and heated at 1100 °C. The original thickness is shown at the extreme left. *Right:* Sandwich of two $SrTiO_3$ single crystals with the oxide between them, also heated at 1100 °C. Although some of the TiO_2 has clearly dissolved, the $SrTiO_3$ crystals show no change at all. (The sandwich configuration was necessary in the second case because there is little or no reaction with the $SrTiO_3$. With an open configuration there would have been excessive evaporation of the oxides.)

[10] M. P. A. Viegers, in: P. Vincenzini (ed.), Science of ceramics, Vol. 12, Ceramurgica, Faenza 1984, pp. 245-256.

15 minutes at 1100 °C, we see that the melt does indeed dissolve some of the TiO_2 (fig. 8, *left*). The original thickness of the specimen is shown on the left of the figure. X-ray diffraction also showed that the affected part had the composition mentioned earlier, $Pb_2Bi_4Ti_5O_{18}$. On the other hand, the $SrTiO_3$ specimen, which was treated in a similar way, shows no visible changes (fig. 8, *right*).

We were also able to experimentally verify the assumption that in the second firing process all the grains are eventually completely surrounded by a liquid phase (see fig. 7*d*). In this situation the grains must be capable of relative movement. Since this implies the loss of the intergranular bonds, it should give a dramatic decrease in the mechanical strength of the material. To check this, we laid narrow strips of $SrTiO_3$ ceramic on a rod of Al_2O_3 (*fig. 9*) and exposed it to a temperature of 1100 °C for 15 minutes. The strip on the left of the figure was not painted with oxides, whereas the strip on the right was. We see that the right-hand strip has sagged under its own weight, following the shape of the alumina rod. This behaviour, and its absence in the other strip, confirms the above assumption that a liquid phase completely surrounds all the grains, as would be expected with the occurrence of selective melting reactions.

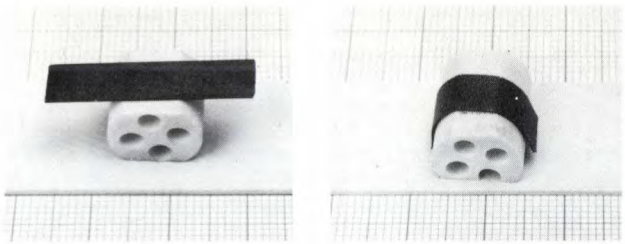

Fig. 9. Heating $SrTiO_3$ ceramic for 15 minutes at 1100 °C had completely different effects, depending on whether the ceramic had been previously painted with oxides or not. In the first case (*right*) the strip sags under its own weight and follows the shape of the alumina rod on which it was laid. This confirms the formation of a liquid phase surrounding all the grains as predicted by the hypothesis of selective melting reactions.

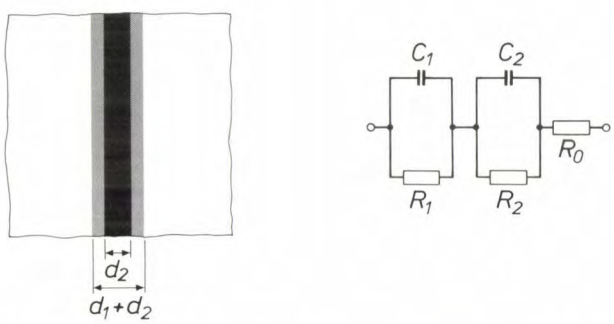

Fig. 10. *Left:* Grain-boundary structure in SBL material: an insulating layer consisting of a second phase (*black*), of thickness d_2, is sandwiched between insulating layers, of thickness $\frac{1}{2}\ d_1$, formed by vacancy diffusion (*shaded*). *Right:* equivalent electrical circuit of the structure.

Model for describing SBL material

To describe SBL materials with the aid of a model it is first of all necessary to find a good approximation for the ceramic microstructure and to obtain significant information about the insulating layers.

Computer calculations have shown that the approximation of the ceramic microstructure by cubic grains, as shown in fig. 2*b*, is not as rough as it might seem at first sight. The calculations were based on a set of statistically distributed points ('nuclei') that were allowed to grow at the same isotropic rate until they touched. The resultant microstructure corresponds well to what is found in practice. Fig. 2*a* is an example of such a simulated microstructure.

Insulating layers were then introduced at the grain boundaries so that the entire structure was equivalent to an electrical network, with each grain representing a node connected to its neighbours by certain impedances. In this way the value of the effective relative permittivity can be calculated for a microstructure as shown in fig. 2*a*.

When this value is compared with the one obtained from eq. (1) for the cubic approximation, the results agree well as long as they are based on 'normal' homogeneities (comparable with that in fig. 2*a*) and a ratio d_c/d_a greater than 10. The approximate value of $\varepsilon_{r,ef}$ from eq. (1) then shows an acceptable deviation (less than 10%), compared with the exact value calculated from the simulation.

For simplicity we shall use this cubic approximation in the rest of this article, because it has the incidental advantage that there is an analytical expression for the effective relative permittivity $\varepsilon_{r,ef}$.

The description of the insulating boundary layers is more of a problem, largely because the second firing takes place in an oxidizing atmosphere, which implies that a diffusion layer will probably form as well as the second-phase layer. During heating in an oxidizing atmosphere, strontium vacancies are likely to arise at the grain boundaries, and these vacancies will diffuse inside the grains, in much the same way as in PTC resistors and boundary-layer capacitors of the type in fig. 1*b* (see page 339). In this way a boundary layer is formed that is built up from two types of layer, as shown in *fig. 10, left*. The central layer consists of a second phase, with a composition differing from that of the grains, while the two adjacent layers are diffusion layers whose composition is practically the same as that of the grains. Assuming that the two diffusion layers are identical, we may describe the electrical

behaviour of the whole structure by an equivalent circuit consisting essentially of two *RC* networks (fig. 10, *right*).

Neglecting the resistance R_0 of the grains, which is significant only at high frequencies, we have an expression for the effective relative permittivity:

$$\frac{1}{\varepsilon_{r,ef}} = \frac{1}{d_a}\left(\frac{d_1}{\varepsilon_{r1}} + \frac{d_2}{\varepsilon_{r2}}\right), \quad (2)$$

where d_1 and ε_{r1} are the thickness and relative permittivity of the diffusion layer, and d_2 and ε_{r2} are the thickness and relative permittivity of the second phase.

Since the formation of the second phase is accompanied by an increase in the volume and weight of the specimen, the thickness d_2 of the associated layer can be related to the relative change in weight $\Delta m/m$ due to the second firing. Assuming that the grains are cubic in shape and that the second phase is homogeneously distributed, and since the volume of the grains is related to the volume of the second phase as d_a^3 is to $6\times\frac{1}{2}d_2\times d_a^2$, then:

$$d_2 = \frac{d_a}{3}\times\frac{\varrho_1}{\varrho_2}\times\frac{\Delta m}{m}, \quad (3)$$

where ϱ_1 and ϱ_2 are the densities of $SrTiO_3$ and the second phase. We thus arrive at the relation:

$$\frac{1}{\varepsilon_{r,ef}} = \frac{d_1}{\varepsilon_{r1}d_a} + \frac{1}{3\varepsilon_{r2}}\frac{\varrho_1}{\varrho_2}\frac{\Delta m}{m}, \quad (4)$$

where ϱ_1/ϱ_2 may vary from 0.8 to 1.0.

Verification of the model

To check the validity of the various assumptions in the previous section, and in particular the validity of eq. (4), a number of measurements were made. To begin with, the reciprocal of the effective relative permittivity $1/\varepsilon_{r,ef}$ was determined as a function of the relative change in weight $\Delta m/m$ of a sample of SBL material when it is fired a second time (*fig. 11*). For sufficiently high values of $\Delta m/m$ the first term of eq. (4) is negligible compared with the second, so that $1/\varepsilon_r$ becomes directly proportional to $\Delta m/m$. In this case only the second-phase layers contribute to $\varepsilon_{r,ef}$. In fig. 11 it can be seen that the curves are indeed straight lines for the higher values of $\Delta m/m$. From the slope of the straight parts we can derive the appropriate value of ε_{r2} for the second phase. Assuming that the second phase and the grains have the same density, we then arrive at a value of about 200 for ε_{r2}. As the compound $Sr_2Bi_4Ti_5O_{18}$, which constitutes the second phase in a number of cases, has a relative permittivity of 280 [11], this is a reasonable value. The deviations from the straight line for small changes in weight indicate that it is here no longer correct to treat the first term in eq. (4) as negligible.

Fig. 12 shows that the temperature of the second firing has a considerable effect on the dielectric properties of SBL material. In fig. 12*a* it can be seen that

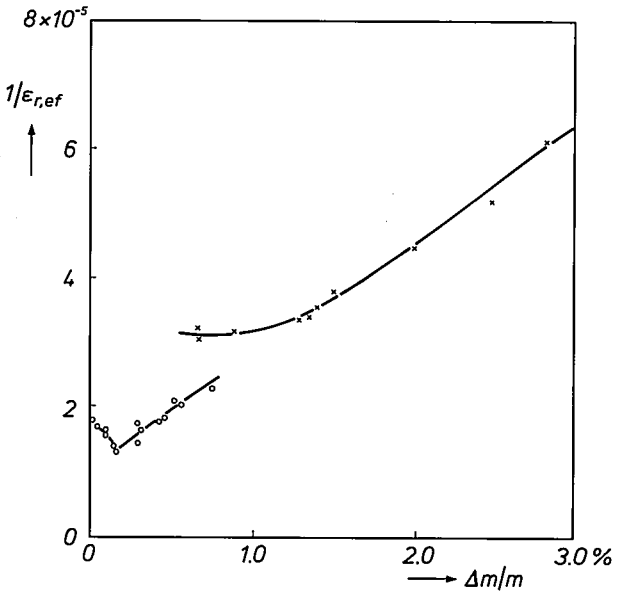

Fig. 11. Reciprocal of the effective relative permittivity $1/\varepsilon_{r,ef}$ of SBL material as a function of relative changes in weight $\Delta m/m$ resulting from the second firing. Measurements were made on material with the composition $Sr(Ti_{0.995}Nb_{0.015})O_3$, to which either 0.2 wt.% SiO_2 (*crosses*) or 0.05 wt.% SiO_2 has been added (*circles*).

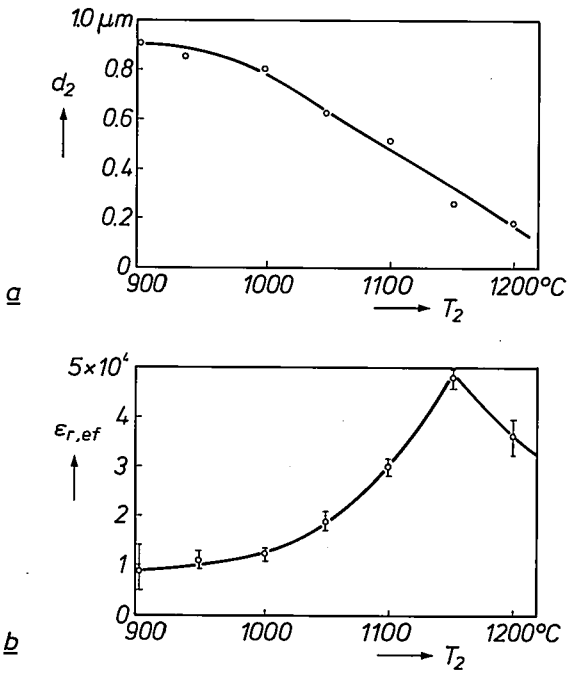

Fig. 12. Shown as a function of the second firing temperature T_2: the average thickness d_2 of the second-phase layers (*a*) and the effective relative permittivity $\varepsilon_{r,ef}$ (*b*). These data relate to material with the composition $Sr(Ti_{1.00}Nb_{0.015})O_3$, to which 0.05 wt.% SiO_2 has been added.

[11] E. C. Subbarao, J. Phys. & Chem. Solids 23, 665-676, 1962.

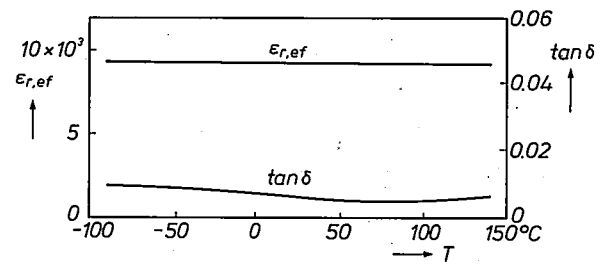

Fig. 13. Effective relative permittivity ($\varepsilon_{r,ef}$) and dielectric loss ($\tan\delta$) of a material developed for use in an SBL capacitor with the smallest possible temperature coefficient, shown here as a function of temperature (T). The material has the composition $Sr(Ti_{1.00}Nb_{0.016})O_3$ with the addition of 0.1 wt.% Al_2O_3 and 0.2 wt.% SiO_2. Sintering was at 1450 °C in a mixture of H_2 and N_2, and the second firing at 1100 °C. On varying the temperature from −55 to +125 °C the change in $\varepsilon_{r,ef}$ is less than 1% compared with the value at 25 °C.

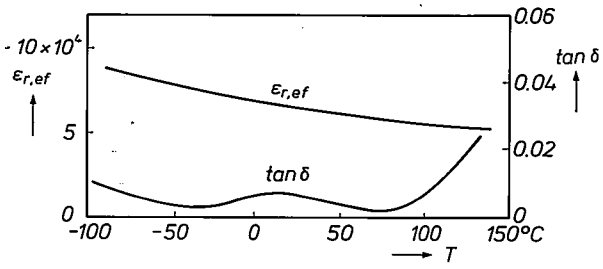

Fig. 14. The result of the development of an SBL capacitor with a high permittivity. The same dielectric properties are shown as in fig. 13. The material has the composition $Sr(Ti_{1.00}Nb_{0.01})O_3$ with the addition of 0.05 wt.% SiO_2. Sintering was at 1470 °C in a gas mixture of H_2 and N_2. The second firing was at 1150 °C. The effective relative permittivity of this material is no less than 65 000 at 25 °C. The temperature characteristic of $\varepsilon_{r,ef}$ is rather less satisfactory, however. On varying the temperature from −55 to +125 °C there is a change in $\varepsilon_{r,ef}$ of about 22% compared with the value at 25 °C.

the average thickness d_2 of the second-phase layers decreases from 0.9 μm at 900 °C to 0.2 μm at 1200 °C. This would be expected, since the liquid phase that forms at the grain boundaries decreases in viscosity at higher temperatures and therefore spreads out in thinner layers. At temperatures between 900 and 1150 °C we see that this reduction in d_2 also appears, as expected, in an increase in $\varepsilon_{r,ef}$ (fig. 12*b*). At temperatures higher than 1150 °C, however, the contribution of the diffusion layers to the dielectric properties becomes more and more dominant. Since their formation is determined by a diffusion mechanism, their thickness increases exponentially with increasing temperature, and from 1150 °C this is expressed in a decrease in $\varepsilon_{r,ef}$, as demonstrated in fig. 12*b*.

Besides the value of $\varepsilon_{r,ef}$ itself, the temperature coefficient also depends on the relative contributions of the two types of layer. Thick layers of the second phase always have a positive temperature coefficient or at best a very small negative one, but thick diffusion layers always have a large negative temperature coefficient, which corresponds to that of the grain material, $SrTiO_3$. This also agrees with the proposed model.

This effect of the relative contributions of the two types of layer on the temperature coefficient can be turned to very good practical use. *Fig. 13* gives the value of $\varepsilon_{r,ef}$ as a function of temperature for a material developed for the smallest possible temperature coefficient. The effective relative permittivity of the material is 9400 and the dielectric loss is less than 1%. In the temperature range from −55 to +125 °C the relative deviation of the effective relative permittivity with respect to the value at 25 °C is less than 1%, which corresponds to a temperature coefficient of 50 ppm/°C. This low temperature coefficient was obtained by careful control of the relative contribution of the two layers, allowing the second-phase layers to be slightly dominant. This was achieved by the addition of a 1.5% excess of TiO_2 and fairly large amounts of SiO_2 and Al_2O_3 to the raw materials [9].

Owing to the fairly large thickness of the second-phase layers, however, the relative permittivity is lowered to the value of 9400 mentioned above. *Fig. 14* demonstrates what happens when the low temperature coefficient is to some extent sacrificed to achieve the highest possible value of $\varepsilon_{r,ef}$. This figure represents the dielectric properties of a specimen whose properties are essentially determined by the diffusion layers. This results in an effective relative permittivity of no less than 65 000, but the temperature dependence is now appreciably higher, about 22%. For comparison, conventional $BaTiO_3$ capacitors with a slightly better temperature dependence (10-15%) have relative-permittivity values of no more than 2000 to 3000.

These examples may indicate the kind of characteristics that can be given to SBL capacitors and also show how these characteristics can be varied by careful adjustment of the preparation conditions.

Summary. The article describes the manufacture and characteristics of ceramic boundary-layer capacitors, in particular SBL capacitors based on $SrTiO_3$. The characteristics are influenced to a considerable extent by the second firing at about 1100 °C. During this firing oxides painted on the surface melt and penetrate the specimen along all the grain boundaries, where they form insulating layers. This oxide melt should selectively dissolve the solid TiO_2 present at the grain boundaries, so that all grains are surrounded by a liquid phase. Experiments verify this hypothesis and show that the ceramic material completely loses its mechanical strength under these conditions. The insulating layers consist of a second-phase layer sandwiched between layers that have become insulating by diffusion. Variation of the thickness of these two types of layer results in very different properties, e.g. an effective relative permittivity of 9400 with a temperature dependence of 1% (relative to the value at 25 °C over the temperature range from −55 to +125 °C), or an effective relative permittivity of 65 000 with a corresponding temperature dependence of 22%.

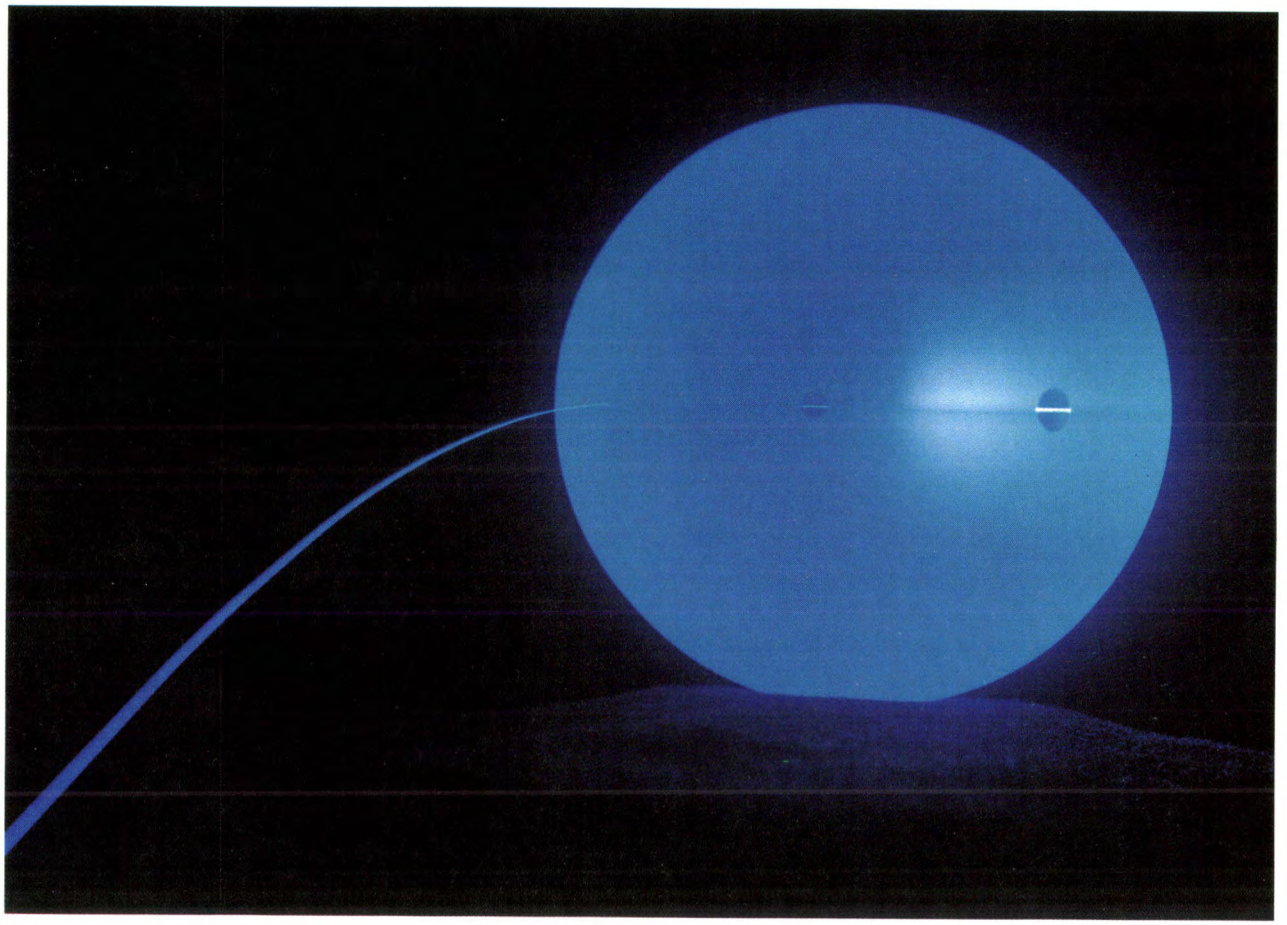

The integrating sphere depicted here is used at Philips Research Laboratories for measuring radiation losses due to scattering in optical fibres. In the situation shown the sphere was not coated with the required reflecting layer of white paint, so that light was able to leave it from all points. As with luminous flux determinations using the Ulbricht sphere, a single measurement seems in principle sufficient. A radiation loss expressed as a power *ratio* (in dB, and per kilometre of fibre length) does require a reference measurement, however. This is because either the intensity of the laser source or the efficiency of the coupling between laser and fibre is an unknown quantity. The second measurement yields the radiant power in the fibre at the given location, the other quantity in the power ratio. The sphere, made of optical glass, has a diameter of 8 cm and consists of upper and lower halves; a recessed capillary channel runs between them along a straight line passing exactly through the centre. Measurements on a fibre are made by passing it through the capillary until the end of the fibre just protrudes outside the sphere. When scattered light escapes through the cladding of the inserted piece of fibre and enters the sphere through a suitable transitional layer (e.g. of glycerine) the lost light will be distributed homogeneously over the wall of the sphere by repeated reflections from the paint layer (in much the same way as reverberations in acoustics). The irradiance at the wall of the sphere thus acquires the same value everywhere. Integration over the surface gives the radiation loss to be determined. Two windows are ground in the spherical surface (visible at the level of the centre plane). A photodiode is applied to the window on the left for measuring the irradiance; the window on the right is used for monitoring measurements. The *absorption loss* inside the piece of fibre can be determined separately by subtracting a scatter loss from the difference, also measured with the sphere, between the radiant power entering and leaving the sphere (the total signal loss). The low values now obtained for such losses, about 0.2 dB/km, will be mentioned in a forthcoming article on colour multiplex and demultiplex. For the reference measurement the fibre is only inserted half-way into the capillary, as shown in the photograph. The light spot to the right of the centre is due to the signal from the fibre end. The separating line between the halves of the sphere shows up as a faint line, partly dark, partly bright.

Philips Tech. Rev. 41, 348-361, 1983/84, No. 11/12

Magnetic bearings

E. M. H. Kamerbeek

In 1725 Jacob Leupold wrote in his book Theatrum Machinarum Hydraulicarum: 'Whosoever therefore seeks to achieve with his Machines as much as the Theory teaches should do away as far as possible with all friction...' [*]. *Today the limitation of friction losses in bearings is still an engineering challenge. The magnetic bearing is distinguished from other types of bearing by an almost complete absence of friction. A difficulty, however, is that in practice magnetic levitation is always accompanied by an unstable equilibrium of forces, so that height control with feedback is necessary. This article shows how the load-carrying capacity and stiffness of magnetic bearings can be calculated and the problems of stability can be solved in certain cases.*

Introduction

Magnetic levitation has a number of advantages as a means of supporting a shaft in a bearing. There is virtually no friction and no wear, so that magnetic bearings can have a long life and run at high speeds. They are quiet, and are particularly suitable for applications in which there should be no contamination from lubricants, as in vacuum. In addition it is fairly easy to adjust the position of the axis of rotation via the bearing forces and suppress the effects of unbalance.

From Earnshaw's theorem [1], formulated in 1842, it can be shown that in a static magnetic field the equilibrium of the forces acting on a body is not stable if the magnetic permeability of the materials in the field is greater than 1. A stable equilibrium in a field of forces (F_x,F_y,F_z) requires negative $\partial F_x/\partial x$, $\partial F_y/\partial y$ as well as negative $\partial F_z/\partial z$; see *fig. 1*. A necessary — but not sufficient — condition for stability is thus

$$\frac{\partial F_x}{\partial x} + \frac{\partial F_y}{\partial y} + \frac{\partial F_z}{\partial z} < 0. \qquad (1)$$

It can be shown that when an object is levitated in a static magnetic field in which there are materials with $\mu_r > 1$ then

$$\frac{\partial F_x}{\partial x} + \frac{\partial F_y}{\partial y} + \frac{\partial F_z}{\partial z} > 0.$$

The equilibrium of forces is then unstable and a small displacement from the unstable equilibrium state causes a greater deflection of the object. In an electrodynamic system — characterized by the action of forces on current-carrying conductors — in air and with constant currents we have

$$\frac{\partial F_x}{\partial x} + \frac{\partial F_y}{\partial y} + \frac{\partial F_z}{\partial z} = 0.$$

This is also true for systems with permanent magnets only with $\mu_r = 1$ ('hard' permanent magnets). In both the last two cases the stability condition is thus not satisfied.

Stable equilibrium is however possible in a magnetic system if the magnetic permeability μ_r is locally less than 1. This is the case in systems with diamagnetic materials and in systems with materials in the superconducting state. In superconducting materials the magnetic permeability is effectively zero. In the diamagnetic materials with the lowest permeability, graphite and bismuth, the value of μ_r differs only slightly from unity. For this reason the load-carrying capacity that can be achieved with these materials in magnetic levitation is very small [2]. Temperatures near absolute zero are necessary to bring materials into the superconducting state. Although the load-carrying capacity that can then be achieved is greater than with diamagnetic materials, 'superconductive' bearing systems have as yet little practical usefulness.

Dr Ir E. M. H. Kamerbeek is with Philips Research Laboratories, Eindhoven.

[*] See page 270 of E. A. Muijderman, New forms of bearing: the gas and the spiral groove bearing, Philips Tech. Rev. 25, 253-274, 1963/64.

To design a magnetic bearing for practical applications it is therefore necessary to compensate for the instability of the equilibrium of forces [3]. By the expedient of adding feedback control loops it is then possible to satisfy the condition of eq. (1).

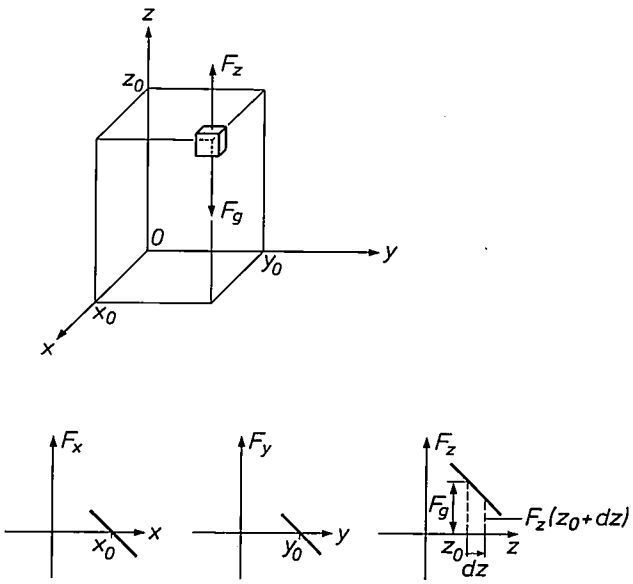

Fig. 1. A stable equilibrium of forces. An object with the gravitational force F_g acting on it is situated at the position (x_0, y_0, z_0) in a rectangular coordinate system (x,y,z). Also defined is a field of forces (F_x,F_y,F_z), whose magnitude is given for a small region around the point (x_0,y_0,z_0) at the bottom of the figure. (F_x, F_y and F_z are taken to be positive in the x-, y- and z-directions; the torques acting on the object are not considered.) When the object is displaced to the point (x_0,y_0,z_0+dz) the resultant force $F_g - F_z(z_0+dz)$ will repel the object back to the starting position. The equilibrium of the forces that act on the object in the z-direction is thus stable. Similar considerations apply to displacements in the x-and y-directions. For stability it is thus necessary in any case to satisfy the conditions $\partial F_x/\partial x < 0$, $\partial F_y/\partial y < 0$ and $\partial F_z/\partial z < 0$.

An object freely levitated in space has in general six degrees of freedom: three translations and three rotations. A shaft supported in a bearing has had five of its degrees of freedom removed. To obtain a stable equilibrium we must therefore provide a maximum of five control loops for the magnetic bearing. With an appropriate geometry only one control loop, relating to a translation, may be sufficient in some cases. The remaining two rotations and two translations are then characterized by a negative stiffness for the corresponding torques and forces [4].

The method of calculating the load-carrying capacity and stiffness of magnetic bearings will next be described. This will be followed by a discussion of some bearing designs we have investigated that have fewer than five control loops. After examining the dynamic behaviour of the control loops, the article concludes with a discussion of the instability of a rotor at very high speeds in a magnetic bearing that we have designed.

Theoretical background

Calculating the load-carrying capacity

There are various ways of determining the force acting on an object in a magnetic field in air or in vacuum. A very straightforward and general method is one in which Maxwell's equations in vector notation are used to calculate a fictitious force density $\boldsymbol{p}$ at a surface that completely encloses the object [5]:

$$\boldsymbol{p} = (\boldsymbol{B}.\boldsymbol{n})\frac{\boldsymbol{B}}{\mu_0} - \frac{1}{2}\boldsymbol{n}\left(\frac{B^2}{\mu_0}\right), \qquad (2)$$

where the vector $\boldsymbol{B}$ is the magnetic flux density, $\boldsymbol{n}$ the outward-directed unit vector perpendicular to the enclosing surface and μ_0 the magnetic permeability of free space; see *fig. 2a*. The total vector force $\boldsymbol{F}$ acting on the object is then found from

$$\boldsymbol{F} = \int_{S'} \boldsymbol{p}\, ds, \qquad (3)$$

where S' is the total area of the enclosing surface with surface element ds. The enclosing surface S'may coincide with the surface S of the object.

After some manipulation, expressions for the component p_n of the force density perpendicular to the surface ('tensile or compressive stress') and the component p_t along the surface ('shear stress') can be derived from (2):

$$p_n = \frac{B_n^2 - B_t^2}{2\mu_0}, \qquad (4)$$

$$p_t = \frac{B_n B_t}{\mu_0}, \qquad (5)$$

where B_n is the normal component and B_t the tangential component of $\boldsymbol{B}$. The relation between the two components of $\boldsymbol{p}$ and the angle ϕ that $\boldsymbol{B}$ makes with the surface is shown in fig. 2*b*: for $\phi = 0$ and for $\phi = \pi/2$ the component $p_t = 0$ and $|p_n|$ is at a maxi-

[1] S. Earnshaw, On the nature of the molecular forces, Trans. Cambridge Phil. Soc. 7, 97-112, 1842.

[2] W. Braunbek, Freischwebende Körper im elektrischen und magnetischen Feld, Z. Phys. 112, 753-763, 1939;
W. Braunbek, Freies Schweben diamagnetischer Körper im Magnetfeld, Z. Phys. 112, 764-769, 1939;
A. H. Boerdijk, Levitation by static magnetic fields, Philips Tech. Rev. 18, 125-127, 1956/57.

[3] An interesting way of obtaining a stable equilibrium by varying the magnitude of the magnetic field is described in: H. van der Heide, Stabilization by oscillation, Philips Tech. Rev. 34, 61-72, 1974.

[4] It is possible to provide the only unstable — and hence uncontrolled — translation with a conventional bearing. A system of this type, with permanent magnets and a conventional axial bearing, is described in: F. T. Backers, A magnetic journal bearing, Philips Tech. Rev. 22, 232-238, 1960/61.

[5] A more general equation is derived in: E. M. H. Kamerbeek, On the theoretical and experimental determination of the electromagnetic torque in electrical machines, Thesis, Eindhoven 1970.
See also pp. 97-103 in: J. A. Stratton, Electromagnetic theory, McGraw-Hill, New York 1941.

mum, and for $\phi = \pi/4$ the component $p_n = 0$ and p_t is at a maximum.

In a magnetic bearing we have a cylindrical object that is levitated in a magnetic field. For the cylindrical surface of the shaft it is then desirable that p_n should be large and p_t small, since p_n produces the load-carrying capacity and p_t usually causes an opposing torque ('friction'). This requirement can be satisfied if $\phi = 0$ or if $\phi = \pi/2$. For $\phi = 0$ the lines of force are tangential to the surface; see fig. 2*c*. It can easily be seen that in this case the force F_z, the force density integrated over the area of the surface, becomes smaller if the shaft is displaced from the region with the largest flux density, i.e. $\Delta F_z/\Delta z < 0$. The equilibrium of F_z with the gravitational force F_g is therefore stable. For $\phi = \pi/2$ the lines of force cut the surface perpendicularly; see fig. 2*d*. We now have $\Delta F_z/\Delta z > 0$, so that the equilibrium between the magnetic force and the gravitational force is unstable.

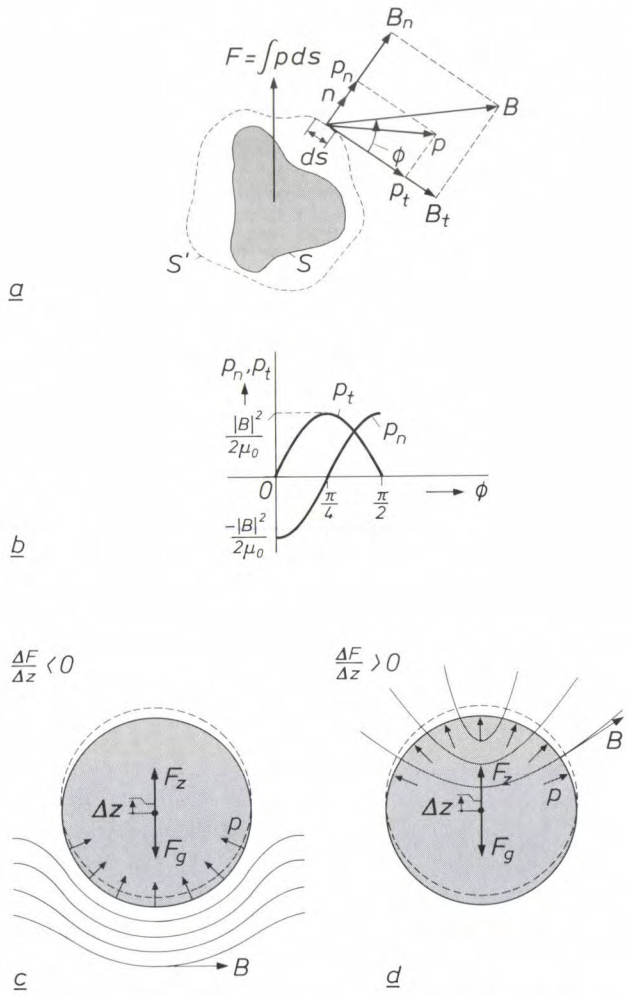

Fig. 2. *a)* Definition of quantities for calculating the force acting on an object in a magnetic field. $\boldsymbol{B}$ magnetic flux density; B_t is the tangential component, B_n the normal component. S' surface completely enclosing the object. S surface of the object. $\boldsymbol{p}$ force density; p_t is the tangential component, p_n the normal component. $\boldsymbol{n}$ unit vector perpendicular to S' (positive outward). $\boldsymbol{F} = \int \boldsymbol{p}\,ds$ resultant force on the object, where ds is a surface element of S'. ϕ angle of $\boldsymbol{B}$ to the surface S'. *b)* The components p_t and p_n of $\boldsymbol{p}$ as a function of the angle ϕ, from equations (4) and (5). *c)* Maximum $|p_n|$ obtained at $p_t = 0$ and $\phi = 0°$. In this way a stable equilibrium is established between the load-carrying capacity F_z and the gravitational force F_g, since $\Delta F_z/\Delta z < 0$. *d)* A similar situation at $\phi = \pi/2$. The equilibrium is now unstable, however, since $\Delta F_z/\Delta z > 0$. Fig. 3 shows how (*c*) and (*d*) are attained in practice.

Obtaining the required direction for the lines of force

A situation as shown in fig. 2*c* can be obtained by making use of the effect of superconductivity. If niobium or lead ('superconductors of the first kind' [6]) are in the superconducting state, any change in the magnetic flux density causes permanent eddy currents at the surface of the material, their magnitude and direction being such as to cancel the effect of this change. No magnetic flux can therefore be generated in these superconductors. This situation corresponds to that in a hypothetical material whose magnetic permeability is equal to zero. The lines of force representing the magnetic field cannot penetrate into the material; see fig. 2*c*. In *fig. 3a* this situation is shown again for the case where the centre-line of the shaft coincides with the plane of the diagram and for a different direction of the flux density. The maximum force density that can be achieved is $|p| = B^2/2\mu_0$, from (4). The flux density at the boundary surface of superconductors of the first kind must remain limited to between 0.1 and 0.3 T (tesla or Wb/m^2), since otherwise the superconductivity would vanish. The corresponding force density is at the most 3×10^4 N/m^2 or 0.3 bar. The load-carrying capacity that can be achieved is thus fairly small. Also, there is the great disadvantage that part of the rotor has to be cooled to a temperature of 10 K or lower. As explained above, the magnetic bearing with superconducting shaft ends does yield a stable equilibrium of forces. This is not in conflict with Earnshaw's theorem, since this theorem only applies to cases where $\mu_r > 1$.

Fig. 3*b* shows the situation for the case where the shaft ends are made of diamagnetic material. The angle that the lines of force make with the surface now has a value between 0 and $\pi/2$. In the material the lines of force diverge, because the flux density here is less than in air. Since μ_r differs very little from unity, the force density is limited. The load-carrying capacity is even less than in the case of fig. 3*a*. It should be noted that the situation shown in fig. 3*b* can also be obtained by means of an alternating electromagnetic field, because eddy currents opposing the alternating magnetic field are then induced into the shaft ends. The eddy currents cause losses, however. A rough calculation shows that the loss on levitating a copper

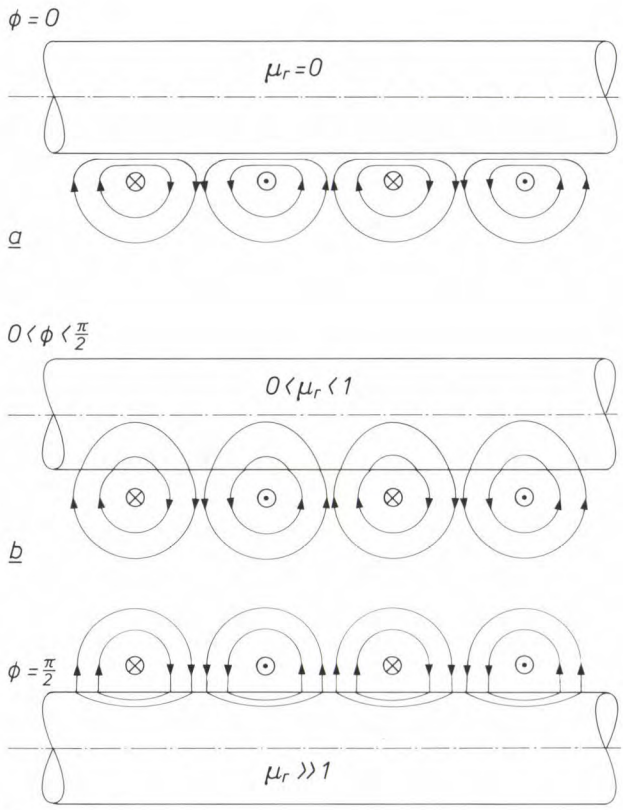

Fig. 3. Three methods of 'levitating' a shaft in a magnetic field (see fig. 2). *a*) With $\phi = 0°$. The shaft must be cooled to a temperature at which the material becomes superconducting. The magnetic permeability μ_r is then effectively equal to zero. *b*) With $0 < \phi < \pi/2$. The shaft must be made of diamagnetic material, for which $0 < \mu_r < 1$. In both these cases the equilibrium of forces in the vertical direction is stable and the shaft 'floats' on the magnetic field. *c*) With $\phi = \pi/2$. The shaft now has to be made of ferromagnetic material, for which $\mu_r \gg 1$. Because of the reversal of the force density, the shaft is suspended in the magnetic field. As Earnshaw's theorem states, however, the equilibrium of forces is not stable.

plate, irrespective of its thickness, is about 2.8 kW per m^2 of bearing surface. The loss with an aluminium plate is about 1.3 kW/m^2 [7].

Fig. 3*c* shows a situation where the direction of the flux is perpendicular to the bearing surface. As in fig. 3*a*, the force density is equal to $B^2/2\mu_0$. We can work here with materials of high magnetic permeability and high saturation flux density. In cobalt iron, for example, the flux density can amount to as much as 2.4 T. The maximum force density is then 23×10^5 N/m^2 or 23 bars. The equilibrium of forces is not stable, however, since Earnshaw's theorem now applies. To obtain an effective bearing the size of the bearing gap must be controlled. The method of control will be discussed later on in this article.

Calculating the load-carrying capacity for a sinusoidal surface-current density

The mean force density $\bar{p}_n$ for the three cases of fig. 3 can be expressed in mathematical terms. We assume that the magnetic field along the surface of a medium of magnetic permeability μ_r is generated by means of a sinusoidal surface-current density of peak value $\hat{A}$ (in A/m); see *fig. 4a*. Using equation (4) we then find for $\bar{p}_n$:

$$\bar{p}_n = -\frac{\mu_0}{4}\frac{1-\mu_r}{1+\mu_r}\hat{A}^2 e^{-4\pi a/\lambda}, \qquad (6)$$

where λ is the wavelength of the surface-current density.

Equation (6) can be derived as follows. We assume that the surface-current density $A = \hat{A} \sin 2\pi y/\lambda$ is located in a rectangular coordinate system (x,y,z) in the plane $z = 0$, with the currents per-

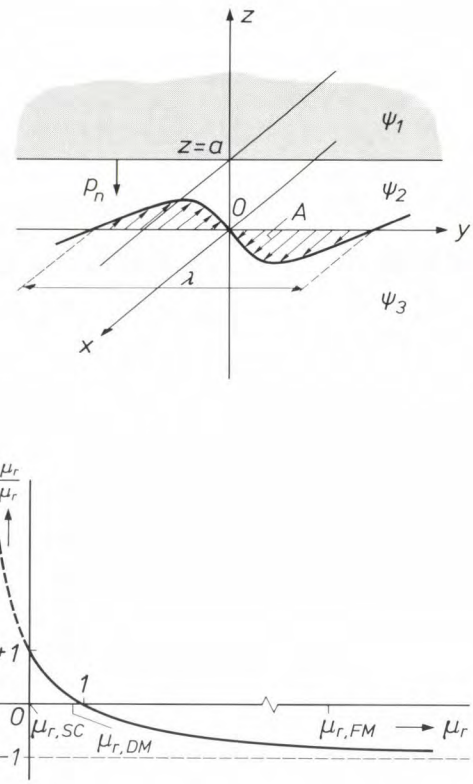

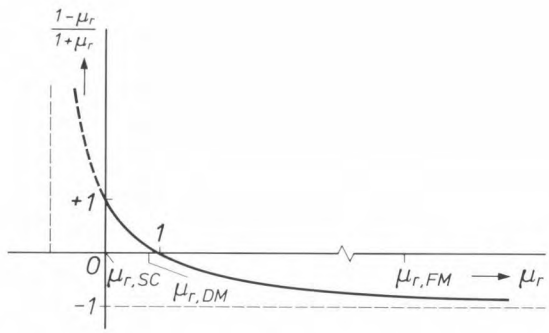

Fig. 4. *a*) Definition of quantities for calculating the density of forces p_n at the interface of two media with $\mu_r = 1$ and $\mu_r \neq 1$ in the presence of a sinusoidal surface-current density of magnitude $A = \hat{A} \sin 2\pi y/\lambda$. The interface coincides with the plane $z = a$ in a rectangular coordinate system (x,y,z). The surface-current density (current sheet) is situated in the (x,y)-plane and extends to infinity in the positive and negative y-directions. Ψ_1, Ψ_2 and Ψ_3 magnetic potential functions in the spaces $z \geqslant a$, $0 \leqslant z < a$ and $z < 0$. *b)* The factor $(1 - \mu_r)/(1 + \mu_r)$ from equation (6) for the mean force density, plotted as a function of μ_r. Here $\mu_{r,SC}$ is the value of μ_r for superconducting material, $\mu_{r,DM}$ the corresponding value for diamagnetic material and $\mu_{r,FM}$ is this value for ferromagnetic material. The diagram shows that higher force densities can be obtained with superconducting and ferromagnetic materials than with diamagnetic materials.

[6] V. L. Newhouse, Applied superconductivity, Vol. 2, Academic Press, New York 1975.

[7] Provided that in both cases the frequency of the alternating field is sufficiently high and that the plate thickness is less than the penetration depth of the eddy currents at that frequency: see H. B. G. Casimir and J. Ubbink, The skin effect, I, Philips Tech. Rev. **28**, 271-283, 1967.

pendicular to the plane $x = 0$ and the surface-current density (current sheet) extending to infinity in the positive and negative y-directions. For $z \geqslant a$ the permeability μ_r is not equal to unity and is constant, and for $z < a$ we have $\mu_r = 1$. Let the space be divided into three parts. In part *1*, for $z \geqslant a$, the magnetic potential function has the value Ψ_1; in part *2*, for $0 \leqslant z < a$, it has the value Ψ_2; in part *3*, for $z < 0$, it has the value Ψ_3. In each of these parts Laplace's equation $\Delta\Psi_i = 0$ applies, with $i = 1$, 2 and 3. We are considering a two-dimensional problem, so that the derivatives with respect to x are equal to 0 and $\partial^2\Psi_i/\partial y^2 + \partial^2\Psi_i/\partial z^2 = 0$. For the magnetic field-strengths in the three parts we can have:

$$H_{1y} = -\frac{\partial\Psi_1}{\partial y}, \quad H_{1z} = -\frac{\partial\Psi_1}{\partial z},$$

$$H_{2y} = -\frac{\partial\Psi_2}{\partial y}, \quad H_{2z} = -\frac{\partial\Psi_2}{\partial z},$$

$$H_{3y} = -\frac{\partial\Psi_3}{\partial y}, \quad H_{3z} = -\frac{\partial\Psi_3}{\partial z}.$$

With the aid of the above differential equations we can calculate the field-strengths along the plane $z = a$. The following boundary conditions then apply:

$$H_{1y} = H_{2y} \text{ and } \mu_r H_{1z} = H_{2z}, \text{ for } z = a;$$
$$H_{1y} = H_{1z} = 0, \text{ for } z = \infty;$$
$$H_{3y} - H_{2y} = A \text{ and } H_{2z} = H_{3z}, \text{ for } z = 0;$$
$$H_{3y} = H_{3z} = 0, \text{ for } z = -\infty.$$

The solutions for the potential functions must then satisfy:

$$\Psi_1 = A_1 \, e^{-2\pi z/\lambda} \cos 2\pi y/\lambda,$$
$$\Psi_2 = (A_2 \, e^{-2\pi z/\lambda} + B_2 \, e^{2\pi z/\lambda}) \cos 2\pi y/\lambda,$$
$$\Psi_3 = A_3 \, e^{2\pi z/\lambda} \cos 2\pi y/\lambda,$$

in which the boundary conditions for $z = \infty$ and $z = -\infty$ have already been included. The remaining boundary conditions give four equations, which we can solve for A_1, A_2, A_3 and B_2. We thus obtain equations for the field-strengths at the boundary plane $z = a$:

$$H_{2y}(z = a) = -\frac{1}{1 + \mu_r} \hat{A} \, e^{-2\pi a/\lambda} \sin 2\pi y/\lambda$$

and

$$H_{2z}(z = a) = -\frac{\mu_r}{1 + \mu_r} \hat{A} \, e^{-2\pi a/\lambda} \cos 2\pi y/\lambda;$$

from this and (4) we obtain an equation for the force density p_n perpendicular to the boundary plane:

$$p_n = \frac{\mu_0}{2(1 + \mu_r)^2} \left\{ \mu_r^2 \hat{A}^2 e^{-4\pi a/\lambda} \cos^2 2\pi y/\lambda - \hat{A}^2 e^{-4\pi a/\lambda} \sin^2 2\pi y/\lambda \right\}.$$

Integrating p_n with respect to y from $-\lambda/2$ to $\lambda/2$ and dividing the result by λ, we find equation (6) for the mean force density $\bar{p}_n$ perpendicular to the boundary plane.

Since $1 - \mu_r$ is very small for diamagnetic materials, the force density obtained with these materials is not very large, as indicated earlier. For bismuth, the diamagnetic material with the lowest permeability, we have $1 - \mu_r \approx 1.6 \times 10^{-4}$. The force density is thus about 0.8×10^{-4} times smaller than for materials in the superconducting state with $\mu_r = 0$ or for ferromagnetic materials with $\mu_r \gg 1$; see fig. 4*b*.

The mean force density at $z = a$ in the z-direction is $-\bar{p}_n$. After differentiating $-\bar{p}_n$ with respect to a we then find the mean vertical stiffness per unit area in the z-direction:

$$\frac{\partial}{\partial a}(-\bar{p}_n) = -\frac{\pi\mu_0}{\lambda} \frac{1 - \mu_r}{1 + \mu_r} \hat{A}^2 \, e^{-4\pi a/\lambda}. \qquad (7)$$

We see from this that for diamagnetic and superconducting materials the mean vertical stiffness is negative. Thus, with these materials, as we have already seen, a stable equilibrium of forces is possible for levitation. With other, 'ordinary' materials this stiffness is positive; the equilibrium of forces is then unstable, as would be expected from Earnshaw's theorem. It also follows from (6) that the conductors of the surface-current density must lie as close as possible to the boundary plane $z = a$ to produce the maximum force density. For $a = 0$ the mean absolute force density $|\bar{p}_n|$ for ferromagnetic and superconducting materials is given by:

$$|\bar{p}_n| = \frac{\mu_0}{4} \hat{A}^2. \qquad (8)$$

In practice the force densities for superconducting materials and ferromagnetic materials are unequal, since, as we noted earlier, in superconducting materials the maximum flux density at the boundary plane must remain limited.

Active magnetic bearings

In active magnetic bearings a stable equilibrium is achieved by means of one or more control loops. In general, five degrees of freedom of the rotor have to be stabilized; see *fig. 5*. For each degree of freedom a sensor is then necessary to measure the displacement of the rotor. The difference between the measured position z and the desired position z_0 is converted in the control loop into a change of the current through the coils that generate the load-carrying capacity.

The five-fold control system required for the magnetic configuration shown in fig. 5 has the advantage that the parameters associated with each degree of freedom can be chosen more or less independently of each other. (The control loop for one pair of magnets is shown in a highly simplified form.) The associated electronics, however, makes the bearing rather complicated and expensive. For this reason magnetic bearings have been designed that have one or more non-controlled degrees of freedom. In these bearings the stiffness in the associated directions is usually smaller than that for the controlled degrees of freedom; but there is a 'natural' stable equilibrium of forces in these directions. We have built three such magnetic bearings, partly based on data from the literature [8][9], and have tested them. Let us now take a closer look at

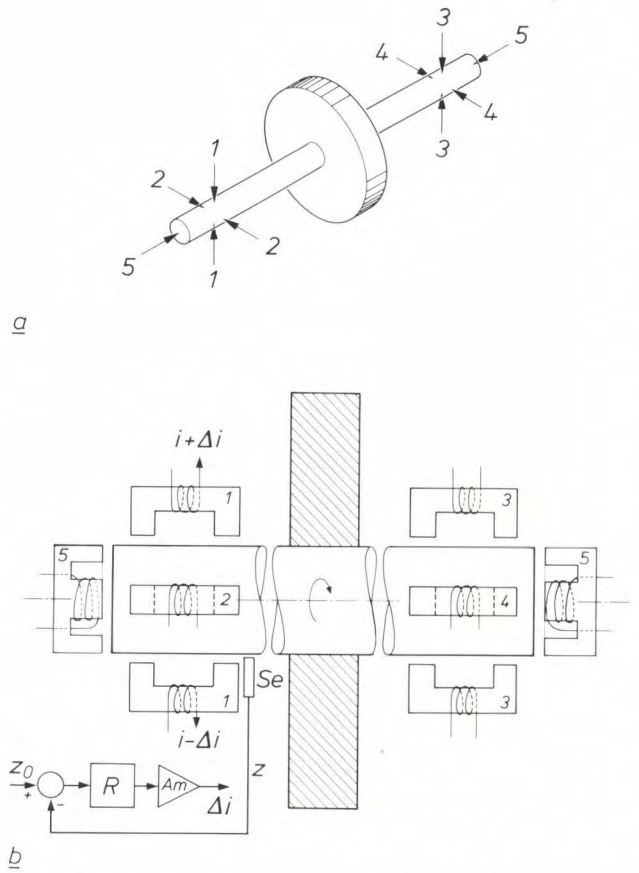

Fig. 5. General configuration of a magnetic bearing for a rotor with five control loops. Each of the pairs of electromagnets *1-1*, *2-2*, *3-3*, *4-4* and *5-5* has its own control loop (shown here simplified for *1-1*) with a displacement sensor. The output signal of the sensor *Se*, which is a measure of the position z of the rotor shaft, is compared with a reference signal for the desired position z_0. The difference signal is converted into a current Δi via a controller *R* and an amplifier *Am*. This signal is added to a direct current i in the one coil and subtracted from the same current in the other coil of the pair of magnets. This produces a resultant force on the shaft, which drives it back to the desired position. The magnet pairs *1-1* and *3-3* control two degrees of freedom of the rotor: a rotation and a translation. The same applies to the magnet pairs *2-2* and *4-4*. The magnet pair *5-5* only controls a translation.

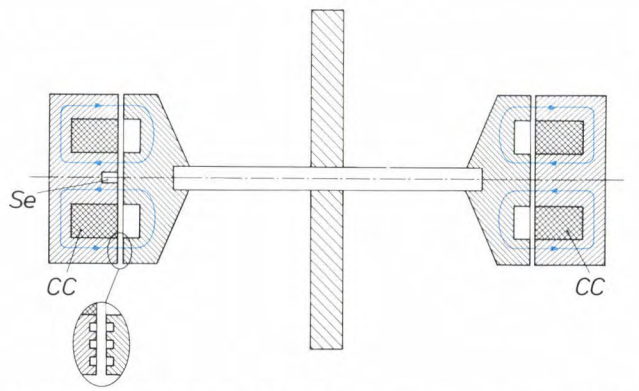

Fig. 6. Magnetic bearing with only one control loop, for the axial direction (see fig. 12). The stiffness in the radial direction is increased by means of concentric grooves in the pole pieces (see inset). In spite of this the stiffness in the radial direction is substantially less than that in the — controlled — axial direction. *Se* displacement sensor. *CC* coils energized by a direct current with a superimposed control current; see fig. 5. The magnitude of the control current is determined by the control loop. The schematized magnetic lines of force are indicated in blue.

the types of bearings we investigated [10], which were designed primarily for use in vacuum.

The magnetic configurations

Fig. 6 shows a configuration in which a control loop is only necessary for the axial direction. In the radial directions the magnetic forces and the external forces are in stable equilibrium. The stiffness and load-carrying capacity in these directions are increased by concentric grooves in the pole pieces. (Approximate equations for calculating the radial stiffness as a function of the groove geometry are given in the next subsection.) The coils are energized by a constant current on which a control current is superimposed. The magnitude of the control current is determined by a control loop with feedback of the axial rotor position, measured by the inductive displacement sensor *Se*.

The configuration in fig. 6 is simple but has the disadvantage that heat is constantly dissipated in the coils. The magnetic bearing in *fig. 7* does not have this disadvantage because it has annular permanent magnets. In coil *CC* the only heat dissipated is the small amount generated by the control current. In the sensor coil *SeC* a voltage is induced when an axial displacement of the rotor changes the linked flux. The output voltage of the sensor coil is a measure of the

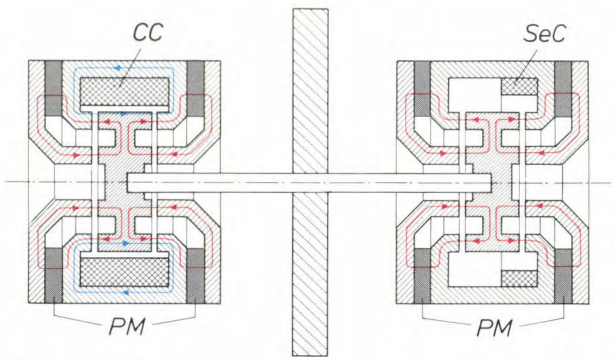

Fig. 7. Magnetic bearing with permanent magnets *PM*. Compared with the bearing in fig. 6, less heat is dissipated, since the coil *CC* is energized only by the control current from the control loop. *SeC* speed sensor. Instead of the axial displacement of the rotor the axial velocity here is the feedback quantity in the control loop (see fig. 13). The pole pieces have concentric grooves as in fig. 6. The schematized magnetic lines of force due to the permanent magnets are shown in red, the lines of force due to the coil *CC* are shown in blue. From the directions of these lines it appears that a current in *CC* increases the flux density in one air gap and reduces it in the other. The current Δi from the control loop can thus be supplied directly to coil *CC* (see fig. 5).

[8] C. L. Henrikson, J. Lyman and P. A. Studer, Magnetically suspended momentum wheels for spacecraft stabilization, AIAA 12th Aerospace Sciences Meeting, Washington, DC, 1974.

[9] A. V. Sabnis, J. B. Dendy and F. M. Schmitt, Magnetically suspended large momentum wheels, AIAA Mechanics and Control Flight Conf., Anaheim, CA, 1974.

[10] For certain aspects of the bearing systems investigated by us, patents have been granted in the United States under the numbers 4 322 624 and 4 357 555.

speed of the rotor, so that this voltage can provide speed information for feedback in the control loop. As in fig. 6, a displacement sensor can also be used. The permanent magnets in the right-hand part serve not only for generating voltage in the sensor coil but also, like the permanent magnets in the left-hand part, for generating radial load-carrying capacity.

As we have seen in the foregoing, the load-carrying capacity of magnetic bearings is proportional to the square of the flux density in the air gap. It is therefore important to make this flux density large, i.e. to ensure that magnetic circuits have a low reluctance. This means that the air gaps must be small: practical considerations dictate a gap of between 0.1 and 0.2 mm. A disadvantage of the magnetic configurations in figs 6 and 7 is that the effect of the rotor temperature on the size of the air gaps is not always negligible. Furthermore, the considerable distance between the outer pole pieces imposes critical manufacturing tolerances on the rotor and the other components.

These disadvantages do not apply to the bearing in *fig. 8*, in which the axial distance between the pole pieces is much smaller. This bearing has three control coils at 120° spacing, three corresponding displacement sensors and one annular permanent magnet. The annular magnet gives a constant magnetic flux in the annular air gaps. There are three control loops. In the radial directions the equilibrium of forces is stable, and the stiffness is again increased by concentric grooves in the pole pieces.

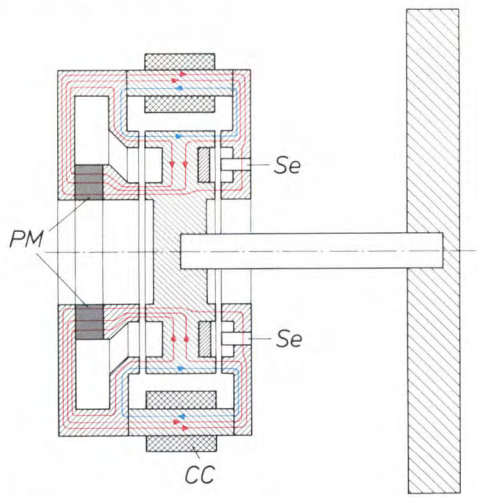

Fig. 8. Magnetic bearing in which the magnitude of the air gaps is less dependent on the rotor temperature than for the bearings in figs 6 and 7. There is one annular permanent magnet *PM* and there are three control coils *CC* spaced at 120° around the circumference. There are also three displacement sensors *Se* and three control loops, each with its own coil *CC*. The pole pieces have concentric grooves. The paths of the schematized lines of force (the red ones relate to *PM*, the blue ones to *CC*) indicate that a current in *CC* increases the flux density locally in one outer air gap and reduces it in the other outer air gap. The three loops control three degrees of freedom: a translation (in the axial direction) and two rotations (about axes perpendicular to the axis of rotation). The three control loops are coupled in a special way for this purpose.

Calculation of the radial load-carrying capacity

Let us first consider *fig. 9a*, which gives a diagram of an iron armature drawn into the air gap of an electromagnet energized by direct current. The force $\boldsymbol{F}$ acting on the armature will be calculated, with the assumption that the air gaps have the same height g so that the vertical forces are in unstable equilibrium. We shall also assume that the gaps between armature and magnet are much smaller than the height of the

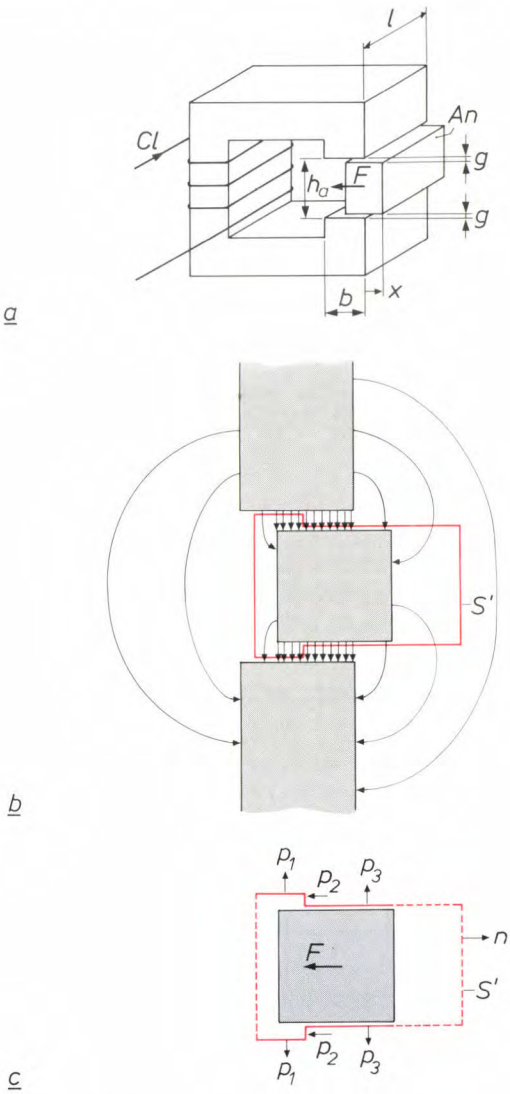

Fig. 9. Magnetic model for calculating the radial load-carrying capacity of the bearings in figs 6, 7 and 8. *a*) The magnetic circuit, in which various dimensional quantities are indicated that are used for calculating the force $\boldsymbol{F}$ on the armature *An*. The displacement x of the armature is positive in the direction indicated. The flux density results from a current in the coil *Cl*. The armature is situated in the centre of the gap of height h_a. *b*) Enlarged cross-section perpendicular to the armature with schematized lines of force. The red line is the line of intersection with a 'convenient' surface S' (see also fig. 2*a*), which completely encloses the armature. *c*) The force densities at the surface S'. Owing to the low flux density in the region indicated by the dashed lines ($h_a \gg g$) the force densities here are negligible. The force densities $\boldsymbol{p}_1$ and $\boldsymbol{p}_3$ oppose one another at opposite sides and make no contribution to $\boldsymbol{F}$. The force density $\boldsymbol{p}_2$ does make a contribution, however. The unit vector $\boldsymbol{n}$ is perpendicular to S' and positive outwards.

armature, i.e. $g \ll h_a$, and that in the iron μ_r is constant and very large. We can calculate F by using equations (4) and (5) for the force densities at a surface enclosing the armature. Fig. 9*b* gives a schematic representation of the lines of force inside and outside the air gap. (The magnetic lines of force are always perpendicular to the surface of a material for which $\mu_r \gg 1$, since the tangential component of the magnetic field-strength at this surface must be zero.) The red line in the figure is the line of intersection of a 'convenient' enclosing surface with the plane of the figure. In the part of the surface indicated by dashed lines in fig. 9*c* the force densities can be neglected, since the flux density there is small compared with that in the air gap ($h_a \gg g$). The force densities p_1 and p_3 on opposite sides of the surface cancel one another out, since the tangential component B_t of the flux density is zero in the associated parts of the surface. Contributions to the force F come only from the force densities p_2. In the associated parts of the surface the normal component B_n of the flux density is equal to zero. The tangential component B_t delivers a negative normal force density, which therefore has the opposite sense to the unit vector n. From (4) we then have

$$p_2 = -\frac{B^2}{2\mu_0} n, \qquad (9)$$

where B is the magnitude of the flux density in the air gap. Using (9) we can calculate the approximate magnitude of the force F on the armature:

$$F \approx \frac{B^2}{\mu_0} gl, \qquad (10)$$

where l is the length of the air gap.

Next we provide the pole pieces on both sides of the air gaps with a large number of grooves perpendicular to the x-direction, as shown in *fig. 10a*. Now the force does depend on the displacement x, and is in addition proportional to the number of grooves N_t [11][12]:

$$F \approx N_t \frac{B^2 gl}{\mu_0} f\left(x, \frac{w}{g}, \frac{t}{g}, \frac{h}{g}\right). \qquad (11)$$

The geometrical factor f depends on x and also takes account of the groove geometry, determined by the ratios of the dimensions w, t and h to the air gap g. (B in (11) is the flux density at the narrowest part of the air gap.) Fig. 10*b* shows the variation of f for $t = s$ and $h/g = 10$ [12]. It can be seen that f is approximately linear with x for values of x up to about $w/10$.

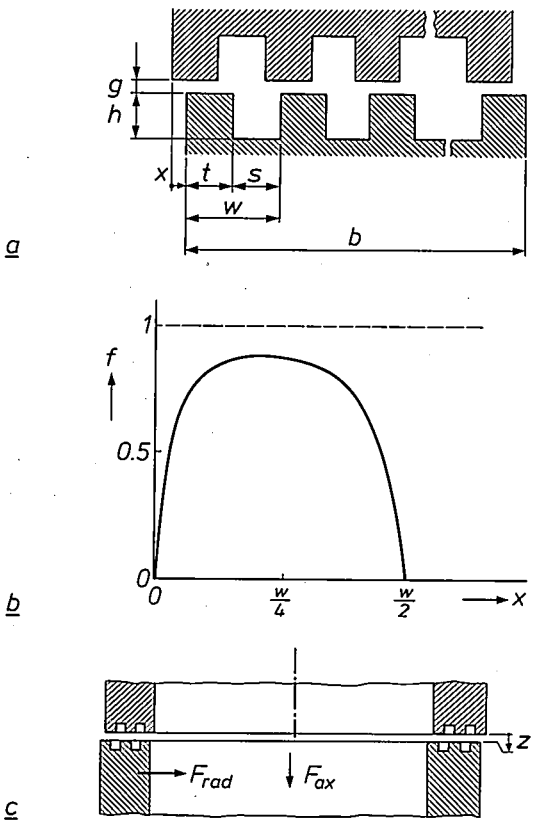

Fig. 10. Modification of the model in fig. 9 with grooves in the pole pieces. *a*) Various dimensional quantities used in the calculation. (The grooves are perpendicular to the plane of the drawing.) *b*) The geometrical factor f as a function of the armature displacement x for $t = s$ and $h = 10g$ (from [12]). For this geometry $f = f(x)$ can be approximated by a sine function. *c*) Application of the model in (*a*) for annular pole pieces. Integration of the calculated value of F (see fig. 9) over the whole annular surface gives F_{rad}, the radial load-carrying capacity. F_{ax} axial load-carrying capacity. F_{rad} cannot be greater than about 0.08 F_{ax}.

The mean magnitude of the 'suction force' F on the grooved armature can be calculated from equation (11):

$$\bar{F} = \frac{2}{w} \int_0^{w/2} F \, dx = 2bl \frac{B^2}{2\mu_0} f_m, \qquad (12)$$

where

$$f_m = \frac{2g}{w^2} \int_0^{w/2} f \, dx.$$

The factor $B^2/2\mu_0$ in equation (12) is equal to the value of the force density p_n perpendicular to the pole pieces, given by (4). Field calculations show that f_m reaches a maximum value of 0.0196 when $w/g \approx 8$, $t/g \approx 3$ and $h \gg g$ [11].

The above expressions can be used for estimating the forces between annular grooved pole pieces of magnetic bearings; see fig. 10*c*. If the function $f = f(x)$ in fig. 10*b* is approximated by a sine function, integra-

[11] K. C. Mukherji and S. Neville, Magnetic permeance of identical double slotting, Proc. IEE 118, 1257-1268, 1971.
[12] H. D. Chai, Permeance between toothed structure, Proc. 7th Ann. Symp. on Incremental motion control systems and devices, Chicago 1978, pp. 45-54.

tion of the force calculated from (12) over the annular surface gives a ratio of the radial to the axial bearing force of

$$\frac{F_{rad}}{F_{ax}} = \frac{\pi f_m w}{2t}. \quad (13)$$

Substituting the maximum value for f_m and the corresponding ratio $t/w = 3/8$, we find that in this case the radial force cannot become greater than about 8% of the axial force.

Calculation of the length/width ratio of the rotor

In the magnetic bearing of fig. 6 stability in the axial direction is obtained through control of the magnitude of the bearing gap. Instability can still occur, however, during an angular rotation of the rotor about a line perpendicular to the centre-line. This instability only occurs when the ratio of the outside diameter to the distance between the pole pieces exceeds a critical value.

Fig. 11 shows the torques that act on the rotor if it is given a small angular rotation α as described above. The total torque M_t acting on the shaft is then:

$$M_t = 2M_\alpha - 2k_{rad}\alpha l^2, \quad (14)$$

where M_α is the torque produced at each pole piece in the tilted position, $2k_{rad}$ is the total radial stiffness of the bearing and $2l$ is the distance between the pole pieces. M_α can be calculated from the force densities in the axial direction. For an annular pole-piece surface:

$$M_\alpha \approx \tfrac{1}{2} R_m^2 k_{ax}\alpha, \quad (15)$$

where k_{ax} is the axial stiffness dF_{ax}/dz for one half of the bearing, see fig. 10c, and R_m is the mean radius of the annulus. The condition for stability is that the stiffness $G = M_t/\alpha \approx -2k_{rad}l^2(1 - k_{ax}R_m^2/2k_{rad}l^2)$ should be negative. This leads to the condition:

$$\frac{R_m^2}{l^2} < \frac{2k_{rad}}{k_{ax}}. \quad (16)$$

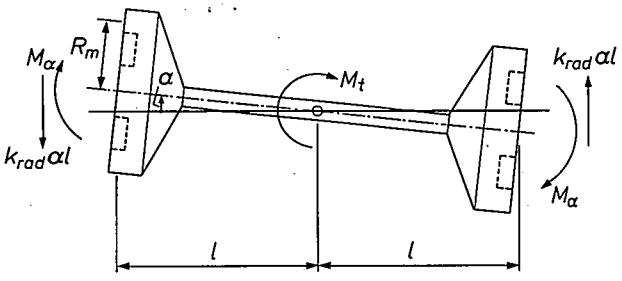

Fig. 11. The forces and torques acting on the rotor in fig. 6 when it is rotated through an angle α about an axis perpendicular to the axis of rotation. $2l$ length of the rotor. k_{rad} radial stiffness of a half-bearing; k_{rad} is positive for the direction chosen here for the vectors $k_{rad}\alpha l$. M_α torque acting on one half-bearing. M_t resultant torque. R_m mean radius of the annular pole pieces.

The ratio $2k_{rad}/k_{ax}$ is almost independent of the radius R_m. In the bearing of fig. 6 that we designed this ratio is about 0.26. To ensure a sufficiently high value for G we made $R_m^2/l^2 \approx 0.1$.

The condition (16) does not apply for a bearing like the one in fig. 8. The three independent control loops here do not only control the axial displacement; they also control the angular rotation about a line perpendicular to the centre-line.

Dynamic stability of the control loops

Control with displacement feedback

As stated above, one control loop is required for the magnetic bearing in fig. 6 or fig. 7 and three control loops are required for the bearing in fig. 8. Let us first consider the behaviour of a control loop with feedback of the displacement, with a 'PID controller'. A PID controller contains elements with proportional, integrating and differentiating action.

The movement of the rotor in the axial direction is described by the differential equation

$$F + F_s = M\frac{d^2z}{dt^2} - k_{PM}z, \quad (17)$$

where z is the displacement of the rotor from the centre position, M is the mass of the rotor, k_{PM} is the (positive) stiffness of the rotor in the field of the permanent magnets in figs 7 and 8 (or in the field due to a constant current in coil CC in fig. 6), F is the force produced by the control current and F_s is a force that perturbs the equilibrium of the rotor. The minus sign for the last term indicates that the equilibrium of the rotor in the magnetic field is unstable. *Fig. 12a* shows the complete block diagram of the control circuit with displacement feedback. The figure also shows the separate transfer functions of the sensor, the controller, the control-coil current amplifier, the control coil and the mass of the shaft. The s in the various transfer functions represents the complex Laplace variable in the usual convention.

The transfer function $H(s)$ of the open control loop is equal to the product of the transfer functions of the individual blocks. We have:

$$H(s) = cKK_cA\frac{(1 + s\tau_i)(1 + s\tau_d)}{s\tau_i(1 + s\tau_d/\gamma)(Ms^2 - k_{PM})}. \quad (18)$$

(The significance of the symbols is explained in the caption to fig. 12.) The poles of $H(s)$ are defined as the values of s for which the denominator is equal to zero. There is therefore one positive pole, $s = \omega_0$, where $\omega_0^2 = k_{PM}/M$.

The behaviour of the control loop for sinusoidal signals of angular frequency ω can be studied by sub-

stituting the imaginary quantity $j\omega$ for s. We then obtain the following expression for the complex transfer function $H(j\omega)$:

$$H(j\omega) = -cKK_cA\frac{(1+j\omega\tau_i)(1+j\omega\tau_d)}{j\omega\tau_i k_{PM}(1+j\omega\tau_d/\gamma)(\omega^2/\omega_0^2+1)}. \quad (19)$$

The stability of the control loop can be investigated by mapping the variation of $H(j\omega)$ for increasing values of ω in the complex plane, thus producing the Nyquist diagram as shown in fig. 12*b*. For $\omega \to 0$ we have $H = \sqrt{Re^2 + Im^2} = \infty$ and the phase angle is $\pi/2$ (arctan Im/Re); for $\omega = \infty$ we have $H = 0$ and the phase angle is π. (Re and Im represent the real and imaginary parts of $H(j\omega)$.) For Nyquist's stability criterion to be satisfied, when the curve is traced out from $\omega = 0$ to $\omega = \infty$, the vector from the point $(-1,0)$ to a point on the curve must rotate anticlockwise through an angle $n\pi$, where n is the number of positive poles of the transfer function [13]. In our case with one positive pole $s = \omega_0$ this vector must therefore rotate through an angle π. For $\omega = 0$ the point of the vector lies at infinity on the negative Re-axis. It is true that for $\omega \to 0$ a phase angle $\pi/2$ was calculated at $H = \infty$, but if the term $j\omega\tau_i$ in the denominator of (19) is replaced by a term $(\delta + j\omega\tau_i)$ the phase angle is π for $\omega = 0$ and $\delta \to 0$. Nyquist's stability criterion is thus satisfied and the control is stable.

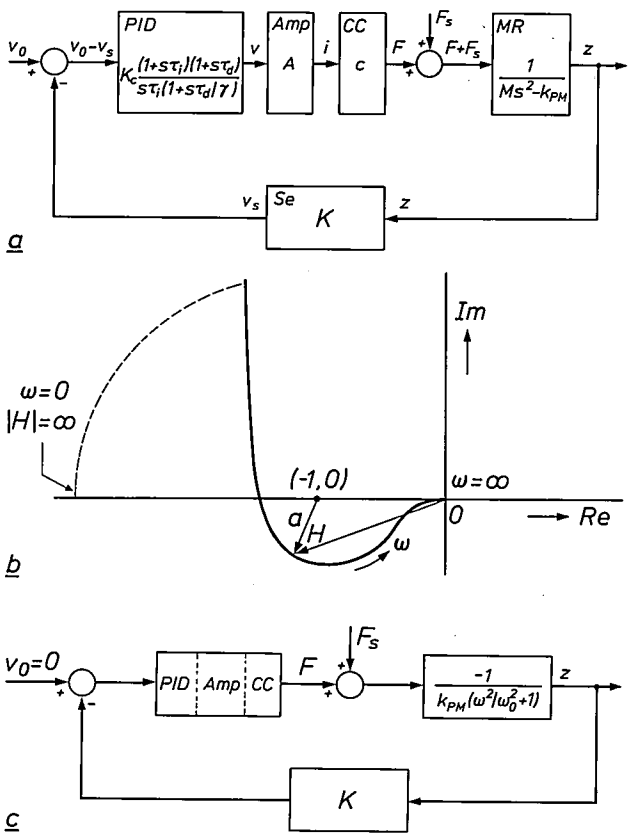

Fig. 12. Control of the height of the bearing gap by rotor-displacement feedback (see fig. 6). *a*) Block diagram of the control loop. v_0 desired signal value. *PID* controller (proportional, integrating and differentiating action) with transfer function $v = (v_0 - v_s)K_c(1 + s\tau_i)(1 + s\tau_d)/\{s\tau_i(1 + s\tau_d/\gamma)\}$ where v is the output voltage of *PID*. K_c gain for the proportional action. τ_i and τ_d time constants of the integrating and differentiating actions. γ factor limiting the differentiating action for high signal frequencies. s complex Laplace variable. *Amp* signal amplifier with transfer function $i = Av$. i output current. A gain. *CC* control coil with idealized transfer function $F = ci$, neglecting eddy-current effects. F axial force. F_s axial perturbing force. *MR* rotor with transfer function $z = (F + F_s)/(Ms^2 - k_{PM})$. M mass. k_{PM} axial stiffness due to the field of the permanent magnets. z axial rotor displacement. *Se* displacement sensor with transfer function $v_s = Kz$. v_s output voltage. K gain. *b*) Corresponding Nyquist diagram. Re real axis. Im imaginary axis. In this diagram the complex value $H(j\omega)$ of the transfer function of the open loop for sinusoidal signals of frequency ω is plotted from the origin for $0 < \omega < \infty$. Here $H(j\omega)$ is the product of the transfer functions of all the blocks, with the imaginary quantity $j\omega$ substituted for s. The distance from the origin O to the curve is equal to $H = \sqrt{Re^2 + Im^2}$, the angle between H and the positive real axis represents the phase angle. The length of the vector $a = 1 + H$, apart from a factor containing ω, is a measure of the stiffness of the bearing to perturbing forces F_s. *c*) Simplified control loop for calculating the stiffness $|F_s/z|$ to perturbing forces.

In reality the behaviour of the control is less satisfactory than indicated in fig. 12*b* because eddy currents are induced in the pole pieces. This means that additional damping terms are included in the transfer function. By laminating the pole pieces or making them of a material of high electrical resistivity such as cobalt iron, this undesirable effect can to some extent be reduced.

The stiffness of the rotor to a perturbing force F_s can also be indicated in fig. 12*b*. Let us consider the simplified control loop shown in fig. 12*c*. It can be shown that

$$z(1 + H) = \frac{-F_s}{k_{PM}(\omega^2/\omega_0^2 + 1)},$$

and from this the stiffness is

$$\left|\frac{F_s}{z}\right| = k_{PM}\left(\frac{\omega^2}{\omega_0^2} + 1\right)|1 + H|. \quad (20)$$

The term $|1 + H|$ is equal to the length of the vector a from $(-1,0)$ to a point on the curve of the Nyquist diagram. From equation (20) and the length of a as a function of ω it follows that the stiffness to perturbing forces is very considerable when $\omega \to 0$ and $\omega \to \infty$. At low frequencies the high stiffness is due to the integrating action of the controller, at high frequencies it is due to the inertia of the rotor mass. We see that for finite frequencies maximum stiffness is achieved when the curve in the Nyquist diagram remains as far away as possible from the point $(-1,0)$. This condition also gives the least amplification of sinusoidal perturbations, i.e. the greatest possible stability.

The perturbing force F_s thus causes a change in the current in the coil *CC* in figs 6, 7 and 8, which acts to

[13] See page 21-10 of: E. M. Grabbe, S. Ramo and D. E. Woolridge, Handbook of automation, computation, and control, Vol. 1, Wiley, New York 1958.

oppose the initial displacement due to $\boldsymbol{F}_s$. A disturbance of the equilibrium therefore brings about extra heat dissipation in the coils. We shall see that with velocity feedback this dissipation is greatly reduced.

Control with velocity feedback

Fig. 13a shows a block diagram of the control loop with velocity feedback. Instead of a PID controller a special controller is used here whose transfer function is $K_c(s\tau + 1)/(s\tau - 1)$, where τ is a time constant and K_c a constant that determines the proportional action [9].

Fig. 13*b* shows the controller network used, with the operational amplifiers to give the required transfer function. Fig. 13*c* shows the equivalent block diagram, in which it is assumed that the operational amplifiers have an infinitely high negative gain. The transfer function of the controller has a positive pole $s = 1/\tau$. The action of the controller alone is thus not stable, but when it is combined with the other elements of the control loop a stable system is obtained.

The transfer function of the open loop of fig. 13*a* for sinusoidal signals of angular frequency ω is:

$$\boldsymbol{H}(j\omega) = cKK_cA\frac{j\omega(1 + j\omega\tau)}{k_{PM}(1 - j\omega\tau)(\omega^2/\omega_0^2 + 1)}.$$

With $K_0 = cKK_cA/k_{PM}$ the real part of $\boldsymbol{H}(j\omega)$ becomes:

$$\mathrm{Re}\,\boldsymbol{H} = \frac{-2\omega^2\omega_0^2\tau K_0}{(\omega_0^2 + \omega^2)(1 + \omega^2\tau^2)},$$

and the imaginary part becomes:

$$\mathrm{Im}\,\boldsymbol{H} = \frac{\omega\omega_0^2 K_0(1 - \omega^2\tau^2)}{(\omega_0^2 + \omega^2)(1 + \omega^2\tau^2)}.$$

Fig. 13*d* gives the corresponding Nyquist diagram with curves for $\omega_0\tau = 1$, $\omega_0K_0 = 4$ and for $\omega_0\tau = 2$, $\omega_0K_0 = 5$. The real axis is intersected for $\omega = 1/\tau$ at the point $\{-\omega_0^2K_0\tau/(1 + \omega_0^2\tau^2), 0\}$. The

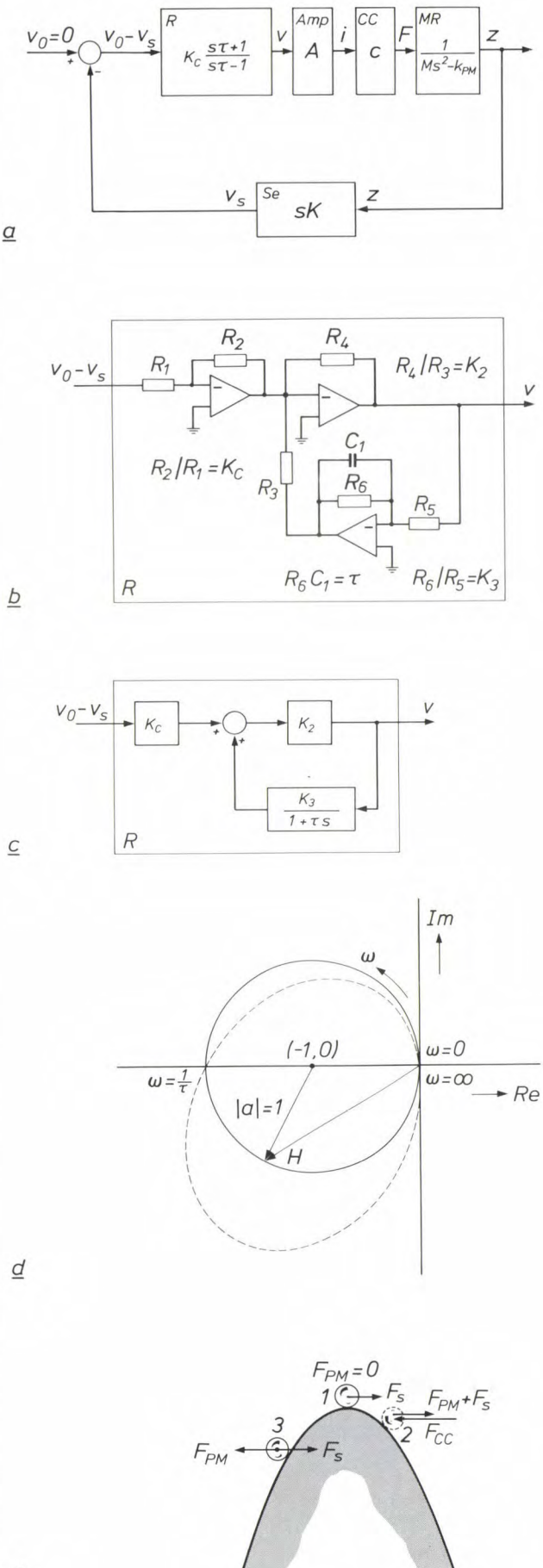

Fig. 13. Control of the height of the bearing gap by means of rotor-velocity feedback (see fig. 7). *a)* Block diagram. The transfer function of the controller R is equal to $K_c(s\tau + 1)/(s\tau - 1)$. τ time constant. The transfer function of the velocity sensor *Se* is equal to sK. See also the caption to fig. 12*a*. *b)* Diagram of the electronic circuit with operational amplifiers which produces the transfer function mentioned above in the controller. *c)* Simplified block diagram of the circuit in (*b*). It is assumed that the operational amplifiers have an infinitely large negative gain. With $K_2 = 1$ and $K_3 = 2$ this diagram gives the required transfer function. *d)* Nyquist diagram corresponding to the complete control loop. For $\omega_0\tau = 1$ the end of $\boldsymbol{H}(j\omega)$ describes a circle with centre $(-K_0/4\tau, 0)$ and radius $K_0/4\tau$, with $\omega_0^2 = k_{PM}/M$ and $K_0 = cKK_cA/k_{PM}$. The continuous curve applies for $\omega_0\tau = 1$ and $\omega_0K_0 = 4$; the dashed curve applies for $\omega_0\tau = 2$ and $\omega_0K_0 = 5$. *e)* Comparison of the behaviour of the control with the equilibrium of a 'ball on a hill'. *1* stabilized equilibrium — the resultant $\boldsymbol{F}_{PM}$ of the forces due to the permanent magnets is zero. $\boldsymbol{F}_s$ perturbing force. *2* the ball is about to roll down the hill with increasing velocity — $F_{PM} + F_s$ increases in magnitude, but the control produces a repelling force $\boldsymbol{F}_{CC}$ from the control coils. *3* stabilized equilibrium state — the ball is driven over the top of the hill by the increase in F_{CC} and finds a position on the other side such that $F_{PM} \approx F_s$. In *3* $F_{CC} = 0$, so that no heat is dissipated in the control coils.

curves start for $\omega = 0$ at the origin and also end there for $\omega = \infty$, in both cases tangential to the imaginary axis at the origin. The transfer function $H(s)$ has two positive poles, $s = \omega_0$ and $s = 1/\tau$. For Nyquist's stability criterion to be satisfied the vector from $(-1,0)$ to the curve must therefore rotate anticlockwise from $\omega = 0$ to $\omega = \infty$ through an angle 2π. For $\omega_0^2 K_0 \tau/(1 + \omega_0^2\tau^2) > 1$ the curve is traced out in such a way that the point $(-1,0)$ is enclosed. Nyquist's stability criterion is then satisfied. It can be shown that for $\omega_0\tau = 1$ the curve becomes a circle with its centre at $(-K_0/4\tau,0)$. The circle shown in fig. 13*d* with $\omega_0 K_0 = 4$ and $\omega_0\tau = 1$ gives the value 1 for $|a| = |1 + H|$ at all frequencies. The stiffness to perturbing forces of angular frequency ω is then, from (20), equal to $k_{PM}(\omega^2/\omega_0^2 + 1)$.

As mentioned above, the system with velocity feedback takes less energy than the system with displacement feedback; see fig. 13*e*. If the rotor is in the central position, the forces of the permanent magnets oppose one another and a stabilized equilibrium of forces prevails. This is represented in the figure as position *1* of a 'ball on a hill'. If the stabilized equilibrium is perturbed by a force F_s, the ball rolls down the hill with increasing velocity. The velocity produces an opposing force, which is generated by a current in the control coils: position *2*. The ball 'shoots over the hill' and finds a stabilized equilibrium at the other side: position *3*. The current in the control coils is then virtually zero.

The position of the rotor with velocity feedback is therefore not always the same but depends on the magnitude of the perturbing force. This is no great problem, because the control behaviour described above takes place in a small region — 10 to 20 μm — of the bearing gap. A disadvantage is that the control has to be 'started', because the rotor is pulled to one side by one of the permanent magnets when the bearing is uncontrolled. This problem is solved by energizing the coil briefly with a current surge from the appropriate direction, thus disengaging the rotor and giving it an initial velocity. The control then comes into operation, and causes the rotor to seek a stable equilibrium.

A version of the bearing system in fig. 7 with velocity feedback and an air gap of 0.25 mm has an average dissipation of only 5 mW at an axial stiffness of 6000 N/mm and a radial stiffness of 345 N/mm.

Dynamic stability of the rotor

The use of a control system to stabilize the unstable equilibrium of a magnetic bearing has been explained in the previous section. The rotor must then have a specific length-to-width ratio for a stable equilibrium of torques to be achieved. A requirement to be met by the control system is that it should be sufficiently stable at all frequencies of periodic disturbances. If a magnetically supported rotor — e.g. the one illustrated in fig. 6 — is set in rotation, its speed of revolution cannot be increased indefinitely, however. In this final section we shall consider the effects — other than the mechanical strength of the rotor — that set limits on the speed of revolution.

Fig. 14a shows the rotor rotating at an angular velocity Ω in a coordinate system (x,y,z). This system is fixed with respect to the non-rotating pole pieces, which we shall refer to as the 'stator pole pieces'. If the rotor rotates without deflection, the y-axis coincides with the axis of symmetry through the central points of the rotor pole pieces. We can write the equations of motion for the centre of mass Z of the rotor (neglecting the movement in the y-direction because the control loop is active in this direction):

$$F_x = M\ddot{x} \tag{21}$$

and

$$F_z + F_g = M\ddot{z}, \tag{22}$$

where F_x represents the external forces in the x-direction, F_z those in the z-direction, F_g the gravitational force and M the mass of the rotor. Similarly, we can write the equations of motion for *small* rotations α and β, which — together with the positions x and z of the centre of mass — establish the position of the rotor-symmetry axis in the coordinate system (x,y,z); see fig. 14*a*. Then we have:

$$T_x = J\ddot{\alpha} - \dot{\beta}\Omega I \tag{23}$$

and

$$T_z = J\ddot{\beta} + \dot{\alpha}\Omega I, \tag{24}$$

where T_x and T_z are the torques acting on the rotor about the x- and z-axes, J is the moment of inertia about an axis perpendicular to the symmetry axis, and I is the moment of inertia about the axis of symmetry. The final terms of equations (23) and (24) are the 'gyroscopic' moments [14].

First of all we shall consider a translation of the rotating rotor as described by (21) and (22), i.e. without the rotations α and β. The axis of symmetry then remains parallel to the y-axis. The terms F_x and F_z contain a component determined by the static stiffness k_{rad} for one half of the bearing as calculated above. Another component of F_x and F_z is a function of the velocity of the rotor pole pieces and the stator pole pieces relative to one another and is due to eddy currents.

Fig. 14*b* shows a rotor pole piece (shaded) that is in motion relative to a stationary stator pole piece, so that forces F_{rs} and F_{rr} act on the rotor pole piece. F_{rs} is the reaction of the sum of the Lorentz forces on the

[14] J. B. Scarborough, The gyroscope, theory and applications, Interscience, New York 1958.

eddy currents in the stator pole piece, $\boldsymbol{F}_{rr}$ is the sum of the Lorentz forces on the eddy currents in the rotor pole piece.

The force $\boldsymbol{F}_{rs}$ acts in the opposite direction to the velocity of the centre-point C' of the rotor pole piece relative to an observer at a point P_s of the stator, and is approximately proportional to this velocity:

$$\boldsymbol{F}_{rs} = -c_{rs}\,\dot{\boldsymbol{r}}_c, \tag{25}$$

where $\dot{\boldsymbol{r}}_c$ is the derivative of the position vector for C' from the centre C of the stator pole piece and c_{rs} is a loss coefficient for the stator.

$\boldsymbol{F}_{rr}$ is proportional to the velocity of C relative to an observer at a point P_r on the rotating rotor pole piece. This velocity is equal to the sum of the vector $-\dot{\boldsymbol{r}}_c$ and the vector product $\boldsymbol{\Omega}\times\boldsymbol{r}_c$. For $\boldsymbol{F}_{rr}$ we can thus write

$$\boldsymbol{F}_{rr} = -c_{rr}(\dot{\boldsymbol{r}}_c - \boldsymbol{\Omega}\times\boldsymbol{r}_c), \tag{26}$$

where c_{rr} is a loss coefficient for the rotor.

There is another way of showing that equation (26) must contain a term in $\boldsymbol{\Omega}$. During one revolution the flux density for part of the surface of the rotor pole pieces varies. A surface element near the point P_r, for example, passes the common region (shown hatched) of the rotor and stator pole piece, where the flux density is at a maximum, twice in one revolution. On the other hand, at a surface element of the stator pole pieces near the point P_s, for example, the flux density is constant during a revolution. Since the loss coefficients c_{rs} and c_{rr} for small values of $\boldsymbol{r}_c$ can be taken as constants, $\boldsymbol{F}_{rs}$ and $\boldsymbol{F}_{rr}$ can be compared with the damping forces in a hydrodynamic bearing.

The summated damping force for a half-bearing may be written as

$$\boldsymbol{F}_{rs} + \boldsymbol{F}_{rr} = -(c_{rs} + c_{rr})\,\dot{\boldsymbol{r}}_c + c_{rr}\boldsymbol{\Omega}\times\boldsymbol{r}_c. \tag{27}$$

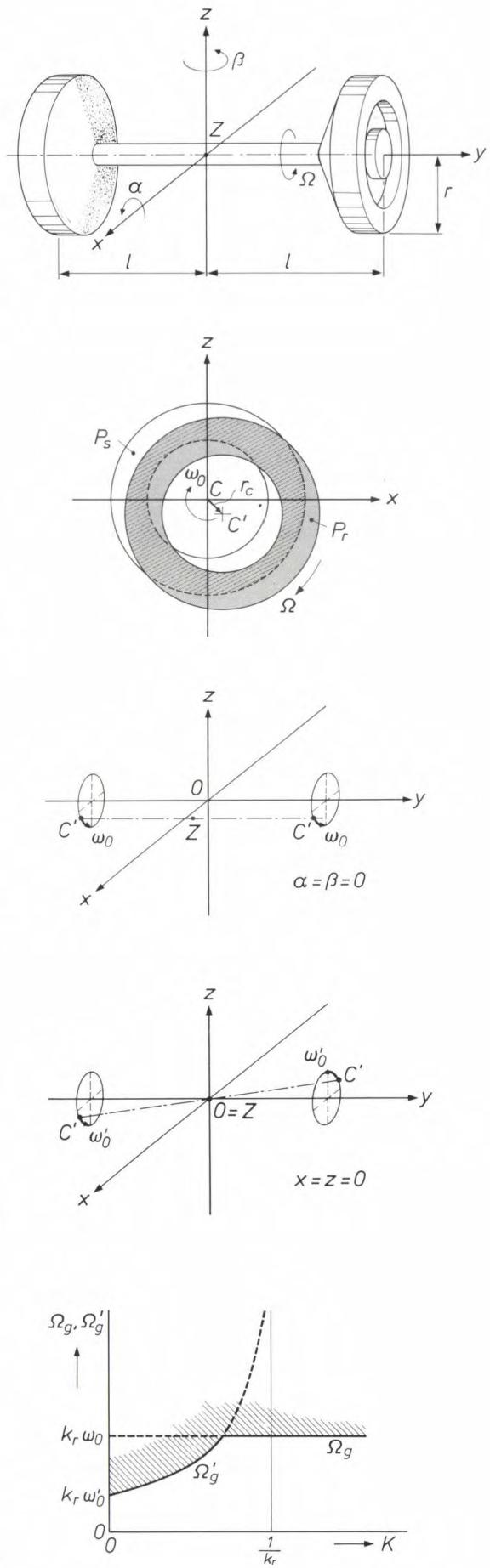

Fig. 14. *a*) Quantities for setting up the equations of motion of a rotating magnetically supported rotor. (x,y,z) rectangular coordinate system. The position of the centre of mass Z of the rotor is determined by the coordinates x and z; the control system keeps Z in the (x,z)-plane. $2l$ length of the rotor. $2r$ diameter of a pole piece. Ω angular velocity of the rotor. α,β angles defining the direction of the axis of symmetry of the rotor. In the situation shown $x = z = 0$ and $\alpha = \beta = 0$. *b*) The outer annular pole pieces of the rotor and stator, seen from Z in the y-direction. The rotor pole piece is shaded. The common region of both pole pieces — with maximum flux density — is shown hatched. C centre of stator pole piece. C' centre of rotor pole piece. r_c vector from C to C'. ω_0 angular velocity corresponding to a rotation of C' about C. P_s (stationary) point of the stator pole piece. P_r (moving) point of the rotor pole piece. *c*) The movement of the centres C' of the rotor pole pieces relative to the centres C of the stator pole pieces at the limiting speed Ω_g. The points C' rotate in phase about C at an angular velocity $\omega_0 = \Omega_g/k_r$; k_r is a function of the loss coefficients of rotor and stator pole pieces. *d*) as (*c*) but at the limiting speed Ω_g'. The points C' rotate with a phase difference π and angular velocity ω_g' about C. The centre of mass Z does not change position, as it did in (*c*). *e*) The limiting speeds Ω_g and Ω_g' as a function of $K = I/J$, the ratio of the moments of inertia along and perpendicular to the axis of symmetry. In the hatched area the rotor becomes unstable. This region should therefore be avoided in the design of magnetic bearings.

In general $F_{rs} + F_{rr}$ has the opposite direction to $\dot{r}_c$, the velocity of the rotor centre. The summated force can however change direction at large values of Ω, giving rise to oscillations and making the bearing unstable. Let us assume that the centre C' of a rotor pole piece describes a circular path with angular velocity ω_0 relative to the point C; see fig. 14*b*. If we substitute $\dot{r}_c = \omega_0 \times r_c$ in (27) we obtain, after some manipulation:

$$F_{rs} + F_{rr} = -\left(c_{rs} + c_{rr} - \frac{\Omega}{\omega_0} c_{rr} \right) \dot{r}_c. \quad (28)$$

We see that when $\Omega > k_r \omega_0$ instability occurs, with $k_r = c_{rs}/c_{rr} + 1$. At the limiting speed $\Omega_g = k_r \omega_0$ the rotor shaft describes a whirling movement relative to the y-axis. The centres C' of the rotor pole pieces at both ends then move in a circular path around the y-axis at an angular velocity ω_0, in the same direction as the rotation Ω of the rotor shaft; see fig. 14*c*. Manipulation of the equations of motion (21) and (22) shows that ω_0 is equal to the frequency $(2k_{rad}/M)^{1/2}$ of the resonance of the rotor mass with the static radial stiffness. If $c_{rs} = c_{rr}$ — which does not necessarily correspond to a practical bearing — $k_r = 2$; the whirling movements of the axis of symmetry of the rotor spinning at an angular velocity $2\omega_0$ may be compared with the 'half-omega whirl' that is known to occur in hydrodynamic bearings [15].

Closer inspection of the equations of motion (23) and (24) reveals that an instability can also occur due to precession of the axis of symmetry of the rotor about the y-axis, with the centre of mass Z remaining in position; see fig. 14*a*. At the corresponding limiting speed Ω_g' of the rotor the centres C' of the rotor pole pieces also describe circular movements, but now at an angular frequency ω_0'. However, there is a phase difference π between the movements at opposite ends and the axis of symmetry describes a conical surface; see fig. 14*d*. The limiting speed depends on the ratio $K = I/J$, where I and J are the moments of inertia about the axis of symmetry and an axis perpendicular to it. Manipulation of (23) and (24) gives the following equation for the critical speed Ω_g':

$$\Omega_g' = \frac{k_r \omega_0'}{\sqrt{1 - k_r K}}, \quad (29)$$

where

$$\omega_0' = \sqrt{\frac{|G|}{J}}. \quad (30)$$

The quantity G is the (negative) stiffness of the rotor for rotation about an axis perpendicular to the axis of symmetry.

In fig. 14*e* the limiting speeds Ω_g and Ω_g' are plotted as a function of the ratio K of the moments of inertia. If $\omega_0' \geqslant \omega_0$ only the limiting speed Ω_g of the translation of the rotor determines the stability. For $\omega_0 > \omega_0'$ both critical speeds determine the stability, each in a particular region of K. For $K = (1/k_r)$, Ω_g' goes to infinity in theory. In all the types of bearings we have investigated it has been found that ω_0' is greater than ω_0, in other words the translation of the axis of symmetry of the rotor determines the stability.

In the derivations described above it has been assumed that the stator pole pieces are connected to the outside world with infinite stiffness. If finite stiffness and damping are taken into account for the mounting of the pole pieces, the limiting speed is not identical with the previously calculated value. By giving the pole-piece mounting an appropriate stiffness and damping, we were able to increase the limiting speed of our bearings. At the same time $k_r = c_{rs}/c_{rr} + 1$ was increased. This was done by making the loss factor c_{rs} larger by introducing short-circuited windings in the concentric grooves of the stator pole pieces. (This was only done for the stator pole pieces in which the magnitude of the flux density is not controlled — the inner pole pieces in fig. 7 — since otherwise the characteristics of the control system would suffer.) In addition the loss factor c_{rr} was limited by making the rotor pole pieces of cobalt iron, which has a high electrical resistivity. With the type of bearing shown in fig. 7 we were finally able to achieve a ratio $k_r = \Omega_g/\omega_0$ greater than 4.4. As a result the limiting speed for this bearing is greater than 20 000 revolutions per minute.

[15] R. Gasch and H. Pfützner, Rotordynamik, Springer, Berlin 1975.

Summary. Magnetic bearings do not wear and have virtually no friction. The consequences of their usually unstable equilibrium of forces have to be corrected by feedback control loops. In general five such loops are required. In each control loop the difference between the displacement measured by a sensor and the desired displacement is converted into a control current through the coils of the magnetic circuit for generating the load-carrying capacity. With a suitable magnetic geometry it is possible to manage with a smaller number of control loops, but this has the disadvantage of reducing the load-carrying capacity and stiffness corresponding to the non-controlled degrees of freedom. This disadvantage can to some extent be overcome by including concentric grooves in the pole pieces. The load-carrying capacity can be calculated fairly easily from Maxwell's equations in vector notation, by expressing the force density at an enclosed surface in terms of the magnetic-flux-density vector. The ratio of the forces in the radial and axial directions of the magnetic bearings investigated, which had grooved pole pieces and one or three control loops, can be calculated from the same equation for the density of forces. The stability of two control methods, one using displacement feedback and the other velocity feedback, is demonstrated with the aid of Nyquist diagrams. The advantage of control with velocity feedback is that less heat is dissipated in the control coils. If a limiting speed is exceeded the magnetically supported rotor is dynamically unstable. This instability is comparable with the 'half-omega whirl' that can occur in hydrodynamic bearings.

Scientific publications

These publications are contributed by staff of laboratories and plants that form part of or cooperate with enterprises of the Philips group of companies, particularly by staff of the research laboratories mentioned below. The publications are listed alphabetically by journal title.

Philips GmbH Forschungslaboratorium Aachen, Weißhausstraße, 5100 Aachen, Germany — *A*

Philips Research Laboratory Brussels, 2 avenue Van Becelaere, 1170 Brussels, Belgium — *B*

Philips Natuurkundig Laboratorium, Postbus 80000, 5600 JA Eindhoven, The Netherlands — *E*

Philips GmbH Forschungslaboratorium Hamburg, Vogt-Kölln-Straße 30, 2000 Hamburg 54, Germany — *H*

Laboratoires d'Electronique et de Physique Appliquée, 3 avenue Descartes, 94450 Limeil-Brévannes, France — *L*

Philips Laboratories, N.A.P.C., 345 Scarborough Road, Briarcliff Manor, N.Y. 10510, U.S.A. — *N*

Philips Research Laboratories, Cross Oak Lane, Redhill, Surrey RH1 5HA, England — *R*

Philips Research Laboratories Sunnyvale P.O. Box 9052, Sunnyvale, CA 94086, U.S.A. — *S*

P. H. Woerlee, P. M. Th. M. van Attekum, A. A. M. Hoeben, G. A. M. Hurkx & R. A. M. Wolters *E*	Observation of anomalous electrical transport properties in $MoSi_2$ films	Appl. Phys. Lett. **44**	876-878	1984
S. Shokoohi (*Bell Labs, Holmdel, NJ*), L. M. Silverman (*Univ. Los Angeles*) & P. van Dooren *B*	Linear time-variable systems: stability of reduced models	Automatica **20**	59-67	1984
G. N. A. van Veen*, T. Baller*, A. E. de Vries* (* *FOM, Amsterdam*) & N. J. A. van Veen *E*	The excitation of the umbrella mode of CH_3 and CD_3 formed from photodissociation of CH_3I and CD_3I at 248 nm	Chem. Phys. **87**	405-417	1984
P. J. van Gerwen, N. A. M. Verhoeckx & T. A. C. M. Claasen *E*	Design considerations for a 144 kbit/s digital transmission unit for the local telephone network	IEEE J. **SAC-2**	314-323	1984
H. Ney *H*	The use of a one-stage dynamic programming algorithm for connected word recognition	IEEE Trans. **ASSP-32**	263-271	1984
L. M. H. E. Driessen *E*	On an infinite series of $[4n, 2n]$ binary codes	IEEE Trans. **IT-30**	392-395	1984
G. F. M. Beenker *E*	A note on extended quadratic residue codes over GF(9) and their ternary images	IEEE Trans. **IT-30**	403-405	1984
W. J. van Gils *E*	Linear unequal error protection codes from shorter codes	IEEE Trans. **IT-30**	544-546	1984
B. M. J. Smets & M. G. W. Tholen *E*	Leaching of glasses with molar composition $20Na_2O{\cdot}10RO{\cdot}xAl_2O_3{\cdot}(70\text{-}x)SiO_2$	J. Am. Ceram. Soc. **67**	281-284	1984
P. Hansen, K. Witter & W. Tolksdorf *H*	Magnetic and magneto-optic properties of bismuth- and aluminum-substituted iron garnet films	J. Appl. Phys. **55**	1052-1061	1984
R. A. de Groot*, F. M. Mueller* (* *Univ. Nijmegen*), P. G. van Engen & K. H. J. Buschow *E*	Half-metallic ferromagnets and their magneto-optical properties	J. Appl. Phys. **55**	2151-2154	1984
P. E. Wierenga & A. J. J. Franken *E*	Ultramicroindentation apparatus for the mechanical characterization of thin films	J. Appl. Phys. **55**	4244-4247	1984
A. G. Dirks, J. J. van den Broek & P. E. Wierenga *E*	Mechanical properties of thin alloy films: ultramicrohardness and internal stress	J. Appl. Phys. **55**	4248-4256	1984
D. E. Lacklison & G. Duggan *R*	Determination of the minority carrier mobility of *n*-type cadmium-mercury-telluride using the Hayes-Shockley method	J. Appl. Phys. **55**	4257-4265	1984
H. A. van Sprang & R. G. Aartsen *E*	The temperature dependence of liquid-crystal tilt angles	J. Appl. Phys. **56**	251-262	1984

M. P. Henaff*, C. Colinet*, A. Pasturel* (* *ENSEEG, St. Martin d'Héres*) & K. H. J. Buschow *E*	Study of enthalpies of formation and crystallization in the system Zr-Ni	J. Appl. Phys. **56**	307-310	1984
C.-P. Klages & W. Tolksdorf *H*	LPE growth of bismuth substituted gadolinium iron garnet layers: systematization of experimental results	J. Cryst. Growth **64**	275-284	1983
D. Mateika, R. Laurien & M. Liehr *H*	Czochralski growth by the double container technique	J. Cryst. Growth **65**	237-242	1983
W. Tolksdorf, B. Strocka & F. Welz *H*	Growth of seeded and unseeded yttrium garnet crystals from high temperature solutions studied by induced striations	J. Cryst. Growth **65**	549-555	1983
C.-P. Klages, W. Tolksdorf & G. Kumpat (*Univ. Hamburg*) *H*	The influence of excess iron oxide in the solubility of yttrium iron garnet and its growth kinetics on (111) substrates	J. Cryst. Growth **65**	556-561	1983
G. M. Blom & D. Y. Lou *N*	Archival life of tellurium-based materials for optical recording	J. Electrochem. Soc. **131**	146-151	1984
H. Baudry & F. Franconville (*Matra, Velizy*) *L*	Rheology and printing of high definition thick-film inks	J. Hybrid Microelectronics **5** (No. 3)	15-23	1982
G. D. Khoe, H. G. Kock, D. Küppers, J. H. F. M. Poulissen & H. M. de Vrieze *E*	Progress in monomode optical-fiber interconnection devices	J. Lightwave Technol. **LT-2**	217-227	1984
J. W. D. Martens, M. Erman & H. M. van Noort *E, L*	A non-destructive analysis of the influence of sputter-etching on the magnetic surface properties of manganeze zinc ferrite (100) surfaces using ellipsometry and the polar magneto-optical Kerr effect	J. Magn. & Magn. Mater. **42**	279-285	1984
E. G. Visser *E*	Analysis of the complex permeability of monocrystalline $MnZnFe^{II}$	J. Magn. & Magn. Mater. **42**	286-290	1984
G. de With *E*	Fracture of translucent alumina: temperature dependence and influence of CaO dope	J. Mater. Sci. **19**	2195-2202	1984
S. H. Hagen & P. J. A. Derks *E*	Photogeneration and optical absorption in amorphous Se-Te alloys	J. Non-Cryst. Solids **65**	241-259	1984
B. M. J. Smets, M. G. W. Tholen & T. P. A. Lommen *E*	The effect of divalent cations on the leaching kinetics of glass	J. Non-Cryst. Solids **65**	319-332	1984
A. L. J. Burgmans & H. J. H. Merks-Eppingbroek *E*	Ionisation by highly excited argon states in mixtures of argon with krypton	J. Phys. D **17**	L93-L96	1984
T. T. M. Palstra*, H. G. C. Werij*, G. J. Nieuwenhuys*, J. A. Mydosh* (* *Univ. Leiden*), F. R. de Boer (*Univ. Amsterdam*) & K. H. J. Buschow *E*	Metamagnetic transitions in cubic $La(Fe_xAl_{1-x})_{13}$ intermetallic compounds	J. Phys. F **14**	1961-1966	1984
H. W. Werner & A. P. von Rosenstiel (*TNO, Apeldoorn*) *E*	Comparison of secondary ion mass spectrometry (SIMS) with electron microprobe analysis (EPMA) and other thin film analytical methods	J. Physique **45** (Colloque C2)	C2/103-C2/113	1984
D. Visser, N. C. J. A. van Hijningen & J. G. Dil *E*	Brillouin scattering near rigid interfaces	J. Physique **45** (Colloque C5)	C5/83-C5/91	1984
F. H. M. Sanders, A. W. Kolfschoten, J. Dieleman, R. A. Haring*, A. Haring* & A. E. de Vries* (* *FOM, Amsterdam*) *E*	Ion-assisted etching of silicon by molecular chlorine	J. Vac. Sci. & Technol. A **2**	487-491	1984
H. W. Werner & N. Warmoltz *E*	Beam techniques for the analysis of poorly conducting materials	J. Vac. Sci. & Technol. A **2**	726-731	1984
P. C. Zalm *E*	Some useful yield estimates for ion beam sputtering and ion plating at low bombarding energies	J. Vac. Sci. & Technol. B **2**	151-152	1984
P. Röschmann, M. Lemke, W. Tolksdorf & F. Welz *H*	Anisotropy fields and FMR linewidth in single-crystal Al, Ga and Sc substituted hexagonal ferrites with M structure	Mater. Res. Bull. **19**	385-392	1984
M. Prins*, J. M. Kuiper* (* *Univ. of Technol., Eindhoven*) & M. P. A. Viegers *E*	The design of an X-ray microprobe at the SRS Daresbury (UK)	Nucl. Instrum. & Methods Phys. Res. **B3**	246-249	1984
H. Decker *H*	A difference technique for automatic inspection of casting parts	Pattern Recognition Lett. **2**	125-129	1983

R. J. Murray & R. W. Gibson	*R*	A coherent digital demodulator for minimum shift key and related modulation schemes	Philips J. Res. **39**	1-10	1984
P. C. Zalm & L. J. Beckers	*E*	In quest of the spike: energy dependence of the sputtering yield of zinc bombarded with neon and xenon ions	Philips J. Res. **39**	11-23	1984
J. Pergrale, C. Berche, D. Iachetti & G. Normand	*L*	Comparison between attenuation correction methods in transaxial single photo emission tomography	Philips J. Res. **39**	24-50	1984
J. H. den Boef, C. M. J. van Uijen & C. D. Holzscherer (*Philips Medical Systems, Eindhoven*)	*E*	Multiple-slice NMR imaging by three-dimensional Fourier zeugmatography	Phys. Med. & Biol. **29**	857-867	1984
K. H. J. Buschow & D. B. de Mooij	*E*	The effect of H_2 absorption on the magnetic properties of Gd-Pd intermetallic compounds	Phys. Stat. Sol. a **84**	207-213	1984
J. W. C. de Vries*, R. C. Thiel* (* *Univ. Leiden*) & K. H. J. Buschow	*E*	The ^{151}Eu Mössbauer isomer shift in intermetallic compounds containing trivalent europium	Physica **124B**	291-298	1984
P. Frey, B. Gabillard & M. Rocchi	*L*	0.25 mW, 1.9 GHz, GaAs T flip-flops	Proc. IEEE GaAs IC Symp., Phoenix 1983	62-65	1983
D. Meignant & M. Binet	*L*	A high performance 1.8 GHz strobed comparator for A/D converter	Proc. IEEE GaAs IC Symp., Phoenix 1983	66-69	1983
S. Makram-Ebeid & P. Minondo	*L*	Side-gating in GaAs integrated circuits: surface and bulk related phenomena	Proc. IEEE GaAs IC Symp., Phoenix 1983	142-144	1983
A. A. Turnbull & R. F. Hall	*R*	A 20-element high performance pyroelectric linear array	Proc. 2nd Int. conf. on Advanced infrared detectors & syst., London 1983	55-58	1983
S. Colak, J. Khurgin & W. K. Zwicker	*N*	Emission cross sections and lifetimes of Er^{3+} eyesafe transitions between $^4S_{3/2} \rightarrow {}^4I_{9/2}$ and $^4I_{13/2} \rightarrow {}^4I_{15/2}$, in $Er_xGd_{1-x}P_5O_{14}$, $Er_xGd_{1-x}LiP_4O_{12}$ and $Er_xGd_{1-x}Al_3(BO_3)_4$	Proc. Int. Conf. on Lasers '82, New Orleans 1982	264-271	1982
J. K. Tyminski*, R. C. Powell* (* *Oklahoma State Univ., Stillwater, OK*) & W. K. Zwicker	*N*	Temperature dependence of the excitation diffusion in $Nd_xLa_{1-x}P_5O_{14}$ crystals	Proc. Int. Conf. on Lasers '82, New Orleans 1982	272-274	1982
M. M. Broer*, W. M. Yen* (* *Univ. Wisconsin, Madison, WI*) & W. K. Zwicker	*N*	Anomalous fluorescence quenching and energy transfer in $La_{1-x}P_5O_{14}:Nd_x^{3+}$	Proc. Int. Conf. on Lasers '82, New Orleans 1982	275-279	1982
J. W. Broer	*E*	Feedforward and metaphoric transfer — natural forces of technical authors and editors	Proc. 31st ITCC, Seattle 1984	RET12-RET14	1984
J. F. van der Veen (*FOM, Amsterdam*), P. K. Larsen, J. H. Neave & B. A. Joyce	*E, L*	The GaAs(001) - $c(4\times4)$ and (2×4) reconstructions: a comparative photoemission study	Solid State Commun. **49**	659-662	1984
R. E. Horstman, E. J. van den Broek, J. Wolter, R. W. van der Heijden*, G. L. J. A. Rikken*, H. Sigg* (* *Univ. Nijmegen*), P. M. Frijlink, J. Maluenda & J. Hallais	*E, L*	Cyclotron resonance from the far-infrared transmission and the photoconductivity of a two-dimensional electron gas in a GaAs/AlGaAs heterojunction	Solid State Commun. **50**	753-756	1984
E. D. Roberts	*R*	Recent developments in electron resists	Solid State Technol. **27** (No. 6)	135-141	1984
P. N. T. van Velzen	*E*	An IETS study of a silane coupling agent; the interaction of 3-(trimethoxysilyl)propanethiol with aluminium oxide and silver surfaces	Surf. Sci. **140**	437-445	1984
W. Tolksdorf & C.-P. Klages	*H*	The growth of bismuth iron garnet layers by liquid phase epitaxy	Thin Solid Films **114**	33-43	1984
P. Hansen & J.-P. Krumme	*H*	Magnetic and magneto-optical properties of garnet films	Thin Solid Films **114**	69-107	1984
G. Martens	*H*	Druckmessung mittels spannungsoptische Effekte	VDI-Berichte **509**	115-118	1984
R. Orlowski & V. Graeger	*H*	Keramische Differenzdrucksensoren in Dickschichttechnik	VDI-Berichte **509**	217-222	1984
W. G. Essers & M. R. M. van Gompel	*E*	Arc control with pulsed GMA welding	Welding J. **63** (No. 6)	26-32	1984
S. Haussühl (*Univ. Köln*) & D. Mateika	*H*	Temperature and pressure derivatives of the elastic constants of hexagonal $Ba_{0.75}Al_{11}O_{17.25}$	Z. Kristallogr. **165**	289-293	1983

Supplement to Philips Technical Review
Bijlage van Philips Technisch Tijdschrift
No. 25

January 1985

Recent United States Patents

Abstracts from patents that describe inventions from the following research laboratories, which form part of or cooperate with the Philips group of companies:

Philips GmbH Forschungslaboratorium Aachen, Weißhausstraße, 5100 Aachen, Germany — *A*
Philips Research Laboratory Brussels, 2 avenue Van Becelaere, 1170 Brussels, Belgium — *B*
Philips Natuurkundig Laboratorium, Postbus 80 000, 5600 JA Eindhoven, The Netherlands — *E*
Philips GmbH Forschungslaboratorium Hamburg, Vogt-Kölln-Straße 30, 2000 Hamburg 54, Germany — *H*
Laboratoires d'Electronique et de Physique Appliquée, 3 avenue Descartes, 94450 Limeil-Brévannes, France — *L*
Philips Laboratories, N.A.P.C., 345 Scarborough Road, Briarcliff Manor, N.Y. 10510, U.S.A. — *N*
Philips Research Laboratories, Cross Oak Lane, Redhill, Surrey RH1 5HA, England — *R*
Philips Research Laboratories Sunnyvale, P.O. Box 9052, Sunnyvale, CA 94086, U.S.A. — *S*

4 443 885

Charge transfer method and device for carrying out the method

A. H. M. van Roermund — *E*

A method and device in which both positive and negative signal charges can be transferred from a first capacitance to a first point via a transistor circuit which exhibits a threshold level. For this purpose the first capacitance contains a reference charge with a positive or a negative polarity. First, the voltage on the first point is switched so that the first capacitance is charged from said first point and subsequently so that the first capacitance discharges towards the first point to its reference charge, which corresponds to said threshold level, in such a way that the net charge transfer from the first capacitance to the first point is equal to the positive or negative signal charge and the charge on the first capacitance is restored to a reference level.

---

4 446 419

Current stabilizing arrangement

R. J. van de Plassche — *E*
E. C. Dijkmans
H. J. Schouwenaars

In a known current source arrangement which generates a current whose temperature coefficient is only equal to zero at one specific temperature, steps are taken, in accordance with the invention, to render the generated current independent of the temperature over a wide temperature range by compensation of the disturbing factor in the relationship between the generated current and the temperature.

---

4 446 548

Apparatus for the point-by-point scanning of an object

G. Bouwhuis — *E*
J. J. M. Braat

An apparatus is described for point-by-point scanning of an object, which may be a phase object, an amplitude object or a combined amplitude and phase object. The object is scanned with a light, sound, electron or X-ray beam which is converged to a spot on the object. A pair of detectors disposed in the path of the modulated radiation coming from the object convert the variations in the radiation into corresponding electrical signals which are fed to a summing circuit. A variable phase shifter connected between at least one of the detectors and the summing circuit is used to introduce a phase shift in the electrical signal such as to optimize the output signal of the summing circuit for the type of object being scanned.

---

4 446 549

Optically readable information disc and method of manufacturing same

G. J. M. Lippits — *E*
J. G. Kloosterboer
G. P. Melis

An optically readable information disc having a substrate plate which on at least one side comprises an information layer of a lacquer cured by irradiation for example by ultraviolet light, said layer carrying an optically readable information track in which the lacquer is a monocomponent lacquer which, in addition to 0.1-5% by weight of auxiliary substances, comprises only one radiation cross-linkable compound in a quantity by weight from 95-99.9% selected from the group consisting of alkanedioldiacrylates, alkanedioldimethacrylates, alkeneglycoldiacrylates and alkeneglycoldimethacrylates having the acrylate or methacrylate groups in end position, of which the alkane moiety and alkene moiety comprise from 4 to 12 carbon atoms, and in which the cured lacquer apart from the auxiliary substances comprises no or substantially no extractable material.

---

4 447 132

Liquid crystal display device

M. de Zwart — *E*

In a matrix display device having a cholesteric liquid crystal the bistability effect is used which some cholesteric liquid crystals show. The liquid crystal shows a frequency-dependent relaxation of a positive to a negative dielectric anisotropy. After writing the information the light-scattering picture elements have a focal-conical

texture and the transparent elements have a homeotropic-nematic texture. The information can be stored for a longer period of time by causing the homeotropic-nematic texture of the transparent elements to change into the substantially transparent planar-conical texture. This is produced rapidly by applying across all picture elements a voltage of a frequency at which the liquid crystal has a negative dielectric anisotropy. The focal-conical texture of the light-scattering elements is substantially not disturbed by this voltage. During the presence of this voltage the written information is continuously visible.

---

4 448 596

Method of operating a bimodal heat pump, as well as bimodal heat pump for using said method

W. L. N. van der Sluys E
M. L. Hermans

A method of operating a bimodal heat pump which in a first mode operates as an absorption heat pump and in a second mode operates as an evaporation-condensation device at a comparatively low ambient temperature. When switching from the first mode to the second mode, an evaporator and absorber are uncoupled from a generator and condensor. The generator and condensor are operated in the second mode as an evaporation-condensation device, an extra quantity of working medium present in the condensor being provided in the system. The heat pump comprises an overflow to the evaporator the level of which is a measure of an extra quantity of the working medium and has a closable transport pipe to the generator for supplying extra working medium to the generator when starting the second mode. The heat pump is meant in particular for heating spaces and presents the possibility of choosings from various working media and solvents having different decomposition temperatures.

---

4 448 635

Method of etching cavities and apertures in substrates and device for carrying out said method

H. K. Kuiken E
R. P. Tijburg

Deep cavities and apertures can be obtained with little undercutting (great etching factor) by etching in an artificial gravitational field (under the influence of centrifugal or centripetal forces).

---

4 449 198

Device for interactive video playback

D. J. Kroon E
K. H. J. Robers

A device for interactive video playback utilizing a modified playback apparatus for video discs. Such a video disc contains stored video information and possibly also audio information. The various playback and addressing modes can be activated by operation of buttons. The information read is directly suitable for playback on a television screen. The playback apparatus is modified for executing these playback and addressing modes also under the control of selection signals received from a computer. There is also provided an extraction element for extracting the frame numbers from the information read and for supplying these numbers as data to the computer. The computer furthermore includes a read/write memory for the storage of the information of alphanumerical characters and of selection signals for the playback apparatus. In some cases, the latter signals are activatable only by a request signal. The computer also includes an output for said alphanumerical characters as additional display information. There is also provided a keyboard suitable on the one hand for inputting instructions for the computer which are expressed in a higher programming language in order to modify the program to be executed by the computer. It can also be used for producing a request signal for activating a selection signal read from the read/write memory.

4 449 287

Method of providing a narrow groove or slot in a substrate region, in particular a semiconductor substrate region

H. G. R. Maas E
J. A. Appels

According to the invention, at least one oxidation-preventing layer is provided on a substrate region, while on this layer there is provided an oxidizable layer. The oxidizable layer is removed above part of the substrate region. An edge portion of the oxidizable layer is oxidized. Subsequently, at least the uncovered part of the oxidation-preventing layer is removed selectively and the exposed part of the substrate region is thermally oxidized through part of its thickness, while practically only at the area of the oxidized edge portion the substrate region is exposed and is etched away through at least part of its thickness in order to form a groove, the oxidizable layer and the oxidized edge portion being removed completely. The substrate region may be a mono- or polycrystalline silicon layer. The oxidizable layer may consist of for instance polycrystalline silicon and may be coated with a second oxidation-preventing layer. If the substrate region is a masking layer, the slots provided therein may be used for doping purposes, for example, for forming channel stoppers, etc. Application in particular for the manufacture of integrated circuits and of gate electrodes spaced apart by very small distances in IGFET and CCD structures.

---

4 450 564

Apparatus for modulating the output signal of a converter

L. J. Meuleman E
A. van de Grijp
E. Roza

Apparatus for modulating the output signal of a converter for converting electric signals into other signals, for example optical signals. An analog signal is applied to a subtraction device the output signal of which controls a limiter. The binary output signal thereof controls a semiconductor laser diode, which is coupled to a photosensitive detector for producing a feedback signal. After being amplified in a broad-band amplifier and integrated in an integrator, this feedback signal is applied to the subtraction device, so that the feedback signal is subtracted from the analog signal. Variations in the optical output signal due to a non-linear conversion characteristic of the laser diode and due to an optical retroaction of a fibre on the laser diode, as well as output noise and signal-dependent amplitude variations, are reduced by the negative feedback.

---

4 451 115

Detachable coupling for optical fibres

A. J. A. Nicia E
C. J. T. Potters
A. H. L. Tholen

A detachable connector for coupling a pair of optical fibers includes two connector elements detachably connected to a connector holder. Each connector element includes a cylindrical housing, a spherical lens, a discshaped fiber holder, means for adjusting the axial displacement of the fiber holder in the housing, and means for adjusting the displacement of the holder perpendicular to the axis. The spherical lens is mounted in a conical bore in the housing, adjacent the fiber holder.

---

4 451 862

Magnetic head mounting mechanism for automatic azimuth control

A. M. A. Rijckaert E
H. M. Ruyten
J. F. Hoefnagels
J. J. M. Schoenmakers

A tape recorder or player with automatic azimuth control, utilizing a single piezoelectric element inside the head's magnetic shield. A bimorph has one end rigidly connected to the head and the other end rigidly connected to the head support, for pivoting the head about an axis in line with the head gap.

4 453 090

MOS field-effect capacitor

A. Sempel E

A field-effect capacitance includes a first region of a first conductivity type in a semiconductor layer, which region is provided with at least one contact electrode connected to a first terminal and with an insulated electrode arranged on said region and connected to a second terminal. A second semiconductor region of a second conductivity type opposite to the first conductivity type is formed in the semiconductor layer, which second region is provided with at least one contact electrode coupled to the first terminal, and with an insulated electrode arranged on said second region and connected to the second terminal. The two capacitances thus formed are then alternatively operative for alternate polarities of the signal voltage. The resulting capacitance structure is suitable for high signal voltage applications, and provides a smooth transition when alternate signal polarities are applied.

4 453 232

Device for generating magnetic bubbles with a high bit rate

G. J. Koel E
K. E. Kuijk

A memory device utilizing magnetic bubbles which are driven by a rotary magnetic field on contiguous disc drive patterns. These disc patterns have mainly a first scale. Each drive pattern also comprises a further disc pattern of a substantially larger scale. These further disc patterns each time comprise an excitation loop. These loops are mutually staggered with respect to the phase of the rotary field and are electrically connected in series. The series connection can be excited during relevant phases of the rotary magnetic field in order to selectively process a bubble then present in a locally formed preferred position from among the magnetic bubbles present on the larger disc patterns. The processing operation may be generating, detecting and annihilating bubbles.

4 454 779

Drive for a variable-stroke swash plate mechanism

J. Vos E

A drive for a variable-stroke swash plate machine, comprising a rotatably journalled shaft and a swash plate mounted so that the plate cannot rotate with respect to the shaft during operation. The plate is journalled on the shaft so that it is rotatable about an axis of rotation which intersects the shaft axis at an acute angle. A first conical gear on the plate engages a second conical gear on a sleeve arranged coaxially around the shaft. Control means rotate the sleeve and second conical gear with respect to the shaft.

4 455 508

Low-pressure mercury vapor discharge lamp

G. A. Wesselink E

Low-pressure mercury vapor discharge lamp having an electrical stabilization ballast which occupies a central position in the lamp. The discharge vessel surrounds the ballast. In order to dissipate the heat generated by the ballast during operation to the environment of the lamp, a thin-walled heat sink of a heat-conductive material which bears on the ballast is provided between the ballast and the discharge vessel, this body having a collar which extends as far as the exterior of the lamp.

4 455 666

Compensation of 1st order transfer inefficiency effect in a C.T.D.

A. H. M. van Roermund E

Charge transfer devices exhibit transfer inefficiencies, so that a part of a transferred charge packet is left and lags the original charge packed. This results in "smearing" of the original charge packet, thereby adversely affecting the unit-function response and the frequency response of the charge transfer device. The invention provides a solution to this problem, utilizing a compensation charge derived from the original charge packet, which at a suitable instant is applied to a point where the residual charge is cancelled via a feedback loop.

4 456 904

Analog-to-digital converter circuit

R. E. J. van de Grift E

In order to avoid errors due to time differences between output signals containing coarse bit information and fine bit information, an insertion circuit is used in an analog-to-digital converter, having a coarse converter and two folding circuits which are each followed by a fine converter, to replace changing coarse bit information with changing fine bit information in the output signals.

4 456 923

Color television display device comprising a plurality of picture display tubes

M. J. J. C. Annegarn E
W. A. L. Heijnemans

A color television display device comprising a plurality of picture display tubes for displaying a color television signal. In order to eliminate a flicker effect which particularly occurs for unsaturated colors at high luminance, the vertical deflection of a first group of the display tubes as well as the video signals applied thereto are delayed by the same time delay with respect to a second group of the display tubes.

4 459 182

Method of manufacturing a display device

T. S. te Velde E

A display device having a transparent supporting plate which is provided with transflective regions. At a short distance from the first supporting plate resilient electrodes are connected which are manufactured from a partially reflective material. By varying the distance between the resilient electrodes and the transflective regions, the reflection of incident light can be controlled from zero to maximum intensity as a result of the occurring interference. Both monocolour and multicolour pictures can be displayed by means of such a display device. Such a display device is particularly suitable for use in a projection television device.

4 459 364

Low-fire ceramic dielectric compositions

R. T. McSweeney S
S. A. Long

A low-fired ceramic dielectric composition, a multilayer capacitor made from such a ceramic dielectric composition provided with silver/palladium electrodes having at least 65 atomic percent silver, and a method of manufacturing such a multilayer capacitor. The ceramic is barium titanate-based and includes Bi_2O_3, Nb_2O_5, and TiO_2 to improve sinterability. $MnCO_3$ is added to increase the insulation resistance. The multilayer capacitor includes high silver-content electrodes to reduce the quantity of expensive noble metals. The multilayer part may be fired at a temperature of 1150 °C or less to yield a capacitor meeting EIA specification X7R. The low firing temperature also inhibits a chemical reaction between bismuth and palladium.

4 459 510

Lamp having a glass lamp vessel and glass (Na-Ca-Ba-SiO_2 with $B_2O_3/Al_2O_3/ZrO_2$) suitable therefor

H. J. M. Joormann E

The invention relates to lamps having a glass lamp vessel and to a glass suitable therefor. The relevant glass is adequately resistant to attack by electrons, is resistant to atmospheric influences and is properly workable in a gas flame. This glass contains 44-60 mole% silicon oxide; 0-7.5 mole% boron oxide; 0-6 mole% zirconium oxide; 0-7.5 mole% aluminium oxide; 5-20 mole% calcium oxide; 12.5-25 mole% barium oxide; 0-15 mole% magnesium oxide; 0-10 mole% strontium oxide; 2-8 mole% sodium oxide. The sum of the alkaline earth metals is 25-42.5 mole%. No discolouration occurs in sodium vapor discharge lamps when the lamp vessel has been made of this glass.

4 459 632

Voltage-limiting circuit

A. J. Nijman E
F. A. C. M. Schoofs

An arrangement for providing protection against overheating in a voltage limiting circuit in the event of overvoltages comprises a series arrangement of a voltage limiting element and a heat sensitive switching element. The voltage limiting element and heat sensitive switching element are connected by a high conductivity heat path so that when the temperature of the element increases this increase is passed to the switching element which reduces or switches off the current in the line between two terminals. In operation a signal supply line is connected to terminal and the protected equipment is connected to terminal. The arrangement may be used to protect telephone exchange equipment from high voltages induced on telephone lines as a result, for example of lightning.

---

4 459 683

Read resettable memory circuit

S. B. Yalamanchili S
S. T. Mahmud

A read resettable memory circuit contains a flip-flop circuit consisting of a flip-flop and an edge-triggered control circuit and a fall-through latch. The control circuit sets the flip-flop in response to a selected edge transition in a first clock when an appropriate external logical set signal is received and resets the flip-flop in response to a selected edge transition in a second clock when an appropriate feedback logical reset signal is received. The latch provides the reset signal at a value corresponding to the current logic state of the flip-flop during each period running from the selected edge transition of the second clock to its opposite edge transition and at a value corresponding to the logic state of the flip-flop that exists just before each opposite edge transition of the second clock during each remaining following period.

---

4 460 911

Semiconductor device with multiple plate vertically aligned capacitor storage memory

R. H. W. Salters E

A high packing density is obtained in a memory by stacking the capacitors of adjacent columns in such a manner that two capacitors of different columns are formed by three conductive layers situated one above the other. The central layer can be connected to a reference voltage, while the uppermost layer is connected to a transistor in one column and the lowermost layer is connected to a transistor in the other column.

---

4 460 914

Programmable semiconductor device and method of manufacturing same

T. S. te Velde E
A. Slob

A blowable fuse is provided over a part of its length separately from the walls of an enveloping cavity and separated from a supporting member. As a result of this the fuse is readily thermally isolated so that it fuses more rapidly and with less energy. In addition, a semiconductor circuit element, for example a Schottky diode, can be realized below a bridging part of a conductor which serves as an upper wall of the cavity, which results in a high bit density.

---

4 460 990

Apparatus for reading an optical record carrier

W. G. Opheij E

An apparatus is described for reading an optical information structure arranged in tracks. By the use of a substantially rotationally symmetrical element having an annular radiation-attenuating peripheral portion cross-talk between the tracks as a result of obliquity of the information structure is substantially reduced.

4 461 016

Method of and device for forming an image of a layer of a three-dimensional object

H. Weiss H
E. Klotz

The invention relates to a method of and a device for forming images of a layer of a three-dimensional object. In order to obtain high-quality images, the object is irradiated by means of a necessarily large number of radiation sources which are arranged in different mutually parallel planes or which are arranged to be displaceable (for example, rotatable) with respect to the object. Alternatively, the object with the record carrier (X-ray film) may be arranged to be displaceable with respect to the radiation sources. In the decoding step (superposition and summing of the shadow images) use is made of the two dimensional distribution of all radiation sources used during coding (irradiation) of the object.

---

4 461 019

Rotary-anode X-ray tube

B. Lersmacher A

A layer of pyrolytic graphite is deposited on the surface of the basic body of the anode of a rotary-anode X-ray tube. On the layer of pyrolytic graphite there is provided a further layer of a high-melting metal on the surface of which the focal path extends during operation of the tube. A basic body which has substantially all advantages of the pyrolytic graphite but whose manufacture is much simpler, faster and hence also more economical than an equivalent carrier body comprising a ring of solid, thick-walled pyrolytic graphite, is obtained in that the basic body consists of a lamination of graphite foils at least in the region beneath the focal path.

---

4 461 540

Optical communication element and optical communication cable comprising such an element

A. J. J. Franken E

An optical communication element comprises an optical fiber bonded in a state of axial compression to a metal tape. The tape may be folded up into a tube and sealed by soldering. Such elements are strong and not sensitive to stress corrosion. Such an optical communication element may be produced by passing a metal tape and an optical fiber in contact around a drum with the optical fiber on the outside. An adhesive, which solidifies or cures during the passage around the drum is applied to the metal tape.

---

4 461 963

MOS power-on reset circuit

J. J. M. Koomen E

A MOS power-on reset circuit includes a Schmitt trigger circuit and an inverter. The Schmitt trigger circuit comprises first, second, and third depletion transistors serially connected between reference potential and supply voltage. The first and second depletion transistors are connected at a first junction point, and the second and third depletion transistors are connected at a second junction point. The gates of the first and second depletion transistors are commonly connected for receiving an input substrate bias voltage. An enhancement transistor is connected between the first junction point and supply voltage. The gates of the enhancement transistor and the third depletion transistor are commonly connected to the second junction point, which is the output of the Schmitt trigger circuit and which is coupled to the inverter from which the output voltage is taken. The transfer characteristic of the circuit exhibits hysteresis, with two trigger levels of input substrate bias voltage that differ sufficiently in magnitude that a triggering at one level, accompanied by a fluctuation in input voltage, will not cause a spurious triggering at the other level. Undesired oscillation of the circuit is thereby avoided.

4 463 367

Frame-transfer charge-coupled image sensor device having channel sounding regions below light-admitting windows

M. G. Collet E

A charge-coupled image sensor device of the frame-transfer type has an electrode system through which windows allow light to enter the device. One group of electrodes extends transverse to charge transport channels in the device. Another group of electrodes extends parallel to the channels. Channel bounding regions that electrically separate the channels lie below substantially the entire areas of the windows.

---

4 463 377

Arrangement for storing or transmitting and for recovering picture signals

D. Meyer-Ebrecht H
J. H. Christiansen

In the conventional transformation coding of pictures the value ranges of the coefficients then produced are extended during the performance of the individual arithmetical steps. As a result thereof these coefficients have a great redundancy. According to the invention, the arithmetical steps which are formed by the basic transformation of two values are performed so that as a result of each arithmetical step only the original word length is obtained, because in each arithmetical step a portion of the value range of the result is mapped onto a different area. An example for the technical implementation of such a mapping on modified coefficients and the retransformation of these modified coefficients is described.

---

4 464 012

Broad-band communication system comprising an optical broad-band cable network

G. D. Khoe E
F. Krahn

Broad-band communication system comprising a broadband cable network arranged between an exchange and a large plurality of subscriber's stations. The network is formed by optical fibers. In order to avoid extra attenuation caused by splices, the incoming bundles of individual cables are split at branching points, without splicing, into a number of separate outgoing bundles of individual cables.

---

4 464 437

Magneto-optical memory element

M. Urner Wille H
P. Hansen

A magneto-optic memory element consisting of a substrate provided with an amorphous layer of an alloy of a rare-earth metal and a transition metal. The layer has a uniaxial magnetic anisotropy. Such memory elements are suitable for storing digital information in the form of magnetized areas, the magnetization direction of which can be read by means of the Kerr effect or Faraday effect. By adding bismuth to the alloy, the Kerr rotation and Faraday rotation can each be increased considerably, so that simpler reading of the stored information is possible.

---

4 464 714

System for transmitting digital information, coding arrangement for use in that system, decoding arrangement for use in that system and record carrier for use in that system

A. Huijser E
M. G. Carasso
J. J. Verboom

A system for transmitting digital information including a coding arrangement, a transfer medium, for example a record carrier, and a decoding arrangement. In the coding arrangement the digital information is received as groups of input words which are encoded to form code words, each code word corresponding to an input word. Each code word has a time duration equal to $s\tau_O$ and each is assembled from M subgroups G_m of I signal positions t_{mi} spaced by equal time intervals τ, where m is a number from 1 to M, inclusive, corresponding to a subgroup G_m and i is a number within each subgroup G_m from 1 to I inclusive. In each subgroup G_m, k of these signal positions t_{mi} are always occupied by a signal which is distinguishable from the signal in unoccupied positions, where k is an integer smaller than I ($1 \leqq k \leqq I - 1$). The first positions of the subgroups G_m are located at mutually different time intervals ε_m from the beginning of the code word, where $O \leqq \varepsilon_m \leqq \tau$ with the restrictions $M \geqq 2$ and $\sum_{m=1}^{M} \varepsilon_m + (I-1)\tau \leqq s\tau_0$ and the group of code words for which it holds that $M = 2$, $I = s = 2$, $k = 1$, $\tau = \tau_O$ and $\varepsilon_2 = \varepsilon_1 + \frac{1}{2}\tau$ being excepted.

---

4 464 733

Office system comprising terminals, a data processor and auxiliary apparatus and a switching device for mass data transport between the auxiliary apparatus

J. S. Misker E
J. A. de Vos

A document and image processing system, used for the updating of document-wise organized information in an office system, has a number of auxiliary apparatus for recording, filing and outputting of such information. Also present are a processor with terminals, peripheral apparatus and a data bus. For the fast execution of mass data transport between the auxiliary apparatus there is provided a switching device which has a number of parallel data highways. Each auxiliary apparatus is connected to the switching module by means of its own switching module in order to be interconnected to either the data bus or, via one of the data highways, to another auxiliary apparatus.

---

4 464 746

Arrangement for correcting pulse distortion in homochronous data transmission

W. A. M. Snijders E
J. J. W. Kalfs
P. J. van Gerwen

In the duplex transmission of data signals over two-wire transmission paths the phenomenon of echo-signals is encountered, while simultaneously intersymbol interference occurs between the data symbols themselves. In order to reduce the influence of both the echo signals, and the intersymbol interference, the arrangement comprises a random access memory which produces a correction value at each sampling instant to correct the received data signal. The memory is addressed from registers and a counter the contents of the registers being determined by the data symbols transmitted last and the data symbols received last, respectively. A D-A converter converts the correction value into a correction signal which in a difference producer is subtracted from the received data signal. A sampling arrangement samples the corrected received data signal. After D-A conversion and multiplication by a predetermined factor α each sample furnishes a number by which the correction value is changed to match it to the value of the pulse distortion at the sampling instant.

---

4 465 546

Method of growing polycrystalline and monocrystalline bodies of volatile 2,6 and 3,5 compounds in graphite crucibles by self-sealing and self-releasing techniques

B. J. Fitzpatrick N
T. F. McGee, III

A large polycrystalline body of a 2,6 or 3,5 volatile compound is produced in a graphite crucible under low external pressure by passing a narrow molten zone through a charge of the compound contained in the graphite crucible the interior of which is coated with pyrolytic graphite. By a similar technique, but by use of a hot zone cooler then the molten zone, the polycrystalline body is converted to a monocrystalline body.

4 466 000

Data communication system

G. L. M. Jansen E
G. J. J. Vos

In a data communication system comprising a plurality of data stations which are interconnected by a common communication medium, simultaneously occurring prospective users of the communication medium undergo an arbitration to determine which one will gain access to it at any time. The system according to the invention provides the arbitration without negatively affecting the capacity of the communication medium. In the system, arbitration takes place during the data communication to decide who will be the next user, arbitration and communication being effected in frequency bands which differ from each other.

---

4 466 013

Tapped integrated resistor

R. J. van de Plassche E
E. C. Dijkmans

The invention relates to an integrated resistor formed in an epitaxial layer and provided with at least one tap. In order to reduce field effect action between the resistor and the epitaxial layer, the voltage on the two ends of the epitaxial layer underneath the resistor tracks the voltage on the two ends of the resistor. Moreover, the epitaxial layer is short-circuited by means of buried layers at the locations where the resistance layer also exhibits a short-circuit, such as underneath the contact area of the tap.

---

4 466 064

Multiprocessor computer system for executing a splittable algorithm, notably a recursive algorithm

A. J. Martin E

A multiprocessor computer system having a two-dimensional array of modules. Each module comprises two source connections for an activation signal for an algorithm, a program memory, a processor element and two destination connections for an activation signal for a corresponding algorithm. The processor element can split the task of a recursive algorithm into two partial tasks (of the same algorithm) or can execute an elementary partial task of this algorithm. The results of the partial tasks are returned in the direction wherefrom the relevant activation signal originated. For this purpose, each module in the array is connected to four neighbouring modules. The peripheral modules are not only connected to at least two neighbouring modules, but also to at least one module on an opposite side of the array. In each module there is one central process and for each connection there is one channel process, the central process communicating only with the channel processes of the relevant module. The latter processes provide the communication between the various modules.

---

4 466 109

Carrier recovery arrangement for sixteen-state amplitude and phase modulation and receiving system for digital data, comprising such an arrangement

H. Sari L

Carrier recovery arrangement in a receiving system for digital data which are transmitted by sixteen-state amplitude and phase modulation (16 QAM), the arrangement having successively six parallel paths each including the series arrangement of a multiplying circuit (M_i) and a low-pass filter; a selection circuit for selecting one of the three pairs of filter output signals thus obtained; a phase control circuit having a Costas signal processing circuit receiving the selected pair of signals and producing a signal representative of the phase error of the received signal, a filter and a voltage-controlled oscillator; and a phase-shifting circuit receiving the output signal of the oscillator in order to couple this output signal to respective second inputs of the multiplying circuits, this signal coupling being effected with a phase shift zero for (M_1), θ for (M_3), 2θ for (M_5), and with a phase shift $\pi/2$ for (M_2), $\theta + \pi/2$ for (M_4), and $2\theta + \pi/2$ for (M_6), where θ is equal to $\tan^{-1}(\frac{1}{2})$.

4 466 171

Method of manufacturing a semiconductor device utilizing outdiffusion to convert an epitaxial layer

P. J. W. Jochems E

A method of manufacturing a semiconductor device having two juxtaposed regions of opposite conductivity types which adjoin a surface and which together constitute a p-n junction which is preferably perpendicular to the surface and the doping concentration of which decreases towards the surface. According to the invention n-type and p-type buried layers are provided beside each other on a semiconductor substrate and on said layers a high-ohmic epitaxial layer is grown. By heating, the dopants diffuse from the buried layers through the whole thickness of the epitaxial layer and into the substrate. With suitably chosen donor and acceptor atoms (for example boron and phosphorus in silicon) n- and p-type regions are formed in the epitaxial layer and form a p-n junction perpendicular to the surface by compensation of the lateral diffusions from the buried layers.

---

4 466 474

Device for rotating a sunshade strip enclosed in an evacuated glass tube

G. Söllner A

A thermally insulating transparent wall element comprises a plurality of paraxially, adjacently arranged evacuated transparent tubes each having an axially arranged shaft journalled therewithin, an elongate sunshade strip being mounted on each shaft. A ratchet wheel is supported on one end of each shaft and has at its circumference engaging elements situated at the same angular distance from one another. An externally operable pawl cooperates with the engaging elements of the ratchet wheel to advance the same in stepwise manner. Means is provided to drive the pawl; and a member is coupled to the pawl drive means for latching the ratched wheel at the end of each movement step, such member being releasable from the ratched wheel by the pawl drive means just before the start of the next movement step.

---

4 466 818

Double crucible method of fabricating optical fibers

H. H. Brongersma E

A method of fabricating an optical fiber by means of the double crucible method. A double crucible is used of which at least the inner crucible has a double-walled construction. The double wall accommodates a metal wire coil. During the fabrication of the optical fiber the core glass is heated by means of a high-frequency electric field and the crucible wall is cooled with a cooling liquid.

---

4 467 291

Delta modulator having optimized loop filter

E. Roza E

A delta modulator comprising a feedback loop incorporating a cascade arrangement formed by a difference producer, a loop filter, a two-level quantizer, a clock pulse-controlled sampler and a feedback path. In order to optimize the signal/quantization noise ratio the minimum phase loop filter has such a phase characteristic that the phase shift in the feedback loop caused by the time delay of the sampler is replenished to approximately 180° with a certain margin, in a frequency range up to a certain cut-off frequency, the phase of the loop filter being constant above the cut-off frequency.

---

4 468 087

Device for coupling two optical fibers

L. R. Milan L
R. R. Gousseau

The coupling device according to the invention comprises two coupling members, each of which has a circularly cylindrical recess on one side. An end of a fiber to be coupled is centered in each recess by means of two sets of balls which are arranged one on top of the other. The first set of balls bears against the fiber end. The second set of balls bears on the first set and against the wall of the recess and presses the first set of balls against the fiber end. A spherical lens is arranged on the second set of balls so that the optical axis of the lens coincides with the axis of the centered fiber.

4 468 413

Method of manufacturing fluorine-doped optical fibers

P. K. Bachmann A

Doped silica glass can be manufactured by reacting gaseous vapors of silica-forming compounds and dopant-forming compounds. Increased fluorine dopant can be provided with less fluorine dopant-forming compound, when the fluorine dopant-forming compound is hexafluoroethane (C_2F_6).

4 468 661

Matrix excitation circuit for an oscilloscope display screen comprising a liquid crystal

C. Z. van Doorn E
J. H. J. Lorteije

For the display of a phenomenon or a small number of phenomena by means of an oscilloscope comprising a liquid crystal display screen, a simple matrix excitation circuit is described wherein a time-division multiplex excitation with a great number of lines and a good contrast appears possible if for each column only one or a few picture elements must be set to the on-state, costly provisions such as voltage and temperature stabilization being required.

4 468 684

High-density charge-coupled devices with complementary adjacent channels

L. J. M. Esser E
L. G. M. Heldens

A CCD includes several juxtaposed channels for hole transport and electron transport. Each channel forms a lateral boundary for an adjacent complementary channel so that high density in combination with a simple structure can be obtained. The CCD channels may include a matrix of photosensitive elements of a solid state image sensor for a camera. The invention may also be used in memory matrices and other CCD devices.

4 468 790

System for the quantization of signals

M. H. H. Höfelt E

A system for quantizing signals having a transmitter section and a receiver section interconnected by a transmission path. The transmitter section includes a quantizer, a difference producer, and a filter. An input signal is differenced with a feedback signal, filtered and quantized to produce a first quantized output signal. The first quantized output signal is filtered to produce the feedback signal. The filtered difference signal is further differenced with the quantized output signal to produce a second difference signal which is quantized to produce a second quantized output signal containing the quantizing noise of the first quantized output signal. In the receiver section a first received signal (proportional to the first quantized output signal) is summed with a second received signal (proportional to the second quantized output signal) to produce a sum signal. The first received signal and the sum signal are each filtered and summed to produce a receiver output signal substantially free of quantizing noise.

4 468 799

Radiation lithography mask and method of manufacturing same

M. Harms H
H. Lüthje
B. Matthiessen

The manufacture of semiconductor systems by means of radiation lithography requires low-stress masks when it is important to achieve very fine structures. In accordance with the invention, such a mask comprises a carrier of boron-doped silicon, a radiation absorbing pattern consisting of a double layer of different metals, such as molybdenum and tungsten, or a double layer of layers of the same metal, such as molybdenum, which are deposited in a different manner.

4 469 440

Short-exposure tomosynthesis apparatus for the formation of layer images with a low artefact-content

W. J. Dallas H

An apparatus for generating images of layers of an object from perspective images recorded from different positions by an array of radiation sources. The apparatus comprises an illumination device, for transilluminating the perspective images, and an imaging matrix comprising imaging elements. An optical system axis extends perpendicularly through the center of the matrix. The matrix superimposes the perspective images on a light-sensitive detector surface. In the apparatus, an optical deflection element is arranged in front of or behind each imaging element. The deflection element blurs the perspective image along a pattern which exhibits a major direction. The relevant deflection element is so arranged that the major direction extends at least substantially perpendicularly to a straight line connecting the optical system axis to the center of the imaging element within the matrix plane. All deflection elements are arranged in such a way relative to each other that the major directions subtend substantially equal angles with each other.

4 469 528

Method of manufacturing a semiconductor device of GaAs by two species ion implantation

M. Berth L
C. Venger
G. M. Martin

The invention relates to a method of treating a substrate of gallium arsenide by a double ion implantation. A first implantation of silicon ions (Si^+) is carried out on the entire surface of the substrate, and a second implantation of oxygen ions (O^+) is carried out in regions intended to become isolated regions. A thermal annealing treatment, preferably under encapsulation, follows these ion implantations. These implantations are carried out in order to obtain at the surface of the substrate regions of n-conductivity type isolating regions separated from each other for subsequent manufacture of semiconductor devices. The invention also relates to a gallium arsenide substrate thus treated and to a semiconductor device obtained by the technique of two ion implantations.

4 469 943

Pyroelectric detector

A. A. Turnbull R

A pyroelectric detector comprises an element of pyroelectric material that responds to variations with time in the intensity of radiation incident on an operative surface region of the detector much larger than the area of a major face of the element. The Noise Equivalent Power of the detector is improved by providing a thermal diffusion means to conduct thermal energy to the element from remote parts of the region. The element is resiliently supported on one or more flexible films and the thermal diffusion means is a thermally conductive layer on a film.

4 469 945

Device for detecting radiation and semiconductor device for use in such a device

A. M. E. Hoeberechts E
G. E. van Rosmalen

In a radiation-sensitive semiconductor element which is divided into a number of sub-elements, the surface potential in the sub-elements varies with incident radiation as a result of charge carriers generated by the radiation. As soon as an adjustable threshold value of this potential is reached in one or more of the sub-elements, a current starts to flow which is signalled by means of a detector and a detection unit. Because the speed of reaching the threshold value depends on the intensity of the radiation, the time measured between the adjustment of the threshold value and the signalling of the current is a measure of the radiation intensity. By means of such a semiconductor element, the associated detection unit and extra electronics, if any, the energy or the cross-section of a beam can be determined and be readjusted, if necessary. Such a semiconductor device can also be used very readily for focusing, for example in LaserVision apparatus.

4 471 260

Oxide cathode

J. Hasker E
J. H. Jacobs
P. Opmeer
J. A. T. Verhoeven

An oxide cathode comprising a metal base substantially consisting of titanium and a heating element for heating said base, on which base a porous layer comprising an alkaline earth metal oxide is provided. The cathode has a comparatively low operating temperature, a short warm up time and a low power requirement.

---

4 471 269

Circuit arrangement for operating a high-pressure gas discharge lamp

H. G. Ganser A
R. Schäfer
H. P. Stormberg

A circuit arrangement for operating a high-pressure gas discharge lamp with high frequency current in which a direct voltage is supplied to a transistor bridge having a transverse branch in which is arranged a choke coil. The switching frequency of the transistor bridge is varied within each period of the AC mains alternating voltage in dependence upon the current derived from the AC mains voltage.

---

4 471 453

Measuring mis-match between signals

H. Ney H
R. Geppert

The degree of mis-match which would be obtained between a test and a reference signal, for example speech signals, should their time-axes be subjected to that relative shift and/or distortion which is required to minimize the degree of mis-match is carried out by sampling the two signals at regular intervals and storing these samples in memories. All the samples of one signal are then read out in succession from one memory; each successive sample of the other signal is read out from the other memory, and the difference between each pair of samples is formed in a subtractor. Each difference value from the subtractor is added to the smallest of three quantities, X, Y and Z and the result stored in a register to form the new quantity X. This new quantity X is also stored in a further memory. The quantity Z is the previous content of the location of memory into which the new quantity X is written, and the quantity Y is the previous value of the quantity Z, obtained by shifting the previous value of the quantity Z in a twostage shift register. Thus the quantities X, Y and Z correspond to the present sample of the other signal and the immediately preceding sample of the one signal, the immediately preceding sample of both signals, and the present sample of the one signal and the immediately preceding sample of the other signal respectively. The result is that each successive value of the quantity X is the optimum cumulative distance value between the two signals for the corresponding pair of samples should these be assigned to each other when matching the two signals to each other. The process is continued until all the sampled values have been read and paired, at which point the value of the quantity X is a measure of the above-defined degree of mis-match.

---

4 471 467

Magnetic domain device

F. A. de Jonge E
A. G. H. Verhulst

A magnetic device comprising at least one thin layer of a magnetizable material which has an easy axis of magnetization approximately normal to the surface of the layer. Magnetic domains are propagated in the layer by a rotating magnetic field in co-operation with a pattern of magnetizable material on the layer. Domains are detected by passing a current through a pattern of magneto-resistive material on the layer. At least in the part of the device where the detection occurs, the propagation and detection patterns have substantially the same configuration and one pattern is situated between the layer of magnetizable material and the other pattern.

---

4 472 734

Television pick-up arrangement comprising a solid state picture pick-up device

L. J. van de Polder E
L. J. M. Esser

A television pick-up arrangement comprising a solid-state picture pick-up device rows of picture pick-up elements of which are connectable to parallel inputs of two output shift registers. At a simultaneous read-out of the shift registers the registers supply at the series outputs picture signals associated with each pair of adjacent rows of picture pick-up elements. In the device the picture pick-up elements in one row are shifted in the row direction to the intermediate position relative to the elements in the other row. A colour strip filter is provided having colour filter strips transverse of the row direction which have a width equal to half the size in the row direction of a picture pick-up element. After the picture signal obtained from the registers are combined with the same polarity they are applied directly and via delay devices to inputs of a matrix circuit outputs of which are coupled to a change-over circuit from which colour signals are obtained. Advantageous use can be made of a device in which pick-up information is obtained by use of both holes and electrons produced by photons.

---

4 472 797

Optical multiplexer

A. J. A. Nicia E

An optical multiplexer whereby the light from a plurality of optical fibers can be combined in an optical transmission fiber via an input lens, a prism and an output lens. The lenses are preferably ball-lenses. The multiplexer does not comprise any colour-selective elements.

---

4 473 772

Colour display tube having improved colour selection structure

A. A. de Keijzer E

In a colour display tube of the post focusing type, a colour selection structure includes first lens electrode means and second lens electrode means situated at a short distance from each other. The second lens electrode means has a number of elongate conductors or groups of conductors extending parallel to each other. The conductors or groups of conductors are interconnected via a resistance material as a result of which the energy released in an electric flash-over between the lens electrode means and a conductor in the flash-over point per unit of time is so small that the colour selection structure is not seriously damaged.

---

4 473 829

Method of recording a digital information signal on a record carrier having a radiation-sensitive information layer, apparatus for carrying out the method, and optical record carrier provided with such a digital information signal

K. A. Schouhamer Immink E
R. M. Aarts
W. G. Opheij

A method of recording a binary information signal on a record carrier having a radiation-sensitive information layer. The information signal is encoded in such a way that at least n ($n \geq 2$) consecutive bit cells are of the same type. This information is recorded as pattern of unitary recording marks on the record carrier. Each unitary recording mark then corresponds to a number of m bit cells of the same first type in the information signal, where $1 < m \leq n$. A greater number of consecutive bit cells of said first type is represented by a plurality of unitary recording marks which are at least contiguous but which preferably overlap each other.